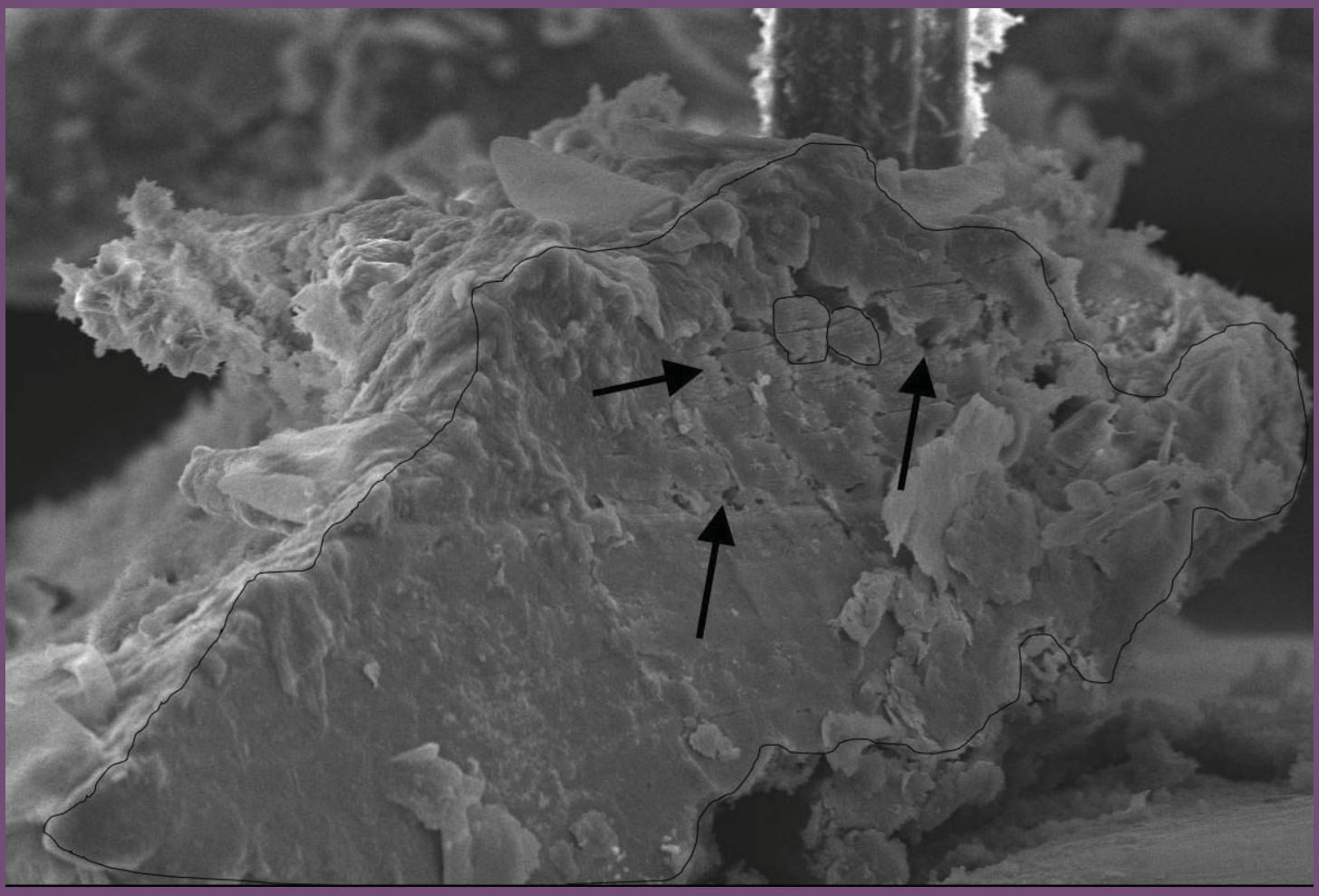
DYNA

Journal of the Facultad de Minas, Universidad Nacional de Colombia - Medellin Campus



DYNA 85 (206), September, 2018 - ISSN 0012-7353
Tarifa Postal Reducida No. 2014-287 4-72
La Red Postal de Colombia, Vence 31 de Dic. 2018.

UNIVERSIDAD NACIONAL DE COLOMBIA
SEDE MEDELLÍN
FACULTAD DE MINAS

UNIVERSIDAD NACIONAL DE COLOMBIA
SEDE MEDELLÍN
FACULTAD DE MINAS

DYNA

http://dyna.medellin.unal.edu.co/

DYNA is an international journal published by the Facultad de Minas, Universidad Nacional de Colombia, Medellín Campus since 1933. DYNA publishes peer-reviewed scientific articles covering all aspects of engineering. Our objective is the dissemination of original, useful and relevant research presenting new knowledge about theoretical or practical aspects of methodologies and methods used in engineering or leading to improvements in professional practices. All conclusions presented in the articles must be based on the current state-of-the-art and supported by a rigorous analysis and a balanced appraisal. The journal publishes scientific and technological research articles, review articles and case studies.

DYNA publishes articles in the following areas:

Organizational Engineering
Civil Engineering
Materials and Mines Engineering
Geosciences and the Environment
Systems and Informatics
Chemistry and Petroleum
Mechatronics
Bio-engineering
Other areas related to engineering

Publication Information

DYNA (ISSN 0012-73533, printed; 2346-2183, online) is published by the Facultad de Minas, Universidad Nacional de Colombia, with a bimonthly periodicity (February, April, June, August, October, and December). Circulation License Resolution 000584 de 1976 from the Ministry of the Government.

Contact information

Web page: http://dyna.unalmed.edu.co
E-mail: dyna@unal.edu.co
Mail address: Revista DYNA
Facultad de Minas Universidad Nacional de Colombia - Medellín Campus
Carrera 80 No. 65-223 Bloque M9 - Of.:107
Telephone: (574) 4255068 Fax: (574) 4255343
Medellín - Colombia

© Copyright 2016. Universidad Nacional de Colombia
The complete or partial reproduction of texts with educational ends is permitted, granted that the source is duly cited. Unless indicated otherwise.

Notice
All statements, methods, instructions and ideas are only responsibility of the authors and not necessarily represent the view of the Universidad Nacional de Colombia. The publisher does not accept responsibility for any injury and/or damage for the use of the content of this journal.
The concepts and opinions expressed in the articles are the exclusive responsibility of the authors.

Institutional Exchange Request
DYNA may be requested as an institutional exchange through the e-mail canjebib_med@unal.edu.co or to the postal address:

Biblioteca Central “Efe Gómez”
Universidad Nacional de Colombia, Sede Medellín
Calle 59A No 63-20
Teléfono: (57+4) 430 97 86
Medellín - Colombia

Indexing and Databases

DYNA is admitted in:

The National System of Indexation and Homologation of Specialized Journals CT+I-PUBLINDEX, Category A1

Science Citation Index Expanded
Web of Science - WoS, Thomson Reuters
Journal Citation Reports - JCR
SCImago Journal & Country Rank - SJR
Science Direct
SCOPUS
Chemical Abstract - CAS
Scientific Electronic Library on Line - SciELO
GEOREF
PERIÓDICA Data Base
Latindex
Actualidad Iberoaméricana
RedALyC - Scientific Information System
Directory of Open Acces Journals - DOAJ
PASCAL
CAPES
UN Digital Library - SINAB
CAPES
EBSCO Host Research Databases

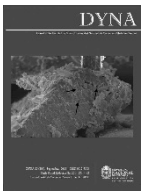
Publisher’s Office
Juan David Velásquez Henao, Director
Mónica del Pilar Rada T., Editorial Coordinator
Catalina Cardona A., Editorial Assistant
Amilkar Álvarez C., Diagrammer
Byron Llano V., Editorial Assistant
Landsoft S.A., IT

Reduced Postal Fee
Tarifa Postal Reducida # 2014-287 4-72. *La Red Postal de Colombia,* expires Dec. 31st, 2018

UNIVERSIDAD NACIONAL DE COLOMBIA
SEDE MEDELLÍN
FACULTAD DE MINAS

DYNA

UNIVERSIDAD NACIONAL DE COLOMBIA
SEDE MEDELLÍN
FACULTAD DE MINAS



DYNA
http://dyna.medellin.unal.edu.co/

COUNCIL OF THE FACULTAD DE MINAS

Dean
Verónica Botero Fernández, PhD

Vice-Dean
Eliana Isabel Arango Zuluaga, PhD

Vice-Dean of Research and Extension
Juan Fernando Ramírez Patiño, PhD

Director of University Services
Santiago Medina Hurtado, PhD

Academic Secretary
Lina María Gómez Echavarría, PhD

Representative of the Curricular Area Directors
Cesar Javier Vinasco Vallejo, PhD

Representative of the Curricular Area Directors
Bibian Alonso Hoyos Madrigal, PhD

Representative of the Basic Units of Academic-Administrative Management
Fernando Jesús Guevara Carazas, PhD

Representative of the Basic Units of Academic-Administrative Management
Andres Osorio Arias, PhD

Professor Representative
Miguel David Rojas López, PhD

Delegate of the University Council
León Restrepo Mejía, PhD

Student representative undergraduate at the Faculty Council
Luis Miguel Gómez Zuluaga

FACULTY EDITORIAL BOARD

Dean
Verónica Botero Fernández, PhD

Vice-Dean of Research and Extension
Juan Fernando Ramírez Patiño, PhD

Members
Oscar Jaime Restrepo Baena, PhD
Juan David Velásquez Henao, PhD
Jaime Aguirre Cardona, PhD
Alfonso Espinosa Parada, PhD
Mónica del Pilar Rada Tobón, MSc

JOURNAL EDITORIAL BOARD

Editor-in-Chief
Juan David Velásquez Henao, PhD
Universidad Nacional de Colombia, Colombia

Editors
George Barbastathis, PhD
Massachusetts Institute of Technology, USA

Tim A. Osswald, PhD
University of Wisconsin, USA

Juan De Pablo, PhD
University of Wisconsin, USA

Hans Christian Öttinger, PhD
Swiss Federal Institute of Technology (ETH), Switzerland

Patrick D. Anderson, PhD
Eindhoven University of Technology, the Netherlands

Igor Emri, PhD
Associate Professor, University of Ljubljana, Slovenia

Dietmar Drummer, PhD
Institute of Polymer Technology University Erlangen-Nürnberg, Germany

Ting-Chung Poon, PhD
Virginia Polytechnic Institute and State University, USA

Pierre Boulanger, PhD
University of Alberta, Canadá

Jordi Payá Bernabeu, Ph.D.
Instituto de Ciencia y Tecnología del Hormigón (ICITECH)
Universitat Politècnica de València, España

Javier Belzunce Varela, Ph.D.
Universidad de Oviedo, España

Luis Gonzaga Santos Sobral, PhD
Centro de Tecnología Mineral - CETEM, Brasil

Agustín Bueno, PhD
Universidad de Alicante, España

Henrique Lorenzo Cimadevila, PhD
Universidad de Vigo, España

Mauricio Trujillo, PhD
Universidad Nacional Autónoma de México, México

Carlos Palacio, PhD
Universidad de Antioquia, Colombia

Jorge Garcia-Sucerquia, PhD
Universidad Nacional de Colombia, Colombia

Juan Pablo Hernández, PhD
Universidad Nacional de Colombia, Colombia

John Willian Branch Bedoya, PhD
Universidad Nacional de Colombia, Colombia

Enrique Posada, Msc
INDISA S.A, Colombia

Oscar Jaime Restrepo Baena, PhD
Universidad Nacional de Colombia, Colombia

Moisés Oswaldo Bustamante Rúa, PhD
Universidad Nacional de Colombia, Colombia

Hernán Darío Álvarez, PhD
Universidad Nacional de Colombia, Colombia

Jaime Aguirre Cardona, PhD
Universidad Nacional de Colombia, Colombia

UNIVERSIDAD
NACIONAL
DE COLOMBIA
SEDE MEDELLÍN
FACULTAD DE MINAS

DYNA
http://dyna.medellin.unal.edu.co/

UNIVERSIDAD NACIONAL DE COLOMBIA
SEDE MEDELLÍN
FACULTAD DE MINAS

DYNA
http://dyna.medellin.unal.edu.co/

DYNA 85 (206), September, 2018. Medellin. ISSN 0012-7353 Printed, ISSN 2346-2183 Online

CONTENTS

Electrochemical analysis of the degradation of nitrided zirconia 3Y-TZP
Kevin Dorado-Bustamante, Sara Leal-Marin & Hugo Estupiñán-Duran 9

Dynamic adjustment of a MLFQ flow scheduler to improve cloud applications performance
Sergio Armando Gutiérrez, Marinho Barcellos & John Willian Branch 16

Use of BOF slag and blast furnace dust in asphalt concrete: an alternative for the construction of pavements
Alfonso López-Díaz, Ricardo Ochoa-Díaz & Gloria Elizabeth Grimaldo-León 24

Impact on the direct costs of social interest and priority interest housing by including new construction standards: Cali case
Mauricio Chávez-Calle, Diego Darío Pérez-Ruiz & María Fernanda Serrano-Guzmán 31

The use of GS1 standards to improve the drugs traceability system in a 3PL Logistic Service Provider
Igor Lopes-Martínez, Lianet Paradela-Fournier, Janett Rodríguez-Acosta, Jenny Laura Castillo-Feu, Martha I. Gómez-Acosta & Alegna Cruz-Ruiz 39

Development of a parametric cable driven planar robot
Juan Pablo Castrillón-Restrepo, Sebastián Jiménez-Gómez & Federico Saldarriaga-Ángel 49

Effect of fly ash and silica fume on rheology, compressive strength and self-compacting in cement mixtures
Jaime Arturo Correa-Yepes, Nestor Rojas-Reyes, Jorge I. Tobón 59

Using a non-reducing sugar in the green synthesis of gold and silver nanoparticles by the chemical reduction method
Wilson Agudelo, Yuliet Montoya & John Bustamante 69

Levelized avoided cost of electricity model based on power system operation
Cristian Camilo Marín-Cano & Diego Adolfo Mejía-Giraldo 79

Heavy metal contribution by runoff in a high-altitude megacity: a method based on the road-deposited sediment characterization
Carlos Zafra-Mejía, Hugo Rondón-Quintana & Álvaro Gutiérrez-Malaxechebarria 85

Design, development, and implementation of an assistive technology device for shoulder telerehabilitation via the Internet
Cristian D. Chamorro-R., Gladys Caicedo-D. & Jose I. Garcia-M. 95

Productive process improvement to elaborate cane train baskets, using Coloured Petri nets
Jesus Filander Caratar-Chaux, Ruth Edmy Cano-Buitrón & José Isidro Garcia-Melo 105

Active geodetic network: application in topography
Enrique Cano-Jódar, Manuel Sánchez-de la Orden & Javier Mesas-Carrascosa 114

Application of OpenFoam solver SettlingFoam to bedload sediment transport analysis
Verónica Carrillo-Serrano & Esteban Pacheco-Tobar 121

Encapsulation of β-carotene extracted from peach palm residues: A stability study using two spray-dried processes
Luis Eduardo Ordoñez-Santos, Jader Martínez-Girón & Rafael Humberto Villamizar-Vargas 128

Synergistic effects in anaerobic codigestion of chicken manure with industrial wastes
Liliana del Pilar Castro-Molano, Humberto Escalante-Hernández, Luis Enrique Lambis-Benítez & José Daniel Marín-Batista 135

Palladium nanoparticles from a surfactant-modified hydroxysalt exchanged with tetrachloropalladate
Maby Mool Martínez, Rogelio Ocampo-Cardona, Jhon Mauricio Aguirre-Cortés, Oscar Giraldo & Luz Amalia Ríos-Vásquez 142

Morphological and nanomechanical characterization of Guadua Angustifolia kunth fiber by means of SEM and AFM
Martin Eduardo Espitia-Nery, Dery Esmeralda Corredor-Pulido, Nelson Javier Rodríguez-Ramírez & Jeimy Natalia Calderón-Bustos 148

Kinetic parameters of lactic acid bacterial isolated from fermented milk "Suero Costeño"
Francia Elena Valencia-García, Karina Edith Motato-Rocha, Madalyd Yurani Vera-Peña & Martha Liliana Sepúlveda-Lindarte 155

Soft Pre-stressed PET Profiles as reinforcing fibers in structural elements made of concrete
Sergio Márquez-Domínguez, Edgar Mejía-Sánchez, Jesús Antonio Arenzano-Altai, Gerson Omar Martínez-Guevara & Dante Tolentino 162

Entropy and negentropy of private electric vehicles in urban systems: homeostasis of mobility in Mexico
Mario Guadalupe González-Pérez 171

Structural, thermal, rheological, morphological and mechanical properties of thermoplastic starch obtained by using hyperbranched polyester polyol as plasticizing agent
Manuel Guzmán & Edwin A. Murillo 178

An evaluation of the controlled release of ammoniacal nitrogen from residual cellulose/polyvinyl alcohol hydrogels as an alternative to traditional fertilization processes
Marybel Montoya-Álvarez, Adriana María Quinchía-Figueroa, Octavio González-Murillo & Pedronel Araque-Marín 187

Design of metacognitive expectations of cognitive functions through ontological representations
Dalia P. Madera-Doval, Manuel F. Caro-Piñeres, Adán A. Gómez-Salgado, Ana M. Cardozo-Soto & Jovani A. Jiménez-Builes 194

Simulation-optimization techniques for closed-loop supply chain design with multiple objectives
William Javier Guerrero, Laura Andrea Sotelo-Cortés & Enrique Romero-Mota 202

Site characterization of a tropical soil by in situ tests
Breno Padovezi Rocha & Heraldo Luiz Giacheti 211

UNIVERSIDAD NACIONAL DE COLOMBIA
SEDE MEDELLÍN
FACULTAD DE MINAS

DYNA
http://dyna.medellin.unal.edu.co/

Sugarcane molasses and vinasse as a substrate for polyhydroxyalkanoates (PHA) production
Alejandro Acosta-Cárdenas, Wilman Alcaraz-Zapata & Mariana Cardona-Betancur 220

Evaluation of water use in food SMEs: Case study of a poultry processing plant in Colombia
Yelitza Angélica Zorrilla-Ortega, Juan Pablo Silva, Valentina Prado & Pablo César Manyoma 226

Nutrient losses due to water erosion using simulated rainfall in southern Brazil
Jeane Cruz Portela, Neroli Pedro Cogo, Jacques Carvalho Ribeiro Filho, Letícia Sequinatto, Rafael Oliveira Batista, Carolina Malala Martins Souza & Joaquim Emanuel Fernandes Gondim 236

Teratogenic effect on bone tissue development in Rattus norvegicus Wistar strain, induced by the presence of arsenic
Mireya Quiterio-Pérez, Juan Carlos Gaytán-Oyarzún, Alberto José Gordillo-Martínez & Francisco Prieto-García 242

Design and Calculation of a Hybrid Solar-Hydraulic Power Station in Gran Canaria
Abian Beltrán, Herberth Gracia-León, Daniella Rodríguez-Urrego & Leonardo Rodríguez-Urrego 250

Electrocoagulation of indigo carmine dye solution with magnesium and AZ31 alloy anodes
Dayana Donneys-Victoria, Cristian Camilo Ospina-Toro, Mónica Vanesa Zapata-Villegas, Nilson Marriaga-Cabrales, Fiderman Machuca-Martínez, Juan M. Peralta-Hérnandez & Carlos A. Martínez-Huitle 258

Integrating SOA and MAS in intelligent environments
Manuel Sánchez, Jose Aguilar & Ernesto Exposito 268

A planning algorithm in a class of discrete event systems
Guelvis Mata, Bladismir Ruiz, Claudia Camacho, Arnaldo Méndez, Sergio Muñoz & Hicher Zambrano 283

Agronomic and environmental benefits of nitrogen fertilizers sources in Ocimum basilicum L
Martha Constanza Daza-Torres, Greydy Selene Ladino-Tabarquino & Norberto Urrutia-Cobo 294

Risk assessment in water treatment processes for the development of a Water Safety Plan – WSP
Andrea Pérez-Vidal, Juan Carlos Escobar-Rivera & Patricia Torres-Lozada 304

Design of a serious emerging games engine based on the optimization algorithm of ant colony
Jose Aguilar, Junior Altamiranda & Francisco Díaz 311

Palladium nanoparticles from a surfactant-modified hydroxysalt exchanged with tetrachloropalladate
Heiner Alexander Vargas-Perea, Robinson Rocha-González, Mónica Andrea Botero-Londoño, Alexander Sepúlveda-Sepúlveda & Clara Lilia Calderón-Triana 321

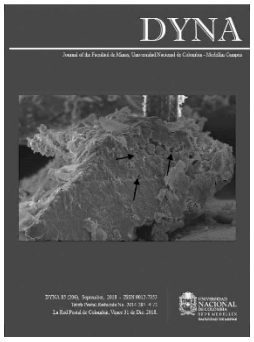
Estimación del retroceso glaciar en los volcanes Nevado del Ruiz, Tolima y Santa Isabel, Colombia a través de imágenes ópticas y Din-SAR
Mario Fernando Monterroso-Tobar, Jhon Makario Londoño-Bonilla & Sergey Samsonov 329

Caracterización de residuos de demolición y construcción para la identificación de su potencial de reúso
Lina María Chica-Osorio & Juan Manuel Beltrán-Montoya 338

Relationship between the particle size and the crystalline phases amount of an aluminum dross
Adriana Gómez-Gómez, Luz Elena Vinasco, Nelson Batista de Lima & Jorge Aberto Soares Tenório 348

Our cover
Image alluding to Article:
Morphological and nanomechanical characterization of Guadua *Angustifolia kunth* fiber by means of SEM and AFM

Authors:
Martin Eduardo Espitia-Nery, Dery Esmeralda Corredor-Pulido, Nelson Javier Rodríguez-Ramírez & Jeimy Natalia Calderón Bustos



UNIVERSIDAD NACIONAL DE COLOMBIA
SEDE MEDELLÍN
FACULTAD DE MINAS

DYNA
http://dyna.medellin.unal.edu.co/

DYNA 85 (206), September, 2018. Medellin. ISSN 0012-7353 Printed, ISSN 2346-2183 Online

CONTENIDO

Análisis electroquímico de la degradación de circonia 3Y-TZP nitrurada 9
Kevin Dorado-Bustamante, Sara Leal-Marin & Hugo Estupiñán-Duran

Ajuste dinámico de un programador de flujos MLFQ para mejorar el desempeño de aplicaciones en la nube 16
Sergio Armando Gutiérrez, Marinho Barcellos & John Willian Branch

Uso de escoria BOF y polvo de alto horno en concretos asfálticos: una alternativa para la construcción de pavimentos 24
Alfonso López-Díaz, Ricardo Ochoa-Díaz & Gloria Elizabeth Grimaldo-León

Impacto en costos directos de vivienda de interés social y de interés prioritario por inclusión de nuevas normas de construcción: caso Cali 31
Mauricio Chávez-Calle, Diego Darío Pérez-Ruiz & María Fernanda Serrano-Guzmán

Uso de los estándares GS1 para la mejora del sistema de trazabilidad de medicamentos en un operador logístico 3PL 39
Igor Lopes-Martínez, Lianet Paradela-Fournier, Janett Rodríguez-Acosta, Jenny Laura Castillo-Feu, Martha I. Gómez-Acosta & Alegna Cruz-Ruiz

Desarrollo de un robot cartesiano parametrizable comandado por cables 49
Juan Pablo Castrillón-Restrepo, Sebastián Jiménez-Gómez & Federico Saldarriaga-Ángel

Efecto de las cenizas volantes y el humo de sílice sobre la reología, resistencia a la compresión y autocompactación en mezclas de cemento 59
Jaime Arturo Correa-Yepes, Nestor Rojas-Reyes, Jorge I. Tobón

Uso de una azúcar no reductora en la síntesis verde de nanopartículas de oro y plata por medio de reducción química 69
Wilson Agudelo, Yuliet Montoya & John Bustamante

Modelo de costo evitado nivelado de electricidad basado en la operación del sistema de potencia 79
Cristian Camilo Marín-Cano & Diego Adolfo Mejía-Giraldo

Contribución de metales pesados por escorrentía en una megaciudad de elevada altitud: un método basado en la caracterización del sedimento vial 85
Carlos Zafra-Mejía, Hugo Rondón-Quintana & Álvaro Gutiérrez-Malaxechebarria

Diseño, desarrollo e implementación de una ayuda tecnológica para rehabilitación de hombro tele-operada vía Internet 95
Cristian D. Chamorro-R., Gladys Caicedo-D. & Jose I. Garcia-M.

Mejora del proceso productivo para elaborar canastas para trenes cañeros, utilizando redes de Petri coloreadas 105
Jesus Filander Caratar-Chaux, Ruth Edmy Cano-Buitrón & José Isidro Garcia-Melo

Red geodésica activa: aplicación en topografía 114
Enrique Cano-Jódar, Manuel Sánchez-de la Orden & Javier Mesas-Carrascosa

Aplicación del solucionador SettlingFoam de OpenFoam para el análisis del transporte de sedimento de carga de lecho 121
Verónica Carrillo-Serrano & Esteban Pacheco-Tobar

Encapsulación de β-caroteno extraído a partir de residuos de chontaduro: Un estudio de estabilidad usando dos procesos de secado por atomización 128
Luis Eduardo Ordoñez-Santos, Jader Martínez-Girón & Rafael Humberto Villamizar-Vargas

Efectos sinérgicos en la codigestión anaerobia de gallinaza y residuos industriales 135
Liliana del Pilar Castro-Molano, Humberto Escalante-Hernández, Luis Enrique Lambis-Benítez & José Daniel Marín-Batista

Nanopartículas de paladio a partir de una hidroxisal modificada con surfactante intercambiada con tetracloropaladato 142
Maby Mool Martínez, Rogelio Ocampo-Cardona, Jhon Mauricio Aguirre-Cortés, Oscar Giraldo & Luz Amalia Ríos-Vásquez

Caracterización morfológica y nanomecánica de la fibra de Guadua Angustifolia kunth mediante SEM y AFM 148
Martin Eduardo Espitia-Nery, Dery Esmeralda Corredor-Pulido, Nelson Javier Rodríguez-Ramírez & Jeimy Natalia Calderón-Bustos

Parámetros cinéticos de bacterias ácido-lácticas aisladas de la leche fermentada “Suero Costeño” 155
Francia Elena Valencia-García, Karina Edith Motato-Rocha, Madalyd Yurani Vera-Peña & Martha Liliana Sepúlveda-Lindarte

Perfiles de PET ligeramente pretensados como fibras de refuerzo en elementos estructurales de concreto 162
Sergio Márquez-Domínguez, Edgar Mejía-Sánchez, Jesús Antonio Arenzano-Altai, Gerson Omar Martínez-Guevara & Dante Tolentino

Entropía y negentropía del vehículo eléctrico particular en sistemas urbanos: homeostasis de la movilidad en México 171
Mario Guadalupe González-Pérez

Propiedades térmicas, reológicas, morfológicas y mecánicas de almidón termoplástico obtenido usando un poliéster poliol altamente ramificado como agente plastificante 178
Manuel Guzmán & Edwin A. Murillo

Evaluación de la liberación controlada de nitrógeno amoniacal a partir de un hidrogel de celulosa residual/polivinil alcohol como una alternativa a los procesos de fertización tradicionales 187
Marybel Montoya-Álvarez, Adriana María Quinchía-Figueroa, Octavio González-Murillo & Pedronel Araque-Marín

Diseño de expectativas metacognitivas de funciones cognitivas a través de representaciones ontológicas 194
Dalia P. Madera-Doval, Manuel F. Caro-Piñeres, Adán A. Gómez-Salgado, Ana M. Cardozo-Soto & Jovani A. Jiménez-Builes

Técnicas de simulación-optimización para el diseño de cadenas de abastecimiento de ciclo cerrado con múltiples objetivos 202
William Javier Guerrero, Laura Andrea Sotelo-Cortés & Enrique Romero-Mota

Caracterización de un suelo tropical por medio de ensayos in-situ 211
Breno Padovezi Rocha & Heraldo Luiz Giacheti

UNIVERSIDAD NACIONAL DE COLOMBIA
SEDE MEDELLÍN
FACULTAD DE MINAS

DYNA
http://dyna.medellin.unal.edu.co/

Melazas y vinaza de la caña de azúcar como sustrato para la producción de polihidroxialcanoatos (PHA) 220
Alejandro Acosta-Cárdenas, Wilman Alcaraz-Zapata & Mariana Cardona-Betancur

Evaluación del uso del agua en PYMES de alimentos: Caso de estudio en una Planta de Beneficio Avícola en Colombia 226
Yelitza Angélica Zorrilla-Ortega, Juan Pablo Silva, Valentina Prado & Pablo César Manyoma

Pérdidas de nutrientes debido a la erosión hídrica con la lluvia simulada en el sur de Brasil 236
Jeane Cruz Portela, Neroli Pedro Cogo, Jacques Carvalho Ribeiro Filho, Letícia Sequinatto, Rafael Oliveira Batista, Carolina Malala Martins Souza & Joaquim Emanuel Fernandes Gondim

Efecto teratogénico sobre el desarrollo del tejido óseo en la cepa Wistar de Rattus norvegicus, inducida por la presencia de arsénico 242
Mireya Quiterio-Pérez, Juan Carlos Gaytán-Oyarzún, Alberto José Gordillo-Martínez & Francisco Prieto-García

Diseño y Cálculo de una Central Hibrida Solar-Hidráulica en Gran Canaria 250
Abian Beltrán, Herberth Gracia-León, Daniella Rodríguez-Urrego & Leonardo Rodríguez-Urrego

Electrocoagulación de soluciones de índigo carmín empleando ánodos de magnesio y de aleación AZ31 258
Dayana Donneys-Victoria, Cristian Camilo Ospina-Toro, Mónica Vanesa Zapata-Villegas, Nilson Marriaga-Cabrales, Fiderman Machuca-Martínez, Juan M. Peralta-Hérnandez & Carlos A. Martínez-Huitle

Integración SOA-MAS en ambientes inteligentes 268
Manuel Sánchez, Jose Aguilar & Ernesto Exposito

Un algoritmo de planificación en una clase de sistemas de eventos discretos 283
Guelvis Mata, Bladismir Ruiz, Claudia Camacho, Arnaldo Méndez, Sergio Muñoz & Hicher Zambrano

Beneficios agronómicos y ambientales de fuentes de fertilizantes nitrogenados en Ocimum basilicum L 294
Martha Constanza Daza-Torres, Greydy Selene Ladino-Tabarquino & Norberto Urrutia-Cobo

Evaluación del riesgo en procesos de tratamiento de agua para el desarrollo de un Plan de Seguridad del Agua – PSA 304
Andrea Pérez-Vidal, Juan Carlos Escobar-Rivera & Patricia Torres-Lozada

Diseño de un motor de juegos serios emergentes basado en el algoritmo de optimización de colonia de hormigas 311
Jose Aguilar, Junior Altamiranda & Francisco Díaz

Herramienta de software para determinar constantes ópticas en celdas solares tipo película delgada 321
Heiner Alexander Vargas-Perea, Robinson Rocha-González, Mónica Andrea Botero-Londoño, Alexander Sepúlveda-Sepúlveda & Clara Lilia Calderón-Triana

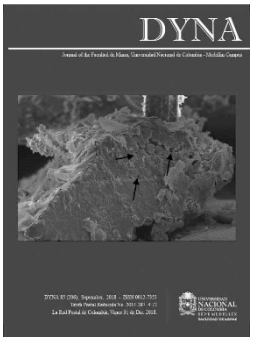
Determination of Glacier retreat at Nevado del Ruiz, Santa Isabel and Tolima Volcanoes, Colombia through optical image and Din-SAR 329
Mario Fernando Monterroso-Tobar, Jhon Makario Londoño-Bonilla & Sergey Samsonov

Demolition and construction waste characterization for potential reuse identification 338
Lina María Chica-Osorio & Juan Manuel Beltrán-Montoya

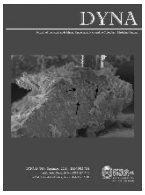
Relación entre el tamaño de partícula y el contenido de las fases cristalinas presentes en una escoria de aluminio 348
Adriana Gómez-Gómez, Luz Elena Vinasco, Nelson Batista de Lima & Jorge Aberto Soares Tenório

Nuestra carátula
Imagen alusiva al artículo:
Caracterización morfológica y nanomecánica de la fibra de Guadua *Angustifolia kunth* mediante SEM y AFM

Autores:
Martin Eduardo Espitia-Nery, Dery Esmeralda Corredor-Pulido, Nelson Javier Rodríguez-Ramírez & Jeimy Natalia Calderón Bustos



UNIVERSIDAD NACIONAL DE COLOMBIA
SEDE MEDELLÍN
FACULTAD DE MINAS



DYNA
http://dyna.medellin.unal.edu.co/

Electrochemical analysis of the degradation of nitrided zirconia 3Y-TZP

Kevin Dorado-Bustamante [a], Sara Leal-Marin [b] & Hugo Estupiñán-Duran [b]

[a] *Departamento de Física Nuclear, Instituto Balseiro, San Carlos de Bariloche, Argentina. kadoradob@gmail.com*
[b] *Grupo de tribología y superficies, Facultad de Minas, Universidad Nacional de Colombia, Medellín, Colombia. slealma@unal.edu.co, haestupinand@unal.edu.co*

Received: October 14th, 2017. Received in revised form: March 2nd, 2018. Accepted: March 20th, 2018

Abstract
Zirconia is a material that is susceptible to changes in its structure from the tetragonal to the monoclinic phase caused by variations in temperature or by contact with water. One way of achieving the stability of the tetragonal phase at low temperatures is by incorporating anionic gaps in its crystal lattice through doping procedures with aliovalent anions such as nitrogen. Nitrogen replaces the oxygen in the crystal lattice, which stabilizes the tetragonal structure of zirconia at low temperatures. The aim of this research was to evaluate the degradation of nitrided zirconia 3Y-TZP after it was immersed in artificial saliva for 0, 7, 14, and 21 days. Interfacial processes such as oxide-formation were assessed simultaneously using the electrochemical impedance spectroscopy test. Additionally, morphological, topographic, and composition changes were analyzed in the degradation process using SEM-EDS and AFM.

Keywords: 3Y-TZP; nitriding; aging; artificial saliva; EIS.

Análisis electroquímico de la degradación de circonia 3Y-TZP nitrurada

Resumen
La circonia es un material susceptible a cambios en su estructura de la fase tetragonal a monoclínica, ocasionados por cambios en la temperatura o contacto con agua. Una manera de alcanzar la estabilidad de la fase tetragonal a bajas temperaturas es a través de la incorporación de vacancias aniónicas en su estructura cristalina por medio de procedimientos de dopado con aniones aliovalentes como el nitrógeno. El nitrógeno reemplaza el oxígeno en la estructura cristalina y estabiliza la estructura tetragonal de la circonia a bajas temperaturas. El objetivo de este trabajo fue evaluar la degradación de la circonia 3Y-TZP nitrurada a través de su inmersión en saliva artificial por 0, 7,14 y 21 días, evaluando los procesos interfaciales como la formación de óxidos a través de espectroscopia por impedancia electroquímica. Adicionalmente se analizó la morfología, topografía y cambios de composición en el proceso de degradación empleando SEM-EDS y AFM.

Palabras clave: 3Y-TZP; nitruración; envejecimiento; saliva artificial; EIE.

1. Introduction

The development of materials in the biomedical field has positioned zirconia as a material that has an increasing number of applications due to its mechanical and biocompatibility properties [1, 2]. However, zirconia under conditions of mechanical loads exhibits slight increases in temperature and a tendency to present structural changes transforming its crystalline structure from a monocyclic to a tetragonal phase. This phase change generates a 3-4% thermal expansion, producing cracks and degradation or material failure [3], and mechanical properties are decreased [4]. In addition, contact with body fluids containing aggressive ions generates phase transformation even after short periods of time [4]. For these reasons, in the zirconia sintering process, it is convenient to add stabilizing oxides to maintain the tetragonal

How to cite: Dorado-Bustamante, K., Leal-Marin, S. and Estupiñán-Duran, H., Electrochemical analysis of the degradation of nitrided zirconia 3Y-TZP. DYNA, 85(206), pp. 9-15, September, 2018.

© The author; licensee Universidad Nacional de Colombia.

structure of the zirconia at room temperature: common aggregated oxides are Yttrium Oxide (Y_2O_3), calcium oxide (CaO), and magnesium oxide (MgO) [5, 6].

The tetragonal polycrystalline zirconia stabilized with 3% mol yttria (3Y-TZP) is one of the ceramics that has been used increasingly in use in dental applications for prostheses, crowns, and implant pillars [2, 7-8]. Nonetheless, in some biomedical applications, the addition of oxides is not enough to obtain adequate degradation resistance. For this reason, this paper explores the ionic nitriding process to improve the mechanical properties and resistance to material degradation in body fluids. In the nitriding process, the inclusion of nitrogen with plasma generates a substitution for anionic vacancies replacing the oxygen with nitrogen in the crystalline lattice to stabilize the surface of the material [9]. Usually, these processes are carried out in ovens at temperatures between 1400 °C and 1900 °C in nitrogen atmospheres for between 2 and 12 hours. However, at 1170 °C there is a phase change in the crystalline structure from monoclinic to tetragonal. This change in the structure of the zirconia affects the material, and there is a consequent deterioration degradation resistance [9-11].

Aging processes are typically characterized by autoclaving at 134°C at a pressure of 200 kPa for approximately 1 h; this may correspond to the material at body temperature aging four years [12-13]. During these processes, the initial state and the final state are evaluated, without considering the deterioration in short periods of time and without following a step by step process of the consequent formation of unstable oxides. Electrochemical impedance spectroscopy is a technique that allows the degradation phenomena that occur in a material exposed to a fluid to be evaluated and the changes in material integrity to be monitored as well as the incidence of the fluid and the formation of oxides or degradation products [14].

The objective of this study was to evaluate the resistance to deterioration of 3Y-TZP samples that have been treated with three different plasma nitriding temperatures (450 °C, 480 °C, and 520 °C). These were used in this research as nitriding temperatures in order to avoid monoclinic transformation and to induce a surface modification with the formation of a semi-crystalline zirconia oxide that increases protection against physiological fluids without the mechanical properties significantly being affected [12, 15]. An experimental setup was performed keeping zirconia samples that were both treated (nitriding) and untreated immersed in an artificial saliva saline solution type Afnor [16] for 21 days. The degradation behavior was evaluated in 7-day intervals using the electrochemical impedance spectroscopy technique. At the same time, other techniques were used to characterize the samples, such as scanning electron microscopy and atomic force microscopy to evaluate the morphology and changes in roughness occasioned with the aging of the material.

2. Materials and methods

2.1. Sample preparation

Pre-sintered 3Y-TZP powder compact blocks with 87-95%ZrO_2, 3-6% Y_2O_3, 1-5% HfO_2, and 1% Al_2O_3 compositions were used. These blocks were sectioned with a microcutter at 250rpm (Isomet 100, Buehler) to obtain samples that were 15x15mm and 2mm thick. Samples were then sintered in a furnace (Ceramill therm®, Armann Girrbach) at 1450 °C for 10 hours using an 8 °C/min heating ramp and then cooled to room temperature. After this process, the surfaces of the samples were polished with silicon carbide sandpaper # 340, 400, 600, and 1200 following the ASTM E3-01 standard. They were rinsed with distilled water, sonicated in isopropyl alcohol, and then dried at room temperature before the nitriding process.

2.2. Nitriding process

The ionic nitriding of the 3Y-TZP zirconia samples was performed at three temperatures (450, 480, and 520 °C) in an industrial furnace using a pulsed direct current. Each temperature was maintained for 2h with a vacuum of 3 Pa, a pressure of 400 Pa, and a 75/25 mixture of H_2/N_2. After the nitriding process was completed, the samples were cooled in the oven to an ambient temperature under a nitrogen atmosphere.

2.3. Immersion in saline solution

The degradation of the samples treated and untreated (NT) was evaluated after immersing the samples for 21 days in plastic sealed containers with an artificial saliva saline solution type Afnor [16]. The composition of this is shown in Table 1; it was prepared in 250mL of distilled water and had a pH of 6.55. All the reagents employed were analytical reagent grade.

2.4. Morphological and compositional analysis

2.4.1. Scanning Electron Microscopy (SEM) - Energy Dispersive X-Ray Spectroscopy (EDS)

The morphological identification was performed using SEM equipment (EVO MA10, Carl Zeiss) and the EDS compositional analysis was performed with an X-Act detector (Oxford Instruments). There was a 10kV acceleration voltage, the composition data was obtained in areas (50*50 µm) by triplicate for each sample, and an average was also reported. During the observation, the samples were covered with a layer of gold.

Table 1.
Chemical composition Afnor artificial saliva

Reagent	Name	Amount (g/250ml)
NaCl	Sodium chloride	0.17
KCl	Potassium chloride	0.30
$NaHCO_3$	Sodium hydrogen carbonate	0.37
KSCN	Potassium Thiocyanate	0.08
$Na_2HPO_4*2H_20$	Disodium phosphate dihydrate	0.06
$CO(NH_2)_2$	Urea	0.32

Source: The authors.

2.4.2. Atomic force microscopy (AFM)

The topographical analysis was assessed using AFM (NX10, Park Systems) equipment in contact mode. Mappings of 10 x 10 µm were performed with a scanning rate of 1 Hz. Topographic images were obtained with a tip (NSC14, Mikromasch) that was 5 N/m, a constant force, and had a 160 kHz resonance frequency. For the height images obtained, the roughness factor Ra was defined as the average arithmetic roughness.

2.5. Electrochemical Impedance Spectroscopy (EIS)

The Electrochemical Impedance Spectroscopy (EIS) and Mott-Schottky (M-S) tests were carried out in a Potentiostat/Galvanostat (Interface 1000®, Gamry instruments) using a three-electrode electrochemical cell. A 99% purity graphite bar was used as a counter electrode, an Ag/AgCl electrode was used as a reference, and the 3Y-TZP (treated and untreated) was used as the working electrode. An artificial saliva type Afnor saline solution was used as the electrolyte. The tests were carried out at body temperature (37 °C) using a thermostat bath (E100, LAUDA) connected to the electrochemical cell with an external circuit. The EIS tests were obtained with a 70 mV amplitude in a frequency range of 100 kHz to 0.01 Hz. The tests were undertaken before starting the immersion process (0 days) and then consecutively every 7 days until the 21-day immersion period was completed. The equivalent circuits proposed to adjust the Bode diagrams were carried out using the software Zview®.

3. Results and discussion

3.1. Morphological and compositional analysis

3.1.1. SEM and EDS

The elemental compositional analysis obtained by EDS (on the polished surface of the sample) was undertaken to identify the presence of nitrogen on the surface; it showed an increase in the percentage of this element with the nitriding treatment. Table 2 shows the results of the elemental composition. Besides nitrogen, elements such as yttria, hafnium, and zirconia (presented as elemental components of the compacted zirconia powders) were identified in all the samples. The additional presence of oxygen may be related to the formation of oxides during the nitriding process.

According to the data in Table 2, it can be seen that the oxygen concentration tends to decrease in all the proposed nitriding treatments, and there is an increase the nitrogen composition. Also, the O/N ratio was lower in the nitriding treatment at 450 °C and higher at 520 °C. The ratio obtained for 520 °C was very close to the untreated sample. This tendency may be related to the phenomenon of oxygen displacement by the nitrogen in the structure of the zirconia, which has already been reported by other authors [9]. Fig. 1 presents the morphological analysis of 3Y-TZP samples with and without nitriding treatment. In these images, no significant differences were observed between treated and untreated samples before immersion. Thus, the nitriding process did not affect the structure of the material in a macroscopic manner since the maximum temperature used was less than the temperature required for the monoclinic phase change of the zirconia (established at 1170 °C) [17]. The morphology observed was similar to other studies that have stabilized zirconia with 3% mol yttria [18].

Table 2.
Elemental composition of different samples

%Atomic	N K	O K	Y L	Zr L	Hf L	O/N
No treatment	2.91	64.76	0.66	31.31	0.37	22.25
450°C	4.03	61.39	0.60	33.39	0.35	15.23
480°C	3.19	63.70	0.90	32.39	0.31	19.96
520°C	2.99	63.11	0.82	33.42	0.38	21.11

Source: The authors.

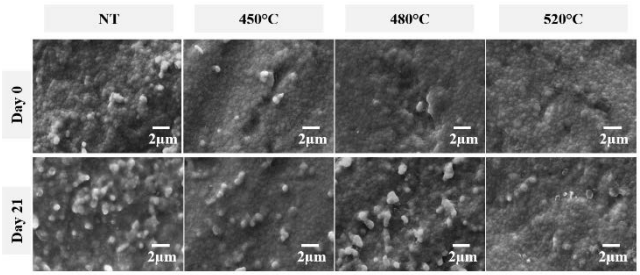


Figure 1. Secondary electron micrographs of samples subjected to different nitriding temperatures: before immersion in artificial saliva and after 21 days of immersion.
Source: The authors.

After being immersed for 21 days in the saline solution, samples revealed morphological changes associated with the degradation of the ceramic structure, they also had rounded particles and more visible bonding interfaces. Additionally Fig. 1 shows a great number of particles with irregular shapes that are observed as whiter areas (day 21); these were generated due to deposition of salts on the surface. However, the quantity of salt accumulation was lower than the detection limited by the EDS technique, thus, the presence of elements such as phosphorus, sodium, or chlorine was not detected. A clear difference between the treated and untreated samples was observed in the morphology of the ceramic aggregation particles. Using the formation of grains in the ceramic with the aggregation of particles as a reference, the untreated grains in the sample (NT) were a round shape and the grains in the nitriding samples were an ovoid elongated shape with fewer spaces between the particles. This phenomenon could be due to the presence of amorphous or semi-crystalline oxides, which were formed mainly in the lower energy zones of the ceramic bonding particles. Specifically, they occupied the spaces left by the bonding interlayers. The presence of this type of oxide has been corroborated with the results and analysis of the electrochemical impedance spectra obtained, especially after being immersed for 21 days in an artificial saliva electrolytic solution. After being immersed for 21 days in saline, there were no defects or cracks in the nitrided samples, as would be expected in unstabilized zirconia on contact with water, in which the tetragonal phase changes to the monoclinic phase [19].

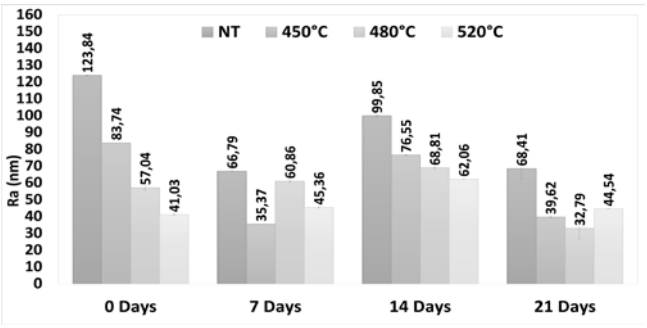


Figure 2. Results of roughness (Ra) for the samples that were immersed in artificial saliva.
Source: The authors.

3.1.2. AFM

The samples were observed using atomic force microscopy, and the topography and roughness are presented in Fig. 2 (samples were analyzed without polishing). The roughness values decreased as the nitriding temperature increased, which confirmed the SEM observations of probable formation of amorphous oxides in the interlayer sites of the bonding particles in the ceramic with nitriding treatment. This increased with the treatment temperature.

In general, from 0 to 21 days immersion in saline, the roughness values decreased 44.76% in the NT sample, and 52.68% and 42.51% in the samples nitriding at 450 °C and 480 °C, respectively. The roughness in the sample at 520 °C, increased to 8.55% at 21 days. The trend in intermediate immersion times (7 and 14 days) represented a drastic decrease in roughness in all samples (less in 480° C) at 7 days, with an increase at 14 days, and then a decrease at 21 days. This trend could be influenced by the occurrence of two simultaneous processes: a) the formation of amorphous oxides that result from the interaction of the ceramics with the aqueous saline solution, and b) the degradation of oxides and particles that are formed in the consolidation and nitriding process. These changes may be related with salt deposition in the surface. In this context, it is notable that the sample that presents the highest percentage of decrease in roughness was the sample with the highest nitrogen content (450 °C), and the sample with the lowest reduction in roughness was the one with the lowest nitrogen content (520 °C). This means that a relationship was established between the nitrogen content added and the increase in the affinity of bonding with either the oxygen presented in the thermal treatment or the aqueous medium for the formation of amorphous oxides. In addition to the changes presented in the roughness value, Fig. 3 shows that there were no notable topographic changes identified.

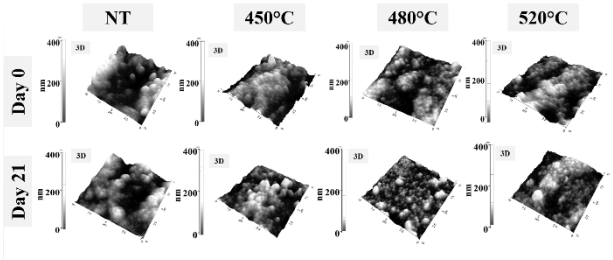


Figure 3. AFM images for the different samples at 0 and 21 days immersion
Source: The authors

Fig. 3 shows structures with robust grains that are more agglomerated in the samples that have been treated at 0 days as well as the structures with small grains and irregular forms at 21 days. This indicates uniform degradation or dissolution of the formed oxides during the nitriding process.

3.2. Electrochemical impedance spectroscopy analysis

The electrochemical test revealed parametric information related to the appearance of oxides that formed on the surface of the nitrided 3Y-TZP samples and the respective defects of these oxides that compromise the integrity of the material. Fig. 4 shows the spectra obtained for each sample both with no treatment and nitriding treatment at 0, 7, 14, and 21 days immersion in saline solution. In the untreated sample, particularly capacitive behavior was initially identified over a large range of frequencies with a wide loop in the phase angle vs. a frequency that was close to 90 degrees. The amplitude of the loop in the frequency range provides an idea of the stability of the sample. The resistance of this material at 0 days was approximately 1010 ohms. The 7, 14 and 21-day spectra showed patterns of untreated zirconia decay with the appearance of RC-transfer relaxations that were related to the formation of amorphous oxides with capacitive behaviors (high frequencies) and resistive behavior between the bulk of the material and these oxides (below 10 Hz). The loops of the phase angle graphs with an increased number of days immersed moved towards the high-frequency region; they became less ample, which is an indication of electrochemical instability due to the formation of amorphous oxides. The maximum deterioration of this sample was observed at 14 days immersion. It then recovered at 21 days until it reached an electrochemical resistance of 108 ohms. The presence of a capacitive region in this sample at 21 days between 0.1 Hz and 10 Hz becomes evident, and it is related to the involvement of the bulk of the zirconia under the action of the saline solution. The resistive behavior observed in this sample at 7 days immersion is part of a cycle of protection and deterioration of the sample due to the formation and dissolution of amorphous oxides and the penetration of aggressive electrolyte species from surface level to the bulk of the material.

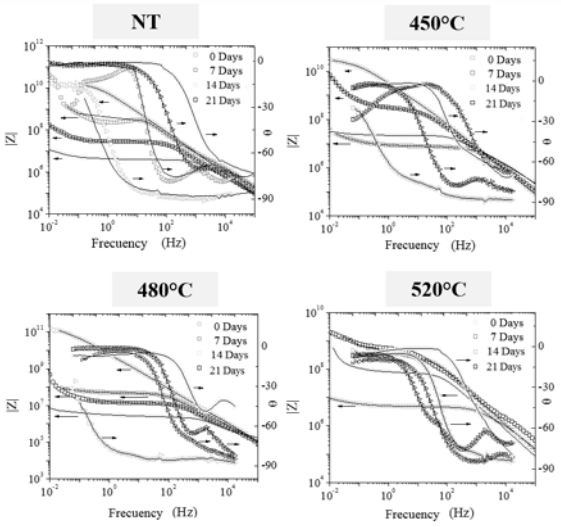


Figure 4. Bode diagrams for nitriding samples at different temperatures.
Source: The authors

The spectra of the samples with nitriding treatment behaved similarly to a sample without nitriding. The electrochemical resistance and stability were the highest at 0 days in the nitrided sample at 480 °C (1011 ohms), followed by the sample treated at 450 °C, which showed a slightly higher resistance in comparison to the untreated sample. The sample treated at 520 °C showed an approximate electrochemical resistance of 10:9 a lower value compared to the resistance of the other samples treated and without nitriding. The highest stability was observed in the sample treated at 480 °C because of its phase angle value in the spectrum which had a constant value of about 90 ° from 1 Hz to more than 10 kHz. With the variation of the residence time, behavior such as that of a sample without nitriding was observed. However, a higher electrochemical resistance was obtained at 21 days in comparison to the untreated sample. The sample nitriding at 520 °C presented an increase in its electrochemical resistance after 21 days in saline solution.

As shown in Fig. 5, for the quantitative analysis of the spectra obtained from the zirconia samples with and without immersion and treated and untreated, two equivalent electrical circuits were proposed. The RC components are related to charge transfer relaxations of the reactions that occur in the interfaces formed from the bulk of the material to the surface. The quantitative determination of the electrical parameters of these models was undertaken by adjusting the experimental parameters with those of the proposed model. Iterations in the software Z-view® were used for impedance analysis until a quantifiable error in four-digit chi-square decimals was found.

The proposed model (Fig. 5b) consists of an element representing the resistance of the artificial saliva (Rsa) used in series with an RC circuit (CPE1-R1), which represents the electrolyte/surface interface of amorphous zirconia formed on samples after 7, 14, and 21 days immersion in artificial solution. This oxidation is a product of the exchange of ions between the electrolyte and the substrate in parallel with a pair of RC elements (CPE2-R2), which represent the interface between the amorphous oxide formed and a zirconia oxide layer generated with the nitriding and the heat treatments. These elements are presented in series with a pair of RC (CPE3-R3) that represents the interface between zirconia samples both treated and untreated. The other model (Fig. 5a) was adjusted for all samples before being immersed in saliva due to the absence of amorphous oxide, which is represented in Bode diagrams with a simpler spectral morphology (Fig. 4).

Pure capacitances in the proposed circuits were replaced by constant phase elements to represent the inhomogeneities of the interfaces showing the formation of an oxide layer with nitriding and the presence of an amorphous zirconia oxide layer. Based on the proposed equivalent circuits, adjustment curves were presented which are shown in Fig. 4 as continuous lines that are superimposed on the dotted lines of the experimental data of the spectra. Table 3 shows the adjustment parameters of these curves for the different elements described.

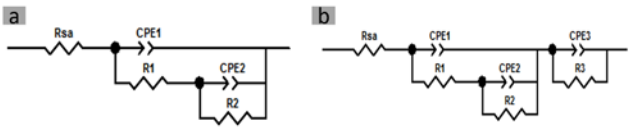


Figure 5. Equivalent circuit models a) at 0 days immersion, b) at 7, 14, and 21 days immersion.
Source: The authors

The CPE1-P values (immersion electrolyte/zirconium oxide) varied very little in a range between 0.8 and 0.9; this means that the hydrolytic degradation of the ceramic could be due to an increase in porosity due to disruption or dissolution of the anionic or cationic elements contained in the 3Y-TPZ. This is caused by oxygen product displacement of the hydrolysis to a local acid pH where reduction is generated and the structure goes through an aging process [20].

The phase values of the CPE1-P capacitance are reduced when immersion takes place, which is related to the formation of defects and porosities in the outermost layer of the zirconia samples. At the same time, the degradation of all samples is reflected in the behavioral changes in the frequency range: approximately between 1 Hz and 1 kHz. In this range, the electrochemical processes refer to the bulk transfer of the material.

The CPE2-P values that represent the transfer of charge restrictions at the interface between amorphous zirconia and nitrided zirconia remained within a range of 0.8 to 0.9. These values represent high integration between both oxides. The smaller CP3-T capacitance values were reached in the nitrided samples, especially in the sample treated at 450 °C which presented the highest impedance value. Moreover, the CPE3-P values showed a clear difference between the treated samples. Lower values in the nitrided samples could be related to the creation of vacancies of anions that generate homogeneities to the transfer of charge. Accordingly, the corresponding effect of an oxygen substitution by nitrogen is characterized by the formation of vacancies of additional anions, as per eq. (1) [9].

$$N_2\ (\text{Gas}) + 3O_x\text{O}\ (\text{YSZ}) = 2\text{NO'}\ (\text{YSZ}) + \text{V''O} + 3/2O_2\ (\text{Gas}) \quad (1)$$

In general, the substitution of oxygen ions for nitrogen ions help to stabilize the structure because of improvement in the concentration of oxygen vacancies (V"O). It has been found that YSZ zirconia with nitrogen doping is an excellent ionic conductor in cubic and tetragonal structures that even showed conductivity of nitrogen ions at high temperatures [9]. Lerch et al. demonstrated that the substitution of the anion (nitrogen) in ZrO2 or Yttrium-doped tetragonal zirconia (Y-TZP) stabilizes the cubic structure and improves the transport properties of these materials [21]. As reported by Cheng and Thompson, it is also possible to nitrate zirconia doped with yttria [22]. The stabilizing effects of both types of dopants are additive. Depending on the proportion of yttria/nitrogen incorporated, the materials show different types of structures with randomly

Table 3.
Adjustment parameters equivalent circuit models a) at 0 days of immersion, b) at 7, 14 and 21 days of immersion.

Immersion time	T (°C)	Rs (Ωcm^2)	R1 (Ωcm^2)	CPE1-T (F/cm^2)	CPE1-P	R2 (Ωcm^2)	CPE2-T (F/cm^2)	CPE 2-P	R3 (Ωcm^2)	CPE3-T (F/cm^2)	CPE 3-P	χ^2 (E^{-4})
0 days	**NT**	5665	2.00E9	2.22E-11	0.97	1.41E10	1.32E-11	0.63	-	-	-	9.78
	450	402	5.29E8	2.76E-11	0.97	3.50E10	4.72E-11	0.64	-	-	-	9.60
	480	4560	2.33E10	2.67E-11	0.94	2.25E11	9.23E-12	0.51	-	-	-	19.23
	520	3927	7.304E7	5.96E-11	0.91	9.438E7	2.15E-8	0.6	-	-	-	11.94
7 days	**NT**	45278	8.18E6	1.73E-11	0.94	3.089E8	9.71E-12	0.99	1.88E9	7.82E-9	0.99	19.35
	450	18372	1.04E9	9.22E-11	0.80	1.03E9	6.13E-15	0.51	7.42E7	1.88E-7	0.55	59.4
	480	17060	-8.63E10	9.09E-11	0.86	8.64E10	5.46E-17	0.99	2.04E7	5.26E-8	0.76	28.53
	520	21185	3.12E8	3.07E-11	0.92	8.91E8	1.90E-9	0.73	2.01E8	5.53E-9	0.72	124.5
14 days	**NT**	6124	1.10E7	1.48E-10	0.84	6.96E6	3.09E-9	0.99	8.95E5	7.72E-7	0.61	83.99
	450	16893	5.94E6	5.18E-11	0.85	1.58E7	5.00E-11	0.90	1.54E7	3.19E-7	0.55	32.57
	480	5.61E7	3.39E7	1.05E-8	0.003	5.23E5	1.26E-10	0.99	1E20	1.63E-7	0.07	151.55
	520	18061	2.94E6	6.53E-11	0.86	1.58E6	6.14E-11	0.98	1.21E7	5.70E-7	0.38	86.19
21 days	**NT**	10077	1.2439E8	1.41E-10	0.84	9.5014E7	4.49E-13	0.99	1.11E7	1.21E-7	0.80	30.50
	450	31599	8.8381E9	8.88E-11	0.86	8.4918E9	9.36E-13	0.99	1.1E20	1.51E-6	0.25	37.67
	480	3505	1.6393E6	4.80E-11	0.92	1.1946E7	4.18E-11	0.95	5.08E6	6.278E-8	0.75	89.91
	520	79699	5.3641E8	7.44E-11	0.82	1.167E9	1.83E-8	0.99	1.3E9	9.44E-9	0.48	11.02

Source: The authors.

ordered or randomly distributed anionic voids [9]. In the Y-Zr-O-N samples, there are anionic voids due to the incorporation of yttria and nitrogen. The incorporation of nitrogen stabilizes the tetragonal structure, which generates remarkable improvements in the resistance to the hydrolytic degradation. Similarly, the properties of protection against degradation are influenced by the formation of amorphous oxides the presence of which is evidenced in the impedance spectra, in the analysis of atomic force microscopy, and in the SEM analysis. The stability of these oxides and their integration with the crystalline oxide structure of zirconia is favored with the presence of anionic voids in the 3Y-TZP structure

4. Conclusions

A significant effect on the increase of resistance to the degradation of 3Y-TZP zirconia with the incorporation of nitrogen by gaseous plasma was analyzed using electrochemical impedance spectroscopy, SEM-EDS microscopy, and AFM atomic force microscopy. 3Y-TZP samples without nitriding and nitrided at different temperatures showed similar hydrolytic degradation patterns, especially the formation of amorphous oxides. These were more stable in the nitriding samples, and they increased in the sample treated at 450 °C, which showed the highest resistance to degradation in artificial saliva. The nitriding processes induced stability in 3Y-TZP zirconia, which favors the electrochemical behavior of these materials that are used as a biomaterial in dental prostheses and bone implants.

Acknowledgements

The authors acknowledge the Sistema General de Regalías de Colombia (SGR) macroproyecto de Salud [BPIN code: 2012000100172] for funding this research.

References

[1] Chevalier, J. and Gremillard, L., 1.6 Zirconia as a biomaterial, in: Compr. Biomater. II, Elsevier, pp. 122-144, 2017. DOI: 10.1016/B978-0-12-803581-8.10245-0.

[2] Yin, L., Nakanishi, Y., Alao, A.R., Song, X.F, Abduo, J. and Zhang, Y., A review of engineered zirconia surfaces in biomedical applications, Procedia CIRP. 65, pp. 284-290, 2017. DOI: 10.1016/J.PROCIR.2017.04.057.

[3] Pieralli, S., Kohal, R.J., Lopez Hernandez, E., Doerken, S. and Spies, B.C., Osseointegration of zirconia dental implants in animal investigations: A systematic review and meta-analysis, Dent. Mater. 34, pp. 171-182, 2018. DOI: 10.1016/J.DENTAL.2017.10.008.

[4] Cattani-Lorente, M., Durual, S., Amez-Droz, M, Wiskott, H.W.A. and Scherrer, S.S., Hydrothermal degradation of a 3Y-TZP translucent dental ceramic: a comparison of numerical predictions with experimental data after 2 years of aging, Dent. Mater. 32, pp. 394-402, 2016. DOI: 10.1016/J.DENTAL.2015.12.015.

[5] Pandoleon, P., Kontonasaki, E., Kantiranis, N., Pliatsikas, N., Patsalas, P., Papadopoulou, L., Zorba, T., Paraskevopoulos, K.M. and Koidis, P., Aging of 3Y-TZP dental zirconia and yttrium depletion, Dent. Mater. 33, pp. e385-e392, 2017. DOI: 10.1016/J.DENTAL.2017.07.011.

[6] Bartolo, D., Cassar, G., Al-Haj Husain, N., Özcan, M. and Camilleri, J., Effect of polishing procedures and hydrothermal aging on wear characteristics and phase transformation of zirconium dioxide, J. Prosthet. Dent. 117, pp. 545-551, 2017. DOI: 10.1016/j.prosdent.2016.09.004.

[7] Sivaraman, K., Chopra, A., Narayan, A.I. and Balakrishnan, D., Is zirconia a viable alternative to titanium for oral implant? A critical review, J. Prosthodont. Res., 62(2), pp. 121-133, 2017. DOI: 10.1016/J.JPOR.2017.07.003.

[8] Abd El-Ghany, O.S. and Sherief, A.H., Zirconia based ceramics, some clinical and biological aspects: Review, Futur. Dent. J. 2, pp. 55-64, 2016. DOI: 10.1016/J.FDJ.2016.10.002.

[9] Berendts, S., Eufinger, J.P., Valov, I., Janek, J. and Lerch, M., Ionic conductivity of low yttria-doped cubic zirconium oxide nitride single crystals, Solid State Ionics. 296, pp. 42-46, 2016. DOI: 10.1016/J.SSI.2016.08.015.

[10] Liu, H., Zhao, W., Ji, Y., Cui, J., Chu, Y. and Rao, P., Determination of fracture toughness of zirconia ceramics with different yttria

concentrations by SEVNB method, Ceram. Int. 43, pp. 10572-10575, 2017. DOI: 10.1016/J.CERAMINT.2017.04.064.
[11] Almeida, P.J., Silva, C.L., Alves, J.L., Silva, F.S. and Martins, R.C., Sampaio-Fernandes, J., Analysis of the stability of 3Y-TZP zirconia abutments after thermocycling and mechanical loading, Rev. Port. Estomatol. Med. Dentária E Cir. Maxilofac. 57, pp. 197-206, 2016. DOI: 10.1016/J.RPEMD.2016.07.003.
[12] Cotič, J., Jevnikar, P. and Kocjan, A., Ageing kinetics and strength of airborne-particle abraded 3Y-TZP ceramics, Dent. Mater. 33, pp 847-856, 2017. DOI: 10.1016/J.DENTAL.2017.04.014.
[13] Cattani-Lorente, M., Scherrer, S.S., Durual, S, Sanon, C., Douillard, T., Gremillard, L., Chevalier, J. and Wiskott, A., Effect of different surface treatments on the hydrothermal degradation of a 3Y-TZP ceramic for dental implants, Dent. Mater. 30, pp. 1136-1146, 2014. DOI: 10.1016/j.dental.2014.07.004.
[14] Pajkossy, T. and Jurczakowski, R., Electrochemical impedance spectroscopy in interfacial studies, Curr. Opin. Electrochem. 1, pp. 53-58, 2017. DOI: 10.1016/J.COELEC.2017.01.006.
[15] Gan, K., Liu, H., Jiang, L., Liu, X., Song, X., Niu, D., Chen, T. and Liu, C., Bioactivity and antibacterial effect of nitrogen plasma immersion ion implantation on polyetheretherketone, Dent. Mater. 32, pp. e263-e274, 2016. DOI: 10.1016/J.DENTAL.2016.08.215.
[16] Romonti, D.E., Gomez-Sanchez, A.V., Milošev, I., Demetrescu, I. and Ceré, S., Effect of anodization on the surface characteristics and electrochemical behaviour of zirconium in artificial saliva, Mater. Sci. Eng. C. 62, pp. 458-466, 2016. DOI: 10.1016/j.msec.2016.01.079.
[17] Platt, P., Mella, R., DeMaio, W., Preuss, M. and Wenman, M.R., Peridynamic simulations of the tetragonal to monoclinic phase transformation in zirconium dioxide, Comput. Mater. Sci. 140, pp. 322-333, 2017. DOI: 10.1016/J.COMMATSCI.2017.09.001.
[18] Zhang, F., Batuk, M., Hadermann, J., Manfredi, G., Mariën, A., Vanmeensel, A., Inokoshi, M., Van Meerbeek, B., Naert, I. and Vleugels, J., Effect of cation dopant radius on the hydrothermal stability of tetragonal zirconia: Grain boundary segregation and oxygen vacancy annihilation, Acta Mater. 106, pp. 48-58, 2016. DOI: 10.1016/J.ACTAMAT.2015.12.051.
[19] Wei, C. and Gremillard, L., Towards the prediction of hydrothermal ageing of 3Y-TZP bioceramics from processing parameters, Acta Mater. 144, pp. 245-256, 2018. DOI: 10.1016/J.ACTAMAT.2017.10.061.
[20] Boccaccini, D.N., Frandsen, H.L, Soprani, S., Cannio, M., Klemensø, T., Gil, V. and Hendriksen, P.V., Influence of porosity on mechanical properties of tetragonal stabilized zirconia, J. Eur. Ceram. Soc. 38, pp. 1720-1735, 2018. DOI: 10.1016/J.JEURCERAMSOC.2017.09.029.
[21] Lee, J.S., Lerch, M. and Maier, J., Nitrogen-doped zirconia: A comparison with cation stabilized zirconia, J. Solid State Chem. 179, pp. 270-277, 2006. DOI: 10.1016/j.jssc.2005.10.012.
[22] Lee, J.S., Fleig, J., Maier, J., Chung, T.J. and Kim, D.Y., Microcontact impedance spectroscopy in nitrogen-graded zirconia, Solid State Ionics. 176, pp. 1711-1716, 2005. DOI: 10.1016/j.ssi.2005.04.036.

K. Dorado-Bustamante, was awarded his BSc. Eng. in Chemical Engineering in 2016 from the Universidad Nacional de Colombia, Medellin. The same year he was awarded a full scholarship from the Instituto Balseiro Patagonia, Argentina and currently, he is working in the department of nuclear physics in the Sp. degree of nuclear energy applications (CEATEN) in Buenos Aires, Argentina. His research interest includes: electrochemical processes, smart materials, and nuclear applications for biomedical devices.
ORCID: 0000-0002-2810-1191

S. Leal-Marin, was awarded her BSc. Eng. in Biomedical Engineering in 2013 from the Universidad EIA, Medellin, Colombia. For two years she worked for in the biomedical devices area, specifically in the neurological and orthopedic field. Currently, she works for the Universidad Nacional de Colombia, Medellin as a characterization devices technician in the laboratory of biomaterials, and she is undertaking a MSc. Eng. Materials and processes. Her research interests include the biological characterization of biomaterials, the development of coatings, and biomedical devices.
ORCID: 0000-0002-0315-1950

H. Estupiñán-Duran, was awarded his BSc. Eng. in Metallurgy Engineering in 2001, his MSc. Eng. in 2005, and his PhD. in Chemical Engineering in 2011, all them from the Universidad Industrial de Santander, Santander, Colombia. He then worked in the corrosion and development of biomaterials. Currently, he is a full professor in the Department of Materials and Minerals, Facultad de Minas, Universidad Nacional de Colombia, Medellin. His research interests include corrosion processes, surface characterization, biosensors, biocompatible and antibacterial coatings, and orthopedic materials.
ORCID: 000-0002-9607-3364



UNIVERSIDAD NACIONAL DE COLOMBIA
SEDE MEDELLÍN
FACULTAD DE MINAS

Área Curricular de Ingeniería
Geológica e Ingeniería de Minas y Metalurgia

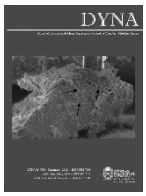
Oferta de Posgrados

Especialización en Materiales y Procesos
Maestría en Ingeniería - Materiales y Procesos
Maestría en Ingeniería - Recursos Minerales
Doctorado en Ingeniería - Ciencia y Tecnología de Materiales

Mayor información:

E-mail: acgeomin_med@unal.edu.co
Teléfono: (57-4) 425 53 68

UNIVERSIDAD NACIONAL DE COLOMBIA
SEDE MEDELLÍN
FACULTAD DE MINAS



DYNA
http://dyna.medellin.unal.edu.co/

Dynamic adjustment of a MLFQ flow scheduler to improve cloud applications performance

Sergio Armando Gutiérrez [ac], Marinho Barcellos [b] & John Willian Branch [a]

[a],*Facultad de Minas, Universidad Nacional de Colombia, Medellín, Colombia, saguti@unal.edu.co, jwbranch@unal.edu.co*
[b] *Instituto de Infiormática, Universidade Federal do Rio Grande do Sul, Porto Alegre, Brazil, marinho@inf.ufrgs.br*
[c] *Facultad de Ingenierías, Universidad de Medellín, Medellín, Colombia, sagutierrez@udem.edu.co*

Received: April 10th, de 2018. Received in revised form: June 7th, 2018. Accepted: June 12th, 2018

Abstract
State-of-the-art solutions for flow scheduling propose the use of Multi Level Feedback Queue (MLFQ) as a mechanism to avoid the requirement of prior information (i.e. agnosticism) regarding flow sizes. This is an important aspect to achieve the performance goals of high responsiveness and high throughput that is expected in Cloud Applications (e.g. search engines, social networks, and e-commerce sites). These goals are tightly associated with the prioritization of short flows (a few KB in size), the majority for these applications rather than long flows (several MB in size). However, these applications usually cannot provide information in advance about the size of the flows. In this paper, we analyze the feasibility of providing dynamic adjustment for a MLFQ-based scheduling system in such a way that it adapts itself to the time and space variations exhibited by Data Center Network (DCN) traffic without requiring prior information about workload properties.

Keywords: Flow scheduling; data center networks; MLFQ; agnostic flow scheduling

Ajuste dinámico de un programador de flujos MLFQ para mejorar el desempeño de aplicaciones en la nube

Resumen
Las soluciones presentes actualmente en el área de conmutación de flujos proponen el uso del concepto de Colas Multinivel con Realimentación (MLFQ por su sigla en inglés) como mecanismo para evitar el requerimiento de información previa (mecanismo agnóstico) con respecto al tamaño de los flujos de datos. Este es un aspecto importante para el logro de las metas de desempeño de alta capacidad de respuesta y alto rendimiento, esperadas en las aplicaciones en la nube (Por ejemplo, motores de búsqueda, redes sociales y sitios de comercio electrónico). Estas metas están estrechamente asociadas a la priorización de los flujos cortos (con tamaños de unos pocos KB), mayoritarios en estas aplicaciones, sobre los flujos largos (con tamaños de varios MB). Sin embargo, estas aplicaciones usualmente no son capaces de proporcionar de antemano la información acerca del tamaño de los flujos. En este artículo, analizamos la viabilidad de proporcionar ajuste dinámico a un esquema de conmutación basado en MLFQ, de tal manera que éste sea capaz de adaptarse a las variaciones espacio temporales que se observan en el tráfico presente en las redes de centro de datos, sin que se requiera información previa sobre las propiedades de las cargas de trabajo.

Palabras clave: Conmutación de flujos; redes de centro de datos; MLFQ; conmutación agnóstica de flujos

1. Introduction

Cloud applications running on Data Center Networks (DCN) have very strict performance requirements which, when unsatisfied, might affect the revenue obtained by the applications' owners [1,2,5-7]. The traffic associated with these applications consists of a mix of short (those transporting a few kilobytes) and long flows (those transporting several megabytes or gigabytes). An important performance goal for these applications is the minimization of the flow completion time (FCT) of short flows without inducing starvation in long flows [3,4].

The literature proposes flow scheduling and queue management as strategies to achieve this goal of minimizing

How to cite: Gutiérrez, S.A., Barcellos, M. and Branch, J.W., Dynamic adjustment of a MLFQ flow scheduler to improve cloud applicationsperformance. DYNA, 85(206), pp. 16-23, September, 2018.

© The author; licensee Universidad Nacional de Colombia.

the FCT of short flows. However, this involves three challenges: First, in many cases, it is not possible to have a-priori information about the flow sizes to plan the scheduling [5,6]. Hence, it is impossible to know whether a flow will be short or long when it starts. Second, even if this information is available, taking advantage of it might imply prohibitive modifications in different elements of the infrastructure (switches and end hosts) and/or the applications themselves [4]. Third, the scheduling mechanisms need to adapt themselves to the time and space variations that the traffic might exhibit [9,19].

Solutions for flow scheduling reported in the literature [4-6,9,13,15] fail to address some or all of the previously mentioned challenges. In particular, although some approaches are agnostic regarding the specific size of flows for its scheduling, they still assume that it is possible to know properties in advance such as the flow size distribution for the workloads present on the network [6,9].

In this paper, we analyze the situation, especially in the context of solutions based on a Multi-Level Feedback Queue (MLFQ) scheduler when the current network traffic does not fit the scheduling configuration. By using simulation, we observe how, despite the fact that this approach introduces agnosticism in the flow scheduling, it is still dependent on previous knowledge of some general features for the workload present on the network to achieve the goal of minimizing FCT for the short flows. To address this dependency, we propose the implementation of a monitoring mechanism system focused on detecting traffic properties that can be used to dynamically adjust the scheduling configuration in such a way that it can handle the space and time variations that the traffic associated to cloud applications usually exhibits [1,7,14,19].

This paper is organized as follows: Section 2 analyzes the demotion threshold problem that might be present in MLFQ-based flow scheduling systems. Section 3 describes our monitoring approach and discusses some assumptions that it leverages. Section 4 presents the results of a preliminary evaluation of the effectiveness of our proposal to minimize the FCT of short flows on a Data Center workload. Section 5 presents the related literature, and Section 6 concludes the paper.

2. Threshold mismatch in agnostic flow scheduling mechanisms

2.1. MLFQ

MLFQ is a concept that has come from Operating Systems [10]. It was conceived for multiuser timeshare systems and it is based on employing a multilevel queue to manage processes, that is, the instances of the programs executed on the system. The goal of MLFQ is to approximate the Shortest Job First (SJF) scheduling heuristic, which theoretically minimizes both the average and tail process completion time. MLFQ aims to prioritize short processes (which are mainly associated with interactive operations and I/O intensive operations) over long processes (usually associated to batch operations), without knowing in advance the exact duration of the former.

Fig. 1 presents the scheme of a MLFQ scheduler in an operating system. It consists of a set of FIFO queues and a scheduling policy. The number of queues goes from two up to a given number according to the implementation (e.g. the Solaris Operating System uses sixty). Each queue has an associated value indicating the maximum quantum for a process to be queued at that given queue (i.e. a given priority level). Higher priority queues have smaller quantum values associated and these values increase between successive queues.

Initially, all the processes enter the highest priority queue. A process is demoted and queued on the next priority queue whenever it exceeds the specified quantum to stay at that queue. Hence, this approach leads to the prioritization of short over long processes. The former tend to complete within the first queues whereas the later tend to sink towards the lowest priority queue.

The scheduling policy in MLFQ is very simple. In order to determine the next process to dequeue, the set of queues is checked following a top-down strategy. Initially, the highest priority queue is checked. If this queue is non-empty, then the first process in the queue is scheduled and runs until blocking. This process is then moved to the end of the same queue (implementing FIFO) or to the end of next queue (demoted to the next lower priority). However, if the highest priority queue is empty, then the next queue (lower priority) is checked just as with the highest one. The scheduling is repeated for the next process, always starting with the highest priority queue.

Recently, the literature on flow scheduling proposed to adapt the notion of MLFQ to schedule data flows. Flow scheduling approaches based on MLFQ aim at approximating scheduling heuristics such as Least Attained Service (LAS) or Shortest Job First (SJF) in order to prioritize short flows [16]. This approximation is performed by dynamically assigning priorities to flows without actually knowing their size in advance. Flows are initially processed at the top priority queue of a MLFQ, and they are progressively demoted according to a given criteria such as deadline meeting, byte count, or associated congestion notifications [3, 5, 6, 9].

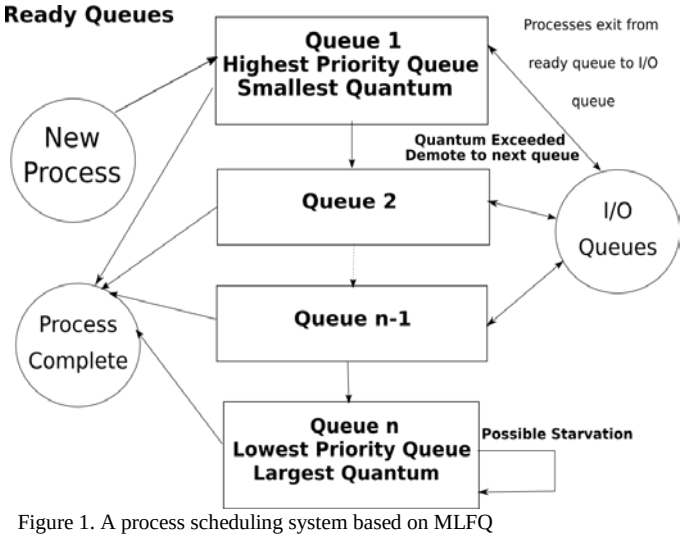


Figure 1. A process scheduling system based on MLFQ
Source: The authors

2.2. Threshold mismatch in MLFQ

Defining the demotion thresholds for an MLFQ scheduler is a challenging task. It involves determining the right values that indicate when the scheduled entity should be moved from a given priority level to another lower level.

This definition is associated with a specific performance goal. In the case of flow scheduling for cloud applications, these thresholds should aim at minimizing the FCT of short flows since it influences the responsiveness as perceived by the end user. However, although approaches based on MLFQ are conceptually agnostic (i.e. they do not require a-priori information about the duration of a process or the size of a flow for the scheduling), they still require some prior information to derive the demotion thresholds. This information is associated to specific properties of the traffic workloads. If the demotion thresholds do not fit these properties, then the threshold mismatch problem arises. Specifically, in the context of flow scheduling, the threshold mismatch problem might hamper the goal of minimizing the FCT, and this might hurt especially short flows.

To illustrate this point, assume a simplified MLFQ with two priority queues and, therefore, a single demotion threshold. Suppose that, for the sake of simplicity, there are only two flow sizes: 10KB and 10MB. Assume that for a given workload, 90% of its flows are 10KB and the remaining 10% are 10MB. In this situation, it would be optimal to set the demotion threshold to 10KB since this would keep the short flows in the high priority queue until their completion. Thus, short flows are prioritized over the long flows, which will ultimately be queued into the low priority queue. Assume that later, there is a shift in the workload. In the new workload, the size of small flows is 20KB instead of 10KB. With the demotion threshold set to 10KB, some of the packets of the short flows will be demoted to the low priority queue. Hence, the latency for these short flows will be larger than it should be. Fig. 2 illustrates this situation.

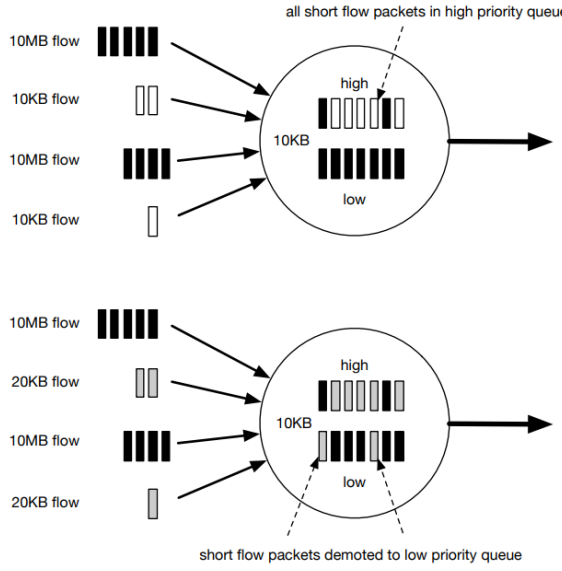


Figure 2. The threshold mismatch problem
Source: The authors

3. Dynamic adjustment of MLFQ scheduler

In this section, we propose an approach to adapt the configuration of a MLFQ scheduler, aiming to achieve workload-agnostic operation. That is, an approach that avoids the requirement of prior information about workload properties that are present in the network.

3.1. Overview

As we previously discussed, state-of-the-art solutions addressing agnostic flow scheduling require information about the distribution of the flow sizes for the workloads. This information is used to derive the demotion thresholds for the MLFQ scheduler. This means that, whenever the workload shifts, there might be a mismatch between the current scheduling configuration and the current workload. This mismatch might adversely affect the FCT for the short flows.

We propose observing the traffic entering into the switch ports. This observation, performed during a given time slot (monitoring window) enables the acquisition of information to infer the traffic behavior associated to the workloads present in the network. Periodically (say, every 100ms), the demotion thresholds are adjusted according to information acquired during the current monitoring window (say 500ms). The rationale behind this approach is to *use the past to try to predict the future*

3.2. Assumptions

Our concept of adaption of MLFQ scheduling leverages the notion of Programmable Switches. Hence, we assume that the MLFQ is implemented with the switch queues associated to each port, and the demotion thresholds are defined and maintained within the switch. The operations of traffic monitoring and threshold adjustment are executed also within the switch (i.e. separated execution threads). This is essentially different to the approach proposed by related work, which considers a packet tagging mechanism based on MLFQ, with strict priority scheduling performed at switches [6, 9].

Although the MLFQ scheduling is implemented at switches, some degree of cooperation is required from the end hosts. Particularly, we assume that end hosts can add a header to packets to inform a) the amount of bytes that a flow has currently sent and b) the final size of the flow. The addition of packet headers has already been used in related work [6,13,15].

Switches receive and process this information sent from end hosts and maintain a sorted list for each port, which contains the size of each flow that is completed during the monitoring window. Then, periodically, the switch calculates a set of predefined percentiles (say 10^{th}, 20^{th}, etc) values from that sorted list. These percentiles provide a clue to adjust the demotion thresholds of the MLFQ scheduler of the particular port. After the adjustment, the list of flow sizes is pruned to make the monitoring window slide forward.

Our observation is that low percentiles can define upper bounds for short flows, which should be associated to higher

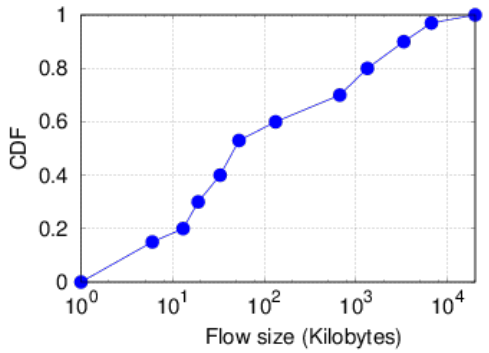


Figure 3. Typical Web Search workload in a production data center
Source: The Authors with data from [19]

priority levels, and higher percentiles can define upper bounds for long flows, which should be associated to lower priority levels. For example, consider the workload Web Search described in Fig. 3. Assume a MLFQ system with two queues (therefore, one demotion threshold). For that workload, the plotted CDF indicates that 80% of the flows are shorter than 10KB. Our intuition is that by calculating low percentiles (say 10th or 20th) in the list of completed flow sizes, we might have a good idea of setting a demotion threshold that approximates the upper bound for the short flows in the workload and then prioritize them by separating from the long flows.

We claim that one advantage of implementing our threshold adjustment mechanism within the switch is avoiding misuse by a malicious host. For example, with packet marking at end hosts, it might happen that a malicious host marks its packets with the highest priority value regardless the amount of bytes that flows have transmitted. In contrast, in our approach, this misuse is avoided since the switch schedules packets according to the amount of bytes transmitted by each flow. Also, since the threshold adjustment is local to switches, it adapts to the time and space variations of the traffic. For example, for different switches, the notion of what is a short flow and the sizes of these flows varies. However, since short flows are the majority in typical data center workloads, the calculation of low percentiles at each switch will yield to prioritize short flows at each switch. This also contrasts with the related work, in which the demotion thresholds are configured globally for all the DCN switches.

4. Experiments and results

4.1. Simulation model

We evaluated our proposal of threshold adjustment via NS-2. This is a discrete time, packet-based network simulator, widely used in the literature to perform large scale evaluation of different solutions in the field of computer networks. Our simulations were executed on a server with an Intel(R) Core(TM) i7-4790S CPU with eight cores @ 3.20Ghz and 8GB of RAM. In our experiments, we compare our proposal of threshold adjustment against the closest related work which is PIAS [6], with static threshold configuration.

4.1.1. Assumptions and input factors

In our experiments, we followed the same guidelines as related work. For our transport protocol, we used DCTCP [1] configured with the recommended values for the parameters K and g (65 and 1/16 respectively) [2]. For the control of the Explicit Congestion Notification, we implemented per-port marking. For a detailed analysis of this choice, please refer to Section IV-A number 2 of [6].

For our evaluation, we considered different traffic load levels ranging from 50% to 90%. We define the monitoring window to be 250ms and we perform the threshold adjustment in 200ms intervals.

4.1.2. Topology

A switch S0 with four connected hosts named from N0 to N3 forms our experimental topology. Links connecting hosts and switches are all full duplex with a bandwidth of 10Gbps and propagation delay of 20.2us. These values correspond to typical values present in infrastructure of production data centers [6]. There are two queues and a single demotion threshold that form the MLFQ system for this configuration. Fig. 4 shows the schematic diagram of the experimental topology.

4.1.3. Workload

The workload consisted of 10000 flows, with 80% being short (10 KB) and 20% being long flows (1000 KB). Nodes N1 and N3 sent long flows towards N0 whereas N2 sent short flows towards N0. In these experiments, we defined that the percent that was going to be calculated from the list of completed flow sizes to update the demotion threshold was the 10^{th} percentile.

4.1.4. Convergence of the Demotion Thresholds

In this section, we analyze the convergence of the demotion threshold. For the sake of comparison, we assess three different values of demotion threshold: 1KB, 10KB and 1000KB that are used for static configuration and for initial value of the demotion threshold. These particular values induce three situations: in the first configuration (1KB), short flows are demoted prematurely. That is, when the flow has transmitted 1KB, its packets are queued into the low priority

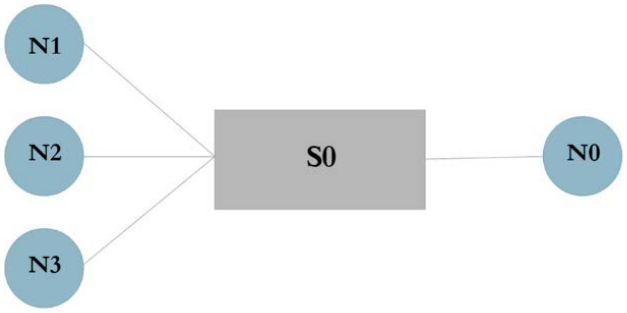
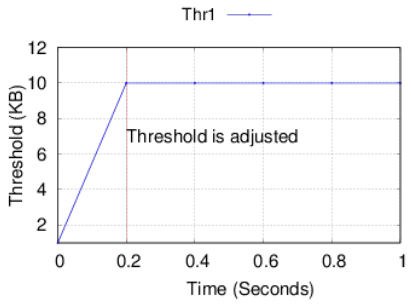


Figure 4. Experimental topology
Source: The authors

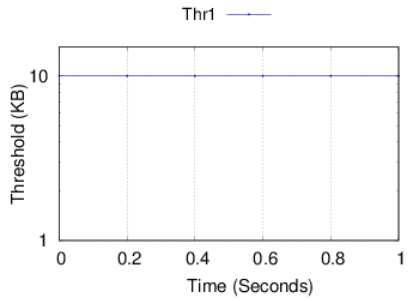
queue. The second configuration (10KB) is optimal as it keeps short flows in the high priority queue until its completion and demotes the long flows towards the low priority queue. The third configuration (1000KB) causes long flows to stay longer at the high priority queue, which hurts the FCT of short flows. The first and third configurations clearly induce the threshold mismatch problem discussed on Section 2.2.

Fig. 5 shows the convergence of the demotion threshold in the explicit threshold mismatch situations. The threshold converges to the value of 10KB, regardless of the initial value. With the threshold configured to the optimal value for this workload, we do not observe changes since the proposed approach detects that the threshold is already set to an adequate value.

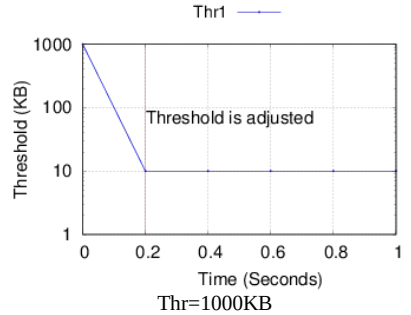
These initial experiments show that the adjustment approach operates adequately in terms of convergence of the demotion threshold. In the next section, we assess the effectiveness of the adjustment mechanism in terms of minimization of the average and tail FCT when compared to the static setting of the demotion threshold.



Thr=1KB



Thr=10KB



Thr=1000KB

Figure 5. Convergence of the demotion threshold in the proposed approach with explicit threshold mismatch
Source: The Authors

4.1.5. Minimization of the FCT

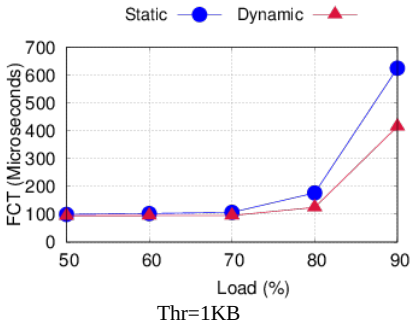
In this section, we present the results after assessing the FCT minimization. In this set of experiments, we compare the average and tail FCT for short and long flows, both in a static threshold configuration and with dynamic adjustment. These experiments consider different levels of link occupation ranging from 50% to 90%.

Short Flows

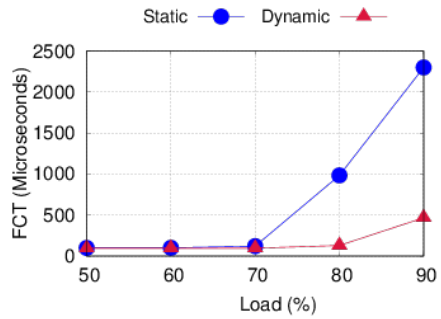
Fig. 6 presents the average FCT of the short flows for the configurations inducing threshold mismatch. It can be observed that the dynamic adjustment improves the metrics in these cases, especially at high traffic loads (higher than 70%). When the demotion threshold is set to 1KB, an average FCT reduction achieved is between 4.9% and 33.5%. When the threshold is set to 1000KB, the reduction is between 3.7% and 86%.

Fig. 7 presents the result for the tail (99th percentile) FCT. In this case, the dynamic adjustment also improves the performance by reducing the FCT in the situation of threshold mismatch, especially at high traffic loads. This improvement goes from 33.9% to 59.5% when the threshold is set to 1KB whereas it is between 51.3% and 93.9% when the threshold is set to 1000KB.

When the threshold is set to the optimal value for this workload (i.e. 10KB), the dynamic adjustment achieves results close to those obtained with the static setting. That is, the dynamic adjustment does not perform further adjustment as it detects that the threshold is already set to an appropriate value for the workload. Due to this, the plot presenting this situation has been omitted.



Thr=1KB



Thr=1000KB

Figure 6. Average FCT of the short flows
Source: The Authors

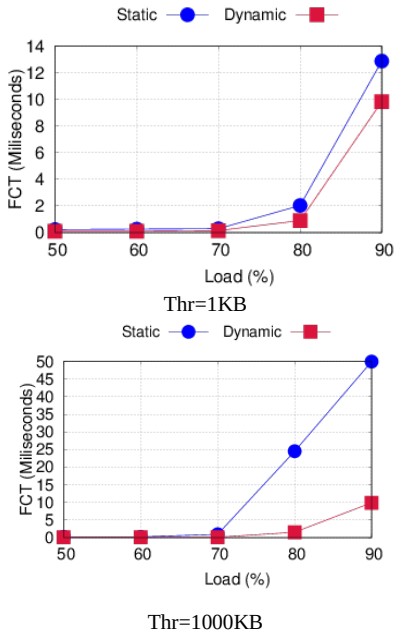


Figure 7. Tail FCT of the short flows
Source: The Authors

Long Flows

Fig. 8 presents the average and tail FCT for the long flows when the demotion threshold is set to 1000KB. The improvement in the metrics is more noticeable at high loads. For the average FCT, the improvement is between 27.1% and 46.7%. For the tail FCT, the improvement is between 24% and 45.8%.

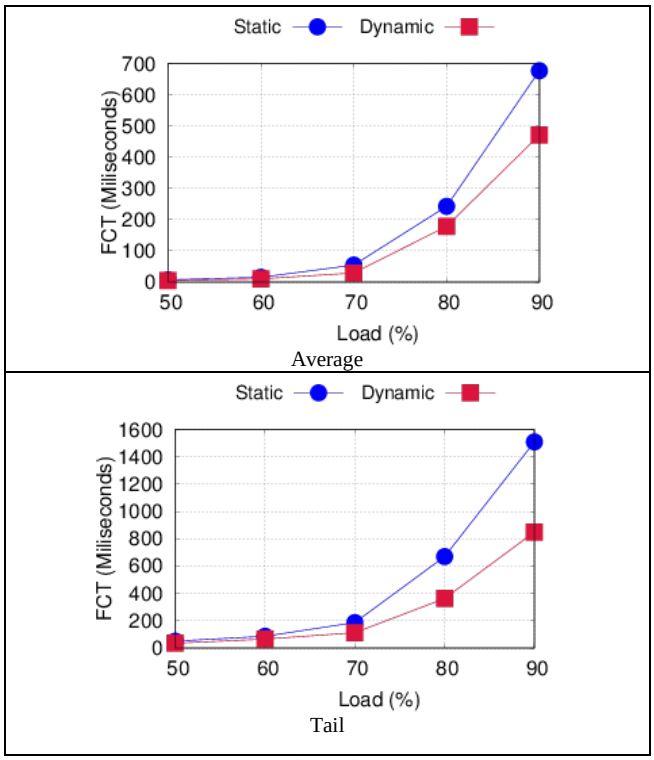


Figure 8. Average and Tail FCT of long flows with threshold set to 1000KB
Source: The authors

With respect to the other cases, the dynamic adjustment does not induce increments for either the average or the tail FCT. As observed in the previous result, the demotion thresholds converges to the size of the short flows. Therefore, it separates the short and the long flows avoiding them becoming mixed. Due to this separation, the long flows are not affected by the prioritization of the short flows.

5. Related work

We present a survey of literature addressing the problem of Information-Agnostic Flow Scheduling in a Data Center Networks context. Information-agnostic is the set of transport mechanisms that try to achieve the performance goals for cloud applications without detailed information for the flow scheduling. For a more extended review of the field's state-of-the-art, the interested reader can refer to [16,18].

HULL [3] and QJUMP [11] are approaches that aim to avoid the queuing delays that might affect especially short flows, but they do not actually require the size of the flow in advance. HULL leverages the concept of Phantom Queues that consists in simulating a queue associated with the egress port in switches. This simulation is implemented through a counter that is updated whenever a packet exits a link at high rate. Congestion signaling (e.g. ECN marking of DCTCP [1]) is associated to the counter instead of the physical switch queue, which can be configured to represent a speed slower than the actual physical link. Thus, some "bandwidth headroom" can be reserved to process high priority traffic. On the other hand, QJUMP focuses on reducing the network interference that throughput-oriented applications might cause by causing high queuing delays. QJUMP claims that applications dominated by short flows exhibit low latency variance and that low throughputs require higher priorities whereas applications with high latency variance and high throughput require lower priorities. In order to reduce this network interference, end hosts perform rate limitation in a non-intrusive way; this enables the applications to specify their required priorities. These approaches are agnostic in the sense that they do not require to know in advance the size of the flows in order to schedule them. However, they do not aim at improving the scheduling but reducing the occupation of switch buffers. That is to say, improving the FCT of short flows is not a primary goal of these works. In addition, in the case of QJUMP, it requires an additional API which implies modifications in the applications in order to use it.

Moreover, PIAS [6] and KARUNA [9] are agnostic flow scheduling approaches that aim to minimize the FCT of short flows by controlling the packet scheduling. They leverage MLFQ to achieve this goal. In PIAS, end host track the amount of bytes sent by each flow. According to this information, end hosts mark packets to match priority levels that are configured at data center switches. This packet tagging is performed following a MLFQ-like approach. That is, packets initially are marked so that they enter into the highest priority queue at switches. When the flow has sent more than a given amount of bytes (i.e. the demotion threshold), packets are marked with the following lower priority level. Hence, the more bytes a flow sends, the lower the priority value used to mark its

packets. This means that demotion thresholds are defined and configured at end hosts whereas switches simply perform priority scheduling. KARUNA [9] can be considered an extension of PIAS, which extends to consider deadline constrained flows. KARUNA divides flows into three categories: deadline-constrained, non deadline-constrained with known sizes, and non deadline-constrained with unknown sizes. Deadline-constrained flows are tagged to enter into the highest priority queue within datacenter switches. Non deadline-constrained flows with known size are tagged to enter into a specific queue. Non-deadline constrained flows with unknown size are sieved through the MLFQ scheduler in a similar way to the approach used in PIAS.

A challenging task associated to MLFQ-based scheduling is the derivation of a set of demotion thresholds that minimizes the average and tail FCT. PIAS and KARUNA calculate these thresholds based on traffic information consisting in the CDF of the flow sizes of the workload that will be present in the network. After the derivation of the thresholds, they are distributed and deployed at end hosts. Then, they use these thresholds to perform the packet tagging procedure [6, 9].

We consider that this approach includes some limitations. Since traffic in DCN presents time and space variations, a set of thresholds that minimizes the FCT of a given workload might not be adequate for a different one [19]. Also, the mentioned state-of-the-art approaches do not update their demotion thresholds dynamically. As previously explained, they need to be derived by considering the properties of the new workload, and they need to be manually deployed at end hosts.

6. Conclusions and future work

In this paper, we have proposed an approach to adjust the demotion thresholds of a MLFQ-based flow scheduling approach. We consider that this approach is an important first step in order to achieve a truly workload-agnostic flow scheduling solution. In this sense, our proposal aims at overcoming some of the limitations present in the state-of-the-art such as the requirement of information about the CDF of the workload that will be present in the network.

We performed a preliminary evaluation of our approach in a small experimental topology as a proof-of-concept of the approach's operation. We verified its adaption capability and confirmed that it provides a minimization of the FCT of short flows at high traffic loads. We also observed that the use of percentiles of the completed flow sizes provide a useful hint for the adjustment of the demotion thresholds.

For future work, we propose to design a smarter mechanism for the definition of the reference percentiles. An important improvement that could be introduced in our proposal is the capacity to determine from the observation of the traffic which would be adequate values to define the percentiles, in order to increase the accuracy of the scheduler.

Finally, an important task to consider for future work would be the integration of this threshold adjustment in a real software switch. Although recent literature presents the concept of programmable switches [8, 21], these devices still have open questions regarding elements such as the structure of their queuing systems. Thus, we consider that well-known software switches [17] with a more robust internal architecture design can provide a more mature starting point in order to develop this threshold adjustment.

Acknowledgments

This work was supported by: the Universidad Nacional de Colombia (UNAL) through the "Outstanding Postgraduate Student" scholarship from 2012 to 2016; Colciencias, through the "567 - National Doctorate Studies" scholarship from 2013 to 2017; the Universidad de Medellín (UDEM); and the Universidade Federal do Rio Grande do Sul (UFRGS), Porto Alegre, Brazil.

References

[1] Alizadeh, M., Greenberg, A., Maltz, D.A., Padhye, J., Patel, P., Prabhakar, B., Sengupta, S. and Sridharan, M., Data Center TCP (DCTCP). Proceedings of the ACM SIGCOMM 2010 Conference, New York, NY, USA, 2010, pp. 63-74. DOI: 10.1145/1851275.1851192

[2] Alizadeh, M., Javanmard, A. and Prabhakar, B., Analysis of DCTCP: stability, convergence, and fairness. Proceedings of the ACM SIGMETRICS Joint International Conference on Measurement and Modeling of Computer Systems, New York, NY, USA, 2011, pp. 73-84. DOI: 10.1145/1993744.1993753

[3] Alizadeh, M., Kabbani, A., Edsall, T., Prabhakar, B., Vahdat, A. and Yasuda, M., Less is more: trading a little bandwidth for ultra-low latency in the data center. Proceedings of the 9th USENIX Conference on Networked Systems Design and Implementation, Berkeley, CA, USA, 2012, pp.19-19.

[4] Alizadeh, M., Yang, S., Sharif, M., Katti, S., McKeown, N., Prabhakar, B. and Shenker, S., pFabric: minimal near-optimal datacenter transport. Proceedings of the ACM SIGCOMM 2013 Conference on SIGCOMM, New York, NY, USA, 2013, pp. 435-446. DOI: 10.1145/2486001.2486031

[5] Bai, W., Chen, L., Chen, K., Han, D., Tian, C. and Wang, H., Information-agnostic flow scheduling for commodity data centers. Proceedings of the 12th USENIX Conference on Networked Systems Design and Implementation, Berkeley, CA, USA, 2015, pp. 455-468.

[6] Bai, W., Chen, L., Chen, K., Han, D., Tian, C. and Wang, H., PIAS: practical information-agnostic flow scheduling for commodity data centers. IEEE/ACM Transactions on Networking. 25(4), pp. 1954-1967, 2017. DOI: 10.1109/TNET.2017.2669216

[7] Benson, T., Akella, A. and Maltz, D.A., Network traffic characteristics of data centers in the wild. Proceedings of the 10th ACM SIGCOMM Conference on Internet Measurement, New York, NY, USA, 2010, pp. 267-280. DOI: 10.1145/1879141.1879175

[8] Bosshart, P., Daly, D., Gibb, G., Izzard, M., McKeown, N., Rexford, J., Schlesinger, C., Talayco, D., Vahdat, A., Varghese, G. and Walker, D., P4: programming protocol-independent packet processors. SIGCOMM Comput. Commun. Rev. 44(3), pp. 87-95, 2014. DOI: 10.1145/2656877.2656890

[9] Chen, L., Chen, K., Bai, W. and Alizadeh, M., Scheduling mix-flows in commodity datacenters with Karuna. Proceedings of the 2016 ACM SIGCOMM Conference, New York, NY, USA, 2016, pp. 174-187. DOI: 10.1145/2934872.2934888

[10] Corbato, F.J., Marjorie Merwin-Daggett and Daley, R.C., An experimental time-sharing system. Classic Operating Systems. P.B. Hansen, ed. Springer New York. 2001, pp. 117-137.

[11] Grosvenor, M.P., Schwarzkopf, M., Gog, I., Watson, R.N., Moore, A.W., Hand, S. and Crowcroft, J., Queues don't matter when you can JUMP Them! Proc. NSDI, 2015.
[12] Hoganson, K. and Brown, J., Intelligent mitigation in multilevel feedback queues. Proceedings of the SouthEast Conference, New York, NY, USA, 2017, pp. 158-163. DOI: 10.1145/3077286.3077319
[13] Hong, C.-Y., Caesar, M. and Godfrey, P.B., Finishing flows quickly with preemptive scheduling. Proceedings of the ACM SIGCOMM 2012 Conference on Applications, Technologies, Architectures, and Protocols for Computer Communication, New York, NY, USA, 2012, pp. 127-138. DOI: 10.1145/2342356.2342389
[14] Joy, S. and Nayak, A., Improving flow completion time for short flows in datacenter networks. 2015 IFIP/IEEE International Symposium on Integrated Network Management (IM), 2015, pp. 700-705. DOI: 10.1109/INM.2015.7140358
[15] Munir, A., Baig, G., Irteza, S.M., Qazi, I.A., Liu, A.X. and Dogar, F.R., Friends, not foes: synthesizing existing transport strategies for data center networks. Proceedings of the 2014 ACM Conference on SIGCOMM, New York, NY, USA, 2014, pp. 491-502. DOI: 10.1145/2740070.2626305
[16] Noormohammadpour, M. and Raghavendra, C.S., Datacenter traffic control: understanding techniques and trade-offs. IEEE Communications Surveys Tutorials. 99, pp. 1-1, 2017. DOI: 10.1109/COMST.2017.2782753
[17] Pfaff, B., Pettit, J., Koponen, T., Jackson, E.J., Zhou, A., Rajahalme, J., Gross, J., Wang, A., Stringer, J., Shelar, P. et al., The design and implementation of Open vSwitch. NSDI, 2015, pp. 117-130
[18] Rojas-Cessa, R., Kaymak, Y. and Dong, Z., Schemes for fast transmission of flows in data center networks. IEEE Communications Surveys Tutorials. 17(3), pp. 1391-1422, 2015. DOI: 10.1109/COMST.2015.2427199
[19] Roy, A., Zeng, H., Bagga, J., Porter, G. and Snoeren, A.C., Inside the social Network's (datacenter) Network. Proceedings of the 2015 ACM Conference on Special Interest Group on Data Communication, New York, NY, USA, 2015, pp. 123-137.
[20] Sivaraman, A., Cheung, A., Budiu, M., Kim, C., Alizadeh, M., Balakrishnan, H., Varghese, G., McKeown, N. and Licking, S., Packet transactions: high-level programming for line-rate switches. Proceedings of the 2016 ACM SIGCOMM Conference, New York, NY, USA, 2016, pp. 15-28. DOI: 10.1145/2785956.2787472
[21] Sivaraman, A., Kim, C., Krishnamoorthy, R., Dixit, A. and Budiu, M., DC.P4: programming the forwarding plane of a data-center switch. Proceedings of the 1st ACM SIGCOMM Symposium on Software Defined Networking Research, New York, NY, USA, 2015, pp. 2:1-2:8. DOI: 10.1145/2774993.2775007
[22] Sivaraman, A., Subramanian, S., Alizadeh, M., Chole, S., Chuang, S.-T., Agrawal, A., Balakrishnan, H., Edsall, T., Katti, S. and McKeown, N., Programmable packet scheduling at line rate. Proceedings of the 2016 ACM SIGCOMM Conference, New York, NY, USA, 2016, pp. 44-57. DOI: 10.1145/2934872.2934899

S.A. Gutiérrez, received the BSc. Eng in Computer Science degree in 2008 from Universidad de San Buenaventura, the MSc., Eng in Computer Science in 2011 from Universidad Nacional de Colombia, sede Medellín, and he is currently candidate to the degree of PhD in Computer Science from Universidad Nacional de Colombia. From 2000 to 2012, he worked as System Administrator and later as Senior Engineer, managing, operating, supporting and developing telecommunication solutions at different scales and criticality levels. He is currently full time lecturer at Universidad de Medellin, and previously he has been also part time lecturer at Universidad de San Buenaventura and Universidad Nacional de Colombia. His research interests include computer networks, security in computer networks, data center networks, software defined networks, programmable devices and application of pattern recognition and machine learning to computer networks.
ORCID: 0000-0003-2880-4601

M. Barcellos, is a CNPq 1D level researcher, senior member of the Association for Computing Machinery (ACM) and the Brazilian Computer Society (SBC). He received BSc. and MSc. degrees in Computer Science from Federal University of Rio Grande do Sul, Brazil (1989 and 1993, respectively) and PhD degree in Computer Science from University of Newcastle Upon Tyne (1998). Between 1999 and 2008, worked as a professor at UNISINOS university, spending 2003-2004 at BT Research Labs working for University of Manchester on high-performance multicast transport. Since 2008 Prof. Barcellos has been with the Federal University of Rio Grande do Sul (UFRGS), where he is an associate professor. He has authored many papers in leading vehicles related to computer networks and security, also serving as PC member, PC chair and General Chair. Prof. Barcellos was the elected chair of the Special Interest Group on Computer Security of the Brazilian Computer Society (CESeg/SBC) 2011-2012. He is the appointed Director of Diversity and Outreach in ACM SIGCOMM for the term 2017-2021. His current research interests are Internet measurements, programmable data planes, and security aspects of those networks.
ORCID: 0000-0002-1505-6408

J.W. Branch, received the BSc. in Mining Engineering, his MSc. degree in System Engineering and his PhD. in Engineering from Universidad Nacional de Colombia, Campus Medellín, in 1995, 1997 and 2007 respectively. Currently, He is full professor in the Department of Computer Science at Universidad Nacional de Colombia, Campus Medellín. His main research interests encompass computer vision, image processing and their applications to the industry field and applications of pattern recognition in the field of Computer Networks.
ORCID: 0000-0002-0378-028X

UNIVERSIDAD NACIONAL DE COLOMBIA
SEDE MEDELLÍN
FACULTAD DE MINAS

Área Curricular de Ingeniería
de Sistemas e Informática

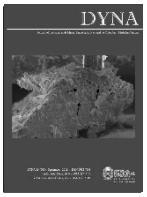
Oferta de Posgrados

Especialización en Sistemas
Especialización en Mercados de Energía
Maestría en Ingeniería - Ingeniería de Sistemas
Doctorado en Ingeniería- Sistemas e Informática

Mayor información:

E-mail: acsei_med@unal.edu.co
Teléfono: (57-4) 425 5365

UNIVERSIDAD NACIONAL DE COLOMBIA
SEDE MEDELLÍN
FACULTAD DE MINAS



DYNA
http://dyna.medellin.unal.edu.co/

Use of BOF slag and blast furnace dust in asphalt concrete: an alternative for the construction of pavements

Alfonso López-Díaz [a], Ricardo Ochoa-Díaz [b] & Gloria Elizabeth Grimaldo-León [c]

[a] *Grupo de Investigación en Materiales Siderúrgicos, Universidad Pedagógica y Tecnológica de Colombia, Tunja, Colombia. alfonso.lopez@uptc.edu.co*
[b] *Grupo de Investigación y Desarrollo en Infraestructura Vial, Universidad Pedagógica y Tecnológica de Colombia, Tunja, Colombia. ricardo.ochoa@uptc.edu.co*
[c] *Grupo de Investigación en Logística, Operaciones, Gestión y calidad, Universidad de Boyacá, Tunja, Colombia. gegrimaldo@uniboyaca.edu.co*

Received: February 12th, 2018. Received in revised form: June 6th, 2018. Accepted: June 12th, 2018.

Abstract
The boom in the construction of large engineering works has boosted the demand for steel, which has generated an increase in the production of steel waste, a situation that causes environmental problems due to the accumulation and inadequate disposal of these by-products. The use of industrial waste in different processes must be focused on sustainable development and the protection of the environment. This work was developed with the objective of ratifying the use of Basic Oxygen Furnace slag (BOF) as coarse aggregate and studying the alternative of using Blast Furnace Dust (BFD) as a fine aggregate; to manufacture asphalt hot mixes for pavements as an alternative to mitigate the environmental problems derived from the accumulation of this steel waste and the exploitation of non-renewable materials, such as gravel and sand. To achieve the objective, three types of asphalt mixtures were analyzed, a mixture with conventional materials (control) and two mixtures that partially and totally replace the coarse aggregate with BOF and the fine aggregate with BFD. The design of the mixtures was made with the RAtional Methodology for COmpacted geomaterials' DEnsification and Strength Analysis (RAMCODES), which is based on the principle of the vacuum polygon. Tests were carried out to evaluate the physical characteristics and the susceptibility to water and plastic deformation of each type of mixture. The results of this study confirm the use of BOF and indicate that it is feasible to use BFD as fine aggregate to partially replace conventional aggregates in road paving.

Keywords: steel waste; BOF slag; blast furnace dust; asphalt concrete.

Uso de escoria BOF y polvo de alto horno en concretos asfálticos: una alternativa para la construcción de pavimentos

Resumen
El auge de la construcción de grandes obras de ingeniería ha impulsado la demanda por acero, lo que ha generado un incremento en la producción de residuos siderúrgicos, una situación que causa problemas ambientales debido a la acumulación y no disposición adecuada de estos subproductos. El uso de residuos industriales en diferentes procesos debe estar enfocado hacia el desarrollo sostenible y la protección del medio ambiente. Este trabajo se desarrolló con el objetivo de ratificar el uso de la escoria de horno al oxigeno (BOF) como agregado grueso y estudiar la alternativa del uso de polvo de alto horno (BFD) como agregado fino; para fabricar mezclas asfálticas en caliente para pavimentos como una alternativa para mitigar los problemas ambientales derivados de la acumulación de residuos siderúrgicos y de la explotación de materiales no renovables, como la grava y la arena. Para lograr el objetivo, se analizaron tres tipos de mezclas asfálticas, una mezcla con materiales convencionales (control) y dos mezclas sustituyendo parcial y totalmente el agregado grueso por BOF y el agregado fino por polvo de AH. El diseño de las mezclas se realizó con la metodología Ramcodes, la cual se basa en el principio del polígono de vacíos. Se realizaron ensayos para evaluar las características físicas y la susceptibilidad al agua y deformación plástica de cada tipo de mezcla. Los resultados de este estudio confirman el uso de BOF e indican que es factible el uso de BFD como agregado fino para reemplazar parcialmente los agregados convencionales en la pavimentación de carreteras.

Palabras clave: residuos siderúrgicos; escoria BOF; Polvo de alto horno; concreto asfáltico.

1. Introduction

The slag produced in the steel industries is a by-product in the manufacture of steel. Three types of slag are known: Granulated Blast Furnace Slag (GBFS), Electric Arc Furnace (EAF) slag, and Basic Oxygen Furnace (BOF) slag [1]. The

How to cite: López-Díaz, A., Ochoa-Díaz, R. and Grimaldo-León, G., Use of BOF slag and blast furnace dust in asphalt concrete: an alternative for the construction of pavements. DYNA, 85(206), pp. 24-30, September, 2018.

© The author; licensee Universidad Nacional de Colombia.

BOF slag is produced during the transformation process of the pig iron coming from the steel blast furnace. The pig iron reacts with lime, silicates, aluminum oxides, manganese oxides, magnesium oxides, and ferrites depending on the quality of steel produced [2]. On the other hand, the Blast Furnace Dust (BFD) is produced during the transformation of iron ore into pig iron. In this process the iron ore, coke, and limestone are melted at a temperature of 1500 ° C. Additionally, during the manufacturing process of pig iron, gases and particulate fine material are generated, and the fine particulate material is decanted into collectors. BOF slag and BFD are produced in integrated steel mills. In Colombia, the only integrated steel mill is *Acerías Paz del Río S.A.* (located in the department of Boyacá, Colombia). This steelmaker produces approximately 50,000 tons of BOF slag and 20,000 tons of AH powder, a situation that generates a problem for the environment.

Taking into account the above, it is necessary to look for an alternative use of BOF slag and BFD. In this regard, the literature reports the use of BOF slag as aggregate in asphalt concrete or hydraulic concrete [3]. A possibility that reduces the use of non-renewable natural aggregates, such as limestone and sand, in the construction and improvement of roads, reducing the environmental impact in the construction of roads.

The use of BOF slag as coarse aggregate and BFD as fine aggregate in asphalt concrete requires knowledge of its physical and chemical characteristics. In this context, the research processes, in general, include two stages. First, the X-Ray Fluorescence characterization (XRF) of the BOF and BFD, as well as the determination of its mineralogical, chemical, and micro-topographic properties using a Scanning Electron Microscope (SEM) system. Second, the design and manufacture of mixtures that incorporate BOF and BFD applying the RAtional Methodology for COmpacted geomaterials' DEnsification and Strength Analysis (RAMCODES), seeking to obtain the basic requirements of stability and flow, susceptibility to water, and resistance to plastic deformation of prepared mixtures. Finally, the results obtained are analyzed and used to determine the feasibility of using this steel waste in the manufacture of asphalt concrete used in road construction.

2. Materials and methodology

2.1. Materials

BOF slag and BFD were supplied by the steel mill Acerías Paz del Río S.A, Fig. 1. The limestone was chosen as coarse aggregate and the sand as fine aggregate for the reference mixture. The basic physical properties of the materials used are shown in Table 1. The tests were carried out in accordance with Colombian standards INVIAS-2013 and international ASTM standards [4]. The asphalt cement used was 80/100 penetration and comes from the company IncoAsfaltos S.A.S. (Colombia). The results of the characterization tests were found within the limits of the specification and are shown in Table 2. The asphalt mixture chosen, for the development of the research, was a MDC-19 according to the specifications INV E-450-13, for a NT3 transit level (ESALs> $5.0x10^6$) [5].

2.2. Methodology

2.2.1. Tests for characterization of BOF and BFD

1. Chemical composition: X-ray fluorescence was used to quantitatively determine the elements in BOF and BFD.
2. Topographical information: scanning electron microscopy (SEM) was used to determine the morphology of BOF and BFD. The digital topographic images of the samples were obtained.

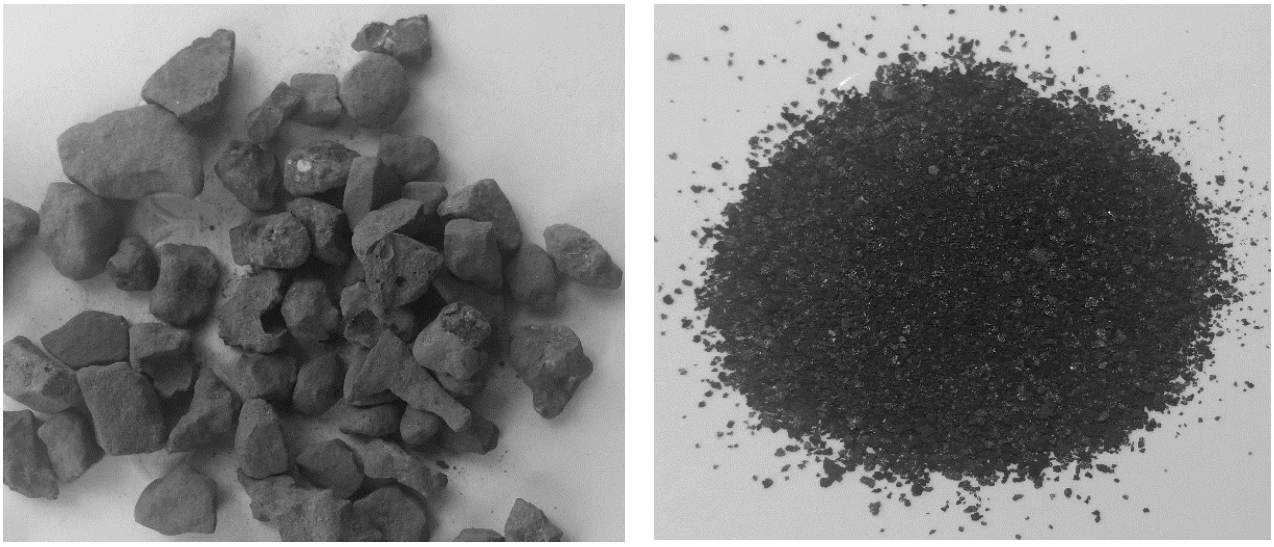


Figure 1. (a) BOF slag (b) BFD
Source: The authors.

Table 1.
Basic physical properties of the aggregates used (BOF, BFD, limestone and sand)

Properties	Coarse aggregate		Fine aggregate		Specification	Standard
	BOF	Limestone	BFD	Sand		
Loss Angeles Abrasion (%)	20	20	N/A	N/A	<25	ASTM C 131
Degradation (Micro-Deval) (%)	20	20	N/A	N/A	<20	ASTM D 6928
Soundness test (%)	1.72	3.20	-	3.21	<18	ASTM C 88
Fractured faces (%)	91.4	94	N/A	N/A	>85	ASTM D 5821
Plasticity index (%)	N/A	N/A	NP	NP	NP	ASTM D 4318
Sand equivalent (%)	N/A	N/A	93.8	68.5	>50	ASTM D 2919
Gsb	2.468	2.593	2.363	2.722	-	
Gss	2.564	2.605	2.496	2.743	-	
Gsa	2.729	2.625	2.727	2.779	-	ASTM C 127/128
Absorption (%)	3.8	0.47	5.6	0.59	-	

Source: The authors

Table 2.
Basic properties of asphalt cement

Properties	Measured values	Specification	Standard
Penetration at 25°C (0.1 mm)	81.35	80 - 100	ASTM D 5-97
Ductility, 5 cm/min, 25°C (cm)	>100	>100	ASTM D 113
Softening point (°C)	50.5	>45	ASTM D 36
Flashpoint (°C)	245	>230	ASTM D 92
Viscosity at 60°C (P)	2336	>1000	ASTM D 2171

Source: The authors

2.2.2. Design of the Mixtures

The chosen gradation has a maximum nominal size of 19 mm and it was designed following Ramcodes design method [6]. This methodology has been successfully applied in the design and quality control of compacted soils for structural fillings and roads, as well as for the design and production control of asphalt mixtures. In the particular case of asphalt mixtures, Ramcodes has two very powerful analysis tools, which are the gradation chart [7] and the polygon of voids [8]. The gradation chart is an analytical environment in which several gradation of asphalt mixtures can be represented simultaneously. This allows to associate the different gradation to the mechanical or hydraulic responses, as well as to the production costs. An advantage that allows optimizing the use of the raw material in the production of asphalt mix. On the other hand, the polygon of voids is a fully automated graphic construction that allows an optimum content of asphalt cement to be determined based on the void specifications and the specific gravities of aggregates and asphalt cement. This method has the advantage to be verified only with the preparation and testing of three briquettes in contrast to the traditional procedures that use 12 to 15 briquettes (Superpave or Marshall, respectively). It is important to emphasize that it has been verified that the results with Ramcodes are very similar to those obtained with the Marshall methodology [9].

Three types of mixtures were initially designed. M1 mixture (control) was prepared using conventional materials (limestone as coarse aggregate and sand as fine aggregate). M2 mixture was prepared by replacing the coarse aggregate with BOF by 50% and the fine aggregate with BFD in equal proportion. M3 has 0% of natural aggregates. The work gradation for the three types of mixture is shown in Fig. 2.

The indicators that were taken into account for the design of each of the asphalt mixtures were: unit weight of the compacted mixture, stability, flow, percentage of voids with air in the mixture, the vacuum between mineral aggregates, and voids filled with binder. The performance tests for each of the mixtures were: susceptibility to water and resistance to plastic deformation.

Susceptibility to water

The water susceptibility test using the indirect tensile test evaluates the change in tensile strength resulting from the effects of saturation and accelerated conditioning to water, on asphaltic mixtures compacted in the laboratory. The test was carried out following the procedure of standard INV E-725-13 and ASTM D4867. Six test pieces were prepared for each type of mixture, three to be tested in dry and three to be tested after partial saturation. The wet group samples were taken to a water bath for 24 hours at a temperature of 60 °C, after which time, the two groups of test pieces were immersed into a water bath at 25 °C for one hour. Indirect tensile strength was determined using equation (1).

$$R_T = \frac{2000P}{\pi h D} \quad (1)$$

Where:
R_T = Tensile strength (kPa)
P = Maximum load applied (N)
h = Thickness of the specimen (mm)
D = Diameter of the specimen (mm)

The tensile strength ratio (RRT) was calculated as the ratio of the average resistance to the tension of the water conditioned subgroup (RTH) and the average resistance to the tension of the subgroup maintained in dry (RTS), as expressed in equation (2).

$$RRT = \left[\frac{R_{TH}}{R_{TS}}\right] * 100 \quad (2)$$

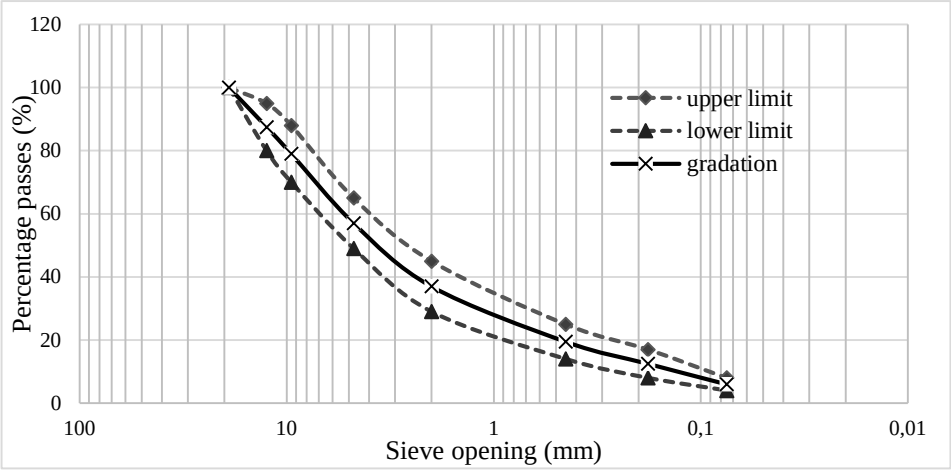


Figure 2. Working gradation for mixtures type MCD-19 according to article 450-13 INVIAS
Source: The authors.

Resistance to plastic deformation

The plastic deformation resistance test was carried out to evaluate the resistance to permanent deformation or rutting. The test was carried out in accordance with the Colombian standard INV E-756-13 and the European standard EN-12697-22, using the "Wheel Tracking Test" equipment. The test was carried out at a constant temperature of 60 °C, passing a metal wheel of 20 cm in diameter, equipped with a tread of solid rubber 5 cm wide and 2 cm thick, which exerts a contact pressure on the surface of the test piece of 900 KN/m^2.

The total deformations were measured in minutes 1, 3 and 5, timing from the beginning of the test. Subsequently, the deformations were measured every 5 minutes until completing 45 minutes, and from this moment, measurements were taken every 15 minutes until the end of the test at 120 minutes. From the deformations obtained at the aforementioned times, the average deformation velocity, corresponding to the time intervals, was calculated by means of equation (3).

$$V_{t2}/V_{t1} = \frac{d_{t2}-d_{t1}}{t_2-t_1} \quad (3)$$

Where:

V_{t2}/V_{t1} = Average speed of deformation, in the time interval between t_1 y t_2 (µm/min)

d_{t1}, d_{t2} = Deformations to t_1 y t_2 respectively (µm)

t_1, t_2 = Times in the established time (min)

3. Results and discussions

3.1. Chemical components of BOF and BFD

The percentage by weight of each of the components present in the limestone and BOF slag are different, the predominant components in limestone are CaO and SiO2 while in BOF slag are CaO and Fe2O3. In BFD the predominant component is Fe2O3 (77.5%) and in sand is SiO2 (88.7%). BOF slag has a higher CaO/SiO2 (4.3) ratio than the one found in limestone (3.8). BFD has a CaO / SiO2 ratio of 0.9 while sand ratio is 0.005, as shown in Table 3. It is important to emphasize that this ratio represents the level of alkalinity of the aggregate, and also, the presence of some high ratios lead to a stronger affinity with asphalt [10].

3.2. Microscopic morphology

Fig. 3 (a) shows the microscopic morphology of the BOF slag at a scale of 1.00KX. The microphotograph shows a rough texture and very irregular angularity, which facilitates the adherence with the asphalt. The microscopic morphology of BFD is shown in Fig. 3 (b) at a scale of 500X, in which a number of micropores are observed, which facilitates the entry of asphalt [11].

3.3. Design of the mixtures

3.3.1. Preliminary design

Initially, the granulometric dosage was made for each mixture. Next, the optimal binder content was determined with Ramcodes, taking into account the results of the characterization of the aggregates and the binder. In this methodology, an analysis of voids in the mixture is carried out: air voids (Va), voids in the mineral aggregate (VMA) and voids filled with asphalt (VFA), which are related to the behavior of the compacted mixtures. Voids based on the percentage of binder (% Pb) and the bulk specific gravity of the mixture (Gmb) are represented in maps with isolines for the values allowed in the specifications (Table 4). The intersection of these lines produces a graphical construction in the space % Pb-Gmb, which gives rise to the polygon of voids. The centroid of the polygon establishes the optimal binder content and the specific gravity bulk (density). Fig. 4 presents the empty polygon for the mixture M2.

Following this methodology, an optimum percentage of asphalt of 5% was obtained and a density of 2.378 gr/cm3 for the mixture M1, 6.5% of asphalt and 2.375 gr/cm3 of density for the mixture M2, and 9.3% of asphalt, and 2.335 gr/cm3 of density for the M3 mixture.

Table 3.
Chemical components of BOF, limestone, BFD and sand

Component (% in weigh)	MgO	Al_2O_3	SiO_2	P_2O_5	CaO	MnO	Fe_2O_3	Others
BOF	2.70	4.90	10.80	2.10	46.80	2.00	28.80	1.73
Limestone	3.80	9.30	16.60	-	63.40	0.17	3.04	3.63
BFD	1.00	3.60	5.50	0.20	4.95	3.32	77.50	0.90
Sand	1.60	7.30	88.70	-	0.46	-	0.99	1.00

Source: The authors, based on laboratory results.

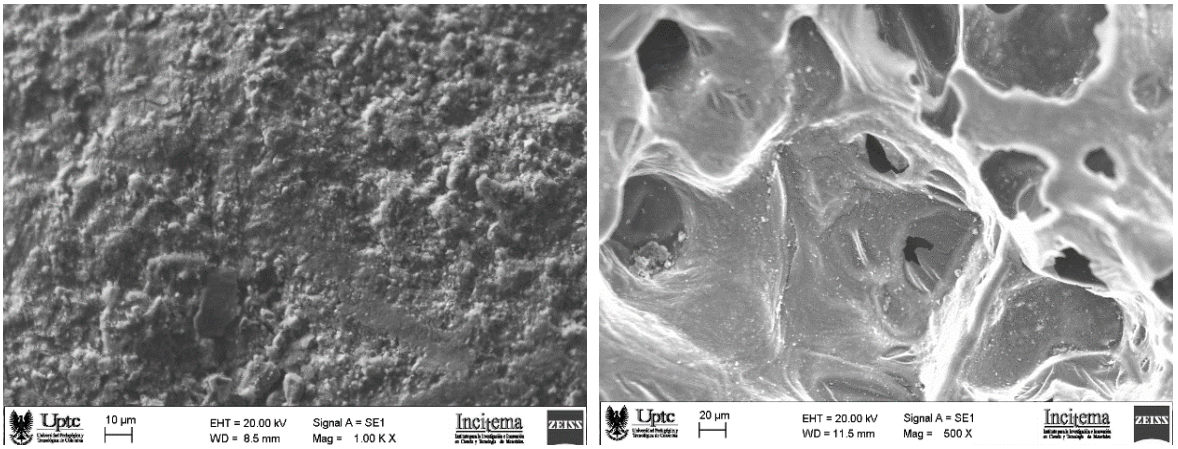


Figure 3. Microscopic morphology (a) BOF slag; (b) BFD
Source: The authors, according to tests carried out in the INCITEMA-Uptc, Tunja.

Once the optimum percentage of asphalt was determined, three test tubes of each mixture were prepared to verify compliance with the requirements established for voids in the specifications. The results are shown in Table 4.

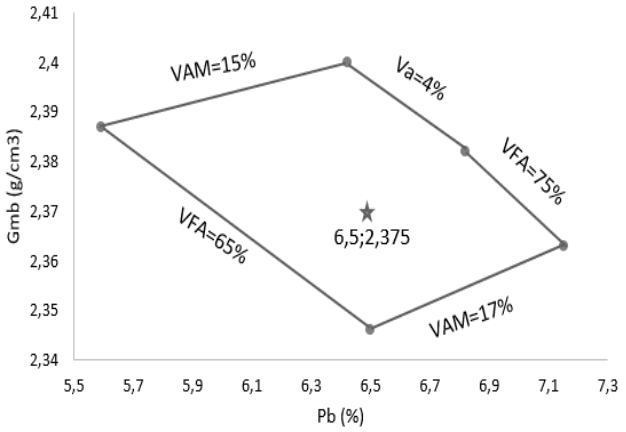


Figure 4. The polygon of voids for the M2 mixture
Source: The authors

Table 4.
Results verification of mixtures parameters

Parameter	M1	M2	M3	Specification INV E 450-13
Va, %	4.70	4.70	4.60	4.0 – 6.0
VMA, % min.	15.20	15.51	15.48	> 15
VFA, %	69.47	69.55	69.645	65 -75

Source: The authors.

Table 5.
Results of mechanical characteristics of the mixtures

Parameter	M1	M2	M3	Specification INV E 450-13
Stability, N	9960	11390	10150	>9000
Flow, mm	2.87	3.40	3.48	2.0 – 3.5

Source: The authors

Table 5 shows the results found in Marshall stability and flow tests. In relation to stability, the three mixtures exceed the minimum requirement of 9000 N established in the specifications of INVIAS-2013. In the case of flow, the three mixtures comply with the values of the requirement. However, M2 and M3 mixtures have higher values than M1 mixture, which is attributed to the substitution of the fine aggregate by BFD in percentages of 50 and 100%, respectively. BFD has a higher percentage of absorption (5.65%) than sand (0.59%), which allows a greater amount of asphalt for the union of the particles.

3.3.2. Performance tests

Once the working formula for each of the mixtures was obtained, the tests for the verification of the design were carried out, as well as the determination of the properties of water susceptibility and resistance to plastic deformation.

Table 6 presents the results of the RRT test performed with the specimens prepared for each type of mixture.

It was determined that the average RRT values of the different mix designs decrease as the content of BOF and BFD increases, but the minimum requirement (80%) required in the standard INV E 450-13 is achieved.

Table 6.
RTT trial results

Condition	Id	P_{ult}(N)	RT(KPa)	RT_{ave}(KPa)	RTT_{ave}(%)
M1					
Wet	M1-3	8030	835.6	825.2	
	M1-5	7880	814.8		95.4
Dry	M1-7	8310	878.6	865.3	
	M1-8	8240	850.0		
M2					
Wet	M2-2	4750	478.6	474.9	
	M2-6	4680	471.1		86.1
Dry	M2-7	5800	569.7	557.2	
	M2-9	5520	544.7		
M3					
Wet	M3-1	3620	340.9	338.9	
	M3-2	3577	336.9		80.0
Dry	M3-5	4610	428.9	426.9	
	M3-6	4460	423.8		

Source: The authors

Fig. 5 shows the results of susceptibility testing to permanent deformation. The M1 mixture showed a maximum deformation of 1.85 mm, while M2 and M3 mixtures (modified with BOF and BFD) showed a greater deformation of 2.2 mm and 2.3 mm, respectively.

The deformation speed was calculated for the intervals between 30 - 45 minutes, 75 - 90 minutes, and 105 - 120 minutes for each of the mixtures. The results are shown in Fig. 6.

In the first interval (30 - 45 minutes) the deformation speed was very similar in the three types of mixtures. In the second interval (75 - 90 minutes) there was a greater difference between the control mixture (M1) and the modified mixtures with BOF and BFD, and the higher deformation rate was observed in the mixture M1. In the case of the third interval (105-120 minutes), like the second interval, a higher deformation speed of the mixture M1 was observed.

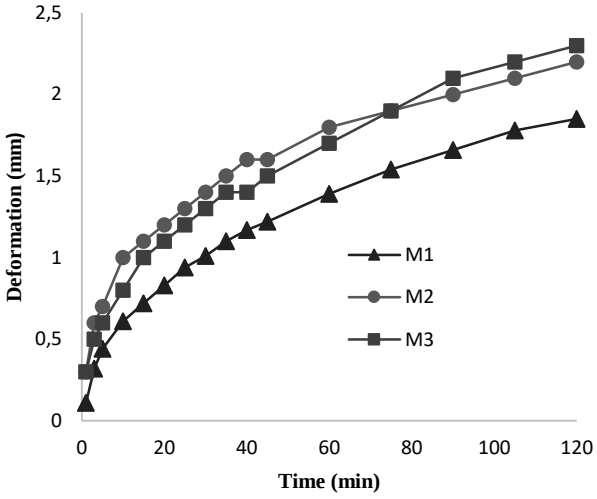


Figure 5. Evolution of deformation
Source: The authors.

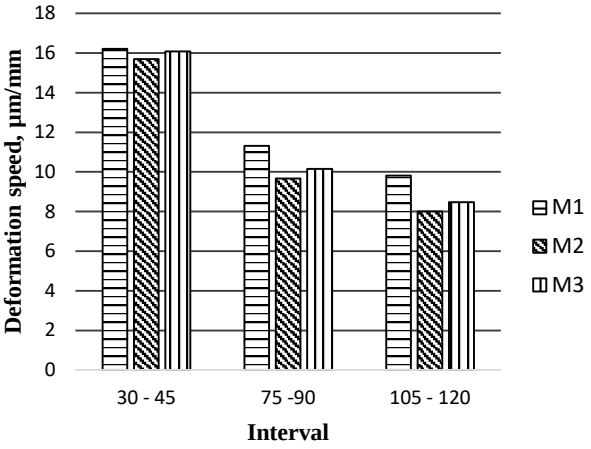


Figure 6. Deformation speed
Source: The authors.

4. Conclusions

This document studies the viability of the use of steel residues (BOF slag and BFD) as aggregates in asphalt mixtures to pave roads to generate an alternative to mitigate the environmental impact derived from the exploitation of non-renewable materials and the inadequate accumulation of this waste. For this purpose, the performance of samples of asphalt concrete was evaluated by partially and totally replacing the conventional aggregates with BOF slag and BFD. Based on the results of this study, the following conclusions are presented:

- The results of the tests to know the chemical composition of the BOF slag and BFD indicate that these materials can be used as aggregates in asphalt mixtures and do not present a risk to the environment.
- The comparison of steel residues with traditional stone aggregates shows that the CaO/SiO2 ratio (which defines the level of alkalinity of the materials) is similar

between the BOF slag and the limestone. On the contrary, in the case of fine aggregates a difference is observed. BFD has a higher alkalinity than sand, which implies a greater affinity of this powder with the asphalt cement.

- The stability improves in the mixtures with slag BOF and BFD, the improvement in the mixture M2 with proportion 50-50 of each material being more noticeable. Likewise, an increase in the flow values was observed for modified mixtures with BOF slag and BFD, being higher in the M3 mixture prepared with 100% residues. This is due to the increase in the optimum content of asphalt cement thanks to the porous characteristics of BFD.
- The results of the RTT test indicate that the ratio between the indirect tensile strengths of the wet and dry samples decreases with the BOF slag and BFD content.
- The deformations obtained in the test of susceptibility to permanent deformation are very similar in the mixtures prepared with BOF and BFD slag. In addition, M2 and M3 mixtures present greater deformation than the control mixture, without being much superior.
- The deformation speed in the test of susceptibility to permanent deformation or rutting indicates a better behavior of the modified mixtures with the passage of time. This is due to the increase in the curing and reaction of steel waste with asphalt cement over time.
- More research should be done to evaluate the feasibility of using other types of slag (mixed or each residue individually) in asphalt mixtures or in base layers for pavements in high traffic road projects. Similarly, it is suggested that the studies include the evaluation of parameters such as resistance to permanent deformation, moisture damage, rigidity, and fatigue of the composite material.
- The results obtained in this research contribute to a better understanding of the implications of the manufacture of asphalt mixtures with unconventional materials or waste, and also, suggest that the incorporation of these waste residues are a feasible alternative for the construction of roads.
- The contribution to the environment in these types of projects focuses on reducing the use of non-renewable natural resources and the accumulation of waste to improve the environmental conditions of the areas surrounding the steel factories.

Acknowledgements

The authors thank the company *Acerías Paz del Río S.A.* for the support and supply of the materials; to the company *IncoAsfaltos S.A.S.* for the supply of asphalt cement; to the *Uptc INCITEMA*, for the development of the chemical characterization tests of the materials and, finally, to the Engineer Manuel Sierra, Coordinator of the Pavement Laboratory of *Universidad Pedagógica y Tecnológica de Colombia* (Tunja, Colombia). The Governorate of Boyacá is also thanked for their support through the COLCIENCIAS announcement 733 of 2015.

References

[1] Kambole, A., Paige-Green, P., Kupolati, W., Ndambuki, J. and Adeboje, A., Basic oxygen furnace slag for road pavements: a review of material characteristics and performance for effective utilization in southern Africa. Construction and Building Materials. 148, pp. 618-631, 2017. DOI: 10.1016/j.conbuildmat.2017.05.036

[2] Xie, J., Wu, S., Zhang, L., Xiao, Y., Liu, Q., Yang, C. and Nie, S., Material characterization and performance evaluation of asphalt mixture Incorporating basic oxygen furnace slag (BFO) sludge. Construction and Building Materials. 147, pp. 362-370, 2017. DOI: 10.1016/j.conbuildmat.2017.04.131

[3] Li, Ch., Chen, Z., Wu, Sh., Li, B., Xie, J. and Xiao, Y., Effects of steel slag fillers on the rheological properties of asphalt mastic. Construction and Building Materials. 145, pp. 383-391, 2017. DOI: 10.1016/j.conbuildmat.2017.04.034

[4] Instituto Nacional de Vías-INVIAS. Especificaciones generales de construcción de carreteras. 2013.

[5] Instituto Nacional de Vías-INVIAS. Normas de ensayos de materiales para carreteras. 2013.

[6] Sánchez-Leal, F., et al., RAMCODES: Metodología racional para el análisis de densificación y resistencia de geomateriales compactados. Descripción de la metodología y campo de aplicación. Publicación Técnica 200 ed. Sanfandila, Querétaro, México, 2002. ISSN 0188-7297.

[7] Sánchez-Leal, F., Gradation chart for asphalt mixes: development. Journal of Materials in Civil Engineering. ASCE. 19(2), 2007. DOI: 1061/(ASCE)0899-1561(2007)19:2(185).

[8] Sánchez-Leal, F., Anguas, P., Larreal, M. and López, D., Polyvoids: analytical tool for Superpave HMA design. Journal of Materials in Civil Engineering ASCE. 23(8), 2011. DOI: 10.1061(ASCE) MT.1943-5533.0000275

[9] Ochoa-Díaz, R., Analysis of the use of coal tar as a binder in bituminous mixtures, using Marshall and Ramcodes. Journal of Physics: Conference Series 466-012034, pp. 1-4, 2013. DOI: 10.1088/1742-6596/466/1/012034

[10] Jun, X., Shaopeng, W., Juntao, L., Jun, C., Zongwu, Ch. and Wei, W., Recycling of basic oxygen furnace slag in asphalt mixture: material characterization & moisture damage investigation, Construction and Building Materials, 36, pp. 467-474, 2012. DOI: 10.1016/J.CONBUILDMAT.2012.06.023.

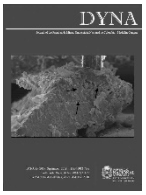
[11] Ochoa-Díaz, R., Blast furnace dust and phosphorous slag, new materials for use in road engineering, Journal of Physics: Conf. Series 935- 012003, pp. 1-4, 2017. DOI: 10.1088/1742-6596/935/1/012003.

A. López-Díaz, received the BSc. in Metallurgical Engineer from the Universidad Pedagógica y Tecnológica de Colombia, Tunja, Colombia; and the PhD. in Engineering from the Rheinisch-Westfälische Technische Hochschule Aachen, Aachen, North Rhine-Westphalia, Germany. He is expert in iron and steel; professor with professional, academic and research experience in the area of steel processes. He has been the main researcher in different research projects funded by with Colciencias, Acerías Paz del Río, Diaco Gerdau and Cerromatoso.
ORCID: 0000-0002-2983-7352

R. Ochoa-Díaz, received the BSc. in Transportation and Roads Engineer and MSc. degree in Road Infrastructure, both from the Universidad Pedagógica y Tecnológica de Colombia, Tunja, Colombia. And PhD. (c) in Engineering and Materials Science at the Universidad Pedagógica y Tecnológica de Colombia, with scholarship from the Gobernación de Boyacá, in accordance with Call 733 of Colciencias 2015. He is professor with professional, academic and research experience in the area of pavements and new materials. He is active researcher of the road infrastructure research and development group, Grinfravial, at the School of Transportation and Roads Engineering the Universidad Pedagógica y Tecnológica de Colombia.
ORCID: 0000-0003-1151-7884

G.E. Grimaldo-León, received the BSc. in Industrial Production Engineer from the Universidad Francisco de Paula Santander, Colombia. MBA in Business Management from the Universidad Autónoma de Bucaramanga, Colombia. She is research professor at the Universidad de Boyacá in the area of business management and researcher of the LOGyCA research group at the Universidad de Boyacá, Colombia.
ORCID: 0000-0002-8211-4305

UNIVERSIDAD NACIONAL DE COLOMBIA
SEDE MEDELLÍN
FACULTAD DE MINAS



DYNA
http://dyna.medellin.unal.edu.co/

Impact on the direct costs of social interest and priority interest housing by including new construction standards: Cali case

Mauricio Chávez-Calle, Diego Darío Pérez-Ruiz & María Fernanda Serrano-Guzmán

School of Engineering, Pontificia Universidad Javeriana, Cali, Colombia. mau_chavez@hotmail.com, ddperez@javerianacali.edu.co, maria.serrano@javerianacali.edu.co

Received: November 24th, de 2017. Received in revised form: May 16th, 2018. Accepted: June 13th, 2018

Abstract
Social interest housing (VIS, in Spanish) and priority interest housing (VIP, in Spanish) programs have been promoted in Colombia to provide affordable housing to low-income households. Currently, in addition to the Colombian Seismic Resistant Construction Regulations, last updated in 2010 (NSR-2010), there are other mandatory construction regulation that have been issued after 2010, producing an additional cost per square-meter of constructed area and exceeding the maximum limits established for these types of residential projects. Adjust the project to the established limits result in area reduction of the areas and quality of construction finishes of the final product. In this research, historical statistics of the construction costs of VIS and VIP in Cali are reviewed, and the impact on the cost of these housing types with respect to the inclusion of new technical dispositions is evaluated. The results reveal that the established maximum values for these types of projects must be adjusted due to the fact that the new standards must be incorporated.

Keywords: social housing; cost; technical requirements.

Impacto en costos directos de vivienda de interés social y de interés prioritario por inclusión de nuevas normas de construcción: caso Cali

Resumen
Los programas de vivienda de interés social (VIS) y de vivienda de interés prioritario (VIP) han sido impulsados en Colombia para proveer una vivienda digna a los hogares de menos ingresos. En la actualidad, además de la existencia del Reglamento Colombiano de Construcción Sismo (NSR-2010), existen otras disposiciones técnicas de obligatorio cumplimiento las cuales están generando costos adicionales en el metro cuadrado de vivienda, excediendo los topes máximos establecidos para este tipo proyectos, con la consecuente repercusión en disminución de áreas y en acabados del producto final. En esta investigación se revisan las estadísticas históricas de costos de la construcción de VIS y VIP en Cali y se evalúa el impacto en los costos de estas viviendas ante la inclusión de las nuevas disposiciones técnicas. Los resultados revelan que, si bien es cierto las nuevas normas deben ser incorporadas, deben ajustarse los valores máximos establecidos para este tipo de proyectos.

Palabras clave: vivienda social; costo; requerimientos técnicos.

1. Introduction

The obligation to comply with Article 51 of the Constitution of Colombia—"All Colombians have the right to a decent housing" [1]—makes it such that this right in Colombia is specifically one of the paths with which the State seeks to guarantee the quality of life of the population. This fact explains the existence of social and priority housing programs to provide housing solutions to low-income households [2].

Currently, private builders are generally responsible for the construction of social interest housing (VIS, in Spanish) and priority interest housing (VIP, in Spanish) [3] for amounts that should not exceed 135 times the statutory monthly minimum wage (SMMLV, in Spanish) and 70 times the SMMLV, respectively [4]. Moreover, from the

How to cite: Chávez-Calle, M., Pérez-Ruiz, D.D. and Serrano-Guzmán, M.F., Impact on the direct costs of social interest and priority interest housing by including new construction standards: Cali case. DYNA, 85(206), pp. 31-38, September, 2018.

© The author; licensee Universidad Nacional de Colombia.

perspective of the State, technical and economic guidelines that govern the construction of these projects are being defined [5], sometimes offering conditions that go beyond economic policies and technical aspects [6].

Currently, construction regulations have arisen in addition to the Colombian Regulation of Earthquake Resistant Construction (NSR-10), including the Technical Regulation of Electrical Installations (RETIE, in Spanish), Technical Regulation of the Drinking Water and Basic Sanitation Sector (RAS-2000), Parameters and Technical Guidelines for Sustainable Construction - Guide for Water and Energy Saving in Buildings, Safe Housing Law, Technical Regulation for Internal Telecommunication Networks (RITEL, in Spanish), Administrative, Operational, Technical and Academic Regulations of Firefighters of Colombia and, in the case of Cali, Earthquake Microzoning of Santiago de Cali. All these technical regulations are generating construction cost overruns and therefore have an impact on the square-meter increase to the final consumer.

Since the VIS and VIP prices are based on the SMMLV, the only increment that is reflected year after year is the annual increase in the statutory monthly minimum wage, for which the builder must build within the established price range, including the mandatory technical provisions for this type of housing, despite the costs entailed.

This research analyzes the impact on direct costs per constructed square-meter that involves the implementation of the new technical criteria of the Colombian Regulation of Earthquake Resistant Construction (NSR-10) in relation to fire protection networks and fire detection equipment, gas networks, and communication networks, which affect the square-meter increase to the final consumer. The study was based on the analysis of detailed technical and budgetary information of four social interest housing projects and two priority interest housing projects, which were designed and built from 2010 onward and were based on technical regulations in force at the time of approval and start of construction.

1.1. Problem statement

Colombia has numerous laws, decrees, resolutions and technical standards issued by multiple state or autonomous entities that mandate or regulate technical aspects of mandatory compliance in the construction of buildings. These regulations, which includes structural design aspects (NSR-10), electrical installations (RETIE, in Spanish), telecommunications (RITEL, in Spanish), hydro-sanitary (RAS2000), and fire protection systems and human safety (Firefighters), among others, are in a process of continuous adjustment, updating or coming into force. In addition, other requirements related to safety, occupational health and the environment are also incorporated in construction projects and demand training and certified personnel for working at heights and handling sector-specific tools.

Even though the introduction of some of these standards has been progressive, it is evident that, to a greater or lesser extent, their application affects the direct construction costs of VIS and VIP projects, either because they affect design parameters, increase the requirements of specifications or include new conditions that did not previously exist and are to apply from the implementation date of the standard. This affects the quality of the delivered housing by decreasing the usable area and eliminating finishes.

2. Social interest housing in Latin America

The main referents regarding social interest housing in Latin America are in Chile, Brazil and Mexico. Particularly, the Chilean model has been incorporated by the Banco Interamericano de Desarrollo (Inter-American Development Bank) due to its tradition and evolution [7], and it is adapted for the Colombian case. Subsidies in Brazil are granted based on income, favoring people with lower incomes. Meanwhile, Chile grants subsidies according to family condition in terms of qualifications such as for vulnerable, emerging and middle-income families, categorization according to which subsidies of US $18,500, US $20,000 and US $13,200 are granted, respectively.

Regarding Mexico, the maximum subsidy is US $4,900 and is granted to families with incomes under US $740. In the Colombian case, the subsidy is US $9,000 for displaced families, and in other cases for amounts of US $6,000. Table 1 summarizes the characteristics of different social housing programs, as previously discussed. The policy models of these countries are very similar and aim mainly to bring the housing supply closer to the economic possibilities of demand, using subsidies, savings and mortgage loans.

3. Social interest housing in Colombia

Throughout the history of Colombia, different programs have been developed to satisfy the need of housing to reach what today is known as social interest and priority interest housing. These changes are outlined in public and legislative policies as well as in regulatory decrees that included the creation of institutions such as the Banco Agrícola Hipotecario (Agricultural Mortgage Bank) (1926), Banco Central Hipotecario (Central Mortgage Bank, BCH in Spanish) (1932), and Instituto de Credito Territorial (Local Credit Institute, ICT in Spanish) (1939) [8]. Subsequently, other programs emerged for financing low-income housing (1946), housing subsidies (1954) and systems of raising funds through private savings with figures such as the UPAC (Units of Constant Purchasing Power, UPAC in Spanish) (1972), until reaching the national system of social interest housing that emerged between 1989 and 2000. Later, between 2006 and 2010 the Friendly Housing (Vivienda Amable) Policy was implemented through the “Friendly Cities and Housing” Plan, the Plan to Promote Productivity and Employment (PIPE, in Spanish), which attempted to stimulate the economic activity in the short and medium term through the priority interest housing program for people with savings, and the expansion of coverage to the interest rate for mortgage loans or housing leasing contracts for the acquisition of new homes between 135 and 335 SMMLV [9].

Table 1.
Comparison of characteristics of social interest housing programs in Latin America.

Country	Brazil	Chile	Mexico	Colombia
Program	My home My life (Mi casa Mi vida)	Buy your home (Comprar tu vivienda)	This is your home (Ésta es tu casa)	Macro-projects of Social Interest and Urban Renovation (Macroproyectos de Interés Social y Renovación Urbana)
Period	2009-2016	2011-2017	2011-2017	2008-2014
Subsidies	For families with monthly incomes below US$1,700	Depends on the family	For families with monthly incomes below US$400	For families with monthly incomes below US$1,150
Value of the home	14,000	18,500	8,908	16,900
% Financing	90	97.56	55	10

Source: Taken and adapted from [7]

3.1. Quality of social interest housing in Colombia

In the guide "Quality of social interest housing", the following attributes are established for the quality concept: population factors for the formulation of the project, quality parameters at the moment of selecting the land, determinants for the formulation of the urban design and determinants for the formulation of the architectural design [10]. However, according to the Information Brochure No. 21, "*the human right to adequate housing*", from the High Commissioner office for Human Rights of the UN, the minimum criteria for adequate housing are tenure security, availability of services, materials, facilities and infrastructure, affordability, habitability, accessibility, location and cultural adequacy.

Taking into consideration the previous referents, it was proposed in Colombia that the new housing should have adequate sleeping area, clothing closets, personal hygiene and laundry and allow for the storage, washing, preparing, and consumption of food; however, no minimum requirements for quality finishes were mentioned for decent habitability conditions of the completed spaces.

Minimum dimensions for interior spaces were considered, which vary according to their type. In the case of bedrooms, the minimum width is 2.70 m, and when building the bedroom with the minimum dimensions, there is only space for a double bed, a walkway, a nightstand and the opening of the door, and in the case of a single bed, there is space to build a closet.

As mentioned, currently the living units are delivered with minimal areas, with partial finishes or without, which generate comfort and hygiene issues for a decent lifestyle.

4. Methodology

For developing the research, the market indicators and the evolution of costs and prices were reviewed as follows:

- Review of housing cost indices in Cali according to reports from the Departamento Administrativo de Estadística (Administrative Department of Statistics, DANE in Spanish) and the Cámara Colombiana de Comercio (Colombian Chamber of Construction, CAMACOL in Spanish) and the database of prices and yields from Construdata;
- Revision of Laws, Decrees and Standards that regulate the construction of social interest housing; and
- Cost comparison of six specific cases of VIS and VIP projects executed by a company in the sector between 2010 and 2015.

5. Analysis of market indicators and evolution of costs and prices for VIS and VIP projects

The following indicators were analyzed in this case study: Construction Cost Index for Housing (ICCV, in Spanish) by DANE, Construction Cost Index for Housing by CAMACOL, Construction Cost Index by Construdata, New Housing Price Index (IPVN, in Spanish) by DANE, Basic Report of Urban Location by CAMACOL, Supply and Demand Study for Housing in Cali by CAMACOL and Building Census (CEED, in Spanish) by DANE.

5.1. Construction cost index for housing (ICCV, in spanish) by DANE

"The ICCV shows the cost behavior of the main inputs used in the construction of housing" [11], and it shows the average cost for the construction of the residential unit as a result of changes in price for construction supplies (materials, labor, tools and equipment).

Its monthly percentage variation allows for variations in the construction cost over time. The compliance of the new constructive standards between 2009 and 2017 has led to the variation shown in Fig. 1

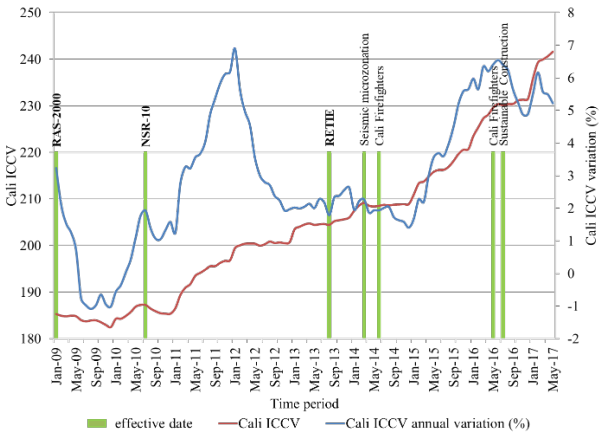


Figure 1. ICCV Cali and historical annual variation (%) 2009-2017.
Source: Authors

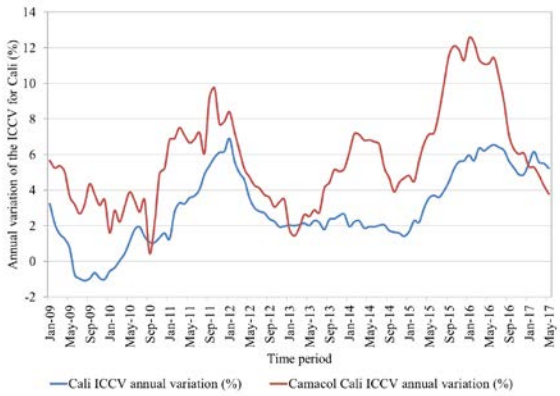


Figure 2. Percentage of annual variation of the ICCV for Cali considering the information reported by CAMACOL.
Source: Authors

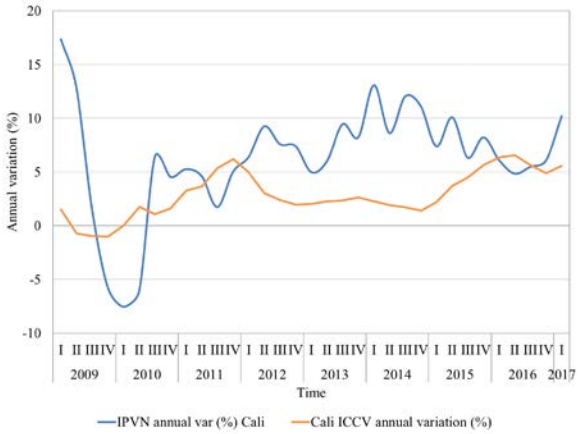


Figure 3. Annual variation percentage of the IPVN and ICCV for Cali.
Source: Authors

prepared with information from the Departamento Administrativo Nacional de Estadisticas (National Administrative Department of Statistics, DANE in Spanish). The greatest increases occurred with the introduction of the NSR-10, RETIE and Firefighters [12].

5.2. Construction Cost Index for Housing (ICCV, in Spanish) by CAMACOL

The Cámara Colombiana de la Construcción (Colombian Chamber of Construction) CAMACOL, Valle del Cauca chapter, publishes monthly Construction Cost Indices for different types of residential buildings in Cali. This report includes the price variation of construction materials for housing in relation to hydro-sanitary installations, internal and external electrical installations, telephone installations and public works. In this study, it was found that the variations between the CAMACOL ICCV and DANE ICCV have a similar trend, which allowed validating the actual behavior of the construction cost, evidencing periods of greater increases after the introduction of the NSR-10 and fire protection regulations (Fig. 2).

5.3. Construction cost indices by Construdata

The construction costs for different projects and the evolution of costs as a whole can be consulted in the Construdata journal, which contains information on the main cities of the country [13]. For this study, related information for the city of Cali was taken from issue No. 156 (third quarter of 2010) to No. 183 (second quarter of 2017), and it was found that as of 2014, the date on which the guidelines for earthquake microzoning, fire brigades and sustainable constructions came into force, a cost increase has been maintained, which reflects a final cumulative cost of 16.31%.

5.4. New housing price index (IPVN, in spanish) by DANE

The New Housing Price Index—IPVN—is a quarterly statistical report that presents the real dynamics of the market

Table 2.
Effective housing demand in Cali.

	2010	2012	2013	2014	2015
50–70 SMMLV	2,391	2,036	1,531	1,923	1,849
70–135 SMMLV	3,913	4,241	3,444	4,808	6,162
OTHERS	2,609	2,651	6,122	6,731	6,780

Source: Authors



Figure 4. Influence of the ICCV on the housing supply in Cali.
Source: Authors

prices [14]. If the behavior of the ICCV is compared with the IPVN, the behavior follows the variation of the ICCV, where the trends in variations of the ICCV are reflected in the IPVN later on (Fig. 3).

6. Considerations in relation to supply and demand

According to the CAMACOL reports between 2012 and 2013, there was a decrease in the effective housing demand from 22.80% to 13.79%, which could infer that this happened because some users had access to the "Free Housing" program [15]; nevertheless, it is evident that the housing demand was increasing throughout the period analyzed for the city of Cali. Table 2 summarizes the housing demand for the city of Cali.

Currently, if the construction ICCV is compared to the housing supply, a decrease in housing supply is observed, a situation that is related to the cost increase generated by the inclusion of the new standards; however, between May 2016 and May 2017, the increase in supply coincided with Government initiatives to provide Colombian families with housing solutions. Fig. 4 shows the housing supply in Cali and the impact of the ICCV.

7. Considerations regarding regulations and their impact on costs

Law 1537 of June 20, 2012, establishes "regulations intending to facilitate and promote urban development and access to housing and other provisions" related to financing social interest housing in Colombia. The Colombian State mainly promotes the construction of social interest and priority interest housing through a subsidies policy. Additionally, local entities may concur in the financial contribution of those projects.

Today, there is a limit on the acquisition value for social interest housing of one hundred thirty-five times the statutory monthly minimum wage (135 SMMLV), and seventy times the statutory monthly minimum wage (70 SMMLV) for priority interest housing, values that incorporate the costs of the real estate market for project development and that include land costs, architectural and engineering fees, urbanization and public services, direct construction costs, indirect costs, financial costs and revenue [16].

7.1. Standards analysis

The regulations and technical standards that directly affect the construction of social interest and priority interest housing in Colombia are now summarized.

7.1.1. Colombian regulation of earthquake resistant construction, NSR–10

This regulation establishes the criteria and minimum requirements for the design, construction and technical supervision of new buildings. Legally, it is supported by Law 400 of 1997 [17], which was initially regulated by Decree 33 of 1998 [18] and later by Decree 926 of 2010 [19], which adopted the Colombian Regulation of Earthquake Resistant Construction NSR-10. That regulation has been modified by Decrees 2525 of July 13, 2010, and Decree 340 of February 13, 2012. It is currently evaluating a new project for the modification of Titles J and K [20].

7.1.2. Technical regulation of electrical installations, RETIE (in spanish)

This regulation standardized the construction, maintenance and operation of the electrical service in Colombia, is legally supported by Law 143 of 1994 [21] and was adopted by Resolution 90708 of 2013 [22]. For the particular issue of social interest and priority interest housing projects, the minimum electrical circuitry and products that buildings must have, technical construction conditions, evaluation and certifications were defined.

7.1.3. Technical regulation of the drinking water and basic sanitation sector, RAS–2000

This regulation specified the mandatory requirements for building sites, equipment and operating procedures that are used in public services of plumbing, sewers, cleaning and their related activities. It was adopted by Resolution 1096 of November 17, 2000 [23], in compliance with the provisions of Law 142 of 1994 [24], which establishes the system of Public Services in Colombia and seeks to guarantee its quality at all levels. In 2009, the "Technical Regulation of plumbing and sewer pipelines" began, which includes the use of equipment, systems and implements of low water consumption in accordance with Decree 3102 of December 30, 1997.

7.1.4. Parameters and technical guidelines for sustainable construction – Guide for water and energy savings in buildings

This standard was issued through Resolution 549 of 2015 [4] and became effective as of July 10, 2016. It establishes the parameters and technical guidelines related to the efficient use of water and energy in new buildings. Due to its recent implementation, there is no clarity regarding the impact on the direct costs of social interest and priority interest housing.

7.1.5. Safe housing law

This regulation was issued through Law 1796 of July 13, 2016 (Ministry of Housing, City and Territory, 2015), by which measures are established focusing on protection of the home buyer, increases in building security and strengthening the public function exercised by City Planners. Certain functions are assigned to the Superintendence of Notaries and Registry, and other provisions are enacted. It came into effect as of July 13, 2016. It mandates that all buildings without exception require a structural inspection by a City Planner or by district or municipal offices [25]; however, in the case of VIS, due to the relatively small footprints of their buildings, only the structural inspection and technical supervision for buildings of 2,000 square meters or greater are required. Due to its recent implementation, there is no clarity regarding the impact on the direct costs of social interest and priority interest housing.

7.1.6. Technical regulations for internal telecommunication networks, RITEL (in spanish)

This regulation established measures related to the design, construction and commissioning of internal telecommunication networks in Colombia. Legally, it is supported by Law 1341 of 2009, which defined the principles and concepts on social information, and the organization of Information and Communication Technologies (TIC, in Spanish) [26]. It is adopted by Resolution No. 4262 of 2013 [27].

Table 3.
Global Budget of VIP projects in Cali.

VIP Global Budget					VIS Global Budget	
Year	1-2013	2-2013	3-2015	4-2015	1-2013	1-2014
Standard	NSR 98	NSR 98	NSR 2010	NSR 2010	NSR 10	NSR 10
Apartment area (m^2)	50.09	49.4	49.4	49.9	59.78	61.77
SMMLV	$ 589.50	$ 589.50	$ 644.35	$ 644.35	$ 616.00	$ 689.46
Item	Vle.SMLV	Vle.SMLV	Vle.SMLV	Vle.SMLV	Vle.SMLV	Vle.SMLV
Common						
Solid waste management	17.35	16.43	16.82	32.68	23.62	24.78
Custodian	7.55	7.55	7.65	7.49	17.18	15.59
Storage tank	103.64	103.64	98.94	108.79	119.44	79.75
Fire protection system	14.77	14.77	53.65	54.2	208.24	501.77
General electrical installations	42.77	42.58	60.19	61.49	360.98	738.67
Fire alarm and fire detection system				55.05		137.56
General hydro-sanitary installations	25.98	23.74	22.71	22.51	598.86	620.16
Enclosure	50.73	52.55	55.25	65.78	111.95	132.83
Complementary services and swimming pool					101.49	127.06
Internal parking for residents					1434.98	2072.63
	262.79	261.26	315.21	407.99	2976.74	4450.8
Apartment Towers						
Tower Structures						
Preliminaries	27	27	25.94	28.06	74.44	89.07
Earthmoving	59.15	63.71	49.76	48.28	228.92	225
Tower concrete structure	2597.95	2669.46	2770.69	2863.59	6542.28	9730.15
Masonry and finishes						
Non-structural masonry	151.05	133.12	98.68	121.05	454.06	595.26
Veneers	131.81	113.19	113.15	113.39	223.34	425.89
Painting	99.76	79.61	120.59	126.07	520.64	926.69
Roof	95.28	116.62	130.72	131.93	378.19	363.55
Carpentry	346.44	345.02	406.01	418.37	1083.02	1577.1
Sanitary, bathroom, and kitchen appliances	94.7	97.2	127.28	96.06	239.94	337.97
Cleaning and delivery	26.11	26.11	43.87	44.93	28.69	
Gas network				176.92	339.29	444.18
Elevator						896.46
Tower electrical installations						
Electrical installations	373.45	373.55	298.37	311.34	762.4	1318.81
Substation, switchboards	329.57	318.95	256.17	258.47	383.99	464.82
Communications network	25.27	27.95	26.92	24.67	93.24	141.09
Screening and protection against light	67.87	68.2	49.29	49.32	151.08	145
Hydro-sanitary installations	207.06	207.06	229.93	219.08	526.44	712.22
Signaling			11.27	6.06	17.9	12.08
Total Direct Costs	4632.47	4666.75	4758.63	5037.58	12047.86	18405.34
Subtotals	4895.26	4927.99	5073.74	5445.57	15024.6	22856.14
Builder AIU	806.74	812.13	836.15	897.43	2476.05	3766.08
Total Construction Costs	5702.00	5740.12	5909.89	6343.00	17500.65	26622.22

Note 1: VIP projects: Project 1 of 2013: 115 apartments of 50.09 m2, 5,760 m2 built with the NSR98; Project 2 of 2013: 115 apartments of 49.40 m2, 5,681 m2 built with the NSR98; Project 3 of 2015: 115 apartments of 49.40 m2, 5,681 m2 built with the NSR10 and dry fire protection system and Project 2 of 2015: 120 apartments of 49.90 m2, 5,988 m2 built with the NSR10, dry fire protection system, and fire detection and alarm system
Note 2: Project 1 of 2013: 220 apartments of 59.78 m2, 13,152 m2 built with the NSR10 and dry fire protection system and Project 2 of 2014: 320 apartments of 61.77 m2, 19,766 m2 built with the NSR10, pressurized fire protection system, and fire detection and alarm system
Source: Taken and adapted from [7]

The RITEL has undergone several modifications and adjustments, and although it does not refer in particular to social interest housing, it categorizes according to the area and stratum of the living unit, design of the minimum grid connection, distribution network and dispersion network of each unit. Its application was suspended by the Communications Regulation Commission (CRC) of Colombia until September 8, 2017 [28], and due to its high incurred costs, a possible definitive suspension is speculated.

7.1.8. Earthquake microzoning of Cali.

It was adopted by Decree 411.0.20.0158 of March 18, 2014 [32] and is supported in NSR–10 [17]. This regulation applies to all types of buildings to be constructed in Cali, including VIS and VIP. According to the earthquake spectrum zone where the project is located, cost overruns may arise due to the geotechnical quality of the soil.

7.2. Project analysis

For the analysis, projects meeting the following conditions were sought:

- Those executed between 2010 and 2017;
- Those within in the range of physical, technical and area characteristics for both VIS and VIP projects; and
- Those for which complete technical and budgetary information is available.

Table 4.
Profit estimation of priority interest and social interest housing projects in Cali.

Costs in SMMLV	VIP				VIS	
	1	2	3	4	1	2
Lot (including external urban planning)	7	7	7	7	20.25	20.25
Construction costs	49.58	49.91	51.39	52.86	79.55	83.2
After sale	0.35	0.35	0.35	0.35	1.32	1.32
Project fees	0.88	0.88	0.88	0.88	1.69	1.69
Supervision	1.98	2	2.06	2.11	3.98	4.16
Management fee and other management expenses	2.28	2.28	2.28	2.28	5.4	5.4
Sales fees	2.1	2.1	2.1	2.1	4.05	4.05
Advertising	2.1	2.1	2.1	2.1	4.05	4.05
Taxes, insurance and guarantees	0.18	0.18	0.18	0.18	0.35	0.35
Trust	0.21	0.21	0.21	0.21	0.64	0.64
Connection of services and administration of non-delivered apartments	0.09	0.09	0.09	0.09	0.18	0.18
Financial costs	1.4	1.4	1.4	1.4	5.63	5.63
Legal expenses	0.18	0.18	0.18	0.18	0.34	0.34
Total Costs	68.34	68.68	70.22	71.74	127.43	131.26
Profit	1.66	1.32	-0.22	-1.74	7.57	3.74

Note: The cost limit is 70 SMMLV for VIP and 135 SMMLV for VIS
Source: Authors

7.2.1. The case of VIP projects

For the VIP case, the information for four projects was analyzed for the south-eastern zone of the city of Cali. The cost estimate in Table 3 was adjusted to the statutory monthly minimum wage on the construction date so the values could be compared.

7.2.2. The case of VIS projects

For the VIS case, the study was performed with available information from two projects carried out in the south-eastern zone of the city of Cali.The costs associated with the construction according to the standards are described in Table 3.

8. Discussion

Regarding the cost structure, it is evident that the requirement to comply with the fire-prevention network and the fire detection and alarm systems by including electrical installations in common areas and solid waste management are impacting the housing cost.

For priority interest housing, it was found that between 2013 and 2015, on average, the solid waste management cost went from 0.145 SMMLV per living unit (p.u.v., in Spanish) to 0.21 SMMLV / p.u.v. Similarly, the economic impact of the fire protection system indicates that on average for 2013, the cost p.u.v. was 0.13 SMMLV / p.u.v., compared to 0.46 SMMLV / p.u.v. in 2015, which on average increased the costs of this system. On the other hand, in relation to general electrical installations, the cost increased to 0.515 SMMLV / p.u.v. in 2015 from 0.37 SMMLV / p.u.v., which was the average cost of those facilities in 2013.

Fire detection systems were not required in 2013, and their inclusion in 2015 incurred a cost of 0.46 SMMLV / p.u.v.

9. Conclusions

Housing is one of the basic needs of every human being. In the case of Colombia, the State has proposed different initiatives that allow the low-income population to access housing through social interest and priority interest housing programs. In addition to the Colombian Regulation of Earthquake Resistant Construction NSR-10, new technical standards have been incorporated to guarantee a better quality of the housing that is being built; constructive provisions, despite being necessary, are affecting the ceilings that the Government has established for the construction of VIS and VIP. The study revealed that with the implementation of the Technical Regulation of Electrical Installations (RETIE, in Spanish), the costs have increased up to 6.56%. This study should continue in order to incorporate the economic impacts that result from the implementation of the Technical Regulations of the Drinking Water and Basic Sanitation Sector – RAS-2000, Parameters and Technical Guidelines for Sustainable Construction, provisions that derive from the Safe Housing Law, Technical Regulation for Internal Telecommunication Networks (RITEL, in Spanish), Administrative, Operational, Technical and Academic Regulations of the Firefighters of Colombia, among others. The results obtained from an economic analysis that incorporates the compliance of those standards can help to support a cost structure that allows the builder to assist the Government with initiatives to serve the unmet housing demand for Colombians.

References

[1] Republica de Colombia., Constitución Política de Colombia, 1991.
[2] Ministerio de Vivienda, Ciudad y Territorio., Decreto 412 de 2016, 7 Marzo 2016. [Online]. Available at: http://www.minvivienda.gov.co/sobre-el-ministerio/conceptos-juridicos/subsidio-familiar-de-vivienda.
[3] Duarte-Quiroga, E., Una reflexión sobre la producción de vivienda social en Bogotá 1998 - 2010, Bogotá: Buenos y Creativos S., 2012.
[4] Ministerio de Vivienda, Ciudad y Territorio, Resolución 549 de 2015, 10 Julio 2015. [Online]. Available at: http://www.minvivienda.gov.co/ResolucionesVivienda/0549%20-%202015.pdf ISBN 978-958-9990-0-4.
[5] Vargas-Lleras, G., Camacol - Noticias, 28 Agosto 2015. [Online]. Available at: http://www.camacol.co/noticias/vargas-lleras-anuncia-derogaci%C3%B3n-de-ritel-y-reglamento-de-bomberos.
[6] CAMACOL., Reglamentos técnicos al cabo del tiempo volverán inviable las VIP, 21 Marzo 2014. [Online]. Available at: http://www.elnuevodia.com.co/nuevodia/actualidad/economica/213518-

reglamentos-tecnicos-al-cabo-del-tiempo-volveran-inviable-las-vip-camaco#sthash.nrfE0mWH.dpuf.
[7] Chirivi-B., E., Quiroz Ó. y Rodríguez-P., D., La vivienda social en América Latina: una revisión de políticas para atender las necesidades habitacionales de la región, Informe Económico 30, Cámara Colombiana de la Construcción Estudios Económicos, Bogotá, 2011.ISSN 2011-7442.
[8] Ministerio de Vivienda, Ciudad y Territorio para el Séptimo Foro Urbano Mundial, Colombia: cien años de políticas habitacionales, Bogotá, 2014. ISBN 978-958-57464-1-1.
[9] Departamento Nacional de Planeación., Docuemento Conpes 3746, 20 Mayo 2013. [Online]. Available at: https://www.dnp.gov.co/programas/vivienda-agua-y-desarrollo-urbano/Vivienda/Paginas/Conpes.aspx.
[10] Ministerio de Ambiente, Vivienda y Desarrollo Territorial , Guías de asistencia técnica para vivienda de interés social, No. 1, Bogotá, 2011.
[11] Departamento Administrativo Nacional de Estadística (DANE), Boletín Técnico - Índice de costos de costrucción de vivienda - ICCV - Junio 2016, Oficina de Prensa DANE, Bogotá, 2016.
[12] Departamento Administrativo Nacional de Estadística (DANE), Boletín de Prensa ICCV, Marzo 2011, Oficina de Prensa DANE, Bogotá, 2011.
[13] Construdata, Construdata Edición 183, Bogotá: Legis, 2017.
[14] Departamento Administrativo Nacional de Estadística (DANE), Ficha metodológica Índice de precios de vivienda nueva, oficina de prensa DANE, Bogotá, 2017.
[15] CAMACOL Valle, Estudio de oferta y demanda de vivienda en Cali, Candelaria, Jamundí, Palmira y Yumbo 2015, Cali: Departamento de Estudios Económicos CAMACOL VALLE, 2015. ISSN 2422-0418.
[16] Ministerio de Vivienda, Ciudad y Territorio., Decreto 1077 de 2015, 26 Mayo 2015. [Online]. Available at: http://www.minvivienda.gov.co/sobre-el-ministerio/normativa.
[17] Congreso de la República de Colombia., Ley 400 de 1997, 19 Agosto 1997. [Online]. Available at: http://www.secretariasenado.gov.co/senado/basedoc/ley_0400_1997.html.
[18] Presidencia de la República de Colombia, Decreto 33 de 1998, 9 Enero 1998. [Online]. Available at: http://www.minvivienda.gov.co/Decretos%20Vivienda/0033%20-%201998.pdf.
[19] Presidencia de la Repúbica de Colombia., Decreto 926 de 2010, 19 Marzo 2010. [Online]. Available at: http://www.alcaldiabogota.gov.co/sisjur/normas/Norma1.jsp?i=39255
[20] Sociedad Colombiana de Ingenieros SCI, Tratemos Temas de Ingeniería, 15 Marzo 2016. [Online]. Available at: http://sci.org.co/sci/media/news_images/memorias/presentacion_jose_alvarez.pdf.
[21] Congreso de la República de Colombia, Ley 143 de 1994., 11 Julio 1994. [Online]. Available at: https://www.minminas.gov.co/documents/10180/667537/Ley_143_1994.pdf/c2cfbda4-fe12-470e-9d30-67286b9ad17e.
[22] Ministerio de Minas y Energía, Resolución 90708 de 2013, 30 Agosto 2013. [Online]. Available at: https://www.minminas.gov.co/documents/10180/23517/22726-Resolucion_9_0708_de_agosto_30_de_2013_expedicion_RETIE_2013.pdf.
[23] Ministerio de Desarrollo Económico., Resolución 1096 de 2000, 17 Noviembre 2000. [Online]. Available at: http://www.minvivienda.gov.co/ResolucionesAgua/1096%20-%202000.pdf.
[24] Congreso de la República de Colombia, Ley 142 de 1994, 11 Julio 1994. [Online]. Available at: http://www.alcaldiabogota.gov.co/sisjur/normas/Norma1.jsp?i=2752.
[25] Congreso de la República de Colombia, Ley 1796 de 2016, 13 Julio 2016. [Online]. Available at: http://es.presidencia.gov.co/normativa/normativa/LEY%201796%20DEL%2013%20DE%20JULIO%20DE%202016.pdf.
[26] Congreso de la República de Colombia, Ley 1341 de 2009., 30 Julio 2009. [Online]. Available at: http://www.mintic.gov.co/portal/604/articles-3707_documento.pdf.
[27] Comisión de Regulación de Comunicaciones, Resolución 4262 de 2013, 15 Julio 2013. [Online]. Available at: https://www.crcom.gov.co/resoluciones/00004262.pdf.
[28] Comisión de Regulación de Comunicaciones, Resolución 4786 de 2015, 8 Septiembre 2015. [Online]. Available at: https://www.crcom.gov.co/resoluciones/00004786.pdf.
[29] Congreso de la República de Colombia, Ley 1575 de 2012, 21 Agosto 2012. [Online]. Available at: http://wsp.presidencia.gov.co/Normativa/Leyes/Documents/LEY%201575%20DEL%20%2021%20DE%20AGOSTO%20DE%202012.pdf
[30] Ministerio del Interior, Resolución 661 de 2014, 26 Junio 2014. [Online]. Available at: http://www.icbf.gov.co/cargues/avance/docs/resolucion_mininterior_0661_2014.htm.
[31] Ministerio del Interior, Resolución 340 de 2016, 30 Marzo 2016. [Online]. Available at: http://www.mininterior.gov.co/la-institucion/normatividad/resolucion-no-340-del-30-de-marzo-de-2016.
[32] Alcaldía de Santiago de Cali, Decreto 411.0.20.0158 de 2014, 18 Marzo 2014. [Online]. Available at: http://www.cali.gov.co/aplicaciones/boletin_publico/detalle_boletin.php?id=869&num=38.

M. Chávez-Calle, is BSc. in Architect. MSc. in Civil Engineering, Construction emphasis, Pontificia Universidad Javeriana Cali, Colombia. Manager of MC Construcciones y Consultoría (MC Construction and Consulting). Specialist in construction management. Specialist in project and works auditing, Cali, Colombia.
ORCID: 0000-0003-1637-5272

D.D. Pérez-Ruiz, is professor at Pontificia Universidad Javeriana de Cali. PhD. in Civil Engineering from the University of Texas in Arlington, MSc. in Traffic and Transportation Engineering from the Universidad del Cauca, Colombia. MSc in Civil Engineering in Water Resources from the Universidad de Puerto Rico Mayaguez Campus, Puerto, BSc. in Civil Engineering from the Universidad del Cauca, Colombia.
ORCID: 0000-0002-9656-2803

M.F. Serrano-Guzmán, is professor at Pontificia Universidad Javeriana Cali, Colombia. PhD in Civil Engineering and MSc. in Engineering from the Universidad de Puerto Rico Recinto Universitario de Mayaguez, Puerto Rico, S. in Construction Project Management at the Universidad Industrial de Santander, Colombia. Sp. in Environmental Engineering from the Universidad Pontificia Bolivariana de Bucaramanga, Colombia. BSc. in Civil Engineering from the Universidad Industrial de Santander, Colombia.
ORCID: 0000-0002-7366-6597/.

UNIVERSIDAD NACIONAL DE COLOMBIA
SEDE MEDELLÍN
FACULTAD DE MINAS

Área Curricular de Ingeniería Civil

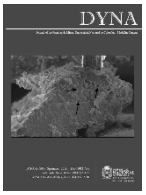
Oferta de Posgrados

Especialización en Vías y Transportes
Especialización en Estructuras
Maestría en Ingeniería - Infraestructura y Sistemas de Transporte
Maestría en Ingeniería – Geotecnia
Doctorado en Ingeniería - Ingeniería Civil

Mayor información:

E-mail: asisacic_med@unal.edu.co
Teléfono: (57-4) 425 5172

UNIVERSIDAD NACIONAL DE COLOMBIA
SEDE MEDELLÍN
FACULTAD DE MINAS



DYNA
http://dyna.medellin.unal.edu.co/

The use of GS1 standards to improve the drugs traceability system in a 3PL Logistic Service Provider

Igor Lopes-Martínez[a], Lianet Paradela-Fournier[a], Janett Rodríguez-Acosta[a], Jenny Laura Castillo-Feu[a], Martha I. Gómez-Acosta[a] & Alegna Cruz-Ruiz[b]

[a] *Industrial Engineering Department, Technological University of Havana José Antonio Echeverría, La Habana, Cuba, ilopes@ind.cujae.edu.cu, lparadelaf@ind.cujae.edu.cu, jracosta@tesla.cujae.edu.cu, jennylaura.castillo@nauta.cu, marthagom@tesla.cujae.edu.cu*
[b] *Havana University, La Habana, Cuba, alegna@psico.uh.cu*

Received: December 29th, 2017. Received in revised form: May 18th, 2018. Accepted: July 16th, 2018

Abstract
The present research has been made based on the analysis of the operation of a 3PL Medication Logistic Service Provider in Cuba. This entity is responsible for managing the distribution of medications to guarantee their offer in health care facilities and communal pharmacies all over the country. The nonexistence of a unique identification and the non-use of international encoding standards for the products in their transit through the chain of supply, the lack of computerization of some fundamental data to support their tracing and incongruences in the readable data found using the entity´s software were the main deficiencies obtained from a diagnosis made to its traceability system. The proposed solutions are centered on a traceability plan conceived by the company from a strategic vision and in a unique-code products procedure for their distribution and merchandising under GS1 international standards.

Keywords: coding system; international standards GS1; traceability system.

Uso de los estándares GS1 para la mejora del sistema de trazabilidad de medicamentos en un Operador Logístico 3PL

Resumen
La presente investigación ha sido realizada a partir del análisis del funcionamiento de un Operador Logístico (OL) 3PL de Medicamentos en Cuba. Esta entidad se encarga de gestionar la distribución de los medicamentos para garantizar su disponibilidad en los centros asistenciales y farmacias comunitarias en todo el país. El diagnóstico realizado al sistema de trazabilidad de la empresa arrojó como principales deficiencias la inexistencia de una identificación única para los productos en su tránsito por la cadena de suministro y la no utilización de estándares internacionales de codificación para ello, la falta de informatización de algunos datos fundamentales para trazar los productos e incongruencias en los datos registrados en el Software que utiliza la entidad. Las propuestas de solución se centran en un plan de trazabilidad que permite a la empresa concebir el sistema de trazabilidad desde una visión estratégica y en un procedimiento de codificación única de los productos para su distribución y comercialización bajo estándares internacionales GS1.

Palabras Clave: sistema de codificación; estándares internacionales GS1; sistema de trazabilidad.

1. Introduction

Elements such as patient´s safety, security in the supply chain, traceability and efficiency in the health care sector, are nowadays at the top of the list of the most relevant issues in the regulations and industries of world governments [1-3]. Various situations have shown the existence of product safety crises in different countries around the world, for example, among the many cases related to illicit drugs, it is estimated in a range of 3.8% to 8.9% of deaths due to malaria-related diseases in Sub-Saharan Africa due to low-quality or warped drugs [4].

The World Health Organization (WHO) has received reports of illicit drugs from many regions of the world, this shows how global and serious the problem is [5], Fig. 1 shows the main countries from where reports were issued between 2013 and 2017.

How to cite: Lopes-Martínez, I., Paradela-Fournier, L., Rodríguez-Acosta, J., Castillo-Feu, J.L., Gómez-Acosta, M.I. and Cruz-Ruiz A., The use of GS1 standards to improve the drugs traceability system in a 3PL logistic service provider. DYNA, 85(206), pp. 39-48, September, 2018.

© The author; licensee Universidad Nacional de Colombia.



Figure 1. Countries from where reports of low-quality or counterfeit medicines were sent to the WHO between 2013 and 2017 (dark color). Source: WHO Global Surveillance and Monitoring System for Substandard and Falsified Medical Products [5].

The regions where the highest incidence of illicit drugs is reported are Central America, South America, Sub-Saharan Africa and India. In these the figures of warped drugs are superior to 20% and go too far up to 50% of the traded medications. The regions of lowest incidence are North America, Europe, Japan and Australia in a range from 1% to 10% [6].

Many reasons can cause the excessive spread of illicit drugs, among them selling through Internet, high cost of patent medications, lack of health policies and the complexity of supply chains [5-7].

A vital strategy for companies must be keeping sustainably competitiveness and offering the best service to the customer; for this, the best methods and tools must be continuously adopted, such as the implementation of traceability systems that allow them to meet the goal [8-10]. These systems involve confronting illegal activities for avoiding illegitimate drugs and the elimination of manual information management procedures, which create doubly manipulation and costly reprocessing, limiting an optimal negotiation among supply chain partners.

In the health sector, as a part of its drugs traceability, it is vitally important to always obtain veracious and reliable information about each product, medicine or service; for this, it is necessary to achieve the unique identification that allows all laboratories, drugstores and pharmacies to use the same communication language, regardless of any distribution channel used or final destination place of goods. The use of GS1 standards for implementing successful traceability systems is proposed as a good solution, since they provide global, interoperable and open results for optimizing the logistics system [11].

The present investigation is focused on the study of the traceability system of a Cuban 3PL drugs Logistic Service Provider (LSP) which is responsible for managing the distribution of medicines throughout all the country, ensuring their availability in health centers and communal pharmacies.

This 3PL has a national coverage and its main difference with other globally existing 3PL in the sector is that it covers 100% of the company´s drugs distribution to all pharmacies, hospitals and other healthcare centers in the country, while in other environments some known 3PLs attend only a part of the market. Due to this characteristic, any proposed solution has an impact on the entire drug system.

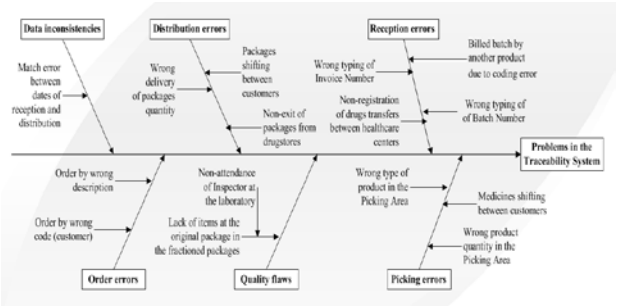


Figure 2. Current problems detected in the company's traceability system. Source: The authors.

Previous studies carried out in the company using the Inventory Reference Model tool called by its Spanish acronym MRInv [12], have shown the existence of problems in products coding that affect the management of inventories and traceability systems: the results of quality claims, the pretends and real drugs called back from the market, gave evidence of a series of deficiencies that represent failures in the traceability system. All these errors and/or deficiencies can be evidenced in the Ishikawa Diagram shown in Fig. 2.

All previously evidences the need to solve the existing deficiencies in the company's traceability system. Thinking of traceability as a system, the aim of this article is to propose a systemic solution for innovating the Traceability System of a drugs 3PL LSP, based on the use of GS1 international standards.

It's necessary for drug Logistics Service Providers to design their traceability plan, supporting the identification of items under the premise of unique identification using proposed GS1 standards. This result can be widespread to several logistics operators.

2. Materials and methods

The research was carried out in a 3PL Logistic Service Provider by performing a diagnosis of the trading and distribution current situation in what concerns drugs identification and traceability. For this, methods such as interviews, direct observations, analysis of technical documents, data processing and resolutions and norms in effect internationally and in Cuba were used. Traceability exercises consisting of following the entire product route throughout its logistics cycle and monitoring activities by tracking the information in the computer systems used in the chain of supply were also carried out, identifying the interoperability of the systems.

In addition, the Products Coding and Classification Systems Module from the Inventory Reference Model was evaluated using the MRInv tool [13], obtaining the main deficiencies of the company in terms of medicines identification.

The main tools used during the investigation were: The Ishikawa Diagram and the V-63 Visualization Pattern. The first one is used to show the current problems of the traceability system in the company and the second one to analyze the information flows among the existing business applications.

The V-63 Visualization Pattern is a part of the Entrepreneurial Architecture Management Patterns that help to manage the information of business applications in an agile and structured way [14].

3. Results

3.1. Regulatory domain

The analysis of the traceability system of the organization begins with the study of the existing environment that regulates Traceability in Cuba in what concerns health sector.

The main legal regulations analyzed [15-20] show that the Center for the State Control of Drugs, Equipment and Medical Devices, CECMED in its acronym in Spanish, establishes the necessary documentation and procedures to guarantee traceability, but it does not specify neither how to be done nor the essential rules to carry it out. To this effect, the Resolution 117/2008 [17], previously issued by an inexistent present organ and currently obsolete, is the most advanced normative as it recognizes the existence in an incipient way of the bar codes in the chain and establishes procedures and registers aimed to guarantee traceability; however, it is still applied by companies because it provides them with methods to comply what´s been established by CECMED. There is a Joint Resolution 1/2001 [18] signed by Ministry of Domestic Trade and Ministry of Foreign Trade that establishes the use of coding standards, for which the GS1 Office in Cuba was constituted, however, it doesn't express a procedure for the implementation of these standards in Cuban companies. On the other hand, Resolution 11/2007 of the Ministry of Finance and Pricing [19] indicates the obligatory documents and information fields that help to guarantee traceability, but it does not mention the use of an internationally standard code.

The regulations issued by the CECMED regarding the post-merchandising surveillance of the products, in spite of including topics such as monitoring to combat illicit drugs and the calls back from the market, do not refer to the existence of traceability systems to support these regulations [15].

In general terms, a delayed regulatory framework regarding to foreign regulations that exist for the health sector in terms of traceability is observed, since work with the GS1 standard codes is not mandatory to have an open, interoperable and global system and there are no master documents that guide the implementation and evaluation of traceability systems in Cuba for the sector.

3.2. Elements that make up the current traceability system

The execution of traceability exercises and monitoring activities through informatics systems allowed knowing the elements that make up the current traceability system and tracing the drugs in the supply chain. The provincial drugstores in which the study was done at this stage, not extended to hospitals, clinics or local pharmacies, allowed to understand the functioning of the current traceability system, being the basis for the design of improvements.

The elements that make up this system are presented below, specifying in each case the type of organizational unit in which they are found:

- Actors: involved in the traceability process are the Informatics Department, Head of Operations, Claims Department, Technical or Quality Department, Economy Department, Warehouse Head and Dependents where the product is receipted, Driver of the distribution vehicles, inspection and storage personnel that receives the goods at the customer's point.
- Documentation: Entry Registers, Entrance Inspection, Entry of products with special conditions, Temperature and Humidity Control, Batch and Expiration Date Control, Control of Expedition Guides, Control of the Cold Chain of products from 2-8°C, Supplier Expedition Guide, Vendor Invoice, Ownership Transfer among areas, Product Master Data, Batch History, Blindly Reception, Report of Reception, Pre-dispatch Grouping by Client and by Product, Customer Invoice, Guide of Expedition to client.
- Sensors: Thermo-hydrometer (instrument for measuring temperature and humidity), Data-Logger, GPS, Infrared pyrometers (temperature measurement instrument), and the Weighing Scales (weight measurement instrument).
- Checkpoints: the verification of the packages weights, the entrance inspection in the Reception Area, the blindly reception in the warehouse, the verification of the number of units delivered in the warehouse, the verification of the batch and code of the product in the Dispatching Area, and the verification of the amount of packages dispatched and delivered in the Shipping area.
- Coding system: The Uniform Product Classifier, CUP in its acronym in Spanish, is used in the company and throughout the drug chain of supply in Cuba. This code, erroneously used as an encoder, was replaced by the Cuban Product Classifier, CPCU in its acronym in Spanish, version 2.0 according to Resolution 49/2017 of the National Office of Statistics and Information, ONEI in its acronym in Spanish. The explanation of how this code is assigned is shown in Fig. 3, which shows that CECMED is involved in both the identification of domestic and imported products. In case of domestic, the decision of the code structure is associated with the regulations of GS1 Cuba, and those imported depend on the Issuing Agencies of codes in origin. This operation is not correctly implemented in the system, but instead an internal coding is used in each link, discarding the GTIN code.
- Computer systems: Fig. 4 shows the V-63 Pattern that illustrates the communication among the informatics systems of the different actors of the chain, which has a direct relationship with the traceability system of the drugs supply chain. The traceability information is introduced for the first time in the laboratories in case of a domestic drug, and/or in the LSP Importing Unit in case of an imported drug, and then, it is transmitted among these informatics systems. The drugstores can have access to a Web Portal, same as laboratories and some hospitals where information about the distribution and availability of drugs is shown, it captures the information of the existing informatics systems and allows to know, among other data and updated every 3 hours, the movements and records of dates, freighters data, place of reception (drugstore).

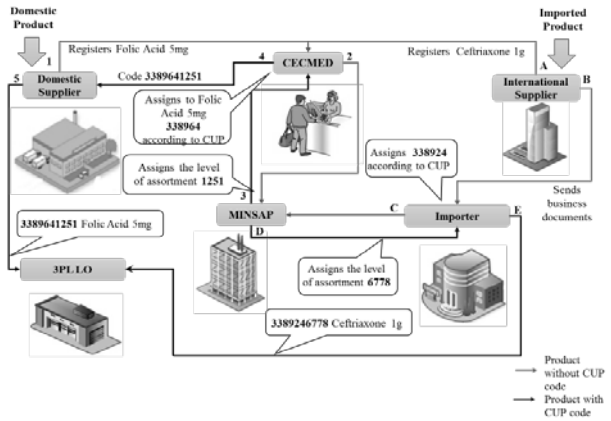


Figure 3. Example of CUP code assignation to a domestic product and an imported one.
Source: The authors.

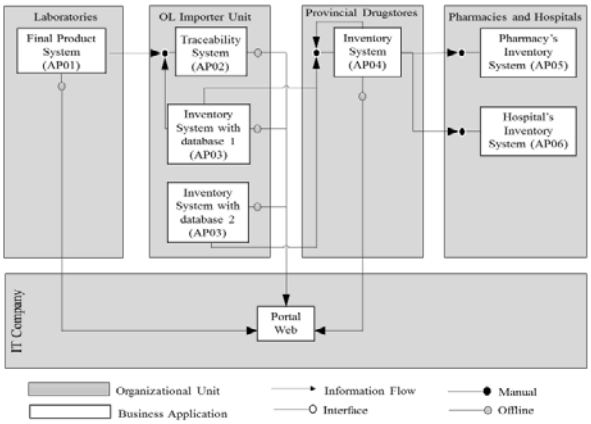


Figure 4. V-63 Pattern – Communication between Computer Systems related to the medicines traceability system.
Source: The authors.

3.3. Deficiencies in the traceability system

As a starting point of the investigation, different deficiencies were checked when detected in previous studies carried out between the Company and the University. However, the problems shown hereinafter constitute a deeper analysis of the traceability system, since they were detected from the realization of traceability exercises and monitoring activities through the informatics systems used in the supply chain, in addition to interviews made to Company specialists. In general, the traceability process in the drug supply chain in Cuba is carried out efficaciously, but it is very inefficient due to the poor use of standards and technologies for the fulfillment of the unique identification traceability principles, communication, data linkage, and recording and data capture [21].

Regarding the existent level of organization in the LSP, the deficient aspects found were:

1. Non-use of a product classifier controlled by the current legislation of the Country.
2. Non-use of an international standard product system for coding and identification.
3. The code of the manufacturer´s product is not sustained in the company.
4. The system for the products description does not guarantee their quick and unmistakable identification.
5. The units of measurement of products in the supply chain are not standard, for example, the unit of milligrams is used as mg or mgs one or the other.
6. The units of measurement of the products are not aligned to the International System of Units, SI in its acronym in Spanish.
7. Non-use of automatic identification systems in the company at the contact points with the client.
8. There are errors in the exchange of data among the different actors in the supply chain. The incorrect typing in the informatics systems of data, numbers of batches and origin of product, among others, are typical examples.
9. During the realization of the traceability exercises, various data could not be obtained, mainly because they were in paper format and were stored without an established filing system, this greatly hindered their search and non-satisfactory results were achieved.
10. Some data referred to the batches, such as the number of boxes, the box serial number and the location inside the warehouse, are not registered.
    a) Regarding the level of technology in the LSP, the negative aspects found were:
    b) The identification usually given to grouping of products that are dispatched is not registered in the informatics systems, only reflected in their packing and sometimes in the conformation work documents of these groupings (Pre-dispatch grouping by Client).
    c) Each laboratory is identified differently in each drugstore.
    d) The registration of data for traceability is not standard in the different drugstores, for example, in the smallest ones the exact date of entry of goods is not recorded, since they do not use the Registry Entry of merchandise to the warehouse, place where this data is required. It was also confirmed that sometimes all the information required by the records is partial or illegible.
    e) In the reception and dispatching operations, data required to know the behavior of the physical movement is not registered in the informatics systems.
    f) Virtually no product batch is linked with others that might have a coincidence on date and place during the travel among areas, in order to prevent cross contamination, even if for good practices, the manipulators know the products that cannot be close.
    g) Problems of data veracity in the informatics systems were detected, because of records that do not match; for example, an entry date of a product to the drugstore appears anticipated regarding to the exit date of the Importing Company, where products come from.
    h) The Web Portal does not illustrate the tracking of

the products by batches, although the information is received from the Inventory systems.

i) There are problems of data veracity in the Web Portal such as repeated and incongruence information, for example, non-registered carrier data (Name and License plate of the vehicle) during the distribution of goods from the Importing Company to the drugstores.

j) The Web Portal does not specify any information in case of cross-docking from harbour to the drugstores. When this happens, the drugstore transmits by phone the required data to the LSP Import Unit who registers it in the Inventory System as an ownership transfer, which affects the necessary information for traceability and generates a false physical movement.

3.4. Implementation of improvements to the traceability system in the logistics system of drug distribution. Proposal of generalization.

One of the challenges faced today by Cuban companies in the health sector to increase their global competitiveness is to achieve the unique identification of each drug and its traceability through the supply chain, from the international or domestic provider to pharmacies, hospitals, institutes and other health care centers.

As previously analyzed, it is observed how the 3PL LSP of the drugs supply chain in Cuba is deficient for the achievement of an effective traceability. For this reason, it is proposed to implement improvements to this system based on the setting-up in a joint way of a Traceability Plan together with the use of the GS1 standards, a contribution in the generalization of this result.

3.4.1. Traceability plan

Based on previous studies of organizations and specialized publications, a Traceability Plan supported in important documents shown in Fig. 5 is proposed, with a reference stated in [22-26], creating the basis for basic notions of the Traceability System and its application by the internal staff and its understanding for any external personnel.

These documents must contain the following information [22-25]:

Document 1- The 3PL logistics Service Provider must define the scope of its Traceability System in both directions according to its commercial objectives, risk analysis or any other criterion. For this, it is also necessary to contact other actors in the supply chain and align their processes if necessary.

Document 2- The traceability plan must contain a provider plan establishing the necessary requirements (in terms of traceability) that suppliers must accomplish.

Document 3- This document must contain the description of staff and departments management responsibilities within the scope of the traceability system.

Document 4- This document should clearly include the descriptions of the handling flow and process, just like the description of the records and registration models.

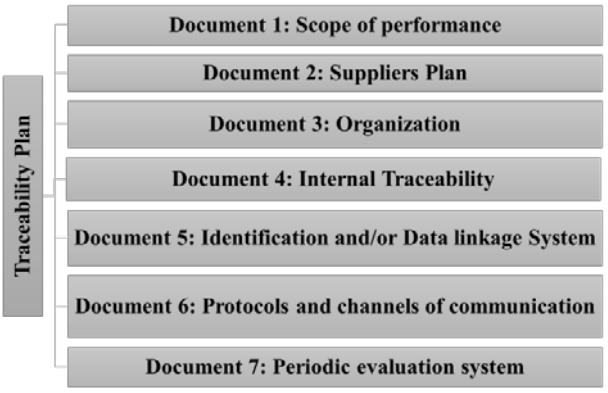


Figure 5. Documents of the Traceability Plan.
Source: The authors.

Document 5- This document holds the traceability system and its technology. The features of the traceability informatics systems and their ways of using them should be described.

Document 6- This document describes the mechanisms to be activated to proceed to locate and withdraw from circulation of an affected batch with finished products.

Document 7- This document must establish the mechanisms to verify that the traceability plan effectively matches the proposed objectives, through the definition of the system evaluation process.

The information and/or procedures proposed in the Traceability Plan are within company documents, considering documents 2 and 6 the most advanced, while the others must be designed in an explicit way based on the proposed procedure for the implementation of GS1 standards.

3.4.2. Procedure for coding products using GS1 standards

The coding procedure to be used based on the GS1 standards was designed with reference to what stated in [21, 27-29] together with company's current procedures.

The success of the procedure will be even safer and larger in scope insofar as actors commitment and understanding increase concerning the need to achieve the unique identification of drugs in Cuba.

3.4.2.1. Principles for the application of the procedure

Carrying out the supply with quality, security and guarantee is not only a responsibility of the Logistics Operator, but from each actor in the supply chain, being that the integration of each one's functions and acting as coordinated organizations, are the basis for efficiency in the logistics system of drug distribution in Cuba. That is the reason of demanding the GS1 standard in the supply chain from the highest regulatory authority in the country, as shown in Fig. 6:

- The CECMED as a regulatory center of drugs merchandising in Cuba must ensure their identification by GTIN code.

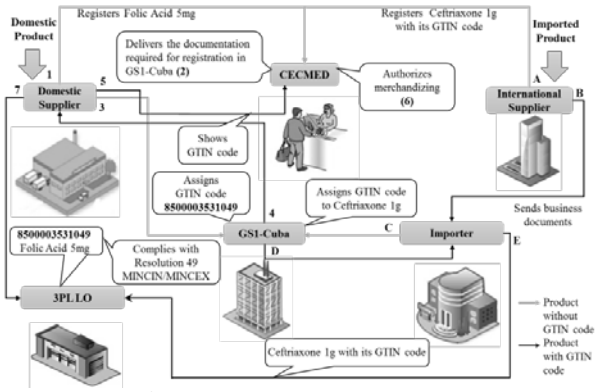


Figure 6. Demand of GTIN code by the CECMED as a register requirement.
Source: The authors.

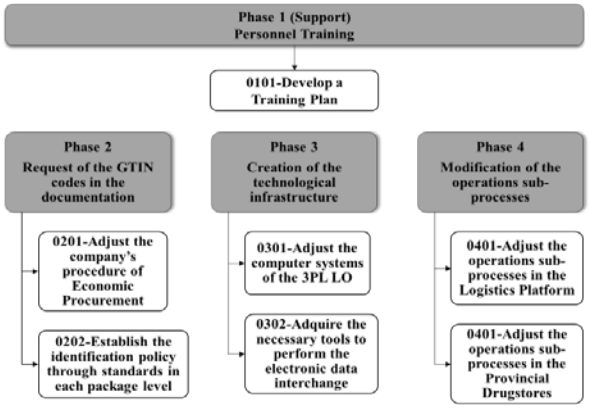


Figure 7. Coding Procedure.
Source: The authors.

- The importer must demand in the contracts the products identification by GTIN code; otherwise it must be registered at the GS1 Office in Cuba´s Chamber of Commerce.
- Domestic suppliers must register their products at the GS1 Office in Cuba´s Chamber of Commerce.

The relationships of CECMED with the rest of the organizations when the use of the GTIN code as a registration requirement is required would be as illustrated in Fig. 6.

3.4.2.2. Objectives of the procedure

General objective

To standardize the coding system in the logistics system of drugs distribution in Cuba.

Specific objectives

1. To achieve the unique identification of the products through the use of the GTIN code.
2. To require the identification of the products in commercial documents, packing and packaging.
3. To carry out the electronic exchange among the actors of the supply chain.
4. To computerize the data record of all operations.
5. To design the operation sub-processes: reception, storage, dispatch and expedition of the LO Importing Unit and the Provincial Drugstores.

3.4.2.3. Scope of the procedure

The procedure extends to all actors in the drug supply chain.

3.4.2.4. Structure of the procedure

The coding procedure consist of four phases as shown in Fig. 7, each one with a set of steps indicating the activities to be performed.

3.4.2.5. First phase: personnel training

Any change in a company may generate resistance, processes redesign, increase of responsibilities, employee cutback and other consequences, which is why training of staff is essential. The plan to be carried out must be as detailed and organized as possible

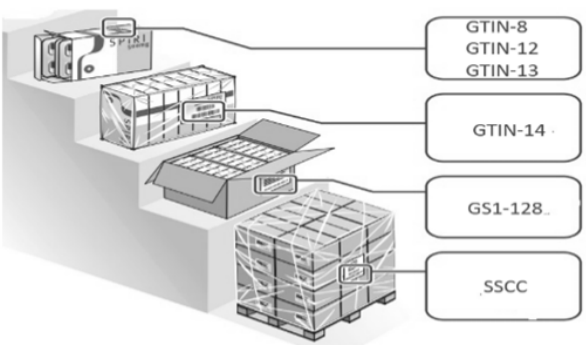


Figure 8. Identification in each level of packaging.
Source: The authors.

to guide both planning and teaching practices. The Training Plan of the company must establish: Scope, Purpose, Objectives, Goals, Strategies, Types, Pattern and Training Levels, Actions to be carried out, Topics to develop, Resources, Financing, Budget and Schedule.

3.4.2.6. Second phase: request of the GTIN codes in the documentation

The results expected at this phase are to achieve the obligatory identification of products with their proper GTIN code. This prevents recoding in other links of the supply chain.

The Economic Contracting Procedure that rules the 3PL LSP contracts with domestic suppliers must be modified, in accordance with stablished legal provisions contained in clauses named *Packing, packaging and marking of the goods*, setting as an additional aspect the identification of products through the GTIN code. Penalties must be established in case that suppliers fail to comply with this clause. This clause must include, as shown in Fig. 8, the policy for the identification by the supplier in each packaging level, as well as the information obtained by the system from the codes. The LSP must also demand the submittal of the documentation that corresponds to the product before its reception.

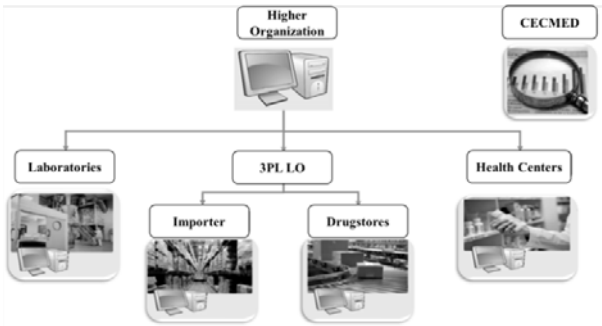


Figure 9. Integration between information systems.
Source: The authors.

3.4.2.7. Third phase: creation of the technological infrastructure

The company must create a technological infrastructure to support its processes to achieve the integrity of data, information exchange with other actors in the supply chain and access in real time. The system of each drugstore and platform must be managed from the Central Office. The database of the company and the remaining actors in the supply chain must be interconnected to a central base managed by the Superior Organization as shown in Fig. 9.

The introduction of the GTIN code in company's operations involves installing a Wi-Fi network to guarantee the connectivity of portable terminals and modifying the information systems, mainly the informatics one. Currently this is not enough to progress, that is why a software for operational management in warehouses is needed. The LSP must adapt it for performing new functions and aiming to convert it into a Warehouse Management System (WMS), or then to acquire a software apart from the current system or to migrate to the use of an ERP system, which leads to other more drastic transformations. The transformations to be carried out are:

- To allow automatic reading of data in the Reception, Storage, Dispatch and Expedition Areas.
- To recognize the GTIN as the unique identification code of the product associated with the minimum presentation unit.
- To assign the barcodes to the products, which will enter the system through Portable Terminals.
- To allow the calculation of the verification digit in the internal use GTIN codes that identify the products without manufacturer's code.
- To facilitate the electronic exchange of documents and the interrelation among the sent and received data using the same structure. Invoices issued by the supplier will enter the system without being typed by a user, decreasing the probability of error and increasing the process reliability.

The introduction of the information corresponding to the products in the database, their description, GTIN code and unit of measure, coming from the domestic supplier or the Importing Company, will be carried out in a centralized manner by an authorized personnel in those companies. The registered information of each product will be automatically displayed in the LSP Importing Unit and Provincial Drugstores through the electronic data interchange (EDI).

The EDI focuses on the transmission of information and supports the processes of the supply chain. It is used to transfer electronic documents or business data from one informatics system to another. In this way the staff of the different drugstores will not be able to introduce codes or descriptions, but the domestic suppliers and the importer the only ones responsible of ensuring the homogeneity through the supply chain.

The LSP, seizing these advantages, must begin to exchange documents beginning by:

- Commercial invoices (Supplier - Drugstores, Importer - LSP Importing Unit, Drugstores - Clients).
- Transfer among agencies (LSP Importing Unit - Provincial Drugstores).
- New products registration (Supplier - Drugstores, Importer - LSP Import Unit, LSP Import Unit - Drugstores).
- Reception confirmation.
- Expedition Guides.
- Claim Report (when applicable).

Tools required for the application of an automatic identification system in the LSP

The application of this automatic identification system, in addition to the modifications to be done in informatics systems, requires a set of necessary tools for the execution of the processes. Table 1 shows the main technological devices to be acquired by the company with their characteristics and functions.

The acquisition of these tools and the installation of a Wi-Fi network by the LSP in all its units that guarantees the connectivity among the terminals is a significant investment for the entity. With the modifications of the informatics systems and the acquisition of these tools, the procedures that regulate the operations in the processes of reception, storage, dispatching and expedition must be modified.

3.4.2.8. Fourth phase: design of operation sub-processes at the 3PL LSP importing unit and provincial drugstores

In this phase, the sub-processes are modified as shown in Fig. 10, taking advantage of the opportunities offered by the unique identification of the products through the GTIN code.

Table 1.
Tools to set up an automatic data capture system.

Tool	Caracteristics
Portable Terminals 	- Provides the processing power and network performance that is needed for applications to run consistently, at high speed and with reliability. - Workers can keep their hands and eyes on the materials they are handling and will not waste any more time with papers. - Eliminates the effort and cost of buying and maintaining various hardware systems for the different types of applications used in a warehouse or distribution center.
Labels Printer 	- Fast production of labels. - Elabeled for processes, products and shipments. - Impression of symbologies of linear and two-dimensional bar codes.

Source: The authors.

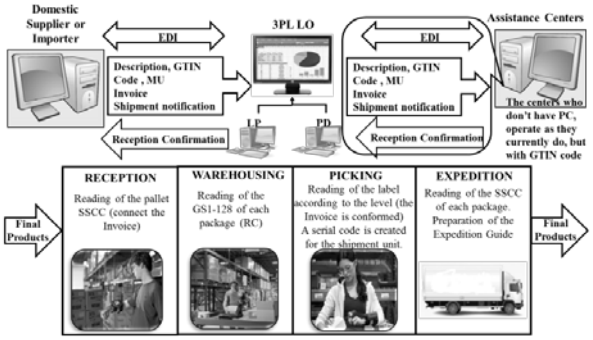


Figure 10. Modification of the sub-processes of operations in the 3PL Logistics Operator.
Source: The authors.

4. Discussion

The efficient implementation of a traceability system in a 3PL LSP under the use of the GS1 standards, cannot be possible if all actors in the drug supply chain do not join this initiative, in this case in Cuba.

One result of the application in the study object has been knowing thoroughly by the health authorities in each country to see the exigency for using a unique identification of products as their direct responsibility in the logistics system. In American continent, it is outstanding the role played by the Food and Drug Administration (FDA) in the United States through rules and regulations contained in Federal Registries, likewise the National Sanitary Surveillance Agency (ANVISA in its acronym in Portuguese) in Brazil, and the National Drugs, Food and Medical Technology Administration (ANMAT in its acronym in Spanish) in Argentina. Then the requirement of the CECMED to national laboratories and the Importing Units of the Superior Organization and the Ministry of Public Health (MINSAP in its acronym in Spanish), which are the drug providers of the LSP about the use of the GS1 standard codes in the different packaging levels is necessary; for this, it is important to comply with the Joint Resolution MINCIN/MINCEX 1/2001, where it is required that any traded product in Cuba must be registered in the Chamber of Commerce, where a GTIN code by GS1-Cuba is assigned. The CECMED must watch over this when approving the merchandising of products, and then claim to be printed on the packaging.

In Cuba, the coding system to be used with the GS1 standards must be implemented together with the CPCU version 2.0 as required by Resolution 49/2017 of the ONEI and the harmonized system; this will enable the standardization of product information in the traceability system. In general, it is important to ensure that article identification systems must integrate the coding and classification systems in a joint and interconnected manner.

Despite the standards are the key to access all the information regarding the product to identify, only with the identification of the product in the packaging is not a guarantee for an optimum performance of 3PL LSP traceability system. The standardization of all data that support the information flow must also be established, such as the unequivocal identification of the actors in the supply chain, the previous definition of each one of the support processes and the necessary technological infrastructure for the capture and registration of the information. All these elements must be shaped into a Traceability Plan to understand the system, and to show its existence to any external entity that requires it to establish businesses. The Traceability Plans proposed in the literature have several formats and contents, but in this article, based on the experience acquired in the research, a structure is proposed, related to the standards of unique product identification, in this case those of GS1.

The above does not mean that with the existing technology improvements based on the GS1 standards in the 3PL LSP cannot be established to the traceability system. For the implementation of these improvements the fundamental thing is the standardization of the information, and the solution to the problems that informatics systems present.

The impossibility of using a technological infrastructure that supports the processes for capturing and recording data or that it is limited, conducts the traceability system to huge risks, that is why the company must perform the necessary analysis to assess the risks and benefits in different technological scenarios according to the capital sum willing to invest.

The implementation of a traceability system based on the GS1 standards provides improvements to the 3PL LSP logistics system such as:

- Guarantee the security of health population and its consequent well-being.
- Allow the efficient and economic evaluation of productivity and quality control.
- Decrease in criminal acts.
- Improves inventory management.
- Control of logistics costs.
- Control of logistics cycles.

The traceability system must be frequently evaluated as a part of the 3PL LSP internal controls, this guarantees its constant valuation and allows the continuous implementation of improvements.

It is important to highlight that the current traceability system in the analyzed logistics system is considered efficacious, but its fundamental weakness is the efficiency by which it is possible to carry out a TRACE or TRACKING process, which reduces its competitiveness when globally -:compared.

In the Traceability Plan and unique identification procedure the use of GS1 standards is proposed, as it is one of the 39 agencies that globally issues unique codes, complying with ISO/IEC 15459 version 2016-07-12, and in case of drugs as a final product its standards are the most used in the different levels of packaging.

The proposed traceability plan and its implementation through its procedure is considered generalizable to any drug logistics Service Provider. The use of the GLN (Global Location Number) for identifying each control point is also recommended, which along with automatic identification technologies with linear, two-dimensional or even RFID (Radio Frequency Identification) patterns allow the Geo-traceability process to be carried out, using qualified 4.0 industry technologies.

All the aforementioned entails not only investment in technology, but also a conviction of the logistics system actors with its consequent learning and training system to achieve the most important thing, which is patient safety and the resiliency of the drugs supply chains.

5. Conclusions

1. The diagnosis of the current traceability system of the LSP allowed to detect as fundamental deficiencies the lack of a unique identification for products in their transit through the supply chain and the non-use of international coding standards, the lack of computerization of some fundamental data to trace the products and incongruences in the data recorded in the Software used by the company.
2. Legal regulations in Cuba regarding identification through GS1 standards and traceability systems are behind existing international regulations in the health sector.
3. The proposed solution is centered on a traceability plan and a unique drugs coding procedure for distribution and trade under GS1 international standards. This proposal is considered liable to generalize to other Logistic Service Providers, regardless of the region where they operate.
4. The use of a traceability plan will allow the company to assess the traceability system from a more strategic view and have it documented as a basis for subsequent evaluations and improvements.
5. The application of the proposed procedure makes it possible to eliminate the detected deficiencies, achieving through the use of the GTIN code throughout the whole supply chain the unique identification of drugs in the Cuban health system and contributing to their traceability. The use of an international standard language facilitates the communication among the different actors in the supply chain, allowing them to communicate in the same language.

References

[1] Chateauvieux, C., Cauchetier, E. and Descoutures, J., PS-067 Traceability intended for patients: investigation of suppliers of implantable medical devices., Eur J Hosp Pharm., 24, pp. A256, 2017. DOI: 10.1136/ejhpharm-2017-000640.573.

[2] Lazarides, H.N. and Goula, A.M., Sustainability and ethics along the food supply chain. In: Costa R. and Pittia P. (eds), Food ethics education. integrating food science and engineering knowledge into the food chain, vol 13. Springer, Cham., 2018. DOI: 10.1007/978-3-319-64738-8_3.

[3] Pérez, M.M., González, G.V. and Dafonte, C., The development of an RFID solution to facilitate the traceability of patient and pharmaceutical data. Sensors, 17(10), pp. 2247, 2017. DOI: 10.3390/s17102247.

[4] World Health Organization (WHO), A study on the public health and socieconomic impact of substandard and falsified medical products, 2017.

[5] World Health Organization (WHO), Global surveillance and monitoring system for substandard and falsified medical products, 2017.

[6] Boletín Electrónico de Salud, Comercio ilegal de medicamentos, un peligro mortal para la salud. [online]. 2010. Available at: http://boletinseps.blogspot.com/2010/02/comercio-ilega…medicamentos-un.html.

[7] World Health Organization (WHO), La falsificación de medicamentos: una amenaza creciente. Boletín de la Organización Mundial de la Salud, 88, pp. 241-320, 2010.

[8] Khan, S., et al., Implementing traceability systems in specific supply chain management (SCM) through critical success factors (CSFs). Sustainability, 10(1), p. 204, 2018. DOI: 10.3390/su10010204

[9] Kumar, V., et al., Contribution of traceability towards attaining sustainability in the textile sector. Textiles and Clothing Sustainability, 3(1), pp. 5. 2017. DOI: 10.1186/s40689-017-0027-8.

[10] Marconi, M., et al., Traceability as a means to investigate supply chain sustainability: the real case of a leather shoe supply chain. International Journal of Production Research, 55(22), pp. 6638-6652, 2017. DOI: 10.1080/00207543.2017.1332437.

[11] Kreysa, U. and Denecker, J., Estándares GS1 en el sector salud: marcando una diferencia en la cadena de abastecimiento del sector salud. Guía de Referencia de GS1 Healthcare, 2010.

[12] Torrens, N.V., Aplicación del modelo de referencia para la evaluación de la gestión de inventarios en los sistemas logísticos en EMCOMED., en: Departamento de Ingeniería Industrial. 2016, Instituto Superior Politécnico José Antonio Echeverría (CUJAE).

[13] Martinez, I.L., Modelo de referencia para la evolución de la gestión de los inventarios en los sistemas logísticos, en: Departamento de Ingeniería Industrial, Instituto Superior Politécnico José Antonio Echeverría, La Habana, Cuba, 2013.

[14] Denert-Stiftungslehrstuhl, E., Enterprise architecture management pattern catalog, 2008.

[15] CECMED, Reglamento para la vigilancia de productos farmacéuticos de uso humano durante la comercialización, 2015.

[16] CECMED, Resolución 11/2012. 2012, Cuba.

[17] QUIMEFA, Resolución 117/2008. 2008, Cuba.

[18] Cuesta, B.C. and Ramírez, R.d.l.N., Resolución Conjunta MINCIN/MINCEX. 2001.

[19] Ministerio de Finanzas y Precios de Cuba, Resolución 11/2007, 2007.

[20] Contraloría General de la República de Cuba., Resolución No.60/11, 2011.

[21] GS1 Argentina, Guía de implementación del estándar GS1 XML en el sector salud. 2012.

[22] Ríos, N.L., Construcción del plan de trazabilidad en las diferentes Líneas (recepción) manejadas por AVINCO S.A. 2010, Corporación Universitarias Lasallista Facultas de Ingeniería en Alimentos.

[23] Pascual, F., El papel del comercio mayorista en la aplicación de la trazabilidad. 2008.

[24] Gaspa, R., Trazabilidad en el comercio mayorista de alimentos frescos. 2007.

[25] Instituto Cerda, A., Estado actual y recomendaciones de la trazabilidad de la trazabilidad en la Mercas, Informe Completo. 2006.

[26] AECID, et al., Manual de trazabilidad para café protegido bajo una indicación geográfica o denominación de Origen. 2011.

[27] Callan, P.V. and Bailey, P., La contratación electrónica (eProcurement) en el Hospital St. James, Dublin. Guía de referencia de GS1 healthcare 2015/2016, 2015.

[28] Ministerio de Salud, Argentina, Regulación e Institutos A.N.M.A.T, Disposición 3683-2011. 2011.

[29] Marin, L.G.G., Soporte a la implementación de un sistema de trazabilidad para el sector salud en Colombia. Guía de referencia de GS1 healthcare 2010/2011, 2010.

I. Lopes-Martínez, is Dr. in Technical Sciences. BSc. in Industrial Engineering, Sp. in Companies Organization. Professor of Industrial Engineering Faculty of CUJAE, Head of Industrial Engineering Department. Member of the research group of Logistics and Production Management, LOGESPRO in its acronym in Spanish. Titular professor of logistics and supply chain topics in pregraduate and postgraduate formation.
ORCID: 0000-0002-1249-8833.

L. Paradela-Fournier, graduated of BSc. in Industrial Engineering. Professor of Industrial Engineering Faculty of CUJAE. Member of the research group of Logistics and Production Management, LOGESPRO. Instructor professor of logistics and supply chain topics in pregraduate and postgraduate formation.
ORCID: 0000-0002-3460-1563.

J. Rodríguez-Acosta, graduated of BSc. in Industrial Engineering. Professor of Industrial Engineering Faculty of CUJAE. Member of the research group of Logistics and Production Management, LOGESPRO. Trained professor of logistics and supply chain topics in pregraduate formation.
ORCID: 0000-0002-4337-6062.

J.L. Castillo-Feu, graduated of BSc. in Industrial Engineering. Professor of Industrial Engineering Faculty of CUJAE.
ORCID ID: 0000-0003-2353-2504.

M.I. Gómez-Acosta, is Dr. in Technical Sciences. Graduated of BSc. in Industrial Engineering. Professor of Industrial Engineering Faculty of CUJAE. Executive coordinator of the research group of Logistics and Production Management, LOGESPRO. Member of the European-Latin-American Center of Logistics and Ecological Projects, CELALE in its acronym in Spanish. Titular professor of logistics and supply chain topics in pregraduate and postgraduate formation.
ORCID ID: 0000-0003-0346-5340

A. Cruz-Ruiz, is MSc. in Social Communication. BSc. of Lic.in Psychology in the Havana University. Professor of the Psychology Faculty in the Havana University. Second Head of Profession Exercise Department.
ORCID ID: 0000-0002-7806-4026

UNIVERSIDAD NACIONAL DE COLOMBIA
SEDE MEDELLÍN
FACULTAD DE MINAS

Área Curricular de Ingeniería Administrativa e Ingeniería Industrial

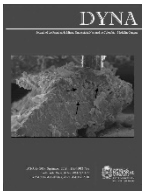
Oferta de Posgrados

Especialización en Gestión Empresarial
Especialización en Ingeniería Financiera
Maestría en Ingeniería Administrativa
Maestría en Ingeniería Industrial
Doctorado en Ingeniería - Industria y Organizaciones

Mayor información:

E-mail: acia_med@unal.edu.co
Teléfono: (57-4) 425 52 02

UNIVERSIDAD NACIONAL DE COLOMBIA
SEDE MEDELLÍN
FACULTAD DE MINAS



DYNA
http://dyna.medellin.unal.edu.co/

Development of a parametric cable driven planar robot

Juan Pablo Castrillón-Restrepo, Sebastián Jiménez-Gómez & Federico Saldarriaga-Ángel

Universidad EIA, Envigado, Colombia. juan.castrillon21@eia.edu.co, sebastian.jimenez1@eia.edu.co, federico.saldarriaga@eia.du.edu.co

Received: December 5th, de 2017. Received in revised form: May 5th, 2018. Accepted: July 24th, 2018

Abstract
Cable driven robots have been a widely researched topic in the last few years, this is due to the advantages that they present over conventional parallel robots. In this paper, all the areas of robotic design have been studied for a planar cable driven robot, with the objective of making it parametric, meaning that the design process and mathematical models used in this paper could be used to implement the suggested architecture to solve any specific need. Finally, using the parametric design approach, a prototype was developed and built in order to validate the design process, evaluate the robot's precision, identify future works and improvements and foresee any trouble that was not considered during the design phase.

Keywords: cable driven parallel robots; kinematics; feasible workspace; control systems; trajectory tracking.

Desarrollo de un robot cartesiano parametrizable comandado por cables

Resumen
Los robots comandados mediante cables han sido muy estudiados en los últimos años, debido a las ventajas que presentan con respecto a otros robots paralelos. En este trabajo, se estudian todas las áreas del diseño robótico para un robot por cables planar cuyo objetivo principal es ser parametrizable, es decir, que el proceso de diseño y los modelos matemáticos utilizados en este trabajo se puedan escalar fácilmente permitiendo implementar la arquitectura trabajada para necesidades específicas. Finalmente, usando el diseño paramétrico, se desarrolló y construyó un prototipo con el fin de validar el proceso de diseño y evaluar precisión en su movimiento, así como identificar futuras mejoras y prever puntos críticos tanto en el diseño mecánico como en los sistemas de actuación no consideradas en el proceso de diseño.

Palabras clave: robot comandado mediante cables; cinemática; espacio de trabajo alcanzable; sistemas de control; seguimiento trayectoria.

1. Introduction

Cable Driven Parallel Robots or CDPR have been widely studied in many areas. For uses such as Contour Crafting [1]] to manipulate patients in medical areas [2], these types of robots are versatile in many applications [3]. Therefore, CDPR are ideal for pick and place operations [4] due to their high speeds and large workspaces. Compared to rigid parallel manipulators, cable-driven parallel robots use cables as links instead of rigid ones to control the motion of the end-effector. CDPR provide desirable characteristics, including potential large workspace, the facility to be reconfigured, high speeds of motion, and high payload capacities to weight ratios [5]. Additionally, CDPR with small to very large cable lengths allow them to be stored on spools or drums thus allowing to build robots with a workspace of wide dimension. Depending on their size they may be less expensive, easier to build, reconfigured, safer and non-invasive [6].

The following paper takes a parametric approach on the design process of CDPR, highlighting one of the main advantages of these types of robots that is scalability. In order to validate and foresee possible errors in this approach, a prototype was developed and tested. Subsequently, the paper details the design and construction process for a suspended planar cable robot starting with the relevant mathematical models shown in section 2. Based on the models, a graphic interface was programed to be able to select the actuators needed for any suspended planar robot to be built, making its design parametric. Section 3 shows

How to cite: Castrillón-Restrepo, J.P., Jiménez-Gómez, S. and Saldarriaga-Ángel, F., Development of a parametric cable driven planar robot. DYNA, 85(206), pp. 49-58, September, 2018.

© The author; licensee Universidad Nacional de Colombia.

the interface and the mechanical, electronic and control design and implementation for a built prototype.

Finally, section 4 presents the measurement results of the said prototype's movements comparing simulations and experimental results in order to validate the design process. Conclusions are shown in the last section for future projects and recommendations for the construction process.

2. Models

Within CDPR, different architectures are identified and can be classified according to [7] in the following ways:

According to their degrees of freedom:

- Planar: They can move and turn in a single plane (2 dimensions)
- Spatial: Allow movement and orientation changes in a three-dimensional space

Depending on the connection between the cables and the end effector:

- Suspended: Constructed so that the vertical components of the tensions in the cables are always opposite to the force of gravity
- Commanded: A robot is considered commanded when some of the components of the cable tensions go in the same direction as gravity

Depending on the number of cables in the system:

- Under-Constrained: When the end effector has infinite positions or orientations for certain lengths of its cables
- Fully-constrained: When, through a combination of cable lengths, the end-effector can find only a single position or orientation
- Over-Constrained: When a single position or orientation can be reached through different cable configurations.

Mathematical models are defined to study robotic cable systems cables. These models vary depending on the architecture selected. This article focuses on a planar suspended robot and will then expose its relevant mathematical models: Inverse kinematics, static and velocity analysis.

2.1. Inverse kinematics

In a robot, kinematics is defined as the relationship between the position and orientation of its end effector with its articular coordinates [8]. In this way, the inverse kinematics allow to obtain the value to be taken by the actuators to achieve a specific position and orientation of the robot`s end.

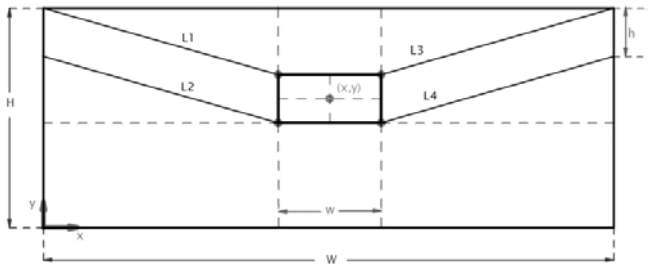


Figure 1. Representation of a suspended CDPR
Source: Authors

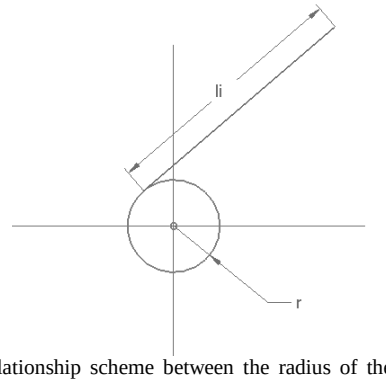


Figure 2. Relationship scheme between the radius of the pulley and the length of the cable
Source: Authors

In the specific case of the CDPR, the inverse kinematics aim to find the lengths of the cables for a certain position of the end-effector. In Fig. 1, a simplified scheme of the implemented architecture is presented:

Geometric relationships are found between the length of the cables (L1, L2, L3 and L4) and the position of the end effector as shown in the equations found at (1)):

$$\begin{aligned} L1_x = x - \frac{w}{2} \;;\; L1_y = H - \left(y + \frac{h}{2}\right) \\ L3_x = W - (x + \frac{w}{2}); L3_y \\ = H - \left(y + \frac{h}{2}\right) \\ Li_{total} = \sqrt{{li_x}^2 + {li_y}^2} \\ L1_{total} = \quad L2_{total} \\ L3_{total} = \quad L4_{total} \end{aligned} \tag{1}$$

Finally, the lengths with the articular coordinates are related making use of the diagram in Fig. 2 and the equation (2).

$$\begin{aligned} \Delta L_i = r * q_i \;\; where\, \Delta L_i \\ = l_{i-actual} - l_{i-desired} \\ q_i = \frac{\Delta L_i}{r} \end{aligned} \tag{2}$$

2.2. Static analysis

In cable driven parallel robots, the work space is limited, not only by the dimensions of the frame, but also by the tension present in each of the cables in a given instant [3]. Therefore, the workspace area of a CDPR is defined by the space within the frame whose Cartesian coordinates ensure that the tension has a positive value in all of its cables. If α is

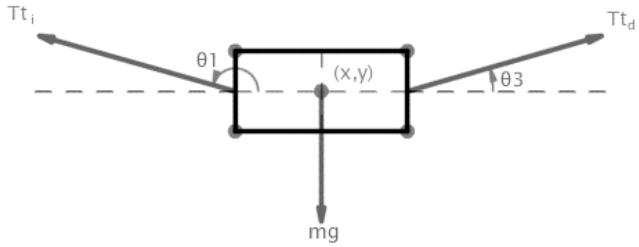


Figure 3. FBD simplification for the suspended cable driven robot
Source: Authors

defined as the set of the points that belong to the workspace, Equation (3) summarizes this definition in the following expression:

$$T(x,y) > 0 \rightarrow (x,y) \in \alpha \tag{3}$$

When defining Tt_i as the sum of tensions on the left side and Tt_d as the sum of tensions on the right side, the tensions can be simplified using a free body diagram (FBD) as shown in the Fig. 3.

By means of geometric relations, the values for the angles of the tensions can be expressed as in Equation (4).

$$\theta_1 = \pi - \tan^{-1}\left(\frac{H-(y+\frac{h}{2})}{x-\frac{w}{2}}\right)$$
$$\theta_3 = \tan^{-1}\left(\frac{H-(y+\frac{h}{2})}{W-(x+\frac{w}{2})}\right) \tag{4}$$

Establishing equilibrium equations ($\sum F_x = 0; \sum F_y = 0$), the Jacobian matrix ($A$) can be obtained and the independent term vector (b) shown in Equation (5).

$$\boldsymbol{A} = \begin{bmatrix} \cos(\theta_1) & \cos(\theta_3) \\ \text{sen}(\theta_1) & \text{sen}(\theta_3) \end{bmatrix}$$
$$\boldsymbol{b} = \begin{bmatrix} 0 \\ mg \end{bmatrix} \tag{5}$$

Lastly, to identify the tensions in the cables, the solution for the equation system is described as follows:

$$\boldsymbol{T} = \begin{bmatrix} Tt_i \\ Tt_d \end{bmatrix} = \boldsymbol{A^{-1}} * \boldsymbol{b} \tag{6}$$

It is then possible to generate the achievable workspace of this type of robots using a computational tool like *Matlab* ®. The result is shown in Fig. 44.

In reality, there are factors that modify the shape of this workspace; factors such as the minimum tension and the maximum tension allowed by the actuators. The evaluation of the effects of these factors on the workspace are observed in Fig. 5 and Fig. 6 respectively.

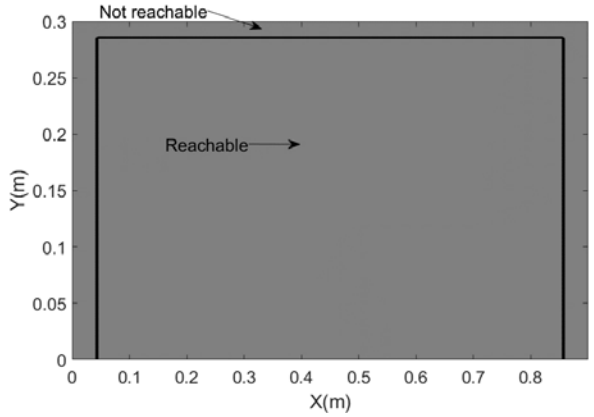


Figure Ideal workspace for a CDPR
Source: Authors.

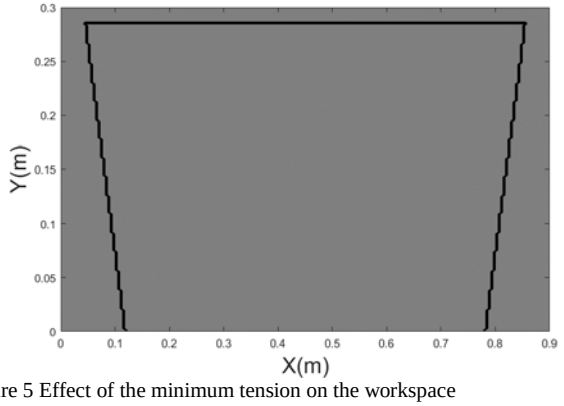


Figure 5 Effect of the minimum tension on the workspace
Source: Authors.

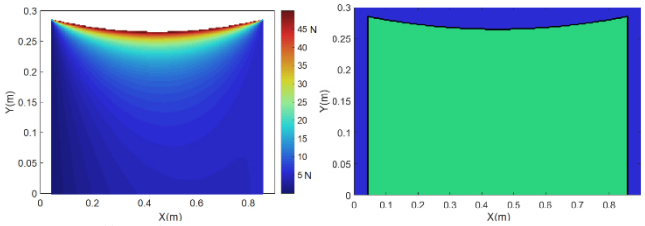


Figure 6. Effect of the maximum tension on the workspace
Source: Authors.

2.3. Velocity analysis

For the speed analysis of the robot, the mathematical model used was the inverse Jacobian matrix. This allows to obtain the speeds of the articulations of the Robot (actuators) starting from speeds defined for the edge [8]:

$$\begin{bmatrix} \dot{q_1} \\ \dot{q_2} \end{bmatrix} = \boldsymbol{J^{-1}} * \begin{bmatrix} \dot{x} \\ \dot{y} \end{bmatrix} \tag{7}$$

Starting from the equations (1) and (2) that describe the inverse kinematics, they can be derived in time and using eq.(7), the inverse Jacobian matrix is defined as shown in (8).

$$\dot{q}_i = \frac{dq_i}{dt} = \frac{dL_i}{dt} * \frac{1}{r} \qquad where\ r = pulleys\ radius$$

$$\begin{bmatrix} \dot{q_1} \\ \dot{q_2} \end{bmatrix} = \begin{bmatrix} \frac{x-w}{L_1 * r} & \frac{y+h-H}{L_1 * r} \\ \frac{x+w-W}{L_2 * r} & \frac{y+h-H}{L_2 * r} \end{bmatrix} * \begin{bmatrix} \dot{x} \\ \dot{y} \end{bmatrix} \quad (8)$$

3. Tools and methods

3.1. Parametric design

Based on the mathematical models explained in the previous section, aiming to develop a parametric system, a program was developed in order to select the actuators required for the construction of any CDPR with the mentioned architecture (planar suspended). Specifying needs of space and load of the robot, the interface also needs the following parameters as entrees for the calculus:

- Height: Vertical dimension of the desired work space and the end effector in meters.
- Payload: Mass in kg to be manipulated by the robot.
- Dimension factor: A factor that relates how large the frame in regar• Length: Horizontal dimension of the desired working space and the end effector in meters
- ds to the desired workspace of the robot (must be greater than 1)
- Minimum tension safety Factor: Percentage of the mass equal to the minimum tension of the robot. This factor guaranties that the tension in the cables is never equal to zero or negative values; therefore, the robot never loses orientation of the end effector.
- Pulley Radius: Radius of the pulleys carrying the actuators.
- X: presents two spaces to enter the initial and final position of the effector in the x-coordinate, in order to calculate the speeds.
- Y: Presents two spaces to enter the initial and final position of the effector in the y-coordinate, in order to calculate the speeds.
- T: time to perform the movement established in the previous entries.

As output parameters, the interface is capable of calculating the minimum torque required, the maximum velocities and the power of the motors or actuators needed for the robot. The interface can be seen in Fig. 7:

Using the developed program, actuators were calculated to create a prototype. It was determined that the robot to be built will handle a load of 1 kg and reach maximum vertical speeds of 20 cm/s. So, the input and output parameters are seen in Table 1 and Table 2 respectively:

3.2. Mechanical system

Once the requirements of the actuators are obtained, the characteristics of the chosen motors are seen in Table 3 [9].

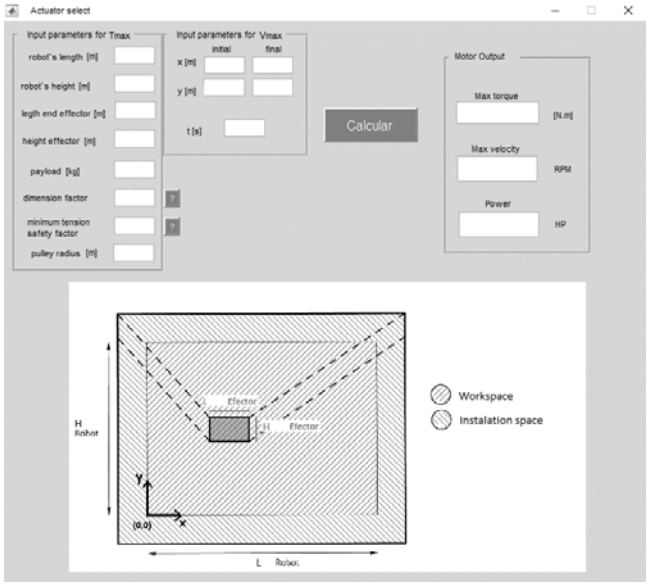


Figure 7. Program interface for the selection of actuators
Source: Authors.

Table 1.
Entre parameters for the user interface

Parameter	Value
Length of the Robot	0.9 m
Height of the Robot	0.3 m
Length of effector	0.12 m
Height of effector	0.04 m
Payload	1 kg
Dimension factor	1.42
Minimum tension safety factor	0.1
Pulley Radius	0.05 m
X Initial	0.45 m
X final	0.45 m
Y initial	0.3 m
Y final	0.1 m
t	1 s

Source: Authors.

Table 2.
Parameters given by the user interface

Output	Value
Minimum torque required	1.3741 Nm
Maximum velocity	16.7119 RPM
Power	0.003224 HP

Source: Authors.

Table 3.
Parameters for the motor used in the prototype

Specifications of the Motor POL1445	
Size	37D x 66L (mm)
Weigh	220g
Shaft diameter	6mm
Transmission relationship	70:1
Free rotation speed @ 12V	150 rpm
Free rotation current @ 12V	300 mA
Stall current	5 A
Stall torque	200 oz-in(1.42 N.m)

Source: Authors.

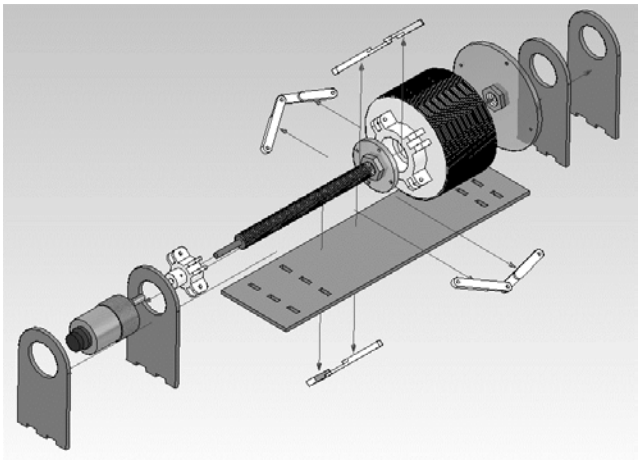


Figure 8 Mechanism to wind the cable
Source: Authors.

Once the actuators were chosen, it was necessary to develop a mechanical system that allowed the cable to be rolled and released. A mechanical system was implemented to ensure that the pulley radius did not change, and the alignment of the cable remained constant. To avoid distorting forces in the end effector movement, a solution was based on [10] and modified to adapt to the specific needs of the prototype.

The mechanism is a threaded drum or pulley, where the cable winds up. This drum spins in a fixed threaded shaft to ensure the same starting point for any instance of time. The details of the adapted mechanism are seen in Fig. 8.

The next elements in the robot's mechanical system are the upper pulleys. These allow the cables to have opposite tensions to gravity, even if the actuators are positioned at ground level. Their design was made in order to eliminate any perpendicular forces to the motion plane of the robot, as well as unwanted output angles. For this reason, they were designed with a minimum thickness so that only a nylon cable could pass between their inner faces (Fig. 9).

Finally, the end effector was designed so that the four cables could be secured ensuring that the distance between cables never changed, as shown in the Fig. 10.

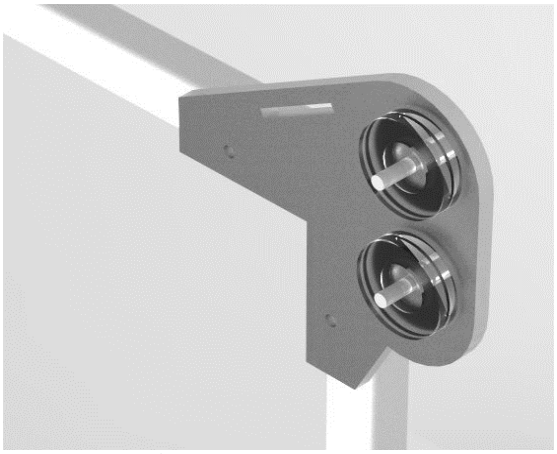


Figure 9. Top pulleys of the CDPR
Source: Authors.

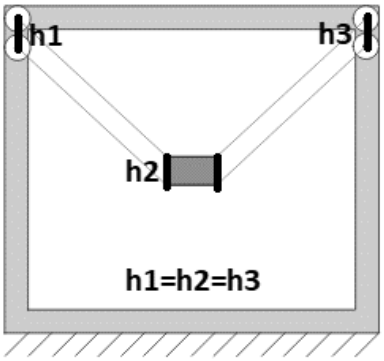


Figure 10. Illustration for equal lengths between cables.
Source: Authors.

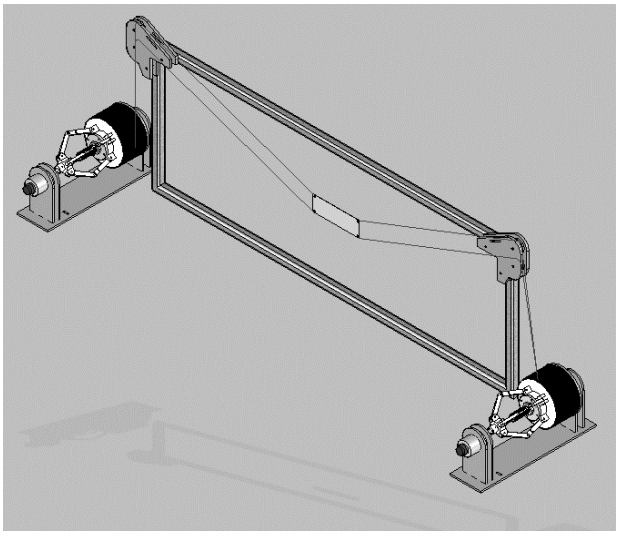


Figure 11 Mechanic assembly of the CDPR
Source: Authors.

Fig. 11 shows the mechanic assembly of the CDPR.

3.3. Control system

To determine the position of the end effector in the robot, position controllers were tuned for the actuators and a decentralized design was implemented to enable perform synchronous tasks. This meaning, being able to perform movements on both motors simultaneously.

The tuning of these controllers starts with the identification of the system then a controller design process and a final performance evaluation [11].

3.3.1. System identification

To appropriately control the actuators, it is first necessary to identify system dynamics using a transfer function. To avoid the inherent destabilizing dynamics in the position of a dc motor, the angular velocity of the system had to be identified, and then proceed to find the position function, using the expression shown in equation (9).

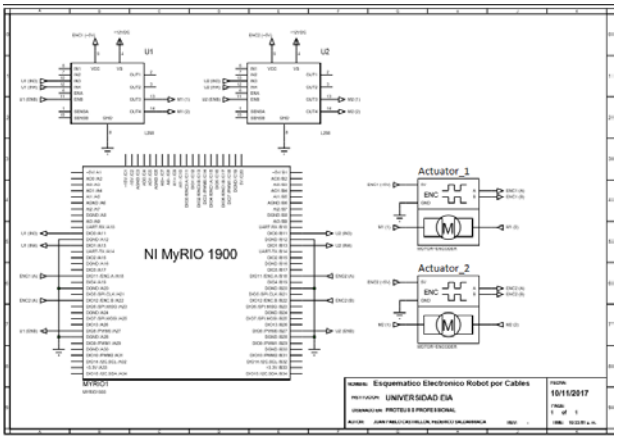


Figure 12. Connection diagram for identification and operation of the DC motors in the CDPR
Source: Authors.

$$\omega(t) = \frac{d\theta(t)}{dt} \rightarrow \omega(s) = \theta(s) * s \tag{9}$$

To identify the system, the motor was stimulated using step signals in PWM percentages and the response of its angular velocity was observed using the incremental Quadrature encoder integrated into the motor. For this, a National Instruments MyRIO acquisition board was used [12] and connected to the actuators as shown (Fig. 12).

Equation (10) shows the formula used to determine the angular velocity of the motor using position measuring elements such as quadrature encoders:

$$\omega\ (rpm) = \frac{\frac{encoder\ pulses\ (process\ output)}{ppr(4480)} * \frac{60\ s}{1\ min}}{sample\ time\ _{(s)}(0.01)} \tag{10}$$

It is necessary to mention that this measurement is possible given the good resolution of the encoders and the acquisition board. Otherwise this identification strategy would not be feasible.

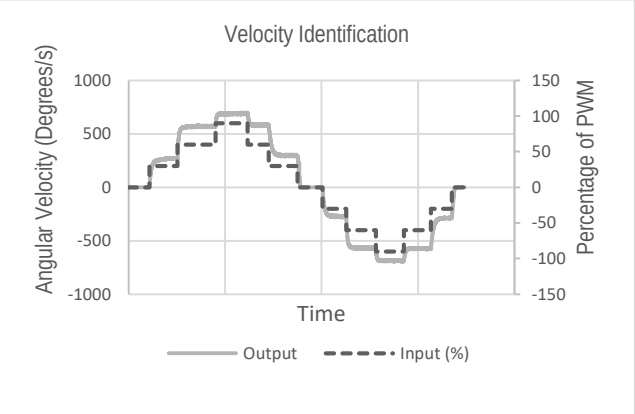


Figure 13. Identification process
Source: Authors.

Table 4.
Tuned controllers for the actuators

Controller	Equation	P	I	D	N
PID	$P + \frac{I}{s} + \frac{D * N}{1 + \frac{N}{s}}$	0.277	0.00598	0.146	285.02
PI	$P + \frac{I}{s}$	0.0475	0.00034	X	X
PD	$P + \frac{DN}{1 + \frac{N}{s}}$	0.2964	X	0.155	304.8

Source: Authors.

The data obtained from the identification experiment is observed in Fig. 13.

The data shown in Fig. 13, was processed using the *Matlab*® identification toolbox which estimates a transfer function (*tf*) and evaluates its accuracy or fit using system data. With a fit of 88.61%, the transfer function obtained can be observed in eq. (11).

The parameters given for the identification process were 1 pole and no zeros in order to get the transfer function (11).

$$tf\ for\ velocity = \frac{17.18}{s + 1.933} \tag{11}$$

The mentioned fit is given by the program and calculated internally by the *Matlab*® identification toolbox [13].

Once the velocity transfer function was established, it was integrated to the time factor to obtain a position transfer function:

$$tf\ for\ position = \frac{17.18}{s^2 + 1.933s} \tag{12}$$

3.3.2. Controller design

Starting 3 main architectures of controllers (PID, PI and PD), these were designed with similar performance parameters to obtain a system with critically damped behavior (ζ=1). Using a sampling time of T=0.01 and settling times 1.5 and 4 seconds, the best controllers of each type were obtained and are described in Table 4.

3.3.3. Performance evaluation

Given the desired settling times and robustness parameters for the tuned controllers [14], a pattern signal was designed (Fig. 14) including sine-type dynamics given their smooth accelerations and ramp-type dynamics in order to obtain constant speeds and step-type references to evaluate their behavior to drastic changes in the reference. This signal tested the three designed controllers (Table 4).

Error metrics were used to evaluate controller performance by means of: ITAE and relative error, related in equations (13) and (14). Table 5 shows the comparison of the results for each controller. It is seen that for both performance parameters the controller PD had the best performance.

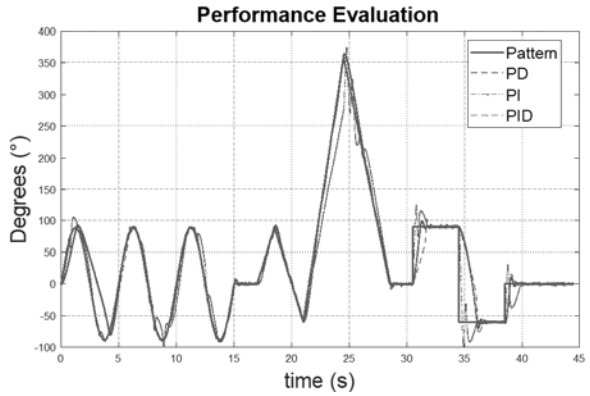


Figure 14. Pattern signal for controller evaluation
Source: Authors.

Table 5.
Controller performance to the pattern signal

Controller	ITAE	$\hat{e}$(%)
PD	8.905	12.501
PI	16.44	15.583
PID	21.68	32.8871

Source: Authors.

Considering the hardware used and its limitations, the error obtained for the PD controller is partially the result of having low specification hardware. Factors such as encoder resolution or gear backlash can greatly affect the controller performance [15]. Improving hardware specifications can resolve smaller errors as shown in [16].

$$ITAE = \int_{to}^{tf} t * |y(k) - \hat{y}(k)| dt \tag{13}$$

$$\hat{e} = \frac{1}{N} * \sum_{k=to}^{tf} \left| \frac{y(k) - \hat{y}(k)}{y(k)} \right| * 100 \tag{14}$$

It is important to consider that the error measured for each controller considers both transient and stable state dynamics. It is also generated by trying to follow an ideal trajectory, which represents the most critical conditions possible in terms of speed and acceleration for the robot's movement and position control system.

3.3.4. Motor synchronization

Because cable driven robots are parallel robots, trajectories of the end effector depend on how synchronized the robot actuators (motors) are. In other words, appropriate and adequate movement of the end effector, the initial and final times for the trajectory of the motors must be as similar as possible. This, not only guarantees the initial and final position of the effector, but also ensures linearity in the trajectories to be performed. To determine dual motor synchronization, an experiment was designed in which, the PD controller was implemented in both actuators and the pattern signal of both motors was measured to compare results.

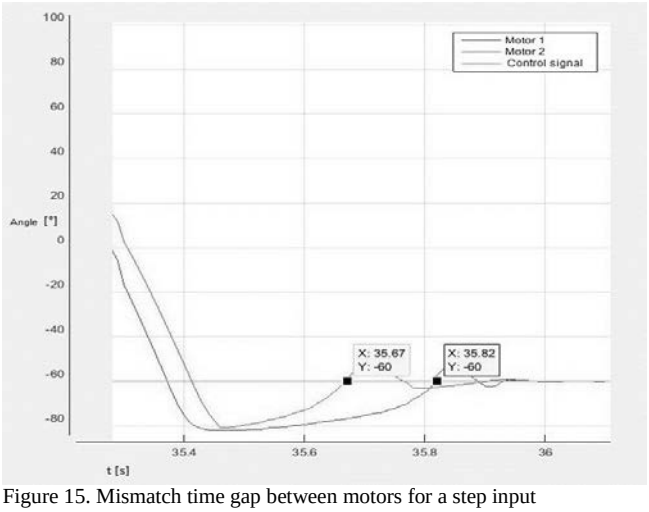


Figure 15. Mismatch time gap between motors for a step input
Source: Authors.

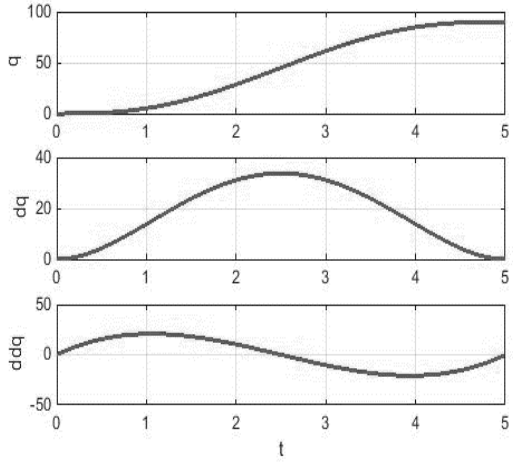


Figure 16. Fifth order trajectories
Source: Authors.

When measuring actuator behavior, the greatest time mismatch for the step type signals was of 0.2 seconds. An example of this behavior is shown in Fig. 15. This gap is considered acceptable because step signal dynamics will not be present in the robot, because as shown in the next section, soft polynomial trajectories were chosen as reference signals for the system.

3.3.5. Trajectory generation

In order to restrict actuator accelerations and speeds in all points of the trajectory, high order polynomial trajectories were selected [17]. From these trajectories, physical restrictions, precision criteria and softness were then contemplated [8]. Otherwise, "in the polynomial trajectories the degree of the polynomial depends on the number of conditions to be satisfied as well as of the smoothness in the resulting movement" [18] fifth-order trajectories were implemented, like those shown in Fig. 16.



Figure 17. Real prototype CDPR
Source: Authors.

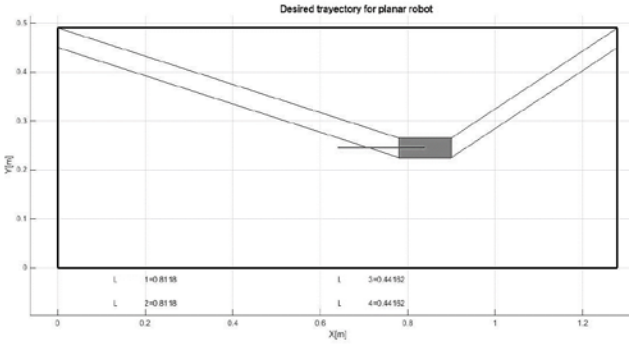


Figure 18. Horizontal trajectory
Source: Authors.

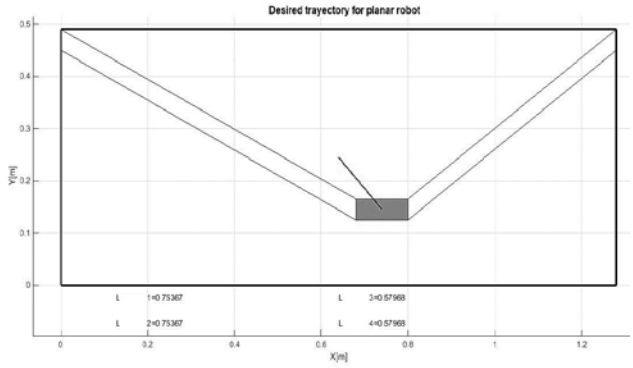


Figure 19. Diagonal trajectory
Source: Authors.

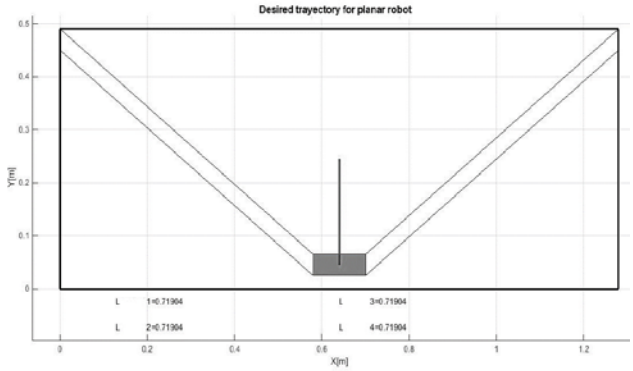


Figure 20Vertical trajectory
Source: Authors.

4. Results

The built robot can be seen in Fig. 17.

Once built, three Cartesian trajectories were designed to test its operation, which are seen in Fig. 18 through Fig. 20.In order to obtain displacement measurements for the end effector to determine the precision of the prototype, two different measurements were used: first, the trajectories in the motors were simulated without having the robot assembled and with the use of the direct kinematics of the robot, an approximate trajectory of the end effector was produced. Second, with the built robot and using the assembly shown in Fig. 21, a video of the robot`s movement was taken and analyzed with video analysis software. Measuring the end-effector position using computer vision, which has proven to be an adequate method that presents the advantage of demonstrating the effects of certain parameters such as the flexible nature of cables. Simultaneously, because it is an external measurement, system performance is not affected [6]. Tracker software works by measuring an object's displacement frame by frame to determine the actual movement of the object in the video [19]. This, to point out that the robot was recorded with a 60 FPS and 1080 p. camera.

Both results (simulation and real movement), as well as the desired trajectory, are showed in Fig. 22 through Fig. 24:

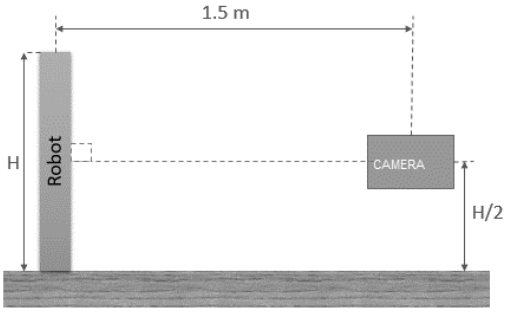


Figure 21. Setup used to record the movement of the robot
Source: Authors.

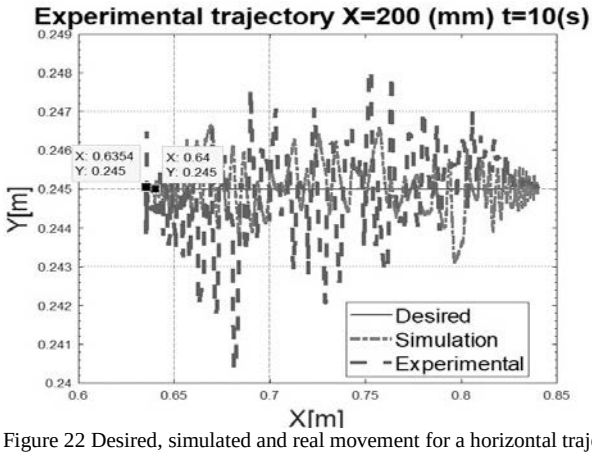


Figure 22 Desired, simulated and real movement for a horizontal trajectory of 20 cm
Source: Authors, 2018.

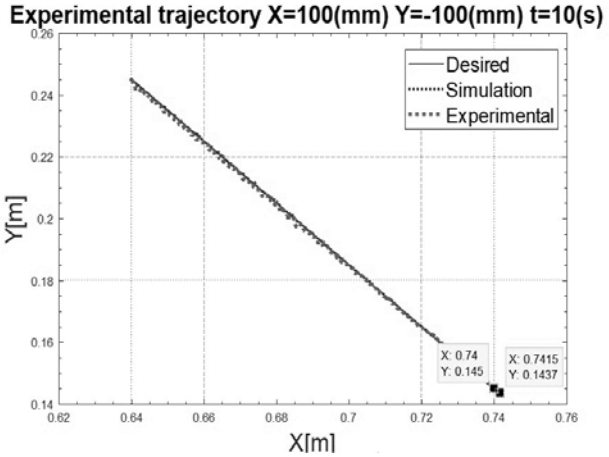


Figure 23. Desired, simulated and real movement for a diagonal trajectory of equal components (10 cm)
Source: Authors.

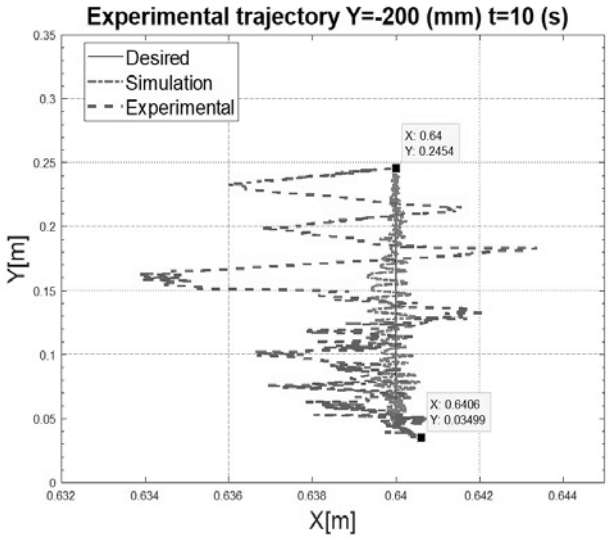


Figure 24. Desired, simulated and real movement for a vertical trajectory of 20 cm
Source: Authors.

In the previous figures, the blue trajectory is the desired, the red trajectory is the simulated using the encoder measurements and the direct kinematics model and the violet trajectory is measured with the non-invasive proposed method. The previous tests show that the maximum deviation for the built prototype was 3% for the trajectory of 200 mm in X.

Errors can be traced back to many factors of the prototype. On the other hand, hardware limitation influence in controller performance, explained in section 3.3.3, proves there are certain inherent factors in cable driven robot dynamics that can affect the precision and accuracy of the robot. These factors include pulley design, cable properties such as material, elongation and mass, and the estimation of the feasible workspace of the robot [15].

As seen in the previous figures, horizontal movements present more errors than vertical. This can be explained due to fact that the motors are not completely synchronized as shown 3.3.4. This time gap between both motors has greater influences on movements requiring both motors to move in the same direction than on those requiring opposite movements. Also, gravity acts as an orthogonal force in horizontal movements which causes undesired behaviors in the cables.

5. Conclusions

Regarding the calculation of the robot's workspace, two fundamental factors are derived for its optimization, the minimum tension factor and the maximum tension. Analyzing the complexity of optimizing both parameters simultaneously one can opt to leave one of these parameters as input (fixed) and calibrate the other. Finally, maximum torque was optimized because it was found that the security factor can be personalized according to the application or scenario in which the robot is going to operate.

The maximum torque calculated using the workspace only takes into consideration static effects. This condition restricts the veracity of the calculation and makes it valid for small speeds and accelerations where the dynamic effects are negligible.

When evaluating motor synchronization, the obtained results were considered satisfactory because both motors were adjusted with the design of one controller.

The use of high-order trajectories is fundamental in these types of applications. Ensuring smooth speeds and acceleration curves causes actuators to make low efforts that do not compromise the mechanical design of the robot.

When transitioning from simulations to the prototype, robot precision and accuracy was smaller than in the simulations. This is because the mechanical components of the robot influence the control of the motors causing the actuator not to move in a linear way and have millimetric errors in its Cartesian position. One of these mechanical factors is the backlash between the threaded shaft and the drum of the cable collection mechanism. In addition, it has been shown [7], that changing the shape of the end effector for one that includes fixed pulleys of the same radius as the pulleys of the structure, significantly improves robot movement.

References

[1] Bosscher, P., et al. Cable-suspended robotic contour crafting system, Automation in Construction, 17(1), pp. 45-55, 2007. DOI: 10.1016/j.autcon.2007.02.011

[2] Burcio, A., Demostración de mejora cinemática para el posicionamiento de robots comandados mediante cables, BSc. Eng. Thesis, Department of Industrial Engineering, Castilla- La Mancha University, Toledo, Spain, 2015.

[3] Garrido, J., Diseño de un robot 3D comandado por cables a partir de un modelo cartesiano convencional, BSc. Eng. Thesis, Department of Industrial Engineering, Castilla- La Mancha University, Ciudad Real, Spain, 2015.

[4] Kawamura, S., et al., Development of an ultrahigh speed robot FALCON using wire drive systems, Journal of the Robotic Society of Japan, 15(1), pp. 82-89, 1997. DOI: 10.7210/jrsj.15.82

[5] Tang, X., An overview of the development for cable-driven parallel manipulator, Advances in Mechanical Engineering, 6, 2015. DOI: 10.1155/2014/823028

[6] Dallej, T., et al., Towards vision-based control of cable-driven parallel robots, Proceedings of 2011 IEEE/RSJ International Conference on Intelligent Robots and Systems, [online]. 2011, pp. 2855-2860. Available at: https://ieeexplore.ieee.org/abstract/document/6094591/
[7] Magán, A., Robot paralelo comandado mediante cables de 4 grados de libertad, BSc. Eng. Thesis, Department of Industrial Engineering, Castilla- La Mancha University, Toledo, Spain, 2015.
[8] Barrientos, A., Fundamentos de robótica., Madrid, McGraw-Hill, 2007.
[9] Pololu.com. (2018). Pololu - 70:1 Metal Gearmotor 37Dx54L mm with 64 CPR Encoder (No End Cap). [online]. Available at: https://www.pololu.com/product/1445
[10] Castillo, F., Video Conferencia. [online]. 2016. Available at: http://enlinea.eia.edu.co/player.php?media=/multimedia/otros/seminario_congreso_ciima_1 [Accessed 1 Aug. 2016].
[11] Dorf, R. and Bishop, R., Modern control systems, 12th ed., Estados Unidos, Prentice Hall, 2011.
[12] I. National Instruments, User Guide and Specifications Ni myRIO-1900 [online]. Available at: http://www.ni.com/pdf/manuals/376047d.pdf
[13] Mathworks, Matlab® 2017. [Online]. Available at: https://es.mathworks.com/products/matlab.html.
[14] Álvarez, C., Soto, A. and Watkins, F., Simulación de controladores digitales, Ingeniare. Revista Chilena de Ingeniería, 17(3), pp. 309-316, 2009. DOI: 10.4067/S0718-33052009000300004
[15] Schmidt, V., Modeling techniques and reliable real-time implementation of kinematics for cable-driven parallel robots using polymer fiber cables, Ph.D Dissertation, Faculty of Design, Production and Vehicle Technology, Universität Stuttgart, Stuttgart, Germany, 2017.
[16] Wei, H., Qin, Y. and Su, Y., Motion control strategy and stability analysis for high-speed cable-driven camera robots with cable inertia effects, International Journal of Advanced Robotic Systems, pp. 1-14, 2016. DOI: 10.1177/1729881416663374
[17] Melchiorri, C., Trajectory planning for robot manipulators, Universit`a di Bologna, 2008. [Online]. Available at: http://www-lar.deis.unibo.it/people/cmelchiorri/Files_Robotica/RIM_09_Traj.pdf
[18] Florez, D., Castro, F. y Castillo, R., Planeación y ejecución de trayectorias en robot delta, Universidad Militar Nueva Granada, 2014. DOI: 10.22517/23447214.11241.
[19] OSP and ComPADRE. Tracker video analysis and modeling tool, 2017. [Online]. Available at: http://physlets.org/tracker/

J.P. Castrillón-Restrepo, is graduated from Universidad EIA, Colombia with a BSc. Eng in Mechatronics Engineering. His bachelor thesis, developed alongside Federico Saldarriaga, explores the implementation of a cable driven planar robot in logistics applications.in 2017, he did an internship in "AKT Motos", developing various mechatronics projects including a pick to light system. He has also participated in the "Motors, Thermal Machines and Automotive Motion" seedbed research group in Universidad EIA.
ORCID: 0000-0002-7832-1344

S. Jiménez-Gómez was born in Medellin - Colombia in 1987. He obtained the BSc. degree of Mechatronic Engineer in 2011 and the MSc. degree in Mechatronics in 2013, both from the Militar Nueva Granada University, Bogota-Colombia. He had an honor distinction for his master thesis called Design and assembly of an experimental setup for characterization and testing of Magneteorheological dampers. Currently he is part of the Department of Automatic and Robotics and is lecturer in control and automation subjects at EIA University, Colombia. His research interest is focused on identification and control of electro-mechanical systems.
ORCID: 0000-0003-3047-8809

F. Saldarriaga-Ángel, has participated in the "Drones & UAVs" seedbed research group in Universidad EIA, Colombia. In 2017, he did an internship in "Avianca" where he focused on projects based on Lean 6 sigma methodology. Graduated from EIA University Colombia, he finished a BSc. in Eng in Mechatronics Engineering in 2017. His bachelor thesis, developed alongside Juan Pablo Castrillón, explores the implementation of a cable driven planar robot in logistics applications.
ORCID: 0000-0001-9420-9742



UNIVERSIDAD NACIONAL DE COLOMBIA
SEDE MEDELLÍN
FACULTAD DE MINAS

Área Curricular de Ingeniería Eléctrica e Ingeniería de Control

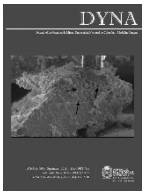
Oferta de Posgrados

Maestría en Ingeniería - Ingeniería Eléctrica

Mayor información:

E-mail: ingelcontro_med@unal.edu.co
Teléfono: (57-4) 425 52 64

UNIVERSIDAD NACIONAL DE COLOMBIA
SEDE MEDELLÍN
FACULTAD DE MINAS



DYNA
http://dyna.medellin.unal.edu.co/

Effect of fly ash and silica fume on rheology, compressive strength and self-compacting in cement mixtures

Jaime Arturo Correa-Yepes [a], Nestor Rojas-Reyes [b] & Jorge I. Tobón [a]

[a] *Group of Cement and Building Materials, Department of Materials and Minerals, Faculty of Mines, Universidad Nacional de Colombia, Medellín, Colombia. jacorreay@unal.edu.co, jitobon@unal.edu.co*
[b] *Cimex Minerals Institute, Department of Materials and Minerals, Faculty of Mines, Universidad Nacional de Colombia, Medellín, Colombia. nrrojasr@unal.edu.co*

Received: November 22th, 2017. Received in revised form: March 11th, 2018. Accepted: April 25th, 2018.

Abstract
In this research the effect of the addition of silica fume (SF) and fly ash (FA) to the ordinary Portland cement (OPC), individually and in combination, on rheology, compressive strength and self-compacting capacity in mixtures of cement were evaluated. At the beginning, the physicochemical characterization of the raw materials was carried out using XRF, SEM and PSD. Subsequently the rheological analysis was done in order to determine yield stress and plastic viscosity, then the compressive strength was measured at 7 and 28 days of normal curing. Finally, the measurement of the self-compacting capacity by means of a V-funnel was performed. It was found that the FA influences positively because it reduces yield stress and self-compacting test times, but decreases the compressive strength in comparison to control sample. The addition of SF increases the yield stress and self-compacting times, but positively influences the compressive strength. By analyzing the combinations of FA and SF additions the effects of each one are maintained allowing finding an addition range that delivered efficient values for the performance of fresh and hardened state of the blended cement pastes.

Keywords: cement rheology; mineral additions; yield stress; viscosity; self-compacting cements.

Efecto de las cenizas volantes y el humo de sílice sobre la reología, resistencia a la compresión y autocompactación en mezclas de cemento

Resumen
En esta investigación se evaluó el efecto de la adición de humo de sílice (SF) y cenizas volantes (FA) al cemento Portland ordinario (OPC) de manera individual y combinada, sobre la reología, resistencia a la compresión y capacidad de autocompactación en mezclas de cemento. Se realizó la caracterización fisicoquímica de las materias primas mediante FRX, SEM y DTP. Se hizo el análisis reológico para determinar el esfuerzo de fluencia y la viscosidad plástica. Se midió la resistencia a compresión a 7 y 28 días de curado normal. Por último, se realizó la medición de la capacidad de autocompactación por medio cono en V. Se encontró que la FA influye de manera positiva al reducir el esfuerzo de fluencia y los tiempos de prueba en la autocompactación, pero disminuye la resistencia a la compresión respecto a la muestra control. La adición de SF incrementa el esfuerzo de fluencia y los tiempos de autocompactación, pero influye de manera positiva en la resistencia a la compresión. Al analizar las combinaciones de adiciones de FA y SF los efectos de cada adición se mantienen permitiendo encontrar un rango de adición que entregó valores eficientes tanto para el desempeño en estado fresco como endurecido de las pastas.

Palabras clave: reología de cemento; adiciones minerales; esfuerzo de fluencia; viscosidad; cementos autocompactantes.

1. Introduction

Nowadays, the use of mineral additions is paramount in reducing energy consumption, emissions of polluting gases and the production costs of both cement and concrete. Nonetheless, it can not be forgotten that all additions will have an impact on

How to cite: Correa-Yepes, J.A., Rojas-Reyes, N. and Tobón, J.I., Effect of fly ash and silica fume on rheology, compressive strength and self-compacting in cement mixtures. DYNA, 85(206), pp. 59-68, September, 2018.

© The author; licensee Universidad Nacional de Colombia.

the performance of both fresh and hardened cement mixtures. Depending on characteristics such as shape and size of particles, reactivity and percentage of substitution of the cement, the rheological properties (yield stress and viscosity), the mechanical strength (at initial and final ages) and the self-compacting capacity of the mixtures will be modified.

1.1. Rheology

The rheology of concrete is an issue of interest both for its influence on the placement of the material as well as for the mechanical response when it reaches the hardened state [1]. The yield stress and the plastic viscosity are two of the parameters that define the rheology of a mixture, where a low yield stress and a moderate viscosity lead to consolidation and increase fluidity without segregation between the cementing material and the aggregates [2].

In recent years there has been growing interest in research on the issue of industrial waste as mineral additions to cement and concrete, such is the case of Fly Ash (FA) and Silica Fume (SF) [3,4].

Some researchers have determined that the inclusion of FA in the cement pastes reduces both yield stress and viscosity, due to its spherical shape and its wide particle size distribution that promotes the fluidity of the mixture; thus functioning as "filling" and increasing the packing factor [4,5]. Regarding compressive strength, FA reduces it at early ages (7-14 days), due to its low reactivity with respect to other additions [4,6].

In the case of SF, due to its purity and its average size of up to four times less than that of the cement, it offers high reactivity, accelerates the hardening of the mixture and at the moment of flow increases the particle to particle interaction; thus generating a high friction and restricting workability [7]. In the same sense, as asserted by Park and col. [3], SF reactivity is also reflected in the final resistance, reaching resistance in some cases over those achieved with pure OPC [8].

In simple additons of OPC plus FA, as stated by Lee and col. [9], the ash itself promotes fluidity by its spherical shape as it sets in the flocs in formation of the OPC and water, but before high replacement percentages, due to its low reactivity derived from both its size and composition; good resistance are not reached at early ages of hardening, this condition is compensated with the addition of SF that in the early ages of the mixture improves the workability and later, compensates for the compressive strength deficiencies with its ability to improve the mechanical strength due to its high reactivity [8], this is the reason why it is sometimes more convenient to think about composite additions rather than simple ones [3,10].

The rheological model used in this study is the Bingham equation (Equation 1), which is widely used for cement-based mixtures, because it describes its behaviour as a viscoplastic fluid in which there is a conversely stress (τ_0) and the rest of the behaviour is similar to a Newtonian fluid [11,12], a necessary condition to be able to apply this model is that the values of shear rate ($\dot{\gamma}$) must be bellow 300 s-1 , this is because research has shown that for higher values the system is distorted and the stress value (τ) increases in an uncontrolled manner [3,13].

$$\tau = \tau_0 + \eta\dot{\gamma} \quad (1)$$

Where:

τ = Shear stress [Pa]
τ_0 = Yield stress [Pa]
η = Plastic viscosity [Pa·s]
$\dot{\gamma}$ = Shear rate [s^{-1}].

2.1. Self-compacting

Self-compacting mixtures can be defined as those that can easily flow by their own weight and self-consolidate without the help of a mechanical vibration system, reaching high deformation capacity and volumetric stability as well [14]. Self-compacting concrete has high fluidity and its implementation allows placement in complicated forms without vibration or without segregation [15]. For self-compacting concrete, insufficient compaction causes the increase of air bubbles which leads to a reduction in concrete strength and durability [16]. Self-compacting cements have provided a promising vision of the concrete industry with respect to environmental impact and cost reduction; however, the use of cement mixtures with mineral mixtures has not developed sufficient applications for the production of these cements [17].

This is the case of Fly Ash (FA) and Silica Fume (SF) [2-4], they have found that these additions affect significantly both the performance and placement of self-compacting cement mixtures.

1.3. Influence of mineral additions

1.3.1. Influence of particle size

Generally, with a smaller particle size of the addition, the packing factor increased by reducing the vacuum ratios per unit volume. As the packing factor increases, fluidity is promoted, because the deformation capacity increases due to the compactness of the mixture, this condition has a certain range of efficiency since the greater number of particles per unit volumen also increase the particle to particle interaction, which at the moment of flow increases the friction among particles, which restricts the movement of the mixture; for this reason the particle size distribution should be as wide as possible so that finer materials improve both the lubrication and packing of the mixture while thicker materials reduce the particle to particle interaction [13,18,7].

1.3.2. Influence of flocculant capacity

The flocculation processes of the cement-based mixtures obey a Brownian movement due to their particle size, variety of electric charges, the flocculation capacity itself and the hydration process. The additions of SF and FA affect the flocculation processes in different ways, with respect to the presence of SF, its great purity and fine size makes it a quite reactive addition, which permits the formation of flocs with cement, accelerating hydration and reducing the workability of the mixture. With regard to FA, its low reactivity interrupts the flocs in formation and its wide particle size distribution reduces the particle to particle interaction; moreover, due to

its low reactivity at early ages, the focculation energies of the cement are reduced, inducing a plasticizing effect, this phenomenon is reflected in the self-compacting capacity since there is a direct relationship between low fluidity effort and viscosity and high fluidity as well [13,4,5].

1.3.3. Influence on compressive strength

Mohamed in 2011 reported that the higher the FA percentage the higher the compressive strength values up to 30%; instead for SF the highest values were found only at 15% of addition; and for ternary mixtures the highest compressive strength values were found with 10% of FA and 10% of SF [19]. Turk in 2012 found that the compressive stress improved with the presence of FA in binary mixtures and with all the ternary mixtures of FA and SF [18]. Jadhav and Chavarekar in 2013 found that mixtures of cement with FA and microsilica increased by 12.9% the compression effort compared to the control sample for 2.5% of each of the additions [20]. Raharjo and col., in 2013 reported a statistical equation to determine the compression strength of cement mixtures with FA, SF and steel slag; however, they warned that the accuracy of the equation depends on the ambient temperature, air humidity, measurement materials and others [21,29].

1.3.4. Influence on self-compacting

To measure the self-compacting, the evacuation time measurements of samples in V funnel are taken [14], the smaller the evacuation times of the cone, the more self-compacting the mixture will be [22,23]. Gesoğlu and col., in 2009, manufactured cement mixtures with SF, FA and steel slag, finding that all samples were 5 s below the flow time under the upper limit of EFNARC [17]. Siddique in 2011 mixed self-compacting cement with FA type F and determined a time between 4 and 10 s for the tests in the V funnel [24]. Turk in 2012 obtained a reduction of time in the tests in the V-funnel with the increase in the content of SF, and an increase in the time with the increase of FA in the content; it also determined that ternary mixtures increase more viscosity compared to binary mixtures [18]. Contrary to this, Kennouche and collaborators in 2013 mixed 15% of FA with two types of cement, finding high fluidity and absence of segregation in all tests [26]. All of the above shows that there are still contradictions in the results and that this is still an issue under discussion [30-33].

In conclusion, a more in depth-study of the influence of mineral addition such as FA and SF is necessary to find the conditions where self-compacting, rheology and compressive strength of a mixture are simultaneously improved, seeking to establish correlations between these three performance parameters in portland cement pastes in binary (OPC + SF and OPC + FA) and ternary (OPC + SF + FA) mixtures [28,30-33].

2. Experimental phase

All the mixtures studied were manufactured with the following raw materials: Ordinary Portland Cement (OPC), manufactured by a Colombian Company; Fly Ash (FA) type F (ASTM C 618 – 99), obtained from a Colombian garment factory; Silica Fume (SF) (ASTM 1240) which was imported. For the characterization of the components, the chemical composition was determined by means of X-ray fluorescence (XRF) in PANalytical AXIOS equipment; the particle size distribution (PSD) using laser diffraction in a Mastersizer 3000 from Malvern Instruments and the morphology was evaluated by scanning electron microscopy (SEM) in an EVO MA10, by Carl Zeiss. The rheological evaluation was carried out in a rotational Kinexus Pro rheometer from Malvern Instruments. The tests of compressive strength were carried out complying with norms ASTM C-109 and ASTM C-305-11, the materials for the manufacture and failure of cubes of cement paste were mixed to 7 and 28 days of curing with a water/cementing material ratio (w/cm) of 0.5 constant for all samples. As a self-compacting measure of the mixtures, the emptying time in the V funnel was determined, according to the recommendations recorded in EFNARC [14,27,28].

2.1. Characterization of materials

The results obtained by XRF of both cement and mineral additions are provided in Table 1. The OPC has low contents of limestone, this due to both low losses on ignition and high content of CaO. The FA is an ash class F, because the sum of its main oxides (SiO_2 + Al_2O_3 + Fe_2O_3) is greater than 75% [27]. Regarding SF, a high purity material with high SiO_2 content and low contents of other oxides is observed [28].

The result of the PSD is featured in Fig. 1, where it can be seen that the OPC is the finest material and the FA the thickest one in comparison with other materials;

Table 2 shows the passing size (in microns) that has a certain amount of material: d_{10}, d_{50} and d_{90} for 10%, 50% and 90%, respectively. In this table it is confirmed that the fine material is the OPC and the thickest one is the FA.

The micrographs for each component of the manufactured mixtures are displayed in Figs 2, 3 and 4. Fig. 2 shows a wide distribution of particle size, in addition that

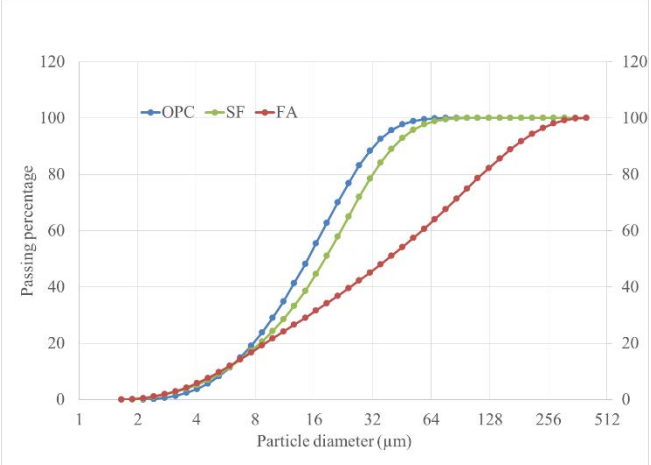


Figure 1. Particle size distribution of materials.
Source: the authors

each particle in general has irregular shapes and ridges, which agrees with what is expected from dry cement without hydration. In Figure 2. Micrography of Ordinary Portland Cement (OPC).

The red arrows show the spherical shapes of the FA of various sizes, some irregular shapes indicated by the blue arrows obey to the unburned ones, which are of the order of 4.37%, measured on the FA by the ASTM D3174 standard. Figure 4 shows SF particles of different sizes and many on the nanometric scale with spherical shapes, this shows that a good part of what is being measured in PSD are agglomerations of SF.

2.1. Preparation of mixtures

15 mixtures and a control mixture, composed of cement and water only, were prepared. The mixtures manufactured with simple additions (OPC + one addition) and composite (OPC + two additions) in certain percentages are shown in Table 3; the name of the simple addition has the following nomenclature: the letter or letters of the material used and on its right side the amount present in percentages (OPC = C).

The red arrows show the spherical shapes of the FA of various sizes, some irregular shapes indicated by the blue arrows obey to the unburned ones, which are of the order of 4.37%, measured on the FA by the ASTM D3174 standard. Figure 4 shows SF particles of different sizes and many on the nanometric scale with spherical shapes, this shows that a good part of what is being measured in PSD are agglomerations of SF.

2.2. Preparation of the mixtures for the rheological analysis

The pastes were prepared in a conventional agitator for 1.5 min at 700 rpm before they were taken to the rheometer. The scheme of the rheological test can be seen in Fig. 5. The mixtures were subjected to a pre-shear for 1 minute at a shear rate of 300 s^{-1} and afterwards were left to rest for 1 minute before starting the rheological measurements.

Table 1.
Chemical composition of raw materials.

OXIDES	OPC	FA	SF
CaO	63.2	5.4	1.4
SiO_2	19.5	44.9	81.5
Al_2O_3	4.5	30.6	0.5
LOI	3.4	3.0	3.5
Fe_2O_3	3.36	6.38	3.6
SO_3	2.87	0.89	0.47
MgO	2.2	4.0	4.6
TiO_2	0.34	1.25	0.02
Na_2O	0.28	1.5	1.05
K_2O	0.16	1.35	3.06

Source: the authors

Table 2. Sizes of raw materials.

Sample	d_{10} (µm)	d_{50} (µm)	d_{90} (µm)
OPC	5.6	14.9	32.7
SF	5.46	18.3	41.4
FA	5.3	44.5	172

Source: the authors

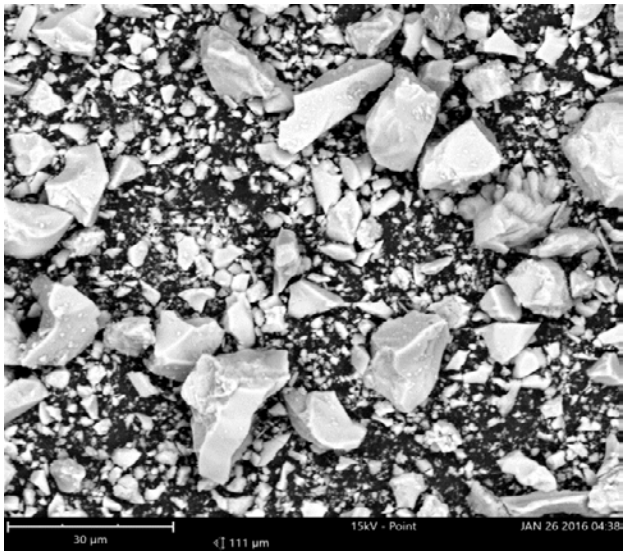


Figure 2. Micrography of Ordinary Portland Cement (OPC).
Source: the authors

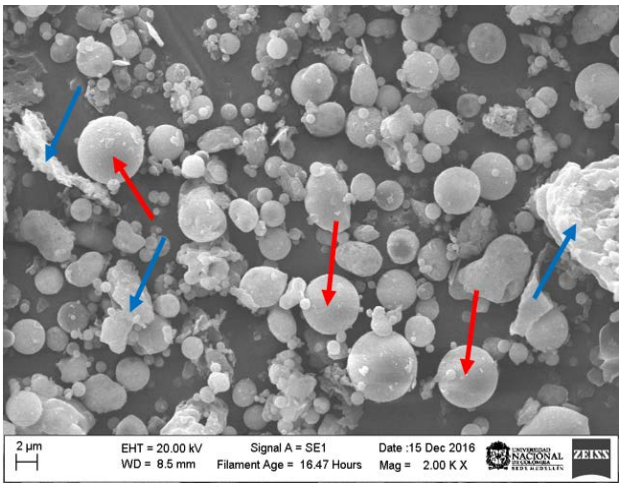


Figure 3. Micrography of Fly Ash (FA).
Source: the authors

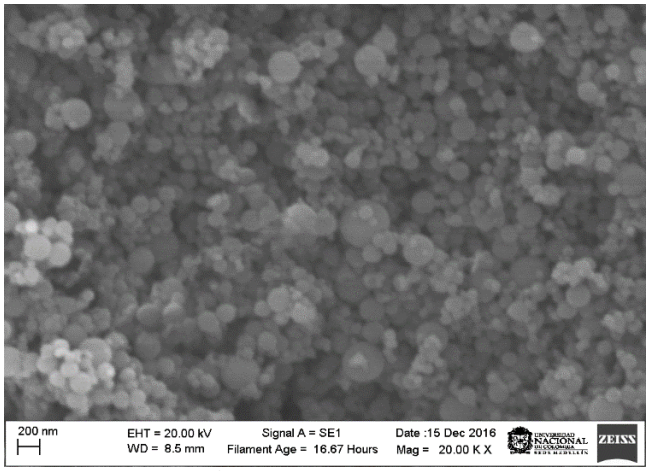


Figure 4. Micrography of Silica Fume (SF).
Source: the authors

Table 3.
Table of dosages for the manufactured mixtures.

Sample	Samples Name	Ratio w/cm	OPC	SF	FA
1	C100SF0FA0	0.5	100%	0%	0%
2	C95SF5FA0	0.5	95%	5%	0%
3	C90SF10FA0	0.5	90%	10%	0%
4	C85SF15FA0	0.5	85%	15%	0%
5	C90SF0FA10	0.5	90%	0%	10%
6	C80SF0FA20	0.5	80%	0%	20%
7	C70SF0FA30	0.5	70%	0%	30%
8	C85SF5FA10	0.5	85%	5%	10%
9	C75SF5FA20	0.5	75%	5%	20%
10	C65SF5FA30	0.5	65%	5%	30%
11	C80SF10FA10	0.5	80%	10%	10%
12	C70SF10FA20	0.5	70%	10%	20%
13	C60SF10FA30	0.5	60%	10%	30%
14	C75SF15FA10	0.5	75%	15%	10%
15	C65SF15FA20	0.5	65%	15%	20%
16	C55SF15FA30	0.5	55%	15%	30%

Source: the authors

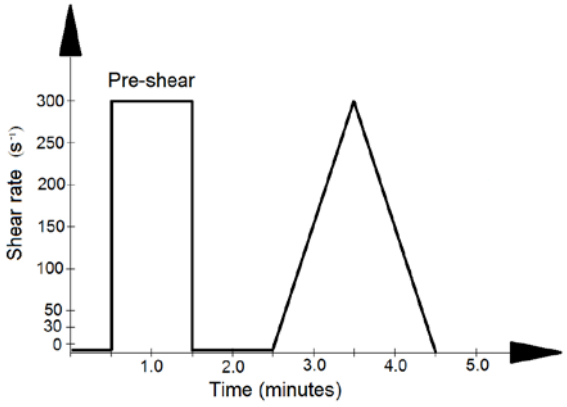


Figure 5. Escheme of the rheological test.
Source: the authors

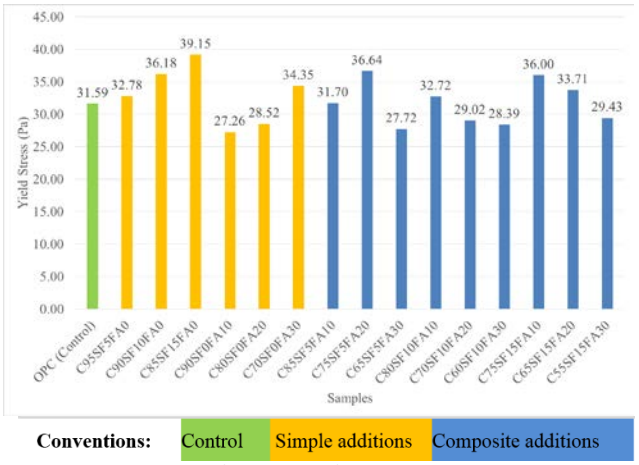


Figure 6. Measurement of yield stress for mixtures.
Source: the authors

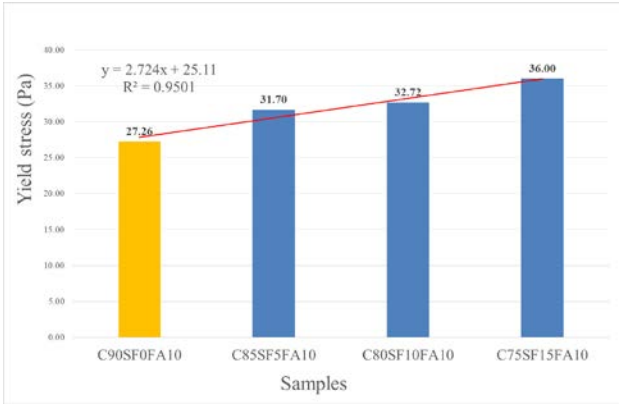


Figure 7. Trend of yield stress for mixtures with 0 to 15% SF and 10% constant FA.
Source: the authors

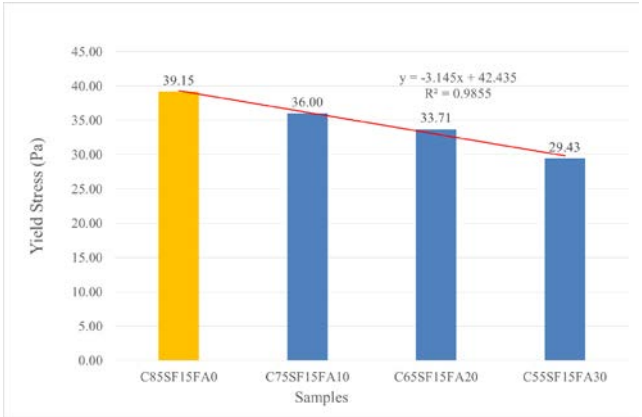


Figure 8. Trend of yield stress for mixtures with 0 to 30% FA with 15% constant SF.
Source: the authors

3. Results

3.1. Yield stress

Fig. 6 shows that for simple additions, yield stress values are lower for samples added with FA than for samples with SF; thus making clear that FA contributes more to the workability of the mixture, with a decrease in the fluidity stress up to 20% on average with respect to the addition of SF. Both for the additions of FA as well as for SF as their amount increases in the mixtures the yield stress increases and only the samples with FA additions of 10% and 20% show values below the control sample. For composite additions it can be noticed that three mixtures are below the value of the control sample, with 20% and 30 % of FA, which corroborates that the presence of FA decreases yield stress in some cases.

Regarding the composite additions, in Fig. 7 the influence of the addition of SF in a mixture with 10% constant FA is observed; a direct proportional relation between the yield stress with the presence of SF is determined, this behaviour can be due to the reactivity and fineness of the material that accelerates the formation of flocs; the beginning of a flow with individual particles demands higher energy compared to the start of flow for flocs, which have sizes larger than the particles. It is noteworthy that with only 10% of FA, in the combined or ternary samples, it is possible to decrease the yield stress for all the evaluated SF percentages, making the yield stress with 5 and 10% of SF very close to the one found for the control sample.

Fig. 8 displays the positive influence on FA variation from 0 to 30% in a mixture with 15% of SF, which shows an inverse relationship between the addition of FA with the yield stress, which is due to the fact that the particles of FA of spherical shape set in among the flocs in formation of the cement and perform a plasticizing work which reduces such yield stress.

3.2. Viscosity

Fig. 9 shows the viscosity value (calculated with the Binghan model) of the analyzed mixtures. In general, it can be noticed that the viscosity of the mixtures increases for all simple additions; however, there is a more pronounced viscosity increase for additions with FA and lower for additions of SF; probably this is because the particle size of the FA is more than 5 times the size of the cement, while the size of the SF is of the order of the size of the OPC and smaller. Regarding the composite additions it can be seen that there are some mixtures with lower viscosity values with respect to the control sample; such mixtures have additions in few proportions, this behaviour is due to the phenomena of rolling and lubrication by small particles and packing phenomena, up to a certain number of particles where energy is spent in moving all the particles present. This again corroborates a complementary effect between these two mineral additions.

3.3. Compressive strength

Fig. 10 summarizes the results obtained for the compressive strength of the mixtures, at 7 and 28 days of curing. Carrying out an analysis first for 7 days of curing, it can be noticed that only greater strength than that of control sample are obtained with simple additions of SF, as the amount of FA increases the compressive strength in relation to the control sample decreases; this evidences the reactive nature of each of these mineral additions. For all composite mixtures the compressive strength decreases as the amount of FA additions increases. For 28 days of curing no mixture, either simple or composite, clearly exceeds the compressive strength of the control sample. Nonetheless, many of the mixtures with percentages of substitution of cement in high percentages have mechanical resistance values similar to control sample, as is the case of the mortars with all SF percentages, with 5% SF + 20% FA; with 10% SF + 10% FA and with 15% SF + 10% FA.

3.4. Self-compacting

Fig. 11 displays the evaluation time for the V -funnel test for each prepared mixture. Regarding simple additions, a direct relationship appears for SF, since as the quantity increases, so does the evaluation time. Conversely, for mixtures with FA the relation is inverse, the evaluation time decreases as its concentration increases. This is due to the fact that SF is quite reactive and it reduces the workability of the mixture, while the FA being less reactive interrupts the formation of flocs serving a plasticizing function. No ternary mixture showed a significantly shorter evacuation time than that of the evacuation time of the control mixture; thus the reactivity of the SF is possibly more decisive than the plasticizing that the FA delivers to the mixture.

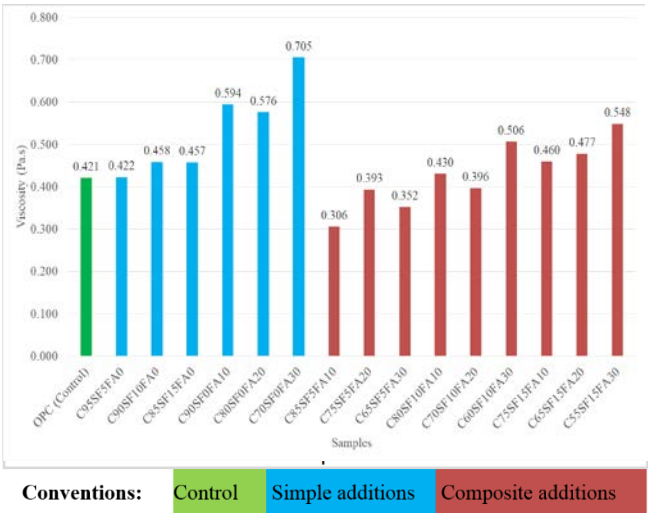


Figure 9. Plastic viscosity values for manufactured mixtures.
Source: the authors

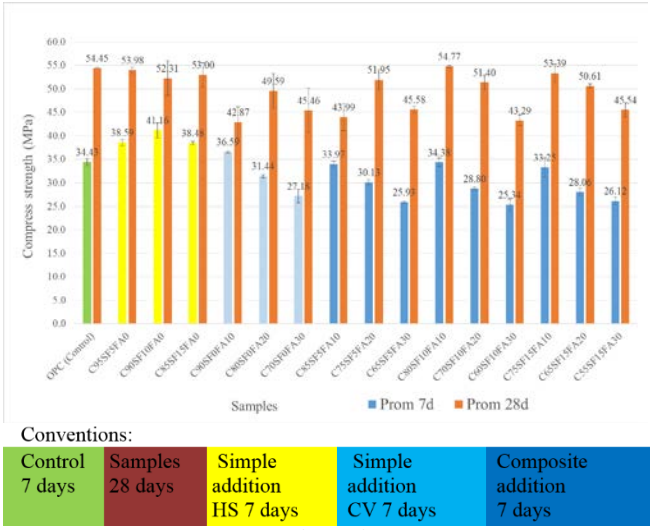


Figure 10. Compressive strength of manufactured mixtures.
Source: the authors

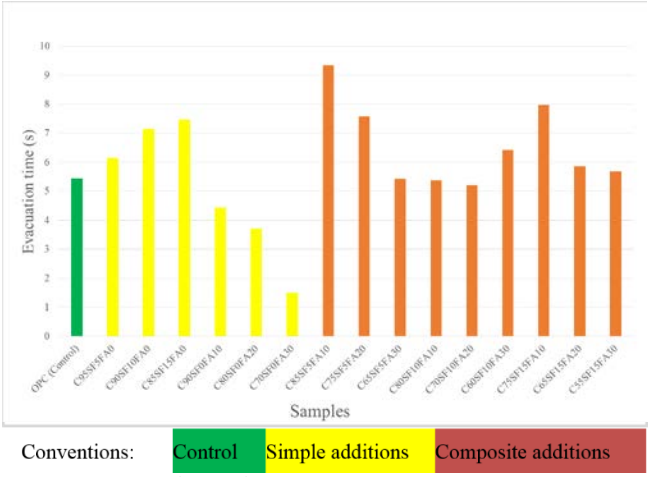


Figure 11. Results of the V-funnel test.
Source: the authors

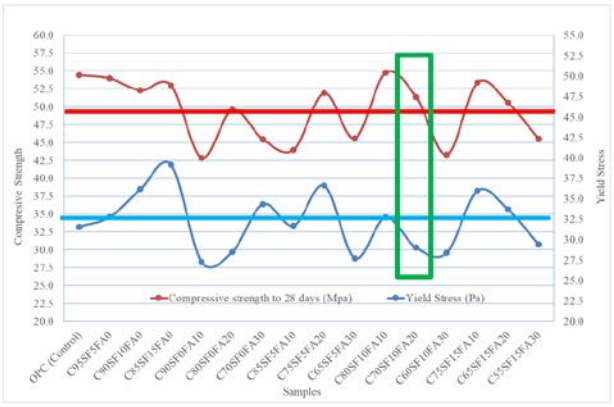


Figure 12. Correlation between compressive strength vs. yield stress. Source: the authors

3.5. Correlations

In order to perform the correlations among variables, the areas where the additions have desirable behaviours were determined by graphical analysis: low yield stress, high compressive strength, low viscosity and short evacuation time (self-compacting test); the objective was to establish areas in which these conditions were met thanks to the presence of mineral additions, that is why these graphs were made:

a) Compressive strength vs. yield stress.
b) Compressive strength vs. viscosity.
c) Yield stress vs. self-compacting cone
d) Self-compacting cone vs. viscosity
e) Compressive strength vs. self-compacting cone.

Each of the graphs shows a median value of the mixtures in a red line and a blue line, for the two properties plotted, and an area of optimal values in green boxes for the mixture that meets the ideal properties simultaneously thanks to the presence of mineral additions.

3.5.1. Compressive strength vs. Yield stress

In Fig. 12 the red line defines the mean value for the compressive strength at 49.51 MPa and the blue line defines the mean value for the yield stress at 32.21 Pa. The green box shows the mixture having a compressive strength avobe average and the yield stress below the mean value. For the present case a single mixture meets the optimal conditions: 10% SF and 20% FA.

3.5.2. Compressive strength vs. viscosity

In Fig. 13 the red line defines the mean for the compressive strength at 49.51 MPa and the blue line defines the mean value for the viscosity at 0.4575 Pa·s. The green boxes show six mixtures that meet the ideal conditions; for this case, all simple mixtures with SF, and composite mixtures with 5% SF + 20% FA; 10% SF with 10% and 20% FA.

3.5.3. Yield stress vs. Self-compacting cone

In Fig. 14 the blue line is the median for the yield stress at 32.21 Pa and the red line defines the median for the self-compacting V funnel test at 5.77 s. The green boxes show 4 mixtures with ideal conditions: two mixtures with simple additions: 10% and 20% FA; and two mixtures with composite additions: 5% SF + 30% FA and 10% SF and 20% FA.

3.5.4. Self-compacting cone vs. viscosity.

In Fig. 15 the red line defines the median for the self-compacting V funnel test at 5.77 s and the blue line defines the mean for the viscosity at 0.4575 Pa·s. The green boxes display 3 compound mixtures with ideal conditions: 5% SF + 30% FA and 10% SF with 10% and 20% FA.

3.5.5. Compressive strength vs. Self-compacting cone

In Fig. 16 the blue line defines the median for the compressive strength at 49.51 MPa and the red lines defines the median for the self-compacting V funnel test at 5.77 s. The green boxes feature 2 compound mixtures with ideal conditions: 10% SF with 10% and 20% FA.

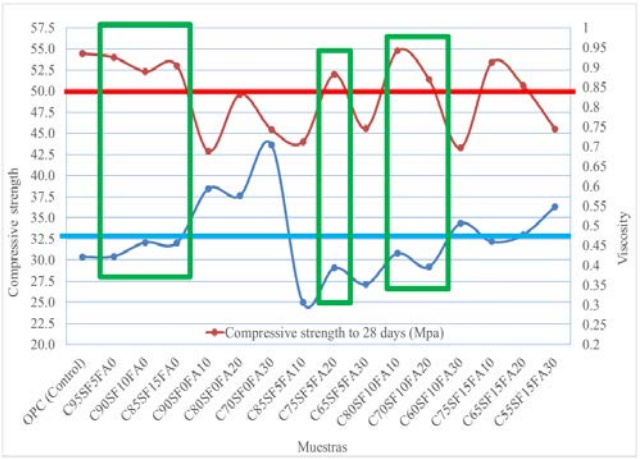


Figure 13. Correlation between compressive strength and viscosity. Source: the authors

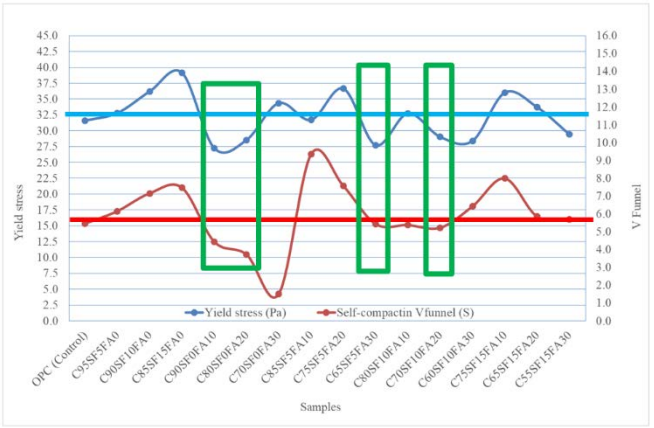


Figure 14. Correlation between yield stress and self-compacting. Source: the authors

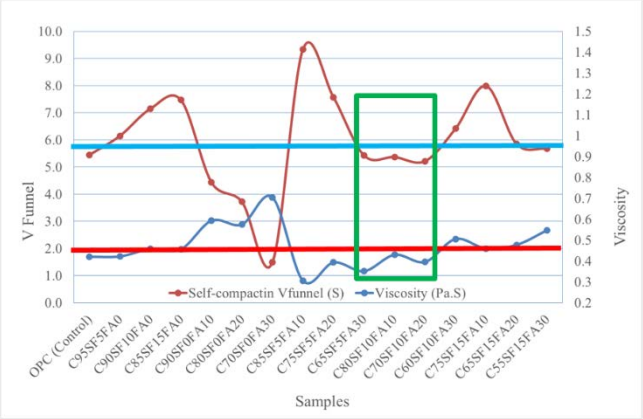


Figure 15. Correlation between viscosity and self-compating V-funnel. Source: the authors

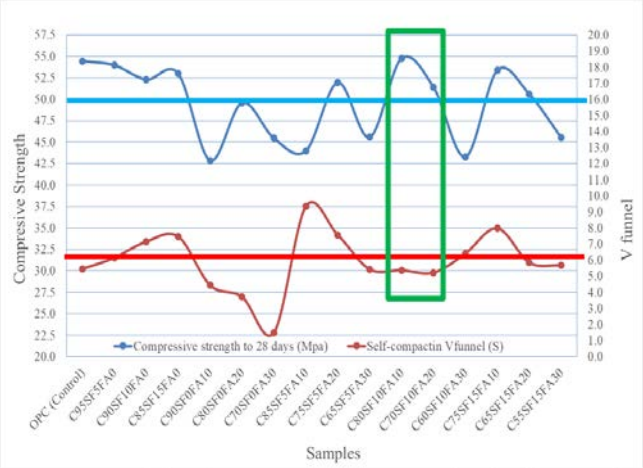


Figure 16. Correlation between compressive strength and self-compacting. Source: the authors

4. Final discussion

Throughout the research it has been possible to determine that during the plastic state of the mixture not only the yield stress, but also the viscosity and the evacuation time increase.

For instance, as the SF increases from 5% to 10% the yield stress increases by about 20%, the viscosity by 10% and the evacuation time by 17%; this due to its particle size and its reactivity that allows it to act as nucleation centers and promotes particle to particle interaction to increase friction among them as well as the formation of flocs. Otherwise happens with the FA, which, due to its larger particle size less reactivity and spherical shape interrupts the formation of flocs and acts as plasticizer or lubricant and also decreases the compressive strength. It can also be established that by mixing these two additions their effects combine and interact, allowing to look for a mixture that meets the parameters of low yield stress, high compressive strength, low viscosity and short evacuation time (self-compacting).

When analyzing the results featured in Figs. 12 to 16, it can be asserted that the composite additions are more efficient than the simple additions, because in the excecuted tests the samples C80SF10FA10 and C70SF10FA20 are the ones that presented the best behaviour; these data are summarized in Table 4 and Fig. 17.

In agreement with several researchers, in the correlation graphs it is observed how when combining the additions, the influence of one addition with the other is compensated, that is, the reductions in compressive strength that could be had with the presence of FA regulates with the reactivity of the SF and on the other hand, the loss of fluidity due to the presence of SF is regulated by the plasticizing effect of the FA [3][4][2][28].

In Table 4 and Fig. 17 it can be seen that the values obtained for these three mixtures are very similar; nonetheless, the recommended mixture is C70SF10FA20; since, although some compressive strength is sacrificed, it improves both in rheology and self-compacting and a very significant aspect is that the percentage of cement replacement is maximized, which, as already mentioned, has paramount effects on environmental as well as economic aspects.

5. Conclusions

Based on the results found throughout this research it can be concluded that:

Both SF and FA have opposite effects on yield stress, viscosity, evacuation times (self-compacting capacity) and compressive strength. This is due to its difference in particle size, reactivity and chemical composition as well.

The SF in the mixture in fresh state promotes more particle to particle interaction and acts as a nucleation center, increasing the friction among them and facilitating the formation of flocs and this results in an increase in yield stress, viscosity and evacuation time. In the mixtures in hardened state and thanks to its chemical composition and pozzolanic activity the compressive strength is increased.

Table 4.
Samples with better results in the parameters evaluated.

Sample	τ_0 (Pa)	η (Pa.s)	f'c at 28 days (MPa)	Desv - f'c at 28 days	V Funnel (S)
C100SF0FA0	31.59	0.4208	54.45	0.08	5.45
C80SF10FA10	32.72	0.4302	54.77	0.28	5.37
C70SF10FA20	29.02	0.3961	51.40	1.62	5.22

Source: the authors

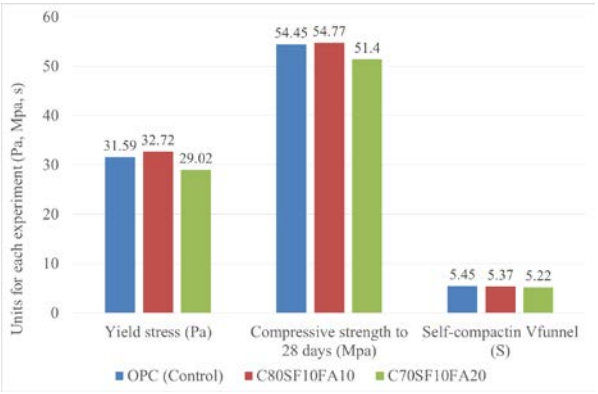


Figure 17. Comparison between control sample and samples selected as optimal in the correlations.
Source: the authors

In the mixtures in fresh state, the FA, thanks to its larger particle size and spherical shape, interrups the formation of flocs and acts as a plasticizer or lubricant. In the mixtures in the hardened state the compressive strength decreases due to its lower reactivity and pozzolanic activity as well.

By mixing these two additions their effects combine and interact allowing finding dosages that are efficient in all measured variables, that is, with good peformance in both fresh and hardened state.

In this study the samples that comply with the proposed variables are C80SF10FA10 and C70SF10FA20, nonetheless, the chosen one is C70SF10FA20 since it allows maximizing the percentage of replaced cement with the corresponding additional benefits, in terms of environmental and economic aspects.

References

[1] Rubio-Hernández, F., Velázquez-Navarro, J., Ordoñez-Belloc, L. Rheology of concrete: a study case based upon the use of the concrete equivalent mortar. Materials and Structures, Vol. 46 (4), pp. 587-605. 2012. DOI: 10.1617/s11527-012-9915-1

[2] Saleh Ahari, R., Kemal Erdem, T., & Ramyar, K. (2015). Effect of various supplementary cementitious materials on rheological properties of self-consolidating concrete. Construction and Building Materials, Vol. 75, pp. 89–98. 2015. DOI: 10.1016/j.conbuildmat. 2014.11.014

[3] Park, C. K., Noh, M. H., & Park, T. H. Rheological properties of cementitious materials containing mineral admixtures. Cement and Concrete Research, 35(5), 842–849. 2005. DOI: 10.1016/j.cemconres.2004.11.002

[4] Bentz, D., Ferraris, C., Galler, M., Hansen, A., & Guynn, J. Influence of particle size distributions on yield stress and viscosity of cement-fly ash pastes. Cement and Concrete Research, Vol. 42(2), pp. 404–409. 2012. DOI: 10.1016/j.cemconres.2011.11.006

[5] Li, Y., & Kwan, A. K. H. Ternary blending of cement with fly ash microsphere and condensed silica fume to improve the performance of mortar. Cement and Concrete Composites, Vol. 49, pp. 26–35. 2014. DOI: 10.1016/j.cemconcomp.2014.02.002

[6] Lorca, Pablo. Efecto de la adición de hidróxido cálcico sobre mezclas con alta sustitución de cemento por ceniza volante. Tesis de Doctorado, Departamento de la construcción y proyectos de Ingeniería Civil. Universidad Politécnica de Valencia - España. Julio de 2014. Descargado desde https://riunet.upv.es/bitstream/ handle/10251/39340/Lorca - EFECTO...

[7] Bustamante-Rua, M., Rojas-Reyes, N., & Quitian-Chila, G. Efecto del material fino en la reología de suspensiones de caolín. DYNA, Vol. 83(195), pp. 105–111. 2016. DOI: 10.15446/dyna.v83n195.48855

[8] Hou, P., Kawashima, S., Wang, K., Corr, D., Qian, J., & Shah, S. Effects of colloidal nanosilica on rheological and mechanical properties of fly ash-cement mortar. Cement and Concrete Composites, Vol. 35(1), pp. 12–22. 2013. DOI: 10.1016/j.cemconcomp.2012.08.027

[9] Lee, S. H., Kim, H. J., Sakai, E., & Daimon, M. Effect of particle size distribution of fly ash-cement system on the fluidity of cement pastes. Cement and Concrete Research, Vol. 33(5), pp. 763–768. 2003. DOI: 10.1016/S0008-8846(02)01054-2

[10] Vance, K., Kumar, A., Sant, G., & Neithalath, N. The rheological properties of ternary binders containing Portland cement, limestone, and metakaolin or fly ash. Cement and Concrete Research, Vol. 52, pp. 196–207. 2013. DOI:10.1016/j.cemconres.2013.07.007

[11] Struble, L., Szecsy, R., Lei, W., and Sun, G., "Rheology of Cement Paste and Concrete," Cement, Concrete and Aggregates, Vol. 20 (2), pp. 269-277, 1998. DOI: 10.1520/CCA10421

[12] Nehdi, M., & Rahman, M. A. Estimating rheological properties of cement pastes using various rheological models for different test geometry, gap and surface friction. Cement and Concrete Research, Vol. 34(11), pp. 1993–2007. 2004. DOI: 10.1016/j.cemconres. 2004.02.020

[13] Feys, D., Verhoeven, R., & De Schutter, G. Why is fresh self-compacting concrete shear thickening?. Cement and Concrete Research, Vol. 39(6), pp. 510–523. 2009. DOI: 10.1016/j.cemconres.2009.03.004

[14] EFNARC. Specification and guidelines for self-compacting concrete. pp. 29-35. 2002. Copia gratuita en pdf descargable desde <http://www.efnarc.org>. Consultada en Febrero de 2017. DOI: 0 9539733 4 4

[15] Kennouche, S., Zerizer, A., Benmounah, A., Hami, B., Mahdad, M., Benouali, H., Bedjou, S. Formulation and characterization of self compacting concrete with silica fume. Journal of Engineering and Technology Research, Vol. 5(5). pp. 160-169. 2013. Descargado desde: http://www.academicjournals.org/journal/JETR/article-full-text-pdf/4ADAE6B2531

[16] Manawadu, A., Wijesinghe1, W., Abeyruwan, H. Rheological behaviour of cement paste with fly ash in the formulation of self-compacting concrete (SCC). 6th International Conference on Structural Engineering and Construction Management 2015, Kandy, Sri Lanka. Descargado desde: www.civil.mrt.ac.lk/ conference/ICSECM.../SECM-15-165.pdf

[17] Gesoğlu, M., Erhan Güneyisi, E., Özbay, E. Properties of self-compacting concretes made with binary, ternary, and quaternary cementitious blends of fly ash, blast furnace slag, and silica fume. Construction and Building Materials, Vol. 23(5), pp. 1847-1854. 2009. DOI: 10.1016/j.conbuildmat.2008.09.015

[18] Turk, K. Viscosity and hardened properties of self-compacting mortars with binary and ternary cementitious blends of fly ash and silica fume. Construction and Building Materials, Vol. 37, pp. 326–334. 2012. DOI: 10.1016/j.conbuildmat.2012.07.081

[19] Mohamed, H. Effect of fly ash and silica fume on compressive strength of self-compacting concrete under different curing conditions. Ain Shams Engineering Journal, Vol. 2, pp. 79–86. 2011. DOI: 10.1016/j.asej.2011.06.001

[20] Jadhav, R., Chavarekar, R. Role of fly ash and silica fume on compressive strength characteristics of high performance concrete. Int. J. Struct. & Civil Engg. Res., Vol 2 (1), pp. 32-39. 2013. Descargado desde: www.ijscer.com/uploadfile/2015/0427/ 20150427030137914.pdf

[21] Raharjo, Da., Subakti, A., Tavio. Mixed concrete optimization using fly ash, silica fume and iron slag on the SCC´s compressive strength. Procedia Engineering, Vol. 54, pp. 827 – 839. 2013. DOI: 10.1016/j.proeng.2013.03.076

[22] Burón, M., Fernández, J., Garrido, L. Hormigón Num. 887, pp. 52-64. 2006. Descargado desde: https://www.ieca.es/show_doc.asp?id_ doc=20

[23] Mebrouki, A., Belas, N., Viña, J., Argüelles, A., Zenasni, R. Aplicación del diseño estadístico de mezclas para la formulación de pasta autocompactante. Materiales de Construcción, Vol. 60 (298), pp. 17-31. 2010. DOI: 10.3989/mc.2010.48308

[24] Siddique, R. Properties of self-compacting concrete containing class F fly ash. Materials and Design, Vol. 32, pp. 1501–1507. 2011. DOI: 10.1016/j.matdes.2010.08.043

[25] Kennouche, S., Zerizer, A., Benmounah, A., Hami, B., Mahdad, M., Benouali, H., Bedjou, S. Formulation and characterization of self compacting concrete with silica fume. Journal of Engineering and Technology Research, Vol. 5(5). pp. 160-169. 2013. Descargado desde: http://www.academicjournals.org/journal/JETR/article-full-text-pdf/4ADAE6B2531

[26] Chen, J. J., Ng, P. L., Li, L. G., & Kwan, A. K. H. (2017). Production of High-performance Concrete by Addition of Fly Ash Microsphere and Condensed Silica Fume. Procedia Engineering, 172, 165–171. https://doi.org/10.1016/j.proeng.2017.02.045

[27] ASTM C618. Standard specification for coal fly ash and raw or calcined natural pozzolona for use in concrete, 1–3, 2015. DOI: 10.1520/C0618-15

[28] Banfill, P. The rheology of fresh cement and concrete - A Review. Proc 11th International Cement Chemistry Congress, Durban, May 2003. Descargado desde: http://www.schleibinger.com/k2003 /banfill/banfill.pdf

[29] De la Cruz, C., Turmo, J., Gettu, R., Barragán, B., & Ramos, G. Beam shear test of structural self-compacting concrete. Ensayos a Cortante

de Vigas de Hormigón Estructural Autocompactable, Vol. 76(159), pp. 35–41. 2009. Descargado desde: http://www.scopus.com/inward/record.url?eid=2-s2.0-77953762021&partnerID=40&md5=091ce99535b19f0aff179af754226212

[30] Ferraris, C., Obla, K., & Hill, R. The influence of mineral admixtures on the rheology of cement paste and concrete. Cement and Concrete Research, Vol. 31(2), pp. 245–255. 2001. DOI: 10.1016/S0008-8846(00)00454-3

[31] Lu, C., Yang, H., & Mei, G. Relationship between slump flow and rheological properties of self compacting concrete with silica fume and its permeability. Construction and Building Materials, Vol. 75, pp. 157–162. 2015. DOI: j.conbuildmat.2014.08.038

[32] Mebrouki, A., Belas, N., Viña, J., Argüelles, A., Zenasni, R. Aplicación del diseño estadístico de mezclas para la formulación de pasta autocompactante. Materiales de Construcción, Vol. 60 (298), pp. 17-31. 2010. DOI: 10.3989/mc.2010.48308

[33] Ferraris, C., Obla, K., & Hill, R. The influence of mineral admixtures on the rheology of cement paste and concrete. Cement and Concrete Research, Vol. 31(2), pp. 245–255. 2001. DOI: 10.1016/S0008-8846(00)00454-3

J.A. Correa-Yepes, is a BSc. in Civil Engineer from Politecnic Jaime Izasa Cadavid and MSc. in Materials and Processes from the Universidad Nacional de Colombia, title received in the year 2017.
ORCID: 0000-0001-6132-4568

N.R, Rojas-Reyes, is BSc. Ing. in Metallurgy in 1999 from the Universidad Pedagógica y Tecnológica of Colombia, Tunja, Colombia, MSc. in Engineering in 2003 at the Universidad de Concepción, Concepción, Chile, and Dr. in Engineering in 2014 at the Universidad Nacional de Colombia, Medellín, Colombia. Between 2004 and 2006 he worked at the Universidad Pedagógica y Tecnológica of Colombia in the area of extractive metallurgy and process modeling and since 2007 for the National University of Colombia. Currently, he is a associated professor at the Faculty of Mines of the Universidad Nacional de Colombia. His research interests include: extractive metallurgy, mineral rheology and physical-chemistry of minerals.
ORCID: 0000-0002-1644-471X

J.I. Tobón, received a BSc. in Geological Engineering in 1992, an MSc. in Engineering in 2003, and a PhD in Materials Science and Technology in 2011, all from the Universidad Nacional de Colombia, Medellin, Colombia. From 1992 to 1995 he worked for different companies in the mining and oil sectors; from 1995 to 1999 he worked for Cementos Argos S.A. while at the same time working at the Universidad Nacional de Colombia as a part-time professor. Since 1999, he has worked full time for the Universidad Nacional de Colombia. Currently, he is a full professor in the Materials and Minerals Department, Facultad de Minas, Universidad Nacional de Colombia. His research interests include: the industrial application of minerals and rocks, chemistry and mineralogy of cements, nanotechnology in construction materials, alternative cementitious materials, and high performance cements and concretes.
ORCID: 0000-0002-1451-1309

UNIVERSIDAD NACIONAL DE COLOMBIA
SEDE MEDELLÍN
FACULTAD DE MINAS

Área Curricular de Ingeniería
Geológica e Ingeniería de Minas y Metalurgia

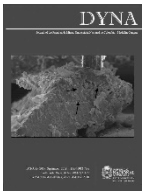
Oferta de Posgrados

Especialización en Materiales y Procesos
Maestría en Ingeniería - Materiales y Procesos
Maestría en Ingeniería - Recursos Minerales
Doctorado en Ingeniería - Ciencia y Tecnología de Materiales

Mayor información:

E-mail: acgeomin_med@unal.edu.co
Teléfono: (57-4) 425 53 68

UNIVERSIDAD NACIONAL DE COLOMBIA
SEDE MEDELLÍN
FACULTAD DE MINAS



DYNA
http://dyna.medellin.unal.edu.co/

Using a non-reducing sugar in the green synthesis of gold and silver nanoparticles by the chemical reduction method

Wilson Agudelo [a], Yuliet Montoya [a,b] & John Bustamante [a,b]

[a] *Grupo de Dinámica Cardiovascular, Universidad Pontificia Bolivariana, Medellín, Colombia. wilson.agudelo@upb.edu.co, yuliet.montoya@upb.edu.co, john.bustamante@upb.edu.co*
[b] *Comité de Trabajo de Bioingeniería Cardiovascular, Sociedad Colombiana de Cardiología y Cirugía Cardiovascular, Bogotá, Colombia.*

Received: May 18th, de 2018. Received in revised form: June 21th, 2018. Accepted: July 24th, 2018

Abstract
The use of more biocompatible and renewable chemical compounds to obtain metal nanoparticles with desired properties and characteristics becomes an alternative route for the reduction of environmental risks and to minimize the incompatibility of these structures when interacting with biological models for their possible application in the health area. The purpose of this research was focused on the use of sucrose, as a reducing agent for gold and silver nanoparticles using different volumes of sodium hydroxide. The nanoparticles obtained were characterized by UV-visible spectrometry, transmission electron microscopy TEM and Fourier transform infrared spectroscopy FTIR, which allowed to determine the surface plasmon resonance, experimental and theoretical particle sizes, morphology and structural changes in the reducing agent, as well as the influence of sodium hydroxide in the synthesis process. The results obtained confirm the generation of gold and silver nanoparticles by the previous formation of reducing sugars and oxidation of the functional group from glucose to salts of carboxylic acid.

Keywords: metal nanoparticles; sucrose; hydrolysis; reduction oxide reaction; salt of carboxylic acid.

Uso de una azúcar no reductora en la síntesis verde de nanopartículas de oro y plata por medio de reducción química

Resumen
El uso de compuestos químicos más biocompatibles y renovables para la obtención de nanopartículas metálicas con propiedades y características deseadas, se convierte en una ruta alternativa para la reducción de riesgos ambientales y del grado de incompatibilidad de estas estructuras al interactuar con modelos biológicos para su posible aplicación en el área de la salud. El propósito de este trabajo se centró en el uso de sacarosa, como agente reductor de nanopartículas de oro y plata al emplear diferentes volúmenes de hidróxido de sodio. Las nanopartículas obtenidas fueron caracterizadas mediante espectrometría UV-visible, microscopía electrónica de transmisión TEM y espectroscopia infrarroja por transformada de Fourier FTIR, la cual permitió determinar los plasmones de resonancia superficial, tamaños de partícula experimentales y teóricos, morfología y cambios estructurales en el agente reductor, así como la influencia del hidróxido de sodio en el proceso de síntesis. Los resultados obtenidos confirman la formación de nanopartículas de oro y plata mediante la previa formación de azúcares reductores. Así mismo, la oxidación del grupo funcional de la glucosa a sales de ácido carboxílico.

Palabras clave: nanopartículas metálicas; sacarosa, hidrólisis; óxido reducción; sales de ácido carboxílico.

1. Introduction

Nanoparticles have been potentiated for the research and development of biosensors, catalytic processes, and biomedical applications, among others. The interest in these materials is due to the fact that is possible to obtain new properties and characteristics by modifying their size and structure depending on the production process employed [1-3]. Currently, different physical and chemical processes are used to synthesize metal nanoparticles (MNPs) to produce

How to cite: Agudelo, W., Montoya, Y. and Bustamante, J., Using a non-reducing sugar in the green synthesis of gold and silver nanoparticles by the chemical reduction method. DYNA, 85(206), pp. 69-78, September, 2018.

© The author; licensee Universidad Nacional de Colombia.

particles with characteristics and properties related to the application area. Two kinds of methodologies are used to obtain nanostructures, i) top-down strategies, in which dimensionally bulk materials are collapsed little-by-little by manual or automated processes until reaching nanoscale [4], and ii) bottom-up where the molecular modification of a precursor agent in order to obtain atoms, which by nucleation processes result in monodisperse nanostructures [5]. However, most of these methods are often expensive, labor-intensive, potentially hazardous to the environment and highly cytotoxic [6]. Therefore, there is a need to carry out new processes to obtain nanoparticles with controlled size and shape, with high performance, high purity, and environmentally friendly conditions and with low levels of cytotoxicity [7,8].

On the other hand, the partial or total substitution of hazardous substances with sustainable processes is known as green chemistry, which arises from the growing demand for more sustainable processes, and is intended to minimize or prevent waste from the reactions involved in the processes of obtaining nanostructured materials while preserving their efficacy [9-11]. This is because, with the obtained characteristics, it is possible to use more biocompatible and renewable chemicals for the development of MNPs with physical, chemical, optical, catalytic and/or electrical properties for their possible application in different areas of science such as medicine [12], biology [13], chemistry [14], and physics [15], among others.

In the search of a nanomaterial for biomedical applications, chitosan (CS), a natural, non-toxic, and biodegradable compound derived from the deacetylation of chitin extracted from the cell walls of some fungi, crustacean exoskeletons and insects, has been studied. [16,17]. Presently, CS is used in the synthesis of gold and silver nanoparticles as a reducing and stabilizing agent at different concentrations of precursor agents, in order to obtain nanomaterials with optical and structural controllable properties, by evaluating with characterization techniques such as UV-visible, infrared spectroscopy by Fourier transform - FTIR, scanning electron microscopy, among others [2].

In addition, the use of gallic acid, present in a variety of plants such as spinach, grapes, green tea, oak bark, red wine and white wine, has been studied as well as chitosan as a reducing agent and stabilizer in the synthesis of gold and silver nanoparticles. In order to compare the catalytic capacity of this material in the process of reducing 4-nitrophenol in the presence of sodium borohydride [18].

Furthermore, the use of ascorbic acid known as vitamin C, present in several fruits and vegetables and used as a dietary supplement, is used as a reducing agent and stabilizer of gold and silver nanoparticles, to evaluate its influence under different conditions of pH for obtaining stable nanostructures and with defined optical properties [19].

On the other hand, the use of sodium alginate, a natural hydrophilic anionic polysaccharide, extracted from brown marine algae [20], which is used in the synthesis of silver nanoparticles as a reducing agent and in turn as a stabilizer of the same, due to this coating provided through the Van der Waals forces. Moreover, its antibacterial effect against Gram-positive (Staphylococcus aureus) and Gram-negative (Pseudomonas aeruginosa) microorganisms have been evaluated for possible use in medical devices or wound dressings [21].

Based on the foregoing, this investigation used a non-reducing sugar such as sucrose, a product of the extraction and refining of sugarcane, as a reducing agent of gold and silver nanoparticles, with the aim to evaluate its influence under different volumes of sodium hydroxide to obtain colloidal nanostructures for its possible application in a cellular microenvironment.

2. Methodology

For this investigation, gold trichloride hydrochloride (HAuCl4·3H2O 99.995 % trace metals basis) was obtained from Aldrich (Sigma-Aldrich), silver nitrate ($AgNO_3$ pure, pharma grade) was obtained from PanReac (PanReac Applichem). Sodium hydroxide (NaOH pellets) was acquired from Merck (Merck Millipore). Sucrose was obtained at a local market.

2.1. Synthesis of silver nanoparticles (AgNPs)

A 1 mM silver nitrate (AgNO3) solution was prepared and mixed with 0.2 % sucrose solution. Then, sodium hydroxide (NaOH) 0.1 M was added at volumes of 0 ml, 0.25 ml, 0.5 ml, 0.75 ml and 1.0 ml, the solutions were mixed at 2000 rpm and left to rest at room temperature until a change in color was observed. Finally, the pH reading was performed on each of the samples obtained, using an Ohaus Starter 2100 pH bench meter at standard conditions for temperature and pressure. In addition, blank solutions from the mixture of reducing agent and the different volumes of sodium hydroxide employed in the reaction were prepared. All assays were performed in triplicate.

2.2. Synthesis of gold nanoparticles (AuNPs)

A 0.5mM chloroauric acid (HAuCl4) was prepared and mixed with 0.1M sucrose solution. Then, 0.1M NaOH was added at volumes of 0 ml, 0.1 ml, 0.15 ml, 0.20 ml and 0.25 ml. Next, the solutions were carried in a water bath at 60 °C by 30 minutes. Once the samples reached standard conditions for temperature and pressure, the pH was read using an Ohaus Starter 2100 pH bench meter. In addition, blank solutions from the mixture of reducing agent and the different volumes of sodium hydroxide employed in the reaction were prepared. All assays were performed in triplicate.

2.3. UV-visible spectrophotometry analysis

Gold and silver nanoparticles were analyzed in a SHIMADZU UV-1800 UV-visible spectrophotometer in a range of 300 - 800 nm; as a control, reducing agent solutions without precursor agent were used. The UV-visible absorbance data obtained for each of the working solutions were subtracted from their respective blank. The result of this subtraction resulted in the resonance associated with the type of metallic particle.

2.4. Fourier transform infrared spectroscopy (FTIR) analysis

The samples were analyzed in an IRAffinity-1S FTIR Spectrophotometer in the range of 500-4000 cm^{-1} to determine the presence of a reducing agent, using attenuated total reflectance (ATR) modulus, with a resolution of 4 cm^{-1}, 128 scans and using Happ-Genzel as apodization function.

2.5. Transmission electron microscopy (TEM) analysis

Analysis by transmission electron microscopy (TEM) was carried out using a Tecnai F20 Super Twin TMP transmission electron microscope operated at 200 kV with the propose to determinate the morphology and particle size.

2.6. Statistical analysis

The synthesis of metal nanoparticles and UV-visible measurements were performed in triplicate in three independent times. In addition, a multivariate statistical analysis was carried out using the Statgraphics Centurion XVI software, which allowed obtaining the population mean, the standard deviation and 95% confidence intervals. For the statistical analysis of the particle size from the TEM images, the ImageJ® software was used, obtaining the population mean, the standard deviation and 95% confidence intervals.

3. Results and discussion

3.1. Non-reducing sugar as a reducing agent in the formation of metal nanoparticles

A reducing sugar is one that through its carbonyl group can donate electrons to molecules that act as oxidants, which accept these electrons. Due to its glycosidic bond, which prevents the opening of the ring of any of its two monosaccharaides, glucose, and fructose, it is not possible to act as reducing sugar of metal nanoparticles in the absence of hemiacetal groups without a process through which the ring opening of either of the two monosaccharaides [22].

This is achieved by a process of hydrolysis of the sucrose molecule, as shown in Fig. 1, in which the dissolution of this structure into glucose and fructose is generated [23]. At the same time, the glucose and fructose molecules may be present in a cyclic or open form.

The presence of carbonyl groups, especially aldehydes in the case of glucose and ketones for fructose, facilitate the synthesis of metal nanoparticles, where glucose is easier to oxidize than fructose, due to the presence of the hydrogen atom in its main group, becoming a strong reducing agent and responsible for the reduction of gold and silver ions to their metallic states [24]. See eq. (1) and (2).

$$AgNO_3 + e^- \rightarrow Ag^0 + NO_3{}^- \quad (1)$$

$$HAuCl_4 + 3e^- \rightarrow Au^0 + H^+ + 4Cl^- \quad (2)$$

For a reduction of gold and silver salts to occur, it is necessary that the reducing agent donates electrons, which will be captured by the oxidizing agents. This is known as a reduction-oxidation reaction, in which the structure acting as a reducer, in this case, glucose, passed from an aldehyde group to form a gluconic acid or salt of gluconic acid, related with pH values in the synthesis process (see Fig. 2), an oxidation reaction. While those structures that act as oxidants, gold salts, and silver are reduced and will result in nanometric structures.

In this research, synthesis of nanoparticles of gold and silver by a non-reducing sugar as sucrose was in an alkaline medium, by the addition of different volumes of sodium hydroxide. Upon which, the expected products in the synthesis are salts of gluconic acid because of the oxidation of glucose and the formation of gold and silver nanoparticles. Also, the use of sodium hydroxide allows for the presence of reducing sugars in a short period of time, due to a low dissolution rate of sucrose, requiring the use of acids, alkaline or enzymatic agents, which increase the reaction rate [25,26].

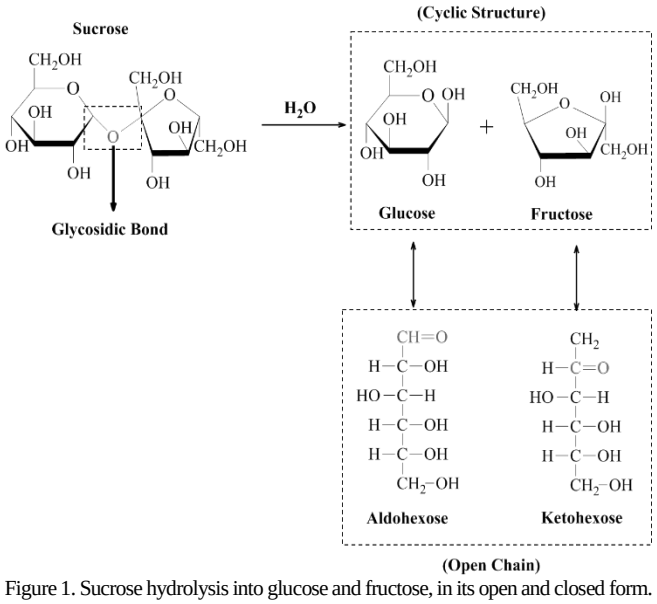


Figure 1. Sucrose hydrolysis into glucose and fructose, in its open and closed form. Source: The authors

3.2. UV-visible spectroscopy

To demonstrate the formation of gold and silver nanoparticles in the different solutions obtained, these were analyzed by UV-visible spectrophotometry, to identify their respective surface plasmon resonance, which indicates the wavelength in where the greatest electronic movement is presented, translated into an increase in absorbance value [27]. Generally, absorbance peaks have a presence at wavelengths between 400 – 500 nm for silver nanoparticles [27,28] and 500 – 600 nm for gold nanoparticles [29,30]. The absorbance spectra obtained in this investigation are shown below (see Figs. 3 and 4).

From Fig. 3 and 4, it is possible to demonstrate that sucrose in presence of different volumes of sodium hydroxide promotes the formation of gold and silver nanoparticles, from hydrolysis and reduction-oxidation reactions, combined with the presence of the absorbance peaks for each kind of metal between the characteristic wavelength ranges.

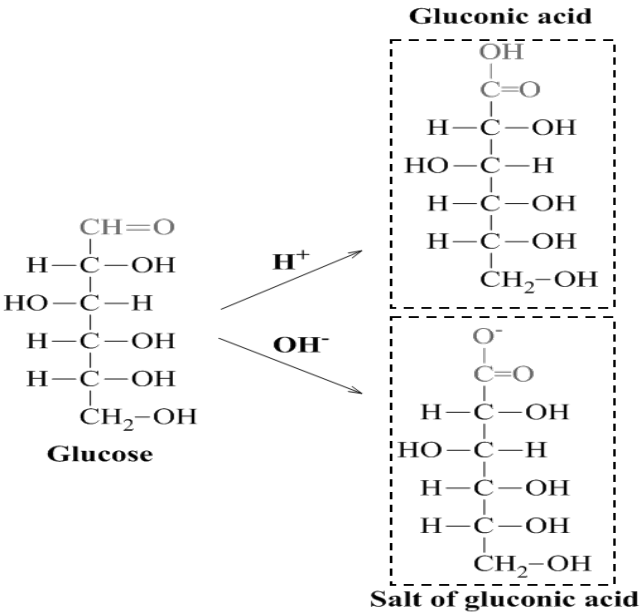


Figure 2. Oxidation of glucose in gluconic acid and gluconic acid salt.
Source: The authors

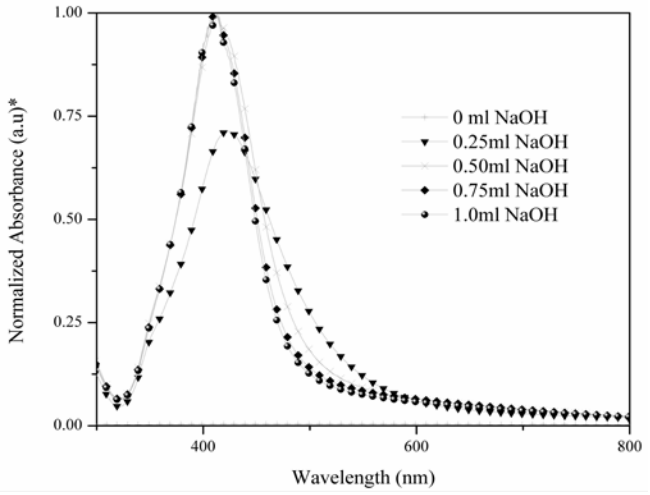


Figure 3. UV-visible spectra of silver nanoparticles at different volumes of sodium hydroxide. As control samples, solutions without reducing agent was used.
*The results presented correspond to the population mean of the replicas made. With n = 3
Source: The authors

In addition, it was possible to show that as of a certain volume of sodium hydroxide is possible to obtain gold and silver nanoparticles. This chemical behavior can be expressed in eq. (3.1) - (3.3) for silver and eq. (4.1) - (4.3) for gold, where is necessary the oxidation of number of glucose moles for the reduction of a particular number of salts precursors moles.

$$C_5H_{11}O_5CHO + 3OH^- \rightarrow C_5H_{11}O_5COO^- + 2H_2O + 2e^- \quad (3.1)$$

v

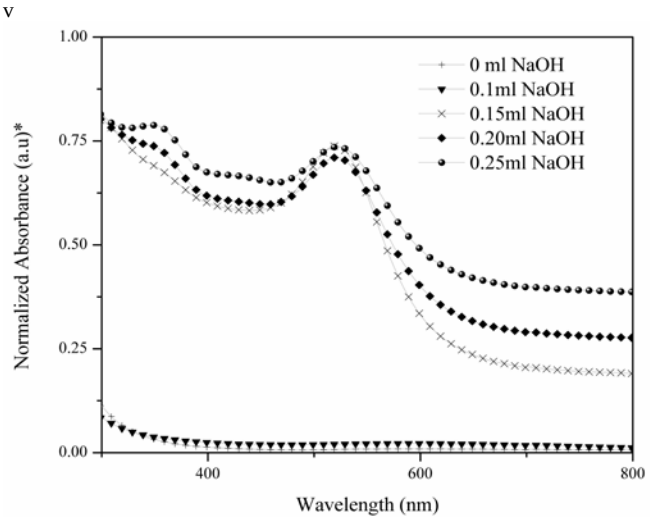


Figure 4. UV-visible spectra of gold nanoparticles at different volumes of sodium hydroxide. As control samples, solutions without reducing agent was used. *The results presented correspond to the population mean of the replicas made. With n = 3
Source: The authors

$$AgNO_3 + e^- \rightarrow Ag^0 + NO_3^- \quad (3.2)$$

$$C_5H_{11}O_5CHO + 3OH^- + 2AgNO_3 \rightarrow 2Ag^0 + C_5H_{11}O_5COO^- + 2H_2O + 2NO_3^- \quad (3.3)$$

$$C_5H_{11}O_5CHO + 3OH^- \rightarrow C_5H_{11}O_5COO^- + 2H_2O + 2e^- \quad (4.1)$$

$$HAuCl_4 + 3e^- \rightarrow Au^0 + H^+ + 4Cl_4 \quad (4.2)$$

$$3C_5H_{11}O_5CHO + 9OH^- + 2HAuCl_4 \rightarrow 2Au^0 + 3C_5H_{11}O_5COO^- + 6H_2O + 2H^+ + 8Cl^- \quad (4.3)$$

From the above equations and as of the addition of 0.25 ml and 0.15 ml of sodium hydroxide for silver and gold respectively [8], it is possible to obtain nanoparticles (see Figs. 5 and 6). Therefore, the presence of sodium hydroxide besides favoring the formation of silver and gold nanoparticles, at the same time increases the pH values, which significantly decreases the efficiency and formation rate of the nanostructures [31]. This behavior can be observed in the absorption spectra of Fig. 3 and 4, where with volumes of sodium hydroxide of 0.5 ml for silver and 0.15 ml for gold, there is no significant variation in the absorbance values (see Tables 1 and 2).

On the other hand, sodium hydroxide plays an important role in the morphology of nanoparticles; this attribute can be evidenced in TEM images (section 3.4). This was possible to evince it from the behavior of the absorption spectrum of gold, where the presence of a second band (see Fig. 4) at volumes of

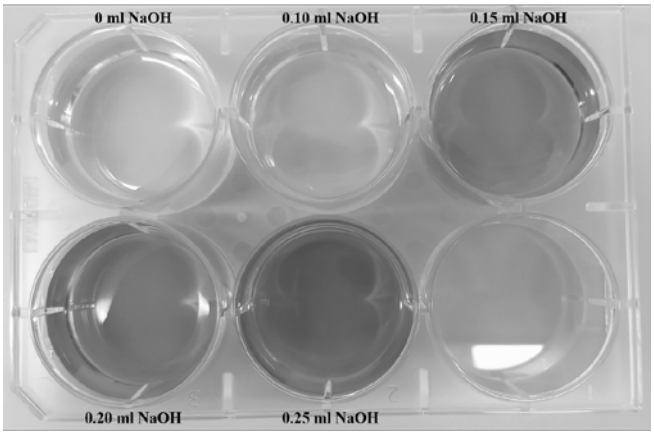


Figure 5. Gold nanoparticles at different volumes of sodium hydroxide.
Source: The authors

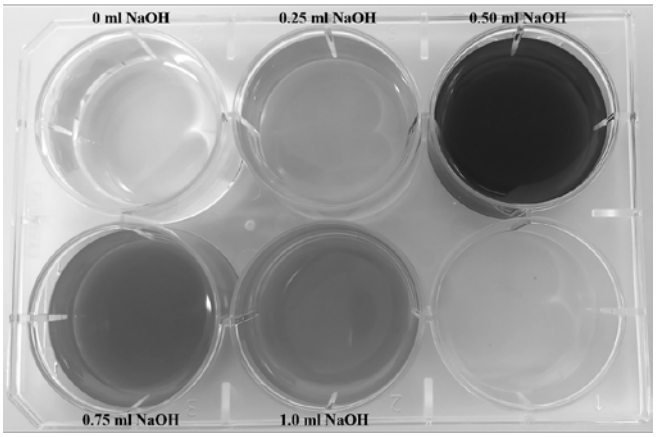


Figure 6. Silver nanoparticles at different volumes of sodium hydroxide.
Source: The authors.

Table 1.
Wavelengths and absorbance of silver nanoparticles at different volumes of sodium hydroxide.

ml NaOH	pH*	Wavelength SPR (nm)*	Normalized absorbance*	Absorbance (u.a)*
0	6.00 ± 1.76	-	-	-
0.25	9.46 ± 1.43	423 ± 6	0.713±0.268	2.385 ± 0.896
0.50	10.66 ± 1.17	413 ± 5	1.000±0	3.382 ± 0.125
0.75	11.02 ± 0.64	411 ± 5	1.000±0	3.526 ± 0.634
1.00	11.17 ± 0.46	412 ± 2	1.000±0	3.586 ± 0.693

*The data are presented with 95% confidence intervals. With n = 3.
Source: The authors

Table 2.
Wavelengths and absorbance of gold nanoparticles at different volumes of sodium hydroxide.

ml NaOH	pH*	Wavelength SPR (nm)*	Normalized absorbance*	Absorbance (u.a)*
0	3.95 ± 0.76	-	-	-
0.1	5.51 ± 0.73	-	-	-
0.15	8.36 ± 1.31	520 ± 2	0.738 ± 0.04	0.195 ± 0.010
0.20	9.49 ± 1.34	522 ± 6	0.710 ± 0.05	0.199 ± 0.010
0.25	10.08 ± 0.51	522 ± 2	0.735 ± 0.04	0.196 ± 0.010

*The data are presented with 95% confidence intervals. With n = 3.
Source: The authors

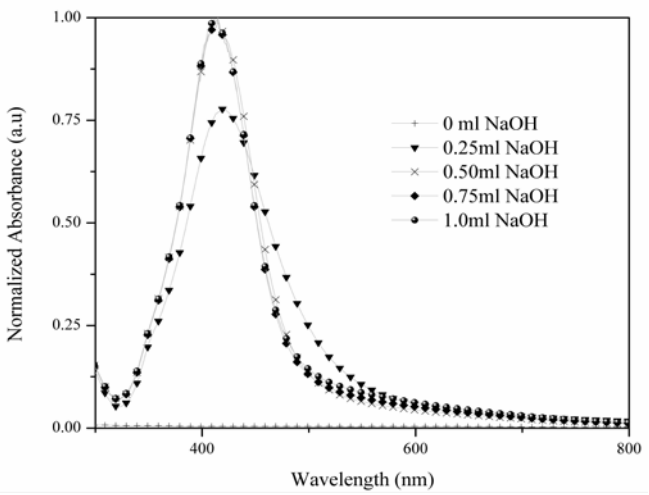


Figure 7. UV-visible spectra of silver nanoparticles at different volumes of sodium hydroxide after four weeks.
Source: The authors

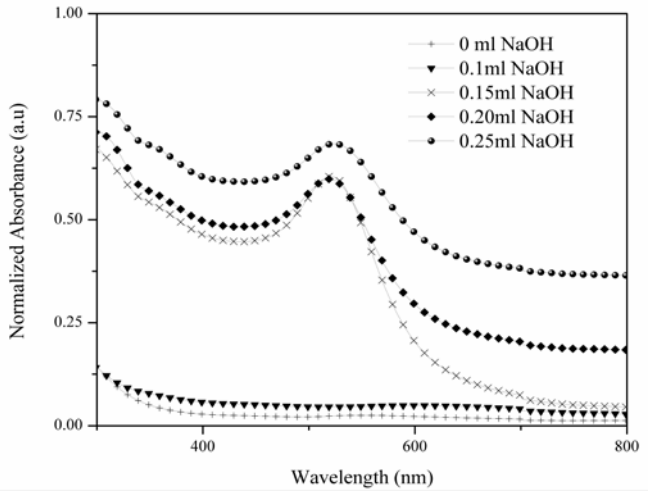


Figure 8. UV-visible spectra of gold nanoparticles at different volumes of sodium hydroxide after four weeks.
Source: The authors

sodium hydroxide of 0.20 and 0.25 ml, can present a different morphology to that obtained by using 0.15 ml of sodium hydroxide [32,33]. To confirm the foregoing, the samples were analyzed after four weeks, with the purpose of evidencing changes in the absorption spectra of the gold and silver nanoparticles (see Figs. 7 and 8).

The first findings after four weeks of synthesis was found in the gold and silver absorption spectra, it is the displacement of the superficial plasmon resonance to those initially recorded (see Tables 3 and 4), which can be associated with changes in the colloidal stability of the nanoparticle solution [35]. Second aspect to highlight, is the decrease of the second gold absorption band. Which indicates that high values of sodium hydroxide at the beginning of the reaction, leads to the formation of specific types of morphologies to evidenced two bands in the absorption spectrum, but with the passage of weeks, the reactions become

Table 3.
Comparison between wavelengths and absorbance weeks 1 and 4 for silver nanoparticles at different volumes of sodium hydroxide.

ml NaOH	Wavelength week. 1 (nm)	Normalized absorbance week 1	Wavelength week. 4 (nm)	Normalized absorbance week 4
0	-	-	-	-
0.25	424	0.79	420	0.77
0.50	415	1.00	411	1.00
0.75	413	1.00	415	1.00
1.00	413	1.00	415	1.00

Source: The authors

Table 4.
Comparison between wavelengths and absorbance weeks 1 and 4 for gold nanoparticles at different volumes of sodium hydroxide.

ml NaOH	Wavelength week. 1 (nm)	Normalized absorbance week 1	Wavelength week. 4 (nm)	Normalized absorbance week 4
0	-	-	-	-
0.1	-	-	-	-
0.15	521	0.72	520	0.60
0.20	520	0.67	519	0.60
0.25	524	0.70	524	0.68

Source: The authors

stabilized in only absorption band could lead to a single morphological structure, this behavior is similar to that reported by Attia et al [32].

3.3. Particle size

From the results obtained in the analysis by UV-visible spectrophotometry, it is possible to determine a particle size approximation from the absorbance and wavelength values obtained for each type of nanoparticle. Using the equations reported by Haiss [35] (5) and Paramelle [34] (6), which are shown below. The results obtained are shown in tables 5 and 6, which are presented as the population mean.

$$dp_{\mathrm{AuNPs}} = e^{(3.0 \cdot A_{spr}/A_{450} - 2.2)} \quad (5)$$

$$dpAgNPs = [(\lambda_{max} - 397)/0.00958]^{0.5} \quad (6)$$

Where A_{spr} and A_{450} correspond to the absorbance obtained at the wavelength of the superficial plasmon resonance and at a wavelength of 450 nm respectively. While λ_{max} is the wavelength of the superficial plasmon resonance. The above equations are valid for a range between [5-80nm] and [20-100nm], respectively.

Additionally, the width at medium height or FWHM was determined, from the UV-vis absorption spectra, to determine experimentally the degree of dispersion of the different synthesized nanoparticles. For this, low FWHM values indicate monodispersity, while high values reflect the polydispersity of particles [36]. The results obtained in this investigation are shown in tables 5 and 6.

Table 5.
The experimental particle size and FWHM of silver nanoparticles at different volumes of sodium hydroxide.

ml NaOH	Particle size (nm)	FWHM (nm)*
0	-	-
0.25	52±6	102±19
0.50	41±7	82±12
0.75	38±8	76±8
1.0	40±4	72±7

*The data are presented with 95% confidence intervals. With n = 3.
Source: The authors

Table 6.
The experimental particle size and FWHM of gold nanoparticles at different volumes of sodium hydroxide.

ml NaOH	Particle size (nm)*	FWHM (nm)*
0	-	-
0.1	-	-
0.15	7 ± 2	126 ± 13
0.20	6 ± 1	142 ± 24
0.25	5 ± 0	161 ± 14

*The data are presented with 95% confidence intervals. With n = 3.
Source: The authors

3.4. Transmission electron microscopy analysis

Fig. 9 shows the TEM images obtained for the gold and silver nanoparticles synthesized using sucrose as a reducing agent, in which the morphology, dispersion and average particle size can be evidenced for each type of synthesis performed.

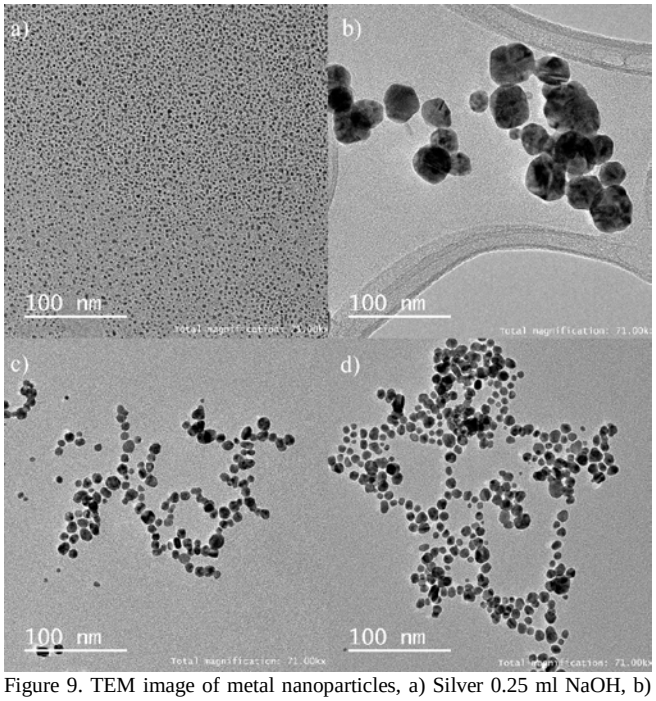


Figure 9. TEM image of metal nanoparticles, a) Silver 0.25 ml NaOH, b) Silver 0.50 ml NaOH, c) gold 0.15 mL of NaOH and d) gold 0.20 ml NaOH.
Source: The authors

Table 7.
Particle size analysis obtained by TEM for gold and silver nanoparticles.

Type of nanoparticle	ml NaOH	Particle size range (nm)*	Particle mean size (nm)*
Silver	0.25	2 - 6	3
Silver	0.50	7 - 48	32
Gold	0.15	2 - 15	9
Gold	0.20	3 - 18	9

*The data are presented with 95% confidence intervals. With n = 3.
Source: The authors

Fig. 9 shows the different morphologies obtained from the gold and silver nanoparticles. In the case of silver, when using a volume of sodium hydroxide of 0.25 ml, the initial phase of nanoparticle formation is observed (Figure 9a), while at a volume of 0.50 ml led to formation of structures with a larger diameter and defined morphologies compared at a volume of 0.25 ml (Figure 9b). This behavior is correlated with the results presented in table 7, where average particle diameters of 3 nm are obtained from a volume of sodium hydroxide of 0.25 ml compared to the 32 nm reached at a volume of 0.5 ml.

In relation to gold nanoparticles (Fig. 9c and 9d), greater nanoparticle formation is contemplated as the volume of sodium hydroxide increases, which could be associated with a greater availability of reducing sugars present in the reaction. The increase in the volume of sodium hydroxide leads to increased polydispersity of particle as shown in Table 6, which relates to the value of width at medium height, where the value changes from 126 nm to a volume of 0.15 ml of sodium hydroxide at 142 nm at a volume of 0.20 ml.

3.5. Fourier-transform infrared spectroscopy analysis

As a complementary technique to UV-vis spectrophotometry transmission electron microscopy, Fourier transform infrared spectroscopy is used to evidence changes in the reducing agent used for the synthesis of metal nanoparticles (see Figs. 10 and 11).

The FTIR spectra of silver nanoparticles exhibit characteristic bands at 3283 and 1637 cm-1, which may be associated with hydroxyl groups either from sucrose, glucose, fructose or gluconic acid [31,37], while the presence of a band at 1738 cm-1 is linked to the stretching of the carbonyl group of the glucose or the gluconic acid. Increasing the volume of sodium hydroxide leads to the appearance and increase of the intensity of the band related to the stretching of the carbonyl group, generated by the breakdown of the glycosidic bond or the oxidation of glucose to gluconic acid.

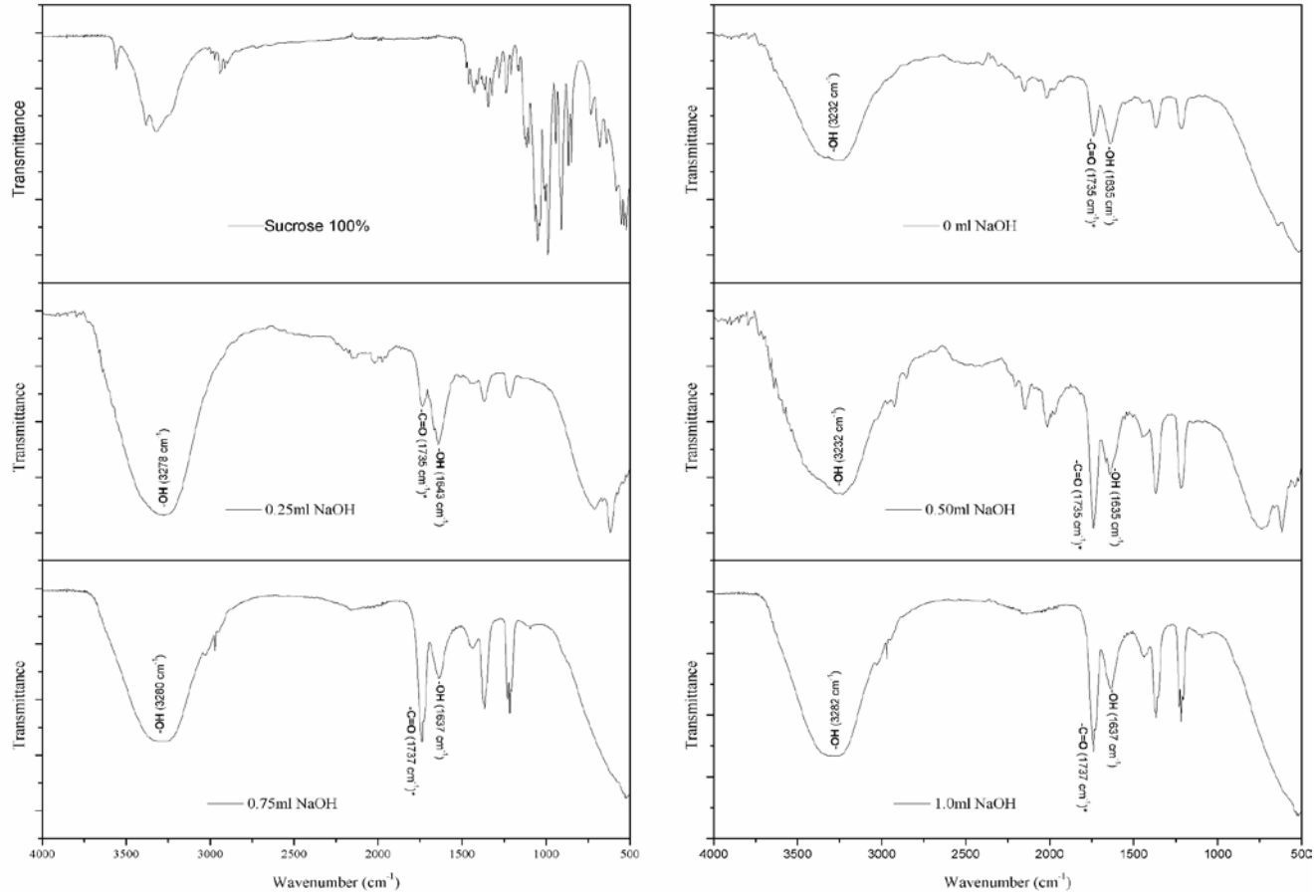


Figure 10. FTIR spectra of silver nanoparticles at different volumes of sodium hydroxide.
*Indicates the change in carbonyl bond intensity (-C=O) as the volume of sodium hydroxide increases in the reaction.
Source: The authors

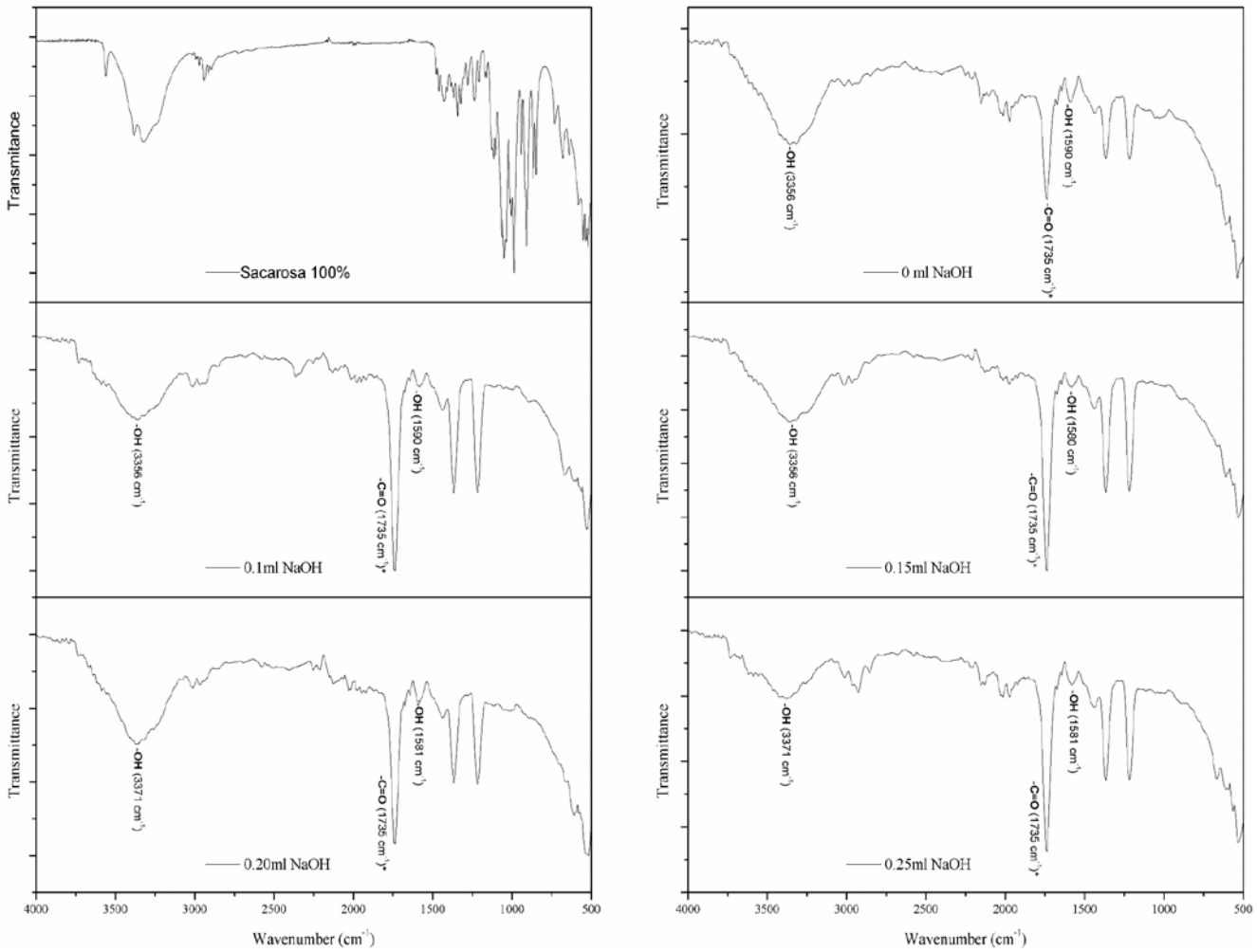


Figure 11. FTIR spectra of gold nanoparticles at different volumes of sodium hydroxide.
*Indicates the change in carbonyl bond intensity (-C=O) as the volume of sodium hydroxide increases in the reaction.
Source: The authors

Moreover, and related with the FTIR spectra of gold nanoparticles (see Fig. 10), it was found that the relative vibration of the hydroxyl group bands are presented at 3371 and 1582 cm-1, while the stretching of the carbonyl group appears at 1736 cm-1. Similarly, to that found in the silver nanoparticles FTIR spectra, the gold nanoparticle FTIR spectra exhibit a higher intensity band associated with stretching of the carbonyl group product of the reduction-oxidation reaction of metal salts and glucose molecule respectively.

4. Conclusion

In this investigation, gold and silver nanoparticles were synthesized by chemical reduction methods using a non-reducing sugar like sucrose, which, through a hydrolysis process leads to structures able of reducing gold and silver salts to its metal states by oxidizing it to salts of carboxylic acid, where these behaviors were evaluated using UV-vis spectrophotometry, TEM and FTIR spectroscopy. Moreover, the effect of sodium hydroxide in the synthesis of MNPs was evaluated, finding that sodium hydroxides, allows the oxidation of reducing sugars in periods of time less or equal to 30 minutes, but also produces different behaviors related to metal nanoparticles formation rate in relation to the volume of sodium hydroxide used, and particle size obtained, which were determined by using the equations reported by Haiss and Paramelle and the analysis of the images obtained by transmission electron microscopy.

The use of environmentally friendly materials such as sugar offers numerous benefits, ranging from the reduction of environmental risks to the integration of these nanomaterials into biologically relevant systems.

5. Ethical responsibility

Authors declare that no human experiments have been conducted for this investigation. For the investigations related in this document, the approval of the Health Research Ethics Committee of the Universidad Pontificia Bolivariana was obtained by Act dated June 8, 2016.

Author contributions

W. Agudelo worked on the experimental development, design and processing of the spectra and chemical structures of the reducing agent. W. Agudelo, Y. Montoya and J. Bustamante worked on the idea, development and analysis of results, as well as contributing to the writing, review and approval of the content of the manuscript.

Conflict of interest

The authors declare that they have no relation, condition or circumstance that constitutes a potential conflict of interest.

Acknowledgment

Thanks to the Universidad Pontificia Bolivariana for the academic support in the formation of a student resource committed in the present research work. Also, to the Department of Science, Technology and Innovation - COLCIENCIAS, Colombia, for the academic support in the formation of a student resource in the announcement of national doctorate 647 of 2014 and project 121074455524 Colciencias.

References

[1] Kaliaraj, G.S., Subramaniyan, B., Manivasagan, P. and Kim, S.-K., Chapter 7 - Green Synthesis of metal nanoparticles using seaweed polysaccharides. In Venkatesan, J., Anil, S. and Kim S.-K., (Edits.), Seaweed Polysaccharides. pp. 101-109, 2017. Elsevier. DOI: 10.1016/b978-0-12-809816-5.00007-4

[2] Wei, D. and Qian, W., Facile synthesis of Ag and Au nanoparticles utilizing chitosan as a mediator agent. Colloids and Surfaces B: Biointerfaces, 62, pp. 136-142, 2008. DOI: 10.1016/j.colsurfb.2007.09.030

[3] Tavakoli, A., Sohrabi, M. and Kargari, A., A review of methods for synthesis of nanostructured metals with emphasis on iron compounds. Chemical Papers, 61, 2007. DOI: 10.2478/s11696-007-0014-7

[4] Razavi, M., Salahinejad, E., Fahmy, M., Yazdimamaghani, M., Vashaee, D. and Tayebi, L., Green chemical and biological synthesis of nanoparticles and their biomedical applications [online], Cham: Springer International Publishing, [online]. 2015 [consulted: may 24th of 2018]. Available at: https://link.springer.com/chapter/10.1007/978-3-319-15461-9_7

[5] Wang, Y. and Xia, Y., Bottom-up and top-down approaches to the synthesis of monodispersed spherical colloids of low melting-point metals. Nano Letters, 4, pp. 2047-2050, 2004. DOI: 10.1021/nl048689j

[6] Makarov, V.V., Love, A.J., Sinitsyna, O.V., Makarova, S.S., Yaminsky, I.V., Taliansky, M.E. and Kalinina, N.O., "Green" nanotechnologies: synthesis of metal nanoparticles using plants. Acta Naturae, [online]. 6, pp. 35-44. 2014. Available at: http://www.ncbi.nlm.nih.gov/pmc/articles/PMC3999464/

[7] Iravani, S., Green synthesis of metal nanoparticles using plants. Green Chemistry, 13, pp. 2638-2650, 2011. DOI: 10.1039/c1gc15386b

[8] Engelbrekt, C., Sørensen, K.H., Zhang, J., Welinder, A.C., Jensen, P.S. and Ulstrup, J., Green synthesis of gold nanoparticles with starch–glucose and application in bioelectrochemistry. Journal of Materials Chemistry, 19, pp. 7839-7847, 2009. DOI: 10.1039/B911111E

[9] Ayala, G., Oliveira-Vercik, L.C., Menezes, T.A. and Vercik, A., A simple and green method for synthesis of Ag and Au nanoparticles using biopolymers and sugars as reducing agent. 1386. Cambridge University Press (CUP), 2012. DOI: 10.1557/opl.2012.645

[10] Silva, L.P., Reis, I.G. and Bonatto, C.C., Green synthesis of metal nanoparticles by plants: current trends and challenges. In Basiuk, V.A. and Basiuk E.V., (Edits.), Green processes for nanotechnology: from inorganic to bioinspired nanomaterials, pp. 259-275, 2015. Cham: Springer International Publishing. DOI: 10.1007/978-3-319-15461-9_9

[11] Duan, H., Wang, D. and Li, Y., Green chemistry for nanoparticle synthesis. Chemical Society Reviews, 44, pp. 5778-5792, 2015. DOI: 10.1039/c4cs00363b

[12] Murthy, S.K., Nanoparticles in modern medicine: state of the art and future challenges. International Journal of Nanomedicine, [online]. 2, pp. 129-141, 2007. Available at: http://www.ncbi.nlm.nih.gov/pmc/ /PMC2673971/

[13] De, M., Ghosh, P.S. and Rotello, V.M., Applications of nanoparticles in biology. Advanced Materials, 20, pp. 4225-4241, 2008. DOI: 10.1002/adma.200703183

[14] Chandra, P., Singh, J., Singh, A., Srivastava, A., Goyal, R.N. and Shim, Y.B., Gold nanoparticles and nanocomposites in clinical diagnostics using electrochemical methods. Journal of Nanoparticles, 2013, pp. 1-12, 2013. DOI: 10.1155/2013/535901

[15] Shipway, A.N., Katz, E. and Willner, I., Nanoparticle arrays on surfaces for electronic, optical and sensor applications. ChemPhysChem, 1, pp.18-52, 2000. DOI: 10.1002/1439-7641(20000804)1:1<18::AID-CPHC18>3.0.CO;2-L

[16] Kheiri, A., Jorf, S.A., Malihipour, A., Saremi, H. and Nikkhah, M., Synthesis and characterization of chitosan nanoparticles and their effect on Fusarium head blight and oxidative activity in wheat. International Journal of Biological Macromolecules, 102, pp. 526-538, 2017. DOI: 10.1016/j.ijbiomac.2017.04.034

[17] Zając, A., Hanuza, J., Wandas, M.,and Dymińska, L., Determination of N-acetylation degree in chitosan using Raman spectroscopy. Spectrochimica Acta Part A: Molecular and Biomolecular Spectroscopy, 134, pp. 114-120, 2015. DOI: 10.1016/j.saa.2014.06.071

[18] Park, J., Cha, S.-H., Cho, S. and Park, Y., Green synthesis of gold and silver nanoparticles using gallic acid: catalytic activity and conversion yield toward the 4-nitrophenol reduction reaction. Journal of Nanoparticle Research, 18, 2016. DOI: 10.1007/s11051-016-3466-2

[19] Malassis, L., Dreyfus, R., Murphy, R.J., Hough, L.A., Donnio, B. and Murray, C.B., One-step green synthesis of gold and silver nanoparticles with ascorbic acid and their versatile surface post-functionalization. RSC Advances, 6, pp. 33092-33100, 2016. DOI: 10.1039/c6ra00194g

[20] Shao, Y., Wu, C., Wu, T., Yuan, C., Chen, S., Ding, T. and Hu, Y., Green synthesis of sodium alginate-silver nanoparticles and their antibacterial activity. International Journal of Biological Macromolecules, 111, pp. 1281-1292, 2018. DOI: 10.1016/j.ijbiomac.2018.01.012

[21] Faried, M., Shameli, K., Ubaidillah, Miyake, M., Hara, H. and Khairudin, N.B., Green synthesis of silver nanoparticles in biopolymer stabilizer and their application as antibacterial efficacy. Author(s), 2017. DOI: 10.1063/1.4968377

[22] Filippo, E., Serra, A., Buccolieri, A. and Manno, D., Green synthesis of silver nanoparticles with sucrose and maltose: morphological and structural characterization. Journal of Non-Crystalline Solids, 356, pp. 344-350, 2010. DOI: 10.1016/j.jnoncrysol.2009.11.021

[23] Hurtado, R.B., Cortez-Valadez, M., Ramírez-Rodríguez, L.P., Larios-Rodriguez, E., Alvarez, R.A., Rocha-Rocha, O. and Flores-Acosta, M., Instant synthesis of gold nanoparticles at room temperature and SERS applications. Physics Letters A, 380, pp. 2658-2663, 2016. DOI: 10.1016/j.physleta.2016.05.052

[24] Darroudi, M., Ahmad, M.M., Abdullah, A.H., Ibrahim, N.A. and Shameli, K., Green synthesis and characterization of gelatin-based and sugar-reduced silver nanoparticles. International Journal of Nanomedicine, 2011(6), pp. 569-574, 2011. DOI: 10.2147/ijn.s16867

[25] Maryan, A.S. and Gorji, M., Synthesize of nano silver using cellulose or glucose as a reduction agent: the study of their antibacterial activity on polyurethan fibers. Bulgarian Chemical Communications, 47, pp. 151-155, 2016.

[26] Suvarna, S., Das, U., Sunil, K.C., Mishra, S., Sudarshan, M., Saha, K.D., Narayana, Y., et al, Synthesis of a novel glucose capped gold nanoparticle as a better theranostic candidate. (Y.K. Mishra, Ed.) PLOS ONE, 12, pp. 1-15, 2017. DOI: 10.1371/journal.pone.0178202

[27] Pettegrew, C., Dong, Z., Muhi, M.Z., Pease, S., Mottaleb, M.A. and Islam, M.R., Silver nanoparticle synthesis using monosaccharides and their growth inhibitory activity against gram-negative and positive bacteria. ISRN Nanotechnology, 2014, pp. 1-8, 2014. DOI: 10.1155/2014/480284

[28] Ashraf, J.M., Ansari, M.A., Khan, H.M., Alzohairy, M.A. and Choi, I., Green synthesis of silver nanoparticles and characterization of their

inhibitory effects on AGEs formation using biophysical techniques. Scientific Reports, 6, 2016. DOI: 10.1038/srep20414
[29] Kikuchi, F., Kato, Y., Furihata, K., Kogure, T., Imura, Y., Yoshimura, E. and Suzuki, M., Formation of gold nanoparticles by glycolipids of Lactobacillus casei. Scientific Reports, 6, 2016. DOI: 10.1038/srep34626
[30] Qi, Z.-m., Zhou, H.-s., Matsuda, N., Honma, I., Shimada, K., Takatsu A. and Kato, K., Characterization of gold nanoparticles synthesized using sucrose by seeding formation in the solid phase and seeding growth in aqueous solution, The Journal of Physical Chemistry B, 108, pp. 7006-7011, 2004.
[31] Meshram, S.M., Gade, A.K., Bonde, S.R., Gupta, I.R. and Rai, M.K., Green synthesis of silver nanoparticles using white sugar. IET Nanobiotechnology, 7, pp. 28-32, 2013. DOI: 10.1049/iet-nbt.2012.0002
[32] Attia, Y.A., Buceta, D., Requejo, F.G., Giovanetti, L.J. and López-Quintela, M.A., Photostability of gold nanoparticles with different shapes: the role of Ag clusters. Nanoscale, 7, pp. 11273-11279, 2015. DOI: 10.1039/c5nr01887k
[33] Cobley, C.M., Skrabalak, S.E., Campbell, D.J. and Xia, Y., Shape-controlled synthesis of silver nanoparticles for plasmonic and sensing applications. Plasmonics, 4, pp. 171-179, 2009, DOI: 10.1007/s11468-009-9088-0
[34] Pimpang, P. and Choopun, S., Monodispersity and stability of gold nanoparticles stabilized by using polyvinyl alcohol. Chiang Mai Journal of Science, 38, pp. 31-38, 2011.
[35] Haiss, W., Thanh, N.T., Aveyard, J. and Fernig, D.G., Determination of size and concentration of gold nanoparticles from UV-Vis spectra. Analytical Chemistry, 79, pp. 4215-4221, 2007. DOI: 10.1021/ac0702084
[36] Paramelle, D., Sadovoy, A., Gorelik, S., Free, P., Hobley, J. and Fernig, D.G., A rapid method to estimate the concentration of citrate capped silver nanoparticles, 2014.
[37] Oliveira J.P., Prado A.R., Keijok W.J., Ribeiro M.R.N., Pontes M.J., Nogueira B.V. and Guimarães M.C.C., A helpful method for controlled synthesis of monodisperse gold nanoparticles through response surface modeling. Arabian Journal of Chemistry, 2017. DOI: 10.1016/j.arabjc.2017.04.003
[38] Janardhanan, R., Karuppaiah, M., Hebalkar, N. and Rao, T.N., Synthesis and surface chemistry of nano silver particles. Polyhedron, 28, pp. 2522-2530, 2009. DOI: 10.1016/j.poly.2009.05.038

W. Agudelo, is MSc. student from Universidad Pontificia Bolivariana, Received the BSc. Eng in Chemical Engineering in 2016. He is currently researcher from Cardiovascular Dynamic Research Group Medellín, Colombia. His areas of interest include cardiovascular tissue engineering and prosthetic, biomaterials development, and characterization of nanomaterials.
ORCID: 0000-0001-5065-166X

Y. Montoya, is PhD. student form Universidad Pontificia Bolivariana. Received the MSc. degree in Engineering from Universidad Pontificia Bolivarian, and BSc. Eng in Biomedical Engineering from Instituto Tecnológico Metropolitano, researcher in Cardiovascular Dynamic Research Group Medellín, Colombia. Her areas of interest include cardiovascular tissue engineering and prosthetic, biomaterials development, and cardiovascular tissue banking.
ORCID: 0000-0002-8402-7109

J. Bustamante, obtained his BSc. degree in Medicine from Universidad Pontificia Bolivariana, Medellín, Colombia. PhD in Medical Sciences in Internal Medicine, Cardiology Program, from the Universitat Autònoma de Barcelona, Barcelona, Spain. Currently, he is Head of the Cardiovascular Dynamic Research Group Medellín, Colombia, and Coordinator of the Doctoral Programme in Medical Sciences at Universidad Pontificia Bolivariana. His areas of interest include cardiac and vascular biomechanics, prostheses and implants in cardiology, cardiovascular instrumentation, modelling and simulation in cardiovascular system, and cardiovascular tissue banking.
ORCID: 0000-0002-4855-9896

UNIVERSIDAD NACIONAL DE COLOMBIA
SEDE MEDELLÍN
FACULTAD DE MINAS

Área Curricular de Ingeniería Química e Ingeniería de Petróleos

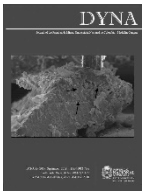
Oferta de Posgrados

Maestría en Ingeniería - Ingeniería Química
Maestría en Ingeniería - Ingeniería de Petróleos
Doctorado en Ingeniería - Sistemas Energéticos

Mayor información:

E-mail: qcaypet_med@unal.edu.co
Teléfono: (57-4) 425 5317

UNIVERSIDAD NACIONAL DE COLOMBIA
SEDE MEDELLÍN
FACULTAD DE MINAS



DYNA
http://dyna.medellin.unal.edu.co/

Levelized avoided cost of electricity model based on power system operation

Cristian Camilo Marín-Cano [a] & Diego Adolfo Mejía-Giraldo [b]

[a] *Grupo de investigación GIMEL, Universidad de Antioquia, Medellín, Colombia. ccamilo.marin@udea.edu.co*
[b] *Departamento de Ingeniería Eléctrica, Facultad de Ingeniería, Universidad de Antioquia, Medellín, Colombia. diego.mejia@udea.edu.co*

Received: December 26th, de 2017. Received in revised form: June 21th, 2018. Accepted: July 24th, 2018

Abstract
This paper presents a methodology to estimate the Levelized Avoided Cost of Electricity (LACE) of new generation projects based on the assessment of economic and operational benefits perceived by an existing power system. The marginal economic benefit caused by the integration of a new generation project is captured using the Differential Revenue Requirement method (DRR); whereas the operational benefits are observed by analyzing the performance of the new project through a preventive DC Security-Constrained Optimal Power Flow (SCOPF) tool. The SCOPF also allows quantifying economic benefits due to replacement of expensive generation, transmission congestion, and N-1 security improvement. Additionally, another metric, called Net Benefit (NB) of a generation project, expressed as the difference between LACE and LCOE (Levelized Cost of Electricity) is also employed in this work. It provides a realistic, easy-to-compute, and intuitive index that helps identifying the most promising generation projects during system expansion planning procedures. Finally, the proposed methodology is applied for computing LACE and NB of different generation projects in Colombia. According to the results, geothermal projects display the most significant LACE and NB. These metrics (LACE and NB) can become useful tools for decision-making in planning process.

Keywords: levelized costs of Electricity; avoided costs of electricity; generation expansion planning; power system optimization; security-constrained optimal power flow.

Modelo de costo evitado nivelado de electricidad basado en la operación del sistema de potencia

Resumen
Este artículo propone una metodología para estimar el Costo Evitado Nivelado de Electricidad (LACE) de nuevos proyectos de generación basados en la evaluación de beneficios económicos y operacionales, percibidos por un sistema de potencia existente. El beneficio económico marginal causado por la integración de un nuevo proyecto de generación es capturado usando el método Requerimiento de Ingreso Diferencial (DRR); mientras los beneficios operacionales son observados al analizar el desempeño del nuevo proyecto de generación a través un Flujo de Potencia Óptimo DC con Restricciones de Seguridad (SCOPF). SCOPF además permite cuantificar beneficios económicos debido al reemplazo de generación costosa, congestión de la transmisión y mejoramiento de la seguridad N-1. Adicionalmente, en este trabajo se emplea otra métrica, llamada Beneficio Neto (NB) de un proyecto de generación, expresado como la diferencia entre LACE y LCOE (Costo Nivelado de Electricidad). NB proporciona un índice intuitivo, realista y fácil de calcular, que ayuda a identificar los proyectos de generación más promisorios durante los procesos de planeación de la expansión del sistema. Finalmente, la metodología propuesta es aplicada para calcular LACE y NB de diferentes proyectos de generación en Colombia. De acuerdo a los resultados, los proyectos geotérmicos muestran los LACE y NB más significantes. Estas métricas (LACE y NB) pueden llegar a ser útiles herramientas para la toma de decisiones en procesos de planeación.

Palabras clave: costo nivelado de electricidad; costo evitado de electricidad; planeación de expansión de generación; optimización de sistemas de potencia; flujo óptimo de potencia con restricciones de seguridad.

1. Introduction

During electrical generation expansion planning process, economic benefits, size and operative performance of different generation alternatives are evaluated by using technical and financial metrics. The well-known Levelized Cost of Electricity (LCOE) is a common financial indicator of different generation projects. According to different authors [1-4], the LCOE is the electricity price, in constant

How to cite: Marín-Cano, C.C. and Mejía-Giraldo, D.A., Levelized avoided cost of electricity model based on power system operation. DYNA, 85(206), pp. 79-84, September, 2018.

© The author; licensee Universidad Nacional de Colombia.

currency, at which energy output must be sold over the generation project life cycle for covering investment and O&M expenses, and return of capital to investors.

Although LCOE of different projects can be used to offer indicative signals for generation expansion planning [5], it has also been exposed that LCOE is not useful for comparing financial performance between intermittent and dispatchable generation technologies [6]. Also, according to [5], LCOE does not capture effects of power system dynamics. In order to overcome potential drawbacks of LCOE, the Energy Information Administration [7] has proposed to use the Levelized Avoided Cost of Electricity (LACE) under the context of the US electricity market. The LACE allows to effectively asses the technical-economic performance of a new generation project. Computing LACE requires the concept of Avoided Cost (AC), which represents potential cost savings in a power system once a new generation project is considered in the power system operations. The levelized term indicates an average cost per MWh of generation. This advantages work presents a novel methodology for computing LACE including operational features of a power system. We evaluate the economic benefit (or even disadvantage) of integrating a particular generation project into the power system by considering its technical operational characteristics and its impact on the economic dispatch. Thus, LACE can be used as a complementary indicator that provides decision makers with realistic and representative signals about generation expansion decisions.

The first contribution of this work is the proposed approach based on combining the DDR method supported by an operational tool like the SCOPF in order to effectively capture benefits (and/or disadvantages) of new generation projects. Not only does this tool evaluate an optimal power flow under normal conditions, but also N-1 post-contingency states are exhaustively considered. If the new project is a non-dispatchable technology (e.g. solar and wind), typical power output profiles are considered for computing LACE. The second contribution is the consideration of different generation scenarios within the power system for computing LACE of the new project. This approach allows to approximately capture the average value of a specific generation project over a set of generation as opposed to LCOE models that only employ a base case generation scenario of the project.

2. Literature review

LACE is conceptually a complementary indicator to LCOE that effectively asses the technical-economic performance of a generation project [7]. It is based on the concept of AC, which has been a public policy tool within energy efficiency context in the US, and it was stated under the Public Utilities Regulatory Policies Act (PURPA) in 1978 [8]. At the international level, several energy-related institutions [7,9-12], have estimated AC as alternative indicators that provide appropriate signals for investors and planners. Besides, references [8,13] argue that AC is based on marginal cost of the power system, and its calculation can provide useful cost saving indicators to investors.

Estimating the AC of a generation project is important for identifying the most promising generation choice [14,15]. Several long-term approaches have been proposed to estimate AC [8,14,15]. One of these approaches is the so-called Differential Revenue Requirement (DRR), which, according to [14], is the most comprehensive. In order to determine the economic and technical effect on the system of a new generation project, the DRR method can be employed. It compares the operational cost of a power system with and without the new generation project.

3. Proposed LACE methodology

Our LACE approach of a specific generation project is based on finding measures that capture the potential impacts, either advantages or disadvantages that the project can offer to the power system. Authors strongly believe these impacts have to be obtained by looking at the potential power system operation under different conditions. The goal of our approach is, therefore, to identify whether the project construction can replace other generation resources due to economic or technical reasons. A new generation project can improve either system security under N-1 contingencies, provide firm energy, offer support during peak demand periods, or replace a more expensive generation. Thus, our LACE indicator not only assesses the economic performance of the project, but also captures operational characteristics of the same.

4. Power system methodology assessment

The power system assessment is performed employing a Preventive DC SCOPF. The SCOPF is an economic dispatch, which ensures a secure power system operation under N-1 transmission contingencies. The interested reader may consult references [16-18] for additional details. Additionally, author propose the use of generation scenarios to provide a more effective LACE that takes into account the performance of the project under different system operating points.

In this setup, the SCOPF model returns the estimated annual operational cost $f_0(\omega)$ of the system under generation scenario ω, which is the optimal objective of the following mixed-integer linear optimization problem:

$$f_0(\omega) = \min \sum_{b\in \mathrm{B}} \sum_{g\in\Psi} c_g(\omega) \cdot P_{g,b,\omega} \cdot h_b \tag{1}$$

subject to:

$$\sum_{g\in\Psi_i} P_{g,b,\omega} - D_{i,b} = \sum_{l\in L_i^+} f_{l,b}^k - \sum_{l\in L_i^-} f_{l,b}^k, \quad \forall i\in\Phi, \forall k\in K, \forall b\in B \tag{2}$$

$$-K_{ol}\cdot F_l^{Max} \le f_{l,b}^k \le K_{ol}\cdot F_l^{Max}, \quad \forall l\in L, \forall k\in K, \forall b\in B \tag{3}$$

$$f_{l,b}^k = \frac{I_{lk}\cdot S_{base}}{X_l}\left(\sum_{i:l\in L_i^-}\theta_{i,b}^k - \sum_{i:l\in L_i^+}\theta_{i,b}^k\right), \quad \forall l\in L, \forall k\in K, \forall b\in B \tag{4}$$

$$U_g \cdot P_{g\min} \le P_{g,b,\omega} \le U_g \cdot A_{g,b}(\omega) \cdot P_{g\max}, \quad \forall g \in \Psi, \forall b \in B \tag{5}$$

$$-\frac{\pi}{2} \le \theta_{i,b}^{k} \le \frac{\pi}{2}, \quad \forall i \in \Phi, \forall k \in K, \forall b \in B \tag{6}$$

Where:

Φ : is the set of the power system buses.

Ψ_i : is the set of existing generators connected at bus i.

$\Psi = \cup_{i\in\Phi} \Psi_i$: is the set of generators.

L: is the set of transmission lines.

K is the set of post-contingency states.

B: is the set of demand blocks. A load duration curve that represents annual demand by a sequence of load blocks is employed. A demand level (peak, medium, minimum) and its corresponding number of hours in a year define each demand block b.

h_b : is the number of hours per year in which demand block b occurs.

c_g (ω): is the operation cost of each generator in generation scenario ω.

S_{base}: base power (100 MVA).

$P_{g,b,\omega}$: is the power generation dispatched by generator g during demand block b when generation scenario ω is simulated.

$f_{l,b}^{k}$: is the power flow through transmission line l during demand block b under contingency state k. k = 0 denotes the pre-contingency or normal condition state.

L_i^+: is the transmission line set that ends at bus i.

L_i^- : is the transmission line set that starts at bus i.

$D_{i,b}$: is the power demand at bus i in block b.

$\theta_{i,b}^{k}$: is the voltage angle at bus i in block b under post-contingency state k.

X_l: is the electrical impedance of the transmission line l.

I_{lk}: is the transmission line status parameter; it is 0 if transmission line l is outaged under contingency k, or 1 otherwise.

F_l^{Max}: represents the maximum power flow on transmission line l.

K_{ol} : is a long-term overload factor that is usually defined in the range [1, 1.3] [19].

U_g : is a binary decision variable; it is 1 if generator g is online, or 0 otherwise.

$A_{g,b}(\omega)$: represents the power availability factor of each generator g. $A_{g,b}(\omega)$ =1 for dispatchable generators, and $A_{g,b}(\omega)$ < 1 for both intermittent and hydro generators only during dry seasons.

$P_{g\ \max}$ and $P_{g\ \min}$: are the maximum and minimum operating power limits of each generator, respectively.

Constraint eq. (1) describes the operational cost of the power system. Constraint eq. (2) represents the power balance constraint under normal and post-contingency operating conditions. Constraint eq. (3) limits power flow on each line under normal and post-contingency operating conditions. Constraint eq. (4) displays the definition of active power flow in terms of voltage angle difference. Constraint eq. (5) shows power output limits of generation. And constraint eq. (6) represents voltage angle limits under normal and post-contingency operating conditions.

5. LACE formulations

LACE of a new generation project *p*, namely $LACE_p$, is defined as the annual cost change (ΔS_p) caused by the project per unit of energy (E_p) it can produce during the year. Thus, LACE can be computed as:

$$LACE_p = \frac{\Delta S_p}{E_p} \tag{7}$$

If $\Delta S_p > 0$, then it can said that project p replaces expensive generation. If $\Delta S_p = 0$, it can said that the project does not offer any economic or operational advantage. ΔS_p is computed as the average cost change caused by project p with respect to the set of generation scenarios Ω. That is,

$$\Delta S_p = \sum_{\omega\in\Omega} w_\omega \left(f_0(\omega) - f_0^{\,p}(\omega) \right) \tag{8}$$

Where w_ω is the weight associated to generation scenario ω. Besides, $\sum_{\omega\in\Omega} w_\omega = 1$. $f_0^p(\omega)$ represents the resulting operating cost of the system when the generation set considers the new project p, i.e., when set Ψ is changed to $\Psi^+ = \Psi \cup \{p\}$. In this work, annual energy produced by each new generation project p is averaged over the generation scenarios, according to the work of [20], as eq. (9) shows:

$$E_p = \sum_{\omega\in\Omega} w_\omega \sum_{b\in B} P_{p,b,\omega}^{*} \cdot h_b \tag{9}$$

Where $P_{p,b,\omega}^{*}$ represents the optimal power dispatched by generation project p in demand block b under generation scenario ω. Finally, LACE can be computed as:

$$LACE_p = \frac{\sum_{\omega\in\Omega} w_\omega \sum_{b\in B} \left(\sum_{g\in\Psi} c_g(\omega) \cdot P_{g,b,\omega}^{*} - \sum_{g\in\Psi^+} c_g(\omega) \cdot P_{g,b,\omega}^{*} \right) \cdot h_b}{\sum_{\omega\in\Omega} w_\omega \sum_{b\in B} P_{p,b,\omega}^{*} \cdot h_b} \tag{10}$$

6. Net Benefit formulations

Another useful indicator for evaluating generation projects is the Net Benefit (NB). The NB of a project can be calculated by subtraction of investment, operating and administrative costs from the cost savings estimated by avoided costs [13]. According to [7], NB_p of project p can be computed as:

$$NB_p = LACE_p - LCOE_p \quad (11)$$

When $LACE_p > LCOE_p$, the project is attractive for the planer or investor since its levelized cost savings can cover the levelized cost. Otherwise, the project does not offer attractive features and might not be considered as a real expansion option. In general, the higher NB_p the better.

7. Numerical results

Our goal is to illustrate LACE and NB of diverse generation projects located in Colombia, which are listed in Table 1. Generation technologies like wind, solar photovoltaic, thermal solar, biomass, hydro, coal, gas, and geothermal of different size were considered. Table 1 presents the variable operational cost c_p of each new generation project p as well as the connection bus. This data were obtained from [21].

Table 1.
Data of the new generation technologies

Generation Technology and nominal capacity	c_p USD/MWh	Connected to the bus:
Geothermal Single Flash (GT-SF 50MW)	0.00	Enea 115 kV
Geothermal Binary Cycle (GT-BC 20 MW)	0.00	Enea 115 kV
Wind (WIND 400 MW)	0.00	Cuestecitas 220kV
Wind (WIND 100 MW)	0.00	Cuestecitas 220 kV
Optimized Thermosolar (OTS 50 MW)	0.00	Cuestecitas 220 kV
Non-Optimized Thermosolar (NOTS 50 MW)	0.00	Cuestecitas 220 kV
Solar Photovoltaic (PV 150 MW)	0.00	Cuestecitas 220 kV
Solar Photovoltaic (PV 20 MW)	0.00	Cuestecitas 220 kV
Biomass (BM 20 MW)	39.01	Viterbo 115 kV
Biomass (BM 40 MW)	35.42	Cerrito 115 kV
Hydropower (HD 820 MW),	3.05	Sogamoso 220 kV
Conventional Pulverized Coal (CPC 70 MW)	32.53	Cerromatoso 110kV
Fluidized Bed Pulverized Coal (FBPC 164 MW)	30.06	Tasajero 230kV
Fluidized Bed Pulverized Coal (FBPC 161 MW)	30.06	Tasajero 230kV
Natural Gas Simple Cycle (NGSC 89 MW)	32.53	Termocol 220 kV
Natural Gas Combined Cycle (NGCC 390 MW)	32.53	Tebsa 220 kV

Source: The Authors

The Colombian network employed consists of 1,487 transmission lines and power transformers, 1018 buses, with a total system demand of 9,500 MW, approximately. Currently, hydro-generation represents 69.9 % of the installed capacity and thermal generation about 29.7 % [22].

Given the high dependence on hydro power, Colombian power system performance is extremely sensitive to weather fluctuations. Geographic location makes of Colombia a tropical country with only two weather seasons: rainy and dry [20]. These conditions allow us to construct two extreme scenarios that capture hydro generation variability. Our generation scenario set is $\Omega=\{H,T\}$, where H represents a heavy "hydro" power production scenario (typical during rainy seasons) and T stands for a heavy "thermal" power production scenario (typical during dry seasons).

Three load blocks were used to model hourly demand variation. These blocks represent peak, medium and minimum demand. According to [23], in Colombia each block is allocated with 2,190 hours/year in peak demand, which occurs during the evening (18:00 h to 0:00 h), 4,745 hours/year in medium demand, which occurs during the daytime (5:00 h to 18:00 h), and 1,825 hours/year in minimum demand (0:00 h to 5:00 h). In order to consider hourly production variability of wind and solar resources, the availability factor $A_{g,b}(\omega)$ was adjusted accordingly to limit power production in the SCOPF model. The availability $A_{g,b}(\omega)$ used for photovoltaic projects under scenario T during peak, medium and minimum demand was 0, 0.8, and 0 respectively; whereas in scenario H, these factors were 0, 0.1 and 0. In the case of wind projects, availability factors were 0.35, 0.45 and 0.2 for each demand block as previously defined for both scenarios. The optimization model presented in section 4 was implemented in GAMS [24].

From Figure 1 some key elements can be highlighted: 1) coal and biomass-based power technologies display a remarkable LACE component during peak hours and under scenario T compared to renewable projects. Coal and biomass projects displace the most expensive generation in the north and southwest regions of the country. Moreover, some of coal-based technologies such as Fluidized Bed Pulverized Coal (FBPC) and Conventional Pulverized Coal (CPC) have a considerable LACE during medium demand blocks under scenario T. 2) Photovoltaic, thermal solar, wind and geothermal projects have a significant LACE under T scenario and medium demand block (when wind availability is high). The displacement of fossil fuel-based expensive generation during dry season is the reason of these results. On the contrary, LACE caused by these projects is low under the H scenario given the lower displacement of low-cost hydro generation.

Figure 2 shows results of LACE, LCOE, and NB. LACE is averaged over scenarios H and T. LCOE data were taken from [4]. The adopted approach is inspired in the work of [1], which facilitates the incorporation of current policy aspects (taxes, incentives). From Figure 2, it can be seen that the geothermal project GT-SF 50 MW reflects the maximum NB given its high LACE. The high availability factor of this resource, its independence from weather conditions to produce energy, and

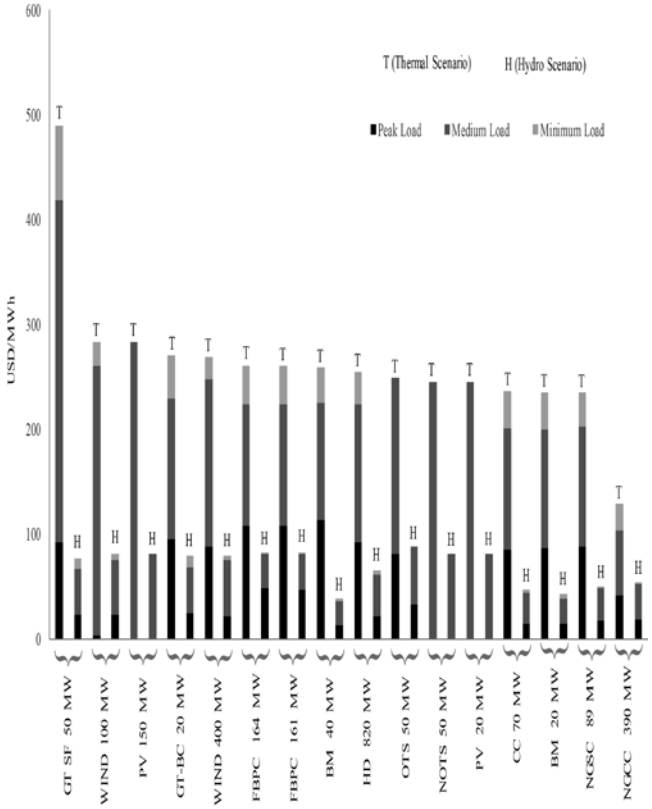


Figure 1. LACE under the different generation and load scenarios
Source: The authors.

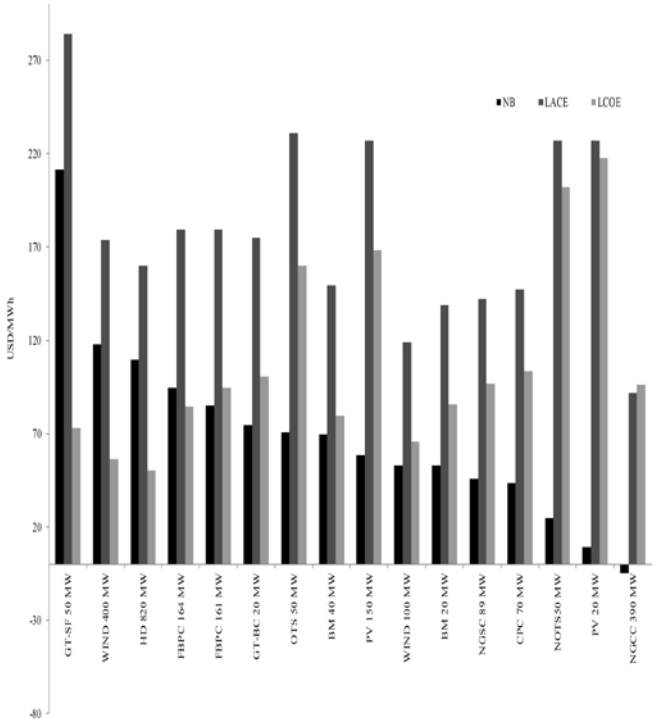


Figure 2. *NB*, *LA*CE and LCOE of the generation technologies in Colombia
Source: The authors.

its null production cost are key factors that justify these results. This is finally reflected in significant cost savings. A similar result is observed in the US according to NB analysis performed in reference [7]. Intermittent generation like wind, photovoltaic, and thermal solar have a positive value of NB due to great economic competitiveness under scenario *T*. The project labeled as NGCC 390 MW has a negative NB since its LACE is not as high as its LCOE. This project does not cause any savings under scenario *H* during minimum load periods.

The SCOPF model is useful to detect transmission congestion and security issues due to the occurrence of a specific contingency. In these cases, a specific project, properly located (and not necessarily economic), can improve these security and/or congestion issues. This benefit is ultimately reflected in high LACE. On the contrary, potential operational impact of generation projects on uncongested networks is null. For instance, the installation of the geothermal project GT-SF 50 MW reduced the congestion level on near three-winding transformers under scenario *T* and peak demand block when the outage of other power transformers was analyzed. The economical and operational advantages of this technology is what makes it valuable.

8. Conclusions

This work proposed a novel methodology for computing LACE considering operational aspects. LACE is a useful index to estimate the unit cost savings produced by new generation project. Our LACE approach also captures important operational aspects, needed to be considered for making investment decisions, such as system security under N-1 contingencies or generation support during peak demand periods. By using the SCOPF as an evaluation tool, the proposed LACE model identifies differences between the power output profiles of both intermittent and dispatchable generation. The proposed LACE model also allows capturing energy resources geographical dependence as well as electrical network topology. Additionally, the consideration of different generation scenarios provides better LACE results, since different operating points are captured. Through NB, it was also possible to identify those candidate projects that effectively balance savings and cost. This formulation can provide decision and policy makers with additional tools to better design expansion plans and policies. According to our results, most of all the renewable generation projects display high values of LACE and NB, especially geothermal technology (GT-SF 50MW).

Acknowledgments

The authors want to thank Colciencias and “Unidad de Planeación Minero Energética” for the financial support under contract 589-2013 (convocatoria # 616 de 2013).

References

[1] Reichelstein, S. and Yorston, M. The prospects for cost competitive solar PV power. Energy Policy, 55(0), pp. 117-127, 2013. DOI: 10.1016/j.enpol.2012.11.003

[2] Castillo-Ramírez, A., Mejía-Giraldo, D.,a,G. and Giraldo-Ocampo, J.D., Geospatial levelized cost of energy in Colombia: GeoLCOE. Paper presented at the Innovative Smart Grid Technologies Latin America (ISGT LATAM), 2015, IEEE PES.

[3] Castillo-Ramírez, A., Mejía-Giraldo, D. and Molina-Castro, J., Fiscal Incentives impact for ret's investments in Colombia. Energy Sources, Part B: Economics, Planning and Policy. [online]. pp. 759-764, 2017. Avilable at: http://www.tandfonline.com/doi/abs/10.1080/15567249.2016.1276648

[4] GIMEL. Costos nivelados de generación de electricidad en Colombia-generalidades: GIMEL-Universidad de Antioquia, Colombia, [en línea]. 2015. Disponible en: http://www.siel.gov.co/Inicio/Generaci%C3%B3n/Estudiodecostosniveladosdegeneracion/tabid/157/Default.aspx

[5] Larsson, S., Reviewing electricity generation cost assessments, MSc. Thesis, Disciplinary domain of science and technology, earth sciences, department of earth sciences, Uppsala University, Sweden, [online]. 2012. Available at: http://www.diva-portal.org/smash/get/diva2:540350/FULLTEXT02

[6] Joskow, P.L., Comparing the costs of intermittent and dispatchable electricity generating technologies. American Economic Association, [online]. 101(3), pp. 4, 2011. Available at: http://citeseerx.ist.psu.edu/viewdoc/download?doi=10.1.1.227.6392&rep=rep1&type=pdf

[7] Energy Information Adminsitration (EIA). Levelized cost and levelized avoided cost of new generation resources in the Annual Energy Outlook 2016: U.S, 2016.

[8] Shalaby, A., Avoided costs: Ontario Hydro's experience. Power Systems, IEEE Transactions on, 4(1), pp. 149-157, 1989. DOI: 10.1109/59.32472

[9] Inter-American Development Bank (IADB). Societal benefits from renewable energy in Latin America and the Caribbean (E. Division, Trans.): Inter American Development Bank: Climate Change and Sustainability Division, [online]. 2014. Available at: https://publications.iadb.org/bitstream/handle/11319/6034/Societal%20benefits%20TN-623.pdf?sequence=1

[10] Synapse Energy Economics, Inc. Avoided energy supply costs in New England: 2013 Report, U.S, [online]. 2013, 289 P. Available at: http://www.synapseenergy.com/sites/default/files/SynapseReport.2013-07.AESC_.AESC-2013.13-029-Report.pdf

[11] Energy and Environmental Economics, Inc. Methodology and forecast of long term avoided costs for the evaluation of California Energy Efficiency Programs, Rocky Mountain Institute, Snowmass, Colorado, U.S, 2004, 279 P.

[12] Exeter Associates, Inc. Avoided energy costs in Maryland- assessment of the costs avoided through energy efficiency and conservation measures in Maryland, U.S, 2014.

[13] Beeche, J.A., Avoided cost: an essential concept for integrated resource planning. Center for Urban Policy and the Environment, Indiana University-Purdue University, Indianapolis, U.S, [online] 1996. Available at: http://opensiuc.lib.siu.edu/cgi/viewcontent.cgi?article=1321&context=jcwre

[14] Elefant, C., Reviving purpa's purpose: the limits of existing state avoided cost ratemaking methodologies in supporting alternative energy development and a proposed path for reform, U.S, [online]. 2011. Avalaible at: http://www.recycled-energy.com/images/uploads/Reviving-PURPA.pdf

[15] Busch, J.F. and Eto, J., Estimation of avoided costs for electric utility demand-side planning. Energy Sources, 18(4), pp. 473-499, 1996. DOI: 10.1080/00908319608908783

[16] Capitanescu, F., Glavic, M., Ernst, D. and Wehenkel, L., Applications of security-constrained optimal power flow, Modern Electric Power Systems Symposium, MEPS06, [online]. 2006. Available at: http://orbi.ulg.ac.be/handle/2268/13538

[17] Phan, D. and Kalagnanam, J., Some efficient optimization methods for solving the security-constrained optimal power flow problem. IEEE Transactions on Power Systems, 29(2), pp. 863-872, 2014. DOI: 10.1109/TPWRS.2013.2283175

[18] Bhaskar-M, M., Srinivas, M. and Sydulu, M., Security constraint optimal power flow (SCOPF) – A comprehensive survey, 11(6), International Journal of Computer Applications, [online]. 2010. Available at: http://www.ijcaonline.org/archives/volume11/number6/1583-2122 DOI: 10.5120/1583-2122

[19] CREG 025. Comision de Regulación de Energia y Gas. Por la cual se establece el Código de Redes, como parte del Reglamento de Operación del Sistema Interconectado Nacional, Colombia, [en línea]. 1995. Dsponible en: http://apolo.creg.gov.co/Publicac.nsf/2b8fb06f012cc9c245256b7b00789b0c/3a940408d14bf2e80525785a007a653b/$FILE/Cr025-95.pdf

[20] Correa-Metrio, A., El cambio climático y el invierno en Colombia: Un juego de niñas y niños. Universo Centro, [en línea]. 21, 2011. Disponible en: http://www.universocentro.com/NUMERO21/ElcambioclimáticoyelinviernoenColombia.aspx

[21] Expertos en mercado-precios de oferta inicial (XM), [en línea]. 2016. [Consultado en: marzo 16 de 2016]. Disponible en: http://www.xm.com.co/Pages/PreciodeOfertaInicial.aspx

[22] UPME. Unidad de Planeación Minero - Energética. Estudio de generacion electrica bajo escenario de cambio climatico: Unidad de Planeación Minero Energética, Colombia, 2017.

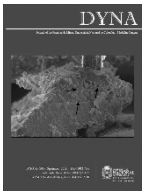
[23] CREG 011. Comision de Regulación de Energia y Gas. Por la cual se establece la metodologia y formulas tarifarias para la remuneracion de la actividad de la tranmision de energia electrica en el STN, Colombia, 2009.

[24] General Algebraic Modeling System. GAMS Development Corporation, Washington DC, USA, 2017. [Online]. Avalaible at: https://www.gams.com/

C.C. Marín-Cano, received the BSc. Eng in Electrical Engineering in 2010, and currently is pursuing the MSc. degree in Engineering, in Universidad de Antioquia, Medellin, Colombia. From 2010 to 2014, he worked for electricity utilities and consulting companies within the power sector. Currently, he is working as auxiliary researcher in GIMEL research group of Universidad de Antioquia and also as freelance consultant. His research interests include: simulation, modeling, and optimization in electrical systems.
ORCID: 0000-0002-8235-4659

D.A. Mejía-Giraldo, received the BSc. and MSc. degrees in Electrical Engineering from Universidad Tecnológica de Pereira, Pereira, Colombia, in 2004 and 2005, respectively, and the PhD. degree in Electrical Engineering from Iowa State University, Ames, IA, USA, 2013. In 2013, he worked as an intern at XM, Colombian ISO, within the long term energy planning team. He is an Assistant Professor of Electrical Engineering for Universidad de Antioquia, Medellin, Colombia.
ORCID: 0000-0001-9287-4810

UNIVERSIDAD NACIONAL DE COLOMBIA
SEDE MEDELLÍN
FACULTAD DE MINAS



DYNA
http://dyna.medellin.unal.edu.co/

Heavy metal contribution by runoff in a high-altitude megacity: a method based on the road-deposited sediment characterization

Carlos Zafra-Mejía, Hugo Rondón-Quintana & Álvaro Gutiérrez-Malaxechebarria

Environmental Engineering, Faculty of Environment and Natural Resources, Universidad Distrital Francisco José de Caldas, Bogotá D.C., Colombia.
czafra@udistrital.edu.co, harondonq@udistrital.edu.co, amgutierrezm@udistrital.edu.co

Received: May 12th, 2017. Received in revised form: March 11th, 2018. Accepted: April 25th, 2018.

Abstract
The objective of this paper is to present the development and application of a method to estimate the heavy metal (HM) contribution derived from the wash-off by runoff on road-deposited sediments (RDS) in a high-altitude megacity (Bogota, Colombia). The method is based on the development of a HM wash-off equation which considers two processes: HM transportation and HM leaching. HM contribution by runoff ranges between 24.7% and 50.3%, relative to the total mass per unit area of HMs associated with dry-weather RDS (Mn, Cd, As, Zn, Cu, Ba, Pb, and Fe). The HMs that show a greater contribution are Cd, Zn, and Mn. RDS size fraction below 250 µm contributes on average 81.6% of the total HM load washed-off by runoff. The findings suggest that the RDS size fraction below 250 µm must be the reference fraction for the control systems design of HM pollution in Bogota city.

Keywords: heavy metal; surface runoff; urban pollution; wash-off; water quality.

Contribución de metales pesados por escorrentía en una megaciudad de elevada altitud: un método basado en la caracterización del sedimento vial

Resumen
El objetivo de este artículo es presentar el desarrollo y aplicación de un método para determinar la contribución de metales pesados (MP) derivados del lavado ejercido por la escorrentía sobre sedimentos viales (SV) en una megaciudad de elevada altitud (Bogotá, Colombia). El método está basado en una ecuación que considera dos procesos: transporte y lixiviación de MP. La contribución de MP por escorrentía varía entre un 24.7-50.3%, con respecto a la masa total por unidad de área de MP asociados con SV de tiempo seco (Mn, Cd, As, Zn, Cu, Ba, Pb y Fe). Los MP que presentan una mayor contribución son Cd, Zn y Mn. La fracción inferior a 250 µm de los SV contribuye en promedio con un 81.6% de la carga total de MP. Los hallazgos sugieren que la fracción inferior a 250 µm es referente para el diseño de sistemas de control de contaminación en Bogotá.

Palabras clave: metal pesado; escorrentía superficial; contaminación urbana; lavado; calidad del agua.

1. Introduction

Public health research agencies reported the growing interest of studying the pollution by heavy metals (HMs) in urban areas due to its continuous emission [1,2], long residence periods in the environment, transport inside of air masses, deposition on road surfaces [3,4], mobility, and bioavailability [5]. Road-deposited sediment (RDS) accumulated in dry weather were used as indicators of the presence of HMs in urban environments because they represented the accumulation more recent of pollutants [6,7]. Namely, they were sinks of HMs and other compounds that came from different urban pollution sources [8,9]. The main advantage of the RDS use as pollution indicators was that they were subjected to transportation processes, which allowed us to evaluate its mobility in the urban environment

How to cite: Zafra-Mejía, C., Rondón-Quintana, H and Gutiérrez-Malaxechebarria, A., Heavy metal contribution by runoff in a high-altitude megacity: a method based on the road-deposited sediment characterization. DYNA, 85(206), pp. 85-94, September, 2018.

© The author; licensee Universidad Nacional de Colombia.

[10]; as for example, the RDS transportation exerted by road runoff during rainfall events.

The pollution caused by road runoff water constitutes a great problem in urban areas, since it has been demonstrated that it contains great loads of HMs (mass quantity of HMs) [11,12]. Diffuse pollution generated by road runoff is known as one of the main reasons for water quality deterioration in urban aquatic bodies [13,14]. The significance and interest in knowing this type of flows relies on many studies reporting the presence of high HM concentrations in dissolved form in the runoff water [15,16]. Additionally, the HM contribution associated with the solid fraction of surface runoff has been considered, namely, the proportion of RDS accumulated in dry weather that is washed-off during rainfall events [17,18]. Therefore, the HM load associated with dry-weather RDS must be determined, and the impacts of surface runoff in the drainage systems and receiving waters must be studied in order to perfect the design of pollution prevention systems.

The studies on the HM wash-off phenomenon by road runoff reported rainfall and previous dry-weather period as leading climatic factors [19,20]. RDS transportation by runoff increased with the rainfall intensity [21] and when the previous dry period was prolonged [13]. Malmquist [22] and Reinertsen [23] reported that intense (> 10 mm/h) and successive (four events) rainfalls decreased the RDS load by nearly 80%. Ball et al. [24] found that only the rainfall events with intensities greater than 7 mm/h could be considered as transportation events of the HM load associated with RDS.

In addition to the RDS transportation process, the leaching process exercised by stormwater runoff on the RDS size fraction which was not transported must be taken into account within the HM wash-off phenomenon. Ellis and Revitt [25] reported the following sequence in RDS leaching studies, from the temporal efficiency in the extraction conducted (leaching test: rainwater, mechanical shaker, pH: 6.5, and t = 28 days): Cd > Zn and Cu > Pb. Stone and Marsalek [26] obtained a similar sequence in leaching tests on RDS (leaching test: mechanical shaker, 0.5 N HCl, and t = 12 hours): Cd and Cu > Zn > Pb. Recent studies have also reported a similar sequence [27,28]: Zn and Cu > Pb. These researchers suggested that RDS acted as effective sinks for Pb, but not for Cd and Cu. Additionally, the optimized BCR sequential extraction procedure (leaching test) developed by Sutherland and Tack was used on RDS to fractionate the HM into the following target phases [29]: acid-extractable, reducible, oxidizable, and residual. The above studies suggested that the acid-extractable phase (water soluble, exchangeable, and bound to carbonate) was most suitable for the simulation of turbulent runoff conditions during storm drainage from the roadside surface (it is the bioavailable fraction of HMs).

In the analysis of HM content on RDS, the size fraction below 250 µm was given attention because the consulted literature suggested that this fraction tended to associate the highest HM concentrations. On average, this size fraction tended to accumulate 69% (between 51.2% and 82.5%) of the total HM load (Mn, Cd, Zn, Cu, Pb, Co, Ni, Fe, and Cr) associated with dry-weather RDS [17,21,25,30-35]. The above studies suggested that the size fraction below 250 µm was representative of the dry-weather RDS to characterize the HM content.

This study was done using data from a Latin-American megacity (8.85 million inhabitants in 2015). Bogota (Colombia) is a high-altitude city located in the Andes Mountains (04°36′35″ N, 74°04′54″ W); its average altitude is 2600 masl. The city's tropical mountain climate is characterized by large hourly temperature variations and average annual rainfall of 797 mm. The city is recognized as the urban center with the greatest population density (26000 inhabitants/km2) and third highest air pollution level in Latin America [36]. In global terms, there have been few published studies that evaluate the behavior of HMs in the urban centers of developing countries with similar physical characteristics and climate conditions; this lack of research has, in part, driven the development of this study.

The objective of this paper is to present the development and application of a method to estimate the HM contribution derived from the wash-off by runoff on RDS in a high-altitude megacity. The above, with respect to the total mass per unit area (load) of HMs associated with dry-weather RDS. The method consists of three phases: climatic characterization of RDS load, evaluation of HM load on dry-weather RDS, and application of a wash-off equation. Two processes are included in the wash-off equation: HM transportation (solid fraction) and HM leaching (dissolved fraction). The method is initially developed on two road surfaces in the cities of Torrelavega (Spain) and Bogotá (Colombia). The development of the method is focused on the following HMs: Zn, Pb, Cu, Cr, Ni, Mn, Cd, Fe, Co, Ba, and As. Subsequently, the method is applied on three road surfaces in Bogota city. The application of the method is focused on two of the HMs most reported by studies on road surfaces: Pb and Cu [37].

2. Materials and methods

2.1. Proposed method

2.1.1. Climatic characterization of RDS load

The two road surfaces for developing the method were in the cities of Torrelavega (Spain, A1) and Soacha (Colombia, A2); Soacha belonged to the metropolitan area of Bogota city (Colombia). A1 road surface was used to validate the results obtained on A2 road surface. Climate data were obtained from stations located at a distance between 300 and 340 m from the road surfaces under study. The three road surfaces to which the proposed method was applied were in Bogota city. These three road surfaces were situated in Fontibón (Z1), Puente Aranda (Z2), and Kennedy (Z3). The climate data were obtained from stations located 10, 38, and 194 meters away from the road surfaces under study, respectively. In A1 road surface, the Atlantic climate (warm) was characterized by abundant rains throughout the year, high humidity, and mild temperatures. In A2, Z1, Z2, and Z3 the Tropical mountain climate (cold) was characterized by abundant rains during the year and a wide variation in temperature (hourly variation between 5 and 22 °C). Table 1 shows the main climatic and physical characteristics of each road surface.

Table 1.
Characteristics of the road surfaces under study.

Characteristic	A1	A2	Z1	Z2	Z3
Coordinates	43°20'17"N 4°02'57"W	4°35'05"N 74°13'12"W	04°40'09"N 74°08'33"W	04°37'49"N 74°07'06"W	04°35'45"N 74°08'48"W
Elevation (mals)	50.3	2560	2548	2557	2560
Annual rainfall (mm)[a]	1230	900	847	854	1236
Daily average wind speed (km/h)[a]	8.0	8.6	10.1	9.4	6.8
Average annual temperature (°C)[a]	14.7	14	14	14	15
Population density (inhabitants/ha)	300	600	600	160	480
Land use[b]	R	R-C	I-R	I-C	R-I
Waterproofing (%)	60	90	95	45	80
Traffic lines/parking	2/2	1[c]/none	1[d]/none	4/none	2/none
Road length (m)	305	120	100	215	105
Longitudinal/cross slope (%)	0.2-4/4	1-2/4	0.7/4	1/4	0.3/4
Pavement type/texture	Asphalt/rough	Asphalt/rough	Asphalt/rough	Asphalt/smooth	Asphalt/rough
Average daily traffic (vehicles/day)	3800	2750	650	13500	12300
Traffic average speed (km/h)	50	20	20	40	50
Traffic composition (%) A1/A2 - Z1/Z2/Z3	Cars: 92/65; light trucks: 5/0; trucks without tow: 2.5/0; trucks with tow: 0.25/0; buses: 0.25/35		Cars: 93/77/83; light trucks: 5/4/3; trucks without tow: 1/2/2; trucks with tow: 0/0/1; buses: 1/17/11 4/Suave-Ádo del tra sentidoe estudio en Puente Aranada.		

Note: [a] during the study period; [b] R-residential, I-industrial, C-commercial; [c] not authorized parking; [d] not authorized parking and automotive maintenance.
Source: The authors.

The protocol for RDS collection was established having as reference the sampling systems used by other studies [17,21,24,25,38]. RDS samplings were collected in dry weather, next to the road curb (0.40 m), at the same hour, and for a period of 65 for A1 (09/28/2004-12/01/2004), 127 days for A2 (01/07/2010-14/05/2010), and 365 days for Z1, Z3 (05/08/2010-08/05/2011) and Z2 (10/03/2010-03/10/2011), respectively. RDS samples were taken daily for A1, every 3 days for A2, and every 10 days for Z1, Z2, and Z3. Slight variations were found in the sampling frequency due to the occurrence of rainfall events that prevented the RDS collection in dry weather.

The sampling surface had an area of 0.50 m^2 (707 mm X 707 mm); the collection area sizes were ensured by placing a wooden frame on the road surface. For the RDS collection a brush with plastic fibers together with a hand dustpan were used. Particle size distribution of RDS (63-2800 μm) was determined using the ISO-11277 method [39]. Fifty-six and 88 RDS samples were collected in A1 and A2, respectively. Finally, a total of 114 RDS samples were collected for application of the proposed method, being 38 samples for each road surface (Z1, Z2, and Z3).

The climatic characterization of RDS load was focused on the following: (i) identification of the climatic periods of dry and rainy weather in the study areas, and (ii) quantification of RDS load (mass quantity of RDS) for each climatic period. Additionally, during the development of the proposed method (A1 and A2), the susceptibility of the RDS to wash-off by runoff (percentage difference relative to the RDS mass before and after each rainfall event) was analyzed as a function of the particle diameter for all rain events during the study period. Finally, we assumed during the application of the proposed method (Z1, Z2, and Z3) that the difference in the RDS load between these climatic periods (i.e., dry and rainy weather) represented the average load washed-off by runoff in rainy weather.

2.1.2. Evaluation of HM load in dry-weather RDS

HM concentration associated with dry-weather RDS was determined by flame atomic absorption spectrometry: ISO-11047 method [39]. RDS samples were previously digested in a mixture of hydrochloric acid and nitric acid (3:1, Aqua Regia): ISO-11466 method [39]. In this study, leaching tests of HMs associated with RDS were carried out considering the DIN 38414-S4 standard [40]: mechanical shaker (10 rpm), deionized water, room temperature (20 °C), and t = 24 hours. In the available literature there were limited discussions on relationship between the sorption behavior of HM species and the water quality of road runoff (e.g., dissolved organic carbon content and pH). Twenty-four leaching tests were performed for each study area (A1 and A2).

The size fraction below 250 μm was chosen as representative of the HM content in dry-weather RDS. An analysis of susceptibility of the HMs to wash-off by runoff was performed and total HM load associated with this size fraction was assumed to be transported by road runoff. The HM load for size fraction was determined from the HM concentration and quantity of RDS by weight associated with each size fraction. Additionally, the leaching effect derived from road runoff on the remaining RDS portion which was not susceptible to wash-off was considered.

2.1.3. Wash-off equation

The wash-off equation was:

$$TLW=\sum_{i=1}^{n}\left[\begin{array}{c}\left(LW_{<250,i}\cdot\frac{ML_{<250,i}}{100}\right)+\\ \left(LE_{<250}\cdot\left(1-\frac{LW_{<250,i}}{100}\right)\cdot\frac{ML_{<250,i}}{100}\right)\end{array}\right]+\left(LE_{\geq 250}\cdot\left(1-\frac{ML_{<250}}{100}\right)\right) \quad (1)$$

Where TLW was the HM contribution washed-off by runoff from RDS (%), $LW_{<250,\ i}$ was the percentage of RDS with size below 250 µm susceptible to transportation (see Table 2), $ML_{<250,\ i}$ was the percentage of HM load associated with RDS of size below 250 µm (see Table 3), $LE_{<250}$ was the percentage of HM leaching associated with RDS of size below 250 µm (see Table 4), and $LE_{\geq 250}$ was the percentage of HM leaching associated with RDS of size greater than or equal to 250 µm (see median for each HM in Table 4). The median was used as a central-tendency measure in light of the extreme values in the information reported in Table 4. The term $(1\text{-}LW_{<250,\ i}/100)$ represented the RDS proportion with size below 250 µm that was not transported by runoff, but which provided HM by leaching.

TLW value depended on the fractions number of size below 250 µm considered (n). Finally, a second term was included to quantify the HM contribution by the size fraction greater than or equal to 250 µm, if this size fraction was not susceptible to transportation, but leached by road runoff. The term $(1\text{-}ML_{<250}/100)$ indicated the HM proportion associated with this size fraction (see Table 3).

Table 2.
Average RDS wash-off after rainfall events.

Site	Road slope (%)	Rainfall intensity (mm/h)	RDS removal (%) Size fraction (µm)		
			< 63	63-125	125-250
A1[a]	0.2	0.7-3.7	27 ± 12	21 ± 9	18 ± 7
	4		40 ± 13	30 ± 19	23 ± 14
A2[b]	1	0.8-4.5	65 ± 15	42 ± 14	22 ± 11
	2		73 ± 17	51 ± 12	29 ± 14

Note: [a] Average over 10 rainfall events; [b] Average over 9 rainfall events.
Source: The authors.

Therefore, the wash-off equation included the following phenomena in its two terms. Term 1: $(LW_{<250,\ i} \cdot ML_{<250,\ i}/100)$, HM transportation (solid fraction) associated with RDS of size below 250 µm; and $(LE_{<250} \cdot (1\text{-}LW_{<250,\ i}/100) \cdot ML_{<250,\ i}/100)$, HM leaching (dissolved fraction) associated with RDS of size below 250 µm. Term 2: $(LE_{\geq 250} \cdot (1\text{-}ML_{<250}/100))$, HM leaching (dissolved fraction) associated with RDS of size greater than or equal to 250 µm.

3. Results and discussion

3.1. Development of the method

3.1.1. Climatic characterization of RDS load

The analysis of susceptibility of the RDS to washing by runoff showed on average for the size fraction below 250 µm, that the percentage of RDS transported by runoff during all rainfall events in A1 (asphalt, slope = 0.2-4%, rainfall intensity = 0.7-3.7 mm/h, Atlantic climate) and A2 (asphalt, slope = 1-2%; rainfall intensity = 0.8-4.5 mm/h, tropical mountain climate) was 26.5% and 47.0%, respectively (Table 2). Zhao and Li [52] reported an average RDS wash-off between 15.8% and 11.6% for the size fraction below 1000 µm, using a rainfall simulator (asphalt, slope = 4.1%, rainfall intensity = 46.7 mm/h, humid continental climate).

Vaze and Chiew [38] reported that the road runoff reached to wash-off up to 45% of RDS accumulated in dry weather (asphalt, slope = 10%; rainfall intensity = 4 mm in single burst, size fraction < 3000 µm, oceanic climate). Finally, Tian et al. [53] reported an average RDS wash-off of 37.9% for the size fraction below 300 µm (humid continental climate). The previous differences reported by the studies were probably linked to the rainfall magnitude, evaluated size fraction, pavement roughness, and accumulated amount of RDS on road surfaces tested (i.e., in dry weather).

3.1.2. Evaluation of HM load in dry-weather RDS

On average for A1 and A2, 62.6% and 58.0% of the total HM load in dry-weather RDS was associated with the size fraction below 250 µm, respectively (Table 3). Sartor et al. [30], Ellis and Revitt [25], German and Svensson [31], Zanders [32], Bian and Zhu [17], Zhao et al. [21], Kayhanian et al. [33], Ma and Singhirunnusorn [34], and Bi et al. [35] reported results between 51.2% and 82.5%, with an average of 69.0%.

Table 3.
Average HM load in dry-weather RDS with a 95% confidence interval.

		HM load (%) - RDS size fraction (µm)										
	Metal	< 63	63-125	125-250	< 250	250-2800		Metal	< 63	63-125	125-250	< 250	250-2800
A1[a]	Pb	18 ± 6	20 ± 5	22 ± 6	60	40	A2[b]	Pb	12 ± 3	18 ± 4	22 ± 5	52	48
	Zn	26 ± 7	24 ± 6	22 ± 5	72	28		Zn	20 ± 5	23 ± 5	22 ± 6	65	35
	Cu	16 ± 4	17 ± 3	24 ± 7	57	43		Cu	13 ± 4	20 ± 4	25 ± 7	58	42
	Cr	22 ± 6	19 ± 5	15 ± 5	56	44		Cd	19 ± 4	23 ± 6	19 ± 4	61	39
	Ni	26 ± 6	20 ± 4	14 ± 3	60	40		Fe	12 ± 3	17 ± 4	20 ± 4	49	51
	Cd	28 ± 8	25 ± 5	17 ± 4	70	30		Mn	13 ± 3	19 ± 4	24 ± 5	56	44
	Fe	17 ± 4	18 ± 5	20 ± 4	55	45		Ba	18 ± 5	24 ± 6	23 ± 5	65	35
	Mn	20 ± 5	21 ± 6	22 ± 5	63	37		As	19 ± 6	21 ± 7	20 ± 4	60	40
	Co	30 ± 7	23 ± 6	17 ± 4	70	30		-	-	-	-	-	-
	Average	22.6 ± 6	20.8 ± 5	19.2 ± 5	62.6	37.4		Average	15.3 ± 4	20.6 ± 5	22.1 ± 5	58.0	42.0
	Std. deviation	5.1	2.7	3.6	6.6	6.6		Std. deviation	3.5	2.8	2.1	5.8	6.2

Note: [a] Average over 56 RDS samples; [b] Average over 88 RDS samples.
Source: The authors.

Table 4.
HM leaching in RDS. Comparison between this study and other research.

Study	Extraction agent	Size fraction (µm)	HM Leaching (%)										
			Pb	Zn	Cu	Cr	Ni	Cd	Fe	Mn	Co	Ba	As
This study, A1	Deionized water	< 250	8.3	18.7	14.4	2.4	6.3	28.9	3.2	32.1	9.2	-	-
This study, A2	Deionized water	< 250	10.3	14.9	12.6	-	-	23.6	2.8	21.7	-	11.8	17.6
Kumar et al. [16]	Acetic acid	< 2000	4.8	38.6	1.5	-	-	15.3	-	-	-	-	-
Kumar et al. [27]	Acetic acid	< 2000	13.3	50.8	21.7	-	-	48.1	-	-	-	-	-
Li et al. [28]	Deionized water	< 2.5	23.5	60.3	36.6	30.4	33.4	42.0	9.7	40.1	-	-	36.9
Sutherland et al. [41]	Acetic acid	< 2000	3.0	34.0	6.4	-	2.6	-	0.05	19.1	8.7	-	-
Li et al. [42]	Acetic acid	< 2000	26.5	64.3	7.9	-	-	55.2	-	-	-	-	-
Sutherland [43]	Acetic acid	< 2000	73.2	50.4	38.2	-	16.9	-	10.8	62.3	57.1	-	-
Banerjee [44]	Acetic acid	< 500	20.3	23.5	4.6	2.3	11.4	49.5	-	-	-	-	-
Sutherland et al. [45]	Acetic acid	< 2000	2.0	29.0	7.0	-	-	-	-	-	-	-	-
Lee et al. [46]	Acetic acid	< 150	13.7	52.8	17.1	1.4	32.9	24.0	-	-	-	-	-
Kartal et al. [47]	Acetic acid	< 74	8.9	25.1	6.0	10.1	13.3	36.4	0.6	25.0	22.6	-	-
Preciado and Li [48]	Acetic acid	< 100	13.0	56.0	42.0	-	-	-	0.9	43.0	-	-	-
Perez et al. [49]	Acetic acid	< 2000	4.1	28.8	1.9	-	-	-	-	-	-	-	-
Zhang et al. [50]	Acetic acid	< 2000	4.8	23.0	5.7	3.1	4.3	7.4	0.5	23.7	5.1	-	-
Li et al. [51]	Acetic acid	< 800	20.4	48.7	3.7	-	-	35.9	-	28.8	-	-	-
	Average		15.6	38.7	14.2	8.3	15.1	33.3	3.6	32.9	20.5	11.8	27.3
	Median		11.7	36.3	7.5	2.8	12.4	35.9	1.9	28.8	9.2	11.8	27.3
	Std. deviation		17.1	16.0	13.5	11.3	12.1	15.0	4.3	13.7	21.5	-	13.6

Source: The authors.

The results of the leaching test performed in A1 and A2 showed that the HMs with higher leaching percentages were Mn and Cd (Table 4). On average, the sequence in leaching tests was the following one: Mn (26.9%) > Cd (26.3%) > As (17.6%) > Zn (16.8%) > Cu (13.5%) > Ba (11.8%) > Pb (9.3%) > Co (9.2%) > Ni (6.3%) > Fe (3.0%) > Cr (2.4%). Average leaching for all HMs under study was 14.1%. Table 4 shows similar results reported by other studies. Nevertheless, differences in the HM leaching tests probably related to the agent and time of extraction, temperature, agitation system, and RDS size fraction were observed. The median of the leaching percentage for all HMs reviewed in Table 4 was 11.8%; median was used as central-tendency measure due to the existence of extreme values in the information reported in Table 4.

3.1.3. Development of the wash-off equation

HM contribution derived from the wash-off by runoff on RDS was calculated from the equation developed for the proposed method (eq. 1). We observed that on average in A1 and A2, 29.0% and 40.3% of the total HM load associated with RDS was washed-off after a rainfall event, respectively (i.e., for Mn, Cd, As, Zn, Cu, Ba, Pb, Co, Ni, Fe, and Cr). Zhao and Li [52] reported that the average HM contribution by road runoff was between 10% and 25% (Pb, Zn, Cu, Cr, and Ni) for the RDS size fraction below 1000 µm and using a rainfall simulator. When calculating for the same HMs reported by these researchers, the present study identified the average HM contribution in A1 and A2 being between 17.1-39.1% and 24.7-48.4%, respectively (see TLW in Table 5). Hamilton et al. [54] and Tian et al. [53] reported a contribution between 6.6-28.9% (Pb, Zn, Cu, and Cd) and 6.1-55.4% (Pb, Zn, Cu, Cr, Ni, and Cd), respectively; this latter being for the RDS size fraction below 40 µm. Thus, we observed that the equation developed for determining the HM contribution tended to overestimate the contribution reported by the previous studies, on average between 1.20 and 2.76 times (Pb, Zn, Cu, Cr, Ni, and Cd). The above, assuming similar climatic and physical characteristics on road surfaces of the studies consulted.

This overestimation of the HM contribution was probably due to the fact that, in the proposed wash-off equation, strong turbulent runoff conditions were considered for the RDS (laboratory leaching tests: DIN 38414-S4 standard, and Tessier and BCR sequential-extraction procedures). It is unlikely that all HMs leached in the laboratory (simulated conditions) would leach with the same intensity during rainfall events (real conditions). Previous comparisons with other studies were useful for validating the proposed simplified method.

In order of precedence, the average contribution for each HM in A1 was: Cd (44.2%) > Mn (42.2%) > Zn (39.1%) > Co (26.0%) > Cu (24.4%) > Pb (24.2%) > Ni (23.6%) > Cr (17.1%) > Fe (16.7%). In A2 the average contribution was: Cd (50.3%) > Zn (48.4%) > Mn (45.4%) > As (44.7%) > Ba (38.7%) > Cu (34.3%) > Pb (32.9%) > Fe (24.7%). On average, the HMs with a greater contribution on road surfaces tested were: Cd (47.3%) > Mn (43.8%), and Zn (43.8%).

We observed that on average for A1 and A2, 83.1% and 81.6% of the total HM load washed-off by runoff was provided by the RDS size fraction below 250 µm, respectively (see T<250 and L<250 in Table 5); this was integrated in the phenomena included in first term of the wash-off equation: transportation (solid fraction of HM) and leaching (dissolved fraction of HM) of RDS < 250 µm (eq. 1). Zhao et al. [21] reported that this size fraction contributed more than 80% of the total HM load washed-off by runoff from RDS.

Table 5.
Results for variables and terms of the wash-off equation.

HM	Road surface	Variable 1	Variable 2	Variable 3	Variable 4	Term 1	Term 2		TLW (%)[a]
		$LW_{<250,\,i}$	$ML_{<250,\,i}$	$LE_{<250}$	$LE_{\geq 250}$	T<250 (%)[b]	L<250 (%)[c]	L≥250 (%)[d]	
Mn	A1	26.5	63	32.1	28.8	16.7	14.9	10.7	42.2
	A2	47	56	21.7	28.8	26.3	6.4	12.7	45.4
Cd	A1	26.5	70	28.9	35.9	18.6	14.9	10.8	44.2
	A2	47	61	23.6	35.9	28.7	7.6	14.0	50.3
As	A1	-	-	-	-	-	-	-	-
	A2	47	60	17.6	27.3	28.2	5.6	10.9	44.7
Zn	A1	26.5	72	18.7	36.3	19.1	9.9	10.2	39.1
	A2	47	65	14.9	36.3	30.6	5.1	12.7	48.4
Cu	A1	26.5	57	14.4	7.5	15.1	6.0	3.2	24.4
	A2	47	58	12.6	7.5	27.3	3.9	3.2	34.3
Pb	A1	26.5	60	8.3	11.7	15.9	3.7	4.7	24.2
	A2	47	52	10.3	11.7	24.4	2.8	5.6	32.9
Ba	A1	-	-	-	-	-	-	-	-
	A2	47	65	11.8	11.8	30.6	4.1	4.1	38.7
Co	A1	26.5	70	9.2	9.2	18.6	4.7	2.8	26.0
	A2	-	-	-	-	-	-	-	-
Ni	A1	26.5	60	6.3	12.4	15.9	2.8	5.0	23.6
	A2	-	-	-	-	-	-	-	-
Fe	A1	26.5	55	3.2	1.9	14.6	1.3	0.9	16.7
	A2	47	49	2.8	1.9	23.0	0.7	1.0	24.7
Cr	A1	26.5	56	2.4	2.8	14.8	1.0	1.2	17.1
	A2	-	-	-	-	-	-	-	-

Note: [a] TLW: HM contribution by runoff from RDS; [b] T<250: RDS transportation < 250 μm (solid fraction); [c] L<250: RDS leaching < 250 μm (dissolved fraction); [d] L≥250: RDS leaching ≥ 250 μm (dissolved fraction).
Source: The authors.

On the other hand, the RDS size fraction greater than or equal to 250 μm represented on average a HM contribution for A1 and A2 of 16.9% and 18.4%, respectively (see L≥250 in Table 5); this was integrated in the only phenomenon included in second term of the wash-off equation: leaching (dissolved fraction of HM) of RDS ≥ 250 μm (eq. 1). Wash-off equation allowed us visualizing the following order of precedence from the included phenomena: Term 1 (RDS < 250 μm), HM transportation (67.1%) > HM leaching (15.2%); and Term 2 (RDS ≥ 250 μm), HM leaching (17.7%). On average, solid and dissolved fractions contribute 67.1 and 32.9% of the total HM load washed-off by runoff from RDS, respectively.

3.2. Application of the method

3.2.1. Climatic characterization of RDS load

According to the Institute of Hydrology, Meteorology, and Environmental Studies of Colombia (IDEAM), three periods were identified in Z1 and Z3 for the climate phenomenon 'La Niña-Southern Oscillation' [55]: (i) 08/05-17/07/2010, (ii) 18/10/2010-09/01/2011, and (iii) 01/03-08/05/2011. In Z2 two periods were identified: (i) 18/10/2010-09/01/2011, and (ii) 24/02-06/06/2011 (see Fig. 1). During the sampling period and in these periods identified, rainfall was 57.7%, 42.3%, and 75.1% higher than the average annual registered by climate stations in Z1 (591 mm/year), Z2 (600 mm/year), and Z3 (706 mm/year), respectively. These periods corresponded to rainy weather, the remaining tested weather being considered as dry one.

Based on the identified climate periods, an estimate of the average RDS wash-off was done for the representative size fraction of HM content (RDS < 250 μm). On average, the RDS load during periods of rainy weather was 28.8 ± 8.1 g/m^2, 36.9 ± 7.3 g/m^2, and 25.1 ± 6.7 g/m^2 in Z1, Z2, and Z3, respectively. RDS load in dry weather was 76.2 ± 9.3 g/m^2, 92.2 ± 14.9 g/m^2, and 67.1 ± 8.8 g/m^2 for Z1, Z2, and Z3, respectively. Therefore, the results showed that during rainy weather there was an average RDS wash-off of 62.2%, 60.0%, and 62.6% for Z1, Z2, and Z3, respectively (Fig. 1).

3.2.2. Evaluation of HM load in dry-weather RDS

On average for Z1, Z2, and Z3, 70%, 48%, and 60% of the total Pb load was associated with the RDS size fraction below 250 μm, respectively. For Cu, there was evidence of a higher association, and more specifically 81%, 57%, and 69%, respectively (Table 6).

Table 6.
Average HM load in dry-weather RDS with a 95% confidence interval.

HM	HM load (%) RDS size fraction (μm) < 63	63-125	125-250	< 250	250-2800
		Z1			
Pb	17 ± 3	18 ± 3	35 ± 6	70	30
Cu	26 ± 5	23 ± 4	32 ± 6	81	19
		Z2			
Pb	11 ± 3	9 ± 3	28 ± 5	48	52
Cu	13 ± 4	10 ± 4	34 ± 6	57	43
		Z3			
Pb	15 ± 3	15 ± 4	30 ± 5	60	40
Cu	18 ± 3	16 ± 5	35 ± 6	69	31

Source: The authors.

3.2.3. Application of the wash-off equation

For applying the method in Z1, Z2, and Z3, the developed wash-off equation (eq. 1) was reduced because only the size fraction below 250 µm was used as indicator of transportation (solid fraction) and leaching (dissolved fraction) of HMs associated with RDS. Thus, there was HM transportation of the size fraction below 250 µm and HM leaching for the size fraction greater than or equal to 250 µm. The reduced wash-off equation was:

$$TLW=\left(LW_{<250}\cdot\frac{ML_{<250}}{100}\right)+\left(LE_{\geq 250}\cdot\left(1-\frac{ML_{<250}}{100}\right)\right) \quad (2)$$

Where TLW was the HM contribution washed-off by runoff from RDS (%), $LW_{<250}$ was the percentage of RDS with size below 250 µm transported by runoff, $ML_{<250}$ was the percentage of HM associated with RDS of size below 250 µm (Table 6), and $LE_{\geq 250}$ was the percentage of HM leaching associated with RDS of size greater than or equal to 250 µm (see median in Table 4). The term $(1-ML_{<250}/100)$ indicated the HM proportion associated with the RDS size fraction greater than or equal to 250 µm (Table 6).

We noted that on average in Z1, Z2, and Z3, 47.1%, 34.9%, and 42.2% of the total Pb load associated with RDS was washed-off after a rainfall event, respectively. For Cu, the contribution was 51.8%, 37.4%, and 45.5%, respectively (see TLW in Table 7). As already observed, Cu tended to show the highest contribution from the application of the reduced wash-off equation because the RDS size fraction below 250 µm associated a higher Cu percentage (average = 69.0%) in comparison with Pb (average = 59.3%), despite showing a lower leaching percentage (Cu = 7.5%; Pb = 11.7%).

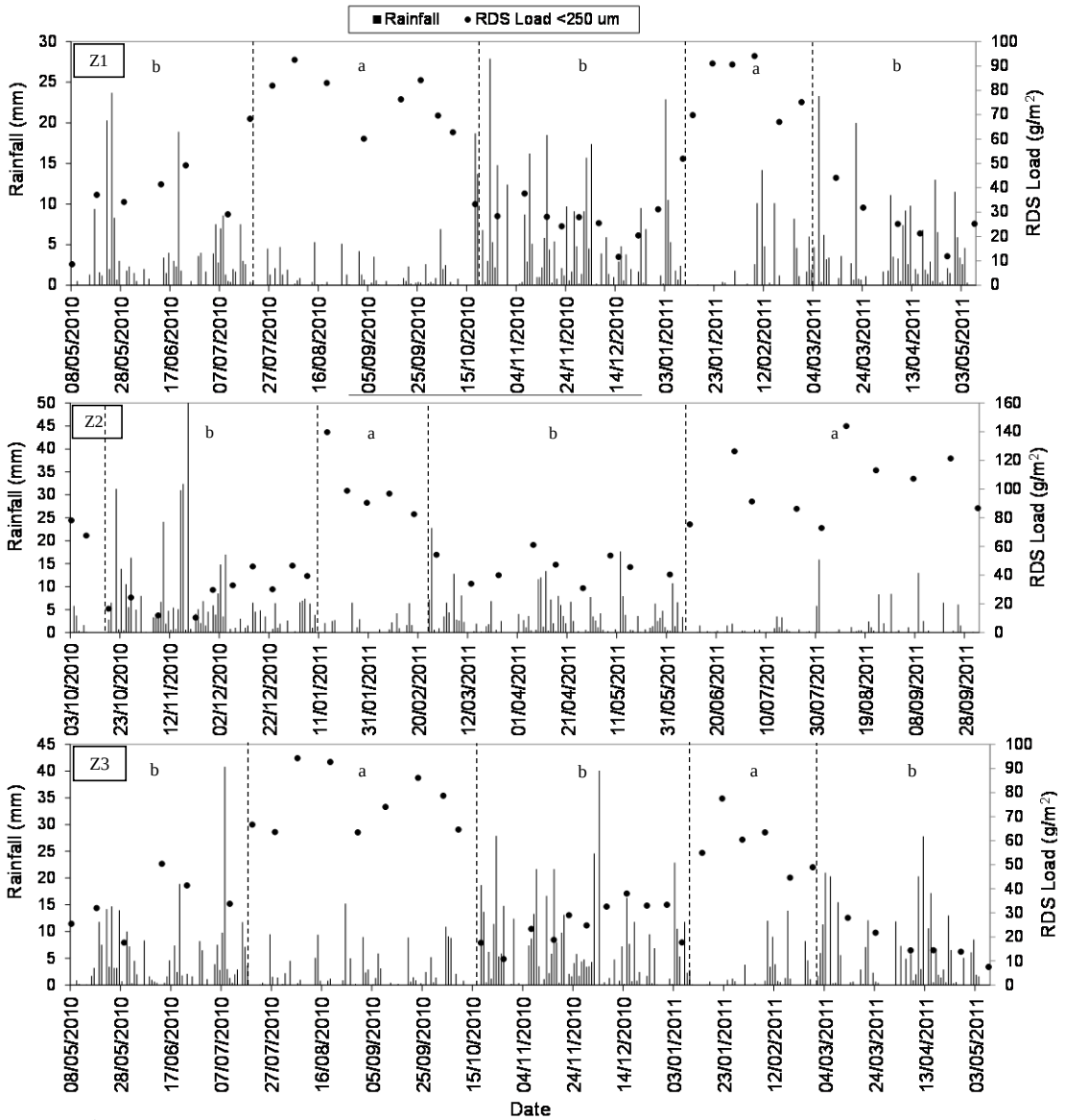


Figure 1. Variation of RDS load in Z1, Z2, and Z3. a) Dry weather period, and b) rainy weather period.
Source: The authors.

Table 7.
Results for variables and terms of the reduced wash-off equation.

HM	Site	Variable			Term		TLW (%)[a]
		1	2	3	1	2	
		$LW_{<250}$	$ML_{<250}$	$LE_{\geq 250}$	T < 250 (%)[b]	L ≥ 250 (%)[c]	
Pb	Z1	62.2	70.0	11.7	43.6	3.5	47.1
	Z2	60.0	48.0	11.7	28.8	6.1	34.9
	Z3	62.6	60.0	11.7	37.5	4.7	42.2
Cu	Z1	62.2	81.0	7.5	50.4	1.4	51.8
	Z2	60.0	57.0	7.5	34.2	3.2	37.4
	Z3	62.6	69.0	7.5	43.2	2.3	45.5

Note: [a] TLW: HM contribution washed-off by runoff from RDS; [b] T < 250: RDS transportation < 250 µm (solid fraction); [c] L ≥ 250: RDS leaching ≥ 250 µm (dissolved fraction).
Source: The authors.

Additionally, the HM contribution for each term of the reduced wash-off equation was quantified. We noted that on average in Z1, Z2, and Z3, 92.5%, 82.6%, and 88.9% of the Pb load was provided by the RDS size fraction below 250 µm (HM transportation phenomenon), respectively. The contribution for Cu was 97.3%, 91.4%, and 94.9%, respectively. For Pb, the RDS size fraction greater than or equal to 250 µm contributed on average 7.5%, 17.4%, and 11.1% in Z1, Z2, and Z3, respectively (RDS leaching phenomenon). The contribution for Cu was 2.8%, 8.6%, and 5.1%, respectively. Therefore, the reduced wash-off equation allowed us visualizing on average the following order of precedence from the included phenomena: Term 1, HM transportation (Pb = 88.0% and Cu = 94.5%; solid fraction); and Term 2, HM leaching (Pb = 12% and Cu = 5.5%; dissolved fraction).

After comparing the results obtained during the development and application of the wash-off equation, we noted that the terms associated with the RDS size fraction below 250 µm contributed, for all HMs under study, 82.4% and 91.3% of the total HM load washed-off by runoff, respectively. The results suggested that the percentage associated with this RDS size fraction tended to increase during the application of the reduced wash-off equation, probably because of the elimination of the leaching phenomenon included in the first term of eq. (1). In other words, the total HM load associated with RDS of size below 250 µm was assumed to be transported by runoff with it.

4. Conclusions

The objective of this paper is to present the development and application of a method to estimate the HM contribution derived from the wash-off by runoff on RDS in a high-altitude megacity (Bogotá, Colombia). The above data and interpretation lead us to the following conclusions.

In the development of the method, the HM contribution by runoff ranges between 24.7% and 50.3%; relative to the total mass per unit area of HMs associated with dry-weather RDS of Bogota city (Mn, Cd, As, Zn, Cu, Ba, Pb, and Fe). The HMs presenting a greater contribution are Cd, Zn, and Mn. Wash-off equation allows us visualizing the following order of precedence from the phenomena included in its terms: HM transportation on RDS < 250 µm (solid fraction), HM leaching on RDS ≥ 250 µm (dissolved fraction), and HM leaching on RDS < 250 µm (dissolved fraction). The RDS size fraction below 250 µm contributes on average 81.6% of the total HM load washed-off by runoff. Similar trends for Pb and Cu are observed during the application of the method in Bogota city. The contribution by runoff for Pb and Cu ranges between 34.9-47.1% and 37.4-51.8%, respectively. The size fraction below 250 µm contributes on average 88.0% and 94.5% of the total load of Pb and Cu washed-off by runoff from RDS. The findings suggest that the RDS size fraction below 250 µm must be the reference fraction for the control systems design of HM pollution in Bogota city.

Therefore, the method presented in this paper is proposed as a management tool for responsible institutions of the urban pollution control. It will be useful to establish control strategies in dry weather (e.g., optimizing the street sweeping frequency schedule); and rainy weather, by improving the storm sewers design, retention-detention ponds, permeable pavements, infiltration-exfiltration trenches and basins, etc. Additionally, this method will suppose a future research improvement on the influence of rainfall events in relation with the HM loads washed-off by runoff from RDS.

Nevertheless, the following limitations form part of this study and require further attention. During the development of the method, we observed that the wash-off equation tends to overestimate the HM contribution reported by other studies. This overestimation was probably due to the fact that, in the proposed wash-off equation, turbulent runoff conditions were considered for the RDS (i.e., laboratory leaching tests: DIN 38414-S4 standard, and Tessier and BCR sequential-extraction procedures); and probably not all HMs that can be leached in the laboratory (simulated conditions) could be leached with the same intensity during rainfall events (real conditions).

Conflict of interest

The authors declare that there are no conflicts of interest.

Acknowledgements

The authors wish to thank the universities 'Francisco José de Caldas' (Colombia) and Cantabria (Spain) for their financial support.

References

[1] Meza-Figueroa, D., De la O-Villanueva, M. and De la Parra, M.L., Heavy metal distribution in dust from elementary schools in Hermosillo, Sonora, México. Atmospheric Environment, 41(2), pp. 276-288, 2007. DOI: 10.1016/j.atmosenv.2006.08.034.

[2] Qing, X., Yutong, Z. and Shenggao, L., Assessment of heavy metal pollution and human health risk in urban soils of steel industrial city (Anshan), Liaoning, northeast China. Ecotoxicology and Environmental Safety, 120, pp. 377-385, 2015. DOI: 10.1016/j.ecoenv.2015.06.019.

[3] Zafra, C., Temprano, J. and Tejero, I., The physical factors affecting heavy metals accumulated in the sediment deposited on road surfaces in dry weather: a review. Urban Water Journal, 14(6), pp. 639-649, 2017. DOI: 10.1080/1573062X.2016.1223320.

[4] Charlesworth, S., de Miguel, E. and Ordóñez, A., A review of the distribution of particulate trace elements in urban terrestrial environments and its application to considerations of risk. Environmental Geochemistry and Health, 33(2), pp. 103-123, 2011. DOI: 10.1007/s10653-010-9325-7.

[5] González, E., Tornero, M.A., Ángeles, Y. and Bonilla Y.N., Total concentration and speciation of heavy metals in urban origin biosolids. Revista Internacional de Contaminacion Ambiental, 25(1), pp. 15-22, 2009.

[6] Yuen, J.Q., Olin, P.H., Lim, H.S., Benner, S.G., Sutherland, R.A. and Ziegler, A.D., Accumulation of potentially toxic elements in road deposited sediments in residential and light industrial neighborhoods of Singapore. Journal of Environmental Management, 101, pp. 151-163, 2012. DOI: 10.1016/j.jenvman.2011.11.017.

[7] Melaku, S., Morris, V., Raghavan, D. and Hosten, C., Seasonal variation of heavy metals in ambient air and precipitation at a single site in Washington, D.C. Environmental Pollution, 155(1), pp. 88-98, 2008. DOI: 10.1016/j.envpol.2007.10.038.

[8] Moreno, T., Karanasiou, A., Amato, F., Lucarelli, F., Nava, S., Calzolai, G. and Gibbons, W., Daily and hourly sourcing of metallic and mineral dust in urban air contaminated by traffic and coal-burning emissions. Atmospheric Environment, 68, pp. 33-44, 2013. DOI: 10.1016/j.atmosenv.2012.11.037.

[9] Liu, E., Yan, T., Birch, G. and Zhu, Y., Pollution and health risk of potentially toxic metals in urban road dust in Nanjing, a mega-city of China. Science of the Total Environment, 476-477, pp. 522-531, 2014. DOI: 10.1016/j.scitotenv.2014.01.055.

[10] Amato, F., Schaap, M., Denier van der Gon, H.A.C., Pandolfi, M., Alastuey, A., Keuken, M. and Querol, X., Short-term variability of mineral dust, metals and carbon emission from road dust resuspension. Atmospheric Environment, 74, pp. 134-140, 2013. DOI: 10.1016/j.atmosenv.2013.03.037.

[11] Hilliges, R., Endres, M., Tiffert, A., Brenner, E. and Marks, T., Characterization of road runoff with regard to seasonal variations, particle size distribution and the correlation of fine particles and pollutants. Water Science and Technology, 75(5), pp. 1169-1176, 2017. DOI: 10.2166/wst.2016.576.

[12] Legret, M. and Pagotto, C., Heavy metal deposition and soil pollution along two major rural highways. Environmental Technology, 27(3), pp. 247-254, 2006. DOI: 10.1080/09593332708618641.

[13] Helmreich, B., Hilliges, R., Schriewer, A. and Horn, H., Runoff pollutants of a highly trafficked urban road - correlation analysis and seasonal influences. Chemosphere, 80(9), pp. 991-997, 2010. DOI: 10.1016/j.chemosphere.2010.05.037.

[14] Wijesiri, B., Egodawatta, P., McGree, J. and Goonetilleke, A., Influence of uncertainty inherent to heavy metal build-up and wash-off on stormwater quality. Water Research, 91, pp. 264-276, 2016. DOI: 10.1016/j.watres.2016.01.028.

[15] Stagge, J.H., Davis, A.P., Jamil, E. and Kim, H., Performance of grass swales for improving water quality from highway runoff. Water Research, 46(20), pp. 6731-6742, 2012. DOI: 10.1016/j.watres.2012.02.037.

[16] Kumar, M., Furumai, H., Kurisu, F. and Kasuga, I., Tracing source and distribution of heavy metals in road dust, soil and soakaway sediment through speciation and isotopic fingerprinting. Geoderma, 211-212, pp. 8-17, 2013. DOI: 10.1016/j.geoderma.2013.07.004.

[17] Bian, B. and Zhu, W., Particle size distribution and pollutants in road-deposited sediments in different areas of Zhenjiang, China. Environmental Geochemistry and Health, 31(4), pp. 511-520, 2009. DOI: 10.1007/s10653-008-9203-8.

[18] Aksoy, H., Unal, N.E., Cokgor, S., Gedikli, A., Yoon, J., Koca, K. and Eris, E., A rainfall simulator for laboratory-scale assessment of rainfall-runoff-sediment transport processes over a two-dimensional flume. Catena, 98, pp. 63-72, 2012. DOI: 10.1016/j.catena.2012.06.009.

[19] Mejía, C.A.Z., Pinzón, E.C.L. and González, J.T., Influence of traffic in the heavy metals accumulation on urban roads: Torrelavega (Spain)-Soacha (Colombia). Revista Facultad de Ingenieria, (67), pp. 146-160, 2013.

[20] Egodawatta, P., Ziyath, A.M. and Goonetilleke, A., Characterising metal build-up on urban road surfaces. Environmental Pollution, 176, pp. 87-91, 2013. DOI: 10.1016/j.envpol.2013.01.021.

[21] Zhao, H., Li, X., Wang, X. and Tian, D., Grain size distribution of road-deposited sediment and its contribution to heavy metal pollution in urban runoff in Beijing, China. Journal of Hazardous Materials, 183(1-3), pp. 203-210, 2010. DOI: 10.1016/j.jhazmat.2010.07.012.

[22] Malmquist, P.A., Atmospheric fallout and street cleaning: Effects on urban storm water and snow, Progress in Water Technology, 10(5), pp. 495-505, 1978.

[23] Reinertsen, T.R., Quality of stormwater runoff from streets, Proceeding of the Second International Conference on Urban Storm Drainage, 1981. pp. 107-115.

[24] Ball, J.E., Jenks, R. and Aubourg, D., An assessment of the availability of pollutant constituents on road surfaces. Science of the Total Environment, 209(2-3), pp. 243-254, 1998. DOI: 10.1016/S0048-9697(97)00319-7.

[25] Bryan-Ellis, J. and Revitt, D.M., Incidence of heavy metals in street surface sediments: solubility and grain size studies. Water, Air, and Soil Pollution, 17(1), pp. 87-100, 1982. DOI: 10.1007/BF00164094.

[26] Stone, M. and Marsalek, J., Trace metal composition and speciation in street sediment: Sault Ste. Marie, Canada. Water, Air, and Soil Pollution, 87(1-4), pp. 149-169, 1996. DOI: 10.1007/BF00696834.

[27] Kumar, M., Furumai, H., Kurisu, F. and Kasuga, I., Potential mobility of heavy metals through coupled application of sequential extraction and isotopic exchange: comparison of leaching tests applied to soil and soakaway sediment. Chemosphere, 90(2), pp. 796-804, 2013. DOI: 10.1016/j.chemosphere.2012.09.082.

[28] Li, H., Wang, J., Wang, Q., Qian, X., Qian, Y., Yang, M. and Wang, C., Chemical fractionation of arsenic and heavy metals in fine particle matter and its implications for risk assessment: a case study in Nanjing, China. Atmospheric Environment, 103, pp. 339-346, 2015. DOI: 10.1016/j.atmosenv.2014.12.065.

[29] Sutherland, R.A., Tack, F.M.G. and Ziegler, A.D., Road-deposited sediments in an urban environment: A first look at sequentially extracted element loads in grain size fractions. Journal of Hazardous Materials, 225-226, pp. 54-62, 2012. DOI: 10.1016/j.jhazmat.2012.04.066.

[30] Sartor, J.D., Boyd, G.B. and Agardy, F.J., Water pollution aspects of street surface contaminants. Journal of the Water Pollution Control Federation, 46(3), pp. 458-467, 1974.

[31] German, J. and Svensson, G., Metal content and particle size distribution of street sediments and street sweeping waste. Water Science & Technology, 46(6-7), pp. 191-198, 2002.

[32] Zanders, J.M., Road sediment: characterization and implications for the performance of vegetated strips for treating road run-off. Science of the Total Environment, 339(1-3), pp. 41-47, 2005. DOI: 10.1016/j.scitotenv.2004.07.023.

[33] Kayhanian, M., McKenzie, E.R., Leatherbarrow, J.E. and Young, T.M., Characteristics of road sediment fractionated particles captured from paved surfaces, surface run-off and detention basins. Science of the Total Environment, 439, pp. 172-186, 2012. DOI: 10.1016/j.scitotenv.2012.08.077.

[34] Ma, J. and Singhirunnusorn, W., Distribution and health risk assessment of heavy metals in surface dusts of Maha Sarakham municipality. Procedia - Social and Behavioral Sciences, 50, pp. 280-293, 2012. DOI: 10.1016/j.sbspro.2012.08.034.

[35] Bi, X., Liang, S. and Li, X., A novel in situ method for sampling urban soil dust: Particle size distribution, trace metal concentrations, and stable lead isotopes. Environmental Pollution, 177, pp. 48-57, 2013. DOI: 10.1016/j.envpol.2013.01.045.

[36] Sarmiento, R., Hernández, L.J., Medina, E.K., Rodríguez, N. and Reyes, J., Respiratory symptoms associated with air pollution in five localities of Bogota, 2008-2011, a dynamic cohort study. Biomedica, 35(3), pp. 167-176, 2015. DOI: 10.7705/biomedica.v35i0.2445.

[37] Eriksson, E., Baun, A., Scholes, L., Ledin, A., Ahlman, S., Revitt and Mikkelsen, P.S., Selected stormwater priority pollutants - a European perspective. Science of the Total Environment, 383(1-3), pp. 41-51, 2007. DOI: 10.1016/j.scitotenv.2007.05.028.
[38] Vaze, J. and Chiew, F.H.S., Experimental study of pollutant accumulation on an urban road surface. Urban Water, 4(4), pp. 379-389, 2002. DOI: 10.1016/S1462-0758(02)00027-4.
[39] ISO. Standards Handbook. Geneva: International Organization for Standardization, 2000.
[40] DIN. Determination of leachability by water, 38414-S4. Berlin: German standard methods for examination of water, wastewater and sludge, 1984.
[41] Sutherland, R.A., Tack, F.M.G., Tolosa, C.A. and Verloo, M.G., Operationally defined metal fractions in road deposited sediment, Honolulu, Hawaii. Journal of Environmental Quality, 29(5), pp. 1431-1439, 2000. DOI: 10.2134/jeq2000.00472425002900050009x.
[42] Li, X., Poon, C. and Liu, P.S., Heavy metal contamination of urban soils and street dusts in Hong Kong. Applied Geochemistry, 16(11-12), pp. 1361-1368, 2001. DOI: 10.1016/S0883-2927(01)00045-2.
[43] Sutherland, R.A., Bed sediment-associated trace metals in an urban stream, Oahu, Hawaii. Environmental Geology, 39(6), 611-627, 2000. DOI: 10.1007/s002540050473.
[44] Banerjee, A.D.K., Heavy metal levels and solid phase speciation in street dusts of Delhi, India. Environmental Pollution, 123(1), pp. 95-105, 2003. DOI: 10.1016/S0269-7491(02)00337-8.
[45] Sutherland, R.A., Tack, F.M.G., Ziegler, A.D. and Bussen, J.O., Metal extraction from road-deposited sediments using nine partial decomposition procedures. Applied Geochemistry, 19(6), pp. 947-955, 2004. DOI: 10.1016/j.apgeochem.2003.11.002.
[46] Lee, H., Lau, S., Kayhanian, M. and Stenstrom, M.K., Seasonal first flush phenomenon of urban stormwater discharges. Water Research, 38(19), pp. 4153-4163, 2004. DOI: 10.1016/j.watres.2004.07.012.
[47] Kartal, S., Aydin, Z. and Tokalioğlu, S., Fractionation of metals in street sediment samples by using the BCR sequential extraction procedure and multivariate statistical elucidation of the data. Journal of Hazardous Materials, 132(1 SPEC. ISS.), pp. 80-89, 2006. DOI: 10.1016/j.jhazmat.2005.11.091.
[48] Preciado, H.F. and Li, L.Y., Evaluation of metal loadings and bioavailability in air, water and soil along two highways of British Columbia, Canada. Water, Air, and Soil Pollution, 172(1-4), pp. 81-108, 2006. DOI: 10.1007/s11270-005-9063-0.
[49] Pérez, G., López-Mesas, M. and Valiente, M., Assessment of heavy metals remobilization by fractionation: Comparison of leaching tests applied to roadside sediments. Environmental Science and Technology, 42(7), pp. 2309-2315, 2008. DOI: 10.1021/es0712975.
[50] Zhang, M. and Wang, H., Concentrations and chemical forms of potentially toxic metals in road-deposited sediments from different zones of Hangzhou, China. Journal of Environmental Sciences, 21(5), pp. 625-631, 2009. DOI: 10.1016/S1001-0742(08)62317-7.
[51] Li, X., Poon, C. and Liu, P.S., Heavy metal contamination of urban soils and street dusts in Hong Kong. Applied Geochemistry, 16(11-12), pp. 1361-1368, 2001. DOI: 10.1016/S0883-2927(01)00045-2.
[52] Zhao, H. and Li, X., Understanding the relationship between heavy metals in road-deposited sediments and washoff particles in urban stormwater using simulated rainfall. Journal of Hazardous Materials, 246-247, pp. 267-276, 2013. DOI: 10.1016/j.jhazmat.2012.12.035.
[53] Tian, P., Li, Y. and Yang, Z., Effect of rainfall and antecedent dry periods on heavy metal loading of sediments on urban roads. Frontiers of Earth Science in China, 3(3), pp. 297-302, 2009. DOI: 10.1007/s11707-009-0042-4.
[54] Hamilton, R.S., Revitt, D.M., Warren, R.S. and Duggan, M.J., Metal mass balance studies within a small highway dominated catchment. Science of the Total Environment, 59(C), pp. 365-368, 1987. DOI: 10.1016/0048-9697(87)90460-8.
[55] García, M.C., Piñeros, A., Bernal, F.A. and Ardila, E., Climate variability, climate change and water resources in Colombia. Revista de Ingenieria, 36, pp. 60-64, 2012. DOI: 10.15446/esrj.v18n1.39966.

C.A. Zafra-Mejía, received the BSc. in Civil Engineering in 2001 (Universidad Industrial de Santander, Colombia), the MSc. degree in Environmental Engineering in 2003, and the PhD. degree in Environmental Engineering in 2012 (Universities de Cantabria y País Vasco, Spain). Since 2006 he worked for the Universidad Distrital Francisco José de Caldas, Colombia. Currently, he is a full professor in the Environment and Natural Resources Faculty. His research interests include: simulation, modeling, and forecasting in stormwater runoff pollution; and time-series analysis and forecasting using statistical and computational intelligence techniques.
ORCID: 0000-0002-4061-4897.

H.A. Rondón-Quintana, received the BSc. in Civil Engineering in 2000 (Universidad Francisco de Paula Santander, Colombia), the MSc. degree in Civil Engineering in 2002, and the PhD. degree in Civil Engineering in 2008 at the Universidad de Los Andes, Colombia. Since 2008 he worked for Universidad Distrital Francisco José de Caldas, Colombia. Currently, he is a full professor in the Environment and Natural Resources Faculty. His research interests include: simulation, modeling and forecasting in environmental impacts for the pavement construction; and time-series analysis and forecasting using statistical and computational intelligence techniques.
ORCID: 0000-0003-2946-9411.

A.M. Gutiérrez-Malaxechebarria, received the BSc. in Civil Engineering in 2001 (Universidad Nacional, Colombia), the MSc. degree in Environmental Engineering in 2004 (Universidad de Los Andes, Colombia), and the PhD. degree in Environmental Studies in 2014 (Universidad Pontificia Javeriana, Colombia). Since 2012 he worked for the Universidad Distrital Francisco José de Caldas, Colombia. Currently, he is an associate professor in the Environment and Natural Resources Faculty. His research interests include: simulation, modeling, and forecasting in urban and rural drainage systems; and time-series analysis and forecasting using statistical and computational intelligence techniques.
ORCID: 0000-0002-2306-1610.



UNIVERSIDAD NACIONAL DE COLOMBIA
SEDE MEDELLÍN
FACULTAD DE MINAS

Área Curricular de Medio Ambiente

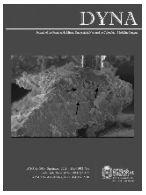
Oferta de Posgrados

Especialización en Aprovechamiento de Recursos Hidráulicos
Especialización en Gestión Ambiental
Maestría en Ingeniería Recursos Hidráulicos
Maestría en Medio Ambiente y Desarrollo
Doctorado en Ingeniería - Recursos Hidráulicos
Doctorado Interinstitucional en Ciencias del Mar

Mayor información:

E-mail: acma_med@unal.edu.co
Teléfono: (57-4) 425 5105

UNIVERSIDAD NACIONAL DE COLOMBIA
SEDE MEDELLÍN
FACULTAD DE MINAS



DYNA
http://dyna.medellin.unal.edu.co/

Design, development, and implementation of an assistive technology device for shoulder telerehabilitation via the Internet

Cristian D. Chamorro-R [a], Gladys Caicedo-D [b] & José I. García-M [b]

[a] *Faculty of Integrated Arts, Universidad del Valle, Cali, Colombia. cristian.chamorro@correounivalle.edu.co*
[b] *Faculty of Engineering, Universidad del Valle, Cali, Colombia. nayiver.gladys.caicedo@correounivalle.edu.co, jose.i.garcia@correounivalle.edu.co*

Received: May 15th, 2017. Received in revised form: March 2nd, 2018. Accepted: April 21th, 2018

Abstract
This study reports the design, development, and validation tests of an assistive technology device for active and passive shoulder telerehabilitation. This application considers range of movement, degrees of freedom, and standard rehabilitation protocols. In addition, it can be operated locally or remotely via the Internet and allows the monitoring of treatment implementation. Its concept was developed using service-oriented architecture, with implementation through web services. Architecture validation was performed with Petri nets to analyze the dynamic performance of the device. This assistive technology device consists of a power unit containing the electronic control, security, and communication cards. This study resulted in an integral rehabilitation system, safe under any eventuality, which can be presented and adapted to the Colombian hospital system. The novelty lies in its safe synchronous operation, allowing treatment traceability and active or passive rehabilitation.

Keywords: assistive technology; active and passive shoulder rehabilitation; telemedicine; service-oriented architecture; web services.

Diseño, desarrollo e implementación de una ayuda tecnológica para rehabilitación de hombro tele-operada vía Internet

Resumen
Este articulo presenta el diseño, desarrollo y pruebas de validación de una ayuda tecnológica tele-operadas para rehabilitación pasiva y activa de hombro, la cual está concebida bajo condiciones definidas por la arquitectura con orientación a servicios para rehabilitación tele-operada y fue modelado en redes de Petri coloreadas para analizar su comportamiento dinámico. Esta ayuda tecnológica está compuesta por una unidad de potencia que es la encargada de generar el movimiento y la resistencia, además contiene las tarjetas de control, seguridad y comunicaciones. La salida de la unidad de potencia se acopla al sistema mecánico que es el encargado de transformar el movimiento a movimientos anatómicos requeridos para lograr la rehabilitación del hombro, la cual puede ser operada en forma local o tele-operada vía internet. También, es posible realizar un monitoreo de las variables de rehabilitación más relevantes sobre la evolución del paciente. En el proceso de diseño se consideraron los protocolos clínicos de rehabilitación, los cuales fueron consultados con expertos en rehabilitación de la ESE de ladera, hospital cañaveralejo ubicado en Santiago de Cali, Colombia, estos protocolos consideraron los movimientos anatómicos del hombro, luego de manera estructurada empleando herramientas de modelado se definieron los requerimientos y determinantes de diseño. Las características de esta ayuda tecnológica benefician la atención en rehabilitación física a una población vulnerable debido a la localización geográfica y condición socioeconómica.

Palabras clave: ayuda tecnológica; rehabilitación de hombro activa y pasiva; tele-medicina; arquitectura con orientación a servicios; servicios web.

1. Introduction

In Colombia, the population with limited movement of the body, hands, arms, and legs is approximately 21% nationally, while it is 35% in Cauca Valley [1]. As a result of these disabilities, patients have limitations in activities of daily living (ADLs); 21% do not perform general tasks and 31% have mobility problems [1]. For this reason, the quality of life of people who suffer some type of injury is affected, as they are unable to perform certain tasks. The 2010 census,

How to cite: Chamorro-R., C., Caicedo-D., G. and Garcia-M., J.I., Design, development and implementation of an assistive technology device for shoulder telerehabilitation via the Internet. DYNA, 85(206), pp. 95-104, September, 2018.

© The author; licensee Universidad Nacional de Colombia.

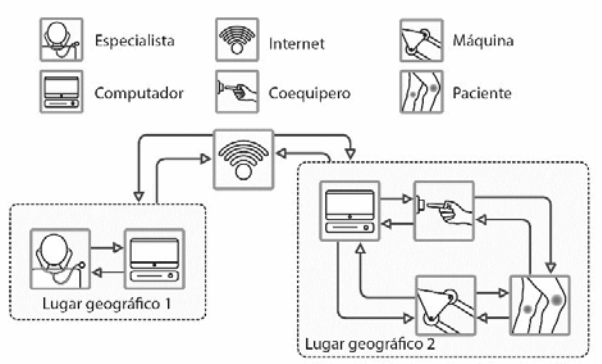


Figure 1. Telerehabilitation system
Source: authors

conducted by DANE, showed that the most accepted methods for rehabilitation treatments are medications with 58%, physical medicine with 16%, and physiotherapy with 22% [3]. Physical rehabilitation treatment includes three procedures: elimination of inflammation and reduction of joint pain, recovery of mobility, and muscle strengthening. According to DANE [3], the quality of the rehabilitation service is commonly negatively affected by the lack of money for travel (64%), lack of a companion (4%), and distance from the care center (6%). These factors are responsible for the increase in risk of geographic vulnerability of the population, so designing telerehabilitation equipment is clearly needed to reduce these effects.

This study focuses on the recovery of mobility and muscle strength by facilitating active and passive rehabilitation treatment protocols in patients with a transitory disability. By using telerehabilitation, the system seeks to minimize the barriers imposed by the centralized medical service in Colombia. This research problem poses major challenges, such as safe remote operation, treatment traceability, basic Internet connection, active and passive rehabilitation, and complying with medical protocols.

In the review of the state of the art equipment for shoulder rehabilitation, several systems or machines were found worldwide [5,6]. These machines run the gamut from conceptual proposals [15] to commercial products [5,8,9], and the following were described: a device with characteristics that provide safe conditions for the patient [5]; a shoulder rehabilitation system at the prototype level [10]; a system allowing several people to be attended to at the same time (although locally) [11]; and a virtual tool guiding the patient in treatment implementation [8]. Other studies had limitations: one prototype did not consider ergonomics or the anthropometrics of patients [9]; one study described a device allowing muscle strengthening, but not the traceability of rehabilitation [12]; and one study explained a conceptual design proposal without describing the machine construction [7]. Kiguchi [13] illustrated an exoskeleton that was developed to ensure treatment continuation and support body weight loading, because it was designed for people with motor skill problems. Finally, Ayala [6] proposed a machine with characteristics that allow treatments to be carried out in a bipedal position, which may be inconvenient for its application in other disabilities.

In the search for related studies, no references were found proposing an integral solution for the population with geographical vulnerability, which should consider aspects of synchronous remote operation, permanent monitoring of the patient by the specialist, implementation of active and passive treatments, patient comfort, anthropometry for the Colombian population, functionality, user safety, and traceability of the rehabilitation protocol, among others. In this context, the importance of this study lies in considering all these aspects, under the framework of one of the branches of telemedicine: remote operation. This would allow decentralizing the Colombian health system related to human rehabilitation, by extending coverage to the population with geographical vulnerability due to problems with access to specialized rehabilitation services [14].

The design of an assistive technology device for shoulder rehabilitation involves high biomechanical complexity because the shoulder joins the trunk with the upper limb, and in conjunction with the elbow and wrist allows positioning of the hand in space. The shoulder involves the gleno-humeral, acromio-clavicular, sterno-clavicular, and scapulo-thoracic joints, which are integrated with the muscles and ligaments, allowing joint mobility [4]. This implies considering three degrees of mechanical freedom in the design, whose movements are: flexion–extension (sagittal plane), abduction and adduction (frontal plane), and internal and external rotation (arm in adduction). In addition, the proposal must be coupled with service-oriented architecture to enable a remote system. Fig. 1 shows the proposed telerehabilitation system.

The modeling of the assistive technology device with colored Petri nets is also shown; this modeling is related to the anatomical movements, as well as the maximum and minimum angles that can be achieved by the assistive technology device according to the anatomical movements. Finally, the tests of a shoulder telerehabilitation service are shown, along with screen captures of the data insertions or modifications in the database verifying the implementation, validation, and integration of web services required for service-oriented architecture.

2. Methods and instruments

2.1. Power unit for the telerehabilitation assistive technology device

The power unit for the assistive technology device was designed with the aim of performing active and passive treatment with the same device because these two treatments are essential for full patient recovery. In passive treatment, the patient regains lost mobility, and in active treatment, the patient regains muscle strength. In addition, rehabilitation procedures will have a traceability that could be consulted by the specialist on duty, which will allow specialists to make decisions for the definition of new rehabilitation protocols.

The power system consists of the following components: a motor-reducer, a clutch, and a magnetic brake. The motor-

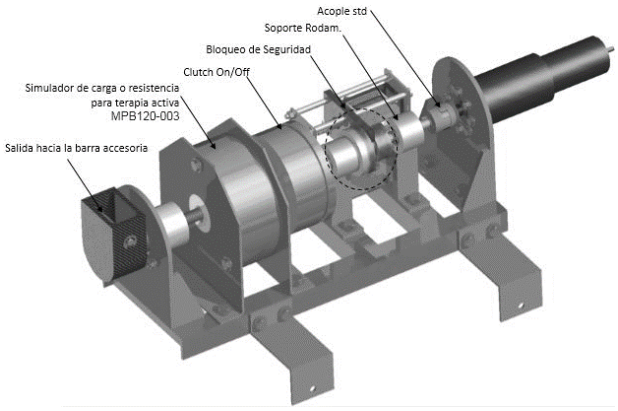


Figure 2. Power unit for rehabilitation assistive technology device
Source: authors

Table 1.
Weight of upper limb segments

Segment name	Segment weight percentage (%)	Segment mass (kg)	Segment weight (N)
Arm	2.7	3.510	34.419
Forearm	1.6	2.080	20.396
Hand	0.7	0.910	8.923
Total		6.500	63.739

Source: authors

reducer is responsible for performing the movement of the patient's limb when in passive treatment, the clutch is responsible for decoupling the motor when switching from passive to active treatment, and the magnetic brake is responsible for opposing resistance to the patient at the time of active treatment. The information from both active and passive treatments is obtained through the control and communication system and is updated in each patient medical record. Fig. 2 shows the power unit for the rehabilitation assistive technology device.

2.2. Biomechanics of the shoulder joint

In the cinematic and kinetic analysis, the maximum range of movement, center of gravity, and static loading conditions were defined, in order to determine the power needed to move the upper limb (arm). Fig. 3 shows the upper limb segments, the points of application of the weight of each limb, and their lengths with respect to the shoulder joint. Based on the free body diagram, the torque needed to move the upper limb were determined. This kinetic analysis was performed considering a person with a weight of 130 kg, which is well above the mean of the Colombian population. This consideration allows the design to be appropriate for the 95th percentile of the population [15].

Table 1 shows the weight of each upper limb segment. Segment 1 corresponds to the arm, Segment 2 to the forearm, and Segment 3 to the hand. The weight ratio of the segment is related to the total weight of the person; in this case, the reference is the above-mentioned 130 kg.

Fig. 3 shows the length of each arm segment. Table 2 shows the lengths of each upper limb segment, determining their centers of gravity.

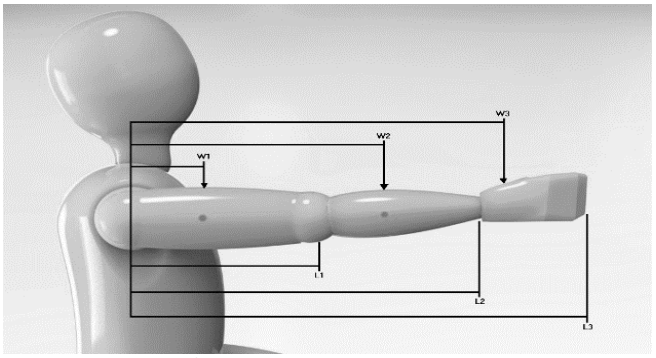


Figure 3. Upper limb free body diagram
Source: authors

Table 2.
Lengths and centers of mass of the arm segments

Upper limb segment	Length (m)	Accumulated length (m)	Location of the center of gravity (m)
Arm	0.36	0.36	0.18
Forearm	0.27	0.63	0.495
Hand	0.19	0.82	0.725

Source: authors

Table 3.
Total torque required to move the arm

Segment	Torque (Nm)
Arm	6.195
Forearm	10.096
Hand	6.470
Total static torque	22.761
Dynamic contribution = 1%	0.23
Safety factor	1.3
Required torque	**29.885**

Source: authors

To select the final control element that will generate arm movement, it is necessary to know the torque necessary to move each segment independently. Where the total torque consists of the static and dynamic torque, the torque calculated for each segment must be added to obtain the total torque needed to move the entire upper limb. Table 3 shows the results of the static torque for each segment. The effect of the dynamic torque is only 1%. In addition, in the total torque, a safety factor of 1.3 was considered to ensure anomalous system operating conditions (undue manipulation of the assistive technology device) and any possible damage.

According to the results shown in Table 3, it was concluded that the actuation system should use a motor-reducer assembly with a minimum torque output of 30 Nm.

3. Results

In the results, the characterization of the variables used by the power unit is initially shown, and then the design of the assistive technology device coupled with the power unit is explained. Subsequently, the modeling with colored Petri nets of the operation of the assistive technology device in terms of anatomical movements and their maximum and minimum ranges

Table 4.
Comparison of theoretical and practical angular velocity data from the power unit

Frequency rate (%)	Experimental data of angular velocity (rad/s)	Theoretical data of angular velocity (rad/s)	Error rate (%)
10	11.53	11.76	1.96
20	22.3	23.52	5.19
30	34.73	35.28	1.56
40	43.9	47.04	6.68
50	56.94	58.8	3.16
60	67.92	70.56	3.74
70	77.92	82.32	5.34
80	87.8	94.08	6.68
90	102.86	105.84	2.82
100	112.5	117.6	4.34

Source: authors

is shown. Finally, the result of a remote treatment system via the Internet is shown with the help of technology integrated into the architecture.

3.1. Characterization of the power unit variables

3.1.1. Speed reference of the power unit

The speed reference will be given in degrees per second; however, motor speed control requires a reference in frequency rates. Next, the data and the graph obtained from the power unit are shown.

The real data obtained from the power unit are compared with the expected data with which the design was made; Table 4 shows these data with their respective error rates.

Fig. 4 shows the two curves, both theoretical and experimental, in order to measure the motion error and take into account the efficiency of the motor reducer. The data of Series 1, represented by triangles, are the experimental data and the data of Series 2, represented by squares, are the theoretical data. From the error calculated in Table 4, it can be determined that the highest error value could be approximately 6.68%, which causes an offset of the angular speed of approximately 1.5 or 2 rad/s, a value that does not affect the provision of the rehabilitation service and does not affect the physical integrity of the patient.

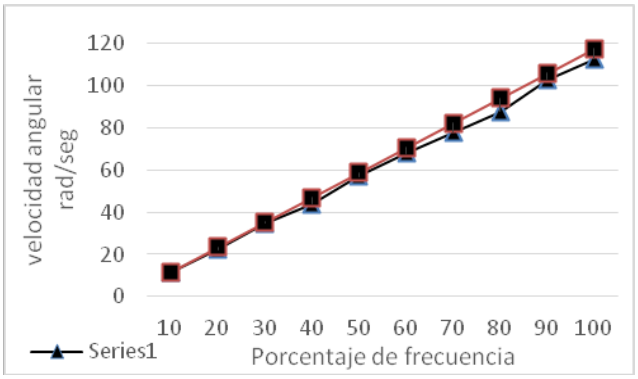


Figure 4. Theoretical and actual angular velocity of the power unit
Source: authors

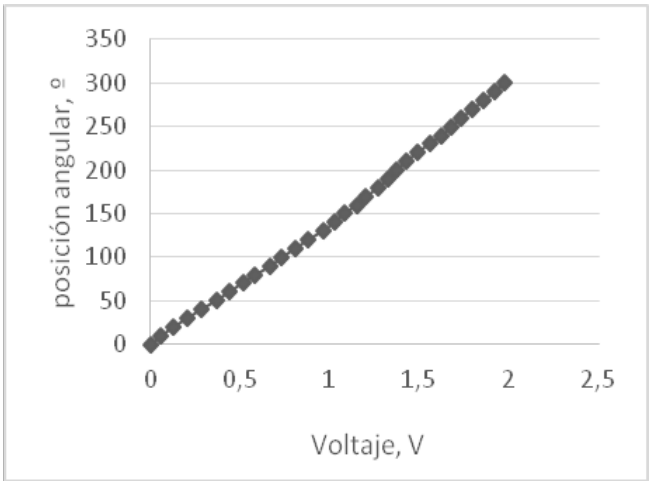


Figure 5. Angular position vs. voltage (V)
Source: authors

3.1.2. Characterization of the angular position of the power unit

It was necessary to test the power system regarding its instrumentation for measuring the angular position at the output of the power unit because these data are essential for recording and updating the rehabilitation treatments in the patient medical records. Calibration of the linear potentiometer was performed by measuring potentiometer voltage versus its angular position; the results were plotted and are shown in Fig. 5. The function obtained in Equation 1 was used in programming the microcontroller, to obtain the desired angular position in degrees (º).

With the obtained data, it was possible to obtain the linear function shown in Eq. (1).

$$\emptyset = 112{,}64V - 0{,}39 \quad (1)$$

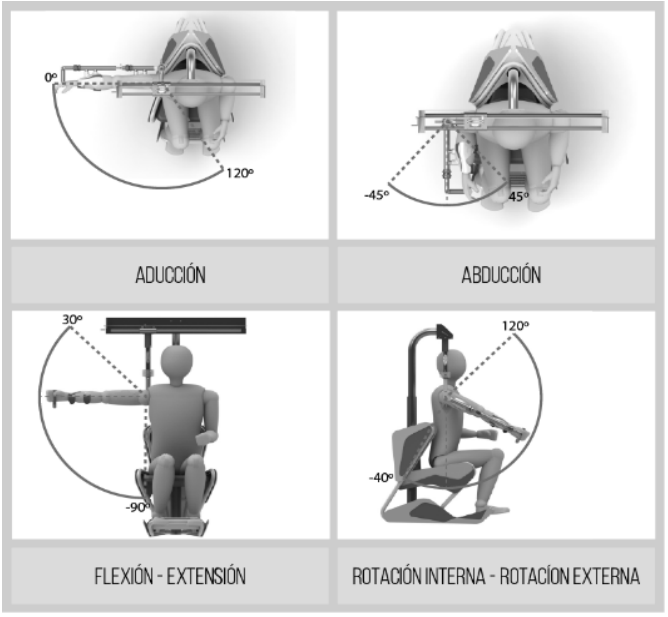


Figure 6. Anatomical movements for rehabilitation
Source: authors

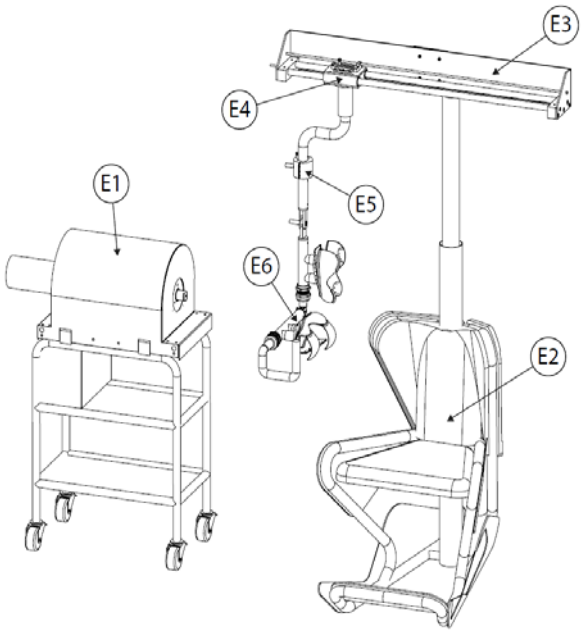


Figure 7. Final design proposal
Source: authors

3.2. Assistive technology device for shoulder rehabilitation

The assistive technology device for shoulder rehabilitation allows the patient to perform active and passive rehabilitation movements in three degrees of freedom, which are shown in Fig. 6; this means that patients recover mobility and muscle strength in six joint movements. These three degrees of freedom are achieved using the power unit coupled to the mechanical system.

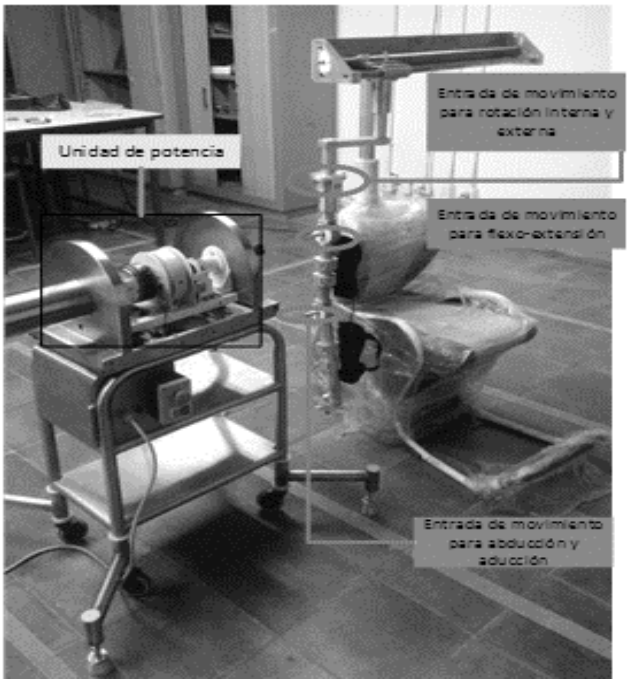


Figure 8. Assistive technology device indicating motion inputs
Source: authors

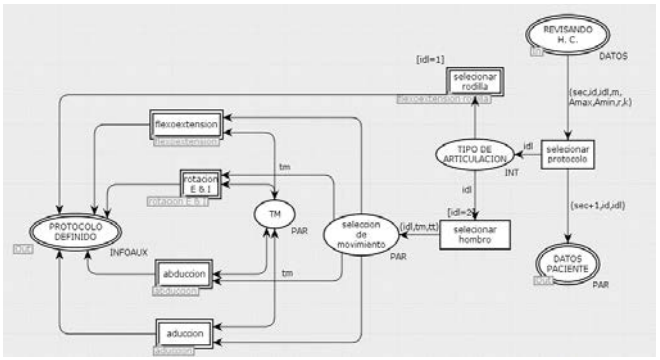


Figure 9. Anatomical shoulder movements modeled with Petri nets
Source: authors

Once all the requirements of the elements were integrated and the conceptual design was established, the design proposal was elaborated, where the building blueprint of the parts and components to be used was developed in detail.

Fig. 7 shows the final design proposal, with all its components and sub-assemblies: power unit (E1), chair (E2), upper frame (E3), carriage (E4), motor unit (E5), and arm (E6).

Next, the prototype of the shoulder assistive technology device was designed, built, and implemented with the service-oriented architecture for telerehabilitation systems. Fig. 8 shows the prototype, indicating motion inputs according to the rehabilitation protocol to be implemented.

3.3 Modeling with colored Petri nets of an assistive technology device for shoulder telerehabilitation

Validation of the assistive technology device design for shoulder rehabilitation was tested by means of simulation with colored Petri nets; these simulations were used to validate the degrees of freedom and maximum and minimum movement ranges of the assistive technology device when carrying out telerehabilitation. Fig. 9 shows the system model detailing all the anatomical movements that can be rehabilitated by the assistive technology device.

In Fig. 9, each movement shown is a substitution transition, which means that it is a new net characterizing each movement independently. Figs. 10-13 show each movement for rehabilitation; this modeling is necessary for characterizing each movement in terms of its maximum and minimum ranges and for decision-making when a protocol is poorly defined by the specialist.

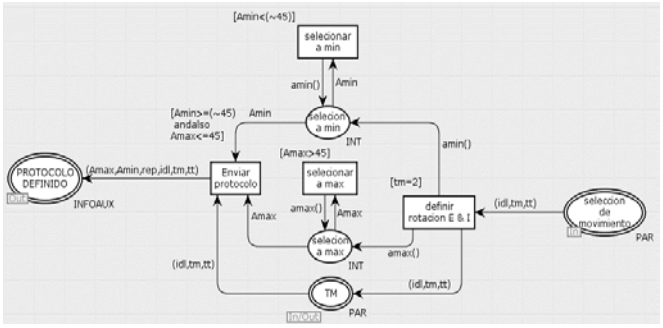


Figure 10. Shoulder internal and external rotation model
Source: authors

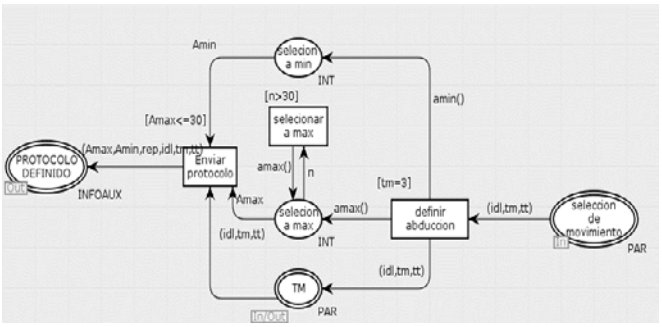


Figure 11. Shoulder abduction model
Source: authors

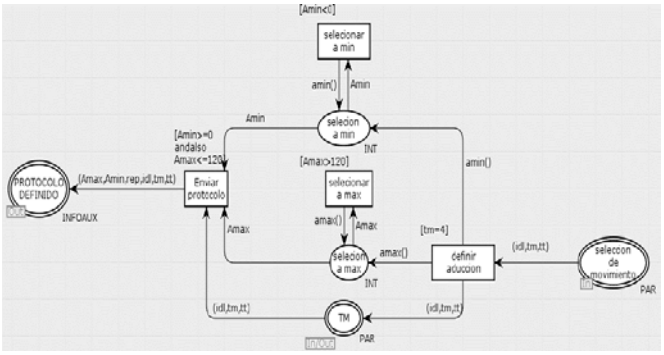


Figure 12. Shoulder adduction model
Source: authors

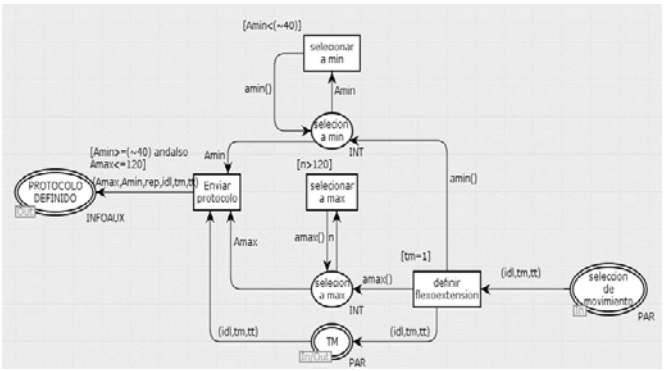


Fig. 13. Shoulder flexion/extension model
Source: authors

The possibility of selecting active or passive treatments was also included in the model, so that validation with colored Petri nets was as close as possible to the proposed system.

3.4. Comparison tests of the angular position of the power unit

To validate the design of the anatomical movements of the shoulder assistive technology device, tests were performed, which consisted of comparing angular values entered by the specialist with measuring the angular output of the power unit. Table 5 presents these values, and Fig. 14 shows comparative graphs between theoretical and experimental values.

Table 5.
Values of angular position tests

Data	Defined angle	Angle of departure	Error rate
1	20	21	5.0
2	40	39	2.5
3	60	60	0.0
4	80	78	2.5
5	100	103	3.0
6	120	117	2.5
7	140	141	0.7
8	160	166	3.8
9	180	179	0.6
10	200	200	0.0
11	220	224	1.8
12	240	242	0.8
13	260	263	1.2
14	280	277	1.1
15	300	298	0.7

Source: authors

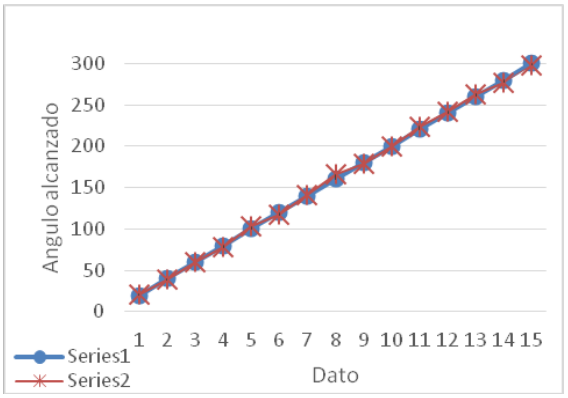


Figure 14. Comparative curves between theoretical and experimental angular positions
Source: authors

Fig. 14 shows the theoretical angular position values of Series 1, represented by circles, and the experimental angular position values of Series 2, represented by asterisks. For these data, error rates are low because the maximum value is approximately 5%, which would indicate that in rehabilitation, an error between 3 and 4 degrees could occur according to what is defined by the specialist in the protocol.

3.5. Design and development of web services for the implementation of service-oriented architecture for telerehabilitation via the Internet

To implement service-oriented architecture, it was necessary to design, develop, and coordinate the web services proposed in the architecture. Next, in Figs. 15-18, the process diagrams of the four services and their interaction with the actors of the telerehabilitation system are shown.

3.5.1. Authentication service

Fig. 15 shows the authentication service model, representing its inputs and outputs. This service is responsible for authenticating users and providing them with an interface, according to their role as a specialist or assistant.

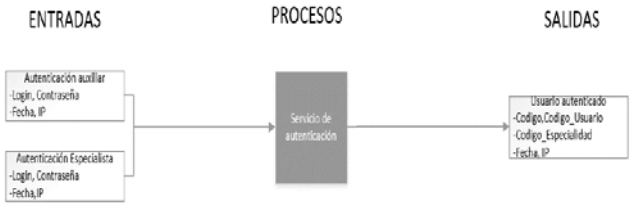


Figure 15. Authentication service
Source: authors



Figure 16. Patient search service
Source: authors

3.5.2. Patient search tool

This tool is responsible for searching in the patient database and classifying patient data in different categories to facilitate access to the appropriate information for each agent in the system. The classified information is related to general patient information and treatment information. Fig. 16 shows the service as a process, indicating its inputs and outputs.

3.5.3. Communication service

This service was present throughout treatment implementation, to maintain a permanent communication between the assistive technology device and system agents. Fig. 17 shows the process diagram of this service.

3.5.4. Medical record update service

Fig. 18 shows the process diagram of the medical record update service, which is responsible for recording in the patient database the information related to the treatment performed or any possible eventuality that may arise and need to be recorded in the medical record.

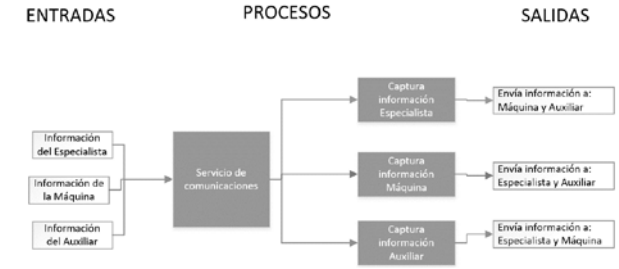


Figure 17. Communication web service
Source: authors



Figure 18. Medical record update service
Source: authors

These four services were designed, developed, and implemented to employ service-oriented architecture for telerehabilitation via the Internet. These services were integrated and coordinated so that the events corresponded to what was defined in the design. The characteristics of the services are that they do not keep the event state—which allows them to return to their initial state—they fulfill specific functions, and they have low coupling—allowing them to be independent—therefore making the system resilient to failures, so that a possible failure in a service does not affect the entire system and is easy to identify. These services are present once they are available, and their access protocol is universal. Finally, the system is scalable, as it can be scaled to one of greater or lesser complexity by coupling or decoupling the required services.

3.6. Implementation tests of service-oriented architecture for the shoulder telerehabilitation system via the Internet

Once the services have been presented, functional tests for shoulder rehabilitation are performed. In this case, the system behaves optimally without any type of eventuality while providing the rehabilitation service; this is done in order to evaluate and validate the architecture and the services developed for its implementation.

The process begins with user authentication, followed by specialist registration, in the application interface, which gives the option of entering a login and password as shown in Fig. 19—according to the data provided by the person to the web service (called "user authentication")—and searches the hospital database to confirm if the authenticated person is a specialist or assistant.

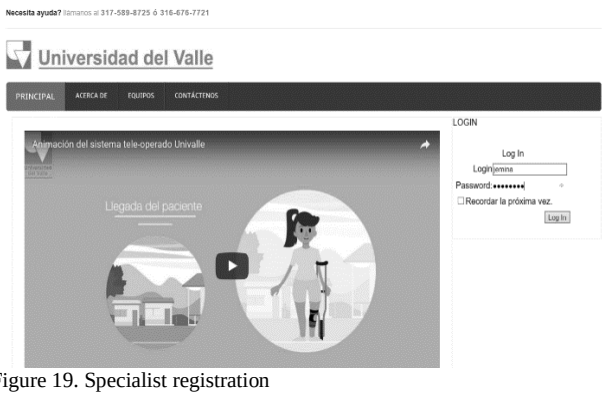
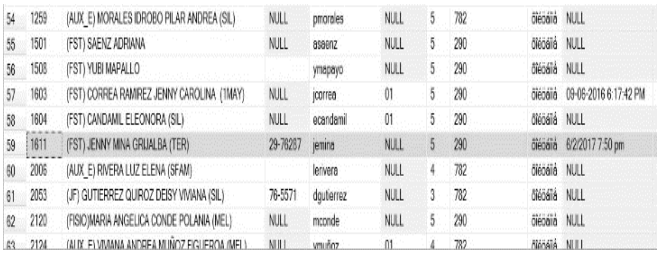


Figure 19. Specialist registration
Source: authors



54	1259	(AUX_E) MORALES IDROBO PILAR ANDREA (SIL)	NULL	pmorales	NULL	5	782	[illegible]	NULL
55	1501	(FST) SAENZ ADRIANA	NULL	asaenz	NULL	5	290	[illegible]	NULL
56	1508	(FST) YUBI MAPALLO		ymapayo	NULL	5	290	[illegible]	NULL
57	1603	(FST) CORREA RAMIREZ JENNY CAROLINA (1MAY)	NULL	jcorrea	01	5	290	[illegible]	09-06-2016 6:17:42 PM
58	1604	(FST) CANDAMIL ELEONORA (SIL)	NULL	ecandamil	01	5	290	[illegible]	NULL
59	1611	(FST) JENNY MINA GRIJALBA (TER)	29-76287	jemina	NULL	5	290	[illegible]	6/2/2017 7:50 pm
60	2006	(AUX_E) RIVERA LUZ ELENA (SFAM)		lenvera	NULL	4	782	[illegible]	NULL
61	2053	(JF) GUTIERREZ QUIROZ DEISY VIVIANA (SIL)	76-5571	dgutierrez	NULL	3	782	[illegible]	NULL
62	2120	(FISIO)MARIA ANGELICA CONDE POLANIA (MEL)	NULL	mconde	NULL	5	290	[illegible]	NULL
63	2124	(AUX_E) VIVIANA ANDREA MUÑOZ FIGUEROA (MEL)	NULL	vmuñoz	01	4	782	[illegible]	NULL

Figure 20. Authenticated specialist database registration
Source: authors

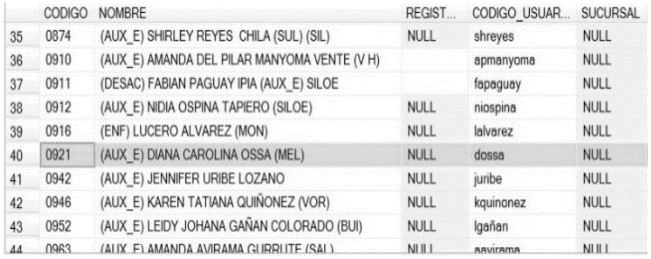


Figure 21. Specialist's interface waiting for patient
Source: authors

When the specialist is authenticated, this event is recorded in the database, as shown in Fig. 20. The database provides information of the authenticated person: their specialty, their last access, and the IP address of the access point; this allows monitoring of the specialists and assistants who perform telemedicine tasks in the respective hospitals.

Once the specialist is authenticated, the application opens a new screen showing the user, connection IP, and date and time of the start of the last session as a specialist, as shown in Fig. 21. In addition, the system is on standby to receive information about the patient waiting for treatment.

Once the assistant is authenticated, the same thing happens as with the specialist; there is an entry in the database with the authenticated assistant information, as shown in Fig. 22.



	CODIGO	NOMBRE	REGIST...	CODIGO_USUAR...	SUCURSAL
35	0874	(AUX_E) SHIRLEY REYES CHILA (SUL) (SIL)	NULL	shreyes	NULL
36	0910	(AUX_E) AMANDA DEL PILAR MANYOMA VENTE (V H)		apmanyoma	NULL
37	0911	(DESAC) FABIAN PAGUAY IPIA (AUX_E) SILOE		fapaguay	NULL
38	0912	(AUX_E) NIDIA OSPINA TAPIERO (SILOE)	NULL	niospina	NULL
39	0916	(ENF) LUCERO ALVAREZ (MON)	NULL	lalvarez	NULL
40	0921	(AUX_E) DIANA CAROLINA OSSA (MEL)	NULL	dossa	NULL
41	0942	(AUX_E) JENNIFER URIBE LOZANO	NULL	juribe	NULL
42	0946	(AUX_E) KAREN TATIANA QUIÑONEZ (VOR)	NULL	kquinonez	NULL
43	0952	(AUX_E) LEIDY JOHANA GAÑAN COLORADO (BUI)	NULL	lgañan	NULL
44	0963	(AUX_E) AMANDA AVIRAMA GURRUTE (SAL)	NULL	aaviirama	NULL

Figure 22. Authenticated assistant database registration
Source: authors



Figure 23. Assistant's interface once authenticated
Source: authors

The assistant performs the same procedure as the specialist in terms of registration. Once registered in the assistant's interface, the following data appear: user, IP, date, last access, and a prompt to enter the identity document of the incoming patient. The requested information is shown in Fig. 23.

Once the assistant enters the patient identity data, a search of the patient database is performed. The web service called "patient search" performs this procedure, and the assistant's interface is updated with patient data. The updated data corresponds to general patient information, as shown in Fig. 24.

Fig. 25 shows medical record data related to rehabilitation treatments. It is observed that the left shoulder is injured; this information is obtained from the treatment order found in the patient medical record.

The patient search is recorded in the database; its record is shown in Fig. 26. This database contains general information and that related to rehabilitation, as well as administrative information such as the medical order, which defines the type of injury and injured side.



Figure 24. General information of the patient waiting for treatment
Source: authors

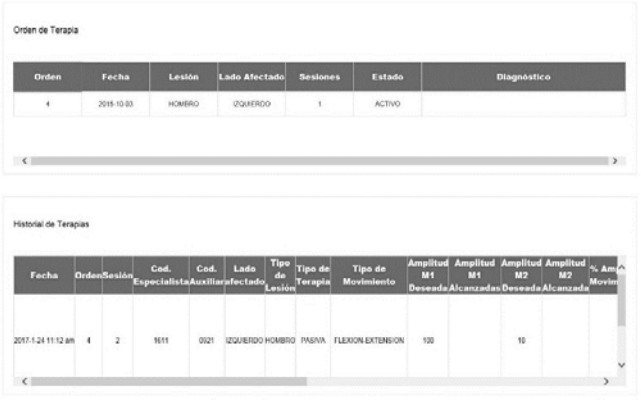
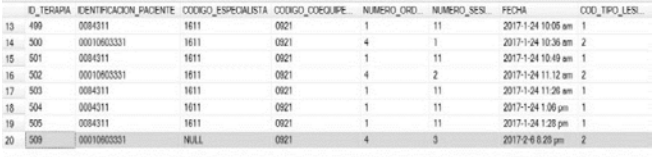


Figure 25. Medical record data and treatment order
Source: authors



	ID_TERAPIA	IDENTIFICACION_PACIENTE	CODIGO_ESPECIALISTA	CODIGO_CODEQUIPE...	NUMERO_ORD...	NUMERO_SESI...	FECHA	COD_TIPO_LESI...
13	499	0084311	1611	0921	1	11	2017-1-24 10:05 am	1
14	500	0001060331	1611	0921	4	1	2017-1-24 10:36 am	2
15	501	0084311	1611	0921	1	11	2017-1-24 10:49 am	1
16	502	0001060331	1611	0921	4	2	2017-1-24 11:12 am	2
17	503	0084311	1611	0921	1	11	2017-1-24 11:26 am	1
18	504	0084311	1611	0921	1	11	2017-1-24 1:06 pm	1
19	505	0084311	1611	0921	1	11	2017-1-24 1:28 pm	1
20	509	0001060331	NULL	0921	4	3	2017-2-6 8:28 pm	2

Figure 26. Patient database search
Source: authors

Because the assistant already registered the patient when entering their identity document number, the information obtained by the patient search service is sent to the specialist's interface, which displays general patient information such as treatment order and treatment history, so that the specialist may have information about the patient to be attended.

Next, the events related to the communication web service are shown. This service is mainly linked to the input and output information of the assistive technology device. As shown in Fig. 27, in the specialist's interface, specialists have the possibility of filling the fields related to the rehabilitation protocol. Unlike knee rehabilitation, the specialist can choose between six anatomical movements to be performed by the shoulder. It should be noted that some fields cannot be modified because they are defined by the treatment order entered in advance into the database. The reason for this is to reduce the possibility of errors by the specialist because of not having direct patient contact.

Fig. 28 shows the protocol sent by the specialist as received by the assistant. This protocol can only be read and cannot be modified by the assistant; also, in this event, patient choice to accept the protocol is shown.



Figure 27. Protocol to be defined by the specialist
Source: authors

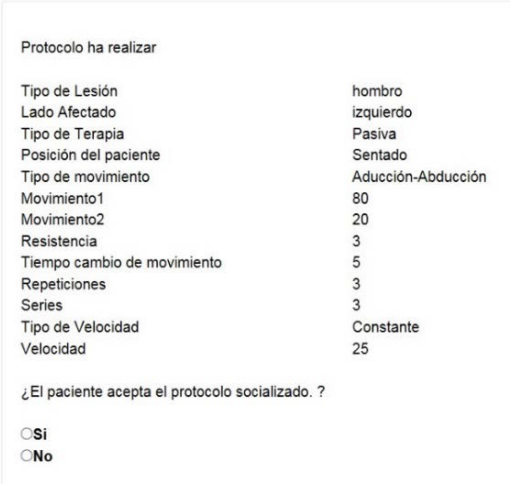


Figure 28. Assistant's interface with the protocol defined by the specialist
Source: authors

	ISI...	ADUCCION_DESEADA	ADUCCION_ALCANZA...	ABDUCCION_DESEADA	ABDUCCION_ALCANZA...	PORCENTAJE_ADU_
13		NULL		NULL		0
14		NULL	NULL	NULL	NULL	NULL
15		NULL		NULL		0
16		NULL	NULL	NULL	NULL	NULL
17		NULL	NULL	NULL	NULL	NULL
18		NULL		NULL		0
19		NULL	NULL	NULL	NULL	NULL
20		80	80	20	20	100

Figure 29. Updated data in the database regarding the treatment performed
Source: authors

Once the protocol is received and accepted by the patient, this information is managed by the assistant and entered through the interface designated for this function.

The confirmation of acceptance of the protocol by the patient and the optional observation entered by the assistant then arrives at the specialist's interface.

Once the specialist receives the confirmation from the patient sent by the assistant, the specialist has the option to start treatment or not; this function is used to ensure patient treatment safety.

The data obtained by the assistive technology device during the course of treatment are recorded both in the specialist's interface and in that of the assistant, in order to monitor treatment implementation and check if the protocol data are correct in comparison with the data available to the assistive technology device for execution.

Once the treatment is finished, the database is updated, and the desired data are compared with the range of motion achieved by the patient during treatment. Fig. 29 shows the entry of this information in the database with the success rate of treatment implementation.

Finally, the system generates a last update of the patient medical record with the data of the treatment performed. In this way, service-oriented architecture was implemented for a telerehabilitation system via the Internet.

4. Discussion

The assistive technology device prototype was verified to comply with the maximum angles defined by the biomechanics of the shoulder, rejecting the rehabilitation protocol when the data exceeded the established values, which proves that the procedure is safe for the patient. In addition, according to the literature found, this is the only prototype incorporating both active and passive rehabilitation.

Web services allow a more efficient remote operation in terms of resource use and connection to the Internet because only plain text is transmitted and the system is resilient to failures.

The system was designed to be synchronous and implemented as such to ensure patient safety, guaranteed by the permanent presence of the specialist during the course of rehabilitation.

The system allows continuous recording in the database of the treatment performed; this information is stored in the patient medical record, allowing traceability of the progress of treatment sessions.

The integration of web services was done in an adequate manner, evidenced by the organized flow of information, and all records were entered into the database.

5. Conclusions

- This assistive technology device for active and passive shoulder rehabilitation was incorporated into a service-oriented architecture, first designed and later implemented, thus allowing patients who are temporarily disabled to achieve rehabilitation. Rehabilitation is ensured because the protocols for active and passive shoulder movements are being followed.
- The information entered into the database allows the specialist to have traceability of the rehabilitation processes of their patients; in addition, remote access to the information recorded in the database is possible.
- Implementing service-oriented architecture with the assistive technology device was successful because it was possible to verify the flow of information between Geographic Location 1, Geographic Location 2, and the server in addition to the correct functioning of the mechatronics of the assistive technology device.
- The results and tests performed in this project are related to prototype construction; in future projects, it is proposed to move from the prototype to product development.

References

[1] DANE. "Censo General" Dirección de censos y demografía. Valle del Cauca; 2005.

[2] Romero, D., Las actividades de la vida diaria. Anales de Psicología; 23(2), pp- 8-9, December, 2007.

[3] DANE, "Censo General" Dirección de censos y demografía. Valle del Cauca; 2010.

[4] Nordin, M. y Frankel, V., Biomecánica básica del sistema musculo-esquelético. McGraw Hill, Madrid, Spain, 2004.

[5] Nef, T., Mihelj, M., Kiefe, G., Pemdl, C., Muller, R. and Riener, R., ARMin exoskeleton for arm treatment in stroke patients. IEEE 10th International Conference on Rehabilitation Robotics, 2007.

[6] Ayala, J., Exoesqueleto para rehabilitación de miembro superior, Tesis de maestría, 2012.

[7] Han, J., Han, C., Jang, H., Jang, J., Lee, Y. and Hong, S., WIPO patent No. 2010071252. Geneva, Switzerland: World Intellectual Property Organization, 2010.

[8] Brokaw, E., Nichols, D., Holley, R., Murray, T., Nef, T. and Lum, P., Time independent functional task training: a case study on the effect of inter-joint coordination driven haptic guidance in stroke treatment. 2011 IEEE International Conference on Rehabilitation Robotics, 2011, pp. 1-6.

[9] Dasheek, N., Riaan, S., Glen, B. and Shaniel, D., A7DOF Exoskeleton arm: shoulder, elbow, wrist and hand mechanism for assistance to upper limb disabled individuals. IEEE Africon, 2011.

[10] Gutierrez, R., Niño-Suarez, P., Avilés-Sanchez, O., Vanegas, F.Y. y Duque, J., Exoesqueleto mecatronico para rehabilitación motora, 8vo Congreso iberoamericano de ingenieria mecánica, 2007, pp. 1-9.

[11] Perry, J.C., Rosen, J.Y. and Burns, S., Upper limb powered exoskeleton design. IEEE/ASME Transactions on Mechatronics; 12(4), 2007, pp 408-417.

[12] Wu, T.M., Wang, S.Y. and Chen, D.Z., Design of an exoskeleton for strengthening the upper limb muscle for overextension injury prevention. Mechanism and Machine Theory, 46(12), pp. 1825-1839, 2011.

[13] Kiguchi, K., Active exoskeletons for upper-limb motion assist. International Journal Humanoid Robotics, 4(3), pp 607-624, 2012.

[14] Busso, G., Vulnerabilidad social: nociones e implicancias de políticas para Latino America a inicios del siglo XXI.

[15] Estrada, J.M., Camacho, J.A., Restrepo, T. y Parra M., Parámetros antropométricos de la población laboral colombiana, acopla95, 1995. Publ. en la Rev. Fac. Nac. Salud Pública, 15(2), pp. 112-139, 1998.

C.D. Chamorro-R. is BSc. In Mechanical Engineer, fron the Universidad Autónoma de Occidente, M.A., Philosophy, form the Universidad del Valle, Cali, Colombia. Engineering, PhD, Universidad del Valle, Cali, Colombia. Is professor of the Department of Design, Universidad del Valle, Cali, Colombia. Member of the DI&ID Research Group, recognized by Colciencias and part of Universidad del Valle, Cali, Colombia.
ORCID: 0000-0002-1792-4555

N.G. Caicedo-D. is BSc. In Electrical Engineer, from the Universidad del Valle, Cali, Colombia. MSc. in Electrical Energy Generation Systems, Universidad del Valle, Cali, Colombia. PhD in Engineering, Universidad del Valle, Cali, Colombia. Is professor, in electrical engineering and electronics, Universidad del Valle. Member of the GRALTA Research Group, recognized by Colciencias and part of Universidad del Valle.
ORCID: 0000-0002-8679-7465

J.I. García-M. IS bsC. IN Mechanical Engineer, from the Universidad Autónoma de Occidente, Colombia. MSc. in Automatics, from the Universidad del Valle, Cali, Colombia. PhD, Engineering, from the Universidad de Sao Paulo, Brazil. Is professor, School of Engineering, Universidad del Valle.
ORCID: 0000-0003-1672-7768



UNIVERSIDAD NACIONAL DE COLOMBIA

SEDE MEDELLÍN

FACULTAD DE MINAS

Área Curricular de Ingeniería Mecánica

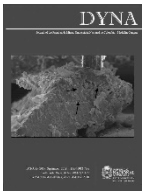
Oferta de Posgrados

Maestría en Ingeniería - Ingeniería Mecánica

Mayor información:

E-mail: acmecanica_med@unal.edu.co
Teléfono: (57-4) 4259262

UNIVERSIDAD NACIONAL DE COLOMBIA
SEDE MEDELLÍN
FACULTAD DE MINAS



DYNA
http://dyna.medellin.unal.edu.co/

Productive process improvement to elaborate cane train baskets, using Coloured Petri nets

Jesus Filander Caratar-Chaux [a], Ruth Edmy Cano-Buitrón [b] & José Isidro Garcia-Melo [b]

[a] *Escuela de Ingeniería Eléctrica y Electrónica, Universidad del Valle, Cali, Colombia. jesus.caratar@correounivalle.edu.co*
[b] *Escuela de Ingeniería Mecánica, Universidad del Valle, Cali, Colombia, Colombia. ruth.cano@correounivalle.edu.co, jose.i.garcia@correounivalle.edu.co*

Received: June 27th, 2017. Received in revised form: May 2nd, 2018. Accepted: May 21th, 2018

Abstract
The search for improvements in production processes that serve a variant market with flexibility and profitability is a subject widely discussed in diverse sectors of the industry. The approach to this type of problem frequently requires a structured and detailed formal study of production systems using tools such as Coloured Petri Nets (CPN). This tool provides a method to propose and evaluate improvements in the system. Considering the production system as a system that evolves through discrete events, this article presents a procedure with a Top-Down approach to identify, simulate and evaluate the current state of a production system using CPN, this model is used to study improvements in order to analyze the impact on the performance of the production system.

Keywords: cane train basket; coloured Petri Net; improvement; productive process.

Mejora del proceso productivo para elaborar canastas para trenes cañeros, utilizando redes de Petri coloreadas

Resumen
La búsqueda de mejoras en los procesos de producción asociadas a variaciones en la flexibilidad y rentabilidad es un tema ampliamente discutido en diversos sectores de la industria. El enfoque de este tipo de problemas requiere con frecuencia un estudio formal estructurado y detallado utilizando herramientas tales como Redes de Petri Coloridas (RPC). Esta herramienta proporciona un método para proponer y evaluar mejoras en el sistema. Considerando el sistema de producción como un sistema que evoluciona a través de eventos discretos, este artículo presenta un procedimiento con un enfoque Top-Down para identificar, simular y evaluar el estado actual de un sistema de producción utilizando RPC, este modelo se utiliza para estudiar mejoras con el fin de analizar el Impacto en el rendimiento del sistema de producción.

Palabras clave: canasta; mejoras; proceso productivo; redes de Petri coloreadas.

1. Introduction

Productive Systems (PS) are defined as those systems that integrate or combine resources (energy, people, raw materials, machines, etc.) to carry out a process for generating goods or services [1,2]. Production systems must address market variations, such as product variety, shortened life cycles, flexibility in production, rapid response to product demand, market expansion, etc.; thus demanding successful system design [3].

Considering the complexities in PS structuring, a design approach using models is recommended to analyze improvements and evaluate behavior before implementation because inadequate specifications for this kind of system can lead to economic or security consequences [4]. Several authors recommend the use of formal models to analyze PS because of processes formality, verification and validation of both structure and dynamics of the system. In this way, the system can be considered a system of discrete events [5-7] where the dynamics are oriented by the occurrence of instantaneous events [7,8].

Coloured Petri Nets (CPN) is a formal tool that uses a high-level programming language to model discrete, concurrent,

How to cite: Caratar-Chaux, J.F., Cano-Buitrón, R.E. and Garcia-Melo, J.I., Productive process improvement to elaborate cane train baskets, using coloured Petri nets. DYNA, 85(206), pp. 105-113, September, 2018.

© The author; licensee Universidad Nacional de Colombia.

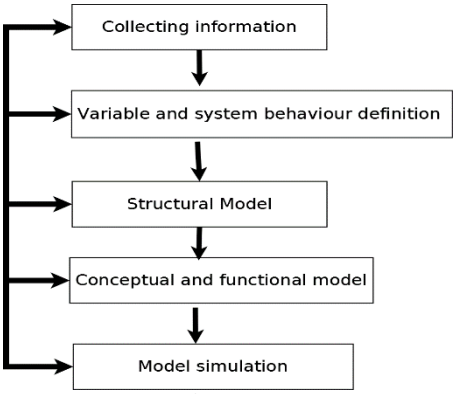


Figure 1. Proposed methodology for modelling.
Source: Modified from [13].

distributed, stochastic and non-deterministic systems [9-13]. A detailed description of the tool can be found in [14] and [15].

Several references can be found that relate to PS model construction with Petri Nets (PN), for example [16-20]. All of these references show the results obtained with the models, but present limited information regarding the methodology used in the modelling; there is little clarity in the procedure followed to enable replication of the process to develop the models. This article presents a procedure for identifying, simulating and evaluating PS using CPN.

The need to evaluate the proposed procedure was considered in this paper. A sugarcane manufacturing train PS was modelled and validated by simulation in order to analyze its current state and evaluate improvements to increase productivity. This work is divided into two sections, the first presents the procedure used to build the model, and the second describes an application where the model was implemented. Finally, conclusions are presented.

2. Modelling procedure

A proposed procedure for modelling a PS is detailed in [21]. A Top-Down approach is defined with five stages that systematically and rationally focus on the characteristics of the analyzed system to establish a representative model. This approach enables progressive construction of a model integrating variables of interest until the desired level of detail of the system is obtained, see Fig. 1.

To study improvements in the PS, the procedure in Fig. 2 was performed once the procedure of Fig. 1 was completed.

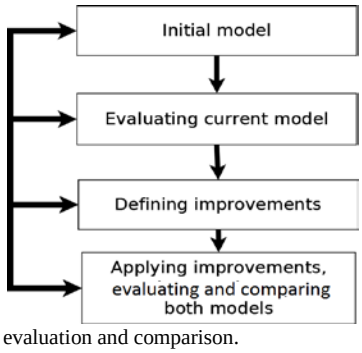


Figure 2. Model evaluation and comparison.
Source: Own elaboration.

2.1. Collecting information

In this stage, it is necessary to collect information related to the current PS in order to identify its behavior, mode of operation, resources and interactions between them, parameters, variables, etc. Plant visits are required to identify and select the processes to model and to consult with the technical and professional staff involved in the PS. In addition, relevant documentation available in manuals, catalogues, books and internet references should be analyzed.

2.2. Variable and system behavior definition

After the information is collected the approach to the model must be defined, i.e., what should be represented in the model, for example production times, material consumption, machinery distribution, etc. To determine the variables that are required to develop the model the following should be considered:

What resources are used in the execution of each process?

What information, signals and data are used in each stage and r related activities?

How do resources interact in each PS stage?

2.3. Structural model

Once the model approach has been defined, a structural survey of the production system is conducted, for example work areas, human and technological resources, etc.

2.4. Conceptual and functional model

The conceptual model represents the process stages and activities involved in the PS. This model considers the approach that has been defined and the relationships between variables and available resources in the real system. The conceptual model is used to define the functional model, which defines the dynamics of each process, activity and operating mode. In this stage, it is necessary to analyze the information acquired in sections 2.2 and 2.3. CPN were used to represent this model; due to the complexity that can be present in a production system, it may be necessary to use hierarchies to represent each system stage in order to avoid an explosion of states. Once the hierarchy is established, refinements can be made.

2.5. Model simulation

The obtained model is analyzed to verify that it is a valid representation of the real PS and satisfies the given approach (validation). Corrections and adjustments must be made until the desired model is obtained. Analysis of the model should consider different operating modes in order to identify bottlenecks, critical activities, and areas for improvements.

2.6. Evaluating the current model

Once the current model has been simulated and validated, the variables of interest must be studied (for example production times, bottlenecks, sequential and concurrent

activities) and intrinsic constraints documented in order to identify activities, resources or processes that can be improved (for example priority activities, environmental and/or legal issues).

2.7. Defining improvements

After identifying the activities, resources or processes that can be improved, the possible solutions that can be applied are defined.

2.8. Applying improvements, evaluating and comparing models

Defined solutions are included in the initial model. The model must be simulated to analyses its new behavior with the same scenarios defined for the initial model.

When the new model has been simulated and validated, the variables of interest are studied once again to identify if the proposed solutions had a positive impact on the selected activities, resources or processes. The impacts of the proposed solutions should be evaluated both independently and collectively to identify the combinations that best suit the process.

When the new model has been simulated and validated, the variables of interest are studied once again to identify if the proposed solutions had a positive impact on the selected activities, resources or processes. The impacts of the proposed solutions should be evaluated both independently and collectively to identify the combinations that best suit the process.

3. Application example

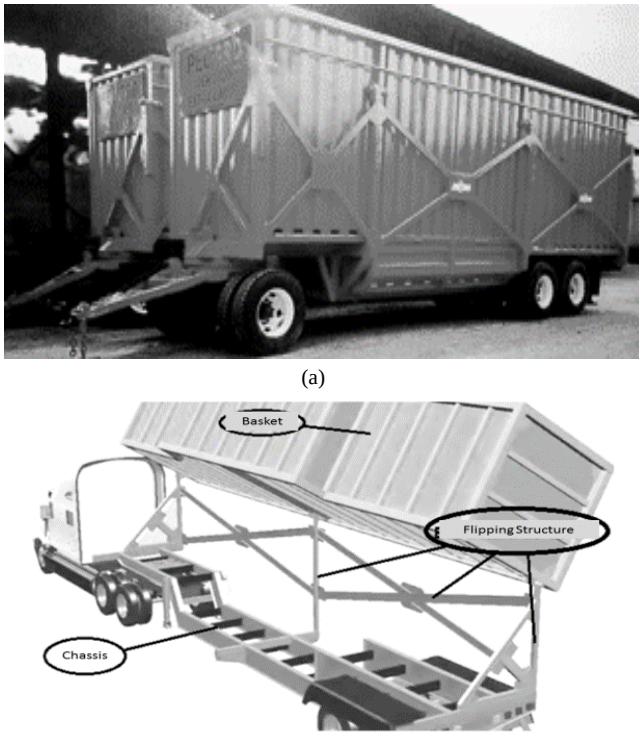
A production system for the manufacture of sugar cane trains was selected as an example. This sector is very important in the Valle de Cauca, Colombia because of the high demand of sugar cane for the production of sugar, alcohol and other derivatives [22]. In the country, the cane is transported over the roads using trains composed of baskets (wagons), pulled by a truck tractor. There are companies exclusively responsible for train design and manufacture; decreases in vehicle weight and production time, and a greater load capacity are important factors in development [23].

Because of the growing demand for sugar cane and the existing competition in the train manufacturing sector, companies have focused on improving their production process [24, 25]. This study was carried out in collaboration with a company in this sector to make improvements to its production system. This work focused on basket manufacture.

3.1. Collecting information

A relevant data summary is shown below: The basket (wagon) has three main components: chassis (main beam, rear and front chassis support), basket (laterals and linings) and flipping structure, see Fig. 3. The chassis supports the load contained in the basket and the flipping structure facilitates the discharge of the transported cane.

The manufacturing process consists of three main activities: cutting, pre-arming and arming.



(a)

(b)

Figure 3. (a) Semi-trailer (b) Cane train components.
Source: Company in the region.

Due to space limitations, Table 1 shows detailed activities descriptions, times and resources used in basket and flipping structure arming and shows global information in the other activities.

3.2. Variable and system behavior definitions

With the available information, the model approach is defined, and in this case, the final objective is to generate proposals for improvements in the current PS; therefore, the focus will be on the production stages, interactions, activity times and restrictions.

The process will be modelled from the approach of the stages of product arming; for this, we have the following as variables:

Work order (O.T in Spanish Orden de Trabajo).

Product reference.

Quantity of product to be produced, according to O.T.

Work pace (E.T in Spanish Espacio de Trabajo) assigned for each product.

As a simplification for the model, workstations (E.T.) will be used as resources, that is, they will be modelled as marks that are consumed. A smart agent will simulate an E.T assignment activity (activity performed by the supervisor); the agent must consider the smallest distance between the chassis manufacturing sections and the empty sides in order to guarantee the manufacturing inputs move as little as possible.

3.3. Structural model

Fig. 4 shows the PS structural model where E.T. 1 to E.T. 10 are generic workspaces that can be used to manufacture

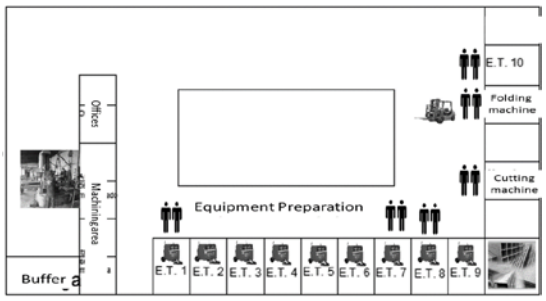


Figure 4. Structural model.
Source: Own elaboration.

any basket component. There are three areas specialized in machining, cutting and bending. A forklift is used to transport raw material between workstations.

3.4. Conceptual and functional model

In this stage, all functional relations between processes are defined, and the variable flow and operations carried out in each stage are described. Fig. 5 presents the conceptual diagram.

A schematic representation was made in Petri nets of the production process, see Fig. 6, using the structural model and conceptual diagram, see Fig. 4 and Fig. 5. In the model, the transitions (rectangles) represent the activities of the process, places (ovals) represent states and arcs (arrows), indicate the relationship between states and activities. In this way, the macro activities (stages) of the process are described, and in a later phase, each stage is refined to involve the functions and variables necessary to obtain a model that meets the required specifications.

Some functional model relations were based on the work order (in Spanish Orden de Trabajo – O.T.) that provided essential information to start the manufacturing process and identify different stages until reaching the finished product.

Different products (references) have similar production processes, i.e., their structure or operation flow has few variations. Therefore, a single general model for the process flow is defined.

Table 1
Time and resources to manufacture a star reference.

PRODUCTION STAGE DESCRIPTION	TIME (h)	ACTIVITIES						PERSONNEL						EQUIPMENT						
		Cut	Bent	Armed	Welding	Transport	Painting	Cutter	Bender	Armer	Assistant	Painter	Welder	S- SMAW	S. MIG	Cutting	Lift truck	Folding	Oxicorte	Compress
CHASSIS ARMING																				
TOTAL CHASSIS ARMING	*53*																			
MAIN BEAM ARMING																				
TOTAL MAIN BEAM ARMING	*9,8*																			
LATERALS PLACING																				
TOTAL LATERALS PLACING	*1*																			
LININGS MANUFACTURE																				
TOTAL LININGS MANUFACTURE	*39,79*																			
BASKET AND FLIPPING STRUCTURE ARMING																				
Cutting of tubular material	8	1						1											1	
Arming first lateral template	6			1						1	1			1						
Arming other sides from template	1,25			1						1	1			1						
Levelling of main beams for chassis assembly	6			1						1	1			1						
Arrangement of basket on chassis	48			1						1	1			1						
Arming turning dump	4			1						1	1			1						
Arming crossbars	14			1						1	1			1						
Arming table top	4			1						1	1			1						
Laying liner in basket	60			1						1	1			1						
Lining Welding	70				1								1		1					
TOTAL BASKET AND FLIPPING STRUCTURE ARMING	*221,25*																			
TOTAL MANUFACTURE	**324,84**	4	1	14	8	1	1	3	1	15	19	1	6	14	6	3	1	1	1	1

Source: Own elaboration.

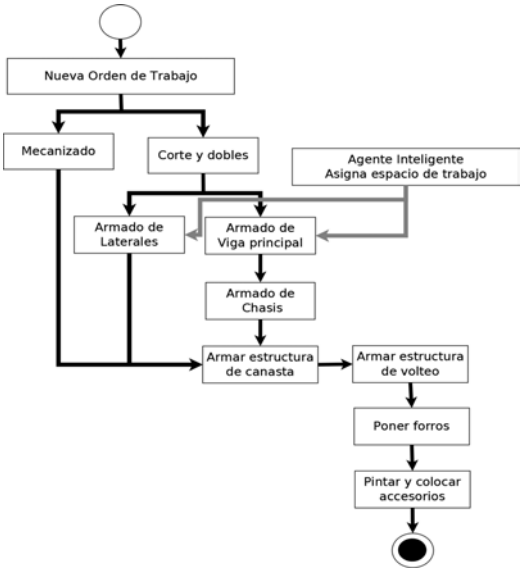


Figure 5. Conceptual diagram.
Source: Own elaboration.

With this general process model, it was necessary to find a variable that defines the E.T. (Workstations) designated on the O.T. (Work Orders). Therefore, at a given time the model can be observed in a state where it is working with two different references, but these operations are carried out in different E.T., therefore, a variable "l" (place) was defined, which will establish the E.T. where this process is found, see Fig. 7. In this figure there is a state «LATERALES UNIDOS» with two marks with values (2, 3) and two marks with values (3, 1), its representation is explained in Table 2.

Because of space limitations, only the process executed by the agent responsible for assigning the workstations (E.T.) is described. This agent has an internal state where the E.T is registered. When an O.T. arrives, this agent is activated and proceeds to assign spaces for the assembly of laterals and chassis. The agent is able to determine how many items are requested for the same reference (product) and allocate the spaces available to comply with the O.T. The agent is aware of the spaces that are enabled at the end of certain tasks and after updating assigns the free spaces to the new products that are pending assignment to an E.T., see Fig. 8.

The agent has two modules, where the module « MÓDULO DE ACCIÓN ASIGNAR ESPACIO EN PLANTA» is the one in charge of supervising the spaces available in the plant and assigning them. This module considers the quantity of products ordered for an O.T. and assigns the required number of spaces, see Fig. 9. An E.T. should be assigned for each part of a product (laterals and chassis), if there are several products for a unique reference, then one E.T should be assigned to manufacture all laterals at the same time and one E.T. for each chassis required, e.g., two products referencing 1070 need only one space for the laterals and two spaces for chassis production, in total there will be three E.T. required.

The module «MÓDULO PERCIBIR ENTORNO Y MODIFICAR ESTADO INTERNO» is responsible for supervising the E.T., which remain free during the process by saving the records in its memory to be assigned later when the space is needed in another O.T., see Fig. 10. Fig. 11 show «NUEVA SOLICITUD». It is the entry point to the agent that assigns spaces. This space contains an initial entry with the values (ot, rf, n); these values are three different O.T.'s with required references and quantities.

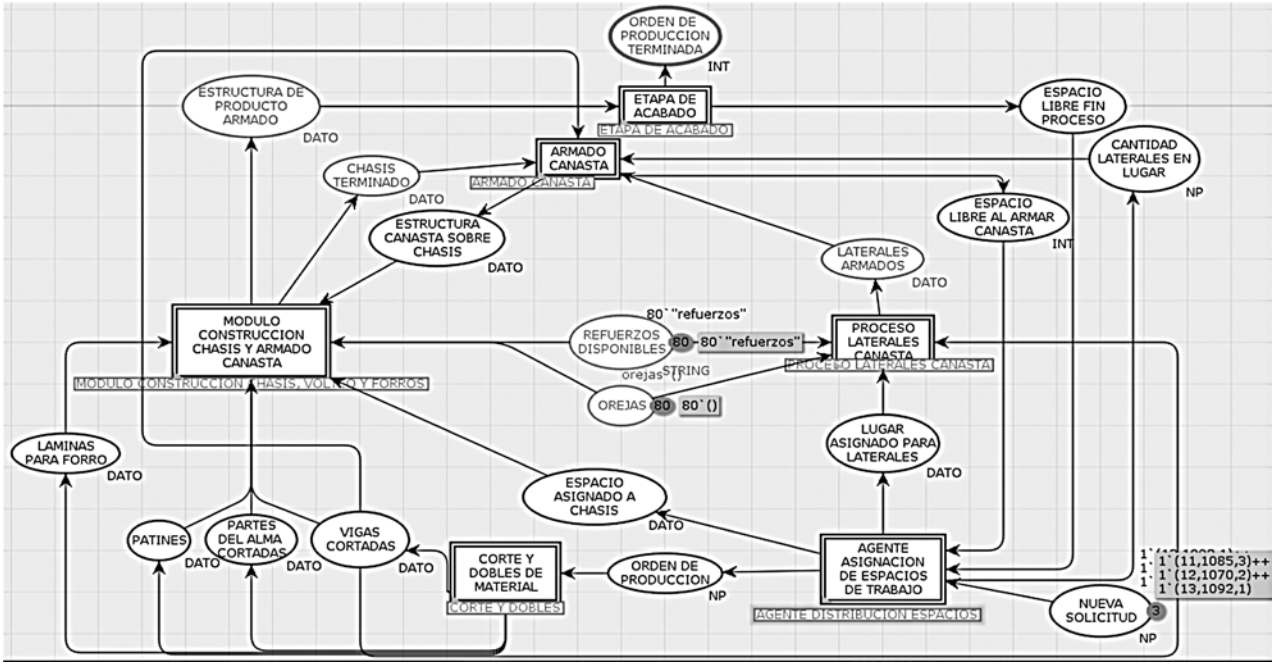


Figure 6. General production model.
Source: Own elaboration.

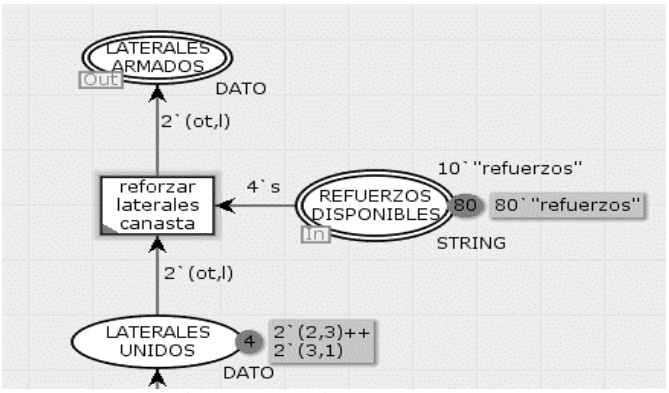


Figure 7. Example of similar status for two products where the process is carried out in different E.T.
Source: Own elaboration

Table 2
Mark description in a place or state.

Mark	First value	Second value	Third value
2`(2,3)	2` represents the amount of resources in that state; in this case, two united laterals	(2, represents the O.T where these sides belong.	,3) represents the place or the E.T. where the sides are located, that is, E.T. 3
2`(3,1)	2` represents the number of resources in that state; in this case, two laterals.	(3, represents the O.T for these laterals.	,1) represents the place or E.T, where the laterals are located, that is, E.T. 1.

Source. Own elaboration.

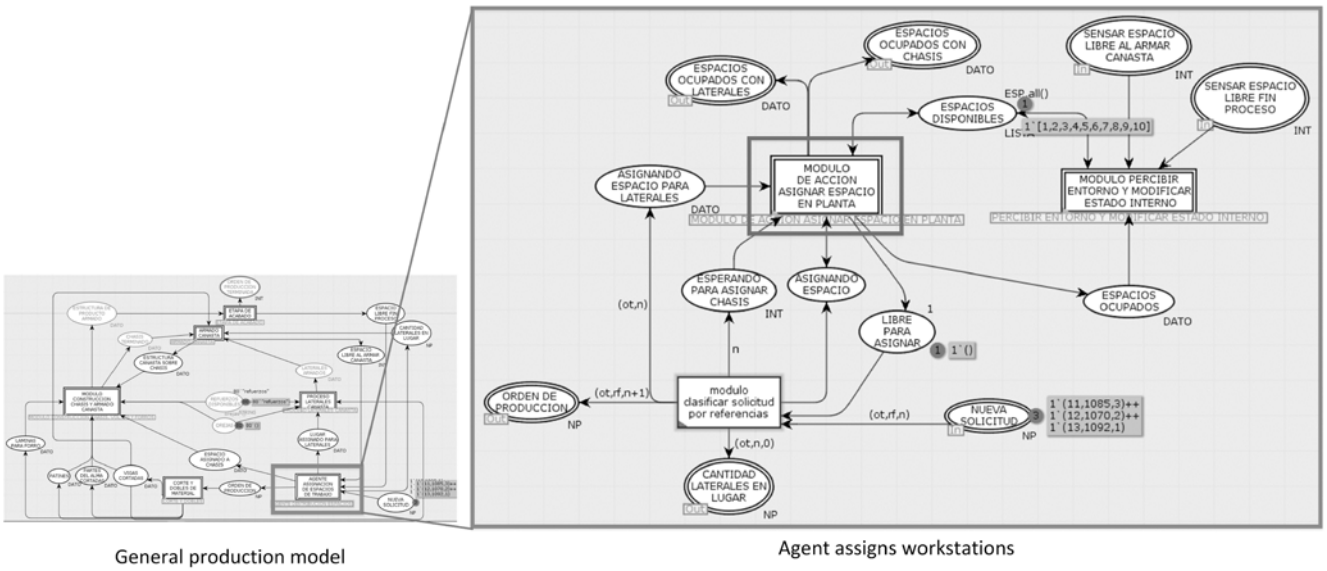


Figure 8. Smart agent model assigns workstations.
Source: Own elaboration

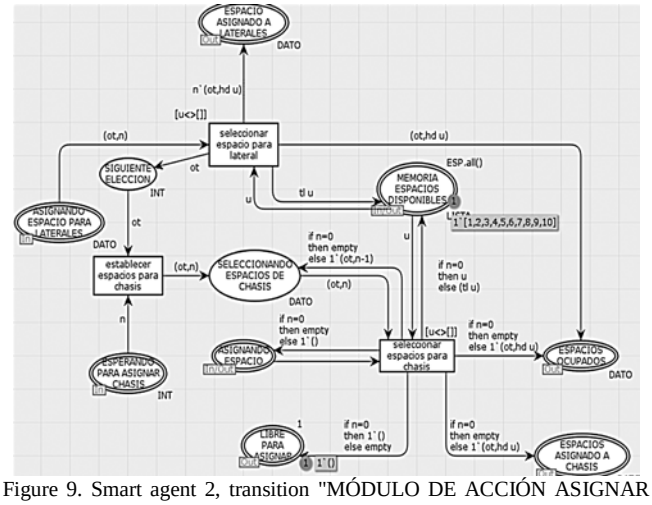


Figure 9. Smart agent 2, transition "MÓDULO DE ACCIÓN ASIGNAR ESPACIO EN PLANTA".
Source: Own elaboration.

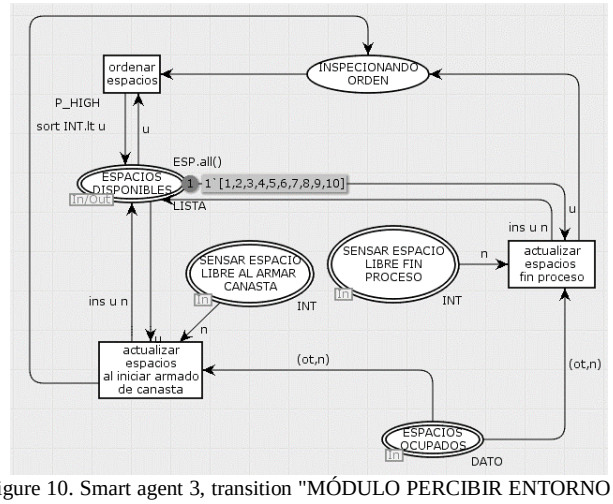


Figure 10. Smart agent 3, transition "MÓDULO PERCIBIR ENTORNO Y MODIFICAR ESTADO INTERNO".
Source: Own elaboration.

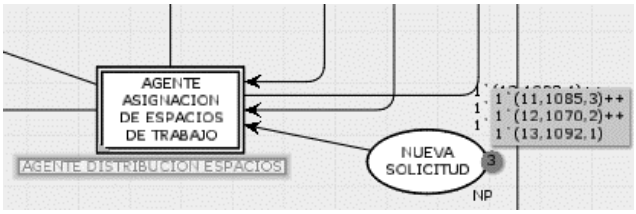


Figure 11. Initial process state, new product request.
Source: Own elaboration.

3.5. Model simulation

The following conditions were defined to simulate:

- In the beginning, all E.T.'s are available.
- All resources necessary for manufacture are available in the company; therefore, delay times due to lack of materials were not considered. The machining process was not considered in the simulation.
- Times and resources given in Table 1 were used.
- No changes of shift or breaks were considered.
- Time taken to prepare workspaces was not considered.

Current PS situation corresponds to the first model in CPN. However, to simulate the improvements in the process, some changes in the CPN model were defined in order to evaluate possible solutions according to what is required. In this context, two scenarios were evaluated. The first one considered the production of several products from the same reference. The second scenario included the production of several products from different references. In both cases, it was taking into account the O.T arrival order. Simulations were performed and model behavior was compared with real systems; each module that conforms to the system was validated. In this case, the functional behavior of the model met the requirements of the real system. All modules were verified to avoid limitations and errors.

3.6. Evaluating the current model

For reasons of space, only some of the results obtained from the model will be shown. The total production time was 306 h distributed as follows: basket and flipping structure arming required 68% of the time, followed by chassis assembly with 17%, lining manufacture with 12% and main beam assembly with 3%, see Fig. 13. It was found that the chassis and laterals assembly are produced in parallel; chassis require 68.8h while laterals need 7.25h; this creates dead time of 61.55 h (laterals must wait until the chassis is finished).

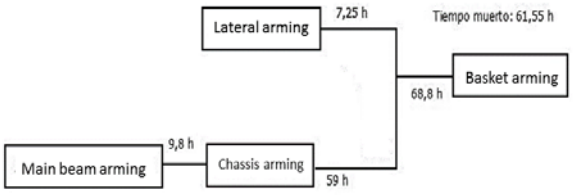


Figure 13. Parallel activities.
Source: Own elaboration.

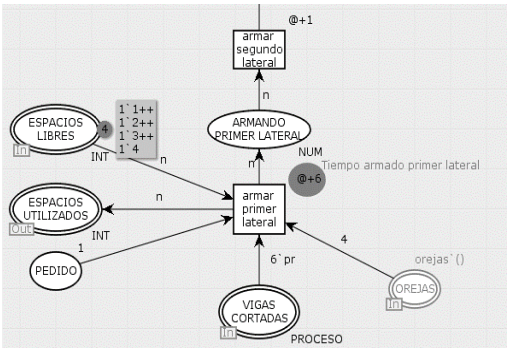


Figure 15. Lateral arming. Source:
Own elaboration.

Information obtained from the model identified some critical phases, for instance, basket and flipping structure arming and chassis assembly, where the activities of reinforcement and welding were representative. The raw material movement between E. T's is other critical phase.

The results of the model show that most of the activities are sequential with the exception of chassis assembly and lateral assembly, which are executed in parallel. However, distribution in the plant makes the sequential process difficult because the E.T.'s are not specialized (any E.T. is available for the execution of all activities). This causes delays due to the transport of materials and dead time due to waiting for the release of available spaces. The model verified that lateral manufacture requires an initial template (fabrication takes 6h), which is used to build the remainder of the laterals (fabrication takes 1.25h); all laterals, including the template, are used in the manufacturing process, see Fig. 15. The first lateral manufactured in each new order generates a delay in production of at least 4.75h per product. Construction of the basket at a height above the floor creates drawbacks for the welders, who require more time to perform this activity compared to working at floor level.

3.7. Defining improvements

Among the possible improvements are the following:

- Plant redistribution: given the characteristics of the production process, distribute processes (sequentially) to adapt the layout to production needs.
- The use of templates: the assembly activity is one of the most time-consuming, it was proposed to use templates for assembly and welding (also called welding tables with modular tools).
- Bridge crane: once the new distribution was established, use devices for handling large loads; the use of a bridge crane facilitates the transportation and location of laterals, baskets, linings, etc.
- Positioning and reinforcement system for chassis arming: to improve welding times and prevent anti-ergonomic welder positions, the use of a positioning and reinforcement system is recommending.
- Welding robot: welding activity represents 28% of the required time; it is advisable to reduce the cost of welding the joints of the main beams.
- Use of tubular cutting devices: at present, tubular cutting

is performed by oxicorte, generating imperfections in the cut, which must be polished to give the required angle and finish. To mitigate this, the use of a band saw was recommended.

Proposed templates are shown in Fig. 16, and the conceptual design consists of two parts. Fig. 16 (a) shows the first template where adjustments are made to manufacture the sides. This template has a series of rods and presses that enable delimiting the initial and final points and the required form for welding. This template will be used to make the laterals (for different products offered by the company). Fig. 16(b) shows the second template, which is the basis for the basket structure. The laterals should be located at the ends of each template using a bridge crane. Once located, they will be welded to manufacture the basket and then moved to the assembly area. The use of these templates facilitates manufacture in a horizontal position.

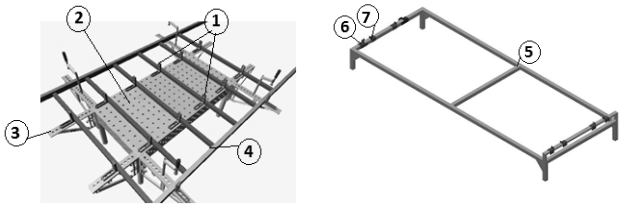
3.8. Apply improvements evaluate and compare both models.

Each improvement was included and simulated individually in the CPN model. It was found that the use of templates represented a considerable saving in the production times.

Template use was added to the current process, see Fig. 17 (a). Simulations were performed and the results are presented in Table 3. The current times to manufacture the basket and the times for the same activities using the proposed improvements are compared; the time for assembly of the first lateral and assembling the basket on the chassis in a horizontal position decrease. The estimated saving of time to assemble the structure

+122W<5

This proposal makes it possible to separate the assembly process from the chassis assembly process because the construction of the basket can be started without having previously armed the reinforced chassis, see Fig. 17 (b). In this way, a reduction of 48 h in the total time of the assembly process can be obtained.



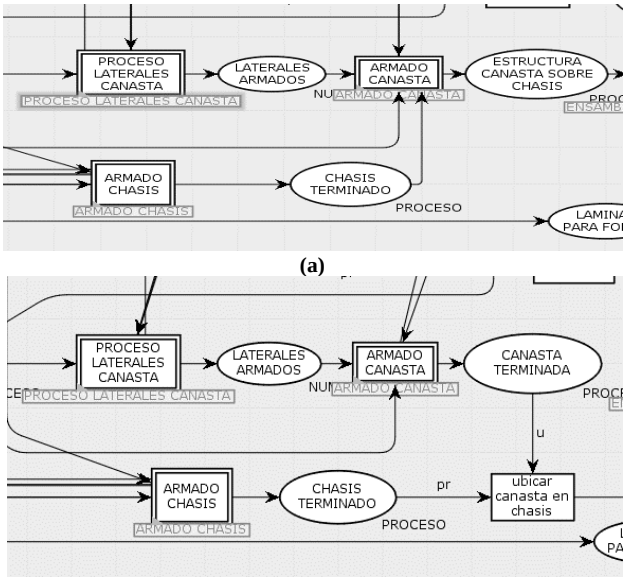
(a) (b)

Figure 16. Structure of templates (a) first one, (b) second one.
Source: Own elaboration.

Table 3.
Time comparison between current model and proposed improvement for basket assembly.

Current process		Proposed process	
Arming first lateral template	6 h	Arming first lateral template	1,8 h
Arming other laterals from template	1,25 h	Arming other laterals from template	1,25 h
Armed basket on chassis	48 h	Armed basket on ground	14,4 h
Total	55.25	Total	17,45

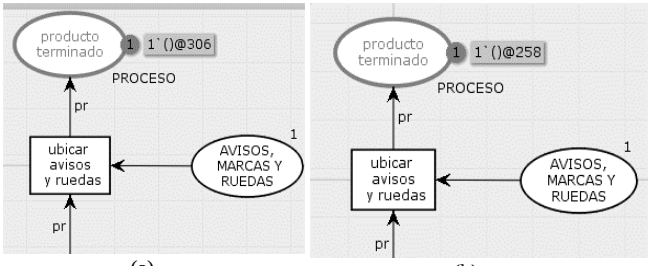
Source: own elaboration.



(a)

(b)

Figure 17. Basket assembly (a) current model, (b) proposed model.
Source: Own elaboration.



(a) (b)

Figure 18. Total production time (a) current model, (b) proposed model.
Source: Own elaboration.

Table 4.
Comparison of actual production times and proposed production times.

Current process	Time (h)	Proposed process	Time (h)
Finished product	306	Finished product	258
Armed basket	55.25	Armed basket	17.45

Source: Own elaboration.

Fig. 18 shows a comparison between the current manufacturing process and the same process with the addition of the templates; the impact on the basket assembly and estimated finished product is presented in Table 4.

Material and personnel resources for the current and new model are the same, i.e., an armer and an assistant, arc welding equipment, MIG welding equipment and transport system.

4. Conclusions

This work presents a procedure that allows the improvement of productive processes using formal tools, such as Coloured Petri Nets. The approach enables structuring the model to improve a production process. The case study shows a time study, where was identified that the

activity that has the greatest impact on the process is basket and flipping structure arming with 68% of the manufacturing time. To improve the processes, seven improvements were proposed. For example, the use of templates allows a reduction of time from 55.25 h to 17.55 h; this represents a reduction of 31.5% in this activity. Other possible analysis would consider the evaluation of more variables such as line efficiency, productivity, costs, etc.

References

[1] Arzola, M. y Mejías, A., Modelo conceptual para gestionar la innovación en las empresas del sector servicios, Revista Venezolana de Gerencia, 12(37), pp. 80-98, 2007.

[2] Cortes, M. et al, Colombia en la era del alcohol carburante, Revista CES, 3(2), pp. 122-132, 2008.

[3] Luna-Gonzáles, A.J., Cock, H., Palma, A.E., Díaz, L.V. y Moreno, C.A., Análisis de la productividad en la agroindustria azucarera de Colombia y perspectivas para aumentarla, en: libro El cultivo de la caña, 1995, pp. 373-394.

[4] Moreno, D.X. y Nieto, Y.O., Incidencia en los trabajadores y empresas que contratan mediante tercerización - Estudio de caso Imecauca S.A., Colección Académica de Ciencias Estratégicas, 1(2), pp. 16-38, 2014.

[5] Du, W., Tang, Y., Leung, S.Y.S., Tong, L., Vasilakos, A.V. and Qian, F., Robust order scheduling in the discrete manufacturing industry: a multiobjective optimization approach. IEEE Transactions on Industrial Informatics, 14(1), pp. 253-264, 2018.

[6] Nogueira, H.S., Controle supervisório para um robô móvel inteligente através de autômatos híbridos. 2015.

[7] Jensen, K. and Kristensen, L.M., Coloured Petri nets, modelling and validation of concurrent systems, 1st ed. Berlin Heidelberg: Springer-Verlag, 2009.

[8] Fanti, M.P., Petri net approaches to deadlock modeling and resolution in automated manufacturing, IEEE Int. Conf. Syst. Man Cybern., 3, 6 P., 2002.

[9] R. Zurawski and Zhou, M., Petri nets and industrial applications: a tutorial, Industrial Electronics, IEEE Transactions on, 41(6). pp. 567-583, 1994.

[10] Silva, M., Teruel, E., Valette, R. and Pingaud, H., Petri nets and production systems, Lect. Petri nets II …, vol. 0452, 1998.

[11] Giua, A. and Silva, M., Modeling, analysis and control of discrete event systems: a Petri net perspective. IFAC-PapersOnLine, 50(1), pp. 1772-1783, 2017.

[12] CPN Group. AIS group, Software de redes de Petri coloridas CPN tools. [Online]. Available at: http://cpntools.org/download.

[13] Tarabuta, O., Workflow optimization and advanced control of systems based on Petri Nets, in: System theory, control and computing (ICSTCC), 2012 16th International Conference, 2012, pp. 1-6.

[14] Murata, T., Petri nets: properties, analysis and applications, Proc. IEEE, 77(4), pp. 541-580, 1989. DOI: 10.1109/5.24143

[15] Jensen, K., Kristensen, L.M. and Wells, L., Coloured Petri nets and CPN tools for modelling and validation of concurrent systems, Int. J. Softw. Tools Technol. Transf., 9(3–4), pp. 213-254, 2007. DOI: 10.1109/87.799667

[16] Drakaki, M. and Tzionas, P., Modeling and performance evaluation of an agent-based warehouse dynamic resource allocation using colored Petri nets. International Journal of Computer Integrated Manufacturing, 29(7), pp. 736-753, 2016.

[17] Yao, A.W.L., Ji, Z. and Liao, H.T., A Petri nets-based process planning system for wastewater treatment, Asian J. Control, 12(3), pp. 281-291, 2010.

[18] Baldwin, W.C., Sauser, B. and Cloutier, R., Simulation approaches for system of systems: Events-based versus agent based modeling. Procedia Computer Science, 44, pp. 363-372, 2015.

[19] Petronijević, J., Petrović, M., Vuković, N., Mitić, M., Babić, B. and Miljković, Z., Integrated process planning and scheduling using multi-agent methodology. In: Applied Mechanics and Materials, Vol. 834, pp. 193-198. Trans Tech Publications, 2016.

[20] Nassar, M. and Melo, J., Modeling and analysing of the material entry flow system in a pickling line process using Petri net, ABCM Symp. Ser. Mechatronics, 3, pp. 444-453, 2008.

[21] García-Melo J.I. and Miyagi, P.E., Modeling and analyzing of the material entry flow system in a pickling line process using Petri net, vol. 3. Universidad de Sao Paulo, Escuela Politécnica, [online]. 2008, Available at: http://www.abcm.org.br/symposiumSeries/SSM_Vol3/Section_III_Industrial_Informatics_and_Discrete_Systems/SSM3_III_07.pdf

[22] Giraldo, F., El cultivo de la caña de azúcar en la zona azucarera de Colombia, 1995, pp. 357-362.

[23] Cappello, F. et al, Methodical redesign of a semitrailer. [online]. Available at: http://library.witpress.com/pages/PaperInfo.asp?PaperID=14975

[24] Medina, N., El proceso de inspección desde la visión de un transportador de fríо. [en líena]. Disponible en: http://www.mincomercio.gov.co/vbecontent/Documentos/intervenciones/2006/TallerSantaMarta7.ppt

[25] República de Colombia, Ministerio de Transporte. Estructura de costos de operación vehicular. En: http://www.mincomercio.gov.co/vbecontent/Documentos/intervenciones/2006/TallerSantaMarta9.ppt

J.F. Caratar-Chaux, is Msc. Mechanical Eng. in 2015, BSc. Mechanical Eng.r in 2012 at the University of Valle, Colombia. Doctoral student in electric and electronic engineering at the Universidad del Valle in 2017. Currently he works as junior researcher with GRALTA group (Grupo de investigación en alta tensión).
ORCID: 0000-0003-0581-7143

R.E. Cano-Buitrón, is graduated the BSc. in Mechanical Eng. in 2014 and Electronic Technology in 2016 at the University of Valle, Colombia. Project engineer in various companies in the industry sector in Santiago de Cali and supports various studies on the BioNovo group (Group of biotechnological innovation) at Universidad del Valle.
ORCID: 0000-0003-4903-4431

J.I. García-Melo, is PhD. in Mechanical Eng. from the University of Sao Paulo-Brazil, 2011. MSc. in Engineering with emphasis in Automation at the Universidad del Valle-Colombia, 2001. BSc. in Mechanical Eng. at the Universidad Autónoma de Occidente, Colombia in 1994. Currently, he is an associated professor at Universidad del Valle and researcher in the Logistics and Production group and BioNovo group at Universidad del Valle.
ORCID: 0000-0003-1672-7768



UNIVERSIDAD NACIONAL DE COLOMBIA
SEDE MEDELLÍN
FACULTAD DE MINAS

Área Curricular de Ingeniería Mecánica

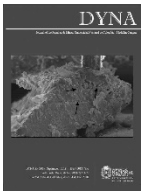
Oferta de Posgrados

Maestría en Ingeniería - Ingeniería Mecánica

Mayor información:

E-mail: acmecanica_med@unal.edu.co
Teléfono: (57-4) 4259262

UNIVERSIDAD NACIONAL DE COLOMBIA
SEDE MEDELLÍN
FACULTAD DE MINAS



DYNA
http://dyna.medellin.unal.edu.co/

Active geodetic network: application in topography

Enrique Cano-Jódar [a], Manuel Sánchez-de la Orden [b] & Javier Mesas-Carrascosa [b]

[a] *Higher Technical School of Belmez, University of Córdoba, Córdoba, Spain. um1cajoe@uco.es*
[b] *Higher Technical School of Agronomic Engineers of Córdoba, University of Córdoba , Spain. ig1saorm@uco.es, ig2mecaf@uco.es*

Received: June 18th, 2017. Received in revised form: March 16th, 2018. Accepted: June 13th, 2018.

Abstract
The objective of this work is to determine the positional quality of the solutions offered by the Andalusia Positioning Network (RAP), an active geodetic network located in the autonomous community of Andalusia in southern Spain. Different tests are performed on the services offered by this active network, especially those that use real-time-Kinematic positioning techniques (RTK). Different parameters are analysed, including precision, accuracy and time of resolution of ambiguities. The system is then analysed from the perspective of the topographic survey; several small-scale topographic surveys are carried out, used for mining and civil engineering projects, with the aim of seeing if an active geodetic network can be used with performance similar to that for conventional RTK.

Keywords: CORS; RTK; RAP; topographical survey.

Red geodésica activa: aplicación en topografía

Resumen
El objetivo de este trabajo es determinar la calidad posicional de las soluciones ofrecidas por la Red de Andaluza de Posicionamiento (RAP). Red geodésica activa situada en la Comunidad Autónoma de Andalucía, en el sur de España. Se realizaron diferentes pruebas a los servicios ofrecidos por esta red activa, especialmente los que utilizan técnicas de posicionamiento en tiempo real (RTK). Se analizaron diferentes parámetros: precisión, exactitud y tiempo de resolución de ambigüedades. Posteriormente, se analizó el sistema desde el punto de vista del levantamiento topográfico, realizándose varios levantamientos de pequeña extensión, utilizados para proyectos de minería e ingeniería civil, con el objetivo de comprobar si una red geodésica activa puede utilizarse con un rendimiento similar a las obtenidos utilizando RTK convencional.

Palabras clave: CORS; RTK; RAP; levantamiento topográfico.

1. Introduction

Over recent years, Global Navigation Satellite Systems (GNSS) have seen major advances, closely related to the increase in the number of satellites and the improvement and development of signal processing algorithms. This has had a direct consequence on the widespread use of these technologies in different areas, mainly in the Engineering and primarily Civil Engineering.

In order to improve the quality metrics and services offered by GNSS systems, several GNSS networks have been installed, both private and public, offering download data services for post-process works and the sending of differential corrections, allowing for precise real time positioning. The scope of these networks can be global like the International GNSS Service (IGS), continental such as the Euref Permanent Network in Europe, national such as the ERGNSS in Spain and local such as the Andalusia Positioning Network (RAP) in Andalusia.

Each of these, Continuously Operating Reference Stations (CORS) are comprised of a certain number of GNSS receivers, distributed homogeneously throughout the area in which it is intended to provide the service, a control centre where the data from said antennae is received a data distribution channel. Using the information received from all the antennae, the control centre determines and models the errors, creating corrections that are sent by the data distribution channel in order to improve the solution obtained in Real Time Kinematic (RTK). Since the 1990s, numerous studies have been carried out in this

How to cite: Cano-Jódar, E., Sánchez-de la Orden, M. and Mesas-Carrascosa, J., Active geodetic network: application in topography. DYNA, 85(206), pp. 114-120, September, 2018.

© The author; licensee Universidad Nacional de Colombia.

area, seeking to improve both the calculation methods and the sending of such corrections. [1]

Today there are different methodologies for calculating the transmission of the corrections based on the unidirectional or bidirectional nature of the communication. In the unidirectional link the user receives the correction directly. Such is the case of the Flächen Korrectur Parameter (FKP) corrections [2,3] and Master Auxiliary Concept (MAC) corrections [4]. With a bidirectional link it is necessary for the mobiles receptor to send its approximate position to the control centre, generating the corrections appropriate for the mobile equipment. Such a concept is used for the following RTK architectures: Virtual Reference Station (VRS) [5] Individualized Master-Auxiliary (I-MAX) [6, 3] and Pseudo Reference Station (PRS) [7]. Today, these

methodologies are allowing for the application of GNSS technology in many areas, such as updating cartography, GIS inventories [8], fleet location and management [9], precision agriculture [10,11], mining applications [12]. Without doubt, this has meant a significant advance in the field of topography, optimising economic costs and improving farmland yields.

While it is important to improve these two factors, it is no less important to ascertain the positional quality obtained in the topographic surveys and stakeouts; fundamental aspects within the field of Civil engineering through compliance testing.

Many authors have studied the functioning and carried out different tests to verify the quality of the RTK service in a network of permanent reference stations. The tests are performed on a series of control points which are situated within the network. Some examples [13] carry out tests on the CORS Net network, which operates in New South Wales, Australia, analysing the difference between a conventional RTK solution and the focuses of the RTK network (NRTK) at different control points, in boundary conditions of distance between reference stations [14] These authors tested the precision of the position in six areas covering England and Wales using two commercial RTK network systems and comparing the coordinates obtained with the precise coordinates determined according to Bernese processing scientific GPS Software obtained through static methods. [15] Other authors perform the preliminary tests of a SmartNet research service from the point of view of the user for the purpose of assessing the quality of the NRTK service; various tests were carried out, applying static and cinematic methods using the same type of equipment as the SmartNet users in Great Britain.

[5] Other examples of RTK tests based on Active Networks have been applied previously, carrying out four simultaneous tests to evaluate RTK performance, using VRS, comparing the results for use of a simple solution and an NRTK solution (network solution) in the BLVA network in Germany.[16] They perform a systematic test that that has been carried out in different places in Shanghai to evaluate the accuracy and reliability that can be reached for VRS, RTK positioning. [17] The CORS GPS Network (GPS Net), created in Victoria (Australia) is described. The evaluation tests for NRTK technologies were performed across extensive surface areas.

Other authors have even performed tests on the periphery of Active Networks that operate in border areas between neighbouring regions [18], performing tests on RTK positioning in three Active local GNSS networks at different testing points located in the border area between the Autonomous Communities of the Region of Murcia and the Valencian Community in the south-east of Spain.

Also, between Active Networks that operate in border areas between neighbouring countries [19] they perform tests of NRTK positions and post-process, simultaneously at different points located in border areas between Portugal and Andalusia, in the south west of the Iberian Peninsula. The analysis is based on the use of two active GNSS networks present in this border region, RENEP (Portugal) and RAP (Autonomous Community of Andalusia, Spain).

The Andalusia Positioning Network (RAP) is an active local network that operates in the Autonomous Community of Andalusia (Spain). It is comprised of 22 reference stations, distributed across the area it services. The approximate separation between stations is 50 to 70 km, as can be observed in Fig. 1.

It offers precision positioning services to be used both in post-process and in real time. It creates solutions based on the Master-Auxiliary Concept (MAC) [3,4], generating different types of differential corrections, from the nearest station or form a station selected in the standard format version 2.3 Radio Technical Commission for Maritime Services (RTCM) and differential corrections based on network solution in the standard format RTCM 3.1, sent through the Internet using the NTRIP protocol (RTCM network transport via Internet Protocol) [20].

The framework of reference is the international ITRF2000; it is made up of RAP stations, linked with the nearest stations belonging to the IGS, UREF or Active Geodetic Networks of a higher order. The calculation and adjustment process is carried out with Bernese 5.0 software developed by the Astronomic Institute of the University of Berna (Switzerland). A daily coordinate is obtained for each RAP station. These solutions are combined, making a least squares adjustment to obtain a weekly solution for each station. The final adjustment of the network is made by setting the IGS or EUREF stations for each period considered. [21].

In summary, the area of study proposed is within the Andalusia Positioning Network, in southern Spain and to the north of the province of Córdoba, as can be seen in Fig.2.

The methodology used is based on locating different control points and using the positioning services of the RAP, basically those that use differential corrections in real time and standard RTCM 2.3 format, from the nearest station to determine different parameters. First the tests to characterise the system are carried out, obtaining precision, accuracy and time to resolve the ambiguities. Subsequently the performance of the system is determined by completing topographic surveys.

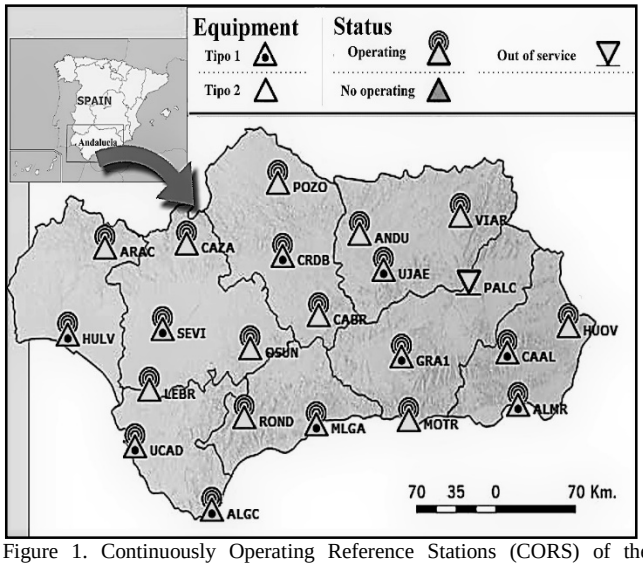


Figure 1. Continuously Operating Reference Stations (CORS) of the Andalusia Positioning Network. Source: authors' own and RAP.

2. Materials

To complete this work, the Andalusia Positioning Network is used, comprised of twenty two permanent GPS stations, of which 10 belong to first phase and consist of the following elements: choke ring geodetic antenna (Dorne-Margolin) Leica AT504 with Domo, Leica GRX1200 Pro double frequency receptors with four RS232 ports and an Ethernet port with three independent IP addresses, uninterrupted electrical feed system, permanent internet connection, weather station and two radio modems: PacifiCrest and Satelline 3AS.

The second phase stations do not have weather stations or radio modems and the geodetic antenna is not the choke ring type.For quality control and data processing, there is the control centre, software, whether scientific (Bernese, Gipsy, etc.) or commercial (Leica Geoffice, Trimble Geomatic office), etc.

The mobile equipment used for data capture is a GX1230 geodetic receiver with double frequency and the possibility of internet connection through GSM link. Siemens MC75, mobile phone integrated in a Leica GFU case, 850, 900, 1800, 1900 MHz, antenna GPS ATX 1220.

3. Methodology

Static and cinematic GPS methods are applied in real time RTK; services which are offered by RAP are applied especially to those that use the positioning techniques using differential corrections in real time (RTK). The parameters to evaluate are: precision, accuracy and performance in the topographic study.

3.1. Precision

Precision allows for the dispersion of the data obtained to be determined, establishing the most probable value for a measured magnitude. The value of said magnitude shall be obtained from the observations made, which suggests an oversized number of repetitions in the measurement process. The measurements will never be exact as there is a series of factors that influence this process; the directions themselves, the instrumentation used, external factors, etc.

When using the GNSS network, this parameter will depend on the different variables, such as the number of satellites, geometry of the constellation, time of observation, precision of the ephemeris used, local effects such as multipath, corrections generated by the system, distance of reference stations, etc.

Other errors, such as ionospheric and tropospheric activity are not controllable. However, the distance between reference stations conditions the dependence of the network with respect to these factors.

Precision is determined numerically by the standard deviation of the measurements collected. To determine the precision of the system, a series of control points are installed on the hard shoulder of several roads in the north of the province of Córdoba, as can be seen in Fig. 2. These points are steel spokes which allow for the data to be taken at the same time and are manufactured so that they can remain stable during the observations. There are six such control points, distributed in groups of three, at an approximate distance of 30 to 40 kilometres respectively from the permanent reference point located in Pozoblanco, Córdoba, belonging to the Andalusia Positioning Network. The data gathering is carried out in real time RTK, configuring the mobile equipment with MAC methodology [3,4] providing differential corrections corresponding to the nearest station in the standard RTCM 2.3 format which are sent through the NTRIP protocol by internet.

To avail of sufficient data in each control point, three different series have been taken and in each series sixty repetitions were made; each data series was taken in different weeks to prevent the collected data from exhibiting a strong temporal correlation (environmental conditions, GNSS constellation configuration, etc.).

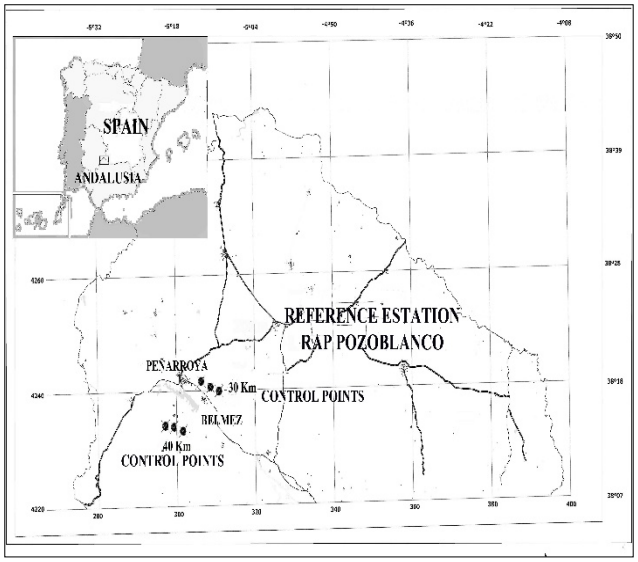


Figure 2. Control points situation.
Source: Authors' own.

3.2. Accuracy

The accuracy of the data offered by the RAP is verified by comparing the coordinates obtained by the mobile receptor in real time RTK, configuring and using MAC architecture with the coordinates of six control points obtained with more precise methods. The coordinates of these control points have been determined through a static survey, with an observation time of approximately sixty minutes at each point. The accuracy obtained in the coordinates will depend, in this case, on the observation time at each point. Once the mobile equipment file is obtained, the corresponding file for the Pozoblanco reference antenna is downloaded from the RAP FTP for the day and time of the mobile observation.

Using Leica Geo Office commercial software, the control point coordinates are calculated in post-process. In general, the parameters used in the post-process are: angle of elevation 15º, type of ephemeris transmitted, type of automatic solution and type of automatic GNSS.

The strategy used is: automatic frequency, set ambiguities up to 80 km, minimum duration for floating solution 300 seconds, sample interval: use all the observations made, Hopfiel tropospheric model, automatic ionospheric model, minimum distance 8 km and automatic ionospheric activity.

To check the deviation of the coordinates obtained by the receiver three series of measurements are taken at different times, taking 60 data in each series. The solution used is that generated by the RAP applying the MAC concept, differential corrections from the nearest station, transmitted in RTCM 2.3 MESSAGES format, through NTRIP [3,4]. The coordinates obtained in real time RTK compared to the coordinates of the control points obtained with the upper range static precision method will allow for the standard deviation to be obtained and thus to establish the accuracy or veracity of the system.

3.3. Ambiguity resolution time

The time a piece of equipment needs to resolve ambiguities depends on a number of factors that can be difficult to determine a priori, such as: distance from the base station, number of satellites observed, algorithm used by the manufacturer, possible loss of cycle during the calculation process, etc.

On this point it is intended to evaluate how much time a field operator needs to take the sample of a determined point. Firstly, the time the receiver takes to achieve a precise positioning is measured and secondly the time taken by the system to recover and the precision after a data loss and the resulting loss of phase.

The first point can be measured easily; it is only necessary to initiate the equipment and measure the time needed to obtain the desired precision. The latter will depend on whether there is an outage in the system, a data loss and loss of phase solution and from this moment measure the time taken to achieve the necessary precision.

In each series, the time a piece of equipment needs to start up has been measured, as has the time taken to connect to the control centre and to obtain the precise position. The recovery time can only be measured if there is a data crash and this is when the recovery time is noted.

3.4. Surveys carried out

The system is analysed from the perspective of a topographic survey, comparing the performance obtained with the classic surveys. For this, several small extension surveys have been carried out, used for different Engineering and Mining projects: surveys of properties, roads, motorways, etc.

Approximately two thousand points have been taken with mean quality of 0.0494m. The method used is in real time (RTK), using the differential correction solution (MAC) from the nearest station, RTCM 2.3 format.

4. Data Analysis

4.1. Precision

The coordinates taken as reference to determine precision are obtained from the filed measurements themselves, determining the most probable value as the average of the measures taken.

Three series of measures are taken at each control point, where 60 repetitions are made. Different statistical tests are applied and the errors are represented to see if they follow a normal distribution.

Table 1 shows the discrepancies in the East, North and Vertical components with respect to the most probable value assigned to each control point.

Table 2 shows the standard deviations σE, σN, σU of the East, North and Vertical components for the three series obtained at each control point, and the average value obtained at the points located 30 and 40 km from the reference station. The results obtained are similar, although the control points are at different distances from the reference station.

Table 1.
Discrepancies with respect to the most probable value.

	Series	dE	dN	dU	dE Mean	dN Mean	dU Mean
1	1	0.004	0.005	0.008	0.005	0.004	0.006
	2	0.005	0.003	0.006			
	3	0.005	0.004	0.005			
2	1	0.004	0.004	0.006	0.005	0.004	0.007
	2	0.005	0.003	0.006			
	3	0.005	0.004	0.008			
3	1	0.004	0.006	0.010	0.004	0.005	0.008
	2	0.004	0.004	0.005			
	3	0.004	0.004	0.008			
4	1	0.005	0.006	0.007	0.004	0.005	0.007
	2	0.003	0.004	0.006			
	3	0.005	0.005	0.007			
5	1	0.007	0.004	0.007	0.006	0.004	0.008
	2	0.004	0.004	0.011			
	3	0.006	0.004	0.007			
6	1	0.005	0.004	0.010	0.005	0.005	0.011
	2	0.005	0.004	0.012			
	3	0.004	0.006	0.010			

Source: Authors' own.

Table 2.
RTK Precision. RAP Solutions.

Control Point	Series	σE	σN	σU	σE Mean	σN Mean	σU Mean
1	1	0.005	0.007	0.010	0.006	0.006	0.008
	2	0.006	0.005	0.008			
	3	0.007	0.005	0.007			
2	1	0.007	0.006	0.011	0.007	0.005	0.009
	2	0.006	0.005	0.008			
	3	0.007	0.005	0.007			
3	1	0.007	0.005	0.008	0.006	0.005	0.008
	2	0.005	0.005	0.006			
	3	0.006	0.005	0.010			
4	1	0.007	0.007	0.008	0.006	0.006	0.008
	2	0.004	0.005	0.008			
	3	0.006	0.006	0.009			
5	1	0.009	0.006	0.009	0.007	0.005	0.010
	2	0.005	0.005	0.013			
	3	0.007	0.005	0.009			
6	1	0.006	0.008	0.013	0.006	0.007	0.013
	2	0.006	0.005	0.014			
	3	0.006	0.008	0.013			

Source: Authors' own.

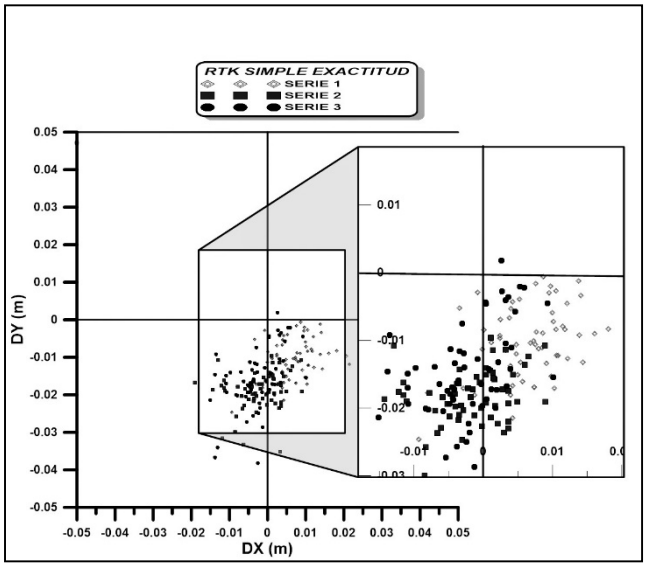


Figure 3. Horizontal discrepancy with respect to the post-process solution and RTK solutions of the RAP for control points 4.
Source: Authors' own.

Table 3.
Accuracy RTK

		RTK SOLUTION			
Control Point	**Accuracy. (m)**	**Series 1**	**Series 2**	**Series 3**	**Mean value**
1	H	0.012	0.015	0.011	0.013
	V	0.011	0.014	0.015	0.013
2	H	0.019	0.016	0.008	0.014
	V	0.011	0.007	0.021	0.013
3	H	0.028	0.008	0.008	0.015
	V	0.025	0.019	0.013	0.019
4	H	0.018	0.014	0.014	0.015
	V	0.013	0.009	0.010	0.011
5	H	0.012	0.007	0.019	0.013
	V	0.009	0.017	0.034	0.020
6	H	0.015	0.021	0.019	0.018
	V	0.022	0.015	0.023	0.020

Source: Authors' own.

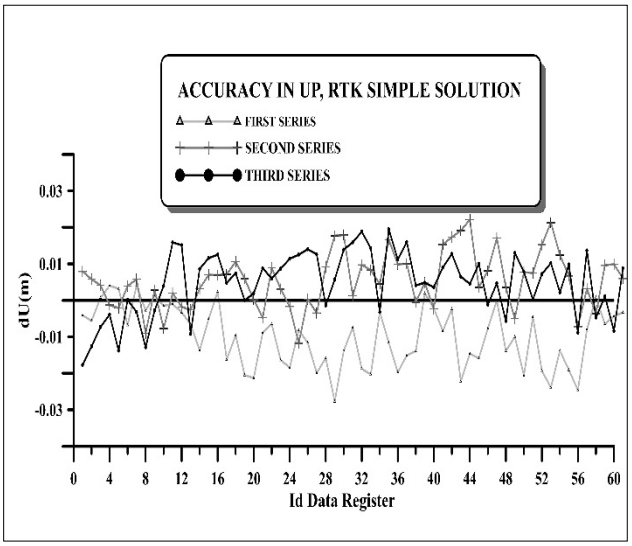


Figure 4. Vertical discrepancy with respect to the post-process solution and RTK solutions of the RAP for control points 4.
Source: Authors' own.

For all the points located 30 to 40 kilometres from the reference station, the mean precision values for the component East, North and Vertical can be observed in Table 2. The variation in precision for the East component ranges between (0.006 - 0.007) m, for the North component, the ranges between (0,005 - 0,007) m and for the vertical component between (0,008 - 0.013) m,

4.2. Accuracy

Accuracy is determined by comparing the coordinates obtained in real time by the mobile equipment with the control points located approximately 30 to 40 km from the nearest reference station, Pozoblanco, of the Andalusia Positioning Network and at the same time shall depend on the coordinates assigned for these control points. The method used to obtain the coordinates of the control points is to perform an autonomous or static positioning and subsequently a post-process with commercial Leica Geo office software.

Table 3 shows the control points, the horizontal and vertical components, the accuracy of each component in the three series of measurements taken and the average value for each component.

The variation in accuracy ranges between (0.013 - 0.018) m and (0.011 - 0.020) for the horizontal and vertical components respectively.

4.3. Ambiguity resolution time

As observed in Fig. 5, the equipment used for performing this work needs an average of 51" to initialise and receive the signal from the constellation, 21" to connect with the control centre of the network and to have precision to complete observations and some 12" to recover precision when it loses a fixed solution.

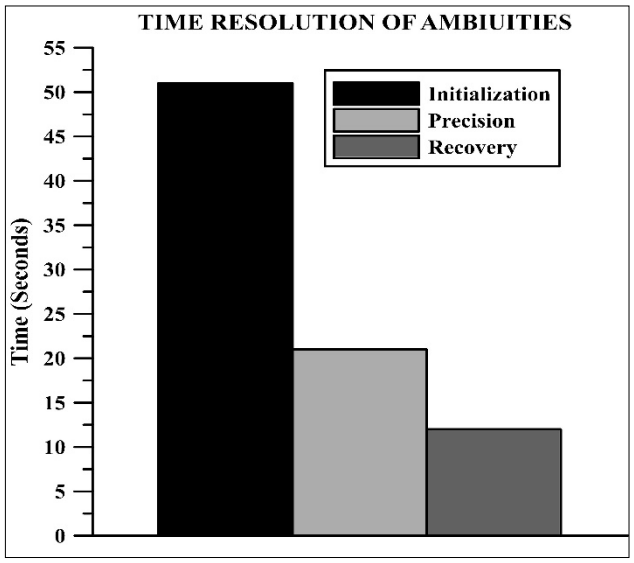


Figure 5. Ambiguity resolution
Source: Authors' own.

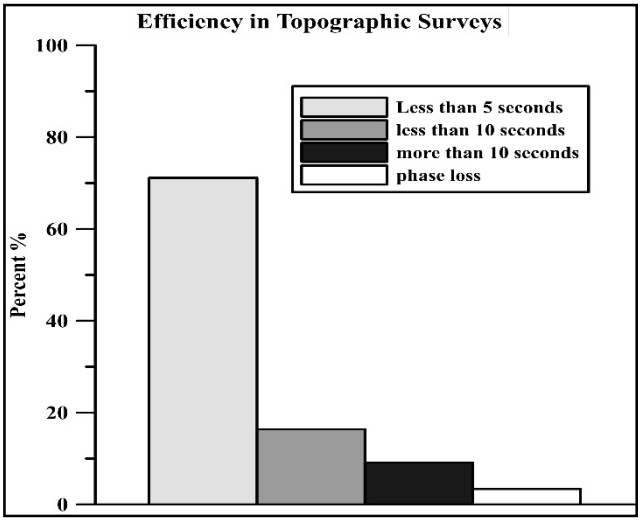


Figure 6. Survey performance
Source: Authors' own

4.4. Survey performance

At this point, the performance of the system is analysed when the topographic survey is carried out. Once the range of the precision and accuracy values is known, the survey is

analysed as a whole: time for sampling a point, quality and outages in the system, errors with coordinates of the points sampled.

Analysing the data for observation times and coordinates of all the surveys carried out, the percentage of points that take a determined time and the average quality of the sampling of all the points can be obtained.

In Fig. 6 the percentage of points that take less than five seconds, less than ten seconds and more than ten seconds can be observed, along with that corresponding to the loss of data with the consequent loss of phase and solution.

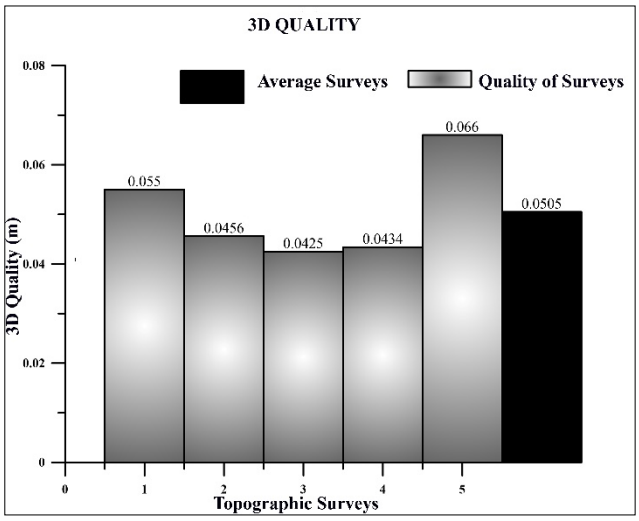


Figure 7. Performance of surveys and 3D quality.
Source: Authors' own.

In Fig. 7, the different surveys are shown on the abscissa axis and the ordinate axis shows the quality in position and height at which the points of all topographic surveys were sampled.

5. Conclusions.

In this work, the services offered by RAP (Andalusia Positioning Network), an Active Local Network located in the Autonomous Community of Andalusia in southern of Spain have been evaluated.

It has been possible to show that the precision and ambiguity resolution times obtained using the permanent GNSS network are similar to those obtained using conventional RTK. The average precision values obtained for the different control points of the East, North and Vertical components are (0.006 - 0,006 - 0,009) m. respectively, Position (3D) 0.012m

If we compare the static method used to obtain the coordinates assigned to the control points, with sampling in (RTK), the accuracy reached in determining said coordinates is high, even though it would probably have been necessary to take a larger number of measurements. The average accuracy values for the six control points, in the horizontal and vertical components are: (0.015 - 0.016) m, respectively. Position (3D) 0.022 m.

The system shows good stability and provides homogeneous solutions, even though the data has been taken at different times and obtained from different reference stations.

In terms of the topographic survey, it is verified that use of an Active Geodetic Network of permanent stations operating continuously is adequate for use in topographic and engineering projects. It offers excellent performance in data sampling, in the acquisition time of same, in the quality of the system and in the processing of data.

References

[1] Rizos, C. and Han, S., Reference station network based RTK System - Concepts & Progress, in 4TH International Symposium on

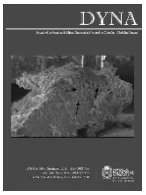
GPS/GNSS, presented at 4th International Symposium ON GPS/GNSS, Wuhan, China, 6−8 November, 2002 .
[2] Wübbena, G., Bagge, A. and Schmitz, M., RTK networks based on Geo+GNSMART concepts, implementation, results, www.geopp.de, in: International Technical Meeting, IONGPS−01, September 11−14, 2001.
[3] Janssen, V., A comparison of the VRS and MAC principles for network RTK. Proceedings of the IGNSS Symposium. Australia, Dec 2009.
[4] Euler, H.J., Keenan, C.R., Zebhauser, C.B. and Wübbena, G., Study of simplified approach in utilizing information from permanent reference station arrays, presented at ION GPS, 2001.
[5] Landau, H., Vollath, U. and Chen, X., Virtual reference station systems, Journal of Global Positioning Systems, 1(2), pp. 137-143, 2002.
[6] Brown, N., Keenan, R., Richter, B. and Troyer, L., Advances in ambiguity resolution for RTK applications using the new RTCM V3.0, Master-Auxiliary messages Leica Geosystems AG, Switzerland Published in proceedings of ION GNSS, Long Beach, CA, September 13-16, 2005.
[7] Wübbena, G., Bagge, A. and Schmitz, M., GNSMART irregularity readings for distance dependent errors, White Paper. July, 2004.
[8] Colombo, O., Brunker, S., Jones, G., Janssen, V. and Rizos, C., Wide-area, sub-decimetre positioning for airborne LiDAR surveys using CORSnet-NSW, in: Proceedings of XXIV FIG International Congress: Facing the Challenges - Building the Capacity, 11-16 April, Sydney, Australia, 2010, pp. 1-20.
[9] Huang, Z., Huang, D., Xu, Z., et al, 3rd International Conference on Environmental Science and Information Application Technology ESIAT 2011, PTC, Book Series: Procedia Environmental Sciences, Part: C, 10, pp. 2498-2504, 2011.
[10] Liu, Z. and Xiong, W., Design of precision fertilization management information system on GPS and GIS, Technologies computer and computing technologies in agriculture PT I, Book series: IFIP, 368, pp. 268-277, 2012.
[11] Freeland, R.S., Buschermohle, M.J., Wilkerson, J.B. and Pierce, J.C., Precision agriculture-assessing virtual and single reference stations, Applied Engineering in Agriculture, 28(6), pp. 913-922, 2012.
[12] Gao, J.-X. and Hu, H., Advanced GNSS technology of mining deformation monitoring. Proceedings of the International Conference on Mining Science & Technology (ICMST2009), Book Series: Procedia Earth and Plantetary Science, 1(2009), 2009, pp. 1081-1088. DOI: 10.1016/j.proeps.2009.09.166
[13] Janssen, V. and Haasdyk, J, Assessment of network RTK performance using CORSnet-NSW, in: Proceedings of the IGNSS Symposium, Sydney, Australia. 15–17 November, 2011.
[14] Edwards, S.J., Clarke, P.J., Penna, N.T. and Goebell, S., An examination of network RTK GPS services in great Britain, Survey Review, 42(316), pp. 107-121, 2010. DOI: 10.1179/003962610X12572516251529
[15] Aponte, J., Meng, X., Dodson, A.H., Moore, T., Hill, C. and Burbidge, M., Quality assessment for a network RTK GPS service in the UK, J. Appl. Geodesy, 3, pp. 25-34, 2009.
[16] Lou, L. and Chen, Y., The precision and accuracy of Shanghai Vs network, in: Observing our Changing Earth, Springer Berlin Heidelberg, 2009, pp. 719-723.
[17] Gordini, C., Kealy, A.N., Grgich, P.M., Hale, M.J. and Gordini, C., Testing and evaluation of a GPS CORS network for real time centimetric positioning–The Victoria GPSnet, in: Proceedings of the IGNSS2006 Symposium, 2006, pp. 17-21.
[18] Garrido, M.S., Giménez, E., de Lacy, M.C. and Gil, A.J., Surveying at the limits of local RTK networks: test results from the perspective of high accuracy users. International Journal of Applied Earth Observation and Geoinformation, 13(2), pp. 256-264, 2011. DOI: 10.1016/j.jag.2010.12.001.
[19] Garrido, M.S., Giménez, E., Armenteros, J.A., Lacy, M.C. and Gil, A.J., Evaluation of NRTK positioning using the RENEP and RAP networks on the southern border region of Portugal and Spain. Acta Geodaetica et Geophysica Hungarica, 47(1), pp. 52-65, 2012
[20] Lenz, E., Networked transport of RTCM via internet protocol (NTRIP) – application and benefit in modern surveying systems, FIG Working Week, Athens, Greece, May 22-27, 2004. Int. paper TS3.2
[21] Berrocoso, M., Páez, R., Jigena, B. and Caturla, C., The RAP net: a geodetic positioning network for Andalusia (south Spain). Riga, Latvia, June 14-17 2006, EUREF Publication No. 16, Mitteilungen des Bundesamtes für Kartographie und Geodäsie, Band 40, pp. 364-368. ICA-UCA.2007

E. Cano-Jódar, is BSC. in Technical Mining Engineer specialised in exploitation of Mines. From 1983 to 1992 he worked for the private company Ferrovial S.A. dedicated to Civil Engineering construction. Civil Servant assigned full time to the corps of Senior University Lecturers, Group A; administrative status: active, by contest; appointment date 07/04/1995. Year 1994/1995, current post. He lectures at the University of Córdoba, Spain, in the Higher Technical School of Belmez, in the degree programmes in civil engineering and energy resources and mining. In 2009 he completed the MSc. in Design and Management of Agro-Industrial Plants. Principal areas of research: active geodetic networks: applications in mining and civil engineering; active geodetic networks: quality control positioning of linear elements; topography; mining cartography and photogrammetry. Coordinator of the degree energy resources and mining, Coordinator of the master in mining engineering.
ORCID. 0000-0002-5036-5564.

M.Sánchez-de la Orden, is university professor in the area of cartographic engineering, geodesy and photogrammetry at the department of graphic and geomatic engineering at the University of Córdoba, Spain. Areas of research: geomatic applications and new sensors (LIDAR air, terrestrial and mobility) for management of agro-forestry and natural resource, teledetection in precision agriculture, photogrammetry applications with unmanned platforms. He has published papers in the international journals Plant & Soil, Weed Science, Agriculture, Ecosystems and Environment, Agronomy for Sustainable Development, Computers and Electronics in Agriculture, and Forest Systems. Management and participation in R&D Projects financed by public tender.
ORCID. 0000-0001-9262-5523

F.J. Mesas-Carrascosa. is BSc. in Eng. in Geodesy and Cartography since 1999, and holds a Dr. in Engineering from the University of Córdoba, Spain awarded in the year 2012. Contracted doctorate professor at the University of Córdoba at the Higher Technical School of Agronomic Engineers. In 2009 he participated as lecturer on a number of Master programmes of the University of Córdoba and the University of Jaén, both in Spain, such as the master in evaluation and management of geographic information or the master in geomatics, teledetection and spatial models applied to forestry management and is currently the co-director of same. He worked as an external consultant for public and private companies from the year 2000 to 2012. His lines of research are those relating to the application of UAV platforms in the energy, agroforestry, civil engineering and heritages sectors as well as the development of applications for mobile devices and the exploitation of open-source sensors and platforms.
ORCID 0000-0002-5674-1292

UNIVERSIDAD NACIONAL DE COLOMBIA
SEDE MEDELLÍN
FACULTAD DE MINAS



DYNA
http://dyna.medellin.unal.edu.co/

Application of OpenFoam solver SettlingFoam to bedload sediment transport analysis

Verónica Carrillo-Serrano & Esteban Pacheco-Tobar

Laboratorio de Hidráulica y Dinámica de Fluidos, Departamento de Ingeniería Civil, Universidad de Cuenca, Cuenca, Ecuador.
veronica.carrillo@ucuenca.edu.ec, esteban.pacheco@ucuenca.edu.ec

Received: August 02nd, 2017. Received in revised form: May 03rd, 2018. Accepted: June 03rd, 2018

Abstract
Sediment transport is an important process for rivers and natural channels. The determination of sediment transport is a very complex process due to the high variability and changing nature of the factors that intervene. As a contribution to the description of this kind of phenomenon and to highlight the problems, the needs and potentials of the numerical approaches, OpenFOAM solver settlingFoam is used to simulate sediment transport in a rectangular channel. The model used constitutes a simplification of a complex procedure based on the application of a single parameter (alpha) to determine the fluid-sediment mixture features. High variability was found between the results from different alpha values. Nevertheless, there is a lack of information to determine the appropriate value of this parameter. However, even though the procedure applied and the results obtained have to be taken as a reference, this study provides valuable criteria for future research of this complex topic.

Keywords: numerical model; sediment transport; mixture theory; turbulence model.

Aplicación del solucionador SettlingFoam de OpenFoam para el análisis del transporte de sedimento de carga de lecho

Resumen
El transporte de sedimento es un proceso importante para ríos naturales, su determinación es un proceso complejo debido a la variabilidad y a la naturaleza cambiante de los factores que intervienen. Como una contribución a la descripción de este fenómeno y para enfatizar los problemas, las necesidades y las potencialidades de los enfoques numéricos, el solucionador settingFoam (OpenFoam) es utilizado para simular el transporte de sedimentos en un canal rectangular. El modelo utilizado constituye una simplificación de basada en la aplicación de un solo parámetro (alpha) para determinar las características de la mezcla fluido-sedimento. Alta variabilidad se reporta en los resultados para diferentes valores de alpha, sin embargo, existe poca información para determinar los valores apropiados para éste parámetro. A pesar de que el procedimiento aplicado y los resultados obtenidos deben ser tomados como referencia, este estudio provee criterios valiosos para la futura investigación de este tema tan complejo.

Palabras clave: modelo numérico; transporte de sedimento; teoría de mezclas; modelo de turbulencia.

1. Introduction

Sediment transport has considerable impact on river processes. It defines river morphology [1] and also has influence on water quality [2]. In North America the water pollution by sediments has an estimated cost of $16 billion per year [3]. Even though sediment transport of fine material $1.56 < d50(mm) < 28.6$ has been studied in detail by [4 -7]. These studies don't apply properly for coarser size sediments. Additionally, the slope plays an important role. The studies developed consider mainly mild slopes [8].

The study of sediment transport in steeper channels with coarse material is a complex process. Continuously changing driving forces, basin sediment production, and river bed conditions such as high gradients and large roughness elements result in high uncertainty in the quantification of sediment transport rates [1,9,10]. The uncertainty reported

How to cite: Carrillo-Serrano, V. and Pacheco-Tobar, E., Application of OpenFoam solver SettlingFoam to bedload sediment transport analysis. DYNA, 85(206), pp. 121-127, September, 2018.

© The author; licensee Universidad Nacional de Colombia.

can reach some orders of magnitude [9,11]. Some equations have been proposed to account for bedload, movement thresholds, and channel roughness of steep channels with coarse material. Nevertheless, it tis concluded that there are more formulae than consistent data to verity them. Besides, no formula is proved to achieve consistent results, and no universal relation has been defines between bedload discharge and hydraulic conditions [12-14. The essence, nature, and physics of sediment transport under these conditions (coarse material and steep channels) make its quantification a difficult process that still needs further investigation to achieve reliable results.

As an initial approach to achieve reliable tools to characterize sediment transport processes, in the present work, a sediment transport numerical model is applied to a study case. The case corresponds to a rectangular steel-glass channel with sediment entrance just at the inlet cross section. Thus, the settling features and transport velocity of a rectangular channel with water and sediment are determined. The main idea of developing the present application is to face the challenges, requirements, and potentialities (for a simple case) of this kind of models in order to project them to a simulation of more complex cases like natural rivers with steep slopes and coarse sediment.

2. Methods

A numerical model that replicates the hydrodynamics of a two-phase (sediment and water) flow is developed to determine the distribution of the two phases along the domain, the sediment transport velocity, and the general flow variables pressure and velocity. The numerical analysis is performed with Open Filed Operation and Manipulation (OpenFOAM), an open source computational fluid dynamics (CFD) software package. It includes built-in applications, but can be used also to create new ones. The applications can be classified as solvers, used to find solutions to specific equations, and as utilities that can be seen as tools for data analysis and manipulation, generally results from the solvers (OpenFOAM 2014). This software is used to solve the Navier-Stokes equations, the governing equations for this problem.

For modeling sediment transport OpenFOAM has a solver called settlingFoam. This model considers the mixture formed by water and sediment as a single phase instead of two separate phases. Considering each phase separately, a proper detail of the flow processes of each individual phase can be obtained. However, in the area where the two phases interact, there are difficulties in simulating the terms of the momentum transfer between the two phases.

The main purpose of this solver is to determine the relative movement between the two phases. The density and pressure of the mixture are respectively defined with the following expressions:

$$\rho_m = \alpha_1\rho_1 + \alpha_2\rho_2, \quad (1)$$

$$P_m = \alpha_1 P_1 + \alpha_2 P_2, \quad (2)$$

The center velocity of the mixture volume is defined as follows.

$$v_m = \frac{\alpha_1\rho_1 v_1 + \alpha_2\rho_2 v_2}{\rho_m}, \quad (3)$$

The governing equations for the mixture flow, including the previous relations, are defined with the next expressions:

Mixture Continuity Equation,

$$\frac{\partial \rho_m}{\partial t} + \nabla.(\rho_m u_m) = 0, \quad (4)$$

Mixture Momentum Equation,

$$\frac{\partial \rho_m u_m}{\partial t} + \nabla.(\rho_m u_m u_m) = -\nabla.P_m + [\tau + \tau^t] - \nabla.\left(\frac{\alpha_d}{1-\alpha_d}\frac{\rho_c\rho_d}{\rho_m} v_{dj} v_{dj}\right) + \rho_m g + M_m, \quad (5)$$

Drift Equation,

$$\frac{\partial \alpha_d}{\partial t} + \nabla.(\alpha_d v_m) = -\nabla.\left(\frac{\alpha_d\rho_c}{\rho_m} v_{dj}\right) + \nabla.\Gamma\nabla\alpha_d, \quad (6)$$

Where, α_d represents the dispersed phase volume fraction. P_m, ρ_m, and u_m account for the average flow properties and v_{dj} for the dispersion phase drift velocity. Finally, Γ is the diffusion coefficient composed by the molecular and turbulent viscosity.

Since the flow features of natural steep channels correspond to turbulent flow, the direct solution of the governing equations is not possible at a reasonable computational cost and simulation time. The resolution required by a DNS of isotropic turbulence that incorporates the viscous dissipation can be projected as four times the Kolmogorov length scale. Even for the smallest length scale the necessary mesh points is proportional to $Re^{9/4}$. In open channel flow the resolution requirement is also dependent on the Reynolds number Re. It can be estimated as $Nxyz = 2x10^6(Re/300)^{2/7}$. Moreover, to solve the smallest eddies adequately the time step does not have to carry a fluid particle further than one cell [15]. Consequently, time step has to be decreased if cell size is decreased. Even for simple laminar cases, direct numerical simulations (DNS) have high costs [16]. A DNS is the most accurate, but even for low Reynolds number cases it has a high computational cost. It is impossible with the available tools to obtain a DNS for a complex geometry. Therefore, an alternative that balances accuracy and computational cost must be used [17].

2.1. Turbulence approach

To solve the Reynolds averaged Navier-Stokes equation, (RANS) two general categories can be applied. The first category, known as the eddy viscosity models, express the components of the Reynolds stress tensor as functions of the gradients of the mean velocity. These models can be classified in turn in isotropic (linear) or non-isotropic (non-linear), depending on which constitutive turbulence law they use. Additionally, depending on the procedure employed to determine the eddy viscosity, these models can be algebraic or differential. The second category depends on Second Moment Closure (SMC) models or Reynolds-Stress Transport (RST) models. For these types of models, the modelled solutions of RST equations are the components of the Reynolds stresses required to close the RANS [18].

2.2. Isotropic eddy viscosity models

The eddy-viscosity concept of Boussinesq is the base of most of the turbulence models. It assumes that the turbulence shear stresses are proportional to the main velocity gradient. Eddy-viscosity models express eddy viscosity v_t as the product of a turbulence length scale, l_t, and a turbulence velocity scale, u_t.

$$v_t = l_t u_t, \tag{7}$$

As a function of the way in which these scales are calculated, the models can be divided in three kinds: zero-equation or algebraic eddy-viscosity models, one-equation models, and two-equation models.

2.3. Two-equation models

These models use one PDE (partial differential equation) for the length scale and one PDE for the velocity scale [18]. These models mostly use the same transport equation for the Turbulence Kinetic Energy (TKE) to calculate a local turbulence velocity scale ($u_t \approx k^{(1/2)}$) [15]. The most common two-equation models are the k-ε model and the k-ω models.

2.4. The k-ε model

This model utilizes an equation for the turbulent energy dissipation $\varepsilon \sim k^{(3/2)}/L$, instead of the direct determination of the length scales, L, together with the kinetic energy k equation [17].

The semi-empirical k-equation and ε-equation are expressed as follows:

For the transport of the kinetic energy k:

$$\frac{\partial k}{\partial t} + \overline{u_i}\frac{\partial k}{\partial x_i} = \frac{\partial}{\partial x_i}\left(\frac{v_t}{\sigma_k}\frac{\partial k}{\partial x_i}\right) + v_t\left(\frac{\partial \overline{u_i}}{\partial x_j} + \frac{\partial \overline{u_j}}{\partial x_i}\right)\frac{\partial \overline{u_i}}{\partial x_j} - \varepsilon, \tag{8}$$

The terms in equation (8), from left to right, correspond to rate of change, convective transport, diffusive transport, production by shear, and dissipation.

For the transport of the dissipation rate ε:

$$\frac{\partial \varepsilon}{\partial t} + \overline{u_i}\frac{\partial \varepsilon}{\partial x_i} = \frac{\partial}{\partial x_i}\left(\frac{v_t}{\sigma_\varepsilon}\frac{\partial \varepsilon}{\partial x_i}\right) + c_{1\varepsilon}\frac{\varepsilon}{k}P - c_{2\varepsilon}\frac{\varepsilon^2}{k}, \tag{9}$$

The terms in equation (9), from left to right, correspond to rate of change, convective transport, diffusive transport, generation-destruction,

$$P = v_t\left(\frac{\partial \overline{u_i}}{\partial x_j} + \frac{\partial \overline{u_j}}{\partial x_i}\right)\frac{\partial \overline{u_i}}{\partial x_j}, \tag{10}$$

where, P is the generation term of the turbulent kinetic energy, and $c_{1\varepsilon}$, $c_{2\varepsilon}$, σ_ε, c_μ are empirical constants.

Turbulent eddy viscosity is then calculated when k and ε have been solved with the Prandtl-Kolmogorov expression [17].

$$v_t = c_\mu\left(\frac{k^2}{\varepsilon}\right), \tag{11}$$

2.5. Domain

The domain chosen for this study corresponds to a rectangular channel 30 cm wide by 45 cm high by 6 m long. As a prismatic small dimensions channel, the flow will be considered just in two dimensions (height and length). The two phases interaction simulated in settlingfoam are the fluid and sediment phase, established as the dispersed phase.

2.6. Boundary conditions

For the flow in a rectangular channel with the dimensions presented above, the boundary conditions include: two walls (upper and lower), inlet, and outlet. One velocity value was given for the inlet and walls. For the lower wall the non-slip condition (zero velocity) is set. The upper wall was given a slip condition. Outlet velocity is calculated. Furthermore, zero differential pressure is assigned to the outlet. For the walls and inlet, pressure is calculated.

Velocity and pressure were established based on laboratory conditions; k and ε were determined from the theory developed for turbulence models [19]. Here, the main relations used to determine the boundary conditions are presented.

$$k = \frac{3}{2}(u \cdot I)^2, \tag{12}$$

$$I = 0.16{R_{eo}}^{-1/8}, \tag{13}$$

$$\varepsilon = C_\mu \frac{k^{3/2}}{L}, \tag{14}$$

$$L = 0.038R, \tag{15}$$

where, u represents the main channel velocity, I is the turbulence intensity, R_{eo} is the jet Reynolds number, L represents the length scale, and R is the hydraulic radius.

Three sediment volume fractions are simulated. There is not any guide to set the alpha (α_d) volume as a function of the sediment conditions. Therefore, values of alpha corresponding to 1%, 0.1% and 0.01% of sediment are simulated to determine the effect of this parameter in the final solution.

2.7. Mesh

The domain is divided in uniform discrete cells of 0.01x0.01m, giving a total of 27,000 cells in the entire domain.

2.8. Schemes

The numerical method used by OpenFOAM is the finite volume method. For the time operator the Euller scheme is used. The Gauss linear scheme is used for the gradient and divergence operators. For the Laplacian operator, the Gauss linear corrected scheme is applied. Additionally, the interpolation scheme is set to linear. All of the schemes used have second-order accuracy [20]. Therefore, the simulations are considered second-order accurate. To verify solution's convergence two parameters are analyzed. First, the residuals for the pressure, velocity and alpha equations are verified to drop to low values. The residuals are obtained from the absolute difference of the solution between the

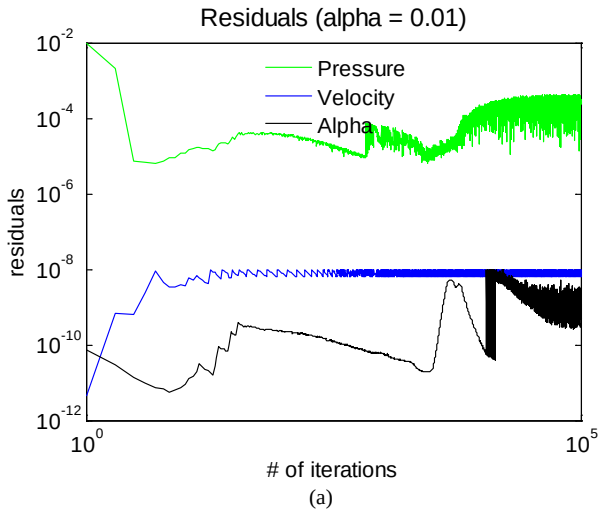
n^{th} and $(n-1)^{th}$. Additionally, change of the solution (alpha, velocity, and pressure) is tracked throughout the entire simulation to ratify that a steady-state solution has been achieved. All the simulations comprised 100,000 iterations. The final time corresponds to 2000s with a variable time step (between 0.01s).

3. Results

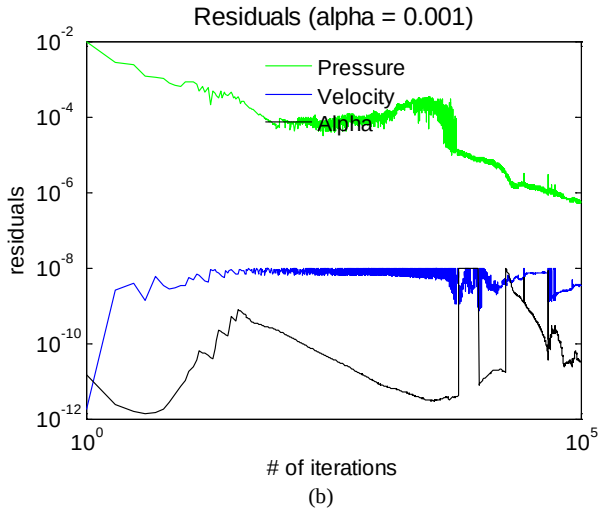
As stated previously, some scenarios are considered to determine the influence of the parameter alpha and also to account for possible circumstances that may arise in the field. Summarizing, the simulations are performed with three different values of alpha: 0.01, 0.001, and 0.0001.

3.1. Residuals

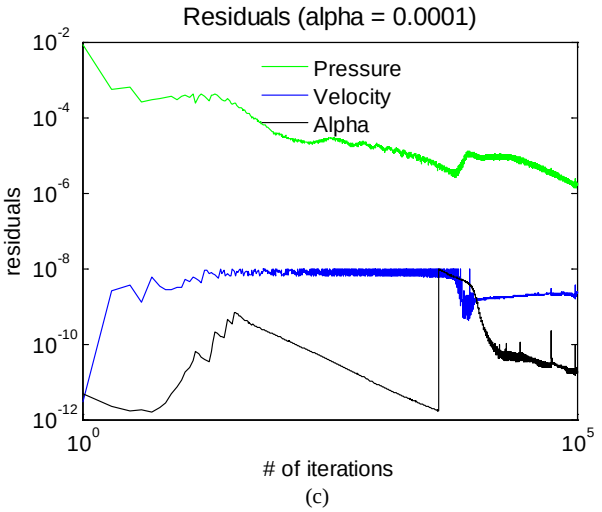
The convergence criteria are verified with the residuals from the pressure, velocity and alpha equation. In Fig. 1 (a), (b) and (c) the residuals are presented for alpha = 0.01, 0.001, and 0.0001 respectively. As can be seen in the figures, the highest residuals correspond to pressure in all three cases. Comparing the different alpha values, the highest residuals correspond to alpha of 0.01.



(a)



(b)



(c)

Figure 1. Residuals of pressure, velocity, and alpha equations (a) $\alpha_d = 0.01$, (b) $\alpha_d = 0.001$, and (c) $\alpha_d = 0.0001$
Source: The authors.

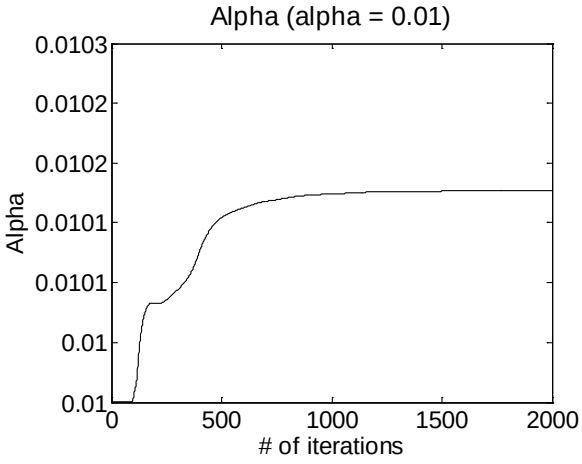
Smaller residuals are obtained with small alpha values. This might indicate that small alpha values produce more stable solutions. For pressure, the residuals decrease two orders of magnitude when alpha decreases one order of magnitude. Similarly, residuals decrease two orders of magnitude when alpha decreases two orders of magnitude. For velocity, the residuals practically maintain their value for all alpha values simulated. A slight diminution is reported for the two smaller alpha values. However, considering the low value of velocity residuals this reduction is considered as non-significant. Alpha equations residuals are the lowest reported values. For the highest alpha value the residuals ranges from 10^{-8} to 10^{-10}. For the two lower alpha values, residuals fall below 10^{-10}. As observed alpha value adopted has considerable impact on the convergence of the solution.

3.2. Monitor point

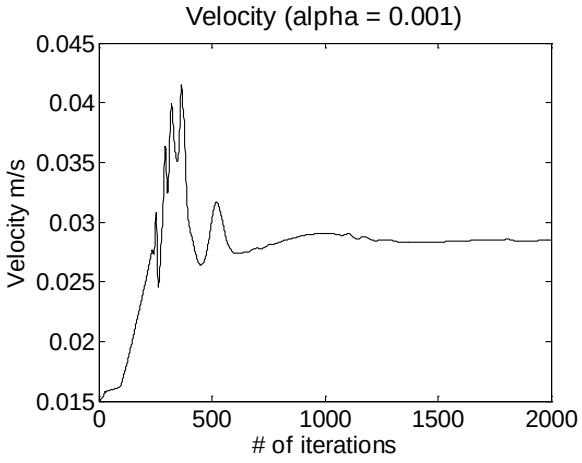
The change in pressure, velocity, and alpha at a selected location (point: 3, 0.15) was monitored over the course of the simulation.

The results presented in Fig. 2 correspond to the parameters analyzed as follows. Fig. 2 (a) presents the alpha variation in the case of $\alpha_d = 0.01$. Fig. 2 (b) details pressure variation for $\alpha_d = 0.001$, Finally, Fig. 2 (c) shows the variation of the velocity for $\alpha_d = 0.0001$.

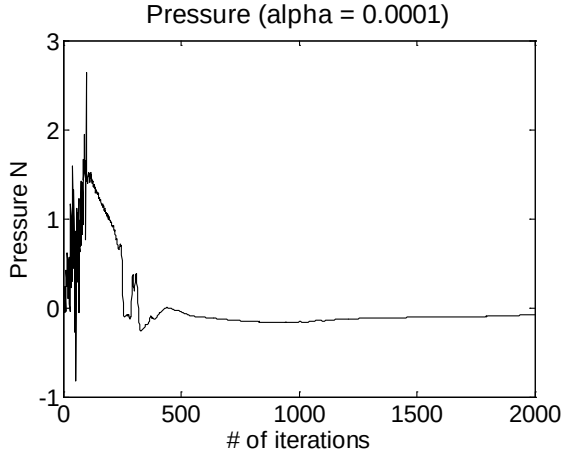
Considering Fig. 2, the following can be reported. The pressure solution for $\alpha_d = 0.01$ does not reach a constant value. However, the variation registered is small. This is in accordance with the small values reported for the residuals. In the case of alpha ($\alpha_d = 0.001$), the constant values is reached around the time 1200s. For velocity and $\alpha_d = 0.0001$, the solution remains constant after the time 1500s. For all simulations (three alpha values), similar characteristics are obtained. In Fig.2, a representative case of each parameter is presented.



(a)



(b)



(c)

Figure 2. Change in the solution over time (a) alpha, $\alpha_d = 0.01$, (b) velocity, $\alpha_d = 0.001$, and (c) pressure, $\alpha_d = 0.0001$
Source: The authors.

3.3. *Alpha*

The alpha variation around the whole domain is presented in Fig. 3 for all three values of alpha considered. As can be seen in the figure, the data scale for (a) and (b) are the same. For (c) the scale is reduced to adjust the figure to the values of that case. Due to the high value of alpha in (a) the dispersed phase (sediment phase) is filling almost the entire domain. Being as the inflow of sediment is permanent during the simulation and the high sediment concentration, in this case the sediment phase occupies a high percentage of the channel.

In Fig. 3 (b), ($\alpha_d = 0.001$) it can be seen that sediment has settled almost entirely approximately the 75% of the domain. The first quarter of the domain contains a higher amount of sediment. Nevertheless, this amount is smaller than the one settled in the channel bottom. For Fig. 3 (c) the reported results are similar to those obtained in Fig. 3 (b); the only difference is the absolute value of alpha.

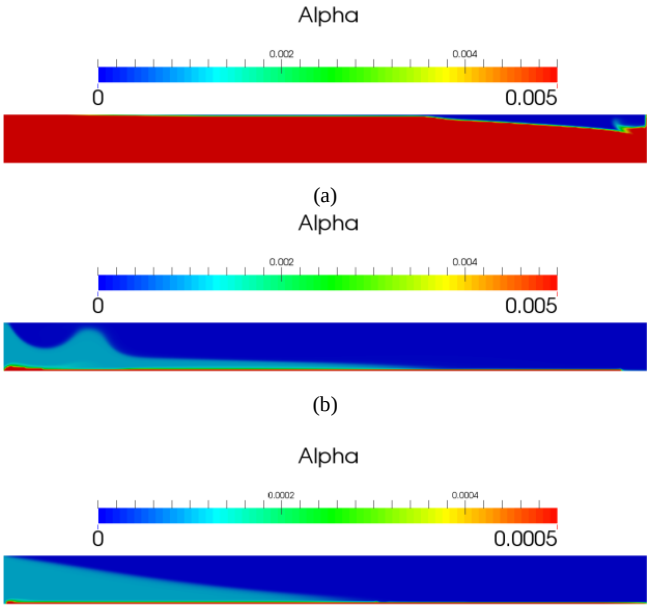
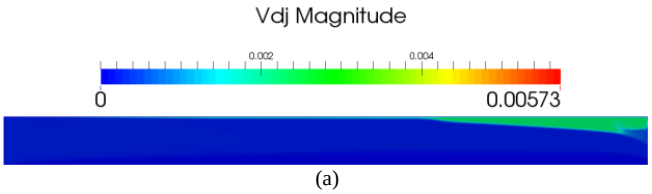


Figure 3. Variation of alpha in the domain (a) $\alpha_d = 0.01$, (b) $\alpha_d = 0.001$, and (c) $\alpha_d = 0.0001$
Source: The authors.

3.4. *Drift velocity*

As can be observed in Fig. 4 (a), (b), and (c), the drift velocity shows exact correspondence to the alpha values. High velocity values correspond to small alpha values and small velocities match with high alpha values. Namely, the sediment phase will be dragged by smaller velocities than the fluid phase.



(a)

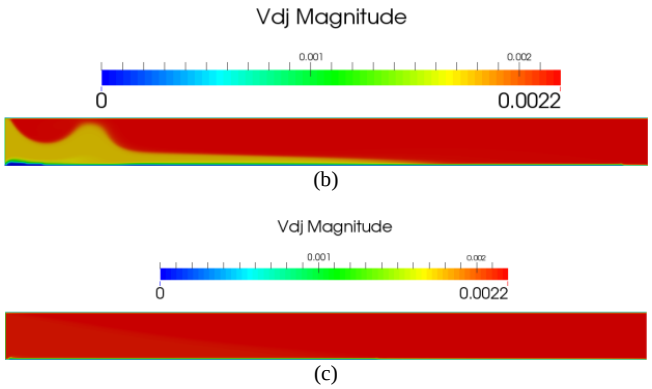


Figure 4. Variation of drift velocity in the domain (a) $\alpha_d = 0.01$, (b) $\alpha_d = 0.001$, and (c) $\alpha_d = 0.0001$
Source: The authors.

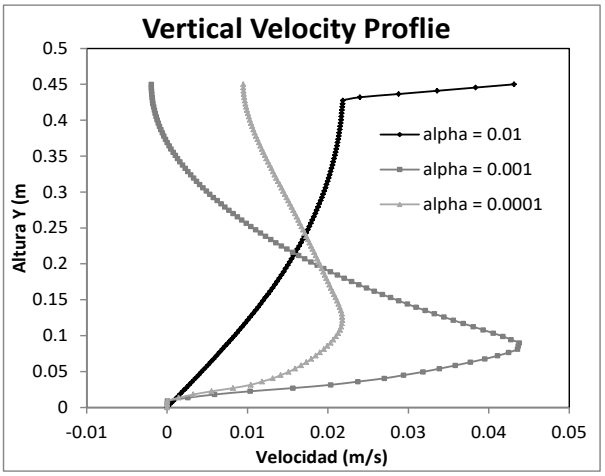


Figure 6. Vertical velocity profiles
Source: The authors.

3.5. Velocity and velocity vectors

As presented in Fig. 5(a), (b), and (c), flow velocity presents a different pattern for αd = 0.001. For high and low alpha the flow configuration is similar. The flow domain, for intermediate alpha, presents recirculation zones following the pattern defined for alpha changes replicating what it is observed with drift velocity.

3.6. Vertical velocity profile

Vertical velocity profiles were obtained at the middle of the domain. The results are presented in Fig. 6. As can be observed, different velocity profiles were obtained with the different alpha values. The maximum flow velocity is reported for α_d = 0.001 with a value of 0.044 m/s. The dissimilar behavior observed in the previous figures is also registered for the velocity profiles for each value of alpha. For $\alpha_d = 0.01$, a severe increase in the velocity is presented in the top of the domain. This can be caused for the change between sediment phase and boundary condition in a small distance (one cell).

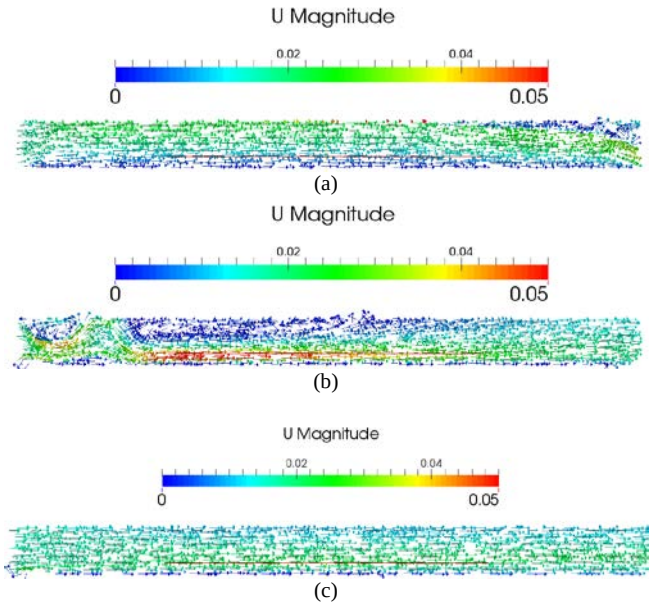


Figure 5. Variation of flow velocity in the domain (a) $\alpha_d = 0.01$, (b) $\alpha_d = 0.001$, and (c) $\alpha_d = 0.0001$
Source: The authors.

4. Conclusions

A numerical model was set to analyze sediment transport processes in a rectangular channel. The numerical model is based on mixtures theory. It constitutes a simple approach to a very complex problem. Well tested and strictly proven procedures like the discrete numerical solution of the Navier-Stokes equations and turbulence models were used in the present simulations. However, a simple method, that just considers a single parameter (alpha) to characterize the mixture, is applied to intend to replicate the natural process. As can be seen in the results, a considerable variability is found with the variation of alpha. Parameters such as flow and drift velocity report a dependence on the alpha value. Specifically, as alpha decreases the channel transport capacity appears to increase (drift velocity increases). Flow velocity presents a different behavior for the medium alpha used. With slight differences, the highest and lowest alphas show similar trends. Additionally, as has been pointed alpha has influence even in the stability and convergence of the equation's solution. Conversely, no hint is available for the correct determination of this parameter. To obtain accurate results, a calibration and validation of the final alpha value must be performed. Thereby, a methodology can be stablished to define the correct alpha value.

This work and the application of settlingFoam can be considered as a first simple approach to the numerical simulation of sediment transport processes. The methodology applied here can be taken as the very first step to achieve a more realistic simulation. The simplicity found in the procedure can lead to the reduction in applicability of the method just for simple cases and the results as a reference of the real values. To set a more realistic numerical model an extensive investigation must be accomplished for both field conditions and model-required parameters.

References

[1] López, R., Vericat, D. and Batalla, R.J., Evaluation of bed load transport formulae in a large regulated gravel bed river: the lower Ebro (NE Iberian Peninsula), J. Hydrol., 510, pp. 164-181, 2014.

[2] Julien, P.Y., Erosion and sedimentation, 2nd ed. Cambridge; New York: Cambridge University Press, 2010.

[3] Pons, L., Helping states slow sediment movement: a high-tech approach to clean water act sediment requirements, Agricultural Research Magazine, 51(12), pp. 12-14, 2003.

[4] DuBoys, M.P., Etudes du regime du Rhone et de l'action exercee par les eaux sur un lit a fond de graviers indefiniment affouillable, Ann. Ponts Chaussees, 18, pp. 141-195, 1879.

[5] Einstein, H.A., Formulas for the transportation of bed load, Trans ASCE, 107, pp. 561-573, 1942.

[6] Meyer-Peter, E. and Müller, R., Formulas for bed-load transport, Proc 2nd Meet. IAHR Stockh., pp. 39-64, 1948.

[7] Shields, Applicatioin of similarity principles and turbulence research to bed-load movement, California Institute of Technology, Pasadena, CA, 1936.

[8] Lamb, M.P., Dietrich, W.E. and Venditti, J.G., Is the critical Shields stress for incipient sediment motion dependent on channel-bed slope?, J. Geophys. Res., 113(F2), May, 2008.

[9] Carling, P.A. and Reader, N.A. Structure, composition and bulk properties of upland stream gravels, Earth Surf. Process. Landf., 7(4), pp. 349-365, Jul. 1982.

[10] Papanicolaou, N., Bdour, A. and Wicklein, E., One-dimensional hydrodynamic/sediment transport model applicable to steep mountain streams, J. Hydraul. Res., 42(4), pp. 357-375, Jan. 2004.

[11] Bathurst, J.C., Effect of coarse surface layer on bed-load transport, J. Hydraul. Eng., 133(11), pp. 1192-1205, Nov. 2007.

[12] Gomez B. and Church, M., An assessment of bed load sediment transport formulae for gravel bed rivers, Water Resour. Res., 25(6), pp. 1161-1186, Jun. 1989.

[13] Habersack H.M. and Laronne, J.B., Evaluation and improvement of bed load discharge formulas based on Helley-Smith sampling in an Alpine Gravel Bed River, J. Hydraul. Eng., 128(5), pp. 484-499, May 2002.

[14] Martin, Y., Evaluation of bed load transport formulae using field evidence from the Vedder River, British Columbia, Geomorphology, 53(1-2), pp. 75-95, Jul. 2003.

[15] Wilcox, D.C., Turbulence modeling for CFD, 3rd ed. La Cãnada, Calif: DCW Industries, 2006.

[16] Reynolds, W.C., The potential and limitations of direct and large eddy simulations, in whither turbulence?, Lumley, J.L., Ed. Turbulence at the Crossroads, Springer, Berlin, Heidelberg, 1990, pp. 313-343.

[17] Sturm, T.W. Open channel hydraulics, 2nd ed. Dubuque, IA: McGraw-Hill, 2010.

[18] Bates, P.D., Lane, S.N. and Ferguson, R.I., Eds., Computational fluid dynamics: applications in environmental hydraulics. Hoboken, NJ: J. Wiley, 2005.

[19] Menter, F.R. Two-equation eddy-viscosity turbulence models for engineering applications, AIAA J., 32(8), pp. 1598-1605, Aug. 1994.

[20] OpenVFOAM, OpenVFOAM. The open source CFD toolbox, user guide, 2014.

V.M. Carrillo-Serrano, received the BSc. Eng in Civil Engineering in 2009, from Universidad de Cuenca, Cuenca, Ecuador, the MSc. degree in Civil Engineering in 2015 from Washington State University, Pullman, Washington, USA. From 2009 to 2013, she worked in the Soil and Water Management Program (PROMAS) of the Universidad de Cuenca as part of the research staff, developing projects in areas such as irrigation, hydraulic structures design, and hydraulic physic and numerical models. From 2015 to the present, she is professor in the Civil Engineering Department, School of Engineering, Universidad de Cuenca, Ecuador. Her main research interests include river hydraulics, sediment transport, hydraulics numerical simulation of structures and natural channels.
ORCID: 0000-0003-3420-0855

E.A. Pacheco-Tobar, received the BSc. Eng in Civil Engineering in 1996 from Universidad de Cuenca, Ecuador, the MSc. degree in Water and Soil Management and Conservation from Universidad de Cuenca and Katholieke Universiteit Leuven K.U. Leuven in 2004. He performed his pre-doctoral program in the Faculty of Science, Katholieke Universiteit Leuven K.U. Leuven in 2008-2009. He has held directive positions such as director of the Civil Engineering program and Graduate Department Director in Universidad de Cuenca, Ecuador. Currently he is full professor of the Engineering Faculty. He is part of the Civil Engineering Department as a member of the Water Engineering Group where projects are executed in the areas of River Hydraulics and Hydraulic structures in mountain areas. Through the Laboratory of Hydraulics & Fluid Dynamics of the Department of Civil Engineering, he participates in several studies related to reduced scale physical modeling in hydroelectric generation projects, river hydraulics and irrigation and drainage engineering.
ORCID: 0000-0001-9292-7193



UNIVERSIDAD NACIONAL DE COLOMBIA
SEDE MEDELLÍN
FACULTAD DE MINAS

Área Curricular de Medio Ambiente

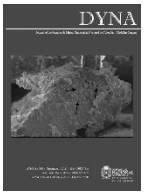
Oferta de Posgrados

Especialización en Aprovechamiento de Recursos Hidráulicos
Especialización en Gestión Ambiental
Maestría en Ingeniería Recursos Hidráulicos
Maestría en Medio Ambiente y Desarrollo
Doctorado en Ingeniería - Recursos Hidráulicos
Doctorado Interinstitucional en Ciencias del Mar

Mayor información:

E-mail: acma_med@unal.edu.co
Teléfono: (57-4) 425 5105

UNIVERSIDAD NACIONAL DE COLOMBIA
SEDE MEDELLÍN
FACULTAD DE MINAS



DYNA
http://dyna.medellin.unal.edu.co/

Encapsulation of β-carotene extracted from peach palm residues: a stability study using two spray-dried processes

Luis Eduardo Ordoñez-Santos [a], Jader Martínez-Girón [a, b] & Rafael Humberto Villamizar-Vargas [c]

[a] *Facultad de Ingeniería y Administración, Departamento de Ingeniería, Universidad Nacional de Colombia-Sede Palmira, Palmira, Colombia. leordonezs@unal.edu.co*
[b] *Facultad de Ingeniería, Universidad del Valle-Sede Palmira, Palmira, Colombia. jader.martinez@correounivalle.edu.co*
[c] *Facultad de Ingenierías, Universidad La Gran Colombia-Seccional Armenia, Armenia, Colombia. villamizarvarrafael@miugca.edu.co*

Received: October 02th, 2017. Received in revised form: January 16th, 2018. Accepted: May 16th, 2018

Abstract
This study aimed to evaluate the stability of β-carotene from peach palm residues (Bactris gasipaes) when using two processes of encapsulation with spray drying: The first process (MC1) consisted of a mixture of maltodextrin: gum arabic as the wall material, an inlet temperature of 160°C, an outlet temperature of 70 °C, flow rate of 12.6 mL/min; the second process (MC2) used gelatin, sugar and lecithin, an inlet temperature of 100°C, an outlet temperature of 65°C, and a flow rate of 3.13 mL/min. The microcapsules (MC1 and MC2) were subjected to physicochemical tests, evaluating their stability for temperature, light, pH and oxygen, as compared to a control of β-carotene extracted from sunflower oil (RCSO). The results indicated that the microcapsules obtained from process (MC2) had better β-carotene stability ($p < 0.05$), as compared to MC1 and RCSO, with higher levels of retention (88.24%), temperature (90.11%), light (67.36%), pH (84.21%) and oxygen (79.23%).

Keywords: peel; ultrasound; sunflower oil; gelatin; morphology

Encapsulación de β-caroteno extraído a partir de residuos de chontaduro: un estudio de estabilidad usando dos procesos de secado por atomización

Resumen
El objetivo de este estudio fue evaluar la estabilidad del β-caroteno procedente de residuos de chontaduro (Bactris gasipaes), mediante dos procesos de encapsulación por secado spray: El primer proceso (MC1) consistió en una mezcla de maltodextrina: goma arábiga como materiales de pared, temperatura de entrada 160 °C, salida 70°C, caudal 12.6 mL/min y en el segundo proceso (MC2) se usó gelatina, azúcar y lecitina, temperatura de entrada 100 °C, salida 65°C, caudal 3.13 mL/min . Las microcápsulas obtenidas de (MC1 y MC2) fueron sometidas a pruebas fisicoquímicas, evaluando su estabilidad ante la temperatura, la luz, pH y oxígeno frente a un control de β-caroteno extraído en aceite de girasol (RCSO). Los resultados indicaron que las microcápsulas obtenidas del proceso (MC2) presentaron una mejor estabilidad de β-caroteno ($p < 0,05$) frente a MC1 y RCSO, al presentar mayores niveles de retención (88.24%), temperatura (90.11%), luz (67.36%), pH (84.21%) y oxígeno 79.23%).

Palabras clave: epicarpio; ultrasonido; aceite de girasol; gelatina; morfología

1. Introduction

Peach palm, pejibaye or chontaduro (*Bactris gasipaes*) is an important fruit, source of carotenoids in the diet of the rural and urban population of tropical America, and is also exported to ethnic markets in USA Rojas-Garbanzo et al. [1]. The yellow orange color of the peach palm pulp is due to the presence of carotenoids (1.1 mg/100g – 22.3 mg/100g) Jatunov et al. [2]. Peach palm fruits are traditionally cooked or turned into flour, preserves, marmalade, or fermented beverages Graefe et al. [3]. When processed, 19% of the fruit becomes residue, mainly the peel and seeds, which are currently not valued and represent an environmental problem. Babbar et al. [4] reported that an effective option for

How to cite: Ordoñez-Santos, L.E., Martínez-Girón, J., and Villamizar-Vargas, R.H., Encapsulation of β-carotene extracted from peach palm residues: a stability study using two spray-dried processes. DYNA, 85(206), pp. 128-134, September, 2018.

© The author; licensee Universidad Nacional de Colombia.

managing fruit residue is the recovery of phytochemicals/bioactive compounds from the fruit residue, which can be used in the food, cosmetic and pharmaceutical industries. Woodside et al. [5] reported that the carotenoids have been proposed to promote health through their antioxidant and anti-inflammatory activity and ability to enhance immune response, with such biological activity being linked to an ability to prevent chronic diseases, such as cancer and cardiovascular disease (CVD), in preserving visual function and protecting against age-related macular degeneration (AMD). In addition to these beneficial effects on health, β-carotene (E160aii), bixin (E160b), paprika extract (E160c), lycopene (E160d) and β-Apo-8´carotenal (E160e), have been broadly used in the food, cosmetic, and pharmaceutical industries.

Autoxidation of carotenoids is one of the factors that significantly restrict the incorporation of carotenoids in processed products Qian et al. [6]; Hojjati et al. [7] comment that carotenoids are unstable and sensitive to light, heat, or oxidants during food processing and storage due to the presence of highly conjugated double bonds in its structure and it loses its color as well as its bioactivity. Microencapsulation is an effective technique that preserves bioactive compounds, such as carotenoids, by providing a protective barrier against the action of oxygen, light, temperature and water vapor Pu et al. [8]. Among the techniques of microencapsulation, such as spray-cooling, spray-drying, freeze-drying, centrifugal extrusion, molecular inclusion and emulsion freeze-drying, however, the spray drying method is most applicable, by offering low installation costs, short drying time, continuous processes, and rapid scaling to industrial level Wang et al. [9]. Different wall materials as β-cyclodextrin, cassava starch, sodium caseinate, lactose, gum Arabic, isolated soy protein and gelatin have been used in the microencapsulation of carotenoids by Spray Drying Pu et al. [8]; Wang et al. [9]; Nunes & Mercadante, [10]; Quek et al. [11]; Rascón et al. [12], Guadarrama-Lezama et al. [13], and Other studies report that carotenoids microencapsulated by spray drying, get a long shelf life, and protection against oxidation Bustos-Garza et al. [14]; Domínguez-Cañedo et al. [15]; Lim et al. [16] and Montero et al. [17]. However, in the literature no reports relating to the microencapsulation of carotenoids present in the fruit of peach palm fruit (*Bactris gasipaes*) by-products, and stability studies of the microcapsule against the action of temperature, light, pH and oxygen. Taking into account all of the above, this study aimed to evaluate the stability of β-carotene extracted from dry residues of peach palm epicarp (peel) (Bactris gasipaes) using two encapsulation processes in order to determine which of the two microencapsulates obtained from each of the processes using spray drying had the best conditions of stability for temperature, light, pH and oxygen for β-carotenes in lipid extracts.

2. Materials and methods

2.1. Materials

Flour from cooked peach palm fruit residue (epicarp) from Palmira (Colombia), dextrose equivalent (DE) 16 maltodextrin (Tecnas), gum arabic especially for spray drying (Sigma-Aldrich), 4X powdered sugar (Colombina), powdered gelatin (Levapan), food grade Solec F lecithin (Cimpa), edible sunflower oil (Lloreda S.A), ethanol (Merck), hexane (Merck), sodium hydroxide (Merck), 98% sulfuric acid (JT Baker), regulating pH buffer solutions (Panreac), silica gel (Yequim), high purity 95-99% oxygen gas (Cryogas), and high purity 95-99% nitrogen gas (Cryogas).

2.2. Obtaining β-carotene extract

Dried peel preparation was conducted as the report by Ordóñez-Santos et al. [18]. Peach palm fruit (Bactris gasipaes) peel was separated with a knife, peel was oven dried at 60 °C until the moisture level was constant (11 % w/w), and reduced to particle size of 0.25 mm, using a sifter (Advantech DT-168, USA). The carotenoid pigments in the flour were extracted with sonification in the lipid phase (3.80 mg of peach palm residue flour per mL of sunflower oil) at 39.96°C, for 27 min using an ultrasonic bath (Ultrasonic Cleaner DC, Hagavishst, Israel): 300 × 155 × 150 mm, 150 W input power, 40 kHz frequency and 6 L capacity. The ultrasonic-assisted extraction of β-carotene in this study correspond to the optimization registered to evaluate the factors solid to solvent ratio (0.51 to 5.9 mg/mL), temperature (28-62 °C) and extraction time (13-47 min). The extract was identified in the study as released carotenoids in sunflower oil (RCSO) that corresponded to the nucleus of the microcapsules. The refined sunflower oil had a peroxide index below 1 Meq O2/ kg and an acidity percentage (oleic) under 0.30%.

2.3. Emulsification and spray drying process

The first encapsulation process (MC1) was carried out according to the method proposed by Guadarrama-Lezama et al. [13] with some modifications, and the second process (MC2) was carried out according to the proposal of Robert et al. [19] with some modifications. DE 16 maltodextrin and gum arabic were used in MC1. The percentages were: 7.58% DE 16 maltodextrin, 7.58% gum arabic, 75.76% water, and 9.09% RCSO. In MC2, the wall materials were powdered gelatin, 4X powdered sugar and commercial grade lecithin. The percentages were: 2.03% powdered gelatin, 1.77% 4X powdered sugar, 0.15% lecithin, 94.28% water and 1.77% RCSO. All of the solid wall materials were hydrated at 60°C in order to release the polymeric material. Each of the wall materials were mixed with RCSO to achieve the required emulsion with an Ultraturrax (T18 IKA Janke and Kunkel, Germany) at 10,000 rpm for 5 min, keeping the temperature below 30°C. The spray drying process was carried out with a YC-105 Spray Dryer (Pilotech Instrument Co., Ltd., Shanghai, China) equipped with a 150 cm x 80 cm spray drying chamber, a cyclone separator, hot air fan and vent fan. The spray drying process variables for MC1 included an injection flow of 12.6 (mL/min), inlet temperature of 160 ± 2 (°C), outlet temperature of 70 ± 2 (°C). In MC2, the process variables included a rate of injection of 3.13 (mL/min), inlet temperature of 100 ± 5 (°C), and outlet temperature of 65 ± 5 (°C).

2.4. Physicochemical characteristics and properties of the microcapsules

The percentage of carotenoid pigment retention was calculated with the eq. (1) reported by Wang et al. [9].

$$\% R = \frac{C_a}{C_b} \times 100 \qquad (1)$$

Where C_b refers to the content of carotenoid pigments in the sample before treatment (emulsion) and C_a refers to the content of carotenoid pigments in the sample after treatment (powder obtained).

The percentage of encapsulation efficiency was calculated with the eq. (2) reported by Alishahi et al. [20] and Rutz et al. [21]

$$\%EE = \frac{TC - TO}{TC} \times 100 \qquad (2)$$

Where TC refers to the β-carotene in the microcapsule and TO refers to the not encapsulated β-carotene in the oil.

The encapsulation yield was determined with eq. (3) as reported by Rutz et al. [21] and Jun-Xia et al. [22].

$$\% Y = \frac{WF}{M1 + M2 + M3 + N} \times 100 \qquad (3)$$

The yield was calculated based on the solid contents of the wall materials: M1 = weight of the maltodextrin or gelatin according to the MC1 and MC2 formulations, respectively; M2 = weight of gum Arabic or 4X powdered sugar according to the CM1 and CM2 formulations, respectively; and M3 = the weight of lecithin in formulation CM2, N = the weight of the core used for the microencapsulation, and WF = final weight of the microparticles.

The water activity of the microcapsules was determined using an Aqualab (Decagon Devices, Model 4 TE, USA) at 25°C and the moisture content of the microcapsules was determined gravimetrically using the official AOAC method [23]. The evaluation of the solubility of the microcapsules was determined by finding the maximum amount of solid materials that was completely dissolved in water, as proposed by [9]. To do this, 10 mg of the microcapsules were weighed and dissolved in 50 mL of distilled water at room temperature. The mixtures were stirred with a magnetic stirrer and the time to reach complete dilution of the samples was measured. The protocol described by Ordóñez-Santos & Ledezma-Realpe, [24] was followed to determine the β-carotene. Approximately 0.01 g of sample were weighed in a capped tube lined with foil. 7 mL of the extractor solvent mixture were added at a ratio of 4:3 of ethanol and hexane. The tubes were deposited in a 250 mL beaker with plastic supports and cold water was added with ice under a nitrogen atmosphere. Subsequently, the samples were placed in a planetary stirrer for 1 hour at 230 rpm. Then, 1 mL of distilled water was added to each tube and the stirring continued for 15 minutes. Once the aqueous phase and the organic phase were separated, 3 mL of the organic phase were extracted with a Fischer micropipette, which were diverted to a clean tube. Finally, the absorbance readings were taken at 453 nm using a Jenway 6320D Spectrophotometer, USA. Before the readings, hexane was used as a base to calibrate the equipment. The total carotenoid content in the hexane extract was calculated using eq. (4):

$$\beta - \text{carotene } (\mu g/g) = \frac{A \times V \times P}{E \times W} \qquad (4)$$

Where: A = absorbance at 453 nm, V = volume of hexane solvent (2.7 mL), P = molecular weight of β-carotene (536.9 g/mol) E = extinction coefficient of β-carotene in hexane (Ɛ = 137.4 mM^{-1}), and W = weight of sample (0.01 g).

The microparticle morphology was captured using a scanning electron microscope (FEI Quanta TM 200-high vacuum mode FEG SEM, Oregon, USA at 30 kV) with a gold coating cathode, 50 second spattering current at 80 mA. The samples were mounted on aluminum stubs with carbon adhesive tape.

2.5. Stability of the microcapsules

The stability of the carotenoids in the microcapsules obtained in MC1, MC2 and RCSO for heat, light, pH and oxygen was observed according to [9], with some modifications; in our study, the samples were tested directly in order to measure the changes in the concentration of β-carotene and in all cases, 1 gram of sample was weighed. The heat effect was evaluated with exposure of the samples between 25-90 °C for 10 min in a controlled thermostatic water bath (Julabo, Germany). The measurement of the experiment time started immediately when the sample temperature reached the temperature set in the equipment, so it was necessary to use a type K thermocouple. After each treatment, the samples were cooled to 10°C to stop the effect of the temperature. In evaluating the stability in light, the samples were placed in Petri dishes and stored in a refrigerator at 4 ° C with a relative humidity of 85%. The refrigerator was fitted with a 25 W lamp 20 cm above the samples. The effect of the pH change on the retention of carotenoids was evaluated at pH 3, 4, 5, 6, 7, 8, 9, 10 and 11, preparing a 1N NaOH solution for the alkaline pH and a solution of 1N H_2SO_4 for the acid pH regulated with a buffer solution. Each solution was used on the samples for 1 hour at room temperature and protected from light. For the oxygen stability tests, the samples were exposed in an oxygen atmosphere for 0, 2, 4, 6, 8 and 10 h. So, a hermetically sealed capsule was used, coupled to a vacuum pump and saturated with an injection of oxygen gas with a purity of 95%, as certified by (Cryogas).

2.6. Statistical analysis

The experimental design was a randomized blocks, with three treatments: MC1, MC2 and RCSO; each treatment had five replications. Data was analyzed with a one-way ANOVA and treatments means were compared using Tukey's test ($p<0.05$). All statistical calculations were performed using SPSS 18 for Windows.

3. Results and discussion

3.1. Physicochemical properties of the microcapsules

The percentage of carotenoid retention (% R) was greater in MC2 with 88.24%, as compared to 66.81% with MC1. These results can be correlated with the inlet temperature in the drying process: in MC2, the working temperature was 100°C and MC1 had an operating temperature of 160°C, which demonstrated that high temperatures resulted in the degradation of carotenoids.

Other studies also obtained this level of retention [19] obtained retentions between 60 and 99% when microencapsulating β-carotene with gelatin of 100 °C. [13] used maltodextrin/gum Arabic coating material of 160 °C, obtaining a carotenoid pigment retention rate of between 84 and 86%. The efficiency (% EE) was greater in MC2 (77.82%), as compared to MC1 (66.81%); however, the encapsulation yield (% Y) was higher in MC1 (71.87%), as compared to MC2 (64.94 %). In other studies of microencapsulation by spray drying, conducted by different researchers as Shu et al. [25] obtained values between 55.30% and 82.20 % EE and R=76.1% to 91.30% in microencapsulation lycopene, using a wall system consisting of gelatin and sucrose. [10] reported values between 94% and 96 % EE and % R = 51% in microencapsulation lycopene with β-cyclodextrin as a carrier. [7] reported values between 78.5% and 90.10 % EE and from 67.40% to 69.70 R% in astaxanthin using soluble soybean polysaccharide as wall system. [10] reported that the efficiency of spray drying processes is related to the physicochemical characteristics of the core and wall materials, and the yield depends heavily on the spray drying equipment configuration. The higher % EE values in MC2 may be associated with the presence of gelatin and lecithin in the formulation because authors such as Turan et al. [26] have noted that the presence of protein and lecithin favors the retention and emulsification of carotenoids. Seybold et al. [27] comment that carotenoids bind to proteins, forming strong protein-carotenoid complexes.

The higher yields (% Y) in MC1 may be associated with the high process temperatures (160°C), which allowed water loss on the surface, increasing the solids of the formulation. The moisture and water activity of MC1 were smaller (4.60% and 0.17, respectively) than in MC2, 5.10% and 0.22, respectively. Another factor that could influence the low humidity and water activity was the presence of maltodextrin in MC1 as wall material because [11] reported that maltodextrin increases solids and reduces the amount of water to be evaporated in the spray drying process.

The solubility in water of microcapsules MC2 at room temperature was 48.96 seconds, with statistically lower than the 51.34 seconds MC1. [9], when microencapsulating lutein with a mixture of starch and gelatin by spray drying, reported solubility 120 seconds at room temperature, that exceeded those recorded in this study. The differences could be attributed to the inverse relationship between the process temperature and the final moisture content of the microcapsules. In previous studies [11] reported that higher drying temperatures can solidify the surface of the microparticles, preventing the diffusion of water molecules and reducing the solubility capacity. The same author alsostated that lower drying temperatures have a smaller evaporation rate, generating microparticles with more moisture and a greater tendency to agglomerate; a situation that benefits the solubility capacity of the microparticles.

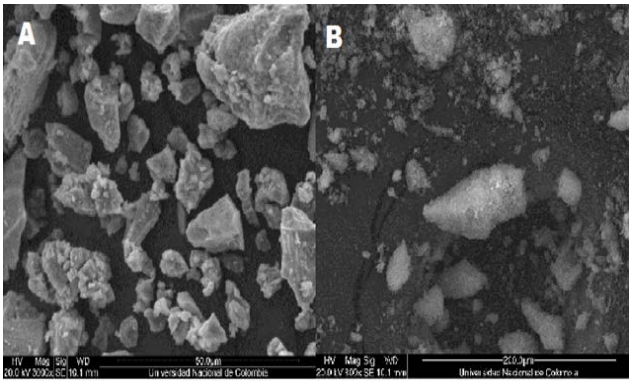


Figure 1. Microcapsule morphology (A: maltodextrin and gum arabic, B: gelatin, sugar and lecithin).
Source: The authors.

3.2. Microcapsule morphology

The morphology of the irregular microcapsules, with a non-characteristic shape, independent of the wall material, presented good protection of the core Fig. 1 (A and B). This result is similar to the findings of [10] who obtained microparticles with irregular structures during spray drying. Authors such as [8] and Handscomb & Kraft, [28] and have reported that the shape of the microcapsules during spray drying directly depends on the droplet size, drying temperature, and viscosity. Pérez-Alonso et al. [29] reported that irregularity on the surface of the microparticles may be desirable for greater dispersibility and microcapsule rehydration.

3.3. Heat stability of the microcapsule

Fig. 2 shows the effect of temperature on the retention of the carotenoids present in the released carotenoids in sunflower oil (RCSO), MC1 and MC2. In the range of 25 to 60°C, a level of carotenoid retention was observed that was similar in both of the evaluated microcapsules, while the level of retention in the RCSO was significantly decreased ($p < 0.05$); at temperatures above 60°C, the effect was significant ($p < 0.05$) in the three studied samples (Fig. 2).

When compared to the released sample, the retention rate was higher in MC2 as the temperature increased; at 90°C, the retention level in MC2 reached 90.11%, MC1 reached 83.18% and RCSO reached 75.23% (Fig. 2) [9] reported values greater than 95% in lutein microencapsulated with gelatin and starch as wall material when evaluated at temperatures of 90°C.

Probably, the hydrophobic interaction between the nucleus, protein and lecithin described by [14] resulted in the thermal insulation of the core and greater stability in MC2. Gharsallaoui et al. [30] comment that the maltodextrin is a poor emulsifying polymer, with emulsion stability and low

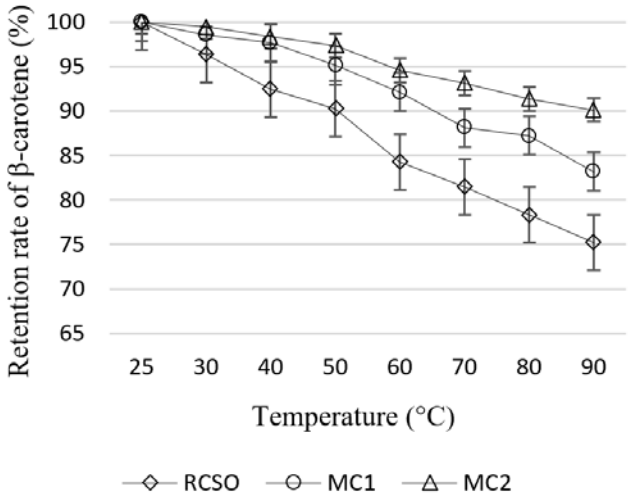


Figure 2. Effect of temperature on stability of β-carotene.
Source: The authors.

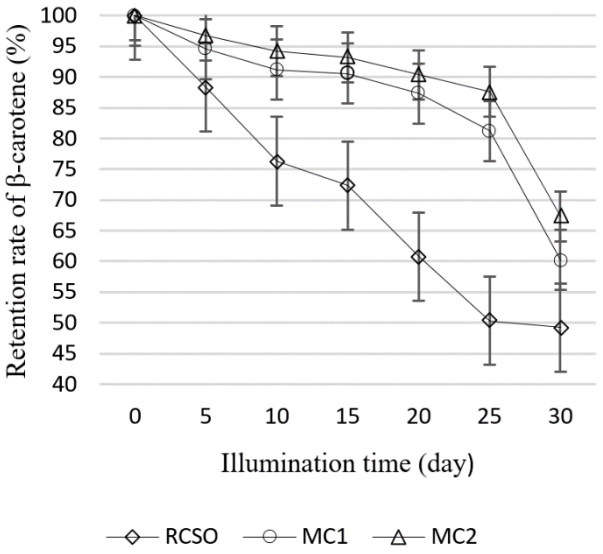


Figure 3. Effect of illumination on light stability of β-carotene.
Source: The authors.

oil retention. This reduces the thermal insulation of the core in MC1 and affecting the carotenoid retention level. The reduction of carotenoids in the RCSO may have resulted from the effect of oxidation of the polyunsaturated fatty acids by temperature action, which in turn triggered co-oxidation reactions in the carotenoids [13].

3.4. Light stability of the microcapsules

The effect of light exposure on the stability of carotenoids in RCSO, MC1 and MC2 can be seen in Fig. 3. After five days of storage, the microcapsules obtained a significantly ($p < 0.05$) higher retention as compared with RCSO and, at 30 days of storage, the retention level in MC2 was 67.36%, followed by MC1 with 60.23% and RCSO with 49.25% (Fig. 3). Authors such as Chen & Huang, [31]; Lee & Chen, [32]; Shi et al. [33] and Boon et al. [34] have reported that light can trigger oxidation and isomerization processes in carotenoids, reducing the concentration; the wall materials in MC2, because they are good emulsifying agents, reduced the action of light in the core of the microparticles, thereby decreasing the processes of oxidation and isomerization in the carotenoids. [9] microencapsulated lutein with porous starch and gelatin as wall materials, and reported retention levels of 90% in microencapsulated lutein exposed to light for 30 days.

3.5. Microcapsule stability in pH changes

The effect of pH variation on the stability of carotenoids in RCSO, MC1 and MC2 can be seen in Fig. 4.

The retention level of carotenoids increased at a pH between 4.00 and 8.00 and decreased in the regions of extreme acidity and alkalinity (Fig. 4) [9] reported a similar behavior in microencapsulated lutein with gelatin and starch as the wall material when exposed to a pH between 1.00 and 11. The retention level in the evaluated pH range presented significant differences ($p < 0.05$) between the three tested samples: MC2, with 84.21%, had a statistically higher retention rate than MC1

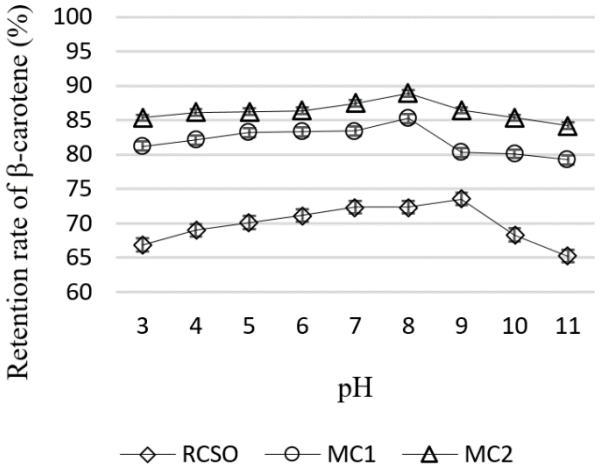


Figure 4. Effect of pH on stability of β-carotene.
Source: The authors.

(79.23%) and RCSO (65.23%). [14] explained the stability of MC2, as compared to RCSO, with the fact that the hydrophobic interaction between the nucleus, protein and lecithin, near the isoelectric point of the protein, can affect the coating, resulting in more stability in the carotenoids present in the core of the microcapsule. Moreover, an extreme pH (acids and alkalis) triggers oxidation and isomerization processes that degrade carotenoids [14] and Seyedrazi, et al. [35].

3.6. Stability of microcapsules in contact with oxygen

In Fig. 5, the effect of oxygen on the retention level in RCSO, MC1 and MC2 can be seen. By increasing the exposure time to oxygen, the retention level was significantly reduced ($p < 0.05$); after 10h, MC2 reached a retention rate of 79.23%, followed by MC1 with 71.24% and RCSO with 54.24% (Fig. 5) [9] obtained

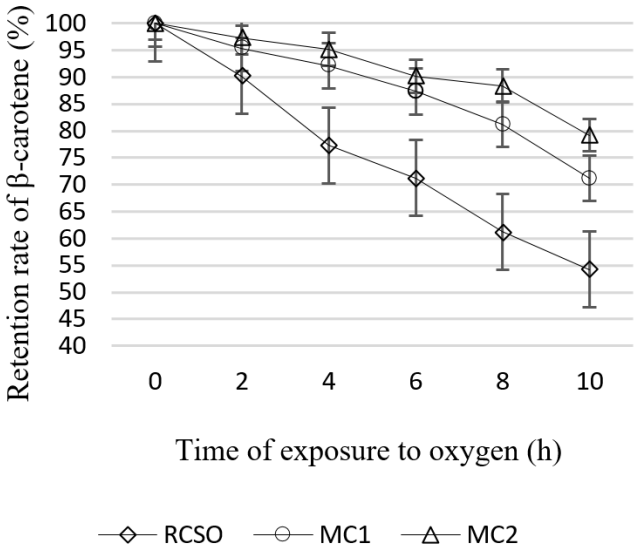


Figure 5. Effect of oxygen on stability of β-carotene.
Source: The authors.

retention levels of 90% in microencapsulated lutein after 10 hours of exposure to oxygen. Comparing RCSO with MC2 and MC1 showed that the wall materials provided an oxygen barrier, reducing the degradation of the carotenoids present in the core of the microparticles because this environmental factor is responsible for degradation by the oxidation and isomerization of carotenoids, as previously reported by [34] and Loksuwan, [36].

4. Conclusions

In this study, the stability of β-carotene extracted from peach palm peel meal (Bactris gasipaes) in a lipid extract of sunflower oil was evaluated using two encapsulation processes (MC1 and MC2), where both the coating materials and the process variables varied (inlet temperature, outlet temperature and flow rate). The microcapsules obtained in both processes were evaluated against the action temperature, light, pH, and oxygen. The results indicate that the microcapsules obtained with the second process (MC2), showed the highest levels of stability against temperature, light, pH, and oxygen, obtain retention rates had been improved about 15-25% than that of free total carotenoids. Future studies are needed to evaluate the potential of this microcapsule as a natural additive in food, pharmaceuticals and cosmetics.

Acknowledgements

The researchers wish to thank the Dirección de Investigaciones e Investigación of the Universidad Nacional de Colombia- Palmira (DIEPAL) under the Proyecto Hermes 19784 and Laboratorio de Biotecnología Alimentaria at Universidad La Gran Colombia-Seccional Armenia, (Quindío).

References

[1] Rojas-Garbanzo, C., Pérez, A.M., Bustos-Carmona, J. and Vaillant, F., Identification and quantification of carotenoids by HPLC-DAD during the process of peach palm (Bactris gasipaes HBK) flour. Food Res. Int. 44(7), pp. 2377-2384, 2011. DOI: 10.1016/j.foodres.2011.02.045

[2] Jatunov, S., Quesada, S., Díaz, C. and Murillo, E., Carotenoid composition and antioxidant activity of the raw and boiled fruit mesocarp of six varieties of Bactris gasipaes. Arch Latinoam Nutr. 60(1), pp. 99-104, 2010.

[3] Graefe, S., Dufour, D., Van Zonneveld, M., Rodriguez, F. and Gonzalez, A., Peach palm (Bactris gasipaes) in tropical Latin America: implications for biodiversity conservation, natural resource management and human nutrition. Biodivers. Conserv. 22(2), pp. 269-300, 2013. DOI: 10.1007/s10531-012-0402-3

[4] Babbar, N., Oberoi, H. and Sandhu, S., Therapeutic and nutraceutical potential of bioactive compounds extracted from fruit residues. Crit Rev Food Sci Nutr. 55(3), pp. 319-337, 2015. DOI: 10.1080/10408398.2011.653734

[5] Woodside, J.V., McGrath, A.J., Lyner, N. and McKinley, M.C., Carotenoids and health in older people. Maturitas. 80(1), pp. 63-68, 2015. DOI: 10.1016/j.maturitas.2014.10.012

[6] Qian, C., Decker, E.A., Xiao, H. and McClements, D.J., Inhibition of β-carotene degradation in oil-in-water nanoemulsions: influence of oil-soluble and water-soluble antioxidants. Food Chem., 135(3), pp. 1036-1043, 2012. DOI: 0.1016/j.foodchem.2012.05.085

[7] Hojjati, M., Razavi, S.H., Rezaei, K. and Gilani, K., Spray drying microencapsulation of natural canthaxantin using soluble soybean polysaccharide as a carrier. Food Sci Biotechnol., 20(1), pp. 63-69, 2011. DOI: 0.1007/s10068-011-0009-6

[8] Pu, J., Bankston, J.D. and Sathivel, S., Production of microencapsulated crawfish (Procambarus clarkii) astaxanthin in oil by spray drying technology. Drying Technol., 29(10), pp. 1150-1160, 2011. DOI: 10.1080/07373937.2011.573155

[9] Wang, Y., Ye, H., Zhou, C., Lv, F., Bie, X. and Lu, Z., Study on the spray-drying encapsulation of lutein in the porous starch and gelatin mixture. Euro Food Res Technol., 234(1), pp. 157-163, 2012. DOI: 10.1007/s00217-011-1630-6

[10] Nunes, I.L. and Mercadante, A.Z., Encapsulation of lycopene using spray-drying and molecular inclusion processes. Braz Arch Biol Technol., 50(5), pp. 893-900, 2007. DOI: 10.1590/S1516-89132007000500018

[11] Quek, S.Y., Chok, N.K. and Swedlund, P., The physicochemical properties of spray-dried watermelon powders. Chem Eng Process., 46(5), pp. 386-392, 2007. DOI: 10.1016/j.cep.2006.06.020

[12] Rascón, M.P., Beristain, C.I., García, H.S. and Salgado, M.A., Carotenoid retention and storage stability of spray-dried encapsulated paprika oleoresin using gum Arabic and soy protein isolate as wall materials. LWT-Food Sci Technol., 44(2), pp. 549-557, 2011. DOI: 10.1016/j.lwt.2010.08.021

[13] Guadarrama-Lezama, A.Y., Dorantes-Alvarez, L., Jaramillo-Flores, M.E., Pérez-Alonso, C., Niranjan, K., Gutiérrez-López, G.F. and Alamilla-Beltrán, L., Preparation and characterization of non-aqueous extracts from chilli (Capsicum annuum L.) and their microencapsulates obtained by spray-drying. Preparation and characterization of non-aqueous extracts from chilli (Capsicum annuum L.) and their microencapsulates obtained by spray-drying. Food Eng. 112(1), pp. 29-37, 2012. DOI: 0.1016/j.jfoodeng.2012.03.032

[14] Bustos-Garza, C., Yáñez-Fernández, J. and Barragán-Huerta, B.E., Thermal and pH stability of spray-dried encapsulated astaxanthin oleoresin from Haematococcus pluvialis using several encapsulation wall materials. Food Res Int., 54(1), pp. 641-649, 2013. DOI: 10.1016/j.foodres.2013.07.061

[15] Domínguez-Cañedo, I.L., Beristaín-Guevara, C.I., Díaz-Sobac, R. and Vázquez-Luna, A., Degradation of carotenoids and capsaicin in the molecular inclusion complex of habanero chili oleoresin (Capsicum chinense) in beta-cyclodextrin. CYTA J. Food, 13(1), pp. 151-158, 2015. DOI: 10.1080/19476337.2014.926459

[16] Lim, A.S., Burdikova, Z., Sheehan, D.J. and Roos, Y.H., Carotenoid stability in high total solid spray dried emulsions with gum Arabic layered interface and trehalose–WPI composites as wall materials. Innov Food Sci Emerg Technol., 34, pp. 310-319, 2016. DOI: 10.1016/j.ifset.2016.03.001

[17] Montero, P., Calvo, M.M., Gómez-Guillén, M.C. and Gómez-Estaca, J., Microcapsules containing astaxanthin from shrimp waste as potential food coloring and functional ingredient: characterization,

stability, and bioaccessibility. LWT-Food Sci Tech., 70, pp. 229-236, 2016. DOI: 10.1016/j.lwt.2016.02.040
[18] Ordóñez-Santos, L.E., Pinzón-Zarate, L.X. and González-Salcedo, L.O., Optimization of ultrasonic-assisted extraction of total carotenoids from peach palm fruit (Bactris gasipaes) by-products with sunflower oil using response surface methodology. Ultrason Sonochem., 27, pp. 560-566, 2015. DOI: 10.1016/j.ultsonch.2015.04.010
[19] Robert, P., Carlsson, R.M., Romero, N. and Masson, L., Stability of spray-dried encapsulated carotenoid pigments from rosa mosqueta (Rosa rubiginosa) oleoresin., J. Am Oil Chem Soc., 80(11), pp. 1115-1120, 2003. DOI: 10.1007/s11746-003-0828-4
[20] Alishahi, A., Mirvaghefi, A., Tehrani, M., Farahmand, H., Shojaosadati, S., Dorkoosh, F. and Elsabee, M., Shelf life and delivery enhancement of vitamin C using chitosan nanoparticles. Food Chem. 126, pp. 935-940, 2011. DOI: 10.1016/j.foodchem.2010.11.086
[21] Rutz, J.K., Borges, C.D., Zambiazi, R.C., da Rosa, C.G. and da Silva, M.M., Elaboration of microparticles of carotenoids from natural and synthetic sources for applications in food. Food Chem., 202, pp.324-333, 2016. DOI: 10.1016/j.foodchem.2016.01.140
[22] Jun-Xia, X., Hai-yan, Y. and Jian, Y., Microencapsulation of sweet orange oil by complex coacervation with soybean protein isolate/gum Arabic. Food Chem., 25(4), pp. 1267-1272, 2011. DOI: 10.1016/j.foodchem.2010.10.063
[23] AOAC, Official methods of analysis. Association of Official Analytical Chemists (AOAC) (16th Ed.) Maryland: AOAC International, 1998.
[24] Ordóñez-Santos, L.E. and Ledezma-Realpe, D.P., Lycopene concentration and physicochemical properties of tropical fruits. Food Nutr Sci., 4(07), pp. 758-762, 2013. DOI: 10.4236/fns.2013.47097
[25] Shu, B., Yu, W., Zhao, Y. and Liu, X., Study on microencapsulation of lycopene by spray-drying. Food Eng., 76(4), pp. 664-669, 2006. DOI: 10.1016/j.jfoodeng.2005.05.062
[26] Turan, F.T., Cengiz, A. and Kahyaoglu, T., Evaluation of ultrasonic nozzle with spray-drying as a novel method for the microencapsulationof blueberry's bioactive compounds. Innov. Food Sci. Emerg. Technol., 32, pp. 136-145, 2015. DOI: 10.1016/j.ifset.2015.09.011
[27] Seybold, C., Fröhlich, K., Bitsch, R., Otto, K. and Böhm, V., Changes in contents of carotenoids and vitamin E during tomato processing, J. Agric Food Chem., 52(23), pp. 7005-7010, 2004. DOI: 10.1021/jf049169c
[28] Handscomb, C.S. and Kraft, M., Simulating the structural evolution of droplets following shell formation. Chem Eng Sci., 65(2), pp. 713-725, 2010. DOI: 10.1016/j.ces.2009.09.025
[29] Pérez-Alonso, C., Fabela-Morón, M.F., Guadarrama-Lezama, A.Y., Barrera-Pichardo, J.F., Alamilla-Beltrán, L. and Rodríguez-Huezo, M.E., Interrelationship between the structural features and rehydration properties of spray dried manzano chilli sauce microcapsules. EV Mex. Ing. Quim., 8(2), pp. 187-196, 2009.
[30] Gharsallaoui, A., Roudaut, G., Chambin, O., Voilley, A. and Saurel, R., Applications of spray-drying in microencapsulation of food ingredients: an overview, Food Res Int., 40(9), pp. 1107-1121, 2007. DOI: 10.1016/j.foodres.2007.07.004
[31] Chen, B.H. and Huang, J.H., Degradation and isomerization of chlorophyll a and β-carotene as affected by various heating and illumination treatments. Food Chem., 62(3), pp. 299-307, 1998. DOI: 10.1016/S0308-8146(97)00201-X
[32] Lee, M.T. and Chen, B.H., Stability of lycopene during heating and illumination in a model system, Food Chem., 78(4), pp. 425-432, 2002. DOI: 10.1016/S0308-8146(02)00146-2
[33] Shi, J., Maguer, M., Bryan, M. and Kakuda, Y., Kinetics of lycopene degradation in tomato puree by heat and light irradiation, J. Food Process Eng., 25(6), pp. 485-498, 2003. DOI: 10.1111/j.1745-4530.2003.tb00647.x
[34] Boon, C.S., McClements, D.J., Weiss, J. and Decker, E.A., Factors influencing the chemical stability of carotenoids in foods. Crit Rev Food Sci Nutr., 50(6), pp. 515-532, 2010. DOI: 10.1080/10408390802565889
[35] Seyedrazi, N., Razavi, S.H. and Emam-Djomeh, Z., Effect of different pH on canthaxanthin degradation, Eng Technol., 59, pp. 532-536, 2011. DOI: 10.1016/j.foodhyd.2006.10.011
[36] Loksuwan, J., Characteristics of microencapsulated β-carotene formed by spray drying with modified tapioca starch, native tapioca starch and maltodextrin, Food Hydrocoll., 21(5), pp. 928-935, 2007.

L.E. Ordoñez-Santos, is associate professor of the Universidad Nacional de Colombia, Sede Palmira, Coombia. Is BSc. in Agroindustrial Engineer, PhD. Food Science and Technology. Leader of the Research Group on Agroindustrial Processes (GIPA). More than forty publications in national and international journals on fruit and vegetable processing, ultrasound processing, food color evaluation, extraction and quantification of bioactive compounds such as carotenoids, anthocyanins, phenolic compounds, vitamin C, among others.
ORCID: 0000-0002-8958-027X.

J. Martínez-Girón, is BSc. in Chemistry and Food Technology. MSc. degree in Agroindustrial Engineering, MSc. in Education, has worked as a quality analyst in Fleischmann Food and Ingenio Manuelita S.A. Coordinator and professor of the academic program of food technology in Universidad del Valle-Sede Palmira, occasional professor at the Universidad Nacional de Colombia-Sede Palmira. His research interests include: color of food, use of fruit waste as a source of bioactive compounds such as carotenoids and chlorophyll, edible oils, cereals and bakery.
ORCID: 0000-0003-4191-5445.

R.H. Villamizar-Vargas, received the BSc. Eng in Chemistry Engineering in 1989, the Sp. degree in Occupational Health, Risk Management and Control in 2001, and MSc. degree in Chemistry in 2012, he worked as a production engineer in the leather industry until 1996, has taught in the area of unitary operations, food analysis and industrial hygiene. Currently, he is a full professor in the Occupational Safety and Health Program of the Faculty of Health Sciences, Universidad del Quindío, Colombia. His research interests include: development of new food products, Exposure to chemical hazards and Hygiene and safety conditions.
ORCID: 0000-0001-6959-0086.

UNIVERSIDAD NACIONAL DE COLOMBIA
SEDE MEDELLÍN
FACULTAD DE MINAS

Área Curricular de Ingeniería Administrativa e Ingeniería Industrial

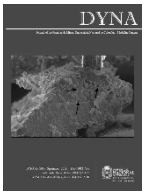
Oferta de Posgrados

Especialización en Gestión Empresarial
Especialización en Ingeniería Financiera
Maestría en Ingeniería Administrativa
Maestría en Ingeniería Industrial
Doctorado en Ingeniería - Industria y Organizaciones

Mayor información:

E-mail: acia_med@unal.edu.co
Teléfono: (57-4) 425 52 02

UNIVERSIDAD NACIONAL DE COLOMBIA
SEDE MEDELLÍN
FACULTAD DE MINAS



DYNA
http://dyna.medellin.unal.edu.co/

Synergistic effects in anaerobic codigestion of chicken manure with industrial wastes

Liliana del Pilar Castro-Molano, Humberto Escalante-Hernández, Luis Enrique Lambis-Benítez & José Daniel Marín-Batista

Escuela de Ingeniería Química, Grupo de Investigación INTERFASE, Universidad Industrial de Santander, Bucaramanga, Colombia. licasmol@uis.edu.co, escala@uis.edu.co, lelb_23@hotmail.com, jdmbatista05@gmail.com

Received: October 9th, 2017. Received in revised form: June 22nd, 2018. Accepted: July 18nd, 2018.

Abstract
Synergy in anaerobic codigestion is described as positive interactions between a substrate and cosubstrate(s). Synergistic effects increase methane production over the weighted average methane production from monodigestion. Limited current knowledge defines synergy as a parameter in the plant control and design and in solving operational problems. In this study, synergy was determined in the anaerobic codigestion of chicken manure with industrial wastes (sugarcane molasses, cheese whey, and crude glycerol). A simplex lattice mixture design was used to determine mixing ratios. Synergy was assessed in terms of substrate composition and ammonia inhibition. The greatest synergistic effects were achieved with ternary mixtures. Synergy was also noticed when total ammonia nitrogen concentrations decreased and the organic load increased. Nonetheless, it was concluded that synergy could be reliably achieved when cosubstrate supplementation reduces ammonia inhibition and increases methane production as increases in organic load.

Keywords: anaerobic codigestion; chicken manure; industrial wastes; mixture design, synergistic effects.

Efectos sinérgicos en la codigestión anaerobia de gallinaza y residuos industriales

Resumen
La sinergia en la codigestión anaeróbica se describe como interacciones positivas entre sustrato y co sutratos. Los efectos sinérgicos aumentan la producción de metano con respecto a la monodigestión. Actualmente, se cuenta con un conocimiento limitado sobre las aplicaciones de la sinergia como parámetro para la solución de problemas operativos en sistemas anaerobios. En este estudio se determinó la sinergia en la codigestión anaeróbica de gallinaza con residuos industriales (melaza de caña de azúcar, lactosuero, y glicerol crudo). Las proporciones de mezclas fueron determinadas a partir de un diseño de mezcla simplex. La sinergia se evaluó en términos de composición de sustrato e inhibición de amoniaco. La sinergia se evidencia cuando reduce la inhibición del amoníaco y aumenta la producción de metano a medida que incrementa la carga orgánica, siendo el efecto más favorable en mezclas terciarias.

Palabras claves: codigestion anaerobia; diseño de mezcla; efectos sinérgicos; gallinaza; residuos industriales.

1. Introduction

Anaerobic digestion (AD) is an effective technology for the conversion of organic wastes into methane-rich biogas and nutrient recovery [1]. In particular, chicken manure (CM) is an attractive substrate for anaerobic digestion owing to its high organic matter content, mainly comprising proteins [2]. Anaerobically, proteins hydrolyse into ammonia, which diffuses within microbial cells and disrupts cellular homeostasis. Ammonia concentrations over 2,500 mg/L reduce the methanogen population affecting methane yields [3].

The Anaerobic digestion of CM mixed with carbon-rich organic wastes has been proven to decrease the probabilities of ammonia inhibition and VFA accumulation [4]. The digestion of two or more substrates together known as anaerobic co-digestion (AcoD) can overcome several inherent problems

How to cite: Castro-Molano, L.dP., Escalante-Hernández, H., Lambis-Benítez, L.E., and Marín-Batista, J.D., Synergistic effects in anaerobic codigestion of chicken manure with industrial wastes. DYNA, 85(206), pp. 135-141, September, 2018.

© The author; licensee Universidad Nacional de Colombia.

associated with single substrate digestion such as the lack of micronutrients, imbalanced C/N ratio, and unfavourable (i.e. too high or too low) organic loading rates [5]. Abouelenien et al., (2014) [4] summarized the operational conditions for the codigestion of CM with agro wastes. In most of studies summarized in this report, mixture ratios were selected randomly to achieve optimal C/N ratios (25 to 30). However, mixtures with low C/N ratios have also been used successfully to achieve low partial increases in methane yield [6]. Moreover, the codigestion assays were conducted under wet conditions (solid concentrations of <10%), which is unfeasible for industrial application because of high water consumption and the too large required digester size [7]. Then, complementariness among physicochemical characteristics of wastes was not a decisive selection criterion to ensure the effectiveness of the mixture against further industrial application.

In AcoD, increased methane production is associated with both synergistic effects and an increase in organic load. Synergistic effects may include additional methane yield for codigestion over the weighted average of the individual substrate's methane yield [8]. This may explain the increase in methane yield via the addition of the cosubstrate. Previous studies have reported stable digestion, enhanced gas yields, and improved economy of biogas plants in conjunction with this synergistic effect [9]. Biochemical methane potential and ammonia inhibition as well as synergy are directly linked to substrate composition [10]. The composition of substrate determines the efficacy of the microbial population, which in turn largely influences biogas yield, long-term process stability, and solid degradation rate [11].

On the other hand, methane production is largely influenced by the organic load or initial volatile solid (VS) concentration of the substrate in the digesters. The organic load and an accumulative volume of biogas are directly correlated [12]. If the organic load is very low, there is a risk of low microbial metabolic activity, in turn leading to low biogas production [13]. In contrast, if the substrate's concentration is too high, the process may be inhibited by an overload of intermediate compounds such as VFA and ammonia [14]. Additionally, Mata-Alvarez et al. [15] documented that industrial AcoD plants should be limited by the transport cost of the cosubstrate from the generation point to plant location. In this sense, the increases in the organic loading rate will impact higher in the biogas plant cost-effectiveness rather than synergy.

Bec.ause of the potential for ammonia inhibition, biogas plants that treat chicken manure are forced to operate below full capacity. It is clear that the concept of synergy is still limited in its application to solving operational problems during the digestion process. Therefore, the impact of synergy on AcoD with high organic load concentrations must be determined in order to increase biogas production and reduce ammonia inhibition. Reliable AcoD modelling is needed to predict, in a clear and quantifiable manner, the effects of mixing two or more wastes in digesters and to mitigate any negative effects of this mixing [10]. Models are also useful in estimating important biochemical parameters, such as biodegradability, hydrolysis rate, and inhibition constant, which are critical in AD design, performance, and troubleshooting [10]. This study aimed to evaluate the synergistic effects of chicken manure with industrial wastes: sugar cane molasses (SCM), cheese whey (CW), and crude glycerol (CG) during AcoD. Cosubstrates were selected based on the ease to introduce them into the production chain of the Colombian poultry industry.

2. Materials and methods

2.1. Inoculum and wastes

The inoculum was cattle manure collected from a cattle slaughterhouse. The cattle manure was incubated at 25 °C to reduce residual organic matter content. The inoculum comprised a soluble chemical oxygen demand (COD) of 777 mg/L, 28.2 g total solid (TS)/kg, and 65% VS-to-TS ratio.

The substrate and cosubstrates were collected from Colombian industries. CM was obtained from a chicken farm, sugarcane molasses (SCM) from a sugar cane refinery, crude glycerol (CG) from an oil refinery and cheese whey (CW) from a dairy company. The characterization of wastes was shown in Table 2.

2.2. Identification of synergistic and antagonistic effects

2.2.1. Experimental set-up

The methanation assay was carried out in triplicate at 37±2 °C for 30 days according to procedures described by [16]. The initial VS ratio of inoculum to substrate was maintained at 2:1 throughout the experimental setup. Each 60-mL reactor contained an organic load of 9 g VS/L, 12 mL of inoculum, and sufficient distilled water to adjust total volume to 35 mL. Reactors were mixed by inverting once per day. Blanks containing inoculum and no substrate were used to correct for background methane potential in the inoculum. All reactors were purged with nitrogen gas and sealed using butyl rubber and an aluminium cap. Methane produced during methanation assay was quantified by the volumetric displacement of an alkaline solution. The volume of methane displaced was normalized and expressed in terms of specific methane production (SMP) m^3 CH_4/kg VS added.

2.2.2. Experimental mixture design

In order to eliminate the randomness of blending, the assay was run based on a simplex lattice design {4,3} augmented with three axial points. The mixture design was created using MINITAB 17 software (license 17.1.0.0) and represented graphically as a tetrahedron made up by a triangular base and three triangular faces called simplex (Fig. 1). Three simplex regions of interest were tested: A {CM, SCM, CG}, B {CM, CG, CW}, and C {CM, SCM, CW}. Each simplex consisted of 13 points (mixture ratios) where vertices corresponded to ratios with 100% single substrate. The upper vertex of the tetrahedron was the pure CM ratio which is also the upper vertex in each simplex. Vertices on the base of tetrahedron comprised pure ratios of 100% SCM, 100% CG, and 100% CW. Points on the axis corresponded to binary mixtures. Interiors points on each simplex corresponded to ternary mixtures. All points of the tetrahedron are listed in Table 1. MINITAB 17 was also used for statistical analysis of the experimental data via one-way ANOVA. Fisher least significant difference was calculated with 95% confidence to conduct pairwise comparisons of the SMP means.

Table 1.
Augmented simplex lattice design {4,3}

Ratios	Simplex A			Simplex B			Simplex C		
	CM	SCM	CG	CM	CG	CW	CM	CW	SCM
1	17	66	17	17	66	17	17	66	17
2	33	0	67	33	0	67	33	0	67
3	0	67	33	0	67	33	0	67	33
4	100	0	0	100	0	0	100	0	0
5	33	67	0	33	67	0	33	67	0
6	34	33	33	34	33	33	34	33	33
7	17	17	66	17	17	66	17	17	66
8	0	0	100	0	0	100	0	0	100
9	67	0	33	67	0	33	67	0	33
10	67	33	0	67	33	0	67	33	0
11	0	33	67	0	33	67	0	33	67
12	66	17	17	66	17	17	66	17	17
13	0	100	0	0	100	0	0	100	0

Source: The authors

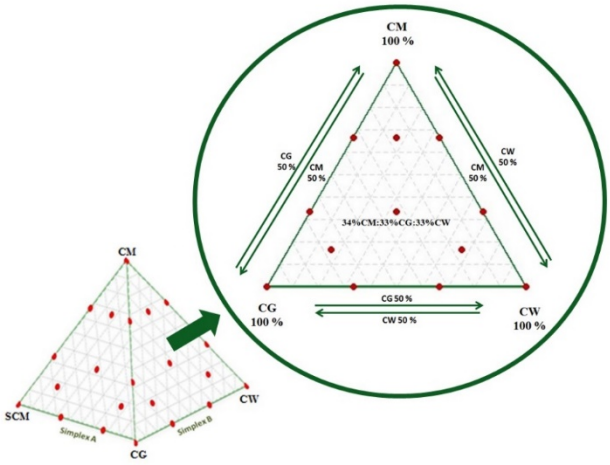


Figure 1 Simplex lattice design for substrate and cosubstrates tested.
Source: The authors

2.2.3. Evaluation of synergistic and antagonistic effects

Synergistic or antagonistic effects were identified as a qualitative parameter for evaluation of process performance. Synergistic effects could be seen as additional SMP obtained during co-digestion over the weighted average of the individual feedstock's SMP [8]. Weighted SMP (WSMP) was calculated using Eq. 1, as follows:

$$WSMP = \frac{(Y_{CM}\times\propto)+(Y_{SCM}\times\beta)+(Y_{CG}\times\delta)+(Y_{CW}\times\theta)}{\alpha+\beta+\delta+\theta} \quad (1)$$

Where Y_{CM} refers to the SMP obtained from the digestion of CM as a mono-substrate. Y_{SCM}, Y_{CG}, and Y_{CW} are the SMPs obtained via singular digestion of their respective co-substrates. Moreover, $\alpha + \beta + \delta + \theta$ corresponds to the sum of the VS fractions added by CM, SCM, CG, and CW, in that order.

Synergistic effects were determined using Eq. 2, as follows:

$$\emptyset = {}^{SMP}/_{WSMP} \quad (2)$$

Where SMP refers to the SMP achieved for the ratio tested. WSMP corresponds to the weighted average experimental SMP calculated using Eq. 1. If $\emptyset > 1$, the mixture presented synergistic effects. If $\emptyset < 1$, the mixture presented antagonistic effects. If $\emptyset = 1$, the effects of the mixture during co-digestion were unclear.

2.3. Analysis of synergistic effects in terms of performance and inhibition

The ratios of each simplex with the highest synergistic effect were evaluated at organic loads of 9 and 18 g VS/L. The methanation assay was performed with the same operating conditions as in the previous stage. SMP and final TAN concentration were considered as response variables. The traditional first-order model was used to evaluate the kinetic degradation of the mixture with highest synergistic effects for both organic loads, according to Eq. 3:

$$SMP(t) = SMP_{max}(1 - \exp(-K_{dis}t)) \quad (3)$$

Where *SMP(t)* refers to the SMY obtained with digestion time *t*, SMP_{max} refers to the highest theoretical SMP, and K_{dis} refers to the first-order hydrolysis constant. Model parameters were calculated using the curve-fitting toolbox (cftool) of MATLAB R2014a, license 271828.

2.4. Analytical techniques

Analyses of total solids (TS), volatile solids (VS), chemical oxygen demand (COD), total Kjeldahl nitrogen, total ammonia nitrogen (TAN), total organic carbon, proteins, and lipids were performed according to standard methods for the examination of wastewater of the American Public Health Association [17] The total amount of carbohydrates was estimated via Van Soest methods [18]. The pH values were determined using a pH meter (691, Metrohm).

3. Results and Discussion

3.1. Characterisation of wastes

The main characteristics of the substrate (CM) and cosubstrates (SCM, CG, and CW) are summarised in Table 2. All residues showed pH values below 6.5, except CM, with a pH value of 7.5. Moreover, residues had VS/TS ratios between 0.52 and 0.98, indicating high potentially biodegradable organic matter content. Organic matter in the co-substrates in particular was readily biodegradable, making the process susceptible to acidification. The SCM had the highest carbohydrate content at 82.5%, while the CG and CW had the highest lipid (49.3%) and protein (23.0%) contents, respectively. On the other hand, each residue presented a C/N ratio outside the optimal range (20 to 25) for the anaerobic degradation process [15]. The CM had the lowest C/N ratio, which is consistent with a high TAN of 843.5 mg/L. Nevertheless, the substrate and co-substrates provided conditions conducive to unprofitable anaerobic process.

Table 2.
Characterization of substrate and cosubstrates

Parameter	Units	CM	SCM	CG	CW
pH	-	7.5	5.6	5.0	3.8
COD	g/L	198.0	1387.8	1914.0	53.0
TS	g/L	224.7	767.2	680.3	42.0
VS	g/L	116.9	561.2	670.4	37.7
VS/TS	-	0.52	0.73	0.98	0.90
Carbohydrates	%	17.1	82.5	41.2	55.3
Protein	%	23.5	5.8	5.6	23.0
Lipid	%	1.8	0.9	49.3	1.9
C/N	-	10.8	53.6	57.5	19.9
TAN	mg/L	843.5	7.8	23.3	46.7

(%) Percentage on wet basis
Source: The authors

Mixtures of residues could improve the biodegradability and stability of the anaerobic system.

3.2. Evaluation of synergy based on substrate composition

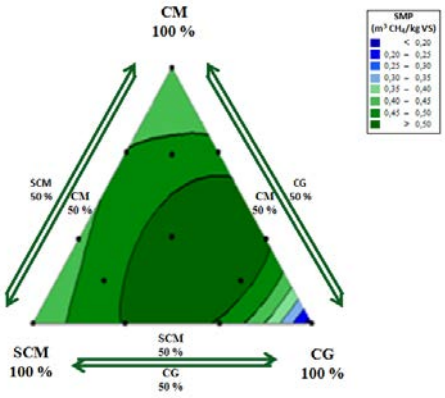
This section describes the synergistic effects of different carbohydrate, lipid, and protein concentrations during codigestion of CM with industrial agro wastes.

3.2.1. Specific methane production throughout simplex lattice design

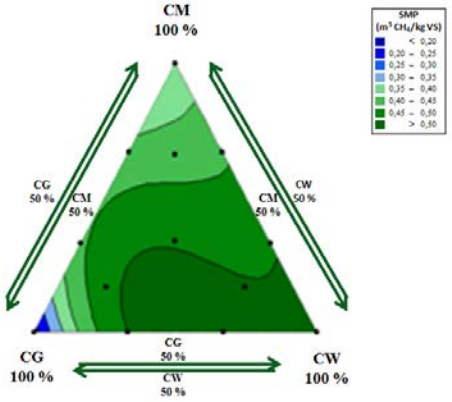
Fig. 2 shows the frontal view of each face of simplexes a, b, and c. Each view corresponds to a contour plot of specific methane production (SMP) created using MINITAB 17. These contour plots were useful in identifying the effects of cosubstrates that were rich in carbohydrates (SCM), lipids (CG), and protein (CW) during the co-digestion process with chicken manure. From the contour plots, the responses were analysed statistically to delimit significant regions. Each region was marked using a colour scale from blue to green according to the magnitude of the response. The darkest green areas had the statistically highest SMP, while deepest blue zones showed the statistically lowest SMP values.

Fig. 2a shows the effects of mixing chicken manure with cosubstrates rich in carbohydrates (SCM) and lipids (CG) in simplex A. The maximum SMP was obtained between the centroid point and the CM:SCM:CG ratio of 17:17:64. The average SMP obtained within this region was 0.45 ± 0.02 m^3 CH_4/kg VS, representing an increase of 32% over the SMP of CM alone. This finding indicates that SMP from the codigestion process was increased due to the increased lipid concentration in the codigestion mixture compared to that when CM was digested alone. The concentrations of CG producing the maximum response areas were 1.53 g VS/L and 5.94 g VS/L. These values are consistent with those recommended by the literature to achieve high rates of solids removal using glycerol as a cosubstrate [19]. Consequently, the simplex zone with lowest SMP corresponded to the right vertex (pure CG), where crude glycerol concentration was 9 g VS/L. Then, the right vertex presented high lipid concentrations in the digestion system with the possible overloading.

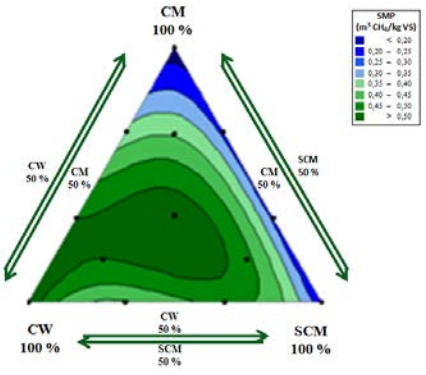
Fig. 2b shows the results of interactions between CM, CG, and CW in simplex B. The maximum response occurred in the area between the centroid point and the right vertex. For this region, the average SMP was 0.56 ± 0.03 m^3 CH_4/kg VS, equivalent to a 64% increase in SMP over that of CM alone. Then, affinity between CM and CW was presented for the simplex B. The affinity between CM and CW in particular could be a consequence of their protein-rich compositions. The affinity among the waste types reduced the lag phase increasing the biodegradability of the mixture [20]. Additionally, the high biochemical methane potential of CW facilitated an increase in SMP.



(2a)



(2b)



(2c)

Figure 2. Contour plots for codigestion of CM with industrial agrowastes.
Source: The authors

For simplex c, the greatest response was achieved at the centroid point, where the mixing ratio was 3 g VS/L for each residue (Fig. 2c). In this zone, the average SMP was 0.55 ± 0.04 m^3 CH_4/kg VS, equivalent to a 62% increase in SMP over that of CM alone. A lower SMP was achieved throughout the right adjacent area, where high concentrations of SCM were present. Moreover, the rapid biodegradation rate of carbohydrate-rich waste supports the elimination of latent phases in proportion with high concentrations of lipids and proteins [10]. Nevertheless, moderate supplementation of carbohydrate-rich residues such as SCM improved the biodegradability of lipid-rich residues such as CG and proteins-rich residues as CM.

3.2.2. Identification of synergistic and antagonistic effects

In AcoD, synergistic and antagonistic effects can be used as stability parameters for further dissection of the SMP data. Synergy mitigates ammonia inhibition and improves digestive process stability [9] and, therefore, SMP. Synergistic effects result from contributions of cosubstrates in terms of alkalinity, trace elements, nutrients, or any other features that the substrate itself is lacking. Similarly, antagonistic effects may be due to several factors, such as a drop in pH, ammonia toxicity, or high concentrations of volatile fatty acid [8].

Table 3 shows the synergistic and antagonistic effects of mixtures of CM with residues rich in carbohydrates (SCM), lipids (CG), and proteins (CW). Synergistic effects occurred for binary mixtures when Ø values were between 1.05 and 1.68. Most binary mixtures achieved synergistic effects, except for the CW:SCM ratio of 67:33, which presented an antagonistic Ø value of 0.86. Antagonism reflects the instability of this mixture, which could have been due to the low pH values of CW and SCM. In general, all ternary mixtures produced synergistic effects, with Ø values between 1.25 and 2.67, a higher range than that of the binary mixtures. The mixing ratios with the highest Ø value in each simplex were considered optimal. For simplex A, the optimal synergistic ratio (Ø = 2.67) was the ternary mixture CM:SCM:CG of 17:17:66. For Simplex B, the optimal synergistic ratio was a CM:CG:CW mixture of 17:66:17, producing a Ø value of 2.29. For Simplex C, the optimal synergistic ratio (Ø = 1.38) was the CM:SCM:CW mixture of 34:33:33. These findings confirmed the advantages of multi-component co-digestion over traditional digestion. [11] also found multi-component co-digestion to be a promising alternative in mitigating inhibition and improving anaerobic stability. According to their study, the synergy in the co-digestion of ternary and quaternary mixtures of solid wastes from dairy slaughterhouse plants (visors, blood, rumen) with manure, various crops, and municipal solid waste resulted in better distribution of nutrients, promoting rapid, beneficial development of microbial consortia.

Table 4 shows the nutritional composition (carbohydrates, lipids, and proteins) of the optimal synergistic mixtures. All optimal synergistic mixtures exhibited high carbohydrate concentrations, indicating that carbohydrates play a supporting role in anaerobic biodegradation process. Furthermore, proteins were found in intermediate concentrations for each optimal synergistic mixture, which could lead to controlled ammonia production in the anaerobic system. The CM:CG:SCM and CM:CG:CW optimal ratios of 17:17:66 and 17:66:17, respectively, had lipid concentrations reaching 33%. Such concentrations could be considered high when compared with those of the CM:CW:SCM optimal ratio of 34:33:33 and CM alone, which were below 1.8%. High lipid concentrations in mixtures seemed to improve Ø values, possibly because of its large theoretical methane potential [21]. However, with high lipid concentrations in the digestion system there is a risk of overloading leading to VFA accumulation. Then, it could be concluded that Synergy could then be linked to the anaerobic system's capability of sustaining a high lipid load during the digestion process. This could translate to hydraulic retention times for continuous optimization, resolving operational problems through synergy.

3.3. Operational outlook of synergy

Synergy was assessed in terms of the impacts of kinetic parameters of biodegradability according to organic load. Fig. 3 shows a comparison between the SMP for optimal synergistic ratios and its uncertainty surfaces for kinetic parameters. Specifically, the maximum SMP and hydrolysis constant (K_{dis}) are the kinetic parameters that describe the substrate's rate of biodegradation [22] (Galí et al., 2009). The size of the uncertainty areas corresponds to the standard deviation of the kinetic parameters. Filled areas correspond to the experiments with an organic load of 18 g VS/L, while the empty areas correspond to experiments with an organic load of 9 g VS/L. As shown in Fig. 3, the uncertainty of the kinetic parameters slightly increased with smaller organic loads, indicating that the substrate concentration must remain high to achieve reliable results.

Table 3.
Synergistic and antagonistic effects (Ø) of cosubstrates in binary and ternary mixtures with CM.

X_1	X_2	X_3	Simplex A	Simplex B	Simplex C
33	0	67	1.58	1.05	1.13
0	67	33	1.68	1.08	0.86
33	67	0	1.13	1.58	1.05
67	0	33	1.59	1.09	1.10
67	33	0	1.10	1.59	1.09
0	33	67	1.32	1.32	1.25
17	66	17	1.38	**2.29**	1.16
34	33	33	1.66	1.48	**1.38**
17	17	66	**2.67**	1.25	1.26
66	17	17	1.54	1.37	1.25

Simplex A {X_1:CM; X_2:SCM; X3:CG}; Simplex B {X1:CM; X2:CG; X3:CW}; Simplex C {X1:CM; X2:CW; X3:SCM}
Source: The authors

Table 4.
Comparison of nutritional composition of optimal synergistic mixtures

Ratios	Carbohydrates (%)	Lipids (%)	Proteins (%)	(Ø)
CM:SCM:CG 17:17:66	44.1	33.0	8.7	2.67
CM:CG:CW 17:66:17	39.5	33.2	11.6	2.29
CM:SCM:CW 34:33:33	51.3	1.5	17.5	1.38
Chicken Manure	23.5	1.8	17.1	1

Source: The authors

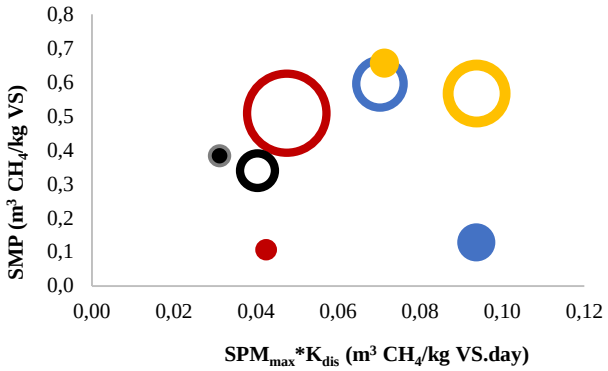


Figure 3. Comparison of uncertainty surfaces for methane production rate. Areas completely filled and empty represent organic loads of 18 and 9 g VS/L, respectively.
Source: The authors

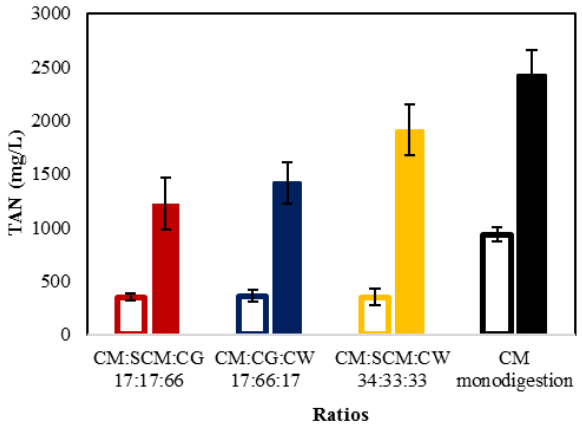


Figure 4. Final TAN for optimal synergistic ratios with organic loads of 9 and 18 g VS/L.
Source: The authors

Fig. 3 also shows that the SMP for the CM:SCM:CW ratio of 34:33:33 significantly increased (p = 0.000) from 0.57 ± 0.02 to 0.66 ± 0.01 m^3 CH_4/kg VS via doubling of the organic load. On the other hand, SMP decreased with the CM:CG:SCM ratio of 17:17:66 and CM:CG:CW ratio of 17:66:17. For the organic load of 18 g VS/L, the CM:CG:SCM ratio of 17:17:66 and CM:CG:CW ratio of 17:66:17 achieved SMPs of 0.11 ± 0.01 and 0.13 ± 0.00 m^3 CH_4/kg VS, respectively. These values were lower than the SMP obtained with the control (CM monodigestion) of 0.38 ± 0.01 m^3 CH_4/ kg VS.

Via doubling of the organic loads, the CM:CG:SCM ratio of 17:17:66 and CM:CG:CW ratio of 17:66:17 increased K_{dis} to 0.38 ± 0.02 and 0.74 ± 0.02 $days^{-1}$, respectively. For these loads, increases in the hydrolysis rate reduced SMP. High K_{dis} values indicate rapid hydrolysis rate of the soluble fractions of the residue [10]. This rapid hydrolysis rate is due to higher acidogenic activity, which is stimulated by increased nutrient availability with greater organic loads [13]. During digestion process, the cellular growth rate ($Y_{x/s}$) of acidogens (0.15 to 0.17 g VS/g COD) is much higher than those of acetogens (0.025 to 0.051 g VS/g COD) and methanogenic archaea (0.020 to 0.054 g VS/g COD) [23]. Consequently, the anaerobic process requires organic loads with hydrolytic activity proportional to both acidogenic and methanogenic activity to avoid process instabilities. On the other hand, K_{dis} for the CM:SCM:CW ratio of 34:33:33 decreased from 0.15 ± 0.02 to 0.11 ± 0.01 $days^{-1}$ when the organic load doubled from 9 to 18 g VS/L. The hydrolytic activity likely decreased proportionally with both methanogenic and acidogenic activity, maintaining cellular homeostasis. K_{dis} constants varied from 0.10 to 0.15 $days^{-1}$, values similar to those commonly reported in the literature for chicken manure codigestion [7]. With an organic load of 9 g VS/L, Kdis values of the optimal synergistic mixtures were equal statistically to that of monodigestion. Codigestion with low organic loads therefore presented no significant benefit over the mono-substrate in terms of biodegradation rate.

In general, an organic load of 18 g VS/L resulted in antagonistic effects for the CM:CG:SCM ratio of 17:17:67 and CM:CG:CW ratio of 17:66:17. Meanwhile, the CM:SCM:CW ratio of 34:33:33 exhibited synergistic effects. Then, toxic compounds may have remained under the inhibition or saturation threshold for CM:SCM:CW ratio of 34:33:33. These results support a new approach for the evaluation of synergistic effects in AcoD. Synergy is effectively achieved with co-substrate supplementation when the organic load increases while negative factors such as pH, fatty acids accumulation, and ammonia toxicity are reduced during the digestion process. Effective synergy facilitates high biogas production rates and low hydraulic retention times, contributing to an optimal anaerobic system.

3.3. Inhibition outlook of synergy

Fig. 4 shows the final TAN values for organic loads of 9 and 18 g VS/L. Monodigestion of CM achieved a final TAN concentration of 935 ± 66 mg/L, while the optimal synergistic ratios achieved TAN concentrations of 368 to 361 mg/L. With organic loads of 9 g VS/L, TAN concentrations for all assays remained below the inhibition threshold of 2,500 to 3,000 mg/L [3]. With organic loads of 18 g VS/L, the CM control achieved a TAN concentration nearly within the inhibition threshold at 2,427 ± 237 mg/L. Otherwise, TAN values of codigestion assays ranged from 1,220 to 1,912 mg/L, indicating that synergy between cosubstrates reduced the risk of ammonia inhibition. This can be explained by an optimum C/N ratio (25:1 and 30:1) Previous report show than CM codigestion present low concentration of TAN [24], which is consistent with the results of this study.

4. Conclusion

Synergy in the anaerobic codigestion of chicken manure with industrial wastes was stimulated with high concentrations of lipids in the mix. Synergy was then conditioned by tolerance and adaptability of the microbial consortia to a high lipid biodegradability rate. Organic loads below 9 g VS/L achieved synergistic effects because TAN concentrations ranged below saturation or inhibition thresholds. However, reliable synergy effects can be achieved to increasing organic load and methane production meanwhile negative impacts in the system are reduced.

Multi-component codigestion is a viable strategy to achieve synergy, increase methane production, and reduce ammonia inhibition. As cosubstrates used in this study are easy introducible into the poultry value chain, anaerobic digesters could be implemented to improve the sustainability of the poultry industry.

References

[1] Wang, M., Sun, X., Li, P., Yin, L., Liu, D., Zhang, Y., Li, W. and Zheng, G., A novel alternate feeding mode for semi-continuos anaerobic co-digestion of food waste with chicken manure. Bioresour. Technol., 164, pp. 309-314, 2014. DOI: 10.1016/j.biortech.2014.04.077

[2] -Batista, J., Castro, L. and Escalante, H., Effect of chicken manure organic load on biomethane potential. Colomb. J. Biotechnol., 17(1), pp. 18-23, 2015. DOI: 10.15446/rev.colomb.biote.v17n1.39971

[3] Niu, Q., Qiao, W., Qiang, H., Hojo, T. and Li, Y., Mesophilic methane fermentation of chicken manure at a wide range of ammonia concentration: Stability, inhibition and recovery. Bioresour. Technol., 137, pp. 358-367, 2013. DOI: 10.1016/j.biortech.2013.03.080

[4] Abouelenien, F., Namba, Y., Kosseva, M., Nishio, N. and Nakashimada, Y., Enhancement of methane production from co-digestion of chicken manure with agricultural wastes. Bioresour. Technol., 159, pp. 80-87, 2014. DOI: 10.1016/j.biortech.2014.02.050

[5] Xie, S., Wickham, R. and Nghiem, L., Synergistic effect from anaerobic co-digestion of sewage sludge and organic wastes. International Biodeterioration and Biodegradatio, 116, pp. 191-197, 2017. DOI: 10.1016/j.ibiod.2016.10.037

[6] Zhang, T., Yang, Y., Liu, L., Han, Y., Ren, G. and Yang, G., Improved biogas production from chicken manure anaerobic digestion using cereal residues as co-substrates. Energy&Fuels, 28, pp. 2490-2495, 2014. DOI: 10.1021/ef500262m

[7] Li, Y., Zhang, R., Chen, C., Liu, G., He, Y. and Liu, X., Biogas production from co-digestion of corn stover and chicken manure under anaerobic wet, hemi-solid, and solid state conditions. Bioresour. Technol., 149, pp. 406-412, 2013. DOI: 10.1016/j.biortech.2013.09.091

[8] Labatut, R., Angenent, L. and Scott, N., 2011. Biochemical methane potential and biodegradability of complex organic substrates. Bioresour. Technol., 102, pp. 2255-2264, 2013. DOI: 10.1016/j.biortech.2010.10.035

[9] Sharma, D., Espinosa-Solares, T. and Huber, D.H., Thermophilic anaerobic co-digestion of poultry litter and thin stillage. Bioresour. Technol., 136, pp. 251-256, 2013. DOI: 10.1016/j.biortech.2013.03.005

[10] Astals, S., Batstone, D.J., Mata-Alvarez, J. and Jensen, P.D., Identification of synergistic impacts during anaerobic co-digestion of organic wastes. Bioresour. Technol., 169, pp. 421-427, 2014. DOI: 10.1016/j.biortech.2014.07.024

[11] Pagés-Díaz, J., Pereda-Reyes, I., Taherzadeh, M., Sárvári-Horváth, I. and Lundin, M., Anaerobic co-digestion of solid slaughterhouse wastes with agro-residues: synergistic and antagonistic interactions determined in batch digestion assays. Chem. Eng., J. 245, pp. 89-98, 2014. DOI: 10.1016/j.cej.2014.02.008

[12] Raposo, F., Borja, R., Martín, M.A., Martín, A., de la Rubia, M.A. and Rincón, B., Influence of inoculum–substrate ratio on the anaerobic digestion of sunflower oil cake in batch mode: process stability and kinetic evaluation. Chem. Eng. J., 149, pp. 70-77, 2009. DOI: 10.1016/j.cej.2008.10.001

[13] Tanimu, M., Ghazi, T., Harun, M. and Idris, A., Effect of feed loading on biogas methane production in batch mesophilic anaerobic digesters treating food waste. Int. J. Chem. Environ. Eng., 5(1), pp. 39-44, 2014.

[14] Wang, B., Strömberg, S., Li, C., Nges, I., Nistor, M., Deng, L. and Liu, J., Effects of substrate concentration on methane potential and degradation kinetics in batch anaerobic digestion. Bioresour. Technol., 194, pp. 240-246, 2015. DOI: 10.1016/j.biortech.2015.07.034

[15] Mata-Alvarez, J., Dosta, J., Romero-Güiza, M.S., Fonoll, X., Peces, M. and Astals, S., A critical review on anaerobic co-digestion achievements between 2010 and 2013. Ren. Sustain. Energy Rev., 36, pp. 412-427, 2014. DOI: 10.1016/j.rser.2014.04.039

[16] Angelidaki, I., Alves, M., Bolzonella, D., Borzacconi, L., Campos, J.L., Guwy, A.J., Kalyuzhnyi, S., Jenicek, P. and van Lier, J.B., Defining the biomethane potential (BMP) of solid organic wastes and energy crops: a proposed protocol for batch assays. Water Sci. Technol., 59 (5), pp. 927-934, 2009. DOI: 10.2166/wst.2009.040

[17] APHA., 21th edition standard methods for the examination of water and wastewater. American public health association, Washington. ISBN 978-0-87553-047-5, 2005.

[18] Malta, E., Ferraz, F., Ribeiro, N., Oliveira, J., Frota, M. and Frische-Neto, R., Comparative efficacy of the conventional and automated methods for determining neutral and acid detergent fiber. Comun. Sci. 7(1), pp. 30-37, 2016. DOI: 10.14295/cs.v7i1.432

[19] Neumann, P., Torres, A., Fermoso, F.G., Borja, R. and Jeison, D., Anaerobic co-digestion of lipid-spent microalgae with waste activated sludge and glycerol in batch mode. International Biodeterioration & Biodegradation, 100, pp. 85-88, 2015. DOI: 10.1016/j.ibiod.2015.01.020

[20] Mao, C., Feng, Y., Wang, X. and Ren, G., Review on research achievements of biogas from anaerobic digestion. Renewable and Sustainable Energy Reviews, 45, pp. 540-555, 2015. DOI: 10.1016/j.rser.2015.02.032

[21] Esposito, G., Frunzo, L., Giordano, A., Liotta, F., Panico, A., Pirozzi, F., Anaerobic co-digestion of organic wastes. Rev Environ. Sci. Biotechnol., 11(4), pp. 325-341, 2012. DOI: 10.1007/s11157-012-9277-8

[22] Galí, A., Benabdallah, T., Astals, S. and Mata-Alvarez, J., Modified version of ADM1 model for agro-waste application. Bioresource Technology, 100, pp. 2783-2790, 2009. DOI: 10.1016/j.biortech.2008.12.052

[23] Viana, M.B., Freitas, A.V., Leitão, R.C., Pinto, G.A.S. and Santaella, S.T., Anaerobic digestion of crude glycerol: a review. Environ. Technol. Rev., 1(1), pp. 81-92, 2012. DOI: 10.1080/09593330.2012.692723

[24] Wang, X., Yang, G., Feng, Y., Ren, G. and Han, X., Optimizing feeding composition and carbon–nitrogen ratios for improved methane yield during anaerobic co-digestion of dairy, chicken manure and wheat straw. Bioresour. Technol., 120, pp. 78-83, 2012. DOI: 10.1016/j.biortech.2012.07.112, DOI: 10.1016/j.biortech.2012.06.058, DOI: 10.1016/j.biortech.2012.02.069

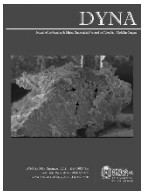
L. Castro-Molano, is graduated the BSc. Chemical Engineer and PhD in Chemical Engineering from the Industrial University of Santander (UIS), Colombia. She has worked in the research lines of biotechnological processes and anaerobic digestion, where she has 12 years of experience. She has published 16 articles (national and international journals) and 2 book chapters in the area of anaerobic digestion. She has participated as a speaker in 14 events (national and international) and has belonged to five research projects. Currently, she is teaching at the Industrial University of Santander, Colombia.
ORCID ID: 0000-0001-8893-6310

H. Escalante-Hernández, is graduated the BSc. Chemical Engineer and MSc. from Universidad Industrial de Santander (UIS) in Colombia. He holds a PhD in Chemical Engineering from the University of Cantabria, Spain, and has worked as a researcher in the field of chemical engineering and industrial biotechnology at UIS. He counts with 10 years of Experience in anaerobic digestion. He has published 30 articles (national and international journals), two books and two book chapters, presented 38 papers (national and international events) and has belonged to fourteen research projects. Nowadays, he is teaching at UIS, Colombia.
ORCID ID: 0000 - 0002 - 6257 – 8110

L. Lambis-Benítez, received the BSc. Eng in Chemical Engineering and MSc. (c) from Universidad Industrial de Santander (UIS), Colombia. He has worked in the research line of bioprocess specifically anaerobic digestion of industrial wastes, where he has 5 years of experience. Currently, he is teaching at the Industrial University of Santader, Colombia.
ORCID ID: 0000-0003-4309-9648

J. Marín-Batista, is a MSc. Chemical Engineer from the Industrial University of Santander, Colombia and currently a PhD student at University Autonoma of Madrid, Spain. He has worked in biotechnological processes which is documented in scientific papers and conferences.
ORCID ID: 0000-0002-4325-9560

UNIVERSIDAD NACIONAL DE COLOMBIA
SEDE MEDELLÍN
FACULTAD DE MINAS



DYNA
http://dyna.medellin.unal.edu.co/

Palladium nanoparticles from a surfactant-modified hydroxysalt exchanged with tetrachloropalladate

Maby Mool Martínez [a], Rogelio Ocampo-Cardona [a], Jhon Mauricio Aguirre-Cortés [a,b,c], Oscar Giraldo [b,c] & Luz Amalia Ríos-Vásquez [a]

[a] *Facultad de Ciencias Exactas y Naturales, Universidad de Caldas, Manizales, Colombia. maby.martinez@ucaldas.edu.co, rogelio.ocampo@ucaldas.edu.co, jhon.aguirre@ucaldas.edu.co, amalia.rios@ucaldas.edu.co*
[b] *Departamento de Física y Química, Universidad Nacional de Colombia, sede Manizales, Manizales, Colombia. ohgiraldoo@unal.edu.co*
[c] *Laboratorio de Materiales Nanoestructurados y Funcionales, Universidad Nacional de Colombia, sede Manizales, Manizales, Colombia*

Received: October 04th, 2017. Received in revised form: June 22nd, 2018. Accepted: July 18nd, 2018.

Abstract
Palladium nanoparticles supported in the interlayer space of hydroxysalts were obtained from zinc hydroxychloride via a prior intercalation of the anionic surfactant sodium dodecyl sulfate (DS), followed by an exchange with potassium tetrachloropalladate and its final reduction to metallic palladium by ethanol. The final materials and their intermediates were characterized by several instrumental techniques such as PXRD, N_2 adsorption, SEM, and TEM. The comparative analyses revealed clearly visible changes on structure, specific surface area and morphology of the reduced material with respect to the starting precursors. The analyses demonstrated that, upon modification of the starting material with the surfactant, the resulting material had a significantly enhanced interlayer space and BET area, which were fairly maintained until the reduced palladium-containing hydroxysalt was obtained.

Keywords: surfactant-modified zinc hydroxychloride; palladium nanoparticles; tetrachloropalladate; anionic clays

Nanopartículas de paladio a partir de una hidroxisal modificada con surfactante intercambiada con tetracloropaladato

Resumen
Se obtuvieron nanopartículas de paladio soportadas en el espacio interlaminar de hidroxisales obtenidas a partir de hidroxicloruro de zinc, mediante la intercalación previa del surfactante aniónico dodecil sulfato de sodio (DS), seguida por intercambio con tetracloropaladato de potasio y la reducción final a paladio metálico mediante etanol. Los materiales finales e intermediarios fueron caracterizados mediante varias técnicas instrumentales tales como PXRD, adsorción de N_2, SEM y TEM. Los análisis comparativos revelaron cambios claramente observables en la estructura, área superficial específica y morfología del material reducido con respecto a los precursores de partida. Los análisis demostraron que, tras la modificación del material de partida con el surfactante, en el material resultante se incrementó el espacio interlaminar y el área BET, los cuales se conservaron considerablemente hasta la obtención de la hidroxisal que contenía nanopartículas de paladio reducido.

Palabras clave: hidroxicloruro de zinc modificado con surfactante; nanopartículas de paladio; tetracloropaladato; arcillas aniónicas

1. Introduction

Clays are interesting materials which have been extensively used for a number of industrial applications, for example, they are applicable in the preparation of nanocomposites [1], controlled-release pharmaceutical systems [2,3], catalytic supports [4,5], and other purposes. A category of clays, layered double hydroxides (LDH), are useful materials because it is possible to modulate several of their physical-chemical properties by proper modification of the preparation method and their chemical composition [6-10]. LDH consist of positively charged layers of metallic

How to cite: Martínez, M,M., Ocampo-Cardona, R., Aguirre-Cortés, J.M., Giraldo, O. and Ríos-Vásquez, L.A., Palladium nanoparticles from a surfactant-modified hydroxysalt exchanged with tetrachloropalladate. DYNA, 85(206), pp. 142-147, September, 2018.

© The author; licensee Universidad Nacional de Colombia.

hydroxides containing water molecules and anions in the interlayer spaces that compensate the charge of the laminae. The positive charge on the layers comes from the substitution of divalent cations by trivalent ones on some octahedral positions, giving rise to structures that are represented according to equation (1):

$$[M(II)_{1-x}^{2+}M(III)_{x}^{3+}(OH)_2]^{x+}\left(A^{n-}\right)_{x/n}.mH_2O \qquad (1)$$

Where *M* may be a divalent or trivalent metal, *x* corresponds to the molar ratio *M(II)/(M(II)+M(III))*, and A^{n-} is the interlayer chemical species with charge *n*, while *m* is the hydration extent [11,12]. These materials have successfully been used for immobilization of metallic nanoparticles based on Au, Pt, Ni or Pd [13-15], useful as heterogeneous catalysts for organic reactions such as alcohol oxidations, hydrogenations, carbon-carbon couplings and others [16-18].

Another kind of clays is constituted by metallic hydroxysalts, which are represented by equation (2):

$$\left[M_3^{oct}(vac)^{oct}M_2^{tetra}(OH)_8\right]^{2+}\left(A^{n-}\right)_{2/n}.zH_2O \qquad (2)$$

Unlike in LDH, the *M* in hydroxysalts corresponds to only one kind of metal, but similarly to the LDH structure, metals in hydroxysalts occupy not only octahedral positions (*oct*) inside the layers but also tetrahedral positions (*tet*) which are differentiated. About one-fourth of octahedral sites are empty $(vac)^{oct}$ and they are compensated by tetrahedral arrangements up and down in that particular point of the layer. As in LDH, this structural feature gives rise to a charge excess that promotes the intercalation of hosted anionic species in the interlayer space [19,20].

Conventionally, laminar hydroxysalts are solid structures resulting from the reaction of a metal oxide and a salt, promoting in one side the metal species that form the laminar inorganic structure and the interspace anion which confers its stability [19, 21-22]. A particularly useful hydroxysalt is zinc hydroxychloride ($Zn_5(OH)_8Cl_2.H_2O$: simonkolleite: ZHC) [22] which has advantages as a supporting material for catalytic systems in comparison to other frequently used materials, especially regarding their easy preparation and modification. Some authors have reported the synthesis of zinc hydroxychloride by adjusting pH around 6 units by the addition of NaOH [22], and others have prepared hidroxysalts hosting nitrate anion in the interspace, through a two-day reaction of zinc oxide and zinc nitrate at temperatures above 60 ºC, but a shorter methodology to prepare ZHC would be welcome, so we prepared a highly crystalline material in a shorter reaction time.

On the other hand, there are reports in the literature [6-10] about chemical modification of clays by inserting hosting molecules in the interlayer space resulting in materials with modulated properties, especially for catalysts. Taking into account the above, we decided to insert a surfactant into the interlayer space of ZHC to generate lipophilicity inside the material, and then it was exchanged with a palladate complex anion and reduced to metal palladium. It would be expected for this new material to be a promising heterogeneous catalysts for C-C coupling reactions [1,2].

This work illustrates the arrangement of palladium nanoparticles on zinc hydroxychloride which was previously exchanged with a surfactant aiming to take advantage of the wide interspace distances which might positively affect the distribution of palladium nanoparticles. The physical-chemical characterization of the intermediate and target materials and their properties such as morphology, textural analysis, crystallinity and particle size are being presented and discussed as well.

2. Materials and methods

2.1. Starting materials

Analytical grade reagents were used: ZnO (Sigma-Aldrich, 99+%), $ZnCl_2$ (Merck, 98%), $CH_3(CH_2)_{11}OSO_3Na$ (DS) (Carlo Erba, 92%), Na_2PdCl_4 (Aldrich, 99,99%). Distilled water was deionized previously in our laboratories. All materials were dried at room temperature and atmospheric pressure without the use of drying solvents.

2.2. Physical-chemical characterization of the materials

All materials (ZHC, ZHC-DS, ZHC-DS-PdCl, and ZHC-DS-Pd^0) were characterized by X-Ray diffraction (PXRD), Scanning Electronic Microscopy (SEM), Transmission Electronic Microscopy (TEM), surface area and pore distribution were measured at the temperature of liquid nitrogen (-196 ºC).

PXRD analyses were carried out on a Rigaku Miniflex II instrument (30 kV and 15 mA) that uses copper as the radiation source (Cu Kα) with a scan rate of 2° per minute in normal environmental conditions. The crystal size of Pd in the ZHC- Pd^0 was estimated from its diffraction pattern by the Debye-Scherrer´s method [25].

Micrograph images were run on a Scanning Electron Microscope SEM, model QUANTA 250 of FEI, while Transmission Electronic Microscopy TEM analyses were run in a JEOL 1200 EX instrument.

Nitrogen adsorption-desorption isothermals and the textural properties of the materials were determined by nitrogen adsorption on a Micromeritics instrument ASAP 2020, using samples of about 0.100 g. Specific surface areas were estimated from the adsorption isothermals by applying the BET method [26].

2.3. Experimental methods

Precursor preparation **(ZHC)**. Zinc hydroxychloride was obtained in an aqueous phase using the reported procedure [27], but in our case, we did not use an autoclave. ZnO (3.5 g) was added to 100 mL of an aqueous solution containing 136 g of $ZnCl_2$. The resulting suspension was shaken at room temperature under a nitrogen atmosphere for 6 hours, and a white precipitate was obtained by centrifugation, and then it was washed several times with distilled deionized water (DDW). The material was dried at room temperature.

Surfactant-modified, ***ZHC-DS***. To a 100 mL of a 0.05M solution of sodium dodecyl sulfate, 1.3 g of ZHC was added.

The entire suspension was shaken at room temperature for 22 hours. A white precipitate was obtained by filtration, and then it was washed several times with distilled deionized water (DDW) and dried at room temperature.

Tetrachloropalladate-exchanged, ***ZHC-DS-PdCl***. The surfactant in ZHC-DS was exchanged with the tetrachloropalladate anion. 1.5 g of Na_2PdCl_4 was added to 50 mL of an aqueous suspension containing 0.3 g of ZHC-DS. The resulting suspension was shaken at room temperature for 5 hours, and a brown precipitate was obtained by filtration. Then, it was washed several times with distilled deionized water (DDW) and dried at room temperature for 12 hours.

Nanoparticles of Pd in surfactant-modified, ***ZHC-DS-Pd^0***. The target material was obtained by reduction of ZHC-DS-PdCl. 72 mg of ZHC-DS-PdCl were suspended in 5.0 mL of CH_3CH_2OH and shaken for 2 hours at room temperature. A black precipitate was obtained by centrifugation and it was washed seven times with 3.0 mL of CH_3CH_2OH each.

3. Results and discussion

Zinc oxide and zinc chloride were combined to form the respective ZHC, a white material that was used as the starting precursor to assemble the palladium nanoparticles inside the ZHC. The target material was obtained through a step-by-step sequence that involved: (1) synthesis of the hydroxysalt (ZHC) according to the standard procedure [19]; (2) intercalation of dodecyl sulfate anion in the interlayer space of the ZHC precursor (**ZHC-DS)**; (3) exchange of dodecyl sulfate by tetrachloropalladate anion (**ZHC-DS-PdCl)**; (4) reduction of the palladium species retained inside the ZHC to be converted into metallic palladium nanoparticles **ZHC-DS-Pd^0**. Visible qualitative changes in the appearance of the materials upon going successively from precursors to intermediates and to the final product are strong suggestions that modifications were occurring properly, and such transformations were confirmed by instrumental analysis as discussed ahead. Our first piece of evidence comes from X-ray diffraction (PXRD patterns) of the materials (Fig. 1), exhibiting the typical lines corresponding to laminar structures.

For the ZHC precursor, Fig. 1a suggests the presence of the expected typical pattern of this kind of materials [28] and shows the crystallographic planes (003), (006), (110) and (0012) corresponding to 2Θ values of 11.2, 22.5, 28.1 and 46.0° respectively, and a basal spacing of 7.8 Å. Fig. 1b-1d exhibits substantial differences of the surfactant-modified hydroxysalt (ZHC-DS, Fig. 1b) and the subsequent materials (ZHC-DS-PdCl, Fig. 1c, and ZHC-DS-Pd^0, Fig. 1d) with respect to the precursor ZHC (Fig. 1a). The disappearing of the characteristic zinc hydroxychloride peaks evidences the transformation of the laminar phase into a new one, with the surfactant molecules being intercalated in the interlayer space, giving rise to an ordered bilayer structure, where the longitudinal axis of the surfactant molecules turns out to be approximately perpendicular to the precursor laminae [29]. In Fig. 1b, two peaks at low 2Θ values are observed, which correspond to two phases with d-spacing of 32.3 Å and 26.2 Å for the main phase. The first value closely resembles the reported data of 31.5 Å for a nitrate-based hydroxysalt that was exchanged with DS in methanol in a theoretical and experimental study [29], which concluded that external variables such as solvent and temperature of the system exert some influence on the structural arrangement of surfactant in the interlayer space. According to it, we believe that in our case the presence of the second phase which is absent in the materials studied by Demel *et al*. [29], may be the result of the use of water instead of methanol as the solvent. In turn, as observed in Fig. 1c for ZHC-DS-PdCl, as a consequence of the intercalation of a $PdCl_4^{-2}$ anion in the interlayer space, a decreased basal spacing is observed. As such, the surfactant-containing material (ZHC-DS) with original basal spacing's of 32.3 Å and 26.2 Å is changed for a material (ZHC-DS-PdCl) with a lowered basal spacing of 25.6 Å and 22.7 Å for the primary phase (Fig. 1c). These data are consistent with an expected diminution in the content of surfactant that induces a bilayer structural change in such way that a decrease in the basal spacing takes place, as reported [29].

Finally, in this sequence, Fig. 1d corresponds to the PXRD pattern of the material resulting from the reduction of the $PdCl_4^{-2}$ anion exchanged ZHC to form palladium nanoparticles (this final material was labeled ZHC-DS-Pd^0). Comparing Fig. 1c and 1d, there are substantial changes in the PXRD pattern and morphology (as shown later in Fig. 3d) of the laminar material upon reduction. As expected, palladium is reduced to metallic palladium with a consequent loss of the structural ordering which is due to the size and distribution of the resulting nanoparticles and the subsequent delamination of the ZHC-DS-PdCl material, so that the characteristic peaks of the clay are not visible anymore.

According to a previous report [21,30], palladium nanoparticles formation is suggested by the diffraction peak at about 40º in 2Θ, which is consistent with our result, and it was also confirmed by TEM images (see ahead in Fig. 3e and 3f). Based on this PXRD peak, palladium nanoparticles size was estimated in about 4 nm by using the Debye-Scherrer´s method [25].

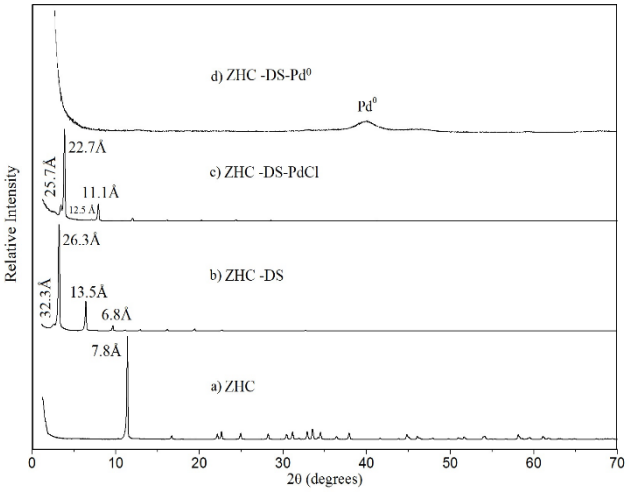


Figure 1. PXRD patterns: (a) ZHC, (b) ZHC -DS (c) ZHC -DS-PdCl, (d) ZHC -DS-Pd^0.
Source: The authors

Table 1.
Textural properties of hydroxysalts materials

Material	BET surface area ($m^2.g^{-1}$)	Pore volume ($cm^3.g^{-1}$)	Average pore size (nm)
ZHC	1.07	0.002	8.19
ZHC-DS	11.66	0.040	13.65
ZHC-DS-PdCl	6.79	0.019	11.14
ZHC-DS-Pd^0	70.11	0.23	13.19

Source: The authors

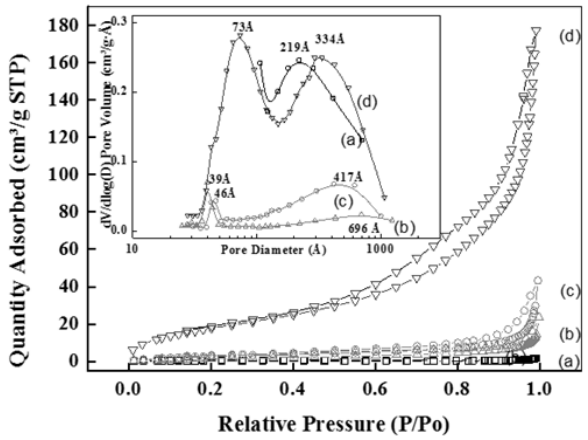


Figure 2. N_2 adsorption-desorption isotermals for (a) ZHC, (b) ZHC-DS, (c) ZHC-DS-PdCl, (d) ZHC-DS -Pd^0. Inset. Mesopore distribution by BJH method for (a) ZHC, (b) ZHC-DS (c) ZHC-DS-PdCl, (d) ZHC-DS-Pd^0.
Source: The authors

Our second piece of evidence of structural changes from precursors to intermediates and to the final material comes from adsorption-desorption isothermals at liquid N_2 temperature (Fig. 2) while the respective analysis of the physical chemical features is summarized in Table 1.

According to IUPAC classification, these are isothermals type II (Fig. 2), typical of materials with big pores, characterized by hysteresis type H2 and H3 of materials with slit-shaped pores. The surfactant-modified hydroxysalt (ZHC-DS) register a slight adsorption enhancement, likely because of the electrostatic attraction between the sulfate groups of surfactant molecules and the positive charges of the ZHC, and also because of the hydrophobic interactions of the surfactant, as other authors have reported [31].

It is important to note that ZHC pore diameter distribution is characterized by a heterogeneous distribution with diameters centered mainly at 219 Å (Fig. 2a), while the surfactant-modified ZHC (ZHC-DS) (Fig. 2b) exhibits a significant diameter decrease (39 Å), probably because the insertion of surfactant forms mesopores. Upon exchange with the $PdCl_4^{-2}$ anions, pore diameters of the resulting material (ZHC-DS-PdCl, Fig. 2c) increase again due to a possible reconfiguration of the interlayer space as explained before. After the reduction to form a palladium-containing surfactant-modified ZHC (ZHC-DS-Pd^0, Fig. 2d), a heterogeneous pore diameter distribution is observed. In Fig. 2d, the first peak suggests the presence of 73 Å-mesopores, and the second peak indicates the occurrence of pores diameters centered at around 334 Å. The first maximum might be the result of palladium nanoparticles being incorporated possibly in the interlayer space, while the second one indicates an increase of the mesopore diameters that are formed in the material due to the incorporation of bigger palladium nanoparticles and mesopores that could be formed between the particles of the material.

According to the trends observed in Table 1, the precursor material ZHC is characterized by a low BET surface area (1.07 m^2g^{-1}) which is significantly increased to 11.6 m^2g^{-1} when DS is intercalated into the material, and is in turn diminished back to 6.79 m^2g^{-1} when the $PdCl_4^{-2}$ anion entered into the material. This latter effect might be the result of a reconfiguration of the interlayer surfactant molecules because of the insertion of the $PdCl_4^{-2}$ in some of the pores, in agreement with a previous literature report [32]. Furthermore, by comparison of BET surface areas for these materials, a drastic increase from 6.79 m^2g^{-1} (in ZHC-DS-PdCl) to 70.11 m^2g^{-1} (in ZHC-DS-Pd^0) was observed, and this should be the result of the formation of palladium nanoparticles that generate mesopores with the consequent substantial increase of the pore volume, which finally results in the loss of the ordered structure in the material (consistent with Fig. 1d).

To study the morphology of the materials, SEM analyses were run for each of them, and the respective micrographies are shown in Fig. 3.

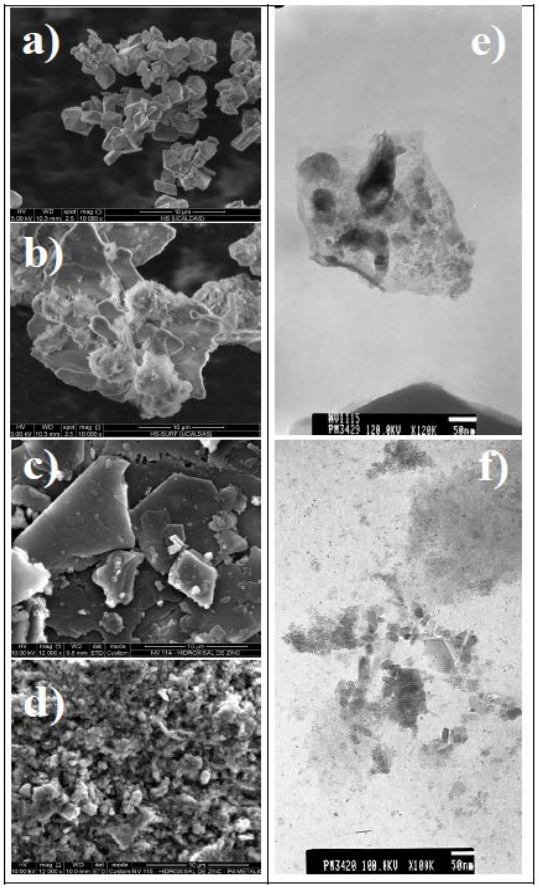


Figure 3. SEM micrographies: (a) ZHC (10.000x), (b) ZHC-DS (10.000x), (c) ZHC-DS-PdCl (12.000x), (d) ZHC-DS-Pd^0 (12.000x). (e) and (f) TEM micrographies of the reduced material ZHC-DS-Pd^0.
Source: The authors

The first image corresponds to the initial hydroxysalt (ZHC), where a crystalline material is observed, and some octahedral crystals with sizes of around 2-3 μm can be distinguished (Fig. 3a). In contrast, the morphology of the surfactant-modified hydroxysalt (ZHC-DS) is characterized by platelets of irregular thickness and irregular aggregates of flakes (Fig. 3b), which suggest the presence of two phases. This drastic change in the morphology of the materials illustrates that a DS intercalation effectively took place.

On the other hand, and according to Fig. 3c, after intercalation of the $PdCl_4^{-2}$ anions, irregularly-shaped laminae are visualized in the resulting material ZHC-DS-PdCl, which upon treatment with refluxing ethanol, changes its morphology to clusters of sub-micrometric particles (see Fig. 3d for ZHC-DS-Pd^0). Additionally, TEM images were run for the material containing reduced palladium (ZHC-DS-Pd^0), Fig. 3e and 3f, where it is possible to differentiate particles with sizes varying approximately from 4-7 nm up to bigger aggregates and even particles of 100 nm in size. Both, TEM images (Fig. 3e and 3f) and PXRD patterns (Fig. 1d) confirm the successful generation of metal palladium particles with nanometric sizes. These particles are characterized by irregular shapes and are heterogeneously dispersed throughout the material.

4. Conclusions

The physical chemical characterization of materials proved that changes were occurring from the structural, textural and morphological point of view, upon going step by step from the ZHC precursor to intermediates and to the final material. PXRD patterns confirm that an intercalation of surfactant into the interlayer space of the hydroxysalt took place, giving rise to an interstratified material (32.3 Å and 26.3 Å). Then, the exchange reaction with a $PdCl_4^{-2}$ anion promotes a decrease in the content of surfactant, which was evidenced by the PXRD analysis (basal spacing changes to 25.7 Å and 22.7 Å). Subsequently, the respective reduced material is constituted by palladium nanoparticles into the surfactant-containing material, and this fact was confirmed by both their PXRD patterns and TEM images.

The possibility of a surfactant-guided preparation of palladium nanoparticles into a hydroxysalt has been demonstrated. The significant increase of BET surface area of the reduced material is closely related to the palladium nanoparticles formation and the laminar material exfoliation. The adsorption of surfactant into a hydroxysalt makes possible to introduce a slight lipophilic character into this highly hydrophilic material, which may be taken advantage of in organic reactions, as suggested by Liu *et al* [33] who reported that a catalyzed Suzuki C-C coupling reaction with palladium nanoparticles supported on a LDH was favored by intercalation of dodecyl sulfate anion.

In order to have some idea about the likely catalytic potential of the new material, a preliminary catalytic test with our reduced material in a Suzuki C-C coupling reaction was performed, starting from iodobenzene and phenylboronic acid, which gave rise to about 90% yield of a white solid, which was not spectroscopically characterized but exhibited identical physical properties than an authentic biphenyl sample.

Acknowledgements

The authors thankfully acknowledge Universidad de Caldas, Vicerrectoría de Investigaciones y Postgrados, for the financial support of this project (code number 0526312) and to the laboratory of scanning electron microscopy (in the Stratigraphy Research Institute) at Universidad de Caldas. We also acknowledge Universidad del Cauca for the TEM analyses.

References

[1] Carmo, D. M., Oliveira, M. G. and Soares, B. G. Effect of the dispersive method in the preparation of the polyurethane/hydrotalcite nanocomposites by in situ polymerization. Applied Clay Science, 101, pp. 128-135, 2014. http://dx.doi.org/10.1016/j.clay.2014.07.027

[2] Ambrogi, V., Perioli, L., Ricci, M., Pulcini, L., Nocchetti, M., Giovagnoli, S. and Rossi, C. Eudragit® and hydrotalcite-like anionic clay composite system for diclofenac colonic delivery. Microporous and Mesoporous Materials, 115 (3), pp. 405-415, 2008. http://dx.doi.org/10.1016/j.micromeso.2008.02.014

[3] Monteiro, M., Lunz, J., Veiga, Sebastião, P. and Tavares, M. Evaluation of Nevirapine Release Kinetics from Polycaprolactone Hybrids. Materials Sciences and Applications, 7 (11), pp. 680-701, 2016. http://dx.doi.org/10.4236/msa.2016.711055

[4] An, Z., Zhang, W., Shi, H. and He, J. An effective heterogeneous L-proline catalyst for the asymmetric aldol reaction using anionic clays as intercalated support. Journal of Catalysis, 241 (2), pp. 319-327, 2006. http://dx.doi.org/10.1016/j.jcat.2006.04.035

[5] Burrueco, M. I., Mora, M., Jiménez-Sanchidrián, C. and Ruiz, J. R. Hydrotalcite-supported palladium nanoparticles as catalysts for the Suzuki reaction of aryl halides in water. Applied Catalysis A: General, 485, pp. 196-201, 2014. http://dx.doi.org/10.1016/j.apcata.2014.07.031

[6] Chen, X., Mi, F., Zhang, H. and Zhang H. Facile synthesis of a novel magnetic core-shell hierarchical composite submicrospheres Fe3O4@CuNiAl-LDH under ambient conditions. Materials Letters, 69, pp. 48-51, 2012. http://dx.doi.org/10.1016/j.matlet.2011.11.052

[7] Diao, Z. Zhang, Y. Hao, X. Wen, Z. Facile synthesis of CoAl-LDH/MnO2 hierarchical nanocomposites for high-performance supercapacitors. Ceramics International, 40 (1), pp. 2115-2120, 2014. http://dx.doi.org/10.1016/j.ceramint.2013.07.127

[8] Xie, L., Sun, G., Xie, L., Su, F., Li, X., Liu, Z., Kong, Q., Lu, C., Li, K. and Chen, C. A high energy density asymmetric supercapacitor based on a CoNi-layered double hydroxide and activated carbon. New Carbon Materials, 31 (1), pp. 37-45, 2016. http://dx.doi.org/10.1016/S1872-5805(16)60003-3

[9] Ma, J., Ding, J., Li, L., Zou, J., Kong, Y. and Komameni, S. In situ reduction for synthesis of nano-sized Cu2O particles on MgCuAl-LDH layers for degradation of orange II under visible light. Ceramics International, 41 (2), pp. 3191-3196, 2014. http://dx.doi.org/10.1016/j.ceramint.2014.10.172

[10] Hoessle, F., Plank, J. and Leroux, F. Intercalation of sulfonated melamine formaldehyde polycondensates into a hydrocalumite LDH structure. Journal of Physics and Chemistry of Solids, 80, pp. 112-117, 2015. http://dx.doi.org/10.1016/j.jpcs.2015.01.008

[11] Chakraborty, S., Kumar, M., Suresh, K. and Pugazhenthi, G. Influence of organically modified NiAl layered double hydroxide (LDH) loading on the rheological properties of poly (methyl methacrylate) (PMMA)/LDH blend solution. Powder Technology, 256, pp. 196-203, 2014. http://dx.doi.org/10.1016/j.powtec.2014.02.035

[12] Zhou, J., Xu, Z. P., Qiao, S., Liu, Q., Xu, Y. and Qian, G. Enhanced removal of triphosphate by MgCaFe-Cl-LDH: Synergism of precipitation with intercalation and surface uptake. Journal of Hazardous Materials, 189 (1-2), pp. 586-594, 2011. http://dx.doi.org/10.1016/j.jhazmat.2011.02.078

[13] Lakshmi Kantam, M., Parsharamulu, T. and Manorama, S. V. Layered double hydroxides supported nano palladium: An efficient catalyst for the chemoselective hydrogenation of olefinic bonds. Journal of

Molecular Catalysis A: Chemical, 365, pp.115-119, 2012. http://dx.doi.org/10.1016/j.molcata.2012.08.017
[14] de Rezende, S. M., Franchini, C. A., Dieuzeide, M. L., Duarte de Farias, A. M., Amadeo, N. and Fraga, M. A. Glycerol steam reforming over layered double hydroxide-supported Pt catalysts. Chemical Engineering Journal, 272, pp.108-118, 2015. http://dx.doi.org/10.1016/j.cej.2015.03.033
[15] Li, Z., Xi, W. and Lu, C. Hydrotalcite-supported gold nanoparticle catalysts as a low temperature cataluminescence sensing platform. Sensors and Actuators B: Chemical, 219, pp. 354-360, 2015. http://dx.doi.org/10.1016/j.snb.2015.05.030
[16] Huang, L., Zhou, J., Hsu, A.T. and Chen, R. Catalytic partial oxidation of n-butanol for hydrogen production over LDH-derived Ni-based catalysts. International Journal of Hydrogen Energy, 38 (34), pp. 14550-14558, 2013. http://dx.doi.org/10.1016/j.ijhydene.2013.09.068
[17] Sahoo, M. and Parida, K. M. Pd(II) loaded on diamine functionalized LDH for oxidation of primary alcohol using water as solvent. Applied Catalysis A: general, 460-461, pp. 36-45, 2013. http://dx.doi.org/10.1016/j.apcata.2013.04.003
[18] Saber, O., Goraba, H. M. and Jaafari, A. A. Catalytic activity and surface characteristics of layered Zn–Al–Si materials supported platinum. Applied Clay Science, 53, pp. 317-325, 2011. http://dx.doi.org/10.1016/j.clay.2010.12.026
[19] Cavani, F., Trifirò, F. and Vaccari, A. Hydrotalcite-type anionic clays: preparation, properties and applocations. Catalysis Today, 11 (2), pp. 173-301, 1991. http://dx.doi.org/10.1016/0920-5861(91)80068-K
[20] Ahmed, I. M. and Gasser, M. S. Adsorption study of anionic reactive dye from aqueous solution to Mg–Fe–CO3 layered double hydroxide (LDH). Applied Surface Science. 259, pp. 650-656. 2012. http://dx.doi.org/10.1016/j.apsusc.2012.07.092
[21] Nityashree, N. and Rajamathi, M. Interstratified composite of the anionic clays, Zn5(OH)8(NO3)2·2H2O and Ni3Zn2(OH)8(NO3)2·2H2O, by delamination-costacking. Journal of Physics and Chemistry of Solids. 74 (8) pp. 1164-1168, 2013. http://dx.doi.org/10.1016/j.jpcs.2013.03.015
[22] Khamlich, S., Abdullaeva, Z., Kennedy, J. V. and Maaza, M. High performance symmetric supercapacitor based on zinc hydroxychloride nanosheets and 3D graphene-nickel foam composite. Applied Surface Science, 405, pp. 329-336, 2017. http://dx.doi.org/10.1016/j.apsusc.2017.02.095
[23] Li, B., Wang, C., Chen, G., and Zhang, Z. Palladium-phosphinous acid complexes catalyzed Suzuki cross-coupling reaction of heteroaryl bromides with phenylboronic acid in water/alcoholic solvents. Journal of Environmental Sciences, 25 (6), pp. 1083-1088, 2013. http://dx.doi.org/10.1016/S1001-0742(12)60132-6
[24] Negishi, E. I. Palladium- or nickel-catalyzed cross coupling. A new selective method for carbon-carbon bond formation Acc. Chem. Res., 15, pp. 340-348, 1982. http://dx.doi.org/10.1021/ar00083a001
[25] Moore, D. M. and Reynolds, R. C., Jr. X-ray diffraction and the identification and analysis of clay minerals, 2nd ed. Oxford: University Press, 1998.
[26] Chui, S. S.-Y., Lo, S. M.-F., Charmant, J. P. H., Orpen, A. G. and Williams, I. D. A chemically functionalizable nanoporous material [Cu3(TMA)2(H2O)3]n. Science, 283 (5405), pp. 1148-1150, 1999. http://dx.doi.org/10.1126/science.283.5405.1148
[27] Tanaka, H., Futoyu, A., Fujioka, A., Kandori, K. and Ishikawa, T. Influence of Ti(IV) on the structure and properties of zinc hydroxychloride. Corrosion Science, 50 (11), pp. 3154-3159, 2008. http://dx.doi.org/10.1016/j.corsci.2008.08.022
[28] Tanaka, H., Tashima, K., Kandori, K., Ishikawa, T. and Nakayama, T. Structure and properties of Ti (IV)-doped zinc hydroxychloride rusts formed at various temperatures. Corrosion Science, 53 (2), pp. 696-702, 2011. http://doi.org/10.1016/j.corsci.2010.10.018
[29] Demel, J., Hynek, J., Kovaŕ, P., Dai, Y., Taviot-Guého, C., Demel, O., Pospíšil, M. and Lang, K. Insight into the Structure of Layered Zinc Hydroxide Salts Intercalated with Dodecyl Sulfate Anions. Journal of Physical Chemistry C, 118 (46), pp. 27131-27141, 2014. http://dx.doi.org/10.1021/jp508499g
[30] Papp, S., Szücs, A. and Dékány, I. Preparation of Pd0 nanoparticles stabilized by polymers and layered silicate. Applied Clay Science, 19 (1-6), pp. 155-172, 2001. http://dx.doi.org/10.1016/S0169-1317(01)00048-5
[31] Pavan, P. C., Gomes, G. de A. and Valim, J. B. Adsorption of sodium dodecyl sulfate on layered double hydroxides. Microporous and Mesoporous Materials. 21 (4-6), pp. 659-665, 1998. https://doi.org/10.1016/S1387-1811(98)00054-7
[32] Wibulswas, R., White, D. A. and Rautiu, R. Adsorption of Phenolic Compounds from Water by Surfactant-Modified Pillared Clays. Process Safety and Environmental Protection, 77 (2), pp. 88-92, 1999. http://dx.doi.org/10.1205/095758299529857
[33] Liu, S., Zhou, Q., Jin, Z., Jiang, H. and Jiang, X. Dodecylsulfate Anion Embedded Layered Double Hydroxide Supported Nanopalladium Catalyst for the Suzuki Reaction, Chinese Journal of Catalysis, 31 (5), pp. 557-561, 2010. http://dx.doi.org/10.1016/S1872-2067(09)60072-3

M.M. Martínez, received her BS. Education degree in Biology and Chemistry in 2005 and the M.Sc. Chemistry in 2010, both degrees obtained from Universidad de Caldas, Manizales, Colombia. She currently works in the Department of Chemistry at Universidad de Caldas. Her present research is developed mainly in heterogeneous organic catalysis using nanostructured materials and in the study of medicinal plants. Contact information: maby.martinez@ucaldas.edu.co
ORCID: orcid.org/0000-0002-7509-9610

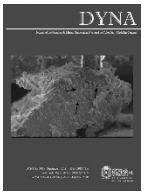
R. Ocampo-Cardona, received his BS. Education degree in Biology and Chemistry in 1984 from Universidad de Caldas, Colombia, and the M.Sc. degree in Chemistry in 1997, and the Ph.D. degree in Chemistry in 1997, from Universidad del Valle, Cali, Colombia. Currently, he is a full professor in the Department of Chemistry at Universidad de Caldas. His present research is mainly developed in organic synthesis, particularly synthesis of molecules with medicinal interest. His research is also focused to heterogeneous organic catalysis using nanostructured materials. Contact information: rogelio.ocampo@ucaldas.edu.co
ORCID: orcid.org/0000-0002-3375-6352

J.M. Aguirre-Cortes, Graduated as Chemical Engineer and Master in Engineering in 2005 and 2008 respectively from the National University of Colombia. He has worked as a professor at the University of Caldas in areas of basic chemistry. His research interests include the synthesis and characterization of nanostructured materials. Contact information: jhon.aguirre@ucaldas.edu.co
ORCID: orcid.org/0000-0002-9700-3544

O. Giraldo, completed his BSc. in Chemistry in 1992, at Universidad del Valle, Cali, Colombia, and his Ph.D. degree in Chemistry in 2000, at the University of Connecticut, USA. He is a full professor in the Physics and Chemistry Department, Universidad Nacional de Colombia, Manizales Colombia. His research interests include: nanostructured functional materials, solid state chemistry, heterogeneous catalysis, hybrid materials, biomaterials, biopolymer-based nanocomposite materials and applications of material chemistry. Contact information: ohgiraldoo@unal.edu.co
ORCID: orcid.org/0000-0002-9213-6348

L.A. Ríos-Vásquez, received her BS. Education degree in Biology and Chemistry in 1987 from Universidad de Caldas, Colombia, and the M.Sc. degree in Chemistry in 1992, and the Ph.D. degree in Chemistry in 1998, from Universidad del Valle, Cali, Colombia. Currently, she is a full professor in the Department of Chemistry at Universidad de Caldas. Her present research is mainly developed in organic synthesis, particularly synthesis of molecules with medicinal interest. Contac information: amalia.rios@ucaldas.edu.co
ORCID: orcid.org/0000-0002-4510-7771

UNIVERSIDAD NACIONAL DE COLOMBIA
SEDE MEDELLÍN
FACULTAD DE MINAS



DYNA
http://dyna.medellin.unal.edu.co/

Morphological and nanomechanical characterization of Guadua *Angustifolia kunth* fiber by means of SEM and AFM

Martin Eduardo Espitia-Nery, Dery Esmeralda Corredor-Pulido, Nelson Javier Rodríguez-Ramírez & Jeimy Natalia Calderón Bustos

Facultad de Ingeniería, Corporación Universitaria Minuto de Dios, Bogotá, Colombia. mespitia@uniminuto.edu, dery.corredor@uniminuto.edu, nrodrigue35@uniminuto.edu.co, jcalderonbu@uniminuto.edu.co

Received: March 7th, 2018. Received in revised form: May 25th, 2018. Accepted: August 4th, 2018.

Abstract
Recent developments in engineering have promoted the use of reinforced composite materials from natural fibers, which provides an opportunity to investigate such materials using state-of the-art tools. Here we present a morphological and nanomechanical characterization of the parallel section of the axis of guadua *Angustifolia kunth* fibers (GAK) from Colombia, focusing on properties such as hardness (nanoindentation), roughness and topography. Our method was based on the application of scanning electron microscope (SEM) and atomic force microscope (AFM). AFM provided curves of force by displacement, as well as characteristics of dynamic nanoindentation systems and images. Their analysis revealed ridges and valleys on the surface of GAK fibers. The estimated surface roughness of 9.51 nm suggests an adequate value to provide superior adhesion between polymer and fiber. The same conclusion follows from our measurements of hardness, reduced modulus and nanoscale topography. Due to their excellent properties, we conclude that GAK fibers represent an ideal reinforcement material in polymer matrices.

Keywords: fibers of Guadua *Angustifolia kunth*; morphology; nanoindentation; SEM; AFM.

Caracterización morfológica y nanomecánica de la fibra de Guadua *Angustifolia kunth* mediante SEM y AFM

Resumen
El desarrollo reciente en la ingeniería propone el uso de materiales compuestos reforzados a partir de fibras naturales, lo cual genera la iniciativa de estudiarlos mediante herramientas sofisticadas. En esta investigación se muestran los resultados de la caracterización morfológica y nanomecánica como dureza (nanoidentación), rugosidad y topografía de la sección paralela al eje axial de fibras de guadua *Angustifolia kunth*, con el fin de encontrar las propiedades mecánicas a nanoescala de las fibras. Para ello se emplearon los microscopios electrónico de barrido (SEM) y de fuerza atómica (AFM), con este último se obtuvieron curvas de fuerza vs desplazamiento, características de sistemas dinámicos de nanoindentación e imágenes, donde a partir de análisis se encontró que la guadua *Angustifolia kunth* (GAK) presenta crestas y ondulaciones en su superficie, las cuales le brindan una rugosidad adecuada otorgando adherencia entre el polímero y la fibra, además la dureza, el módulo reducido y la topografía a escala nanométrica, lo que permite concluir que las fibras de GAK presentan mejores propiedades para ser utilizadas como material de refuerzo en matrices poliméricas.

Palabras claves: fibras de Guadua *Angustifolia kunth*; morfología; nanoindentación; SEM; AFM.

1. Introduction

Polymer matrix composites consist of a continuous phase (polymer matrix) and a dispersed phase (particles or fibers) [1,2]. Usually the dispersed phase consists of fibers. Most studies have shown that synthetic fibers such as graphite [3,4] glass [5,6], carbon [7, 8], and thermoplastic resins such as polyesters and polypropylenes [9,10] among others, can be used as reinforcement for composite materials through the incorporation of fibers, thereby improving their properties

How to cite: Espitia-Nery, M.E., Corredor-Pulido, D.E., Rodríguez-Ramírez, N.J., and Calderón-Bustos, J.N,. Morphological and nanomechanical characterization of Guadua Angustifolia kunth fiber by means of SEM and AFM. DYNA, 85(206), pp. 148-154, September, 2018.

© The author; licensee Universidad Nacional de Colombia.

[11]. However, many studies have ignored the high energy requirements and negative impact on the environment associated with the production of those materials. While some fibers are widely used in industry due to their excellent properties, they may on the other hand generate health problems such as asbestosis [12]. In Colombia, a considerable volume of organic waste derived from the production of fique, guadua, coconut, rice husk, bagasse, husk and other husk fibers have contributed to increasing pollution levels [13,14]. Therefore, the incorporation of organic fibers as reinforcement in polymeric matrices would not only avoid the use of synthetic or artificial fibers, but also reduce the environmental impact generated by their disposal.

2. Materials and methods

For our study, fibers of guadua *Angustifolia kunth* were collected in El Peñón, Cundinamarca Department, Colombia. Fiber extraction was mechanically carried out, so that fiber diameter was under 1mm and lengths under 5mm. Surfaces of GAK fibers were then modified with 5% sodium hydroxide (NaOH) solution to remove impurities [36], continuously stirred for half an hour at room temperature, and finally washed with distilled water (neutral pH) to completely eliminate NaOH. Fibers were then left to dry for 12 hours at room temperature, and 24 hours at 60 ° C [37].

2.1. Scanning electronic microscopy (SEM)

Fibers were coated with gold to increase conductivity of samples and enable analysis by a Scanning Electron Microscope, JEOL brand, model JSM 6490-LV. ImageJ software was used for processing of digital images and measurement of average diameter and cross-sectional area of fibers.

2.2. Atomic force microscopy (AFM)

To investigate the mechanical behavior of natural fibers at low scale through instrumented indentation tests, we used the AFM brand ASYLUM RESEARCH, model MFP-3D-BI. Fibers were cut down to a length of 5mm, and appropriate points for nanoindentation were identified on their surface. This process consists in applying a force to the fiber with the tip of an indenter or cantilever to create indentation marks. The tip is pressed continuously against the fiber for about 2 seconds, and the resulting displacement is measured. Data on force vs. displacement, and on indenter geometry, were used to calculate hardness (H), reduced modulus (Er), rupture modulus (H/Er), resistance to plastic deformation (H^3/Er^2) and elastic module, after the method proposed in 1992 by Oliver and Pharr. In addition, fibers were swept before and after the indentation at low force using the same indentation tip, thereby generating a topographic record on nanometric scale. The obtained nanoscale topographic images of fiber and indentation traces enabled quantification of the stacking of ductile material around the indenter. For the nanoindentation test, an AC 160 TS Olympus indenter was selected based on the principle that the indenter tip must have an elastic modulus equal to or greater than the sample in order to generate a deformation. Finally, water left over from the NaOH treatment was slowly neutralization (until neutral pH) by diluted acetic acid (vinegar) and disposed by a hazardous waste management company with a valid environmental license.

3. Results and discussion

3.1. Morphological characterization

Fig. 1 shows the cross section of a GAK fiber from the interior of the cluster and treated with 5% NaOH. The fiber has an irregular and elongated shape, while its transversal area is composed of irregularly shaped microfibers. Average value was 13301.806 μm^2.

Fig. 2 shows a comparison between two GAK fibers with and without the 5% sodium hydroxide treatment. The untreated fiber presents irregularities due to the presence of lignin and hemicellulose [38], while the treated fiber exhibits no imperfections, and instead consists of visible microfibrils (observable in the cross-section). Treatment exposes microfibers aligned in the axial direction, which is relevant for applications to composite materials by providing stronger adherence between the polymer matrix and natural fibers.

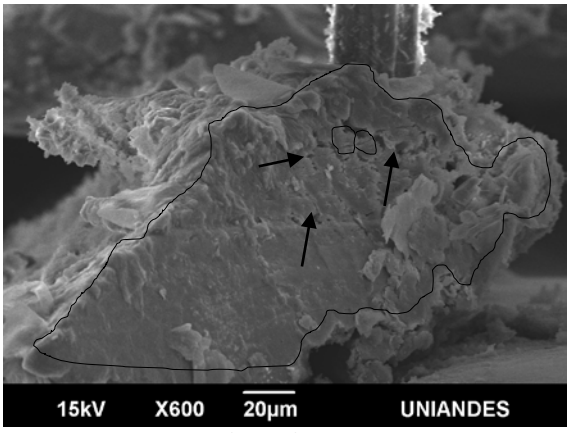


Figure 1. Transversal section of GAK fiber.
Source: Authors.

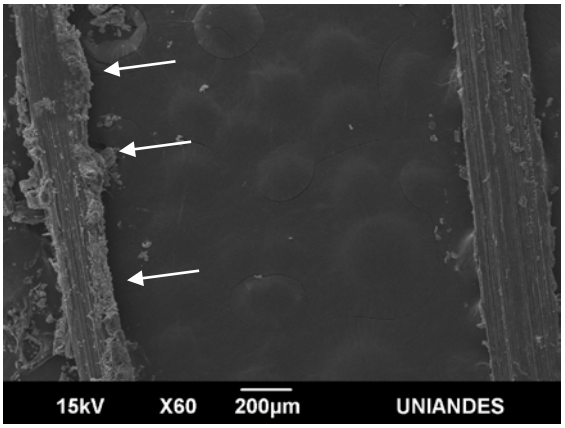


Figure 2. Longitudinal section of GAK fiber, with and without 5% NaOH treatment.
Source: Authors.

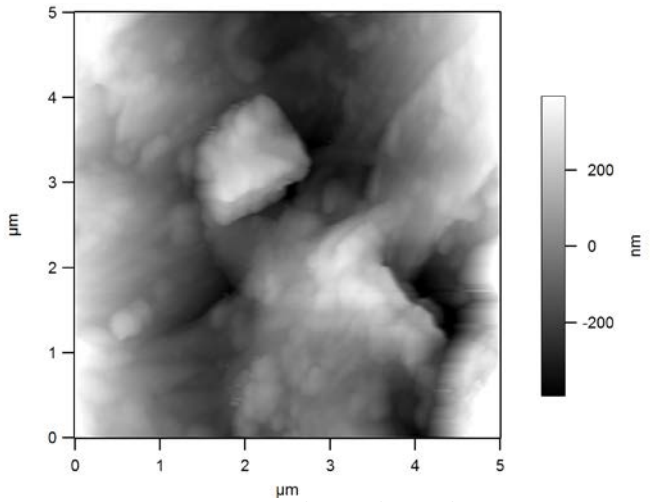


Figure 3. Longitudinal section of GAK fiber before indentation. AFM altitude image.
Source: Authors.

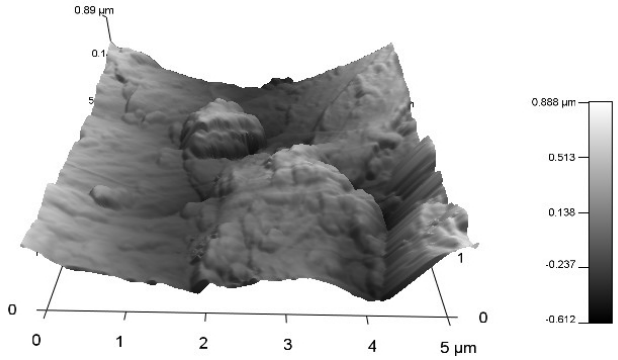


Figure 4. 3D morphology of the longitudinal surface of GAK fiber.
Source: Authors.

3.2. GAK topography

Prior to indentation, we recorded the longitudinal topography of a section of GAK fiber measuring 5um x 5um. Fig. 3 shows that the GAK fiber displays an irregular structure on most of its surface.

Fig. 4 is a 3D section along the longitudinal axis of the GAK fiber, revealing surfaces without defined shape that protrude between 0.888µm-0.612µm relative to the general surface. It exhibits superior roughness (Ra) to the areca palm [39], but inferior to flax [40]. This level of roughness may facilitate adhesion between polymer matrices and GAK fibers, confirming our SEM findings.

3.3. Nanoindentation

Figs. 5 and 6 show a longitudinal section of GAK fibers before and after nanoindentation. In Fig. 5, cellulose microfibers are observed in lignin within the hemicellulose matrix [34] and aligned with the main axis of the GAK fiber. Due to their orientation, microfibers confer guadua superior resistance to tension along the main axis of the fiber. In addition, the distribution of microfibers confirms that guadua is an orthotropic material [41]. Moreover, Fig. 6 shows 10 nanoimprints with different indentation depths, as shown in Table 2. Nanoimprints 2, 3 and 4 cannot be clearly seen in Fig. 6 since the nanoindentation zone exhibits elastic behavior, recovering by 98.7%, 96.70 and 96.13% respectively after removal of the indentation load, therefore presenting no residual deformation. In contrast, nanoimprints 1, 5-10 presented only minor and non-identifiable recovery.

Fig. 7 shows the loading and unloading curve of nanoimprint 1. The curve is similar for indentations on other nanoimprints, which is most likely explained by the similar elastic properties of GAK fibers in most of their surface.

Following the analysis of curves and the method proposed by Oliver and Pharr, Table 1 presents measures of hardness, reduced modulus, modulus of rupture and resistance to plastic deformation for each of the 10 nanoimprints. Hardness ranges between 10.27 and 13.48MPa, demonstrating the homogeneity of the longitudinal section.

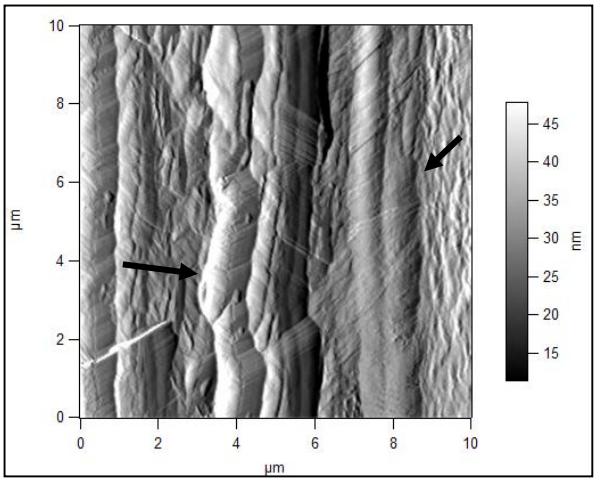


Figure 5. Longitudinal section of GAK fiber prior to indentation. AFM amplitude image.
Source: Authors.

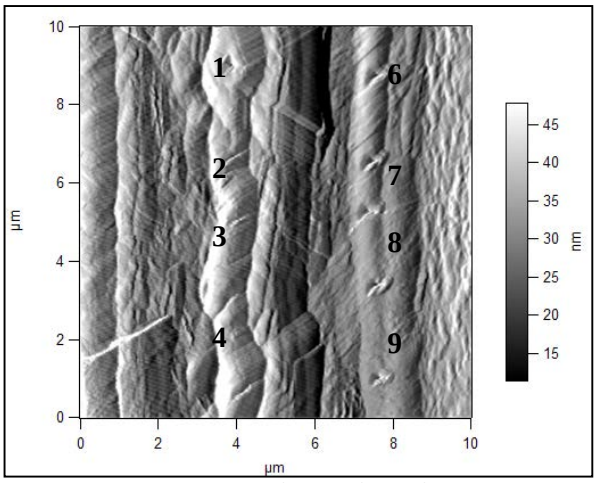


Figure 6. Longitudinal section of GAK fiber after indentation. AFM amplitude image.
Source: Authors.

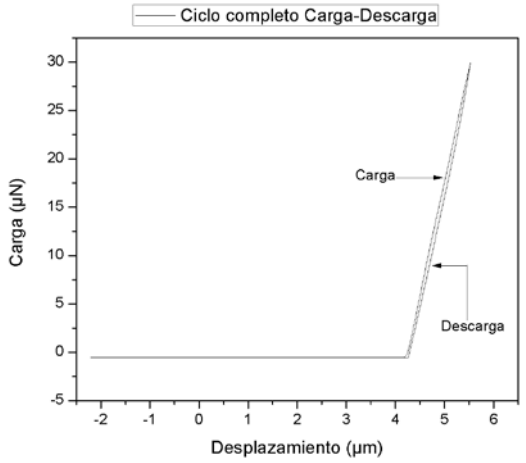


Figure 7. Full loading-unloading cycle of nanoimprint 1.
Source: Authors.

Table 1.
Mechanical properties at the nanoscale of GAK fibers.

777777-curves (Fig. 8), as well as residual depth values (h) for each nanoimprint and the percentage of elastic recovery.

Residual deformation of nanoimprints is variable; however, nanoimprints 2, 3 and 4 show the highest residual difference, with values of 17.49, 42.31 and 52.15 nm. This confirms that they exhibit the highest values of elastic recovery (Table 2), as shown in Fig. 6 where they do not exhibit an indentation mark. On the other hand, the nanoimprints with the most visible marks in indentation (Fig. 6) show the highest values of residual deformation.

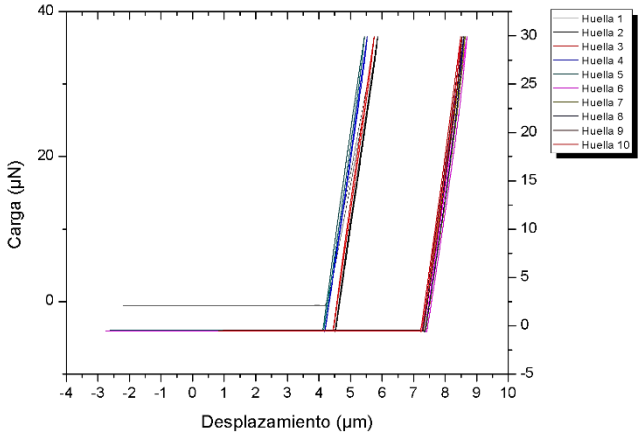


Figure 8. Loading-unloading curves of the 10 nanoimprints on GAK fibers.
Source: Authors.

Table 2.
Elastic properties of GAK fibers.

Nanoimprint	hmax (nm)	h (nm)	Recovery (nm)	Recovery (%)
1	1280,90	92,44	1188,46	92,78
2	1342,21	17,49	1324,72	98,70
3	1298,23	42,31	1255,92	96,74
4	1346,93	52,15	1294,78	96,13
5	1294,50	81,30	1213,20	93,72
6	1273,86	80,50	1193,36	93,68
7	1281,23	92,79	1188,44	92,76
8	1236,41	66,06	1170,35	94,66
9	1242,99	85,57	1157,42	93,12
10	1251,23	86,46	1164,77	93,09
Mean	1284,85	69,71	1215,14	94,54

Source: Authors.

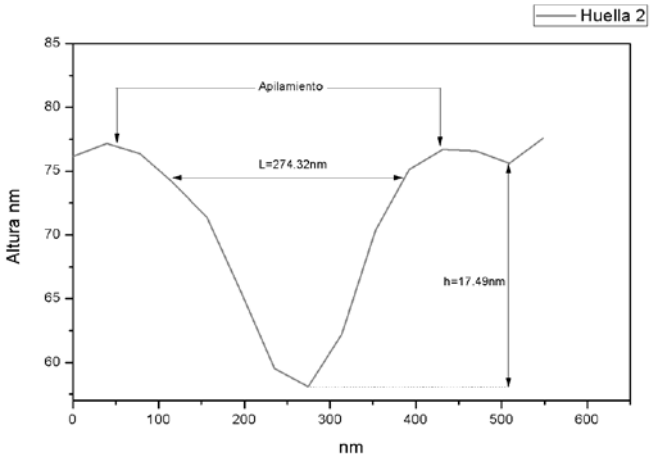


Figure 9. Topographic profile of residual deformation in nanoimprint 2.
Source: Authors.

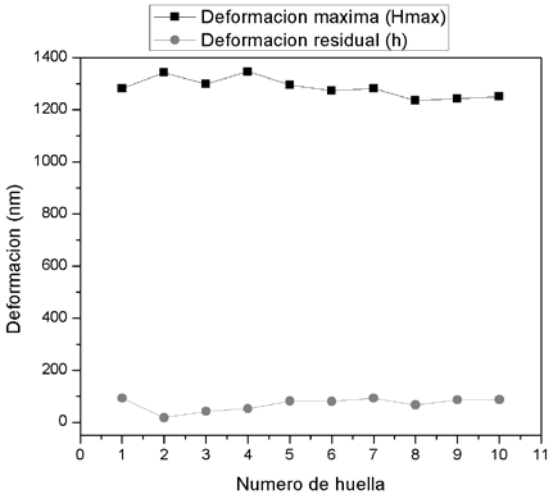


Figure 10. Elastic recovery of GAK fibers after nanoindentation essay.
Source: Authors.

Table 3.
Elastic properties of GAK fibers.

Mechanical properties	Unit	Value
Hardness (H)	MPa	11,75
Reduced modulus (Er)	MPa	12,97
Rupture modulus (H/Er)	-	0,91
Resistance to plastic deformation (H^3/Er^2)	MPa	9,68
Elastic recovery	%	94,54

Source: Authors.

Fig. 9 shows the residual deformation on nanoimprint 2 after application of load. Residual depth on all nanoimprints is obtained from the topographic profile, with a value of 17.49nm in nanoimprint 2, which displays a minimum amount of stacking on the sides but no sinking nonetheless. This is due to the characteristics of plasticity and elasticity of the material.

Application of the maximum indentation load (29,91uN) on all nanoimprints resulted in maximum deformations (hmax) of 1290 ± 60um of the GAK fibers (Table 2). When the load is removed, fibers recover from deformation by an amount ranging between 1160 and 1320 nm (Fig. 10). This demonstrates the elastic recovery of GAK fibers, which averaged 94.54%. Recovery occurs since the atoms in the fiber are not permanently displaced, with the force applied in the indentation being stored as a distortion of fiber interatomic bonds [43].

Table 3 shows the summary of average mechanical properties of GAK fibers resulting from instrumented nanoindentation.

4. Conclusions

Due to their characteristics, fibers of *Angustifolia kunth* guadua are a viable alternative to reinforcement of composite materials. Our sampled fibers had an average cross-sectional area of 13301.806 μm^2 as measured by SEM. GAK fibers also exhibited ridges and undulations resulting in considerable levels of rugosity, which constitutes a key feature by enabling stronger adhesion to polymer matrices.

Furthermore, AFM characterization demonstrated that the cross section of GAK fibers is formed by microfibrils in the longitudinal direction, providing excellent resistance to tension in that direction. In addition, most of the nanoimprints on the GAK fibers presented minimal stacking, and no sinking. The findings validate the view that GAK fibers are ideally suited to be used as reinforcement in compound materials. Similarly, characterization of the GAK fiber longitudinal section revealed irregularities, which can nonetheless be removed through application of 5% NaOH.

Mechanical characterization at nanometric scale revealed that *Angustifolia kunth* guadua fibers had an average hardness of 11,75MPa, a reduced modulus of 12.97MPa and break of and 0.91 respectively. Characterization also showed that GAK fibers exhibited a plastic deformation resistance of 9.68MPa and an elastic recovery of 94.54%.

Acknowledgements

We thank the Microscopy Center, Universidad de los Andes; the Faculty of Engineering and Basic Sciences, Department of Electronic Engineering; Solid State, Micro and Nanostructures Unit; and the NBIC Research Cluster at the Universidad Central.

References

[1] Hidalgo, M.A., Muños, M.F. and Quintana, K.J. Desempeño mecánico del compuesto aluminio reforzado con agro fibras contínuas de fique. Revista Latinoamericana de Metalurgia y Materiales, 31 (2), pp. 187-194, 2011.

[2] Ru-Min, W., Shui Rong Z. and Ya Ping, Z. Polymer matrix composites and technology. Georgia: Woodhead Publishing, 1, pp. 1-28, 2011.

[3] Baptista, R., Mendão, A., Rodrigues, F., Figueiredo, C. G., Guedes, M. and Marat, R. Effect of high graphite filler contents on the mechanical and tribological failure behavior of epoxy matrix composites. Theoretical and Applied Fracture Mechanics, 85, pp. 113-124, 2016. DOI: http://doi.org/10.1016/j.tafmec.2016.08.013

[4] Khalili, P., Tshai, K.Y. and Kong, I., Natural fiber reinforced expandable graphite filled composites: evaluation of the flame retardancy, thermal and mechanical performances. Composites: Part A, 100, pp. 194-205, 2017. DOI: 10.1016/j.compositesa.2017.05.015

[5] Pedrazzoli, D. and Pegoretti, A., Expanded graphite nanoplatelets as coupling agents in glass fiber reinforced polypropylene composites. Composites: Part A, 66, pp. 25-34, 2014. DOI: 10.1016/j.compositesa.2014.06.016

[6] Papageorgiou, D.G., Kinloch, I.A. and Young, R.J., Hybrid multifunctional graphene/glass-fibre polypropylene composites. Composites Science and Technology, 137, pp. 44-51, 2016. DOI: 10.1016/j.compscitech.2016.10.018

[7] Kwan, K., Hye, L., Jeong, A., Dong, C., Kay, A. and Byung, K., Recycling and characterization of carbon fibers from carbon fiber reinforced epoxy matrix composites by a novel super-heated-steam method. Journal of Environmental Management, 203, pp. 872-879, 2017. DOI: 10.1016/j.jenvman.2017.05.015

[8] Sharma, M., Rao, I. and Bijwe, J., Influence of orientation of long fibers in carbon fiber-polyetherimide composites on mechanical and tribological properties. Wear, 267, pp. 839-845, 2009. DOI: 10.1016/j.wear.2009.01.015

[9] Serrano, R., Cobo, A., Prieto, M.I. and González, M., Analysis of fire resistance of concrete with polypropylene or steel fibers. Construction and Building Materials, 122, pp. 302-309, 2016. DOI: /10.1016/j.conbuildmat.2016.06.055

[10] Kakooe, S., Md-Akil, H., Jamshidi, M. and Rouhi, J., The effects of polypropylene fibers on the properties of reinforced concrete structures. Construction and Building Materials, 27, pp. 73-77, 2012. DOI: 10.1016/j.conbuildmat.2011.08.015

[11] Amine, M., Hegde, K., Rouissi, T., Kaur, S., Galves, R., Sorelli, L., Ben, R., Paiva, M. and Abokitse, K., Green synthesis of novel biocomposites from treated cellulosic fibers and recycled bio-plastic polylactic acid. Journal of Cleaner Production, 164, pp. 575-586, 2017. DOI: 10.1016/j.jclepro.2017.06.235

[12] Ramos, J. and Cely, M., Exposición personal a asbestos en dos talleres de frenos para vehículos de flota pesada en la ciudad de Bogotá. Fundación Mapfre, [Online]. 2011. [date of reference: November 4th of 2017]. Available at: https://es.scribd.com/document/384252215/ASBESTO-EN-LOS-TALLERS-DE-VEHICULOS

[13] Jaramillo, G. y Zapata, L.M., Aprovechamiento de los residuos sólidos orgánicos en Colombia, Esp. Tesis, Facultad de Ingeniería, Universidad de Antioquia, Medellín, Colombia, 2008.

[14] Águila, I. y Sosa, M., Evaluación físico química de cenizas de cascarilla de arroz, bagazo de caña y hoja de maíz y su influencia en mezclas de mortero, como materiales puzolánicos. Revista de la Facultad de Ingeniería U.C.V [Online]. 23(4), 2008. [date of reference November 4th of 2017]. Available at: http://saber.ucv.ve/ojs/index.php/rev_fiucv/article/view/5078

[15] Bordoloi, S., Hussain, R., Garg, A., Sreedeep, S. and Zhou, W.-H., Infiltration characteristics of natural fiber reinforced soil. Transportation Geotechnics, 12, pp. 37-44, 2017. DOI: 10.1016/j.trgeo.2017.08.007

[16] Steffens, F., Steffens, H. and Ribeiro, F., Applications of natural fibers on architecture. Procedia Engineering, 200, pp. 317-324, 2017. DOI: 10.1016/j.proeng.2017.07.045
[17] Balakrishnan, P., John, M., Pothen, L., Sreekala, M. and Thomas, S., Natural fibre and polymer matrix composites and their applications in aerospace engineering. Advanced Composite Materials for Aerospace Engineering, pp. 365-383, 2016. DOI: 10.1016/B978-0-08-100037-3.00012-2
[18] Ashik, K.P. and Sharma, R., A review on mechanical properties of natural fiber reinforced hybrid polymer composites. Journal of Minerals and Materials Characterization and Engineering, 3, pp. 420-426, 2015. DOI: 10.1016/j.matpr.2017.11.276
[19] Rodríguez, L., Sarache, W. and Orrego, C., Compuestos de poliéster reforzados con fibra de plátano/banano (musa paradisiaca) modificada químicamente. Comparación con Fibra de Vidrio y Fique (Furcraea andina). Información tecnológica, 25(5), pp. 27-34, 2014. DOI: 10.4067/S0718-07642014000500005
[20] Danso, H., Properties of coconut, oil palm and bagasse fibres: as potential building materials. Procedia Engineering, 200, pp. 1-9, 2017. DOI: 10.1016/j.proeng.2017.07.002
[21] Wang, W. and Chouw, N., The behaviour of coconut fibre reinforced concrete (CFRC) under impact loading. Construction and Building Materials, 134, pp. 452-461, 2017. DOI: 10.1016/j.conbuildmat. 2016.12.092
[22] Mwaikambo, L., Review of the history, properties and application of plant fibres. African Journal of Science and Technology (AJST) [Online]. 7(2), 2006. [date of reference November 17th of 2017]. Available at: https://www.researchgate.net/publication/284760719_ Review_of_the_history_properties_and_application_of_plant_fibres
[23] Hidalgo, M., Muñoz, M. y Quintana, K., Análisis mecánico del compuesto polietileno aluminio reforzado con fibras cortas de fique en disposición bidimensional. Revista Latinoamericana de Metalurgia y Materiales [Online]. 32(1), 2012. [date of reference November 19th of 2017]. Available at: http://www.rlmm.org/ojs/index.php/rlmm/ article/view/117
[24] Pietroniro, M. y Bloem, C., Ventajas del algodón frente al fique como refuerzo en compuestos poliméricos. Ciencia e Ingeniería [Online]. 36(1), 2015. [date of reference November 20th of 2017]. Available at: http://erevistas.saber.ula.ve/index.php/cienciaeingenieria/article/view/5495/0
[25] Karaduman, Y., Gokcan, D. and Onal, L., Effect of enzymatic pretreatment on the mechanical properties of jute fiber-reinforced polyester composites. Journal of Composite Materials, 47(10), pp. 1293-1302, 2012. DOI: 10.1177/0021998312446826
[26] Bursi, N., Gualtieria, A.F., Pollastria, S. and Tibaldib, E., Assessment of asbestos body formation by high resolution FEG-SEM after exposure of Sprague-Dawley rats to chrysotile, crocidolite, orerionite. Journal of Hazardous Materials, 306, pp. 95-104, 2016. DOI: 10.1016/j.jhazmat.2015.11.050
[27] Fang, C.-H., Jiang, Z.-H., Sun, Z.-J., Liu, H.-R., Zhang, X.-B., Zhang, R. and Hua Fei, B., An overview on bamboo culm flattening. Construction and Building Materials, 171, pp. 65-74, 2018. DOI: 10.1016/j.conbuildmat.2018.03.085
[28] Kaminski, S., Lawrence, A. and Trujillo, D., Structural use of bamboo: Part 1: Introduction to bamboo. The Structural Engineer [Online]. 94(8), 2016. [date of reference November 20th of 2017]. Available at: https://www.researchgate.net/publication/305808084_Structural_use_of_bamboo_Part_1_Introduction_to_bamboo
[29] Zakikhani, P., Zahari, R., Sultan, M. and Majid, D., Extraction and preparation of bamboo fibre-reinforced composites. Materials & Design, 63, pp. 820-828, 2014. DOI: /10.1016/j.matdes.2014.06.058
[30] Valarezco, L.E., Obtención experimental de un material biocompuesto a base de una matriz polimérica y reforzada con fibras naturales de guadúa angustifolia proveniente del Ecuador, Pregrado. Tesis, Facultad de Ingeniería, Universidad Politécnica Salesiana, Cuenca, Ecuador, 2013.
[31] Luna, P., Marriaga, J. and Mariño, A., Guadua angustifolia bamboo fibers as reinforcement of polymeric matrices: An exploratory study. Construction and Building Materials, 116, pp. 93-97, 2016. DOI: 10.1016/j.conbuildmat.2016.04.139
[32] AL-Oqla, F.M. and Sapuan, S.M., Natural fiber reinforced polymer composites in industrial applications: feasibility of date palm fibers for sustainable automotive industry. Journal of Cleaner Production, 66, pp. 347-354, 2014. DOI: 10.1016/j.jclepro.2013.10.050
[33] Salas, E., Actualidad y futuro de la arquitectura de bambú en Colombia, PhD. Tesis, Departamento de Construcciones Arquitectónicas, Universidad Politécnica de Cataluña, Barcelona, España, 2006.
[34] Hao, H., Tam, L.-H., Lu, Y. and Lau, D., An atomistic study on the mechanical behavior of bamboo cell wall constituents. Composites Part B: Engineering, In Press, 2018. DOI: /10.1016/j.compositesb.2018.05.046
[35] Rao, J., Bao, L. Wang, B., Fan, M. and Feo, L., Plasma surface modification and bonding enhancement for bamboo composites. Composites Part B: Engineering, 138, pp. 157-167, 2018. DOI: 10.1016/j.compositesb.2017.11.025
[36] Mohanty, A., Khan, M. and Hinrichsen, G., Influence of chemical surface modification on the properties of biodegradable jute fabrics—polyester amide composites. Composites Part A: Applied Science and Manufacturing, 31(2), pp. 143-150, 2000. DOI: /10.1016/S1359-835X(99)00057-3
[37] Herrera, P. and Valadez, A., Mechanical properties of continuous natural fibre-reinforced polymer composites. Composites Part A: Applied Science and Manufacturing, 35(3), pp. 339-345, 2004. DOI: 10.1016/j.compositesa.2003.09.012
[38] Focher, B., Palma, M., Canetti, M., Torri, G., Cosentino, C. and Gastaldi, G., Structural differences between non-wood plant celluloses: evidence from solid state NMR, vibrational spectroscopy and X-ray diffractometry. Industrial Crops and Products, 13, pp. 193-208, 2001. DOI: /10.1016/S0926-6690(00)00077-7
[39] Shanmugasundaram, N., Rajendran, I. and Ramkumar, T., Characterization of untreated and alkali treated new cellulosic fiber from an Areca palm leaf stalk as potential reinforcement in polymer composites. Carbohydrate Polymers, 195, pp. 566-575, 2018. DOI: 10.1016/j.carbpol.2018.04.127
[40] Chegdani, F. and El Mansori, M., Friction scale effect in drilling natural fiber composites. Tribology International, 119, pp. 622-630, 2018. DOI: 10.1016/j.triboint.2017.12.006
[41] Sreenivasulu, S. and Chennakeshava, A., Mechanical properties evalution of bamboo fiber reinforced composite materials. International Journal of Engineering Research, [Online]. 3(1), pp. 187-194, 2014. [date of reference November 20th of 2017]. Available at: https://www.researchgate.net/publication/269412025_Mechanical_ Properties_Evaluation_of_Bamboo_Fiber_
[42] Huanga, Y., Benhua, F., Penglian, W. and Chang, Z., Mechanical properties of bamboo fiber cell walls during the culmdevelopment by nanoindentation. Industrial Crops and Products, 92, pp. 102-108, 2016. DOI: 10.1016/j.indcrop.2016.07.037
[43] Arroyave, M., Nanocaracterización estructural y macánica de recubrimeintos duros de TiN y ZrN producidos por descarga de arco pulsado, MSc. Tesis, Departamento de física y química, Facultad de Ciencias y Administración, Universidad Nacional de Colombia, Manizales, Colombia, 2004.

M.E. Espitia-Nery, is a BSc. Physical Engineer, Sp. in Production and Operations Management, MSc. in Industrial Engineering, MSc. in Business Administration, and currently a student in the MBA program at the Universidad de los Andes. He has 10 years of experience in teaching, research and management of strategic plans, specialized in companies in the services and manufacturing sector in areas of production, operations and R&D + i. Consultant and lecturer in countries such as Spain, Brazil, Mexico,

among others, in topics related to engineering, science and materials technology. He is currently a principal investigator in the GEIIC group.
ORCID: 0000-0001-5626-3051

D.E. Corredor-Pulido, is a BSc. in Metallurgy Engineer, MSc. in Metallurgy at the Universidad de Concepción in Chile, and a researcher in the GEIIC research group. She is currently a full professor at the Corporación Universitaria Minuto de Dios, Colombia, Faculty of Engineering, a national and international speaker, and expert in ONAC scanning electron.
ORCID: 0000-0003-3148-9219

N.J. Rodríguez-Ramírez, is a BSc. Civil Engineer at the Minuto de Dios University Corporation, Colombia. He is currently a member at SINCE, the Sustainable Construction and Structures Seedbed. He has delivered presentations on the characterization of composite materials at national and international events
ORCID: 0000-0003-2062-3021

J.N. Calderón-Bustos, is a BSc. in Civil Engineer at the Minuto de Dios University Corporation, Colombia. She is currently a member at SINCE, the Sustainable Construction and Structures Seedbed. She has delivered presentations on the characterization of composite materials at national and international events.
ORCID: 0000-0002-3570-6439



UNIVERSIDAD NACIONAL DE COLOMBIA
SEDE MEDELLÍN
FACULTAD DE MINAS

Área Curricular de Ingeniería
Geológica e Ingeniería de Minas y Metalurgia

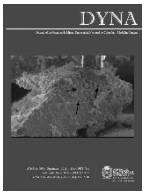
Oferta de Posgrados

Especialización en Materiales y Procesos
Maestría en Ingeniería - Materiales y Procesos
Maestría en Ingeniería - Recursos Minerales
Doctorado en Ingeniería - Ciencia y Tecnología de Materiales

Mayor información:

E-mail: acgeomin_med@unal.edu.co
Teléfono: (57-4) 425 53 68

UNIVERSIDAD NACIONAL DE COLOMBIA
SEDE MEDELLÍN
FACULTAD DE MINAS



DYNA
http://dyna.medellin.unal.edu.co/

Kinetic parameters of lactic acid bacterial isolated from fermented milk "Suero Costeño"

Francia Elena Valencia-García [a], Karina Edith Motato-Rocha [b], Madalyd Yurani Vera-Peña [a] & Martha Liliana Sepúlveda-Lindarte [a]

[a] *Biotransformation Research Group. Industrial Microbiology and Environmental Program. School of Microbiology. Universidad de Antioquia. Medellín, Colombia. francia.valencia@udea.edu.co, madalyd.vera@udea.edu.co, lilianasepulveda13@gmail.com*
[b] *Bioali Research Group. Food Engineering Program. Faculty of Pharmacy and Food Science. Universidad de Antioquia. Medellín, Colombia. karina.motato@udea.edu.co*

Received: March 13th, 2018. Received in revised form: July 12th, 2018. Accepted: August 15th, 2018.

Abstract
The isolation of bacteria from artisanal dairy products has increased in different countries, it has reported special technological properties, responsible for giving to dairy products unique characteristics. The kinetic parameters of native microorganisms are important for biotechnological scaling. This research, to evaluated the kinetics of bacterial growth under optimal conditions of lactic acid bacterial isolated from artisanal fermented milk "Suero Costeño" *Lactobacillus plantarum* (*Lp*), *Streptococcus infantarius* (*Si*) and *Lactococcus lactis* (*Ll*), identified by 16S rRNA. There were fast rate acidification of *Si* and *Ll* as a typical dairy starter culture. *Lp* showed a slowly rate acidification and highest pH resistance. It is necessary a pH control between 5,3 and 5,7 in order to obtain higher consume of substrate and yield biomass. *Si* and *Ll* can be used as primary cultures in fermentations as a result of their rapid acidification and *Lp* as an adjunct culture through the slow acid production.

Key words: traditional fermented foods; kinetic growth; lactic acid bacterial.

Parámetros cinéticos de bacterias ácido-lácticas aisladas de la leche fermentada "Suero Costeño"

Resumen
El aislamiento de bacterias a partir de productos lácteos artesanales ha incrementado en diferentes países, debido a que éstas han reportado características de interés tecnológico únicas. Conocer los parámetros cinéticos de estos microorganismos caracterizados es importante para escalamiento biotecnológico. Este estudio, evaluó tres bacterias ácido lácticas de "Suero Costeño" de preparación artesanal: *Lactobacillus plantarum (Lp), Streptococcus infantarius* (Si) y *Lactococcus lactis (Ll),* identificados por 16S rRNA. Las cinéticas de crecimiento en condiciones ideales fueron evaluadas. Los resultados muestran que los microorganismos presentaron comportamientos diferentes de crecimiento, *Si* y *Ll presentaron una rápida* acidificación, lo que indica que podrían ser usados como cultivos primarios en fermentaciones y Lp como cultivo adjunto por la lenta producción de ácido y mayor resistencia a pH bajo. Además, el estudio mostró que es necesario controlar el pH entre 5,3 y 5,7 para favorecer el consumo de sustrato y el aumento de la biomasa.

Palabras clave: alimentos tradicionales fermentados; cinéticas de crecimiento; bacterias ácido lácticas.

1. Introduction

In recent years, the isolation of lactic acid bacteria from traditional fermented foods has increased promoting the production of the regional healthy foods and recovering the traditions which allows to improve the nutrition of the population[1].The microorganisms involved in these artisanal fermentation processes, in their great majority correspond to the group of lactic acid bacteria, many of these

How to cite: Valencia-García, F.H., Motato-Rocha, K.E., Vera-Peña, M.Y. and Sepúlveda-Lindarte, M.L., Kinetic parameters of lactic acid bacterial isolated from fermented milk "Suero Costeño". DYNA, 85(206), pp. 155-161, September, 2018.

© The author; licensee Universidad Nacional de Colombia.

are generally recognized as safe by the food industry (GRAS), and some also have the name of probiotic microorganisms that provide, in addition to the technical benefits, specific health benefits to the hosts [2][3].

Among the traditional products of Colombia, the "Suero Costeño" (SC) is an artisanal soured cream produced in the Northern-Caribbean regional coast of Colombia. It is widely produced by the rural population in the regions of Córdoba, Sucre and Bolívar, manufactured mainly in households on a small scale, and represents a gastronomic heritage of Colombian cuisine [4] (Simanca et al., 2010). Microorganisms that are not commonly used in dairy products have been isolated from this product [5]. After distinguishing the existent microorganisms in the local products and identifying the shared probiotic technical characteristics and their molecular identification [6], it is necessary to think about the application of biotechnological scaling techniques in order to bioaugment the specific ferments and consequently make them available to improve the quality during the production of the specific products, which often is the financial support of many families depending on this production.

Scaling techniques of native potential probiotic/starter dairy strains involves the study of basic growth dynamic microorganisms, such as kinetic parameters, which is not very documented with lactic acid bacterial in Colombia; probably due to biotechnological dairy starter production of these microorganisms, has been restricted to few industrialized companies that offer starter cultures for massive use to develop food products.

This shows how the kinetic parameters of each microorganism in ideal conditions provide information that can be used to establish suitable conditions in the inoculum, among other purposes for: suggest alternative industrial culture methods, production of specific metabolites, [7], establish conditions in the concentration of cells in order to standardize probiotic and technological tests and / or cell conservation.

The purpose of this research is to establish the kinetic parameters of lactic acid bacteria isolates obtained from the fermented milk "Suero Costeño" of artisan manufacture.

2. Methodology

2.1. Bacterial strains

Native microorganisms from the fermented milk "Suero Costeño" produced in the Colombian Caribbean region were isolated and identified through partial amplification of the sequencing gene, 16S rRNA (Young et al., 1991), whose genomic sequences were determined using the BLAST program and the Ribosomal Database Project as *Lactobacillus plantarum* (60-1), *Streptococcus infantarius* (46-3) and *Lactococcus lactis* (25-2) [5].

2.2. Conservation and activation of cells

Each lactic acid bacteria (LAB) strains isolated from the fermented milk "Suero Costeño", was inoculated in a liquid medium and incubate under microaerophilic atmosphere to the proposed conditions (See Table 1). The overnight cultures were centrifuged at 5000 rpm, washed with phosphate buffered saline (PBS), added with 20% of glycerol and stored in 2mL vials to preserve at -80°C.

Table 1.
Conditions of microorganisms growth

Number code strain	T ° (C) Incubation	Broth culture	Agar	Incubation time (h)
60-1 *Lactobacillus plantarum*	32	MRS	MRS	12
46-3 *Streptococcus infantarius*	37	BHI+Glucose	M17	18
25-2 *Lactococcus lactis*	32	BHI+Glucose	M17	12

Source: Author.

In order to activate the strains, each vial was defrosted at room temperature and 50µL of sample were inoculated into the corresponding agar by a loopful of the turbid culture streaked on specified agar (Table 1), and incubated in microaerophilic atmosphere at the temperature (Tº in ºC) and time (h) established in order to reach the early stationary phase, overnight culture. After this time, a single colony was selected and it was inoculated in 5mL of liquid culture and them second culture was made (2 generation).

Cells was obtained by centrifugation of culture liquid at 5000 rpm / 10-15 minutes at room temperature in a Sigma 3-16K 10280 centrifuge. The supernatant was discarded and cells was washed. In addition, sterile phosphate buffered saline (PBS) was added to the cell buttons, and it was mixed in the vortex (KMC 1300v), this procedure was performed two times. After this wash, the cells were resuspended in the culture liquid using an vortex, subsequently the initial optical density (OD600) concentration was standardized at 0,8±0,1 in a Spectronic® spectrophotometer 3w2R179001 genesys 2PC.

2.3. Kinetic growths in conventional culture media

To establish the growth parameters, the activated cells were inoculated (5%) in 8 tubes each containing 7mL of the corresponding liquid culture. Immediately after inoculation one of the tubes was taken and set aside for the analytical determinations, the other tubes were placed in incubation at the temperatures established in Table 1. To perform the growth curve for 24 hours. During the incubation, one tube was taken every 2h, in total 8 tubes were taken at different times (t_0= startup, t_1=2h, t_2=4h, t_3=6h, t_4=8h, t_5=10h, t_6=12h y t_7=24h). The analytical determinations were made to the taken samples. Each sample was made in triplicate.

2.4. Analytical determinations

2.4.1. Determination of biomass concentration (g/L)

The quantification of the microorganism growth was carried out by three methods which were correlated through a linear equation and statistical analysis. (1) Cell growth was measured spectrophotometrically based on the optical density

at 600 in a Spectronic® spectrophotometer 3w2R179001 genesys 2PC. (2) The UFC/ml was performed using the microdrop technique, plated on to the surface of an agar plate 10µL in duplicate of the last 4 serial dilutions. The cultures were incubated for 48 hours at the established temperature conditions (Table 1), after incubation, counting colony was made. To precise the results it was considered, the average number of the grown colonies in the dilution per 100 (correction factor adjusting to 1ml) and multiplied by the inverse of the dilution. (3) The dry weight was measured to 5mL of harvesting liquid culture by membrane filtration (filters 0.2 µm x 47mm ADVANTE Brand) previously weighed in the analytical balance Adventurer AR2140 or AV-210 Ohaus Corporation, using Thomas lab vacuum pump, the filters were placed in a Binder ED53 01-27082 incubator a 70°C for 24h hours. After this time, the filters were weighed, and the biomass were calculated using eq. 1.

$$Biomass\ \frac{g}{L} = \frac{Dry\ weight\ sample}{Wet\ weight\ sample} \quad (1)$$

2.4.2. Substrate concentration

The glucose concentration was determined by the Glucose GO-PAD enzymatic method of Sigma Aldrich, using 10µL of the filtered culture plus 1mL of the reagent, dilutions were prepared for samples that presented OD > 1. The samples were mixed and incubated for 10 minutes at 22°C± 2°C. After this time, the reading of the samples and the standard (1g / L) was performed against the reagent blank. The glucose concentration was calculated using eq. 2

$$Glucose\ \frac{g}{L} = \frac{Abs\ sample}{Abs\ pattern} \quad (2)$$

2.4.3. Determination of pH and acidity

The pH was measured in real time using a device manufactured by the Interfaculty Instrumentation Center of the University of Antioquia. The electrode was maintained for 24 hours in contact with inoculated liquid culture. The acidity was calculated using eq. 3 which corresponds to the chemical reaction of the acid (lactic acid) dissociation, taken into account the change in the pH value during the fermentation time, the pH which is equal to–log [H3O+] and the acidity constant (Ka) of lactic acid that equals to 1,38 x10-4 M [11]. These calculations were expressed in mg/L of lactic acid.

$$C_2H_5OCOOH + H_2O \rightleftharpoons C_2H_5OCOO^- + H_3O^+.$$

$$C_2H_5\text{COOH} = \frac{[H_3O^+]*[H_3O^+]}{K_a} - Log_{10}[H_3O^+] \quad (3)$$

2.4.4. Kinetic calculations parameters

The specific speed growth calculations were made using the analytical techniques data (µ) which depends of the limiting substrate concentration (glucose) and the microorganism growth over time (eq. 4) [12].

$$\mu = \frac{Ln\frac{x}{x_0}}{t} \quad (4)$$

μ=Growth rate
Xo= inicial count of microorganism.
X= Final count of microorganism.
t= time (hours)

The biomass yield coefficient was calculated for each microorganism used eq. 5 [13]:

$$Y\frac{x}{s} = \frac{g\ produced\ biomass}{g\ substrate\ consumption} \quad (5)$$

The doubling time of cells was obtained from the specific growth rate [12,13].

2.5. Data analysis

The kinetic processed data were obtained from two independents trials and each analysis (biomass concentration (g/L and substrate concentration g/L) was made triplicate. Obtained data was processed through the Statgrafics Centurion 17.2.00 software, using ANOVA and Fisher's LSD comparison test with a 5% of significance.

3. Results

The results of the kinetic growth for the three species of microorganisms are presented in Figs. 1A, 1B and 1C.

Figs. 1A, 1B and 1C present the biomass growth and substrate consumption during the fermentation and substrate consumption in commercial media for each of the isolations. The initial glucose concentration initial concentration in the BHI+glucose broth was 14,5g/L, while the initial concentration of glucose for the MRS broth was 16g/L. During the first 12 hours of fermentation they were consumed 59,6%, 65,9% and 68,9% leaving a remnant at the end of the process of 29%, 31,5% and 7% substrate for strains *L. lactis* 25-2, *S. infantarius* 46-3 and *L. plantarum* 60-1, respectively.

Although the initial concentration of the inoculum in the three strains did not present statistically significant differences, at the end of fermentation *L. plantarum* 60-1 was the isolation with the highest growth (6,46 +/- 0,71) (Fig. 1).

The independent terms and the slope obtained for the curves of OD vs Log UFC/mL and OD Vs Dry weight g/mL. In addition, the correlated coefficients and the R^2 for each curve are presented on Table 2.

In general, for all microorganisms, a greater adjustment was observed between the curves that correlate the OD vs LogUFC/mL (0,94 – 0,97) that the curves that correlate OD Vs dry weight g/mL (0,85 – 0,88). For the isolates, highest correlation obtained was *L. lactis* 25-1 (0,97).

L. lactis 25-2 and *S. infantarius* 46-3 have a similar behaviour and decreasing of pH was faster than *L. plantarum* 60-1. Therefore, *L. lactis* 25-2 and *S. infantarius* 46-3 strains isolated from the fermented milk “Suero Costeño” can be considered starter culture, because in five hours the pH decreased two pH-metric units, after this time pH was maintained stable.

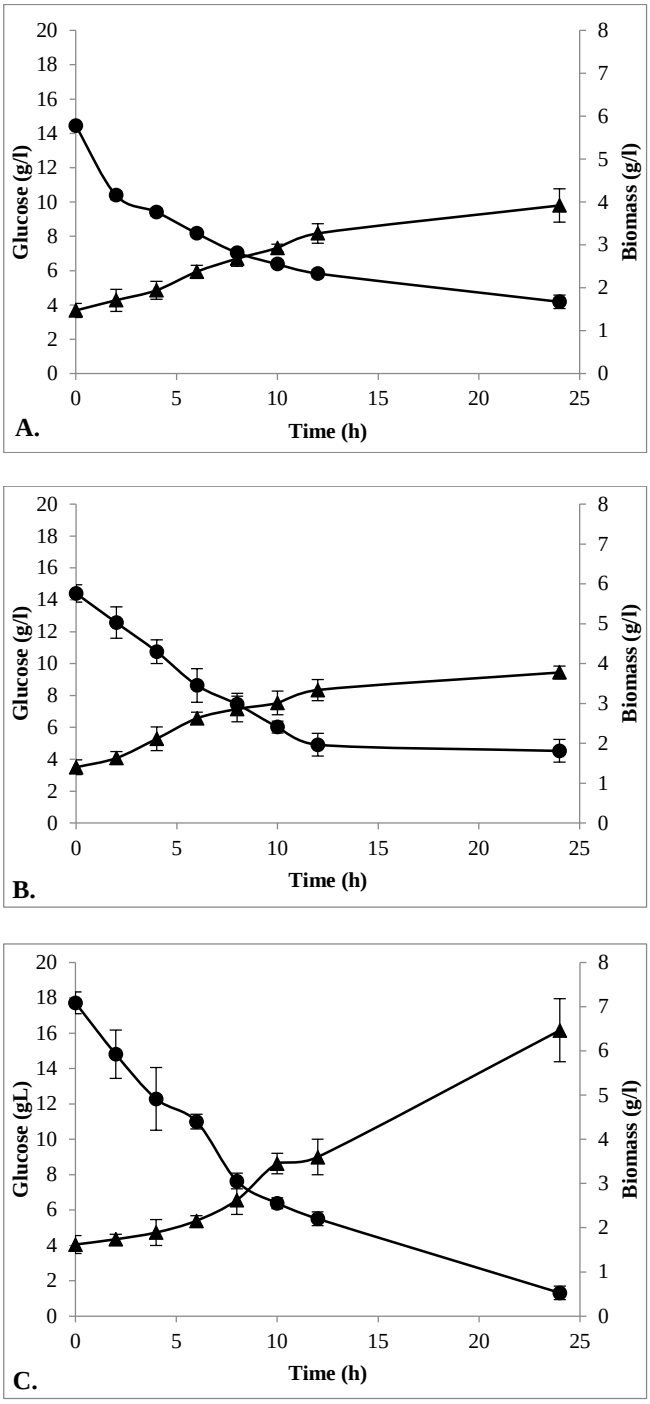


Figure 1. The kinetics of cell growth (▲) and substrate utilization (•)in a conventional culture media. 1A. *Lactococcus lactis* 25-2, 1B. *Streptococcus infantarius* 46-3 y C. *Lactobacillus plantarum* 60-1.
Source: Author.

The behaviour of the *L. plantarum* 60-1 did not show a fast decrease in pH, but after 10h decrease more than 4 pH-metric units, reaching a better ΔpH with a value of 3.17 units.

Fig. 3 presents the results of the pH values at time 0, 6, 12 and 24 hours.

Table 2.
Equations terms for biomass yields of the different LAB isolates.

Strain LAB	Correlated variable	Independent term	Slope	Correlation coefficient	R2
Lactococcus lactis 25-2	OD 600 vs CFU/ml	-256849,00	33,96	0,97	94,4
	OD 600 vs dry weight	-4,44	13,36	0,85	72
Streptococcus infantarius 46-3	OD 600 vs CFU/ml	-18,52	23,87	0,94	89,1
	OD 600 vs dry weight	-5,47	15,36	0,88	77,1
Lactobacillus plantarum 60-1	OD 600 vs CFU/ml	-23,18	27,78	0,96	91,2
	OD 600 vs dry weight	-3,81	14,51	0,87	95

Source: Author.

Fig. 2 presents the results of the three LAB strains pH change studied during the time.

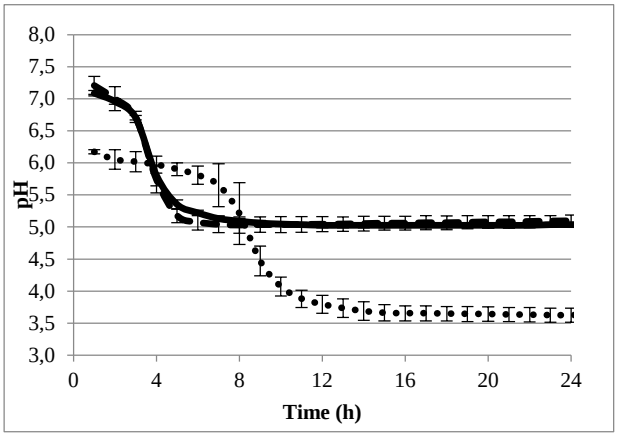


Figure 2. pH dynamic *L. lactis* 25-2 ( ), *S. infantarius* 46-3 (-----) and *L. plantarum* 60-1 (……..).
Source: Author.

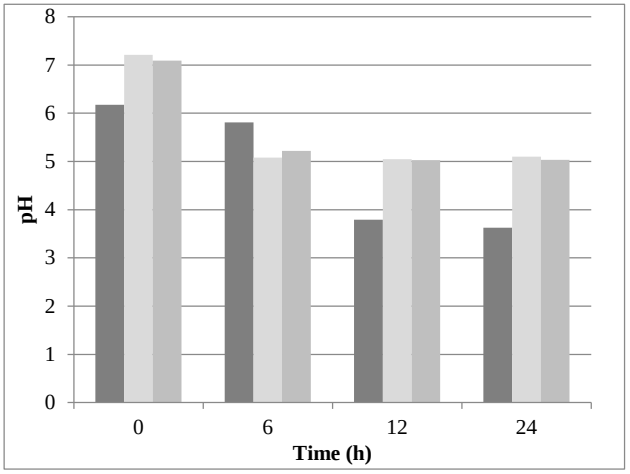


Figure 3. pH of *L. lactis* 26-2, *S. Infantarius* 46-3 and *L. plantarum* 60-1 at different times of incubation
Source: Author.

During the first six hours, pH changes more faster for the *L. lactis* 26-2 and *S. Infantarius* 46-3, (1,87 y 2,13 respectively)

Table 3.
Acidity (mg/L) calculated during the growth of the strains.

Time (h)	*Lactococcus lactis* 25-2	*Streptococcus infantarius* 46-3	*Lactobacillus plantarum* 60-1
0	0,01	0,01	0,06
6	0,57	0,80	0,14
12	0,91	0,87	31,41
24	0,89	0,76	58,43

Source. Author.

Table 4.
Kinetic calculation parameters and performance for the different isolates

Parameters	Unit	*L. Lactis* 25-2	*S. infantarius* 46-3	*L. plantarum* 60-1
Yx/s	gX/gS	0,24	0,24	0,30
μ	1/hour	0,08	0,10	0,08
td	hours	8,66	6,93	8,66

Source: Author.

isolations while the *L. plantarum* 60-1 was of 0,36 units; after 12 hours of fermentation the changes were *L. lactis* 26-2 (0,19), *S. Infantarius* 46-3, (0,04) and *L. plantarum* 60-1(2,02), after 24 hours of process, the change was observed only in the *L. plantarum* 60-1 (0,17) isolation.

Table 3 presents the results of the acidity calculated (mg/L) from equation 3.

The highest acidifying activity was for *L. plantarum* with a 24-hour value of 58.43 (mg /L), the values for *L. lactis* and *S. infantarius* were 0.89 and 0.76 respectively.

Table 4 presents the results of biomass performance based from the substrate, specific growth rate and doubling time for the studied isolates.

The highest yield biomass was for *L. plantarum* 60-1 with a value of 0.3 (gX/gS), followed by *L. lactis* 26-2 and *S. infantarius* 46-3 with a value of 0,24 (gX/gS). The specific growth velocity (μ) in the exponential phase was greater for *S. infantarius* 46-3. The doubling time of cells was similar for *L. lactis* 26-2 and *L. plantarum* 60-1 and almost 1.5h less for *S. infantarius* 46-3 which obtained the shortest doubling time.

4. Discussion

The selected commercial culture media are suitable for the lactic acid bacteria growth of fermented milk "Suero Costeño" (Fig. 1), since adaptation phase is not evident from the moment of inoculation. Logarithmic phase is concluded between 10 and 12h for the microorganisms in discontinuous growth, which does not coincide with others authors: Escobar et al. carried out the fermentations with enriched buttermilk for lactobacillus species for almost 170 hours [18]; Peñuela et al. performed fermentations in yogurt for the *L. plantarum* and *L. lactis* growth with almost a duration of 72 hours; Agudelo et al. develop fermentations with time duration of 48 hours [19]. However, it was observed that after hour 13, the pH was stabilized as well as the biomass production, and at 24 hours, no change in the biomass. As a result, the early stationary phase is adequate, for the performance of many tests or procedures which is achieved in a time shorter than 13h for the established growth conditions.

The results of the pH curves indicates that the strains studied are good candidates to be used in industrial processes as starter microorganisms, some as primary cultures and others as adjuvants [10]. In the elaboration of dairy products a rapid decrease in pH causes the destabilization of casein micelles (milk protein) due to the solubilization of their calcium phosphate, the pH values reached are close to the isoelectric point of the milk, with which coagulation takes place. *L. plantarum* 60-1 having a decrease in the higher pH but need more time compared to the other two strains, could be used as an adjunct culture [20]

L. plantarum 60-1 had the highest yield biomass probably to resistance pH stress. According to Chungking et al (2017), *L. plantarum* could maintain constant pH gradient between the inside of the cell (cytoplasm) and culture media (extracellular) in the presence of high lactate concentrations, therefore it is capable of supporting acid culture media in comparison with the other microorganisms and finish completely the fermentation [21].

In the growth and substrate consumption pH curves and due to the lactic acid nature of the isolates such as the fermentation metabolites, it is possible for either *L. lactis* 25-2 or *S. infantarius* 46-3 in addition to the carbón source, the occurrence of an inhibition per product, that even though with a decrease evidence in the substrate concentration, did not allow the microorganisms the glucose consumption, therefore; there was a decrease in the expected growth, this is due to the fact that most of the bacteria have an optimal pH value and when the decreasing occurred in the first 8 hours this could inhibit cell growth.

L plantarum 60-1 not show an inhibition by the acidity, probably, this microorganism use a mechanism known as F1-F0 ATPase as protection under acidic conditions. The F1-F0 ATPase is a multiple enzymatic subunit, which contains a catalytic portion (F1), incorporating subunits for the hydrolysis of ATP; and an integral membrane portion (F0) that includes subunits that function as membrane channels for proton translocation [22]. To obtain a higher yield biomass and improve the performance of the strains *L. lactis* 25-2 and *S. infantarius* 46-3, it is necessary to carry out a pH control in the optimal growth values, since the cellular metabolism tends to turn slower when it is not operating in optimal conditions [23].

The kinetic parameters values obtained in this work differ from those reported in the literature; Georgieva et al. present a Yx/s of 0,143 for *L. plantarum* in MRS culture médium with glucose [24] obtaining 48% better results. The speed depends on several factors among which are the nutrients concentration, products, pH and temperature. The results of the three strains studied show a specific growth rate lower than that reported by other authors. Agudelo *et al*. 2010, reported a 0,53 (h^{-1}) for *L. plantarum* [19]. When the specific growth rate depends only on a limiting substrate, when the substrate is added in high concentrations, the specific velocity reaches maximum values, up to the point at which substrate inhibition occurs. The results obtained seem to indicate that, although we worked with a simple substrate (glucose) we would expect a higher specific growth rate, therefore, it is assumed that the kinetics growth was of

order 1 where the low substrate concentration makes that the values of u are below the maximum growth rate.

The doubling time values indicate the time it takes for LABs to double their population. For *L. plantarum* 60-1 doubling times between 1.1 and 1.98 hours have been reported, therefore, the effect of some variables such as the change in pH over the doubling time could be evidenced.

5. Conclusions

The culture media used was suitable for the growth of the microorganism, since the adaptation phase was not observed in the studied isolates, despite being bacterias that can be used as starter culture. For its production and bioaugmentation it is necessary to carry out a pH control during the fermentation since it is not possible to consume all the substrate and an inhibition by product is observed without reaching the best performance in biomass.

Kinetic parameters were obtained from lactic acid bacterial isolates from the fermented milk “Suero Costeño”, which can be used in different fermentation processes in the food industry, taking into consideration the acidifying capacity and kinetic growth.

Acknowledgements

This research was financed through the research Project funds:

"Production of indigenous starter culture of lactic acid bacterial LAB for the production of traditional fermented milk “Suero Costeño" code 111572553287 aproved by Colciencias in call 725 of 2015.

Bibliography

[1] Misihairabgwi, J., Cheikhyoussef, A. Traditional fermented foods and beverages of Namibia. J Ethn Foods. Vol 4, (3), pp. 145-153. 2017. DOI: 10.1016/j.jef.2017.08.001

[2] Singh, D., Lee, S. and Hwan Lee, C. Metabolomics for empirical delineation of the traditional Korean fermented foods and beverages. Trends in Food Science & Technology Vol 61, (2), pp. 103-115. 2017. DOI: 10.1016/j.tifs.2017.01.001.

[3] La Anh, N. Health-promoting microbes in traditional Vietnamese fermented foods: A review. Food Science and Human Wellness. Vol 4 (4), pp. 147–161. 2015. DOI: 10.1016/j.fshw.2015.08.004

[4] Simanca, M. Arteaga, M., Pérez, Y. Soto, M. and Salcedo, J. Caracterización y estudio de la fermentación espontánea del Suero Costeño producido en Montería. Rev.MVZ Córdoba. Vol 15, (1), pp. 1944-1953, 2010. DOI: DOI: 10.21897/rmvz.332

[5] Motato, K. E., Milani, C., Ventura, M. Valencia-García, F. E., Ruas-Madiedo, P., Delgado, S. Bacterial diversity of the Colombian fermented milk “Suero Costeño” assessed by culturing and high-throughput sequencing and DGGE analysis of 16S rRNA gene amplicons. Food Microbiology. Vol. 68 (1), pp. 129-136. 2017. DOI: 10.1016/j.fm.2017.07.011

[6] Vakev ainen, K., Valderrama, A., Espinosa, J., Centurionc , D. Rizo, J., Reyes-Duarte, D., Díaz-Ruiz, G., Wright, A., Elizaquível, P., Esquivel, K., Simontaival, A., Aznar, R., Wacher, C. and Plumed-Ferrer, C. Characterization of lactic acid bacteria recovered from atole agrio, a traditional Mexican fermented beverage. LWT - Food Science and Technology. Vol. 88 (1), pp. 109-118. 2018. DOI: 10.1016/j.lwt.2017.10.004

[7] Scragg, A. Biotecnología para ingenieros: Sistemas biológicos en procesos tecnológicos. Limusa: México. 2004.

[8] Liu, X., Kuda, T., Takahashi, H. and Kimura,B. Bacterial and fungal microbiota of spontaneously fermented Chinese products, Rubing milk cake and Yan-cai vegetable pickles. Food Microbiology. Vol. 72 (1), pp. 106-111, 2018. DOI: 10.1016/j.fm.2017.11.014

[9] Jimenez, E., Yepez, A., Perez-Catalu A., Ramos, E., Zúniga-Avila, D., Vignolo, G., Aznar, R. Exploring diversity and biotechnological potential of lactic acid bacteria from tocosh - traditional Peruvian fermented potatoes - by high throughput sequencing (HTS) and culturing. LWT - Food Science and Technology Vol. 87 (1), pp. 567-574. 2018. DOI: 10.1016/j.lwt.2017.09.033

[10] Gobbetti, M., De Angelis, M., Di Cagno, R., Mancini L. and Fox, P. F. Pros and cons for using non-starter lactic acid bacteria (NSLAB) as secondary/adjunct starters for cheese ripening. Trends in Food Science & Technology. Vol 4 (1), 167-178. 2015. DOI: 10.1016/j.tifs.2015.07.016

[11] Universidad de Cordoba. Química General. Córdoba. Departamento de Química Agrícola y Edafología. 2015. http://www.uco.es/~qe1marim/PractQGenIAgroalimentaria 2015_16.pdf

[12] Diaz, M. Ingeniería de Bioprocesos. Madrid: Paraninfo. 2012.

[13] Doran, P.M. Principios de Ingeniería de los Bioprocesos. Zaragoza: Acribia. 1998.

[14] Rizo-Porro, M., González-Fernández, N., Pérez-Martínez, A. & Ramos-Sánchez, L. Diseño de un medio de cultivo con base en sacarosa para la producción de un probiótico para camarones. ICIDCA Sobre los Deriv la Caña Azúcar. 49 (2), pp. 8–16. 2015. Available at: www.redalyc.org/articulo.oa?id=223143421002

[15] Armando, M.R., Galvagno, M.A., Dogi, C.A., Cerrutti, P., Dalcero, A.M. & Cavaglieri, L.R. Statistical optimization of culture conditions for biomass production of probiotic gut-borne *Saccharomyces cerevisiae* strain able to reduce fumonisin B1. Journal Applied Microbiology. 114 (5), pp.1338–46. 2013. http:// doi:10.1111/jam.12144

[16] Hwang, C.F., Chang, J.H., Houng, J.Y., Tsai, C.C., Lin, C.K., Tsen, H.Y. Optimization of medium composition for improving biomass production of *Lactobacillus plantarum* Pi06 using the Taguchi array design and the Box-Behnken method. Biotechnology and Bioprocess Engineering. 17 (4) pp. 827–34. 2012. http://doi 10.1007/s12257-012-0007-4

[17] Aguirre-Ezkauriatza, E. J., Ramírez-Medrano, A., Aguilar-Yáñez, J. M., Álvarez, M.M. Producción de proteína y biomasa probiótica de *Lactobacillus casei* liofilizadas a partir de suero de leche de cabra. Revista Mexicana de Ingeniería Química. 8 (1), pp. 67–76. 2013. http://www.redalyc.org/articulo.oa?id=62011375006

[18] Escobar, L.F, Rojas, C.A., Giraldo, G.A. & Padilla, L. Evaluación del crecimiento de *Lactobacillus casei* y producción de ácido láctico usando como sustratoe el suero de leche vacuno. Revista Universidad Del Quindio. 20, pp. 42-49. 2010.

[19] Agudelo, C., Ortega, R., Hoyos, J.L. Determinación de parámetros cinéticos de dos inóculos lácticos: *Lactobacillus plantarum* A6 y bacterias ácido lácticas de yogurt. Facultad de Ciencias Agropecuarias. 8 (2), pp. 8-16, 2010.

[20] Olivera, J. Caracterización tecnológica de cepas de bacterias ácido lácticas aisladas de la leche. Facultad de Agronomia, Universidad de la República, Montevideo. 2011. 43 P.

[21] Changkun, L., Jihong, S., Lai-yu, K., Jicheng, W., Yan, D., Haijing, Y., Qiangchuan, H., Heping, Z. & Yongfu, C. Influence of *Lactobacillus plantarum* on yogurt fermentation properties and subsequent changes during postfermentation storage. Journal of Dairy Science. 100 (4), pp. 2512–24. 2017. DOI: 10.3168/jds.2016-11864.

[22] León, M.F. Evaluación in vitro de Cepas de Bacterias Ácido Lácticas Nativas con Potencial Probiótico. Facultad de Agronomia, Universidad de la República, Montevideo. 2012. 52 P.

[23] Jurado-Gámez, H., Calpa-Yamá, F., Chaspuengal-Tulcán, A. Determinación de parámetros cinéticos de *Lactobacillus casei* en dos medios probióticos. Facultad de Ciencias Agropecuarias. 8 (2), pp. 15-35 2014. https://doi: 10.17151/vetzo.2014.8.2.2

[24] Georgieva, R., Koleva, P., Nikolova, D., Yankov, D., Danova, S. Growth Parameters of Probiotic Strain *Lactobacillus plantarum*, isolated From Traditional White Cheese. Biotechnology & Biotechnological Equipment. 23 (1), pp. 861–864. 2009. http:// doi: 10.1080/13102818.2009.10818558

F.E. Valencia-García, received the BSc. Bacteriology and Technology in Clinic Laboratory in 1989 from Universidad Católica de Manizales. The MSc. in Food Technology in 1998 from the Universidad Nacional Sede Medellín, Colombia. The MSc. degree in Pharmaceutical Science with emphasis in Food in 2006 and the PhD. In Pharmaceutical and Food Science in 2012, both of them from the Universidad de Antioquia, Colombia. From 1990 to 1998 was working in different clinic laboratories. Since 2000 she has been working in some universities as a teacher. Currently, she is a full professor of the Industrial and Environmental Microbiology Program of Microbiology, School of the Universidad de Antioquia, Colombia. Her research interests include: technology and nutrition foods, development of functional foods, Acid lactic bacterial. probiotics, prebiotics and food quality control.
ORCID: 0000-0002-4167-2167

K.E. Motato-Rocha, is BSc. in Food Scientific and Technologist: Undergraduate studies of the University of Antioquia, Medellín, Colombia, 2001. MSc. of Biotechnology of the University of Antioquia, Medellín, Colombia, 2006. Dr. in Biotechnology programme: PhD studies of the University of Antioquia, Medellín, Colombia, 2018. Assistant professor of the University of Antioquia, Medellín, Colombia, in the Food Technology Department, Faculty of the Phamaceuticals and Food Sciences. Research performance in biotechnology of acid lactic bacterial and probiotics, food microbiology, isolation and characterization of microorganism in traditional fermented foods.
ORCID: 0000-0002-1974-3301

M.Y. Vera-Peña, Student (c) PhD in Biology at the University of Antioquia. Received her BSc. in Biotechnological Production Engineering at Francisco de Paula Santander University and she is MSc. of Science in Chemical Engineering at University of Nacional de Colombia. She is part time Professor at the University of Antioquia, School of Microbiology, Industrial and Environmental Microbiology program. Belongs to the biotransformation research group of the University of Antioquia; She has belonged to the biotechnology and biological control research groups of the Biological Research Corporation, the Dynamic Processes Research Group (KALMAN) of the Universidad Nacional de Colombia, all registered in Colciencias. The courses taught are bioprocesses modeling and drying technology in microorganism; in her doctoral research she is studing the protection mechanisms during spray dryer process of lactic acid starter cultures.
ORCID: 0000-0002-0128-1188

M.L. Sepúlveda-Lindarte, is the BSc. in Biotechnological Engineer of the Universidad Francisco de Paula Santander, Cúcuta, Colombia in 2015. Diploma in Human Genetics and Clinical, form the Universidad de Pamplona, 2006. Professional practice in the area of Cytogenetics, Genetics and Molecular Biology laboratory LTDA, Bogotá, 2009. Undergraduate degree thesis: Mycorrhization in Guadua: behavior in the field and response to biofertilizers in the nursery Laboratory of Soil-Plant-Microorganism Associations (LAMIC), Pontificia Universidad Javeriana, Bogotá, 2011. Technical Specialization “Preparation of bio-inputs and vegetable extracts for organic farming production”. Servicio Nacional de Aprendizaje (SENA), Cúcuta, 2011. Currently, belongs to the Biotransformation Group of the University of Antioquia, collaborated in the project research production of indigenous enzymes from native strains for the production of fermented milk “Suero Costeño" endorsed by Colciencias.
ORCID: 000-0002-0894-9451

UNIVERSIDAD NACIONAL DE COLOMBIA
SEDE MEDELLÍN
FACULTAD DE MINAS

Área Curricular de Ingeniería Química e Ingeniería de Petróleos

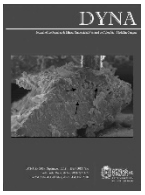
Oferta de Posgrados

Maestría en Ingeniería - Ingeniería Química
Maestría en Ingeniería - Ingeniería de Petróleos
Doctorado en Ingeniería - Sistemas Energéticos

Mayor información:

E-mail: qcaypet_med@unal.edu.co
Teléfono: (57-4) 425 5317

UNIVERSIDAD NACIONAL DE COLOMBIA
SEDE MEDELLÍN
FACULTAD DE MINAS



DYNA
http://dyna.medellin.unal.edu.co/

Soft Pre-stressed PET profiles as reinforcing fibers in structural elements made of concrete

Sergio Márquez-Domínguez [a], Edgar Mejía-Sánchez [a], Jesús Antonio Arenzano-Altaif [a], Gerson Omar Martínez-Guevara [a] & Dante Tolentino [b]

[a] *Facultad de Ingeniería, Universidad Veracruzana, C. Z. Mendoza, Veracruz State, México; semarquez@uv.mx, edmejia@uv.mx, jarenzano@uv.mx, germartinez@uv.mx*
[b] *Sección de Estudios de Posgrado e Investigación, ESIA Zacatenco, Instituto Politécnico Nacional, México, dtolentinolsro@gmail.com*

Received: April 20th, 2018. Received in revised form: june 27th, 2018. Accepted: July 16, 2018

Abstract
The inclusion of pre-stressed PET profiles as reinforcing fibers in structural elements is proposed. The PET-profiles are placed in a unidirectional and bidirectional fiber matrix with soft pre-tensioned condition that they could have advantages in structural members made of concrete in some precise applications, for instance, road safety barriers. A universal machine (WDW-200E) is used to test PET-profiles with different width, knots and even other conditions. The desired PET profile is chosen and the concrete mixture is designed under the ACI standard guidance. Pre-stressed PET-profiles are included in wood molds shaped in beam-type and subsequently flexural strength is estimated. Furthermore, experimental tests results are presented for PET-profiles as structural reinforcement of beams made of concrete under pure flexural. Finally, a probabilistic model is used to estimate the PET contribution in terms of exceedance of the rupture modulus.

Keywords: PET profiles; fiber matrix; beams-type; concrete; Pre-stress; PET fibers; probabilistic model

Perfiles de PET ligeramente pretensados como fibras de refuerzo en elementos estructurales de concreto

Resumen
Se propone la inclusión de perfiles de PET pretensados como fibras de refuerzo en elementos estructurales. Los perfiles de PET se colocan en una matriz de fibra unidireccional y bidireccional con una condición de pretensado suave que podría tener ventajas en elementos estructurales de concreto en algunas aplicaciones precisas, por ejemplo, barreras de contención para seguridad vial. Una máquina universal (WDW-200E) se usa para probar los perfiles de PET con diferentes anchos, nudos e incluso otras condiciones. Se elige el perfil de PET deseado y el concreto se diseña según la norma ACI. Los perfiles de PET pretensados se incluyen en moldes de madera con forma de vigas y, posteriormente, se estima la resistencia a la flexión. Los resultados de las pruebas experimentales de flexión son presentados. Finalmente, se usa un modelo probabilístico para estimar la contribución de PET en términos de excedencia del módulo de ruptura.

Palabras clave: Perfiles de PET; matriz de fibra; tipo viga; concreto; pre-tensados; fibras de PET; modelo probabilístico.

1. Introduction

1.1. State of the art

Environmental pollution is a serious issue that must be addressed as soon as possible. Polyethylene Terephthalate (PET or PETE) is considered a serious environmental problem that need to be studied in order to decrease its environment impact. According with INEGI [1], 44.646 million tons of urban solid waste were generated in Mexico by 2017; of which around 10% was classified as plastic waste. Carcaño [2], made an important prediction based on a study of supply-demand of PET products, establishing that the demand of PET products is going to be higher. One way to decrease this problem can be by implementing *"green building"*. These alternatives provide the opportunity to reuse

How to cite: Márquez-Domínguez, S., Mejía-Sánchez, E., Arenzano-Altai, J.A., Martínez-Guevara, G.O. and Tolentino, D., Soft Pre-stressed PET profiles as reinforcing fibers in structural elements made of concrete. DYNA, 85(206), pp. 162-170, September, 2018.

© The author; licensee Universidad Nacional de Colombia.

toxic products and developed new building techniques, hence solid waste or polluting products can be integrated into useful structural elements that can even improve the building processes and also contribute to the mechanical properties of the structural elements. In order to understand the mechanical properties of concrete containing PET waste, several manuscripts have been conducted taken into account parameters such as elastic modulus [3-5], flexural tensile strengths [6-8], impact resistance [10], fresh and hardened properties of concrete [11] including abrasion resistance [9]. This research is presented as a structural context where PET-profiles were used as an alternative structural reinforcement, and also a probabilistic model is used to estimate the PET contribution in terms of exceedance of the rupture modulus.

2. Main scope

The main objective of this paper is to be the first national incursion on the subject of sustainable development through a prototype proposed to be implemented in the highway infrastructure. Here, the results are presented in order to assess the importance of using a PET-profiles matrix within concrete beam-type specimens where the flexural properties of concrete specimens reinforced by a soft pre-tensioned PET-profile matrix placed on in specially designed molds should be increased. PET-profiles settled as a fiber matrix with soft pre-tensioned condition could have advantages in structural members in some precise applications, as for instance, structural support for road safety barriers. Laboratory Tests are performed using a universal machine (WDW-200E) in order to estimate the tensile strength capacity of PET profiles with different width, number of "knots" and other conditions. The desired PET profile is chosen and the concrete mixture is designed under the ACI standard guidance [17]. The main stage is to estimate the flexural properties of reinforced concrete beams by including pre-stressed PET-profiles in order to develop a sustainable prototype that can be used in the highway infrastructure which are basically designed with a specified compressive strength of concrete (f'_c=30MPa).

2.1. The research process will cover the following phases

1. Analyze the mechanical and physical properties of the PET-profiles with different width, different number of "knots" and also many other conditions.
2. Perform Bending tests of concrete beams with loads in the thirds of their length.
3. Perform Bending tests of concrete beams including pre-stressed PET profiles in a unidirectional fiber matrix.
4. Perform bending tests of concrete beams with pre-stressed PET-profiles placed on a bidirectional fiber matrix in a mesh form.

In this paper a probabilistic assessment is used to estimate the PET contribution of the rupture modulus [12]**.** Here, the beam-type specimens are casted with concrete with a (f'_c=30MPa) complying with NMX-C-159-ONNCCE-2004 [13] and NMX-C-160-ONNCCE. 2004, MEXICO: ONNCCE [14]. These standard codes are used for the preparation of test specimens. In order to estimate the flexural strength capacity of beam-type specimens, it is worth to mention that, the molds are built with a cross section of 0.15 x 0.15 m and length equal to 0.60 m, made of wood. The wooden molds will include different aluminum accessories necessary to hold the PET-fibers, then it is possible make a soft pre-stressing, see Fig. 1.



Figure 1. Wooden molds within aluminum accessories and PET-profiles matrix: 5 layers with 11 threads every layer.
Source: The authors.

3. PET-profiles: Tensile strength capacity

The PET-profiles and/or PET-threads were tested one by one in blocks with similar geometric properties in order to estimate an average of the tensile strength capacity and deformation of each block. The PET-profiles were cut and prepared from recycled PET-bottles coming from commercial sodas. In Table 1 to 6, valuable information is given obtained for PET-profile with different width (Table 1), number of "knots" (Tables 2) and also other properties were analyzed such as for instance the temperature effect. It is worth to mention that the tensile strength was estimated in a Universal Testing Machine (WDW-200E),

The necessity of workability, when the PET-profiles are implemented in the wooden molds is very important. For this reason and according with the tests results given in Table 1, it was decided to use PET-profiles with 3.5 x 10^{-3} m of width. On the other hand, knotted PET-profiles have the "anchorage"

Table 1.
Tensile strength capacity of PET-profiles with different widths and a length equal to 0.25 m and Thickness 4.5 x10^{-4} m

No. of specimens	Width (m)	Deformation (m)	Tensile strength capacity (N)
10	3.5 x10^{-3}	0.06690	180.11
10	5.0 x10^{-3}	0.05213	240.15
10	7.0 x10^{-3}	0.03712	344.23
10	1.0 x10^{-2}	0.04175	392.20

Source: The authors.

Table 2.
Tensile strength capacity from knotted PET-profiles with a width 3.5 x10^{-3} m, length equal to 0.25 m and Thickness 4.5 x10^{-4} m

No. of specimens	No. of Knots	Deformation (m)	Tensile strength capacity (N)
10	1	0.03893	160.10
10	2	0.03579	140.09
10	3	0.10731	160.09
10	5	0.11929	152.06
10	7	0.08620	124.10
10	10	0.17620	136.06

Source: The authors

Table 3.
Tensile strength capacity from PET-profiles baked at 50 °C with a width 3.5 x10^{-3} m, length equal to 0.25 m and Thickness 4.5 x10^{-4} m

No. of specimens	Baking time (s)	Deformation (m)	Tensile strength capacity (N)
5	900	0.04108	248.19
5	1,800	0.04025	280.17
5	2,700	0.04198	224.16
5	3,600	0,04720	248.19

Source: The authors

Table 4.
Tensile strength capacity from PET-profiles baked at 100 °C with a width 3.5 x10^{-3} m, length equal to 0.25 m and Thickness 4.5 x10^{-4} m

No. of specimens	Baking time (s)	Deformation (m)	Tensile strength capacity (N)
5	900	0.09516	272.13
5	1,800	0.11167	264.18
5	2,700	0.06349	216.11
5	3,600	0.05337	176.11

Source: The authors

function working together with concrete; these knots will be like the corrugations in the steel rods. In this study, Knotted PET-profiles are the most viable option granting the anchorage between PET-Profiles and concrete, see Fig. 1.

Knotted PET-profiles provide similar tensile strength capacity than not knotted PET-profiles, see Table 2 where a total of 60 test specimens were tested in blocks each one with 10 specimens with similar knotted conditions in order to estimate an average of the tensile strength capacity and deformation of each block. Even, in this research work, the effect of temperature on the PET is reviewed since the particles of the material could be crystallized providing a change in their mechanical properties. The Tensile strength estimated from PET- profiles baked at different temperatures are presented in Tables 3 to 5 where 5 tests are reported for each time step and temperature, these number of tests were considered enough evidence to observe the behavior of the effect of temperature on PET-profiles.

Table 5.
Tensile strength capacity from PET-profiles baked at 150 °C with a width 3.5 x10^{-3} m, length equal to 0.25 m and Thickness 4.5 x10^{-4} m

No. of specimens	Baking time (s)	Deformation (m)	Tensile strength capacity (N)
5	900	0.10644	200.12
5	1,800	0.08161	176.09
5	2,700	0.09000	160.10
5	3,600	0.06491	184.13

Source: The authors

Table 6.
Tensile strength capacity of extruded Plastic-profiles made off with commercial plastic bags; length 0.15 m.

No. of specimens	Diameter (m)	Deformation (m)	Tensile strength capacity (N)
7	3.50 x10^{-3}	0.21484	125.76
7	4.85 x10^{-3}	0.24998	240.15
7	5.75 x10^{-3}	0.24976	314.21

Source: The authors



Figure 2. Extruded Plastic-Profiles.
Source: The authors.

The Plastic-profiles can be made off with recycled plastic material coming from commercial plastic bags, See Fig. 2 where extruded Plastic-profiles are shown. In Table 6, is clear that the deformation of the Plastic-profiles is greater than that experienced by the PET-profiles given in Table 1. In fact, the tests carried out under controlled laboratory test conditions proved that "Plastic-profiles", with circular cross-section, resist a certain tensile strength capacity without reaching their rupture, it means that the Plastic-profiles are working in the plastic zone area.

A considerable number of Tests were carried out with different diameters of extruded Plastic-profiles, see Table 6 where it is shown that the Plastic-profile of 5.75 x10^{-3} m in diameter has the highest tensile strength capacity.

It is worth to mention that for 1 kg of plastic material; the following material is required:

- 0.772kg of recycled Linear Low-Density Polyethylene (LLDPE).
- 0.154kg of recycled High Density Polyethylene (HDPE).
- 0.074kg. of recycled Low Density Polyethylene (LDPE)

The last three materials can be recycled from commercial plastic bags.

4. Concrete Beam-type specimens: Flexural strength capacity

The concrete was designed with a specified compressive strength of $(f'c = 30\text{MPa})$. The compressive strength of concrete is measured to ensure that the concrete satisfy the quality control. To measure the compressive strength of the concrete, cylindrical-test specimens of 0.15 x 0.30 m are prepared and stored until the concrete hardens. The whole testing procedure was carried out in laboratory test conditions following the standard codes, see [13-15].

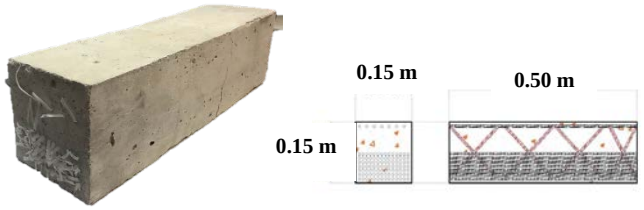


Figure 3. Beam-type specimen with PET-profiles settled in a bidirectional fiber matrix in a mesh form.
Source: The authors



Figure 4. Concrete Flexural Resistance using a simple concrete beam with load in the middle third of the clearing. NMX-C-191-ONNCCE [15].
Source: The authors

Once the concrete mixture is designed and tested. The concrete is casted in molds made off wood with cross-section 0.15 x 0.15 x 0.50 m. Every PET-thread had knots every 0.02 m to provide traction and an additional pre-tension was induced (approximately - 1 kg per thread). A cast beam-type specimen with the PET-profile matrix is shown in Fig. 3.

Now, it is possible to perform bending tests in order to estimate the flexural strength of concrete beams-type specimens with loads in the thirds of their length with and without PET-profiles embedded following a unidirectional fiber matrix or a bidirectional fiber matrix in a mesh form.

According with NMX-C-191-ONNCCE [15], the modulus of rupture is a material property obtained to determine the flexural strength of the concrete by the bending test of a beam. There are two types of failure in terms of the rupture modulus, when the fracture is presented in the middle third of the clearing, see Fig. 4 and when the rupture is not presented within the middle third.

Therefore, on average, two beam-type specimens were casted per every test stage so that in total around 18 tests beam-type specimens were done obtaining the following results. In Table 7, the bending test results for beam-type specimens made of simple concrete are shown with loads in the thirds of their length.

Table 7.
Main data obtained from Beam-type specimens made of simple concrete

Day	3	7	28
Maximum load (KN)	24.255	28.838	23.894
Deformation (m)	2.4 x10^{-3}	1.6 x10^{-3}	7.8 x10^{-3}
Modulus of rupture (MPa)	3.66	4.35	3.60
Rotation (θ-grades)	8°	5°	14°

Source: The authors

Table 8.
Main data obtained from Beam-type specimens made with PET-profiles placed in a unidirectional fiber matrix

Day	3	7	28
Maximum load (KN)	37.093	36.673	36.743
Deformation (m)	6.4 x10^{-3}	5.4 x10^{-3}	5.8 x10^{-3}
Modulus of rupture (MPa)	5.60	5.53	5.54
Rotation (θ-grades)	21°	17°	19°

Source: The authors

Table 9.
Main data obtained from Beam-type specimens made with PET-profiles placed in a bidirectional fiber matrix (45°, Fig. 3).

Day	3	7	28
Maximum load (KN)	29.858	28.857	25.836
Deformation (m)	7.3 x10^{-3}	7.5 x10^{-3}	6.5 x10^{-3}
Modulus of rupture (MPa)	4.50	4.35	3.90
Rotation (θ-grades)	23°	24°	21°

Source: The authors

In Table 8 and 9, the bending tests results coming from beam-type specimen whit pre-stressed PET profiles in a unidirectional and bidirectional fiber matrix are given, respectively.

The average of the maximum load capacity and deformation are obtained from beam-type specimens casted at different ages; see Tables 7 to 9 where Fluctuated load capacity values are observed. The PET-profiles in a unidirectional and bidirectional matrix arrangement have influence in the flexural strength capacity of the beams-type specimens. In Tables 7 to 9, The deflection has also an considerable importance in the load capacity and modulus of rupture where a soft increment in the value are observed in beam-type specimens with PET-profiles settled in a uni and bi-directional matrix. It is because the beam-type specimens with PET-profiles can support more deflection. The influence of the PET-profiles is higher in the test specimens with a unidirectional arrangement than in a bidirectional matrix where the PET-profiles settled with a 45° angle could affect the behavior of the unidirectional PET-Profile arrangement which could work once the concrete have failed. In Tables 7 to 9, the rotation is estimated using the data of maximum load and deformation. It is easy to see that the PET-profiles provide a better rotation degree to the beam where, the beam-type specimens made with PET-profiles placed in a bidirectional fiber matrix placed to 45° have higher rotation and flexibility with similar flexural strength those beam-type specimens with a unidirectional fiber matrix.

In Table 2 is shown that a thread with 10 knots can resist a load of 135.97 N. But according to data in Tables 7 to 9, it is not easy to see the contribution of tensile and flexural strength. For this reason, it is necessary to analyze the Figs. 5-7.

In Fig. 5, the beam specimen reaches the maximum load and after that a fragile failure is presented. That is not the case for beam specimens with unidirectional and bidirectional PET fiber matrix where, the PET profiles provides a 62-63% average resistance after the failure of concrete, see Fig. 6 and 7. In Fig. 7, PET-profiles placed in a bidirectional matrix with 45° provide a 6.46% more compared to profiles settled in a

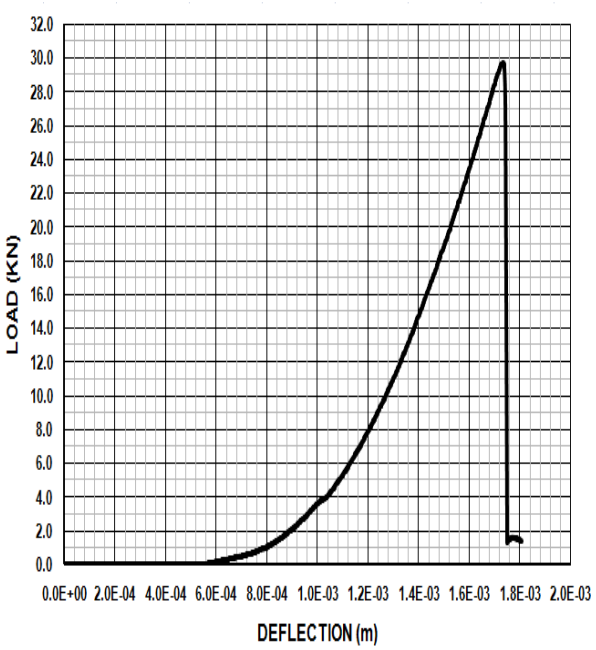


Figure 5. Load-Deflection for a simple concrete beam loaded in the middle third of the clearing. NMX-C-191-ONNCCE [15].
Source: The authors

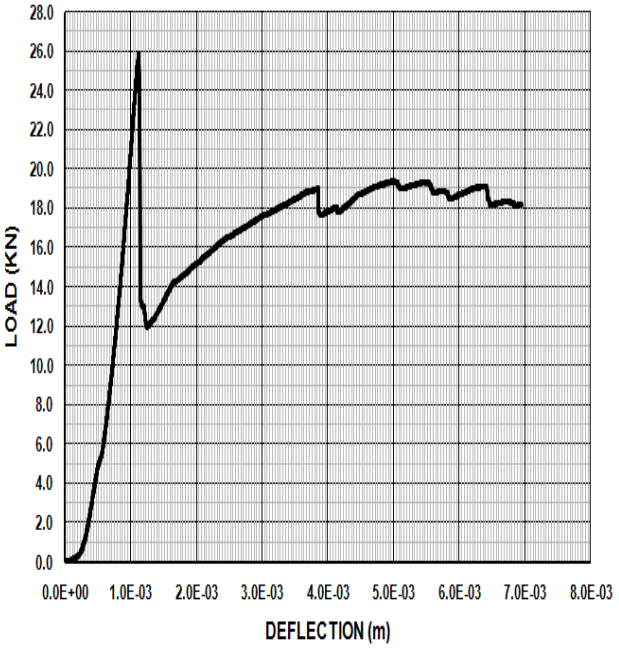


Figure 7. Load-Deflection for a beam-type made off concrete with bidirectional fiber matrix loaded in the middle third of the clearing. NMX-C-191-ONNCCE [15].
Source: The authors

unidirectional way. Therefore, PET-profiles settled in a bidirectional matrix with 45° provides around 69.31% more than a simple concrete beam after the fragile failure, it should be mentioned that these test specimens with PET-profiles shown a remarkable strength increase upwards compared to the profiles placed in a unidirectional way; showing a "constant" or linear contribution.

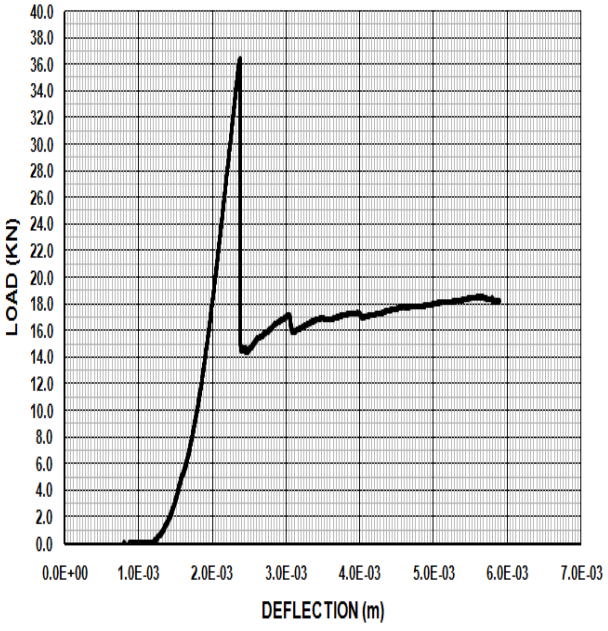


Figure 6. Load-Deflection for a beam-type made off concrete with unidirectional fiber matrix loaded in the middle third of the clearing. NMX-C-191-ONNCCE [15].
Source: The authors

Fig. 5 shows a tests specimen with fragile failure, it is because the PET profiles are not included. In Fig. 6 and 7, the contribution of the PET profiles are working once the concrete fail. Therefore, the curves in the figures show that the tests specimen is holding strength and lead to a ductile failure.

Fig. 8 shows that PET-profiles have the characteristic to keep the concrete fragments confined due to the action or anchoring provided by knotted PET profiles. Therefore, the PET-profiles inclusion in the concrete can be useful in structural support for road safety barrier where the car impact can spread small concrete fragments and the PET-profiles or PET-threads could keep the concrete fragments confined. Future work can be planned where impact tests and energy dissipation can be carried out, since the PET profiles has the ability to confine the concrete particles where the main objective of this project is to save the life of the road users and protect the environment.



Figure 8. Fragments confined in a beam specimen due to the anchoring provided by knotted PET profiles placed in a bidirectional fiber matrix.
Source: The authors

5. Probabilistic estimation of PET-profiles contribution

In this section, a probabilistic approach is proposed to evaluate PET-Contribution in terms of capacity and failure. In Table 10, the stochastic variables are enumerated. It is worth to mention that PET contribution affects more the vicinity of flexural failure stage when these profiles are delaying the Rupture modulus (RM) while the flexural beam upper compression block is increasing (or decreasing) to balance the flexural capacity. Therefore, the rupture modulus test considers an early state during beam behavior before tension-cracking condition where it is always expected a sudden and brittle beam failure.

The values shown in Table 10 are based on preliminary test studies which have been carry out in [12] where a modulus of rupture of 3.54MPa was obtained for a beam-type specimen made of 20MPa and beams including pre-stressed PET profiles in a unidirectional fiber matrix a modulus of rupture of 3.788MPa was estimated, which clearly is compatible with the results presented in Tables 7 to 9 where Beam-type specimens with a compressive strength of 30MPa which have been tested.

Eq. (1) is used to estimate the tension stress in the bottom fiber where rupture is taking place:

Table 10.
Stochastic variables and models for Probabilistic simulation of PET-contribution before flexure rupture

No.	Variable	Values	Description
1	$h \sim LN(\mu_h, \sigma_h)$	$\mu_h = 0.15$, $\sigma_h = 0.2$ (%)	Beam height (m)
2	$b \sim LN(\mu_b, \sigma_b)$	$\mu_b = 0.15$, $\sigma_b = 0.2$ (%)	Beam base (m)
3	$P \sim LN(\mu_P, \sigma_P)$	μ_P, σ_P, according analysis	Rupture test load (N)
4	$f_t \sim LN(\mu_{ft}, \sigma_{ft})$	$\mu_{ft} = 3.54$, $\sigma_{ft} = 0.4$ (%)	RM (MPa)
5	$\varepsilon_{cu} \sim LN(\mu_{cu}, \sigma_{cu})$	$\mu_{cu} = 0.000038$ $\sigma_{cu} = 0.000002$	Ultimate compressive deformation
6	$l_w \sim LN(\mu_{lw}, \sigma_{lw})$	$\mu_{lw} = 0.60$ $\sigma_{lw} = 0.4$ (%)	Beam total length (m)
7	$l_P \sim LN(\mu_{lP}, \sigma_{lP})$	$\mu_{lP} = 0.50$, $\sigma_{lP} = 0.4$ (%)	Beam test length (m)
8	$w_{tot} \sim LN(\mu_{wt}, \sigma_w$	$\mu_{wt} = 255.06$ $\sigma_{wt} = 10$	Total beam weight (N)
9	$f'_c \sim LN(\mu_{fc}, \sigma_{fc})$	$\mu_{fc} = 20$ $\sigma_h = 1.5$	Design compressive of concrete (MPa)
10	$n_{sim} \sim D$	According analysis	Number of simulations
11	$n_{pp} \sim D$	Matrix of 3 layers, 6 profiles within layer.	Number of PET-profiles. Total 18 profiles.
12	$p_t \sim N(\mu_{pt}, \sigma_{pt})$	$\mu_{pt} = 0.000635$ $\sigma_{pt} = 0.0001$	Thickness of PET-profile (m)
13	$p_b \sim N(\mu_{pb}, \sigma_{pb})$	$\mu_{pb} = 0.003$, $\sigma_{pb} = 0.0005$	Cross-section base of PET-profile (m)
14	$p_{yi} \sim N(\mu_{yi}, \sigma_{yi})$	$\mu_{yi} = (0.02, 0.04, 0.06)$ $\sigma_{yi} = (0.1, 0.1, 0.1)$ (%)	i-th distance of layer from the bottom of the beam (m).
15	$p_E \sim N(\mu_{pE}, \sigma_{pE})$	$\mu_{pE} = 7138.0135$ $\sigma_{pE} = 120$	Commercial Young's modulus of PET-profile (MPa)

Note: D: Deterministic value, N: Normal distribution and LN: Log-normal distribution.

Source: Taken from [12]

$$f_c = f_{Hm}\left[{f_H}^{-1}\left[\frac{\left(\frac{w_{tot} l_w}{16} + \frac{P\, l_p}{6}\right)(d_f)}{\left(\frac{b\, h^3}{12}\right)}, f'_c, E_c\left(\frac{w_{tot}}{h\, b\, l_w}, f'_c, f_t\,,\, \varepsilon_{cu}\right)\right]\right] \quad (1)$$

Where ${f_H}^{-1}(\cdot)$ and $f_{Hm}(\cdot)$ are the inverse Hognestad's stress-deformation model for nonconfined concrete and simple numerical modification of Hognestad's stress-deformation model for nullifying tension stresses in the lower part of the beam, see reference [16]. The first term in ${f_H}^{-1}(\cdot)$ is the flexural normal stress σ and the last is a Young's modulus that is calculated using a former ACI contribution [17]. The total weight of the specimen is considered as uncertainty. The variable d_f is the distance to the section fiber in which one is interested on. Thinking in the top or bottom layers, $d_f = h/2$.

With the inclusion of PET-profile, the bottom stress (σ_b) and top stress (σ_t) may change with the hand of the stress diagram of a supposed plain remaining face. In Fig. 9, it is shown the case 9-a where PET-profiles are not included. Also, the condition of PET embedded is considered in 9-b and 9-c. In the Fig. 9-b, it is shown the case in which any reinforcing fibers (general case) are contributing to the tension wedge force and as a result, the compression force should increase in a manner of an area increasing. In the case of Fig. 9-c, the condition of a reinforcing soft fiber is prevailing. In the former case, the fibers are reducing concrete area at tension wedge and hence, the tension force should increase (with an increasing of tension wedge area). Previous cases in Fig. 9-b, 9-c, can be the cases of PET-profiles. The diverse behavior depends directly on the Young's modulus of PET-profiles as theory is describing but also any initial pre-tensioning of PET-fibers (as is the case) according the PET variety and conditions.

Assuming the behavior in Fig. 9-b, the PET contribution may be positive for increasing RM or generating cases where σ_b is less than σ_t. The experimental data of the beams in this work, confirm this belief. In order to include in the eq. (1) with the variation of d_f and using:

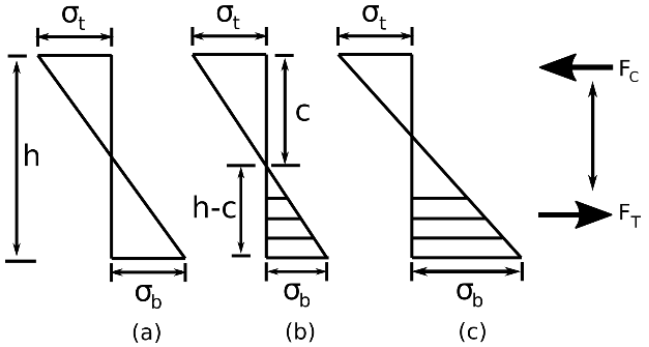


Figure 9. Effects of PET-profiles. (a) Stress diagram without PET-profiles. (b) Stress diagram with PET-profile and increasing of compression wedge area. (c) Stress diagram with PET-profile and decreasing of compression wedge area.
Source: [12]

$$c = \frac{2\left(F_C \pm \sum_{i=1}^{n_f} f_i\right)}{b\sigma_b} \quad (2)$$

where c is the compression wedge depth, F_C is the Compression resulting force, f_i is the fiber force, b is the cross-sectional base and σ_b is the bottom tension stress. The signs $\pm$ are referring to soft-fibers (+, sign) and acting-fibers (-, sign), respectively. Using the eq. (2), it is possible to calculate (1) and estimate the modification of the stress profile. When the eq. (1) is modified by (2), it is possible to simulate by Monte Carlo technique and then find the positive or negative contribution of the PET-profile.

The limit state equation can be described by:

$$g(\tilde{x}) = f_{tb} - f_{cb} \quad (3)$$

where $\tilde{x}$ is the vector of stochastic and deterministic parameter shown in Table 10 and f_{tb} is the stochastic variable representing the maximum tension stress at the bottom line of the cross section and f_{cb} is the bottom stress calculated with f_c using the eq. (3) as d_f.

6. Application case

In Table 11, the results are shown which they basically address the tests made in beam-type specimens with simple concrete (f'_c=20 MPa), where two different molds were used: a conventional 0.15 x 0.15 x 0.45 m and other with 18 holes to introduce the PET-profiles which have been carry out in [12].

From Table 11, it is possible to see an increase of reliability (β) for specific values of P, coming from expected forces for particular compressive strength of concrete in specific tested beams. And also low reliability β-values are referring to the tension cracking condition from the fact that this condition is not preventable. However, it is more important to be concentrated in the difference between beam's reliability indexes ($\boldsymbol{\beta}$) with and without PET-profiles. The differences are mainly what this work is about.

In this paper, the tests are made in beam-type specimens with simple concrete (f'_c=30MPa). This is done mainly for structural applications mainly for a Highway Safety barrier prototype complying with the standard code "NMX-C-159-ONNCCE-2004" [13], where two different molds were used: a conventional 0.15 x 0.15 x 0.50 m and other with 55 holes to introduce the PET-profiles in a matrix with 5 layers with 11 threads every layer. Every PET-thread had knots every 0.02 m to provide traction and an additional pre-tensioning was induced (approximately 1 kg per thread). Beam-test specimens without PET-profiles has a Rupture modulus in average equal to 3.60MPa and Beam-type specimens made with PET-profiles placed in a unidirectional fiber matrix has an estimated Rupture Modulus around 5.54MPa (see Table 8) and 3.90MPa with PET-profiles placed in a bidirectional fiber matrix (45°, Table 9).

National Road Accident Statistics is widely addressed in [18]. In fact, injuries caused by traffic accidents are still among the ten leading causes of death in Mexico, in 2014, 15,886 deaths were registered. Therefore, a rate of 13.3 deaths per 100 thousand inhabitants is estimated. According with above, the possibility of a car accident is high and should be taken into account carefully.

Table 11.
Reliability results for beam specimen made of 20MPa

P Rupture test load parameters (KN)	RM-Exceedance probability without PET	RM-Exceedance probability with PET	$\boldsymbol{\beta}$ without PET-profiles	$\boldsymbol{\beta}$ with PET-profiles
$\mu_P = 25.0$, $\sigma_P = 0.5$	0.078	0.072	1.4186	1.4610
$\mu_P = 25.0$, $\sigma_P = 1.0$	0.164	0.155	0.9781	1.015
$\mu_P = 27.0$, $\sigma_P = 0.5$	0.072	0.069	0.588	0.5129
$\mu_P = 27.0$, $\sigma_P = 1.0$	0.0642	0.0617	0.3638	0.2976

Source: Taken from [12]

7. Highway safety barrier prototype

Car accidents are presented due to various conditions and it is easy that the vehicles lose their trajectory causing accidents that endanger the lives of passengers and other road users. For this reason, the development of new technologies in this area is important. In consequence, road safety barriers are installed and designed in accordance with strict technical criteria, in order to achieve maximum efficiency avoiding major damage to road users. Highways have mostly road safety barriers dividing the main lanes. Due to the above, PET profiles can be added to the safety barriers potentializing considerably the PET recycling.

Safety barriers with PET-profiles matrix is an initial prototype as a proposal that need to be studied in detail, see Fig. 10 and 11. The initial model has PET-profiles placed in a bidirectional matrix where PET-profiles are settled with 0.15 m between each one following the vertical direction of the cross section, this arrangement is an initial purpose thinking in easy enabled and placed inside the mold of the safety barrier. For future investigations, it is recommended to conduct impact studies to determine the effectiveness of the proposed model and determine the release of energy as presented in the prototype. Therefore, the PET-profiles inclusion in the concrete can be useful in structural support for road safety barrier where the car impact can spread small concrete fragments and the PET-profiles or PET-threads could keep the concrete fragments confined.

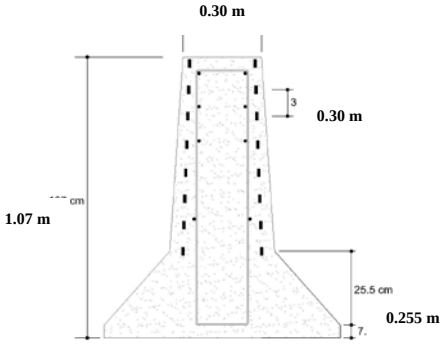


Figure 10. Pure bending device built according to NMX-C-191-ONNCCE [15] standard.
Source: The authors

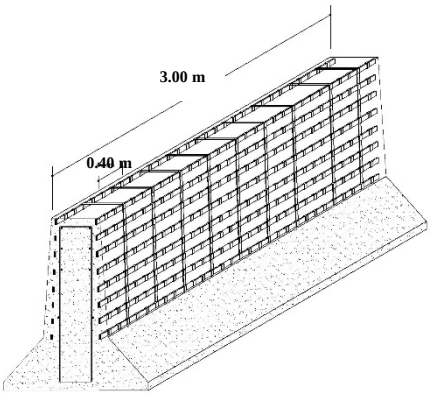


Figure 11. Pure bending device built according to the NMX-C-191-ONNCCE [15] standard.
Source: The authors

8. Conclusions

Green building is the opportunity to reuse toxic products and developed new building techniques in such a way that polluting products can be integrated into useful building elements that can even improve the building processes and also contribute to the mechanical properties of the structural elements. Therefore, this paper is an initial addressing PET-profiles reinforcing for failure structural states. In fact, it is presented experimental tests of a PET-profile matrix as tension reinforcement of beams made of concrete under pure flexural test. It was shown that PET-profiles used in unidirectional and bidirectional fiber matrix with soft pre-tensioned condition could have advantages in structural members in some precise applications, as for instance members impose to impact such as road safety barriers implemented in the highway infrastructure where PET-profiles inclusion in the concrete can be useful in structural support when a car impact can spread small concrete fragments and the PET-profiles or PET-threads could keep the concrete fragments confined and also the PET-fibers can be helpful in the vicinity of cracking failure condition, having three main aspects: a subtle increasing rupture modulus, crack mitigating in the failure plane and providing an additional plastic PET-capacity after failure. From the structural reliability perspective, PET-threads have influence, rising the reliability levels for expected forces for a particular compressive strength of structural members. It is worth to say that the stochastic model match properly with the experimental test.

Acknowledgements

The authors acknowledge the support of Program for Professional Teacher Development, for the Higher Type (PRODEP) through the project called **SA/103.5/16/10438 /PTC-835.** The authors want to make a special thanks to the students Sergio Jesús López-Castañeda, José Melesio Sánchez-Morales, Abelardo Molohua-Texoco due to the valuable help and effort by carrying out the laboratory tests

References

[1] National Institute of Statistic and Geography (INEGI). Statistical and Geographical Yearbook of the United Mexican States, National Institute of Statistic and Geography. 2017, Mexico, 1066 P.
[2] Reyes-Carcaño, J.R., Estudio de factibilidad para la instalación de una planta recicladora de envases de PET. BSc. Thesis, Unidad Profesional Interdisciplinaria de Ingeniería y Ciencias Sociales y Administrativas (UPUESA), Instituto Politécnico Nacional, México, 2009.
[3] Hannawi, K., Kamali-Bernard, S. and Prince, W., Physical and mechanical properties of mortars containing PET and PC waste aggregates. Waste Management, 30, pp. 2312-2320, 2010. DOI:10.1016/j.wasman.2010.03.028
[4] Mohammed, A.A., Flexural behavior and analysis of reinforced concrete beams made of recycled PET waste concrete. Construction and Buildings Materials, 155, pp. 593-604, 2017. DOI: 10.1016/j.conbuildmat.2017.08.096
[5] Mohammed, A.A., Modeling the mechanical properties of concrete containing PET waste aggregate. Construction and Buildings Materials, 150, pp. 595-605, 2017. DOI: 10.1016/j.conbuildmat.2017.05.154
[6] Bhogayata, A.C. and Arora, N.K., Fresh and strength properties of concrete reinforced with metalized plastic waste fibers. Construction and Buildings Materials, 146, pp. 455-463, 2017 DOI: 10.1016/j.conbuildmat.2017.04.095
[7] Rebeiz, K.S., Precast use of polymer concrete using unsaturated polyester resin based on recycled PET waste. Construction and Buildings Materials, 10(3), pp. 215-220, 1996.
[8] Rinu-Isah, R.J. and Shruthi M.V., Utilization of waste PET bottle fibers in reinforced concrete. International Journal of Pure and Applied Mathematics, 116(13), pp. 579-584, 2017. ISSN: 1311-8080 (printed version); ISSN: 1314-3395 (on-line version)
[9] Saikia, N. and De Brito, J., Mechanical properties and abrasion behavior of concrete containing shredded bottle waste as a partial substitution of natural aggregate, Construction and Buildings Materials, 52, pp. 236-244, 2014. DOI: 10.1016/j.conbuildmat.2013.11.049
[10] Saxena, R., Siddique, S. Gupta, T., Sharma, R.K. and Chaudhary, S., Impact resistance and energy absorption capacity of concrete containing plastic waste, Construction and Buildings Materials, 176, pp. 415-421,2018. DOI: 10.1016/j.conbuildmat.2018.05.019
[11] Pacheco-Torgal, F., Ding, Y. and Jalali, S., Properties and durability of concrete containing polymeric wastes (tire rubber and polyethylene terephthalate bottles): an overview, Construction and Buildings Materials, 30, pp.714-724, 2012. DOI: 10.1016/j.conbuildmat.2011.11.047
[12] Márquez-Domínguez, S. et al., Residual PET profiles as tension reinforcing fibers in beams. Proceedings of 6th Structural Engineers World Congress (SEWC). Cancún, Mexico. November 14-17, 2017.
[13] National Agency for Standardization and Certification of Construction and Building. Mexican Standard- NMX-C-159-ONNCCE. 2004, MEXICO: ONNCCE.
[14] National Agency for Standardization and Certification of Construction and Building. Mexican Standard- NMX-C-160-ONNCCE. 2004, MEXICO: ONNCCE.
[15] National Agency for Standardization and Certification of Construction and Building. Mexican Standard-NMX-C-191-ONNCCE. 2004. Concrete flexural resistance using a simple beam with load in the clear thirds. MEXICO: ONNCCE.
[16] Hognestad, E., A Study of combined bending and axial load in reinforced concrete members. University of Illinois Engineering Experimental Station, Serie number 399, November 1951, 128 P.
[17] ACI Committee 318, Building Code Requirements for Reinforced Concrete, American Concrete Institute, Detroit, 1971.
[18] Report on the situation of road safety, Mexico 2015. Secretariat of Health/STCONAPRA. Mexico, [online]. 2016. ISBN: 978-607-460-534-1. Available at: http://conapra.salud.gob.mx/Interior/Documentos/Informe2015.pdf

S. Márquez-Dominguez, received the BSc. Eng in Civil Engineering in 2004 by the Universidad Veracruzana, the MSc. degree in Engineering in 2006 from Universidad Nacional Autónoma de Mexico (UNAM), both in Mexico and the PhD degree in Civil Engineering in 2013 from Aalborg

University in Denmark. From 2013 to 2014, he worked as a full professor in civil engineering in Universidad de Guanajuato, Mexico and since 2014, he is a full professor in the Civil Engineering Department, Facultad de Ingeniería, Universidad Veracruzana; Mexico. His research interests include: structural reliability, materials and sustainable construction or green building as an opportunity to reuse toxic products and developed new building techniques.
ORCID: 0000-0002-4864-3238

E. Mejía-Sánchez, received the BSc. Eng in Electromechanical Engineering in 2001 by the Instituto Tecnológico de Apizaco, the MSc. degree in Mechanical Engineering in 2004 from Centro Nacional de Investigación y Desarrollo Tecnológico (CENIDET) and the PhD degree in Engineering and Applied Sciences in 2010 from Universidad Autónoma del Estado de Morelos, all in Mexico. From 2001 to 2009, he worked as a full professor in Mechanical Engineering in Universidad Tecnológica Emiliano Zapata (UTEZ), Morelos, Mexico and since 2009, he is a full professor in the Mechanical Engineering Department, Facultad de Ingeniería, Universidad Veracruzana. His research interests include: materials and sustainable construction.
ORCID: 0000-0002-9806-6141

J.A. Arenzano-Altaif, Completed his BSc. degree in Industrial Engineering in 1998 and a MSc. degree in Industrial Engineering in 2004, both at Instituto Tecnologico de Orizaba, also completed a Doctorate in Engineering in 2017 at Universidad Veracruzana. He is currently full time professor at the Faculty of Engineering, campus Cd. Mendoza, of Universidad Veracruzana. His research works include advanced materials in the area of polymers.
ORCID: 0000-0001-5201-1527

G.O. Martinez-Guevara, received the BSc. Eng in Civil Engineering in 2004 by the Technological Institute of Tehuacan, the MSc. of Applied Engineering in 2015 from Universidad Veracruzana, both in Mexico. And since 2011, he is a full professor in Facultad de Ingeniería, Universidad Veracruzana in the Engineering Department and responsible for the laboratory of soil and materials mechanics. His research interests include: technology in materials, as an opportunity to implement the use of materials in new technologies.
ORCID: 0000-0002-8040-9097

D. Tolentino, completed his BSc. in Civil Engineering at Instituto Politécnico Nacional in 2007, a MSc. in Engineering in 2009 and a PhD in Engineering in 2013 all of them at Universidad Nacional Autónoma de Mexico. He is currently professor at the Seccion de Estudios de Posgrado e Investigación of the Escuela Superior de Ingeniería y Arquitectura Unidad Zacatenco at the Instituto Politécnico Nacional. He is an expert in structural reliability and optimization.
ORCID: 0000-0003-3930-3562

UNIVERSIDAD NACIONAL DE COLOMBIA
SEDE MEDELLÍN
FACULTAD DE MINAS

Área Curricular de Ingeniería Civil

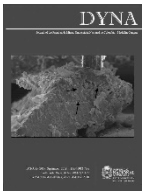
Oferta de Posgrados

Especialización en Vías y Transportes
Especialización en Estructuras
Maestría en Ingeniería - Infraestructura y Sistemas de Transporte
Maestría en Ingeniería – Geotecnia
Doctorado en Ingeniería - Ingeniería Civil

Mayor información:

E-mail: asisacic_med@unal.edu.co
Teléfono: (57-4) 425 5172

UNIVERSIDAD NACIONAL DE COLOMBIA
SEDE MEDELLÍN
FACULTAD DE MINAS



DYNA
http://dyna.medellin.unal.edu.co/

Entropy and negentropy of private electric vehicles in urban systems: homeostasis of mobility in Mexico

Mario Guadalupe González-Pérez

División de Ingenierías e Innovación Tecnológica, Centro Universitario de Tonalá, Universidad de Guadalajara, México. inge_united@hotmail.com

Received: May 29th, 2018. Received in revised form: July 11th, 2018. Accepted: August 10th, 2018.

Abstract
Since many years ago, private electric vehicles threaten to interact massively and substitute a large proportion of internal combustion vehicles; nevertheless, the homeostasis of the speed and the elapsed time in domestic journeys fluctuate between the phases critical and sub-critical due to the entropy of the production and consumption processes that pressure urban mobility subsystems and vice versa. This work considers from the *Systems Theory* the interaction of the entropic components of Mexican urban mobility through the model entropy-homeostasis-negentropy, which is an adaptation of the model pressure-status-response, issued by the Organization for Economic Cooperation and Development with the intention of showing qualitatively which is the most probable scenario of the private electric vehicle for urban mobility. The results show that a larger number of vehicles produce a higher intra-systemic entropy. Thus, it is essential to implement definitive negentropies to favour electric mobility.

Keywords: entropy; homeostasis; urban mobility; negentropy; private electric vehicles.

Entropía y negentropía del vehículo eléctrico particular en sistemas urbanos: homeostasis de la movilidad en México

Resumen
Hace años que el vehículo eléctrico de uso particular amenaza con interactuar masivamente y sustituir buena parte de la carga vehicular de combustión interna; sin embargo, actualmente la homeostasis de la movilidad urbana relacionada con la velocidad y el tiempo en los trayectos motorizados cotidianos transitan entre las fases sub-crítica y crítica, por la entropía de los procesos de producción y consumo que presionan a este subsistema y viceversa. Este trabajo analiza desde la teoría de los sistemas la participación de los componentes entrópicos de la movilidad urbana en México, a través del modelo entropía-homeostasis-negentropía; una adecuación del modelo presión-estado-respuesta de la Organización para la Cooperación y el Desarrollo Económico, con el objetivo de mostrar cualitativamente el escenario más probable en la interacción vehículo eléctrico particular-movilidad urbana. Los resultados indican que un mayor número de unidades vehiculares generan mayor entropía intra-sistémica. En este sentido, es indispensable implementar negentropías definitivas para la automovilidad eléctrica.

Palabras clave: entropía; homeostasis; movilidad urbana; negentropía; vehículo eléctrico particular.

1. Introduction

The work done by Sadi Carnot and Rudolf Clausius enable the formulation of the second principle of thermodynamics: "*in a closed system, a certain quantity, called entropy, must increase to a maximum, and eventually the process comes to a stop at a state of equilibrium"* [1]. At first, entropy was defined in terms of thermodynamics; however, after the arrival of mechanical statistics this concept has been defined from the notions of probability proposed by Ludwig Boltzmann [2]. Latter, "*in 1948, by analogy with the Boltzmann probability expression of the classical concept of entropy, Shannon introduced the abstract entropy as a way to measure information or uncertainties from arbitrary probable experiments*" [3].

As time goes by, in isolated systems entropy tends to increase, which is a natural and irreversible feature of the

How to cite: González-Pérez, M.G., Entropy and negentropy of private electric vehicles in urban systems: homeostasis of mobility in Mexico. DYNA, 85(206), pp. 171-177, September, 2018.

© The author; licensee Universidad Nacional de Colombia.

physical universe both for living and inanimate things. However, it has been explained that technology may decrease, at least to a certain degree, the natural growing of entropy in open systems, and that might happen through restrictions applied in the environment [4,5]. In other words, the developments in this field might contribute to minimize the entropy originated by the anthropic performance, through contrary entropic actions; which are also defined as negative entropies, negentropies, and sintropies.

According to Shannon in the context of *Information Theory*, the aforementioned entropy can be used to reduce the entropy of the system [6], or as stated by Wiener [7, 8] the information would become a measure of order, especially in living beings; therefore, "*entropy is ameasure of the lack of detailed information about a physical system. The greater is the information, the smaller will be the entropy"* [9]. In this way, what Shannon understands as entropy, other authors define it as negentropy [7-10]; in summary, Shannon and Weaver define information as *"(…) an expression isomorphic to negative entropy of thermodynamics"* [1].

At present, it is possible to find the expression entropy linked to a number of concepts and categories of concepts associated with energy availability but not used in connection with labour production, disorder, instability, intra systemic disorder, heat, irreversibility, wear, deterioration, chaos, uncertainty, lack of information, ignorance, among other expressions [2,3,9-18]. Nonetheless, in the urban context it has become highly complex to associate the concept due to the degree of abstraction and the difficulty to determine isomorphisms in the structure of the boundary and the behaviour of the elements of the urban system.

On one hand, it is presumed the existence of an internal systemic concatenation configuring urban morphology through positive and negative interactions, and on the other hand, there may be functional problems occurring in one of the system´s elements and that might alter homeostasis in one or more of its different phases; however, there is consensus respecting the following conclusión *"the city is a system that causes deterioration, and in some way order depends on such deterioration, which it is the basis for its structure and functioning"* [16].

Urban systems depending on auto-mobility experience some functional problems related to:

a) *financial cost*, due to the continual investment on paved surfaces, huge investments in concrete constructions, investment and maintenance in signalling and traffic lights, financial availability to deal with sanctioning issues due to high speed and other related matters, measuring alcohol level systems, preventive or corrective maintenance liabilities, fuel expenses, vehicle taxes, registration certificates, emissions certificates, car insurance for own and third parties damage protection.
b) *Social expenses* due to imbalance in the formula vehicle-user-road, increase in the likelihood of accidents with physical and emotional temporary or permanent implications, down time due to traffic congestion, physical or mental damages caused by gas emissions, noise, stress.
c) environmental impact due to alterations in land topography, induced vibrations, changes in vegetal cover, pollution emissions, infiltration of oils to drainage systems, pollution of superficial and groundwater systems, among other negative conditions.

In contrast with the aforementioned expenses, there are some benefits associated with the quality of the journey (comfort) as follows: availability, flexibility, freedom and the minimization of the time factor in the periurban journeys, as time has become a very limited resource for people. In this way, intervention in the motorway physical urban area intends to take the maximum advantage of time at commuting that is to say *"spending less time in mobility affairs, because the most quantity of time invested in mobility implies greater economic or social cost"* [10].

Indeed, vehicles have become a type of catalyser to access different locations in the city and outside, and their ample availability has produced an increase in entropy *"(…) pushing the global order of the urban system forward and nobody knows how or when it will end"* [16]. In summary, auto-mobility is a trend that unsettles the system and its subsystems mainly due to the pressure from extra systemic components (matter and energy) and due to the limitations and the dimensions of the roadways infrastructure able to contain a maximum load of intra systemic vehicle circulation; then it is not completely accurate to suppose as constant the inter nodal geometric distance (*d*) and the restrictions in the maximum speed limit settled by intra urban law (*v*), therefore, indiscriminate introduction of new vehicles into the roads system, implies the generation of entropies linked with time increase (*t*) according the following equation:

$$t = \frac{\mathrm{d}}{\mathrm{v}} \tag{1}$$

On this basis, the quantity and the capacity of the roadways infrastructure becomes unable to keep up with a limitless increase of vehicle usage. Overcrowding at certain times decreases speed and therefore travelling time increases. *"The geographic distance or Euclidean distance does not change at all. Notwithstanding, time, may vary in terms of speed and position respectively"* [10]. Therefore, with the aim of showing the most probable scenario of interaction of electric vehicles particularly in urban mobility, the research poses the following questions: What are the possible scenarios in connection with speed and time in Mexico City?, and Is there any contribution from private electric vehicles to the issue of speed and time?

2. The city in the prospection of the *systems theory*

This theory was introduced no longer than a century ago, however, its principles have permeated different fields of scientific research. At the same time, there have been a number of methodologies and models based in the considerations of Bertalanfffy´s theory. Respecting the planning and behaviour of the city the systemic approach has been pretending to be incorporated since many years ago [19-27]. Therefore, this works assumes that the city represents to the pressured and pressing system, in other words, the city, hereinafter *the urban* is identified as the open urban system

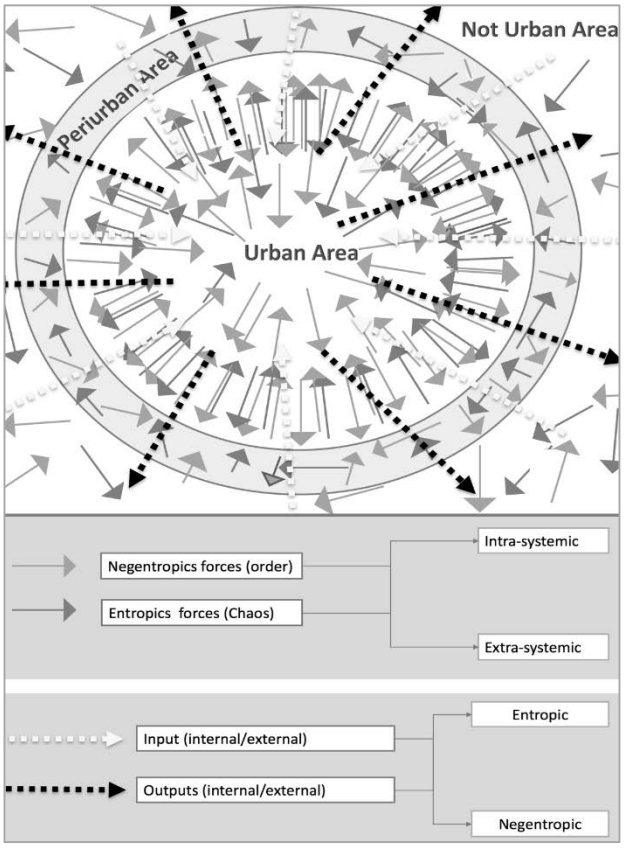


Figure 1. Entropic and negentropic forces in the *urban system* and supporting systems (not urban area).
Source: The author.

and what it occurs there does not belong to the urban system which is identified as no urban, or the environment that does not contribute to the urban pressure system. At the same time, in the boundary between the *urban* and *not urban* it will be found what is known by many as *periurban*.

Consequently, the triad *system-boundary-environment*, or *urban-periurban-not urban* entails intentional and unintentional forces affecting the morphology of the system and its subsystems. That morphology of the system becomes an hybrid, which is a complex combination depending of the *in situ* performance of the entropy and negentropy struggle (Fig. 1).

Periurban areas never have a static position, their location is not permanent, they are continually subject to movements to the no urban areas and not on the contrary. The *urban system* and its components *"press the supporting systems by the extraction of raw materials with the intention of increasing organization or complexity"* [28].

In mobility affairs and in certain circumstances private vehicles solve some problems associated with time when commuting from peri-urban to urban areas or vice-versa. Under these conditions the force temporarily counteracts the entropy caused by the geometric prolongation of the disperse housing model. Nevertheless, if private vehicles reduce entropy in the urban-not urban interphase, some conditions such as: a) absence or inefficacy of alternative options to private vehicles, b) poor physical infrastructure, and c) insecurity that threatens physical integrity from t_0 to t_1, from t_1 to t_2 and from t_2 to t_3, where:

t_0 = represents the place of origin of each user.
t_1 = represents the time where the user enters to an alternative means of transport.
(t_1, t_2) = represents the elapsed time in transport.
t_3 = represents the place of interest where the user must go; it also represents the place where the user left the transport means up to his final destination.

Indeed, it is necessary to consider the travel time from t_0 up to t_1, and the waiting time in t_1. In this way a private vehicle becomes a limited negentropy with positive temporary effects, which is conditioned by the relationship cost-benefit where not using a private vehicle results in larger financial and social costs in contrast with not using it; however, at getting near to *the urban*, the private vehicle does not solve the time concern, but it becomes an environmental entropic component, as well as a financial and social problem.

3. Materials and methods: from the Pressure-State-Response (PSR) model to the Entropy-Homeostasis-Negentropy (EHN) model

The model PSR *"(…) allows the establishment and redirection of public policies and the criteria required for decision making in main State sectors (...)*" [29]; that occurs by the provision of a conceptual-theoretical framework working through environmental indicators which measure and report the state of the environment [30].

On the other hand, the model EHN classifies qualitatively each phase of the exerted pressure, the existing conditions of the open system and the undertaken responses to reduce entropy caused by pressure forces. In this way, vehicles are understood as a casual force of entropy in the urban system, and it they become an intra systemic component that make pressure upon the other elements in urban and not urban systems; and a pressure for itself as a subsystem. Therefore, entropy can be identified in three phases: subcritical, critical and hypercritical. Homeostasis of the process of urban mobility as an intra systemic and inter systemic product can be: reversible, quasi reversible or irreversible, and the implemented negentropy as: non-existing, occasional, or definitive (Fig. 2).

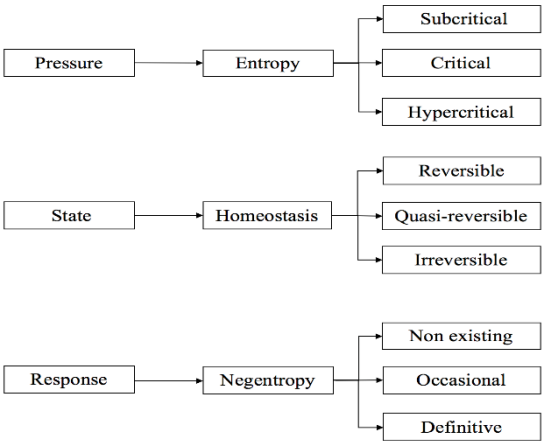


Figure 2. Subclassifications of the EHN Model.
Source: The author.

Entropy in its subcritical phase does not inhibit the functioning of the system; in other words, the system works even when abnormalities occur in internal processes that may affect operability, or due to the interventions of external forces. In such a case, the systems homeostasis is not severely affected, and therefore, it can revert entropies or buffer impacts preventing significant residual damages due to the intrinsic contention of dissipation structures able to regulate processes, or it may produce own or induced negentropies that contribute to the configuration of adaptive states for the development of emerging subsystems. On the other hand, in systems with a critical phase of entropy it is urgent a negentropic intervention; in that case, the system homeostasis has been affected with a resulting malfunctioning of the system. Even more, some elements and processes hardly ever are able to reverse the entropic affectations or reach adaptative states. Then, the prospective scenario is uncertain, because while some components are not able to recover their original shape, others, in contrast may become hybrid and may adapt and work according new conditions. Finally, for systems with an entropy in a hypercritical phase the structure of the system will not be able to recover its previous state, and the outworking in terms of time effectiveness has exceeded both its components and environment severely.

In this context, and according to the EHN Model, it is possible to minimize the different levels of entropy in each of the three phases of system homeostasis up to get even instances of stable conditions. In such a way non existing negentropy does not consider any intervention to reduce the levels of entropy; the system worsens its homeostasis by itself and increases the entropy as time goes by. In this case negative entropy is null. On the other hand, some *in situ* strategies to reduce the levels of entropy derived from abnormalities in one element that does not take into account the relationship system-environment do not solve the problema but prolong the irreversibility of the damage for a certain time. The effects of this negentropy are occasional and are limited in time. Finally, definitive negentropy reduce entropy levels due to the correction of abnormalities intra and inter systemic; this negentropy pretends to reach a steady state, because *"living systems, maintaining themselves in a steady state, can avoid the increase of entropy, and may even develop towards states of increased order and organization"* [1].

4. Results and discussion of urban motoring in Mexico

Since its very beginning, vehicles enabled the inter nodal relocation in a territory. In the United States alone the number of registrations rose from 8 to 23 million between 1920 and 1930. At the same time since the middle of 1940 up to the oil crisis in 1973, the number of vehicles increased from 25 million up to more than 100 million units [31]. This information is an indication of the social and financial impact that private vehicles generated in the XX century; and that occurred because a large number of direct and indirect delivery subunits and businesses began to depend of the utilisation of internal combustion engine vehicles. At the same time other types of businesses began to benefit from it as spare parts manufacturers, accessories providers, fuels,

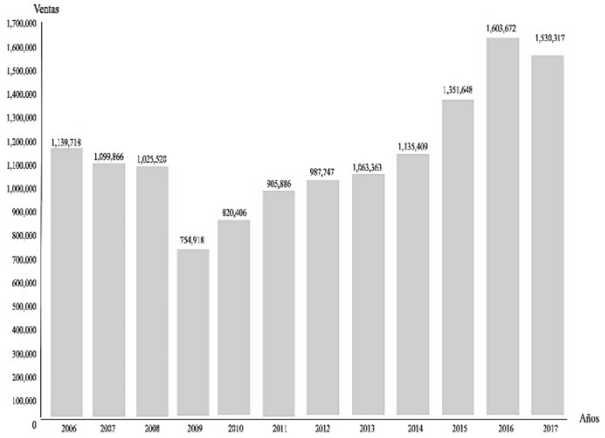


Figura 3. Vehicle yearly sales in Mexico
Fuente: The author. Information reported by [33] was used.

oils and additives distributors; as well as other kind of companies such as credit companies, car dealers, insurance companies, mechanic workshops, electrical and electronic service providers, car-washes, and the like.

In Mexico, nearly two decades after starting the XXI century, internal combustion engine private vehicles continue to be in the social consciousness a symbol of status in connection with their possession. It is believed that it is not the same traveling by private cars in comparison with traveling by bus, or having a new brand car worth USD $7,500 in comparison with a USD $25,000 (or even more expensive) vehicle. In addition, at present private vehicles and related services such as the so called 'shared automobility', or other related activities in the context of 'collaborative economy' are solving occasionaly some abnormalities in the everyday urban mobility but especially in periurban areas.

In 2015, Mexico had around 294 vehicles per 1,000 inhabitants [32] y according to the information provided by the Asociación Mexicana de Distribuidores de Automotores (AMDA), in Mexico the number of light vehicles sold in 2016 was higher compared to what had happened in the previous 10 years; the total number was 1,603,672 units, which included subcompact, compact, luxury, sports, and multiple usage vehicles, as well as light and heavy-duty trucks. Notwithstanding, in 2017 a decreased number of 1,530,317 vehicles were sold, which meant a decrease in 73,355 vehicles, a negative variation of 4.6% in comparison with the previous year (Fig. 3). The forecast for 2018 is near to 1,545,245 units, a 1% increase respecting 2017 [33].

In all Mexican metropolitan cities, the proliferation of private vehicles has exceeded motorways capacity at certain hours of the day, and that occurs due to the disparity between the dimensioning of the physical works and loading excess generated by motorized journeys. However, it is known that widening the dimensions of the motor roads does not solve traffic issues in the long term. After expansion traffic issues can be resolved in a significant way; nevertheless, that occasional negentropy which initially has positive effects in time starts decreasing in effectiveness in reducing negentropy levels.

Private vehicles require matter and energy in order to exist as mechanical, electrical and electronic systems, and in

some way understood as autonomous. In summary, the system-vehicle requires of a system-user, and a system-roadway in order to operate for motorized mobility. However, vehicles building industry, and the construction and conservation of motor roads infrastructure, as well as the rapid consumption of raw materials (*not urban*), such as oil materials, row materials for the production of concrete, asphalt roads, additives, paintings, plastic elements, glues, rubber, minerals, water resources, among others, is transforming the homeostasis of these supporting systems. At the same time, in connection with this entropic context it is necessary to add the current trend of horizontal property promotion in *periurban* areas, which implies shortages and deficiencies in mobility alternatives that turn vehicles as the only transportation means able to provide swiftness, comfort, and physical safety, which means a negentropy in the short term [34]. If the above mentioned habitability-mobility trend continues developing in the surroundings of *the urban*, apart from the time factor concern, there would be other serious implications in the structure and infrastructure of the system implying greater risks of accident rates due to the increased and sometimes uncontrolled loads of transit [35,36]. As explained in the attached information about habitability-mobility, habitability sets conditions respecting the most appropriate means to provide mobility in terms of time. Periurban habitability powered by the diffused city model favours the use of vehicles, and that is given due to the lack of infrastructure and alternate transport subsystems. Urban habitability, on the other hand, favours the use of alternative transport means.

4.1. Private vehicles: production and sales forecast

The use of electric vehicles dates back to the middle of the XIX century. These vehicles were produced experimentally before the use of private internal combustion vehicles. However, "*in the 1930´s with the introduction of the internal combustion vehicle, electric vehicles almost disappeared"* [37]. Given the fact that use of electricity was poorly promoted, as well as the introduction of gasoline, added to the fast improvement of internal combustion engines, and weight reduction, electrical vehicles were not produced any more [38]. Sure enough, it has been said that the use of electric vehicles is far superior. Electric vehicles do not depend on the usage of fossil fuels, their efficiency in engines performance is well known, and they produce lesser impact and affectations on the environment [37]. Notwithstanding, *"(…) consumers perceive them to be more expensive due to their higher capital cost"* [39].

In 2011, the International Energy Agency (IEA) estimated there were around 45,000 electrical vehicles in use. In 2012 the figure reached nearly 180,000 units [40]. For 2015, the threshold of 1 million vehicles was surpassed; and in 2016, the number of electric vehicles around the world was above 2 million units. Moreover, the same organization forecasts that the number of electric vehicles will be between 9 and 20 million for 2020, and for 2025 between 40 and 70 million units [41]. In the particular case of Mexico in 2017 a number of 257 private electric vehicles were sold, which is

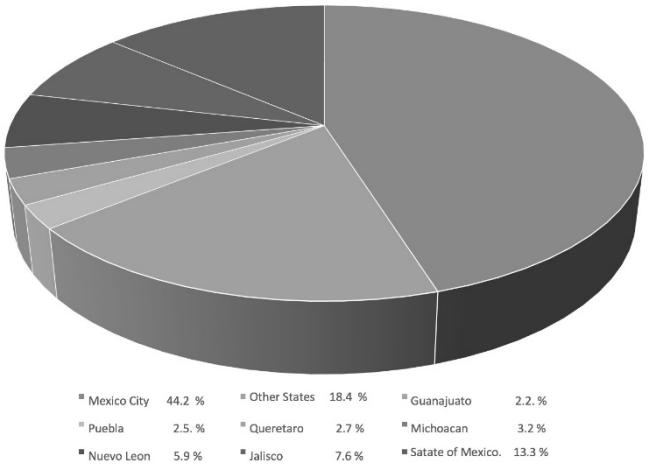


Figure 4. Sales of electric and hybrid vehicles in 2017 in Mexico. Source: The author. Information reported by [42] was used.

14 private electric vehicles less than in 2016, with a number of 271 units. Notwithstanding, for hybrid vehicles the figure increased from 7,989 vehicles in 2016 to 10,255 in 2017 (Fig. 6) [42].

At considering Figs. 4, 5 and 6, electric vehicles usage trend for the coming decades is growing globaly. However, current vehicle load has become a critical issue in urban mobility of Mexico. Nevertheless, this prospection of vehicle usage it is subject to a number of conditions that would not solve the problem of speed, and commuting time.

4.2. Some urban mobility possible scenarios for private electric vehicles of Mexico

In connection with the variables of speed and time, and urban mobility, two possible scenarios have been identified for private electric vehicles. The first scenario is optimistic and implies an entropy in the subcritical phase. But nevertheless, it is less likely to occur because at present speed

Table 1.
Speed and commuting times for private electric vehicles in Mexico

Variable	Current Scenario	Less likely to occur scenario	Most probable scenario
Speed consumed	Optimistic with sub critic entropy at hours without traffic, and critical entropy at peak hours, or subcritical entropy in both cases	Optimistic with subcritic entropy at hours without traffic and critical at peak hours, or subcritical entropy in both cases	Pesimistc with entropies surpasing the critical phase
Time consumed	Subcritical entropy at hours without traffic and critical entropy at peak hours	Optimistic with sub critical entropies at hours without traffic and critical at peak hours, or sub critical entropy in both cases	Pesimistc with entropies surpasing the critical phase

Source: The autor.

of urban mobility shows significant reductions, and important increases at rush hours. Therefore, it can be said that the current situation of homeostasis varies between subcritical and critical phases; and expecting a scenario where entropy may be constant or reduced in connection with time it is less likely to occur keeping into account the second principle of thermodynamics, and that corresponds to higher estimates in vehicle sales and the consequent vehicles load. The second scenario is pessimistic; with a growing entropy surpassing the critical phase due to the lack of definite negentropies aimed to reduced intra systemic entropy levels (Table 1).

According to the characteristics that identify homeostasis which at present are quasi irreversible, the most likely scenario to occur is pessimistic. There are deficiencies of integrated plans to encourage the use of private non-motorized vehicles to improve urban mobility.

At the same time, there is also a huge lack of balance in habitability-mobility; as well as lack of or absence of infrastructure of sustainable urban mobility systems, and lastly, recurring investments in works to favour the use of vehicles, all of this despite the fact electric vehicles benefit environment in terms of pollutants reduction and noise among others. Nonetheless, due to the excessive use of traditional private vehicles, the processes of substitution of these traditional vehicles in exchange of private electric vehicles, and the consolidation of this means of transport entail entropic forces in the urban system, or negentropic forces with occasional impacts.

The substitution of these private mobility subsystems (internal combustion, hybrid, or electric vehicles), for massive mobility systems such as long articulated busses, electric urban trains, trams, and the like; and the use of mechanical means of mobility (bicycles), pedestrian prioritization; and the systemic interconnection of habilitability-mobility lead to a definitive negentropy, which is required to reduce the current levels of high intra systemic entropy.

5. Conclussions

The conception of *the urban* from the perspective of the systemic analysis implies both the conjunction and the struggle of social, financial, and environmental elements that work as subsystems in the configuration of its structure. The system is transformed by its anthropogenic activity, in other words, embodies a shape, which sometimes faces troubles, worsens and self regulates due to, entrance, process or emission of matter and energy coming from the not urban systems, where the shape of the system allows to monitor and measure qualitatively its homeostasis.

Based on the implementation of the EHN Model it is possible to identify the critical phase in which intra-systemic time and speed is found, even though when some entropic actions might be omitted in order to revert the current system homeostasis; that is possible due to the quasi-reversible phase in which is found. For that reason, these actions necessarily require definite negentropies aimed to discourage the use of private vehicles regardless its power source. Likewise, *"(...) the interests of groups that have temporary social representation are greater than the carrying capacity of the system and, therefore, exceed the set of forces that tends to generate negentropy (...)"* [43].

In light of this, the possible scenarios of the time of connection of the speed of private vehicles in Mexico seem to be pessimistic, because at present the daily flow of these vehicles is in the subcritical phase that tends to escalate to the critical phase. For that reason, the introduction of particular electric vehicles does not solve the main problem or solve other secondary problems. In other words, the most important problem is related to the preservation of the current paradigm: automobility is not resolved; and, in addition, secondary problems such as road congestion, the accident rate, pollution and the like, in relation to the speed of the journey in different metropolitan urban systems is neither improved.

Referencias

[1] Bertalanfy, Von L. General system theory. Foundations, development, applications. New York: George Braziller, 1968.

[2] Marin, C., Entropía: un cadaver exquisito, AusArt Journal for Research in Art [En línea]. 2(1), 2014. [consulta, 8 de enero de 2018]. Disponible en: http://www.ehu.eus/ojs/index.php/ausart/ article/view/ 11953/1171 4

[3] Pardo, L., Teoría de la información estadística, Estadística Española [En línea]. 35(133), 1993. [consulta, 20 de enero de 2018]. Disponible en: http://www.ine.es/ss/Satellite?blobcol=urldata&blobh eader=application%2Fpdf&blobheadername1=ContentDisposition&blobh eadervalue1=attachment%3B+filename%3D583%2F542%2F133_1.pdf& blobkey=urldata&blobtable=MungoBlobs&blobwhere=583%2F542%2F1 33_1.pdf&ssbinary=true

[4] Cressie, N., Statistícs for spatial data. New York: Wiley, 1991.

[5] Pardo-Llorente, L., Teoría de la información estadística, Estadística Española [En línea]. 35(133), pp. 195-268, 1993. [consulta, 20 de enero de 2018]. Disponible en: http://www.ine.es/ss/ Satellite?blobcol=urldata&blobheader=application%2Fpdf&blobheaderna me1=ContentDisposition&blobheadervalue1=attachment%3B+filename% 3D583%2F542%2F133_1.pdf&blobkey=urldata&blobtable=MungoBlobs &blobwhere=583%2F542%2F133_1.pdf&ssbinary=true

[6] Marcos, A., Información y entropía, Arbor: Ciencia, pensamiento y cultura, 1(549), 1991, pp. 111-138

[7] Wiener, N., Cybernetics: or control and communication in the animal and machine. Cambridge, Massachusetts: MIT. Press, 1948.

[8] Wiener, N., The human use of human beings. Boston: Houghton Mifflin Company, 1950.

[9] Brillouin, L., Science and information theory. London: Academic Press, 1962.

[10] González, M., Movilidad motorizada e infraestructuras de transporte en Culiacán: una situación entrópica, cap 1. Poder, Cultura y Desarrollo. [en línea]. México, Universidad de Guanajuato, 2007. [consulta, 12 de enero de 2018], Disponible en: http://www.investigacion. colpospuebla.mx /pdf/2018/capitulos%20de%20libros/prespectivas%20migratorias%20inter nacinales%20de%20estudiantes%20de%20bachillerato%20de%20san%20 francisco%20tetlanochcan,%20tlaxcala.pdf

[11] Shannon, C. y Weaver, W., Teoría matemática de la comunicación. Madrid: Forja, 1981.

[12] Margalef, R., Ecología. Barcelona: Omega, 1982.

[13] Wiener, N., Cibernética y sociedad. México: Consejo Nacional de Ciencia y Tecnologia, 1981.

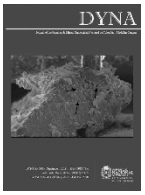
[14] Brooks, D., Collier, J., Maurer, B.A., Smith, J.B.H. and Wiley, E.O., Entropy and information in evolving biological systems, Biology and Philosophy [online]. 4(4), 1989 [consulted, January 9th of 2018]. Available at: https://link.springer.com/article/10.1007/BF00162588

[15] Georgescu, N., The entropy law and the economic process, Cambridge, Massachusetts: Harvard University Press, 1971. DOI: 10.4159/harvard.9780674281653

[16] Fariña, J. y Ruiz, J., Orden, desorden y entropía en la construcción de la ciudad, Urban. [En línea]. 1(7), 2002. [consulta, 10 de enero de 2018]. Disponible en: http://polired.upm.es/index.php/ urban/article/ view/339/339
[17] Prigogine, 1997. El fin de las certidumbres. Santiago de Chile: Andrés Bello, 1997.
[18] Herrmann, F., Comencemos con la entropía, Revista Cubana de Física. [En línea]. 27(2), 2018. [consulta, 4 de enero de 2018]. Disponible en: http://www.physikdidaktik.unikarlsruhe.de/publication/Entropia _RCF .pdf
[19] Guillén, D., Hacia una planificación urbana sistémica. Una experiencia universitaria de aprendizaje y aplicación de nuevos instrumentos técnicos en la planificación urbana tradicional, Espacio y desarrollo. [En línea]. 1(20), 2008. [consulta, 10 de marzo de 2018]. Disponible en: http://revistas.pucp.edu.pe/index.php/espacioydesar rollo/article/view5452/5449
[20] Alfonso, W.H. y Galindo, L.M., Evolución de la visión sistémica en el pensamiento urbano del siglo XX. La integración de las disciplinas hacia la ciudad sustentable. [En línea]. Facultad de Ciencia Política y Gobierno, Universidad del Rosario, Bogotá, 2011. [consulta, 12 de enero de 2018]. Disponible en: http://repository.urosario.edu.co/ bitstream/handle/10336/11719/Biekistica02web2.pdf?sequence=7
[21] Brocolini, S.M., El evento urbano. La ciudad como un sistema complejo lejos del equilibrio, Quid 16, [En línea]. 1(6), 2016. [consulta, 8 de marzo de 2018]. Disponible en: http://publicaciones.s ociales.uba.ar/index.php/quid16/article/view/2073/1765
[22] Sepulveda, R., De la Puente, P., Torres, M., Arditi, C. y Muñoz, P., Enfoque sistémico y lugar. Una perspectiva para el studio de habitat residenciales urbanos, Documento de trabajo FONDECYT 1114-92, Instituto de la Vivienda, Facultad de Arquitectura y Urbanismo, Universidad de Chile, Santiago de Chile, 1992, 44 P.
[23] Leleur, S., Systemic planning. Principles and methology for planning in a complex world. Denmark: Schultz Grafisk, 2008.
[24] Posada, A., Paredes, A.D. y Ortiz, G.E., Enfoque sistémico aplicado al manejo de parques metropolitanos, una posición desde Bogotá D.C. 2016, Colombia, Actualidad & Divulgación Científica [En línea]. 19(1) [consulta, 21 de enero de 2018]. Disponible en: http://www.scielo.org. co/pdf/rudca/v19n1/v19n1a24.pdf
[25] Solano, E.E., Crítica sistémica. Un enfoque hermenéutico del fenómeno arquitectónico. Revista de Arquitectura [En línea]. 16(1), pp. 68-76, 2014. DOI: 10.14718/RevArq.2014.16.8
[26] Boisier, S., ¿Y si el desarrollo fuese una emergencia sistémica? Documento de trabajo Nº 6, Instituto de Desarrollo Regional, Fundación Universitaria, [En línea]. 2002. [consulta, 17 de enero de 2018]. Disponible en: http://www.upo.es/ghf/giest/ODTA/documentos/Mar coTeorico/ILPES/boisier_desemesis.pdf
[27] Ruíz, L., Sistemas urbanos complejos acción y comunicación, Cuadernos de Investigación Urbanística. [En línea]. 1(32), 2001 [consulta, 22 de febrero de 2018]. Disponible en: http://polired.upm. es/index.php/ciur/article/view/246/ 242
[28] Rueda, S., Modelos e indicadores para ciudades más sostenibles, Fundació Fòrum Ambiental, Cataluña, [En línea]. 1999. [consulta, 10 de diciembre de 2017]. Disponible en: https://www.researchgate.net/ publication/41393067_Analisis_territorial_de_las_condiciones_de_habitabilidad_en_el_periurbano_de_la_ciudad_de_Mar_del_Plata_Argentina_a_partir_de_la_construccion_de_un_indice_y_de_la_aplicacion_de_metodos_de_asociacion_e/fulltext/57e4fbc708ae9e8425a4e533/41393067_Analisis_territorial_de_las_condiciones_de_habitabilidad_en_el_periurbano_de_la_ciudad_de_Mar_del_Plata_Argentina_a_partir_de_la_construccion_de_un_indice_y_de_la_aplicacion_de_metodos_de_asociacion_e.pdf?origin=publication_detail
[29] González, M. y López, L., Entropía del crecimiento habitacional en el río Blanco de la metrópoli de Guadalajara, México, RIHA [En línea]. 39(2), 2018. [consulta, 15 de mayo de 2018]. Disponible en: http://scielo.sld.cu/scielo.php?script=sci_arttext&pid=S1680-03382018000200008
[30] OECD. Rumo a um desenvolvimento sustentável indicadores ambientais: indicadores ambientais, Série Cadernos de Referência Ambiental, Centro de Recursos Ambientais, Salvador, Brasil, 2002, 244 P.
[31] Clapson, M., Suburban century, social change and urban growth in England and the United State. New York: Oxford Bearg, 2003.
[32] OICA. World vehicles in use- all vehicles. Organización Internacional de Constructores de Automóviles, Francia, [En línea]. 2015. [consulta, 11 de marzo de 2018]. Disponible en: http://www.oica.net/ wp-content/uploads//Total_in-use-AllVehicles.pdf
[33] AMDA. Reporte de mercado interno automotor. Asociación Mexicana de Distribuidores de Automotores, México, [En línea]. 2017. [consulta, 11 de marzo de 2018]. Disponible en: https://www.amda.mx/wpcontent/uploads/2018/02/1712_Reporte_Mercado_Automotor.pdf
[34] González, M., Uberficación y movilidad urbana en el Área Metropolitana de Guadalajara: entropía en las nuevas configuraciones de acceso al transporte motorizado, Ciencia Ergo-sum [En línea]. 25(2), 2018. [consulta, 30 de abril de 2018]. Disponible en: http://cienciaergosum.uaemex.mx/article/view/9500
[35] Marchesini, P. and Weijermars, W., The relationship between road safety and congestion on motorways, Institute for Road Safety Research. [online]. 25(2), 2010. [consulted, April 20th of 2018]. Available at: https://www.swov.nl/sites/default/files/publicaties/rapport/r-2010-12.pdf
[36] Johnston, I., Beyond best practice road safety thinking and systems management, Safety Science [En línea]. 9(48), pp. 1175-1181, 2010. DOI: 10.1016/j.ssci.2009.12.003
[37] Sanz, I., Análisis de la evolución y el impacto de los vehículos eléctricos en la economía europea. Facultad de Ciencias Económicas y Empresariales, Universidad Pontificia Comillas ICAI-ICADE, España, [En línea]. 2015. [consulta, 30 de enero de 2018]. Disponible en: https://repositorio.comillas.edu/xmlui/bitstream/handle/11531/3803/TFG001112.pdf
[38] De la Herrán, J., El auto eléctrico: una solución apremiante. Universidad Nacional Autónoma de México, México, [En línea]. 2014. [consulta, 12 de enero de 2018]. Disponible en: http://www.dgdc.unam.mx/ assets/cienciaboleto/cb_auto_electrico.pdf
[39] Wu, G., Inderbitzin A. and Bening, C., Total cost of ownership of electric vehicles compared to conventional vehicles: a probabilistic analysis and projection across market segments, Energy Policy, 80(1), pp. 196-214, 2015. DOI: 10.1016/j.enpol.2015.02.004
[40] IEA. Understanding the electric vehicle landscape to 2020. Global EV Outlook, International Energy Agency, Francia, [online]. 2013 [consulted, January 7th of 2018]. Available at: https://www.iea.org/ publications/freepublications/publication/GlobalEVOutlook_2013.pd
[41] IEA. Two million and counting. Global EV Outlook, International Energy Agency, Francia, [online]. 2017 [consulted, January 7th of 2018]. Available at: https://www.iea.org/publications/freepublications/publication/GlobalEVOutlook2017.pdf
[42] AMIA. Boletín híbridos y eléctricos. Asociación Mexicana de la Industria Automotriz, México, [En línea]. 2017 [consulta, 17 de enero de 2018]. Disponible en: http://www.amia.com.mx/bhye/
[43] García-de Quevedo-Najar, F., González-Pérez, M.G. y Asprilla-Lara, Y., Determinación de los componentes entrópicos de la accidentalidad: el trinomio vehículo/usuario/camino en la metrópoli de Guadalajara, México. Revista Tecnura, [En línea]. 22(55), pp. 51-65, 2018. Disponible en: http://revistas.udistrital.edu.co/ojs/index.php/Tecnura/article/view/13245/14071. DOI: 10.14483/22487638.13245

M.G. González-Pérez, graduated the BSc. in in Civil Engineering from the Faculty of Culiacan Engineering of the UAS in 2004, from the MSc. Degree in Civil Engineering with a specialization in Construction Administration from the Faculty of Engineering of the UNAM, Mexico in 2006 and the Dr. in City, Territory and Sustainability by the University Center of Art, Architecture and Design of the UdeG, Mexico, in 2013. He has worked as a consultant, builder and teacher in various universities of the private sector and since the year 2014 he joined to the University Center of Tonalá of the University of Guadalajara, Mexico as a research professor in the Division of Engineering and Technological Innovation. His research interests include: entropic systems in the urban system associated with urban mobility, transportation systems, natural resource management, housing construction and systems dynamics. He is currently a distinguished member of the National System of Researchers.
ORCID: 0000-0002-5457-5948

UNIVERSIDAD NACIONAL DE COLOMBIA
SEDE MEDELLÍN
FACULTAD DE MINAS



DYNA
http://dyna.medellin.unal.edu.co/

Structural, thermal, rheological, morphological and mechanical properties of thermoplastic starch obtained by using hyperbranched polyester polyol as plasticizing agent

Manuel Guzmán [a] & Edwin A. Murillo [b]

[a] *Departamento de Ingeniería de Materiales, Universidad de Antioquia, Medellín, Colombia. polimetal9@hotmail.com*
[b] *Departamento de Química, Universidad Francisco de Paula Santander, Cúcuta, Colombia. edwinalbertomr@ufps.edu.co*

Received: April 23th, 2018. Received in revised form: June 6th, 2018. Accepted: June 12th, 2018.

Abstract
In this work, the effect of the proportion of a hyperbranched polyester polyol (HBP) of fourth generation on the structural, thermal, rheological, morphological and mechanical properties of tapioca starch/HBP blends (TPS) was evaluated. For this purpose, the ratios of starch:HBP employed to prepare the TPS were: 30:70 (TPS30), 40:60 (TPS40) and 50:50 (TPS50). Using infrared (IR) analysis, it was observed that the presence of HBP produced a displacement at the absorptions of the C-OH, C-O and C-O-C bonds of the TPS. The X-ray diffraction (DRX) analysis showed that the starch crystallinity is A and B type, which increased with the HBP amount. The glass transition temperature (T_g) of the TPS, increased with the HBP content, but the thermal stability and viscosity (at an angular frequency of 1 Hz) presented an opposite behavior. The scanning electronic microscopy analysis (SEM) revealed that the granular structure of the starch was not completely destructured.

Keywords: starch; hyperbranched polyester polyol; TPS; plasticization; properties.

Propiedades térmicas, reológicas, morfológicas y mecánicas de almidón termoplástico obtenido usando un poliéster poliol altamente ramificado como agente plastificante

Resumen
En este trabajo, se evaluó el efecto de la proporción de un poliéster poliol altamente ramificado (HBP) de cuarta generación en las propiedades estructurales, térmicas, reológicas, morfológicas y mecánicas de mezclas de almidón de yuca/HBP (TPS). Para este propósito las relaciones de almidón:HBP empleadas para preparar los TPS fueron: 30:70 (TPS30), 40:60 (TPS40) and 50:50 (TPS50). Por análisis infrarrojo (IR) se observó que la presencia de HBP produjo un desplazamiento en las absorciones de los enlaces C-OH, C-O and C-O-C del TPS. El análisis de difracción de rayos X mostró que la cristalinidad del almidón es tipo A y B, las cuales incrementaron con la cantidad de HBP. La temperatura de transición vítrea (T_g) de los TPS, incrementó con el contenido de HBP, pero la estabilidad térmica y la viscosidad (a una frecuencia angular de 1 Hz) presentaron un comportamiento opuesto. El análisis de microscopia de barrido electrónica (SEM), reveló que la estructura granular del almidón no fue completamente desestructurada.

Palabras clave: almidón; poliéster poliol altamente ramificado; TPS; plastificación; propiedades.

1. Introduction

The last years, the investigations have been focused mainly toward the replace of materials derived from petrochemical resources for biodegradable materials with mechanical properties comparable to those of the no-biodegradable materials [1]. The biodegradable plastic materials offer a solution to the accumulation of synthetic

How to cite: Guzmán, M. and Murillo, E.A., Structural, thermal, rheological, morphological and mechanical properties of thermoplastic starch obtained by using hyperbranched polyester polyol as plasticizing agent. DYNA, 85(206), pp. 178-186, September, 2018.

© The author; licensee Universidad Nacional de Colombia.

plastic materials [2]. Starch is probably a more promissory material for the production of environmental friendly plastics among biodegradable polymers. This is due to its great abundance, low cost and easy of degradation [3]. Starch is a polysaccharide. Depending on the extraction sources, starch may have varying proportion of amylose and amylopectin, which confers to it several properties [3]. Furthermore, starch has a granular structure whereas thermoplastic polymer does not. Therefore, to obtain a thermoplastic starch (TPS), starch has to be plasticized [3]. The plasticizing agents are generally hydrophilic compounds, such as, urea [1], ethanolamine [4], glycerol [5], xylitol, sorbitol [6] and water [7].

During the plasticization process of the starch, the plasticizing agents form hydrogen bonds that decrease the interaction between starch macromolecules. Thus, there is a reduction of the granules sizes and increased mobility of the polymeric chains. Consequently, the processability and ductility are improved [7]. The starch proportion and chemical nature, strongly influenced the physical properties in two ways: 1) control the starch destructuration (it increases) and 2) affect the final properties of the materials such as, T_g and Young's modulus [1,7].

A great deal of plasticizing agents has already been widely employed [4-7]. One material that may be employed as plasticizing agent to starch is the HBP of fourth generation. This material has been prepared from pentaeritritol and dimethylol propionic acid by polycondensation reaction by using a combination of the methods in a series of systematic approach [8-10]. This material has small hydrodynamic dimensions (3,28 nm) [8], an average number of terminal units of 9,36 (around 18 OH groups in the periphery) [9], lowest viscosity in molten state (lower than 2×10^1 Pa.s) [10] and its average number molar mass is 5030 g/mol [8].

There is little or no literature on HBP of fourth generation for this application. HBP have high structural packing, great OH groups number in the periphery, low viscosity in solution and molten state, lowest molecular entanglement and good solubility in commons organic solvents [11]. These materials may be a good alternative to the plastization of starch because their high OH groups number, which may interact and form hydrogen bonds with those of the starch. It may possibly reduce the interaction between OH groups of the starch and produce the destructuration of starch granules.

In a previous study, the use of a HBP of fourth generation in plasticizing of starch was reported [12]. The proportion of the HBP of fourth generation was 40 wt% relative to that of the starch (60 wt%). This material was named TPS60 [12]. The HBP was effective in the plastization of starch, since the crystallinity of starch was reduced. Furthermore, the thermal stability of the starch was higher than that of the TPS. In another study, was plasticized maize starch with hyperbranched polyesters, terminated with either hydroxyl (HBPET-H) or carboxyl groups (HBPET-C), these polyesters were prepared from glycerol and citric acid [13]. The plasticizing agents did not change the crystal structures of the starch films, but decreased the crystallinities. Also, both plasticizing agents increased the chain mobility. On the other hand, the HBPET-C was not as good plasticizing agent as HBPET-H. A hyperbranched poly(trimellitic glyceride) (PTG) was used on starch plasticization [14]. The tensile strength decreased with the PTG amount. Moreover, PTG did not change the crystal type of starch film, but reduced the crystallinities.

The effect of the proportion of a HBP of fourth generation on the starch properties has not been studied nor reported (according our literature review). Therefore, in this work, the influence of HBP amount on the structural, thermal, morphological, rheological and mechanical properties of TPS was evaluated. Furthermore, the properties of a TPS60 obtained in a previous study via the same methodology [12], will be compared with those of the materials prepared in the present study.

2. Experimental part

2.1. Materials

Tapioca starch was supplied by the Factory ALICO (Colombia), this material has a 17 wt% of amylose and 83 wt% of amylopectin. This material was previously dried at 50 °C in an oven for 12 h before being used. HBP was prepared by Murillo et al. and their properties have already been previously reported [8-10].

2.2. Preparation of the TPS

In order to prepare the TPS, the respective proportions of starch and HBP were carry out to the torque rheometer Thermo SCIENTIFIC and submitted to mixed process at 150 °C and a rate of 100 rpm during 8 min. The ratio of starch:HBP employed to prepare the TPS were: 30:70 (TPS30), 40:60 (TPS40) and 50:50 (TPS50).

2.3. Characterization of the materials

In order to characterize the materials, the TPS were kept in a desiccator before realization of IR, DRX, differential scanning calorimetry (DSC), thermogravimetric analysis (TGA) and compression analyses. In the case of IR analysis, pills of the samples were prepared with KBr and were analyzed in a Perkin Elmer spectrometer model spectrum one. For every analysis 8 scans were done. In order to make DRX analysis, the samples were analyzed in a PANalytical X'Pert PRO MPD diffractometer by using Cu Kα= 1,54 A, the voltage and current operation were 45 kV y 40 mA respectively. The difractogramas were obtained in the interval of Bragg angle (2θ) of 4 and 70°. DSC analysis was performed in a TA Instruments Q-100 equipment in a temperature range between -80 and 150 °C by using a heating rate of 20 °C/min. TGA analysis was done in a TA instruments Q-500 equipment, the heating rate was 10 °C/ min. The DSC and TGA analyses were done in nitrogen atmosphere. SEM analysis was done to starch granules and cryofractured surfaces of the TPS, for it was

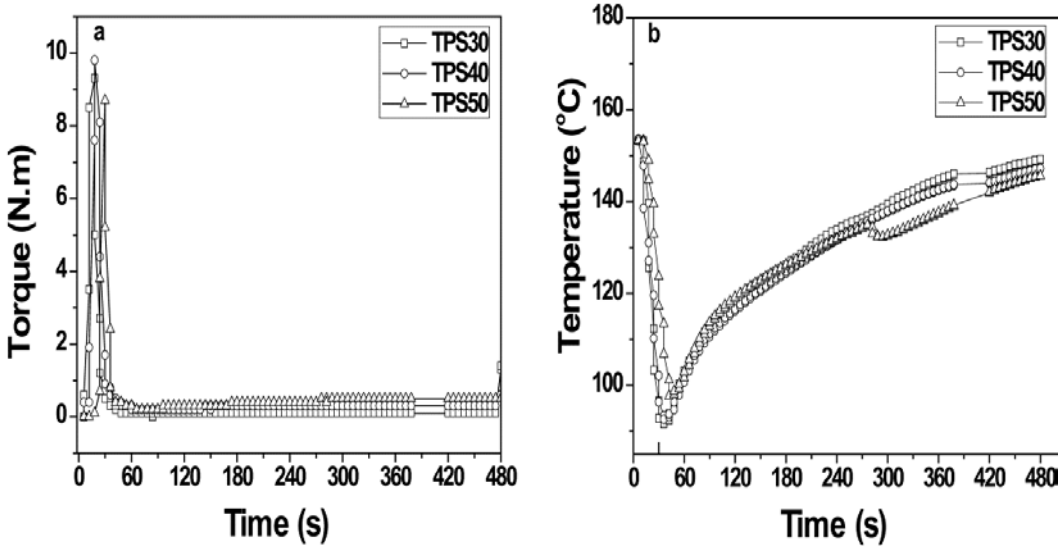


Figure 1. Torque rheometry of the TPS a) Torque vs time and b) Temperature vs time.
Source: Authors

used a JEOL JSM-6490LV microscopy. The samples were submitted in gold bath and the analysis were done using a voltage acceleration of beam 20 kV. Rheological analysis was performed in a Malvern Kinexus rotational rheometer by using plate-plate geometer of 20 mm of diameter at 130 °C under dynamic conditions in the range of angular frequency between 0,10 and 100 Hz and a strain of 0,2 %. Compression test was done only to compare the mechanical properties of the materials. Therefore, for it, were obtained cylindrical specimens of 3 cm of diameter and one cm of thickness. Compression test was performed in quadruplicate.

3. Results and Discussion

3.1. Torque rheometry

Fig. 1 presents the results of torque rheometry of the TPS. Initially, for all the samples, at 30 s of mixed process, the torque increased and then decreased and finally was stabilized (Fig. 1a). The samples exhibit a reduction in temperature (Fig. 1b). This may be because the melting process was endothermic and the increasing of torque (Fig. 1a) was produced for incomplete melting of the HBP. With the increasing of the HBP amount (melting temperature: 108,5 °C) [8], more heat for melting all the materials is required. On the other hand, the torque decreased with the enhancing of temperature, because in the same sense the HBP was melting. Finally, the torque reached a constant value at 280 s, this means that under conditions of mixed, the optimum time for obtaining the TPS (Fig. 1a) was established. The final torque value of the TPS, increased slightly with the proportion of starch employed. It was expected because the starch is not thermoplastic material. Therefore, the shear increased with the starch content. Possibly, the torque also is enhanced with the increasing of the interactions trough OH groups of HBP and starch. Once the torque was stabilized, no order reduction was observed, which indicates that, there was no degradation process during the processing. The same behavior was observed with TPS60 [12].

3.2. IR Analysis

In order to show evidence of interactions between starch and HBP the IR analysis was done. Fig. 2 presents IR spectra of the samples. Fig. 2a shows the IR spectra at high frequencies. The signal at 3399 cm^{-1} in starch is due to stretching of O-H bond of C-OH, which are bonded inter and intramolecular into starch structure. At 2940 cm^{-1} appear a signal corresponding to stretching of C-H bond of $-CH_2-$.

The signal observed in all TPS at 1309 cm^{-1} is assigned to bending of C-O bonds of the ester groups of HBP. This signal is absence in the starch spectrum. In the other hand, the signals at 1159 and 1081 cm^{-1} into IR spectrum of starch are attributed to C-O stretching of C-OH bonds [15]. These signals in the TPS IR spectra were observed to be displaced to lower frequencies (1128 and 1145 cm^{-1} respectively).

At 1015 cm^{-1} a signal which corresponds to stretching of C-O bond of C-O-C groups in the pyranose was observed [5]. This signal appeared into TPS spectra at 1010 cm^{-1} and its intensity was low with respect to that of starch. According to results obtained by IR analysis, it was evidenced that the presence of HBP in the TPS produced a displacement C-OH, C-O y C-O-C signals assigned to starch. This was attributed to the formation of hydrogen bonds between starch and HBP; which reduced the interactions between OH groups of starch. The displacement exhibited by these signals has been employed to show the evidence of the interactions between starch and plasticizing agents [1,4]. Therefore, all the samples exhibited interactions between starch and HBP. A schematic representation of these interactions can be observed in Fig. 3. The same behavior exhibited by the TPS in this study was also observed in TPS60 [12].

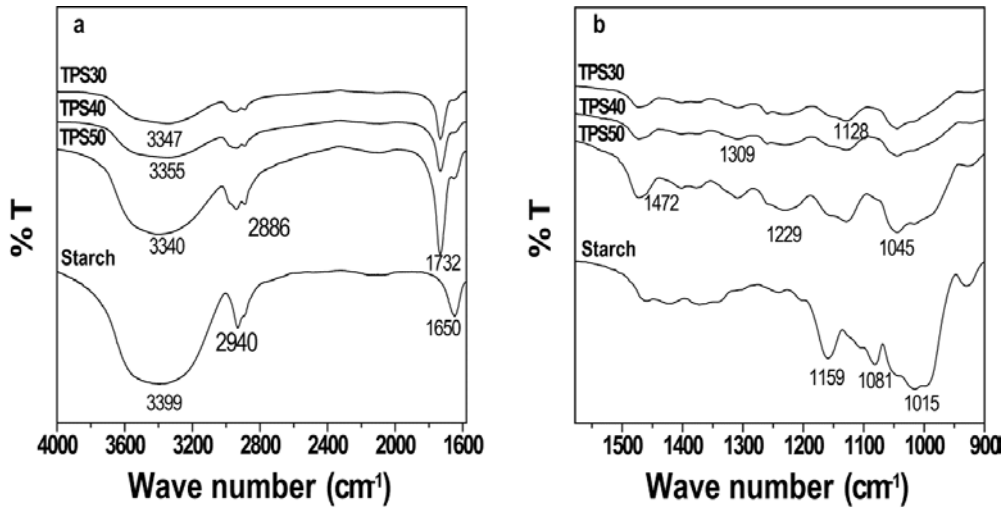


Figure 2. IR spectra of the starch and TPS a) High frequencies and b) Low frequencies.
Source: Authors

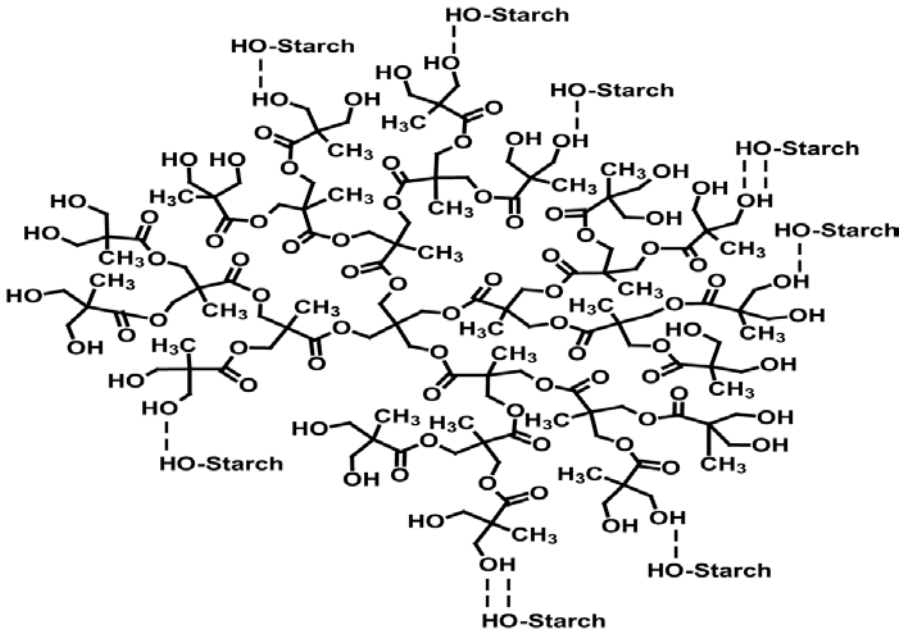


Figure 3. Schematic representation of the interactions between starch and HBP.
Source: Authors.

3.3. DRX analysis

The difractograms of the sample can be seen in Fig. 4. Starch exhibited peaks of low intensity at 2θ=5,6º, 14.9º, 17,0º y 22,9º. Furthermore, three weak peaks at 2θ=9,8º, 11,4º and 26,5º were observed. The presence of peaks at 2θ=14,9º, 17,0º y 22,9º, indicate that the crystalline structure of the starch is mainly A type, but also there is a B type crystalline structure (2θ=5,6°) [16]. On the other hand, the C type crystallinity is considered a mix of crystallinities A and B types, which exhibit the same diffraction patron of an A type crystal with an additional peak around 2θ=5.0º, which is characteristic of B type crystallinity [16].

The TPS difractograms did not exhibit the peaks at 2θ=5,6º, 9,8º and 11,4º and the peaks at 2θ= 14,9° and 22,9°, ostensibly reduced their intensity. The reduction of the intensity of these peaks and the absence of other can be interpreted as a reduction on crystallinity of starch in TPS. Although the peak in the TPS difractograms at 2θ=17° increased slightly its intensity with regards to that of the neat starch.

The peaks at 2θ=14.9° and 22,9° enhanced in intensity with the HBP content, which can be interpreted as an increasing of the A type crystallinity in these samples. This may be attributed to those samples with high proportion of HBP. The shear is low due to the reduction on viscosity and it reduces the destructuration of starch,

thus, it can be corroborate from results obtained by rheometry, since final torque increased with the proportion of starch (Fig. 1). The TPS50 was the sample that showed the lowest reduction on crystallinity.

The TPS60 exhibited the same peaks of the TPS [12], but in the case of the peaks at 2θ=14,9° and 22,9°, their intensities were slightly higher than those of the TPS obtained in this study. This behavior may be attributed to high proportion of starch. Possibly this sample exhibited high resistance to the mixed (was obtained with highest proportion of starch) and different interaction or destructuration degrees.

In this study, there was no evidence of the formation of V type crystallinity, since it was not observed in new peaks, as in the case of the other plasticizing agents such as, glycerol, sorbitol and ethylenglycol [17]. This indicates that HBP is more efficient in restrict the formation of this type of crystallinity. The absence of this type of crystallinity in TPS was probably due to the interaction between OH groups of the amylose and HBP, which possibly produced the stabilization of amylose helix.

According to the results, it can be concluded that the HBP acts as plasticizing agent of the starch, since HBP reduced the crystallinity of starch. The efficiency of HBP possibly was due to this material exhibiting high structural packing, low viscosity in molten state and high OH groups number OH [8-10].

In this study, was not observed the recrystallization (retrogradation) for the TPS, which was due to the interaction between starch and HBP, since it reduced the hydrogen bonds between the starch chains [18].

According to results obtained by DRX, A type crystallinity was eliminated by HBP and the B type crystallinity of starch was reduced. In a study of the starch plastization by using HBPET-H, HBPET-C and PTG, it was observed that these plasticizing agents did not change the crystal type of starch, but they decreased the crystallinities [13,14].

3.4. Thermal analysis

The DSC (Fig. 5a) and TGA (Fig. 5b) thermograms of the samples are displayed in Fig. 5. In DSC thermograms

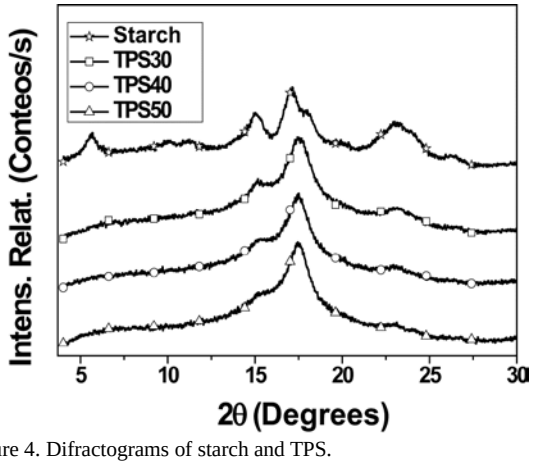


Figure 4. Difractograms of starch and TPS.
Source: Authors.

(Fig. 5a) it can be seen that starch did not exhibit a T_g. All TPS presented only a T_g value and it was higher than that of the HBP (28 °C) [8]. The absence of T_g of HBP in these samples is another indication that there was interaction between starch and HBP. Furthermore, in previous study it was observed that a small endothermic peak to HBP was assigned to the melting of ordered domains of hydrogen bonds due to the interaction of terminal OH groups [8]. This peak was not detected to TPS, which means that the HBP is interacting through OH groups with starch. All T_g values of the TPS are presented in Table 1. The T_g values increased with the HBP amount. The sample TPS50 exhibited the lowest T_g value (40 °C), which means that this sample showed highest destructuration of the starch granules and dissociation of interactions between OH groups of starch. Therefore, the mobility of the starch chains was consequently increased. [19]. The sample TPS60 presented a T_g value of 31 °C [12], which indicate that this sample has a higher interaction between starch and HBP than the TPS obtained in this study. An explanation for the behavior showed by TPS and TPS60 is that when the content of HBP is higher than 50 wt% (TPS30 and TPS40), the starch granules are more disperses into the HBP and as consequence of the shear, these were separated, but their interaction with the HBP was lowest, which probably was due to low viscosity. Therefore, the interactions between HBP and starch are lowest for these samples, because probably there is great piece of HBP without interact with starch. In another account, plasticized corn starch with glycerol (15 wt%) and urea (15 wt%), el T_g value was 37 °C [1], this value is comparable with the TPS50 and TPS60. Kaur et al. [20] obtained a T_g value of 63 °C for plasticized potato starch with glycerol monoestearate and water (1:10).

In the TGA thermograms of the samples (Fig. 5b). The starch and HBP exhibited only one peak, the thermal stability of the starch is higher than that of the HBP. The TPS presented two peaks, the first peak (T_{onset1}) increased your intensity and your thermal stability (TPS30→TPS50) with the enhancing of the starch amount, but its thermal stability was lower than that of the starch. These results indicate that this peak is related to starch. Furthermore, the increase in thermal stability of this peak may be associated with enhancing of the interactions between starch and HBP. On the other hand, the reason for the lowest thermal stability of this peak with regards to that of starch is probably attributed to the interactions into starch are more strong than those into TPS. The second peak (T_{onset2}) decreased its intensity and thermal stability with the reduction of HBP amount (Fig.6b and Table 1), which indicate that this peak is associated to HBP present into the TPS. The same behavior was observed to TPS60 whose values of T_{onset1} and T_{onset2} were 302 °C and 339 °C, respectively [21].

The displacement of the T_{onset} of starch and HBP in the TPS is a proof that the interaction between starch and HBP was carried out and it decreased with the proportion of HBP. The presence of peaks due to starch and plasticizing agents has been reported in the plasticization of starch with glycerol [22].

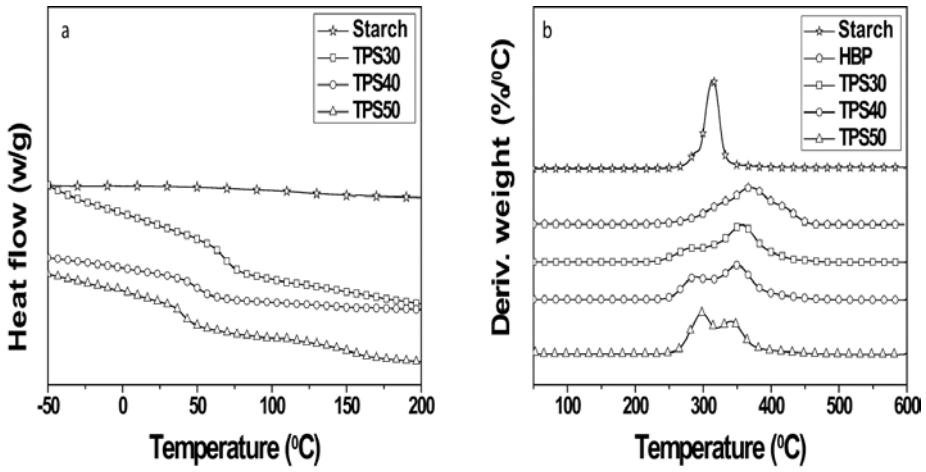


Figure 5. Thermograms of the samples a) DSC and b) TGA.
Source: Authors.

3.5. Rheological analysis

Fig. 6 shows the rheological behavior of the samples. The result of dynamic analysis (Fig. 6a) shows that all samples exhibited a reduction on complex viscosity (η*), in the case of HBP it was due to dissociation of interactions through OH groups, which has been seen in HBP [11]. On the other hand, the reduction on viscosity of TPS probably corresponded to dissociation of interactions and disentanglement of starch chains (amylose or amylopectin). The η* values of the samples at angular frequency of 1 Hz are as follow: HBP: 16,89 Pa.s, TPS30:16,99 Pa.s, TPS40:30,39 Pa.s and TPS50:58,03 Pa.s. Accordingly, this result means that the order of the interactactions degree is as follows: TPS50>TPS40>TPS30. Furthermore, this result followed the same trend exhibited by these samples on final torque. In addition, the TPS50 presented a lowest reduction on η*, this means that this sample exhibited a highest stability under conditions used to make this analysis; this is corroborate by TGA results. Furthermore, this sample showed a great displacement of the T_{onset1} and T_{onset2} regards to T_{onset1} of the starch and HBP, which was due to highest interaction between these materials. TPS60 exhibited a η* at 1 Hz of 486,99 Pa.s [12], this value is highest relative to that of the TPS. This may be due to high number of interactions and the starch content. On the other hand, at an angular frequency of 20 Hz, it was observed that a considerable increase on η* value for all TPS (shear thickening), the same was observed with TPS60 [12]. This can be interpreted as a formation of a microstructure, which is the ability of elastically deformation when exposed to external stress. This behavior has already been detected for tapioca starch dispersions [23]. The formation of this microstructure has been assigned to complexation reaction between amylose and lipids [24]. The angular frequency value, at which the increasing abrupt appear on η* did not showed a trend with the starch and HBP proportions. The rheological behavior exhibit by the HBP and TPS (Fig. 6b) was mainly viscous because loss modulus (G") was higher than elastic modulus (G'). The considerable increase on G" and G', was due to the microstructure formed, but did not occur a transition from viscous to elastic (G" < G'), which has been observed in starch gels [25]. The η* values of the samples at angular frequency of 1 Hz are as follow: HBP: 16,89 Pa.s, TPS30:16,99 Pa.s, TPS40:30,39 Pa.s and TPS50:58,03 Pa.s. This result followed the same trend exhibited by these samples on final torque. In addition, the sample TPS50 presented a lowest reduction on η*, this means that this sample exhibited a highest stability under conditions used to make this analysis; this is corroborate by TGA results. Furthermore, this sample showed a great displacement of the T_{onset1} and T_{onset2} regards to T_{onset1} of the starch and HBP, which was due to highest interaction between these materials. TPS60 exhibited a η* at 1 Hz of 486.99 Pa.s, this value is highest relative to that of the TPS. This may be due to high number of interactions and the starch content. On the other hand, at an angular frequency of 20 Hz, it was observed that a considerable increase on η* value for all TPS (shear thickening), the same was observed for TPS60 [12].

This can be interpreted as a formation of a microstructure, which is the ability of elastically deformation when exposed to external stress. This behavior has already been detected for tapioca starch dispersions [23]. The formation of this microstructure has been assigned to complexation reaction between amylose and lipids [24]. The angular frequency value, at which the increasing abrupt appear on η* did not showed a trend with the starch and HBP proportions. This means that the size of these microstructures and the interactions are different.

The rheological behavior exhibit by the HBP and TPS (Fig. 6b) was mainly viscous because loss modulus (G") was higher than elastic modulus (G'). The considerable increase on G" and G', was due to the microstructure formed, but did not occur a transition from viscous to elastic (G" < G'), which has been observed in starch gels [25]. These results indicate that the gel content or microstructures present in TPS is lowest.

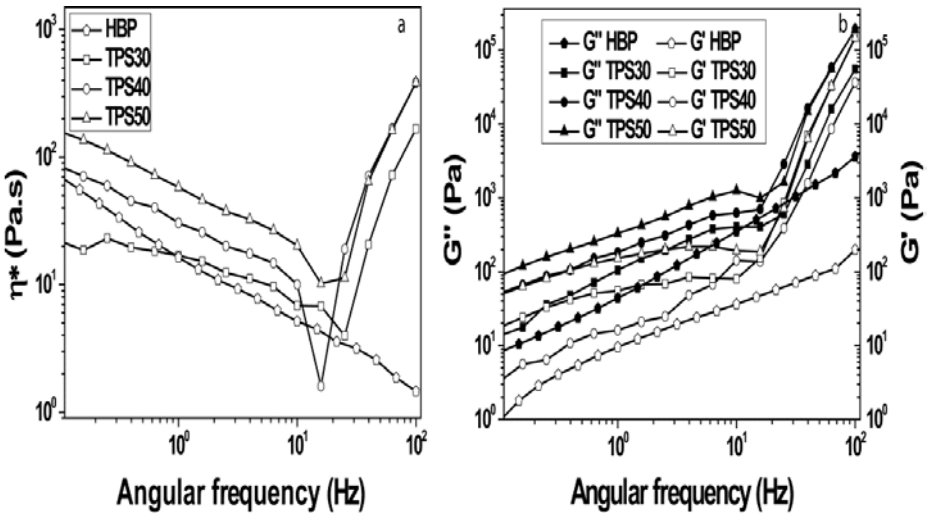


Figure 6. Rheological behavior of the HBP and TPS a) η* vs angular frequency and b) G" and G' vs angular frequency.
Source: Authors

3.6. SEM analysis

The morphology of the samples is presented in Fig. 7. It can be observed that the starch granules sized into TPS are smaller than those of the neat starch. That was as a result of destructuration produced by shear and HBP. In addition, similar results were found for starch plasticized with a mix of urea-ethanolamine [1]. In a study of the plasticization of starch with glycerol was reported that the addition of polyol to starch matrix changed the microstructural arrangement of starch chains and are less dense [26,27]. The samples TPS30 and TPS40 exhibited in some regions without starch granules. Big domains without starch particles were observed in TPS50, which indicates that this sample has a greatest interconnection.

This behavior is possibly due to the increasing of shear during the processing since this sample was obtained with the highest amount of starch. TPS60 [12] displayed the same behavior to that of TPS50. The results obtained in this study corroborated the results found by DSC analysis, since it was observed that TPS50 showed better interaction between HBP and starch than TPS30 and TPS40. The results obtained by SEM confirmed the reduction on crystallinity observed with the samples TPS30 and TPS40. This was possibly due to high dispersion of starch due to smallest starch amount present in these samples and not the high interaction between starch and HBP. Furthermore, it is possible that the effect of HBP in these samples be mainly as a result of dispersant agent present in these proportions. HBP is the dispersant phase.

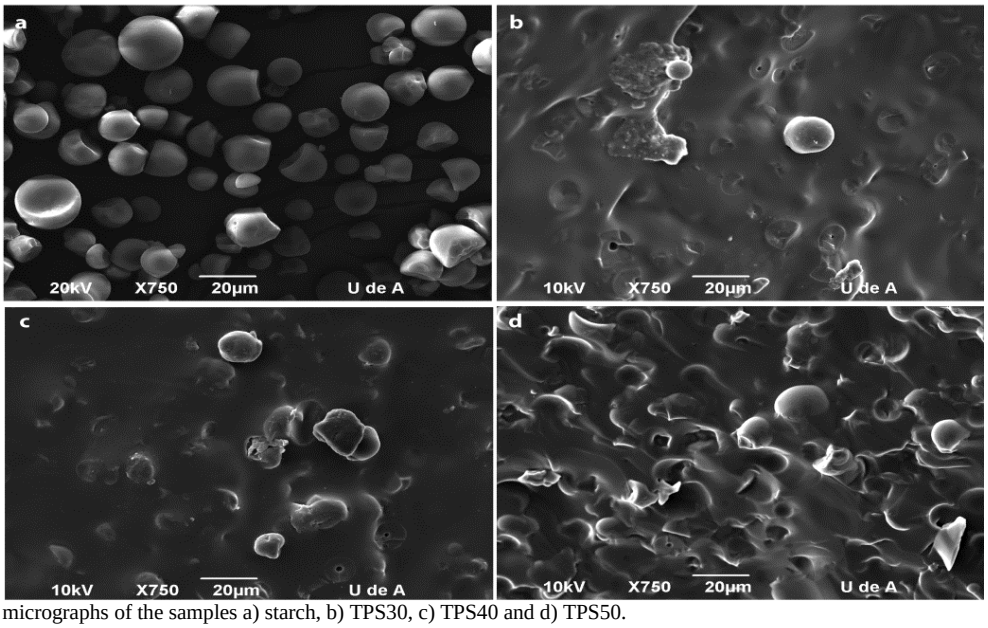


Figure 7. SEM micrographs of the samples a) starch, b) TPS30, c) TPS40 and d) TPS50.
Source: Authors

Table 1.
Results of the thermal and compression test.

Samples	T_g (°C)	$T_{Onset\ 1}$ (°C)	$T_{Onset\ 2}$ (°C)	Young's modulus (MPa)	Compression strength (MPa)
HBP	28,0	372	-	23,21 ± 2,1	1,25 ± 0,23
Starch	-	314	-	-	-
TPS30	54	282	358	38,98 ± 1,0	2,14 ± 0.10
TPS40	48	289	350	40,98 ± 1,0	2,25 ± 0,12
TPS50	40	299	341	44,08 ± 1,4	2,79 ± 0,18

Source: Authors

3.7. Compression test of the samples

The Young's modulus and tensile strength of the TPS decreased with the HBP content and these were higher than those of the HBP (Table 1). This is possibly due to the highest interaction between HBP and starch and to the presence of starch in the TPS. The results of Young's modulus, are lower than those reported to starch plasticized with ethylene glycol, propylene glycol and sorbitol (10-40 wt%), whose values were between 59 and 219 MPa [17]. According to the results, TPS did not improve the mechanical properties of the TPS, probably because the material is fragile.

4. Conclusions

In this study, TPS was obtained by employing a HBP as plasticizing agent. All the TPS present an interaction between starch and HBP. The proportion of HBP affect the shear degree of the materials during the processing, because the TPS prepared with lowest proportion of HBP, exhibited the best interaction between starch and HBP. This was due to highest viscosity of the system. Therefore, it favored the destructuration of the starch granules. The crystallinity of the TPS was lower than that of the starch and it increased with the proportion of HBP. None of the TPS exhibited V type crystallinity, which indicate that HBP restrict this crystallinity type, it can be interpreted as a high stability against retrogradation of starch, which is an important result. The rheological behavior of the TPS in the range of angular frequency studied was manly viscous. Furthermore, all TPS exhibited the formation of a microstructure. On the other hand, the size of the starch granules decreased comparably to the neat starch. The increase of HBP amount reduced the viscosity and mechanical properties of the TPS. However, the HBP may be an alternative for plastization of starch. According to the results, HBP affect the structural, thermal, morphological, rheological and mechanical properties of the TPS, since this material interacted with starch.

References

[1] Ma, X.F, Yu, J.G. and Wan, J., Urea and ethanolamine as a mixed plasticizer for thermoplastic starch. Carbohydrate Polymers, 64(2), pp. 267-273, 2006. DOI: 10.1016/j.carbpol.2005.11.042

[2] Vaverková, M., Toman F., Adamcová, D. and Kotovicová, J., Study of the biodegrability of degradable/biodegradable plastic material in a controlled composting environment. Ecological Chemistry and Engineering, 19(3), pp. 347-358, 2012. DOI: 10.2478/v10216-011-0025-8.

[3] Bertolini, A., Starches, characterization, properties and applications. Editorial CRC Press, United States, [online]. 2009, 6 P. Available at: https://books.google.com.co/books/about/Starches.html?id=iv2u5fM2as8C&source=kp_cover&redir_esc=y. DOI: 10.1201/9781420080247

[4] Huang, M., Yu, J. and Ma, X.F., Ethanolamine as a novel plasticizer for thermoplastic starch. Polymer Degradation Stability, 90(3), pp. 501-507, 2005. DOI: 10.1016/j.polymdegradstab.2005.04.005

[5] Yang, J., Yu, J. and Ma, X., Study on the properties of ethylenebisformamide and sorbitol plasticized corn starch (ESPTPS). Carbohydrate Polymers, 66(1), pp. 110-116, 2006. DOI: 10.1016/j.carbpol.2006.02.029

[6] Mesias, R. and Murillo, E., Hyperbranched polyester polyol modified with polylactic acid as a compatibilizer for plasticized tapioca starch/polylactic acid blends. Polímeros, 28(1), pp. 44-52, 2018. DOI: 10.1590/0104-1428.09516

[7] Janssen, L. and Moscicki, L., Thermoplastic starch. Editorial Wiley, Germany, [online]. 2009, 4 P. Available at: https://books.google.com.co/books?id=nHbLfoCoMvQC&pp=PA218&lpg=PA218&dq=Janssen+L.+and+Moscicki+L.,+%22Thermoplastic+starch%22.&source=bl&ots=sHq0LxS7nk&sig=6tE-DjgQFg8y5A109zj9gy8Q4Q&hl=en&sa=X&ved=0ahUKEwjRmry77MnaAhVQvVMKHaLpD

[8] Murillo, E.A., Vallejo, P.P. and López, B.L., Characterization of hydroxylated hyperbranched polyesters of fourth and fifth generation. E-Polymer, 10(1), pp.1347-1358, 2010. DOI: 10.1515/epoly.2010.10.1.1347

[9] Murillo, E.A., Vallejo, P.P., Sierra, L. and López B.L., Characterization of hyperbranched polyol polyesters based on 2,2-bis (methylol Propionic Acid) and pentaerythritol. Journal of Applied Polymer Science, 112(1), pp. 200-207, 2009. DOI: 10.1002/app.29397

[10] Murillo, E.A., Cardona, A. and López B.L. Rheological behavior in the molten state and solution of hyperbranched polyester of fourth and fifth generation. Journal of Applied Polymer Science, 119(2), pp. 929-935, 2011. DOI: 10.1002/app.32774

[11] Zagar, E. and Zigon, M., Aliphatic hyperbranched polyesters based on 2,2 bis(methylol)propionic acid—Determination of structure, solution and bulk properties. Progress in Polymer Science, 36(1), pp. 53-88, 2011. DOI: 10.1016/j.progpolymsci.2010.08.004

[12] Guzmán, M. and Murillo, E.A., The properties of blends of maleic anhydride-grafted polyethylene and thermoplastic starch using hyperbranched polyester polyol as a plasticizer. Polymer Engineering and Science, 55(11), pp. 2526-2533, 2015. DOI: 10.1002/pen.24143

[13] Zhang, K., Cheng, X., Cheng, F., Lin, Y., Zhou, M. and Zhu, P., Poly(citrate glyceride): a hyperbranched polyester for starch plasticization. Polymer International, 67(4), pp. 399-404, 2018. DOI: 10.1002/pi.5520

[14] Zhang, K., Cheng, F., Lin, Y., Zhou, M. and Zhu, P., Effect of hyperbranched poly(trimellitic glyceride) with different molecular weight on starch plasticization and compatibility with polyester. Carbohydrate Polymers, 195 (1), pp. 107-113, 2018. DOI: 10.1016/j.carbpol.2018.04.080

[15] Chang, P., Jian, R., Zheng, P., Yu, J. and Ma, X., Preparation and properties of glycerol plasticized-starch (GPS)/cellulose nanoparticle (CN) composites. Carbohydrate Polymers, 79(2), pp. 301-305, 2010 DOI: 10.1016/j.carbpol.2009.08.007.

[16] Zobel, H.F., Starch crystal transformations and their industrial importance. Starch/Stärke, 40(1), pp. 1-7, 1988. DOI: 10.1002/star.19880400102.

[17] Da Roz, A.L., Carvalho, A., Gandini, A. and Curvelo, A., The effect of plasticizers on thermoplastic starch compositions obtained by melt processing. Carbohydrate Polymers, 63(3), pp. 417-424, 2006. DOI: 10.1016/j.carbpol.2005.09.017.

[18] Yoon, S.D., Chough, S.H., and Park, H.R., Properties of starch-based blend films using citric acid as additive. II. Journal of Applied Polymer Science, 100(3), pp. 2554-2560, 2006. DOI: 10.1002/app.23783.

[19] Mathew, A.P., and Dufresne, A., Plasticized waxy maize starch: effect of polyols and relative humidity on material properties. Biomacromolecules, 3(5), pp. 1101-1108, 2002. DOI: 10.1021/bm020065p

[20] Kaur, L., Singh, J. and Singh N., Effect of glycerol monostearate on the physico-chemical, thermal, rheological and noodle making

properties of corn and potato starches. Food Hydrocolloids, 19(5), pp. 839-849, 2005. DOI: 10.1016/j.foodhyd.2004.10.036.
[21] Guzmán, M., Obtención y caracterización de mezclas de polietileno de baja densidad modificado con anhídrido maleico y almidón termoplástico. Trabajo de Investigación, Universidad de Antioquia, 2013, pp. 56-63.
[22] Canché, G., Canché, M., Duarte, S., Cáceres, M. and Borges, R., Mechanical properties and biodegradation of thermoplastic starches obtained from grafted starches with acrylics. Carbohydrate Polymers, 86(4), pp. 1501-1508, 2011. DOI: 10.1016/j.carbpol.2011.06.052.
[23] Rao, M. and Tattiyakul, J., Granule size and rheological behavior of heated tapioca starch dispersions. Carbohydrate Polymers, 38(2), pp. 123-132, 1999. DOI: 10.1016/S0144-8617(98)00112-X.
[24] Rodríguez, F.J., Ramsay, B.A. and Favis, B.D., Rheological and thermal properties of thermoplastic starch with high glycerol content. Carbohydrate Polymers, 58(2), pp. 139-147, 2004. DOI: 10.1016/j.carbpol.2004.06.002.
[25] Nagano, T., Tamaki, E. and Funami T., Influence of guar gum on granule morphologies and rheological properties of maize starch. Carbohydrate Polymers, 72(1), pp. 95-101, 2008. DOI: 10.1016/j.carbpol.2007.07.028.
[26] Jagadish, R.S., and Raj, B., Properties and sorption studies of polyethylene oxide-starch blended films. Food Hydrocoloids. 25(6), 1572-1580, 2011. DOI: 10.1016/j.foodhyd.2011.01.009
[27] Basiak, E., Lenart, A. and Debeaufort, F., How glycerol and water contents affect the structural and functional properties of starch-based edible films. Polymers, 10(4), pp. 412-429, 2018 DOI: 10.3390/polym10040412

M. Guzmán, received the BSc. in Mechanical Engineering in 1994, the MSc. degree in Engineering in 2010. Actually he is studying a PhD in Materials Engineering in University of Antioquia, Colombia. His research interests include: biodegradable polymers, polymer blends, rubber and characterization of materials. He is currently a member of the Grupo de Materiales Poliméricos de Ingeniería, Universidad de Antioquia, Colombia
ORCID: 0000-0003-2722-7259

E.A. Murillo, received the BSc. in Chemistry in 2003 in University of Antioquia, Colombia. Furthermore, he received the MSc. degree in Chemistry Sciences in 2007 and PhD degree in Chemistry Sciences in 2010. He is currently a professor and head of the Research Group in Polymeric Materials (GIMAPOL) of the Department of Chemistry of the Universidad Francisco de Paula Santander in Cúcuta, Colombia. His research interests include: synthesis and characterization of polymers, polymer blends, hyperbranched polymers, alkyd resins and biodegradable polymers.
ORCID: 0000-0002-0617-2327

UNIVERSIDAD NACIONAL DE COLOMBIA
SEDE MEDELLÍN
FACULTAD DE MINAS

Área Curricular de Ingeniería
Geológica e Ingeniería de Minas y Metalurgia

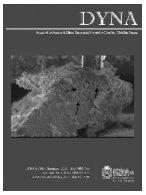
Oferta de Posgrados

Especialización en Materiales y Procesos
Maestría en Ingeniería - Materiales y Procesos
Maestría en Ingeniería - Recursos Minerales
Doctorado en Ingeniería - Ciencia y Tecnología de Materiales

Mayor información:

E-mail: acgeomin_med@unal.edu.co
Teléfono: (57-4) 425 53 68

UNIVERSIDAD NACIONAL DE COLOMBIA
SEDE MEDELLÍN
FACULTAD DE MINAS



DYNA
http://dyna.medellin.unal.edu.co/

An evaluation of the controlled release of ammoniacal nitrogen from residual cellulose/polyvinyl alcohol hydrogels as an alternative to traditional fertilization processes

Marybel Montoya-Álvarez [a], Adriana María Quinchía-Figueroa [a], Octavio González-Murillo [b] & Pedronel Araque-Marín [a]

[a] *Escuela de Ingeniería y Ciencias Básicas. Universidad EIA, Envigado, Colombia. marybel.montoya@eia.edu.co, adriana.quinchia@eia.edu.co, pedronel.araque@eia.edu.co*
[b] *Grupo SOBIOTECH. Sobiotech S.A.S, Guarne, Colombia., Colombia. octaviog@abonamos.com*

Received: August 28th, de 2017. Received in revised form: May 5th, 2018. Accepted: July 24th, 2018

Abstract
Soil fertilization improves yield and quality of produce, but nutrient loss from fertilized soil produces alterations in the ecosystems (e.g., eutrophication); it also increases costs in the agribusiness. In this research, we developed a device from residual cellulose/polyvinyl alcohol hydrogel for the controlled release of ammoniacal nitrogen in soil. Total Kjeldahl Nitrogen (TKN) method was used to determine the fraction of nitrogen released, and the effect of the device on a bioindicator (*Zea mays*) was studied in greenhouse conditions. Structural damage to the device after its application to soil was analyzed using scanning electron microscopy (SEM). Kjeldahl tests showed the device released less than 15% of total nitrogen across a 60 day evaluation period, displaying a Fickian diffusion pattern. Seedlings produced two times more biomass in device-fertilized soil.

Keywords: hydrogel; residual cellulose; poly(vinyl alcohol); controlled release; ammoniacal nitrogen.

Evaluación de la liberación controlada de nitrógeno amoniacal a partir de un hidrogel de celulosa residual/polivinil alcohol como una alternativa a los procesos de fertilización tradicionales

Resumen
La fertilización del suelo mejora el rendimiento y la calidad en la producción, pero la pérdida de los nutrientes del suelo provoca alteraciones en los ecosistemas (por ejemplo, la eutrofización) y también incrementa los costos en el sector agrícola. En este trabajo se evaluó la liberación controlada de nitrógeno a partir de un hidrogel de celulosa-residual/alcohol-polivinilico, como alternativa de lenta liberación para procesos de fertilización. El método de nitrógeno Kjeldahl fue utilizado para determinar el porcentaje de nitrógeno liberado y se valoró su efecto sobre *Zea mays* como bioindicador en condiciones de invernadero y la pérdida de estructura del hidrogel se analizó por microscopía electrónica de barrido (SEM). El porcentaje de liberación de nitrógeno fue inferior al 15% tras 60 días de evaluación, ajustándose a un mecanismo de difusión Fickiana, con un aumento en la producción de biomasa del 100% en las plántulas bioindicadoras.

Palabras clave: hidrogel; celulosa residual; polivinil alcohol; liberación controlada; nitrógeno amoniacal.

1. Introduction

Nitrogen deficiency in soil limits the yield and quality of produce [1]. Soil matrices can lose nitrogen via volatilization, lixiviation and denitrification processes; these affect soil recovery and fertilizer performance [2] —they also generate pollution [3]. Thus, researchers have tried different approaches to reduce N exit from soil: choosing the right source of N, adjusting the dose of fertilizer and setting the correct time and method of application.

Controlled-release fertilizers are gathering momentum

How to cite: Montoya-Álvarez, M., Quinchía-Figueroa, A.M., González-Murillo, O. and Araque-Marín, P., An evaluation of the controlled release of ammoniacal nitrogen from residual cellulose/polyvinyl alcohol hydrogels as an alternative to traditional fertilization processes. DYNA, 85(206), pp. 187-193, September, 2018.

© The author; licensee Universidad Nacional de Colombia.

due to their ability to prevent nutrient loss [4]. Researchers have recognized their capacity to minimize environmental impact [5,6]. Still, controlled-release fertilizers remain in a stage of development and require further research to minimize production costs —in that way, a trend toward waste-based fertilizers has surfaced over the past few years [7].

The pulp and paper industry, one of the largest contributors to pollution, generates large amounts of waste that constitute an environmental puzzle. Recycling of this waste produces enormous environmental benefits, but so far, researchers have only used it as material for construction[8]. We expect this material could work to produce new fertilizers, but although paper sludge waste is widely available, we have not found any prior research stating that.

Some authors have used raw materials derived from agribusiness waste, and they highlight the importance of adjusting preparation parameters to match the nutritional requirements of the plants [7]. Other authors have added materials such as Bentonite clay and copolymers to waste-based fertilizers; these improve mechanical strength and release performance, which translates into a smaller nutrient loss [9]. Although these authors have demonstrated that changes to the composition of the device can improve its performance, the effect of the physicochemical parameters of different matrices on that performance remains unknown.

In this research, we developed a residual cellulose/polyvinyl alcohol controlled-release fertilizer. We then used the Total Kjeldahl Nitrogen method to determine the amount of ammoniacal nitrogen lost from soil and sand matrices and finally, assessed the effect of the physicochemical properties of these matrices on nutrient release.

2. Materials and methods

2.2. Reagents

Analytical grade sulfuric acid (98%), hydrogen peroxide (50%), Nessler polyvinyl alcohol, Kjeldahl Nitrogen indicator and 12N potassium hydroxide were obtained from Hach. Lactophenol blue was obtained from Merck. Glucose Sabouraud agar (4%) was obtained from Becton Dickinson GmbH. Diammonium phosphate (DAP) with a composition of 18% nitrogen, 46% phosphorus and 0% potassium was obtained from Delcorp.

2.3. Materials for planting

Residual cellulose/polyvinyl alcohol hydrogel was manufactured at Universidad EIA (Table 1). Sieved and washed sand (2 mm) and Andisol (Fulvudand), were provided by SOBIOTECH (Table 2) and characterized by Grupo Interdisciplinario de Estudios Moleculares-GIEM at Universidad de Antioquia and Laboratorio de Suelos at Universidad Nacional de Colombia, in Medellin, respectively.

Zea mays seeds (Poaceae) 96 % pure and 80 % Germ were kept away from light, at a relative humidity of 30 % and a temperature of 4 °C, to inhibit germination. The seeds' surfaces were disinfected with water and 70 % alcohol for 2 min. Then, they were immersed in 0.05 % sodium hypochlorite for 5 min, under constant stirring. After disinfection, the seeds were washed with sterile water and laid over wet sterile paper sheets for two days to complete germination. Germinated seeds were placed in plastic cylindrical holders (11 cm x 9 cm) with 200 g andisol type soil and thinned after 15 days to limit the number of plants to one per holder.

Table 1
Physicochemical analysis of residual cellulose/polyvinyl alcohol, data in (m/m) %. RC = Residual Cellulose, PVA = polyvinyl alcohol.

Component	(w/w) %	Component	(w/w) %
Humidity	71.18	P_2O_5	2.9
RC	1.78	Na_2O	0.14
PVA	8.07	K_2O	0.8
$CaCO_3$	0.36	TiO_2	0.03
MgO	0.03	SiO_2	0.26
Al_2O_3	0.16	NH_4^+	2.94
Fe_2O_3	0.01	NO_3^-	10.1
B_2O_3	0.61	------	------

Source: The authors

Table 2
Physicochemical analysis of andisol, data in (w/w) %.

Component	(w/w) %	Component	(w/w) %
Sand	70	K_2O	$6.58x10^{-6}$
Lime	10	P_2O_5	$1.30x10^{-3}$
Clay	15	CaO	$3.61x10^{-5}$
Organic matter	4.3	pH	4.8
MgO	$1.29x10^{-3}$	CIC (cmolc*kg^{-1})	3

Source: The authors

2.4. Equipment

DR/200 UV/Vis spectrophotometer (Hach). 400-900nm. Tungsten halogen lamp. Spectral band: 7nm. Wavelength: ± 2 nm. Resolution: 1nm. Photometric linearity: ± 0.002 A. Photometric reproducibility: ± 0.005 A.

Digesdahl Digestor (Hach). Model 23130-20. Temperature range: 100 °C - 400 °C. Temperature control ± 15 °C. Flushing capacity: 11.5 L/min at a water flow rate of 6.5 L/min. Minimum pressure: 51.7 kPa.

Phenom Scanning electron microscope. Optical zoom: 20x -135x. SEM zoom 80x - 130000x. Sample size 32 nm. Acceleration voltage: 5 kV - 10 kV.

Olympus optical microscope CX21. 10x/18 ocular. Binocular tube inclined at 30°. Interpupilar distance range: 45 mm - 75 mm. Rotatable quadruple lense holder. 4x, 10x, 40x and 100x lenses. Halogen lamp 6V/20W. Fixed mechanical slide with cable movement: 120 x 132mm. Range of displacement: 76 mm(X) by 30 mm(Y).

2.5. Methods

2.5.1. Nitrogen quantification

Solid sample treatment: 0.1 g to 0.5 g of residual cellulose/polyvinyl alcohol hydrogel were crushed with mortar and pestle and then placed in a 100 mL Digesdahl® flask alongside 25 mL of distilled water. Then, 3 mL of 98 % sulfuric acid were added into the flask and stirred. 10 min later, the flask was placed in a digester and heated at 440 °C. Once reflux started, the flask was allowed to set for 16 min,

and then, 10 mL of 50 % hydrogen peroxide were added through the capillary funnel. Once hydrogen peroxide was added, heating was suspended, and the flask was again left to set for 30min. The digested solution was filtered through a 595 Rundfilter paper (∅ 110 mm) and taken to a 100 mL volumetric flask, where the final volume of the mixture was adjusted using distilled water.

Liquid sample treatment: 25 mL of the leachate were taken to a 100 mL Digesdahl® flask, and the same method used in the treatment of the solid sample was followed.

For the determination of ammoniacal nitrogen as Total Kjeldahl Nitrogen by Nessler 399 method, Hach 0875 method was used: 3 mL of the prepared solution were taken to a 25 mL volumetric flask, and then, a drop of TKN indicator was added into the flask, alongside three drops of mineral stabilizer, three drops of a dispersing agent (polyvinyl alcohol), 200 uL of 12 N potassium hydroxide and 1mL of Nessler's reagent. Distilled water was added until a 25 mL solution was obtained. The solution was then taken to the spectrophotometer.

2.5.2. Evaluation of the hydrogel's degradation

The hydrogel was cut in 1 cm x 1cm pieces. The pieces were dried at 20 °C for 48 h and weighed. Then, they were placed in distilled water (pH 6.8) for 30 days, and dried every five days at 20 °C for 48 h and weighed again. All tests were run in triplicate.

2.5.3. Assembly for nitrogen release leaching tests

Polyvinyl chloride (PVC) cylindrical columns (20 cm long by 3.8 cm wide) were adapted with a nylon filter at the lower end. Each column was packed with 200g of the substrate (andisol or sand) and 525 mg of the hydrogel. The columns were washed using 120 mL of distilled water, and then, the leachate was collected for analysis; this process was performed on days 3, 5, 15, 25, 30 and 60. All tests were run in triplicate. 194 g of diammonium phosphate were used as positive control [10]. Presence of nitrogen was determined by spectrophotometry using the Nessler 399 method.

2.5.4. Assembly for greenhouse tests

Hydrogel and diammonium phosphate were added to the soils where *Zea mays* seeds had previously germinated. The plants were grown in natural light in SOBIOTECH's greenhouse in Antioquia (6°15´07" N; 75°25´42" W, 2117 masl). The soil was kept around 50 % to 60 % of its maximum moisture retention capacity. The plants were harvested 60 days after planting, their height was measured, and then, they were dried at 50 °C for 48 h to determine their total dry mass. All tests were quintupled.

2.5.5. Microbiological analysis of soil

Microbiological analysis of the soil used in the greenhouse tests was performed to determine the presence of mold, yeast, or bacteria before and after 60 days of treatment. A pattern solution was obtained by mixing 10 g of soil and 90 mL of distilled water. Serial dilutions of this solution were obtained by mixing 1 mL of the solution and 9 mL of distilled water until a concentration in the order of 10^{-7} was obtained. 100 uL solutions of concentrations $1x10^{-1}$, $1x10^{-3}$, $1x10^{-5}$ and $1x10^{-7}$ g/L were placed in Sabouraud Agar.

2.5.6. Statistical analysis

Results were compared using ANOVA analysis; this was followed by a set of tests to determine the differences between the mean values. The analysis was performed on STATGRAPHICS Centurion XVIII.

3. Results and discussion

3.1. Degradation of the hydrogel

Fig. 1 shows that, from day five on, hydrogel loses up to 10% of its structure. This reduction in mass is related to the erosion of residual cellulose and polyvinyl alcohol chains that failed to crosslink during hydrogel formation; this behavior indicates low disintegration during the evaluation period.

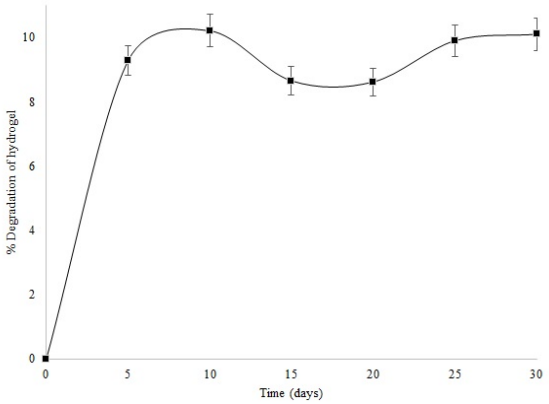


Figure 1 Hydrogel's weight loss in liquid media.
Source: The authors..

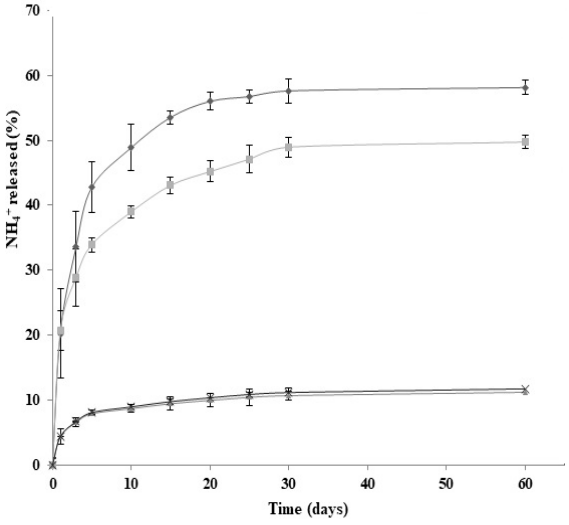


Figure 2 Release of NH4+ in water: ◆ diammonium phosphate in soil, ■ diammonium phosphate in sand; ▲ hydrogel in soil, × hydrogel in sand.
Source: The authors

3.2. Release of NH_4^+ by leaching

Fig. 2 shows the release profiles for NH_4^+ (diammonium phosphate and hydrogel) from day 0 to day 60 of the evaluation period.

During the first five days of evaluation, diammonium phosphate released 43 ± 2 % and 34 ± 2 % of NH_4^+ in soil and sand matrices, respectively. The high solubility of diammonium phosphate in water (57.5 g / 100 mL at 10ºC) produced this rapid release (called Tigger effect). On day 30, NH_4^+ release reached levels of 58 ± 2 % and 48 ± 1 %; these data are similar to those found on day 60 —this indicated that migration of NH_4^+ from the fertilizer to the soil matrix had reached equilibrium. During the evaluation period, larger concentrations of NH_4^+ were found in solutions obtained from soil (pH 4.8), than in those obtained from sand (pH 7.2); this was to be expected as pH was an essential factor in determining the solubility of nutrients in soil, where NH_4^+, NO_3^-, CO_3^{2-} and SiO_3^{2-} displayed a larger displacement of oxidation equilibria (nitrification and denitrification), and also dissociation of NH_4^+ ions (eq. 1 and 2) to the left side of the equation, increasing the concentration of NH_4^+ ions in the soil solution and favoring leaching [11]. In addition, the soil exchange complex displays a lower pH, which increases protonation at the points of exchange; this translates into positive charging of the colloidal mycelia, avoiding adsorption of NH_4^+ on the surface.

$$NH_{4(ac)}^{+} + 13H_2O_{(l)} \leftrightarrow NO_{3(ac)}^{-} + 10H_3O_{(ac)}^{+} + 8e^{-} \quad (1)$$

$$NH_{4(ac)}^{+} + H_2O_{(l)} \leftrightarrow NH_{3(ac)} + H_3O_{(ac)}^{+} \quad (2)$$

The different media did not exhibit statistical differences when hydrogel was used. Release of NH_4^+ after days 5, 30 and 60 was 8 ± 2 %, 11 ± 1% and 12 ± 2%, respectively. The first stage of release from the hydrogel can be attributed to the erosion of residual cellulose and polyvinyl alcohol chains as mentioned before [12]; structural loss also plays a role. According to the European Standardization Committee [13], a fertilizer is called "a controlled release fertilizer" when:

- It releases no more than 15% after 24 h.
- It releases no more than 75% after 28 days.

Once NH_4^+ finds its way into the substrate, water can wash it out via pore saturation, or it can remain available to plants and microorganisms [14]. Although the release profile in water does not represent the real span in which nutrients exit soil, it allows for comparison between commercial fertilizers and the hydrogel. In this way, we can test the capacity of our hydrogel to release NH_4^+.

To analyze NH_4^+ release data, we used the Korsmeyer-Peppas empirical model [15] (eq 3), for polyvinyl alcohol hydrogel controlled-release systems in soil [16,17].

$$\frac{M_t}{M_\infty} = Kt^n \quad (3)$$

In eq 3, $\frac{M_t}{M_\infty}$ is the fraction of drug or fertilizer used by time t, K is the constant that marks the speed of release and n is the release exponent.

To estimate n and K values, eq. 3 was linearized

$$log\left(\frac{M_t}{M_\infty}\right) = log(k) + n\ log(t) \quad (4)$$

Fig. 3 shows log (% NH_4^+) versus time, Table 3 shows the statistical results of NH_4^+ release data linearization. The data exhibits significant statistical correlation (p-value < 0.05) between log (NH_4^+) and log (t), with a 95% confidence level; the correlation coefficients for the models used were larger than 0.99 —this indicates a strong correlation between variables.

From the equations shown in Table 3, the following equation was obtained:

$$log(\%NH_4^+) = a + n\ log(t) \quad (5)$$

Assuming $a = log\ k$:

$$log(\%NH_4^+) = logk + n\ log(t) \quad (6)$$

Using the antilog function on both sides of the equation:

$$\%NH_4^+ = kt^n \quad (7)$$

By representing $\%NH_4^+$ as $\frac{M_{NH_4^+}}{M_\infty}x100$, then

$$\frac{M_{NH_4^+}}{M_\infty} = \frac{k}{100}t^n \quad (8)$$

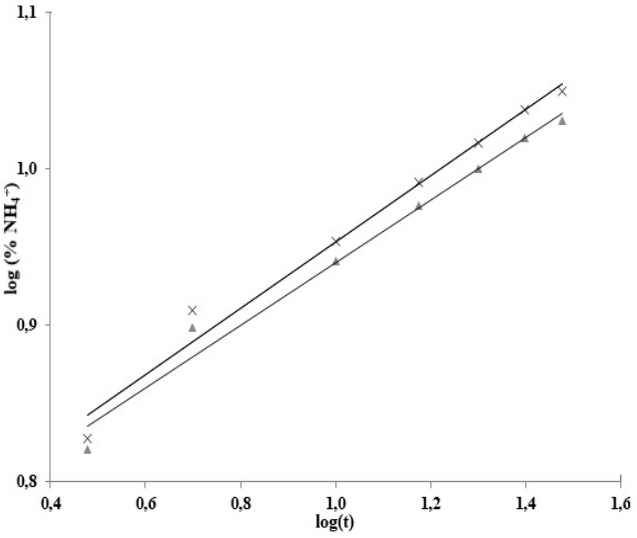


Figure 3 Adjustment to the Korsmeyer-Peppas model for the release of NH_4^+ in water: ▲hydrogel in soil, ×hydrogel in sand.
Source: The authors..

Table 3.
Linear parameters of residual cellulose/polyvinyl alcohol hydrogel.

Media	Regression equations	r^2	p-value
Soil	$log(\%NH_4^+)$ = 0,741 + 0,199*$log(t)$	0,991	0,003
Sand	$log(\%NH_4^+)$ = 0,742 + 0,211*$log(t)$	0,991	0,002

Source: The Authors.

$$\frac{M_{NH_4^+}}{M_\infty} = \frac{k}{100} t^n \quad (8)$$

Since k is constant then $\frac{k}{100}$ must also be a constant:

$$\frac{M_{NH_4^+}}{M_\infty} = K t^n \quad (9)$$

In this way, the leaching of NH_4^+ in water adjusts to the Korsmeyer-Peppas model [18](eq. 3), which adequately describes the leaching process. This model explains the NH_4^+ release mechanisms for residual-cellulose/polyvinyl-alcohol hydrogel; the derived n and K values can be seen on Table 4.

For polyvinyl alcoholhydrogels with different degrees of hydrolysis, a Fickian diffusion mechanism (n = 0.45) was proposed. For hydrogels with chitosan, xanthan and starch contents the mechanism proposed is not Fickian (0.45 < n < 0.89) as hydrogels disintegrated easily.

Hydrogel shows no significantly different n values for treatments in soil and sand, but values of n < 0.45 indicate a lower rate for water infiltration into the hydrogel than the rate at which its polymeric chains can relax. This phenomenon has been attributed to the high content of calcium carbonate in the hydrogel's structure; even so, the process remains Fickian —such behavior is called "Less Fickian" [19,20].

3.2. Evaluation of the hydrogel in greenhouse conditions

Fig. 4 shows the control (left), diammonium phosphate-treated (center) and hydrogel-treated (right) samples used in the greenhouse tests; it is evident that plants in the right-hand side column are taller and display broader leaves.

Table 4.
Parameters of the Korsmeyer-Peppas model for release of NH4+ in water by leaching from RC/PVA.

Nutrient	System	*n*	*K* (min^{-n})
NH_4^+	Soil	0.20 ± 0.01	5.508
	Sand	0.21 ± 0.02	5.521

Source: The authors.



Figure 4 *Zea mays* parts and treatment used in greenhouse tests: a) leaf (control), b) leaf (diammonium phosphate); c). leaf (hydrogel), d) root (control), e) root (diammonium phosphate); f) root (hydrogel).
Source: The authors.

Table 5.
Effect of Diammonium phosphate (DAP) and residual cellulose/polyvinyl alcohol hydrogel (RC/PVA) on *Zea mays* morphology. Data presented as: mean ± sd.

System	Control	DAP	RC/PVA
Length (cm)	24 ± 1	31 ± 2	34 ± 2
Mass of root (g)	1,5 ± 0,4	1,6 ± 0,4	2,4 ± 0,3
Mass of stem (g)	0,13 ± 0,02	0,29 ± 0,01	0,35 ± 0,07
Mass of leaves (g)	0,30 ± 0,07	0,52 ± 0,08	0,7 ± 0,2
Total mass (g)	1,9 ± 0,6	2,4 ± 0,5	3,4 ± 0,5

Source: The authors.

Table 5 shows the average heights of the hydrogel-treated plants and the diammonium phosphate-treated plants; p > 0.05 suggests there are no significant differences in the treatments. However, both treatments are significantly different from the control group. The mass of the plants grown in hydrogel-fertilized soil was larger than that of diammonium phosphate-fertilized plants; these findings show the positive effects of hydrogel-fertilized soil on the bioindicator. The results shown confirm that nitrogen fertilizers can be optimized, averaging lower production costs and reducing environmental impact produced by traditional fertilization processes [21].

3.3. Analysis of the morphological changes in the Hydrogel

Hydrogel produced the largest release of NH_4^+. When hydrogel interacts with solid fractions in soil (organic and inorganic) it releases NH_4^+, but the rate at which that release takes place is dependent on the degradation of the cellulose matrix. Degradation was verified on day 60 using scanning electron microscopy (SEM). Fig. 5b shows the presence of a microorganism growing on the surface of the hydrogel; given the characteristics of the material, microorganisms can exhibit cellular activity and contribute to its degradation.

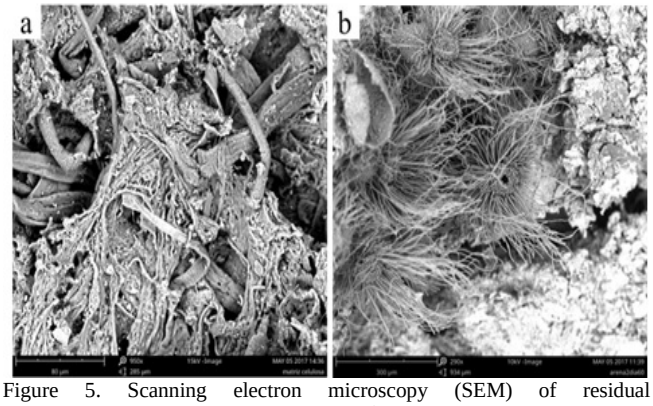


Figure 5. Scanning electron microscopy (SEM) of residual cellulose/polyvinyl alcohol hydrogel: a) before application to soil, 950x and b) 60 days after application, 290x.
Source: The authors.

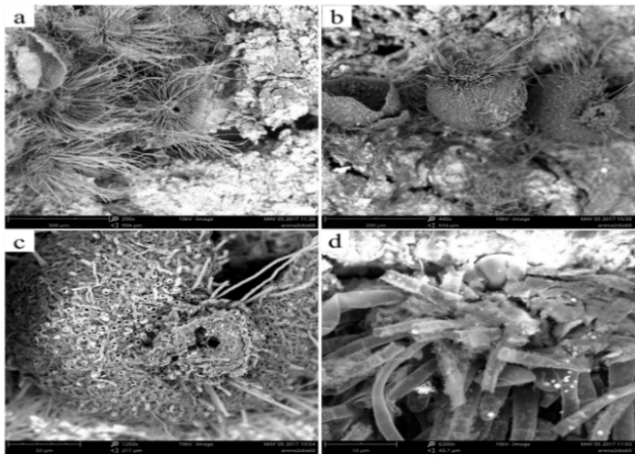


Figure 6. Scanning electron microscopy (SEM) of the isolated fungus: a) 290x; b) 440x; c) 1250x; d) 6200x.
Source: The Authors.

Fig. 6 shows a filamentous fungus with cylindrical hyphae, spherical structures, ascomata (flask-like, some already broken due to the release of ascospores to the media) and conical-shaped porous hyphae (characteristic of the ascomycota) [22].

3.4. Microbiological characterization of the soil isolates

After 60 days, we isolated (in 4 % Glucose Sabouraud agar) from hydrogel-fertilized soil, a fungus with the same characteristics as those found on the hydrogel's surface. None of the tests performed revealed the presence of enterobacteria or *E. coli* (both regulated by Colombian legislation and the National Health Institute).

On the sixth day of isolation (Fig. 7a), an unlimited number of white cottony colonies was discovered throughout the Petri dish, all of which exhibited radial growth. On the backside of the plate, a diffused brown shade appeared (Fig. 7b). After ten days of isolation (Fig. 7c) the cottony colonies, once white, turned purplish, and then covered the entire agar, adhering to the walls. Meanwhile, the brown shade on the back of the plate turned pink (Fig. 7d).

Table 6.
Microbiological analysis.

Treatment	Soil	DAP	RC/PVA
Mold	+	+	+
Yeast	+	+	+
Enterobacteria	-	-	-
E. coli	-	-	-
Fungus	-	-	+

Source: The Authors.

Figure 7 Development of the isolated fungus on Sabouraud agar; a) Cottony mycelia on day 6, b) Backside of the plate on day 6, c) Cottony mycelia on day 10 and d) Backside of the plate on day 10.
Source: The Authors.

Fig. 8 shows images (at 40x) of the culture plates in lactophenol blue. On the images we observe the fungus' mycelium, composed of thin septate hyaline hyphae (Fig. 8a), lateral phialides (Fig. 8b), oval and ellipsoidal microconidia and ascospores (Figs. 8c and 8d) [22]. The macroscopic and microscopic taxonomic characters identified in the fungal isolate match those of *Fusarium spp*.

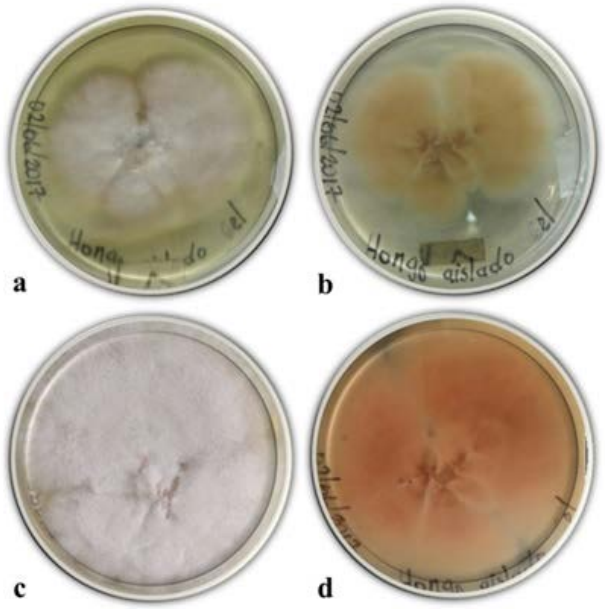


Figure 8. Development of the isolated fungus on Sabouraud agar; a) Cottony mycelia on day 6, b) Backside of the plate on day 6, c) Cottony mycelia on day 10 and d) Backside of the plate on day 10.
Source: The Authors.

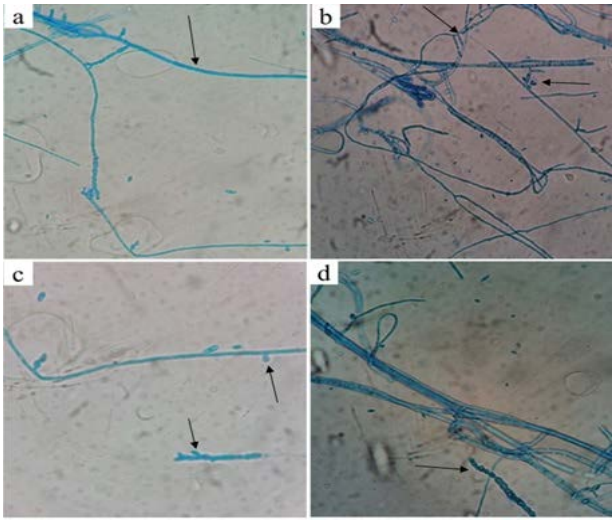


Figure 9 Microscopic characterization of the colonies in fungal isolate: a) hyphae; b) phialides; c) macro and microconidia; d) ascospores.
Source: The Authors.

4. Conclusions

NH_4^+ release data adjusts well to the Korsmeyer-Peppas empirical model, suggesting a Fickian diffusion mechanism.

A controlled-release system was manufactured to improve nutrition in plants (especially *Zea mays*). Increased height and biomass in the plants indicate a substantial contribution of NH_4^+; this makes the hydrogel a compelling alternative to traditional chemical fertilization processes. It is, however necessary, to adjust first the conditions that facilitate the application of this technology to different types of plants and soils.

Acknowledgments

We, the authors, would like to extend our acknowledgments to Colciencias, who supported this research through the National Program of Agricultural Science and Technology, grant program number 669-2014, contract number 1333-669-45305.

References

[1] Kumar, K. and Goh, K.M., Crop residues and management practices: effects on soil quality, soil nitrogen dynamics, crop yield, and nitrogen recovery, Adv. Agron., 68, pp. 197-319, 1999. DOI: 10.1016/S0065-2113(08)60846-9
[2] Kanampiu, F.K., Raun, W.R. and Johnson, G.V, Effect of nitrogen rate on plant nitrogen loss in winter wheat varieties, J. Plant Nutr., 20(2-3), pp. 389-404, 1997. DOI: 10.1080/01904169709365259
[3] Tong, Z., Bischoff, M., Nies, L., Applegate, B. and Turco, R.F., Impact of fullerene (C60) on a soil microbial community, Environ. Sci. Technol., 41(8), pp. 2985-2991, 2007. DOI: 10.1021/es061953l
[4] Marschner, B., DOM-enhanced mobilization of benzo(a)pyrene in a contaminated soil under different chemical conditions, Phys. Chem. Earth, 23(2), pp. 199-203, 1998. DOI: 10.1016/S0079-1946(98)00013-5
[5] Golman, R., Ito, B. and Shinohara, K., Design of multi-layer coated particles with sigmoidal release pattern, Chem. Eng. Sci., 60(20), pp. 5415-5424, 2005. DOI: 10.1016/j.ces.2005.04.023
[6] Xu, L., Luo, M., Yang, L., Wei, X., Lin, X. and Liu, H., Encapsulation of pannonibacter phragmitetus LSSE-09 in alginate- carboxymethyl cellulose capsules for reduction of hexavalent chromium under alkaline conditions, J. Ind. Microbiol. Biotechnol., 38(10), pp. 1709-1718, 2011. DOI: 10.1007/s10295-011-0960-5
[7] Purnomo, C., Respito, A., Sitanggang, E.P.,and Mulyono, P., Slow release fertilizer preparation from sugar cane industrial waste, Environ. Technol. Innov., 10, pp. 275-280, 2018. DOI: 10.1016/j.eti.2018.02.010
[8] de Azevedo, A.R.G., Alexandre, J., Xavier, G.deC. and Pedroti, L.G., Recycling paper industry effluent sludge for use in mortars: a sustainability perspective, J. Clean. Prod., 192, pp. 335-346, 2018. DOI: 10.1016/j.jclepro.2018.05.011
[9] Wen, P., Han, Y., Wu, Z., He, Y., Ye, B.C. and Wang, J., Rapid synthesis of a corncob-based semi-interpenetrating polymer network slow-release nitrogen fertilizer by microwave irradiation to control water and nutrient losses, Arab. J. Chem., 10(7), pp. 922-934, 2017. DOI: 10.1016/j.arabjc.2017.03.002
[10] Instituto Colombiano Agropecuario ICA Subgerencia de Protección y Regulación, Comercialización de fertilizantes y acondicionadores de suelos, Bogotá, 2014.
[11] López-Ritas, J. and López-Melida, J., El diagnóstico de suelos y plantas. Métodos de campo y laboratorio, 4th ed. Madrid, 1990, 363 P.
[12] Esser-kahn A.P., Odom, S.A., Sottos, N.R., White, S.R. and Moore, S., Triggered release from polymer capsules, Macromolecules, 44(14), pp. 5539-5553, 2011. DOI: 10.1021/ma201014n
[13] Aguilar, Y., Preparación y evaluación en suelo de fertilizantes de liberación controlada (NPK) cubiertos con polímeros biodegradables, Tesís de Maestría, Departamento de Química, Universidad Nacional de Colombia, Bogotá, Colombia, 2014.
[14] Kramer, P.J., Plant and soil water relationships: a modern synthesis. New York: McGraw-Hill, 1969.
[15] Dash, S., Murthy, P.N., Nath, L. and Chowdhury, P., Kinetic modeling on drug release from controlled drug delivery systems, Acta Pol. Pharm. — Drug Res., 67(3), pp. 217-223, 2010.
[16] Azhar, F.F., Shahbazpour, E. and Olad A., pH sensitive and controlled release system based on cellulose nanofibers-poly vinyl alcohol hydrogels for cisplatin delivery, Fibers and Polymers, 18(3), pp. 416-423, 2017. DOI: 10.1007/s12221-017-6958-5.
[17] Balcerzak, J. and Mucha, M., Analysis of model drug release kinetics from complex matrices of polyactide-chitosan, Prog. Chem. Appl. Chitin Its Deriv., 15, pp. 117-126, 2010.
[18] Korsmeyer, R.W., Gurny, R., Doelker, E., Buri P. and Peppas, N.A., Mechanisms of solute release from porous hydrophilic polymers, Int. J. Pharm., 15(1), pp. 25-35, 1983. DOI: 10.1016/0378-5173(83)90064-9
[19] Wang, J., Wu, W. and Lin, Z., Kinetics and thermodynamics of the water sorption of 2-hydroxyethyl methacrylate/styrene copolymer hydrogels, J. Appl. Polym. Sci., 109(5), pp. 3018-3023, 2008. DOI: 10.1002/app.28403
[20] Ritger, P.L. and Peppas, N.A., A simple equation for the description of solute release, J. Control. Release, 5(1), pp. 23-36, 1987. DOI: 10.1016/0168-3659(87)90034-4. DOI:10.1016/0168-3659(87)90035-6
[21] Ammar, H., Abid, M. and Abid, S., Cellulose fibers obtained by organosolv process from date palm rachis (Phoenix dactylifera L.), in: IOP Conference Series: Materials Science and Engineering, 28, 2012. DOI: 10.1088/1757-899X/28/1/012002
[22] Summerell, B.A., Leslie, J.F. and Bullock, S., The fusarium laboratory manual. Ames: Wiley-Blackwell, 2006.

M. Montoya-Álvarez, is Msc. Grupo Sostenibilidad, Infraestructura y Territorio-SITE. Universidad EIA, Envigado, Colombia.
ORICID: 0000-0001-9488-1037

A.M. Quinchía-Figueroa, is PhD. Directora de Maestrías y Doctorado, Universidad EIA. Grupo Sostenibilidad, Infraestructura y Territorio-SITE. Universidad EIA, Envigado, Colombia.
ORICID: 0000-0003-3362-4410

O.González-Murillo, is Msc. Director de Investigación y Desarrollo Grupo Abonamos - Sobiotech. Guarne, Colombia.
ORICID: 0000-0003-4922-6986

P. Araque-Marín, is PhD(c), Director Grupo de Investigación e Innovación en Formulaciones Químicas, Universidad EIA, Envigado, Colombia.
ORICID: 0000-0002-8225-472X

UNIVERSIDAD NACIONAL DE COLOMBIA
SEDE MEDELLÍN
FACULTAD DE MINAS

Área Curricular de Ingeniería Química e Ingeniería de Petróleos

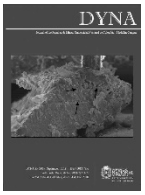
Oferta de Posgrados

Maestría en Ingeniería - Ingeniería Química
Maestría en Ingeniería - Ingeniería de Petróleos
Doctorado en Ingeniería - Sistemas Energéticos

Mayor información:

E-mail: qcaypet_med@unal.edu.co
Teléfono: (57-4) 425 5317

UNIVERSIDAD NACIONAL DE COLOMBIA
SEDE MEDELLÍN
FACULTAD DE MINAS



DYNA
http://dyna.medellin.unal.edu.co/

Design of metacognitive expectations of cognitive functions through ontological representations

Dalia P. Madera-Doval [a], Manuel F. Caro-Piñeres [a], Adán A. Gómez-Salgado [a], Ana M. Cardozo-Soto [a] & Jovani A. Jiménez-Builes [b]

[a] *Departamento de Informática Educativa, Universidad de Córdoba, Montería, Colombia. dmaderadoval@correo.unicordoba.edu.co, manuelcaro@correo.unicordoba.edu.co, aagomez@correo.unicordoba.edu.co, acardozosoto30@correo.unicordoba.edu.co*
[b] *Facultad de Minas, Universidad Nacional de Colombia, Medellín, Colombia. jajimen1@unal.edu.co*

Received: April 13th, 2018. Received in revised form: August 28th, 2018. Accepted: September 7th, 2018.

Abstract
This paper presents a model of metacognitive expectations about the running time of cognitive functions in the metacognitive architecture CARINA. A formal and ontological representation is created that establishes the relationship between the process of observing a fact in the self-model and a belief stored in the semantic memory of the system. The cognitive ontology evidenced tracing and interchange information process among different kind of memories, such as: sensorial memory, semantic memory, procedural memory, prospective memory and working memory. The experiment carried out demonstrated the functionality of the model where expectations were generated for each observation and could be compared with the observed values in real time. Another type of result was the conceptual advance of an expectation, the formal mathematical representation, the design of the ontology and the model as a mechanism of implementation in CARINA architecture.

Keywords: artificial intelligence; expectations; computational metacognition; cognitive architecture CARINA; cognitive agent.

Diseño de expectativas metacognitivas de funciones cognitivas a través de representaciones ontológicas

Resumen
Este artículo presenta un modelo de expectativas metacognitivas sobre el tiempo de funcionamiento de las funciones cognitivas en la arquitectura metacognitiva CARINA. Se crea una representación formal y ontológica que establece la relación entre el proceso de observar un hecho en el auto-modelo y una creencia almacenada en la memoria semántica del sistema. La ontología cognitiva evidenció el proceso de búsqueda e intercambio de información entre diferentes tipos de recuerdos, tales como: memoria sensorial, memoria semántica, memoria de procedimientos, memoria prospectiva y memoria de trabajo. El experimento realizado demostró la funcionalidad del modelo en donde se generó expectativas para cada observación y podía compararlas con los valores observados en tiempo real. Otro tipo de resultado fue avance conceptual de una expectativa, la representación matemática formal, el diseño de la ontología y el modelo como un mecanismo de implementación en la arquitectura CARINA.

Palabras clave: inteligencia artificial; expectativas; metacognición computacional; arquitectura cognitiva; agente cognitivo.

1. Introduction

Humans and other agents are able not only to coordinate their actions with their current sensorimotor state, but also plan and act in view of the future. They can propose to achieve distal goals using anticipatory mechanisms named expectations [1].

A crucial feature of an Intelligent Agent is being proactive and not just reactive, i.e., they have a capacity to use anticipatory mechanisms [2]. This ability allows them to deal with the future by mental representations or specific forms of learning [3]. The use of this anticipation determines the purposive character of the behavior of the Intelligent Agent for its own internal explicit goal representation and

How to cite: Madera-Doval, D.P., Caro-Piñeres, M.F., Gómez-Salgado, A.A., Cardozo-Soto, A.M. and Jiménez-Builes, J.A., Design of metacognitive expectations of cognitive functions through ontological representations. DYNA, 85(206), pp. 194-201, September, 2018.

© The author; licensee Universidad Nacional de Colombia.

allows self-modification of its own mental representation for virtually 'exploring' possible actions, events, and results: "what will/would happen if…?" [4]. The metacognitive ability may be to explain errors in a cognitive task or it may be to select between cognitive "algorithms" to perform reasoning.

An Intelligent System with metacognitive abilities makes explicit its components, capabilities, actions, percepts, and internal state information in a structure called a self-model. It uses this information to declare expectations about how its activities will affect perceptual and state information as well as monitoring the operation of its actions and its sensory feedback against its expectations, waiting for violations to occur [5]. The execution time, or running time, is the time of continued system operation required in a given environment in order to execute a program or algorithm [6].

Several authors have addressed the generation of expectations regarding the execution time of programs. Duda [6] defines the elapsed time *t*, as the time required to execute a program correctly in a given computing system, where the expectation of the elapsed time will be derived as functions of the execution time *t*. The expectation depends on: i) frequency and duration of failures, (ii) workload of the system and (iii) minimum execution time *t.* Sun and Peterson [7] propose a formal model where the estimation of the system execution time is calculated from the expectation of the maximum execution time of all processors in the computing system.

In the described context, our motivation is to provide a model of metacognitive expectations that represents a hypothesis or projection of current knowledge about running time of a cognitive function that is executed at the object-level. Expectations enable the reasoner to be prepared for the future, the reasoner can thus generate contingency plans to avoid anticipated failures [8]. The identified problem is related to the modeling of metacognitive expectations based on an observation process that uses information obtained from the self-model of a cognitive agent when a cognitive function is executed at its object-level.

This paper is organized as follows: Section 2 "Materials and Methods" describes the formal representation of metacognitive expectation based on observation and presents a general panorama about the structure of the CARINA cognitive architecture. Section 3 "Model of expectations in CARINA" presents the process of triggering a metacognitive expectation in the CARINA architecture. Section 4 "Computational implementation of metacognitive expectations" describes the internal representation of a metacognitive expectation; and some components of the memory system that use the ontology. Section 5 "Validation, result and discussion" presents empirical results within a metacognitive architecture demonstrating the ability to generate metacognitive expectations; and the final section presents the conclusions of this research.

2. Materials and methods

2.1. Formal definition of expectations

In this section we describe the formal representation of metacognitive expectation using elements of denotational mathematics proposed by Wang [9].

An expectation represents a hypothesis or projection of current knowledge [10]. A metacognitive expectation with respect to the execution time of a cognitive function that is executed at the object-level has an observation of a metacognitive sensor (o), an attribute of the observation that represents the execution time (ϱ), the expected value (ν) and the set of rules that generates the expectation (P). Formally a metacognitive expectation (η) about observation (o) is a 4-tuple, i.e.:

$$\eta \triangleq < o, \varrho, \nu, P > \quad (1)$$

Where:

η is an expectation about an observation o.

o represents an observation from a sensor ς, with $o \triangleq < \psi, \tau, \upsilon >$, where:

ψ is the instance of a profile of a cognitive function that is running in the object level.

τ is the current execution time of cognitive function.

υ is the unit in which the execution time is measured in milliseconds.

ϱ is an attribute of the observation o, with $o \prec \psi \triangleq A_o \supset A_\psi$. A_o represents the set of attributes of the observation o from the sensor ς. A_ψ represents the set of attributes of profile ψ of a cognitive function χ.

ν is expected value for the field ρ; the field is retrieved from semantic memory. With $o = \beta \triangleq A_o = A_\beta$, where β is a belief in the semantic memory and ϱ is a common field for o and β.

P is a set of rules that retrieve information from different types of memory in order to generate an expectation.

2.2. CARINA cognitive architecture

CARINA is a meta-cognitive architecture for artificial intelligent agents. CARINA is derived from the MISM Metacognitive Metamodel [11]. CARINA integrates self-regulation and meta-memory with support for the meta-cognitive mechanisms of introspective monitoring and meta-level control. In this sense CARINA assumes a functional approach to philosophy of mind, according to Piccinini, Fodor, and Scheutz [12-14]. According to Machamer, Darden, and Craver [15], the term ''mechanism" includes entities and activities involving entities (i.e., including both static and dynamic aspects). The entities in CARINA are called "cognitive elements".

In accordance with MISM, CARINA is composed of three types of cognitive elements: structural elements, functional elements, and basic elements. Structural elements are containers into which the functional and basic elements are embedded. The main structural element is the "Cognitive level". The functional elements are tasks that enable reasoning and decision-making. Basic elements consist of the set of elements that participate and interact in reasoning and meta-reasoning processes. The main functional elements in CARINA are reasoning task and meta-reasoning task. Reasoning tasks (RT) are actions that enable the processing (transformation, reduction, elaboration, storage and retrieval) of information by applying knowledge and decision making in order to meet the objectives of the system. A meta-reasoning task (MT) may be used to explain errors in some

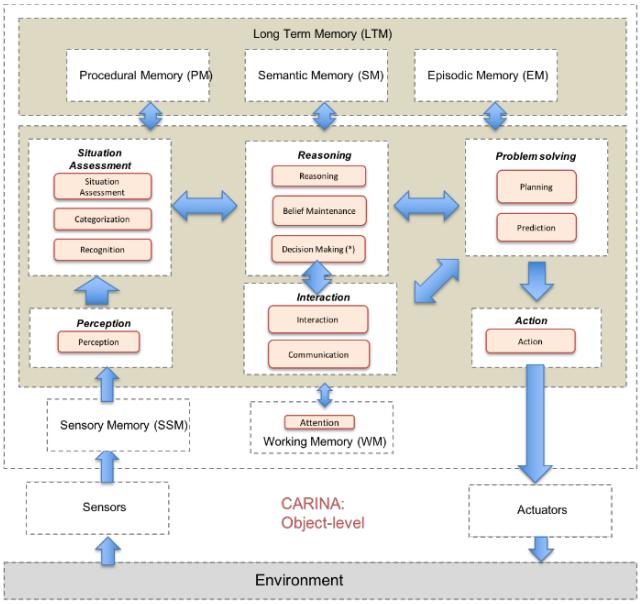


Figure 1. CARINA: Cognitive architecture for artificial intelligent agents. Source: Image Generated by Authors

reasoning task or it may be used to select between "cognitive algorithms" to perform the reasoning [16].

CARINA ≙ (OL, ML)
Where OL ≙ (PS, SAS, RS, IS, PSS, AS, MoW)
With PS ≙ (perception)
SAS ≙ (situation assessment, categorization, recognition)
RS ≙ (reasoning, belief maintenance, decision making)
IS ≙ (interaction, communication)
PSS ≙(planning, prediction)
AS≙ (action)
MoW

In CARINA, object-level has stages which are sets of cognitive functions (CF): Perception Stage (Perception CF), Situation Assessment Stage (Situation Assessment CF, Categorization CF, and Recognition CF), Reasoning Stage (Reasoning CF, Belief Maintenance CF, and Decision Making CF), Problem Solving Stage (Planning CF and Prediction CF), Interaction Stage (Interaction CF and Communication CF) and Action Stage (Action CF) as shown in Fig. 1. The meta-level contains a dynamic model of the object-level.

The meta-level includes the components, knowledge and mechanisms necessary for a system to monitor and control its own learning and reasoning processes. The meta-level of CARINA has two types of metacognition:

ML ≙ (SR, M)
SR ≙ (M, C)
M≙(Identification,Detection, Explanation, Goal Generation)
C ≙ (Strategy Selection)
MM≙ (MS, MKSS, JS, CS)
MS ≙ (Identification, Detection)
MKSS ≙ (Goal Generation, Explanation)
JS ≙ (Judgment)
CS ≙ (Strategy Selection)

i. Self-regulation: this type of metacognition monitors and controls the reasoning process that takes place at the object-level. Self-regulation contains two stages, which are sets of meta-cognitive functions (MCF): Monitoring Stage (Identification MCF, Detection MCF, Explanation MCF, and Goal Generation MCF) and Control Stage (Strategy Selection MCF).
ii. Meta-memory: is a component of meta-cognition [17]. The meta-memory in CARINA is a mechanism that allows adaptation to change in the constraints of a memory task [18].This meta-memory mechanism contains four stages which are sets of metacognitive functions (MCF): Monitoring Stage (Identification MCF and Detection MCF), Meta-Knowledge Search Stage (Goal Generation MCF and Explanation MCF), Judgment Stage (Judgment MCF) and Control Stage (Strategy Selection MCF).

3. Model of expectations in CARINA

Introspective monitoring is a meta-reasoning mechanism implemented at the meta-level in CARINA. Using the common terms of cognitive science, the notion of ''mechanism" involves both representations as well as cognitive mechanisms and processes operating on them [19]. Introspective monitoring includes mechanisms for detecting reasoning failures at the object-level. The main purpose of monitoring is to provide enough information to make effective decisions in the meta-level control [20]. The monitoring process is done through information feedback that is gathered at the meta-level from the object level, see Fig. 2. Thus, each cognitive task executed in the object level has a performance profile that is continuously updated in the meta-level. The performance profile is used to evaluate the results of each reasoning task.

CARINA is conformed by two cognitive levels called object level and meta-level i.e.

CARINA ≙ (OL, ML)

The object level (OL) contains the working memory where the self-model is located.

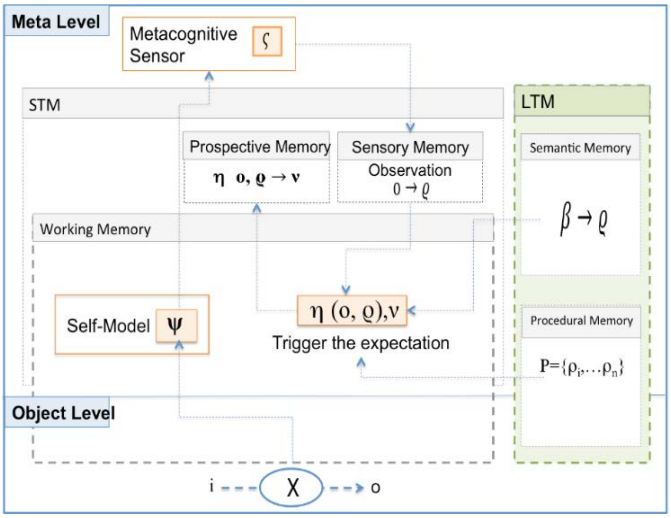


Figure 2. Process of triggering metacognitive expectations in CARINA. Source: Image Generated by Authors

According to Caro, Gomez, and Giraldo [20], when the cognitive function (χ) is executed at the object level with an input (IP), output (OP) and start time (B), a profile is automatically generated for the cognitive function in the self-model with the fields.

$\psi \triangleq (ID, B, E, S, C, IP, OP)$, with:

ID is the identifier of the cognitive function.
B is the time stamp of when the cognitive function was started.
E is the time stamp of when the cognitive function is finished.
S is the state of the cognitive function, s∈S and S={active, inactive}
C is the priority level for focus attention c∈C and C={low, medium, high}.
IP is the set of parameters used as input of the cognitive function.
OP is the output of the cognitive function.

The self-model contains the profile (ψ) of the cognitive function (χ). The meta-level includes the necessary mechanisms for a system to monitor its own learning and reasoning processes. In the meta-level of CARINA there is a metacognitive sensor (ς). A metacognitive sensor is an element of the meta-level. The function of metacognitive sensor is to monitor the profile of the cognitive function; this sensor has a sensory memory that stores the observation (o), taking into account that:

$$o \prec \psi \triangleq A_O \supset A_\psi \quad (2)$$

In formula (2), we can appreciate the fields of profile of cognitive function expressed as: $A_\psi \triangleq (ID, B)$ and the fields that are observed $A_O \triangleq (ID, B, E, S, C, IP, OP)$.

Whereas in semantic memory a field (ρ) is created, which consists of the average time of execution of all cognitive functions.

$$\varrho_e = \frac{\sum_{i=1}^{n} \beta_i \cdot \varrho_\nu}{n} \; With \; o = \beta \triangleq A_o = A_\beta \quad (3)$$

The formula (3) is based in [10] who affirms that expectations may emanate from a mental process such as an arithmetic check of a mathematics computation [10], For this, formula (3) represents the average of the execution time where (β) represents a belief retrieved from the semantic memory, (o) is a fact of the observation that is generated in the sensorial memory taking into account $A_o = A_\beta$. In this case, they are equivalent and the belief (β) is extracted from the semantic memory and all the values of A_β are compared with the values of A_o. In the working memory the expectation is generated with the observation field (ρ) The expected value of the semantic memory is generated with the average time and the unit of time, which causes an expectation. This is based in [21] which establishes that specific mental process that forms an expectation may be a memory process that retrieves an expectation from memory.

To verify the expectation (η) refer a set of rules (P), which are in the procedural memory. There are two types of rules to trigger and one [10] to validate; the rule we use is the process of triggering the expectation.

Prospective memory is a particular type of short-term memory, understood as the anticipatory capacity for the future, where it is expected to develop at a given time and the expected value (ν). If the field of observation (o) does not match, then a violation of expectation will be determined..

4. Computational implementation of metacognitive expectations

In this section we describe the internal representation of a metacognitive expectation and some components of memory system using ontology. Ontology is an explicit specification of knowledge level of a conceptualization, which can be affected by a particular domain or task, for which it has been created [22].

According to Gómes, Benjamins [23], Stojanovic, Maedche, Motik and Stojanovic [24]. Ontologies are comprised of several components:

- A set of concepts (also known as classes) and a hierarchy among concepts.
- A set of relationships between concepts.
- A set of properties, which are a special case of relationship.
- A set of axioms, rules that are always valid.

Table 1.
Piece of code: Structure of the cognitive ontology.

1	ObservationField ⊑ Field
2	ObservationCFIP ⊑ ObservationField
3	ObservationCFP ⊑ ObservationField
4	ObservationTime ⊑ ObservationField
5	ObservationUnitOfTime ⊑ ObservationField
6	ObservationField ⊑ Field
7	Field ⊑ Thing
8	MetacognitiveSensor
9	MetacognitiveSensor ⊑ Thing
10	CognitiveFunction ⊑ Belief
11	CognitiveFunctionInstanceProfile ⊑ Belief
12	CognitiveFunctionProfile ⊑ Belief
13	ComputationalStrategy ⊑ Belief
14	Number ⊑ Belief
15	UnitOfTime ⊑ Belief
16	CognitiveFunction ⊑ Belief
17	Belief ⊑ SemanticMemoryUnit
18	SemanticMeroryUnit ⊑ Thing
19	Observation ⊑ Fact
20	Fact ⊑ Thing

Source: Author's own elaboration

4.1. Metacognitive representation in ontology

Our ontology generates a metacognitive expectation of time with respect to the execution of a cognitive function in the metacognitive architecture. The implementation of the ontology was done using Protégé, version 5.2.0. This tool allows good level of details and its interface is user-friendly. WOL-DL (Web Ontology Language – Description Logic) was the formal language used for representation, World Wide Web Consortium (W3C) recommends WOL-DL. In this context the metacognitive problem is noted as ρ. ρ represents how to generate a metacognitive expectation with respect to the execution time of a cognitive function that is executed at the object level. Metacognitive expectation is represented as a hierarchical structure in ontology. First, the taxonomy of terms was created with the main concepts (classes): SemanticMemoryUnit. Creating subclasses Beliefs and Facts from derived concepts refined this hierarchy. Next, the fields of the Observation were defined. Malviya, Mishra, and Sahu define Object Properties as relationships between two instances of classes, whereas data properties describe relationships between instances and data values [25].

According to the structure of the ontology the classes depend on a super class Thing, the classes contain individuals and the object properties. The structure of the ontology is shown in Table 2 which contains an example of object and data properties of the cognitive ontology.

In the object properties, the domain and the range are created.

Table 2.
Piece of code: Object and Data Properties

```
1  hasCFIP(CogitiveFunctionInstanceProfile),
   (CognitiveFunction)
2  hasCFIP(CogitiveFunctionInstanceProfile),
   (CognitiveFunctionProfile)
3  hasCFIP(CogitiveFunctionInstanceProfile),
   (ComputacionalStrategy)
4  hasCFIPRunningTime(CogitiveFunctionInstan
   ceProfile),(Number)
5  hasCFIPUnitOfTime(CogitiveFunctionInstanc
   eProfile), (UnitOfTime)
6  hasCFP(CogitiveFunctionProfile),(Cogitive
   FunctionInstanceProfile)
7  hasObservation(Observation),(ObservationC
   FIP)
8  hasObservation(Observation),(ObservationC
   FP)
9  hasObservation(Observation),(ObservationT
   ime)
10 hasObservationUnitOfTime(Observation),(Ob
   servationUnitOfTime)
11 triggerRunningTimeExpectation(Observation
   ),(ObservationTime)
```

Source: Author's own elaboration

Table 3.
Piece of code: ID Data Properties

```
1  DataProperty(hasIDConcept)
```

Source: Author's own elaboration

Table 4.
Piece of code: Range and Domain of the data properties

```
1  hasIDConcept(SemanticMemoryUnit),(xsd:st
   ring)
```

Source: Author's own elaboration

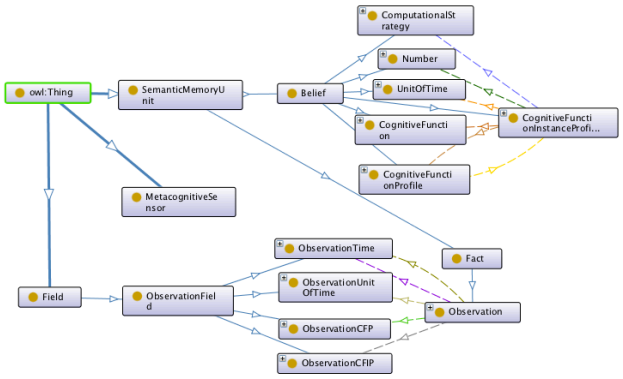


Figure 3. Network of concepts
Source: Image Generated by Authors

The data property has `IDConcept` which defines the identifier of the semantic memory unit. In the same way, the properties pertaining to each concept were represented as is shown in Table 4.

Ontology Instantiation is implemented as a simulation of the process of triggering expectations in CARINA. The next step is the use of the ontology as a simulation of triggering expectations at meta-level. This work explores the role of different types of memories in the triggering of metacognitive expectations in CARINA. We use production rules for representing the procedural knowledge needed to generate a metacognitive expectation. Table 5 shows a rule named R1. R1 gets the current observation from the sensory memory and generates an expectation for the field running time.

The sensorial memory contains the observation flow from the metacognitive sensor. In the ontology an observation has a relation (`hasObservationCFP`) that points to the profile of a cognitive function, and based on the observation, it looks for the beliefs (β) in the semantic memory to verify and extract the field of cognitive function profile (OCFP). Since the fact field of the observation must be equal to the beliefs (β), then the fields in the ontology should not be equal. One way to identify it is to make a datum of the `hasIDConcept` property of script type when the value is the same.

As stated by Gordon, Hobbs and Cox the reasoner calculates some expected outcome and compares it with the actual outcome that constitutes the feedback [26]. The observation field (OCFP) and the field (ϱ) in the belief (BCFP) are extracted and the two script data are matched to obtain the execution time.

Table 5.
Piece of code: Rule R1. R1 gets the current observation from the sensory memory and generate an expectation.

<Rule1001>	
1	Observation(?O)∧
2	hasObservationCFP(?O, ?OCFP) ∧
3	Belief(?B) ∧
4	hasCFIPCognitiveFunctionProfile(?B,?BCFP) ∧
5	hasIDConcept(?OCFP, ?IDO) ∧
6	hasIDConcept(?BCFP, ?IDB) ∧
7	equal(?IDO, IDB) ∧
8	hasCFIPRunningTime(?B, ?RT)
9	→triggerRunningTimeExpectation(?O,?RT)

Source: Author's own elaboration

`hasCFIPRunningTime` is the average of the sum of i=1 to *n* of the field (ϱ) in equation (3), the field (ϱ) of the belief about in formula (3), the field (ϱ) of the belief is automatically extracted in a new relationship called `triggerRunningTimeExpectation`.

4.1. Validation, result and discussion

An experiment was conducted to validate the performance of the model and its ability to generate expectations regarding the execution time of cognitive functions that are executed in the object-level of a cognitive agent based on CARINA. The syntactic analysis of a sentence was the cognitive task of the real world used in the experiment. In this experiment a cognitive agent identified the different grammatical categories in which the words of the language are grouped. These categories include the word's meaning, its grammatical function and the way in which it is structured, combined and modified.

The Left-corner is the algorithm implemented in the cognitive agent to decide if the chain of input symbols is a sentence in a given language. The algorithm determines the syntactic structure of the sentence according to a grammar [27].

We collect data from 200 executions of the cognitive task in CARINA, varying the available resources such as the size of the content of the semantic memory with respect to the domain of the cognitive task. Figure 4 shows the results of CARINA in terms of the expectations created with respect to the observations of the profile of cognitive functions that were executed in each cognitive cycle at object-level. The x-axis represents the 12 cognitive functions that were executed in CARINA to perform the cognitive task. The y-axis represents the execution time in milliseconds.

The blue bars represent the run-time expectation of 12 cognitive functions that were executed in CARINA to perform the cognitive task. CARINA calculates the run-time values using equation (3). The blue lines represent the observed runtime values at a time t_i. This is a clear example of the functionality of the model, because it generates expectations for each observation and is able to compare them against the observed values in real time.

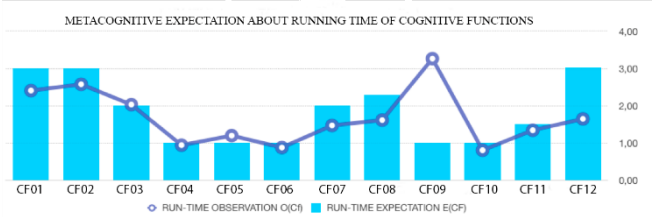


Figure 4. Metacognitive Expectations about Running Time of Cognitive Functions
Source: Image Generated by Authors

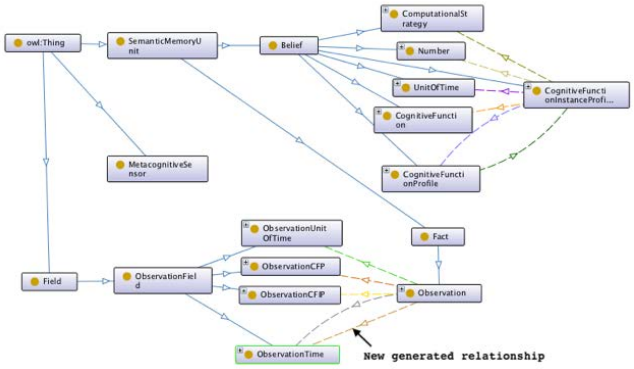


Figure 5. New generated relationship
Source: Image Generated by Authors

The scope of this investigation only applies to the generation of execution time expectations. In this sense, the model tests demonstrate the ability to generate expectations and the possibility of detecting anomalies in the expected execution times for cognitive functions. An interesting aspect for future investigations is to analyze the reasoning trace of the function that presents the anomaly, with the goal to determine the cause and possible corrective actions.

Another type of result obtained in this research was in terms of the conceptual advance of an expectation, the formal mathematical representation, the design of ontology and the model as an implementation mechanism. The cognitive ontology for reasoning about expectations in CARINA architecture facilitates the visualization of the expectations generated from the observations of the profiles of cognitive functions, as shown in Figure 5.

In Figure 5, the new relationship in ontology represents an expectation generated by the CARINA meta-level in the process of introspective monitoring. This result is promising because it will serve as a basis for the implementation of predictive capabilities of introspective monitoring in Carina's meta-level.

5. Conclusions

In this paper we have proposed an ontology based on an approach to automatically generate Metacognitive expectation about observations of the self-model. The ontology is based on [28], In this way, formal model represents the average of the execution time of a cognitive function executed at the object-level, using elements of the denotational mathematics proposed by Wang [9]. In this

formal model, the beliefs (β) (stored in semantic memory), and the observation process of facts (o) (stored in sensorial memory), are compared, expecting that $A_o = A_\beta$. In the working memory, the expectation is generated with the observation field (ρ), the expected value of the semantic memory (average running time of cognitive function) and the unit of time of execution.

Cognitive Ontology allowed us to develop a reasoning test according to a specific cognitive task in the CARINA Metacognitive Architecture. In this test, we applied rules that represent the necessary procedural knowledge to trigger the metacognitive expectations.

Also, the cognitive ontology resulted in the tracing and interchange of information process among different kind of memories, such as: sensorial memory, semantic memory, procedural memory, prospective memory and working memory. The above reaffirms what is proposed by Cox "a specific mental process that forms an expectation may be a memory process that retrieves an expectation from memory" [29]. This work provides advances in the implementation of metacognitive mechanisms such as introspective monitoring in CARINA architecture.

References

[1] Pezzulo, G., Coordinating with the future: the anticipatory nature of representation. Minds and Machines, 18(2), pp. 179-225. 2008. DOI: 10.1007/s11023-008-9095-5

[2] Castelfranchi, C. and Lorini, E., Cognitive anatomy and functions of expectations 1. Artificial Intelligence, (October). 2001.

[3] Castelfranchi, C. and Lorini, E., Cognitive anatomy and functions of expectations. In: IJCAI03 Workshop on Cognitive Modeling of Agents and Multi-Agent Interactions, 2003, pp. 9-11. DOI: 10.1109/IAT.2006.2

[4] Castelfranchi, C., For a systematic theory of expectations. BVAI, 3704, 2007, pp. 258-276. DOI: 10.1007/s11229-006-9156

[5] Haidarian, H., Dinalankara, W., Fults, S., Wilson, S., Perlis, D., Schmill, M.D. and Anderson, M.L., The metacognitive loop : an architecture for building robust intelligent systems. AAAI Fall Symposium, (II), 2010, pp. 33-39.

[6] Sevcik, C., The Effects Andrzej Duda. Information Processing Letters, 16, pp. 221-229,1983.

[7] Sun, J. and Peterson, G.D., An effective execution time approximation method for parallel computing. IEEE Transactions on Parallel and Distributed Systems (TPDS), 23(11), pp. 2024-2032, 2012. DOI: 10.1109/TPDS.2012.21

[8] Fox, S. and Leake, D., Introspective reasoning for index refinement in case-based reasoning. Journal of Experimental & Theoretical Artificial Intelligence, 13(1), pp. 63-88, 2001. DOI: 10.1080/09528130010029794

[9] Wang, Y., On contemporary denotational mathematics for computational intelligence. Lecture Notes in Computer Science (Including Subseries Lecture Notes in Artificial Intelligence and Lecture Notes in Bioinformatics), 5150 LNCS, 2008, pp. 6-29. DOI: 10.1007/978-3-540-87563-5_2

[10] Cox, M.T. and Ashwin, R., Introspective multistrategy learning: on the construction of learning strategies. Artificial Intelligence, 112(1), pp. 1-55. 1999. DOI: 10.1016/S0004-3702(99)00047-8

[11] Caro, M., Josyula, D., Cox, M. and Jiménez, J., Design and validation of a metamodel for metacognition support in artificial intelligent systems. Biologically Inspired Cognitive Architectures, 9, pp. 82-104, 2014. DOI: 10.1016/j.bica.2014.07.002

[12] Piccinini, G., The mind as neural software? Understanding functionalism, computationalism, and computational functionalism. Philosophy and Phenomenological Research, 81(2), pp. 269-311, 2010. DOI: 10.1111/j.1933-1592.2010.00356.x

[13] Fodor, J.A., The language of thought. New York (Vol. 4). 1975. DOI: 10.1016/0093-934X(77)90028-1

[14] Scheutz, M., Computational versus causal complexity. Minds and Machines, 11(4), pp. 543-566, 2001. DOI: 10.1023/A:1011855915651

[15] Machamer, P., Darden, L. and Craver, C.F., Thinking about mechanisms. Philosophy of Science, 67(1), pp. 1-25, 2000. DOI: 10.1086/392759

[16] Cox, M. and Raja, A., Metareasoning: an introduction. In: Cox and Raja (Ed.), In Metareasoning: Thinking about thinking, 2012, pp. 1-23, Cambridge. MA: MIT. DOI: 10.7551/mitpress/9780262014809.003.0001

[17] Cox, M., Oates, T. and Perlis, D., Toward an integrated metacognitive infrastructure. 2011 AAAI Fall Symposium, 2011, pp. 74-81. DOI: 10.1016/j.procs.2014.11.107

[18] Caro, M., Diaz, D. and Josyula, D., MetaThink: a MOF-based metacognitive modeling tool. Ieeexplore.Ieee.Org, pp. 351-358, 2013. DOI: 10.1109/ICCI-CC.2016.7862059

[19] Sun, R., Theoretical status of computational cognitive modeling. Cognitive Systems Research, 10(2), pp. 124-140, 2009. DOI: 10.1016/j.cogsys.2008.07.002

[20] Caro, M., Gomez, A. and Giraldo, J., Algorithmic knowledge profiles for introspective monitoring in artificial cognitive agents. In: 2017 IEEE 16th International Conference on Cognitive Informatics & Cognitive Computing (ICCI*CC), 2017, pp. 475-481. DOI: 10.1109/ICCI-CC.2017.8109792

[21] Cox, M., Introspective multistrategy learning: constructing a learning strategy under reasoning failure. Doctoral dissertation - Cox - 1996.

[22] Gruber, T.R., A translation approach to portable ontology specifications. Knowledge Acquisition, 5(2), pp. 199-220, 1993. DOI: 10.1006/knac.1993.1008

[23] Gómez, A. and Benjamins, R., Overview of knowledge sharing and reuse components: ontologies and problem-solving methods. In: IJCAI-99 Workshop on Ontologies and Problem-Solving Method (KRR5), 1999, pp. 1-15. DOI: 10.1.1.39.249.

[24] Stojanovic, L., Maedche, A., Motik, B. and Stojanovic, N., User-driven ontology evolution management. In: Knowledge Engineering and Knowledge Management: Ontologies and the Semantic Web, 2002, pp. 133-140. DOI:10.1145/637411.637413

[25] Malviya, N., Mishra, N. and Sahu, S., Developing university ontology using protégé OWL tool: process and reasoning. International Journal of Scientific & Engineering Research, 2(9), pp. 1-8, 2011.

[26] Gordon, A., Hobbs, J. and Cox, M., Anthropomorphic self-models for metareasoning agents. Metareasoning: Thinking about Thinking, 129-135. 2011. DOI: 10.7551/mitpress/9780262014809.003.0019

[27] La Serna, N., Un analizador sintático eficiente para gramáticas del español, Rev. investig. sist. inform., 1(1), pp. 19-26, 2004.

[28] Zhang, Z.J., Shi, T.Y. and Yu, Z.H., A method for building geographical conditions ontology attribute library: taking Tianjin as an example. Applied Mechanics and Materials, 156, pp. 411-414, 2013. DOI: 10.4028/www.scientific.net/AMM.411-414.156

[29] Cox, M., Introspective multistrategy learning: constructing a learning strategy under reasoning failure, Thesis Dr. of Philosophy in Computer, Science Georgia Institute of Technology Introspective Mu. 1996b.



D.P. Madera-Doval, received a BSc. in Computer Science and Audiovisual Media (2017) from the Universidad de Córdoba, Colombia. She is currently a junior researcher in the Computer Research and Cognitive Computing Group at the Faculty of Education of the Universidad de Córdoba, Colombia. His research interests include: cognitive informatics, cognitive computing and artificial intelligence in education.
ORCID: 0000-0003-3451-9110



M.F. Caro-Piñeres, received a PhD. in Engineering - Systems and Information (2015) at the Universidad Nacional de Colombia - Medellín. Currently, he is an associate professor in the Department of Educational Computing and coordinator of the Computer Science and Cognitive Computing Research Group at the Faculty of Education of the Universidad de Córdoba, Colombia. His research interests include: cognitive informatics, cognitive computing and artificial intelligence in education.
ORCID: 0000-0001-6594-2187



A.A. Gómez-Salgado, received MSc. in Technology of Information Applied to Education (2012) in the Universidad Pedagógica Nacional, Esp. in Informatic and Multimedia (2006) in the Fundación Universitaria los Libertadores, Lic. in Educational Informatic and Audiovisual Media (2001). Currently, he is associate professor in the Department of Educational Computing at the Faculty of Education of the Universidad de Córdoba, Colombia. His research interests include: artificial intelligence - educational software development, knowledge representation, cognitive informatic, cognitive computing.
ORCID: 0000-0002-7676-8492



A.M. Cardozo-Soto, received a BSc. in Computer Science and Audiovisual Media (2017) from the Universidad de Córdoba, Colombia. His research interests include: cognitive informatics, cognitive computing and artificial intelligence in education.
ORCID: 0000-0002-0915-6015



J.A. Jiménez-Builes, is a full time professor, at the Facultad de Minas, Universidad Nacional de Colombia, Medellín, Colombia. He holds a BSc. degreee in Computer Teaching Universidad de Medellin, Colombia and received an MSc. in System Engineering, and a PhD. Engineering from Universidad Nacional de Colombia, Medellín, Colombia. His research areas include: artificial intelligence in education, knowledge management, E-learning and T-learning.
ORCID: 0000-0001-7598-7696

UNIVERSIDAD NACIONAL DE COLOMBIA
SEDE MEDELLÍN
FACULTAD DE MINAS

Área Curricular de Ingeniería
de Sistemas e Informática

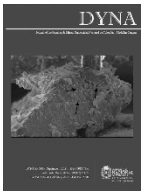
Oferta de Posgrados

Especialización en Sistemas
Especialización en Mercados de Energía
Maestría en Ingeniería - Ingeniería de Sistemas
Doctorado en Ingeniería- Sistemas e Informática

Mayor información:

E-mail: acsei_med@unal.edu.co
Teléfono: (57-4) 425 5365

UNIVERSIDAD NACIONAL DE COLOMBIA
SEDE MEDELLÍN
FACULTAD DE MINAS



DYNA
http://dyna.medellin.unal.edu.co/

Simulation-optimization techniques for closed-loop supply chain design with multiple objectives

William Javier Guerrero [a], Laura Andrea Sotelo-Cortés [b] & Enrique Romero-Mota [b]

[a] *Facultad de Ingeniería, Universidad de la Sabana, Chía, Colombia. william.guerrero1@unisabana.edu.co*
[b] *Escuela Colombiana de Ingeniería Julio Garavito, Bogotá, Colombia. l.sotelo-c@escuelaing.edu.co, enrique.romero@escuelaing.edu.co*

Received: February 23th, de 2018. Received in revised form: August 6th, 2018. Accepted: August 17th, 2018

Abstract
This paper presents a methodology for determining the optimal supply chain design with economic, environmental and risk management considerations. A multi-objective model based on mixed integer programming is proposed seeking three objectives: First, to minimize the total cost of transportation and the costs associated to the use of intermediate nodes. Second, to minimize the risks of product losses in transportation. Third, to minimize the environmental impact of CO2 emissions produced by transportation and storage operations. The proposed model is solved with two approaches: First, a commercial solver to compute the Pareto-optimal set of solutions. Second, a simulation-based optimization approach that allows to obtain statistically different but efficient solutions such that the decision-maker will be able to trade-off objectives while considering only Pareto optimal solutions. Experiments on random instances demonstrate the capability of the models and methods.

Keywords: supply chain design; risk; sustainability; simulation.

Técnicas de simulación-optimización para el diseño de cadenas de abastecimiento de ciclo cerrado con múltiples objetivos

Resumen
El objetivo de este trabajo es determinar el diseño óptimo para una cadena de suministro de tres eslabones de acuerdo a consideraciones económicas, ambientales y de gestión de riesgo. Se plantea un modelo de programación entera mixta que busca simultáneamente: Primero, minimizar el costo total del transporte y el costo asociado al uso de nodos intermedios; Segundo, minimizar las pérdidas de producto en el transporte como factor de riesgo; Tercero, minimizar el impacto ambiental por emisiones de CO2 en cada una de las conexiones y nodos. El modelo se resuelve utilizando un método exacto y métodos de optimización vía simulación que permiten obtener distintas soluciones de tal manera que el usuario podrá escoger de acuerdo a sus prioridades. Experimentos en instancias aleatorias demuestran la capacidad de los modelos y métodos propuestos.

Palabras clave: diseño de cadena de abastecimiento; riesgo; sostenibilidad; simulación.

1. Introduction

A firm is considered to be successful when it positions its brand on the market with profitable operations. This is achieved by an efficient supply chain that allows managing the resources strategically. In this manner, accomplishing satisfactory service levels and highly attractive margins result in a differentiating advantage.

Configuring a supply chain design requires coordinating the flow of goods, money, and information between suppliers, manufacturers, distributors and retailers [1,2]. At the design stage of a supply chain, coordination is performed considering the decisions of facility location and transportation of goods in order to achieve high performance.

The performance of a supply chain design is often measured as the total cost of inventory management, transportation, and the fixed cost of using the facilities and other resources. Nevertheless, current requirements of the

How to cite: Guerrero, W.J., Sotelo-Cortés, L.A. and Romero-Mota, E., Simulation-optimization techniques for closed-loop supply chain design with multiple objectives. DYNA, 85(206), pp. 202-210, September, 2018.

© The author; licensee Universidad Nacional de Colombia.

environment force companies to consider other performance metrics to evaluate the sustainability of the operations. Thus, operational risks, social impacts and environmental aspects must be considered in the decision making process of designing supply chains.

This paper proposes to study a non-hierarchical, or non-tier, supply chain design problem. This means that the product is shipped to the customers through different network levels, without any hierarchical sequences. E.g.: Products can be supplied directly from the production center or through intermediate nodes without any specific order.

Moreover, this work will use as solution method the combination of optimization models and Monte Carlo simulation. This represents a powerful development, since simulation enables to examine impacts while taking into account variability of the parameters, which makes the model to represent more realistic situations and to gain confidence in the solutions.

Then, the main contribution of the article is to carry out a comprehensive study of a supply chain design problem with the following features: 1) A supply chain design model with a generic structure is analyzed, by assuming a non-hierarchical closed-loop configuration, which generalizes the topology of a hierarchical supply chain. 2) Three objective functions are involved in the decision-making process in order to tackle the green challenge of supply chain designs and the trade-off with profitability. These objectives are associated to the economic, environmental, and risk dimensions of the considered operations. 3) Variability of the performance indicators associated to uncertainty is studied by integrating simulation techniques while evaluating the performance of the supply chain designs.

This paper is structured as follows: section 2 presents the state of the art, section 3 presents the proposed mathematical model, section 4 corresponds to the methodologies of developed solutions, and sections 5 and 6 present the results and the conclusions, accordingly.

2. State of the art

The supply chain refers to all activities related to the flow and transformation of goods and services from raw materials to final consumption [3]. Supply chain management can be classified into two broad categories: configuration and coordination. First, the configuration relates to the high-level design and the basic infrastructure of the supply chain. On the other hand, coordination is related to tactical and operational decisions [4]. This work is focused on the configuration category, which integrates elements of risk management and sustainability. For this reason, the literature review is presented around these concepts and their relationship.

Closed-loop supply chains are defined by Guide & Van Wassenhove [5] as the design, control and operation of a system to maximize the value creation over a product's life cycle. The literature on the topic shows that progressive attention is focused on public awareness and laws to make the designs less harmful for the environment [6]. A closed-loop supply chain includes the concept of reverse logistics, in which residuals are collected at the customer after consumption to be recycled or destroyed.

Some works in the literature propose different approaches and variables to take into account relevant variables such as the prices, which affect the demand and thus the flow [7], provider's ratings [8], as well as the extensions to more than one distribution channel [9], and even for more than one period [10]. Hierarchical models that take into account social and environmental impacts are proposed by [11] or diverse combinations of the previous ones, adding variables such as multi period time horizon [12].

Specifically, the design of supply networks that involve more than one objective to be optimized, comprises a wide variety of works that include objectives of different nature such as the minimization of transportation costs based on risk neutral criteria [13], economic and environmental performance according to life cycle assessment (LCA) principles [14], minimization of total daily cost and environmental impacts when applied to a hydrogen supply chain [15], decision analysis of a supply network integrating costs, customer service, and volume of deliveries [16].

According to the supply chain design supported in different models, environmental issues have not always been integrated to these models, or have not been evaluated explicitly. Nonetheless, based on the review by Eskandarpoura, Dejaxa, Miemczykb & Péton [17], it is concluded that some models include one measure regarding the environment and the social impact, either in the objective function or in the model constraints, while optimizing decisions related to the supply chain design, including location of facilities, means of transportation, design of production processes, technological options, among others [17]. This dimension has been treated with models such as: Life Cycle Assessment, reasoning maps, Analytic Hierarchy Process, Analytic Network Process, Data Envelopment Analysis, equilibrium models, simulation, and others. The main measure to estimate environmental impacts is based on carbon emission indicators, wastes, energetic consumption and recycled material [18]. Authors like Quariguasi Frota Neto, Bloemhof-Ruwaard, van Nunen, & van Heck [19] show that advantages of solving problems using multi-objective programming.

Additionally, regarding risk management, the literature shows that several works have been formulated for supply chain design models considering some kind of risk. For example, a multi-objective stochastic programming for the supply chain design considering financial risks is proposed in [20]; a stochastic model for risk management in global supply chain networks of multiple-stage, incorporating demand, exchange rate and the disruption risks is presented in [21]; a case-oriented approach to a lead-acid battery closed-loop supply chain network design under risk and uncertainty is studied in [22]; [23] presents a conceptual model for managing supply chain network risk. Tuncel and Alpan [24] propose the use of Petri nets to model and analyze a supply chain network subject to various risks. Moreover, simulation is a powerful tool to evaluate scenarios of the supply chain and to generate different options to improve operations. Further, tools for measuring and managing risks have been proposed, such as the "Supply Chain Resilience Assessment and Management (SCRAM™)". This tool focuses on environmental risks only and has proven to increase of the recovery capacity and a higher performance of the supply chain [25].

Table 1.
Literature review

Author	Sust.	Risk	Uncert.
Azarona, Browna, Tarima, & Modarrese [20]		X	X
Pan & Nagi[28]			X
El-Sayed, Afia, & El-Kharbotly [29]		X	
PrasannaVenkatesan & Kumanan [30]		X	
Pishvaee & Razm [31]	X		X
Pishvaee, Razmi, & Torabi [32]	X		X
Ruiz-Femenia, Guillén-Gosálbez, Jiménez, & Caballero [33]	X		X
Hamed & Govindan [34]	X	X	
Yang, Liu, & Yang [13]		X	X
Nooraie & Mellat Parastb[35]		X	
Jindal & Sangwan [36]	X		X
Mota, Gomes, Carvalho, & Barbosa-Povoa[37]	X		
Montoya-Torres[38]	X		

Source: Own elaboration

For this work the solution methods are based on methodologies that combine simulation with optimization. The integration of optimization with simulation, is a process whose objective is to minimize the resources spent while maximizing the information obtained in a simulation experiment [26]. Simulation-optimization techniques have been used for a few decades, firstly with a stochastic approximation during the 1950s. However, this technique has become more powerful in recent years due to the increase in computational capacity, that allowed providing alternative solutions of high-quality systems and promoting the introduction of uncertainty and risks [27]. Some examples of this kind of methods include the following: search methods based on probability gradients, finite differences and perturbation analysis; stochastic optimization; Surface response methodology; Heuristic methods such as genetic algorithms, evolutionary strategies and statistical methods such as classification and selection [27].

Table 1 summarizes relevant works of this literature review, developed in the last decade, which highlights interesting features of the chain design problems: sustainability (Sust), the risks (Risk) and other sources of uncertainty (Uncert.), as applicable:

According to the review developed, it is concluded that several authors have worked on subjects related to supply chain design, risks and sustainability, while including uncertainty in order to consider variability of parameters. However, it is not common to find works that explicitly consider these aspects under uncertainty in an integral manner. Furthermore, stochastic programming modeling techniques predominate over simulation techniques as a solution tool. Nevertheless, it is well known that simulation techniques are more flexible and scalable to tackle large scale design problems.

3. Mathematical formulations

We consider a supply chain (SC) composed by 6 levels or echelons. Four levels are available to connect the production sites with the nodes representing the final customers. Further, two additional levels are included: one for recollection sites

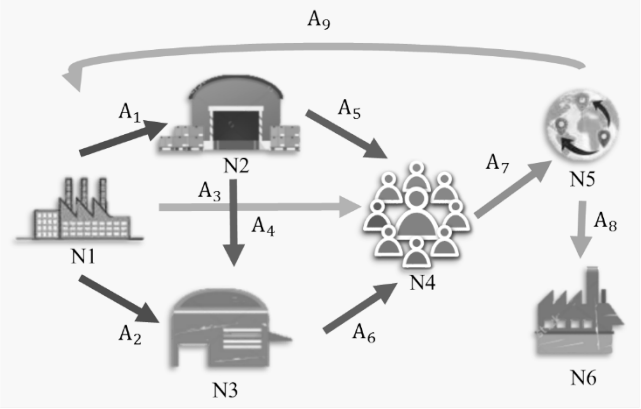


Figure 1. Supply network graph.
Source: Own elaboration

N1: Level 1; N2: Level 2; N3: Level 3; N4: Level 4; N5: Level 5; N6: Level 6.

for collecting recyclable materials such as packing boxes, and the second one are destruction sites for the non recyclable waste. The assumptions made for the proposed model are the following: First, to satisfy the final customer's demand (at level 4 of the SC), the product is delivered from the production centers (level 1) and distributed through warehouses or distribution centers, passing through retailers if necessary (levels 2 and 3, accordingly). Each facility is characterized for having a limited capacity, with known costs associated to CO2 emissions when the node is used.

Product transportation can be performed by two types of vehicles (Type I and Type II) whose characteristics change according to load capacity, cost, and the amount of CO2 emissions. Product may flow within the facilities at the same level of at different levels until the consumption nodes.

Additionally, product flow decisions consider a proportion to product loss in the arcs previous to customer delivery as a risk measure. After the product fulfils its function with the final customer, a proportion of this is picked and transported towards recollection centers (level 5). There, the selection process to decide whether the product can return to the plants to be reused or if it is sent to a destruction level is made (level 6). At this stage of the network, the closed-cycle is implemented. In Fig. 1, the studied network is shown.

The problem can be formulated using the following notation. A directed, completed and weighted graph G={N,A} is defined, consisting of a set of nodes N, which represents the total number of facilities and customers of the supply chain. This set N includes the following subsets:

N1: Set of production plants
N2: Set of distribution centers
N3: Set of retailers
N4: Set of customers
N5: Set of collection centers
N6: Set of destruction centers

Additionally, the graph consists of a set of directed arcs A composed of the following arcs:

A_1 : Arcs connecting production plants (N_1) to distribution centers (N_2)

A_2 : Arcs connecting production plants (N_1) to retailers

(N_3)

A_3 : Arcs connecting production plants (N_1) to customers (N_4)

A_4 : Arcs connecting distribution centers (N_2) to retailers (N_3)

A_5 : Arcs connecting distribution centers (N_2) to customers (N_4)

A_6 : Arcs connecting retailers (N_3) to customers (N_4)

A_7 : Arcs connecting customers (N_4) to collection centers (N_5)

A_8 : Arcs connecting collection centers (N_5) to destruction centers (N_6)

A_9 : Arcs connecting collection centers (N_5) to production plants (N_1)

A set of transport modes M and a set of product types $T = \{new, recycled\}$ are considered. Furthermore, the following model parameters are considered:

C_{ijm}^T : Unitary transportation cost in the arc $(i,j) \in A$ using transportation mode $m \in M$

C_u^F: Financial cost for using the intermediate node $u \in N_2 \cup N_3$

C_{ti}^P: Unitary production cost of product type $t \in T$ at production plant $i \in N_1$

E_{ijm}^T: Unitary CO_2 emissions for transporting product in the arc $(i,j) \in A$ using transportation mode $m \in M$

E_u^F: CO_2 emissions for using the intermediate node $u \in N_2 \cup N_3$

S_{ijm}: Percentage of product loss in the arc $(i,j) \in A$ with transportation mode $m \in M$

Q_u: Reception and processing capacity at node $u \in N_1 \cup N_2 \cup N_3 \cup N_5 \cup N_6$

D_j: Customer's product demand in node $j \in N_4$

α_j: Expected proportion of product recovered from customers $j \in N_4$ to be taken to collection centers.

β_k: Expected proportion of product recovered from the collection center $k \in N_5$ to be sent back to production centers.

H: Very large number.

The proposed decision variables define the product flow on the network and activate the corresponding costs.

P_{ti}: Amount of product type $t \in T$ manufactured in the production center $i \in N_1$

X_{ijm}: Amount of product to transport in the arc $(i,j) \in A_1 \cup A_2 \cup A_3 \cup A_4 \cup A_5 \cup A_6$ by transportation mode $m \in M$.

Y_{ijm}: Amount of product to transport in the arc $(i,j) \in A_7$ by transportation mode $m \in M$

Z_{klm}: Amount of product to transport in the arc $(i,j) \in A_8$ by transportation mode $m \in M$

R_{kim}: Amount of product to transport in the arc $(i,j) \in A_9$ by transportation mode $m \in M$

$B_u = 1$, if the node $u \in N_2 \cup N_3$ is used to transport the product. 0, otherwise.

$W_{ijm} = 1$, if the arc $(i,j) \in A$ is used with the means of transport $m \in M$. 0, otherwise.

The proposed model seeks to optimize simultaneously the following three objectives:

1. Minimizing the total transportation cost + fixed cost of using nodes (location cost) + production cost. This is expressed in eq. (1).

$$Min\ A = \sum_{m\in M}\sum_{(i,j)\in A_1\cup A_2\cup A_3\cup A_4\cup A_5\cup A_6} C_{ijm}^T X_{ijm} + \sum_{u\in N_2\cup N_3} C_u^F B_u + \sum_{t\in T}\sum_{i\in N_1} C_{ti}^P P_{ti} + \sum_{m\in M}\sum_{(i,j)\in A_7} C_{ijm}^T Y_{ijm} + \sum_{m\in M}\sum_{(i,j)\in A_8} C_{ijm}^T Z_{ijm} + \sum_{m\in M}\sum_{(i,j)\in A_9} C_{ijm}^T R_{ijm} \quad (1)$$

2. Minimizing the total amount of CO2 emissions in transportation, and the operations at nodes. This is expressed by eq. (2).

$$Min\ G = \sum_{m\in M}\sum_{(i,j)\in A} E_{ijm}^T W_{ijm} + \sum_{u\in N_2\cup N_3} E_u^F B_u \quad (2)$$

3. Minimizing the risk of product losses in transportation, computed by eq. (3).

$$Min\ Q = \sum_{m\in M}\sum_{(i,j)\in A_1\cup A_2\cup A_3\cup A_4\cup A_5\cup A_6} S_{ijm} X_{ijm} + \sum_{m\in M}\sum_{(i,j)\in A_7} S_{ijm} Y_{ijm} + \sum_{m\in M}\sum_{(i,j)\in A_9} S_{ijm} R_{ijm} \quad (3)$$

The model is subject to the following constraints:

First, the demand must be completely fulfilled at each demand node:

$$\sum_{m\in M}\sum_{i\,|\,(i,j)\in A_1\cup A_2\cup A_3\cup A_4\cup A_5\cup A_6} (1 - S_{ijm}) X_{ijm} \geq D_j \quad \forall\, j \in N_4 \quad (4)$$

Also, the SC has limited capacities. Thus, eq. (5) limits the reception capacity of products at each node.

$$\sum_{m\in M}\sum_{i\,|\,(i,u)\in A_1\cup A_2\cup A_4} X_{ium} \leq Q_u B_u \quad \forall\, u \in N_2 \cup N_3 \quad (5)$$

Eq. (6) limits the production and reception capacity at each production center:

$$\sum_{t\in T} P_{ti} \leq Q_i \ \forall\, i \in N_1 \quad (6)$$

Eq. (7) limits the amount of products that leave each production plant to be equal to the existing products:

$$\sum_{m\in M}\sum_{j\,|\,(i,j)\in A_1\cup A_2\cup A_3} X_{ijm} = \sum_{t\in T} P_{ti} \quad \forall i \in N_1 \quad (7)$$

Eq. (8) limits the reception capacity of products going from the collection center to each plant:

$$\sum_{k|(k,i)\in A_9}\sum_{m\in M} R_{kim}(1 - S_{kim}) \leq Q_i \ \forall\, i \in N_1 \quad (8)$$

Eq. (9) limits the reception capacity of products at collection centers.

$$\sum_{j|(j,k)\in A_7}\sum_{m\in M} Y_{jkm}(1 - S_{jkm}) \leq Q_k \quad \forall\, k \in N_5 \quad (9)$$

The following constraints coordinate the decision variables. Eq. (10) forces that if an arc is used, the associated nodes must be used:

$$\sum_{i|(i,u)\in A_1\cup A_2\cup A_3\cup A_4}\ \sum_{m\in M} W_{ium} \leq B_u Q_u \quad \forall u \in N_2 \cup N_3 \quad (10)$$

Eq. (11)-(15) coordinate the integer and binary decision variables associated with transportation decisions:

$$H \cdot X_{ijm} \leq W_{ijm} \quad \forall (i,j) \in A_1 \cup A_2 \cup A_3 \cup A_4 \cup A_5 \cup A_6, \forall m \in M \tag{11}$$

$$H \cdot Y_{ijm} \leq W_{ijm} \quad \forall (i,j) \in A_7, \forall m \in M \tag{13}$$

$$H \cdot Z_{ijm} \leq W_{ijm} \quad \forall (i,j) \in A_8, \forall m \in M \tag{14}$$

$$H \cdot R_{ijm} \leq W_{ijm} \quad \forall (i,j) \in A_9, \forall m \in M \tag{15}$$

Eq. (16)-(19) are flow conservation constraints. The amount of product arriving at a destination node must be equal to the flow minus the proportion of product lost on the arc depending on the mode of transportation:

$$\sum_{i|(i,j)\in A_1 \cup A_2 \cup A_3 \cup A_4} \sum_{m \in M} X_{ijm} (1 - S_{ijm}) = \sum_{i|(j,i)\in A_4 \cup A_5 \cup A_6} \sum_{m \in M} X_{jim} \quad \forall j \in N_2 \cup N_3 \tag{16}$$

$$\sum_{i|(i,j)\in A_3 \cup A_5 \cup A_6} \sum_{m \in M} X_{ijm} (1 - S_{ijm}) = \sum_{k \in N_5} \sum_{m \in M} Y_{jkm} \quad \forall j \in N_4 \tag{17}$$

$$\sum_{j|(j,k)\in A_7} \sum_{m \in M} Y_{jkm}(1 - S_{jkm}) = \sum_{i|(k,i)\in A_9} \sum_{m \in M} R_{kim} + \sum_{l|(k,l)\in A_8} \sum_{m \in M} Z_{klm} \quad \forall k \in N_5 \tag{18}$$

Eq. (19) guarantees that the amount of product arriving at the production centers from the collection center must be equal to the amount of products recovered, discounting the loss factor:

$$\sum_{k|(k,i)\in A_9} \sum_{m \in M} R_{kim} (1 - S_{kim}) = P_{1i} \quad \forall i \in N_1 \tag{19}$$

Eq. (29) guarantees that the expected proportion of products is sent from the customers to the collection centers:

$$\sum_{k \in N_5} \sum_{m \in M} Y_{jkm} \geq \alpha_j D_j \quad \forall j \in N_4 \tag{20}$$

Eq. (21) and (22) guarantee that the products fraction must be sent from the collection centers to the nodes of origin and to the destruction centers:

$$\sum_{i \in N_1} \sum_{m \in M} R_{kim} \geq \beta_k \sum_{j \in N_4} \sum_{m \in M} Y_{jkm} (1 - S_{jkm}) \quad \forall k \in N_5$$

$$\sum_{l \in N_6} \sum_{m \in M} Z_{klm} \geq (1 - \beta_k) \sum_{j \in N_4} \sum_{m \in M} Y_{jkm} (1 - S_{jkm}) \quad \forall k \in N_5 \tag{21}$$

Eq. 22 guarantees that the customer's demand is fulfilled completely from a single source by using a unique transportation mode, where split deliveries are not allowed:

$$\sum_{i|(i,j)\in A} \sum_{m \in M} W_{ijm} = 1 \quad \forall j \in N_4 \tag{22}$$

The following equations define the nature of the decision variables:

$$B_u \in \{0,1\} \quad \forall u \in N_2 \cup N_3$$
$$W_{ijm} \in \{0,1\} \quad \forall (i,j) \in A, \forall m \in M$$
$$X_{ijm} \geq 0, \quad \forall (i,j) \in A_1 \cup A_2 \cup A_3 \cup A_4 \cup A_5 \cup A_6, \forall m \in M$$
$$Y_{ijm} \geq 0, \forall (i,j) \in A_7, \forall m \in M$$
$$Z_{ijm} \geq 0 \quad \forall (i,j) \in A_8, \forall m \in M$$
$$R_{ijm} \geq 0 \quad \forall (i,j) \in A_9, \forall m \in M$$

4. Proposed solution methodology

Three methods to solve the proposed problem are compared. These methods are classified according to the solution technique. The first one is based on mixed integer linear programming. The other methods include optimization and simulation. Combining optimization with simulation allows generating attractive solutions for the different objectives exposed, where simulation is a tool to replicate scenarios with several values for random variables.

4.1. Methods based on mixed-integer programming

Solving a multi-objective problem requires to compute a number of solutions belonging to the Pareto-optimal set. The solution method chosen is the ε-constraint implemented as in Mavrotas [39]. It is briefly described next.

Consider the following multi-objective problem where x ∈ S, is a decision variable vector in the search space S. Let *f1 (x),.., Fp (x)* be objective functions.

In the ε-constraint method, one of the objective functions is optimized by using the other objective functions as constraints. Thus, iteratively, each constraint is allowed to deteriorate to improve the performance of other objective functions.

Max F1(x)
Subject to:
F2(x) ≥e2
F3(x) ≥e3
…
Fp(x) ≥ep
x ∈ S

As performance measures for multi-objective optimization the hyper-volume, spread measure and spacing are typically used for multi-objective problems [40].

4.2. Methods based on optimization via simulation

Simulation has the advantage of being a tool that replicates situations with many relations among variables. A simulation engine is developed in VBA running with MS Excel and with the optimization model implemented in GAMS. This integration allows computing attractive solutions to solve the proposed objectives. Two different approaches are studied. Each one is explained next:

4.3. Approach 1: First stage: optimization. Second stage: simulation

This approach is developed by using the following method: First, the solutions of the Pareto-optimal set for the

problem are obtained by using the ε-constraint method. Then, by using simulation methods, the solutions that do not show statistically significant differences are deleted. The steps for this method are the following:

1. Compute the Pareto optimal set of solutions using the method described in [40].
2. Each solution in the Pareto-optimal set is simulated in the SC simulation engine. This simulation varies the costs, CO2 emissions, and the proportion of product losses with a known probability distribution. The confidence interval is determined for each objective function with a defined significance level of 5%. The number of iterations in this step must be determined by the decision maker.
3. Then, the dominance of the solutions is analyzed by comparing all of them. The Pareto Set of solutions is said to be set of statistically non- dominated solutions. Thus, a solution is said to dominate another if there is at least a single objective that is statistically better without deteriorating the others.
4. When the solutions are classified, the total set of statistically different solutions is shown. With this input, the decision maker may select the one that fits better for the specific case.

4.4. Approach 2: Optimization-simulation cooperation

This model seeks to converge to attractive solutions in fewer simulation and optimization runs. This variant is explained with the following steps:

1. Solve the optimization problem with the most important objective function without restricting the values of the other two objective functions. The ideal value for that objective is computed.
2. Simulate the obtained solution to compute the confidence intervals for each one of the objective functions. Denote the lower limit of each confidence interval as f_i'
3. Include in the mathematical model a set of constraints to the value of the constraints in the right side associated to the other two objective functions (secondary functions) taking into account the lower levels of the confidence intervals. For example:
4. - Quantity of emissions

$$\sum_{m\in M}\sum_{(i,j)\in A} E_{ijm}^{T} W_{ijm} + \sum_{u\in N_2\cup N_3} E_u^F B_u \le f_2'$$

-Amount of product loss

$$\sum_{m\in M}\sum_{(i,j)\in A_1\cup A_2\cup A_3\cup A_4\cup A_5\cup A_6} S_{ijm}X_{ijm} + \sum_{m\in M}\sum_{(i,j)\in A_7} S_{ijm}Y_{ijm} + \sum_{m\in M}\sum_{(i,j)\in A_9} S_{ijm}R_{ijm} \le f_3'$$

5. These constraints are treated similar to the ε-constraint method.
6. Solve the mathematical programming model once again, adjusting the right side of these two constraints.
7. Solve steps 2 – 5 until the main objective function has deteriorated until a tolerable limit or unfeasibility of the solution.
8. Check the dominance of computed solutions.
9. The number of solutions will depend on the analyst criteria, according to the acceptable range of each of the objective functions that can operate the supply chain.

5. Computational results

Results of the developed experimental studies are tested on 48 randomly generated instances, changing the number of nodes in each of the six levels of the supply chain, with three or six nodes per level and five or ten customers, which correspond to 24 different configurations. All the experiment are carried out in a computer with an Intel(R) Core(TM) i7-3930k CPU @ 3.20 GHz. Processor. 12 GB RAM. Operative system: 64-bit Windows 8. The mathematical models are solved using GAMS and CPLEX, and the simulation engine is developed in VBA.

5.1. Parameterization

In the ε-constraint method, the number of grid points define discrete limits within the range in which each objective function is optimized to search for Pareto-optimal solutions. The larger the number of grid points, more solutions are likely to be computed since the step size in which objective functions are allowed to deteriorate is smaller. Our experiments work with 5 and 10 grid points.

Fig. 2 is an example of the Pareto-optimal set solutions for one instance. It shows the location of the different solutions with respect to the objective functions and highlights those three that have the minimum value cost (C), emissions (E) and product losses (P).

Table 2 details the results of the performance measures for the performed experiments using the traditional ε-constraint method with five and ten grid points. Note that the higher the number of grid points, the denser the representation of the efficient set, but with a higher computation time requirement. The solution distribution measuring throughout the Pareto-optimal set (spacing) is presented with better performance that those instances run with more grid points. The hyper volume is higher when the number of grid points increases.

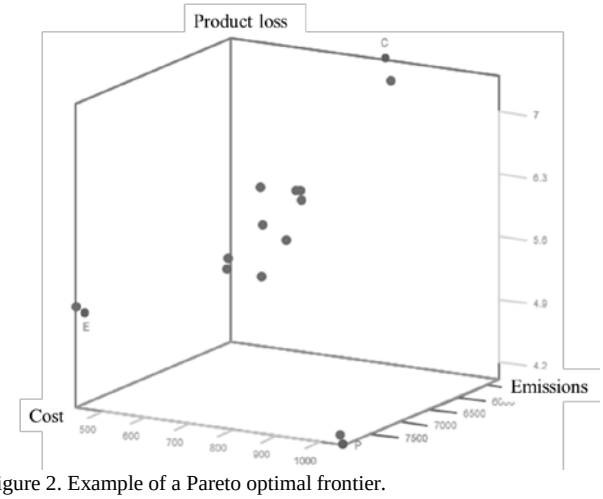


Figure 2. Example of a Pareto optimal frontier.
Source: Own elaboration

Table 2.
Summary of the performance measures for the ε-constraint method

Grid points=5				
Customers	CPU (Seg)	Spread	Hypervolume	# Solutions
5	39	471	7.40E+09	13
10	128	758	3.50E+09	16
Grid points=10				
Customers	CPU (Seg)	Spread	Hypervolume	# Solutions
5	151	125	7.50E+09	51
10	618	333	3.90E+09	49

Source: Own elaboration

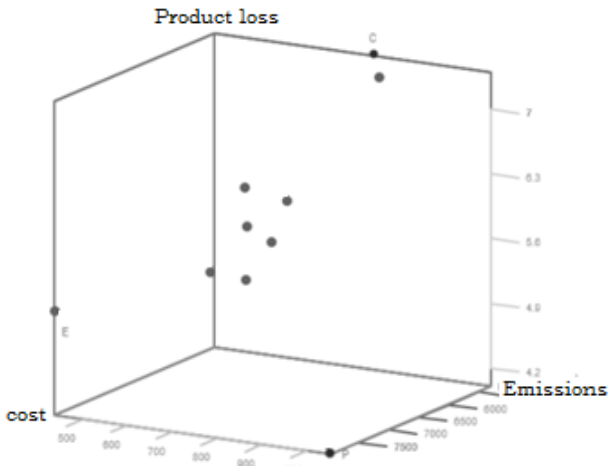


Figure 3. Example of Pareto frontier – Sim-Opt approach 1
Source: Own elaboration

For the experimental development of these methods, 10 instances are randomly chosen. For the first proposed method, the simulation engine works with the solutions belonging to the Pareto Frontier obtained from the optimization model after applying the ε-constraint method. The Tukey test with a significance level of 5%, allows identifying which of the solutions show statistical differences. On average, about 60% of the solutions do not present statistical differences and therefore, these are discarded. Fig. 3 presents an example of the resulting Pareto frontier with solutions that are statistically different between each other.

In our experiments, the percentage of recovered product that may be recycled varies from 40%-60% of the total sold product. Also, when minimizing economic costs, the objective function is 5,289 in average. When minimizing exclusively one of the other two objective functions, the cost may be increased up to 50%. When minimizing CO2 emissions, the average optimal solution is 43,8Kg. This KPI is increased by 81% when the objective function is economic cost, and 140% when the objective function is minimizing risks. By setting the objective function to minimize the operational risks, the amount of lost product may be reduced up to 45%.

In Table 3, the configuration of the 10 studied instances is presented, together with the spacing and hyper volume values obtained for each developed Sim-Opt approaches. In general, the second approach presents a spacing measure of approximately 51% higher than the first one, since the search of solutions there lacks a reference point to move within the Pareto-optimal set, different from the first one. Instances 3 and 5 present better results since the intention was to move within closer values to reduce costs. The second approach requires less computational time and is more dedicated to finding statistically different solutions with limited economical costs. Fig 4. Presents the Pareto frontier approximation for this approach.

6. Conclusions and future work

This work proposes two multi-objective supply chain design approaches combining optimization and simulation techniques. Further, a generic closed-loop supply chain design is considered, in which product flow may happen between consecutive and non-consecutive echelons of the network, respecting the required steps for production and consumption.

The purpose of the considered approach is to build Pareto frontier solutions that are statistically different, and robust, so that the decision maker has different options to choose from. The traditional exact methods generate good results in theoretical terms. The Pareto-optimal set found there for each instance allows visualizing a large set of solutions.

Nevertheless, although multiple options are presented, this does not guarantee that these are statistically different, since this method does not take into account the variability from randomness in parameters.

Therefore, the cooperation between optimization and simulation methods is studied to bound the set of solutions, thus allowing the decision maker choose among the most convenient configurations. Computational results show that the proposed approaches reduce the number of solutions to 40% for not being statistically different.

The first solution approach is a two stage approach in which all the solutions obtained from a ε-constraint method are simulated using our simulation engine, and statistical tests are performed to determine statistical differences. If no statistical difference is proven, the solution is discarded. The second approach simulates each solution that is being evaluated by the ε-constraint method to determine confidence intervals of the solutions that constitute the bounds in which the objective functions must not be explored in subsequent iterations.

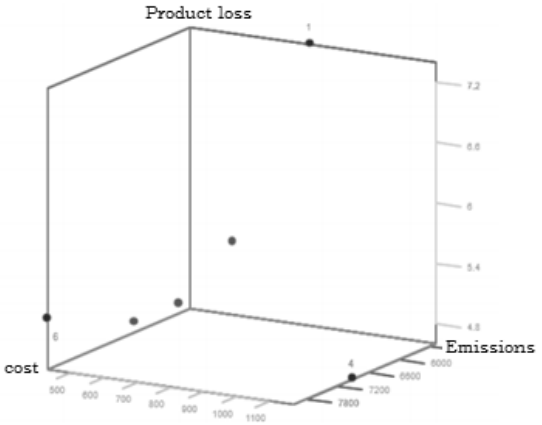


Figure 4. Example of Pareto frontier – Sim-Opt approach 2
Source: Own elaboration

Table 3.
Comparison of indicators of the optimization via simulation methods.

Method	Instance	Production Plants	Distribution Centers	Retailers	Customers	Collection centers	Destruction Centers	Performance indicator		
								spread Measure	Hyper-Volume	Time [H]
1° stage: Optimization, 2° stage: Simulation	1	3	3	3	5	3	3	848	1,27E+08	37,26
	2	6	3	3	5	3	3	363	1,22E+08	41,47
	3	3	6	3	5	3	3	433	1,12E+08	41,18
	4	3	3	6	5	3	3	697	1,44E+08	42,19
	5	3	3	3	5	3	3	1025	9,68E+07	39,09
	6	3	3	3	10	3	3	1003	3,40E+07	37,60
	7	3	6	3	10	3	3	1811	8,11E+07	35,81
	8	3	3	6	10	3	3	980	8,56E+07	41,35
	9	3	3	3	10	6	3	1232	1,26E+07	40,57
	10	3	6	3	10	3	6	1429	6,65E+06	39,36
1° stage: Optimization, 2° stage: Simulation, 3° stage: Optimization	1	3	3	3	5	3	3	1760	3,37E+08	17,11
	2	6	3	3	5	3	3	1742	5,59E+07	14,26
	3	3	6	3	5	3	3	384	8,40E+07	15,81
	4	3	3	6	5	3	3	1466	6,15E+08	15,78
	5	3	3	3	5	3	3	402	2,07E+08	17,76
	6	3	3	3	10	3	3	2287	7,12E+07	16,79
	7	3	6	3	10	3	3	912	4,76E+07	14,63
	8	3	3	6	10	3	3	2167	8,31E+07	16,84
	9	3	3	3	10	6	3	2176	6,59E+07	16,80
	10	3	6	3	10	3	6	1529	6,90E+08	15,61

Source: Own elaboration

The main advantage of the second proposed approach is that the computational time requirements are considerably lower than in the first approach since fewer solutions are simulated.

Future works include a finer tuning of the number of replications required to compute the confidence intervals. Also, to consider a multi-objective supply chains design with hierarchical and multi-product settings, considering manufacturing operations. Besides that, it can contain multiple period decisions and routing decisions as in [41]. Moreover, other performance measures may be included, such as the financial risks and social sustainability. Furthermore, optimization methods based on meta-heuristic methods may also be taken into account in future works.

References

[1] Sahin, F. and Robinson, E., Flow coordination and information sharing in supply chains: review, implications and directions for future research. Decision Science, 33(4), pp. 505-536, 2002. DOI: 10.1111/j.1540-5915.2002.tb01654.x

[2] Chopra, S. and Meindl, P., Supply chain management, 2° Edición: Pretince-Hall, 2004.

[3] Ballou, R.H., Logística: administración de la cadena de suministro, Mexico: Pearson Education, 2004.

[4] Xiaoyuan, L. and Swaminathan, J.M., Supply chain management. International Encyclopedia of the Social & Behavioral Sciences (Second Edition), 2015, pp. 709-713.

[5] Guide, D. and Van Wassenhove, L., The Evolution of Closed-Loop Supply Chain Research. Operations Research, 57(1), pp. 10-18, 2009.

[6] Govindan, K., Soleimani, H. and Kannan, D., Reverse logistics and closed-loop supply chain: a comprehensive review to explore the future. European Journal of Operational Research, 240(3), pp. 603-626, 2015. DOI: 10.1016/j.ejor.2014.07.012

[7] Rezapour, S., Zanjirani, R., Fahimnia, B., Govindan, K. and Mansouri, Y., Competitive closed-loop supply chain network design with price-dependent demands. Journal of Cleaner Production, 93, pp. 251-272, 2015. DOI: 10.1016/j.jclepro.2014.12.095

[8] Amin, S.H. and Zhang, G.Z., An integrated model for closed-loop supply chain configuration and supplier selection: multi-objective approach. Expert Systems with Applications, 39, pp. 6782-6791, 2012. DOI: 10.1016/j.eswa.2011.12.056

[9] Easwaran, G. and Üster, H., A closed-loop supply chain network design problem with integrated forward and reverse channel decisions. IIE Transactions, 42(11), pp. 779-792, 2010. DOI: 10.1080/0740817X.2010.504689

[10] Kannan, G., Sasikumar, P. and Devika, K., A genetic algorithm approach for solving a closed loop supply chain model: A case of battery recycling. Applied Mathematical Modelling, 34(3), p. 655-670, 2012. DOI: 10.1016/j.apm.2009.06.021

[11] Metta, H. and Badurdeen, F., Optimized closed-loop supply chain configuration selection for sustainable product designs. In: 2011 IEEE International Conference on Automation Science and Engineering, Trieste, 2011, pp. 438-443, DOI: 10.1109/CASE.2011.6042416

[12] Ramezani, M., Ali, K., Karimi, B. and Hejazi, T., Closed-loop supply chain network design under a fuzzy environment. Knowledge-Based Systems, 59, pp. 108-120, 2014. DOI: 10.1016/j.knosys.2014.01.016

[13] Yang, G., Liu, Y. and Yang, K., Multi-objective biogeography-based optimization for supply chain network design under uncertainty. Computers & Industrial Engineering, 85, pp. 145-156, 2015. DOI: 10.1016/j.cie.2015.03.008

[14] Ruiz-Femenia, R., Guillén-Gosálbez, G., Jiménez, L. and Caballero, J., Multi-objective optimization of environmentally conscious chemical supply chains under demand uncertainty. Chemical Engineering Science, 95, pp. 1-11, 2013. DOI: 10.1016/j.ces.2013.02.054

[15] De-León-Almaraz, S., Azzaro-Pantel, C., Montastruc, L. and Baez-Senties, O., Design of an hydrogen supply chain using multiobjective optimization. Computer Aided Chemical Engineering, 30, pp. 292-296, 2012. DOI: 10.1016/B978-0-444-59519-5.50059-9

[16] Sabri, E.H. and Beamon, B.M., A multi-objective approach to simultaneous strategic and operational planning in supply chain design. Omega, 28, pp. 581-598, 2000. DOI: 10.1016/S0305-0483(99)00080-8

[17] Eskandarpour, M., Dejax, P., Miemczyk, J. and Péton, O., Sustainable supply chain network design: an optimization-oriented review. Omega, 54, pp. 11-32, 2015. DOI: 10.1016/j.omega.2015.01.006

[18] Brandenburg, M., Govindan, K. and Sarkis, J.S., Quantitative models for sustainable supply chain management: developments and directions. European Journal of Operational Research, 233(2), pp. 299-312, 2014. DOI: 10.1016/j.ejor.2013.09.032

[19] Quariguasi-Frota-Neto, J., Bloemhof-Ruwaard, J., van Nunen, J. and van Heck, E., Designing and evaluating sustainable logistics networks. Int. J. Production Economics, 111(1), pp. 195-208, 2006. DOI: 10.1016/j.ijpe.2006.10.014

[20] Azaron, A., Brown, K., Tarim, S. and Modarres, M., A multi-objective stochastic programming approach for supply chain design considering risk. International Journal of Production Economics, 116(1), pp. 129-138, 2008.
[21] Goh, M., Lim, J. and Meng, J., A stochastic model for risk management in global supply chain networks. European Journal of Operational Research, 182(1), pp. 164-173, 2007. DOI: 10.1016/j.ijpe.2008.08.002
[22] Subulan, K., Baykasoğlu, A., Özsoydan, F.B., Tasan, A.S. and Selim, H., A case-oriented approach to a lead/acid battery closed-loop supply chain network design under risk and uncertainty. Journal of Manufacturing Systems, 37, 2014. DOI: 10.1016/j.jmsy.2014.07.013
[23] Trkman, P. and McCormack, K., Supply chain risk in turbulent environments—A conceptual model for managing supply chain network risk. International Journal of Production Economics, 119(2), pp. 247-258, 2009. DOI: 10.1016/j.ijpe.2009.03.002
[24] Tuncel, G. and Alpan, G., Risk assessment and management for supply chain networks: a case study, Computers in Industry, 61(3), pp. 250-259, 2010. DOI: 10.1016/j.compind.2009.09.008
[25] Pettit, T.J., Croxton, K.L. and Fiksel, J., Ensuring supply chain resilience: development and implementation of an assessment tool. Journal of Business Logistics, 34(1), pp. 46-76, 2013. DOI: 10.1111/jbl.12009
[26] Carson, C,. Simulation and optimization: methods and applications. State University of New York at Binghamton, New York, 1997.
[27] Juan, A.A., Faulin, J., Grasmanc, S.E., Rabe, M. and Figueira, G., A review of simheuristics: extending metaheuristics to deal with stochastic. Operations Research Perspectives, 2, pp. 62-72, 2015. DOI: 10.1016/j.orp.2015.03.001
[28] Pan, F. and Nagi, R., Robust supply chain design under uncertain demand in agile manufacturing. Computers & Operations Research, 37(4), pp. 668-683, 2010. DOI: 10.1016/j.cor.2009.06.017
[29] El-Sayed, M., Afia, N. and El-Kharbotly, A., A stochastic model for forward–reverse logistics network design under risk. Computers & Industrial Engineering, 58(3), pp. 423-431, 2010. DOI: 10.1016/j.cie.2008.09.040
[30] Prasanna-Venkatesan, S. and Kumanan, S., Multi-objective supply chain sourcing strategy design under risk using PSO and simulation. The International Journal of Advanced Manufacturing Technology, 61(4), pp. 325-337, 2012. DOI: 10.1007/s00170-011-3710-y
[31] Pishvaee, S. and Razmi, J., Credibility-based fuzzy mathematical programming model for green logistics design under uncertainty. Computers & Industrial Engineering, 62(2), pp. 624-632, 2012. DOI: 10.1016/j.cie.2011.11.028
[32] Pishavee, M., Razmi, J. and Torabi, S., Robust possibilistic programming for socially responsible supply chain network design: a new approach. Fuzzy Sets and Systems, 206, pp. 1-20, 2012. DOI: 10.1016/j.fss.2012.04.010
[33] Ruiz-Femenia, R., Guillén-Gosálbez, G., Jiménez, L. and Caballero, J., Multi-objective optimization of environmentally conscious chemical supply chains under demand uncertainty. Chemical Engineering Science, 95, pp. 1-11, 2013. DOI: 10.1016/j.ces.2013.02.054
[34] Hamed, S. and Govindan, K., Reverse logistics network design and planning utilizing conditional value at risk K. Govindan, 237(2), pp. 487-497, 2014. DOI: 10.1016/j.ejor.2014.02.030
[35] Nooraie, V. and Mellat-Parast, M., A multi-objective approach to supply chain risk management: integrating visibility with supply and demand risk. International Journal of Production Economics, 161, pp. 192-200, 2015. DOI: 10.1016/j.ijpe.2014.12.024
[36] Jindal, A. and Sangwan, K., Multi-objective fuzzy mathematical modeling of closed-loop supply chain considering economical and environmental factors. Annals of Operations Research, pp. 1-26, 2016. DOI: 10.1007/s10479-016-2219-z
[37] Mota, B., Gomes, M., Carvalho, A. and Barbosa-Povoa, A., Towards supply chain sustainability: economic, environmental and social design and planning. Journal of Cleaner Production, 105, pp. 14-27, 2015. DOI: 10.1016/j.jclepro.2014.07.052
[38] Montoya-Torres, J.R., Designing sustainable supply chains based on the triple bottom line approach, in: Proceedings of the 2015 International Conference on Advanced Logistics and Transport (ICALT 2015), Valenciennes, France, 2015.
[39] Mavrotas, G., Effective implementation of the e-constraint method in multi-objective mathematical programming problems. Applied Mathematics and Computation, 213(2), pp. 455-465, 2009. DOI: 10.1016/j.amc.2009.03.037
[40] Deb, K., Thiele, L., Laumanns, M. and Zitzler, E., Scalable multi-objective optimization test problems, Congress on Evolutionary Computation, 2002, pp. 825-830.
[41] Pérez-Kaligari, E. y Guerrero, W.J., Métodos de optimización para el problema de ruteo de vehículos con inventarios y ventanas de tiempo duras. Revista Ingeniería Industrial, 3(1)4, pp. 31-49, 2015.

W.J. Guerrero, received the BSc. Eng in Industrial Engineering in 2008, and MSc.degree in Industrial Engineering in 2010, and the PhD.degree in Engineering in 2014, all of them from the Universidad de Los Andes in Colombia. He received the PhD. degree in Systems Optimization and Dependability from Université de Technologie de Troyes, in France. He works in projects of the transportation area, with emphasis on developing heuristic and metaheuristic algorithms. Since 2017, he is associate professor at the engineering school at Universidad de La Sabana.
ORCID: 0000-0002-9807-6593

L.A. Sotelo Cortés, received the BSc. Eng in Industrial Engineering in 2012, and MSc. degree in Industrial Engineering in 2017, both from the Escuela Colombiana de Ingeniería Julio Garavito in Colombia. She works at Belcorp Co. as Sales and Operations Analyst.
ORCID: 0000-0003-3398-4408

E. Romero-Mota, received the BSc. Eng in Industrial Engineering in 1999 from Escuela Colombiana de Ingeniería Julio Garavito (ECIJG), MSc. degree in Logistics, Materials and Supply Chain Management from Florida Institute of Technology and MSc. in Corporate Innovation Management from Universidad de Barcelona, Spain. Currently he is lecturer in ECIJG and innovation manager at Process Innova SAS.
ORCID: 0000-0003-3427-0765

UNIVERSIDAD NACIONAL DE COLOMBIA
SEDE MEDELLÍN
FACULTAD DE MINAS

Área Curricular de Ingeniería Administrativa e Ingeniería Industrial

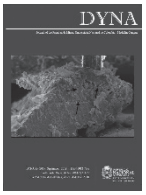
Oferta de Posgrados

Especialización en Gestión Empresarial
Especialización en Ingeniería Financiera
Maestría en Ingeniería Administrativa
Maestría en Ingeniería Industrial
Doctorado en Ingeniería - Industria y Organizaciones

Mayor información:

E-mail: acia_med@unal.edu.co
Teléfono: (57-4) 425 52 02

UNIVERSIDAD NACIONAL DE COLOMBIA
SEDE MEDELLÍN
FACULTAD DE MINAS



DYNA
http://dyna.medellin.unal.edu.co/

Site characterization of a tropical soil by in situ tests

Breno Padovezi Rocha [a] & Heraldo Luiz Giacheti [b]

[a] *Department of Geotechnical Engineering, University of São Paulo, São Carlos, Brazil. brenop@sc.usp.br*
[b] *Department of Civil and Environmental Engineering, São Paulo State University, Bauru, Brazil. h.giacheti@unesp.br*

Received: September 26th, 2017. Received in revised form: June 6th, 2018. Accepted: August 10th, 2018.

Abstract
This paper compiles site characterization data of an unsaturated tropical soil profile in an experimental research site in Bauru, São Paulo State, Brazil. Several in situ campaigns comprised geophysical borehole tests (cross-hole, down-hole and up-hole together with the SPT), as well as mechanical tests (SPT, CPT and SDMT) have been performed. According to the MCT Classification System for tropical soils, the first 13 m depth is a colluvium with lateritic soil behavior (LA') over the residual soil with non-lateritic behavior (NA'). The ratio between seismic (G_o) and mechanical (q_n, N_{60}, E_D, K_D *and* M_{DMT}) parameters was useful to identify the presence of microstructure and to confirm unusual soil behavior for this tropical soil site. CPT and SDMT were efficient for detailed stratigraphic logging, however, the estimative of geotechnical parameters cannot be solely been done base on just conventional correlations defined for sedimentary soil.

Keywords: site characterization; tropical soils; CPT; SDMT; seismic tests.

Caracterización de un suelo tropical por medio de ensayos in-situ

Resumen
Este artículo presenta la caracterización geotécnica de un perfil de suelo tropical no saturado de un campo experimental localizado en la ciudad de Bauru, São Paulo, Brasil. Fueron ejecutadas varias campañas in-situ, que incluyen ensayos geofísicos (cross-hole, down-hole y up-hole con ensayos SPT) y ensayos mecánicos (SPT, CPT e SDMT). Según el sistema de clasificación MCT, los primeros 13 m del sitio de estudio corresponden a un colúvio de matriz arenosa con comportamiento laterítico (LA'), seguido por un suelo residual de comportamiento no laterítico (NA'). La relación obtenida entre los parámetros sísmicos (G_o) y mecánicos (q_n, N_{60}, E_D, K_D *e* M_{DMT}) permitió identificar la presencia de microestructuras y confirmar el comportamiento específico de este material. Los ensayos de CPT y SDMT fueron eficientes para definir detalladamente el perfil estratigráfico; no obstante, la estimativa de los parámetros geotécnicos no puede ser realizada basada únicamente en correlaciones convencionales definidas para suelos sedimentares.

Palabras clave: caracterización del suelo; suelos tropicales; CPT; SDMT; ensayos sísmicos.

1. Introduction

The site characterization must be performed to define the geotechnical profile, which includes layers identification, thickness and type of soil, water level position and mechanical and hydraulic parameters of each layer. For this purpose, both in situ and laboratory tests can be used. However, although the laboratory tests permit test conditions controlling, as well as accomplishing a series of simulations, in situ tests have been increasingly employed for being simple, operator-independent, rapid and covering a larger volume of soil.

Tropical soils are mostly formed by geological and pedological processes typical of tropical wet regions [1]. It is mainly composed of two horizons. The top horizon, which has suffered intensive pedogenetic evolution is so-called lateritic soils. This horizon overlays a deep layer of residual soil with relict structures from parent rock, which is called as saprolites. The lateritic soil has evolved from residual soils as well as colluvium soils. Tropical soils present a bonding structure, which generates a cohesive-frictional nature, anisotropy due to relic structure, genesis, destructuration under shear conditions and low influence of stress history [2]. Therefore, it is becoming increasingly important to understand the soil behavior of the tropical soils, since they cannot be properly assessed by means of models and correlations developed by the Classical Soil Mechanics.

How to cite: Rocha, B.P. and Giacheti, H.L., Site characterization of a tropical soil by in situ tests. DYNA, 85(206), pp. 211-219, September, 2018.
© The author; licensee Universidad Nacional de Colombia.

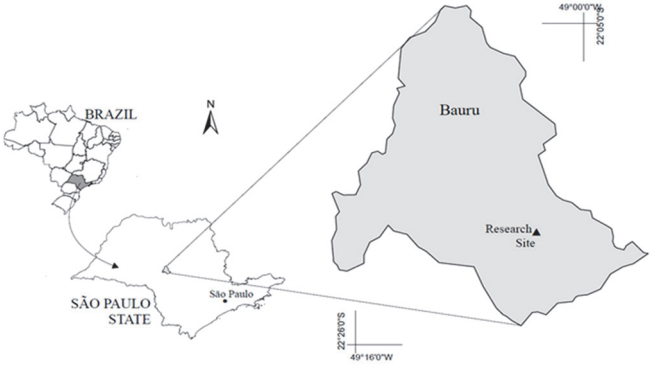


Figure 1. Location of the Unesp research site.
Source: The authors.

This paper aims to present and discuss extensive site characterization campaigns carried out by in situ tests performed at one relatively well-studied unsaturated tropical soil profile at Unesp research site, in the State of São Paulo, Brazil. CPT, SDMT and seismic test data were interpreted and compared to available reference soil parameters determined based on laboratory and others in situ tests. In addition, G_o/q_c, G_o/N_{60}, G_o/E_D and G_o/M_{DMT} were discussed to identify microstructure in the studied site profile.

2. Geology and site conditions

Geotechnical site characterization campaigns were carried out at the Unesp research site – Bauru Campus, in northwest of São Paulo state, Brazil (Fig. 1). This site has been extensively studied via laboratory and in situ tests.

Sandstone rocks from Bauru Group (Upper Cretaceous), which recovers the volcanic rocks from Serra Geral Formation, geologically characterize the soil profile. These rocks emerge in the direction of the Tiete River. Sedimentary rocks from Marilia Formation are predominant at this region, which are experiencing weathering processes over tropical conditions. According to [3], these soils exhibit characteristics from the parent rocks such as sequence of layering and modifications on these geological materials by pedogenetic and morphogenetic processes (softening caused by water migration by the fracture zones and recovering by colluvial soils in several phases). These profiles are generally unsaturated porous sandy soils with a high-saturated permeability and low degrees of saturation (below 30%). An important geotechnical problem in this area is the soil collapsibility caused by wetting.

The study site is characterized by an upper lateritic soil layer (colluvium) about 13.0 m thick followed by a saprolitic soil (residual soil) which reach depths up to 30 m. The groundwater is not found up to 30 m depth. The MCT Classification System (Mini, Compacted, Tropical) proposed by [4] for tropical soils was used to define and classify the soils with regards to their lateritic behavior.

3. In situ tests

3.1. SPT and SPT-T

SPT is still the most current in test for geotechnical site characterization. The test is simple and provides a disturbed soil sample while the penetration resistance (N-value) is measured. Geotechnical design parameters can be estimated from the N-value; however, it has been found to be very dependent on the test equipment and procedure [5-7]. Furthermore, N-values are usually recorded every 1.0 to 1.5 m and that is relatively discontinuous when compared to other tests, such as CPT and DMT.

[8] suggested supplementing the conventional SPT with measurement of the torque required to turn the split spoon after driving. This is called the standard penetration test with torque measurement (SPT-T). According to [8], the torque (T) provides a 'static' component for a 'dynamic' test.

Three SPT tests were carried out in the site. Fig. 2a shows a soil profile consisting of a red, clayey fine sand. Average N-values increase almost linearly with depth, up to 13 m depth (Fig. 2b). One SPT test complemented by torque measurement was carried out at the site and Fig. 2c shows the T/N ratio profile. There are two different trends for the T/N ratio with average values of 1.3 for the top 12.5 m depth and 2.0 bellow this depth (Fig. 2c). The interpretation of MCT classification test data separated lateritic (LA') from non-lateritic (NA') soil behavior almost at the same depth (13 m).

Grain size distribution for the soil samples retrieved every meter from one of the SPT tests were determined using dispersant (Fig. 2d) and with no dispersant (Fig. 2e). Oxides and hydroxides of iron and aluminium, which are typical on tropical soil profiles, naturally aggregate clay and silt particles and explains the observed differences.

3.2. CPTu

CPTu is another in test for geotechnical site characterization where cone resistance (q_c), sleeve friction (f_s) and pore pressure (u) are measured during the probe penetration at a constant rate of 20 mm per second. The piezocone probe has a 60-degree apex angle and a diameter of 35.7 mm (10 cm² cross-sectional area). The partially saturated nature of tropical soils does not allow pore pressure measurements, so it cannot be used to help the identification of the drainage conditions during cone penetration. [9] suggested a framework for interpretation of

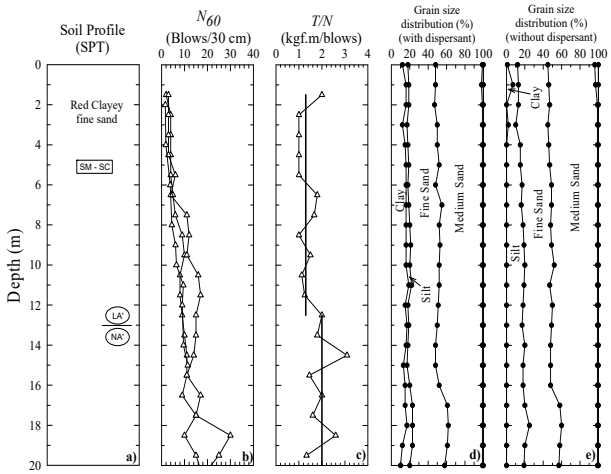


Figure 2. SPT, SPT-T results and grain size distribution.
Source: The authors.

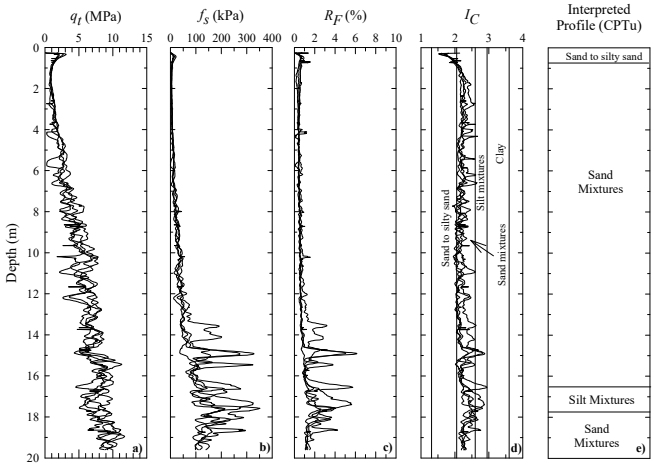


Figure 3. CPT data and interpretation for the studied site.
Source: The authors.

cone penetration tests in tropical soils, which depends largely on semi-empirical approaches using other in situ or laboratory test results.

CPTu does not provide soil samples. For this reason, soil type is identified by using classification charts (SBT charts) that relate corrected cone resistance (q_t) and friction ratio (R_f) as discussed by [10]. Four CPTu were carried out in the site in March, 2016. Fig. 3 shows the CPTu data and their interpretation. Water table was not found up to 20 m depth. Due to the unsaturated condition of the studied site, pore pressure was note measured and cone resistance (q_c) was assumed to be equal to corrected cone resistance (q_t).

The corrected cone resistance (q_t) and the sleeve friction (f_s) increase almost linearly with depth up to 13 m leading to a friction ratio (R_f) between 0.5 and 1.0 % (Fig. 3). The I_c index profile, calculated as defined by the Unified Approach [11], is also shown in Fig. 3 and it was used to interpret the soil profile. The CPTu interpreted profile indicated that a sand to silty sand occurs from 0 to1.0 m depth, sand mixtures from 1.0 to 16.5 m depth, silt mixtures from 16.5 to 17.8 m depth and sand mixtures from 17.8 to 19.6 m depth.

Robertson [12] updated the CPT-based SBT classification chart [11] based on the work of Idriss and Boulanger [13]. This modified classification system is based on the soil behavior characteristics, which consider either dilative or contractive behavior at large strains and soils that are predominately more sand-like (susceptible to cyclic liquefaction) or more clay-like (not susceptible to cyclic liquefaction). Moreover, this classification system captures soils in transition from more sand-like to more clay-like.

Fig. 4 shows that the use of Robertson's chart [12] in the interpretation of the CPTus identified sand-like soils up to 16.5 m depth (Fig. 4a). The soil was classified as transitional between 16.5 to 17.8 m depth, and as a sand-like soil below 17.8 m depth (Fig. 4b). It is also interesting to note that at 13 m depth, where there is a boundary between lateritic (LA') and non-lateritic (NA') soil behavior, the CPT response was also different: up to 13 m depth the soil contracts at large strains and below 13 m depth the soil dilates at large strains. It was also observed that soil from the top layer (up to 1.0 m depth) is classified as sand-like soil with dilative behavior at large strains.

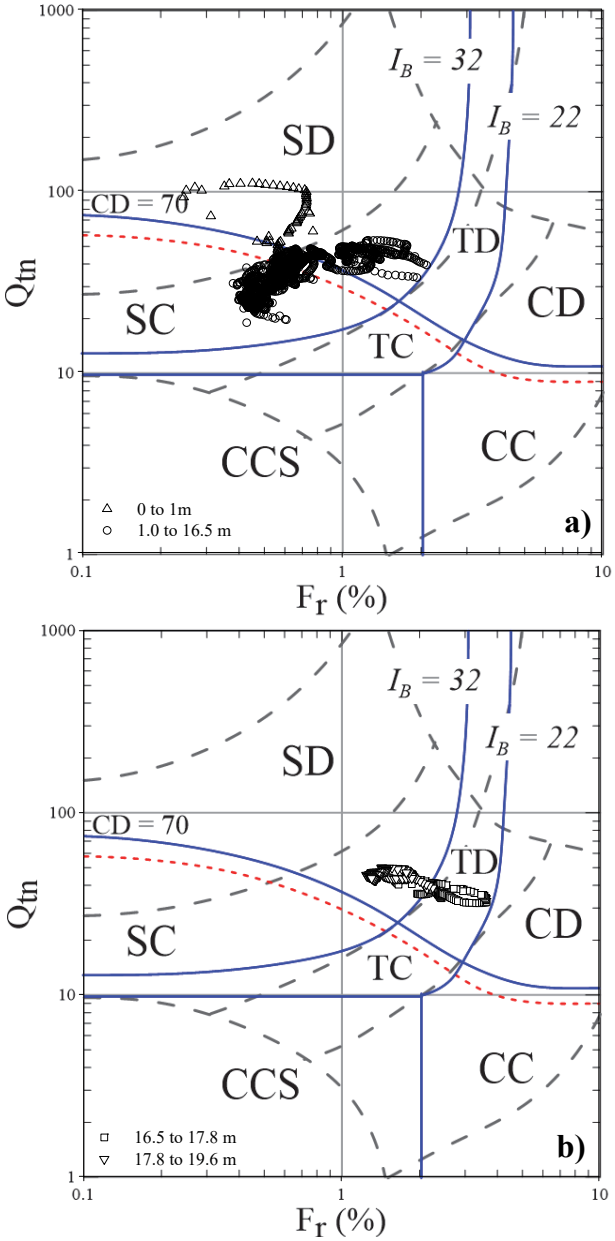


Figure 4. CPT data from the studied site in the normalized CPT soil behavior chart.
Source: modified from [13].

Besides stratigraphic logging, the CPTu data are used to estimate geotechnical parameters based on classical empirical correlations [14,15]. Empirical correlations to estimate soil unit weight (γ), friction angle (ϕ'), constrained modulus (M) and maximum shear modulus (G_o) were used to compare calculated and measured parameters. The reference G_o was determined in situ via one cross-hole [16], one seismic cone [3] and one downhole test [17]. Moreover, the reference of soil unit weight (γ) and friction angle (ϕ') was determined based on direct shear tests carried out on undisturbed samples [18].

Fig. 5 shows the comparison between measured and estimated parameters in terms of average values for all CPTs. Fig. 5a shows that estimative of soil unit weight (γ) using the

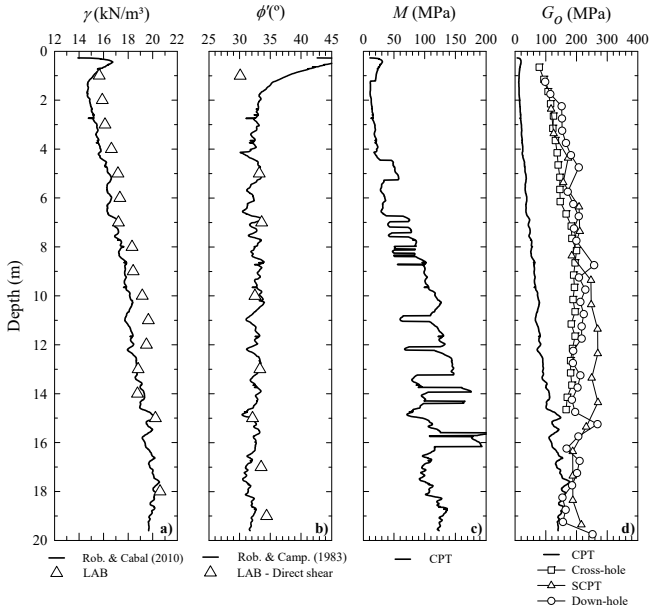


Figure 5. Measured and estimated parameters from average CPT data. Source: The authors.

Equation 1, presented by [19], is lower than then those determined by undisturbed soil samples up to 13 m depth and they are in a reasonable agreement bellow this depth.

$$\gamma/\gamma_w = 0.27\left[\log R_f\right] + 0.36[\log(q_t/p_a)] + 1.236 \quad (1)$$

Fig. 5b presents the comparison between predicted friction angle by Robertson and Campanella [14]'s equation (equation 2) and reference (laboratory data) values.

$$tan\,\phi' = \frac{1}{2.68}\left[log\left(\frac{q_c}{\sigma'_{vo}}\right) + 0.29\right] \quad (2)$$

The reference friction angles were determined by direct shear tests under consolidated drained condition (CD) on undisturbed soil samples at its natural water content. The estimated CPTu friction angle values are in good agreement with those obtained from shear tests. In this case, average estimated ϕ' angle was equal to 32.5º and the average measured ϕ' angle of about 33º. However, the estimated ϕ' values are much higher than the reference ones for the 1 m topsoil. This difference is caused by the influence of soil suction, which provides mainly an increase on the intercept of cohesion. The estimated ϕ' values incorporate the component of cohesion as a friction angle, since it assumes the soil behave like sands.

The constrained modulus (M) is a key engineering parameter in evaluating the settlements behavior of foundations. Constrained modulus can be obtained by oedometer test in laboratory and in situ tests. Fig. 5c shows the *M-values* against depth obtained from equation 3 presented below.

$$M = \alpha_M(q_t - \sigma_{vo}) \quad (3)$$

Robertson [11] suggested the following simplified correlation:

when $I_c > 2.2$ use

$$\alpha_M = Q_{tn} \text{ when } Q_{tn} \leq 14$$
$$\alpha_M = 14 \text{ when } Q_{tn} > 14 \quad (4)$$

and, when $I_c > 2.2$ use

$$\alpha_m = 0.03\left[10^{(0.55I_c+1.68)}\right] \quad (5)$$

Unfortunately, there are no oedometer test data for this site to be used as reference values.

Maximum shear modulus (G_o) is a fundamental parameter for predicting the dynamic response of soil and can be determined from elastic theory for equation 6:

$$G_o = \rho\, V_s^2 \quad (6)$$

where ρ is mass density of the soil (kg/m³) and Vs is shear wave velocity (m/s).

Fig. 5d presents the G_o profile obtained from cross-hole, seismic cone and downhole test and the estimated profile from average CPTu data G_o was estimated from equation 7 developments for uncemented Holocene to Pleistocene age soils [11]:

$$G_o = 0.0188\left[10^{(0.55I_c+1.68)}\right](q_t - \sigma_{vo}) \quad (7)$$

G_o measured values are much higher than estimated one for this site. It can be associated to the weakly cemented structure of these soils (microstructure), which increases the low strain shear modulus while the penetration of the cone breaks down all cementation [12, 20, 21, 22].

The observed differences between estimated and measured parameters in tropical soils can be attributed the unusual behavior (e.g. a cohesive-frictional nature, anisotropy due to relic structure, destructuration under shear conditions and low influence of stress history). As a result, although CPTu is an excellent tool for soil profiling, it cannot serve as an exclusive site investigation tool for tropical soils, since genetic characteristics affect soil behavior and soil sampling and extra tests are required.

3.3. DMT and SDMT

The DMT was developed by [23] and consists of a blade of 14 mm thick, 95 mm wide and 220 mm length. The SDMT incorporates the traditional "mechanical" Flat Dilatometer with a seismic module placed above the DMT blade. The SDMT module is a probe outfitted with two receivers, spaced 0.5 m, for measuring the shear wave velocity (Vs), which allows obtaining the maximum shear modulus (G_o) based on Elastic theory [24]. One flat dilatometer (DMT) and three seismic dilatometer (SDMT) tests were carried out in the site in Abril, 2016. Fig. 6 shows the DMT and the SDMT data for the studied site. [23] proposed a series of correlations based on Italian soils for estimating soil parameters (i.e., unit weight - γ, at-rest earth pressure - K_o, overconsolidation ratio - OCR, friction angle - ϕ, undrained shear strength - c_u and constrained modulus - M).

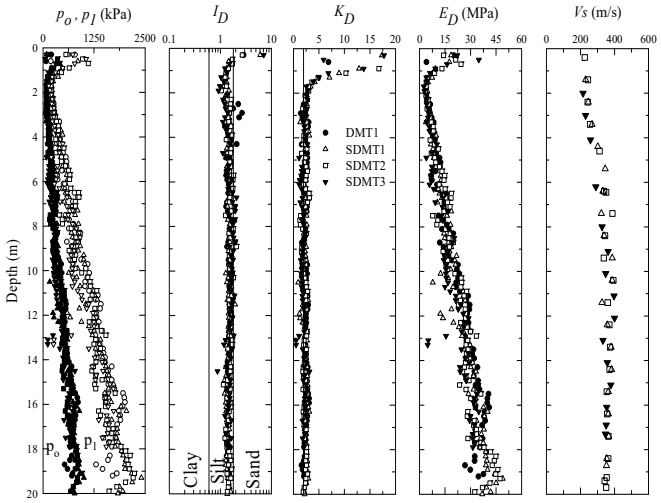


Figure 6. DMT and SDMT data for the studied site.
Source: The authors.

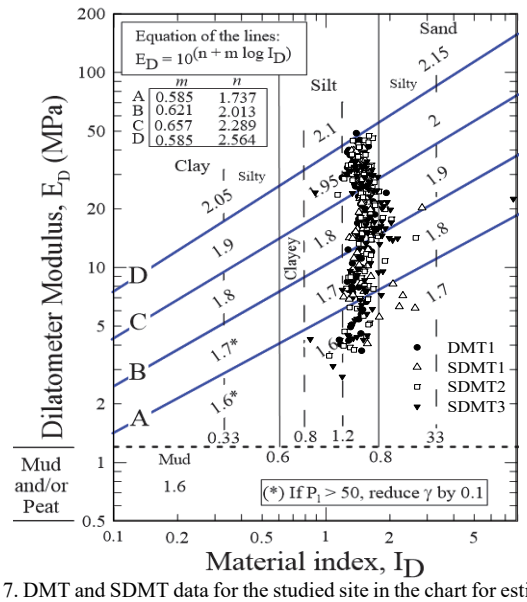


Figure 7. DMT and SDMT data for the studied site in the chart for estimating soil type and unit weight.
Source: modified from [25].

The material index $I_D = (p_1 - p_0)/(p_0 - u_0)$ was calculated from DMT and SDMT data to identify soil type. The pressures p_0 and p_1 are recorded when the center of the membrane is displaced 0.05 mm and 1.1 mm respectively, and u_o is the hydrostatic pore pressure.

The material index I_D (Fig. 6b) indicates that a sand silty occurs in the studied site. This classification can also be observed in the Marchetti and Crapps [25] chart, which can be used for estimating soil type as well as unit weight (Fig. 7). However, the real texture of this soil is a clayey fine sand, as can be seen in the Fig. 2a (SPT samples). [26] affirms that material index (I_D) should not be used to classify the soil as it is done by grain size analysis, but as an index which reflects mechanical behavior (a kind of "rigidity index"). For example, if a clay for some reasons behaves "more rigidly" than most clays, such clay will be probably interpreted by I_D as silt.

Interpretation of soil properties and parameters obtained from the average DMT and SDMT data are presented in the Fig. 8. Unit weight estimated based on the I_D vs E_D chart [25] is in good agreement with those obtained from undisturbed samples (Fig. 8a).

The dilatometer modulus (E_D) is obtained from p_0 and p_1 with the Elastic Theory. Fig. 8b shows the E_D profile, which demonstrates the linear increase with depth. These data were compared with E_{pmt} determined from Menard Pressuremeter. E_{pmt} and E_D (DMT and SDMT) are very close in agreement up to about 11 m depth. Epmt was one third lower than E_D after that depth. This behavior can be explained by soil disturbance, as discussed by [27]. According to [28], dilatometer modulus represents a measure of the elastic-plastic response of sands, since it is defined through the slope of the DMT expansion curve.

The DMT data can also be used to estimate the coefficient of at-rest earth pressure (K_o). The original correlation suggested by [23] was elaborated for clayey soils. [29] suggested a K_o chart for sands. This chart estimates K_o for a given value of corrected cone resistance (q_t) and K_D. [30] updated it converting into the following equation for sandy soils:

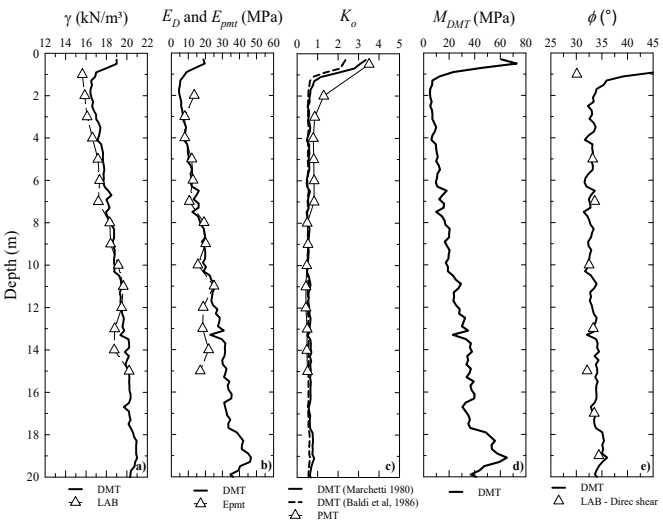


Figure 8. Measured and estimated parameters from average DMT and SDMT data.
Source: The authors.

$$K_o = 0.376 + 0.095K_D - 0.0017\ q_c/\sigma'_{vo} \qquad (8)$$

Fig. 8c presents K_o values estimated based on SDMT and DMT data using [23] and [30] correlations, as well as K_o interpreted based on PMT data. K_o from PMT is equal to 3.5 at 0.5 m depth and 1.3 at 1.5 m depth. It assumes a constant value almost equal to 0.8 up to about 8 m depth and 0.5 below this depth. The K_o values estimated from [30] correlation is equal to 2.2 at 0.5 m depth, 0.5 between 1 and 12 m depth and 0.6 below 12 m depth. K_o values predicted by [23] is 3.0 at 0.5 m depth, 0.5 between 1 and 13 m depth and 0.7 below 13 m. DMT K_o values calculated using [30] and [23] correlations better matches with PMT K_o values between 8 to 15 m depth.

Predicting settlements of foundations is the main DMT

application. Constrained modulus (M) is derived from the original correlation proposed by [23]. Fig. 8d shows the constrained modulus obtained via SDMT and DMT data. The M_{DMT} increases almost linearly with depth. The average M_{DMT} is equal to 10 MPa up 7 m depth, 23.5 MPa between 7 to 14 m depth and 41 MPa below 14 m depth. Unfortunately, there are no oedometer tests in this site to be used as reference values.

The strength parameters are amongst the most important information in geotechnical design. Fig. 8e presents friction angle estimated thorough Equation 9 suggested by [31] and the values determined in laboratory by direct shear tests (CD type).

$$\phi' = 28 + 14.6 \log K_D - 2.1 \log^2 K_D \quad (9)$$

The average estimated ϕ' angle was equivalent to the average measured ϕ' one of about 33º. For the 1 m topsoil, the estimated ϕ' angle based on DMT test data was little higher than determined by the direct shear tests. [32] monitored the water content and estimated the soil suction indirectly by the retention curve with depth and observed significant changing on both along the year up to about 4 m depth. This unsaturated soil has a cohesive-friction behavior and the estimative of the shear strength based on DMT data represents it just in terms of the friction angle. It could justify the higher DMT ϕ' angle for the top 1 m depth.

3.4. Seismic tests

Shear wave velocity (Vs) is an important mechanical parameter for geotechnical projects. Most seismic tests induce low shear strains and Vs can be used to compute initial shear modulus at very small strains, corresponding to a nondestructive testing ($\gamma_s < 10^{-6}$ %). The small-strain shear modulus or the maximum shear modulus (G_o) is mainly a stiffness parameter to predict the response of machine foundations, dynamic response of soil, earthquake and shallow and deep foundation design [33,34].

One cross-hole [16], two down-holes [17], one seismic cone [3] and one seismic SPT [35] tests previously carried out in the site were reinterpreted. The seismic SPT consists in the up-hole seismic technique carried out together with SPT [33,35]. The shear wave velocity (Vs) and maximum shear modulus (G_o) profiles, when the latter was calculated from total mass density determined using undisturbed soil samples collected in a sample pit excavated in the site, are illustrated in Fig. 9. The differences observed in both Vs and G_o profiles can be associated to different degree of weathering [36] as well as soil anisotropy [37]. [38] discussed variability for this site based on several CPT data and conclude that it could be affected by soil suction in the upper part of the soil profile.

Fig. 9c and Fig. 9d present G_o/q_t and G_o/N_{60} ratios from average values of G_o, q_t and N_{60}. Fig. 9c shows that the average G_o/q_t ratio tends to decrease with depth, with an average value equal to 111 between 1 and 4 m depth, 75 between 4 to 7 m depth, 41 between 7 to 14 m depth and 27 below 14 m depth. This behavior can also be observed in Fig. 9d, when the average G_o/N_{60} ratio was equal to 40 between 1 and 7 m depth, 21 between 7 to 16 m depth and 12 below 16 m depth.

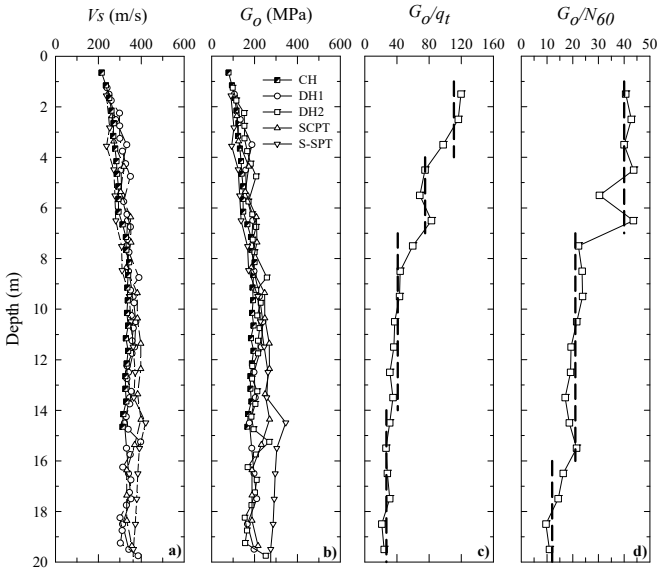


Figure 9. Seismic tests data and interpretation for the studied site.
Source: The authors.

These data indicate that G_o/q_t and G_o/N_{60} ratios are higher in the lateritic soil layer and tend to decrease as residual soil is less developed as presented by [38-40].

Tropical soils are typically unsaturated, so the pore pressure (u) are inconsistent and cannot be used as an extra information for soil classification. The ratio between maximum shear modulus (G_o) and cone resistance (q_t) is characteristic for clays and sands, as well as for a wide range of well-behaved soils [10]. [41,42,12] suggest the seismic cone (SCPT) as a useful tool to assess unusual geomaterials such as unsaturated soils, tailings, coarse-grained cemented aged materials. The ratio between the elastic stiffness (G_o) and ultimate strength (q_t) can be expected to increase with cementation and age, since these factors have higher influence G_o than on q_t [42].

[12], based on [43], proposed a chart and boundaries to evaluate the possible effects of microstructure (e.g. cementation, bonding and ageing) for a given profile. The author proposed the use of a modified normalized small strain rigidity index (K^*_G), the small strain rigidity index (I_G) and normalized cone resistance with a variable stress exponent (Q_{tn}). The I_G is defined as:

$$I_G = \left(\frac{G_o}{q_n}\right) = \left(\frac{G_o}{q_t - \sigma_v}\right) \quad (10)$$

Q_{tn} is defined as:

$$Q_{tn} = \left[\frac{q_t - \sigma_v}{p_a}\right]\left(\frac{p_a}{\sigma'_v}\right)^n \quad (11)$$

where p_a is the atmospheric pressure, σ'_v is the vertical effective stress, σ_v is the vertical stress and n is a stress exponent that varies with soil behavior type index (I_C), and n is calculated by:

$$n = 0.381(I_C) + 0.05\left(\frac{\sigma'_v}{p_a}\right) - 0.15 \quad (12)$$

The K^*_G is defined as:

$$K^*_G = (G_o/q_n)(Q_{tn})^{0.75} \quad (13)$$

[12] also demonstrated that soils with $K^*_G < 330$ are likely young and uncemented and where main models and empirical correlations for CPT can be applied. Moreover, soils with K^*_G higher than 330 tend to have significant microstructure, where main models and empirical correlations for CPT can be less reliable and local adjust may be needed.

Fig. 10 presents I_G vs Q_{tn} chart and the data for the studied site. It indicates that the bonded structure of tropical sandy soils always produced K^*_G values higher than 330. Moreover, it is also interesting to note in this Fig. that the lateritic soils have a higher G_o/q_n ratio than the saprolitic ones. Therefore, the models and empirical correlations for CPT data should be carefully used and local adjusts are necessary.

[44] also proposed interpretation charts for detecting the presence of cemented structures on soils based on DMT and SDMT data. The author carried out DMT and seismic tests in a calibration experiment inside an artificially cemented block samples prepared in a large chamber (CemSoil box). Fig. 11a and Fig. 11b show the G_o/E_D vs I_D and G_o/M_{DMT} vs K_D chart, respectively, and the three lines and one equation define the limits for the DMT sedimentary international database and upper bounds for cemented soil (CemSoil data).

SDMT data plotted in G_o/E_D vs I_D and G_o/M_{DMT} vs K_D charts are above the line which separates the DMT sedimentary international database and in the range proposed for residual soils. It indicates that the bonded structure of the studied tropical sandy soil produces G_o/E_D and G_o/M_{DMT} that are systematically higher than those observed in sedimentary soils. The differences on G_o/E_D and G_o/M_{DMT} for lateritic and saprolitic soils are also observed, similarly to what was as shown by [18,39] on G_o/q_c ratio from SCPT and by [40] and the based on based on G_o/N_{60} ratio from S-SPT. These ratios can be used to assess unusual soil behavior and they also indicated that the lateritic soils have higher ratios than the saprolitic ones.

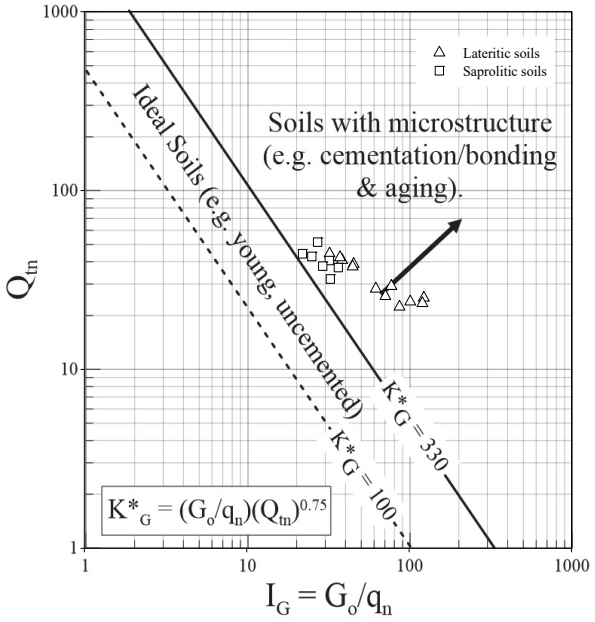


Figure 10. Q_{tn} vs I_G chart to identify soils with microstructure.
Source: modified from [12].

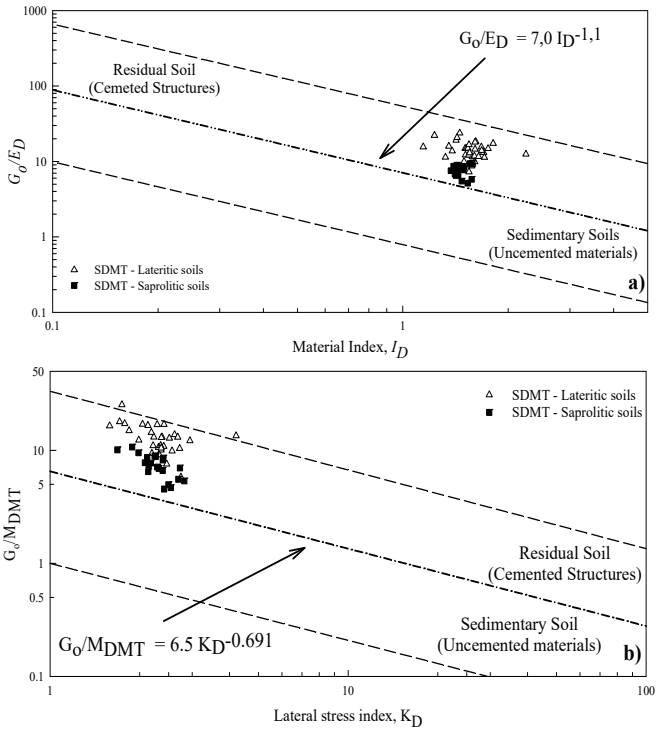


Figure 11. (a) G_o/E_D vs I_D and (b) G_o/M_{DMT} vs K_D charts.
Source: modified from [44].

4. Conclusions

This paper aims to present and discuss site investigation campaigns carried out via SPT, CPT, SDMT and seismic tests at a tropical soil profile. The main conclusions are:

- The soil profile was classified as red clayey fine sand by SPT samples. Both I_c index and I_D parameter were not appropriate to identify soil texture since mixtures of sand and clay were identified as silty sand to sandy silt. The soil description in terms of grain size distribution should be confirmed with soil samples for tropical soil.
- The estimated total unit weight based on CPT and SDMT worked well for the study site. The estimated CPT and DMT friction angle also worked well for the soil below 1 m. The unsaturated condition, as well as the cohesive-friction behavior could justify higher CPT and DMT ϕ' angle for the top 1 m depth.
- G_o was estimated for the study site assuming that the soil is uncemented quartz sand using current correlations. This approach underestimated G_o especially up to 13 m depth in the soil with lateritic behavior (LA'). It can be associated to the weakly cemented structure of these

soils, which increases the low strain shear modulus.

- DMT Modulus (E_D) was equivalent to PMT modulus (E_{pmt}) up to about 11 m depth and E_{pmt} was almost one third lower than E_D after that depth. The lateritic soil layer ends close to this depth (between 12 to 13 m depth), based on MCT Classification System.
- K_o predicted from DMT using Marchetti (1980) and Baldi et al. (1986) correlation basically matched PMT K_o values below to 8 m depth.
- Robertson [13] proposed a chart to identify the existence of microstructure in soils. Average G_o, Q_{tn} and q_n data were plotted in this chart. The tropical soil study has significant microstructure (e.g. $K^*_G > 330$). As a result, the proposed SBTn charts and most empirical correlations should be carefully applied, and site or geologic specific modifications are required.

Acknowledgments

The authors are grateful to the São Paulo Research Foundation – FAPESP (Grand # 2010/50680-3, 2011/09031-0, 2014/23767-8 and 2015/17260-0) and to the National Council for Scientific and Technological Development – CNPq (Grant # 446424/2014-5 and 310867/2012-6) for supporting their researcher.

References

[1] Vargas, M., The concept of tropical soils. keynote lecture, Proceedings of 1st International Conference on Geomechanics in Tropical Lateritic and Saprolitic Soils, Keynote Lecture, 1985. 3, pp. 101-134.

[2] Vaughan, P.R., Maccarini, M. and Mokhtar, S.M., Indexing the engineering properties of residual soils. Quarterly Journal of Engineering Geology, 21(1), pp. 69-84, 1988.

[3] De Mio, G., Condicionantes geológicos na interpretação de ensaios de piezocone para identificação estratigráfica na investigação geotécnica e geoambiental, PhD. Thesis, Department of Geotechnics Escola de Engenharia de São Carlos, Universidade de São Paulo, São Carlos, SP, Brasil, 2005.

[4] Nogami, J.S. and Villibor, D.F., A new soil classification for highway purposes, Proceedings of Symposium on Tropical Soils in Engineering], 1, 1981, pp. 30-41 [in Portuguese].

[5] Schmertmann, J.H. and Palacios, A., Energy dynamics of SPT. Journal of Geotechnical Engineering Division, ASCE, 105(8), pp. 909-926, 1979. DOI: 10.1680/geot.1986.36.3.425

[6] Skempton, A.W., Standard penetration test procedures and the effects in sands pf overburden pressure, relative density, particle size, ageing and overconsolodation, Géotechnique, 36(3), pp. 425-447, 1986. DOI: 10.1680/geot.1986.36.3.425

[7] Belincanta, A., Avaliação dos fatores intervenientes no índice de resistência à penetração do SPT, PhD. Thesis, Department of Geotechnics, Escola de Engenharia de São Carlos, Universidade de São Paulo, São Carlos, SP, Brasil, 1998.

[8] Ranzine, S.M.T., SPTF, Solos e Rochas, 11, 1988, pp. 29-30.

[9] Schnaid, F., Consoli, N.C. and Averbeck, J.H., Aspects of cone penetration in natural weakly-cemented deposits, Proceedings of 1st International Conference on Site Characterization, 2, 1998, pp. 1159-1163.

[10] Lunne, T., Robertson, P.K. and Powell, J., Cone penetration test in geotechnical practice. London: Blackie Academic Professional, 1997.

[11] Robertson, P.K., Interpretation of cone penetration tests - a unified approach, Canadian Geotechnical Journal, 46(11), pp.1337-1355, 2009. DOI: 10.1139/T09-065.

[12] Robertson, P.K., CPT-based soil behavior type (SBT) classification system – an update. Canadian Geotechnical Journal, 53(12), pp.1910-1927, 2016. DOI: 10.1139/cgj-2016-0044.

[13] Idriss, I.M. and Boulanger, R.W., Soil liquefaction during earthquakes, Oakland, Earthquake Engineering Research Institute, 2008. (Monograph MNO-12).

[14] Robertson, P.K. and Campanella, R.G., Interpretation of cone penetration tests. Part I: sand. Canadian Geotechnical Journal, 20(4), pp. 718-733, 1983. DOI: 10.1139/t83-078

[15] Robertson, P.K. and Campanella, R.G., Interpretation of cone penetration tests. Part II: clay. Canadian Geotechnical Journal, 20(4), pp. 734-745, 1983. DOI: 10.1139/t83-079

[16] Giacheti, H.L., Estudo experimental de parâmetros dinâmicos de alguns solos tropicais do Estado de São Paulo, PhD. Thesis, Department of Geotechnics, Escola de Engenharia de São Carlos, Universidade de São Paulo, São Carlos, SP, Brasil, 1991.

[17] Vitali, O.P.M., Pedrini, R.A.A., Giacheti, H.L. and Oliveira, L.P.R., Developing a system for down-hole seismic test together with the CPTU. Soil and Rocks, 35(3), pp. 75-88, 2012.

[18] Giacheti, H.L., Peixoto, A.S.P., De Mio, G. and Carvalho, D., Flat dilatometer testing in Brazilian tropical soils. Proceedings from the Second International Flat Dilatometer Conference. ASCE, [online].1, 2006,pp. 103-110. Available at: http://www.marchetti-dmt.it/wp-content/uploads/bibliografia/giacheti_2006_DMT_in_Brazilian_tropicalsoils. pdf

[19] Robertson, P.K. and Cabal, K.L., Estimating soil unit weight from CPT. Proceedings of 2nd International Symposium on Cone Penetration Testing, CPT'10, 2, 2010, pp. 447-454.

[20] Viana-da Fonseca, A., Identifying the reserve of strength and stiffness characteristics due to cemented structure of a saprolitic soil from granite. Proceedings of 2nd International Symposium on Hard Soils – Soft Rocks, 1, 1998, pp. 361-372.

[21] Viana-da Fonseca, A., Ferreira, C., Carvalho, J., Sousa, C., Costa, E. and Santos, J., Geotechnical characterization of residual soil profile: the ISC'2 experimental site, Porto. Proceedings of Geotechnical and geophysical site characterization, 2, 2004, pp. 1361-1370.

[22] Viana-da Fonseca, A., Carvalho, J., Ferreira, C., Santos, J.A., Almeida, F., Pereira, E., Feliciano, J., Grade, J. and Oliveira, A., Characterization of a profile of residual soil from granite combining geological, geophysical, and mechanical testing techniques. Geotechnical and Geological Engineering, 14(5), pp. 1307-1348, 2006.

[23] Marchetti, S., In situ tests by flat dilatometer. Journal of the Geotechnical Engineering Division, ASCE, 106 (GT3), pp. 299-321, 1980.

[24] Marchetti, S., Monaco, P., Totani, G. and Marchetti, D., In situ tests by seismic dilatometer (SDMT). Symposium Honoring Dr. John H. Schmertmann for His contributions to civil engineering at research to practice in geotechnical engineering Congress, 2008, pp. 292-311.

[25] Marchetti, S. and Crapps, D.K., Flat dilatometer manual: internal report of G.P.E. Washington, The Global Partnership for Education, Washington, 1981.

[26] Marchetti, S., Monaco, P., Totani, G. and Calabrese, M., The flat dilatometer test (DMT) in soil investigations. Proceedings of International Conference on In situ Measurement of Soil Properties and Case Histories, TC16 Report, 2001, 41 P.

[27] Ortigão, J.A.R., Cunha, R.P. and Alves, L.S., In situ tests in Brasília porous clay. Canadian Geotechnical Journal, 33(1), pp. 189-198, 1996. DOI: 10.1139/t96-035.

[28] Campanella, R.G., and Robertson, P.K., Use and interpretation of a research DMT. Soil Mechanics Series No. 127. British Columbia, Vancouver, Department of Civil engineering, The University of British Columbia, Vancouver, 1989.

[29] Marchetti, S., On the field determination of K_0 in sand. Proceedings of XI International Conference of Soil Mechanics and Foundation Engineering. Discussion Session n. 2A. 5, 1985, pp. 2667-2673.

[30] Baldi, G., Bellotti, R., Ghionna, V., Jamiolkowski, M., Marchetti, S. and Pasqualini, E., Flat dilatometer tests in calibration chambers. Proceedings of Conference on Use of In Situ Tests in Geotechnical Engineering, In Situ' 86(6), 1986, pp. 431-446.

[31] Marchetti, S., The flat dilatometer: design applications. Proceedings of 3rd International Geotechnical Engineering Conference, Keynote Lecture, 2007, pp. 421-448.
[32] Rocha, B.P. Santos, R.A., Bezerra, R.C., Rodrigues, R.A. and Giacheti, H.L., Characterization of unsaturated tropical soil site by in situ tests. Proceedings of 5th International Conference on Geotechnical and Geophysical Site Characterization. [online]. 2, Sydney, Australia, 2016, pp. 1129-1136. Available at: https://www.issmge.org/uploads /publications/25/26/ ISC5_168.pdf
[33] Bang, E.S. and Kim, D.S., Evaluation of shear wave velocity profile using SPT based up-hole method. Soil Dynamics and Earthquake Engineering, 27(7), pp. 741-758, 2007. DOI: 10.1016/j.soildyn.2006.12.004.
[34] Ku, T., Mayne, P.W. and Cargill, E., Continuous-interval shear wave velocity profiling by auto-source and seismic piezocone tests. Canadian Geotechnical Journal, 50(4), pp. 382-390, 2013. DOI: 10.1139/cgj-2012-0278.
[35] Pedrini, R.A.A., Developing a system for up-hole seismic testing together with the SPT test. MSc. Thesis, Department of Civil and Environmental Engineering, Faculdade de Engenharia de Bauru, Universidade do Estado de São Paulo, Bauru, SP, Brasil, 2012.
[36] Hoyos, L.R. and Macari, E.J., Influence of in situ factors on dynamic response of piedmont residual soils. Journal of Geotechnical and Geoenvironmental Engineering, 125(4), pp. 271-279, 1999. DOI: 10.1061/(ASCE)1090-0241 (1999) 125:4(271)
[37] Powell, J.J.M. and Butcher, A.P., Small strain stiffness assessments from in situ tests. Proceedings of 2nd International Conference on Geotechnical and Geophysical Site Characterization. 2, 2004, pp. 1717-1722.
[38] Giacheti, H.L., Peixoto, A.S.P. and Marques, M.E.M., Cone penetration testing on Brazilian tropical soils. Proceedings of XII Pan-American Conference on Soil Mechanics and Foundation Engineering. 1, 2003, pp. 397-402.
[39] Giacheti, H.L. and De Mio, G., Seismic cone penetration tests on tropical soils and the ratio G_o/q_c. Proceedings of 3rd Geotechnical and Geophysical Site Characterization Conference. 1, 2008, pp. 1289-1295.
[40] Rocha, B.R., O emprego do SPT sísmico (S-SPT) na investigação de solos tropicais. MSc. Thesis. Department of Geotechnics, Escola de Engenharia de São Carlos, Universidade de São Paulo, São Carlos, SP, Brasil, 2013.
[41] Eslaamizaad, S. and Robertson, P.K., A framework for in-situ determination of sand compressibility. Proceedings of 49th Canadian Geotechnical Conference. 1, 1996, pp. 419-428.
[42] Schnaid, F., Fahey, M. and Lehane, B., In situ test characterization of unusual geomaterials. Keynote Lecture. Proceedings of Geotechnical e Geophysical Site Characterization. 1, 2004, pp. 49-74.
[43] Schneider, J.A. and Moss, R.E.S., Linking cyclic stress and cyclic strain based methods for assessment of cyclic liquefaction triggering in sands. Géotechnique Letters, 1(2), pp. 31-36, 2011. DOI: 10.1680/geolett.11.00021.
[44] Cruz, N., Modelling geomechanics of residual soils with DMT tests. PhD. Thesis, Faculdade de Engenharia, Universidade do Porto, Porto, Portugal, 2010.

B.P. Rocha, received his BSc. in Civil Engineering in 2011 from the São Paulo State University, Brazil. He earned his MSc. and DSc. in Geotechnical Engineering, both from the University of São Paulo, Brazil in 2013 and 2018, respectively. During his Master's degree and doctorate, he has been working with in situ and laboratory testing for site characterization of soils mainly for foundations engineering (SPT, cone penetration, seismic flat dilatometer and laboratory tests).
ORCID: 0000-0002-6534-0482

H.L. Giacheti, received his BSc. in Civil Engineering in 1982 from São Paulo State University, Brazil. He earned his MSc. and DSc. in Geotechnical Engineering, both from the University of São Paulo, Brazil in 1987 and 1991, respectively and a Post-doctorate at the University of British Columbia, Canada, during 1997 to 1999. Full professor at the São Paulo State University and Brazilian representative in the TC-102: Ground Property Characterization from In-Situ Tests for the ISSMGE. His research interests include: site investigation, in situ testing, piezocone, flat dilatometer, foundation engineering and geo-environmental geotechnics.
ORCID: 0000-0001-7999-0956

UNIVERSIDAD NACIONAL DE COLOMBIA
SEDE MEDELLÍN
FACULTAD DE MINAS

Área Curricular de Ingeniería Civil

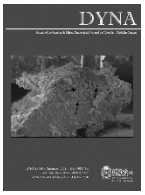
Oferta de Posgrados

Especialización en Vías y Transportes
Especialización en Estructuras
Maestría en Ingeniería - Infraestructura y Sistemas de Transporte
Maestría en Ingeniería – Geotecnia
Doctorado en Ingeniería - Ingeniería Civil

Mayor información:

E-mail: asisacic_med@unal.edu.co
Teléfono: (57-4) 425 5172

UNIVERSIDAD NACIONAL DE COLOMBIA
SEDE MEDELLÍN
FACULTAD DE MINAS



DYNA
http://dyna.medellin.unal.edu.co/

Sugarcane molasses and vinasse as a substrate for polyhydroxyalkanoates (PHA) production

Alejandro Acosta-Cárdenas, Wilman Alcaraz-Zapata & Mariana Cardona-Betancur

Research Group on Biotransformation, School of Microbiology, University of Antioquia, Medellin, Colombia, alejandro.acosta@udea.edu.co, wilman.alcaraz@udea.edu.co, mariana.cardona@udea.edu.co

Received: October 20th, de 2017. Received in revised form: July15th, 2018. Accepted: August 15th, 2018

Abstract
Polyhydroxyalkanoates (PHA) are fully biodegradable biopolymers of microbial origin, with physicochemical characteristics similar to those of conventional synthetic plastics. However, their current production is highly expensive mainly due to the substrate or culture medium employed. In this research, a mixture of cane molasses and residual vinasse from the alcohol industry was evaluated as a substrate using the reference strain *Ralstonia eutropha* ATCC 17699 to produce PHAs. The results showed the potential of the mixture as a culture medium, after reaching polymer concentrations of 3.17 g/L in MSM medium and 2.71 g/L in M/V medium with a molasses/vinasse ratio of 25/75. There was a sugar (sucrose, fructose, and glucose) consumption yield of 70.7%, and a biopolymer accumulation of 97.8% with respect to the biomass produced. The biopolymer characterization showed a correlation with the standard polyhydroxybutyrate sample - PHB of 99.25%.

Keywords: biopolymers; polyhydroxyalkanoates; *Ralstonia*; sugarcane molasses; sugarcane vinasse.

Melazas y vinaza de la caña de azúcar como sustrato para la producción de polihidroxialcanoatos (PHA)

Resumen
Los Polihidroxialcanoatos (PHAs) son biopolímeros de origen microbiano totalmente biodegradables con características físicoquímicas similares a los plásticos sintéticos convencionales, sin embargo, su producción actual es altamente costosa debido principalmente al sustrato o medio de cultivo. En esta investigación se evaluó como sustrato, una mezcla de melaza de caña y vinaza residuales de la industria licorera empleando la cepa referencia *Ralstonia eutropha* ATCC 17699 para la producción de PHAs. Los resultados obtenidos mostraron potencial en el uso de este medio de cultivo, alcanzando concentraciones de polímero de 3,17 g/L en medio MMS y de 2,71 g/L en el medio M/V con una relación melaza/vinaza de 25/75. El rendimiento de consumo de azucares (sacarosa, fructosa y glucosa) fue del 70,7% y una acumulación del biopolímero del 97,8% respecto a la biomasa producida. La caracterización del biopolímero presento una correlación con la muestra patrón de polihidroxibutirato - PHB del 99,25%.

Palabras clave: biopolímeros; polihidroxialcanoatos; *Ralstonia*; melaza de caña de azúcar y vinaza de caña de azúcar.

1. Introduction

Polyhydroxyalkanoates (PHA) are fully biodegradable biopolymers of microbial origin with physiochemical characteristics similar to those of conventional synthetic plastics, from rigid and brittle plastics to rubber-like plastics [1-5]. There are different microbial strains employed in the production of PHAs; *Rasltonia eutropa*, for example, can metabolize different carbon sources and accumulate the biopolymer [6,7].

Despite the environmental advantages that PHAs represent and their wide field of application in comparison with petrochemical plastic, their use and industrial profitability is limited by high production costs which, in 2010, reached estimated values of 6.25 USD/kg, surpassing prices of petroleum-based polymers, which had reached an estimated cost of 1.45 USD/kg [8], preventing them from being economically competitive.

How to cite: Acosta-Cárdenas, A., Alcaraz-Zapata, W. and Cardona-Betancur, M., Sugarcane molasses and vinasse as a substrate for polyhydroxyalkanoates (PHA) production. DYNA, 85(206), pp. 220-225, September, 2018.

© The author; licensee Universidad Nacional de Colombia.

Much of PHAs high costs respond to the culture medium employed, which accounts for up to 50% of the total production cost [9]. In view of this, the study and evaluation of low-cost non-conventional substrates to elaborate such a culture medium is increasing.

Molasses emerge as a good alternative because of its nutritional composition, rich in sugar, protein, amino acids and microelements such as Mg, P and K. Given the large extent of sugarcane crops in Colombia, it is possible to obtain residual molasses, from the sugar refinement process, at a low cost [10]. Vinasse, another residue obtained from ethanol distillation processes, is rich in salts [11]. Therefore, it could be used as a complement to the elaboration of culture media for fermentative processes.

The use of vinasse in PHA production could reduce its negative impact on the environment since it would reduce the amount of water and salts necessary for the elaboration of the culture medium and its effects if not properly disposed, caused by its high levels of BOD and COD between 35,000-50,000 and 100,000-150,000 mg O_2/L respectively [11,12], which exceed the permissible discharge limits for the production of agroindustrial activities (sugar and derivatives from sugar cane) and for non-domestic wastewater discharge - nDWD to surface water bodies, BOD 500 mg/L O_2, COD 900 mg/L O_2 [13], according to Resolution 0631 of 2015 (Ministry of Environment - Colombia). All things considered, this study evaluated different molasses/vinasse ratios to obtain a non-conventional culture medium for PHA production by *Rastonia eutropha* ATCC 17699, given its ability to metabolize different carbon sources.

2. Materials and methods

2.1. Microbial strain and culture condition

Ralstonia eutropha ATCC 17699 (*Cupriavidus necator*) was purchased from ATCC (Manassas, VA, USA) through CES University. The bacterium was cryopreserved at -20 °C in tryptic soy and broth medium (TSB) in 30% glycerol, inside a 1.5 mL vial, and subcultured in TSB under standard monthly conditions.

The inoculum used for culture in the reactor was carried out in 1L Erlenmeyer flasks containing 300 mL of TSB medium, at 30°C and 150 rpm for 12 hours, using a vial with the bacterial strain cryopreserved.

The culture was carried out in a 5L bioreactor (New Brunswick) with automatic control of agitation at 200 rpm, a temperature of 30ºC, air flow of 5 L/min and pH 7.0, controlled with 1N HCL and NaOH solutions.

2.2. Treatment and characterization of raw materials used as a substrate

The vinasse for experimentation was donated by a sugar-alcohol company in Colombia. It was centrifuged at 8,000 rpm for 7 min to remove particulate matter. The supernatant was then characterized to determine total sugar, Ca, Mg and K content. On the other hand, commercial molasses employed (high viscosity sugar syrup) contained 60-63 % (w/w) sucrose and 3-5 % (w/w) reducing sugars. Due to the high sugar content, this was diluted to obtain the ratio and concentration of sugar required for experimentation.

Mineral salt medium (MSM) employed in the culture as a reference medium contained (per liter): Glucose 20 g; $Na_2HPO_4.7H_2O$ 6,7 g; KH_2PO_4 1,5 g; $(NH_4)_2SO_4$ 1,0 g; $MgSO_4.7H_2O$ 0,2 g; iron and ammonium citrate 60 mg; $CaCl_2.2H_2O$ 10 mg; element trace solution 1 ml. Element trace solution (per liter): H_3BO_3 0,3 g; $CoCl_2.6H_2O$ 0,2 g; $ZnSO_4.7H_2O$ 0,1 g; $MnCL_2.4H_2O$ 30 mg; $NaMoO_4.2H_2O$ 30 mg; $NiCl_2.6H_2O$ 20 mg; $CuSO_4.5H_2O$ 10 mg [14].

2.3. Biomass determination

Biomass concentration was determined by gravimetry, using dry weight determination with 5mL samples of culture broth. The samples were passed through membrane filters (Millipore, 0.45 µm filters) in a filtration equipment with a vacuum pump, to be then dried at 70°C for 24 hours and weighed in an analytical balance to constant weight.

2.4. Sugars determination

A high-performance liquid chromatography (HPLC) Agilent Technologies 1200, model 61362A, with a column of separation ionic interchange Animex HPX-87H, 300x7.8mm was employed in sugars determination. The samples were centrifuged at 7,000 rpm for 5 min and aliquots of the supernatant were taken, which were diluted in mobile phase according to the concentration range of the standard curve employed. Each diluted sample was run through 0.2 µm regenerated cellulose filters and injected under the following conditions: 20 µL sample, 0.6 mL/min flow, 35ºC and 12 min run time. All samples were analyzed in triplicate.

2.5. PHA extraction, and characterization by FTIR

The extraction of the PHA produced was carried out following Yu & Chen methodology, where the sample was subjected to a sterilization process at 120ºC for 30 min, to be then is recovered by centrifugation at 5,000 g for 12 min and washed with distilled water; then, 200 mL of 0.1 M H2SO4 are suspended in solution and subjected to digestion at 100 ºC for 2 hours, adjusted to pH 10 with 5N NaOH and centrifuged at 4,000 rpm for 20 min to recover the biopolymer. This is resuspended in a 6% NaCl solution to be bleached and is again recovered by centrifugation and washed with distilled water. Determination of the PHA production was performed using dry basis quantification [15].

For the characterization of the PHA produced, Fourier Transform Infrared Spectroscopy (FTIR) technique was used, with a Perkin-Elmer Spectrum BX infrared spectrophotometer and ART module from 4,000 to 400 cm^{-1} and a Sigma-Aldrich branched PHB (Polyhidroxibutyrate) standard with 99% purity.

2.6. Experimental design and statistical analysis

Three one-way experimental designs were performed. The first factor was evaluated with different relations of molasses/vinasse (M/V: 100/0, 75/25, 50/50, 25/75); the second factor was the nitrogen source (with and without nitrogen source); the third factor was the salts supplement

Table 1.
Characterization of vinasse

Parameters	Results
Sucrose	3.72 ± 1.05 g/L
Glucose	2.44 ± 1.25 g/L
Fructose	5.48 ± 1.35 g/L
Mesophiles	$2.67x10^7$ UFC/mL
pH	4.85 ± 0.2
Conductivity	21,180 ±30 uS/cm
Total solids (dry weight)	5.0 ± 0.7 g/L
Ca	1.28 %
Mg	0.36 %
K	1.66 %

Source: The authors.

(with and without salts supplement). The nitrogen and salts from the MSM medium were used as a reference for the second and third factor. All experiments were carried out in triplicate, using biomass, sugars, and biopolymer as response variables.

A one-way variance analysis (ANOVA) and a Tukey HSD multiple comparisons test were performed to evaluate the data. The results that presented values of *p-value* < 0.05 were interpreted as statistically significant variables using the software StatGraphics Centurion 17.1 Demo.

3. Results and discussion

3.1. Characterization of vinasse

Vinasse was characterized according to available sugar content, which was quantified by HPLC; this, together with other components that can be seen in Table 1, were analyzed at the Laboratory of Physicochemical Analysis, Institute of Chemistry (Laboratorio de Análisis Fisicoquímico del Instituto de Química - LAFQ) , University of Antioquia.

According to Table1, the sugar content in the vinasses reached 11.64 g/L, so it was required to complement the medium with an additional carbon source such as molasses, according to the carbon requirements of the MSM. The pH also needed to be adjusted but Ca, Mg and K contributions exceeded those required by the reference medium [14]. However, Zuñiga et al. (2013) report pH values in vinasse of 4.6-4.7 and 7.4 - 8.4 g/L in total solids [11], in agreement with the values in this work.

3.2. Evaluation of different molasses/vinasse ratios

Table 2 shows the concentration of sugars consumed by *R. eutropha* under different molasses/vinasse ratios. The growth of bacteria in all cultures was evidenced by microscopy. It was also observed that the highest yield of total sugars was reached in the proportion 25/75 molasses/vinasse, presenting a statistically significant difference between the other proportions (*p-value <0.05*). Similarly, Dos Santos et al. reported a yield of 0.79 or 79 % of sugars consumed in an *R. eutropha* culture, using vinasse obtained from cane ethanol production [16].

Fig. 1 shows a profile of time-quantified sugars for the cultivation of *R. eutropha* at an M/V ratio of 25/75 with supplementation of nitrogen and salt sources (1.0 g/L of $(NH_4)_2SO_4$)

Table 2.
Consumption of sugars performance under different proportions of molasses/vinasse in cultures of *R. eutropha* ATCC 17699 in the 5L bioreactor.

Proportion molasses/vinasse (v/v)	Y (Total sugars consumed/initial sugars*)
100/0	0.15±0.01
75/25	0.08±0.02
50/50	0.26±0.01
25/75	0.79±0.09

*Sugars, corresponding to the sum of sucrose, glucose, and fructose
Source: The authors.

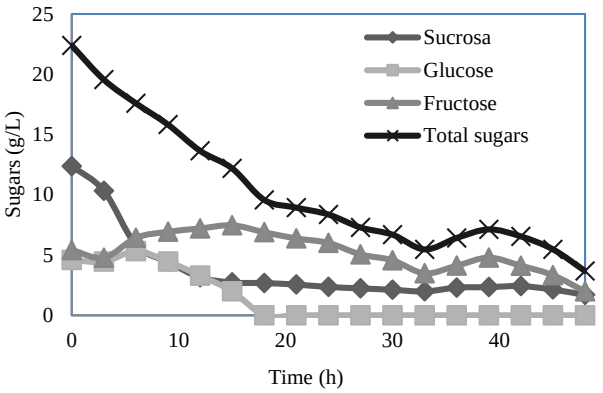


Figure 1. Consumption of sugars by *R. eutropha* ATCC 17699 of an M/V ratio: 25/75, with nitrogen and salt supplementation, in the 5L bioreactor.
Source: The authors.

and according to the MSM culture medium. It also shows the consumption of total sugars (sucrose, glucose, and fructose), the gradual consumption of sucrose, and how at 18 hours post-culture the total glucose had been consumed.

The results in Table 3 correspond to the evaluation of the culture supplemented with nitrogen and salt sources, with M/V of 25/75. Although there were no statistically significant differences between treatments, PHA productivity, $Y_{p/s}$ and consumption of sugars were higher in the mixture supplemented with nitrogen and salt sources.

Table 3.
Experimental results of *R. eutropha* ATCC 17699 in molasses/vinasse: 25/75 culture with or without nitrogen and/or salt supplementation.

Parameter	Molasses/vinasse with N and salts	Molasses/vinasse with N and without salts	Molasses/vinasse without N and without salts
Total sugars consumed (g/L)	18.71±3.98	15.43±4.65	14.80±4.05
Polymer concentration (g/L)	3.84±0.41	2.11±0.43	1.92±0.38
Yp/s (g/g)	0.21±0.319	0.14±0.50	0.13±0.47
PHA Productivity (g/L.h)	0.080±0.012	0.043±0.021	0.040±0.019

Yp/s = Product yield coefficient relative to the substrate = dry polymer produced per unit of consumed sugars.
Source: The authors.

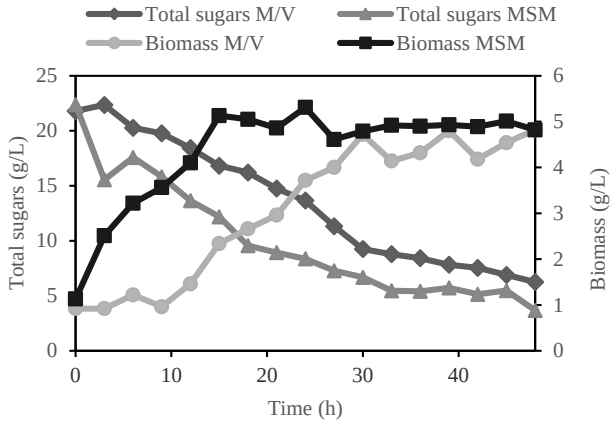


Figure 2. Growth of *R. eutropha* ATCC 17699 in molasses/vinasse: 25/75 with addition of nitrogen and salts and in MSM reference medium, grown in a 5L bioreactor.
Source: The authors.

Finally, in Fig. 2, a comparison was made between the MSM reference culture and the culture using an M/V ratio of 25/75 supplemented with nitrogen and salt sources. In both cultures, the consumption of total sugars with values of 18.60 and 15.56 g / L is appreciated, which represents an efficiency in the consumption of sugars of 83.1 and 71.3%, respectively.

In the culture with molasses/vinasse, a lag phase of 9 hours could also be observed, unlike the culture with the MSM medium. This difference in the lag phase may be related to the low concentration of glucose in the medium forcing *R. eutropha* to hydrolyze the available sucrose.

Table 4 shows the results of the parameters determined for each crop; no statistically significant differences were found between the parameters evaluated except the total of sugars consumed. In this way, the M/V medium can be considered suitable for the cultivation of *R. eutropha*, with the capacity to accumulate up to 97.8 % of PHA with respect to the produced biomass and a yield of 97.8 % in total sugars consumed. However, Nonato et al. cultivated *R. eutropha* with a medium enriched with cane molasses with a productivity of 1.44 g PHA/L.h, but with a biopolymer content of 65-70% [17].

Table 4.
Comparison of the parameter for *R. eutropa* ATCC 17699 in MSM and culture with M/V: 25/75 supplemented with nitrogen source and salts.

Parameter	*R. eutropha* ATCC 17699 with MSM	*R. eutropha* ATCC 17699 with M/V
Total sugars consumed (g/L)	18.60 ± 0.93	15.56 ± 1.22
Biomass concentration (g/L)	3.69 ± 0.07	3.90 ± 0.32
Polymer concentration (g/L)	3.17 ± 0.47	2.71 ± 0.56
Yx/s (g/g)	0.20 ± 0.068	0.25 ± 0.016
Yp/s (g/g)	0.17 ± 0.019	0.17 ± 0.028
Yp/x (g/g)	0.86 ± 0.167	0.69 ± 0.288
PHA Productivity (g/L.h)	0.066 ± 0.014	0.056 ±0.020

Yx/s = Biomass yield coefficient relative to substrate = dry biomass produced per unit of consumed sugars.
Yp/x = Product yield coefficient relative to biomass = dry biopolymer produced per unit of dry biomass.
Source: The authors.

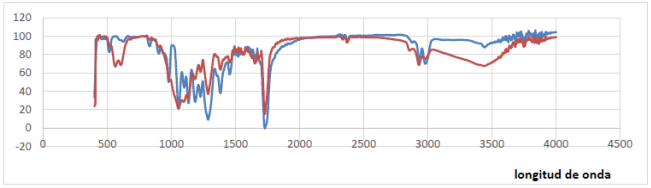


Figure 3. Spectra of the polymer produced with *R. eutropha* ATCC 17699 in the medium MV and the reference polymer PHB brand Sigma-Aldrich, using the Fourier transform infrared spectroscopy (FTIR).
Source: The authors.

Other researchers, such as El-Sayed et al., also carried out cultures with mixtures of glucose and sucrose obtaining 0.8 g/L PHB, but with a change in the culture, strategy reached 7.31 g/L PHB [18]. On the other hand, Pramanik A et al. also used vinasse as a culture medium for the production of PHAs but using the strain *Haloarcula marismortui*, with which a content of 23-30% was obtained in the dry biomass with a productivity between 0.015 and 0.020 g / L.h of polymer [19].

3.3. Biopolymer characterization by FTIR

By comparing the spectra of the polymers obtained in Fig. 3 with the *R. eutropha* strain versus the polyhydroxy butyrate standard (PHB), an equal pattern is observed in the formed bands. The peaks corresponding to the region of the spectrum of 1,740 cm^{-1} and 2,970 cm^{-1} are characteristic of C = O and CH_3 functional groups of the monomeric PHB [20].

The spectra obtained from *R. eutropha* showed a correlation of 99.25% with the pattern of bands in the PHB commercial polymer employed, indicating thus that the polymer obtained from *R. eutropha* is of the PHB type [21] [22]. According to reports, this polymer is highly crystalline (> 50%). The melting and glass transition temperature is about 180 ° C and 4 ° C, respectively. It has some mechanical properties comparable to degradable synthetic polyesters, such as PLA. During the storage time at room temperature, it undergoes a secondary crystallization of the amorphous phase, as a result, the tensile and elongation modulus increase while the polymer becomes more brittle and harder [23] [24].

This biopolymer is an attractive material for tissue engineering due to its inherent biocompatibility. It has been shown to enhance the proliferation of different cell types and since PHB is susceptible to various processing methods, it can be mixed with other types of biocompatible molecules such as the hydroxyapatite mineral to create films, fibrous mats or non-crystalline chains, adaptable to a specific use [25] [26].

4. Conclusions

Both molasses and vinasse can be used as a non-conventional culture medium in the production of PHA, thanks to their contributions to carbon and micronutrient sources.

Vinasses alone do not provide a sufficient carbon source to achieve high amounts of biomass and PHA production. Therefore it is essential to supplement the culture with an additional carbon source.

The most suitable proportion of the molasses/vinasse mixture was 25/75, achieving a substrate consumption efficiency of 83.6%. On the other hand, *R. eutropha* ATCC 17699, has the ability to consume sucrose as a substrate.

The FTIR analysis between the PHB Polyhydroxybutyrate sample and the polymer produced by *R. eutropha* showed a correlation between its bands of 99.25%, which allows us to state that the biopolymer produced was of the polyhydroxybutyrate type.

Acknowledgments

The authors thank the Biotransformation Group of the School of Microbiology and the Technological Management Program of the University of Antioquia for the financial support of the project CIEMB-072-12; the students Lina Marcela Serna, Adis Andrea Acevedo and Diana Marcela Rodríguez for their support in the execution of the project; and the professor Luis Fernando Giraldo for the interpretation of the FTIR.

References

[1] Mozumder, M.S.I., De Wever, H., Volcke, E.I.P. and Garcia-Gonzalez, L., A robust fed-batch feeding strategy independent of the carbon source for optimal polyhydroxybutyrate production, Process Biochem., 49(3), pp. 365-373, 2014. DOI: 10.1016/j.procbio.2013.12.004

[2] Costa, M.M.E., Cabral-Albuquerque, E.C.M., Alves, T.L.M., Pinto, J.C. and Fialho, R.L., Use of polyhydroxybutyrate and ethyl cellulose for coating of urea granules, J. Agric. Food Chem., 61(42), pp. 9984-9991, 2013. DOI: 10.1021/jf401185y

[3] Bressan, E., Favero, V., Gardin, C., Ferroni, L., Iacobellis, L., Favero, L., Vindigni, V., Berengo, M., Sivolella, S. and Zavan, B., Biopolymers for hard and soft engineered tissues: application in odontoiatric and plastic surgery field, Polymers (Basel)., 3, pp. 509-526, 2011. DOI: 10.3390/polym3010509

[4] Esha, M., Tissue engineering applications of polyhydroxybutyrate, MSc. Thesis. Cornell University, Nueva York, EE.UU., 2008.

[5] Castilho, L.R., Mitchell, D.A. and Freire, D.M.G., Production of polyhydroxyalkanoates (PHAs) from waste materials and by-products by submerged and solid-state fermentation, Bioresour. Technol., 100(23), pp. 5996-6009, 2009. DOI: 10.1016/j.biortech.2009.03.088

[6] Du, C., Sabirova, J., Soetaert, W. and Ki C., Lin, S., Polyhydroxyalkanoates production from low-cost sustainable raw materials, Curr. Chem. Biol., 6(1), pp. 14-25, 2012. DOI: 10.2174/187231312799984394

[7] Mozumder, S.I., De Wever, H., Volcke, E.I.P. and Garcia-Gonzalez, L., A robust fed-batch feeding strategy independent of the carbon source for optimal polyhydroxybutyrate production, Process Biochem., 49(3), pp. 365-373, 2014. DOI: 10.1016/j.procbio.2013.12.004

[8] Chanprateep, S., Current trends in biodegradable polyhydroxyalkanoates, J. Biosci. Bioeng., 110(6), pp. 621-632, 2010. DOI: 10.1016/j.jbiosc.2010.07.014

[9] Naranjo-Vasco, J.M., Design and analysis of the polyhydroxybutyrate (PHB) production from agroindustrial wastes in Colombia, PhD. Thesis, Universidad Nacional de Colombia, Colombia, 2014.

[10] Fajardo-Castillo, E.E. y Sarmiento-Forero, S.C., Evaluación de melaza de caña como sustrato para la producción de *Saccharomyces cerevisiae*, Thesis, Pontificia Universidad Javeriana, Bogotá, Colombia, 2007.

[11] Zúñiga-Cerón, V. and Gandini-Ayerbe M.A., Environmental characterization of stillage from sugar cane waste from the production of ethanol, DYNA, [en linea], 80(177), pp. 124-131, 2013. [Consulted: August 27th of 2018] Availavle at: en: http://www.redalyc.org/articulo.oa?id=49625661016. ISSN: 0012-7353

[12] Dávila, J., Machuca, F. y Marrianga, N., Peroxidación y flotación electrolítica de vinazas de destilería, Rev. Ing., [online]. 32, pp. 38-44, 2010. [Retrieved: August 27th of 2018]. Available at: http://www.scielo.org.co/scielo.php?script=sci_arttext&pid=S0121-49932010000200005&lng=en&tlng=.

[13] Minambiente, Resolución 0631 -17 Marzo 2015, Ministerio de Ambiente y Desarrollo Sostenible, Bogotá, Colombia, ., [online]. 2015. [Retrieved: August 27th of 2018]. Available at: http://www.minambiente.gov.co/images/normativa/app/resoluciones/d1-res_631_marz_2015.pdf

[14] Ramsay, B.A., Lomaliza, K., Chavarie, C., Dube, B., Bataille, P. and Ramsay, J.A., Production of poly- (beta-Hydroxybutyric-Co-beta-Hydroxyvaleric) acids, Appl. Environ. Microbiol., 56(7), pp. 2093-2098, 1990.

[15] Yu, J. and Chen, L.X.L., Cost-effective recovery and purification of polyhydroxyalkanoates by selective dissolution of cell mass, Biotechnol. Prog., 22(2), pp. 547-553, 2006. DOI: 10.1021/bp050362g

[16] dos Santos, E., Gai, C., Zanfonato, K., Martinhago, F., Steffen, W. and Quines, L.K., Production of polyhydroxyalkanoate biopolymer from vinasse using *Ralstonia eutropha*, BMC Proc., 8(Suppl 4), pp. P132, 2014. DOI: 10.1186/1753-6561-8-S4-P132

[17] Nonato, R.V., Mantelatto, P.E. and Rossell, C.E.V, Integrated production of biodegradable plastic, sugar and ethanol, Appl. Microbiol. Biotechnol., 57(1-2), pp. 1-5, 2001. DOI: 10.1007/s002530100732

[18] Sayed, El-, Azhar, A., Abdelhady, H.M., Abdel-Hafez, A.M. and Khodair, T.A., Batch production of polyhydroxybutyrate (PHB) by *Ralstonia Eutropha* and *Alcaligenes latus* using bioreactor different culture strategies, J. Appl. Sci. Res., [online]. 5(5), pp. 556-564, 2009. [Retrieved: August 27th of 2018]. Available at: https://docplayer.net/48081542-Batch-production-of-polyhydroxybutyrate-phb-by-ralstonia-eutropha-and-alcaligenes-latus-using-bioreactor-different-culture-strategies.html

[19] Pramanik, A., Mitra, A., Arumugam, M. et al., Utilization of vinasse for the production of polyhydroxybutyrate by *Haloarcula marismortui*, Folia Microbiol. (Praha)., 57(1), pp. 71-79, 2012. DOI: 10.1007/s12223-011-0092-3

[20] Aarthi, N. and Ramana, K.V., Identification and characterization of polyhydroxybutyrate producing *Bacillus cereus* and *Bacillus mycoides* strains, Int. J. Environ. Sci., [online]. 1(5), pp. 744-756, 2011. [Retrieved: August 27th of 2018]. Available at: http://www.ipublishing.co.in/jesvol1no12010/EIJES2030.pdf

[21] Barbosa, M., Espinosa-Hernández, A., Malagón-Romero, D. and Moreno-Sarmiento, N., Producción de Poli- β -Hidrobutirato (PHB) por *Ralstonia eutropha* ATCC 17697, Univ. Sci. Rev. la Fac. Ciencias. Pontif. Univ. Javeriana., [online]. 10(1), pp. 45-54, 2005. [Retrieved: August 27th of 2018]. Available at: http://revistas.javeriana.edu.co/index.php/scientarium/article/view/4936

[22] Saratale, G.D. and Oh, M.K., Characterization of poly-3-hydroxybutyrate (PHB) produced from *Ralstonia eutropha* using an alkali-pretreated biomass feedstock, Int. J. Biol. Macromol., 80, pp. 627-635, 2015. DOI: 10.1016/j.ijbiomac.2015.07.034

[23] El-Hadi, A., Schnabel, R., Straube, E., Muller, G. and Henning S., Correlation between degree of crystallinity, morphology, glass temperature, mechanical properties and biodegradation of poly (3-hydroxyalkanoate) PHAs and their blends, Polym. Test., 21(6), pp. 665-674, 2002. DOI: 10.1016/S0142-9418(01)00142-8

[24] Vroman, I. and Tighzert, L., Biodegradable polymers, Materials (Basel)., 2(2), pp. 307-344, 2009. DOI: 10.3390/ma2020307

[25] Priyadarshi S, Shukla, A and Bhaskarrao-Borse, B. Polyhydroxyalkanoates: Role of *Ralstonia eutropha*. Int J Biomed Adv Res. 05(02), pp. 68-76, 2014. DOI: 10.7439/ijbar

[26] Wu, Q., Wang, Y. and Chen, G.-Q., Medical application of microbial biopolyesters polyhydroxyalkanoates, Artif. Cells Blood Substitutes Immobil. Biotechnol., 37(1), pp. 1-12, 2009. DOI: 10.1080/10731190802664429

A. Acosta-Cárdenas, received the BSc. of Chemical Engineer in 2001, a mMSc. degree in Biotechnology in 2007 and from 2007 to 2016 he was a professor at the School of Microbiology at the University of Antioquia, Colombia. At the moment he carries out his PhD studies in Biotechnology at the University of Antioquia, Colombia.
ORCID: 0000-0002-2435-4060

W. Alcaraz-Zapata, received the BSc. of Industrial and Environmental Microbiologist in 2011 and the MSc. degree in Biology in 2018, both at the University of Antioquia, Colombia. Since 2016 he teaches at the School of Microbiology of the University of Antioquia, Colombia.
ORCID: 0000-0001-6121-4916

M. Cardona-Betancur, received the BSc. of Chemical Engineer in 2008, the MSc. degree in Engineering in 2011, both at the University of Antioquia, Colombia. Between 2010 and 2014 she was a teacher at the UdeA School of Microbiology and currently works as research and development specialist on new technologies of the Company Anhydrides and Derivatives of Colombia - ANDERCOL S.A.
ORCID: 0000-0002-9011-0865



Área Curricular de Ingeniería
Química e Ingeniería de Petróleos

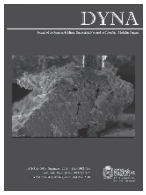
Oferta de Posgrados

Maestría en Ingeniería - Ingeniería Química
Maestría en Ingeniería - Ingeniería de Petróleos
Doctorado en Ingeniería - Sistemas Energéticos

Mayor información:

E-mail: qcaypet_med@unal.edu.co
Teléfono: (57-4) 425 5317

UNIVERSIDAD NACIONAL DE COLOMBIA
SEDE MEDELLÍN
FACULTAD DE MINAS



DYNA
http://dyna.medellin.unal.edu.co/

Evaluation of water use in food SMEs: case study of a poultry processing plant in Colombia

Yelitza Angélica Zorrilla-Ortega [a], Juan Pablo Silva [a], Valentina Prado [b] & Pablo César Manyoma [a]

[a] *Facultad de Ingeniería, Universidad del Valle, Cali, Colombia. yelitza.angelica.zorrilla@correounivalle.edu.co, juan.silva@correounivalle.edu.co, pablo.manyoma@correounivalle.edu.co*
[b] *Institute of Environmental Sciences (CML), Department of Industrial Ecology, Leiden University P.O., Leiden, The Netherland. & EarthShift Global LLC, Kittery, USA. v.prado@cml.leidenuniv.nl*

Received: November 12h, 2017. Received in revised form: june 27th, 2018. Accepted: July 16, 2018

Abstract
Water resources and the food sector in developing countries are key elements in ensuring the goals of sustainable development. The challenge is even greater, considering that the 90% of companies in these countries are small and medium enterprises (SMEs). To evaluate water management in food SMEs in Colombia, a case study was conducted in a poultry processing plant. Operation was determined by technical visits, measurements and water balances and the performance was evaluated by a sensitivity analysis. Total water consumption was 206,2$m^3 \cdot d^{-1}$ finding performances between 10,9 and 28,8 L.$chicken^{-1}$. The areas of plucking and evisceration were responsible for 62% and cleaning for 19% of water use. Daily, a volume of 32,4m^3 water was used as a means of transport. It was found that water consumption exceeds the recommended values of the Environmental Technology Best Practice Programme. Proposals for improvement in situ focused on prevention and minimization were suggested.

Keywords: water consumption; SMEs; poultry slaughter; sensitivity analysis; cleaner production.

Evaluación del uso del agua en PYMES de alimentos: caso de estudio en una planta de beneficio avícola en Colombia

Resumen
El sector de alimentos y el agua en países en desarrollo, son elementos fundamentales para alcanzar los objetivos del desarrollo sostenible. Este reto a enfrentar es mayor cuando el 90% de las empresas son pequeñas y medianas (Pymes). Para evaluar cómo es el manejo del agua en las Pymes, un estudio de caso fue desarrollado en una planta de beneficio avícola colombiana. Visitas técnicas, monitoreos y balances de agua determinaron el funcionamiento. El desempeño fue evaluado por un análisis de sensibilidad. El consumo promedio de agua fue 206,2$m^3.d^{-1}$ hallando desempeños entre 10,9 y 28,8 L.$pollo^{-1}$, con las áreas de desplume y evisceración responsables del 62% y la limpieza del 19%. Diariamente 32,4m^3 de agua son empleados como medio de transporte. Se encontró que el consumo de agua excede los valores recomendados del Programa de Mejores Prácticas de Tecnología Ambiental. Propuestas de mejora enfocadas en prevención y minimización fueron planteadas.

Palabras clave: consumo de agua; PYMES; sacrificio avícola; análisis de sensibilidad; producción más limpia.

1. Introduction

Only 2,5% of the water available on the planet is fresh water, and only 0,006% (2120 km^3) is contained in rivers [1]. Factors such as the global population of 7400 million people and economic growth (the world's Gross Domestic Product (GDP) doubled over the last 30 years) [2], have increased the pressure on water resources mainly fresh water. For example, human and industrial consumption are supplied mainly by fresh water in 80% and 87%, respectively [3]. It has been determined that to meet production needs and population requirements, the demand for water by the industrial sector

How to cite: Zorrilla-Ortega, Y.A., Silva, J.P., Prado, V. and Manyoma, P.C., Evaluation of water use in food SMEs: case study of a poultry processing plant in Colombia. DYNA, 85(206), pp. 226-235, September, 2018.

© The author; licensee Universidad Nacional de Colombia.

must increase to 1170 km^3 by 2025, which will lead to a strict dependence on the status and the quality of the resource.

This demand of water by the industrial sector depends on the size of the company, as does the efficiency of its water management [4,5]. Small and medium-sized enterprises (SMEs) are particularly important because they account for 90% of companies worldwide [6] and contribute 50% of GDP and 60% of global employment [7]. In terms of environmental performance, SMEs have certain common characteristics, such as high levels of non-compliance with environmental regulations that can impact the environment [8]. Statistical data on environmental impacts in SMEs are scarce in many countries. Among the few available data, SMEs in Europe account for 50% of the total industrial environmental impact, and in Asia it reaches 70% [5,9].

All agroindustry processes require water for operations, especially the food sector. According to reports from the European Commission, this sector contributes 23% of the global consumption of water resources and generates between 43% and 54% of organic pollutants in water in both developed and developing countries, the latter having primary economies, meaning those based on agriculture [10].

The meat subsector is an important group within the food sector. It demands a significant volume of water; the consumption of meat and dairy alone represent 29% of the human water footprint [12]. By 2014, world meat production was estimated at 311.6 million tons, with poultry at 35%, beef 22%, pork 37%, sheep 4% and others 2% [13]. The poultry subsector, thanks to certain competitive advantages, stands out against the other meat products due to the low area intensity, the reduced rearing and processing times and the low price of the final product versus the others [14]. Worldwide, the main producers of broiler chicken are the United States, China, Brazil and the European Union. In Latin America, the countries that represent 77% of production as of 2013 are Brazil (5608 million chickens), Mexico (1472 million), Argentina (810 million) and Colombia (631 million) [15].

In Colombia, the poultry subsector accounts for 11% of agricultural GDP and 28% of livestock GDP, which also includes other meats such as cattle and pork and products such as milk and eggs. Poultry production has a production value of $14,8 billion (USD $4934 million) [16] and generates approximately 400000 jobs. Some 60% of this activity is located in the departments of Cundinamarca, Santander and Valle. Per capita consumption of poultry at the national level reached 30 kg, requiring 97 million broilers, measured in the capacity of the broiler, equivalent to a production of 1,42 million tons of chicken meat by 2015 [17]. Current water indicators for productive activities in Colombia, such as the water footprint, have been quantified [18]. In terms of demand for surface water or blue water footprint (BWF) at the national level, the Ministry of Environment (ME) estimated 26 $m^3 \cdot year^{-1}$ per animal for broiler chicken processing, $4,6x10^6$ $m^3 \cdot year^{-1}$ for poultry slaughtering activities and $1,7x10^6$ $m^3 \cdot year^{-1}$ for the processing and preservation of meat and meat products [18,19].

According to the Ministry of Information Technologies and Communications, in Colombia there are 306 Poultry Processing Plants, but by 2017 47% were reported closed [20], evidencing strong needs and shortcomings in their processes. Therefore, the present study sought to identify the critical points that generate a high water consumption, and then developed a sensitivity analysis to establish an evaluation of the management, in order to make the right decisions in relation to their management of water, and finally, and thus proposing improvement strategies that contribute to reducing and mitigating the pressure on the water resource caused by Poultry Processing Plants.

2. Materials and methods

2.1. Characterization of the chicken processing plant

The Plant under study was located in the rural area of Valle del Cauca, at an altitude of 1200 m, and temperatures between 25°C in the shade, with a water supply of rivers, streams and creeks. Its economic objective was the slaughter and commercialization of chicken in carcasses without viscera, legs, head or neck. The work week was Monday to Saturday from 5:30 a.m. to 15:30 p.m. It had 69 employees distributed among plant and administrative personnel, with breaks of one hour for breakfast and lunch.

The form of operation was by batches, between 3 and 6. For each truck with chickens that arrived at the plant, there was a sacrifice batch. These were manually unloaded and were heavy. Those that died during the journey were placed in sacks as a confiscation. The chickens were then lifted, stunned, slaughtered, scalded, plucked, skinned, eviscerated, washed, then cooled or hydrated and then packaged, stored and/or dispatched. The length of time from lifting to packing is 76,5 minutes. Before each break and batches, the workers quickly rinsed their work areas. At the end of the day, a general cleaning was carried out at the plant.

The auxiliary operations with water demand included administrative activities, water purification (DWTP), washing baskets, ice generation, general cleaning and disinfection, activities in the by-product area, activities in the wastewater treatment plant (WWTP) and the bathroom service. The latter has eight toilets with a tank capacity of 6 liters and for handwashing two metal structures each with four wrenches under pressure. There is also a boiler for the generation of steam, which consumes $1m^3.day^{-1}$ of water. Fig. 1 shows the general outline of the plant.

The by-product area received, by pipes and channels, waste from each of the areas, such as feathers, cuticle, viscera, guts and undigested food. In this area, solid waste was collected manually in sacks (feathers, cuticle and feed) and in buckets (viscera). Blood was stored in jars. These waste products were withdrawn daily and purchased by an outside company. Regarding wastewater was sent to the WWTP, with a treatment system consisting of a grease trap, oxidation trench, secondary settler and gravel-sand filters.

At the end of the shift, general disinfection of equipment, walls and floors was carried out in each area. Typically, it started at 17:00 pm with an average duration of 7 hours, being carried out by three operators to clean the eight areas. Depending on the area, the cleaning lasted 20-120 minutes. It started with a manual rinse, using buckets and hoses without

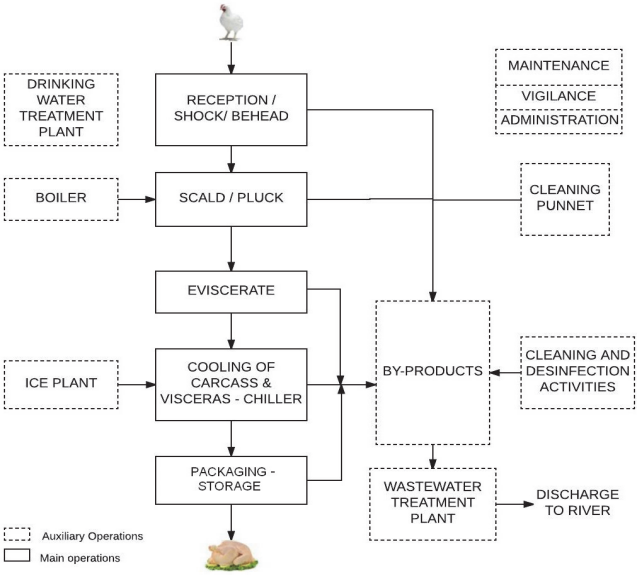


Figure 1. Main processing activities in the Benefit Plant
Source: The authors

valves to turn them off. Although washing equipment (pressure hydro-washer of handgun) was available, it was damaged. Then, the areas were scrubbed, and the final rinse removed detergent. At the end a spray disinfectant is applied.

To establish the typical operation at the plant, 114 days of operation were studied, from February to August 2016. With this information the operation was evaluated from Monday to Saturday, using the box diagram.

2.2. Water consumption estimation

Visits were made to a poultry processing plant to understand the processes performed there. Each area of the enterprise was inspected with regard to water use on equipment and activities performed by the operators, including the state of the infrastructure. The daily logs of the process and the technical feature of the teams were also evaluated. Primary and secondary information from the literature review was compiled and then contrasted with our collected data. All points of access to water in the plant were identified and inventoried by area, identifying the points where the water was used and where it was poured, as well as a photographic survey of the leaks. In addition, we identified which units were directly required for the process and which were only auxiliary operations. For water supply, the company had two supplies, the main one came from a surface water source that worked on gravity and provided 95% of the water which supplied average flow of 4 $L.s^{-1}$ and the another came from the local public aqueduct destined for the generation of ice. This requires to be driven by pumping. Due to the lack of water flow meters in the plant, it was necessary to carry out a water balance. With the volumetric method, the flow rates of the productive areas were calculated. For this, chronometers and buckets (12L) were used, and for each measurement 3 replicates were made. Finally, an material flow analysis was performed using the trial version of the software e!Sankey 4 calc, 4.4.07513 for 14 days of august of 2017.

The water balance equation was:

Accumulation = Inputs - Outputs + Production - Consumption

With: Accumulation, Production and Consumption = 0, we had eq. (1):

$$\frac{dv}{dt} = \sum_{i=1}^{N} Qe,i - \sum_{j=1}^{M} Qs,j = 0 \qquad (1)$$

Then,

$\frac{dv}{dt}$ = Accumulated volume over time;

$\sum_{i=1}^{N} Qe,i$ = Flow Inputs

$\sum_{j=1}^{M} Qs,j$ = Flow Outputs

2.3. Sensitivity analysis

A sensitivity analysis of the water consumption in the productive process was carried out. Thus, the information was grouped with respect to the number of batches processed, the number of chickens processed, the average time of a batch and the duration of slaughter. The operating range was established with the maximum and minimum value found in the records. The minimum found was 50 minutes, so an increase of 15 in 15 minutes was established until 140 minutes. These were analyzed by varying the time of the batch between 50 and 140 minutes. The unit used to compare the performance efficiency was liters consumed per chicken.

3. Results and discussion

3.1. Characterization of the productive process

With the recognition of each area and the variation in the number of chickens slaughtered from one batch to another and from one day to another, it was necessary to analyze the behavior and dispersion with respect to the number of slaughtered batches and then, to establish the typical operation at the plant.

Fig. 2 shows the number of chickens slaughtered for each batch. For all period evaluated the median was around to 2780 chickens. In terms of interquartile range this oscillates between 2600 and 2860 chickens, such difference was due to the capacity of the truck and / or production on the farm. The size of the boxes shows a very similar dispersion from one day to another, being minimal in the case of Friday, showing homogeneous batch, perhaps by factors such as the allocation of the same farm. The minimum and maximum atypical values found for the number of slaughtered chickens per batch were 2290 and 3140 respectively, thus indicating the flexibility of operation that the plant has by batch. Such variations are caused by the number of chickens caged according to the sex and weight of the animal sent in each batch.

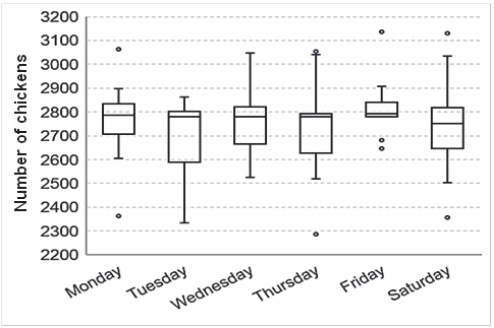


Figure 2. Processing capacity: slaughtered chickens per batch
Source: The authors

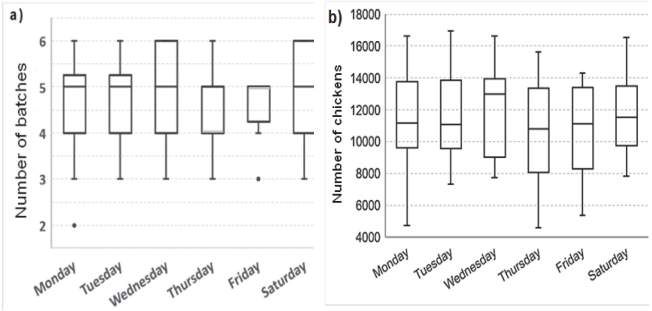


Figure 3. Slaughter capacity average per day. (a) Number of batches per day; (b) Processing capacity: total slaughtered chickens per day
Source: The authors

The Fig. 3(a) shows numbers of batches per day. The median was 5 batches by day, except on Thursday. Wednesday and Saturday had the greatest dispersion with an interquartile range between 4 and 6 batches. This is reflected in the processing capacity of a day of sacrifice, Fig. 3(b), where the median of Wednesday was the highest with 13000 chickens to coincide with the highest number of batches processed. For the other days, the median was reiterative, close to 11200 chickens, with a homogeneous distribution and an interquartile range between 8000 and 14000 chickens, as well extreme values between 4200 and 17000 chickens were observed.

In addition, to quantify the water consumption by the areas it was necessary to describe the operating times. This measurement considered (a) the time to hoist a batch for slaughter and (b) the total duration per day. It should be noted that few studies describe the operating times. The Fig. 4(a), shows a low dispersion of data for the different days, being between 75 and 80 minutes, except Tuesday with 70 minutes coinciding with a smaller number of chickens to be sacrificed. Atypical values were reported between 63 and 90 minutes. In terms of the total day of operation, Fig 4(b) shows an average of 320 minutes with a discrepancy of Wednesday that reaches 353 minutes, because it coincides with the day of greatest production. On Thursday a time of only 293 minutes was registered, with 4 process batches in the day. The extreme values were between 123 and 485 minutes. It should be highlighted that these were net values of the hoisting time of the chickens, and do not include recess and other stops of operation.

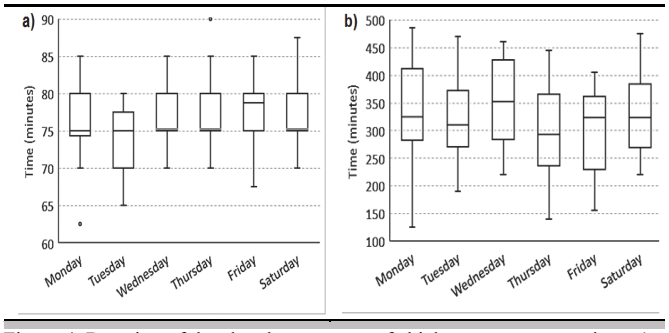


Figure 4. Duration of the slaughter process of chickens, average per day. a) Total operating time and duration of each batch; b) Total batches time and total duration per process day.
Source: The authors

Table 1.
Daily Average operation conditions

Description	Unit
Average processing capacity	13630 chickens.d^{-1}
Average time per 1 batch hoist	80 min
Number of batches per day of processing	5 batches.d^{-1}

Source: The authors

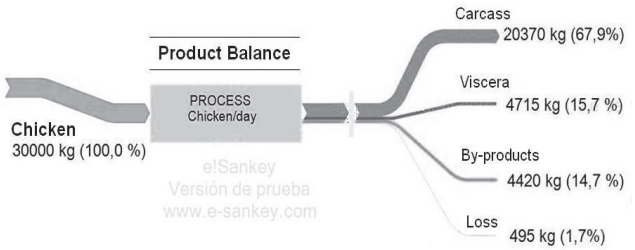


Figure 5. Balance of the product (e!Sankey software)
Source: The authors

The above is important to mention because the operating time is linked to the amount of water consumed and it will vary according to the number and type of equipment, as well as the way of operation. Such disinformation can lead to underestimation of total water demands. As a result of the characterization, a 5 batches operation was established for the Plant. Of the 114 days, 47% were performed under this condition. Therefore, the average operation of the plant was established with the values shown in Table 1.

Based on average operation conditions, the mass balance indicated that the chicken carcass product amounted to 67,9% of the total, edible viscera 15,7% and by-products and losses the remaining 16,4% (Fig. 5). The percentages found correspond to the reported for a chicken carcass weight between 67% and 75% [29] and a by-product weight of 20% [27].

3.2. Estimation of consumption

The main water uses in the plant were: the production process, cleaning of equipment, use of bathrooms and general cleaning. Throughout the plant, 58 water supply points were inspected, also the presence and absence of leaks in them. In



Figure 6. Photographic record
Source: The authors

the toilet service was not recorded leakage. Of the eleven water leaks found, they were located in the joints of the equipment, in the faucets or in the water main pipes (see Fig.6), wasting 3621 liters of water per day. One of the causes was the type of valve used, as a direct seal caused a pressure blow on the joints, causing misalignments and leaks. On the other hand, leaks are a contributing factor in the generation of wastewater, which can sometimes affect the removal efficiency of treatment systems, having very dilute loads.

To estimate water consumption, it was necessary to establish the management of the demand and the frequency of consumption of the equipment, operation activities and routine cleaning as well as the instruments used for its execution (faucets, hoses, buckets, etc.). Fig. 7 shows the areas and required volume of 206,2 m^3 of water to slaughter 13630 chickens in one day of processing. The net consumption of the process was 140,0 m^3 (68%) excluding auxiliary operations, ice demand and cleaning at the plant. The distribution of water demand that each area generates is shown in Fig. 8. Evisceration, plucking and scalding accounted for 62% of the total water consumption that the plant used. This coincides with the 68% reported in the literature [22].

Plucking and evisceration were the activities with the highest demand, at 103,8 m^3. It should be mentioned that 35,8m^3 was for the use of water as a means of transport. The activities are described in Table 2. Point 1 used a hose with a constant flow of water to transmit the waste to the by-product zone. At point 2, a raised metal channel received the chicken and slid it with water towards the evisceration area. Point 3 carried the viscera, discharging water through the ducts. As for the cooling area it represented 11,7% including ice. The literature reports values between 14% and 16,7% [22,26]. Routine cleaning activities in each area depend on the number of breaks and how long each batch of chickens is processed. This represented 8,2% of total consumption, with 16,9 m^3. The area with the highest water consumption was the reception where the chickens arrived, where constant cleaning of the truck, cages and place of unloading was required. For [22,26] this was reported in 15%.

Cleaning and disinfection at the end of the shift had a consumption of 39,4 m^3. The volume depended on how the operator performed the cleaning, the instruments used and the time required to do it. The use of hoses without faucets to shut them off caused a waste, which doubled the consumption when compared to the use of pressure-washing equipment.

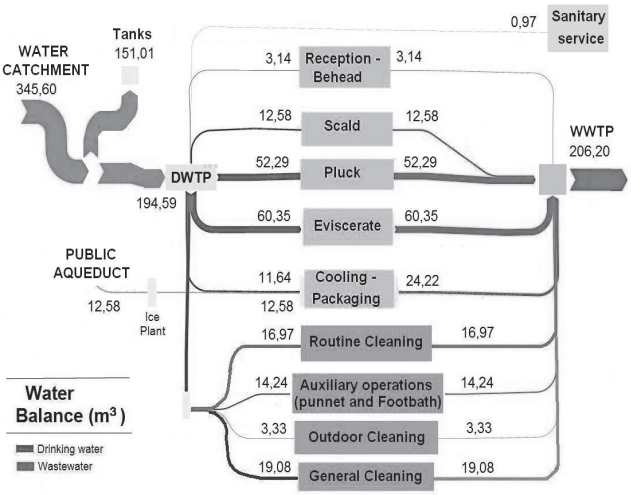


Figure 7. Water balance for a day of process using the e! Sankey software. Note: DWTP: Drinking water Treatment Plant; WWTP: Wastewater Treatment Plant.
Source: The authors

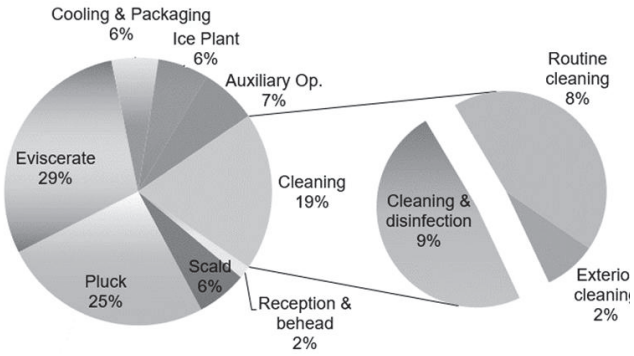


Figure 8. Distribution of water consumption
Source: The authors

The cleaning activity accounted for 19% of the total consumption quantified, but when compared with the main operations only, it reached 25%. According to the companies evaluated by [21], cleaning ranged between 10% and 22% of the total consumption. Values of 9% were reported by [22] for industrial cleaning, and including the washing activity of the baskets and cages, it reached 18%. It should be mentioned that for the present study, washing baskets and washing cages were considered ancillary activities because each task had its own personnel, day and area. In the literature only one study was found that quantified the water consumption for a poultry processing plant. It did not specify the operating conditions, but it presented consolidated values for the companies in terms of water consumption per month, as well as the number of birds slaughtered for each studied plant [21]. Another study evaluated water minimization, reporting values only in percentages [22]. Other it reported data in terms of water effluent in $m^3 \cdot ton^{-1}$ but without information on chicken weight and slaughtering capacity [23]. These reports thus presented water consumption in different ways, which makes it difficult to make an adequate comparison between companies, together with the lack of relevant information.

Table 2.
Use of water as a means of transport

Point	Water use for:	Consumption ($m^3.d^{-1}$ Process)
1.	Conduction of feathers and cuticle to the by-products area	11,7
2.	To slide the carcasses by metal channel that connects pluck with evisceration	3,4
3.	Conduction of edible and non-edible viscera	20,6
	Total	35,8

Source: The authors

Table 4.
Results of operating ranges

Description	Operation		
	Maximum	Average	Minimun
Average capacity (chickens)	16919	13630	7085
Batches per day (units)	6	5	3
	Average Batch Time (minutes)		
1 Batch hoist	110	80	55
Total Batches hoist	504	400	188
Average (#chickens.batch^{-1})	3190	2726	2203
Date	22-03-2016		25-07-2016

Source: The authors

Table 5.
Sensitivity Analysis Average Operating Values

Description	Average Function	Analysis #1
Average capacity (chickens)	13630	Fixed
Number of process batches (Batches.d^{-1})	5	Fixed
Average Time of Batch hoist (min)	80	110
Chickens per Average Batch hoist	2726	Fixed
Time of Batches.d^{-1}	400	550
CONSUMPTION DAY (m^3)	206,2	244,7
Process	81%	84%
Cleaning	19%	16%
CONSUMPTION L.chicken^{-1}	15,1	18,0

Source: The authors

Table 3 shows the consolidation of available studies with information in terms of slaughtering capacity, water consumption and volume of effluent generated. It should be noted that when the study did not indicate the days per month, 26 days of operation were assumed. In addition, we considered the minimum number of chickens that a plant of similar size would sacrifice in an hour. Based on this, the minimum operating hours of the plant were estimated.

For the 17 processing plants referenced for Colombia, it was estimated that, there would be a total of 186 million chickens slaughtered per year, requiring 2,09x$10^6 m^3$ of water. If it is compared with the value reported by the Ministry ME, there is an underestimated value of only 4,6 x$10^6 m^3$ for all Poultry Processing Plants. Thus, it is critical to study how water management is being carried out in this sector because it may be underestimated. However, the range found to sacrifice a single chicken was between 6,4 to 29,8L/chicken, indicating how there are companies that can consume up to five times more water per processed chicken than others. According to Environmental Technology Best Practice Programme-ETBPP for chicken slaughter activity having 8,0 L.chicken^{-1}, is a recommended value of operation and this evidenced inefficient water management, generating pressure on the water resource. Due to the different ways in which each plant can operate, it is important that studies report the quantified values and the areas included and not included as precisely and specifically as possible, to enable correct comparisons. What promotes working on how water management is carried out in these production processes.

3.3. Sensitivity analysis of the production process

In order to analyze the liters consumed per chickens and to evaluate trends and behaviors of the water consumption in a day of operation, values such as the number of chickens processed, the number of batches and their duration were analyzed. In Table 4, the actual plant performance values and their maximum, average and minimum processing capacities are presented. These values established the operating range of the plant, between 50 and 140 minutes per hoist one batch.

A sensitivity analysis for 110 minutes was presented as an example, indicating the fixed values. For this case, the 20-minute delay in the process, from hoisting to packing, resulted in an increase of 38,5 m^3, equivalent to 3L more for each processed chicken. Table 5 consolidates the results obtained. For this analysis the activities of the process were grouped (main and auxiliary operations), as well as cleaning (general, routine and outdoor).

Table 6 shows the increase of water consumption by processed chicken for periods of 15 minutes for each capacity. For the reported maximum slaughter capacity, consumptions were obtained between 10,9 and 19,1 L per chicken, almost double the value. According to these data, for every minute would have a consumption of 1529 L more approximately. Considering the average value, the range found was 12,3 and 20,8L per chicken with an increase of 1279L. In terms of the minimum production capacity of 7085 chickens, the results found were 18,9 to 28,8 L per chicken, giving an average increase of 780 L·min^{-1}. When compared with the maximum values, the minimum number of chickens slaughtered per process caused a higher rate of water consumption per chicken. This is explained by the minimum operating requirements, in water and equipment, that are needed for its execution. This indicates the importance of working with appropriate water management in this sector, confirming that inefficient use doubles water demand.

Identifying the critical points that generate an inadequate water performance is fundamental for a sustainable water management and thus successful decision making and not only the remediation of end-of-pipe (for example, WWTP) with high costs in the alternatives, causing a strong economic impact for SMEs.

Table 3.
Poultry Slaughterhouse water consumption

		Slaughter		Consumption			Wastewater	Reference
Country	Capacity	Chicken.h^{-1}	Chicken.d^{-1}	Ice (kg.chicken^{-}	Process (m^3.d^{-1})	Demand L.chicken^{-1}	Effluent (m^3.d^{-1})	Author
BOLIVIA, Tarija	Operation 365 days	-	1900	1,21	16	-	-	[24]
COLOMBIA, Valle	Employees: 69, Workday: 10h.d^{-1}, Discharge: 17h	2726	13630	0,92	206	15,10	206	PS
COLOMBIA, Santander	470234 CSM; Workday: 8h.d^{-1} and 26 d.month^{-1},* Discharge: 12h		18086		213	11,77	199	[25]
COLOMBIA, Bogotá	480000 CSM. Employees: < 100		18462		154	8,33±0,54		[21]
COLOMBIA, Tolima	Displume: 60 chicken.min^{-1};	3600		0,63	-	-		[27]
COLOMBIA, Bogotá	520000 CSM. Employees: < 100		20000		162	8,06±0,65		[21]
COLOMBIA, Bogotá	620000 CSM. Employees: < 100		23846		158	6,60±0,42		[21]
COLOMBIA, Bogotá	625000 CSM. Employees: < 100		24038		154	6,43±0,41		[21]
COLOMBIA, Santander	783924 CSM. Workday: 10h.d^{-1}*, Discharge: 18h*		30151		656	21,84	651	[25]
COLOMBIA, Santander	859969 CSM. Workday: 8h.d^{-1}*, Discharge:10h		33076		270	8,23	248	[25]
BOLIVIA, Cochabamba	Workday: 10h.d^{-1} and 308 d.year^{-1}	3800	38000			20,40		[24]
COLOMBIA, Bogotá	880000 CSM. Employees: 100 - 250		33846		335	9,91±0,50		[21]
COLOMBIA, Bogotá	883000 CSM. Employees: 100 - 250		33962		327	9,64±0,52		[21]
COLOMBIA, Bogotá	1295000 CSM. Employees: 100 - 250		49808		346	6,96±0,65		[21]
COLOMBIA, Santander	Workday: 13h.d^{-1}; Integrated plant Employees: 180, Discharge: 20h.d^{-1}	4500	40000	0,80	480		390	[29]
COLOMBIA, Santander	Integrated plant Employees: 300.	7000	50000	0,80				[28]
COLOMBIA, Santander	1380582 CSM, Workday: 20h.d^{-1}*, Discharge: 24h		53099		1828	29,83	1232	[25]
COLOMBIA, Bogotá	1400000 ch.month^{-1}. Employees: 100 - 250		53846		385	7,19±0,51		
COLOMBIA, Santander	2488731 CSM, Workday: 12h.d^{-1}*, Discharge: 15h		95720		1081	11,58	826	[25]
BRAZIL	103000-120000.CSD	8000	120000		1800	14,50	1500	[26]
SPAIN						8,00		Quoted by [21]
FINLAND						17,80 – 18,70		idem
DENMARK						16,10		idem

Note: Chickens slaughtered per day: CSD; Chickens slaughtered per Month: CSM; The present study -PS. * Values estimated
Source: The authors

The cleaning activity was between 13% and 23% of the water use (Table 6), both in the maximum and in the average of one day of operation. However, it is important to note that the percentages of cleaning variation indicated are not because this activity increased with the duration of the slaughter process, because 94% of it was independent of the process. The increase found was due to a faucetless hose used to rinse the floor located in the scalding and plucking areas. The consumption for this activity was between 38,8 and 41,0 m^3 representing 2,9 and 5,5 L per chicken, for the average and minimum capacity. The lowest capacity is explained by the minimum requirements of slaughter process, since cleaning must be performed for one or six batches, the carried out the same throughout the plant.

Table 6.
Sensitivity analysis for the maximum, average and minimum production day

Maximum Capacity [16919 chickens.d^{-1} with 6 batches]							
Batch Duration on hoist (min)	50	65	80	**95**	**110**	**125**	**140**
Consumption day (m^3)	184,8	207,7	230,7	253,6	276,5	299,4	322,4
Process	79%	81%	83%	84%	85%	86%	87%
Cleaning	21%	19%	17%	16%	15%	14%	13%
CONSUMPTION L.Chicken^{-1}	*10,9*	*12,3*	*13,6*	*15,0*	*16,3*	*17,7*	*19,1*
Average Capacity [13630 chickens.d^{-1} with 5 batches]							
Batch Duration (min)	50	65	80	**95**	**110**	**125**	**140**
Consumption day (m^3)	168,0	187,2	206,2	225,5	244,7	263,9	283,1
Process	77%	79%	81%	82%	84%	85%	86%
Cleaning	23%	21%	19%	18%	16%	15%	14%
CONSUMPTION L. Chicken^{-1}	*12,3*	*13,7*	15,1	*16,6*	*18,0*	*19,4*	*20,8*
Minimum Capacity [7085 chickens.d^{-1} with 3 batches.d^{-1}]							
Batch Duration (min)	50	65	80	**95**	**110**	**125**	**140**
Consumption day (m^3)	133,9	145,6	157,3	169,0	180,7	192,4	204,1
Process	71%	74%	75%	77%	78%	80%	81%
Cleaning	29%	26%	25%	23%	22%	20%	19%
CONSUMPTION L. Chicken^{-1}	*18,9*	*20,6*	*22,2*	*23,9*	*25,5*	*27,2*	*28,8*

Source: The authors

3.4. In situ improvement proposals

In brief, a group of improvement strategies focused on the prevention and minimization of water consumption, considered low cost and easy to implement for SMEs, are presented.

3.4.1. Dry handling of byproducts

Instead of continuing to use water as a means of transportation, it is proposed to consider dry management as a water minimization strategy, seeking a gradual change in water use as a means of transportation. In this case, the change of 50% would allow a reduction of 16,2 m^3.d^{-1}, equivalent to 8% of the total average consumption of the production process, and thereby encourage an environmental awareness regarding the management of the resource within the business. Actions like these have been reported by [24].

3.4.2. Records management and control

Starting from the premise "what is not measured cannot be controlled", it is proposed to install a meter, when possible and even if it is second-hand but in good condition, to quantify the volume that enters the Plant. Another recommendation is to plan when an adaptation is achieved at the plant, consider a design of the supply network by areas that have their own measurement record. For example, for the area of scalding, plucking and evisceration have a measuring point. This type of control and measurement are performed by large companies in all areas. Also recommended by Kist et al.[26].

3.4.3. Water leakage management

An option to avoid leaks and their recurrence could be to change to butterfly valves that close gradually. This type of valve located at strategic points (eg water as transport of by-products and high consumption areas), contributes to the reduction of consumption by not being open to the full. The amount of expenditure was 3621 L in 24 hours, representing 2% of the total volume. Although this percentage could be considered negligible by the volume that it represents, it influences the perception of the workers, evidencing a corporate culture of water waste by showing a lack of interest in the maintenance of leaks. Which is why having a periodic maintenance plan for leakage and the state of the networks is critical. At least one revision is proposed per month.

3.4.4. Implementation of low consumption equipment and / or equipment

The elements that are recommended of immediate implementation for the minimization of consumption, are the control devices of closing in the ten hoses. The importance of acquiring and / or repairing the pressure hydro-washer equipment is also highlighted. An example is to consume 0,30L.s^{-1} with the hose and with the hydro-washed device only 0,09L/s was required. Only this option can represent a decrease in consumption up to 30% for routine and general cleaning activities.

3.4.5. Business environmental education

It is important to promote a business environmental education interested in the care of the water resource because can lead to actions that reduce the impacts arising from water withdrawals and disposal. For example, the greater the demand for water, the greater the generation of wastewater. This awareness also covers the handling of by-products (blood, viscera), and how it can affect the quality of the effluent and the performance of the treatment system. The

implementation of minimization strategies with posters or banners, as well as training on improvement in water management, allows moving towards a better performance of the water in companies. It is also recommended to make a periodic check during breaks, to avoid open faucets. Management strategies that help encourage staff in each area to perform better, with a recognition at the end of the month are also very assertive.

3.4.6. Reuse of cleaning water

Due to strong restrictions that food companies must meet, this option has limitations. However, it is a valuable resource to employ, 41m^3 daily. Unlike the other proposals, these require a characterization of the water, the storage tank and the location conducive to its use. Depending on the quality of the wastewater of cleaning, this could be used for washing the truck and cages, washing exterior roads, rinsing the byproduct areas and the too, the plant of wastewater treatment [22, 26]. This option has also been reported in the literature, attaining that a 40% of the effluents can be reused, nevertheless, it can be higher if a treatment system for reuse is projected [30].

4. Conclusions

An evaluation of the use of water in a poultry benefit plant was presented. The results show that characterizing the plant allows to recognize variations in its operation and therefore, have more accurate estimates. A consumption of 206,2 m^3.d^{-1} was recorded, equivalent to 15,1L per chicken. This depended on the number of areas, the forms of operation and the execution time in each line of production and cleaning. Additionally, a strong trend of water management as a means of transportation was found 35,8m^3, corresponding to 17% of total consumption.

The sensitivity analysis allowed to evaluate the efficiency of the process and to quantify the increase of the water consumption to the maximum, average and minimum capacity. For each, an increase of 1529L, 1279L and 780L per minute was found, respectively, showing a range between 10,9 and 28,8L per chicken. This sensitivity analysis corroborated a lower number of slaughtered chickens, corresponds to a higher water demand. The high consumption of water also responded to practices of water wastage included prolonged leakage, lack of maintenance, hoses without control valves for closure and water based transport. This condition is partly propitiated by having an abundant water supply at a low cost. Inattention to water wastage encourages high consumption in the facilities.

The literature reported water consumption values per chicken of 6,4L, lower than the 8,0L recommended by ETBPP, being a benchmark for good performance and efficiency in water management. Consumptions above this value are considered operationally inefficient. This situation shows the need to work on approaches to sustainable consumption of water resources for this productive process. Finally, to help water management in these sectors, the need to integrate this type of production process with the academy by the strengthening and shaping of work teams is evident. This would allow companies to identify the critical points that generate an inadequate water performance and thus help to mitigate the needs and limitations that exist in the productive processes of SMEs.

Acknowledgments

In particular, we wish to thank the poultry processing plant for access to its facilities. We thank FENAVI Seccional Occidente as a facilitator, COLCIENCIAS as a funding body for the doctoral fellowship, Universidad del Valle for financing the project (CI 2953-2017) and the professor Camilo Micán and colleagues of EIDENAR.

References

[1] AQUASTAT. ¿Sabía qué…? Datos y cifras sobre. FAO´s Information System on Water and Agriculture. [En línea]. 2017. [Consulta: 15 de agosto de 2017]. Disponible en: http://www.fao.org/nr/water/aquastat/didyouknow/indexesp.stm

[2] WWF. World Wildlife Fund. Una mirada a la agricultura de Colombia desde su Huella Hídrica. Reporte Colombia, [En línea]. 2012. [Consulta: 1 de Septiembre de 2014]. Disponible en: http://www.huellahidrica.org/Reports/Arevalo-2012-HuellaHidricaColombia.pdf

[3] UNESCO. World Water Assessment Programme. The United Nations World Water Development Report 3: Water in a Changing World. Paris: UNESCO, and London: Earthscan, 2009, 429 P.

[4] Cardozo, E., Velásquez, Y. y Rodríguez, C., El concepto y clasificación de Pyme en América Latina. Global Conference on Business and Finance Proceedings, (GCBF), [En línea]. 2012, pp. 1630-1641. Disponible en: http://oa.upm.es/10940/2/Actas_del_Congreso_theibfr_CardozoNaimeMonroy[1].pdf

[5] Singh, M., Brueckner, M. and Padhy, P.K., Insights into the state of ISO14001 certification in both small and medium enterprises and industry best companies in India: the case of Delhi and Noida. Journal of Cleaner Production, 69, pp. 225-236, 2014. DOI: 10.1016/j.jclepro.2014.01.040

[6] Daude, C., Perspectivas económicas de América Latina. Políticas de pymes para el cambio estructural. Centro de Desarrollo de la OCDE, [En línea]. 2013. [Consulta: 1 de Septiembre de 2014]. Disponible en: http://www.oecd.org/dev/americas/PPT_%20LEO%202013%20Presentation%20Maison%20de%20l%20Amerique_ES.pdf.

[7] ONUDI. Acceso a los mercados y comercio responsable: ¿Oportunidades u obstáculos para las PYME de los países en desarrollo?, [En línea]. 2006. [Consulta: 1 de marzo de 2014]. Disponible en: http://catedrarses.com.do/backadmin/media/files/Acceso%20a%20los%20mercados%20y%20comercio%20responsable%20Oportunidades%20u%20obst%C3%A1culos%20para%20la%20PyME%20de%20los%20pa%C3%ADses%20en%20desarrollo,%202006.pdf.

[8] Fernández, V.M.B., Gómez, N.T. and Capuz, R.S., Diagnóstico de la implantación de la ecoeficiencia en las pequeñas y medianas industrias venezolanas [En línea]. 9(2), 2009. [Consulta: 26 de septiembre de 2014]. Disponible en: http://ares.unimet.edu.ve/academic/revista/anales9.2/documentos/pag-119.pdf

[9] Pimenova, P. and Van der Vorst, R., The role of support programmes and policies in improving SMEs environmental performance in developed and transition economies, Journal of Cleaner Production, 12(6), pp. 549-559, 2004. DOI: 10.1016/j.jclepro.2003.07.001

[10] Bengtsson, J. and Seddon, J., Cradle to retailer or quick service restaurant gate life cycle assessment of chicken products in Australia, Journal of Cleaner Production, 41(0), pp. 291-300, 2013. DOI: 10.1016/j.jclepro.2012.09.034

[11] IDEAM-MAVDT., Estudio nacional del agua. Instituto de Hidrología, Meteorología y Estudios Ambientales de Colombia. Subdirección de Hidrología, [En línea]. 2010. [Consulta: 12 de febrero de 2016]. Disponible en: http://www.ins.gov.co/lineas-de-accion/Red-Nacional-

Laboratorios/Documentacin%20en%20Salud%20Ambiental/Estudio%20Nacional%20de%20Agua%20IDEAM,2010.pdf
[12] Hoekstra, A.Y., Sustainable, efficient and equitable water use: the three pillars under wise freshwater allocation. Wiley Interdisciplinary Reviews: Water, 1(1), pp. 31-40, 2013. DOI: 10.1002/wat2.1000
[13] FAO. Perspectivas alimentarias. Resúmenes de mercado [En línea]. 2014, [Consulta: 12 de febrero de 2016]. Disponible en: http://www.fao.org/3/a-i3915s.pdf
[14] González-García, S., Gomez-Fernández, Z., Dias, A.C., Feijoo, G., Moreira, M.T. and Arroja, L., Life cycle assessment of broiler chicken production: a Portuguese case study. Journal of Cleaner Production, 74(0), pp. 125-134, 2014. DOI: 10.1016/j.jclepro.2014.03.067
[15] Poultry Trends. WATT executive guide to world. The statistical reference for Poultry Executives. [En línea], 2014. Poultry Trends, 2014 [Consulta: 9 de septiembre de 2016]. Disponible en: http://www.poultrytrends.com/2014/.
[16] FENAVI-FONAV and CAF. Estrategia competitiva y sostenible de la industria avícola en Santander. Cámara de Comercio de Bucaramanga. Bucaramanga, Colombia, 2010, 124 P.
[17] FENAVI. Federación Nacional de Avicultores & Fondo Nacional Avícola. Programa técnico y estadísticas. [En línea]. 2015. [Consulta: febrero 10 de 2016]. Disponible en: http://www.fenavi.org/
[18] CTA. Resumen de resultados. Evaluación de la huella hídrica en la cuenca del río Porce. [En línea]. 2013. Centro de Ciencia y Tecnología de Antioquia. [Consulta: 11 de noviembre de 2014]. Disponible en: http://www.goodstuffinternational.com/images/PDF/LibroHuellahidrica.pdf
[19] CTA, GSI-LAC, COSUDE and IDEAM. Evaluación multisectorial de la huella hídrica en Colombia. Resultados por subzonas hidrográficas en el marco del Estudio Nacional del Agua 2014, Medellín, Bogotá. [En línea]. 2015. [Consulta: 15 agosto de 2016]. Disponible en: http://documentacion.ideam.gov.co/openbiblio/bvirtual/023272/HH_ENA2014.pdf
[20] MINTIC. Ministerio de Tecnologías de la Información y las Comunicaciones. Datos abiertos Colombia. Planta de beneficio animal. Datos Industria avícola en Valle. [En línea]. 2017. [Consulta: febrero 8 de 2017]. Disponible en: https://www.datos.gov.co/Salud-y-Protecci-n-Social/PLANTAS-DE-BENEFICIO-ANIMAL/g5gy-3pge/data
[21] Casas Forero, A.M., Estimación del consumo requerido de agua para un subsector del sector agroalimentario de la ciudad de Bogotá. MSc. Tesis, Departamento de Ingeniería Química y Ambiental, Universidad Nacional de Colombia, Bogotá, Colombia, 2012.
[22] Amorim, A.K.B., Nardi de, I.R. and Nery, D.V., Water conservation and effluent minimization: case study of a poultry slaughterhouse. Resources, Conservation and Recycling, 51, pp. 93-100. 2007. DOI: 10.1016/j.resconrec.2006.08.005
[23] Silva, d.P.V., van der Werf, H.M.G. and Roberto-Soares, S. Environmental impacts of French and Brazilian broiler chicken production scenarios: an LCA approach. Journal of Environmental Management, 133, pp. 222-231, 2014. DOI: 10.1016/j.jenvman.2013.12.011
[24] CPTS. Centro de Promoción de Tecnologías Sostenibles CPTS Bolivia. 30 Estudios de caso. [En línea]. 2007. [Consulta: 23 de marzo de 2017] Disponible en: http://www.academia.edu/31592328/Estudios_Caso_PML_1_
[25] Arenas, R.S.M. and Nuncira, P.A., Evaluación de humedales artificiales para el tratamiento de aguas residuales del sector industrial avícola, Monografía, Esp., Facultad de Ingeniería, Universidad Industrial de Santander, Bucaramanga, Colombia, 2010.
[26] Kist, L.T., Moutaqi, S. and Machado, E.L., Cleaner production in the management of water use at a poultry slaughterhouse of Vale do Taquari, Brazil: a case study. Journal of Cleaner Production, 17, pp. 1200-1205, 2009. DOI: 10.1016/j.jclepro.2009.04.006
[27] Reyes-Méndez, L., Osorio-Tangarife, M. y Salamanca-Grosso, G., Criterios de diseño para una planta de beneficio de pollo, establecimiento de un sistema de aseguramiento de calidad e implementación de un programa de trazabilidad. Revista de la Asociación Colombiana de Ciencias Biológicas [En línea]. 23, pp. 121-133, 2011. [Consulta: 31 de agosto de 2015]. Disponible en: http://www.asocioncolombianadecienciasbiologicas.org/download/revistas/2011/Art.11%20ACCB2011.pdf
[28] Sánchez-Álvarez, E.J., Análisis y mejoramiento de los procesos de producción de pollo entero y presas en la Planta de Beneficio de Pollosan S.A. Monografía, Esp., Universidad Industrial de Santander, Bucaramanga, Colombia, 2010.
[29] Guauque-Vásquez, C.G., Impacto ambiental generado por plantas de beneficio avícola. Monografía, Facultad de Ingeniería, Universidad Industrial de Santander, Bucaramanga, Colombia, 2012.
[30] De Nardi, I.R., Del Nery, V., Amorim, A.K.B., Dos Santos, N.G. and Chimenes, F., Performance of SBR, chemical-DAF and UV disinfection for poultry slaughterhouse wastewater reclamation. Desalination, 269(1), pp. 184-189, 2011. DOI: 10.1016/j.desal.2010.10.060

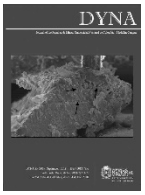
Y.A. Zorrilla-Ortega, is currently a doctoral candidate with emphasis in Sanitary and Environmental Engineering at the Universidad del Valle, Colombia. Her field of research has focused on the integrated management of water resources, addressing the planning and modeling of urban watersheds also environmental management system in Public Utilities Company Domiciliary. In 2010 she was part of the SWITCH project team (Sustainable Water Management Improves Tomorrow's Cities Health). Her lines of research include wastewater treatment, industrial ecology, multicriteria analysis and LCA.
ORCID: 0000-0001-5737-0297

J.P. Silva, received his BSc. Chemical Engineering degree in 1990, Sp. in Sanitary and Environmental Engineering in 1996 and MSc. in Sanitary and Environmental Engineering in 2000 from Universidad del Valle, Colombia. He is a doctoral candidate of the Institute of Hydraulic Water Resource (IHE), Holland. He is an associate professor in the School of EIDENAR, Universidad del Valle, Colombia. His lines of research include air quality, environmental processes, air pollution, biological gas treatment, Industrial Ecology and waste management in industry.
ORCID: 0000-0002-1134-1252

P.C. Manyoma-Velásquez, received his BSc. in Industrial Engineering in 1994, Sp. in Management Systems in 1997, MSc. in Industrial Engineering in 2006 and Dr. with emphasis in Sanitary and Environmental Engineering in 2015. He is currently an associate professor attached to the Industrial Engineering School of the Universidad del Valle, Colombia. He is an associate researcher, Colciencias. Some areas of interest are multi-criteria decision analysis (MCDA), unwanted service centers and work methods and process improvement.
ORCID: 0000-0003-1479-5986

V. Prado, is a BSc. in Civil Engineer at Jackson State University in Mississippi, EE UU. She holds an MSc and PhD in Sustainable Engineering from Arizona State University, EE UU. Her work is published in the Handbook of LCA (ed. Mary Ann Curran), the International Journal of LCA, the Journal of Industrial Ecology, and Environmental Science and Technology. Since May 2015 she is an assistant professor in the department of Industrial Ecology-CML of the University of Leiden, The Netherland, teaching courses in the Master's program in Industrial Ecology. Related research topics include: standardization, weighting, uncertainty, sensitivity analysis and decision analysis.
ORCID: 0000-0003-4974-0504

UNIVERSIDAD NACIONAL DE COLOMBIA
SEDE MEDELLÍN
FACULTAD DE MINAS



DYNA
http://dyna.medellin.unal.edu.co/

Nutrient losses due to water erosion using simulated rainfall in southern Brazil

Jeane Cruz Portela [a], Neroli Pedro Cogo [b], Jacques Carvalho Ribeiro Filho [a], Letícia Sequinatto [c], Rafael Oliveira Batista [a], Carolina Malala Martins Souza [a] & Joaquim Emanuel Fernandes Gondim [b]

[a] *Centro de Ciências Agrárias, Mossoró, Universidade Federal Rural do Semiárido, RN, Brasil. jeaneportela@ufersa.edu.br, jaquesfilho1@hotmail.com, rafaelbatista@ufersa.edu.br, carolmalala@ufersa.edu.br, joaquimcg_rn@hotmail.com*
[b] *Departamento de Ciência do Solo, Universidade Federal do Rio Grande do Sul, Porto Alegre, RS, Brasil. neroli@ufrgs.br*
[c] *Centro de Ciências Agroveterinárias – CAV, Departamento de Solos e Recursos Natuaris, Universidade do Estado de Santa Catarina, Lages – SC, Brasil. leticia.sequinatto@udesc.br.*

Received: March 17th, 2018. Received in revised form: August 14th, 2018. Accepted: August 18th, 2018.

Abstract
Erosion is the main form of degradation in the world, consequently of loss of soil, water and nutrients, provoking direct and indirect damages. The objective of this work is to quantify N, P and K losses by water erosion under simulated rainfall conditions by the application of six erosion tests in continuous cultivation of seasonal cycle species, including isolated and intercropped crops. The study was carried out in the field at the Experimental Station of Agronomy in Eldorado do Sul (RS), Brazil, in a typical Dystrophic Red Argisol. For the analysis of nutrient loss, six erosion tests with simulated rainfall were applied to the treatments between the end of October and mid-December, using the rain simulator with swivel arms of Swanson. The losses of N and P were influenced by surface conditions, with the partial removal of crop residues and the non-mobilization of the soil. The exception was K, due to its high solubility in the soil with a low colloidal activity, which was easily lost in the soil water surface runoff, regardless of total soil surface coverage by crop residues.

Keywords: erosive process; runoff; cultural sequences; ground cover.

Pérdidas de nutrientes debido a la erosión hídrica con la lluvia simulada en el sur de Brasil

Resumen
La erosión es la principal forma de degradación en el mundo, en consecuencia de la pérdida de suelo, agua y nutrientes, provocando daños directos e indirectos. El objetivo de este trabajo es cuantificar las pérdidas de N, P y K por erosión hídrica en condiciones de lluvia simulada mediante la aplicación de seis pruebas de erosión en cultivo continuo de especies de ciclo estacional, incluyendo cultivos aislados y cultivos intercalados. El estudio se llevó a cabo en el campo en la Estación Experimental de Agronomía en Eldorado do Sul (RS), Brasil, en un Argisol Rojo Distrófico típico. Para el análisis de la pérdida de nutrientes, se aplicaron seis ensayos de erosión con lluvia simulada a los tratamientos entre finales de octubre y mediados de diciembre, utilizando el simulador de lluvia con brazos giratorios de Swanson. Las pérdidas de N y P se vieron influenciadas por las condiciones de la superficie, con la eliminación parcial de los residuos del cultivo y la no movilización del suelo. La excepción fue K, debido a su alta solubilidad en el suelo con baja actividad coloidal, que se perdió fácilmente en la escorrentía superficial del agua del suelo, independientemente de la cobertura total de la superficie del suelo por los residuos de los cultivos.

Palabras clave: proceso erosivo; escorrentía; secuencias culturales; cobertura del suelo.

1. Introduction

The undue use of soil, including the removal of vegetation cover, stands out as one of the main factors associated with accelerated erosion, represented by soil loss rates by erosion that exceed the natural rates of renewal and replenishment of this resource. Soil loss rates in Brazil generally vary from 15 to 25 Mg ha^{-1} $year^{-1}$, while soil formation rates are in the range of 1 Mg ha^{-1} $year^{-1}$ [1].

How to cite: Portela, J.C., Cogo, N.P., Filho, J.C.R., Sequinatto, L., Batista, R.O., Souza, C.M.M. and Gondim, J.E.F., Nutrient losses due to water erosion using simulated rainfall in southern Brazil. DYNA, 85(206), pp. 236-241, September, 2018.

© The author; licensee Universidad Nacional de Colombia.

Soil erosion is considered one of the major environmental problems in the world, as it causes soil and nutrient losses and is associated with flooding, sedimentation and pollution of water bodies [2,3] According to [4], an inadequate soil management may lead to erosive processes such as water erosion, whose sediment transport culminates in the loss of soil, water, nutrients and organic matter.

As there is an increase in soil losses, they are accompanied by losses of organic matter and nutrients, notably phosphorus, for example, which is very susceptible to losses in floods, and potassium [5]. Soil preparation methods vary in extent surface area of the land under of preparation and degree of mass fragmentation solo mobilized [6]. Notably, the loss of nutrients by erosion is affected by the method of preparation of the soil used in the growing process.

As for rainwater erosion, specifically, soils must fulfill their functions to freely let rainwater infiltrate its surface and resist degradation and transport of its particles by the action of rainfall and associated runoff.

Nutrients in the soil are those adsorbed to mineral or organic solid particles or dissolved in surface runoff water, which can be removed by water erosion processes [6].

[7] stated that with regard to nutrient losses caused by this type of erosion, they are more related to sediment losses than to water losses.

[8] quantified total water, soil and nutrient losses in the native field and verified that the removal of the vegetal cover by the burning of the native field phytomass decreased the infiltration of water in the soil, besides increasing the maximum rate of flood, water and soil losses due to water erosion and total nutrient losses (P, K and NH_4^+). For the quantification of losses of soil, water and nutrients, the use of the rainfall simulator is a tool that allows the control of rainfall characteristics, such as diameter and drop distribution, height and time of fall, terminal velocity, duration time, intensity and kinetic energy, which is not possible under natural rainfall conditions (Ribeiro et al. [9]).

The objective of this work is to quantify N, P and K losses by water erosion under simulated rainfall conditions by the application of six erosion tests in continuous cultivation of seasonal cycle species, including isolated and intercropped crops.

2. Material and methods

The study was conducted at the Experimental Erosion Area with Simulated Rain III at the Agronomic Experimental Station of the Federal University of Rio Grande do Sul (EEA/UFRGS) in the municipality of Eldorado do Sul (RS) in the interval of six (6) months for six (6) rain simulation tests.

The EEA/UFRGS is located in the Central Depression, RS, between the geographic coordinates 30°00' and 30°15' S and 51°30' and 51°45' W, at an average altitude of 46 m. According to the Köppen classification, the climate is Cfa, subtropical humid with a hot summer and temperature of the coldest month oscillating between -3°C and 18°C and temperature of the hottest month higher than 22°C, with an annual mean rainfall around 1,400 mm and a monthly average of about 120 mm (BERGAMASCHI; GUADAGNIN [10]).

The soil is classified as a typical Dystrophic Red Argisol [11-13], presenting the following characteristics: sandy loam surface texture, A moderate to B moderate textural horizons, moderate depth and drainage, mean slope of 0.115 mm^{-1} and effective depth lower than 0.80 m [14].

The treatments consisted of seasonal crop species (autumn-winter and spring-summer) arranged in a continuous succession mode, including isolated cultivations and intercropped crops, most often in line and tratorized as for the sowing method (except for the first crop, depending on the soil adaptation operation in the experimental area, in which the grid was used).

The cultivars constituting the crop sequences of the autumn-winter period were *Avena strigosa* (black oat), *Vicia sativa* (vetch), *Raphanus sativus* L. (forage turnip), (*Trifolium alexandrinum*) (Alexandrian clover - cultivar Calipso), and *Lolium multiflorum* L. (ryegrass), while crops from the spring-summer period were *Zea mays* L. (maize), *Pennisetum americanum* (millet), *Euchlaena mexicana* Schrad (teosinte), *Vigna unguiculata* (kidney bean) and *Canavalia ensiformes* L. (jack bean).

For the analysis of nutrient loss, six erosion tests with simulated rainfall (T1 to T6) were applied to the treatments between the end of October and mid-December, with no more plants in the experimental plots (only their crop residues - dried - were used in this phase), using the rain simulator with swivel arms or Swanson. Each test consisted of a rainfall with a planned constant intensity of 64.0 mm h^{-1} and variable duration (60 to 180 minutes), depending on the behavior of the runoff, basically start and equilibrium times, in a given treatment, and were characterized as described below:

Test 1 (T1): unmoved soil, dead roots, natural crust, 100% surface cover (consisting of herbicide-dried plants, scrubbed with a costal scrubber and evenly scattered on the soil surface in experimental plots).

Test 2 (T2): unmoved soil, broken crust (manually and slightly, with a plastic rake, during the operation of removal of cultural residues from the experimental plots after T1), 18% (average values of 15% to 20%) of surface cover (remaining from the operation described immediately above, which could not be removed to avoid changing the soil surface in the experimental plots).

Test 3 (T3): unmoved soil, dead roots, thin or recent crust (naturally formed after T2), 18% (mean values between 15% and 20%) of surface cover (remaining from T2).

Test 4 (T4): recently scarified soil, dead roots, 100% of surface cover (added manually using the crop residues removed for the performance of T2).

Test 5 (T5): soil previously scarified (before T4), 18% (average values between 15% and 20%) of surface cover (remaining from the operation of removal of cultural residues after T4), which was not possible to remove so as not to change the soil surface in the experimental plots.

Test 6 (T6): recently gridded soil (after T5), 0% surface coverage (the small amount of remaining T5 cultural residue was incorporated into the topsoil during its harrowing operation), performed on December 13 and 14, 2007.

In the course of the research, several samplings and determinations were made in the field and in the laboratory, including soil management variables (measured in the experimental plots) and soil water erosion variables (measures in the runoff). For the elaboration of this study, only the results of measurements regarding the water erosion were used.

For the collection of runoff, directly under its flow, graduated test tubes of 500, 1,000 and/or 2,000 ml were used, according to the intensity of the flow. At the same time, samples were also collected for laboratory determination of sediment concentrations. For this, 1.0 L plastic pots were used, most of the time filled to the limit (except in cases where the flow was very small). At the end of the collection, the plastic pots were sealed, taken to the laboratory and weighed to later quantify the amount of nutrients lost in water and soil samples.

Subsequently, 3 to 5 ml (depending on the sediment charge in the sample) of the commercially available saturated solution (5%) of commercial potassium alum, used as a precipitant, were added to each pot and allowed to stand for 24 to 48 hours for decantation. After this time and using a small-diameter plastic hose, the supernatant from the plastic pots was sucked off and set to oven drying at 60°C for three to four days. Afterwards, the pots were weighed with and without sediments, and the appropriate subtractions were made. Once the sediments and the runoff were obtained, N, P and K determinations were performed on the samples using the methodologies described by [15]

3. Results and discussion

It was verified that, for soil nitrogen losses caused by rainwater erosion, the highest averages refer to Test 2, in which there was no soil mobilization regardless of the crop sequence. However, after the first erosion test, the surface cover of the soil was removed, which now represented about 18% of the total (Table 1), whereas for all treatments of the Test 1, for example, where the soil was 100% covered, the values of losses were much lower, being the soil cover by crop residues a condition of physical protection of its surface, essential with respect to the control of water erosion and the associated runoff. For all tests performed, the crop sequence 1Av,3Av+Er/3Fm presented the highest nitrogen losses in relation to the others (Table 1). [16], studying soil losses due to water erosion in corn crops in two erosion tests, observed that in treatments where the soil was completely covered by vegetation, there were no losses since the beginning of the experiment. This evidences the importance of maintaining the residues of crops on the surface for the conservation of the soil. For the nitrogen lost and quantified in the runoff water, the tests differed significantly from each other, and, in general, the lowest values were recorded for the Test 2. The Tests 1, 4 and 5 presented higher values of losses for the different cultural sequences, which are 1Av,Tr, Nf,Az/1Fm, 2Mi+Fm1Sc, Av+Er, Av+Nf, Av+Az/1Fm,2Mt. For the Test 2, the 4Av/1Fm,2Te was the only sequence that differed statistically from the others, with the lowest mean losses of nitrogen in the runoff (Table 2). [17], studying nutrient losses due to water erosion, observed that nitrogen losses (NH^{4+}) in the runoff water were higher in the treatment with burning, therefore, in a soil with absence of vegetal cover, corroborating values found in this study.

Phosphorus levels found in the soil lost due to rainwater erosion accompanied nitrogen losses, in which the highest averages were recorded in all cultural sequences for the Test 2, ranging from 0.35 to 0.62 kg ha^{-1}. For the remaining tests, these amounts were 0.02 to 0.45 kg ha^{-1} (Table 3).

[18] adds that the adoption of the no-tillage system is one of the main forms of soil P transfer through surface runoff. It can be observed that the losses of phosphorus in the runoff were higher when the cultural sequence 4Av/1Fm,2Te was used, differing

Table 1.
Nitrogen loss for crop sequences in six water erosion tests with simulated rainfall in southern Brazil.

Crop Sequence[1]	Nitrogen losses (kg ha^{-1})					
	Test 1	Test 2	Test 3	Test 4	Test 5	Test 6
1Av,3Av+Er/3Fm	0.47	5.58	1.12	0.18	1.61	2.41
4Av/1Fm,2Te	0.09	1.35	0.14	0.08	0.72	0.47
1Av,Tr,Nf,Az/1Fm,2Mi+Fm	0.70	1.32	0.53	0.10	0.75	0.30
1Sc,Av+Er,Av+Nf,Av+Az/1Fm,2Mt	0.37	3.09	0.99	0.23	0.64	0.27
1Av,3Er/1Fm,2Mi+Fp	0.31	4.24	0.99	0.29	0.64	1.25

Source: The authors

Table 2.
Nitrogen loss for crop sequences in six water erosion tests with simulated rainfall in southern Brazil at a 5% of significance according to the Tukey test.

Crop Sequence[1]	Nitrogen (mg L^{-1})					
	Test 1	Test 2	Test 3	Test 4	Test 5	Test 6
1Av,3Av+Er/3Fm	5.400 aB	16.750 aA	6.225 aB	2.050 aB	6.975 aB	8.950 abA
4Av/1Fm,2Te	2.400 aB	5.355 bcB	3.125 aB	1.900 aB	6.525 aB	15.000 aA
1Av,Tr,Nf,Az/1Fm,2Mi+Fm	4.575 aA	3.475 cA	3.050 aA	1.750 aA	5.325 aA	4.900 bA
1Sc,Av+Er,Av+Nf,Av+Az/1Fm,2Mt	3.475 aA	6.400 bcA	4.425 aA	2.375 aA	5.500 aA	6.075 bA
1Av,3Er/1Fm,2Mi+Fp	3.050 aB	12.100 abA	5.525 aA	1.700 aB	3.575 aB	9.175 abAB

[1]In the listed crop sequences, using no-tillage, the algorithm preceding the crop or combination of crops indicates the number of times it took part in the experiment, while the underlined crop or combination of crops means that it was the one that prevailed earlier to the moment of evaluation, being the following the conventions adopted: Av = Black oats, Er = vetch, Fm = Kidney beans, Te = Teosinte, Tr = Calypso clover, Nf = forage turnip, Az = rye grass, Mi = Corn, Sc = without cultivation, Mt = Millet and Fp = jack beans. [2]cs = cover only by cultural residue. 1 Means followed by the same uppercase letters in rows and lowercase letters in lines do not differ by Tukey test at 5% probability.
Source: The authors

Table 3.
Phosphorus loss for crop sequences in six water erosion tests with simulated rainfall in southern Brazil.

Crop Sequence[1]	Phosphorus losses (kg ha^{-1})					
	Test 1	Test 2	Test 3	Test 4	Test 5	Test 6
1Av,3Av+Er/3Fm	0.26	0.41	0.21	0.05	0.23	0.16
4Av/1Fm,2Te	0.05	0.35	0.04	0.02	0.11	0.01
1Av,Tr,Nf,Az/1Fm,2Mi+Fm	0.45	0.38	0.12	0.04	0.11	0.04
1Sc, Av+Er,Av+Nf,Av+Az/1Fm,2Mt	0.22	0.39	0.13	0.04	0.05	0.03
1Av,3Er/1Fm,2Mi+Fp	0.11	0.62	0.17	0.05	0.13	0.09

Source: The authors

Table 4.
Phosphorus loss for crop sequences in six water erosion tests with simulated rainfall in southern Brazil at a 5% of significance according to the Tukey test.

Crop Sequence[1]	Phosphorus					
	Test 1	Test 2	Test 3	Test 4	Test 5	Test 6
1Av,3Av+Er/3Fm	2.925 aA	1.225 abB	1.115 aB	0.590 aB	0.990 aB	0.590 aB
4Av/1Fm,2Te	1.400 bA	1.370 abA	0.855 aA	0.535 aA	0.997 aA	0.460 aA
1Av,Tr,Nf,Az/1Fm,2Mi+Fm	2.925 aA	0.992 abB	0.675 aB	0.605 aB	0.792 aB	0.592 aB
1Sc,Av+Er,Av+Nf,Av+Az/1Fm,2Mt	2.025 abA	0.812 bB	0.587 aB	0.415 aB	0.452 aB	0.687 aB
1Av,3Er/1Fm,2Mi+Fp	1.150 bAB	1.775 aA	0.912 aAB	0.285 aB	0.732 aB	0.657 aB

[1]In the listed crop sequences, using no-tillage, the algorithm preceding the crop or combination of crops indicates the number of times it took part in the experiment, while the underlined crop or combination of crops means that it was the one that prevailed earlier to the moment of evaluation, being the following the conventions adopted: Av = Black oats, Er = vetch, Fm = Kidney beans, Te = Teosinte, Tr = Calypso clover, Nf = forage turnip, Az = rye grass, Mi = Corn, Sc = without cultivation, Mt = Millet and Fp = jack beans. [2]cs = cover only by cultural residue. 1 Means followed by the same uppercase letters in rows and lowercase letters in lines do not differ by Tukey test at 5% probability.
Source: The authors

Table 5
Potassium loss for crop sequences in six water erosion tests with simulated rainfall in southern Brazil.

Crop Sequence[1]	Potassium Losses (kg ha^{-1})					
	Test 1	Test 2	Test 3	Test 4	Test 5	Test 6
1Av,3Av+Er/3Fm	3.30	3.55	1.12	0.76	3.18	3.84
4Av/1Fm,2Te	0.83	2.35	0.29	0.32	1.34	0.15
1Av,Tr,Nf,Az/1Fm,2Mi+Fm	7.86	2.23	0.82	0.69	1.41	0.61
1Sc,Av+Er,Av+Nf,Av+Az/1Fm,2Mt	6.63	5.94	1.45	1.21	1.64	0.54
1Av,3Er/1Fm,2Mi+Fp	2.48	3.56	0.89	1.6	2.00	1.96

Source: The authors

statistically from the other treatments, except for the Test 1, in which the phosphorus lost did not differ statistically between the sequences, and for the Test 2, where the phosphorus lost at 4Av/1Fm,2Te did not differ statistically from 1Av,3Er/1Fm,2Mi+Fp, and was higher than the others (Table 4). These results show that for all crop sequences, there was an efficient soil restoration, with emphasis on the cultural sequence that has a predominance of teosinte (grassy), 4Av/1Fm,2Te. [19], when assessing soil and water losses in cultural sequences, emphasizes that grasses, act as a soil builder, with positive impacts on minimizing soil and water losses, and, consequently, of nutrients.

The highest potassium losses in the soil were in the Test 1 for the crop sequences. In this test, the results were obtained for 1Av,Tr,Nf,Az/1Fm,2Mi+Fm and 1Sc,Av+Er,Av+Nf,Av+Az/1Fm,2Mt, which reached on average 7.0 kg ha^{-1}. This loss of K may be associated with a higher mobility of this ion in the soil, although the soil has 100% coverage. In the other evaluations, a loss pattern of this element was not observed (Tabla 5). This lack of pattern is linked to a starting time of the runoff that varied in both shape and magnitude [20]. Potassium lost in runoff was not influenced by the different crop sequences planted in the research and, for all of them, did not differ statistically (Table 6). Similar tendencies were observed by [21] in different plant cover conditions, where potassium losses were influenced by the magnitude of rainfall events. Potassium was easily lost in the soil condition without mobilization and with 100% coverage (Test 1). This is due to the soil class under study (typical Dystrophic Red Argisol) because it presents a low colloidal activity and a low affinity with ions, being easily released in runoff water (floodwater), which can be attributed to the low affinity of K with soil constituents.

4. Conclusions

- Soil preparation methods and crop sequences influenced losses of Nitrogen and Phosphorus due to water erosion with simulated rainfall.
- Potassium, in function of its high solubility in a soil condition of low colloidal activity, was easily lost in surface runoff water, regardless of the total cover of the soil surface by crop residues and the unmoved condition.

Table 6.
Potassium loss for crop sequences in six water erosion tests with simulated rainfall in southern Brazil at a 5% of significance according to the Tukey test.

Crop Sequence[1]	Potassium					
	Test 1	Test 2	Test 3	Test 4	Test 5	Test 6
1Av,3Av+Er/3Fm	37.500 bcA	10.675 aB	6.225 aB	8.525 aB	13.750 aB	14.250 aB
4Av/1Fm,2Te	22.750 dA	9.275 aAB	6.775 aB	7.875 aB	12.175 aAB	9.550 aAB
1Av,Tr,Nf,Az/1Fm,2Mi+Fm	51.250 abA	5.850 aB	4.750 aB	11.725 aB	9.950 aB	10.050 aB
1Sc,Av+Er,Av+Nf,Av+Az/1Fm,2Mt	61.500 aA	12.325 aB	6.500 aB	12.250 aB	14.000 aB	12.350 aB
1Av,3Er/1Fm,2Mi+Fp	25.250 cdA	10.150 aB	4.075 aB	9.300 aB	11.175 aAB	5.250 aAB

[1]In the listed crop sequences, using no-tillage, the algorithm preceding the crop or combination of crops indicates the number of times it took part in the experiment, while the underlined crop or combination of crops means that it was the one that prevailed earlier to the moment of evaluation, being the following the conventions adopted: Av = Black oats, Er = vetch, Fm = Kidney beans, Te = Teosinte, Tr = Calypso clover, Nf = forage turnip, Az = rye grass, Mi = Corn, Sc = without cultivation, Mt = Millet and Fp = jack beans. [2]cs = cover only by cultural residue. 1 Means followed by the same uppercase letters in rows and lowercase letters in lines do not differ by Tukey test at 5% probability.
Source: The authors

- The 100% coverage in Test 1 and lack of soil preparation was effective in controlling nutrient loss for N and P by water erosion in all cultural sequences.
- The highest nitrogen loss occurred with the removal of cultural residues from the soil surface, with the same tendency for phosphorus. The highest losses occurred in Test 2 (18% coverage).

References

[1] Bertoni, J. and Lombardi Neto, F., Eds., Conservação do solo, São Paulo, Ícone, 2012.

[2] Cogo, N.P., Levien, R., Schwarz, R.A. Perdas de solo e água por erosão hídrica influenciadas por métodos de preparo, classes de declive e níveis de fertilidade do solo. Revista Brasileira de Ciência do Solo [online]. 27, pp 743-753, 2003. Available at: http://www.scielo.br/pdf/rbcs/v27n4/a19v27n4.pdf.

[3] Wang, X., Zhao, X., Zhang, Z., Yi, L., Zuo, L., Wen, Q., Liu, F., Xu, J., Hu, S. and Liu, B., Assessment of soil erosion change and its relationships with land use/cover change in China from the end of the 1980s to 2010. Catena, 137, pp. 256-268, 2016. DOI: 10.1016/j.2015.10.004.

[4] Thomazini, A. Azevedo, H.C.A. and Mendonça, E.S., Perdas de solo, água e nutrientes em sistemas conservacionistas e convencionais de café no sul do estado do Espírito Santo. Revista Brasileira de Agroecologia [online]. 7(2), pp. 150-159, 2012 Available at: http://orgprints.org/22945/1/Thomazini_Perdas.pdf

[5] Cassol, E.A., Levien, R., Anghinoni, I. and Badelucci, M.P., Perda de nutrientes por erosão em diferentes métodos de melhoramento em pastagens nativa no Rio Grande do Sul. Revista Brasileira de Ciência do Solo [online]. 26(3), pp. 705-712, 2002. Available at: http://www.redalyc.org/pdf/1802/180218340015.pdf

[6] Gilles, L., Cogo, N.P., Bissani, C.A., Bagatini, T. and Portela, J.C., Perdas de água, solo, matéria orgânica e nutriente por erosão hídrica na cultura do milho implantada em área de campo nativo, influenciadas por métodos de preparo do solo e tipos de adubação. Revista Brasileira de Ciência do Solo [online]. 33, pp. 1427-1440, 2009. DOI.org/10.1590/S0100-06832009000500033

[7] Oliveira, L.C., Bertol, I., Barbosa, F.T., Campos, M.L. and Júnior, J.M., Perdas de solo, água e nutrientes por erosão hídrica em uma estrada florestal na Serra Catarinense, Revista Ciência Florestal. [online]. 25(3), pp. 655-665, 2015. DOI:10.5902//1980509819616.

[8] Bertol, I., Gobbi, E., Barbosa, F.T., Paz-Ferreiro. J., Gebler, L., Ramos, J.C. and Werner, R.S., Erosão hídrica em campo nativo sob diversos manejos: perdas de água e solo e de fósforo, potássio e amônio na água de enxurrada. Revista Brasileira de Ciência do Solo [online]. 35(4) pp, 1421-1430, 2011. DOI: 10.1590/S0100-06832011000400036.

[9] Ribeiro, B.T., Magalhães, C.A.S., Lima, J.M. and Silva, M.L.N., Calibração e uso de minissimulador de chuva para estudos de erosão e poluição do solo. Boletim Técnico n. 17, Lavras: UFLA, 2007, pp. 1-17.

[10] Bergamaschi, H. and Guadagnin, M.R., Agroclima da Estação Experimental Agronômica/UFRGS. Porto Alegre, UFRGS, 1990, 96 P.

[11] BRASIL. Ministério da Agricultura. Departamento Nacional de pesquisa agropecuária. Divisão de pesquisa pedológica. Levantamento de reconhecimentos dos solos do Estado do Rio Grande do Sul. Recife: Boletim técnico, 1973, 431 P.

[12] EMBRAPA. Empresa Brasileira de Pesquisa Agropecuária. Sistema brasileiro de classificação de solos. Rio de Janeiro, 2006, 306 P.

[13] Streck, C.A., Reinert, D.J., Reichert, J.M. and Horn, R., Relações dos parâmetros S para algumas propriedades físicas de solos do Sul do Brasil, Revista Brasileira de Ciência do Solo [online]. 32(4) pp, 2606-2612, 2008. DOI: /10.1590/S0100-06832008000700001

[14] Lopes, P.R.C., Relações da erosão com tipos e quantidades de resíduos culturais espalhados uniformemente sobre o solo. Msc. Dissertation, Departamento de Ciência do Solo, Universidade Federal do Rio Grande do Sul, Porto Alegre, RS, 1984.

[15] Tedesco, M.J., Gianello, C., Bissani, C.A., Bohnen, H., Volkweiss, S.J., Análise de solo, plantas e outros materiais. 2da ed. Porto Alegre, Universidade Federal do Rio Grande do Sul, 1995, 174 P.

[16] Gilles, L., Cogo, N.P., Bissani, C.A., Bagatini, T. and Portela, J.C. Perdas de água, solo, matéria orgânica e nutriente por erosão hídrica na cultura do milho implantada em área de campo nativo, influenciadas por métodos de preparo do solo e tipos de adubação. Revista Brasileira de Ciência do Solo [online]. 33, pp. 1427-1440, 2009. DOI: 10.1590/S0100-06832009000500033

[17] Bertol, I., Gobbi, E., Barbosa, F.T., Paz-Ferreiro. J., Gebler, L. Ramos, J.C. and Werner, R.S., Erosão hídrica em campo nativo sob diversos manejos: perdas de água e solo e de fósforo, potássio e amônio na água de enxurrada. Revista Brasileira de Ciência do Solo [online]. 35(4) pp. 1421-1430, 2011. DOI: 10.1590/S0100-06832011000400036.

[18] Bertol, I., Mafra, A.L., Engel, F.L. and Ritter, S.R., Phosphorus, potassium and organic carbon concentrations in runoff water and sediments under different soil tillage systems during soybean growth. Soil and tillage Research, [online]. 94(1), pp. 142-150, 2007. DOI: 10.1016/j.still.2006.07.008

[19] Portela, J.C., Cogo, N.P., Amaral, A.J., Gilles, L., Bagatini, T., Pardo Chagas, J. and Portz, G., Hidrogramas e sedimentogramas associados à erosão hídrica em solo cultivado com diferentes sequências culturais, com diferentes condições físicas na superfície. Revista Brasileira de Ciência do Solo [online]. 35, pp. 225-240, 2011. Available at: http://www.scielo.br/pdf/rbcs/v35n1/a21v35n1.pdf

[20] Araújo, Y.R., Souza, C.A., Araújo-Neto, J.R., Ribeiro-Filho, J.C., Lima, J.W.C., Perda de nutriente e custo da erosão em microbacias no Semiárido Brasileiro. Revista Geonorte, [online]. 7 (26), 2016. Available at: http://www.periodicos.ufam.edu.br/revista-geonorte/article/view/2768

[21] Portela, J.C., Cogo, N.P., Bagatini, T., Chagas J.P. and Portz, G., Restauração da estrutura do solo por sequências culturais implantadas em semeadura direta, e sua relação com a erosão hídrica em distintas condições físicas de superfície. Revista Brasileira de Ciência do Solo, [online]. 34(4), pp. 1353-1364, 2010. DOI:/10.1590/S0100-06832010000400032.

J.C. Portela, received the BSc. in Agronomist Engineer, from the Faculty of Agronomy of the Federal University of Bahia, Brazil, in 1997, MSc. in Agronomy Soil and Plant Nutrition, in 2000. In 2009 received the Dr. in Agronomy (soil science) from University Federal university of Rio Grande Sul, Brazil. Currently, and attached teacher IV of the University Federal Rural Semi-arid. Has experience in the field of agronomy, with emphasis on management and conservation, working mainly in the following Topics: semi-arid, Caatinga, fertility, environment and education.
ORCID: 0000-0002-9207-5530

N.P. Cogo, received the BSc. in Agronomist Engineer from the Federal University of Santa Maria, in 1969, MSc. degree in in Soil Science emphasis on morphology, genesis and soil classification by Federal University of Rio Grande do Sul, Brasil, in 1972. In 1981 received the Dr. in PurdueUniversity, EUA. He is currently associate professor IV and soil researcher at the Department of Soils of the Faculty of Agronomy of the Federal University of Rio Grande do Sul and ad hoc consultant of the National Council for Scientific and Technological Development (CNPq) and the Coordination of Improvement of Higher Level Personnel (CAPES). He works in undergraduate and postgraduate education and research in the area of soil and water management and conservation, emphasizing the study of rainwater erosion of the soil and associated runoff, using simulated rainfall under conditions field.
ORCID: 0000-0002-8172-7062

J.C.R. Filho, received the BSc. in Technologist in Irrigation and Drainage by the Federal Institute of Education Science and Technology of Ceará. MSc. in soil and water management by the Semi-Arid Rural Federal University, in 2018. He is currently a student of the Graduate Program in Agricultural Engineering, Federal University of Ceará, with a concentration area: Management of Hydrographic Basins in the Semi-Arid.
ORCID: 0001-0001-9544-009x

L. Sequinatto, received the BSc. In Agronomist Engineer Federal University of Santa Maria, in 2005, MSc. in Soil Science by Federal University Santa Maria, in 2007. In 2010 received the Dr. in soil science by Federal University Rio Grande do Sul, Brazil. Currently is adjunct professor III in the Department of Soils and Natural Resources, Agroveterinary Sciences Center (Lages, SC). Participates in the research groups CNPq Characterization of soils and relationship soil plant and Management and Conservation of Subtropical and water soils Coordinates the Santa Catarina Soil Museum and the Soil Extension Program at the School
ORCID: 0000-0002- 4368-6079

R.O. Batista, received the BSc. in Agricultural Engineer at the Federal University of Viçosa, in 2002, MSc. in Agricultural Engineering by Federal University of Viçosa, in 2004. In 2007 received the Dr. in Agricultural Engineering by Federal University of Viçosa, Brazil. Currently adjunct professor IV of the Federal Rural Semi-Arid University. Works mainly in the following subjects: irrigation engineering; environmental sanitation; and treatment and management of agroindustrial and urban waste.
ORCID: 0000-0002-3083-6808.

C.M.M. Souza, received the BSc. in Agronomist Engineer Semi-Arid Rural Federal University. MSc. in Agronomy (soil science), in 2009. In 2012 received the Dr. in Agronomy Soil and Plant Nutrition from University Federal of Viçosa, Brazil. Currently, and attached teacher III of the University Federal Rural Semi-arid. Has experience in the field of agronomy, with emphasis on management and conservation, working mainly in the following topics: semi-arid, Caatinga, fertility, geneses and soil morphology.
ORCID: 0000-0002-9553-9126

J.E.F. Gondim, received the BSc. in Agronomist Engineer Federal University Rural Semi-Arid, in 2015. Currently holds a MSc. in Soil Science from the CCA /UFPB with Emphasis in the line of research on soil management and conservation.
ORCID: 0000-0002-86906553

UNIVERSIDAD NACIONAL DE COLOMBIA
SEDE MEDELLÍN
FACULTAD DE MINAS

Área Curricular de Medio Ambiente

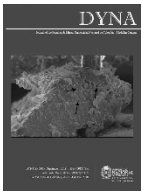
Oferta de Posgrados

Especialización en Aprovechamiento de Recursos Hidráulicos
Especialización en Gestión Ambiental
Maestría en Ingeniería Recursos Hidráulicos
Maestría en Medio Ambiente y Desarrollo
Doctorado en Ingeniería - Recursos Hidráulicos
Doctorado Interinstitucional en Ciencias del Mar

Mayor información:

E-mail: acma_med@unal.edu.co
Teléfono: (57-4) 425 5105

UNIVERSIDAD NACIONAL DE COLOMBIA
SEDE MEDELLÍN
FACULTAD DE MINAS



DYNA
http://dyna.medellin.unal.edu.co/

Teratogenic effect on bone tissue development in *Rattus norvegicus* Wistar strain, induced by the presence of arsenic

Mireya Quiterio-Pérez [a], Juan Carlos Gaytán-Oyarzún [a], Alberto José Gordillo-Martínez [b], & Francisco Prieto-García [b]

[a] *Academic Area Biology, University of the State of Hidalgo. Pachuca, Hidalgo, Mexico. quiterio@hotmail.com, jcgaytan@uaeh.edu.mx*
[b] *Chemistry Academic Area, University of the State of Hidalgo. Pachuca, Hidalgo, Mexico, gordillo@uaeh.edu.mx, prietog@uaeh.edu.mx*

Received: November 10th, 2017. Received in revised form: August 14th, 2018. Accepted: September 10th, 2018

Abstract
In this study we evaluated the possible teratogenic effects of arsenic (As) in the same concentrations recorded in water Zimapan, Hidalgo, using specimens of *Rattus norvegicus* Wistar strain, pregnant. Were subjected to varying concentrations of sodium arsenate (1887.9 mg/L, 943.9 mg/L and 0.5 mg/L), concentration, 0.5 mg/L corresponds to the registered Zimapan water, Hidalgo and chromium trioxide (166.0 mg/L) used as positive control and 5% sucrose as a negative control. The specimens were exposed from day 7 through 15 of gestation, and were sacrificed on day 19 of gestation by inhalation of chloroform. We analyzed reproductive harm the mother, as well as alterations and lack of ossification of the bone tissue of the fetus. The highest dose tested (1887.9 mg/L) produced more reproductive harm in mother resorptions caused by preventing the continuation of embryonic development. Concentrations of 0.5 mg/L to 943.9 mg/L, resulted in lack of ossification ribs, sternebrae, metacarpals, phalanges previous metatarsals and phalanges posterior sacral vertebrae.

Keywords: sodium arsenate; teratogenic; reproductive harm; lack of ossification; *Rattus norvegicus.*

Efecto teratogénico sobre el desarrollo del tejido óseo en la cepa Wistar de *Rattus norvegicus*, inducida por la presencia de arsénico

Resumen
En este estudio evaluamos los posibles efectos teratogénicos del arsénico (As) en las mismas concentraciones registradas en el agua de Zimapan, Hidalgo, usando especímenes de la cepa Wist de *Rattus norvegicus*, preñada. Se sometieron a concentraciones variables de arseniato de sodio (1887.9 mg/L, 943.9 mg/L y 0.5 mg/L), concentración, 0.5 mg/L corresponde al agua registrada de Zimapan, Hidalgo y trióxido de cromo (166.0 mg/L) utilizados como control positivo y 5% de sacarosa como control negativo. Las muestras se expusieron del día 7 al 15 de gestación y se sacrificaron el día 19 de gestación por inhalación de cloroformo. Analizamos el daño reproductivo de la madre, así como las alteraciones y la falta de osificación del tejido óseo del feto. La dosis más alta probada (1887.9 mg/L) produjo más daño reproductivo en las resorciones de la madre causado por la prevención de la continuación del desarrollo embrionario. Concentraciones de 0.5 mg/L a 943.9 mg/L, resultaron en la falta de costillas de osificación, esternebras, metacarpianos, falanges metatarsales previos y falanges de vértebras sacras posteriores.

Palabras clave: arseniato de sodio; teratogénico; daño reproductive; falta de osificación; *Rattus norvegicus*.

1. Introduction

Pollution in natural water, both chemical contaminants (polychlorinated biphenyls (PCBs), heavy metals, dioxins, chemicals, etc) such as biological, is a worldwide problem. Actually, few populated areas in developed and developing countries, which are not subject to contamination [1].

The accumulation of heavy metals in the environment and in biological systems, either by adsorption, precipitation and other forms of natural association, including bioaccumulation, are one way to minimize transport and spreading. However, this can have negative consequences for the ecological environment due

How to cite: Quiterio-Pérez, M., Gaytán-Oyarzún, J.C., Gordillo-Martínez, A.J. and Prieto-García, F., Teratogenic effect on bone tissue development in Rattus norvegicus Wistar strain, induced by the presence of arsenic. DYNA, 85(206), pp. 242-249, September, 2018.

© The author; licensee Universidad Nacional de Colombia.

to leaching of chemical species in significantly higher amounts, are accessible to aqueous systems. Consequently man can be incorporated by the ingestion of water and/or through food chains [2].

Arsenic (As) is not a metal, however it has properties of heavy metals, their toxic effect is similar to that of Mercury (Hg) and Lead (Pb). Forms As (III) or arsenite, are the most toxic [3]. Arsenic (As) is highly distributed in nature and is present in many work activities. With the growth of industrial activities, the sources of environmental contamination with this element and other heavy metals have increased significantly [4]. The leaching of mine tailings from gold and other minerals left in previous decades and centuries, are a significant source of As contamination in groundwater systems, such as the State of Hidalgo, which has a long tradition of mining activity [1].

The arsenic found in the oceans is very low values, close to 0.001 - 0.008 mg/L. Their concentration in the rivers is highly variable and has been identified from 0.1 mg/L to 1 mg/L [5]. As the average content in drinking water is approximately 2.4 mg/L. Arsenic in water, acid commonly found as As (V), H3AsO4 or deprotonated form, which is a less toxic form. Also, is the ace in the form of As (V) (as H2AsO4 and [HAsO4]-2) a less toxic As (III) [6].

It has been reported that the ingestion of small amounts of As, at a prolonged level, produces affectations to the bone marrow and the placenta and are stored in the bone tissue. Also has been associated with various processes carcinogenic and teratogenic in several bioassays [7]. In some regions has been identified endemic regional chronic hydroarsenism, reported at concentrations of 0.21 mg/L to 12.6 mg/L. Concentrations sufficient to cause long-term poisoning in the human population [5].

They have identified a large number of natural areas with groundwater, which present As content exceeding 50 µg/L in different parts of the world (Fig. 1). The major problems cited in the literature are located in Argentina, Bangladesh, Nepal, Chile, China, Hungary, India (West Bengal), Mexico (Laguna Region and Zimapan Valley), Romania, Taiwan, Vietnam and the U.S., being in latter and in Bangladesh where they have been the subject of further study. In addition there are other areas directly related to hydrothermal processes in Argentina, Chile, Japan, New Zealand, USA, Iceland, France, Dominican Republic and Kamchatka. Areas with arsenic contamination problems related to mining and mineral deposits have been recognized in many parts of the world, being the most outstanding cases of Ghana, Greece, Thailand, Chile and the U.S. [8].

In Hidalgo, the State Office of the National Water Commission is aware of the presence of high levels of As in the water is supplied by wells Zimapan City (Fig. 2).

A study on the concentrations of this element during the period March 1992 to March 1993, confirmed the presence of As in these wells [6]. Recorded concentrations exceeded the maximum permissible limits for 2005, which is 0.025 mg/L, according to Mexican legislation in 2000 [9]. Also, there were several monitoring of As to 1998, concluding with the closing of Well No. 4 (the Muhi) presented a concentration of 1.5 mg/L of As. The results of the analysis of Zimapán water samples (September 2002) show that the content of As in concentrations ranging from 0.30 mg/L to 0.50 mg/L, 12 to 20 times more than what is established by the NOM -127-SSA1-1994 [2,9-10]. The World Health Organization (WHO) has concluded that 1/10,000 population at risk of getting skin cancer caused by the daily intake of water with As at concentrations of 0.002 mg As/L. Therefore, the maximum As for water intended for human consumption in some European Union countries such as Spain, has been reduced to values of 0.010 mg/L [6].

It is essential to evaluate the causes and effects caused by environmental pollution. This leads to environmental monitoring is absolutely necessary to identify risks on human health and the ecosystem [11]. The monitoring of environmental pollution can be done primarily through chemical analysis. However, it should be reinforced through a biological assessment of toxicology, assessing the effects of xenobiotics on ecosystems and individuals using bioindicators or biomonitors, which together provide a comprehensive assessment of the environment and biological systems [12].



Figure 1. Global distribution of aquifers with high contents of As
Source: taken from [8].

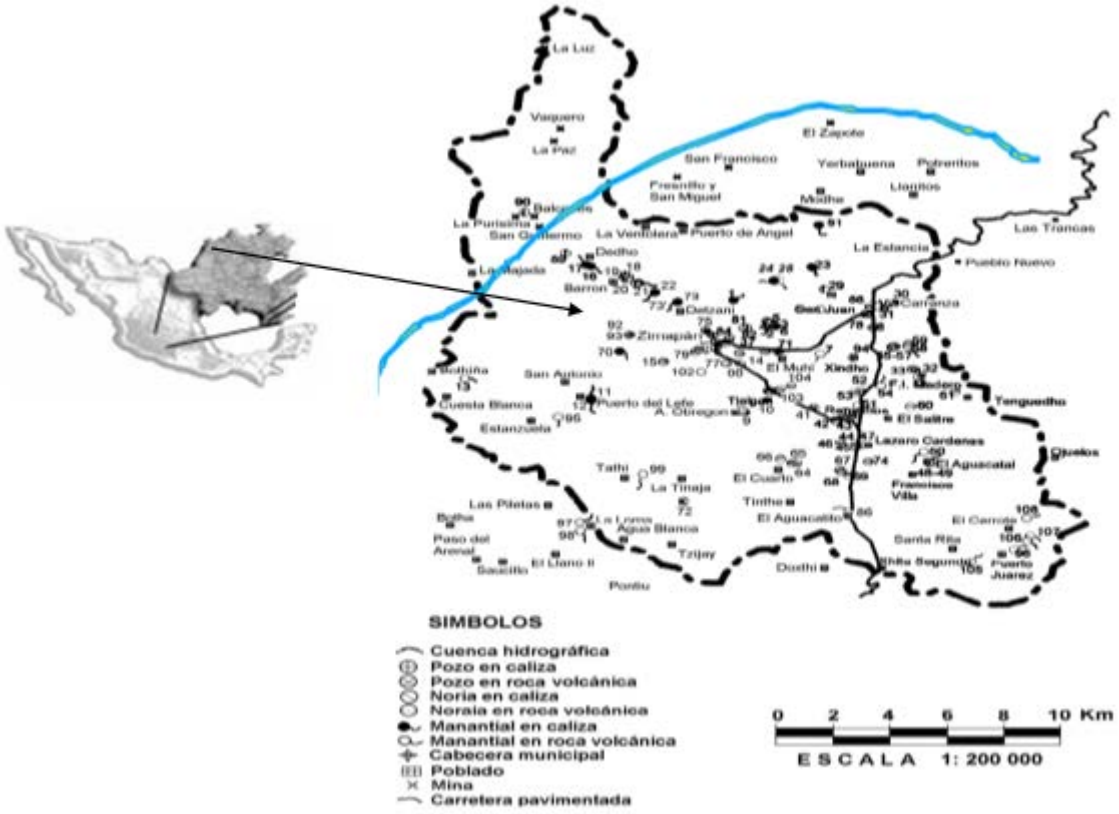


Figure 2. Zimapán City, Hidalgo, belongs to RH-26 hydrological Panuco northern part of the Basin of Mexico, Sub-basin of Rio Moctezuma. Blue line border area in the northern part of the Basin of Mexico
Source: taken from [10].

Bioassays are a type of biomarker that may be from viruses to human tissue culture, which under controlled conditions (in vivo and in vitro) allowed us to correlate the effect of the agent and/or physical chemical biological level [13]. There are different levels where you can express the hurt biological level, these can be, morphological, physiological and/or behavioral. Of these, the mutagenic, carcinogenic and teratogenic effects are important, because of their frequency and effects that impact on social, economic and health [14].

A lot of bioassays were used to assess environmental quality, one of the most used is that of *Rattus norvegicus*. This bioassay has many advantages for use in the laboratory, can evaluate the genotoxic effect and/or teratogenic induced by various pollutants. Furthermore, it is a mammal, allowing to correlate the results between rat and man [15].

The technique that is apparent in fetuses can observe the skeletal system, as it is in other organisms, because no dislocation of the same. One advantage of this technique is that organisms are preserved for a long time, allowing occasions carefully review them as necessary. This technique is used in rats to observe skeletal malformations to identify ossification centers thereof and/or delayed development, among others, naturally or induced by exposure to xenobiotic agent [16-17].

2. Metodology

2.1. Establishment of experimental plots

We used 50 individuals (pregnant females) of *R. norvegicus* who were on their first day of gestation. They were randomly divided into five treatment groups with 10 specimens each:

- Lot 1: 5% Sucrose, concentration corresponding to a negative control competitor.
- Lot 2: 166.00 mg/L of chromium trioxide (CrO_3) [18], concentration corresponding to a concurrent positive control.
- Lot 3: 0.5 mg/L of sodium arsenate (Na_2HAsO_4) corresponding concentration Zimapan waters, as it is of interest for this work to know their teratogenic effects on the skeletal system of *R. norvegicus.*
- Lot 4: 943.9 mg/L of Na_2HAsO_4, concentration corresponding to the quarter of the CL_{15} subtoxic concentration.
- Lot 5: 1887.9 mg/L Na_2HAsO_4, concentration corresponding to half the CL_{15} subtoxic concentration.

The administration of the compound to all experimental plots was performed by mouth with chronic exposure. The administration was performed during organogenesis of *R. norvegicus*, from the 7th to 15th day of gestation. The specimens were examined daily for signs of toxicity notorious,

Table 1.
Dawson made transparent technique

Skeletal abnormalities	Control	Experimental treatments			
	Sucrose, %	CrO_3, mg/L	Na_2HAsO_4, mg/L		
	5	166	0.5	943.9	1887.9
Total analyzed fetuses	85	85	85	85	85
*Ribs Nº Supernumerical	0	1/1.17	0	2/2.35	2/2.35
*Ribs Lack ossification, Nº/%	0	43/50.58*	21/24.70*	17/20.00*	5/5.88*
*Estenebras Nº Merged	0	0	0	0	0
*Estenebras Lack ossification, Nº/%	0	70/82.35*	49/57.64*	32/37.64*	50/8.82*
*Pastern Nº Absence	0	0	0	0	0
*Pastern Lack ossification, Nº/%	0	40/7.05*	30/35.29*	32/37.64*	8/9.41*
* Previous phalanges Nº Absence	0	0	0	0	0
* Previous phalanges Lack ossification, Nº/%	0	66/77.64*	56/65.88*	65/76.47%	48/56.47
*Hocks Nº Absence	0	0	0	0	0
*Hocks Lack ossification, Nº/%	0	40.47*	31/36.47	32/37.64	8/9.41
* Phalanges later Nº Absence	0	0	0	0	0
* Phalanges later Lack ossification, Nº/%	0	76/89.41*	75/88.23*	69/81.17*	66/77.64*
* Sacral vertebrae Nº Absence	0	0	0	0	0
* Sacral vertebrae Lack ossification, Nº/%	1/1.17	71/83.52*	76/89.49*	70/82.35*	69/81.17*

* Significant difference from control group, Dunnett's test, $p<0.05$ [23-24].
Source: Own elaboration, modified by Stapler [19]

impending abortion or premature delivery. In the last two cases, the specimens were sacrificed before the 19th day of gestation.

2.2. Sacrifice

The animals of all lots were sacrificed on gestation day 19th by inhalation of chloroform [19].

2.3. Hysterectomy and recording in the rat reproductive harm progenitor

After sacrifice of copies, a hysterectomy is practical to each individual pregnant, assessing reproductive damage by assessing the number of fetuses, number of implantations, early and late resorptions. Independently, fetuses were removed, recording the number of them and placing them in 96% alcohol for later evaluation teratogenic damage these.

Made transparent fetuses: To assess teratogenic damage through skeletal abnormalities and lack of ossification of the bone tissue, the analysis was performed according to the technique bone Dawson Staples modified in order to detect damage induced by the treatment (Table 1) [19].

Analysis and recording of changes in bone tissue in fetuses: For the record of the present skeletal changes were taken into account the number and condition of ribs, sternebrae, metacarpals, phalanges, metatarsals and sacral vertebrae because they are the main centers of ossification (Fig. 3) recommended for analysis [16,19].

- Ribs: We recorded whether there is a lack of ossification (by staining the sternebrae), and if numerary or not.
- Sternebrae: We record if there is a lack of ossification (according to the sternebrae staining), and whether it has merged or not
- Pasterns recorded whether there is a lack of ossification (according to the staining of the metacarpals), and the absence or not of metacarpals.
- Phalanges of forelimb: There was no lack of ossification if (according to the staining of the phalanges), and the lack or absence of phalanges.
- Hocks: We recorded whether there is a lack of ossification (as staining of metatarsals phalanges), and the absence or metatarsal.
- Phalanges of the hind: We recorded whether there is a lack of ossification (as phalanges staining), and the absence or phalanges.
- Sacral vertebrae: We recorded whether there is a lack of ossification (as staining of the phalanges), and the absence or not of these.

3. Results and discussion

3.1. Analysis in the rat reproductive harm parent

Table 2 presents the effect of treatment and the level of reproductive harm in female specimens of *R. norvegicus*. The total number of fetuses (134) and implants (89) concentration 0.5 mg/L is statistically significant, independent of treatment because not reflected an increase in the number of resorptions. Likewise, in Table 2 is shown the significant difference in total early resorptions the highest concentration

Table 2.
Effect of sodium arsenate (Na_2HAsO_4) and chromium trioxide (CrO_3) at reproductive harm in *R. norvegicus*

Variable	Control	Experimental treatments			
	Sucrose, %	CrO_3, mg/L	Na_2HAsO_4, mg/L		
	5	166	0.5	943.9	1887.9
Nº Pregnant females	10	10	10	10	10
Nº Total fetuses	88	111	134*	119	85
Rate fetuses/mother*	8.8 ± 2.4	11.1 ± 3.4	13.4 ± 2.7	11.9 ± 4.2	8.5 ± 3.2
Nº Total implantations	89	113	136*	119	113
Relac. Implant./mother	8.0 ± 2.2	11.2 ± 3.3	13.6 ± 2.9	11.9 ± 4.2	11.3 ± 2.0
Nº Total resorption tempreanas	1	1	2	0	25**
Rate resorption tempreanas /mother*	0.1 ± 1.3	0.1 ± 1.3	0.2 ± 0.4	0	2.5 ± 2.5
Nº Total late resorptions	0	1	0	0	3
R ate late resorptions /mother*	0	0.1 ± 0.3	0	0	0.3 ± 0.9

Not:* = mean ± standard deviation; ** = Significant difference from control group, Dunnett's test , p<0.05 [23-24].
Source: Own elaboration

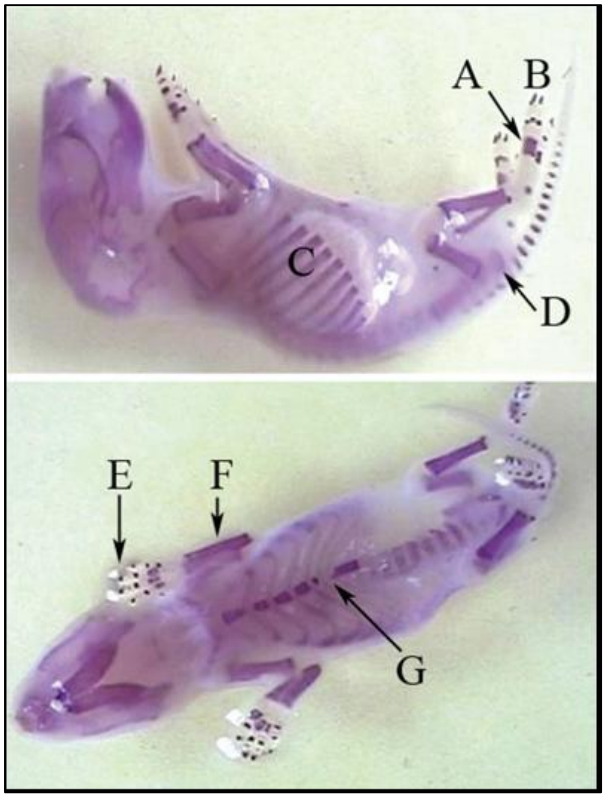


Figure 3. Major centers of ossification in rats. A. metatarsals; B. posterior phalanges, C. ribs, G. sternebrae, D. sacral vertebrae; E. previous phalanges; F. metacarpals.
Source: Own elaboration

(1887.9 mg/L), which indicates a toxic effect at the beginning of embryonic development, which is reflected in the total number of fetuses obtained in this concentration. It is particularly important to note that the reference teratogen CrO_3, which has been reported in mice, shows no statistically significant harm pregnant females of *R. norvegicus* at the concentration tested.

3.2. Analyzing changes in the bone tissue in the fetus

Teratogenic effect in fetuses (Table 2), seven markers skeletal abnormalities with two variables each, statistically determined by Dunnett's test.

The lack of ossification in the relevant variable, being nonsignificant variables supernumerary ribs, fused sternebrae, metacarpals absence of previous phalanges, metatarsal, phalanges and sacral vertebrae later. To 166.00 mg/L of CrO_3 (Fig. 4B), 0.5 mg/L Na_2HAsO_4 (Fig. 4C) and 943.9 mg/L Na_2HAsO_4 (Fig. 4D) were statistically significant variables ossification faults in the ribs, sternebrae, metacarpals, phalanges above, metatarsals, phalanges and sacral posterior (Table 3).

For the highest concentration of Na_2HAsO_4 (1887.9 mg/L) (Fig. 4E), the variables that showed statistical significance were the lack of ossification in sternebrae, previous phalanges, phalanges later and sacral vertebrae (Table 3).

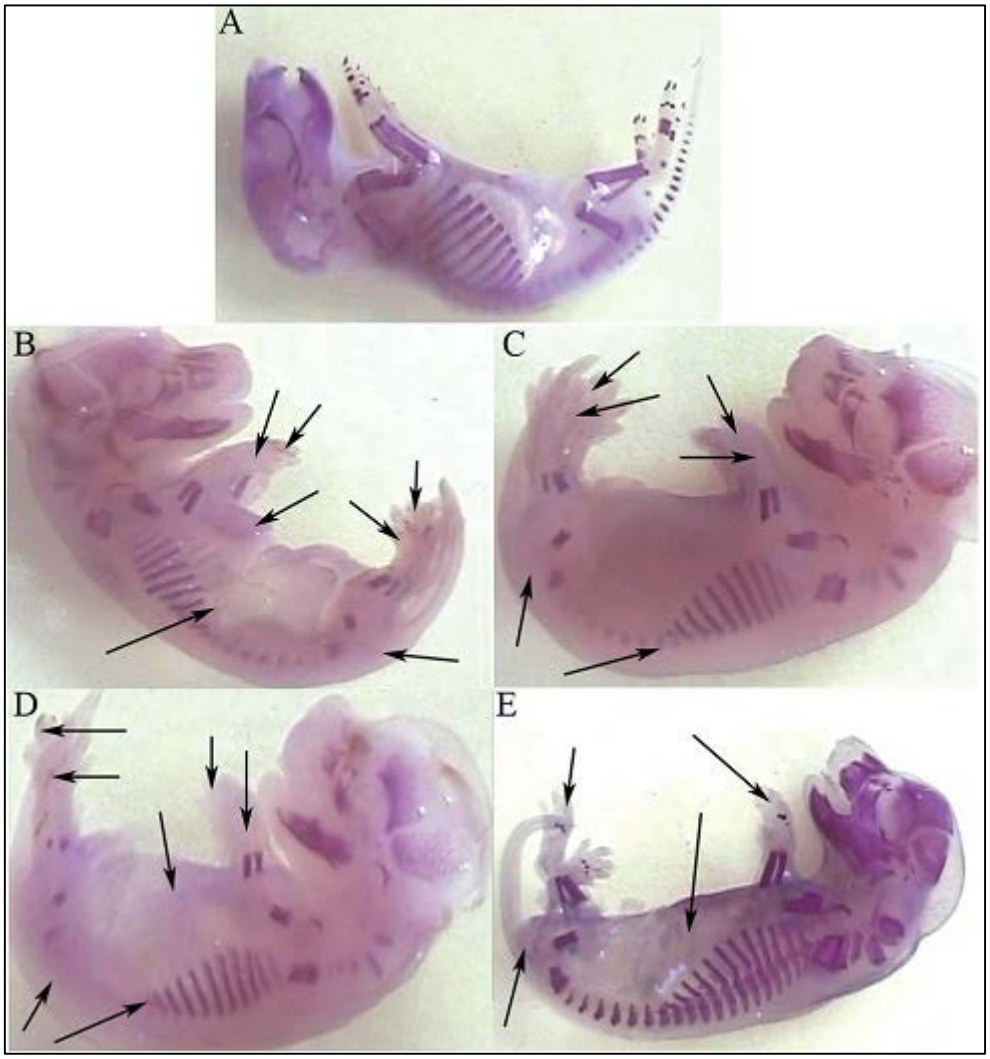


Figure 4. Effect of treatments on the process of ossification. A. Witness. B. Lack of ossification in ribs, sternebrae, metacarpals, phalanges above, metatarsals, phalanges sacral posterior and produced by administration of chromium trioxide (CrO3). C. Lack of ossification in ribs, sternebrae, metacarpals, phalanges above, metatarsals, phalanges sacral posterior and produced by administration of 0.5 mg/L of sodium arsenate (Na2HAsO4). D. Lack of ossification in ribs, sternebrae, metacarpals, phalanges above, metatarsals, phalanges sacral posterior and produced by administration of 943.95 mg/L of sodium arsenate (Na2HAsO4). E. Lack of ossification in sternebras, phalanges previous and subsequent phalanges sacral vertebrae, caused by administration of 1887.91 mg/L of sodium arsenate (Na2HAsO4). Note: Magnification is not the same in each photo; arrows indicate points without ossification.
Source: Own elaboration

Based on the results, it was determined that Na_2HAsO_4 induces reproductive harm in female progenitors of *R. norvegicus* and teratogenic damage in fetuses, because it shows statistically significant toxicity in the rat mother to the highest concentration of 1887.9 mg/L, which was established based on the ratio of the number of implantations and the number of fetuses obtained.

Furthermore, it was determined that the toxic effect acting in the early stages of embryonic development, indicating that one of the possible causes of these Na_2HAsO_4 resorption is not a metabolite of it, and acting toxic level. Also, it demonstrates that there is a different sensitivity for each of the stages of embryonic development.

Teratogenic damage caused by Na_2HAsO_4 in fetuses is statistically significant in the process of ossification in the seven markers analyzed in two of the three concentrations tested (0.5 mg/L and 943.9 mg/L).

Being relatively important to mention that the lowest concentration is found in the water used for human consumption in Zimapan, Hidalgo. So the effect caused by the Na_2HAsO_4 can be associated with a social and health problem in this town.

This allows corroborating the mechanisms and factors described above that may affect the expression of a teratogenic effect and, therefore, the difficulty of its evaluation. The results can vary from one experimental organism to another, genetic susceptibility of each organism, by the influence of maternal genome because it may interact with the metabolism of other compounds that come from mother to fetus. And participate in the resistance to infection, biochemical and molecular processes that can affect the product. Another factor that can affect the susceptibility teratogenic response of organisms, which may vary between different stages of embryonic development at the time of

Table 3.
Effect of sodium arsenate (Na_2HAsO_4) and chromium trioxide (CrO_3) in the development of the fetal bone treated in the prenatal period

Skeletal abnormalities	Control	Experimental treatments			
	Sucrose, %	CrO_3, mg/L	Na_2HAsO_4, mg/L		
	5	166	0.5	943.9	1887.9
Total analyzed fetuses	85	85	85	85	85
*Ribs Nº Supernumerical	0	1/1.17	0	2/2.35	2/2.35
*Ribs Lack ossification, Nº/%	0	43/50.58*	21/24.70*	17/20.00*	5/5.88*
*Estenebras Nº Merged	0	0	0	0	0
*Estenebras Lack ossification, Nº/%	0	70/82.35*	49/57.64*	32/37.64*	50/8.82*
*Pastern Nº Absence	0	0	0	0	0
*Pastern Lack ossification, Nº/%	0	40/7.05*	30/35.29*	32/37.64*	8/9.41*
* Previous phalanges Nº Absence	0	0	0	0	0
* Previous phalanges Lack ossification, Nº/%	0	66/77.64*	56/65.88*	65/76.47%	48/56.47
*Hocks Nº Absence	0	0	0	0	0
*Hocks Lack ossification, Nº/%	0	40.47*	31/36.47	32/37.64	8/9.41
* Phalanges later Nº Absence	0	0	0	0	0
* Phalanges later Lack ossification, Nº/%	0	76/89.41*	75/88.23*	69/81.17*	66/77.64*
* Sacral vertebrae Nº Absence	0	0	0	0	0
* Sacral vertebrae Lack ossification, Nº/%	1/1.17	71/83.52*	76/89.49*	70/82.35*	69/81.17*

Note: * Significant difference from control group, Dunnett's test, $p<0.05$; # number of exemplary [23-24].
Source: Own elaboration

exposure. In addition, we have to consider the different mechanisms of action that may arise in cells and tissues by different types of teratogens, hence the importance of selecting a good bioassay, concentration, route of administration and the time of exposure [20].

In terms of CrO_3, its effect was tested on the positive control at the level of lack of ossification in the bone tissue at the concentration tested, which corroborates the sensitivity of the bioassay to a chemical agent. This emphasized the potential of CrO_3 to induce at least lack of ossification in the bone tissue and serves as an index for comparison with other chemical agents to determine effect [18].

Na_2HAsO_4 at the highest concentration used in this work, causes damage in rats progenitor player. Its effect on ossification was significant only in four of the seven markers (lack of ossification in sternebrae, previous phalanges, phalanges later and sacral vertebrae).

It is evident that these markers, called ossification centers are sensitive to Na2HAsO4 in the concentrations evaluated, while the other three markers (lack of ossification in the ribs, metacarpals and metatarsals) were not sensitive to this compound, that is, they show an apparent sensitivity different depending on the chemical and / or concentration evaluated [21-22]. There are reports of some heavy metals, although the fetal toxic effects expressed at high and low concentrations thereof, are capable of inducing alterations in several embryonic developments [23-24]. It is recommended to conduct more experiments at different concentrations and with other compounds to assess the level of risk in human populations.

5. Conclusions

Teratogenic damage caused by Na_2HAsO_4 in fetuses is statistically significant in the process of ossification in the seven markers analyzed.

Based on these results, it is recommended further studies using Na_2HAsO_4 and try it in different kinds of organisms and trophic levels.

With this, it can be concluded that these markers, called ossification centers are sensitive to Na_2HAsO_4 in the concentrations analyzed. The other three markers (lack of ossification in ribs, metacarpals and metatarsals) are not sensitive to this compound

References

[1] Baird, C., Environmental chemistry. 3rd Edition, Reverté, S.A., Barcelona, Spain, 2006, 622 P. DOI: 10.1021/ed083p217

[2] Lechuga-Vargas, M.Á., Prieto-García, F., Gaytán-Oyarzún, J.C., Barrado-Esteban, E. and del Razo-Jiménez, L., Study of genotoxic damage accumulation and cell tissues sensitive for the presence of arsenic in water and soils of Zimapán, Hidalgo, Mexico. Bio-Press, 7, pp. 1-13, 2003.

[3] Patnaik, P., A comprehensive guide to the hazardous properties of chemical substances. 3rd Edition, Van Nostrand Reinhold, New York, E.U.A., 2007, 763 P. ISBN: 978-0-471-71458-3

[4] Lippmann, M., Environmental toxicants: Human exposures and their health effects. 3rd Edition, Van Nostrand Reinhold, New York, E.U.A., 2009, 699 P. ISBN: 978-0-471-79335-9
[5] Galvao, L.A.C. and Corey, G., Arsenic. Watch Series, 3, CPEHS-PPS-OMS, Metepec, México, 1987, 70 P.
[6] Pérez-Moreno, F., Prieto-García, F., Rojas-Hernández, A., Galán-Vidal, C.A., Marmolejo-Santillán, Y., Romo-Gómez, C., Castañeda-Ovando, A., Rodríguez-Ávila, J.A. and Barrado-Esteban, E., Chemical characterization of groundwater wells and water distributor Zimapan, State of Hidalgo, Mexico. Hidrobiológica, 13, pp. 95-102, 2003.
[7] Ramos-Morales, P. and Rodríguez-Arnaiz, R., Genotoxicity of two arsenic compounds in germ cells and somatic cells of Drosophila melanogaster. Environmental and Molecular Mutagenesis, 25, pp. 288-299, 1995. DOI: 10.1002/em.2850250405
[8] Dopp, E., Kligerman, A.D. and Diaz-Bone, R.A., Organoarsenicals. uptake, metabolism, and toxicity. Royal Society of Chemistry, 2010. ISBN: 978-1-84973-082-2. DOI: 10.1039/9781849730822-00231
[9] Secretaría de Salud., Water for human use and consumption. Permissible limits of quality and must undergo treatment to the water to make it drinkable. Amendments to the Official Standard NOM-127-SSA1-1994, Environmental Health. Official Journal, First section, Federal District, México, pp. 73-79, 2000
[10] Pérez-Moreno, F., Dynamics of arsenic in groundwater wells and sediments general distributor Zimapán drinking water, Hidalgo. Doctoral Thesis in Chemical Sciences, University of the State of Hidalgo, Pachuca, Hidalgo, México, 2004, 132 P.
[11] de Fernícola, N.A.G.G., Risk Assessment. In: Reyes, F.G.R. and Waldemar, A., Prospective toxicology and chemical safety: International programme of chemical safety (PISSQ/PNUMA-OIT-OMS). The Pan American Center for Human Ecology and Health (ECO/OPS/OMS). pp. 53-63, Metepec, State of México, México, 1992a
[12] de Fernícola, N.A.G.G., Biological assessment of human exposure. In Reyes, F.G.R. and Waldemar, A., Prospective toxicology and chemical safety: International programme of chemical safety (PISSQ/PNUMA-OIT-OMS). The Pan American Center for Human Ecology and Health (ECO/OPS/OMS). pp. 23-34, Metepec, State of México, México, 1992b.
[13] Markert, B., Oehlmann, J. and Roth, M., General aspects of heavy metal monitoring by plants and animals. In Subramanian, K. and Iyengar, G., Environmental biomonitoring: Exposure assessment and specimen banking. American Chemical Society, pp. 19-29, Washington, D.C., E.U.A, 1997.
[14] Reyes, F. and Waldemar, A., Prospective toxicology and chemical safety: International programme of chemical safety (PISSQ/PNUMA-OITOMS). The Pan American Center for Human Ecology and Health (ECO/OPS/OMS). Metepec, State of México, México, 1992, 231 P.
[15] Gad, S. and Chengelis, P., Acute toxicology testing. Academic Press, San Diego, CA, E.U.A., 2011, 534 P.
[16] Kaufman, M., The atlas of mouse development. Academic Press, San Diego, CA, E.U.A., 1992, 512 P.
[17] Acuña, O., Silva, G., Lemus, D., Fuenzalida, M., Román, D., Rivera, Y. and Varela, H., Copper ion poisoning in pregnant rats and their effect on the formation of centers of ossification in fetuses. Revista Chilena de Anatomía, 17, pp. 217-224, 2005.
[18] García-Rodríguez, M., López-Santiago, V. and Altamirano-Lozano, M., Study of genotoxic and teratogenic effect of CrO3 during mouse fetal development in vivo, Proceedings of the National Congress of Genetics. Research Unit Genetics and Environmental Toxicology, FES-Zaragoza, National Autonomous University of México, DF, México, 2002.
[19] García, A., Teratogenic interaction of 4-hydroxy, 4-ethyl, 4-phenyl-butyramide (HEPB) and lower homologues carbamazepine and phenytoin in mice. Master Thesis in Science in Toxicology, National Polytechnic Institute, México, 1999, 85 P.
[20] Sadler, T., Langman: Medical Embryology. Editorial Médica Panamericana, DF, México, 2000, 424 P.
[21] Earl, F. and Vish, T., Teratogenicity of heavy metals. In: Oehme, F., Toxicity of heavy metals in the environment, Part 2. Marcel Dekker, pp. 617-637, New York, E.U.A., 1979.
[22] Vega-G., S., Epidemiological evaluation of risks caused by environmental chemicals. Toxicology V: Genotoxicity and reproductive system reproductive harm. The Pan American Center for Human Ecology and Health (ECO / PAHO / WHO). Metepec, State of México, México, 1985, 47 P.
[23] Infante-Gil, S. and Zárate-de Lara, G.P., Statistical methods interdisciplinary approach. Editorial Trillas S.A. de C.V., Mexico, 2000, 643 P.
[24] Ronal, W., Probability and statistics for engineers. Prentice-Hall, Hispanoamericana S.A., México, 1999, 739 P.

M. Quiterio-Pérez, is PhD in Environmental Sciences from the Autonomous University of the State of Hidalgo, Mexico. Professor-researcher at the Universidad del Valle del Mezquital, Hidalgo Mexico.
ORCID: 0000-0003-2481-4378

J.C. Gaytán-Oyarzún, is Doctor in Environmental Sciences from the Autonomous University of the State of Hidalgo, Mexico. Research professor B. Academic Area of Biology. Institute of Basic Sciences and Engineering.
ORCID: 0000-0003-3498-0441

A.J. Gordillo-Martínez, is Doctor of Science from the Polytechnic University of Madrid, Spain. Research professor at the Autonomous University of the State of Hidalgo, Mexico.
ORCID: 0000-0002-5266-5982

Francisco Prieto-García, PhD in Chemistry from the University of Valladolid, Spain. Research Professor Holder C at the Autonomous University of the State of Hidalgo, Mexico. prietog@uaeh.edu.mx.
ORCID: 0000-0001- 8878-3908



UNIVERSIDAD NACIONAL DE COLOMBIA
SEDE MEDELLÍN
FACULTAD DE MINAS

Área Curricular de Ingeniería Química e Ingeniería de Petróleos

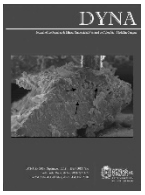
Oferta de Posgrados

Maestría en Ingeniería - Ingeniería Química
Maestría en Ingeniería - Ingeniería de Petróleos
Doctorado en Ingeniería - Sistemas Energéticos

Mayor información:

E-mail: qcaypet_med@unal.edu.co
Teléfono: (57-4) 425 5317

UNIVERSIDAD NACIONAL DE COLOMBIA
SEDE MEDELLÍN
FACULTAD DE MINAS



DYNA
http://dyna.medellin.unal.edu.co/

Design and calculation of a hybrid solar-hydraulic power station in Gran Canaria

Abian Beltrán [a], Herberth Gracia-León [b], Daniella Rodríguez-Urrego [c] & Leonardo Rodríguez-Urrego [b]

[a] *Facultad de Ingeniería, Universidad Las Palmas de Gran Canaria. abian.beltran101@alu.ulpgc.es*
[b] *Facultad de Ingeniería, Universidad EAN, Bogotá, Colombia. hgracia@universidadean.edu.co, lrodriguezu@universidadean.edu.co*
[c] *Facultad de Ingeniería, Universidad Católica, Bogotá, Colombia. drodriguez@ucatolica.edu.co*

Received: February 21th, de 2018. Received in revised form: July 25th, 2018. Accepted: August 15th, 2018

Abstract
This paper propose the design, calculation and feasibility study of a reversible hydroelectric plant located in the island of Gran Canaria, with the support of a solar power plant to cover a part of the energy demand of the pumping of water from a lower reservoir to a higher one. This work is motivated in order that the island of Gran Canaria has the first hydroelectric power station in its history, and has energy storage to cover peak hours of demand between 18 and 22 hours. At the same time, it is intend to increase the installed capacity of renewable sources to the detriment of fossil fuels. Finally, this paper conclude with an economic study where a budget and its corresponding prefeasibility study are estimated, considering a construction period of 4 years and a useful life of the installation of 25 years.

Keywords: solar; photovoltaic; design; hydropower; hybrid energy; Isla Gran Canaria; non-conventional energy.

Diseño y cálculo de una central híbrida solar-hidráulica en Gran Canaria

Resumen
Este artículo propone el diseño, cálculo y estudio de factibilidad de una planta hidroeléctrica reversible ubicada en la isla de Gran Canaria, con el apoyo de una planta de energía solar para cubrir una parte de la demanda de energía del bombeo de agua desde un depósito inferior a uno superior. Este trabajo está motivado para que la isla de Gran Canaria tenga la primera central hidroeléctrica de su historia y tenga un almacenamiento de energía para cubrir las horas pico de demanda entre 18 y 22 horas. Al mismo tiempo, tiene la intención de aumentar la capacidad instalada de fuentes renovables en detrimento de los combustibles fósiles. Finalmente, este trabajo concluye con un estudio económico donde se estiman un presupuesto y su estudio de prefactibilidad, considerando un período de construcción de 4 años y una vida útil de la instalación de 25 años.

Palabras clave: energía solar; fotovoltaica; diseño; hidroeléctrica; energía hibrida; Isla Gran Canaria; energía no convencional.

1. Introducción

Actualmente, los combustibles fósiles atienden la demanda energética mundial actual correspondiente al 90% aproximadamente, dadas estas condiciones se presenta la necesidad de potencializar las nuevas fuentes energéticas permitiendo el desarrollo de las energías renovables en su totalidad sin presentar limitaciones técnicas o financieras [1]. Dentro de los casos más destacados es el de las zonas aisladas, puntos no conectados a la red por distancia o geografía, donde las nuevas opciones de energías renovables se han convertido en la forma más efectiva para un desarrollo energético en estas áreas.

La combinación de dos o más sistemas de energías renovables se denominan sistemas híbridos [2], los cuales complementan hoy en día aquellas energías que en el momento de implementarse no tienen una disponibilidad de recurso permanentemente o no producen energía durante algunas franjas diarias como es el caso de la solar fotovoltaica. En efecto, uno de los sistemas híbridos más

How to cite: Beltrán, A., Gracia-León, H., Rodríguez-Urrego, D. and Rodríguez-Urrego, L., Diseño y cálculo de una central híbrida solar-hidráulica en Gran Canaria. DYNA, 85(206), pp. 250-257, September, 2018.

© The author; licensee Universidad Nacional de Colombia.

implementados en sistemas aislados en el mundo son Eólico-solar [3], así mismo en menor medida se han realizado sistemas híbridos con energía hidráulica [4,5]. Por tal razón de acuerdo a las condiciones topográficas, geográficas y meteorológicas, es necesario revisar los recursos que se presentan en las zonas a estudiar para así hacer partícipe de la combinación de energías con el fin de implementar los mejores recursos y así obtener mayores eficiencias y posibles soluciones económicas/viables para los proyectos en zonas aisladas.

Las islas son un caso de estudio que, dependiendo de su tamaño, podrían ser entendidas como zonas no interconectadas o como zonas conectadas, pero por su ubicación geográfica en si misma ya genera retos a la hora de poder abastecer de energía a su población. Investigar como podrían mantenerse sólo con energías renovables, reconociendo que en su mayoría se abastecen a través de combustibles fósiles es un reto. Hay que tener en cuenta muchos factores como el transporte y la logística, que en estos casos genera un alto incremento en costos y algunos perjuicios ambientales, sin dejar de lado los análisis técnicos y financieros del propio proyecto. IRENA por ejemplo, presenta el apoyo a 2700 islas de la comunidad europea ante el título "Energía limpia para las islas" en el año 2017 [6]. Bajo esta finalidad se hace énfasis en el caso de la Isla de Gran Canaria, España, donde el aumento de la demanda eléctrica exige la implementación de un nuevo medio de generación energética dentro del sistema actual para conseguir la demanda promedio de 503 MW [7]. Como solución, se podría recurrir a centrales térmicas convencionales, pero éstas provocan problemas de emisiones y mala aceptación social debido al impacto ambiental que producen en su entorno. Por ello, se convierte en reto enfrentarse en las próximas décadas a la búsqueda de fuentes de energías renovables y sostenibles para cubrir la demanda energética tanto en Canarias como en otras islas del mundo [8]. Este artículo presenta el diseño de una central híbrida solar-hidráulica reversible en la isla Gran Canaria [9], estudiando su viabilidad y sostenibilidad desde lo técnico financiero y social.

Entre algunas de las distintas soluciones existentes dentro de las energías no convencionales se encuentran las instalaciones solares, eólicas e hidroeléctricas. Como ejemplo, las centrales hidroeléctricas de acumulación por bombeo, consisten en elevar agua de un desnivel en un depósito inferior a uno superior mediante bombeo, para luego turbinar en sentido descendente. Este tipo de centrales presenta múltiples ventajas. La primera es la posibilidad de servirse de las fases de bombeo como sistema de almacenaje de energía, donde la energía que se puede almacenar proviene de fuentes no regulables como la energía solar o eólica [10]. Por ello, las centrales eléctricas de bombeo resultan rentables si el sistema de bombeo se utiliza durante las horas valle, asegurando así una producción máxima durante las horas pico. La segunda posibilidad son las centrales hidroeléctricas de bombeo que pueden funcionar en circuito cerrado, es decir, bombear y turbinar la misma agua con pocas pérdidas hidráulicas, aprovechando las horas de gran consumo (horas pico) permitiendo tener una rentabilidad consecuente de la instalación.

El mayor problema encontrado en este tipo de instalación es la inversión inicial. Por eso existen muy pocos proyectos de centrales hidroeléctricas de bombeo de pequeña o mediana potencia. A continuación, se presentan algunos proyectos de este tipo en España y en el mundo [11]:

- Sistema de La Muela, Comunidad Valenciana
- La central hidroeléctrica de Aguayo, ubicada en San Miguel de Aguayo (Cantabria)
- La central hidroeléctrica de acumulación por bombeo Bath County, situada en Virginia (EEUU
- La central de Entracque, Italia

La propuesta desarrollada dentro del articulo puede ser aplicada dentro de cualquier isla que cuente, en su topografía, con una región a mayor altitud donde pueda ser instalada la central hidráulica. En el mundo existen más de 2000 islas según el observatorio mundial y en el 50% se encuentran problemas de abastecimiento energético como lo es el caso de Puerto Rico y de Isla Canaria. La presente solución, además, puede validar el modelo en cualquier zona no interconectada con características similares que pretenda un abastecimiento de energía a su población.

Sin embargo, y como se mencionó anteriormente, los sistemas energéticos alternativos como el solar y los eólicos tienen algunos inconvenientes como lo son la disponibilidad y el cargo por confiabilidad. Estos problemas los hacen inestables para las redes de grandes poblaciones aisladas, como es el caso del mayor porcentaje de islas. Algunos proyectos cuentan con baterías plomo ácido, sin embargo, por costos y temas de mantenimiento son insostenibles en el tiempo. Una de las soluciones es utilizar sistemas híbridos con combustibles fósiles como es el caso de la mayoría de proyectos del caribe [12]. En estos proyectos, la energía alternativa da el aporte energético principal y la energía a partir de combustible fósil da la confiabilidad, aunque es una importante solución, sigue teniendo problemas asociados al componente y el impacto ambiental. Esto se soluciona con una batería natural tal cual se explicó anteriormente bombeando a una cota más alta y turbinando después. Estas cotas existen en todas y cada una de las islas del mundo y no se están aprovechando energéticamente.

2. Recurso energético de Gran Canaria

El sistema eléctrico canario cuenta con seis sistemas eléctricamente aislados, de pequeño tamaño, con una red de transporte de energía débilmente mallada y además de la imposibilidad de conexión a una red continental. Estas condiciones hacen que estos sistemas sean menos estables y fiables que los grandes sistemas interconectados en los que es posible garantizar el suministro ante picos de demanda o ante determinadas situaciones de falta de generación.

El sistema eléctrico está configurado el torno a dos centros de generación, la central de Jinámar y la central de Barranco de Tijarana, compuestas por grupos de generación de gas, vapor y diésel. Así mismo, hay instalados en torno a 100 MW de energía eólica de gran antigüedad en la zona sureste de la isla [8]. Siendo la distribución porcentual de la demanda de un 79.13% a partir de productos petrolíferos y un 0,24% solar [8].

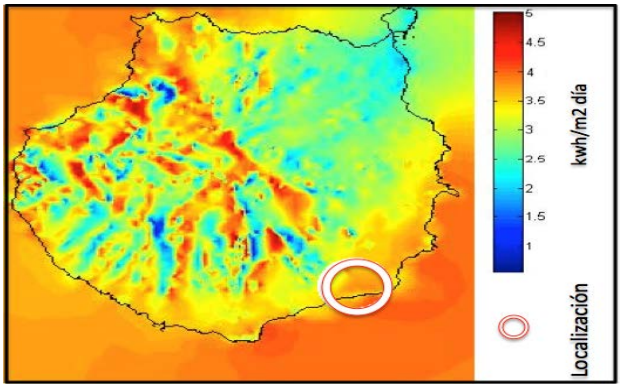


Figura 1. Recurso Solar en canaria.
Fuente: [1] Anuario Energético de Canarias.

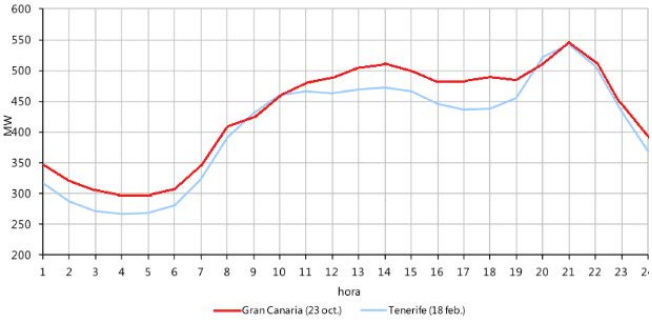


Figura 2. Recurso Solar en canaria.
Fuente: [1] Anuario Energético de Canarias.

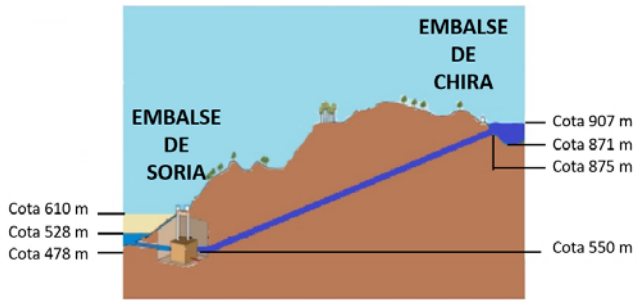


Figura 3. Salto neto entre embalses.
Fuente: Los autores.



Figura 4. Localización central hidráulica y solar
Fuente: Google maps modificado por los autores

En los últimos años se ha notado un decrecimiento de la energía generada por la red pasando de 3.593 GWh a 3.389 GWh de 2010 a 2014 respectivamente, disminuyendo un 5% de la cobertura sobre la demanda total de la isla. Es necesario entonces, estudiar los recursos con los que cuenta la isla para desarrollar nuevas formas de generación energética. En la actualidad existen en la isla 60 presas, y todas las de mayor tamaño se encuentran en la zona centro–oeste y noreste de la isla, ya que son las zonas en las que más llueve, entre ellas y las de más importancia son la presa Soria y la de Chira.

En la Fig.1 se observa la radiación solar media que recibe la isla de Gran Canaria durante un año, en el cual se aprecia una radiación promedio de 3.7 kwh/m^2 día. Así mismo se identifica la zona donde se localizará la central solar del presente estudio.

3. Estado y localización del sistema de generación híbrido

Existen varios tipos de sistemas híbridos con la finalidad de aumentar la producción de energía renovable[13] con la simulación y control de instalaciones híbridas solares-eólicos. El sistema propuesto plantea utilizar un sistema híbrido de energía solar e hídrica óptimos [14], el primero para el funcionamiento del sistema de bombeo y el segundo para cubrir las demanda de la isla. Se analiza la demanda horaria de la isla como se muestra en la Fig.2, donde se observa que la demanda horaria promedio equivale a 450 MW y la mayor demanda se presenta entre las 13 y 21 horas.

Respecto al estado y ubicación de la presa, con el fin de realizar el diseño de la parte hidráulica del sistema, los informes del estado de las presas justifican que existe un aterramiento de la presa de Chira con un volumen disponible de 4,03 hm^3. El salto útil será el que tiene lugar desde la descarga de la presa de Chira hasta la caverna donde se encuentran las turbinas, en la presa de Soria, y es de 325m. Según esto, considerando unas pérdidas del 9%, el salto nominal neto es de 295 metros [15]. En la Fig.3 se identifica el salto neto que tendría el flujo de agua.

La energía necesaria para bombear el agua desde el embalse inferior hasta el superior se extrae de una central de energía solar fotovoltaica. La potencia a instalar, por costos y factibilidad, es 2,247 MW lo cual requiere un área amplia para instalar la cantidad de módulos solares que requiere. Se ha optado por un área de 280 x 400 m^2. En la Fig.4 se identifica la posición las instalaciones correspondientes al sistema hibrido, la zona 1 es donde se encuentra la central hidroeléctrica y la zona 2 donde se sitúa la central solar.

La energía eléctrica que circula por la red de transporte lo hace en forma de corriente alterna, la corriente continua generada en los paneles solares debe ser transformada a corriente alterna a través de los inversores de red.

Posteriormente la energía eléctrica producida pasa por un centro de transformación donde se adapta a las condiciones de las líneas de transporte para su utilización [15,16].

4. Formulación y cálculos

La central hidroeléctrica cuenta con tres grupos formado cada uno por una turbina Francis, un generador y un transformador.

$$nTurbina = 0.85$$
$$nGenerador = 0.9$$
$$nTransformador = 0.95$$

- La velocidad del agua debe estar comprendida entre 3 y 5 m/seg. Por esta razón, se fija una velocidad de 4 m/seg.
- El caudal fijado para cada una de las 3 turbinas Francis de la central es de 2 m^3/seg, para el total es de 6 m^3/seg.
- Es importante la implementación de un sistema para diagnóstico de fallos dentro de las turbinas, obteniendo un mayor tiempo de vida y conocimiento del estado del sistema [18].
- Se procede al cálculo del diámetro de las tuberías conectadas a cada turbina, de la turbina forzada y la galería de conducción:

$$Q = v \cdot 2\pi \frac{D^2}{4} \quad (1)$$

$$D = \sqrt{\frac{4 \cdot Q}{v \cdot \pi}} \quad (2)$$

Diámetro Turbinas (Dt)	0.8 m
Diámetro Forzada (DF)	1.4 m

La longitud del tubo desde las turbinas hasta el embalse superior es de L = 2.225 m.

La central hidroeléctrica funcionará durante 4 horas ininterrumpidas, entre las 18 y 22 horas. Por tanto, la cantidad de agua necesaria para el correcto funcionamiento de la central es de 86.400 m^3/día:

La potencia eléctrica generada en turbina según la fórmula 3:

$$P_{eTURBINA} = n_{TURBINA} \cdot g \cdot \rho \cdot H_n \cdot Q \quad (3)$$

$$P_{eTURBINA} = 4.919.715W \approx 4{,}920\ MW$$

Tenemos entonces la potencia eléctrica en bornas del generador:

$$P_{eG} = \mathrm{n}_{GENERADOR} \cdot P_{eTURBINA} \approx 4{,}428\ MW \quad (4)$$

Aplicando la ecuación 5 la potencia eléctrica en la salida del trasformador seria:

$$P_{eTRANSF} = \mathrm{n}_{TRANSF} \cdot P_{eG} \quad (5)$$

$$P_{eTRANSF} \approx 4{,}206\ MW$$

Por tanto, tenemos que la potencia eléctrica a la salida de los tres transformadores es de:

$$Potencia\ total = 12{,}618\ MW$$

Además, se considera que la central hidroeléctrica funcionará durante 360 días al año, estableciendo 5 días para mantenimiento.

La energía eléctrica anual generada en turbina descrita en la fórmula 6.

$$E_{Turbina} \approx 7{,}08 \frac{GWh}{año} \quad (6)$$

Por lo tanto, la energía eléctrica anual en bornas del generador

$$E_{eG} = P_{eG} \,.\, t = 6.375{,}95 \frac{MWh}{año} \approx 6{,}379 \frac{GWh}{año} \quad (7)$$

Tenemos entonces la energía eléctrica anual en la salida del transformador

$$E_{eTRANSF} = \mathrm{n}_{TRANSF} \cdot E_{eG} \approx 16{,}83 \frac{MWh}{día} \quad (8)$$

Por tanto, la energía eléctrica anual a la salida de los tres transformadores es de:

$$Energía\ eléctrica\ anual\ total \approx 50{,}5 \frac{MWh}{día} \quad (9)$$

Y según las características del tendido eléctrico y la conexión a red, con una tensión de 66 kV y una intensidad de 350 A. la potencia máxima que podremos inyectar a la red será:

$$P_{MÁX} = V \cdot I = 66kV \cdot 350A = 23{,}1\ MW \quad (10)$$

4.1. Central de bombeo

El periodo de bombeo se considera de 20 horas, que abarca desde las 22 horas que acaba el turbinado hasta las 18 horas que vuelve a empezar. La cantidad de agua necesaria para el turbinaje, que resultó ser de 86.400 m^3. Se proyecta un bombeo del 60% de dicha cantidad debido a:

- El consumo queda notablemente reducido los fines de semana, días festivos y los meses de verano.
- Las lluvias caídas durante el año.
- Y, por último, la capacidad sobrante de agua en el embalse superior (Presa de Chira).

Se dispone de una capacidad útil para la central de 2.600.000 m^3 de agua:

$$Caudal\ a\ bombear/dia = 0{,}7\ \frac{m^3}{seg}$$
$$Velocidad = 0{,}46\ m/seg$$

Según las siguientes consideraciones:

Table 1.
Cálculos del sistema de bombeo

Descripción	Valor
Margen de días sin bombear agua.	$\mathbf{30{,}09\ días}$
Cantidad de caudal que falta diariamente para que el bombeo fuera del 100%.	$\mathbf{86.400\ \frac{m^3}{día} - 56.000\ \frac{m^3}{día} = 30.400\ \frac{m^3}{día}}$
Margen de días bombeando el 60% de la cantidad de agua turbinable.	$\mathbf{\frac{2.600.000\ m^3}{30.400\ m^3/día} \approx 85\ días}$

Fuente: Los autores.

Table 2.
Consideraciones de bombeo

Descripción	Valor
Temperatura del agua a 30ªC	$\boldsymbol{Densidad = \rho = 995,7\ kg/m^3}$
	$\boldsymbol{Viscosidad = 0,8 \cdot 10^{-3} kg/m \cdot seg}$
	$\boldsymbol{Peso\ específico = 9,375 \cdot\ 10^3\ \frac{kg}{m^2 \cdot seg^2}}$
Rendimiento de la bomba (μ_B)	0,9
Caudal (Q)	0,7 m^3/seg
Diámetro	1,4 m
Longitud	2225 m
Altura	325 m
Velocidad	0,46 m/seg
Rugosidad relativa ε/D	$3,5 \cdot 10^{-5}$

Fuente: Los autores.

Table 3.
Coordenada central solar

Descripción	Coordenada
Latitud	27°48'12" Norte
Longitud	15°28'51" Oeste
Elevación	20 m.s.n.m

Fuente: Google maps.

Según la Tabla 2 se obtiene que las pérdidas de carga son de 1,3 metros, adicionales a los 325 metros de diferencia de cotas entre las dos presas (altura útil). El resultado es muy pocos metros debido a que se bombea a muy poco caudal para un diámetro de tubería elevado[19]. Por consiguiente, se obtiene una potencia de la bomba hidráulica de:

$$P_{BRUTA} = h_A \cdot \gamma \cdot Q = \ 2.134.781,25\ W \qquad (11)$$

$$P_{BOMBA} = \frac{P_{BRUTA}}{\mathrm{n}_B} = 2,247\ MW \qquad (12)$$

$$Energía/dia = \ 44,94\ \frac{MWh}{día}$$

$$Energía/anual\ = 16,18\ \frac{GWh}{año}$$

4.2. Central de energía solar

La orientación de los paneles solares viene definida por el ángulo de Azimut (α), que es el ángulo entre la proyección sobre el plano horizontal de la normal a la superficie del módulo y el meridiano del lugar [20]. Para el presente diseño se considera un ángulo α = 0º, hacia el sur geográfico

La inclinación de los paneles solares viene definido por el ángulo de inclinación (β), que es el ángulo que forma la superficie de los paneles con el plano horizontal.

$$Inclinación = \ 27,7º - 10º = 18º \qquad (13)$$

No obstante, se considerará un ángulo de inclinación β = 26º, ya que es el ángulo de inclinación óptimo que determina el software fotovoltaico PVGIS.

Dado que la instalación se encuentra en campo abierto, las únicas pérdidas posibles son las propias, que pueden estar producidas por otros seguidores solares, casetas de transformadores, apoyos de las líneas aéreas y vallado perimetral, entre ellas. Se calcula con la siguiente fórmula:

Se obtiene los siguientes resultados: $\begin{cases} d = 2,90\ metros \\ d_1 = 1,1\ metros \\ d_2 = 1,8\ metros \end{cases}$

La central de energía solar se ubica en la zona de Gran Canaria llamada Juan Grande, y tiene las siguientes coordenadas:

Considerando nulas las pérdidas por sombras, se expone en la siguiente tabla la irradiación global del lugar:

H_h	Irradiación sobre plano horizontal (Wh/m2/día)
H_{OPT}	Irradiación sobre un plano con la inclinación óptima (Wh/m2/día)
$H(18)$	Irradiación sobre plano inclinado:18grados (Wh/m2/día)
DNI	Irradiación directa normal (Wh/m2/día)
I_{OPT}	Inclinación óptima (grados)

Table 4.
Irradiación global sobre la instalación solar

Mes	H_h	H_{OPT}	$H(18)$	DNI	I_{OPT}
Enero	3890	5440	5050	5300	54
Febrero	4800	6120	5810	5850	46
Marzo	6300	7110	6970	6270	32
Abril	6810	6900	6990	6820	15
Mayo	7440	6930	7200	7230	1
Junio	7750	6910	7280	7620	-6
Julio	7930	7200	7550	7950	-3
Agosto	7290	7140	7310	7310	10
Septiembre	6070	6590	6540	6200	26
Octubre	5260	6410	6150	6030	41
Noviembre	4030	5490	5120	5350	52
Diciembre	3540	5090	4690	4990	57
Año	**5930**	**6450**	**6390**	**6410**	**26**

Fuente: Los autores.

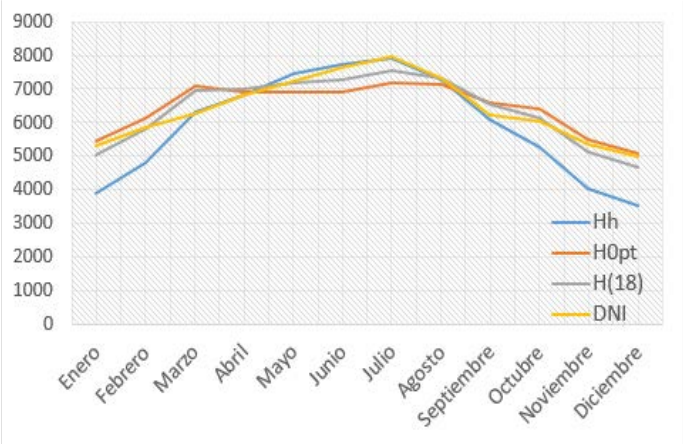


Figura 5. Irradiación del lugar
Fuente: Los Autores

Table 5.
Consideraciones de la central eléctrica

Descripción	Valor
Potencia nominal del sistema FV	2980,8 kW
Inclinación de los módulos	26ª
Orientación (azimut) de los módulos	0º
Pérdidas estimadas debido a la temperatura y niveles bajos de irradiación (utilizando la temperatura ambiente local):	11,2%
Pérdidas estimadas debido a los efectos de la reflectancia angular:	2,6%
Otras pérdidas (cables, inversor, etc.):	4,0%
Pérdidas combinadas del sistema FV:	17,0%

Fuente: Los autores.

Table 6.
Caracterización de componentes.

Datos del módulo		Datos del inversor	
P (W)	345	P. entrada (kW)	1500
Voc (V)	47,13	Imáx entrada (A)	2500
Vmp (V)	38,39	P. salida (kW)	1250
Icc (A)	9,48	Imáx salida (A)	2123
Imp máx (A)	8,99	Icc (A)	3065
		Tensión en la entrada	500/800

Fuente: Los autores.

Table 7.
Simulación de producción eléctrica mes a mes

Mes	E_d	E_m	H_d	H_m
Enero	13700.00	424000	5.44	169
Febrero	15300.00	428000	6.12	171
Marzo	17600.00	546000	7.11	220
Abril	17000.00	511000	6.90	207
Mayo	17100.00	529000	6.93	215
Junio	17000.00	509000	6.91	207
Julio	17600.00	545000	7.20	223
Agosto	17300.00	537000	7.14	221
Septiembre	16000.00	481000	6.59	198
Octubre	15700.00	486000	6.41	199
Noviembre	13600.00	408000	5.49	165
Diciembre	12800.00	396000	5.09	158
Año	15900.00	483000	6.44	196

Fuente: Los autores.

Como se mencionó, de acuerdo a el software PVGIS se determinó que el ángulo de inclinación óptimo es β = 26º y de acuerdo a éste se halla la generación de irradiación como se enseña en la Fig. 5.

Tomando como referencia un panel y un inversor de un fabricante reconocido tenemos:

E_d Producción de electricidad media diaria por el sistema dado (kWh)

E_m Producción de electricidad media mensual por el sistema dado (kWh)

H_d Media diaria de la irradiación global recibida por metro cuadrado por los módulos del sistema dado (kWh/m2)

H_m Suma media de la irradiación global por metro cuadrado recibida por los módulos del sistema dado (kWh/m2)

La Tabla 7 proporciona la producción de electricidad media mensual (483.000kWh), que anualmente se obtendría una energía anual producida de 5,796 GWh.

En la Fig.6 se observa la producción mensual de energía del sistema FV con ángulo fijo durante el año.

La conexión de paneles por inversor, de acuerdo a la estimación de la dimensión de la central solar es:

$$\text{Nº de paneles máx del inv} \approx 4340 \text{ módulos por inv}$$

Elección del número de módulos que debe tener el panel solar a usar:

$$\text{Nº mín de paneles en SERIE} = 14 \text{ módulos}$$

$$\text{Nº máx de paneles en SERIE} = 20 \text{ módulos}$$

El número de paneles debe estar comprendido entre 14 y 20. Se elige 20 paneles por inversor. Se procede a calcular el número de ramas máximo que soporta cada inversor. Se eligen 216 ramas. Se comprueba que las condiciones impuestas por el inversor están garantizadas eligiendo 20 módulos por inversor en serie:

$$V_{mp} = 38{,}39 \text{ V} \rightarrow 20 \text{ módulos} \rightarrow 767{,}8 \text{ V} \rightarrow \text{Cumple}$$

$$I_{mp} = 8{,}99 \text{ A} \rightarrow 216 \text{ ramas} \rightarrow 1950{,}83 \text{ A} \rightarrow \text{Cumple}$$

$$\text{P pk} = 20 \frac{\text{mód}}{\text{serie}} \cdot 345\text{W} \cdot 216 \text{ ramas} = 1490{,}4 \text{ Kw} \quad (14)$$

Con la configuración planteada, se conectará a cada inversor (2) 4.320 módulos distribuidos en 216 ramas compuestas cada una por 20 módulos en serie. Por lo tanto, la instalación tendría una potencia pico instalada de 2980,8 kW con unas pérdidas aproximadas del 17%, se tendría una potencia útil de 2.474 KW, superior a la potencia necesaria que exige la bomba hidráulica (2,25 MW).

El tendido eléctrico existente en los alrededores de la zona tiene una tensión de 66 kV y una intensidad de 575 A. Por tanto, aplicando la ecuación 15 la potencia máxima que se podrá inyectar a la red será:



Figura 6. Producción Mensual
Fuente: Los autores

Table 8.
Análisis de utilidad

	Energía (GWh/año)	Precio €/kW	Beneficios anuales en euros (€)
Energía anual hidroeléctrica	18,171	0,19	3.452.490
Energía anual solar	5,796	0,15	869.400
Energía bombeo	-16,18	0,06	-970.800
			3.351.090

Fuente: Los autores.

$$P_{MÁX} = 66kV \cdot 575A = 37,95\,MW \qquad (15)$$

Esta potencia máxima es mayor que la potencia generada a la salida del transformador, por tanto, el cableado eléctrico aéreo no limita la potencia instalada de la central hidroeléctrica.

5. Análisis financiero

Los datos de partida para analizar la rentabilidad y viabilidad del proyecto son las siguientes:

- Presupuesto de inversión: 39.473.500 €.
- Plazo de ejecución: 4 años.
- Vida útil: 25 años.
- Coste de bombeo: 0,06 €/kWh.
- Precio de venta de energía hidroeléctrica: 0,19 €/kWh.
- Precio de venta de energía solar: 0,15 €/kWh.
- Tasa de descuento: 4%.

Se entiende, por consiguiente, que la central tendrá ingresos cuando entre en funcionamiento, esto es a partir de los primeros 4 años. Los ingresos y los gastos están definidos en la Tabla 8, y su correspondiente balance:

El mercado diario establece el precio de la energía en función de la demanda prevista por cada hora del día siguiente. Según los datos del eurostat, en el 2015 el precio promedio de la energía en España cerro en 0,23 €/KWh, y algunas tecnologías como la hidráulica y de bombeo son las que fijan el precio del mercado, sin embargo, su precio de venta es de 0,19 y 0,06 según la agencia internacional de energías renovables IRENA[6] Por su parte el precio de venta de energía solar se encuentra en el informe de la comisión Europea de Mapas de costo de electricidad fotovoltaica.

Con el fin de profundizar en la viabilidad de un proyecto de esta índole se puede tomar como referencia el proyecto que adelanta actualmente Red Eléctrica de España, en el cual se planea construir una central hidroeléctrica entre las represas de Soria y Chira, la cual a futuro podría ser el primer componente del sistema hibrido que se propone[21].

Volviendo a la instalación Solar-Hidráulica, estudiando el flujo de caja se observa que a partir del decimosexto año (16º), en el año 2033, se ha recuperado la inversión y se obtiene unas primeras ganancias de 739.580 €.

Se ha considerado una vida útil de 25 años, y su flujo neto

Según el VAN (Valor Actual Neto), se empieza a obtener valores positivos a partir del decimoséptimo año (17º), en el año 2034. Y al final de su vida útil (25 años) el valor del VAN es de 12.877.496 €.

El valor de la TIR (Tasa Interna de Retorno) es del 7%.

6. Conclusiones

Teniendo en cuenta la energía anual producida por la central hidroeléctrica (18,17 GWh) y la central de energía solar (5,796 GWh), y la energía anual consumida por el bombeo (16,18 GWh), tenemos un balance energético anual positivo de 7,786 GWh.

Según el anuario 2015 del Gobierno de Canarias, la isla de Gran Canaria inyectó a red en el año 2015 una energía de 3389,02 GWh, por lo que la central proyectada aportaría un 0,23%.

Con respecto a la viabilidad económica, se obtiene un flujo de caja en el que a partir del decimosexto año (16º), en el año 2033, se ha recuperado la inversión y se obtiene unas primeras ganancias de 739.580 €. Además, se ha obtenido una TIR (Tasa Interna de Retorno) del 7%, lo que quiere decir es que, si se financiase la inversión a un coste equivalente a esa tasa, el proyecto ni aportaría riqueza ni supondría costo económico alguno.

En cuanto a la satisfacción de la demanda en la isla de Gran Canaria, el consumo medio en la franja horaria que está centrado este trabajo (entre las 18 y 22 horas) es de 504,37MW, y la central aporta una potencia de 12,62MW, lo que supone un aporte de 2,5% de origen renovable.

La solución de una central hibrida solar-hidráulica y su aplicación en zonas aisladas o de distribución descentralizada, denota una oportunidad aprovechable a la hora de desarrollar soluciones energéticas en zonas isleñas, como lo es el presente caso. Además, su análisis financiero en cuanto a inversión, rentabilidad y sostenibilidad en el tiempo, contribuye a la viabilidad de proyectos de esta magnitud en cualquier lugar del mundo, creando sinergias al momento de crear sistemas híbridos renovables con el fin de abastecer una región.

Referencias

[1] Hussain, A., Arif, S.M. and Aslam, M., Emerging renewable and sustainable energy technologies: State of the art. Renewable Sustainable Energy Reviews, 71, pp. 12-28, 2017. DOI: 10.1016/j.rser.2016.12.033

[2] Avila-Prats, D., Alesanco-García, R. and Veliz-Alonso, J., Sistemas híbridos con base en las energías renovables para el suministro de energía a plantas desaladoras. Ing. Mecánica [En línea]. 14, pp. 22-30, 2011. [fecha de referencia: Agosto 14 de 2018]. Disponible en: http://scielo.sld.cu/scielo.php?script=sci_arttext&pid=S1815-59442011000100003

[3] Huang, Q., Shi, Y., Wang, Y., Lu, L. and Cui, Y., Multi-turbine wind-solar hybrid system. Renew. Energy, 76, pp. 401-407, 2015. DOI: 10.1016/j.renene.2014.11.060

[4] Balta, S., Talat-Birgonul, M. and Dikmen, I., Buffer sizing model incorporating fuzzy risk assessment: case study on concrete gravity dam and hydroelectric power plant projects, J. risk uncertain. Eng. Syst. Part A Civil. Eng., 4(1), 2018. DOI: 10.1061/AJRUA6.0000948

[5] Rios, R., Ortigoza, E., Romero, C. and Morinigo, L., Analysis and optimization of energy resources of the city of Bahía Negra Chaco [Online], Proceedings of the 2017 IEEE URUCON, pp. 1-4, Montevideo, UR, 2017. Available at: https://ieeexplore.ieee.org/document/8171887/

[6] International Renewable Energy Agency. IRENA. [Online]. [date of reference August 14th of 2018]. Available at: http://www.irena.org/publications/2017/May/Renewable-Energy-and-Jobs--Annual-Review-2017.

[7] Red Eléctrica de España. Sistema eléctrico canario [En línea]. 2015. [fecha de referencia: Agosto 14 de 2018]. Disponible en: http://www.ree.es/es/actividades/sistema-electrico-canario.
[8] Gobierno de canarias, Anuario Energetico de Canarias [En línea]. 2016. [fecha de referencia: Agosto 14 de 2018]. Disponible en: http://www.gobiernodecanarias.org/ceic/energia/doc/Publicaciones/AnuarioEnergeticoCanarias/ANUARIO-ENERGETICO-CANARIAS-2016.pdf
[9] de Faria, F., Davis, A., Severnini, E. and Jaramillo, P., The local socio-economic impacts of large hydropower plant development in a developing country. Energy Econ., 2017. DOI: 10.1016/j.eneco.2017.08.025
[10] Dujardin, J., Kahl, A., Kruyt, B., Bartlett, S. and Lehning, M., Interplay between photovoltaic, wind energy and storage hydropower in a fully renewable Switzerland. Energy, 135, pp. 513-525, 2017. DOI: 10.1016/j.energy.2017.06.092
[11] PROYECTOS HIDROPROYECTOS INGENIEROS CONSULTORES [En línea]. [fecha de referencia: Agosto 14 de 2018] Disponible en: http://www.hidroproyectos.com/Proyectos..
[12] Rodríguez-Urrego, D. and Rodríguez-Urrego, L., Photovoltaic energy in Colombia: Current status, inventory, policies and future prospects. Renew. Sustain. Energy Rev. 92, pp. 160-170, 2018. DOI: 10.1016/j.rser.2018.04.065
[13] Saidi, A. and Chellali, B., Simulation and control of Solar Wind hybrid renewable power system, Proceedings of the 6th International Conference on Systems and Control (ICSC), pp. 51-56, Batna, Algeria, 2017.
[14] Coban, H., Moskins, I. and Sauhats, A., The optimization capabilities of combined solar/hydropower plant operation, Proceedings of the IEEE 4th Workshop on Advances in Information, Electronic and Electrical Engineering (AIEEE), pp. 1-6, Vilnius, Lithuania, 2016.
[15] Chaer, R. and Zeballos, R., Simplified model of a hydroelectric generation plant for teaching purposes. IEEE Lat. Am. Trans., 4(3), pp. 198-211, 2006. DOI: 10.1109/TLA.2006.4472114
[16] Kabalci, Y., Kabalci, E., Canbaz, R. and Calpbinici, A., Design and implementation of a solar plant and irrigation system with remote monitoring and remote control infrastructures. Sol. Energy, 139, pp. 506-517, 2016. DOI: 10.1016/j.solener.2016.10.026
[17] Rodriguez-Urrego, L., Valencia, J., Rodriguez-Urrego, D. and Martinez, A., Design, implementation and operation of a solar hybrid system in a remote area in the Colombian Guajira desert. WIT Transactions on Ecology and the Environment, 195, pp. 427-438, 2015. DOI: 10.2495/ESUS150361
[18] Rodriguez-Urrego, L., Garcia, E., Morant, F., Correcher, A. and Quiles, E., Hybrid analysis in the latent nestling method applied to fault diagnosis. IEEE Trans. Autom. Sci. Eng., 10(2), pp. 415-430, 2013. DOI: 10.1109/TASE.2012.2229706
[19] Chen, Q., Chen, T., Guo, J., Zeng, H. and Xiao, Z., Study and design of digital simulation system for pumped storage hydropower units, Proceedings of the 10th World Congress on Intelligent Control and Automation, pp. 3068-3071, 2012. DOI: 10.1109/WCICA.2012.6358398
[20] Relva, S.G., Udaeta, M.E.M., Gimenes, A.L.V. and Grimoni, J.A.B., Solar energy analysis supported on hydropower modelling for taking advantage of photovoltaic power plants, Proceedings of the 5th International Youth Conference on Energy (IYCE), pp. 1-8, 2015. DOI: 10.1109/IYCE.2015.7180814
[21] Red Eléctrica de España. Soria-Chira - Central Hidroeléctrica Reversible [En línea]. [fecha de referencia: Agosto 14 de 2018]. Disponible en: http://www.ree.es/html_chira_soria/index.html.

A.K.Beltrán-Nordahl, es Ing. Técnico Industrial en la especialidad de Mecánica por la Universidad de Las Palmas de Gran Canaria (ULPGC), España, Ingeniero de Organización Industrial por la misma Universidad. MSc. en Prevención de Riesgos Laborales por la Universidad de San Pablo-CEU en Madrid, España y MSc. en Energías Renovables y Sostenibilidad Energética por la Universidad Internacional de Barcelona (UNIBA), España.
ORCID: 0000-0001-6985-9751

H. Gracia-León, es Ingeniero de Producción de la Universidad EAN, Colombia. Becario Colciencias como Joven investigador dentro de la Universidad EAN trabajando en análisis de vibraciones estáticas. Sus intereses principales se encuentran enfocados en sostenibilidad, energías renovables, automatización, monitorización y control a partir del uso de herramientas IoT (Internet of Things). Actualmente es investigador dentro de la Universidad EAN.
ORCID: 0000-0002-7171-8656

D.Rodríguez-Urrego, es Ingeniera Civil de la Universidad Católica de Colombia. Ingeniera de Obras Públicas y MSc. en Transporte, Territorio y Urbanismo de la Universidad Politécnica de Valencia, España. MSc. en Energías Renovables y Sostenibilidad Energética de la Universidad de Barcelona, España. En el campo profesional y como investigadora cuenta con 6 años de experiencia en el área de ingeniería de tráfico, pavimentos energéticos, movilidad sostenible y sostenibilidad energética. Actualmente profesora titular de la Universidad Católica de Colombia
ORCID: 0000-0001-5354-0092

L. Rodriguez-Urrego, es Ingeniero en Mecatrónica de la Universidad San Buenaventura, sede Bogotá, Colombia. Ingeniero en Automática y Electrónica Industria de la Universidad Politécnica de Valencia, España, MSc. en Automática, Robótica e Informática Industrial, MSc. en Tecnología Energética para el Desarrollo y Dr. en Automática, Robótica e Informática Industrial de la misma Universidad española. En su realización profesional e investigadora cuenta con 14 años de experiencia en el área de automatización industrial y energías renovables, control de sistemas de eventos discretos, control de sistemas híbridos, sistemas de diagnóstico y recuperación de fallos y sistemas de supervisión y control. Actualmente es profesor titular de la Universidad EAN, Colombia.
ORCID: 0000-0001-6973-1280

UNIVERSIDAD NACIONAL DE COLOMBIA
SEDE MEDELLÍN
FACULTAD DE MINAS

Área Curricular de Ingeniería Eléctrica e Ingeniería de Control

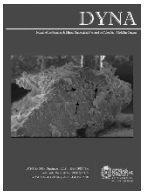
Oferta de Posgrados

Maestría en Ingeniería - Ingeniería Eléctrica

Mayor información:

E-mail: ingelcontro_med@unal.edu.co
Teléfono: (57-4) 425 52 64

UNIVERSIDAD NACIONAL DE COLOMBIA
SEDE MEDELLÍN
FACULTAD DE MINAS



DYNA
http://dyna.medellin.unal.edu.co/

Electrocoagulation of indigo carmine dye solution with magnesium and AZ31 alloy anodes

Dayana Donneys-Victoria [a], Cristian Camilo Ospina-Toro [a], Mónica Vanesa Zapata-Villegas [a], Nilson Marriaga-Cabrales [a], Fiderman Machuca-Martínez [a], Juan M. Peralta-Hérnandez [b] & Carlos A. Martínez-Huitle [c]

[a] *Facultad de Ingeniería, Universidad del Valle, Cali, Colombia. dayana.donneys@correounivalle.edu.co, cristian.ospina.toro@correounivalle.edu.co, monica.zapata@correounivalle.edu.co, nilson.marriaga@correounivalle.edu.co, fiderman.machuca@correounivalle.edu.co*
[b] *Departamento de Química, Universidad de Guanajuato, Guanajuato, México juan.peralta@ugtomx.onmicrosoft.com*
[c] *Instituto de Química, Universidade Federal do Rio Grande do Norte, Natal-RN, Brasil. carlosmh@quimica.ufrn.br*

Received: March 16th, de 2018. Received in revised form: June 12th, 2018. Accepted: July 17th, 2018

Abstract
Indigo carmine is one of the most polluting components found in the textile industry effluents. It was carried out an exploratory study about the performance of the high purity magnesium and the alloy AZ31 used as sacrifice electrodes for removing color and dissolved organic carbon (DOC) in indigo carmine solutions treated by the electrocoagulation process. Tests were developed through a two levels fractionate factorial design. Factors and levels were: stirring speed (zero or 840 rpm), temperature (28 or 50 °C), dye concentration (100 or 300 mg/L) and current density (20 or 50 A/m^2). It was used a concentration NaCl as support electrolyte, and contrary to other studies all the runs were carried out at the same electric charge (5,000 C/L). Removals around 99% colour and 84% in DOC were obtained. Both materials were competitive for colour and DOC removal..

Keywords: carmine indigo; electrocoagulation; colour removal; DOC removal; magnesium electrode; alloy AZ31.

Electrocoagulación de soluciones de índigo carmín empleando ánodos de magnesio y de aleación AZ31

Resumen
El índigo carmín es uno de los componentes más contaminantes encontrados en los efluentes de la industria textil. Se exploró el desempeño del magnesio de alta pureza y la aleación AZ31 como ánodos de sacrificio en la electrocoagulación de soluciones de índigo carmín para la disminución de color y carbono orgánico disuelto (COD). Los experimentos se llevaron a cabo empleando un diseño factorial fraccionado a dos niveles con los siguientes factores: velocidad de agitación (cero y 840 rpm), temperatura (28 y 50 °C), concentración de colorante (100 y 300 mg/L) y densidad de corriente (20 y 50 A/m^2). Como electrolito se utilizó NaCl y la magnitud de la carga eléctrica específica se mantuvo constante en 5,000 coulomb/litro (C/L). Se alcanzaron disminuciones cercanas al 99% en color y 84% en COD. Se evidenció que ambos materiales son competitivos en relación con la remoción de color y de COD alcanzadas.

Palabras clave: índigo carmín; electrocoagulación; remoción de color; remoción de COD; electrodo de magnesio; aleación AZ31.

1. Introducción

En años recientes se ha incrementado la conciencia ciudadana en relación con la polución de las fuentes de agua por causa de efluentes contaminados con sustancias como fertilizantes, pesticidas, tintes sintéticos, fármacos, entre otros. En particular, la industria textil genera entre 200 y 500 litros de agua residual por tonelada de producto terminado [1,2]; estas aguas se caracterizan por presentar altas fluctuaciones en la magnitud de algunos parámetros como la demanda química de oxígeno (DQO), la demanda biológica de oxígeno (DBO), el pH, el color, la salinidad y, adicionalmente, presentan baja biodegrabilidad.

How to cite: Donneys-Victoria, D., Ospina-Toro, C.C., Zapata-Villegas, M.V., Marriaga-Cabrales, N., Machuca-Martínez, F., Peralta-Hérnandez, J.M. and Martínez-Huitle, C.A., Electrocoagulación de soluciones de índigo carmín empleando ánodos de magnesio y de aleación AZ31. DYNA, 85(206), pp. 258-267, September, 2018.

© The author; licensee Universidad Nacional de Colombia.

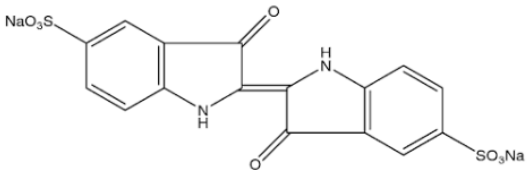


Figura 1 Estructura del tinte índigo carmín.
Fuente: Adaptado de [7].

La producción mundial de tintes es alrededor de 700 mil toneladas por año y se estima que 200 mil ton/año se emplean en la industria textil [3,4]. Debido a su alto peso molecular y a sus complejas estructuras químicas los tintes presentan alta resistencia a la degradación [3,5]. Uno de los componentes más contaminantes encontrados en los efluentes textiles es el índigo carmín, un tinte azul oscuro de la clase indigoides ácidos, usado principalmente en la industria del teñido de fibras de poliéster y denim [4,6]. Esta sustancia es clasificada como material peligroso debido a que confiere alta coloración a las aguas lo que perturba la vida acuática; además de ser resistente a la acción de agentes químicos, a la luz y al calor, también se considera una sustancia cancerígena y puede causar irritaciones en la piel, en los ojos y dañar la córnea. La estructura química del índigo carmín se esquematiza en la Fig. 1[7].

Para el tratamiento de aguas residuales de la industria textil se han ensayado diversas alternativas. Han sido empleados agentes como H_2O_2, O_3 y técnicas avanzadas de oxidación; no obstante, aunque estos métodos presentan buenos desempeños, la principal limitación son los altos costos involucrados en su implementación y su operación [1,8]. Asimismo, entre los métodos fisicoquímicos, la coagulación y floculación química ha demostrado ser ineficaz en el tratamiento de algunos tintes como los reactivos y el tipo tina, debido a sus pobres resultados en la disminución de color y a la alta generación de lodos [1]. Mientras la adsorción, especialmente con carbón activado tiene un alto costo operativo asociado a la regeneración del carbón, aunque presenta buenos resultados respecto a la disminución del contenido de una gran variedad de tinte [1,2]. Ramesh & Sreenivasa investigaron la adsorción del colorante índigo carmín en hidróxido de magnesio para pH 6-7 y 12-13 y encontraron que el proceso es endotérmico, espontáneo, sigue una cinética de velocidad de pseudo segundo orden y se favorece a pH 6-7 a temperatura ambiente [9].

En cuanto a los métodos biológicos, se han empleado microorganismos en procesos aerobios, anaerobios y en procesos combinados; aunque estos sistemas son amigables con el medio ambiente, tienen baja producción de lodos, aseguran la mineralización completa y consumen poca agua, requieren una correcta selección de los microorganismos y las enzimas a emplear para lograr buenas eficiencias, además de que suelen requerir prolongados tiempos de operación [1].

Por otra parte, la electrocoagulación (EC) es un método simple en el que, a diferencia de la coagulación química, los cationes metálicos se generan *in situ* por medio de reacciones electroquímicas. El proceso de EC involucra tres etapas: a) formación de cationes metálicos mediante la electrodisolución de ánodos de sacrificio; b) hidrólisis de los cationes y formación de coágulos y c) la agregación y desestabilización de los coloides a través de la formación de flóculos. En la EC los cationes generados en el ánodo de sacrificio se hidrolizan formando aglomerados amorfos insolubles del metal correspondiente, los cuales proveen superficies activas para la adsorción de coloides presentes en el agua. Por su parte, en el cátodo se descompone electroquímicamente el agua produciendo pequeñas burbujas de hidrógeno, estas burbujas pueden adicionalmente atrapar flóculos y llevarlos a la superficie por efecto de la flotación [2,10].

La reacción catódica correspondiente a un medio ácido y a un medio alcalino es como sigue, eq. (1)-(2), respectivamente:

$$2H^+ + 2e^- \rightarrow H_{2(g)} \quad (1)$$

$$2H_2O + 2e^- \rightarrow 2OH^- + H_{2(g)} \quad (2)$$

Existen antecedentes del uso de ánodos de aluminio y de hierro para el tratamiento de soluciones de índigo carmín mediante electrocoagulación [11,12] sin embargo, el aluminio tiene por desventaja generar costos de operación hasta tres veces superiores a los del hierro por kg de DQO removido [13]; mientras que en el caso del hierro, las concentraciones de colorante estudiadas son hasta 18 veces inferiores a las que se reportan en efluentes reales [14]. En este contexto, el uso de electrodos de magnesio en la electrocoagulación de índigo carmín en novedosa.

En el caso ánodos de magnesio se presentan las siguientes reacciones eq.(3)-(5):

$$Mg \rightarrow Mg^{2+} + 2e^- \quad (3)$$

$$Mg_{ac}^{2+} + 2OH^- \rightarrow Mg(OH)_2 \downarrow \quad (4)$$

$$Mg_{ac}^{2+} + H_2O \rightarrow MgO \downarrow + 2H^+ \quad (5)$$

Para ánodos de la aleación AZ31 las reacciones son las siguientes eq. (6)-(10):

$$Mg \rightarrow Mg^{2+} + 2e^- \quad (6)$$

$$Mg_{ac}^{2+} + 2OH^- \rightarrow Mg(OH)_2 \downarrow \quad (7)$$

$$Mg_{ac}^{2+} + H_2O \rightarrow MgO \downarrow + 2H^+ \quad (8)$$

$$Al \rightarrow Al^{3+} + 3e^- \quad (9)$$

$$Al_{ac}^{3+} + 3H_2O \rightarrow Al(OH)_3 \downarrow + 3H^+ \quad (10)$$

Además de las reacciones anteriores, los ánodos de magnesio pueden producir hidrógeno durante su polarización. Esto se denomina efecto diferencial negativo y es particular del magnesio [15].

$$2Mg^+ + 2H_2O \rightarrow 2Mg^{2+} + 2OH^- + H_2 \quad (11)$$

El propósito de la presente investigación fue estudiar el desempeño de la electrocoagulación de soluciones sintéticas de índigo carmín empleando ánodos de magnesio de alta

pureza y de aleación AZ31 sobre la disminución de color y COD, teniendo como variables la densidad de corriente, la concentración de tinte, la temperatura y la velocidad de agitación, para una carga eléctrica especifica de 5,000 C/L.

2. Materiales y métodos

Los ánodos se construyeron utilizando láminas de magnesio de alta pureza (99.5% p/p) y de aleación AZ31 (composición en peso: 95.56 % magnesio; 3.0 % aluminio; 1.0 % de zinc; 0.043 % manganeso; 0.01 % de silicio; cobre < 0.01%; níquel <0.001% y 0.003 % de hierro); mientras que para el cátodo se empleó una lámina de acero inoxidable AISI 304. Las dimensiones de todos los electrodos fueron de 9 cm × 8 cm.

Se empleó índigo carmín marca Sigma Aldrich con 85 % de contenido de tinte; asimismo, se empleó cloruro de sodio grado reactivo marca Sigma Aldrich como electrolito. Las soluciones de índigo carmín se prepararon empleando agua purificada obtenida por destilación de agua potable, previamente filtrada (0.45 µm) y empleando adsorción con carbón activado, en un equipo marca Water Pro PS Labconco. Las propiedades del agua purificada fueron: 1 mg/L de carbono orgánico disuelto (COD), conductividad eléctrica (k) de 17.95 µs/cm y pH de 7.83. Para la medición del pH y la conductividad eléctrica estandarizada a 25 °C (mS/cm) se utilizó un sensor multiparamétrico marca Thermo Scientific (Orion Star A329).

Para la determinación del COD (mg/L) se filtraron previamente las muestras utilizando un filtro de 0.45 µm y luego fueron analizadas en un equipo de medición de TOC con el equipo Shimadzu TOC-VCPH. Se realizó una curva de calibración entre 0 y 60 mg/L de COD.

Por espectrofotometría se llevó a cabo la determinación de la concentración de índigo carmín. Se realizó un barrido para hallar la longitud de onda a la cual se tiene la máxima absorbancia (612 nm) y posteriormente se construyó la curva de calibración en un equipo marca Jasco (UV Visible Spectrophotometer V-730).

Para la determinación del magnesio total, primero se ajustó el pH de las muestras a un valor menor a dos con ácido nítrico (HNO_4) al 35%. Las muestras se sometieron a digestión suave con adición de ácido clorhídrico. Posteriormente se añadió cloruro de lantano heptahidratado con el fin de eliminar interferencias por ionización del analito. Finalmente se analizaron las muestras mediante absorción atómica con llama de aire-acetileno a una longitud de onda de 253 nm. Se usó un espectrofotómetro de absorción atómica marca Thermo Scientific (ICE 3000 Spectrometer).

2.1. Pretratamiento de electrodos

Previo a cada ensayo se lijaron manualmente las dos caras del ánodo con papel lija grano 100; 200; 400; 600 y 1,200; posteriormente ambos electrodos, ánodo y cátodo, se sumergieron durante 5 minutos en ácido clorhídrico al 10% (v/v), se lavaron varias veces con agua destilada y se secaron a condiciones ambiente.

2.2. Montaje experimental

La celda de EC consistió de un vaso de borosilicato de 1000 mL talla alta en el que se ubicaron verticalmente un ánodo y un cátodo separados 0.8 cm, los electrodos se suspendieron por medio de un soporte de polietileno y se conectaron a una fuente de poder de corriente directa marca BK Precisión DC Regulated Power Supply modelo 1665 con un amperaje máximo de 5 A. Para las pruebas con agitación se utilizó un agitador magnético de 3 cm de longitud y 0.5 cm diámetro. Para el calentamiento y la agitación se utilizó una plancha marca Thermo Scientific modelo SP131635Q. El montaje experimental se muestra en la Fig.2.

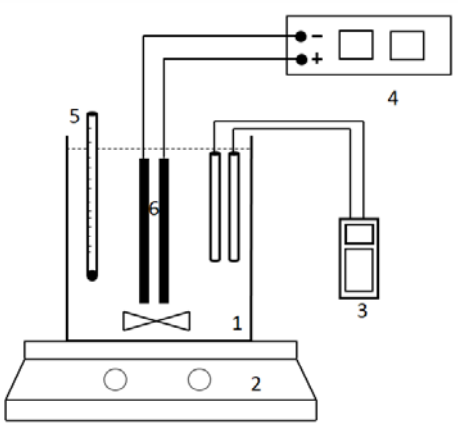


Figura 2. Esquema del montaje experimental; 1) celda EC; 2) plancha de agitación y calentamiento; 3) multímetro de alta impedancia; 4) fuente de poder; 5) termómetro; 6) electrodos.
Fuente: Los autores.

2.3. Pruebas experimentales

Ensayos de EC fueron realizados variando la densidad de corriente (A/m^2), la temperatura (°C), la velocidad de agitación (rpm), la concentración de colorante (mg/L) y se suministró la misma carga eléctrica específica a cada ensayo (5000 culombios por litro equivalente a 0.944 A-h/L). Para cada ensayo se empleó un litro de solución de IC y se adicionó NaCl como electrolito soporte para mejorar la conductividad eléctrica (1,800 mg/L) sin ajustar ni controlar el pH, con base a los resultados obtenidos en pruebas preliminares (datos no mostrados). La celda electrolítica se cubrió con papel aluminio para evitar posibles efectos de fotólisis del IC. Se tomaron seis muestras para cada ensayo de 62; 67; 12; 67; 12 y 67 (ml) correspondientes a los puntos de carga de 250; 900; 1800; 2700; 4050 y 5000 culombios por litro (C/L) respectivamente, equivalentes a 0.063; 0.21; 0.386; 0.569; 0.779 y 0.944 amperio-hora por litro (A-h/L).

Las placas fueron suspendidas, de tal manera que pudieran descender a medida que la altura de la solución disminuía con el objetivo de evitar la pérdida de área sumergida de los electrodos. Además, se realizó una corrección de la carga eléctrica a suministrar para cada punto de muestreo debido al volumen extraído en cada muestra. Las muestras fueron analizadas en términos de COD, absorbancia (color), magnesio total (soluble y precipitado) y consumo eléctrico (kW-h/kg de COD removido); además, durante cada experimento se monitoreo el pH, la conductividad eléctrica, y el contenido de oxígeno disuelto.

Para evaluar el efecto de los cuatro factores y sus interacciones: velocidad de agitación (rpm), temperatura (°C),

Tabla 1.
Diseño Factorial.

Prueba	Temperatura (°C)	Agitación (rpm)	Densidad de corriente (A/m^2)	Concentración de IC (mg/L)
1	25	0	20	100
2	50	0	20	300
3	25	840	20	300
4	50	840	20	100
5	25	0	50	300
6	50	0	50	100
7	25	840	50	100
8	50	840	50	300

Fuente: Los autores

concentración de colorante (mg/L) y densidad de corriente (A/m^2) sobre el desempeño del material del ánodo, se empleó un diseño factorial fraccionado 2^{4-1} [16]. Los factores, sus respectivas interacciones y la significancia de los mismos, se evaluó a través de la metodología de Daniel, donde se evalúan los efectos tanto de los factores como de sus interacciones en un gráfico de probabilidad normal [16]. Los niveles evaluados se presentan en la Tabla 1.

Se utilizaron concentraciones de colorante entre 100 y 300 mg/L y concentraciones de NaCl de 1,800 mg/L considerando abarcar las concentraciones bajas que suelen emplearse en estudios de fotocatálisis o estudios de electrocoagulación con hierro [11,17] y las concentraciones que se reportan para efluentes reales [18].

Por otra parte, las densidades de corriente fueron seleccionadas a través de una polarización potenciostática realizada para AZ31 en una solución de 1022 mg/L de NaCl, donde se evidenció que para densidades de corriente mayores a 50 A/m^2, el voltaje del electrodo de trabajo se incrementa en 0.6V vs Ag/AgCl (datos nos mostrados).

2.4. Calculo de parámetros del proceso

La magnitud de la disminución de color se calculó mediante la eq. (12).

$$Y = \frac{C_0 - C}{C_0} x100 \quad (12)$$

Donde C_0 es la concentración inicial de índigo carmín (mg/L^{-1}) y C es la concentración de índigo después de cierto tiempo de operación.

La magnitud de la disminución del contenido de carbono orgánico se calculó con la eq. (13).

$$Z = \frac{COD_0 - COD}{COD_0} x100 \quad (13)$$

Donde COD_0 (mg/L) es el carbono orgánico disuelto inicial y COD (mg/L) es el carbono orgánico disuelto en el tiempo t de operación.

El consumo específico de energía eléctrica se calculó como sigue, eq. (14).

$$E = \frac{U.I.t}{g\ COD\ removido * 1000} \quad (14)$$

Donde E es el consumo de energía eléctrica (kW-h/g de COD removido); U es el voltaje (V); I es la corriente (A); t el tiempo de operación (h).

La cantidad teórica de coagulante (magnesio), se calculó a partir de la ley de Faraday, eq. (15).

$$w = \frac{I.t.M}{F.n} \quad (15)$$

Donde w es la cantidad de coagulante (*g*); *I* es la corriente (*A*); t tiempo (*s*); M es el peso molecular (*g/mol*); F es la constante de Faraday equivalente a *96500* (*C/mol*); y *n* es el número de electrones involucrados en la reacción, que para el caso específico es de *2*.

Por otro lado, según Secula et al [19] para el cálculo del costo del uso de la electrocoagulación como tecnología para para la disminución de índigo carmín se tienen las eq. (16)-(18):

$$EOC = UED.EEP + UEM.EMP \quad (16)$$

$$UED = \frac{I.U.t}{100.V.C_i\frac{Y_t}{100}} \quad (17)$$

$$UEMD = \frac{I.t.M}{n.F.VC0_i.\frac{Y_t}{100}} \quad (18)$$

Donde U es el voltaje de celda (V); I densidad de corriente (A); t tiempo (s); n número de electrones involucrados en la reacción; F constante de Faraday (C/mol); M peso molecular (g/mol); UED unidad de demanda de energía (kWh/kg de COD removido); V volumen de solución tratada (m3); Yt disminución de COD (%); UEM unidad de demanda del material del electrodo (kg/kg COD removido); EOC costo operacional (USD$/kg COD removido); EEP precio de la energía eléctrica (USD$/kW-h), considerado como 0.315 USD$/kW-h; EMP costo del material del electrodo (USD$/kg) estimado de proveedores internacionales como 2.42 USD$/kg para el magnesio de alta pureza y 25 USD$/kg para el AZ31.

2.5. Cinética aparente de electrodisolución.

La cinética de electrodisolución de magnesio para todas las condiciones de proceso, se determinó ajustando los datos de concentración de magnesio vs tiempo a la ecuación (19), según lo reportado por Panaiotova [20]:

$$Ln\ (Mg) = kt + Ln(Mg_0) \quad (19)$$

Donde k (h^{-1}) es una constante aparente de reacción de primer orden.

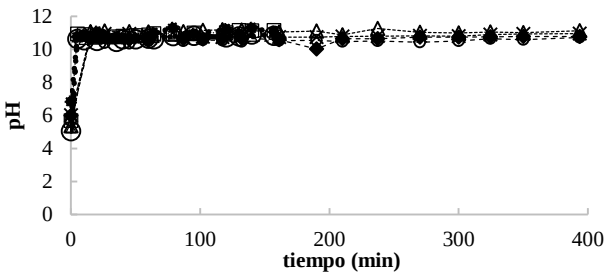


Figura 3. Evolución del pH para todas las condiciones experimentales, aleación AZ31. Las condiciones para todas las pruebas (1-2-3-4-5-6-7 y 8) se reportan en la tabla 1.
Fuente*:* Los autores.

3. Resultados y análisis

3.1. Evolución del pH

En la Fig.3, se presenta la evolución del pH en el tiempo para las pruebas realizadas con el ánodo de AZ31, en ella se observa el aumento casi instantáneo del pH hasta un valor de 11 durante los primeros minutos de operación, valor alrededor del cual, el pH se estabilizó. Para el caso del magnesio de alta pureza el comportamiento fue similar (datos no mostrados). De esta figura es posible afirmar que independiente de las condiciones de los ensayos, del tipo de material y del tiempo del proceso, el pH aumentó rápidamente y permaneció constante hasta el final de la prueba. Este comportamiento puede asociarse a que la tasa de acumulación de los OH^- entregados al medio fue mayor que el consumo de los mismos para la formación del hidróxido de magnesio $Mg(OH)_2$. Esto, se debe a que los iones hidroxilo (OH^-) se entregan al medio a través de dos reacciones, una reacción química en el ánodo eq. (11) y la reacción convencional electroquímica en el cátodo eq. (2); la primera reacción ocurre como consecuencia del efecto diferencial negativo en el que se asume que los ánodos de magnesio entregan magnesio univalente Mg^+ además de Mg^{2+}, por lo tanto los hidroxilos entregados al medio son la suma de la reacción anódica y catódica [15]. Si bien no se encontraron reportes para ánodos de magnesio, Secula et al [11] estudiaron ánodos de acero dulce para el tratamiento de soluciones acuosas de IC y encontraron que el pH se incrementó paulatinamente hasta estabilizarse en el mismo valor de 11 para varios pHs iniciales. Chantaraporn, Suprangpag & Warangkana (2010), reportaron el aumento del pH en aproximadamente 10 minutos en efluentes textiles tratados por el método de EC con electrodos de hierro y aluminio [21].

3.2. Pruebas finales

3.2.1. Variables de respuesta del proceso.

La Fig. 4 presenta la disminución de COD para la aleación AZ31 usando concentraciones de IC de 100 y 300 mg/L. la disminución del COD alcanzó un valor entre 70 y 85% para todas las condiciones de proceso después de 150 minutos de tratamiento. De la Fig. 4b, aunque la carga orgánica fue mayor, la disminución de COD fue cercana a 82% para las pruebas realizadas a la mayor densidad de corriente. Estos resultados evidencian que no es necesario tener tiempos de electrolisis tan extensos como los empleados en las pruebas 1, 2, 3 y 4, debido a que a 150 min ya se habían alcanzado disminuciones satisfactorias.

Con ánodo de magnesio se alcanzaron disminuciones de COD entre 62 y 83 % para 100 mg/L de IC y, entre 30 y 75%, para 300 mg/L de IC Fig. 5a y 5b. Para las dos concentraciones de IC las disminuciones de COD fueron más favorables para las pruebas que emplearon menores tiempos de operación, es decir a densidad de corriente de 50 A/m^2. Este mismo comportamiento se observó al utilizar ánodos de AZ31 y puede atribuirse a que a menores tiempos de operación, es decir, a mayor densidad de corriente, la tasa de generación de burbujas se incrementó y el tamaño de las mismas disminuyó mejorando así la remoción del contaminante [11].

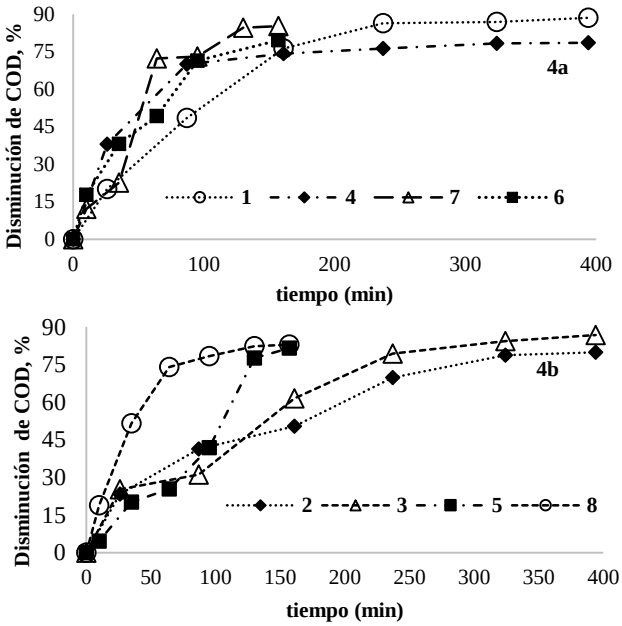


Figura 4. Disminución de COD para cada prueba usando la aleación AZ31; **a)** [IC]=100 mg/L. **b)** [IC]= 300 mg/L.
Fuente: Los autores.

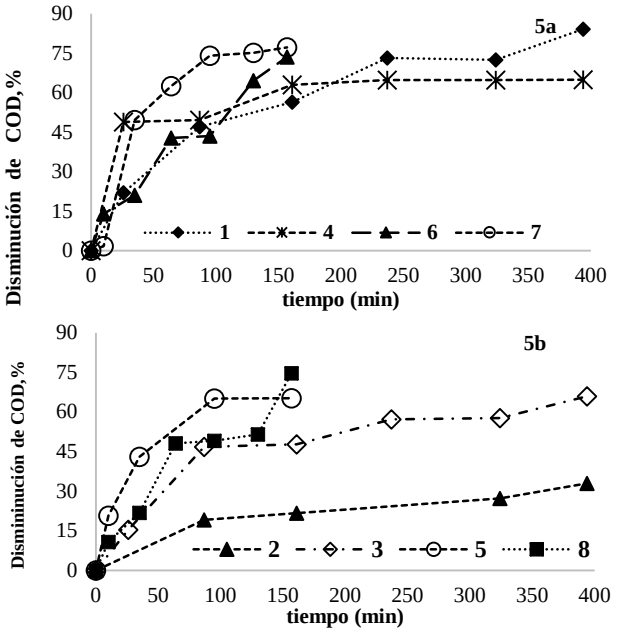


Figura 5. Disminución de COD para cada prueba usando magnesio de alta pureza; **a)** [IC]=100 mg/L. **b)** [IC]=300 mg/L.
Fuente: Los autores.

Utilizando el ánodo de AZ31 y 100 mg/L de IC se alcanzaron disminuciones de color hasta del 100% después de 100 min de tratamiento para una densidad de corriente de 50 A/m^2; el mismo resultado se obtuvo después de 240 minutos de operación para las pruebas a densidad de corriente de 20 A/m^2 Fig.6a. Por otra parte, al incrementar la concentración de IC a 300 mg/L Fig.6b, fueron necesarios tiempos de operación entre 100 y 150 minutos para obtener disminuciones entre 90 y 98% en color para las pruebas a densidad de corriente de 50 A/m^2; en contraste, fueron

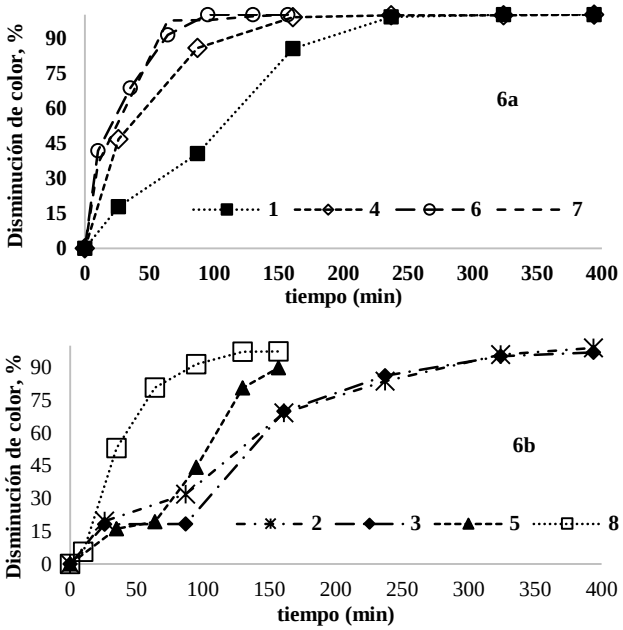


Figura 6. Disminución de color para cada prueba usando la aleación AZ31; **a)** [IC]= 100 mg/L. **b)** pruebas a concentración de índigo carmín de 300 mg/L.
Fuente: Los autores.

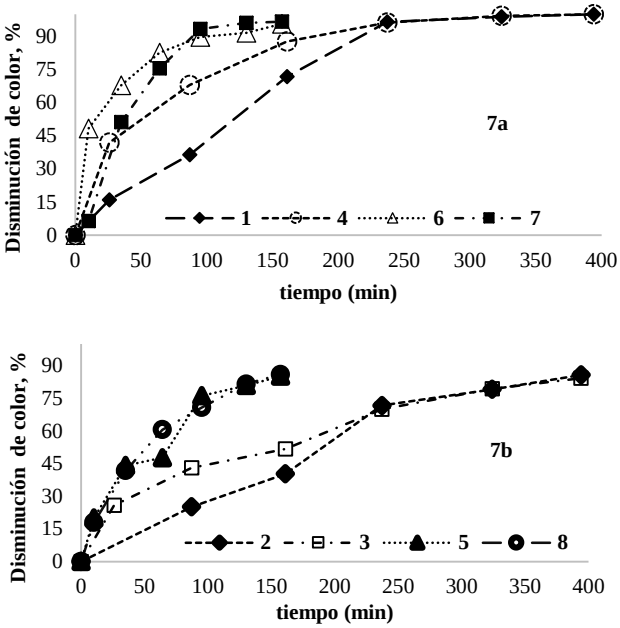


Figura 7. Disminución de color para cada prueba usando magnesio de alta pureza; **a)** [IC]= 100 mg/L. **b)** [IC]= 300 mg/L.
Fuente: Los autores.

necesarios tiempos de operación de 300 minutos para alcanzar disminuciones de 90% en color para las pruebas realizadas a densidad de corriente de 20 A/m^2.

Para las pruebas con ánodo de magnesio y 100 mg/L de IC Fig.7a, la disminución de color fue del 100% después de 100 minutos de operación y una densidad de corriente de 50 A/m^2 mientras que, con la menor densidad de corriente 20 A/m^2, se requirieron 240 minutos de operación para alcanzar el mismo resultado. Para las pruebas a 300 mg/L de IC Fig.7b, se lograron disminuciones de 90% en el color independientemente de la carga; este mismo comportamiento fue observado para el electrodo de AZ31. Para ambos materiales y para la concentración de 100 mg/L de IC, se lograron disminuciones de 100% en color en tiempos más cortos, es decir, a mayor densidad de corriente, en contraste con las pruebas a la concentración de 300 mg/L de IC que requirió tiempos de operación de aproximadamente 400 minutos para lograr la misma disminución en el color. En comparación con los resultados obtenidos con la aleación AZ31, las disminuciones de color y COD obtenidas al utilizar magnesio de alta pureza fueron menores. Estos resultados pueden atribuirse a la disolución paralela de aluminio cuando se utilizó como ánodo la aleación AZ31. A pH básico los cationes Al^{3+} pueden formar diferentes complejos poli-nucleares insolubles de hidróxido de aluminio [21].

Además, para el caso de 300 mg/L de IC para ambos materiales la reducción de COD y de color disminuyó respecto a los valores obtenidos para 100 mg/L, probablemente como consecuencia de la disminución de la capacidad de adsorción del colorante sobre la superficie del hidróxido de magnesio. N. Daneshvar et al, estudiaron el tratamiento de tintes ácidos por medio de EC con ánodo de hierro y encontraron que para una concentración de colorante mayor a 80 mg/L, la disminución de color fue relativamente constante, atribuyendo dicho comportamiento al agotamiento de la capacidad de adsorción de los flóculos [22].

Se ha evidenciado que existe una velocidad de agitación apropiada por encima de la cual el desempeño de la electrocoagulación disminuye debido a que ocurre el rompimiento de los coágulos [23]. Khaled, Wided, Béchir et al (2015), estudiaron el efecto de la agitación en el desempeño de la electrocoagulación para remover cadmio empleando electrodos de aluminio y encontraron que la velocidad de agitación adecuada fue de 450 rpm; por encima de esta velocidad el desempeño del proceso disminuyó drásticamente [24]. Aunque en el presente estudio se utilizaron valores de agitación de 0 y 840 rpm, no fue posible demostrar estadísticamente el efecto negativo de la agitación sobre la electrocoagulación que refieren otros autores.

Por otra parte, se obtuvieron disminuciones comparables de COD para ambos materiales tanto a temperatura ambiente como a 50 °C. Son pocos los estudios que evalúan el efecto de la temperatura en la EC; a este respecto, algunos estudios sostienen que la temperatura tiene un efecto positivo al favorecer los fenómenos de transferencia de masa en la capa límite de difusión del electrodo [3]. Sin embargo, VamshiKrishna, Omprakash, & Venkata, afirman que la temperatura puede tener o no un efecto positivo; esto, debido a que a bajas temperaturas puede reducirse la velocidad de disolución anódica, mientras a mayores temperaturas, la formación de flóculos densos que se depositan sobre la superficie de los electrodos puede afectar la disolución [22,25]

En general, usando ánodos de magnesio se alcanzaron disminuciones de 100% en color y hasta 83% en COD; para la aleación AZ31 se obtuvieron disminuciones de 100% en color y hasta 88% en COD, aplicando en ambos casos, los niveles inferiores de los factores estudiados. Esto sugiere que la magnitud de la carga eléctrica empleada en el presente estudio (5,000 C/L) fue superior a la requerida para alcanzar un buen desempeño; además, sugiere que futuros experimentos deberían llevarse a cabo a temperatura ambiente y sin agitación.

Según lo obtenido del diseño experimental, independientemente del material empleado en el ánodo (AZ31 ó Mg) se evidenció que los rangos empleados en las variables independientes no alteraron significativamente el desempeño del proceso ya que los efectos siguieron una distribución aproximadamente normal localizándose en una línea recta sobre el gráfico de probabilidad normal (datos no mostrados).

El consumo eléctrico específico por kilogramo de COD removido para los dos materiales se presenta en la Fig.8 solamente para las pruebas con el máximo y el mínimo consumo eléctrico, los demás ensayos tuvieron un comportamiento intermedio. Esta variable de respuesta tuvo un comportamiento similar para los dos materiales y aunque con el AZ31 se obtuvo una disminución más alta en color y COD, el consumo eléctrico específico para la mayor densidad de corriente, fue el doble que para el magnesio, alcanzando valores cercanos 10 kW-h/kg COD removido Fig.8a y Fig 8b; los consumos acumulados alcanzaron valores cercanos a 12 y 6 kW-h/kg COD removido para AZ31 y magnesio respectivamente (datos no mostrados) probablemente debido a la acción del ion cloruro ya que la aleación tiende a pasivarse más en comparación con el electrodo de magnesio de alta pureza [26]. El aluminio que entrega la aleación AZ31 al medio reacciona espontáneamente con el agua o con oxígeno eq.(10), (20) y (21) para formar una capa de óxido; esta capa afectaría el desempeño de la electrocoagulación aumentando el consumo eléctrico [27]; además, a partir de estudios de disolución realizados por Harish & Adka (2017), para la aleación AZ31 y el magnesio de alta pureza en una solución de etilenglicol a diferentes temperaturas y concentraciones de NaCl, se demostró que el electrodo de magnesio de alta pureza y la aleación AZ31 son muy sensibles a crear capas corrosivas en solución con iones cloruro, siendo mayor la corrosión para la aleación AZ31 con lo cual se favorece la formación parcial del complejo $Mg(OH)_2$ que actúa como una capa pasivante sobre el electrodo [28].

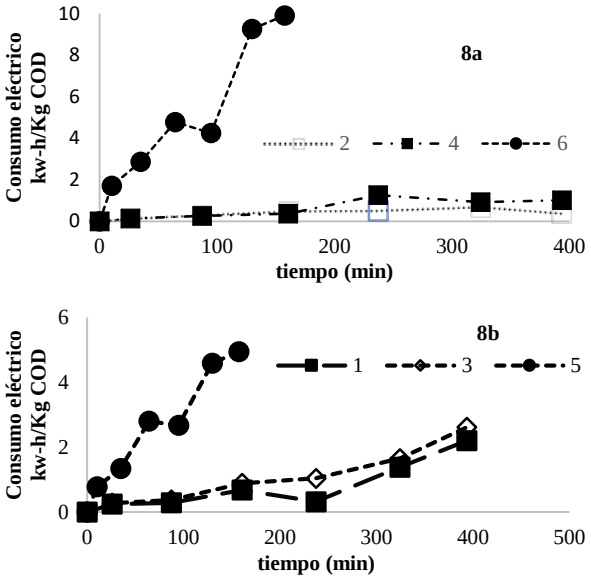


Figura 8. Consumo eléctrico específico para cada prueba. a) consumo eléctrico para la aleación AZ31. b) consumo eléctrico, magnesio de alta pureza.
Fuente: Los autores.

Chantaraporn, Suprangpak & Warangkana (2010), emplearon ánodos de hierro y aluminio para el tratamiento de un efluente textil y encontraron que el consumo eléctrico fue mayor para el electrodo de aluminio debido a que por algunas características de los flóculos formados por la difícil sedimentación de los mismos, estos obstruían el transporte de los iones en el medio, aumentando la resistencia del medio y por ende el consumo eléctrico; lo anterior puede también explicar el comportamiento de la aleación AZ31 debido a que uno de los componentes en mayor proporción es el aluminio [21,28].

$$2Al + \frac{3}{2}H_2O \rightarrow Al_2O_3 + 3H_2 \quad (20)$$

$$2Al + \frac{3}{2}O_2 \rightarrow Al_2O_3 \quad (21)$$

La concentración de magnesio en la solución final después del tratamiento, se presenta en la Fig. 9. El material que presentó mayor disolución de magnesio en algunos casos fue el AZ31 Fig.9a, obteniéndose concentraciones entre 500 hasta 1,900 mg/L, en comparación con el magnesio Fig.9b, con el que se alcanzaron concentraciones de magnesio disuelto desde 500 hasta 850 mg/L. Este resultado coincide con las disminuciones de COD y de color obtenidos para cada material, ya que, al entregarse más magnesio al medio en forma de Mg^{2+} se favoreció la formación del complejo de hidróxido de magnesio mediante la eq. (3), el cual es un material con gran capacidad de adsorción sobre su superficie [23]. Para ambos materiales la eficiencia de corriente eléctrica Tabla 2, en todos los casos, fue mayor a 100%, esto puede ser explicado porque la ley de Faraday solo asume que el magnesio se entrega al medio por disolución electroquímica sin considerar la pérdida de masa del ánodo que ocurren por otros mecanismos como por ejemplo la corrosión química ocasionada por agentes oxidantes como el ion cloruro. Zongo, Amadou, Josep et al (2009), reportaron un valor de 200% para la eficiencia de corriente usando ánodo de aluminio, resultado explicado por disoluciones laterales que no son consideradas por la ley de Faraday [29]. Así mismo, Kobya & Demirbas (2015), reportaron en su estudio de EC con electrodo de aluminio que a mayor densidad de corriente, la ley de Faraday se desvió fuertemente de los resultados experimentales obtenidos, fenómeno atribuido a la corrosión superficial del metal [30,31].

Los resultados de la constante de velocidad aparente k ajustada para una cinética de electrodisolución de primer orden se presentan en la Fig. 10, se observa que las pruebas realizadas a menor densidad de corriente (1, 2, 3,4) presentan un menor valor de la constante de velocidad aparente k, comparado con las pruebas a la mayor densidad de corriente (5, 6, 7, 8), esto es consistente con el incremento de iones metálicos generados al aumentar la corriente aplicada. Balasubramanian, Kojima & Srinivasakannan (2009), reportaron que para la remoción de arsénico por EC con ánodos de aluminio y acero dulce, a densidades de corriente entre 50 y 150 A/m^2 la constante de velocidad para aluminio fue dependiente y proporcional a la densidad de corriente [32].

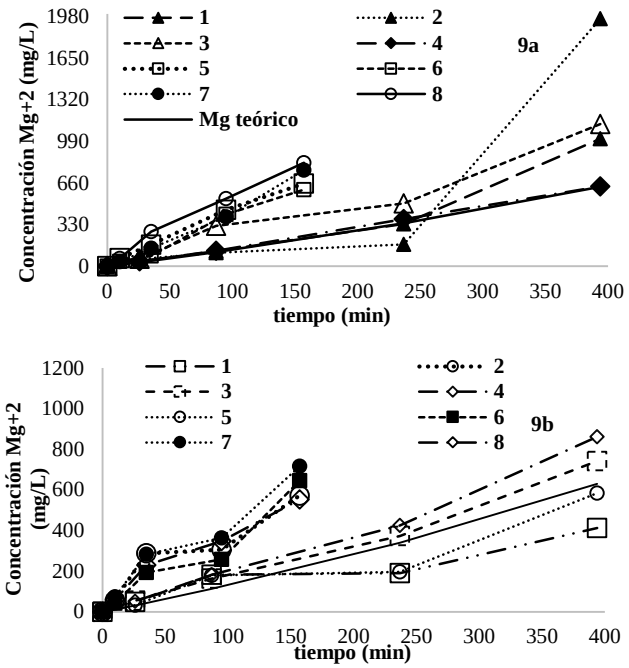


Figura 9. Concentración de magnesio total teórico y experimental para cada prueba. **a)** concentración de magnesio para la aleación AZ31. **b)** concentración de magnesio total para el electrodo de magnesio de alta pureza.
Fuente: Los autores.

Tabla 2.
Eficiencia de corriente eléctrica.

	Prueba							
material	**1**	**2**	**3**	**4**	**5**	**6**	**7**	**8**
AZ31	124	386	208	222	276	199	359	229
Mg	109	344	147	395	161	401	246	327

Fuente**:** Los autores.

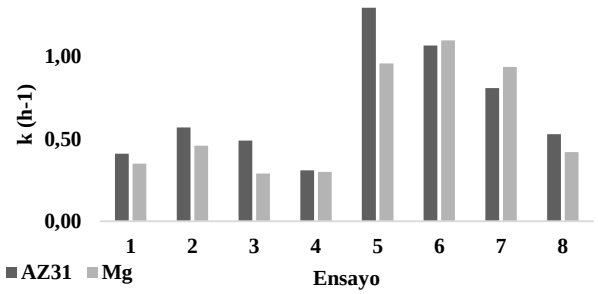


Figura 10. Cinética de electrodisolución, valores de k aparente.
Fuente**:** Los autores.

3.3. Costo operacional

Para determinar el costo operacional de la EC con electrodos de magnesio de alta pureza y la aleación AZ31, se utilizó la eq. (16) tomada de Secula et al [19]. El costo promedio operacional para el AZ31, fue de 3,8 USD$/kg de COD removido y para el magnesio de alta pureza fue de 2 USD$/kg de COD removido. Según lo reportado en el artículo citado anteriormente, el costo aproximado de la misma tecnología con electrodos de acero dulce y agregando carbón activado granular para mejorar la eficiencia del proceso fue de 7.25 USD$/ kg de contaminante removido, lo que sugiere que el uso de electrodos de magnesio de alta pureza y de aleación AZ31 sería económicamente viable.

4. Conclusiones

El desempeño de ánodos de magnesio y de aleación AZ31 en la electrocoagulación de soluciones sintéticas de índigo carmín arrojó resultados favorables en relación con la remoción de color y de COD. Empleando ánodos de aleación AZ31 se alcanzaron disminuciones cercanas al 100% en color y 88% en COD; mientras que con ánodos de magnesio se lograron disminuciones de 99 % en color y 84 % en COD. Además, se alcanzó un bajo consumo eléctrico acumulado, cercano a 12 kW-h/kg COD removido para el caso de la aleación AZ31 y 6 kW-h/g COD removido para el magnesio de alta pureza. Asimismo, pudo inferirse que no son necesarios tiempos de operación mayores a 250 minutos operando a las densidades de corrientes empleadas.

Por otra parte, para ambos materiales los valores finales de COD y de color disminuyeron con el incremento de la concentración de índigo carmín posiblemente como consecuencia de la reducción en la capacidad de adsorción del colorante sobre la superficie del hidróxido de magnesio. En general, se alcanzaron mayores disminuciones de COD para las pruebas realizadas a 50 A/m2.

Los resultados evidenciaron la viabilidad técnica del empleo del magnesio y sus aleaciones como ánodo de sacrificio en la electrocoagulación de soluciones de índigo carmín, además, este material a diferencia del aluminio se distribuye de forma natural en el medio ambiente y no representa peligro para los seres vivos.

Agradecimientos

Los autores desean agradecer a la Universidad del Valle por financiar la investigación “Electrocoagulación de efluentes provenientes de la industria textil empleando magnesio. Caso de estudio: Soluciones modelo de índigo carmín.” CI 2863 y el Departamento Administrativo de Ciencia, Tecnología e Innovación-Colciencias (Colombia) por la Beca de Doctorado Nacional de uno de los autores. Adicionalmente, se reconoce el aporte de los estudiantes de Estadística de la Universidad del Valle: Carlos Taimal y Laura Orozco por su contribución en el análisis del diseño experimental y la participación de la Universidad del Valle, la Universidad de Guanajuato (México) y la Universidad Federal do Rio Grande do Norte (Brasil).

Bibliografía

[1] Chandrakant, R., Ananda, J., Dipak, V., Naresh, M. and Aniruddha, B., A critical review on textile wastewater treatments: Possible Approaches. Environmental Management, 182, pp. 351-366, 2016. DOI: 10.1016/j.jenvman.2016.07.090.

[2] Can-Zeng, L., Shi-Peng, S., Fu-Yun, L., Yee-Kang, O. and Tai-Shung, C., Treatment of highly concentrated wastewater containing multiple synthetic dyes by a combined process of coagulation/flocculation and nanofiltration. Journal of Membrane

Science, 469, pp. 306-315, 2014. DOI: 10.1016/j.memsci.2014.06.057.
[3] Khandegar, V. and Anil, K., Electrocoagulation for the treatment of textile industry effluent - A review. Journal of Environmental Management, 128, pp. 949-963, 2013. DOI: 10.1016/j.jenvman.2013.06.043.
[4] Chequer, F.M.D., De Olivera, G.A.R., Ferraz, E.R.A., Cardoso, J.E., Zanoni, M.V.B. and De Olivera, D.P., Textile Dyes: Dyeing Process and Environmental Impact. In: Eco-Friendly Textile Dyeing and Finishing, Croacia: Intech open science open minds, 2013, pp. 151-176. DOI: 10.5772/53659.
[5] Barun, K. and Sunil, P., Effects of operational parameters on the removal of brilliant green dye from aqueous solutions by electrocoagulation, Arabian Journal of Chemistry, 10(2), pp. S2961-S2968, 2017. DOI: 10.1016/J.ARABJC.2013.11.032.
[6] Agileo, H., Vicente, R., Socorro, O. and Ricardo, G., Photodegradation of indigo carmine dye by CdS nanostructures underblue-light irradiation emitted by LEDs, Catalysis Today, 266, pp.27-35, 2016. DOI: 10.1016/j.cattod.2015.09.001.
[7] Sabnis, R.W. Handbook of biological dyes and stains: synthesis and industrial applications [online], Canada, 2010 [consulted, November 5th of 2017]. Available at: https://onlinelibrary.wiley.com/doi/book/10.1002/9780470586242
[8] Lucyna, B, Marta, G. and Stanisław, L., Comparison between industrial and simulated textile wastewater treatment by AOPs – Biodegradability, toxicity and cost assessment, Chemical Engineering, 306, pp. 550-559, 2016. DOI: 10.1016/j.cej.2016.07.100.
[9] Ramesh, T.N. and Sreenevisa, V.P., Removal of indigo carmine dye from aqueous solution using magnesium hydroxide as an adsorbent, Journal of Materials, 11, pp. 1-10, 2015. DOI: 10.1155/2015/753057.
[10] Elmira, P., Mokhtar, A. and Niyaz, M., Binary system dye removal by electrocoagulation from synthetic and real colored wastewaters, Journal of the Taiwan Institute of Chemical Engineers, 43(2), pp. 282-290, 2012. DOI: 10.1016/j.jtice.2011.10.014.
[11] Marius, S., Igor, C. and Stelian, P., An experimental study of indigo carmine removal from aqueous solution by electrocoagulation, Desalination, 277(1-3), pp. 227-235, 2011. DOI: 10.1016/j.desal.2011.04.031.
[12] Mall, I., Taneja, N. and Thakur, C., Treatment of indigo carmine dye bearing wastewater by electrocoagulation. Kuala Lumpur (Malaysia), 2nd International Conference on Environment, Agriculture and Food Sciences (ICEAFS'2013), [online]. 2013, pp. 86-90. Available at http://psrcentre.org/images/extraimages/20%20813080.pdf.
[13] Martínez-Huitle, C.A. and Brillas, E., Decontamination of wastewaters containing synthetic organic dyes by electrochemical methods: A general review. Appl. Catal., B., 87(3-4), pp. 105-145, 2009. DOI: 10.1016/j.apcatb.2014.11.016.
[14] Butrón, E., Juarez, M., Solis, M., Teutli, M., Gonzalez, I. and Nava, J., Electrochemical incineration of indigo textile dye in filter-press-type FM01-LC electrochemical cell using BDD electrodes. Electrochim. Acta, 52(4), pp. 6888-6894, 2007. DOI: 10.1016/j.electacta.2007.04.108.
[15] Thomas, S., Medhekar, N., Frankel, G. and Birbilis, N., Corrosion mechanism and hydrogen evolution on Mg, Current Opinion in Solid State and Materials Science, 19(2), pp. 85-94, 2015. DOI: 10.1016/j.cossms.2014.09.005.
[16] Douglas, C., Montgomery, Diseño de análisis de experimentos, 4ta edición, México editorial Limusa, 2004, 218 P. ISBN: 968-18-61516.
[17] Mendes, S., Oliveira, A., Buss, D., Magalhães, D., Pavesi, T., Jimenez, M. et al, Photo-decolorization and ecotoxicological effects of solar compound parabolic collector pilot plant and artificial light photocatalysis of indigo carmine dye. Dyes Pigments, 113, pp. 571-580, 2015. DOI: 10.1016/j.dyepig.2014.09.029.
[18] García-Morales, M. et al, An integrated electrocoagulation and ozonation process for removal of indigo carmine dye from denim processing effluent. Sustain. Environ. Res., [online]. 23(4), pp. 241-245, 2013. Available at: http://ser.cienve.org.tw/download/23-4/23-4-2.pdf.
[19] Secula, M., Igor, C., Benoit, C., Liliana, M., Corneliu, S. and Luliana, B., Fractional factorial design study on the performance of GAC-enhanced electrocoagulation process involved in color removal from dye solutions, Materials [Online], 6(7), pp. 2723-2746, 2013. Available at: https://www.ncbi.nlm.nih.gov/pmc/articles/PMC5521228/. DOI: 10.3390/ma6072723.
[20] Panaiotova, M., Kovatcheva, V. and Parlapanski, M., Kinetics of dissolution of iron inaqueous media containing chloride and sulphate ions, Indian Journal of Chemistry, [online]. 39A, pp.1000-1004, 2000. Available at: http://nopr.niscair.res.in/bitstream/123456789/26077/1/IJCA%2039A%289%29%201000-1004.pdf.
[21] Chantaraporn, P., Suprangpak, P. and Warangkana, T., Electrocoagulation of blue reactive, red disperse and mixed dyes, and application in treating textile effluent, Journal of Environmental Management, 91(4), pp. 918-926, 2010. DOI: 10.1016/j.jenvman.2009.11.008.
[22] Daneshvar, N., Oladegaragoze, A. and Djafarzadeh, N., Decolorization of basic dye solutions by electrocoagulation: an investigation of the effect of operational parameters, Journal of Hazardous Materials, 129(1-3), pp.116-122, 2006. DOI: 10.1016/j.jhazmat.2005.08.033.
[23] Jianhai, Z., Runxi, S., Xiaoyu, G., Wenpu, L. and Na, F., Role of mixing conditions on coagulation performance and flocs breakage formed by magnesium hydroxide, Journal of the Taiwan Institute of Chemical Engineers, 45(4), pp. 1685-1690, 2014. DOI: 10.1016/j.jtice.2013.12.014.
[24] Khaled, B., Wided, B., Béchir, H., Elimame, E. and Mouna, L., Investigation of electrocoagulation reactor design parameters effect on the removal of cadmium from synthetic and phosphate industrial wastewater, Arabian Journal of Chemistry, [Online], December, 2015. Available at: DOI: 10.1016/j.arabjc.2014.12.012.
[25] VamshiKrishna, K., Omprakash, S. and Venkata, M., Bioelectrochemical treatment of paper and pulp wastewater in comparison with anaerobic process: integrating chemical coagulation with simultaneous power production, Bioresource Technology, 174, pp.142-151, 2014. DOI: 10.1016/j.biortech.2014.09.141.
[26] Fuyong, C., Ling, G. and Andrej, A., Corrosion and passivation of magnesium alloys, Corrosion Science, CS 6802, pp. 1-40, 2016. DOI: 10.1016/j.corsci.2016.05.04.
[27] Baya, P., Nadjib, D., Salaheddine, A, and Kenza, B., Cost-effective electrocoagulation process for the remediation of fluoride from pretreated photovoltaic wastewater, Journal of Industrial and Engineering Chemistry, 22, pp. 127-131, 2015. DOI: 10.1016/j.jiec.2014.06.033.
[28] Harish, M. and Adka, N., Electrochemical corrosion study of Mg–Al–Zn–Mn alloy in aqueous ethylene glycol containing chloride ions, Journal of Materials Research and Technology, 6(1), pp. 40-49, 2017. DOI: 10.1016/j.jmrt.2016.04.003.
[29] Inoussa, Z., Amadou, H., Joseph, W., Gérard, V., Jean-Pierre, L., Gérard, P., Francois, L., Electrocoagulation for the treatment of textile wastewaters with Al or Fe electrodes: compared variations of COD levels, turbidity and absorbance, Journal of Hazardous Materials, 169(1-3), pp. 70-76, 2009. DOI: 10.1016/j.jhazmat.2009.03.072.
[30] Song, G., Atrens, A. and John, D., The anodic dissolution of magnesium in chloride and sulphate solutions, Corrosion Science, 39(10-11), pp. 1981-2004, 1997. DOI: 10.1016/S0010-938X(97)00090-5.
[31] Kobyaa, M. and Demirbas, E., Evaluations 9of operating parameters on treatment of canmanufacturing wastewater by electrocoagulation, Journal of Water Process Engineering, 8, pp. 64-74, 2015. DOI: 10.1016/j.jwpe.2015.09.006.
[32] Balasubramanian, N., Kojima, T. and Srinivasakannan, C., Arsenic removal through electrocoagulation: kinetic and statistical modeling, Chemical Engineering Journal, 155, pp.7682, 2009. DOI: 10.1016/j.cej.2009.06.038.

D. Donneys-Victoria, es Ing. Química de la Universidad del Valle, Colombia en 2010, MSc. en Ingeniería Química en 2014 y candidata a PhD en Ingeniería con énfasis en Ingeniería Química de la Universidad del Valle, Colombia. Cuenta con experiencia en desarrollo de investigaciones en electroquímica, materiales avanzados, tratamiento de aguas residuales y procesos avanzados de oxidación. Pertenece al grupo Procesos Avanzados de Oxidación para Tratamientos Biológicos y Químicos (GAOX), de la Universidad del Valle y hace parte de la International Society of electrochemistry (ISE) desde el año 2012.
ORCID ID 0000-0002-1943-6328

C.C. Ospina-Toro, es Ing. Químico de la Universidad del Valle, Colombia, en 2018, donde realizó su investigación para el tratamiento de soluciones de índigo carmín mediante electrocoagulación, dirigido por el grupo de investigación Procesos Avanzados de Oxidación para Tratamientos Biológicos y Químicos (GAOX).
ORCID ID 0000-0002-9792-6963

M.V. Zapata-Villegas, es Ing. Química de la Universidad del Valle, Colombia, en 2018. Realizó su investigación para el tratamiento de soluciones de índigo carmín mediante electrocoagulación, dirigido por el grupo de investigación Procesos Avanzados de Oxidación para Tratamientos Biológicos y Químicos (GAOX).
ORCID ID 0000-0002-8793-7634

N. Marriaga-Cabrales, es Ing. Químico de la Universidad Industrial de Santander (UIS), MSc. de la misma universidad en 2001 y PhD en Ingeniería Química de la Universidad del Valle, Colombia. Profesor titular, docente e investigador de la escuela de Ingeniería Química en la Universidad del Valle. Miembro del grupo de investigación Procesos Avanzados de Oxidación para Tratamientos Biológicos y Químicos (GAOX). Su línea de investigación está enfocada en el tratamiento de aguas residuales con procesos electrolíticos y procesos de oxidación avanzada. Cuenta con más de 11 publicaciones en revistas nacionales e internacionales y dos patentes vía PTC.
ORCID ID 0000-0002-5046-9371

F. Machuca-Martínez, es Investigador Sénior en Colombia, realizó sus estudios de pregrado, maestría y doctorado en Ingeniería Química, en la Universidad Industrial de Santander, Colombia. Es el director de la escuela de Ingeniería Química de la Universidad del Valle, y Sub-director del grupo de investigación de procesos Avanzados de Oxidación para Tratamientos Biológicos y Químicos (GAOX). Su línea de investigación está enfocada en procesos de modelamiento, análisis y simulación de procesos catalíticos y desarrollo de productos catalíticos heterogéneos.
ORCID ID 0000-0002-4553-3957

J.M. Peralta-Hernández, es Lic. en Ingeniería Química por el Instituto Tecnológico de Toluca, México, MSc.y PhD en Electroquímica por el Centro de Investigación y Desarrollo Tecnológico en Electroquímica CIDETEQ, México. Actualmente trabaja en el Departamento de Química, División de Ciencias Naturales y Exactas, de la Universidad de Guanajuato, México. Su foco de investigación es el control de la contaminación del agua, con procesos avanzados de oxidación. Cuenta con más de 60 publicaciones en revistas internacionales, 2 libros publicados, 10 capítulos de libros y 3 patentes en México. Actualmente es miembro del comité editorial del Journal Sustainable Environment Research (SER).
ORCID ID 0000-0003-2733-4126

C.A. Martínez-Huitle, es Químico de Universidad de las Américas-Puebla, México. PhD en Ciencias Químicas en la Universidad de Ferrara, Italia. En 2008 se vinculó como profesor del Instituto de Química en la Universidad Federal de Rio Grande do Norte, Brasil. Recibió el premio "Oronzio and Niccolo" de Nora Fundación (2005), y el premio "Oronzio and Niccolò" de Nora Fundación, en electroquímica ambiental por la sociedad internacional de electroquímica (2009). También fue reconocido por el gobierno alemán en 2009 con el "Green Talent Award", por su contribución en el campo de desinfección y tratamiento del agua con nuevas tecnologías electroquímicas. Cuenta con 190 publicaciones en revistas internacionales y 6 capítulos de libros. Sus investigaciones incluyen procesos electroquímicos avanzados de oxidación para el tratamiento del agua, materiales electrocatalíticos, electrolisis, fotocatálisis y electroanálisis.
ORCID ID 0000-0002-6209-5426

UNIVERSIDAD NACIONAL DE COLOMBIA
SEDE MEDELLÍN
FACULTAD DE MINAS

Área Curricular de Ingeniería Química e Ingeniería de Petróleos

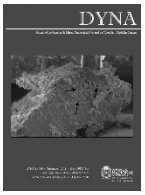
Oferta de Posgrados

Maestría en Ingeniería - Ingeniería Química
Maestría en Ingeniería - Ingeniería de Petróleos
Doctorado en Ingeniería - Sistemas Energéticos

Mayor información:

E-mail: qcaypet_med@unal.edu.co
Teléfono: (57-4) 425 5317

UNIVERSIDAD NACIONAL DE COLOMBIA
SEDE MEDELLÍN
FACULTAD DE MINAS



DYNA
http://dyna.medellin.unal.edu.co/

Integrating SOA and MAS in Intelligent Environments

Manuel Sánchez [a,c], Jose Aguilar [b] & Ernesto Exposito [c]

[a] Departamento de Ing. en Informática, Universidad Nacional Experimental del Táchira, Venezuela. mbsanchez@unet.edu.ve
[b] Centro de Estudios en Microelectrónica y Sistemas Distribuidos (CEMISID), Universidad de Los Andes, Mérida, Venezuela. aguilar@ula.ve
[c] Univ Pau & Pays Adour/E2S UPPA, Laboratoire d'informatique de L'universite de Pau et des Pays de L'adour, Pau, France. m.sanchez@univ-pau.fr, ernesto.exposito@univ-pau.fr

Received: November 2nd, 2017. Received in revised form: April 27th, 2018. Accepted: May 7th, 2018.

Abstract
Service Oriented Architecture (SOA) has emerged as the dominant architecture for interoperability between applications, by using a weak-coupled model, based on the flexibility provided by Web Services, which has led to a wide range of applications, in what is known as cloud computing. On the other hand, Multiagent System (MAS) is widely used in the industry, because it provides an appropriate solution to complex problems in a proactive and intelligent way. Specifically, the Educational Smart Environments (AmI) obtain great benefits by using both architectures, because MAS endows intelligence to the environment, while SOA enables users to interact with academic services in the cloud. The purpose of this article is to propose an architecture for bidirectional integration SOA-MAS to be used on educational AmI. The proposed solution allows taking advantages of both architectures, and solves integration problems raised in previous researches.

Keywords: ambient intelligence; SOA; MAS; cloud computing.

Integración SOA-MAS en Ambientes Inteligentes

Resumen
SOA (Service Oriented Architecture) ha emergido como una arquitectura dominante para la interoperabilidad entre aplicaciones, por medio de un modelo de acoplamiento débil basado en la flexibilidad que proveen los servicios web, esto ha dado lugar a una amplia gama de aplicaciones, en lo que se conoce hoy en día como computación en la nube. Por otro lado, los MAS (Multiagent System, por sus siglas en inglés) son usados ampliamente en la industria, ya que brindan soluciones apropiadas a problemas complejos, de forma proactiva e inteligente. En particular, los Ambientes Inteligentes (AmI) educativos se benefician de estás dos arquitecturas, ya que por un lado los MAS dotan al AmI de inteligencia, mientras que SOA permite a los usuarios interactuar con servicios académicos en la nube. El propósito de este artículo es proponer una arquitectura de integración bidireccional SOA-MAS para AmI educativos. La solución propuesta aprovecha las ventajas de ambas tecnologías (SOA-MAS), y resuelve problemas de integración planteados en investigaciones previas.

Palabras clave: ambiente inteligente; SOA; MAS; integración; computación en la nube.

1. Introducción

En educación, la Inteligencia Ambiental permite aportar grandes beneficios, al adaptar el ambiente de forma dinámica a las necesidades de enseñanza-aprendizaje de los usuarios [1-5]; por ejemplo: brindando contenidos digitales basados en el estilo de aprendizaje de los estudiantes, adecuando el ambiente (aula) para realizar las actividades adecuadas al contexto educativo, poniendo en contacto estudiantes que estudien temas similares para fomentar el aprendizaje colaborativo, entre otras cosas.

Por otro lado, el aprendizaje en la nube (C-Learning) consiste en mantener y usar servicios educativos de manera distribuida, usando los mecanismos y herramientas que ofrece la computación en la nube [6-7]. Los servicios educativos clásicos que brinda C-Learning son cursos, actividades y contenidos. El C-Learning incluye actividades síncronas y asíncronas, para fomentar el aprendizaje colaborativo por medio del uso de la nube. C-Learning brinda servicios educativos disponibles en la nube, tal que los recursos educativos son almacenados en un ambiente virtual que puede ser accedido de maneras y ubicaciones distintas, por medio del del paradigma SOA [8-9].

En investigaciones pasadas se ha propuesto AmICL, un

How to cite: Sánchez, M., Aguilar, J. and Exposito, E., Integración SOA-MAS en ambientes inteligentes. DYNA, 85(206), pp. 268-282, September, 2018.
© The author; licensee Universidad Nacional de Colombia.

medio de gestión de servicios (middleware) para Ambientes Inteligentes Educativos basado en el aprendizaje en la nube [10-15]. La inteligencia de AmICL está soportada por un MAS cuya arquitectura es descrita en [11]. Para implementar este MAS se utiliza el estándar FIPA [16-17] por medio de un conjunto de agentes básicos descritos en [18]. Por otro lado, la arquitectura SOA permite a AmICL hacer uso de los servicios académicos de la nube en la búsqueda por mejorar el proceso de enseñanza-aprendizaje de los usuarios del ambiente.

Debido a que SOA y MAS [19] utilizan estándares y especificaciones diferentes [20-22], no es posible su comunicación de manera natural y directa. Mientras que un MAS utiliza protocolos FIPA para la comunicación, y más específicamente el lenguaje FIPA-ACL [16, 23-24], en SOA se utiliza generalmente el protocolo de comunicación SOAP [25-27], el cual es un estándar que define cómo objetos en diferentes procesos pueden comunicarse usando mensajes escritos en XML [28-29] con un protocolo de transporte como HTTP [30]. Es así que desde hace algún tiempo se vienen proponiendo soluciones que permiten la integración de ambas arquitecturas [20,31-37], de tal manera que éstas puedan descubrirse e invocar instancias de la otra, para aprovechar las ventajas de ambas tecnologías.

Por otra parte, en AmICL se hizo una primera propuesta que busca dar solución al problema planteado, a través de los agentes SMA y WSA definidos en [10]; Sin embargo, estos agentes solo permiten la integración de forma unidireccional entre el MAS y la nube (SOA). Esto significa que AmICL puede hacer uso de los servicios académicos en la nube, pero las aplicaciones externas basadas en SOA no pueden usar los servicios de AmICL, lo que limita que los servicios de la nube puedan integrarse con el ambiente, y a su vez, se limitan las capacidades de AmICL, ya que su proactividad e inteligencia depende en gran medida de estos servicios.

En definitiva, el objetivo fundamental de este artículo es analizar las posibles arquitecturas de integración MAS-SOA, que puedan ser usadas en AmICL, las cuales, a su vez, deben ser genéricas, tal que puedan ser de utilidad para cualquier sistema que requiera interconectar MAS y SOA.

En consecuencia, el artículo se organiza de la siguiente manera: En la sección 2 se especifica la arquitectura de AmICL, en la sección 3 se presenta el estado del arte en cuanto a que se ha hecho en integración MAS-SOA, para posteriormente, en la sección 4 presentar posibles soluciones de integración, analizando sus ventajas y desventajas, finalizando con algunas conclusiones y trabajos futuros.

2. Especificación de AmICL

2.1. Caracterización de AmICL

AmICL es un Middleware Reflexivo Autonómico [38-40] que permite la integración de los objetos (inteligentes o no) del ambiente educativo, con recursos educativos en la nube, de una manera flexible, proactiva y adaptativa, tal que estos objetos pueden ajustar su comportamiento de acuerdo al contexto y requerimientos del usuario (Ver Fig. 1, arquitectura multi-capa de AmICL), posibilitando ubicar, analizar y compartir el conocimiento).

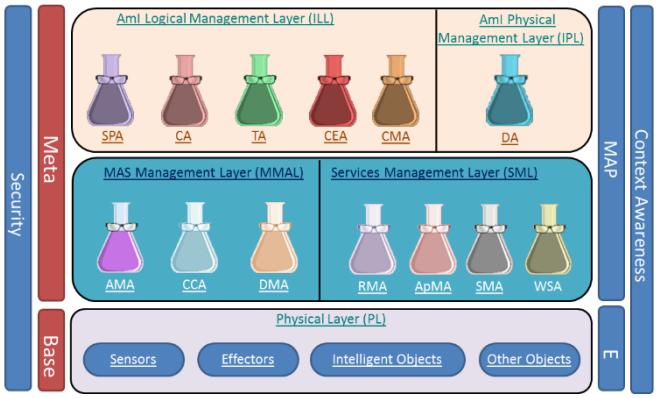


Figura 1. Arquitectura multi-capa de AmICL.
Source: [10].

En AmICL, los servicios académicos en la nube se combinan con objetos inteligentes que integran el ambiente, para adaptarse y responder a los requerimientos de enseñanza aprendizaje de los usuarios. Esto posibilita poner a disposición de los usuarios de forma inteligente, los servicios apropiados que permitan mejorar el desarrollo de las actividades académicas que realizan en un momento específico, adaptados a la forma de aprender del estudiante.

AmICL está compuesto por un MAS de cinco capas (Ver Fig. 1). La capa física (PL) representa los diversos dispositivos físicos del ambiente, definidos como agentes dispositivos en la capa de gestión de AmI Físico (IPL). PL está conectada con el Sistema Operativo, y trabajan en conjunto para realizar las diferentes actividades que se llevarán a cabo en el entorno. La capa de gestión de AMS (MMAL) está compuesta por una comunidad de agentes que soporta la ejecución de aplicaciones multi-agentes. Esta capa se basa en el estándar FIPA [18] y ha sido definida en artículos previos [10-11]; Ésta capa es una abstracción del estándar FIPA, donde el agente AMA representa al directorio facilitador (DF [18]), y el agente CCA sirve como punto de enlace para coordinar la comunicación entre los demás agentes, tanto internos como externos al MAS (ver [18] para más detalles de esos agentes). La capa de gestión de servicios (SML) es donde se registran, descubren, invocan, etc., los servicios requeridos por el ambiente en un momento determinado. La capa AmI lógico (ILL) representa los diferentes componentes de software que son usados en la plataforma educativa. En adición, esta capa tiene dos agentes, el agente perfil de estxcudiante (SPA) y el agente tutor (TA), que caracterizan a estudiantes y profesores, respectivamente.

Los detalles de AmICL pueden encontrarse en [8]. En general, los agentes del middleware son, en MMAL: el Agente Administrador de Agentes (AMA), Agente Controlador de Comunicación (CCA) y el Agente Gestor de Datos (DMA), este último encargado de poner a disposición de los demás agentes, los datos que requieran para llevar a cabo sus funciones; La SML está compuesta por el Agente Gestor de Servicios (SMA, se encarga de gestionar el directorio de servicios en la nube), El Agente de Servicio (WSA, un proxy que sirve para invocar servicios web), el Agente Gestor de Recursos (RMA, gestiona el uso de los recursos requeridos por los demás agentes) y el agente gestor

de aplicaciones (ApMA, encargado de gestionar el uso de las aplicaciones por parte de los demás agentes). Los agentes de CAL son: el Agente Perfil de Estudiante (SPA, caracteriza un estudiante en el AmI), el agente colaborativo (CA, posibilita el aprendizaje colaborativo entre estudiantes), el Agente Tutor (TA, caracteriza al profesor de la clase y sirve como un tutor virtual para el estudiante), el Agente de aplicaciones de Gestión de Contenido (CMA, gestiona el ambiente virtual de aprendizaje agregando dinámicamente los recursos recomendados de acuerdo al estilo de aprendizaje del estudiante), y el Agente de aplicaciones de Espacio Colaborativo (CEA, similar a CMA pero solo para aplicaciones de trabajo colaborativo). Finalmente, la IPL está compuesta de un único agente, el Agente Dispositivo (DA, representa los diversos dispositivos desplegados en el aula inteligente).

2.2. Subsistema de gestión de la nube en AmICL

En particular, el aspecto que permite unir el AmI con el paradigma de computación en la nube, se encuentra en SML. Esta capa contiene algunos agentes, que son una extensión del estándar FIPA (ver [18]), para gestionar tanto los recursos y aplicaciones presentes en el sistema operativo, como los servicios educativos en la nube, lo que permite que otros agentes de AmICL puedan usar servicios académicos en la nube, para mejorar las actividades de los usuarios del ambiente educativo. En particular los agentes RMA y ApMA manejan recursos y aplicaciones del sistema operativo en el MAS [18]; mientras que los agentes que representan un puente entre el AmI y la nube se detallan a continuación:

El Agente Gestor de Servicios (SMA) Controla, registra y administra los servicios web disponibles en el Sistema; de esta forma, cuando un agente del MAS requiere un servicio específico, debe contactar al SMA, para que éste ubique al Agente de Servicio (WSA) que caracteriza, en el MAS, al servicio web requerido. SMA caracteriza lo que se conoce dentro del tema de Servicios Web como UDDI [41] (Universal Description, Discovery and Integration, por sus siglas en inglés).

Por su parte, el Agente Servicio (WSA) es la representación lógica de un servicio web. Es decir, éste agente caracteriza a un servicio web (un agente por cada servicio web), por esa razón éste sabe cómo invocarlo (tiene su interfaz) y cuáles son los requerimientos necesarios para acceder al endpoint del servicio web. El WSA tiene acceso al archivo de descripción del servicio (WSDL [42], por sus siglas en inglés). El diseño de estos agentes se describe con mayor detalle en [10-11].

El mayor problema que tiene este subcomponente de AmICL es que solo permite la integración en forma unidireccional (desde AmICL hacia la nube), eso significa que el AmI no podrá exponer sus servicios a otros sistemas desarrollados bajo el paradigma SOA, limitando las capacidades de integración de AmICL. En esta investigación se analizarán dos propuestas de integración bidireccional SOA-MAS y se realizarán un conjunto de pruebas que permitirán determinar cuál de las dos presenta mayores ventajas en cuanto a escalabilidad, tiempo de respuestas, entre otras.

3. Trabajos relacionados

La integración entre MAS y SOA ha sido objeto de diversos estudios durante los últimos años [20,31-37,43-45]. Esas propuestas se dividen en dos grandes grupos: aquellas que utilizan agentes proxy (Gateway) y aquellas que son completamente orientadas a servicios.

3.1. Estudios basados en Agente Proxy

Las investigaciones realizadas en [20-31] permiten realizar composición y descubrimiento de servicios por medio de agentes. La arquitectura propuesta se basa en el uso de una pasarela (Gateway Proxy) para la integración de servicios web (WSIG, por sus siglas en inglés), que permite el registro y descubrimiento, tanto de agentes como de servicios web. El registro/deregistro es realizado por medio del componente "GatewayRegistry", éste a su vez utiliza el "Service Description Translator" para traducir de WSDL a ACL/OWL y viceversa, de tal forma que el servicio web (WS, por sus siglas en inglés) sea registrado en el DF como un agente, y los agentes sean registrados en el UDDI como servicios web. De esta manera, los agentes pueden hacer descubrimiento de servicios web a través del DF, mientras que los servicios web descubrirán a los agentes usando el UDDI.

Cuando un agente requiere invocar un WS, WSIG pasa el requerimiento al componente "Web Service Invocation", el cual traduce el mensaje a SOAP usando el "Message Translator", y lo envía al endpoint del WS, espera su respuesta, y la retorna al agente solicitante. De forma similar, para que un servicio web comunique a un agente su solicitud la pasa al componente "AgentService Invocation", el cual traduce el mensaje de SOAP a ACL, y lo envía al agente especificado, espera su respuesta en ACL, y una vez recibida, la remite al WS solicitante en forma de mensaje SOAP. Para que todo este proceso pueda llevarse a cabo, la plataforma debe contar con un servidor web y un UDDI, ejecutándose como servicios de JADE [46-47].

Por su parte, en [32] proponen AgentWeb Gateway, el cual es un middleware que permite la integración de MAS con SOA de forma muy similar a la realizada por [20,31], ya que se basa en los mismos principios. Su arquitectura está integrada por 3 componentes. El primero es el "Search query converter", el cual se encarga de procesar las búsquedas de agentes y servicios web, a fin de que puedan descubrirse entre ellos. El modulo "DF to UDDI" permite a los agentes descubrir servicios web registrados en el UDDI, mientras que su contraparte (UDDI to DF) permite a un servicio web ubicar a los agentes. El siguiente componente (Service Description Converter) se compone de dos módulos, el "DFAgentDesc to WSDL" permite a los agentes de software publicar sus servicios en el directorio UDDI de la plataforma web, a fin de que puedan ser consumidos por otros servicios web, mientras que el módulo "WSDL to DFAgentDesc" permite que un servicio web publique sus servicios en el DF del MAS, de tal manera que los agentes puedan consumir dichos servicios de forma transparente. El tercer componente, denominado "Communication protocol converter", permite la invocación entre agentes y servicios web. En particular, el módulo "ACL to SOAP" permite a los agentes del MAS

invocar un servicio web (traduce el mensaje de ACL a SOAP), mientras que el módulo "SOAP to ACL" permite a un servicio web invocar los servicios ofrecidos por los agentes, traduciendo los mensajes de SOAP a ACL.

Otra investigación basada en la integración por medio del uso de agentes Gateway es la que se realizó en [33]. WS2JADE permite a los agentes de JADE descubrir y consumir servicios web, con un alto grado de automatización al desplegar los mismos como agentes de JADE en tiempo de ejecución. A su vez, puede generar agentes a partir del archivo WSDL. De igual forma, WS2JADE permite el mapeo M a N entre agentes y servicios web, lo que posibilita que varios agentes puedan consumir un servicio web de forma concurrente. Las capas que componen la arquitectura de WS2JADE son de dos tipos, la capa de interconexión y la capa de administración. La primera capa contiene entidades (agentes de servicios web, ontologías y protocolos) que permiten interconectar agentes y servicios web. La capa de administración crea y gestiona dichas entidades de forma dinámica. Los agentes de servicios web (WSAG) son creados por la capa de administración de forma dinámica en tiempo de ejecución, para ello, el descubrimiento de servicios web se debe realizar de forma activa (mapea, registra, etc.). Los servicios web son vistos por los agentes de JADE como servicios ofrecidos por algún WSAG. Al ofrecer el mismo servicio web en diferentes WSAG, se logra el acceso concurrente a los servicios web.

Una solución para la integración MAS-SOA usando agentes proxy y Java Business Integration (JBI) es propuesta por [34]. La idea fundamental es crear un servicio web (servicio proxy) dentro del contenedor JBI, que actúe como proxy entre el NMR (Normalized Message Router) y el MAS, el cual pueda interactuar tanto con los servicios desplegados en el contenedor JBI como con los agentes de JADE. Para que el servicio proxy pueda comunicarse con los agentes en el MAS debe crearse un agente proxy en el MAS, que actuará como puente entre la comunidad de agentes y el servicio proxy. En consecuencia, esta propuesta contiene dos entidades fundamentales, el servicio proxy desplegado en el contenedor JBI, y el agente proxy desplegado en la plataforma Multiagentes; todo el tráfico entre servicios web y agentes debe pasar a través de estas dos entidades, que funcionan como los extremos de un puente de comunicación. De esta forma, cuando un servicio web en el JBI requiere usar las capacidades de un agente, enviará un mensaje al servicio proxy por medio del NMR, el servicio proxy transformará el mensaje a ACL, y lo remitirá al agente proxy asociado con él, el agente proxy lo enviará al agente especifico, esperará la respuesta, y la transmitirá nuevamente al servicio proxy en formato SOAP, el cual lo remitirá al servicio que hizo la solicitud inicialmente. Por otra parte, cuando un agente de la comunidad requiere usar un WS, envía un mensaje ACL al agente proxy, el cual lo transforma en un mensaje SOAP, y remite al servicio proxy que tiene asociado, quien debe enviarlo al servicio destino, esperar la respuesta, y retransmitirla nuevamente al agente proxy en ACL, para que éste la remita al agente que realizó la solicitud inicialmente. Es importante resaltar que el servicio proxy y agente proxy deben crearse manualmente.

En [36] se desarrolló una librería denominada JADE Gateway Library, que actúa como puente entre un MAS y los servicios que se encuentran desplegados en un Bus de Servicios Empresarial (ESB por sus siglas en inglés) [48]. La librería está compuesta por dos elementos fundamentales, el primero es el Jade-Gateway, que se encarga de gestionar los mensajes que se reciben desde y hacia el ESB; el otro es el Gateway Agent, que tiene como objetivo principal retransmitir los mensajes entre el MAS y el ESB. Cuando un agente quiere consumir un WS, debe enviar un mensaje al GatewayAgent, que a su vez lo retransmite al ESB; por otro lado, cuando un WS necesita enviar un mensaje a un agente, debe hacerlo a través del EntryPoint ESB Service, este lo pasará al Jade-Gateway, y luego al GatewayAgent, que lo retransmitirá al agente solicitado. Durante el proceso de comunicación el Jade-gateway debe realizar conversiones SOAP-ACL y ACL-SOAP, para que cada parte reciba el mensaje en el lenguaje apropiado. De igual forma, Jade-gateway resuelve el problema de integración de las comunicaciones síncronas de los servicios web con las comunicaciones asíncronas de un MAS, bloqueando el hilo del GatewayAgent hasta obtener la respuesta del MAS.

3.2 Estudios basados en Agentes Orientados a Servicios

Las investigaciones realizadas en [35,37,43] proponen SoMAS (Service oriented MultiAgent System) como una arquitectura completamente orientada a servicios, donde tanto agentes como servicios web utilizan SOAP como lenguaje de comunicación. En la arquitectura SoMAS, los agentes deben publicar sus servicios en el directorio de servicios, donde enviaran para ello el archivo WSDL correspondiente a los servicios que ofrece. Cuando un agente o servicio web requiere usar un servicio particular, debe buscarlo en el directorio de servicios, y una vez encontrado establecer la comunicación con el mismo por medio de mensajes SOAP. Esta arquitectura deja a un lado el estándar FIPA, ya que el sistema no utiliza DF ni el lenguaje de comunicación ACL, aunque el autor indica que se pueden usar ambas interfaces de comunicación, lo que supone hacer un trabajo adicional. SoMAS es la propuesta más relevante de este tipo, en la literatura.

Para finalizar esta sección, se presenta un resumen de los problemas encontrados en los trabajos estudiados. En general, las grandes desventajas de las propuestas son: algunas integran en una sola dirección, esto quiere decir que solo permite que los agentes puedan consumir servicios web (como WS2JADE). Otras, no logran traducir el modelo de comunicación con estado de los agentes al modelo de comunicación sin estado de los servicios web, lo que dificulta la comunicación asíncrona entre ambos paradigmas. En algunos casos, los servicios y agentes proxy deben crearse manualmente, y son muy dependientes de la arquitectura. De igual forma, las propuestas que no usan conversión ACL/SOAP dejan de ser FIPA-Compliant.

4. Arquitecturas propuestas

En la siguiente sección se describe la propuesta de integración SOA-MAS, en la cual se muestran dos enfoques de integración. Ambos enfoques son independientes, es decir cada uno define una forma de integración usando diferentes

paradigmas, componentes y tecnologías. Por esta razón es necesario realizar un análisis comparativo, que permita determinar cuál enfoque brinda mejores rendimientos, respecto a los trabajos relacionados, así como entre ellos.

En general, en AmICL (o cualquier SMA basado en la nube) es fundamental que los agentes puedan consumir servicios de la nube, ya que de ello depende que los usuarios puedan usar los servicios ofrecidos por C-Learning. De igual manera, exponer los servicios de AmICL hacía la nube es indispensable, para que otros sistemas puedan interactuar con el AmI (Ej: para describir los dispositivos en el AmI, conocer el contexto de aprendizaje, entre otras cosas). Así, las características que deben cumplir las propuestas de integración se enumeran a continuación:

1. Permitir las comunicaciones bajo ambos estándares (FIPA para comunicaciones agente-agente, FIPA ACL-SOAP y SOAP-FIPA ACL para comunicaciones agente-WS y WS-agentes).
2. Permitir la transformación de mensajes SOAP a FIPA-ACL y FIPA-ACL a SOAP.
3. Crear automáticamente los Agentes Gateway, que servirán como punto intermedio entre las comunicaciones MAS-SOA y SOA-MAS.
4. Permitir las comunicaciones síncronas y asíncronas, esto implica transformar las comunicaciones síncronas que se reciban de parte de los servicios web, en comunicaciones asíncronas para la comunidad con agentes, y viceversa.
5. Permitir el mapeo M a N entre agentes y servicios web. Esto significa: a) Que M agentes puedan consumir un mismo servicio web en el mismo instante, b) Que N servicios web puedan comunicarse con un mismo agente.
6. Especificar la arquitectura, independiente de su implementación.

4.1. Propuesta 1: basada en Agentes Proxy orientados a servicios

En la Fig. 2 se muestra la primera propuesta de integración, la cual permitirá a AmICL consumir los servicios de la nube por medio de agentes proxy convencionales (WSA), y exponer las capacidades de los agentes en el MAS como servicios, por medio de agentes proxy orientados a servicios (WSOA).

La arquitectura propuesta es una mezcla entre el enfoque de agente gateway convencional y el enfoque de agentes orientados a servicios (SoMAS). En la Fig. 2 se pueden ver los agentes que intervienen en el proceso de integración. El agente SMA se encarga de controlar el directorio de Servicios (UDDI), y todo lo referente al registro/de-registro, modificación y búsqueda de servicios web. Cada vez que un servicio web es registrado en el UDDI, se registra en el SMA un WSA que caracteriza dicho servicio web, usando para ello el módulo "WSDL Translator". Por otro lado, WSOA tiene el rol de servir de fachada a los agentes del SMA, para que sus capacidades puedan ofrecerse como servicios a través de la nube, y SRPA representa a cualquier agente del MAS que en momento determinado puede necesitar invocar un Servicio Web (en cuyo caso se llamará RA, ver Fig. 3-4); o a un agente que expone sus funcionalidades como servicios web (en este caso se denominará SA, ver Fig. 5).

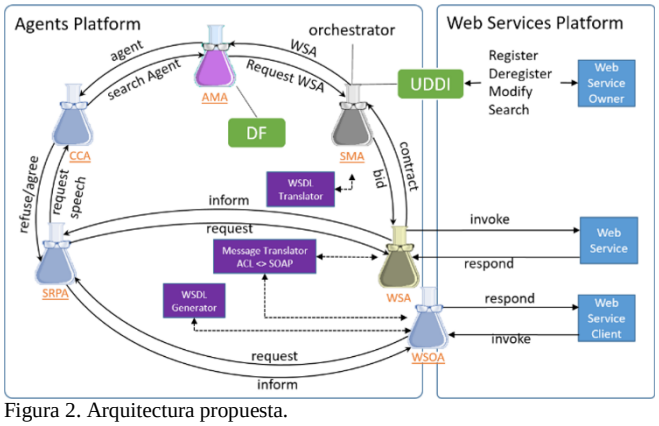


Figura 2. Arquitectura propuesta.
Source: Los autores.

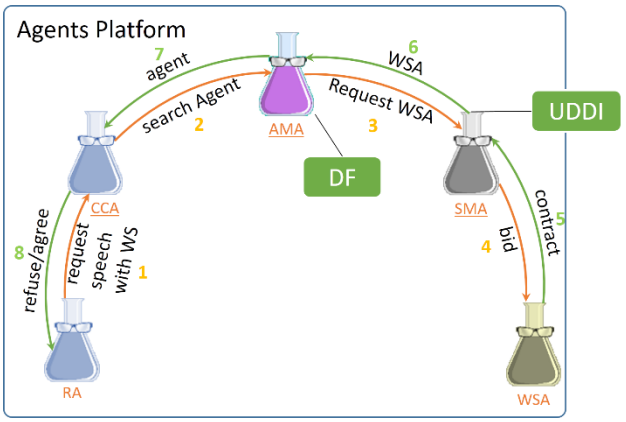


Figura 3. Descubrimiento de servicios web por agentes.
Source: Los autores.

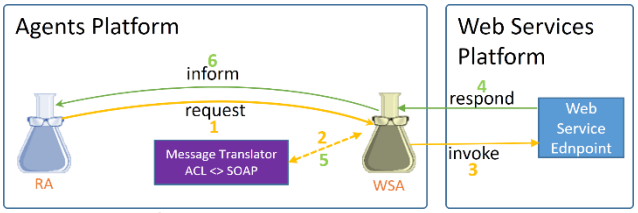


Figura 4. Invocación de servicios web por agentes.
Source: Los autores.

A diferencia de lo propuesto por [20,31-32], el WSA no se registra en el AMA (DF), ya que el encargado de administrar los agentes WSA es el SMA. Por su lado, el Agente AMA es el encargado de controlar el DF, donde se encuentran registrados los agentes de la plataforma Multiagentes; cuando un agente requiere descubrir a otro, AMA busca primero en el DF, si lo encuentra lo retorna, si no lo consigue en el DF, remite el requerimiento al SMA (ya que puede estar requiriendo un WSA). SMA buscará en su directorio, y de encontrarlo, retornará el WSA que sirve como proxy para consumir el servicio web requerido. De esta forma, un agente puede descubrir tanto a otros agentes (registrados en el DF), como a los servicios web disponibles en el ambiente (registrados en el UDDI). La Fig. 3 muestra los pasos seguidos en este proceso, las flechas de color

naranja (mensajes 1-4) muestran el camino seguido hasta encontrar el servicio web requerido, mientras que las flechas de color verde (mensajes 5-8) muestran como el servicio solicitado llega hasta el agente que hizo el requerimiento (RA), con lo cual ya pueden entablar comunicación.

Una vez que RA tiene la información del Agente que caracteriza al servicio solicitado, puede iniciar el proceso de comunicación para consumir el servicio web. En la Fig. 4 se detalla este proceso. Inicialmente RA hará el requerimiento para consumir el servicio web, enviando un mensaje ACL a WSA (1), WSA transformará el mensaje de ACL a SOAP usando el Módulo "Message Translator" (2), y retransmitirá el mensaje al endpoint del servicio web (3). Si es una comunicación asíncrona, WSA debe bloquear su hilo hasta recibir una respuesta del WS. Una vez recibida está respuesta (4), WSA transformará el mensaje de SOAP a ACL (5), usando nuevamente el módulo "Message Translator", y remitirá la información (6), al agente solicitante.

Por otro lado, como se dijo antes, los agentes WSOA (ver Fig. 2) sirven como fachada para exponer las capacidades de los agentes del MAS como servicios web. Estos agentes son creados de forma automática, cuando el agente al que sirven se registra en el AMA (1 WSOA por cada agente registrado en el AMA). El archivo WSDL de cada WSOA será registrado en el UDDI, usando para ello el módulo "WSDL Generator". Sin embargo, ningún WSA es creado en este proceso (no tiene sentido que los WSOA tengan un WSA que los caracterice como servicios web en el MAS), de esta manera, los WS externos pueden descubrir a los WSOA (y por ende, al agente al que sirven de fachada) realizando una búsqueda en el UDDI. Los servicios ofrecidos por cada WSOA deben ser desplegados en un servidor web, o por medio de un framework como Apache CXF [49], lo cual debe ser decidido al momento de la implementación. La Fig. 5 detalla tanto el proceso de descubrimiento de los WSOA por parte de un servicio web (1), como el proceso seguido para consumir los servicios expuestos por los agentes del MAS.

Una vez que el "Web Service Client" ha encontrado al agente WSOA que expone los servicios del agente SA por medio del UDDI, puede invocar dichos servicios, enviando un mensaje SOAP al WSOA (2), el WSOA tomará el requerimiento y lo transformará en un mensaje ACL (3), usando para ello el modulo "Message Translator", para luego remitirlo al agente (SA) (4). Debido a la naturaleza asíncrona de las comunicaciones entre agentes, WSOA debe esperar hasta recibir respuesta del SA (5), y una vez que tenga la información transformarla en un mensaje SOAP (6) por medio del "Message Translator", y reenviarla al "Web Service Client" (7) que realizó la solicitud inicialmente.

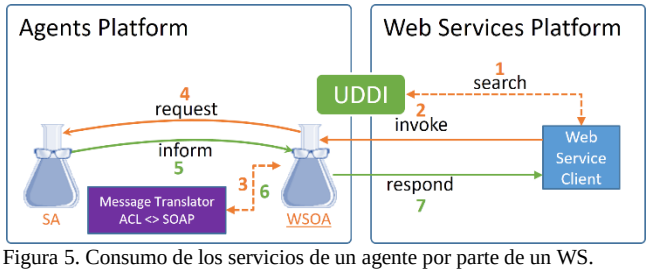


Figura 5. Consumo de los servicios de un agente por parte de un WS.
Source: Los autores.

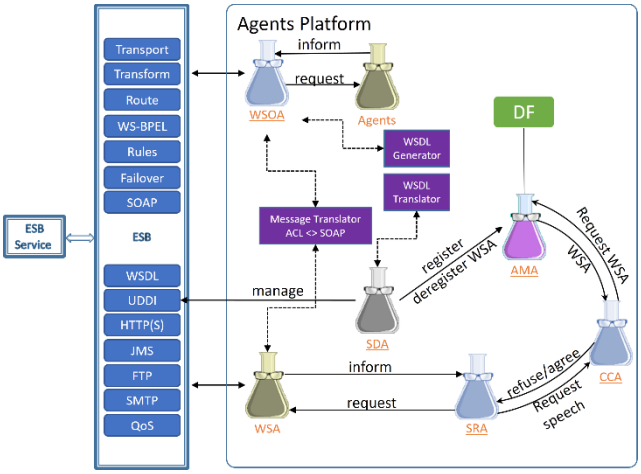


Figura 6. Arquitectura propuesta.
Source: Los autores.

4.2. *Propuesta 2: basada en un ESB usando Agentes Proxy orientados a servicios*

La arquitectura de ésta segunda propuesta se muestra en la Fig. 6. Ésta propuesta no solo permite aprovechar las características del enfoque de agentes Gateway y el enfoque SoMAS, sino que además incorpora elementos importantes del paradigma orientado a servicios, puesto que la integración se da por medio de un Bus de Servicios Empresarial (ESB, por sus siglas en inglés).

El ESB brinda al componente de la nube de AmICL características importantes, tales como: transporte, transformación y ruteo de mensajes, de esta manera, se pueden utilizar múltiples protocolos de transporte como HTTP(S)/REST [50], FTP [51], SMTP [52], etc. y estandarizarlos en un solo protocolo como SOAP, lo cual mejora en gran medida la integración con otros sistemas.

En la Fig. 6 se observan los elementos de la arquitectura que permiten lograr la integración MAS-SOA. Los agentes WSOA y SMA tienen las mismas funciones de la propuesta 1, sin embargo, en esta propuesta existe un nuevo agente denominado SDA (Service Discovery Agent), encargado de administrar el UDDI del ESB, y ejecutar los cambios correspondientes en el MAS. Así mismo, el SRA representa agentes del AMS que requieren consumir servicios web registrados en el ESB, mientras que "Agents" se refiere a todos aquellos agentes del MAS que exponen sus funcionalidades como servicios web usando un WSOA como fachada.

En las Fig. 7-11 se detallan los procesos básicos que se realizan en esta arquitectura: Registro de un servicio web, Descubrimiento de servicios web por agentes, Invocación de servicios web por agentes, Registro de agentes del MAS y WSOA, y Consumo de los servicios de un agente por parte de un WS. Vemos que, en esta arquitectura, hay dos procesos básicos extras. Por otro lado, el SRA representa los agentes RA que consumen los servicios web (ver Fig. 8-9), mientras que "Agents" son los agentes SA que exponen sus funcionalidades como servicios web (ver Fig. 10-11).

En la Fig. 7 se detalla como un Proveedor de servicios publica sus servicios en el ESB (1), el ESB lo registra en el

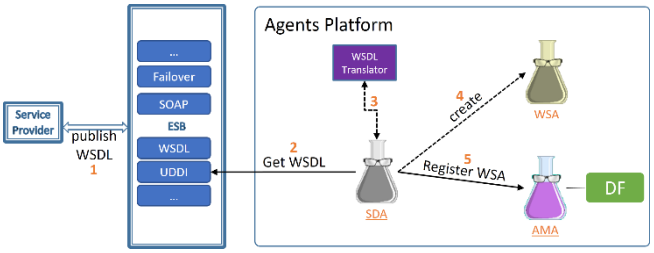


Figura 7. Registro de un servicio web.
Source: Los autores.

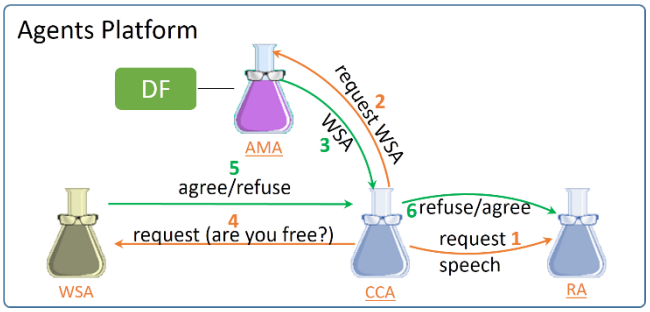


Figura 8. Descubrimiento de servicios web por agentes.
Source: Los autores.

UDDI, el SDA, al detectar el nuevo registro debe obtener el archivo WSDL correspondiente al servicio web registrado (2), utilizar el módulo "WSDL Translator" para obtener la descripción de un agente que caracterice a dicho servicio (3), para luego crear el agente WSA (4), y registrarlo (5) en el directorio facilitador administrado por el AMA. De forma similar, el SDA respondería cuando se modifica o de-registra un servicio web, efectuando los cambios necesarios en la plataforma.

Debido a que los WSA son registrados en el AMA, los agentes del MAS pueden descubrir sus servicios, como si de otro agente se tratase (buscando en el AMA). En la Fig. 8 se detalla el proceso.

En primera instancia, el agente RA debe preguntar (1) al CCA si es posible establecer comunicación con un WSA (CCA siempre está presente al inicio de la comunicación entre dos agentes, y es quien controla si los agentes pueden entablar una conversación o no). CCA debe buscar si el agente solicitado se encuentra registrado en el AMA (2). De ser así, el AMA responderá con la referencia del agente solicitado (3); CCA preguntará al WSA si está disponible para ejecutar una tarea (4), a lo cual el WSA puede responder afirmativo o negativo (5), dependiendo de esta respuesta, el CCA permitirá o no el inicio de la conversación entre el RA y el WSA (6).

Una vez que el RA tenga permiso para hablar con el WSA, puede invocar sus servicios (ver Fig. 9). Para ello, envía un requerimiento al WSA (1) por medio de un mensaje ACL. WSA usa el módulo "Message Translator" para transformar el mensaje de ACL a SOAP (2), y lo remite al ESB (3), el ESB se encarga de entregar dicho mensaje al endpoint del WS requerido (4 y 5), el WS procesa el mensaje y envía la respuesta al ESB (6) en un mensaje SOAP. El ESB se encarga de entregar este mensaje (en comunicaciones síncronas, WSA bloquea su hilo

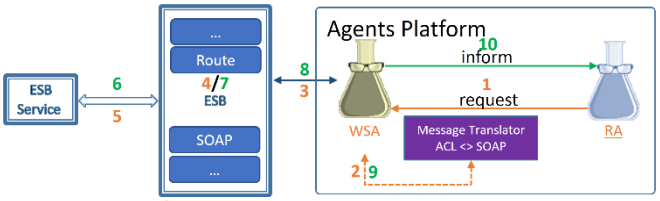


Figura 9. Invocación de servicios web por agentes.
Source: Los autores.

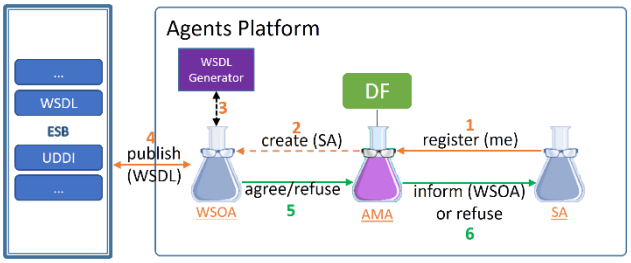


Figura 10. Registro de agentes del MAS y WSOA.
Source: Los autores.

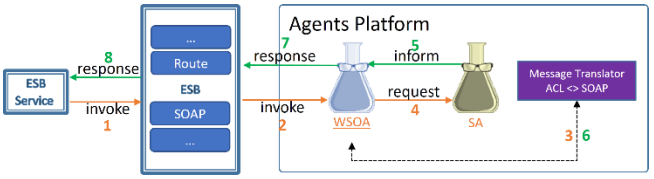


Figura 11. Consumo de los servicios de un agente por parte de un WS.
Source: Los autores.

hasta obtener respuesta del ESB) al WSA solicitante (7 y 8), quien usa nuevamente el "Message Translator" para transformar (9) el mensaje SOAP a ACL, y remitirlo al agente que realizó el requerimiento inicialmente (10).

Por otro lado, cuando un agente del MAS es registrado en el AMA, se debe crear automáticamente el WSOA (excepto si el agente que se registra es un WSA) que servirá de fachada para exponer sus capacidades como servicios web en el ESB (el mensaje de registro enviado a AMA, debe contener información que indique cuando crear o no el WSOA). La Fig. 10 refleja cómo se realiza esta tarea. En primer lugar, el agente del MAS (SA) solicita registrarse en el AMA (1); AMA lo registra en su DF y al conocer que el agente requiere un WSOA, lo creará (2). Una vez que el WSOA es creado, utiliza el módulo "WSDL Generator" para obtener un archivo WSDL (3) correspondiente a las capacidades del SA, que serán expuestas como servicios web y publicadas (4) en el ESB (WSOA guarda la referencia del SA al cual presta servicios, ya que lo necesitará para consumir sus servicios). WSOA responderá al AMA si fue posible o no publicar los servicios en el ESB, y dependiendo de la respuesta, AMA informará al SA quien es su WSOA o rechaza el registro del agente.

Debido a que los agentes WSOA tienen registrados sus servicios en el UDDI del ESB, cualquier servicio web que esté acoplado al ESB puede descubrir esos servicios por medio del mismo ESB. De esta manera, servicios web del ESB pueden invocar las capacidades de los agentes del MAS (ver Fig. 11).

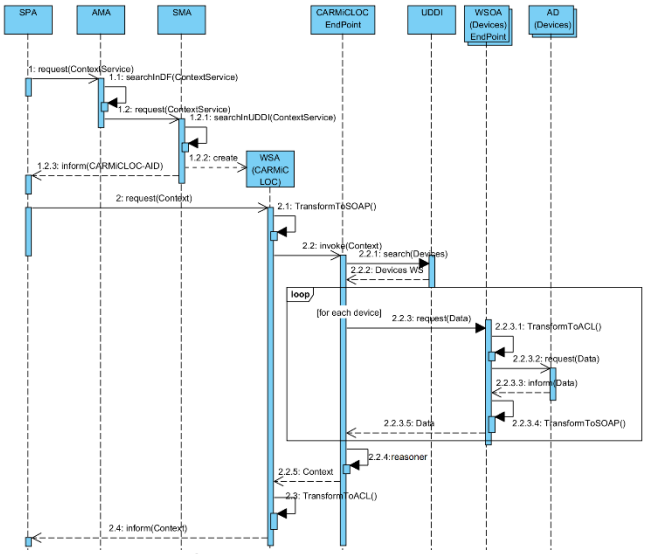


Figura 12. Conversación entre SPA y CARMiCLOC de la Propuesta 1. Source: Los autores.

El proceso se inicia cuando el ESB recibe un mensaje (1) para invocar un servicio de agente específico, el ESB se encarga de entregar el mensaje al endpoint del WS perteneciente al WSOA que expone ese servicio (2), WSOA transforma el mensaje de SOAP a ACL (3) usando el "Message Translator", y remite el resultado al agente SA al cual sirve de fachada (4). En comunicaciones síncronas, WSOA quedará en espera (bloqueo del hilo de ejecución), hasta que SA emita una respuesta. SA procesa los datos e informa el resultado al WSOA (5), el cual debe transformar nuevamente el mensaje de ACL a SOAP (6) usando el "Message Translator", y remitir el mensaje ya en SOAP al ESB (7), para que éste se encargue de entregarlo al servicio web que realizó el requerimiento inicialmente.

5. Experimentación

5.1. Instanciación de los dos enfoques en un caso de estudio

Para validar las propuestas de integración MAS-SOA presentadas en la sub-sección anterior, se presenta un caso de estudio, en el cual uno de los agentes de AmICL (SPA, Agente Perfil de Estudiante por sus siglas en inglés) descubre e invoca un servicio web de consciencia contextual (denóminado CARMiCLOC [53]), el cual a su vez, debe descubrir y comunicarse con los dispositivos presentes en el AmI (los cuales están caracterizados como agentes dispositivos en AmICL), para poder caracterizar el contexto (eso le permite a CARMiCLOC, descubrir y modelar el contexto). De esta manera, en este caso de estudio se requiere una comunicación bidireccional entre MAS y SOA (Agente consumen servicios web por medio de WSA, y los servicios web usan las funcionalidades de los agentes por medio de los WSOA). La información del contexto recibida por SPA puede usarse para tomar decisiones que permitan mejorar las actividades del estudiante en el AmI, de acuerdo a la situación del momento.

Se asume que CARMiCLOC ya se encuentra registrado en el SMA, así como los dispositivos del ambiente (camáras, pizarras electrónicas, sensores, etc.) caracterizados como agentes dispositivos (DA), y expuestos como servicios web a través de los WSOA, los cuales publican su archivo de descripción de servicios en el UDDI de la plataforma de servicios web. La conversación que se da entre agentes del AMS y los servicios web en la nube para la Propuesta 1, se muestra en la Fig. 12.

Inicialmente, el agente SPA hace una solicitud al agente AMA (DF), para ubicar un agente que provea un servicio de consciencia de contexto (1); AMA realiza la búsqueda en su directorio (1.1), y no lo encuentra debido a que no existen agentes con esas capacidades en el AMS, y delega la búsqueda al SMA (UDDI), para que verifique si existen servicios que provean consciencia contextual (1.2). SMA busca en su directorio (1.2.1) y consigue a CARMiCLOC, y crea un WSA que caracteriza a este servicio web (1.2.2). Este WSA se encarga de servir como proxy entre el SPA y el mismo CARMiCLOC; el Id del Agente (AID) de este WSA se envía al SPA que realizó la solicitud inicialmente (1.2.3). Nótese que todas estas conversaciones se dan en FIPA-ACL, ya que todas las entidades involucradas son agentes. Una vez que SPA tiene el AID del WSA que brinda el servicio de consciencia contextual, realiza un requerimiento de contexto (2) al WSA; por su parte, el WSA recibe el mensaje, y como está en FIPA-ACL realiza la transformación a SOAP (2.1), y lo remite al EndPoint de Servicio Web de CARMiCLOC (2.2). Como CARMiCLOC necesita tomar datos en AmICL para descubrir y modelar el contexto, debe comunicarse con los sensores y dispositivos presentes en el ambiente que le permitan realizar tal acción. Para ello, debe invocar los servicios de los Agentes que caracterizan dichos dispositivos en AmICL, que son los agentes DA. CARMiCLOC puede descubrir los DA como servicios, realizando una búsqueda de Servicios de Dispositivos en el UDDI de AmICL (2.2.1), donde encontrará los Endpoint de servicio web de los WSOA que sirven de fachada a los DA (2.2.2). De esta forma, CARMiCLOC se comunica con cada WSOA para obtener información del ambiente (2.2.3); cada WSOA transforma el mensaje de SOAP a ACL (2.2.3.1), y lo remite al DA (2.2.3.2), que es quien realmente obtiene la data del dispositivo físico, y una vez que obtiene los datos, los retorna a su WSOA en un mensaje ACL (2.2.3.3), el cual después lo transforma a un mensaje SOAP (2.2.3.4) y lo retorna al EndPoint de CARMiCLOC (2.2.4). CARMiCLOC le entrega el contexto al WSA proxy de CARMiCLOC (2.2.5), quien se encuentra esperando por el resultado. Como WSA recibe los datos en SOAP, transforma el mensaje a ACL (2.3), y remite la información al SPA (2.4), el cual lo usará para razonar y tomar decisiones, de acuerdo a la situación que indique el contexto en ese momento.

Por otra parte, la Fig. 13 muestra la conversación entre los agentes y los servicios web, para el mismo caso de estudio, usando ahora la Propuesta 2.

En este caso, el agente SPA envía un mensaje al AMA (1) para localizar un agente que provea servicios de consciencia contextual. En esta propuesta, en AMA se encuentran registrados tanto los agentes del MAS como los agentes de servicios web (WSA). Es así que AMA busca en su directorio

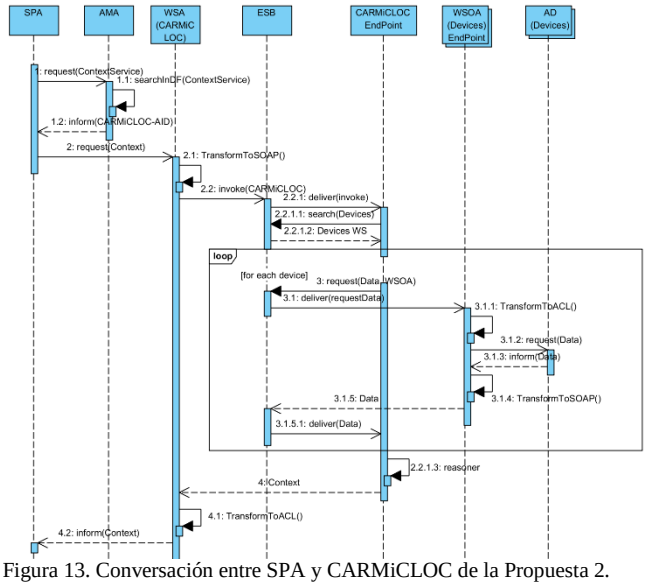


Figura 13. Conversación entre SPA y CARMiCLOC de la Propuesta 2. Source: Los autores.

de servicios (1.1), y consigue al agente WSA que caracteriza al servicio web CARMiCLOC como un agente, el cual es retornado a SPA (1.2). Una vez que SPA conoce cual agente puede ayudarlo a reconocer el contexto, realiza un requerimiento de contexto a dicho agente (2), WSA, recibe la solicitud en FIPA-ACL y la transforma a SOAP (2.1), para remitirla al ESB (2.2), el cual se encargará de entregar el mensaje al EndPoint de CARMiCLOC (2.2.1), quien actúa de la misma forma que en la conversación de la Fig. 12 (el comportamiento de CARMiCLOC es el mismo para ambas propuestas). Ahora bien, todo mensaje enviado por CARMiCLOC será puesto en el ESB, y este se encargará de transportarlo a su destinatario. Es así como CARMiCLOC inicia el descubrimiento de los servicios web de dispositivos presentes en el ambiente (2.2.1.1), y es el ESB quien usa su UDDI para localizar los servicios y entregar a CARMiCLOC los Endpoint de los WSOA que sirven de fachada a todos los dispositivos en AmICL (2.2.1.2). Con esta información, CARMiCLOC inicia la solicitud de datos, para recabar la información del ambiente que le permita descubrir el contexto, poniendo un mensaje en el ESB (3) para solicitar la información a cada WSOA. El ESB entregará el mensaje al WSOA correspondiente (3.1), quien a su vez, lo transformará a un mensaje ACL (3.1.1), y lo remitirá al AD que caracteriza (3.1.2). El AD tomará los datos requeridos del dispositivo físico, y los retornará a su WSOA en un mensaje ACL (3.1.2). Por su parte, el WSOA transforma el mensaje a SOAP (3.1.4) y lo pone en el ESB (3.1.5), para que sea entregado a CARMiCLOC (3.1.5.1). Una vez que éste obtiene toda la información necesaria, inicia el proceso de modelado (2.2.1.3), para finalmente distribuir el contexto al WSA correspondiente (4), el cual está a la espera de la respuesta. El WSA toma el mensaje recibido en SOAP y lo transforma a ACL (4.1), enviando el resultado al SPA (4.2) que inició el proceso.

5.2. Comparación preliminar entre los dos enfoques

Las propuestas presentadas en las subsecciones anteriores, mezclan los enfoques de integración discutidos en la sección 3. (Agente Proxy y SoMAS). La diferencia principal entre ambas, radica en que la segunda propuesta utiliza un ESB, que se hará cargo de enrutar los mensajes desde el endpoint solicitante hacia el enpoint que presta el servicio, sin vincular el emisor del mensaje con el recibidor (acoplamiento débil); y de hacer transformaciones de mensajes, posibilitando la integración con otras tecnologías web, como es el caso de los servicios web REST, cuyo protocolo de comunicación no es SOAP. De igual manera, el ESB tiene componentes para brindar seguridad a las comunicaciones, así como para asegurar la calidad del servicio (QoS), entre otras cosas. Así, la segunda propuesta podría brindar más beneficios en la integración de MAS con SOA.

Sin embargo, en la primera propuesta el número de mensajes intercambiados y elementos que intervienen en las comunicaciones generalmente es menor; Por ejemplo, en las conversaciones de la Fig. 12 (primera propuesta) y Fig. 13 (segunda propuesta), para la primera propuesta se intercambian 13 mensajes, mientras que en la segunda se requieren 15, lo que podría indicar que las comunicaciones en la primera propuesta tendrán mejor rendimiento. Con respecto a los requerimientos de cómputo, en ambas propuestas los agentes WSOA, y WSA tienen los mismos requerimientos computacionales; sin embargo, los agentes AMA y SMA de la primera propuesta requerirán un mayor costo computacional al momento de realizar las búsquedas, pero equivalente al necesitado por el AMA de la segunda propuesta, ya que las tareas del SMA de la primera propuesta pasan a formar parte del AMA en la segunda propuesta. Adicionalmente, el agente SDA de la segunda propuesta requerirá revisar periódicamente el UDDI del ESB, para determinar cambios y hacerlos efectivos en el MAS. De forma similar, el ESB requerirá un costo computacional adicional al momento de usar elementos de ruteo, transformación, entre otros;

Por otra parte, la primera propuesta utiliza el agente SMA, cuyas funciones son administrar el UDDI y los agentes WSA (creación, búsqueda, composición, orquestación de WSA, entre otros); en cambio, en la segunda propuesta muchas de esas tareas son realizadas por el propio ESB (composición, orquestación, etc.), y en parte por el SDA (creación, modificación, entre otros), pero la ubicación de WSA queda delegada al AMA, tal que los agentes del MAS pueden ubicar a los WSA como si de otro agente de la plataforma se tratase.

En ambas propuestas, el agente CCA es el encargado de definir cuando un agente del MAS puede establecer comunicación con un WSA, dependiendo de la ocupación que éste tenga. Además, es él fundamental para garantizar el mapeo M a N entre servicios y agentes. Los objetivos y tareas de los agentes WSOA y WSA en ambas propuestas son los mismos. El WSOA sirve como puente en la dirección SOA-MAS, mientras que el SMA es el puente de comunicación en la dirección MAS-SOA.

En general, analizando criterios como pase de mensajes y agentes participantes en las propuestas, para los casos de descubrimiento y consumo de servicios web y uso de las capacidades de los agentes desde un servicio web (son los casos más importantes), tenemos que:

Para que un agente pueda descubrir un servicio web, en la primera propuesta se utilizan 8 pasos, mientras que en la segunda se requieren 6 (ver las Figs. 3, 8, 12, 13). Además, en la primera propuesta intervienen 5 agentes, mientras que en la segunda intervienen 4. Finalmente, en la primera propuesta los WSA se deben buscar tanto en el DF como en el UDDI, mientras que en la segunda solo se busca en el DF (ver Figs. 3, 8).

Con respecto a la invocación del servicio web en sí, en la primera propuesta se utilizan 6 pasos mientras que en la segunda se utilizan 10 (ver las Figs. 4, 9, 12, 13). De forma similar, en la primera propuesta intervienen 2 agentes, los módulos de transformación de mensaje y el servicio web cliente, mientras que en la segunda intervienen, además, el ESB y sus componentes de ruteo y transformación de mensajes.

Para que un WS haga uso de una tarea de un agente (consuma), en la primera propuesta se utilizan 8 pasos e intervienen 2 agentes y el servicio web cliente; mientras que en la segunda propuesta se utilizan 8 pasos, intervienen 2 agentes, el WS cliente, y los componentes del ESB de ruteo y transformación de mensajes (ver Figs. 5, 11-13).

5.3. Simulaciones

Con el fin de realizar una comparación cuantitativa de ambas propuestas en términos de rendimiento, se realizaron un conjunto de simulaciones. El modelo de simulación comprende los nodos necesarios para medir el comportamiento del sistema real. Estos nodos puede ser agentes (SMA, WSA, WSOA, Otros Agentes del Sistema, etc.) o elementos de hardware y software como: internet, red local, traductor de mensajes, endpoint de servicios web, entre otros. Las variables consideradas en las simulaciones son las siguientes: a) Número de agentes de AmICL que ofrecen sus funcionalidades como servicios b) Número de servicios web registrados en el UDDI (Servicios en la nube usables por los agentes) c) Número máximo de agentes WSA soportados por la plataforma, el cual depende de los recursos del SMA d) Tiempo medio de generación de nuevos requerimientos de servicios web, por parte de los agentes (Agente→WS) e) Tiempo medio de generación de nuevos requerimientos de servicios a los agentes, por parte de los servicios web (WS→Agente).

También existen otras variables en la simulación que se mantuvieron constantes, ya que afectan a ambas propuestas por igual e influirán de la misma manera en ambos casos. Estás variables son: a) Tiempo medio de atención de requerimientos por parte de los servicios web (tiempo que tarda un servicio web en atender una solicitud) b) Desviación estándar del tiempo de atención de requerimientos por parte de los servicios web c) Tiempo medio de atención de requerimientos por parte de los agentes (tiempo que tarda un agente en atender una solicitud) d) Desviación estándar del tiempo de atención de requerimientos por parte de los agentes e) Tiempo promedio de atención de solicitudes del agente SMA f) Tiempo promedio de traducción de mensaje (SOAP-ACL, ACL-SOAP) g) Latencia de Internet h) Latencia de la red local.

Se diseñaron tres escenarios de simulación que se detallan más adelante. Para todos los escenarios se estableció un tiempo de simulación de 1800 segundos y un máximo de agentes WSA de 2000, es decir, la plataforma SMA no puede crear más de 2000 agentes WSA. Eso significa que, si hay muchas invocaciones concurrentes de servicios web, y se supera el valor máximo de WSA soportados, las solicitudes siguientes serán rechazadas, hasta que el número de WSA baje nuevamente.

Las métricas consideradas en estos escenarios, son las siguientes: a) **Tiempo total de atención promedio de los servicios en la nube**: es el tiempo promedio que dura una solicitud de servicio web en ser procesada, esto incluye el pase de mensaje entre el agente solicitante y el SMA, la búsqueda en el UDDI, el pase de mensajes entre el agente solicitante y el WSA, la invocación del servicio, el envío de los datos a través de internet, la traducción de los mensajes (ACL/SOAP, SOAP/ACL), y el retorno de los resultados por parte del servicio. b) **Tiempo total de atención promedio de las tareas de agentes como servicios**: Es el tiempo promedio que tarda una solicitud a una tarea de agente en ser procesada, esto incluye el tiempo de búsqueda del servicio de agente en el UDDI, el pase de mensajes a través de internet desde los servicios de la nube hasta los agentes WSOA, el pase y traducción de mensajes (SOAP/ACL, ACL-SOAP) entre el WSOA y el agente destino, y el cálculo y el retorno de los resultados hasta el servicio web solicitante. c) **Número de WSA creados**: Indica el número de agentes WSA que se deben crear para atender todas las solicitudes que llegan al sistema, lo cual depende directamente de los recursos del propio SMA. Esta variable nos ayuda no solo a medir la cantidad de recursos que se necesitan para poner en marcha el sistema, sino, además, cómo se comporta la concurrencia en la invocación de servicios. d) **Otras variables**: Para realizar análisis más exhaustivos de las simulaciones, también se tomarán en cuenta variables, como longitud de la cola de espera en los nodos, el tiempo de atención de cada uno de los nodos de la simulación, así como la cantidad de solicitudes atendidas en cada nodo.

Escenario 1: En este escenario se probará la comunicación en el sentido MAS-SOA, donde son los agentes del sistema los que invocan servicios de la nube por medio del uso de los mecanismos de integración presentados en las dos propuestas. Se probará cómo se comporta el sistema con pocos servicios registrados (10), regular cantidad de servicios registrados (80), y muchos servicios registrados (1000). También se variará el número de solicitudes por segundo, empezando con 2 solicitudes por segundo, luego 4 solicitudes por segundo, 8 solicitudes por segundo, y terminando con casos extremos de 50 y 100 solicitudes por segundo. Al utilizar muchas solicitudes por segundo, también se prueba el sistema ante llamadas concurrentes de servicios, de tal forma que podamos observar cómo crece la cantidad de agentes WSA para poder atender todas las solicitudes.

En la Fig. 14, se muestra la comparación de ambas propuestas, tomando en cuenta el tiempo de atención total promedio de cada solicitud de servicio hecha por parte de los agentes.

Se puede observar claramente, que los tiempos de atención siempre son mayores en la segunda propuesta y a medida que aumenta el número de solicitudes de servicios

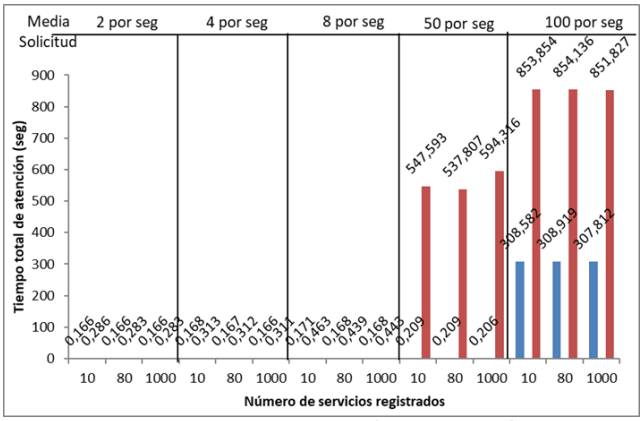


Figura 14. Tiempo total promedio de atención respecto al número de servicios en el UDDI (azul propuesta 1, rojo propuesta 2).
Source: Los autores.

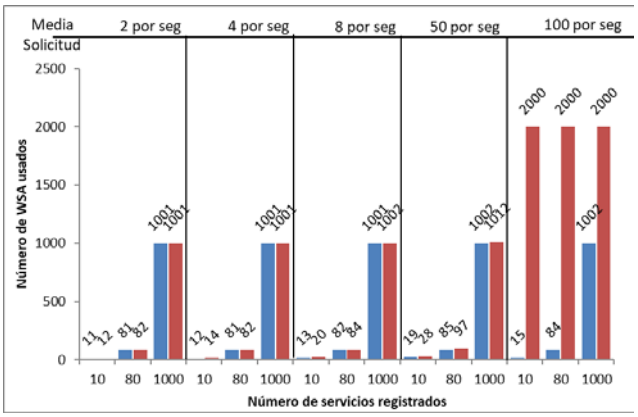


Figura 15. WSAs requeridos respecto del número de servicios en el UDDI (azul propuesta 1, rojo propuesta 2).
Source: Los autores.

por parte del SMA, aumenta también el tiempo de atención total de las solicitudes, siendo mayor la discrepancia en el caso de la Propuesta 2. También se logra apreciar que ambas propuestas son independientes del número de servicios registrados en el UDDI con respecto al tiempo de atención, ya que el tiempo se mantiene más o menos constante para 10, 80 y 1000 servicios para una misma media de solicitud. Por ejemplo, para una media de 2 solicitudes por segundos, el tiempo total de atención promedio en la primera propuesta siempre es de 0,166; mientras que para la segunda propuesta es de 0,283; independientemente del número de servicios registrados en el UDDI. Eso significa que podemos agregar o quitar servicios del UDDI, sin afectar el rendimiento de la plataforma.

De la Fig. 14 también se observa que los tiempos de atención promedio se mantienen por debajo de 1 segundo en ambas propuestas, para medias de solicitud de 2, 4 y 8 solicitudes por segundo, lo cual es bueno. Sin embargo, para los casos extremos de 50 y 100 solicitudes por segundos, se observa que para la segunda propuesta el tiempo total de atención promedio, crece considerablemente, tomando valores de más de 500 y 800 segundos, respectivamente; mientras que la primera propuesta solo se ve afectada cuando la media de solicitudes es de 100 solicitudes por segundo.

Analizando un poco más los resultados de la simulación, se aprecia, en el caso de la primera propuesta, que el nodo que representa la comunicación con la nube (internet) se encuentra sobresaturado debido a la gran cantidad de datos enviados por el canal de comunicación, mientras que, para la segunda propuesta, están sobresaturados tanto el nodo de comunicación con la nube como el nodo que representa al ESB, lo cual deriva en un incremento del tiempo total de atención promedio.

Por otra parte, en la gráfica de la Fig. 15, se analiza la dependencia de la plataforma, con respecto al número de agentes WSA necesarios para atender las solicitudes de servicios (como se indicó anteriormente, se estableció un límite superior de 2000 WSAs).

En este caso, se puede apreciar que ambas propuestas no dependen en gran medida de los agentes WSA, pero si requieren tener suficientes recursos para contar con al menos un WSA por cada servicio registrado en el UDDI, puesto que la cantidad de WSA adicionales que se requieren para atender solicitudes en paralelo en este escenario es poco. Note que si hay 10 servicios registrados se requieren 12 o 13 WSA para cada propuesta, para 80, se requieren entre 81 y 86, y para 1000 se requieren menos de 1015 agentes WSA, manteniéndose estos valores prácticamente independientes del número de solicitudes de servicio, lo que también indica que el sistema puede lidiar con la concurrencia en la invocación de servicios, sin ningún problema. El único caso donde se presenta una variación considerable del número de agentes WSA, es para la segunda propuesta cuando la media de solicitudes es de 100 solicitudes por segundo. En este caso, el sistema alcanza el valor máximo establecido de 2000 WSAs.

Al analizar en detalle el proceso de simulación, se nota que al estar congestionados el nodo ESB y el nodo de comunicación con la nube, se empiezan a generar muchas solicitudes paralelas que se van acumulando, hasta alcanzar el límite de 2000 WSA, debido a que ningún WSA termina su requerimiento (el tiempo total de atención promedio es superior a 800 segundos), y se están generando 100 solicitudes cada segundo. A partir de allí el sistema empezará a denegar las solicitudes de servicio, puesto que no se cuentan con los recursos para atenderlas.

Escenario 2: En este segundo escenario se busca probar la comunicación SOA-MAS, donde los servicios en la nube invocan las tareas de los agentes del sistema como servicios. Se probará cómo se comporta el sistema con pocos agentes que ofrecen sus capacidades como servicios (10), una cantidad regular (80), y con muchos agentes (1000). De igual manera, se variará el número de solicitudes por segundo, tomando valores de 2, 4, 8, 50 y 100 solicitudes por segundo.

La Fig. 16, muestra una gráfica en la cual se puede deducir rápidamente que la propuesta 2 tiene problemas con el tiempo promedio total de servicio de los agentes, cuando el número de solicitudes por segundo es superior a 8, llegando a superar los 400 segundos, independientemente del número de agentes que ofrecen sus tareas como servicios, lo cual es inconcebible para sistemas que requieren una respuesta inmediata.

De forma similar, la propuesta 1 presenta problemas cuando la media de solicitudes es de 100 solicitudes por segundo,

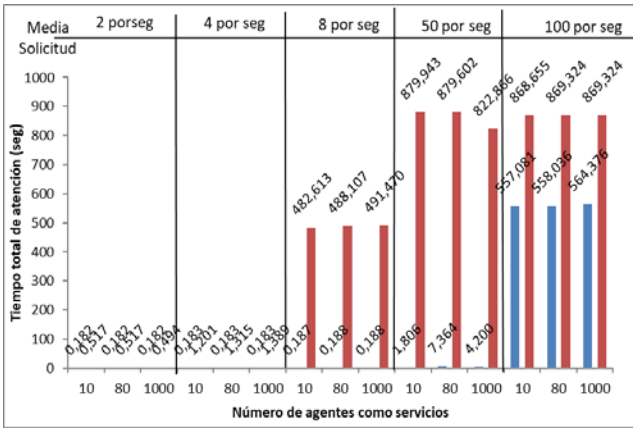


Figura 16. Tiempo de atención promedio respecto del número de agentes que ofrecen tareas como servicios (azul propuesta 1, rojo propuesta 2).
Source: Los autores.

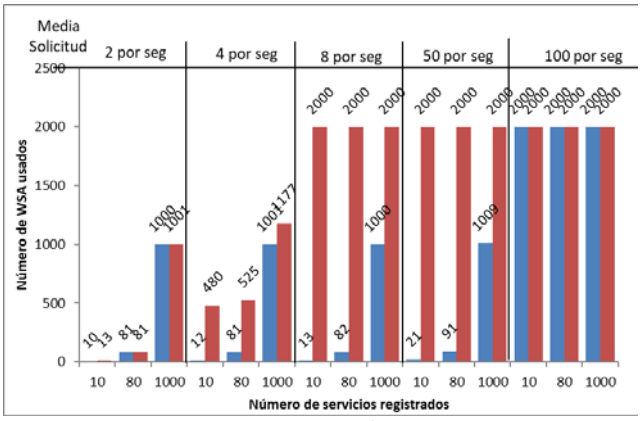


Figura 18. WSAs requeridos respecto del número de servicios en el UDDI (azul propuesta 1, rojo propuesta 2).
Source: Los autores.

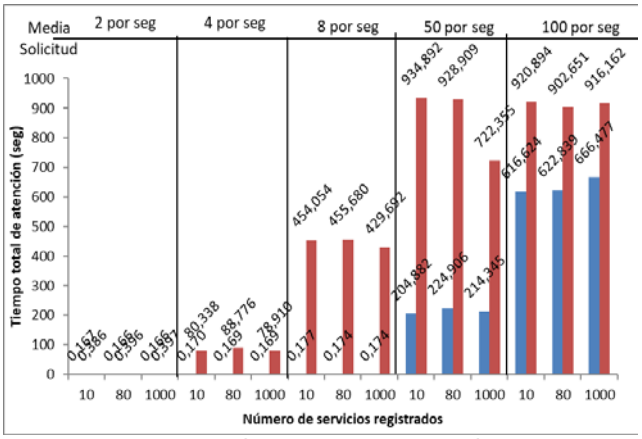


Figura 17. Tiempo de atención promedio respecto del número de servicios en el UDDI (azul propuesta 1, rojo propuesta 2).
Source: Los autores.

alcanzando tiempos superiores a los 500 segundos, aunque nunca tan malo como la propuesta 1. En general, cuando el número de solicitudes por segundo es inferior a 50, la propuesta 1 se comporta de manera adecuada, mientras que la propuesta 2 lo hace cuando el número de solicitudes por segundo es menor a 8, ya que se observa que el tiempo total de atención promedio es inferior a 2 segundos.

Al analizar más a fondo los resultados de la simulación, se observa nuevamente que el problema se presenta en el nodo de comunicación con la nube para la propuesta 1, y para la propuesta 2 se observa congestionamiento en los nodos ESB y de comunicación con la nube, lo cual hace que los tiempos de atención totales aumenten considerablemente cuando la red se satura.

Escenario 3: En este escenario se prueba la comunicación en ambos sentidos (bidireccional), con el fin de verificar si se afectan entre sí y se generan conflictos. Los valores que se toman para las variables son los mismos de los escenarios anteriores, solo que esta vez actúan en conjunto, indicando que habrá el doble de solicitudes, ya que se generan tanto solicitudes de servicios web, como solicitudes de tareas de agente como servicio.

Una vez realizadas las simulaciones se crearon tres gráficas, que se presentan en las Fig. 17-19.

En la Fig. 17 se muestra el comportamiento del sistema respecto del número de servicios registrados en el UDDI y el tiempo total de atención promedio. Se aprecia en esta figura, que cuando la media de solicitud de servicios es baja (2 solicitudes por segundos), ambas propuestas tienen un comportamiento aceptable, incluso similares, en cambio, cuando la media de solicitud es regular (8 solicitudes por segundo) o alta (50 y 100 solicitudes por segundo), la propuesta 2 comienza a presentar resultados muy poco aceptables, pues el tiempo de atención se incrementa considerablemente, mientras que la propuesta 1 comienza a presentar problemas para medias de solicitudes altas (50 y 100 solicitudes por segundo).

Analizando más a fondo los resultados, se consigue que nuevamente para la propuesta 2, el nodo ESB y el nodo de comunicación con la nube están saturados, mientras que para la propuesta 1 solo el nodo de internet se congestiona, lo cual produce que los tiempos de atención aumenten, debido a la cantidad de datos que deben pasar por la red. En este escenario esto aún más ocurre, debido a que están activos ambos sentidos de la comunicación, lo que significa que están pasando el doble de datos por la red que en los escenarios 1 (comunicación solo en sentido MAS-SOA) y 2 (comunicación solo en sentido SOA-MAS). Debido a lo anterior, los problemas en este escenario empiezan con medias de solicitud más bajas, con respecto a los dos escenarios anteriores. De igual manera, en este escenario, la propuesta 2 también presenta un mayor tiempo total promedio de atención con respecto a la propuesta 1, ya que los datos deben pasar primero por el ESB para que sean reenviados a los destinos correspondientes.

Análogamente, en la Fig. 18, donde se presenta el número de WSAs necesarios para cumplir con los requerimientos de consumo de servicios web por parte de los agentes.

De la Fig. 18 se tiene que para la propuesta 1, el número de WSAs requeridos es muy cercano al número de servicios registrados en el UDDI en todos los casos, excepto para una media de solicitud de 100 solicitudes por segundo, donde el sistema alcanza el límite máximo de 2000 WSA. Sin embargo, para la propuesta 2 el número máximo de WSA es

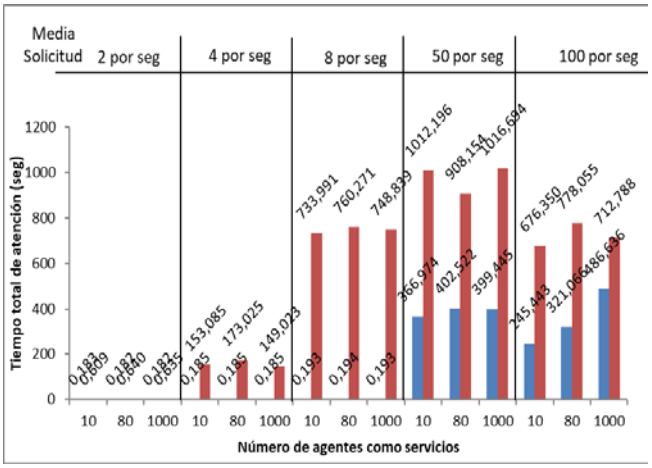


Figura 19. Tiempo de atención promedio respecto del número de agentes que ofrecen tareas como servicios (azul propuesta 1, rojo propuesta 2). Source: Los autores.

alcanzado para cuando la media es de 8 solicitudes por segundo. Esto se debe al congestionamiento que ocurre en los nodos ESB y comunicación con la nube, lo cual provoca que el tiempo total de atención promedio se eleve, ya que se generan muchas solicitudes concurrentes, debido a que los WSA no terminan de atender una solicitud cuando ya se genera otra gran cantidad, lo cual provoca que se vayan acumulando las solicitudes y el número de WSA se dispare hasta alcanzar su valor máximo.

Por otro lado, respecto a la comunicación SOA-MAS, se observa (ver Fig. 19) que en el caso de la primera propuesta los tiempos se mantienen bajos cuando la media de solicitud es menor a 8 solicitudes por segundo, con valores muy similares a los del segundo escenario. En cambio, en el caso de la propuesta 2, los tiempos de respuesta se mantienen bajos solo cuando la media es de 2 solicitudes por segundo, pero cuando la media cambia a 4 solicitudes por segundo o más, los tiempos de respuesta pasan a ser inaceptables.

Revisando con mayor detalle la simulación, se observa, que el tiempo total de atención también se ve afectado debido al retardo generado en los nodos ESB y comunicación con la nube, viéndose mayormente afectada la segunda propuesta, debido a la inclusión del ESB, donde todos los datos de la comunicación deben pasar a través del bus de servicios, para que sean ruteados a su destino final.

Según estos resultados, se puede deducir que la propuesta 1 tiene siempre mejor rendimiento que la propuesta 2, puesto que siempre los tiempos de atención promedios y el número de WSA máximo requerido siempre son menores que para el caso de la propuesta 2. A pesar que la propuesta 1 se ve afectada cuando el número de solicitudes es muy alto (100 solicitudes cada segundo), el problema se debe mayormente al canal de comunicación que se satura debido a la alta cantidad de datos que deben pasar a través de él, y no a la propuesta en sí misma. En cambio, para la propuesta 2, siempre los tiempos son superiores a los de la propuesta 1, debido a que el ESB genera un retardo para procesar y enrutar los datos, lo que afecta al tiempo de atención total.

En general, se observa que el rendimiento de la propuesta 1 es mejor el de la propuesta 2.

Table 1.
Comparación de las propuestas con trabajos previos.

# Car.	[20,31,32]	[33]	[34]	[36]	[35,37,43]	Prop. 1 y 2
1	✓	×	✓	✓	✓	✓
2	✓	✓	✓	✓	×	✓
3	×	✓	×	×	n/a	✓
4	×	×	✓	×	✓	✓
5	×	✓	×	×	✓	✓
6	✓	×	×	×	✓	✓

Source: Los autores.

5.4. Comparación con trabajos previos

Debido a que los autores de las propuestas anteriores, no presentaron resultados cuantitativos, la comparación de las propuestas se hará en forma cualitativa, en base a lista de 6 características presentadas al inicio de la sección 4. El resultado se resume en la Tabla 1, donde se observa que los trabajos previos a esta investigación no cumplen con todas las características deseadas para la integración MAS-SOA. Además, algunos son muy poco automatizados, y otros no saben cómo lidiar con la naturaleza sin estado/con estado de MAS y SOA.

La investigación que cumple con la mayoría de requerimientos es [35, 37, 43], pero la misma no es compatible con el estándar FIPA-ACL, limitando la integración con otros MAS que sí lo sean.

Por su parte, las propuestas 1 y 2 realizadas en esta investigación poseen todos los requerimientos planteados, lo cual se mostró en las anteriores subsecciones de esta sección. Sin embargo, en estás subsecciones no queda muy claro cómo resolver el problema para mapeo M a N. El mismo se resuelve de la siguiente forma:

1. Si un agente cualquiera (RA1) del MAS está consumiendo un servicio web caracterizado como WSA1, y algún otro agente (RA2) necesita consumir el mismo servicio web; en el momento que el agente de servicio sea solicitado al CCA, éste se dará cuenta que el WSA1 está ocupado atendiendo otro requerimiento, por lo cual debe solicitarle al SMA (en la primera propuesta) o al AMA (en la segunda) que cree un nuevo agente WSA2 que caracterice el mismo servicio; de esta forma, WSA2 podrá atender los requerimientos del RA2, posibilitando así la concurrencia al servicio.
2. Para controlar que no haya un crecimiento exponencial de agentes de servicio (WSA), el AGS o AMA (dependiendo de la propuesta), debe eliminar el registro de los WSA en el MAS, cuando se determine que tienen un tiempo específico sin atender solicitudes.
3. De manera similar se procedería con los agentes WSOA, cuando dos servicios intenten comunicarse con un mismo agente en un mismo momento.

6. Consideraciones finales

Se puede ver que ambas propuestas permiten la integración bidireccional MAS-SOA; igualmente, sus arquitecturas son FIPA-compliant. De igual forma, también son orientadas a servicios, ya que por medio de los WSOA se estará usando el paradigma SOA. Los agentes Gateway (WSA y WSOA) se crean

de manera automática, cuando servicios y agentes son registrados en los directorios respectivos. La transformación entre comunicaciones síncronas y asíncronas se hace en los agentes WSA y WSOA. El componente "Message Translator" se hará cargo de transformar los elementos semánticos que acompañan los mensajes, para que sean entendibles tanto por servicios web como por agentes.

En el mismo sentido, el mapeo M a N se realiza al crear varios agentes WSA y WSOA para un mismo servicio web o agente, eso se realizaría cuando el agente CCA determine que el WSA (o el WSOA) que caracteriza a un servicio (o agente) no se encuentra disponible. Finalmente, la arquitectura propuesta fue especificada de forma independiente a la implementación ya que no está ligada a ninguna librería particular, y a la hora de implementarla será cuando se decida que librerías deben utilizarse.

Por su parte, cada propuesta permite a los agentes de AmICL consumir servicios en la nube, así como exponer sus funcionalidades como servicios web (integración bidireccional de AmICL con la nube). Por otro lado, debido a que los agentes necesarios para integrar MAS y SOA son los agentes AMA, CCA, WSA, SMA y WSOA para la primera propuesta, y AMA, CCA, WSA, SDA y WSOA para la segunda propuesta, y debido a que AMA y CCA son abstracciones del estándar FIPA (en JADE por ejemplo, AMA es el DF y CCA es el CCA proveído por el framework), estás propuestas pueden ser extendidas a cualquier plataforma de despliegue de sistemas multi-agente que requiera servirse de la integración SMA y SOA. A dichas plataformas, solo se les deberá incorporar (implementar) los respectivos agentes establecidos en cada propuesta no considerados por FIPA (por ejemplo, en la propuesta 1 a WSA, SMA y WSOA).

De acuerdo a los experimentos realizados, se puede concluir que la primera propuesta brinda un mejor rendimiento, en cuanto a tiempos de respuesta y consumo de recursos del sistema, la cual podría utilizarse en AmIs donde el número de solicitudes no sea tan elevado y la latencia de internet sea muy baja.

El trabajo futuro está orientado a mejorar los tiempos de respuesta ante números de solicitudes elevados, para lidiar con problemas de tiempo real y latencia de internet altas, mediante la incorporación de un componente basado en Fog Computing, que servirá para poder usar este componente en sistemas a gran escala, como es el caso de las ciudades inteligentes.

Referencias

[1] Mhiri, F. and Ratté, S., AARTIC: development of an intelligent environment for human learning. SIGCSE Bulletin, 41(3), pp. 359-359, 2009. DOI: 10.1145/1562877.1563001

[2] Mikulecký, P., Smart environments for smart learning, Proceedings of the 9th International Scientific Conference on Distance Learning in Applied Informatics DIVAI, Sturovo, Slovakia, 2012.

[3] Shi, Y., Qin, W., Suo, Y. and Xiao, X., Smart classroom: bringing pervasive computing into distance learning [Online]. pp. 881-910, 2010. Available at:https://goo.gl/7VK6Bc

[4] Stenvall-Virtanen, S. and Nordell, K., Smart environments: technology, protocols and applications. Tech. Rep.: University of Turku, Turku, Finland, 2014.

[5] Duraes, D., Castro, D., Bajo, J. and Novais, P., Modelling an intelligent interaction system for increasing the level of attention, Proceedings of the International Symposium on Ambient Intelligence [Online]. pp. 210-217, 2017. Available at: https://goo.gl/gGVzkq

[6] Bai, Y., Shen, S., Chen, L. and Zhuo, Y., Cloud learning: A new learning style, Proceedings of the International Conference on Multimedia Technology, 2011. DOI: 10.1109/ICMT.2011.6002268

[7] Castillo-Rodríguez, C. and Rios-Moyano, S., Promoción del c-learning a través del uso de herramientas, software y entornos virtuales. Historia y Comunicación Social [En línea]. 18(1), pp. 305-317, 2013. Disponible en: https://goo.gl/3TWifL

[8] IBM, Introducción a SOA y servicios web [En línea]. 2007. [fecha de referencia: Febrero 27 de 2018]. Disponible en: https://goo.gl/aQSnjZl.

[9] Serrano, N., Hernantes, J. and Gallardo, G., Service-oriented architecture and legacy systems. IEEE software, 31(5), pp. 15-19, 2014. DOI: 10.1109/MS.2014.125

[10] Sanchez, M., Aguilar, J., Cordero, J. and Valdiviezo, P., A smart learning environment based on cloud learning. International Journal of Advanced Information Science and Technology (IJAIST), 39(39), pp. 39-52, 2015.

[11] Sánchez, M., Aguilar, J., Cordero, J. and Valdiviezo, P., Basic features of a reflective middleware for intelligent learning environment in the cloud (IECL), Proceedings of the Asia-Pacific Conference on Computer Aided System Engineering, 2015. DOI: 10.1109/APCASE.2015.8

[12] Valdiviezo, P., Cordero, J., Aguilar, J. and Sánchez, M., Conceptual design of a smart classroom base on multiagent system, Proceedings of the International Conference on Artifitial Intelligence (ICAI'15), 2015.

[13] Aguilar, J., Sánchez, M., Cordero, J., Valdiviezo-Díaz, P., Barba-Guamán, L. and Chamba-Eras, L., Learning analytics tasks as a services in smart classrooms. International Journal of Universal Access in the Information Society [Online]. pp. 1-17, 2017. Available at: https://goo.gl/YV4xWN.

[14] Aguilar, J., Sánchez, M., Valdiviezo, P. and Cordero, J., Mecanismos de coordinación en un salón inteligente, Proceedings of the 6to Congreso Iberoamericano de Estudiante de Ingeniería Eléctrica, 2015.

[15] Sánchez, M., Aguilar, J., Cordero, J., Valdiviezo, P., Barba-Guamán, L. and Chamba-Eras, L., Cloud computing in smart educational environments: application in learning analytics as service. New advances in information systems and technologies, 444(1), Springer International Publishing, pp. 993-1002, 2016. DOI: 10.1007/978-3-319-31232-3_94

[16] FIPA. IEEE [Online]. 2013. [date of reference: Febrary 27th of 2018]. Available at: http://www.fipa.org.

[17] Deen, S.M., Agent-based manufacturing: advances in the holonic approach. Springer, 2013.

[18] Aguilar, J., Ríos, A., Hidrobo, F. and Cerrada, M., Sistemas multiagentes y sus aplicaciones en automatización industrial, 2nd ed., Mérida: Talleres Gráficos, Universidad de Los Andes, 2013.

[19] Lopes, F. and Coelho, H., Negotiation and argumentation in multi-agent systems: Fundamentals, theories, systems and applications. Bentham Science Publishers, 2014.

[20] Greenwood, D., Buhler, P. and Reitbauer, A., Web service discovery and composition using the web service integration gateway, Proceedings of the IEEE International Conference on e-Technology, e-Commerce and e-Service, 2005. DOI: 10.1145/1329125.1329458

[21] Sánchez, A., Villarrubia, G., Zato, C. and Chamoso, P., A gateway protocol based on FIPA-ACL for the new agent platform PANGEA. Trends in Practical Applications of Agents and Multiagent Systems [Online]. Springer, pp. 41-51, 2013. Available at: https://goo.gl/yHNNKJ

[22] Marin, C., Monch, L., Leitao, P., Vrba, P., Kazanskaia, D., Chepegin, V., Liu, L. and Mehandjiev, N., A conceptual architecture based on intelligent services for manufacturing support systems, Proceedings of the IEEE International Conference on Systems, Man, and Cybernetics (SMC), pp. 4749-4754, 2013. DOI: 10.1109/SMC.2013.808

[23] Singapogu, S.S., Gupton, K. and Schade, U., The role of ontology in C2SIM, Proceedings of the 21st ICCRTS, London, 2016.

[24] Geetha, R. and Shunmuganathan, K., Intelligent query processing from biotechnological database using co-operating agents based on FIPA standards and Hadoop, in a secure cloud environment, Proceedings of the 4th International Conference on Advanced Computing and Communication Systems [Online]. pp. 1-4, 2017. Available at: https://goo.gl/HwSVBz

[25] Oracle, Simple object access protocol overview [Online], Oracle Corporation, 2001 [date of reference: February 27th of 2018]. Available at: https://goo.gl/MR1ZJv.

[26] De-la-Cruz, A., Una aproximación MDA para la conversión entre servicios web SOAP y RESTful, Universidad complutense de Madrid,

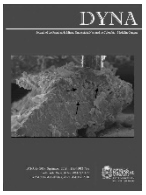
Madrid, 2013.
[27] López, M., Carrillo, R. and Martínez, P., Subsistema Informático para la Interoperabilidad de la Plataforma SIUDERLAN desarrollada en la empresa ETECSA. Universidad y Sociedad, 8(4), pp. 100-105, 2016.
[28] Tang, J., Liu, S.L., Gu, Z. and Gaudiot, J.L., Acceleration of xml parsing through prefetching. IEEE Transactions on computers, 62(8), pp. 1616-1628, 2013. DOI: 10.1109/TC.2012.88
[29] W3C, Extensible Markup Language (XML) [Online], W3C, 2016 [date of reference: February 27th of 2018]. Available at: https://goo.gl/9FLm2E
[30] Fielding, R. and Reschke, J., Hypertext transfer protocol (HTTP/1.1): Message syntax and routing [Online], 2014 [date of reference: February 27th of 2018]. Available at: https://goo.gl/qdae7f
[31] Greenwood, D. and Calisti, M., Engineering web service-agent integration, Proceedings of the IEEE International Conference on Systems, Man and Cybernetics, 2004. DOI: 10.1109/ICSMC.2004.1399962
[32] Shafiq, M.O., Ding, Y. and Fensel, D., Bridging multi agent systems and web services: towards interoperability between software agents and semantic web services, Proceedings of the IEEE International Conference on Enterprise Distributed Object Computing Conference [Online]. 2006. Available at: https://goo.gl/JeSFGm
[33] Nguyen, X.T. and Kowalczyk, R., WS2JADE: Integrating web service with jade agents, Proceedings of Service-Oriented Computing: Agents, Semantics, and Engineering. Springer, Berlin, Heidelberg, pp. 147-159, 2007. DOI: 10.1007/978-3-540-72619-7_11
[34] Mordacci, P., Poggi, A., Tiso, C.G. and Turci, P., Using agent technology as a support for an enterprise service bus, Proceedings of the Workshop on Objects and Agents (WOA 2008), 2008.
[35] Leitão, P., Towards self-organized service-oriented multi-agent systems. In: Service orientation in holonic and multi agent manufacturing and robotics. Springer, pp. 41-56, 2013. DOI: 10.1007/978-3-642-35852-4_3
[36] Fuksa, M., Methods and tools for intelligent ESB, Czech Technical University in Prague, Prague, 2014.
[37] Pinto-Pereira, A., Towards robustness and self-organization of ESB-based solutions using service life-cycle management [Online], Polytechnic Institute of Bragança, 2014. Available at: https://goo.gl/RLDfDi
[38] Vizcarrondo, J., Aguilar, J., Exposito, E. and Subias, A., ARMISCOM: Self-healing service composition. Service Oriented Computing and Applications, 11(3), pp. 345-365, 2017.
[39] Vizcarrondo, J., Aguilar, J., Exposito, E. and Subias, A., ARMISCOM: Autonomic Reflective MIddleware for management Service COMposition, Proceedings of the Global Information Infrastructure and Networking Symposium. pp. 1-8, 2012. DOI: 10.1109/GIIS.2012.6466760
[40] Lalanda, P., McCann, J. and Diaconescu, A., Autonomic Computing, Springer, 2013.
[41] Su, Z., Song, C., Dai, L., Ge, F., Yang, R. and Biennier, F., A security criteria regulation middleware using security policy for Web Services on multi-Cloud tenancies, Proceedings of the 3rd International Conference on Computational Intelligence & Communication Technology (CICT), 2017. DOI: 10.1109/CIACT.2017.7977320
[42] Paik, H., Lemos, A., Barukh, M.C., Benatallah, B. and Natarajan, A., Web Services-SOAP and WSDL. In: Web Service Implementation and Composition Techniques. Springer, pp. 25-66, 2017, DOI: 10.1007/978-3-319-55542-3_2
[43] Colombo, A., Karnouskos, S., Mendes, J. and Leitão, P., Industrial agents in the era of service oriented architectures and cloud based industrial infrastructures. In: Industrial Agents: Emerging Applications of Software Agents in Industry, Elsevier, 2015. DOI: 10.1016/B978-0-12-800341-1.00004-8
[44] Greenwood, D., Lyell, M., Mallya, A. and Suguri, H., The IEEE FIPA approach to integrating software agents and web services, Proceedings of the 6th international joint conference on autonomous agents and multi-agent systems, 2007. DOI: 10.1145/1329125.1329458
[45] Kumar, A., Tayal, A., Kumar, S. and Bindhumadhava, B.S., Multi-agent autonomic architecture based agent-web services, Proceedings of the 16th International Conference on Advanced Computing and Communications (ADCOM), 2008. DOI: 10.1109/ADCOM.2008.4760469
[46] Buitrago, S. and Sánchez, M., VMAS-Modeller: Una aplicación visual para el modelado de sistemas multi-agentes guiado por la metodología MASINA. ReVeCom, 4(1), pp. 47-58, 2017.
[47] JADE, JAVA Agent DEvelopment Framework [Online]. 2017 [date of reference: February 27th of 2018]. Available at: http://jade.tilab.com/
[48] Kress, J., Maier, B., Normann, H., Schmeidel, D., Schmutz, G., Trops, B., Utschig-Utschig, C. and Winterberg, T., Enterprise Service Bus [Online]. Oracle Corporation, 2013 [date of reference: February 27th of 2018]. Available at: https://goo.gl/sQBzBk
[49] CXF, Apache CXF [Online]. Apache, 2007 [date of reference: February 27th of 2018]. Available at: https://cxf.apache.org/
[50] Richardson, L. and Ruby, S., RESTful web services, Beijing: O'Reilly, 2008.
[51] Postel, J. and Reynolds, J., File transfer protocol [Online]. 1985 [date of reference: February 27th of 2018]. Available at: https://goo.gl/KaiEaz
[52] Hoffman, P., SMTP service extension for secure SMTP over transport layer security [Online]. 2002 [date of reference: February 27th of 2018]. Available at: https://goo.gl/yyDGWu
[53] Jerez, M., Aguilar, J., Exposito E. and Tierry, V., CARMICLOC: Context Awareness Middleware in Cloud Computing, Proceedings of the XLI Conferencia Latinoamericana en Informática, pp. 532-541, 2015. DOI: 10.1109/CLEI.2015.7360013

M. Sánchez, recibió el título de Ingeniero de Sistemas en 2002 por la Universidad de los Andes, Venezuela. El grado de MSc. en Ciencias de la Computación por la Universidad de los Andes, Venezuela, en 2012. Actualmente, está desarrollando una tesis doctoral para obtener el título de Doctor en Ciencias Aplicadas (Ambientes Inteligentes) en la Universidad de los Andes, Venezuela. Es profesor asociado del Departamento de Ingeniería en Informática en la Universidad Nacional Experimental del Táchira, Venezuela. Sus intereses en investigación incluyen Inteligencia Artificial, Ambientes de Aprendizaje, Computación Gráfica y lenguajes de programación.
ORCID: 0000-0002-3310-3394.

J. Aguilar, recibió el título de Ingeniero de Sistemas de la Universidad de los Andes, Venezuela en 1987, el grado de MSc. en Ciencias de la Computación en 1991 de la Universite Paul Sabatier, France, y el grado de PhD en Ciencias de la Computación en 1995 de la Universite Rene Descartes, France. Realizó estudios post-doctorales en el Departamento de Ciencias de la Computación en la Universidad de Houston (1999-2000). Es profesor titular del Departamento de Ciencias de la Computación en la Universidad de los Andes, Mérida, Venezuela, y fue investigador Prometeo en la Universidad Técnica Particular de Loja, y en la Escuela Politécnica Nacional, Ecuador. Es miembro de la Academia de Ciencias de Mérida y de la IEEE CIS Technical Committee on Neural Networks. Ha publicado más de 500 artículos y 10 libros, en el campo de computación paralela y distribuida, inteligencia computacional, ciencias y gestión tecnológica, etc. Sus intereses de investigación incluyen Inteligencia Artificial, Minería semántica, Big Data, Computación Emergente y Ambientes Inteligentes.
ORCID: 0000-0003-4194-6882.

E. Exposito, es profesor titular en la Université de Pau et des Pays de l'Adour en la UFR ST Côte Basque en Anglet, Francia. En 1994, obtuvo el grado de Ing. en Ciencias de la Computación de la Universidad Centro-Occidental Lisandro Alvarado, Venezuela. En 2003, obtiene su grado de Dr. en Informatique et Télécommunications, del Institut National Polytechnique de Toulouse, Francia. En 2004, trabajó como investigador en el centro de investigación de NICTA (National ICT Australia Limited) en Sydney, Australia. Entre 2006 y 2016 trabajó como profesor asociado en INSA Toulouse e investigador en LAAS/CNRS en Toulouse, Francia. En 2010, obtuvo la Habilitation à diriger des recherches del Institut Nacional Polytechnique de Toulouse. Ha sido presidente y miembro de muchos Comités. Ha participado y coordinado diversas acciones en varios proyectos de investigación europeos y franceses, incluyendo el proyecto europeo IMAGINE relacionado con las Redes de Fabricación Dinámica. Entre 2014 y 2016, trabajó en actividades de coordinación de innovación pedagógica y fue responsable de asuntos internacionales entre el INSA de Toulouse y América Latina.
ORCID: 0000-0002-3310-3394

UNIVERSIDAD NACIONAL DE COLOMBIA
SEDE MEDELLÍN
FACULTAD DE MINAS



DYNA
http://dyna.medellin.unal.edu.co/

A planning algorithm in a class of discrete event systems

Guelvis Mata [a], Bladismir Ruiz [a], Claudia Camacho [b], Arnaldo Méndez [c], Sergio Muñoz [d] & Hicher Zambrano[e].

[a] *Facultad de Ingeniería, Universidad Nacional de Chimborazo, Riobamba, Ecuador. & Departamento de Matemáticas, Facultad de Ciencias, Universidad de Los Andes, Mérida, Venezuela. gemata@unach.edu.ec, lbruiz@unach.edu.ec*
[b] *Universidad Politécnica Territorial de Mérida, "Kléber Ramírez", Venezuela. claucamacho11@gmail.com*
[c] *Dpto. de Física y Matemáticas, Facultad de Ingeniería, Universidad Nacional Experimental Francisco de Miranda, Venezuela. mendez.arnaldo@ula.ve*
[d] *Universidade do Estado do Rio de Janeiro, Resende, Brasil. sergio.munoz@uerj.br*
[e] *Facultad de Ingeniería, Universidad de Los Andes, Mérida, Venezuela. zhichert@gmail.com*

Received: November 25th, 2017. Received in revised form: May 24th, 2018. Accepted: June 8th, 2018.

Abstract
In this article, we will propose an approach to generate a planning based on the concepts of k-interaction and consensus, showing for this an algorithm that couples the plant with these concepts. In this sense, the resulting models will be reduced and, consequently the computational complexity.

Keywords: discrete event systems; planning; k-interactions and consensus.

Un algoritmo de planificación en una clase de sistemas de eventos discretos

Resumen
En este artículo, nosotros proponemos un enfoque para generar una planificación fundamentada en los conceptos de k-interacción y consenso, mostrando para ello un algoritmo que acopla la planta con dichos conceptos. En este sentido, se reducirán los modelos resultantes y en consecuencia la complejidad computacional.

Palabras clave: sistemas de eventos discretos; planificación; k-interacciones y consenso.

1. Introducción

Los sistemas distribuidos, de transporte, logísticos, redes de comunicación, entre otros, son Sistemas de Eventos Discretos (SED), y en general las disciplinas teóricas que soportan su estudio incluyen la teoría de sistemas, la investigación de operaciones, la ciencia de la computación y la ingeniería industrial (ver [2,5,11-14,16]).

Usualmente, un SED es referido como un conjunto discreto de eventos, junto con un mecanismo que especifica las ordenes posibles en que estos pueden ocurrir. Así, la no linealidad inherente de los SED clasifica a esta clase de sistemas como complejos (ver [1]). Ellos consisten de un conjunto de procesos independientes asincrónicos (componentes) que operan concurrentemente e interactúan sobre un medio ambiente compartido (ver [9]). La planificación inapropiada de la ocurrencia de eventos puede conducir a estos sistemas a estancamientos (bloqueo del sistema), a sobreflujos de capacidad, etc, degradando la ejecución deseable para el logro de objetivos. Así, uno siempre quiere que los SED sean funcionalmente correctos en términos de propiedades deseables. En consecuencia, el análisis formal es un aspecto primordial para la verificación de dichas propiedades. Más aun, el análisis automático (enfoque algorítmico) nos permite construir herramientas de software para el estudio adecuado de la dinámica del sistema.

Actualmente, (ver [3,4,6,8,17]) la generación de una planificación en los SED esta direccionada desde:

1. La comparación de metodologías para la toma de decisiones;
2. La aplicación de hojas de cálculo;
3. La modelación de redes de Petri, para señalar las rutas del

How to cite: Mata, G., Bladismir Ruiz, G.M., Camacho, C., Méndez, A., Muñoz, S. and Zambrano, H., Un algoritmo de planificación en una clase de sistemas de eventos discretos. DYNA, 85(206), pp. 283-293, September, 2018.

© The author; licensee Universidad Nacional de Colombia.

sistema.

Cualquiera de estos enfoques es potencialmente útil para ordenar el flujo de eventos resultantes. Nosotros presentamos en este artículo un algoritmo para la construcción de una planificación basada en las nociones propias de k-interacción y consenso, entre las componentes asincrónicas de un SED. Este incluye:

a. Consenso en cada paso: expresado desde criterios de ordenamientos racionales para la toma de decisiones;
b. Solamente las componentes de cambio en el estado actual: determinadas por las k-interacciones físicamente posibles;
c. Flexibilidad y opción de reconfiguración del sistema.

Formalmente, dado un SED $\mathcal{A}$ con comportamiento dinámico $\mathcal{L}$, y una planificación $\mathcal{L}_p$ capturada por un autómata $\mathcal{H}$, $\mathcal{A} \parallel \mathcal{H}$ es el SED sujeto a la planificación, donde $\parallel$ es la composición paralela de las componentes asincrónicas de $\mathcal{A}$, condicionadas por $\mathcal{H}$ bajo consenso.

La organización de este artículo comienza con una sección de Preliminares, que incluye las definiciones básicas de la teoría de lenguajes y autómatas, las cuales constituyen fundamentalmente el piso de nuestro modelo; a saber, la composición paralela. Posteriormente, presentamos una metodología de modelación en el contexto de manufactura, que finaliza en una expresión genuina que llamaremos k-interacción. Ella junto con el concepto de consenso, apertura la base teórica que permitirá la generación de un algoritmo para la planificación de un SED. Luego, presentaremos una aplicación en sistemas de producción, para finalmente establecer algunas conclusiones y trabajos futuros.

2. Preliminares

Sea Σ un conjunto cualquiera y consideremos el conjunto Σ^* de todas las combinaciones finitas de elementos de Σ, es decir, el conjunto conformado por n-uplas $s = (\alpha_1, \alpha_2, \cdots, \alpha_n)$, con $\alpha_i \in \Sigma$, para todo $1 \leq i \leq n$. El entero n será llamado la longitud de s y es denotado por $|s|$.

Convenimos reescribir a s como $\alpha_1\alpha_2\cdots\alpha_n$, si $n > 0$, al tomar a α en lugar de la 1-upla (α). Sobre este conjunto definimos una operación binaria como sigue: si $\omega = \sigma_1\sigma_2\cdots\sigma_m$, con $\sigma_j \in \Sigma$, para todo $j > 0$; es otro elemento de Σ^*, entonces el producto $s\omega = \alpha_1\alpha_2\cdots\alpha_n\sigma_1\sigma_2\cdots\sigma_m$ es también un elemento de Σ^*. Esta operación binaria, nombrada concatenación le da a Σ^*estructura de monoide con unidad θ; la 0-upla . Cualquier subconjunto $\mathcal{L}$ de Σ^* es llamado un lenguaje sobre Σ; en consecuencia, la unión, intersección, diferencia y complemento de lenguajes son lenguajes sobre Σ. Más aún, si $\mathcal{L}_1$ y $\mathcal{L}_2$ son lenguajes sobre un alfabeto Σ entonces

$$\mathcal{L}_1\mathcal{L}_2 = \{s \in \Sigma^* : s = s_1 s_2, \quad s_1 \in \mathcal{L}_1, s_2 \in \mathcal{L}_2\} \tag{1}$$

$$\overline{\mathcal{L}_1} = \{s \in \Sigma^* : \exists\, t \in \Sigma^*, st \in \mathcal{L}_1\} \tag{2}$$

son lenguajes sobre Σ. Sea $s, t \in \Sigma^*$ será llamado un segmento de s si $s = utv$, para algunos $u, v \in \Sigma^*$. Si $u = \theta$, entonces t será llamado un prefijo de s. Por lo tanto, $\overline{\mathcal{L}_1}$ es el conjunto de todos los prefijos de todas las palabras en $\mathcal{L}_1$. Claramente, por definición, $\mathcal{L}_1 \subseteq \overline{\mathcal{L}_1}$. Cuando $\mathcal{L}_1 = \overline{\mathcal{L}_1}$ entonces $\mathcal{L}_1$será llamado prefijo-cerrado o simplemente cerrado (ver [7,10,15]).

Otro tipo de operación que se realiza con frecuencia entre lenguajes es la proyección natural, o simplemente la proyección. Formalmente, sean Σ_i, $i = 1,2,\cdots,n$; alfabetos y pongamos $\bigcup_{i=1}^{n} \Sigma_i = \Sigma$. Las proyecciones naturales, $\pi_i : \left(\bigcup_{i=1}^{n} \Sigma_i\right)^* \longrightarrow \Sigma_i^*$, $i = 1,2,\cdots,n$; son dadas por

$$\begin{aligned} &\pi_i(\theta) = \theta_i \\ &\pi_i(\alpha) = \begin{cases} \alpha, & si\ \alpha \in \Sigma_i \\ \theta_i, & si\ \alpha \notin \Sigma_i \end{cases} \\ &\pi_i(s\alpha) = \pi_i(s)\pi_i(\alpha), \\ &\text{para cualquier } s \in \left(\bigcup_{i=1}^{n} \Sigma_i\right)^* \ \ y\ \ \alpha \in \bigcup_{i=1}^{n} \Sigma_i \end{aligned} \tag{3}$$

Sea Σ un alfabeto. Un Generador Finito Determinístico (GFD) $\mathcal{G}$ sobre Σ (Σ-generador finito), es un séxtuple $(Q, \Sigma, \delta, \mathcal{E}, i, T)$, donde Q es un conjunto finito de estados, i y $T \subseteq Q$ llamados respectivamente estado inicial y conjunto de estados finales, δ es un subconjunto de $Q \times \Sigma \times Q$ de eventos y $\mathcal{E}$ es un subconjunto de $Q \times \Sigma$ de eventos activos (o habilitados) sobre los elementos de Q (ver [7]). Un evento (q, σ, p) será denotado $q \overset{\sigma}{\rightarrow} p$. Así, obtenemos un grafo dirigido ponderado: los estados son los vértices y los eventos determinan los arcos, con marca en Σ. El conjunto de todas las trazas $c: i \longrightarrow q$, $q \in Q$ es denotado por $\mathcal{L}(\mathcal{G})$, y será llamado lenguaje generado por $\mathcal{G}$. Una traza $c: i \longrightarrow t$ en $\mathcal{G}$, con $t \in T$, será llamada una tarea. El conjunto de las etiquetas de tareas en $\mathcal{G}$ forman un lenguaje $\mathcal{L}_m(\mathcal{G})$ de Σ^* llamado el comportamiento de $\mathcal{G}$; es decir,

$$\mathcal{L}_m(\mathcal{G}) = \left\{ \begin{matrix} s \in \Sigma^* : s \text{ es una etiqueta de la traza} \\ c: i \longrightarrow t\ en\ \mathcal{G}, t \in T \end{matrix} \right\}. \tag{4}$$

Un lenguaje $\mathcal{L}$ de Σ^* es llamado regular si existe un Σ-generador finito $\mathcal{G}$ tal que $\mathcal{L} = \mathcal{L}_m(\mathcal{G})$. Ahora dado un Σ-generador finito $\mathcal{G} = (Q, \Sigma, \delta, \mathcal{E}, i, T)$ un estado $q \in Q$ será llamado accesible si existe una traza $c: i \longrightarrow q$. Si todos los estados de $\mathcal{G}$ son accesibles, entonces diremos que $\mathcal{G}$ es accesible. Se llama parte accesible de $\mathcal{G}$ al Σ-generador finito $\mathcal{G}^a = (Q^a, \Sigma, \delta^a, \mathcal{E}^a, i, T^a)$, donde Q^a es el conjunto de estados accesibles de $\mathcal{G}$, $T^a = T \cap Q^a$, $\delta^a = \delta/Q^a$, $\mathcal{E}^a \subset \delta^a$. Note que $\mathcal{L}_m(\mathcal{G}) = \mathcal{L}_m(\mathcal{G}^a)$. Por otro lado, δ determina la función parcial $\delta: Q \times \Sigma \longrightarrow Q$. Algebraicamente podemos extender δ a una función parcial $\hat{\delta}: Q \times \Sigma^* \longrightarrow Q$ satisfaciendo las siguientes condiciones

$$\begin{aligned} \hat{\delta}(q, \theta) &= q, \quad \forall\, q \in Q, \\ \hat{\delta}(q, st) &= \delta\left(\hat{\delta}(q, s), t\right), \quad \forall\, q \in Q, s \in \Sigma^*, t \in \Sigma. \end{aligned} \tag{5}$$

Luego, $\hat{\delta}$ así definida, es efectivamente una extensión de δ. Por lo tanto, en lo que sigue, no se hará distinción entre $\hat{\delta}$ y δ. Sean $\mathcal{G}_i = (Q_i, \Sigma_i, \delta_i, \mathcal{E}_i, i_i, T_i)$ $i = 1,2,\cdots,n$; n Σ-generadores finitos determinístico. Se llama Composición Paralela (o síncrona) de los $\mathcal{G}_i$; al GFD accesible $| \; |_{i=1}^{n}\mathcal{G}_i = \mathcal{G}^a$ donde $\mathcal{G} = (\times_{i=1}^{n} Q_i, \cup_{i=1}^{n}\Sigma_i, \delta, \mathcal{E}, (i_1, i_2, \cdots, i_n), \times_{i=1}^{n} T_i)$

con $\delta\big((q_1, q_2, \cdots, q_n), \alpha\big) = (P_1, P_2, \cdots, P_n)$, $P_i = \delta_i(q_i, \alpha)$, y $P_j = q_j$, si para $i, j = 1,2,\cdots, n\alpha \in \cap_i \mathcal{E}_i(q_i) \setminus \bigcup_{j:j\neq i} \Sigma_j$;;

e indefinida en otro caso, y $\mathcal{E}(q_1, q_2, \cdots, q_n) = \bigcap_i \mathcal{E}_i(q_i) \setminus \bigcup_{j:j\neq i}\Sigma_j$; $i, j = 1,2,\cdots,n$. Se puede chequear sin dificultad que si los $\mathcal{L}_i$, son lenguajes regulares de los $\mathcal{G}_i$ sobre Σ_i, tales que $\mathcal{L}_m(\mathcal{G}_i) = \mathcal{L}_{mi}$, $i = 1,2,\cdots,n$, entonces se satisfice

(i) $$\mathcal{L}(| \; |_{i=1}^{n}\mathcal{G}_i) = \bigcap_{i=1}^{n} \pi_i^{-1}\big(\mathcal{L}(\mathcal{G}_i)\big). \tag{6}$$

(ii) $$\mathcal{L}_m(| \; |_{i=1}^{n}\mathcal{G}_i) = \bigcap_{i=1}^{n} \pi_i^{-1}\big(\mathcal{L}_m(\mathcal{G}_i)\big). \tag{7}$$

3. Metodología y construcción del modelo en manufactura

Un sistema de manufactura es un par de conjuntos: conjunto de actividades y conjunto de recursos; que interactúan para obtener un producto. Este incluye un plan de proceso de producción (programa) que especifica las actividades y los tipos de recursos, así como también las relaciones de precedencia entre actividades. Sea $\mathcal{G}$ un sistema de manufactura. La metodología incluida en este artículo para llevar a cabo la modelación será establecida mediante la composición paralela, organizada desde las interpretaciones de condiciones locales de estados (o estatus) y eventos tal como sigue:

1. Identificar las actividades y recursos necesarios para la producción de un artículo (o producto).
2. Ordenar las actividades por las relaciones de precedencia tal como lo establece el programa.
3. Para cada actividad, crear un generador componente que represente el estatus oci:=<<ocioso>> o eje:=<ejecución>>.
4. etiquetar un evento α=<<comienzo de ejecución de la actividad>> creando un arco desde oci hasta eje, y un evento β=<<completación de actividad>> para incluir un arco desde eje hasta oci. En general, el evento de completación para una actividad será el evento de comienzo para la nueva actividad (ver Fig. 1).

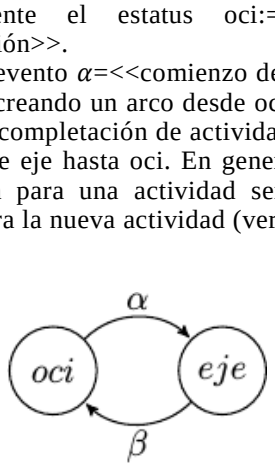


Figura 1. Un generador componente para una actividad.
Fuente: Los autores.

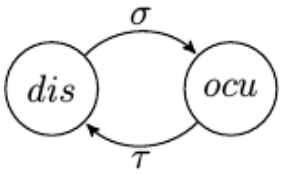


Figura 2. Un generador componente para un recurso.
Fuente: Los autores.

5. Para cada actividad, crear un generador componente para cada recurso necesario para el comienzo de la actividad dis:=<<disponible>> y ocu:<<ocupado>> etiquetar un evento σ:=<<comienzo de utilización del recurso>> el cual será igual al comienzo de la actividad; creando un arco desde dis hasta ocu. Finalmente, un evento τ:=<<finalización de utilización del recurso>> el cual será igual al de finalización de dicha actividad; para incluir un arco desde ocu hasta dis. En general, el evento de completación para una actividad con recurso de entrada corresponde a la disponibilidad de dicho recurso comienzo para la nueva actividad (ver Fig. 2)
6. Establecer el estado inicial; para cada actividad y cada recurso los estatus ocioso y disponible determinan respectivamente el estado inicial.

El modelo para el sistema de manufactura $\mathcal{G}$ será establecido por $| \; |_{i=1}^{n}\mathcal{G}_i$, con $\mathcal{L} = \cap_{i=1}^{n} \pi_i^{-1}(\mathcal{L}_i)$, donde los $\mathcal{G}_i$ determinan las dinámicas de las n componentes constituyentes $\mathcal{G}_i, i = 1,2,\cdots,n$; del sistema. La construcción del modelo para el sistema de manufactura $\mathcal{G} = (Q, \Sigma, \delta, \mathcal{E}, q_0, Q_m)$ será establecido desde la interpretación, organización y conjugación de los generadores componentes. Para ello,

Definición 1. Sea $\mathcal{G}$ el generador que representa un sistema global. Un evento $\alpha \in \cup_{i=1}^{n}\Sigma_i$ será llamado una k-interacción en $\mathcal{G}$ si cada vez que ocurre α éste produce cambios en k-componentes, $k \leq n$, siempre que $\alpha \in \bigcap_i \mathcal{E}_i(q_i) \setminus \cup_{j:j\neq i}\Sigma_j$, $i, j = 1,2,\cdots,k$.

Convendremos en lo que sigue que una k-interacción en $\mathcal{G}$ es simplemente un evento de orden k en $\mathcal{G}$ y al conjunto constituido por las k-interacciones lo denotamos Σ_k, $0 < k \leq n$. Luego, $\Sigma = \bigcup_{k=1}^{n}\Sigma_k$ es una partición de Σ ($\Sigma_i \cap \Sigma_k = \emptyset, i \neq j$). Una k-interacción no es más que una expresión simbólica de la ocurrencia simultanea de eventos de ciertos generadores componentes. Estos eventos representan acciones distintas (con etiquetas distintas) pero podríamos darles una interpretación que nos permita conjugarlas mediante un mismo evento. Otro hecho aún más significativo para la construcción del modelo, ocurre cuando una actividad en el sistema requiere de uno o más recursos; donde el comienzo y la completación de dicha actividad tiene una relación directa con el comienzo y la finalización del uso de esos recursos. Igualmente, estos eventos tienen representaciones distintas en el sistema, pero la interpretación de este hecho por el mismo evento nos permitirá simplificar la construcción del modelo. Por lo tanto, diremos que las componentes $\mathcal{G}_i$, $i = 1,2,\cdots,n$; del sistema de manufactura $\mathcal{G}$ estarán determinadas bajo simetría de los eventos que representan los comienzos y finalizaciones de las actividades, así como de la adquisición y liberación de los recursos. Finalmente, en la

composición paralela de los $\mathcal{G}_i$, un evento común solo ocurre si ocurre simultáneamente en los $\mathcal{G}_i$ relacionados a través de dicho evento. Por lo tanto, los $\mathcal{G}_i$ están sincronizados sobre los eventos comunes. Los eventos no comunes no están sujetos a esta restricción y pueden ocurrir siempre que sea posible. Por lo tanto, $\mathcal{G} = |\ |_{i=1}^{n}\mathcal{G}_i$.

4. Condiciones y planificación por consenso

Sea $\mathcal{G} = (Q, \Sigma, \delta, \mathcal{E}, q_0, Q_m)$ (sistema de manufactura) la composición síncrona de n componentes (subsistemas) $\mathcal{G}_i = (Q_i, \Sigma_i, \delta_i, \mathcal{E}_i, q_{0_i}, Q_{m_i}), i = 1, \cdots, n$. Sabemos que, para cualesquiera $\mathcal{L}_i$ y $\mathcal{L}_{m_i}$, $i = 1, \cdots, n$; existe un generador finito determinístico $\mathcal{G}_i$ tal que $\mathcal{L}_i = \mathcal{L}(\mathcal{G}_i)$ y $\mathcal{L}_{m_i} = \mathcal{L}_m(\mathcal{G}_i)$, $i = 1,2, \cdots, n$. Sea $\mathcal{C}$ una condición (expresada como un lenguaje) para $\mathcal{G}$ y para cada i, con $i = 1,2, \cdots, n$; sea $\mathcal{C}_i = \pi_i(\mathcal{C})$ la proyección i-ésima de $\mathcal{C}$. La afectación que puede producir $\mathcal{C}$ sobre $\mathcal{G}$ puede ser proyectada a las dinámicas de las componentes. Más aún, existen condiciones no únicas que producen el efecto global impuesto por las condiciones locales. Por lo tanto, conocer $\mathcal{L} \cap \mathcal{G}$ (lenguaje global ante una condición) es conocer los $\mathcal{L}_i \cap \mathcal{C}_i$, $i = 1, \cdots, n$; es decir, conocer la afectación $\mathcal{C}$ sobre el sistema $\mathcal{G}$ es conocer las afectaciones $\mathcal{C}_i$ sobre las componentes $\mathcal{G}_i$. Note que la condición $\mathcal{C}$ no tiene sentido lógico, en relación al acoplamiento con $\mathcal{G}$, si ésta no está reflejada en la dinámica del sistema. En este sentido, para la construcción de la metodología por consenso podemos suponer que la planificación $\mathcal{L}_p$ es un sublenguaje de $\mathcal{L}(\mathcal{G})$.

Definición 2. Sean $\mathcal{G}$ un sistema global y $\mathcal{C}$ una condición sobre $\mathcal{G}$. Para cualesquiera $q = \delta(q_0, s)$ y $\alpha \in \mathcal{E}(q)$ una k-interacción, sean $j_1, j_2, \cdots, j_k$; los índices de las componentes de cambio por la ocurrencia de α en q. Diremos que α es obtenida por consenso si para todo $j_l, l = 1, \cdots, k$ se tiene que $\pi_{j_l}(s)\alpha \in \pi_{j_l}(\mathcal{C} \cap \mathcal{L})$.

De acuerdo a la definición 2 establecemos el conjunto de todos eventos permitidos en q obtenidos por consenso, el cual denotaremos por $\mathcal{J}(q)$. La construcción para la planificación en los sistemas de manufactura; $\mathcal{G} = (Q, \Sigma, \delta, \mathcal{E}, i, Q_m)$ establecida por el producto síncrono, está fundamentada en el consenso como sigue: Para cada estado del sistema de manufactura; $q = \delta(i, s)$, donde $s \in \left(\bigcup_{i=1}^{n}\Sigma_i\right)^*$ e $i = (i_1, i_2, \cdots, i_n)$ es el estado inicial, consideramos el conjunto de todos los eventos habilitados en q; $\mathcal{E}(q)$: para cada k-interacción $\alpha \in \mathcal{E}(q)$, donde $j_1, j_2, \cdots, j_k$ son los índices de las componentes de cambio por la ocurrencia en q, α deberá satisfacer: $\pi_{j_l}(s)\alpha \in \pi_{j_l}(\mathcal{C} \cap \mathcal{L})$, $\forall\, j_i,\ i = 1, \cdots, k$, para ser obtenida por consenso. Comenzamos el procedimiento desde el estado inicial i, y consideremos el subconjunto de eventos obtenidos por consenso en i; $\mathcal{J}(i)$. La ocurrencia de un evento α en $\mathcal{J}(i)$ determinará un nuevo estado q, y por ende se genera un arco dirigido desde i al nuevo estado q etiquetado por el evento α; $i \xrightarrow{\alpha} q$. Ahora, esto ocurrirá eventualmente para todo evento α en $\mathcal{J}(i)$. Y en el estado actual q se repetirá el proceso antes mencionado con respecto a $\mathcal{J}(q)$, generando de esta manera bajo consenso el árbol que determina el generador que reconoce la planificación desde un punto de vista constructivo. El procedimiento repetido sucesivamente generará un conjunto de estados bajo consenso y puede ser representado gráficamente. Finalmente, el proceso resultante será un reconocedor de la planificación y será denotado por $\mathcal{P}(\mathcal{G})$. Formalmente,

Definición 3. Sea $\mathcal{P}(\mathcal{G})$ como antes. El lenguaje generado por $\mathcal{P}(\mathcal{G})$ será llamado lenguaje de planificación y es dada por

- $\theta \in \mathcal{L}(\mathcal{P}(\mathcal{G}))$;
- para cada $s \in (\bigcup_{i=1}^{n}\Sigma_i)^*$, y para cada $\alpha \in \bigcup_{i=1}^{n}\Sigma_i$ se tiene que: $s \in \mathcal{L}(\mathcal{P}(\mathcal{G}))$, $s\alpha \in \mathcal{L}(\mathcal{G}) = \mathcal{L}$, α es obtenido por consenso, si y solo si, $s\alpha \in \mathcal{L}(\mathcal{P}(\mathcal{G}))$.

El lenguaje de planificación marcado por $\mathcal{P}(\mathcal{G})$ es dado por $\mathcal{L}_m(\mathcal{P}(\mathcal{G})) = \mathcal{L}(\mathcal{P}(\mathcal{G})) \cap \mathcal{L}_m(\mathcal{G})$.

Para facilitar la escritura, denotaremos a los lenguajes de planificación y planificación marcada por $\mathcal{L}_p$ y $\mathcal{L}_{p_m}$ respectivamente. El conjunto de todos los estados generados por consenso desde el estado inicial i está dado por $Q_p = \{q \in Q: \exists\, s \in \mathcal{L}_p,\ \delta(i, s) = q\}$, y el generador determinístico accesible $\mathcal{P}(\mathcal{G}) = (Q_p, \Sigma, \delta, \mathcal{J}, i, Q_{p_m})$ es el reconocedor de $\mathcal{L}_p$. La selección de eventos comunes en la composición paralela, lo cual determina el acoplamiento entre las componentes, junto con la reducción en cuanto a la navegación de estados sometidas a las condiciones impuestas localmente permite lidiar eficientemente con la complejidad computacional resultante del modelo completo.

5. Algoritmo para la planificación

Para la construcción de $\mathcal{P}(\mathcal{G})$ mediante el algoritmo son necesarias las siguientes especificaciones (ver Fig. 3):

- Los elementos del generador composición paralela $\mathcal{G}$: el estado inicial $(q_{0_1}, \cdots, q_{0_n})$, el conjunto de estados finales $\times_{i=1}^{n} Q_{i_m}$, el conjunto $\times_{i=1}^{n} Q_i$ de estados, el conjunto de eventos activos $\mathcal{E}$ y la función de transición δ;
- el conjunto de las k-interacciones; Σ^k, $k \in \{1,2, \cdots, n\}$, donde n representa el número de componentes constituyendo a $\mathcal{G}$;
- $\mathcal{L}$ el lenguaje generado por el generador composición paralela; y
- $\mathcal{C}$ expresando el condicionamiento global sobre la dinámica del sistema.

Proposición 1. Sea n el cardinal del conjunto Q_p. La planificación $\mathcal{P}(\mathcal{G})$ se puede llevar a cabo a la sumo en $n - 1$ pasos.

Demostración. Supongamos que para $q_i \in Q_p$; $i = 0,1, \cdots, n-1$ $(q_j \neq q_i; i \neq j)$; se tiene que $\mathcal{J}(q_i) = \alpha_{i+1}$, tal que $\delta(q_i, \alpha_{i+1}) = q_{i+1}$; $i = 0,1, \cdots, n-2$. Ahora, si $\mathcal{J}(q_{n-1}) = \emptyset$, entonces el nivel del nodo que representa a q_{n-1} está dado por

$$l(q_{n-1}) = \sum_{i=0}^{n-1} |\mathcal{J}(q_i)| \leq \sum_{i=0}^{n-1} 1 = n. \qquad (8)$$

Algoritmo 1 Para la construcción de $\mathcal{P}(\mathcal{G})$

Entrada: $\mathcal{G} = \left(\bigtimes_{i=1}^{n} Q_i, \bigcup_{i=1}^{n} \Sigma_i, \delta, \mathcal{E}_i, (q_{01}, \ldots, q_{0n}), \bigtimes_{i=1}^{n} Q_{im}\right), \Sigma^k, \mathcal{L}, \mathcal{C}$

Salida: $\mathcal{P}(\mathcal{G}), \mathcal{L}_p$

inicio : Alcanzados $\leftarrow \{(q_{01}, \ldots, q_{0n})\}$, $\mathcal{J}((q_1, \ldots, q_n)) \leftarrow \emptyset$, $\mathcal{E} \leftarrow \emptyset$, $(q_{01}, \ldots, q_{0n})$ no etiquetado, $s \leftarrow \theta$, $\mathcal{L}_p \leftarrow \emptyset$
mientras $(q_1, \ldots, q_n) \in$ Alcanzados $\wedge$ $(q_1, \ldots, q_n)$ no etiquetado **hacer**
  para $\alpha \in \mathcal{E}((q_1, \ldots, q_n))$ **hacer**
    para $k \in \{1, 2, \ldots, n\}$ **hacer**
      si $\alpha \in \Sigma^k$ **entonces**
        $l = k$, interrumpir
      fin si
      para $i \in \{j_1, \ldots, j_l\}$ **hacer**
        si $\pi_i(s)\alpha \in \mathcal{C}_i \cap \mathcal{L}_i$ **entonces**
          Imprimir: La componente i-esima no viola la condición $\mathcal{C}$
          en otro caso
          Imprimir: La componente i-esima viola la condición $\mathcal{C}$
        fin si
      fin para
      $\mathcal{J}((q_1, \ldots, q_n)) \leftarrow \alpha$, $s \leftarrow s \cdot \alpha$, $\mathcal{L}_p \leftarrow \mathcal{L}_p \cap \{s\}$
      Imprimir: α es obtenida por consenso en $(q_1, \ldots, q_n)$
      si $\delta((q_1, \ldots, q_n), \alpha) = (q_1', \ldots, q_n') \notin$ Alcanzados **entonces**
        Alcanzados $\leftarrow$ Alcanzados $\cup \{(q_1, \ldots, q_n) \wedge (q_1', \ldots, q_n')\}$ no etiquetado
      fin si
    fin para
    $(q_1, \ldots, q_n)$ etiquetado
  fin para
fin mientras
devolver $\mathcal{P}(\mathcal{G}), \mathcal{L}_p$

Figura 3. Algoritmo para la construcción de $\mathcal{P}(\mathcal{G})$.
Fuente: Los autores.

Si $\mathcal{J}(q_{n-1}) \neq \emptyset$, entonces $\delta(q_{n=1}, \alpha_n) = q_n$. Esto implica que necesariamente $q_n = q_i$, para algún i; $i = 0,1, \cdots, n-1$. Sea $l: Q_p \longrightarrow \mathbb{N}\$, \mathbb{N} = \{0,1,2, \cdots\}$, una función de nivel: para cada $q_j \in Q_p$, $l(q_j) \in \mathbb{N}$ es el nivel del estado q_j definida como $l(q_j) = \sum_{i=0}^{n-1} |\mathcal{J}(q_i)|$; entonces, $l(q_n) \leq l(q_{n-1}) = n-1$. Finalmente, $l(q_{n-1}) \leq n-1$.

■

Nosotros construimos al conjunto $\mathcal{J}(q)$ cuyos elementos son las k-interacciones obtenidas por consenso, $\mathcal{I}(q) \subseteq \mathcal{E}(q)$, para obtener posteriormente, para cada $\alpha \in \mathcal{J}(q)$ una nueva bolsa $\mathcal{J}(\delta(q, \alpha))$. Este proceso continua considerando la nueva bolsa $\mathcal{J}(\delta(q, \alpha)) \subseteq \mathcal{E}(\delta(q, \alpha))$, obteniendo de esta manera el lenguaje de planificación $\mathcal{L}_p$, en algún sentido, por sucesiones de bolsas de la forma $\mathcal{J}_0(q_0), \mathcal{J}_1\left(\delta(q_0, \alpha_1)\right), \cdots, \mathcal{J}_n(\delta(\cdots \delta(\delta(q_0, \alpha_1), \alpha_2), \cdots), \alpha_n)) \cdots$ Finalmente, $\mathcal{P}(\mathcal{G})$ es una realización de $\mathcal{L}_p$ construida desde las afectaciones locales $\mathcal{C}_i$, $i = 1, \cdots, n$; sobre las componentes $\mathcal{G}_i$, $i = 1, \cdots, n$. La justificación por la cual una condición $\mathcal{C}$ sobre $\mathcal{G}$ es dada, es por la necesidad de establecer una planificación sobre el sistema. Por ello estableceremos el acoplamiento con $\mathcal{G}$.

Teorema 1. Dado una condición $\mathcal{C}$ sobre $\mathcal{G}$. Sea para cada j, $j = 1, \cdots, n$, $\mathcal{C}_j = \pi_j(\mathcal{C})$ la condición local para $\mathcal{G}_j$. Entonces, $\mathcal{C} \cap \mathcal{L} = \mathcal{L}_p$ (más restrictivamente, $\mathcal{C} \cap \mathcal{L}_p = \mathcal{L}_{p_m}$).

Demostración.

$$
\begin{aligned}
s \in \mathcal{L}_p \iff & \text{admites una descomposición de la forma} \\
& \alpha_1\alpha_2 \cdots \alpha_n \ \ con \ \ \alpha_i \in \mathcal{J}_{i-1}, \ \ i = 1, \cdots, n \\
\iff & \omega\alpha_n, con\ \omega = \alpha_1\alpha_2 \cdots \alpha_{n-1} \wedge \alpha_n \in \mathcal{J}_{n-1} \\
\iff & \omega\alpha_n, con\ \omega \in \mathcal{J}_0\mathcal{J}_1 \cdots \mathcal{J}_{n-2} \wedge \alpha_n \in \mathcal{J}_{n-1} \\
\iff & \pi_j(\omega)\alpha_n \in \mathcal{C}_j \cap \mathcal{L}_j, \ \text{para todo } j \\
\iff & \pi_j(\omega)\pi_j(\alpha_n) \in \pi_j(\mathcal{C} \cap \mathcal{L}), \ \text{para todo } j \\
\iff & \pi_j(\omega\alpha_n) \in \pi_j(\mathcal{C} \cap \mathcal{L}), \ \text{para todo } j \\
\iff & \bigcap_{j=1}^{n} \pi_j^{-1}(\pi_j(s)) \in \bigcap_{j=1}^{n} \pi_j^{-1}(\pi_j(\mathcal{C} \cap \mathcal{L})) \\
\iff & s \in \mathcal{C} \cap \mathcal{L}
\end{aligned}
\tag{9}
$$

Análogamente, se puede probar que $\mathcal{C} \cap \mathcal{L}_p = \mathcal{L}_{p_m}$. ■

El resultado anterior; teorema 1 expresa que la planificación global sobre el sistema $\mathcal{G}$ puede ser obtenida desde las planificaciones locales de las componentes $\mathcal{G}_i$, mostrando de esta manera el análisis global desde un punto de vista local.

6. Aplicación

6.1. Un sistema de producción por lote

Consideremos un sistema de producción de pinturas constituido solo por tres líneas de producción, ya que la gama de productos elaborados por la empresa podría ser muy amplia. Para cada línea de producción las unidades que la conforman establecen los subsistemas. Un sistema de producción de pinturas es un sistema de producción por lote, porque la finalización de producción de una pintura especifica dará comienzo a la fabricación de otra pintura quizás con características distintas. La materia prima (recursos) utilizada para la elaboración de las pinturas son: los pigmentos, los vehículos y los solventes, a los que se suman los aditivos. Para la construcción del modelo asumiremos la existencia de estos recursos. Para cada subproceso (o subsistema) en el proceso de fabricación de pinturas cada actividad es llevada a cabo por una unidad de producción. Las actividades son descritas a continuación:

1. La dispersión es la fase inicial y de mayor duración en el proceso, en la cual se agita la carga del vehículo, el agregado de solventes y aditivos. Luego, se agregan sucesivamente los diferentes tipos de pigmento, empezando con los de más difícil mojado. En esta fase se logra obtener una pasta llamada pasta de molienda.
2. En una segunda fase; molienda, se consigue obtener una mayor finura de la pasta de molienda por medio de los llamados molinos.
3. En una última etapa dilución o mezcla se ajusta la consistencia de la pintura con el agregado de solventes y/o resinas compatibles con la base de molienda y generalmente se incluyen aditivos que ayudan en la estabilización.

A continuación, describiremos las líneas de producción del sistema de producción de pinturas; pintura blanca, pintura de color y pintura texturizada (o masilla), en la que se pueden distinguir algunas de las etapas discutidas anteriormente (ver Fig. 4):

a) $PB :=$ subsistema de producción de base incolora. Éste

está constituido por dos unidades de producción distinguidas por sus operaciones para la elaboración de este producto:

i) $PB_1 :=$ unidad de dispersión de la base concentrada incolora;
ii) $PB_2 :=$ unidad de mezclado de terminación de base incolora.

Luego de estas etapas, se obtiene la base incolora, la cual puede continuar a envasado, a completar el proceso de fabricación de pintura texturizada o a completar el proceso de fabricación de pintura de color.

b) $MA :=$ subsistema de producción de pintura texturizada. Para este producto se distinguen las siguientes operaciones llevadas a cabo por las correspondientes unidades de producción:
   i) $MA_1 :=$ unidad de dispersión de base de alta viscosidad;
   ii) $MA_2 :=$ unidad de mezclado del concentrado con la base blanca.

   Una vez obtenido el concentrado producto de la mezcla con la base blanca, la culminación se logra con el envasado del producto.

c) $PC :=$ subsistema de producción de pintura de color. Éste se caracteriza por las siguientes actividades:
   i) $PC_1 :=$ unidad de dispersión del pigmento para formar una pasta de color;
   ii) $PC_2 :=$ unidad de molienda de la pasta de color para formar empaste;
   iii) $PC_3 :=$ unidad de mezclado del empaste con resinas y solventes formando un concentrado de color;
   iv) $PC_4 :=$ unidad de mezclado del concentrado de color con la base incolora.

   La pintura de color es el resultado de la mezcla del concentrado de color con la base incolora. La culminación de este proceso se logra con el envasado de la pintura, luego de haber pasado previamente por control de calidad.

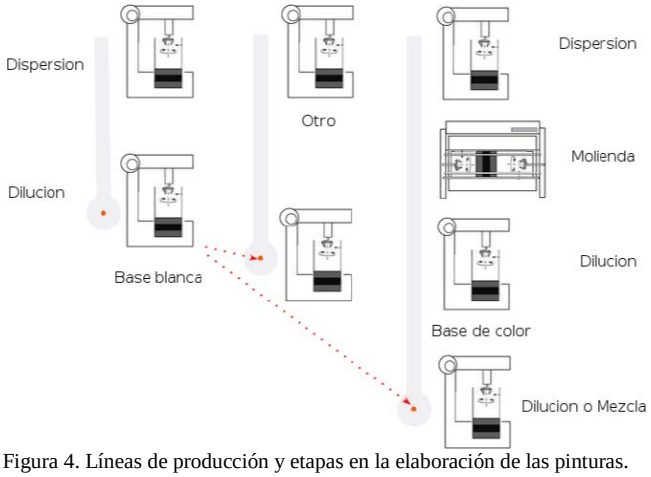


Figura 4. Líneas de producción y etapas en la elaboración de las pinturas.
Fuente: Los autores

En la producción de la pintura de color se utiliza la técnica tirada de color, que consiste de un proceso (reiniciable) que se lleva a cabo para disminuir gradualmente el valor del color (o diferencia luminosa) hasta alcanzar el color más oscuro. Esto reduce al mínimo la limpieza y la nueva configuración de la maquinaria entre cada lote de pintura de color. El blanco (pintura opaca, tinta no transparente) es el único color que no es utilizado en esta técnica, ya que, una pequeña cantidad de pigmento blanco puede afectar negativamente a los colores medios. Con la idea de facilitar los cálculos en la construcción de la metodología de modelación para esta clase de sistemas de manufactura solo consideraremos los casos expuestos anteriormente. Excluiremos, por ejemplo, los subprocesos de filtrado y envasado en los procesos de fabricación de pintura texturizada (o masilla) y pintura de color. Además, consideraremos que un producto obtenido en cada unidad de producción es un recurso para la siguiente unidad en cada subproceso. Más aún, la base incolora en PB es un recurso necesario para continuar el envasado de la misma o completar los procesos de fabricación en MA y PC.

6.2. Interpretaciones en el sistema de producción

Para el subsistema de producción de pintura blanca PB, para la actividad dispersión (llevada a cabo por la unidad PB_1) representando los estatus $q_{0_1} = \ll ocioso \gg$ y $q_{1_1} = \ll ejecución \gg$ los eventos σ_1 y σ_3 etiquetan el comienzo y la completación respectivamente (ver Fig. 9), y para la actividad de mezclado o dilución (llevada a cabo por la unidad PB_2) representando los estatus $q_{0_2} = \ll ocioso \gg$ y $q_{1_2} = \ll ejecución \gg$ los eventos σ_3 y σ_5 etiquetan el comienzo y su completación respectivamente de dicha actividad (ver Fig. 5).

La composición síncrona de los $G_i = (Q_i, \Sigma_i, \delta_i, \mathcal{E}_i, q_{0_i}, Q_{m_i})$, $i = 1,2\$$; representa al subsistema PB, donde cada uno de sus elementos pueden distinguirse en la Fig. 6.

Su comportamiento es dado por

$$\mathcal{L}_{m_1} = (\sigma_1\sigma_3\sigma_5 + \sigma_1\sigma_3\sigma_1(\sigma_5\sigma_3\sigma_1)^*\sigma_5\sigma_3\sigma_5)^*.$$

Para el subsistema de producción de masilla MA, para la actividad dispersión (llevada a cabo por la unidad MA_1)

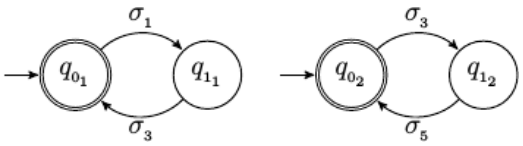


Figura 5. Unidades de producción PB_1 y PB_2.
Fuente: Los autores.

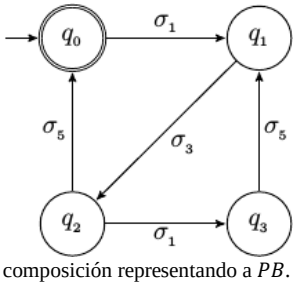


Figura 6. Generador composición representando a PB.
Fuente: Los autores.

representando los estatus $q_{0_3} = \ll ocioso \gg$ y $q_{1_3} = \ll ejecución \gg$ los eventos σ_{17} y σ_{19} etiquetan el comienzo y la completación de dicha actividad (ver Fig. 7). Así mismo, para la actividad mezclado (llevada a cabo por la unidad MA_2) representando los estatus $q_{0_4} = \ll ocioso \gg$ y $q_{1_4} = \ll ejecución \gg$ los eventos σ_{19} y σ_{21} etiquetan el comienzo y la completación respectivamente (ver Fig. 7).

Las $\mathcal{G}_i = (Q_i, \Sigma_i, \delta_i, \mathcal{E}_i, q_{0_i}, Q_{m_i})$ $i = 3{,}4$; representan las dos unidades de producción del subsistema MA y la composición síncrona de estas dos unidades se muestra en la Fig. 8.

Su comportamiento es dado por

$$\mathcal{L}_{m_2} = (\sigma_{17}\sigma_{19}\sigma_{21} + \sigma_{17}\sigma_{19}\sigma_{17}(\sigma_{21}\sigma_{19}\sigma_{17})^*\sigma_{21}\sigma_{19}\sigma_{21})^*.$$

Para el subsistema de producción de pintura de color PC, para la actividad dispersión (llevada a cabo por la unidad PC_1) representando los estatus $q_{0_5} = \ll ocioso \gg$ y $q_{1_5} = \ll ejecución \gg$ los eventos σ_7 y σ_9 etiquetan el comienzo y la completación (ver Fig. 9) y para la actividad molienda (llevada a cabo por la unidad PC_2) representando los estatus $q_{0_6} = \ll ocioso \gg$ y $q_{1_6} = \ll ejecución \gg$ los eventos σ_9 y σ_{11} etiquetan el comienzo y su completación respectivamente (ver Fig. 9).

Para el mezclado del empaste con resinas y solventes (concentrado de color llevado a cabo por la unidad PC_3) representando los estatus $q_{0_7} = \ll ocioso \gg$ y $q_{1_7} = \ll ejecución \gg$ los eventos σ_{11} y σ_{13} etiquetan el comienzo y la completación (ver Fig. 9) y el mezclado del concentrado de color con la base incolora (llevada a cabo por la unidad PC_4) representando los estatus $q_{0_8} = \ll ocioso \gg$ y $q_{1_8} = \ll ejecución \gg$ los eventos σ_{13} y σ_{15} etiquetan el comienzo y la completación respectivamente (ver Fig. 9).

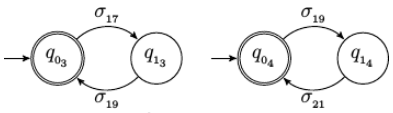


Figura 7. Unidades de producción MA_1 y MA_2.
Fuente: Los autores.

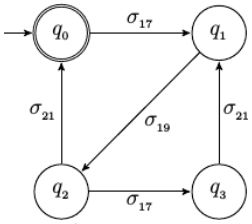


Figura 8. Generador composición representando a MA.
Fuente: Los autores.

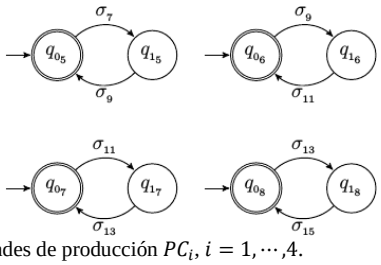


Figura 9. Unidades de producción PC_i, $i = 1, \cdots, 4$.
Fuente: Los autores.

Igualmente, la composición síncrona de los $\mathcal{G}_i = (Q_i, \Sigma_i, \delta_i, \mathcal{E}_i, q_{0_i}, Q_{m_i})$, $i = 5, \cdots, 8$; representando las unidades de producción del subsistema PC, se ilustra en la Fig. 10.

Su comportamiento es dado por

$$\mathcal{L}_{m_3} = (\sigma_7\sigma_9\sigma_{11}\sigma_{13}\sigma_{15} + \sigma_7\sigma_9(\sigma_7\sigma_{11} + \sigma_{11}\sigma_7)\sigma_{13} + \sigma_{11}\sigma_{13}\sigma_7) \cdots + \cdots$$

Para el envasado de la pintura blanca (denotamos esta actividad por EN representado los estatus $q_{0_9} = \ll ocioso \gg$ y $q_{1_9} = \ll ejecución \gg$ los eventos σ_{23} y σ_{25} etiquetan el comienzo y la completación de dicha actividad respectivamente (ver Fig. 11).

Su comportamiento es $\mathcal{L}_{m_4} = (\sigma_{23}\sigma_{25})^*$. Para los subsistemas de producción EN, MA y PC requerimos la disponibilidad de la base blanca, para este recurso representado $q_{0_{10_i}} \ll ocioso \gg$ y $q_{1_{10_i}} \ll ejecución \gg$ $i = \{1{,}2{,}3\}$: el evento σ_5 etiqueta el comienzo de disponibilidad del recurso (agregación de la base blanca por PB), mientras que, los eventos σ_{13}, σ_{19} y σ_{23} etiquetarán la finalización de disponibilidad del mismo (uso de la base blanca por los subsistemas de producción EN, MA y PC respectivamente). El generador composición paralela representando el uso de la base blanca por parte de EN, MA y PC, es denotado por Re y está dado a continuación en la Fig. 12.

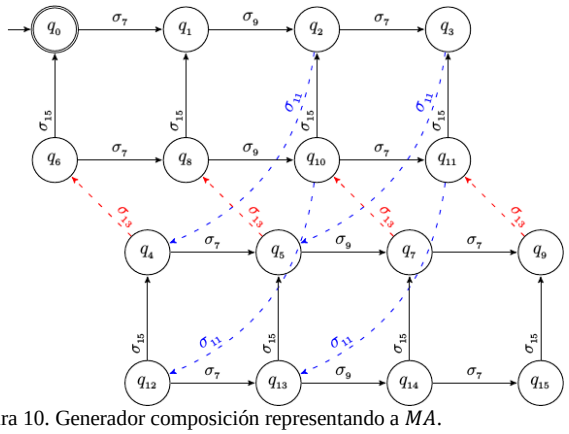


Figura 10. Generador composición representando a MA.
Fuente: Los autores.

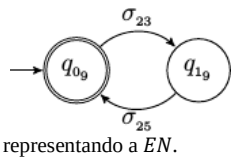


Figura 11. Generadores representando a EN.
Fuente: Los autores.

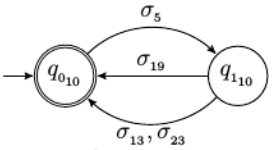


Figura 12. Generador composición representando Re.
Fuente: Los autores.

Su comportamiento dado por

$$\mathcal{L}_{m_5} = \left(\sigma_5(\sigma_{13} + \sigma_{19} + \sigma_{23})\right)^*.$$

Sean $\mathcal{G}_i = (Q_i, \Sigma_i, \delta_i, \mathcal{E}_i, q_{0_i}, Q_{m_i}), \quad i = 1, \cdots, 5;$ los subsistemas y el recurso, entonces la composición sincronía $\mathcal{G} = ||_{i=1}^{5}\mathcal{G}_i = \mathcal{G}_1||\mathcal{G}_2||\mathcal{G}_3||\mathcal{G}_4||\mathcal{G}_5,$ representando el comportamiento cooperativo global del sistema de producción el cual posee 1024 estados y 4608 transiciones, tiene como lenguajes generado y marcado a

$$\mathcal{L}(\mathcal{G}) = \bigcap_{i=1}^{5} \pi_i^{-1}(\mathcal{L}(\mathcal{G}_i)) \quad y \quad \mathcal{L}_m(\mathcal{G}) = \bigcap_{i=1}^{5} \pi_i^{-1}(\mathcal{L}_m(\mathcal{G}_i)) \tag{10}$$

respectivamente. El sistema fue probado usando el software TCT desarrollado por Wonham [10].

6.3. Condicionamiento sobre el sistema

En relación a la composición paralela dada anteriormente, establecemos la especificación siguiente: cada línea de producción de la planta se interrumpe por cada lote de producción requerido; fabricación de una cantidad determinada del mismo producto, y las cantidades de lotes producidas por ésta son limitadas. Esto sugiere que el sistema de producción es de capacidad finita con cardinal igual a $k_1 + \cdots + k_n$, donde $k_i \in \{1, \cdots, n\}$; indica la capacidad máxima de lotes para la i-ésima línea de producción. Si denotamos por $N_\sigma(s)$ el número de ocurrencia de un evento σ (interpretando el inicio o la finalización de una actividad) en $s \in \Sigma^*$ (interpretando una tarea del sistema de producción), entonces una especificación sobre el sistema de producción está dada por el siguiente conjunto $\mathcal{K} = \{s \in \mathcal{L}(\mathcal{G}): N_\sigma(s) \leq k, \sigma \in \Sigma\}$ donde $k = k_1 + \cdots + k_n$. Las afectaciones de estas especificaciones pueden ser reflejadas en el sistema de producción $\mathcal{L}_m \cap \mathcal{K}$. Más aún, las afectaciones pueden ser proyectadas a cada componentes; interpretando a cada línea de producción (conformada por unidades de producción), del sistema de producción, es decir, $\pi_i(\mathcal{L}_m(\mathcal{G}) \cap \mathcal{K}), \ i \in \{1, \cdots, n\}$ es la afectación local inducida por la afectación global. Supongamos que la empresa de pintura desea producir los tres tipos de pinturas para satisfacer un pedido: dos lotes de pintura de color, dos lotes de masilla y un lote de pintura blanca. De esta manera, se requerirá de cinco lotes de base incolora, de los cuales cuatro lotes se disponen para completar el proceso de fabricación de masilla y el proceso de fabricación de pintura de color. El lote restante es requerido para el envasado de la pintura blanca. Asumiremos la disponibilidad de todos los recursos (materias primas) necesarios para la producción de estos lotes y consideramos que el suministro de base blanca para los tres tipos de producto; pintura blanca, masilla y pintura de color, es limitado y una vez usado un lote de base incolora (recurso) se deberá espera su producción para su nuevo uso. Deseamos saber de qué manera cada uno de líneas de producción pueden producirlos con el objeto de satisfacer la demanda. La especificación reflejada sobre el sistema de producción es dada por

$$\mathcal{K} = \left\{ \begin{matrix} s \in \mathcal{L}(\mathcal{G}): N_{\sigma_{13}}(s) = 2, N_{\sigma_{19}}(s) = 2, N_{\sigma_{23}}(s) = 1, \\ \sigma_{13}, \sigma_{19}, \sigma_{23} \in \Sigma \end{matrix} \right\}$$

donde, $N_{\sigma_5}(s) = N_{\sigma_{13}}(s) + N_{\sigma_{19}}(s) + N_{\sigma_{23}}(s)$. Esta especificación puede ser proyectada a cada componente; $\mathcal{K}_i = \pi_i(\mathcal{K}), \ i \in \{1, \cdots, 5\}$. Así, las afectaciones locales sobre la i-ésima componente para $i \in \{1, \cdots, 5\}$ están dadas a continuación:

$$\begin{aligned} \mathcal{K}_1 &= \left\{s \in \mathcal{L}_{m_1}: N_{\sigma_5}(s) \leq 5, \sigma_5 \in \Sigma_1\right\} \\ \mathcal{K}_2 &= \left\{s \in \mathcal{L}_{m_2}: N_{\sigma_{19}}(s) \leq 2, \sigma_{19} \in \Sigma_2\right\} \\ \mathcal{K}_3 &= \left\{s \in \mathcal{L}_{m_3}: N_{\sigma_{13}}(s) \leq 2, \sigma_{13} \in \Sigma_3\right\} \\ \mathcal{K}_4 &= \left\{s \in \mathcal{L}_{m_4}: N_{\sigma_{23}}(s) \leq 1, \sigma_{23} \in \Sigma_4\right\} \\ \mathcal{K}_5 &= \left\{ \begin{matrix} s \in \mathcal{L}_{m_5}: N_{\sigma_5}(s) = N_{\sigma_{13}}(s) + N_{\sigma_{19}} \\ (s) + N_{\sigma_{23}}(s), \\ \sigma_5, \sigma_{13}, \sigma_{19}, \sigma_{23} \in \Sigma_5 \end{matrix} \right\} \end{aligned} \tag{11}$$

La clasificación de los eventos (k-interacciones) según la sincronización de las componentes $\mathcal{G}_i, i = 1, \cdots, 5;$ es dada en la Tabla 1.

En efecto, los eventos $\sigma_1, \sigma_7, \sigma_{15}, \sigma_{17}, \sigma_{21}$ y σ_{25} son 1-interacciones: σ_1, σ_7, y σ_{17}, representan los comienzos de las actividades de dispersión ejecutadas por PB_1, PC_1 y MA_1 respectivamente, mientras que, los eventos σ_{15}, σ_{21}, y σ_{25} representan las completaciones de las actividades de mezclado y envasado llevadas acabos por la unidades PC_4, MA_2, y EN respectivamente. Por otro lado, los eventos $\sigma_3, \sigma_5, \sigma_9, \sigma_{11}$ y σ_{23} son 2-interacciones: σ_3 representa la completación y el comienzo de las actividades de dispersión y mezclado por parte PB_1 y PB_2, σ_5 representa la completación de mezclado por parte PB_2 y el comienzo de disponibilidad del recurso Re, σ_9 representa la completación de la actividad dispersión llevada a cabo por la unidad PC_1 y el comienzo de la actividad molienda llevada a cabo por la unidad PC_2, σ_{11} representa la completación de actividad de molienda llevada a cabo por la unidad PC_2 y el comienzo de la actividad de mezclado del concentrado de color llevado a cabo por la unidad PC_3 y σ_{23} representa la finalización del uso de la base blanca por PC y el comienzo de la actividad de envasado de la pintura blanca. Finalmente, los eventos σ_{13} y σ_{19} son 3-interacciones: σ_{13} representa la completación de la actividad de mezclado de concentrado de color llevado a cabo por la unidad PC_3, la finalización del uso de la base blanca por MA y el comienzo de la actividad de mezclado del concentrado de color con la base incolora llevada a cabo por la unidad PC_4 y σ_{19} representa la finalización del uso de la base blanca por PC, la completación de la actividad de dispersión llevada a cabo por la unidad MA_1 y el comienzo de la actividad mezclado llevada a cabo por la unidad MA_2.

Tabla 1.
Valores de las k-interacciones.

Σ_i-ORDEN	$K = 1$	$K = 2$	$K = 3$
Σ_1	σ_1	σ_3, σ_5	
Σ_2	σ_{17}, σ_{21}		σ_{19}
Σ_3	σ_7, σ_{15}	σ_9, σ_{11}	σ_{13}
Σ_4	σ_{25}	σ_{23}	
Σ_5		σ_5, σ_{23}	σ_{13}, σ_{19}

Fuente: Los autores.

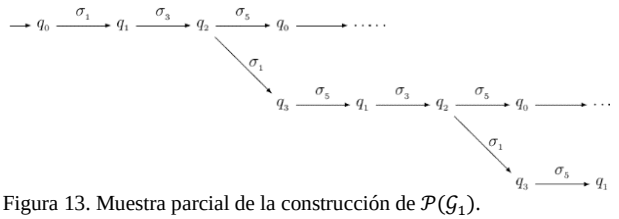


Figura 13. Muestra parcial de la construcción de $\mathcal{P}(\mathcal{G}_1)$.
Fuente: Los autores.

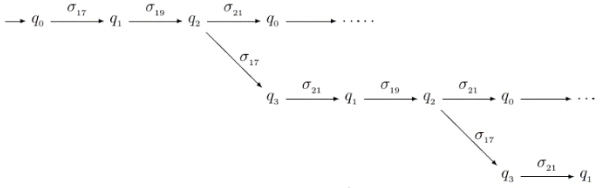


Figura 14. Muestra parcial de la construcción de $\mathcal{P}(\mathcal{G}_2)$.
Fuente: Los autores.

6.4. Planificaciones locales

Para cada estado del sistema de producción de pintura; $q = \delta(q_0, s)$, donde $s \in \Sigma^*$ y $q_0 = \left(q_{0_1}, q_{0_2}, \cdots, q_{0_5}\right)$ es el estado inicial, consideramos el conjunto de todos los eventos habilitados en q; $\mathcal{E}(q)$: para cada k-interacción $\sigma \in \mathcal{E}(q)$, donde $j_1, j_2, \cdots, j_5$ son los índices de las componentes de cambio por la ocurrencia en q, σ es consensuada sí $\pi_{j_i}(s) \in \mathcal{K}_i,\ \forall\, j_i,\ i = 1, \cdots, 5$. Para el subsistema de producción PB, las actividades de dispersión y dilución son llevadas a cabo siempre que $\pi_1(s)\sigma \in \mathcal{K}_1,\ \ \sigma \in \Sigma_1$. El procedimiento repetido sucesivamente generará un conjunto de estatus Q_{p_1} obtenidos por consenso y su dinámica puede ser representada gráficamente (ver Fig. 13).

Donde $\mathcal{L}_{p_1} = (\sigma_1\sigma_3\sigma_5)^5 + \sigma_1\sigma_3\sigma_1(\sigma_5\sigma_3\sigma_1)^3\sigma_5\sigma_3\sigma_5$; es lenguaje de planificación local. Para el subsistema de producción MA, las actividades de dispersión y mezclado con la base blanca se ejecutarán siempre que $\pi_2(s)\sigma \in \mathcal{K}_2, \sigma \in \Sigma_2$. El procedimiento repetido sucesivamente generará un conjunto de estatus Q_{p_2} obtenidos por consenso y su dinámica puede ser representada gráficamente (ver Fig. 14).

Donde

$\mathcal{L}_{p_2} = (\sigma_{17}\sigma_{19}\sigma_{21})^2 + \sigma_{17}\sigma_{19}\sigma_{17}(\sigma_{21}\sigma_{19}\sigma_{17})^0\sigma_{21}\sigma_{19}\sigma_{21}$;

es el lenguaje de planificación local. Para el subsistema de producción PC, las actividades de dispersión, molienda, dilución y mezclado con la base blanca se efectuaran siempre que $\pi_3(s)\sigma \in \mathcal{K}_3,\ \ \sigma \in \Sigma_3$. Repetido sucesivamente el procedimiento se generará un conjunto de estatus Q_{p_3} obtenidos por consenso y su dinámica puede ser representada gráficamente (ver Fig. 15).

Donde $\mathcal{L}_{p_3}$ lenguaje de planificación local es

$\mathcal{L}_{p_3} = (\sigma_7\sigma_9\sigma_{11}\sigma_{13}\sigma_{15})^{2+}$

$\sigma_7\sigma_9\sigma_7\sigma_{11}\sigma_{13}\sigma_9(\sigma_{11}\sigma_{15}\sigma_{13}\sigma_7\sigma_9)^0\sigma_{11}\sigma_{15}\sigma_{13}\sigma_{15} + \cdots$

Para el subsistema de producción EN, la actividad de envasado se cumple si $\pi_4(s)\sigma \in \mathcal{K}_4, \sigma \in \Sigma_4$.

El procedimiento repetido sucesivamente generará un conjunto de estatus Q_{p_4} obtenidos por consenso y su dinámica puede ser representada gráficamente (ver Fig. 16).

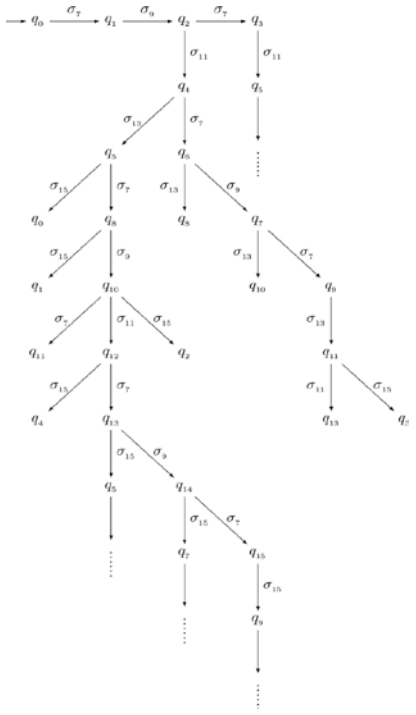


Figura 15. Muestra parcial de la construcción de $\mathcal{P}(\mathcal{G}_3)$.
Fuente: Los autores.

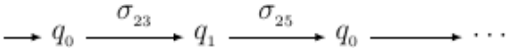


Figura 16. Muestra parcial de la construcción de $\mathcal{P}(\mathcal{G}_4)$.
Fuente: Los autores.

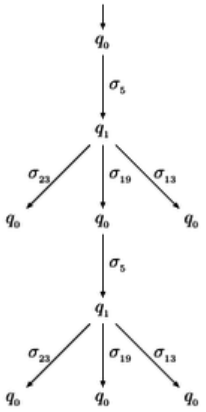


Figura 17. Muestra parcial de la construcción de $\mathcal{P}(\mathcal{G}_5)$.
Fuente: Los autores.

Donde $\mathcal{L}_{p_4} = (\sigma_{23}\sigma_{25})^1$ es lenguaje de planificación local. Para el sistema de producción, la distribución de la base blanca proporcionada por PB a los subprocesos EN, MA, y PC se efectuaran siempre que $\pi_5(s)\sigma \in \mathcal{K}_5,\ \ \sigma \in \Sigma_5$. Mientras, este requerimiento se cumpla se generará un conjunto de estatus Q_{p_5} obtenidos por consenso y su dinámica puede ser representada gráficamente (ver Fig. 17).

Donde $\mathcal{L}_{p_5} = (\sigma_5\sigma_{13})^2 + (\sigma_5\sigma_{19})^{+2}(\sigma_5\sigma_{23})^1$; es el lenguaje de planificación local.

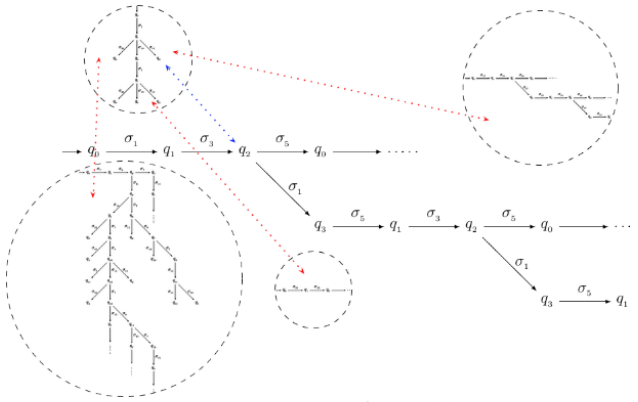


Figura 18. Muestra parcial de la construcción de $\mathcal{P}(\mathcal{G})$.
Fuente: Los autores.

6.5. Planificación por consenso

Finalmente, para el sistema de producción de pintura la sincronización de los subsistemas $(PB, EN, MA\ y\ PC)$ es establecida desde la agregación de la base blanca por parte de PB y el posterior uso de la misma por parte de EN, MA y PC (ver Fig. 18).

Así, la planificación $\mathcal{P}(\mathcal{G})$ es construida desde la sincronización de las planificaciones locales $\mathcal{P}(\mathcal{G}_i) = (Q_i, \Sigma_i, \delta_i, \mathcal{J}_i, q_{0_i}, Q_{p_{im}})$, con $i = 1, \cdots, 5$; sobre PB, MA, PC, EN y Re respectivamente y está dada por $\mathcal{P}(\mathcal{G}) = (Q_{p_1} \times \cdots \times Q_{p_5}, \Sigma, \delta, \mathcal{J}, (q_{0_1}, \cdots, q_{0_5}), Q_{p_{1m}} \times \cdots \times Q_{p_{5m}})$

donde

- $Q_{p_1} \times \cdots \times Q_{p_5}$ es el conjunto de estados;
- Σ es el alfabeto y representa a $\Sigma_1 \cup \cdots \cup \Sigma_5$;
- $(q_{0_1}, \cdots, q_{0_5})$ es el estado inicial;
- $Q_{p_{1m}} \times \cdots \times Q_{p_{5m}}$ es el conjunto de estados finales;
- $\delta\big((q_1, \cdots, q_5), \alpha\big) = (P_1, \cdots, P_5)$, $P_i = \delta_i(q_i, \alpha)$, y $P_j = q_j$, si para $i, j = 1, \cdots, 5$; $\alpha \in \bigcap_i \mathcal{J}_i(q_i) \setminus \bigcup_{j:j\neq i} \Sigma_j$,

e indefinida en otro caso;

- $\mathcal{J}(q_1, \cdots, q_5) = \bigcap_i \mathcal{J}_i(q_i) \setminus \bigcup_{j:j\neq i} \Sigma_j$; $\quad i, j = 1, \cdots, 5$;

  el cual tiene como lenguaje (de planificación) $\mathcal{L}_p = \mathcal{L}_{pm} = \cap_{i=1}^{5} \pi_i^{-1}(\mathcal{L}_{pm_i})$.

7. Conclusión

La descomposición de una planificación en planificaciones locales, direcciona el análisis global desde un punto de vista local, lo cual permite bajo modularidad, unificación de criterios y juicios, flexibilidad, capacidad de gestión, viabilidad e implementación reducida; en consecuencia, un proceso ágil desde el punto de vista de automatización. En efecto, las descomposiciones son

$$\mathcal{L}_p = \bigcap_{i=1}^{n} \pi_i^{-1}(\mathcal{L}_{p_i}) \quad y \quad \mathcal{L}_{p_m} = \bigcap_{i=1}^{n} \pi_i^{-1}(\mathcal{L}_{p_{mi}}) \qquad (12)$$

expresadas por lenguajes cerrados y $\mathcal{L}_{p_m}$-cerrados respectivamente; de donde, se avanza modularmente a la reducción e implementación óptima. A propósito, enfatizamos que la planificación en SED siempre será una intención que posiblemente no pueda ser llevada a cabo completamente; por ejemplo, cuando estamos en teoría de control, debido a los eventos no controlables. Por otro lado, el modelo construido para la clase de sistemas de manufactura con componentes cooperantes (unidades de producción) puede ser considerado para el estudio de las k-interacciones cuando las unidades del sistema toman opciones cooperativas. Más precisamente, si el número de opciones cooperativas crece, entonces seguramente se generarán nuevas interacciones indeseables entre estas, produciendo problemas de funcionalidad en el sistema; pero nuevamente será establecido el acoplamiento entre las componentes por consenso (reconfiguración del sistema), con lo cual podríamos abordar propiedades de seguridad y no bloqueo desde un punto de vista local.

En relación a los trabajos futuros se puede considerar el desarrollo de programas de software para ejecutar cálculos referentes al algoritmo de planificación. También, comparar la planificación por consenso con diseños establecidos por Redes de Peri, representadas por bases de Gröbner, por razones de explosión de estados. Finalmente, se pueden extender nuestros argumentos teóricos de planificación, como una herramienta a un nivel de abstracción temporal para el análisis de SED.

Bibliografía

[1] Aldaniyazov, K.N., Main factors for the improvement of a complex system of strategic production cost management. Revista Espacios, 39(11), pp. 29, 2018.

[2] Al-Jaar, R.Y. and Desrochers, A.A., Petri nets in automation and manufacturing. Advances in Automation and Robotics, 2, pp. 153-225, 1990.

[3] Andrade, H.deS. and Loureiro, G., Proposta de um modelo de planejamento estratégico baseado em engenharia de sistemas. Revista Espacios, 39(13), pp. 10, 2018.

[4] Arias-Bolzmann, L., Agurto, W.F., Chávez, Á.M., Pantoja, R. and Pinto, A., Decisions in hierarchical production planning: goals, heuristics and bias. Revista Espacios, 30(14), pp. 3, 2018.

[5] Caspi, P., Model of discrete event systems in computer science, Proceedings of the European Control Conference (ECC 91), Grenoble, France, 1991.

[6] Dante, O., Coromings, A. and Lusa, A., Estado del arte sobre planificación agregada de la producción. Tesis Doctoral, Instituto de la Organización y Sistemas Industriales, Universidad Politécnica de Cataluña, Barcelona, 2007.

[7] Eilenberg, S., Automata, languages and machines. Academic Press, New York, 1974.

[8] Gradišar, D. and Mušič, G., Production-process modelling based on production-management data: A Petri-net approach. International Journal of Computer Integrated Manufacturing, 20(8), pp. 794-810, 2007. DOI: 10.1080/09511920601103064.

[9] Guo-zhu, J.I.A. and Cheng, Yan., Reengineering method of production system based on theory of constraint and system dynamics. Computer Integrated Manufacturing Systems, 4, 2007.

[10] Hopcroft, J.E., Motwani, R. and Ullman, J.D., Automata theory, languages, and computation. Addison Wesley, Press Reading, Massachusetts, 1979.

[11] Lapulus, E., Fang, S., Rang, C. and Van-Gerwen, R., Manufacturing Integration, Computers in Industry, 1995.

[12] Marsan, M.A., Balbo, G., Bobbio, A., Chiola, G., Conte, G. and Cumani, A., The effect of execution policies on the semantics and

analysis of stochastic Petri nets. IEEE Transactions on Software Engineering, 15(7), pp. 832-846, 1989. DOI: 10.1109/32.29483
[13] Mata, G., Lugo, A. and Rojas, G., Aplicación de bases de Gröbner en el problema de alcanzabilidad de estados de sistemas de eventos discretos modelados por redes de Petri. Lecturas Matemáticas, 37(1), pp. 5-23, 2016.
[14] Murata, T., Petri Nets: Properties, analysis and applications, Proceedings of the IEEE, 77(4), 1989. DOI: 10.1109/5.24143
[15] Peterson, J., Petri Net Theory and the Modeling of Systems. Prentice Hall, PTR Upper Saddle River, NJ, USA, 1981.
[16] Wonham, W., Design Software: TCT [Online]. Systems Control Group, Dept. of ECE, Univ. of Toronto, 2015. Available at: http://www.control.toronto.edu/DES.
[17] Yan, H.S., Zhang, X.D. and Jiang, M., Hierarchical production planning with demand constraints. Computers & Industrial Engineering, 46(3), pp. 533-551, 2004. DOI: 10.1016/j.cie.2004.01.012

G.E. Mata-Díaz, received a Dr. degree in mathematical sciences: Doctor Applied Science, Universidad de Los Andes, ULA, Mérida-Venezuela in 2016. From 1997, he is currently a full professor in the department of mathematics at Universidad de Los Andes, Venezuela. Has experience in mathematics, with emphasis on dynamic systems of discrete events (analysis and control).
ORCID: 0000-0001-7147-1422

L.B. Ruiz-Leal, received a PhD degree in mathematical sciences: Doutor em Ciências, from the National Institute of Pure and Applied Mathematics: Instituto Nacional de Matemática Pura e Aplicada IMPA Rio de Janeiro-Brasil in 2005. From 2005, he is currently a full professor in the department of mathematics Universidad de Los Andes, Venezuela. Has experience in Mathematics, with emphasis on ergodic theory and hyperbolic dynamical systems. His research interests include: transitive and robustly transitive invariant sets, infinite ergidic theory and symbolic dynamics.
ORCID: 0000-0002-7737-3847

C.C. Camacho-Camacho, received a MSc. degree in alternative pedagogy in the teaching of mathematics from Universidad Politécnica Territorial de Mérida "Kleber Ramírez", Venezuela in 2018. Has experience in mathematics, with emphasis on teaching systems and didactic.
ORCID: 0000-0003-3630-2812

A.J. Méndez-Urrieta, received a Dr. degree in mathematical sciences: Doctor Applied Science, Universidad de Los Andes, ULA, Mérida-Venezuela in 2017. Has experience in mathematics, with emphasis on Control engineering and automation.
ORCID: 0000-0002-6406-6805

S. Muñoz, received a PhD degree in mathematical sciences: Doutor em Ciências, from the National Institute of Pure and Applied Mathematics: Instituto Nacional de Matemática Pura e Aplicada IMPA Rio de Janeiro-Brasil in 2005. From 2017 he is currently a full professor in the department of mathematics, physics and computers (Dpto. de Matemática, Física e Computação DMFC) at the university: Universidade do Estado do Rio de Janeiro UERJ Resende, Rio de Janeiro, Brasil. Has experience in Mathematics, with emphasis on ergodic theory and dynamical systems. His research interests include: transitive and robustly transitive invariant sets, infinite ergidic theory and symbolic dynamics.
ORCID: 0000-0002-6952-6102

H.B. Zambrano-Garcia, received the Lcdo. Mathematics in 1994, from the Universidad de los Andes. Mérida, Venezuela. Has experience in mathematics, with emphasis on programmer in systems, and in control and automation. His research interests include: analysis of complex systems and control of hybrid systems.
ORCID: 0000-0002-6059-5136



UNIVERSIDAD NACIONAL DE COLOMBIA
SEDE MEDELLÍN
FACULTAD DE MINAS

Área Curricular de Ingeniería
de Sistemas e Informática

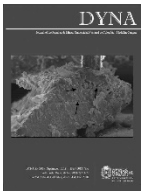
Oferta de Posgrados

Especialización en Sistemas
Especialización en Mercados de Energía
Maestría en Ingeniería - Ingeniería de Sistemas
Doctorado en Ingeniería- Sistemas e Informática

Mayor información:

E-mail: acsei_med@unal.edu.co
Teléfono: (57-4) 425 5365

UNIVERSIDAD NACIONAL DE COLOMBIA
SEDE MEDELLÍN
FACULTAD DE MINAS



DYNA
http://dyna.medellin.unal.edu.co/

Agronomic and environmental benefits of nitrogen fertilizers sources in *Ocimum basilicum* L

Martha Constanza Daza-Torres [a], Greydy Selene Ladino-Tabarquino [b] & Norberto Urrutia-Cobo [c]

[a] *Escuela de Ingeniería de Recursos Naturales y del Ambiente, Universidad del Valle, Cali, Colombia. martha.daza@correounivalle.edu.co*
[b] *Programa de Agronomía. División de suelos. Centro de Investigación de la Palma de Aceite, Agustín Codazzi, Cesar, Colombia. gladino@cenipalma.org*
[c] *Escuela de Ingeniería de Recursos Naturales y del Ambiente, Universidad del Valle, Cali, Colombia. Norberto. urrutia@correounivalle.edu.co*

Received: November 29th, de 2017. Received in revised form: May 10th, 2018. Accepted: May 29th, 2018

Abstract
This work evaluated slow release fertilizers in basil cultivated in soil of Valle del Cauca (Colombia). A completely random design was established with 14 treatments in lysimeters and two fast liberation fertilizers (calcium nitrate and ammonium sulphate), urea coated with sulphur and two organic fertilizers (vermicompost and chicken manure) in different doses (100, 150 y 200 kg ha^{-1}) were evaluated. At 96 days, measurements of nitrogen leached, dry mass, foliar nitrogen, pH, electric conductivity and soil organic matter were determined. In addition, apparent efficiency of recovery, internal efficiency of use and efficient use of water were calculated. The organic fertilizer caused changes in porosity, producing nitrogen leaching. The fast liberation fertilizers obtained better performance of percentage of dry mass, foliar nitrogen and efficiency of recovery, while slow release fertilizers did so in soil properties, internal efficiency of use and efficient use of water.

Keywords: nitrate leaching; organic fertilizer; efficiency; water productivity; basil.

Beneficios agronómicos y ambientales de fuentes de fertilizantes nitrogenados en *Ocimum basilicum* L

Resumen
Este trabajo evaluó diferentes fuentes de fertilizantes nitrogenados en albahaca cultivada en un suelo del Valle del Cauca (Colombia). Se realizó un diseño completo al azar con 14 tratamientos en lisímetros y se compararon dos fertilizantes de rápida liberación (FRL) (nitrato de calcio y sulfato de amonio) y tres fertilizantes de lenta liberación (FLL) (urea recubierta, lombricompost y gallinaza). A los 84 días se midió nitrógeno lixiviado, masa seca foliar, (%MS), nitrógeno foliar (NF), pH, conductividad eléctrica, materia orgánica y nitrógeno total del suelo. También se determinaron la eficiencia aparente de recuperación (ER), la eficiencia interna de utilización (EI) y el uso eficiente de agua (UEA). Como principales resultados se encontró que los abonos orgánicos ocasionaron cambios en la porosidad, produciendo lixiviación de nitrógeno. Los FRL obtuvieron mejor comportamiento en %MS, NF y ER, mientras que los FLL lo hicieron en las propiedades del suelo, la EI y UEA.

Palabras clave: lixiviación de nitrato; abono orgánico; eficiencia; productividad del agua; albahaca

1. Introducción

Para la producción agrícola de alto rendimiento, es necesaria la aplicación de fertilizantes nitrogenados (FN); sin embargo, la eficiencia de uso del nitrógeno (N) es menor al 50 %, debido a las pérdidas por lixiviación, desnitrificación y volatilización de compuestos nitrogenados [1]. La lixiviación de N está directamente relacionada con el inadecuado manejo del riego, aplicaciones excesivas y no oportunas de la fertilización nitrogenada, características y uso del suelo y las condiciones climáticas, entre otros factores [2]. También, la pérdida de nitrato está en función de la fuente de fertilizante (orgánico o inorgánico) y de las fases

How to cite: Daza-Torres, M.C., Ladino-Tabarquino, G.S. and Urrutia-Cobo, N., Beneficios agronómicos y ambientales de fuentes de fertilizantes nitrogenados en Ocimum basilicum L. DYNA, 85(206), pp. 294-303, September, 2018.

© The author; licensee Universidad Nacional de Colombia.

fenológicas de las plantas, presentándose la mayor lixiviación en las primeras etapas [3].

Una de las estrategias empleadas para reducir las pérdidas de N por lixiviación y aumentar la eficiencia de la fertilización nitrogenada en sistemas agrícolas, es el uso de fertilizantes de liberación lenta (FLL). Estos fertilizantes pueden ser de síntesis química o ser orgánicos, donde los primeros a su vez pueden ser inhibidores o pueden estar hechos con materiales recubiertos. Los inhibidores consisten en fertilizantes con concentraciones de sustancias capaces de inhibir la actividad microbiana responsable de la nitrificación, específicamente de bacterias del género *Nitrobacter* sp, retrasando la oxidación del nitrito a nitrato. Los segundos hacen referencia a fertilizantes como la urea, recubierta con películas de sustancias de lenta descomposición como el azufre (urea acidulada) o con polímeros que retrasan la transformación a formas inorgánicas [4].

Los abonos orgánicos (AO) también pueden ser considerados como FLL puesto que su mineralización sucede gradualmente, aportando de forma progresiva el N para las plantas [5]. Incluso algunos tectosilicatos como las zeolitas son considerados como FLL, al ser capaces de retener, tanto el amonio como el nitrato, e irlo liberando lentamente a la solución del suelo, lo que retrasa la nitrificación [6]. Estos fertilizantes permiten un mayor aprovechamiento del N por parte de la planta, gracias a su lento suministro.

Existen varios estudios relacionados con el uso de FLL y sus beneficios en aspectos como la disminución de la tasa máxima e incremento del periodo de nitrificación [7], reducción de las pérdidas de N por volatilización en cultivo de maíz [8], incremento del rendimiento de albahaca [9], incremento en el carbono orgánico (CO) del suelo en cultivo de albahaca [10] y canola [11] y en el caso de los orgánicos se ha reportado mayor retención de humedad [12], aumento del contenido de N orgánico en el suelo, aumento del proceso de mineralización [13], incremento de la actividad microbiana [14], y reducción en la lixiviación de nitrato [15].

La principal desventaja de los FLL de origen inorgánico es su alto precio, aunque es posible que éste se vea compensado por el aumento en la eficiencia de la fertilización nitrogenada en los cultivos [16]. En el caso de los orgánicos, la desventaja es la alta variabilidad en las tasas de mineralización de los AO, haciendo difícil la determinación de dosis nitrogenadas adecuadas, pese a los beneficios que brinda a las propiedades de los suelos [5].

Los FLL son poco usados en los países en desarrollo. Sin embargo, son estos países los que consumen más FN con muy baja eficiencia de uso, la cual está entre el 20 % y el 35 % [17]. En América Latina, Colombia es el segundo país con el mayor consumo de FN, 5,8 veces por encima de la media regional de 84,2 kg·ha^{-1} cultivable, superando a países como Chile, Brasil, México y Argentina [18], con eficiencia de uso por debajo del 30 %. Sumado a lo anterior, la producción de FN de síntesis industrial no está contemplada en la política colombiana por sus altos costos energéticos y de infraestructura, que hacen que sea más viable importarlos que producirlos [19]. Ante este panorama, es importante realizar estudios de diversas estrategias como el uso de FLL, para aumentar la eficiencia del N en sistemas productivos agrícolas.

La albahaca (*Ocimum basilicum* L.) es una planta aromática de la familia de las lamiáceas, muy apetecida para su comercialización en fresco o para la extracción de aceites esenciales para usos medicinales y cosméticos principalmente. En Colombia, los principales productores de albahaca se encuentran en los departamentos de Boyacá, Cundinamarca y Valle del Cauca. El cultivo de albahaca es promisorio para pequeños y medianos agricultores, por su gran potencial de comercialización y exportación. Sin embargo, ante los altos precios de los FN, aún faltan estudios que permitan mejorar la eficiencia de la fertilización, para que sus sistemas productivos sean más competitivos en el mercado.

En el presente trabajo se realizó un estudio en condiciones controladas para investigar mediante el uso de lisímetros de drenaje, cómo los FN, tanto los FRL (nitrato de calcio y sulfato de amonio) como los FLL (urea recubierta, lombricompost y gallinaza) contribuyen con beneficios ambientales y agronómicos de producción, en un suelo cultivado con albahaca (*Ocimum basilicum* L).

2. Materiales y métodos

El experimento se realizó entre los meses de diciembre de 2015 y marzo de 2016 en los invernaderos del Laboratorio de Aguas y Suelos Agrícolas (LASA) de la Universidad del Valle, ubicados en el municipio de Santiago de Cali, Valle del Cauca, a una altura de 979 msnm; coordenadas latitud 3° 22’ 22.29’’ N, longitud -76° 31’ 49.22’’ W. Los valores de temperatura y precipitación promedio anual son de 25º C y 909 mm respectivamente.

El suelo utilizado provino de la finca “Las Palmas” (N 03 26.767’ W 076 27.551’), vereda Cauca Seco, corregimiento de Juanchito (Candelaria) en el Valle Cauca (Colombia). El suelo utilizado corresponde a la clasificación taxonómica Fluventic Haplustepts [20], cuyas principales características físico químicas fueron: textura franco arcillosa, pH (7,47); materia orgánica (2,32 %); Ca2+, Mg2+, K+ y Na+ (10,66; 5,95; 1,69 y 0,44 cmol(+)·kg-1 respectivamente), P disponible (29,56 mg·kg-1) y contenido de N total (0,12 %).

Los abonos orgánicos fueron caracterizados siguiendo la norma técnica NTC 5167 [21], los cuales presentaron pH ligeramente alcalino, alta capacidad de intercambio catiónico (CIC) y baja relación C/N (Tabla 1.).

Tabla 1.
Caracterización de los abonos orgánicos utilizados en la experimentación.

Abono	pH	CIC	CO	NT	K	Ca	Mg	C/N
		cmol(+)·kg^{-1}			%			
L	7,3	24,6	13,0	1,22	1,0	3,8	1,1	13,0
G	7,5	34,5	16,0	1,43	1,2	11,2	0,4	12,3

CIC = capacidad de intercambio catiónico; CO = carbono orgánico; NT = Nitrógeno total; L= lombricompost; G= gallinaza.
Fuente: Los autores

Con el propósito de determinar los volúmenes de riego a aplicar, se construyó un tanque evaporímetro clase A de 0,60 m de diámetro y 0,19 m de altura, el cual se ubicó a 0,10 m de la superficie del suelo siguiendo las especificaciones de Allen et al. (2006) [22]. La calibración del tanque evaporímetro se realizó registrando el valor diario de evaporación, tanto del prototipo como del tanque ubicado en la estación climatológica de la Universidad del Valle sede Meléndez. Con el registro de los datos de ambos tanques, se realizó una regresión lineal con la cual se obtuvo una confiabilidad en la correlación de los datos registrados; con ello se garantizó que la lectura de evaporación registrada en el tanque evaporímetro del prototipo, se ajustara a la lectura real de evaporación registrada por el tanque evaporímetro clase A. El coeficiente de tanque utilizado fue de 0,75. El coeficiente de regresión alcanzado fue de 0,9764 ($p<0,01$).

Los lisímetros consistieron en recipientes plásticos de 0,25 m de altura por 0,20 m de diámetro, recubiertos con malla y grava en el fondo, donde se dispuso el suelo. El recipiente se perforó en la parte inferior lateral y se instaló una manguera conectada a un segundo recipiente debidamente tapado, dentro del cual se ubicó un vaso graduado para la recolección del lixiviado. Se estableció una diferencia de altura de 0,30 m entre el lisímetro y el recipiente recolector para favorecer el flujo. Cada lisímetro fue inclinado con un ángulo de 10º con el fin de garantizar el flujo total del lixiviado. La recolección se realizó diariamente y la muestra fue guardada en condiciones refrigeradas hasta cuando se contó con 30 mL para ser analizado.

El diseño del experimento utilizado fue unifactorial (tipo de abono) completamente al azar con 14 tratamientos y tres repeticiones. Se evaluaron tres FLL: urea recubierta con azufre (U) (con 40 % de N, 6 % de S y 2 % de polietileno) y dos AO (lombricompost y gallinaza). También se evaluaron dos fertilizantes de rápida liberación (FRL): nitrato de calcio (NC) con 15,5 % de N-amoniacal y 18,5 % de Ca^{2+} y sulfato de amonio (SA) con 21 % de N-amoniacal y 24 % de S respectivamente. Los 14 tratamientos fueron: testigo sin ninguna aplicación (TA), NC en dosis de 150·kg ha^{-1}, SA, U, en dosis de 100, 150 y 200 kg ha^{-1} y gallinaza (G) y lombricompost (L) en dosis de 200, 250 y 300 kg·ha^{-1} de N. Cada tratamiento tuvo tres repeticiones para un total de 42 unidades experimentales; cada unidad experimental (UE) consistió en un lisímetro de drenaje el cual fue llenado con suelo previamente tamizado por 4 mm y una planta de albahaca.

Los AO fueron aplicados a los 8 días antes del trasplante mientras que los FRL (NC, SA) fueron adicionados disueltos en el agua de riego en el momento del trasplante. La urea recubierta (U) fue adicionada tres días antes del trasplante.

Durante los primeros 15 días después del trasplante (ddt), se mantuvo el suelo a capacidad de campo (CC), con ayuda de un Time Domain Reflectometry (TDR marca MPKit-406 ICT Internacional, Australia). En los siguientes 69 ddt se utilizó una lámina de riego basada en la evaporación potencial medida en el tanque evaporímetro, utilizando los coeficientes del cultivo (Kc) de 0,59 y 0,42 para las etapas comprendidas entre 26-50 días y 51-71 días, respectivamente [23]. La aplicación de la lámina de riego para cada UE se realizó diariamente. Los volúmenes de riego estuvieron entre 70 y 500 mL·$planta^{-1}$·$día^{-1}$.

A los 25 y 84 ddt se determinó el contenido de N amoniacal (nitrato y amonio) en lixiviados por el método de extracción con KCl 2N. Al inicio de la floración, a los 84 ddt se realizó la cosecha y se determinó el porcentaje de masa seca foliar a partir de los pesos de la masa aérea fresca y seca. La masa fresca fue puesta a secar en estufa a 55 ºC por 24 horas, para luego adquirir el peso seco. Igualmente, el porcentaje de nitrógeno foliar (NF) fue estimado por el método de Kjeldahl modificado, realizando predigestión por 24 horas con H_2SO_4 reactivo analítico y catalizadores compuestos por sulfato de cobre y sulfato de potasio. Posteriormente se realizó la digestión sometiendo la muestra foliar a 250 ºC por 30 minutos y luego a 350 ºC por dos horas, hasta lograr que las muestras quedaran verdes traslúcidas. Luego, se realizó la destilación de la misma usando soda al 40 % y recogiendo el N amoniacal en ácido bórico con indicador. El NF fue cuantificado usando ácido sulfúrico en la titulación.

También se determinaron al final del experimento, (84 ddt) variables del suelo como el pH (potenciómetro, relación suelo: agua 1:1), conductividad eléctrica (CE) (conductímetro, relación suelo: agua 1:2), materia orgánica del suelo (MOS) (Método de Walkley Black) y nitrógeno total del suelo (NTS) por el método de Kjeldahl, donde una muestra de suelo se puso en digestión con ácido sulfúrico y catalizadores por 2,5 horas a 350 ºC hasta alcanzar coloración transparente. Seguidamente se destiló con soda al 40 % y se recogió el N volatilizado en ácido bórico con indicador. La titulación se realizó con ácido sulfúrico, Así mismo, se calcularon los indicadores "eficiencia aparente de recuperación" (ER) y "eficiencia interna de utilización" (EI) propuestos por Dobermann [24] para calcular la eficiencia de la fertilización nitrogenada, así como el índice "uso eficiente del agua" (UEA) calculado como la relación entre la masa fresca y seca producida y el volumen de agua empleado durante el ciclo de cultivo evaluado.

La verificación de la distribución normal de los datos se hizo siguiendo la prueba de Shapiro Wilk y la homogeneidad de varianzas se determinó con la prueba de Levene. Se realizó un análisis estadístico descriptivo y análisis de varianza para determinar diferencias significativas entre tratamientos. Para las variables que siguieron distribución normal y tuvieron varianzas homogéneas se realizó un análisis de postanova mediante los test de Tukey y Duncan ($p=0,05$). Para el caso de las variables volumen de lixiviados, porcentaje de masa seca (MS) y NTS, que no mostraron homogeneidad de varianza, se realizó el análisis de varianza por el test de Welch y la comparación de medias mediante la prueba de Dunnett ($p= 0.05$). Se utilizó el programa estadístico IBM SPSS Statistics 20.

3. Resultados y discusión

3.1. Lixiviación total de nitrógeno

Solamente los tratamientos con AO fueron los que presentaron lixiviación durante el periodo experimental (Fig. 1). Los volúmenes de lixiviados estuvieron entre 50 y 270 mL para los tratamientos con gallinaza y lombricompost. El

tratamiento G300 presentó la mayor cantidad de lixiviados, siendo estadísticamente diferente de G250 y del lombricompost (L). A pesar de que todos los tratamientos recibieron la misma cantidad de riego, la cual fue calculada para llevar el suelo a capacidad de campo, solamente los AO presentaron pérdida de agua por lixiviación. Lo anterior se explica por la capacidad de los AO para la formación de agregados del suelo estables en agua, disminuyendo la densidad aparente del suelo e incrementando la porosidad del suelo [25]. Estas condiciones mejoran la infiltración y favorece el movimiento del agua dentro del suelo, llevándola inclusive más allá del sistema de raíces, lo que alimenta los depósitos de agua subterránea, pero reduce la eficiencia del uso del recurso hídrico por la planta, para lo cual debería contemplarse la determinación de la humedad de capacidad de campo para estas nuevas condiciones. De acuerdo con Moreno [26], se debe tener precaución con la aplicación de AO, puesto que en condiciones que favorezcan su mineralización, podrían incrementar significativamente la lixiviación de nitrato.

La aplicación del riego (cantidad de agua y método de aplicación) debe ir en concordancia con la aplicación de los AO. Cuando se empleó el Kc del cultivo para la determinación de la lámina de riego, la pérdida de agua por lixiviación se redujo sustancialmente en un 92 %.

El nitrógeno lixiviado (NL) estuvo por debajo de un kg·ha^{-1} para los tratamientos con AO (Fig.1A). A medida que se aumentó la dosis de gallinaza, la pérdida de NL también tendió a aumentar, mientras que en los tratamientos con lombricompost ocurrió lo contrario, la mayor dosis presentó la menor pérdida de N, aunque sin diferencias estadísticas con las otras dosis. Los tratamientos con urea recubierta y los FRL no presentaron lixiviación, indicando que, a pesar de la mayor disponibilidad de N, el manejo del agua es más determinante, a la hora de mejorar la retención de N en el suelo, que incluso, la dosis y el tipo de fertilizante [27]. Resultados opuestos fueron reportados por Alfaro et al., [28] quienes valoraron la lixiviación de nitrato en un suelo andisol al aplicar 150 kg·ha^{-1} de N por medio de AO e inorgánicos y encontraron que la concentración de nitrato en los lixiviados fue 50 % más alta en los tratamientos con fertilizantes inorgánicos que con los AO, utilizando la misma lámina de agua de 1260 mm. Estos resultados pueden deberse a la diferencia de suelos utilizados en ambas investigaciones, ya que los suelos pesados con presencia de arcillas expandibles como el utilizado en esta investigación, pueden mejorar su porosidad drenable con la aplicación de AO.

La mayor y menor concentración de amonio en el lixiviado encontrada fue para los tratamientos G200 y L200 respectivamente, siendo los únicos que presentaron diferencias estadísticas entre ellos (Tabla 2). Estos resultados pudieron deberse a la menor CIC que tenía el lombricompost que retuvo menor cantidad de amonio. También es posible que el proceso de mineralización sea mucho más lento, al contar con menor cantidad de nutrientes para los microorganismos del suelo.

El mayor y menor contenido de nitrato presente en los lixiviados fueron para los tratamientos de L250 y L200, sin superar los 50 mg·L^{-1} admisibles en el agua para consumo humano establecida por la WHO [28]. Superiores concentraciones fueron

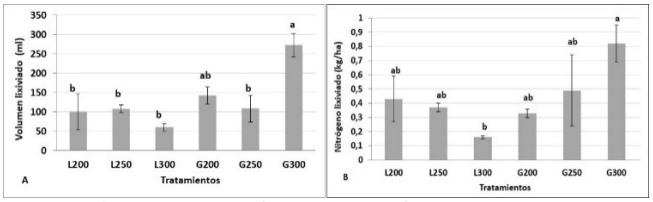


Figura 1. Efecto de la aplicación de abonos orgánicos usados en albahaca en: A. volumen de lixiviados, (F=6,76; p<0,001; Dunnett 95 %). B. Nitrógeno lixiviado total (F=2,72; p=0,07; Duncan 95 %). Letras iguales indican que no hay diferencias significativas entre tratamientos Las barras indican el error estándar. L= lombricompost; G= gallinaza; Los números indican las dosis de N empleadas en kg ha^{-1}
Fuente: Los autores.

Tabla 2.
Efecto de abonos orgánicos en la lixiviación de amonio, nitrato y total amoniacal durante el periodo experimental de 80 días después del trasplante de albahaca

Tratamiento	NH_4^+ mg·L^{-1} (1)	NO_3^- mg·L^{-1} (2)	N-amoniacal mg·L^{-1} (2)
L200	3,09±0,70 a	21,01±0,9 a	24,1±0,90 a
L250	2,81±0,43 ab	12,07±1,11 a	14,88±1,30 a
L300	1,91±0,05 ab	10,38±1,72 a	12,29±1,76 a
G200	1,47±0,61 b	8,93±0,09 a	10,39±0,64 a
G250	2,92±0,16 ab	15,10±3,46 a	14,88±3,52 a
G300	2,38±0,44 ab	10,72±0,35 a	13,09±0,68 a
F	1,89	1,03	1,26
p	0,17	0,44	0,34

Promedio de tres repeticiones ± error estándar. Letras iguales indican que no hay diferencias significativas entre tratamientos [1] comparación de promedios mediante la prueba de Duncan 95% [2]comparación de promedios mediante la prueba de Dunnett (95%). L= lombricompost; G= gallinaza. Los números indican las dosis de N empleadas en kg·ha^{-1}
Fuente: Los autores

encontradas por Ortuzar et al. [30], al utilizar FN para el cultivo de trigo, los cuales reportaron niveles de nitrato del orden de 40 mg·L^{-1}, respectivamente en lixiviados. Civeira y Rodríguez, [31] reportaron niveles más bajos de nitrato de 6,25 mg·L^{-1} en cultivos de maíz, debido al uso de enmiendas como la zeolita enriquecida con amonio. Daza et al. [15] encontraron en estevia concentraciones de nitrato en lixiviados entre 0,21 y 3,10 mg·L^{-1} al utilizar gallinaza y lombricompost, utilizando una menor lámina de riego y aseguran que el manejo del agua es fundamental en la prevención de la lixiviación.

A pesar de los valores bajos encontrados, es importante resaltar la cantidad de N lixiviado que se podría acumular en el tiempo, lo que puede llevar a pérdidas significativas. Zhang et al., [32] encontraron que la pérdida de nitrato por lixiviación en cultivos de hortalizas por año fue de 48,1 mg·L^{-1}, equivalente al 36 % del N aplicado en fertilizantes.

3.*2. Porcentaje de masa seca y N foliar*

A medida que se aumentó la dosis de N aplicado, el porcentaje de MS se incrementó, sin diferencias significativas, tanto en los tratamientos con AO como con los fertilizantes convencionales de síntesis industrial, con excepción de la urea recubierta (Tabla 3). Los tratamientos con U y SA presentaron porcentajes de MS, entre 31 % y 43 % aproximadamente, indicando que dichos tratamientos suministraron una adecuada cantidad de N para el crecimiento y la formación de tejidos y órganos vegetales. La

mayor dosis de SA fue estadísticamente diferente del TA, de los tratamientos con lombricompost y de las dosis de 200 y 250 kg ha^{-1} de N de gallinaza. Similares resultados fueron encontrados por Gao et al. [33], quienes reportaron un aumento hasta de 26,46 % de aumento en la cosecha de tomate, con el uso de urea de liberación lenta, en comparación con la urea convencional.

Al comparar las dosis evaluadas, la aplicación de 100 y 150 kg·ha^{-1} fueron las que mayor porcentaje de MS obtuvieron, sin diferencias significativas entre ellas, pero sí con las demás dosis evaluadas. (Fig. 2). Los FRL fueron los que mayores porcentajes de MS consiguieron, siendo significativamente diferentes de los FLL; los fertilizantes convencionales proporcionaron mayor porcentaje de MS que los AO. Estos últimos posiblemente favorecieron la absorción de agua y nutrientes pero su concentración de sales minerales fue menor y el suministro de N fue más lento, mientras que los FRL permitieron mayor concentración de sales minerales, mayor disponibilidad de N y por tanto mayor porcentaje de masa seca. Estos resultados sugieren que, dependiendo del destino final de la albahaca, se deben aplicar diferentes tipos de fertilizantes, de tal manera que, para su comercialización en fresco, el uso de AO resulta ser más apropiado y para forma deshidratada o extracción de aceites, la fertilización con fertilizantes como el SA o la U resultan mejor.

El NF estuvo entre 0,1 % y 3,5 % para T y SA150 respectivamente (Tabla 3.) Los tratamientos con SA fueron los que presentaron los mayores valores, estadísticamente diferentes de los AO, del T y del NC, pero similares a los alcanzados por los tratamientos con urea recubierta (U). Esto podría indicar que el S, elemento secundario indispensable para el crecimiento de las plantas y para el proceso de fotosíntesis, jugó un papel importante en los resultados observados. Tanto el SA como la U contienen una cantidad representativa de S que pudo haber favorecido la absorción de N [33].

Las dosis de 100, 150 y 200 kg·ha^{-1} de N obtuvieron los mayores porcentajes de NF sin diferencia significativas entre ellos, pero sí fueron diferentes del TA y de las dosis más altas de N aplicadas (Fig. 3). Los FRL fueron los que obtuvieron los valores más altos sin diferencias significativas con los FLL.

Los fertilizantes convencionales (NC, SA y U) presentaron los mayores contenidos de NF, mientras que los AO (lombricompost y gallinaza) mostraron una disminución de hasta un 90 % con respecto a los primeros; el contenido de NF en TA fue menor, posiblemente debido a que el N contenido en el suelo es orgánico en su mayor parte y no está disponible para la planta. Los AO presentaron 80,6 % por encima de la concentración de NF encontrada en TA, aunque no se pudieron encontrar diferencias estadísticas, debido a la alta variabilidad de los datos. Los AO mostraron mayor producción de masa que TA, debido posiblemente al suministro de N que pudo ser absorbido por la planta.

Tabla 3.
Contenidos foliares de masa seca y de nitrógeno en plantas de albahaca al ser tratadas con diferentes tipos de fertilizantes nitrogenados.

Tratamiento	Masa seca (%)	NF (%)
TA	25,1±1,2c	0,1±0,0c
NC	32,5±0,6abc	0,7±0,2c
U100	36,6±1,3abc	2,7±0,6ab
U150	31,1±1,1abc	2,8±0,4a
U200	29,4±1,7abc	0,4±0,0c
SA100	30,8±1,0abc	2,7±0,0ab
SA150	38,7±3,5ab	3,5±0,4a
SA200	43,0±7,9a	3,0±0,2a
L200	26,0±1,2bc	0,6±0,1c
L250	26,0±2,5bc	0,3±0,0c
L300	29,3±1,2bc	0,6±0,2c
G200	24,6±0,9c	0,5±0,1c
G250	26,6±0,5bc	1,4±0,4bc
G300	30,0±2,0abc	0,9±0,0c
F	4,31	9,68
p	<0,001	<0,001

Promedio de tres repeticiones ± error estándar. Letras iguales indican que no existen diferencias significativas entre las medias. 1Comparación de promedios por el Test de Dunnett (95%); NF= nitrógeno foliar; TA= testigo absoluto; NC= nitrato de calcio; U= urea recubierta; SA= sulfato de amonio; L= lombricompost; G= Gallinaza. Los números indican las dosis evaluadas de N en kg·ha^{-1}.
Fuente: Los autores

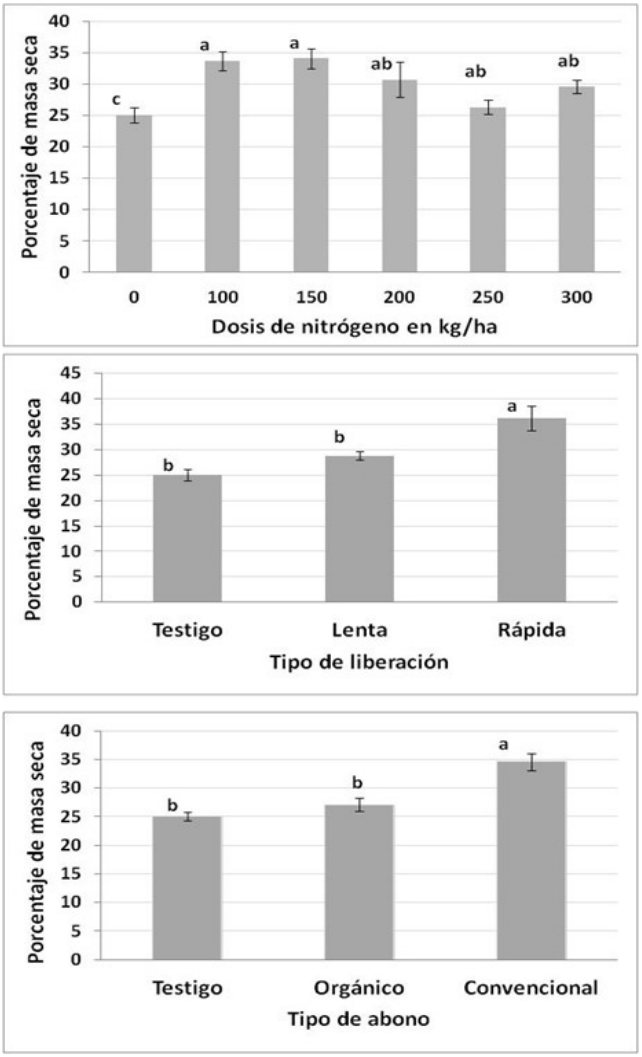


Figura 2. Efecto de la dosis (F= 1,98; P= 0,11), el tipo de liberación (F=9,16; P<0,001) y el tipo de fertilizante nitrogenado (F=11,56; P<0,001) en el porcentaje de masa seca de albahaca Comparación de medias por la prueba de Tukey (p<0,05). Las barras indican el error estándar.
Fuente: Los autores

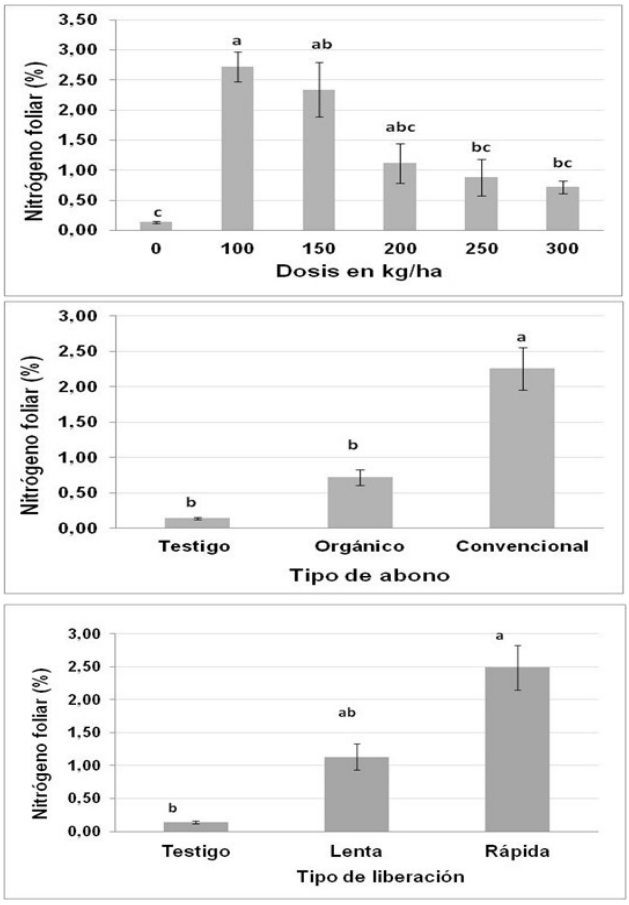


Figura 3. Efecto de la dosis (F=5,99; p=0,00), el tipo de abono (F= 16,2; p< 0,001) y el tipo de liberación (F=9,68; p< 0,001) en el porcentaje de nitrógeno foliar en albahaca. Comparación de medias mediante la prueba de Tukey al 95 %. Las barras indican el error estándar.
Fuente: Los autores

Tabla 4.
Efecto del uso de abonos nitrogenados de liberación lenta en propiedades del suelo después de la cosecha de albahaca

Tratamiento	pH[1*]	CE (dS·m^{-1})[2]	MOS (%)[1]	NTS (%)[3]
TA	7,37±0,10ab	0,51±0,06fg	4,08±0,39abc	0,22±0,04
NC	7,44±0,05ab	0,96±0,07cd	3,73±0,16bc	0,11±0,05
U100	7,42±0,19ab	0,64±0,05defg	3,76±0,12bc	0,17±0,01
U150	7,17±0,63ab	0,87±0,05cde	3,87±0,20abc	0,10±0,02
U200	7,23±0,02ab	0,96±0,09cd	3,68±0,23c	0,13±0,06
SA100	7,36±0,48ab	1,08±0,10bc	3,73±0,24bc	0,14±0,05
SA150	7,11±0,38b	1,35±0,07ab	3,84±0,29bc	0,06±0,01
SA200	7,21±0,35ab	1,44±0,06a	3,76±0,12bc	0,21±0,01
L200	7,37±0,16ab	0,69±0,09defg	4,62±0,21abc	0,14±0,03
L250	7,44±0,11ab	0,49±0,03g	5,18±0,31ab	0,16±0,04
L300	7,41±0,19ab	0,60±0,04efg	4,08±0,05abc	0,09±0,01
G200	7,48±0,21a	0,63±0,06efg	3,97±0,42abc	0,15±0,04
G250	7,40±0,60ab	0,82±0,08cdef	4,99±0,33abc	0,12±0,00
G300	7,47±0,19a	0,78±0,05cdefg	5,31±0,49a	0,19±0,03
F	2,95	21,19	4,27	1,96
p	0,01	<0,001	<0,001	0,07

Promedio de tres repeticiones de la concentración de hidrógeno ± error estándar. [1]Comparación de promedios mediante el Test de Tukey (95%); [2] Comparación de promedios mediante el Test de Duncan (95 %); [3] Comparación de promedios mediante el Test de Dunnett (95 %). Letras iguales indican que no existen diferencias significativas entre las medias. Promedio de tres repeticiones ± error estándar. CE= conductividad eléctrica; MOS = Materia orgánica del suelo; NT= nitrógeno Total del suelo. TA= testigo absoluto; NC= nitrato de calcio; U= urea recubierta; SA= sulfato de amonio; L= lombricompost; G= Gallinaza. Los números indican las dosis evaluadas de N en kg·ha^{-1}
Fuente: Los autores.

En estudios previos de albahaca como el de Búfalo et al. [35] se obtuvieron valores promedio de NF entre 1,64 % y 2,75 %, siendo el máximo para un tratamiento orgánico; Singh et al. [10] encontraron valores promedio de 2,28 % y 2,37 % en albahaca con tratamientos inorgánicos y orgánicos respectivamente. Estos valores fueron similares a los encontrados en el presente trabajo para SA en sus tres dosis, U100 y U150, indicando que estos tratamientos brindaron la cantidad de N adecuada. Los AO obtuvieron valores por debajo de los reportados por estos autores, indicando posiblemente que se presentó inmovilización del N y que estos abonos deben aplicarse con mayor antelación antes de la siembra, de acuerdo a su tasa de mineralización, para un mejor aprovechamiento de N.

3.3. Propiedades del suelo

Los resultados promedio de las propiedades del suelo obtenidas después del ciclo del cultivo se encuentran en la Tabla 4. Los pH del suelo, después de la cosecha de albahaca, estuvieron por encima de 7,0 para todos los tratamientos. No se encontraron diferencias estadísticas entre AO, ni de estos con la urea y los FRL, pero si entre los tratamientos G200 y G300 con SA150. Esta situación se atribuye a la reacción de los fertilizantes, al poder amortiguador del suelo mismo, así como a la absorción de cationes por las plantas. Similares resultados fueron encontrados por Hailing et al. [36] quienes argumentaron que la disminución en el pH del suelo producto de la fertilización nitrogenada es debida al proceso de nitrificación llevado a cabo por los microorganismos del suelo. El proceso de nitrificación en SA150 fue más rápido debido a la mayor disponibilidad del amonio, liberando hidrógeno y acidificando el medio.

Los valores de CE estuvieron entre 0,49 y 1,44 dS m^{-1} para L250 y SA200 respectivamente, propios de un suelo normal no salino, aunque superiores a los hallados en la caracterización inicial del suelo (0,454 dS m^{-1}). Tanto el SA como la urea de liberación lenta, modificaron significativamente la CE del suelo, donde la dosis de 200 kg ha^{-1} la incrementó en 65 % y 47 % con respecto al TA. Los valores más bajos de CE en los AO están relacionados con la presencia de lixiviados en las primeras etapas del cultivo, ocasionando el lavado de nutrientes.

La CE aumentó con la dosis, independientemente de la fuente aplicada. La cantidad de N aplicado tuvo un efecto significativo en la CE (p= 0,01), donde las dosis de 150 kg·ha^{-1} obtuvieron los valores más altos de CE, estadísticamente diferente del T y de las dosis más altas empleadas con los AO. Así mismo, los AO obtuvieron los menores registros de CE que los convencionales o de síntesis química, encontrando diferencias significativas con ellos (p < 0,01), mientras que no cambiaron el valor de esta variable en comparación con el T. Los FLL, tanto orgánicos como de síntesis, obtuvieron menores CEs y fueron diferentes de los FRL (p < 0,01).

Todos los tratamientos incrementaron el contenido de MOS con respecto a su valor inicial (2,32 %), debido a la presencia de la planta que aporta MOS a través de sus exudados y al desarrollo de la actividad microbiana en la zona cercana a las raíces. Los resultados obtenidos fueron superiores a los presentados por Singh et al. [10] quienes encontraron aumentos de hasta 0,25 % en MOS

utilizando AO y FRL en albahaca.

El análisis por factores (datos no mostrados) demostró que los AO incrementaron significativamente la MOS con respecto a los fertilizantes convencionales de síntesis química (NC, SA y U), siendo las dosis de 250 y 300 kg·ha^{-1} las que contribuyeron a aumentar el contenido de forma significativa ($p< 0,01$). Por otro lado, el tipo de liberación no tuvo incidencia significativa en la MOS ($p= 0,032$), debido a que los FRL y la U no contienen materia orgánica como tal en su composición.

El porcentaje de NTS estuvo entre 0,06 % y 0,22 % con una alta variabilidad en los datos obtenidos, estando en los rangos habituales para suelos cultivados [37]. No se encontraron diferencias entre tratamientos, ni se incrementaron los valores sustancialmente con respecto a los iniciales, como se esperaba. Probablemente los AO perdieron parte del N por lixiviación ocurrida en las primeras semanas del experimento o también pudo haberse perdido por volatilización, en el proceso de amonificación de los compuestos orgánicos nitrogenados constituyentes de dichos abonos.

En el caso de la U, es muy probable que el N liberado haya sido absorbido por la planta, como se pudo apreciar anteriormente, al presentar los mayores valores de NF. Singh et al. [10] encontraron un incremento en el NTS de hasta 62,4 kg·ha^{-1} utilizando AO y FRL al cabo del ciclo de la albahaca, y explican que se debió posiblemente al manejo efectivo del agua, y a la ausencia de minerales de arcilla expansivos que forman grietas creando flujos preferenciales y promoviendo la lixiviación del N, como los que se presentaron en la presente investigación.

3.4. Eficiencia de la fertilización nitrogenada

Las ER obtenidas con los AO fueron las más bajas, por debajo del 10 %, similares a la del TA, mientras que los tratamientos con SA obtuvieron las mayores eficiencias, por encima del 30 % (Fig. 4A). La U obtuvo la ER mayor al 10 % para las dosis más altas (100 y 150 kg·ha^{-1}), mientras que la dosis de 200 kg·ha^{-1} fue la más baja, sin diferencias significativas con las de los AO. Estos resultados pueden obedecer a que los FLL, sean orgánicos o de síntesis industrial, necesitan un tiempo prudencial de aplicación para suministrar el N, para asegurar que éste sea disponible para la planta. El NC, obtuvo una eficiencia menor, debido a la alta movilidad del nitrato y a la baja densidad de raíces en edades tempranas de la planta para absorber, lo que pudo haber generado su movimiento a capas más profundas.

No hay muchos estudios donde se muestre el cálculo de eficiencias en la fertilización nitrogenada de albahaca. En comparación con otras aromáticas, Berti et al. [38] encontraron valores de ER entre 8,2 % y 18,2 % utilizando dosis entre 75 y 300 kg·ha^{-1} de salitre sódico en hierba de San Juan, y argumentaron que la ER disminuyó con el aumento en la dosis de N, similares a los resultados obtenidos en este estudio, aunque los resultados expuestos deben interpretarse con precaución puesto que, para mayor certeza, el uso de isótopos es lo más indicado.

De acuerdo a la dinámica de mineralización, el L y la G deben aplicarse con tiempo de anterioridad, para permitir la mineralización del N y aumentar su disponibilidad. De acuerdo con Figueroa – Barrera et al. [39], los AO como L y G, en alrededor de la segunda semana después de su aplicación, liberan aproximadamente el 50 % del N mineralizable, por lo tanto, lo ideal es que este período de liberación de N coincida con la etapa de crecimiento o desarrollo de la planta. En la presente investigación es posible que el tiempo de antelación con la que se aplicó fuera insuficiente, por lo que posiblemente no se liberó suficiente N, y no se hizo disponible para la planta en el momento oportuno, como lo muestran algunos valores de NT en el suelo, al final del experimento.

Vale la pena aclarar que para el cálculo de la ER de los AO se tuvo en cuenta todo el N contenido en el abono, el cual solo un pequeño porcentaje estará disponible para la planta, el resto está en formas orgánicas, cuya mineralización puede tardar un tiempo prudencial de meses e incluso de años. En el caso de la U, es posible que haya ocurrido la misma situación, y que sea necesario aplicarla con mayor anterioridad, puesto que necesita de tiempo para solubilizar la parte azufrada de recubrimiento y empezar a aportar el N al medio.

De acuerdo con Roberts [40], las ER para cereales generalmente están entre 20 % y 30 % en cultivos de secano y pueden alcanzar hasta un 40 % en cultivos bajo irrigación; estos bajos valores no significan un aspecto negativo, porque no necesariamente alta eficiencia significa buenas cosechas y viabilidad para el agricultor o para el ambiente. En efecto, se ha demostrado que las bajas cosechas vienen acompañadas de altas eficiencias de uso de nutrientes y viceversa, como se encontró en este experimento, pero los aspectos ambientales como, por ejemplo, la protección contra la erosión del suelo se vería comprometida por la reducción en la producción de residuos de cosecha.

A pesar de que los AO presentaron bajas ER, las EI estuvieron dentro de las más altas (Fig. 4B), puesto que el N suministrado por los AO se manifestó en mayor producción

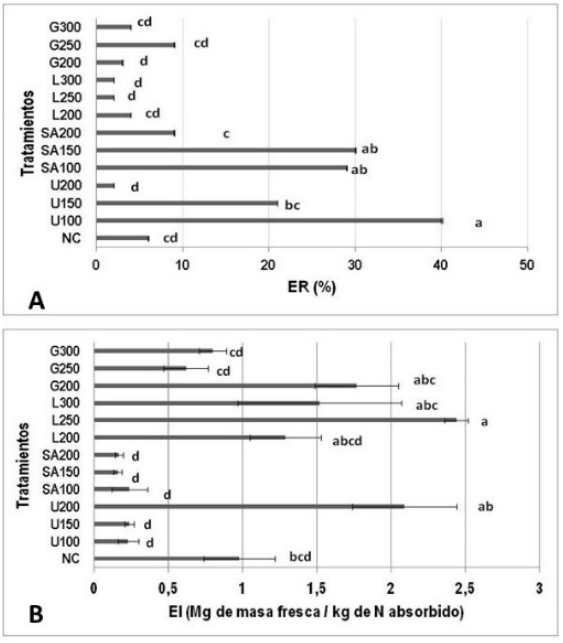


Figura 4. (A) Eficiencia aparente de recuperación ER ($F=14,85$; $p<0,001$) (B) Eficiencia interna de utilización EI ($F=12,27$; $p<0,001$) del nitrógeno para diferentes tipos de fertilizantes utilizados en albahaca. Promedio de tres repeticiones. Las barras indican el error estándar. Letras iguales indican que no hay diferencias estadísticas (test de Tukey al 95%). TA= testigo absoluto; NC= nitrato de calcio; U= urea recubierta; SA= sulfato de amonio; L= lombricompost; G= Gallinaza. Los números indican las dosis evaluadas de N en kg·ha^{-1}.
Fuente: Los autores.

de masa fresca. Además, la adición de AO trae beneficios adicionales como, por ejemplo, mejor acondicionamiento físico del suelo, aporte de otros nutrientes, y mayor actividad microbiana. En el caso de la G la dosis de 200 kg·ha^{-1} produjo más de 1,5 Mg de masa fresca por cada kg de N absorbido por la planta, mientras que para el L fue la dosis de 250 kg·ha^{-1}, la cual obtuvo valores cercanos a los 2,5 Mg·kg^{-1} de N absorbido.

Para la U, la mayor dosis fue la que obtuvo mayor EI, cercano a los 2 Mg·kg-1 de N absorbido, debido a que la planta tuvo mayor oportunidad de aprovechar el N y se presentaron menores pérdidas ya sea por lixiviación a capas más profundas o por volatilización. Gao et al. [33] encontraron que la urea recubierta aumentó la eficiencia agronómica de papa, pero redujo la eficiencia fisiológica con respecto a la urea convencional, opuesto a lo encontrado en este trabajo. Estas diferencias pueden deberse a que son cultivos diferentes, con sistemas radicales diferentes, lo que influye en la absorción del nutriente.

Los FRL obtuvieron EI por debajo de un Mg·kg^{-1} de N absorbido, lo cual puede deberse probablemente a la volatilización del N en los procesos de aminificación y amonificación, que se vieron favorecidos por el pH básico del suelo o por inmovilización del N ocasionado por la actividad microbiana del mismo. La eficiencia interna de utilización (EI) superó los rangos óptimos reportados para cereales (55- 65 kg·kg-1) presentados por Dobermann, [24]. Vale la pena aclarar que estos valores de eficiencia fueron calculados sólo para permitir la comparación entre tratamientos durante el tiempo experimental. Los valores no pueden ser aplicados como valores de referencia, puesto que para conocer la eficiencia del N es necesario tener en cuenta otros factores y procesos implicados en la dinámica a largo plazo del ciclo del N [40].

3.5. Eficiencia del uso del agua (EUA)

Todos los tratamientos obtuvieron similares valores de EUA, entre 3 y 6 y entre 1 y 1,5 kg·m^{-3} de masa fresca y seca (Fig. 5). Los valores hallados son similares a los reportados a cereales como el maíz, que están entre 1,3 y 1,5 kg·m^{-3} [41] y arroz que están 0,6 y 1,6 kg·m^{-3} [42].

A pesar de no encontrarse diferencias estadísticas, los AO mostraron tendencia a presentar mayores eficiencias de uso del agua, que los fertilizantes convencionales de síntesis industrial, lo cual se relaciona positivamente con la EI. Una mayor eficiencia implica menores pérdidas por lixiviación, garantizando que tanto el agua como los nutrientes se queden en la zona de raíces y las plantas tengan mayores oportunidades de aprovecharlos. A pesar que los AO presentaron pérdidas por lixiviación al inicio del experimento, su contribución a mejorar las propiedades físicas del suelo y el suministro de nutrientes pudieron tener un efecto positivo en el desarrollo radicular de la planta y, por tanto, en la producción de biomasa. Los valores más bajos de EUA pueden deberse a que el dosel de cobertura de las plantas es menor, quedando la superficie del suelo expuesta a mayor evaporación. Además, a medida que se aumenta la concentración de sales, la EUA se reduce, debido al incremento del potencial osmótico del suelo, como se puede apreciar en los tratamientos con SA [43].

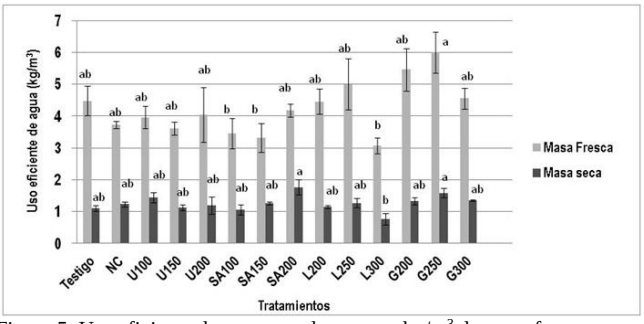


Figura 5. Uso eficiente de consumo de agua en kg/m^3 de masa fresca y seca en función del tipo de fertilizante nitrogenado en albahaca. Comparación de medias realizada con la prueba de Tukey al 95 % (F=4,33; p=0,00) para masa fresca y (F=2,83; p=0,01) para masa seca. TA= testigo absoluto; NC= nitrato de calcio; U= urea recubierta; SA= sulfato de amonio; L= lombricompost; G= Gallinaza. Los números indican las dosis evaluadas de N en kg·ha^{-1}.

4. Conclusiones

Los AO presentaron mayor lixiviación de N que los fertilizantes NC, SA y U cuando el riego se realizó llevando el suelo a capacidad de campo, debido probablemente a cambios en la porosidad y en la retención de humedad del suelo. El empleo del Kc por etapa redujo significativamente la lixiviación, ratificando que el manejo del agua es el factor más importante para la reducción de las pérdidas de los iones nitrato y amonio.

Las dosis de 100 y 150 kg ha^{-1} obtuvieron los mayores porcentajes de MS independiente del tipo de abono, aunque sin diferencias con las dosis empleadas con los AO (200, 250 y 300 kg ha^{-1}. Las plantas fertilizadas con dosis de 100 y 150 kg ha^{-1} independiente del tipo de abono, presentaron mayores concentraciones de NF que las demás dosis. Los FRL (NC y SA) obtuvieron mayores porcentajes de MS y NF que los FLL (U, AO) y que el TA. Los abonos convencionales de síntesis industrial (NC, SA y U) alcanzaron mayores porcentajes de MS y NF que los AO y el TA, indicando que una oportuna disponibilidad del N es importante para el crecimiento y desarrollo del cultivo, y que la definición de la época de aplicación es indispensable para garantizar dicha disponibilidad. Este tiempo de aplicación antes de la siembra dependerá de la velocidad de disolución de los FLL convencionales o de la tasa de mineralización de los AO. Los resultados obtenidos sugieren que, para la comercialización de albahaca en fresco, el uso de AO puede ser más apropiado y para forma deshidratada o extracción de aceites, la fertilización con FRL es mejor. Sin embargo, se requieren otros estudios para confirmar lo anterior.

Todos los fertilizantes empleados mantuvieron el pH cerca a la neutralidad, mientras que el SA y la U aumentaron significativamente la CE, indicando una mayor disponibilidad de nutrientes. Ni los tipos de abono evaluados ni las dosis aplicadas tuvieron incidencia en la MOS y en NTS después de la cosecha.

La U y el SA consiguieron mayores kg de N absorbido por kg de N aplicado mientras que los AO consiguieron mayores kg de MS por kg de N absorbido, resultando más eficientes en la producción de biomasa. Los AO permitieron obtener mayor productividad de agua, al conseguir más kg de MS por m^3 de agua aplicada, gracias a la capacidad de estos

para la retención de humedad y al mejoramiento de las propiedades físicas del suelo.

Es necesario realizar estudios más profundos que evalúen el efecto de estos fertilizantes en contenidos de aceites y compuestos aromáticos en albahaca, así como la investigación en cultivos comerciales con seguimiento por mayor tiempo, tanto de variables agronómicas, como de variables ambientales, relacionadas con el agua y el suelo.

Referencias

[1] Jamali, H., Quayle, W. and Baldock, J., Reducing nitrous oxide emissions and nitrogen leaching losses from irrigated arable cropping in Australia through optimized irrigation scheduling. Agricultural and Forest Meteorology, 208, pp. 32-39, 2015. DOI: 10.1016/j.agrformet.2015.04.010G

[2] Arauzo, M. and Valladolid, M., Drainage and N-leaching in alluvial soils under agricultural land uses: implications for the implementation of the UE Nitrates Directives. Agriculture, Ecosystems & Environment, 179, pp. 94-107, 2013. DOI: 10.1016/j.agee.2013.07.013.

[3] Reyes, A., Figueroa, U., Ochoa, E., Verastegui, J., Sánchez, J.I. and Núñez, G., Lixiviación de nitratos provenientes de estiércol y fertilizante en forrajes cultivados en lisímetros de volumen. Agrofaz [En línea], 12(4), pp. 95-101, 2012. [fecha de referencia: Noviembre 25 de 2017]. Disponible en: http://www.agrofaz.mx/wp-content/uploads/articulos/2012124V_1.pdf

[4] IDAE – Instituto para la Diversificación y Ahorro de la Energía., Ahorro, eficiencia energética y fertilización nitrogenada. Ahorro y eficiencia energética en la agricultura. IDAE: Madrid, 2007, 44 P.

[5] Hadas, A., Agassi, M., Zhevelev, H., Kautsky, L., Levy, G.J., Fizik, E. and Gotessman, M., Mulching with composted municipal solid wastes in the Central Negev Israel. II Effect on available nitrogen and phosphorus and on organic matter in soil. Soil Tillage Research, 78, pp. 115-128, 2004. DOI: 10.1016/j.still.2004.02.020

[6] Soca, M. and Daza, M.C., Evaluation of particle size fractions and doses of zeolite for agriculture. Agrociencia [Online]. 50(8), pp. 965-976, 2016. [date of reference: November 25th of 2017]. Available at: http://www.colpos.mx/agrocien/Bimestral/2016/nov-dic/nov-dic-16.html

[7] Barrios, M. and Killorn, R., Nitrificación del amonio a partir de un fertilizante de liberación controlada y urea convencional en dos suelos de Iowa, EEUU. Bioagro [En línea]. 22(3), pp. 193-200, 2010. [fecha de referencia: Noviembre 25 de 2017]. Disponible en: http://www.ucla.edu.ve/bioagro/Rev22(3)/4.%20Nitrificaci%C3%B3n%20del%20amonio.pdf

[8] Barbieri, P.A., Echeverría, H.E., Saínz, H.R. and Maringolo, M., Fertilización de maíz con urea de liberación lenta: pérdida por volatilización y eficiencia de uso de nitrógeno. Ciencia del Suelo (Argentina) [En línea]. 28(1), pp 57-66, 2010. [fecha de referencia: Noviembre 25 de 2017]. Disponible en: https://www.suelos.org.ar/publicaciones/vol_28n1/28(1)%2057-66.pdf

[9] Moncayo, M., Alvarez, V., González, G., Salas, L. and Chaves, J., Producción orgánica de albahaca en invernadero en la Comarca Lagunera. Terra Latinoamericana [En línea]. 33(1), pp. 69-77, 2015. [fecha de referencia: Noviembre 25 de 2017]. Disponible en: https://www.terralatinoamericana.org.mx/index.php/terra/article/view/46

[10] Singh, K., Chand, S. and Yaseen, M., Integrated nutrient management in Indian basil (*Ocimum basilicum*). Industrial Crops & Products, 55, pp. 225-229, 2014. DOI: 10.1016/j.indcrop.2014.02.009

[11] Lu, Y., Sun, Y., Liao, Y., Nie, J., Xie, J., Yang, Z. and Zhou, X., Effects of the application of controlled release nitrogen fertilizer on rapeseed yield, agronomic characters and soil fertility. Agricultural Science & Technology [Online], 16(6), pp. 1216-1226, 2015. [date of reference: November 29th of 2017]. Available at: https://search.proquest.com/openview/c5861a601cf5a7bb94f8bce494ae448e/1?pq-origsite=gscholar&cbl=1596357

[12] Xie, L., Liu, M., Ni, B., Zhang, X. and Wang, Y., Slow release nitrogen and boron fertilizer from a functional superabsorbent formulation based on wheat straw and attapulgite. Chemical Engineering. Journal [Online], 167(1), pp. 342-348, 2011. [date of reference: November 25th of 2017]. Available at: https://www.sciencedirect.com/science/article/pii/S1385894711000180

[13] Cristobal-Acevedo, D., Álvarez, M.E., Hernández, E. and Améndola, R., Concentración de Nitrógeno en suelo por efecto de manejo orgánico y convencional. Terra Latinoamericana [En línea], 29(3), pp. 325-332, 2011. [fecha de referencia: Noviembre 25 de 2017]. Disponible en: http://www.redalyc.org/articulo.oa?id=57321283011

[14] Li, J., Zhao, B., Li, X., Jiang, R. and So, H.B., Effects of long-term combined application of organic and mineral fertilizers on microbial biomass, soil enzyme activities and soil fertility. Agricultural Sciences in China, 7(3), pp. 336-343, 2008. DOI: 10.1016/S1671-2927(08)60074-7

[15] Daza, M.C., Díaz, J., Aguirre, E. and Urrutia, N., Efecto de abonos de liberación lenta en la lixiviación de nitratos y nutrición nitrogenada en estevia. Revista Colombiana de Ciencias Hortícolas [En línea], 9(1), pp. 112-123, 2015. [fecha de referencia: Noviembre 25 de 2017]. Disponible en: http://revistas.uptc.edu.co/index.php/ciencias_horticolas/article/view/3750/pdf_20

[16] Nielsen, S., Minchin, T., Kimber, S., van-Zwieten, L., Caporaso, J.G., Gilbert, J., Munroe, P., Joseph, S. and Thomas, T., Comparative analysis of the microbial communities in agricultural soil amended with enhanced biochar or traditional fertlizers. Agriculture Ecosystems & Environment, 191, pp. 73-82, 2014. DOI: 10.1016/j.agee.2014.04.006

[17] Ni, X., Wu, Y., Wu, Z., Wu, L., Qiu, G. and Yu, L., A novel slow-release urea fertiliser: Physical and chemical analysis of its structure and study of its release mechanism. Biosystems engineering, 115(3), pp. 274-282, 2013. DOI: 10.1016/j.biosystemseng.2013.04.001

[18] Sánchez, D., Gutierrez, J., Campo, J. and Herrera, J.P., Estudio sobre el sector de fertilizantes en Colombia. Grupo de Estudios Económicos Sectoriales, Superintendencia de Industria y Comercio, Bogotá, 2013, 198 P.

[19] DNP – Departamento Nacional de Planeación., Política nacional para la racionalización del componente de costos de producción asociado a los fertilizantes en el sector agropecuario. CONPES 3577, Bogotá, 2009, 33 P.

[20] IGAC/CVC (Instituto Geográfico Agustin Codazzi/Corporación Autónoma Regional del Valle del Cauca), Levantamiento de suelos y zonificación de tierras del departamento del Valle del Cauca. IGAC, Bogotá, COL, 2004.

[21] ICONTEC. NTC Norma Técnica Colombiana 5167., Productos para la industria agrícola. Productos orgánicos usados como abonos o fertilizantes y enmiendas o acondicionadores de suelo. Instituto Colombiano de Normas Técnicas y Certificación, Bogotá, 2011.

[22] Allen, R., Pereira, L., Raes, D. and Smith, M., Crop evapotranspiration. Guidelines for computing crop water requirements. FAO. Irrigation and Drainage, 56, Rome, Italy, 2006, 300 P.

[23] Daza, M.C., Arias, P., Reyes, A. and Urrutia, N., Basil (*Ocimum basilicum* L) water needs calculated from the crop coefficient. Ingeniería e Investigación, 37(3), pp. 8-16, 2017. DOI: 10.15446/ing.investig.v37n3.65058

[24] Dobermann, A., Nutrient use efficiency-measurement and management, Proceedings of the International Fertilizer Industry Association (IFA) Workshop on Fertilizer Best Management Practices, Brussels, Belgium, 267 P, 2007.

[25] Mitran, T., Kumar-Mani, P., Kumar-Bandyopadhyay, P. and Basak, N., Influence of organic amendments on soil physical attributes and aggregate associated phosphorus under long-term rice-wheat cropping. Pedosphere, In press, 2017. DOI: 10.1016/S1002-0160(17)60423-5

[26] Moreno, G., López, M.L., Oliveira, F. and Chuna, M., Eficacia de los sistemas agroforestales en el control de la lixiviación de nitrato. Cuadernos de la sociedad española de ciencias forestales [En línea]. 22, pp. 113-118, 2007. [fecha de referencia: Noviembre 25 de 2017]. Disponible en: http://secforestales.org/publicaciones/index.php/cuadernos_secf/article/view/9589/9507

[27] Cavero, J., Barros, R., Sellam, F., Topcu, S., Isidoro, D., Hartani, T., Lounis, A., Ibrikci, H., Cetin, M., Williams, J.R. and Aragüés, R.,

APEX simulation of best irrigation and N management strategies for off-site N pollution control in three Mediterranean irrigated wastersheds. Agricultural Water Management. 103, pp. 88-99, 2012. DOI: 10.1016/j.agwat.2011.10.021

[28] Alfaro, M., Salazar, F., Endress, E., Dumont, J.C. and Valdebenito, A., Nitrogen leaching losses on a volcanic ash soil as affected by the source of fertiliser. Journal of Soil Science and Plant Nutrition [Online]. 6(2), pp. 54-63, 2006. [date of reference: November 25th of 2017]. Available at: http://jsspn.ufro.cl/index.php?option=com_docman&task=doc_download&gid=76&Itemid=6

[29] WHO – World Health Organization., Guidelines for drinking-water quality. Fourth edition. WHO library cataloguing in publication data, 564 P, 2011.

[30] Ortuzar, M.A., Aizpurua, A., Castellón, A., Alonso, A. and Estavillo, J.M., Evolución del contenido de nitrato y amonio en lixiviados bajo diferentes formas de fertilización nitrogenada en trigo. Estudios de la zona no saturada del suelo [En línea]. 6, pp. 45-50, 2003. [fecha de referencia: Noviembre 25 de 2017]. Disponible en: http://www.zonanosaturada.com/zns03/publications_files/p045-050.pdf

[31] Civeira, G. and Rodríguez, M.B., Nitrógeno residual y lixiviado del fertilizante en el sistema suelo-planta-zeolitas. Ciencia Del Suelo [En línea]. 29(2), pp. 285-294, 2011. [fecha de referencia: Noviembre 25 de 2017]. Disponible en: https://dialnet.unirioja.es/servlet/articulo?codigo=4346877

[32] Zhang, B., Li, Q., Cao, J., Zhang, C., Song, Z., Zhang, F. and Chen, X., Reducing nitrogen leaching in a subtropical vegetable system. Agriculture, Ecosystems and Environment. 241, pp. 133-141, 2017. DOI: 10.1016/j.agee.2017.03.006

[33] Gao, X., Li, C., Zhang, M., Wang, R. and Chen, B., Controlled release urea improved the nitrogen use efficiency, yield and quality of potato (*Solanum tuberosum* L.) on silt loamy soil. Field crops research. 181, pp. 60-68, 2015. DOI: 10.1016/j.fcr.2015.07.009

[34] Osorio, N.W., Manejo de nutrientes en suelos del trópico. Ed L Vieco S.A.S, Medellín, pp. 185-187, 2014.

[35] Búfalo, J., Cantrell, C.L., Astatkie, T., Zheljazkov, V.D., Gawde, A. and Boaro, C.S.F., Organic versus conventional fertilization effects on sweet basil (*Ocimum basilicum* L.) growth in a greenhouse system. Industrial Crops and Products. 74, pp. 249-254, 2015. DOI: 10.1016/j.indcrop.2015.04.032

[36] Hailing, Y., Qiang, G., Zeqiang, S., Anning, Y., Yuyang, S., Jingwei, L. and Zhang, B., Decreasing nitrogen fertilizer input had little effect on microbial communities in three types of soils. PLoS One. 11(3), pp. 1-13, 2016. DOI: 10.1371/journal.pone.0151622

[37] Navarro, S. and Navarro, G., Química agrícola. El suelo y los elementos químicos esenciales para la vida vegetal. Segunda edición, Ediciones Mundiprensa, Madrid, España, 438 P, 2003.

[38] [38] Berti, M., Hevia, F., Wilckens, R. and Joublan, J., Fertilizacion nitrogenada del cultivo de hierba de San Juan (*Hypericum perforatum* L.) en Chillan, Provincia de Nuble, Chile. Ciencia e Investigación Agraria [En línea]. 107-116, 2000. [fecha de referencia: Noviembre 25 de 2017]. Disponible en: http://www.submission.rcia.uc.cl/index.php/rcia/article/view/1002/859

[39] Figueroa-Barrera, A., Álvarez-Herrera, J.G., Forero, A.F., Salamanca, C. and Pinzón, L.P., Determinación del nitrógeno potencialmente mineralizable y la tasa de mineralización de nitrógeno en materiales orgánicos. Temas Agrarios [En línea]. 17(1), pp. 32-43, 2012. [fecha de referencia: Noviembre 25 de 2017]. Disponible en: https://dialnet.unirioja.es/descarga/articulo/4230882.pdf

[40] Roberts, T., Improving nutrient use efficiency. Turkish Journal of Agriculture and Forestry [Online]. 32(3), pp. 177-182, 2008. [date of reference: November 25th of 2017]. Available at: http://journals.tubitak.gov.tr/agriculture/issues/tar-08-32-3/tar-32-3-4-0801-9.pdf

[41] Reta, D.G., Figueroa, U., Faz, R., Núñez, G., Gaytán, A., Santos, J. and Payán, J.A., Sistemas de producción de forraje para incrementar la productividad del agua. Revista Fitotecnia Mexicana [En línea]. 33(4), pp. 83-87, 2010. [fecha de referencia: Noviembre 25 de 2017]. Disponible en: http://www.scielo.org.mx/pdf/rfm/v33nspe4/v33nspe4a17.pdf

[42] Sander, J. and Win, G.M., Review of measured crop water productivity values for irrigated wheat, rice, cotton and maize. Agriculture Water Management. 69(2), pp. 115-133, 2004. DOI: 10.1016/j.agwat.2004.04.007

[43] Steduto, P., Hsiao, T., Fereres, E. and Raes, D., Crop yield response to water. Food and Agriculture Organization of United Nations – FAO, Irrigation and drainage paper N° 66, 530 P, 2012.

M.C. Daza-Torres, recibió su título de Ing. Agrícola en 1997 y su grado de MSc. en el año 2005 ambos de la Universidad Nacional de Colombia sede Bogotá. Fue profesora e investigadora en el área de suelos de la Facultad de Ciencias agropecuarias de la Universidad de Cundinamarca entre los años 2003 y 2006. Desde el 2007 trabaja como profesora de tiempo completo en el área de suelos en la Universidad del Valle, Cali, Colombia, en el área de Ingeniería Agrícola y Recursos Hídricos. Ha participado en proyectos de investigación en temas relacionados con el uso de abonos orgánicos de diferente procedencia y su repercusión en sistemas productivos y en los recursos suelo y agua.
ORCID: 0000-0002-7200-0443.
Google analytics: UA-99323342-1

G.S. Ladino-Tabarquino, recibió su título de Ing. Agrícola en 2017 de la Universidad del Valle, Cali, Colombia. Participó como pasante en Cenipalma entre noviembre de 2016 y agosto de 2017. Actualmente trabaja como investigadora en CENIPALMA en el Programa de Agronomía en el área de suelos.
ORCID: 0000-0003-1542-9267.

N. Urrutia-Cobo, recibió su título de Ing. Agrícola de la Universidad del Valle, Cali, Colombia, en convenio con la Universidad Nacional de Colombia sede Palmira en 1977. Realizó una Esp. en ingeniería de regadíos del Centro de Estudios y de Experimentación de Obras Públicas de España en 1988. También realizó MSc. en ingeniería hidráulica en el International Institute for Infrastructural Hydraulic and Environmental Eng (IHE – Holanda) entre 1995 y 1997. Es Dr. en ingeniería hidráulica de la Agricultural University – Wageningen. Ha trabajado como profesor e investigador del área de ingeniería agrícola y recursos hídricos de la Universidad del Valle, Cali, Colombia, desde 1979. Actualmente es profesor titular e investigador principal del grupo de investigación Gestión integral del riego para el desarrollo agrícola y la seguridad alimentaria (REGAR).
ORCID: 0000-0002-7163-3708.

UNIVERSIDAD NACIONAL DE COLOMBIA
SEDE MEDELLÍN
FACULTAD DE MINAS

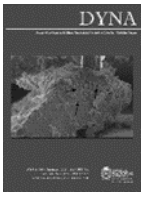
Área Curricular de Medio Ambiente

Oferta de Posgrados

Especialización en Aprovechamiento de Recursos Hidráulicos
Especialización en Gestión Ambiental
Maestría en Ingeniería Recursos Hidráulicos
Maestría en Medio Ambiente y Desarrollo
Doctorado en Ingeniería - Recursos Hidráulicos
Doctorado Interinstitucional en Ciencias del Mar

Mayor información:
E-mail: acma_med@unal.edu.co
Teléfono: (57-4) 425 5105

UNIVERSIDAD NACIONAL DE COLOMBIA
SEDE MEDELLÍN
FACULTAD DE MINAS



DYNA
http://dyna.medellin.unal.edu.co/

Risk assessment in water treatment processes for the development of a Water Safety Plan – WSP

Andrea Pérez-Vidal [a], Juan Carlos Escobar-Rivera [b] & Patricia Torres-Lozada [c]

[a] *Facultad de Ingeniería, Universidad Santiago de Cali. Cali, Colombia. andrea.perez00@usc.edu.co*
[b] *Departamento Producción Agua Potable, Empresas Municipales de Cali EMCALI EICE-E.S.P. Cali, Colombia. jcescobar@emcali.com.co*
[c] *Facultad de Ingeniería, Universidad del Valle. Cali, Colombia. patricia.torres@correounivalle.edu.co*

Received: June 01rd, 2017. Received in revised form: January 20th, 2018. Accepted: march 13th, 2018.

Abstract
Drinking Water Treatment Plants (DWTP) must ensure safe water supply; to this end, we applied risk assessment tools for the development of the Water Safety Plan (WSP) in a DWTP from Cali-Colombia, which supplies 1.4 million inhabitants. For the identification of hazards and risk assessment, four tools were used: exploratory analysis of turbidity data, inspection visits, hazard/hazardous event matrix and semiquantitative matrix. Under normal and extreme conditions of turbidity (>400 - 2500 UNT), it has been guaranteed the turbidity of treated water of 0.39 ± 0.15 UNT, showing the robustness of the DWTP. It was found that sixty percent of the 40 hazardous events had a very high risk level without considering control measures and it was possible reduce to 7% with existing control measures. The improvement or support programs should be directed towards the treatment phases identified as priority (chemical conditioning, coagulation, flocculation/clarification and filtration).

Keywords: drinking water; hazardous event; hazard identification; water safety plan; risk.

Evaluación del riesgo en procesos de tratamiento de agua para el desarrollo de un Plan de Seguridad del Agua – PSA

Resumen
Las Plantas de Tratamiento de Agua (PTA) deben garantizar el suministro de agua segura; con este fin, se aplicaron herramientas de evaluación del riesgo para el desarrollo del Plan de Seguridad del Agua (PSA) en una PTA de Cali-Colombia que abastece 1.4 millones de habitantes. Para la identificación de peligros y valoración del riesgo, se usaron cuatro herramientas: análisis exploratorio de datos de turbiedad, visitas de inspección, matriz de peligros/eventos peligrosos y matriz semicuantitativa. En condiciones normales y extremas de turbiedad (>400 – 2500 UNT) se garantiza turbiedad del agua tratada de 0.39±0.15 UNT, mostrando la robustez de la PTA. El 60% de los 40 eventos peligrosos presentaron nivel de riesgo muy alto sin considerar medidas de control y se redujeron hasta 7% con medidas de control existentes. Los programas de mejoramiento o soporte se deben orientar hacia las fases del tratamiento identificadas como prioritarias (acondicionamiento químico, coagulación, floculación/clarificación y filtración).

Palabras clave: agua potable; evento peligroso; identificación de peligros; plan de seguridad del agua; riesgo.

1. Introducción

Para garantizar la seguridad del agua de consumo humano, las guías de calidad de agua potable de la Organización Mundial de la Salud – OMS promueven la aplicación de un enfoque preventivo e integral de evaluación y gestión del riesgo denominado Plan de Seguridad del Agua – PSA, cuyo objetivo principal se centra en el aseguramiento de la calidad del agua a través de la minimización de la contaminación en la cuenca de abastecimiento, la eliminación o reducción de contaminantes durante los procesos de tratamiento y la prevención de la contaminación en el sistema de distribución, almacenamiento y manipulación del agua a nivel intradomiciliario [1].

How to cite: Pérez-Vidal, A., Escobar-Rivera, J. C. & Torres-Lozada, P., Evaluación del riesgo en procesos de tratamiento de agua para el desarrollo de un Plan de Seguridad del Agua – PSA. DYNA, 85(206), pp. 304-310, September, 2018.

© The author; licensee Universidad Nacional de Colombia.

La Evaluación del Riesgo - ER y la Gestión del Riesgo en los Sistemas de Abastecimiento de Agua Potable – SAAP, son de gran importancia para disminuir la vulnerabilidad y garantizar la seguridad del agua [2]. La ER, además de señalar los posibles peligros y eventos peligrosos (eventos que introducen peligros o impiden su eliminación en el SAAP) y valorar o determinar el nivel de riesgo (probabilidad de ocurrencia de un evento peligroso), permite identificar las medidas pertinentes para controlar los riesgos señalados y sirve para confirmar si se cumplen las normas y metas establecidas por la empresa prestadora del servicio de agua [1,3].

La calidad del agua entregada al usuario final dependerá siempre de la cuenca de abastecimiento, los procesos de tratamiento y el sistema de distribución, por lo que todos estos componentes deben ser la base de la evaluación y gestión del riesgo [2,4,5]. Este estudio hace parte de la evaluación del sistema de abastecimiento de la Ciudad de Cali, alimentado por el río Cauca, en el cual se estudiaron todos los componentes del sistema, desde la cuenca de abastecimiento hasta el usuario final [6-8]. En esta investigación se presentan los resultados asociados al componente procesos de tratamiento, para el cual se adaptaron herramientas de evaluación del riesgo orientadas al desarrollo de un Plan de Seguridad del Agua en la Planta de Tratamiento de Agua Potable - PTA de Puerto Mallarino.

2. Materiales y métodos

Durante el estudio se contó con el soporte del equipo del Plan de Seguridad del Agua - PSA constituido por personal operativo y técnico de la empresa prestadora del servicio de agua, asesores con experiencia en operación y mantenimiento del SAAP de la ciudad y profesionales e investigadores del sector académico. Inicialmente se recopiló y procesó información secundaria disponible en la entidad prestadora del servicio de agua (planos, manuales de operación y mantenimiento, reportes de calidad de agua, etc.), la cual sirvió de insumo para la ER en la PTA de Puerto Mallarino.

Para realizar la ER articulada con la metodología de los PSA, se tomaron como referencia los conceptos y estructuras planteadas en diferentes enfoques [1,9-11]. Se seleccionaron y adaptaron herramientas de apoyo para la ER, la cual comprendió dos etapas: la identificación de peligros y la valoración del riesgo.

2.1. Identificación de peligros

En esta etapa del estudio se aplicaron las siguientes herramientas:

2.1.1. Análisis exploratorio

Se analizó el registro de 15 años de los datos horarios de turbiedad a lo largo del tren de tratamiento, empleando gráficos de dispersión y diagramas de boxplot. La selección de la variable turbiedad se fundamentó en su importancia como indicador de rápida y fácil interpretación para los operadores de PTA [12], utilidad en el monitoreo operacional de las medidas de control a lo largo de todo el SAAP [1], por estar reglamentada por [13] y ser empleada para la determinación del índice de riesgo por calidad de agua (IRCA). Los datos horarios de turbiedad del agua cruda se clasificaron según [14] en condiciones normales y eventos extremos de turbiedad, estos últimos definidos como i) el incremento de la turbiedad del agua cruda igual o superior a 100 UNT en 1 hora y ii) la turbiedad horaria del agua cruda igual o superior a 400 UNT.

2.1.2 Visitas de inspección sanitaria

Se realizaron 5 visitas, en las cuales se inspeccionaron todas las etapas del tratamiento, estructuras, equipos, laboratorios, etc., intentando establecer los diferentes peligros y eventos peligrosos. Se contó con la presencia del personal operativo de la empresa que contribuyó a retroalimentar la información obtenida.

2.1.3. Matriz de peligros y eventos peligrosos

A partir del análisis de la información obtenida en las actividades anteriores y la retroalimentación con miembros del equipo PSA, se elaboró la matriz de peligros y eventos peligrosos para cada una de las fases del tratamiento y se incluyeron estructuras adicionales como canales, tuberías y estaciones de bombeo. La matriz consideró la clasificación de los eventos en las categorías de diseño, operación, mantenimiento, emergencias y factores externos (Ej. Amenazas naturales, deforestación de la cuenca, vandalismo, etc.). Los peligros fueron clasificados en las categorías de biológico, químico, físico, radiológico, asociado a la infraestructura física (daños en instalaciones) y asociado a la cantidad de agua (insuficiencia de agua).

2.2. Valoración del riesgo

El desarrollo de esta etapa comprendió dos actividades, la estimación del riesgo y la identificación de medidas de control, esta última acompañada de la reestimación del riesgo que permitió determinar la eficacia de las actuales medidas de control y generar insumos para la gestión del riesgo:

2.2.1. Estimación del riesgo

Se adaptaron los significados de probabilidad e impacto de la matriz semicuantitativa recomendada por [15,3,1] (Tabla 1). La frecuencia del evento peligroso, definida en la columna de probabilidad, se estableció en función de la gran variabilidad en la calidad del agua de la fuente de abastecimiento (río Cauca) y el elevado riesgo sanitario asociado a los usos del suelo y eventos extremos de turbiedad y contaminación, los cuales han sido reiterativos en el tiempo [6,14].

2.2.2. Identificación de medidas de control y reestimación del riesgo

Bajo la dirección del equipo PSA, el apoyo de personal técnico de la empresa y lo reportado en investigaciones previas, se identificaron las medidas de control del riesgo existentes y su eficacia para mitigar cada evento peligroso. Finalmente, se realizó la reestimación del riesgo haciendo uso nuevamente de la matriz semicuantitativa y considerando el nivel de eficacia de las medidas de control.

Tabla 1.
Matriz de riesgo semicuantitativa para estimar el riesgo en los procesos de tratamiento.

			Impacto				
	Descripción		**INSIGNIFICANTE** cusión. No detectable Suministro de agua segura	**MENOR** ro de agua con incumplimiento de características organolépticas	**MODERADO** ncias en salud pública a largo plazo (riesgo crónico) **y/o** características organolépticas. **No** hay insuficiencia de agua	**MAYOR** Incumplimiento reglamentario con repercusión en la salud pública a corto (riesgo agudo) **o** largo plazo (riesgo crónico).Insuficiencia de agua **< 24 h**	**CATASTRÓFICO*** limiento reglamentario con repercusión en la salud pública a corto (riesgo agudo) **y** largo plazo (riesgo crónico). Insuficiencia de agua **> 24h**
			Valor: 1	**Valor: 2**	**Valor: 3**	**Valor: 4**	**Valor: 5**
Probabilidad	**CASI CERTEZA*.** Ha ocurrido en varias oportunidades; existe certeza que pueda volver a ocurrir. Frecuencia: diaria/varias veces/mes	**5**	5	10	15	20	25
	PROBABLE. Ha ocurrido en algunas oportunidades. Frecuencia: una o varias veces al año	**4**	4	8	12	16	20
	MODERADO. Ha ocurrido alguna vez. Frecuencia: al menos 1/5 años	**3**	3	6	9	12	15
	IMPROBABLE. Es posible y no puede descartarse totalmente. Frecuencia: al menos 1/ 5 - 10 años	**2**	2	4	6	8	10
	RARO. No ha ocurrido anteriormente y es improbable que ocurra en el futuro. Frecuencia: 1 vez en más de 10 años	**1**	1	2	3	4	5

Puntuación del riesgo	< 6	6-9	10-15	≥ 16
Nivel de riesgo	Bajo	Medio	Alto	Muy alto

*Si no hay datos suficientes para determinar si un riesgo es alto o bajo, deberá considerarse significativo hasta que investigaciones posteriores aclaren la incertidumbre (Bartram et al., 2009)
Fuente: Adaptado de [3,1].

3. Resultados y discusión

La PTA evaluada tiene una capacidad máxima instalada de 6.6 m^3/s y aunque actualmente suministra agua potable al 56% de la población de Cali – Colombia (aprox., 1.4 millones de habitantes), tiene la capacidad para abastecer hasta el 77% de la misma [16]. Como resultado de la etapa de recopilación y procesamiento de la información y de las visitas de inspección sanitaria, se elaboró la descripción detallada de la PTA y la elaboración del diagrama de flujo del proceso (Fig. 1).

La configuración de la PTA de Puerto Mallarino presenta mayor complejidad comparada con una planta convencional, por incluir tratamientos complementarios, debido a las características de la fuente de abastecimiento, que se encuentra fuertemente impactada por vertimientos industriales, domésticos, escorrentía agrícola, minería, ganadería y deforestación en las subcuencas tributarias [6,14]. El uso de tratamientos específicos como estrategia complementaria del proceso, se articula con el concepto de barreras múltiples [17].

3.1. Identificación de peligros

A partir del análisis exploratorio, se construyeron los boxplots mostrados en las Figs. 2 y 3, en las que se observa la variación de los datos horarios de turbiedad a lo largo del tren de tratamiento bajo condiciones normales de operación y eventos extremos de turbiedad.

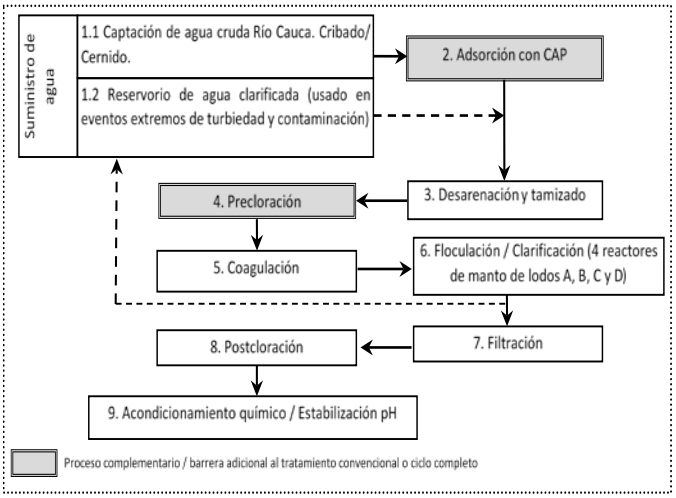


Figura 1. Diagrama de flujo simplificado de la PTA de Puerto Mallarino.
Fuente: Los autores

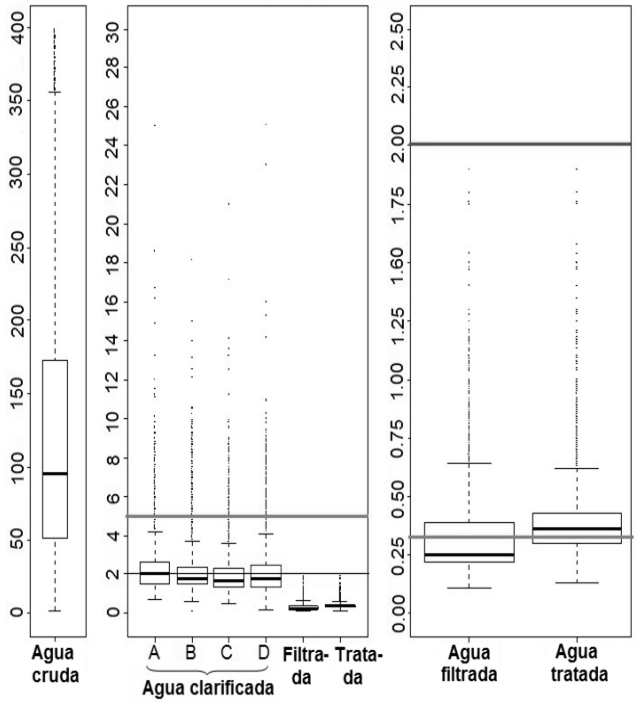


Figura 2. Variación de la turbiedad en el tren de tratamiento bajo condiciones normales de operación.
Fuente: Los autores

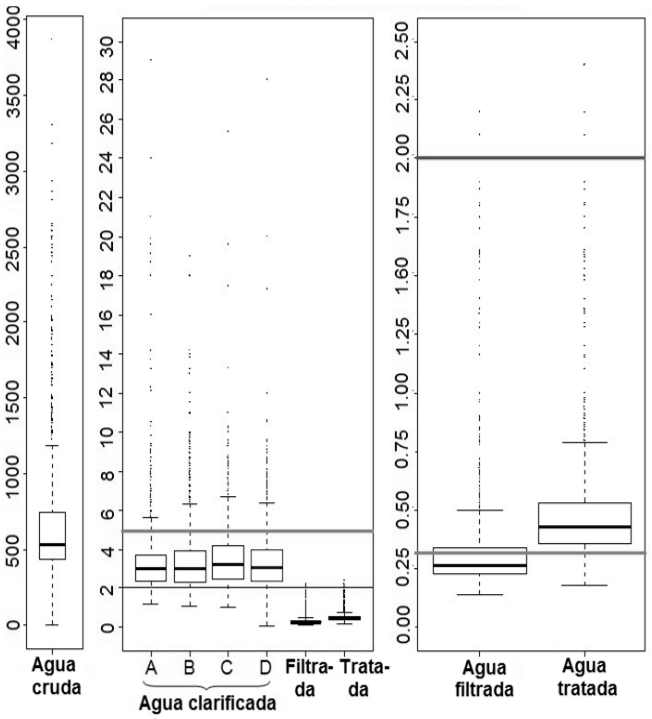


Figura 3. Variación de la turbiedad en el tren de tratamiento bajo condiciones de evento extremo de turbiedad.
Fuente: Los autores

La comparación entre las dos condiciones de operación (turbiedad promedio agua cruda = 168±218 UNT y > 400 UNT) evidencia algunas variaciones en el comportamiento global del tren de tratamiento, principalmente en la fase de clarificación, en la cual se desmejora ligeramente la turbiedad durante los eventos extremos (mayor amplitud del boxplot y desplazamiento de la mediana > 2.0 UNT), sin embargo, la robustez de la tecnología de clarificación por manto de lodos permite el tratamiento de este tipo de aguas con alta variabilidad de turbiedad [14]. Adicionalmente, la barrera de filtración puede asumir las posibles deficiencias en la clarificación, lográndose en ambas condiciones operativas una calidad de agua tratada que cumple con la reglamentación Colombiana (turbiedad $\leq$ 2 UNT) y en la mayoría de los datos, el cumplimiento de lo establecido por la Unión Europea [18], la EPA [19,20] y reglamentaciones de países como Brasil, Paraguay y Uruguay (turbiedad $\leq$ 1.0 UNT).

Con relación al agua filtrada, 75% de los datos estuvieron entre 0.11 – 0.38 UNT (promedio 0.31±0.16 UNT), valor muy cercano al límite de 0.3 UNT recomendado por la EPA [20] y WHO [1] antes de la desinfección para lograr la eliminación de patógenos resistentes al cloro; adicionalmente, solo el 0.8% de datos superó el valor de 1.0 UNT establecido para el agua filtrada previa desinfección en reglamentaciones de países como Brasil, Paraguay y Uruguay en las cuales, la turbiedad se asocia a riesgos en la salud, además de los aspectos estéticos y organolépticos [21].

El agua tratada (mediana 0.36 UNT – promedio 0.39 ±0.15 UNT) muestra un ligero incremento de la turbiedad comparada con el agua filtrada (mediana 0.25 UNT) debido a la adición de cal en la fase de acondicionamiento químico, la cual contiene material particulado que aunque incrementa la turbiedad, no compromete la calidad final del agua.

Los resultados del análisis exploratorio, las visitas de inspección sanitaria y la discusión y retroalimentación al interior del equipo PSA permitieron identificar 40 eventos peligrosos parte de los cuales también fueron considerados en otras experiencias PSA [22,23]. La Tabla 2 sintetiza algunos eventos peligrosos y peligros identificados en las fases de tratamiento y componentes del sistema.

La mayoría de los eventos peligrosos se clasificaron en las categorías de mantenimiento, factores externos y operación; el control de los factores externos se puede dificultar, principalmente, por estar fuera de la gobernabilidad de la empresa prestadora del servicio de agua, lo que podría incrementar los niveles de riesgo, siendo indispensable en la implementación de los PSA la participación de todos actores involucrados en los diferentes componentes del sistema de abastecimiento de agua.

En cuanto al tipo de peligros, predominaron de tipo biológico, químico y físico, asociados a la calidad del agua cruda y la eficiencia del tratamiento, sin desconocer que el peligro asociado a la cantidad de agua disponible también resultó relevante, principalmente por las características de la fuente de abastecimiento cuyo progresivo deterioro ha incrementado el número de paradas de planta [16]; se resalta que no se evidenciaron peligros radiológicos.

Aunque todas las fases del tratamiento de agua influyen considerablemente en la calidad del agua tratada, se identificó que, en lo referente a infraestructura física, el componente canales y tuberías, además de presentar el mayor número de eventos peligrosos (9), resultó un componente muy vulnerable del sistema de tratamiento por su difícil acceso, grado de exposición a corrosión externa y la ausencia de conducciones alternas que suplan sus funciones de transporte.

Tabla 2.
Fragmento de la matriz de peligros y eventos peligrosos en los procesos de tratamiento.

Evento Peligroso												
Descripción	Clasificación					Peligro					
	D	O	M	EM	E	B	Q	F	R	C	Inf
Captación y Estructuras (Nº total de eventos peligrosos = 7)											
Presencia de obstáculos físicos (flotantes, material de arrastre, sedimentos, barro y residuos, etc.) que pueden afectar la captación y estructuras (rejas, tamices y tranquilizadores).	-	X	X	X	X	X	X	X	-	X	X
Reducción del caudal del río debido a largos periodos de sequía.	-	-	-	X	X	X	X	X	-	X	-
Reservorio Agua Clarificada (Nº total de eventos peligrosos = 3)											
No disponibilidad del reservorio por fallas operativas o de mantenimiento, vandalismo etc.	-	X	X	-	X	X	X	X	-	X	X
Contaminación del agua del reservorio por animales, crecimiento de algas, vandalismo, etc.	-	X	X	-	-	X	X	X	-	X	-
Pretratamiento (Nº total de eventos peligrosos = 3)											
Obstrucción de los tamices	-	X	X	-	X	X	X	X	-	X	-
Deficiente funcionamiento del sistema de desarenación	X	X	X	-	X	X	X	X	-	X	X
Procesos Complementarios (Nº total de eventos peligrosos = 4)											
Dosificación inadecuada de carbón activado. Ineficiencia del proceso de Adsorción. (No remoción de sustancias productoras de olores y sabores, fenoles y plaguicidas)	X	X	X	-	X	-	X	X	-	-	-
Dosificación inadecuada de cloro gaseoso (exceso o deficiencia)	-	X	X	X	X	X	X	-	-	-	-
Escape o fugas de cloro en las instalaciones de la planta o durante su transporte	X	X	X	-	X	-	X	-	-	-	X
Coagulación (Nº total de eventos peligrosos = 1)											
Fallas en el proceso de coagulación por inadecuada: -distribución del caudal de agua, -dosificación de coagulante, -pH, -gradiente y tiempo de mezcla, -calidad de materia prima, etc.	-	X	X	-	-	X	X	X	-	-	-
Floculación/Clarificación (Nº total de eventos peligrosos = 2)											
Inadecuada calidad del agua decantada causada por pérdida del manto de lodos, recirculación y purga inadecuadas, corrientes de densidad, fallas en el proceso de coagulación etc.	-	X	X	-	X	X	X	X	X	-	X
Inadecuada aplicación de ayudantes floculación.	X	X	-	-	-	X	X	X	-	-	-
Filtración (Nº total de eventos peligrosos = 3)											
Deficiente lavado de los filtros	X	X	X	-	-	X	X	X	-	X	X
Falla en procesos anteriores a la filtración (precloración, coagulación y floculación/clarificación) que causan mala calidad del afluente.	X	X	X	-	X	X	X	X	-	X	X
Postcloración (Nº total de eventos peligrosos = 4)											
Insuficiente tiempo de contacto del cloro con el agua	-	X	-	-	-	X	-	-	-	-	-
Inadecuada remoción de materia orgánica antes de la aplicación del cloro	X	-	-	-	X	-	X	-	-	-	-
Acondicionamiento Químico (Nº total de eventos peligrosos = 2)											
Ajuste incorrecto del pH (inadecuado acondicionamiento químico del agua tratada)	X	X	X	-	-	X	X	X	-	-	X
Canales y Tuberías (Nº total de eventos peligrosos = 9)											
Fugas o rotura de tubería de agua cruda por corrosión interna y externa. Acumulación de sólidos gruesos y sedimentos que disminuyen la capacidad de transporte. Formación de biopelículas.	X	X	X	-	X	X	X	X	-	X	X
Fugas y roturas de las cuatro tuberías de agua coagulada	X	-	X	-	-	X	X	X	-	X	X
Fallas en las estaciones de bombeo de agua cruda y tratada de la planta	-	X	X	-	-	X	X	X	-	X	X
Falla en la estación de bombeo de aguas residuales (aguas residuales y lluvias de la planta y lodos procedentes de los decantadores y del lavado de filtros son evacuados por esta estación)	-	X	X	-	-	X	X	X	-	X	X

D: Diseño; O: Operación; M: Mantenimiento; EM: Emergencia/Contingencia; E: Factores externos; B: Biológico; Q: Químico; F: Físico; R: Radiológico; C: Insuficiencia de agua; Inf: Asociado a la infraestructura
Fuente: Los autores

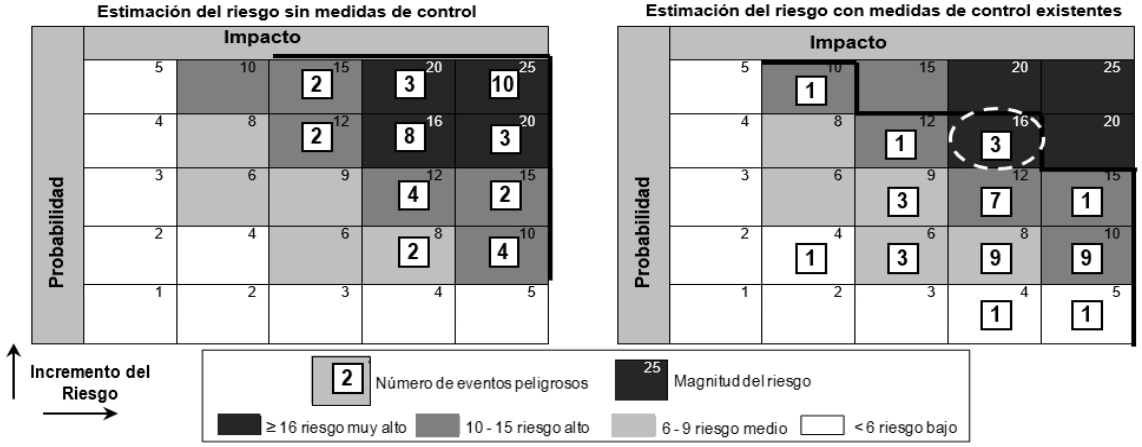


Figura 4. Estimación del riesgo sin y con medidas de control.
Fuente: Los autores

3.2. Valoración del riesgo

La estimación del riesgo para los 40 eventos peligrosos sin considerar las medidas de control existentes, permitió clasificarlos en: 24 en nivel de riesgo muy alto (60%), 14 en nivel alto (35%) y 2 en nivel medio (5%). Una vez identificadas las medidas de control y considerando su nivel de eficacia, se reestimó el riesgo, obteniéndose una nueva clasificación: 3 en nivel muy alto (7%), 19 en nivel alto (47%), 15 en nivel medio (38%) y 3 en nivel bajo (8%). La Fig. 4 esquematiza el número de eventos peligrosos asociados a cada nivel de riesgo estimado sin y con medidas de control

Se destaca que las medidas de control existentes permitieron mitigar el nivel de riesgo de los 40 eventos peligrosos de manera significativa; los 3 eventos peligrosos que aún permanecen en el nivel de riesgo muy alto están relacionados con la fase de acondicionamiento químico y el componente de canales/tuberías debido a la insuficiencia o ineficacia de las medidas de control existentes.

La Fig. 5 muestra los valores promedio y desviación estándar de los riesgos estimados sin y con medidas de control por cada fase del tratamiento y principales componentes.

Aunque la eficiencia de las medidas de control existentes permite reducir considerablemente los niveles de riesgo, aún es necesario concentrar esfuerzos en algunas fases del proceso para reducir los riesgos clasificados como alto y muy alto, siendo prioritarias en su orden las fases de acondicionamiento químico del agua potable, coagulación, floculación/clarificación y filtración, ratificando lo encontrado en el análisis exploratorio. Aunque los resultados de la valoración del riesgo son particulares y específicos para cada SAAP, en algunas experiencias de PSA, las fases de filtración y desinfección en PTA convencionales han resultado con niveles de riesgo alto [22,24,25].

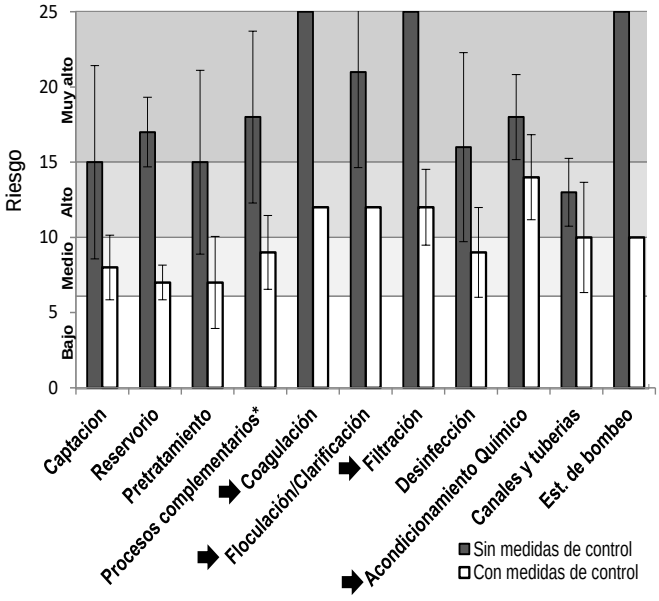


Figura 5. Valores promedio de los riesgos estimados sin y con medidas de control por cada fase del tratamiento.
Fuente: Los autores

Vale la pena destacar tres medidas de control existentes, dos de las cuales implicaron una importante inversión económica por parte de la empresa prestadora del servicio y que han mostrado su efectividad para reducir el nivel de riesgo de varios de los eventos peligrosos identificados en la PTA, principalmente los relacionados con la elevada turbiedad y bajo nivel de oxígeno disuelto – OD en la cuenca de abastecimiento: i) suspensión de la captación cuando se alcanzan niveles de turbiedad > 2500 UNT, ii) estación de alerta temprana en el río Cauca aguas arriba de la captación que cuenta con medición en línea de OD y turbiedad y iii) reservorio de agua clarificada para garantizar continuidad del servicio durante la suspensión de la captación.

En general, la evaluación del riesgo realizada contribuye al desarrollo del PSA en el SAAP de la ciudad de Cali, permitiendo priorizar los eventos peligrosos sobre los cuales es necesaria la formulación de programas de mejoramiento, soporte o apoyo al PSA que incluyan nuevas medidas de control y correctivas, la optimización de las existentes, programas de capacitación y concientización, mantenimiento y calibración, investigación y desarrollo e importantes obras de inversión en infraestructura, equipos, etc., todo ello como parte de la gestión del riesgo y estrategia de aseguramiento de la calidad del agua.

4. Conclusiones

Las herramientas empleadas para la evaluación del riesgo (análisis exploratorio de datos de turbiedad, visitas de inspección, matriz de peligros/eventos peligrosos y matriz semicuantitativa de riesgo) evidenciaron su potencialidad de uso y adaptación para diferentes sistemas de abastecimiento, facilitando la identificación y priorización de los eventos peligrosos, lo que a su vez contribuye al desarrollo de los PSA y facilita la toma de decisiones en las empresas prestadoras de servicios de agua.

El análisis exploratorio de los datos horarios de turbiedad evidenció la robustez y capacidad de las barreras de tratamiento en la reducción de la turbiedad a niveles adecuados para el control del riesgo microbiológico en las fases de filtración y desinfección. Aunque se observó una asociación entre los eventos extremos de turbiedad en la cuenca de abastecimiento, la robustez de la tecnología de clarificación por manto de lodos evitó incrementos bruscos de la turbiedad del agua clarificada; adicionalmente, la barrera de filtración contribuyó a garantizar niveles de turbiedad acordes a la reglamentación.

La valoración del riesgo mostró la eficacia de las medidas de control existentes en la PTA, logrando reducir el nivel de riesgo de los eventos peligrosos clasificados en un nivel muy alto (60%) al 7%. Sin embargo, es necesario la formulación de varios programas de mejoramiento, soporte o apoyo al PSA orientados a las fases prioritarias, que en su orden fueron: acondicionamiento químico del agua potable, coagulación, floculación/clarificación y filtración.

Teniendo en cuenta la interrelación entre los componentes de un sistema de abastecimiento de agua, es indispensable garantizar de manera integral la evaluación y gestión del riesgo con la participación de todos los actores involucrados en los diferentes componentes (cuenca, procesos de tratamiento, sistema de distribución y usuario final).

Agradecimientos

Los autores agradecen a las Empresas Municipales de Cali (EMCALI EICE ESP) por permitir la ejecución del proyecto de investigación y a COLCIENCIAS, la Universidad del Valle y la Universidad Santiago de Cali por la financiación Proyecto 1106-744-54937.

Referencias

[1] World Health Organization. Guidelines for Drinking-water Quality. Genéva: WHO, 2011.

[2] Lindhe, A., Rosén, L., Norberg, T. and Bergstedt, O., Fault tree analysis for integrated and probabilistic risk analysis of drinking water systems. Water Research, 43(6), pp. 1641-1653, 2009. DOI: https://doi.org/10.1016/j.watres.2008.12.034

[3] Bartram, J., Corrales, L., Davison, A., Deere, D., Drury, D., Gordon, B., Howard, G. and Stevens, M., Water safety plan manual: step-by-step risk management for drinking-water suppliers. Genéva: WHO, 2009.

[4] Davies, J. and Mazumder, A., Health and environmental policy issues in Canada: the role of watershed management in sustaining clean drinking water quality at surface sources. Journal of Environmental Management, 68(3), pp. 273-286, 2003. DOI: 10.1016/S0301-4797(03)00070-7

[5] Tuhovcak, L., Rucka, J. and Juhanak, T.B., Risk analysis of water distribution systems, en Pollert, J. & Dedus, B., Security of water supply systems: from source to tap, Netherlands, Springer, 2006. pp 169-182.

[6] Pérez-Vidal, A., Torres-Lozada, P. and Escobar-Rivera, J.C., Hazard identification in watersheds based on water safety plan approach: case study of Cali-Colombia. Environmental Engineering and Management Journal, 15(4), pp. 861-872, 2016.

[7] Pérez Amezquita-Marroquin, C.P., Pérez-Vidal, A. and Torres-Lozada, P., Evaluación del riesgo en sistemas de distribución de agua potable en el marco de un plan de seguridad del agua. Revista EIA, 21, pp. 157-169, 2014.

[8] Pérez-Vidal, A., Amezquita-Marroquin, C. and Torres-Lozada, P., Water safety plans: risk assessment for consumers in drinking water supply systems. Ingeniería y Competitividad, 15(2), pp. 237-251, 2013.

[9] National Research Council, Committee on Toxicants and Pathogens in Biosolids Applied to Land, Board on Environmental Studies and Toxicology, Division on Earth and Life Studies. Biosolids applied to land: Advancing standards and practices. Washington: National Research Council; 2002.

[10] Rosén, L., Hokstad, P., Lindhe, A., Sklet, S. and Rostum, J., Generic framework and methods for integrated risk management in water safety plans [online]. TECHNEAU, Europa, 2007, 102 P. Available at: http://www.techneau.org/fileadmin/files/Publications/Publications/Deliverables/D4.1.3.pdf

[11] Rinehold, A., Corrales, L., Medlin, E. and Gelting, R., Water safety plan demonstration projects in Latin America and the Caribbean: lessons from the field. Water Science & Technology: Water supply, 11(3), pp. 297-308, 2011. DOI: 10.2166/ws.2011.050

[12] Burlingame, G.A., Pickel, M.J. and Roman, J.T., Practical applications of turbidity monitoring. Journal of American Water Works Association, 90(8), pp. 57-69, 1998.

[13] Ministerio de Protección Social, Ministerio de Ambiente, Vivienda y Desarrollo Territorial. Resolución 2115 del 22 de junio de 2007: por medio de la cual se señalan características, instrumentos básicos y frecuencias del sistema de control y vigilancia para la calidad del agua para consumo humano. República de Colombia, Bogotá D.C., 2007.

[14] Montoya, C., Loaiza, D., Torres, P., Cruz, C.H. y Escobar, J.C., Efecto del incremento en la turbiedad del agua cruda sobre la eficiencia de procesos convencionales de potabilización. Revista EIA, 16, pp. 137-148, 2011.

[15] Lindhe, A., Integrated and probabilistic risk analysis of drinking water system, BSc. Thesis, Department of Civil and Environmental Engineering oral, Chalmers University of Technology, Göteborg, Sweden, 2008.

[16] Pérez, A., Delgado, L.G. y Torres, P., Evolución y perspectivas del sistema de abastecimiento de la ciudad de Santiago de Cali frente al aseguramiento de la calidad del agua potable. Ingeniería y Competitividad, 14(2), pp. 69-81, 2012.

[17] Fournier, B., Gestión del riesgo sanitario en la regeneración del agua, Tesis de especialización, Universidad Politécnica de Cataluña, España, 2006.

[18] Unión Europea. Directiva 98/83/CE del Consejo, de 3 de noviembre de 1998, relativa a la calidad de las aguas destinadas al consumo humano [online]. UE, 1998, 23 P. Available at: http://eur-lex.europa.eu/legal-content/ES/TXT/PDF/?uri=CELEX:31998L0083&rid=1

[19] Environmental Protection Agency. Optimizing water treatment plant performance using composite correction program – 1998. Edición (EPA/625/6-91/027). USA: EPA, Office of Research and Development, 1998.

[20] Environmental Protection Agency. National primary drinking water regulations. EPA 816-F-09-004 [online]. EPA, USA, 2009, 6 P. Available at: http://pbadupws.nrc.gov/docs/ML1307/ML13078A040.pdf

[21] Pinto, V., Heller, L. and Bastos, R.K.X., Drinking water standards in South American countries: convergences and divergences. Journal of Water and Health, 10(2), pp. 295-310, 2012. DOI: 10.2166/wh.2012.087

[22] Vieira, J. and Morais, C., Planos de Segurança da Água para consumo humano em sistemas públicos de abastecimento. Portugal: Instituto Regulador de Águas e Resíduos - Universidade do Minho, Braga, Portugal 2005.

[23] Marini-Bulbarela, E.C., Plan de seguridad del agua para la UNAM. Aplicación de la metodología de los planes de seguridad del agua potable. México: Editorial Académica Española, 2016.

[24] Environmental & Engineering Managers LTD. Documento técnico lecciones aprendidas del desarrollo del plan de seguridad del agua para el sistema de abastecimiento de agua de Spanish Town en Jamaica [online], Jaimaca, 2008, 16 P. Available at: http://www.bvsde.paho.org/bvsacg/red_lac_psa/casos/jamaica/technicalesp.pdf

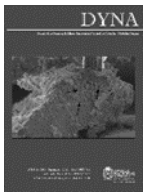
[25] Caribbean Environmental Health Institute (CEHI). Water Safety Plan Linden Guyana [online]. CEHI, Guyana, 2009, 111 P. Available at: http://www.bvsde.paho.org/bvsacg/red_lac_psa/casos/guyana/WSPFinal.pdf

A. Pérez-Vidal, obtuvo el título de Ing. Sanitaria en el 2002, de MSc. en Ingeniería en 2007 y Dra. en Ingeniería con énfasis en Ingeniería Sanitaria y Ambiental en 2013, por la Universidad del Valle, Cali - Colombia. Se desempeñó como asistente de investigación y docente cátedra en la Universidad del Valle, como docente tiempo completo en la Universidad de Boyacá y actualmente es profesora titular en la Universidad Santiago de Cali – USC, Colombia. Está categorizada por Colciencias como investigadora asociada. Sus áreas de investigación han sido el tratamiento de agua para consumo humano, tratamiento de aguas residuales y manejo de biosólidos.
ORCID: 0000-0001-6989-0441

J.C. Escobar-Rivera, obtuvo el título de Ing. Sanitario en 1982 de la Universidad del Valle, Cali – Colombia, de MSc. (1993) y Dr. (2001) en Engenharia Civil: Hidráulica e Saneamento de la Universidade de São Paulo – Brasil. Desde 1982 se desempeña como profesional operativo en las Empresas Municipales de Cali EMCALI-EICE-ESP y ha trabajado como docente cátedra en la Universidad Nacional sede Palmira, la Universidad del Valle y la Universidad Santiago de Cali, Colombia. Su área de investigación es la calidad y el tratamiento de agua.
ORCID: 0000-0002-2504-0557

P. Torres-Lozada, obtuvo el título de Ing. Sanitaria en 1982 de la Universidad del Valle, Cali – Colombia, de MSc. (1993) y PhD. (2001) en Engenharia Civil: Hidráulica e Saneamento de la Universidade de São Paulo – Brasil. Desde 1995 hasta la fecha, se encuentra vinculada a la Universidad del Valle como profesora titular. Está categorizada por Colciencias como investigadora senior y es líder del Grupo de Investigación Estudio y Control de la Contaminación Ambiental ECCA con categoría A1. Sus áreas de investigación son calidad del agua, tratamiento de agua para consumo humano, tratamiento de aguas residuales y residuos sólidos.
ORCID: 0000-0001-9323-6677

UNIVERSIDAD NACIONAL DE COLOMBIA
SEDE MEDELLÍN
FACULTAD DE MINAS



DYNA
http://dyna.medellin.unal.edu.co/

Design of a serious emerging games engine based on the optimization algorithm of ant colony

Jose Aguilar, Junior Altamiranda & Francisco Díaz

CEMISID, Facultad de Ingeniería, Universidad de los Andes, Mérida, Venezuela. aguilar@ula.ve, altamira@ula.ve, francisco.diaz@ula.ve

Received: January 19th, 2018. Received in revised form: Junio 18th, 2018. Accepted: June 27th, 2018.

Abstract
An engine for a serious emergent game (MJSE due its Spanish acronym) must make explicit the possibility of emergence in a serious game, from the coordination of game frames, adapted to the specific educational context where the game is being used. In particular, in previous works have proposed a hierarchical architecture for a MJSE, composed of sub-motors. The main objective of this work is to specify the sub-motors responsible for the emergence process of the serious game, which are based on the algorithm of optimization based on ant colonies (ACO). These sub-motors carry out the management of the set of game frames according to the educational context of interest, in such a way to merge them into a single frame, in order to make the dynamic of the serious game emerge. Additionally, this paper analyzes the behavior of the sub-motors in a case study, with very encouraging results.

Keywords: games engine; serious emerging games; optimization algorithm based on ants colonies.

Diseño de un motor de juegos serios emergentes basado en el algoritmo de optimización de colonia de hormigas

Resumen
Un motor de juegos serios emergentes (MJSE) debe hacer explícito la posibilidad de emergencia en un juego serio, a partir del manejo coordinado de tramas de juegos, adaptadas al contexto educativo especifico donde se esté desarrollando el juego. En particular, en anteriores trabajos se ha propuesto una arquitectura jerárquica para el MJSE, constitutiva de submotores. El objetivo principal de este trabajo es especificar los submotores encargados del proceso de emergencia del juego serio, los cuales se basan en el algoritmo de optimización basado en colonias de hormigas (ACO). Dichos submotores realizan la gestión del conjunto de tramas de juego según el contexto-dominio educativo de interés, de tal manera de fusionarlas en una única trama, para hacer de esta forma emerger la dinámica del juego serio. Adicionalmente, en este trabajo se analiza el comportamiento de dichos submotores en un caso de estudio, mostrando resultados muy alentadores como MJSE.

Palabras claves: motor de juegos; juegos serios emergentes; algoritmo de optimización basado en colonias de hormigas.

1. Introducción

Un motor de juego es un conjunto de programas que permiten la creación, la representación y la ejecución de un juego. Hoy en día, existen una gran variedad de motores para que el usuario pueda crear sus propios juegos. Ahora bien, no se han desarrollado motores de juegos para juegos emergentes, y mucho menos para juegos serios emergentes.

El objetivo específico de este trabajo, es realizar la especificación de un MJSE. En particular, nosotros estamos interesados en MJSEs, cuyo objetivo es diferente al de meramente jugar, tal que puede ser educativo, de entrenamiento, de rehabilitación, entre otros fines, y en particular, cuya dinámica surja en función de lo que va aconteciendo en el contexto [1]. Los juegos serios emergentes parten de dos teorías, la de juegos serios que establece que es un juego que tiene un propósito específico, el cual puede estar relacionado con el aprendizaje, con la comprensión de un tema complejo [2,19-21]; y la de sistemas emergentes, que son sistemas cuyos comportamientos surgen a partir de las interacciones espontáneas de los elementos relativamente simples que los componen, sin leyes explícitas [3,4]. En ese

How to cite: Aguilar, J., Altamiranda, J. and Díaz, F., Diseño de un motor de juegos serios emergentes basado en el algoritmo de optimización de colonia de hormigas. DYNA, 85(206), pp. 311-320, September, 2018.

© The author; licensee Universidad Nacional de Colombia.

sentido, estos tipos de juegos requieren de un MJSE específico a sus características.

A continuación, comentamos rápidamente los trabajos de mayor interés para nuestra propuesta. En [1] se ha propuesto la arquitectura de un MJSE estructurada en capas, para el cual se hace la propuesta de los submotores encargados del proceso de emergencia en este trabajo. En [5] exponen el modelo conceptual de un motor de juegos basado en capas jerárquicas. En [6] se introduce la noción de juegos emergentes, bajo el enfoque basado en guiones, como un juego en la que su dinámica va surgiendo en función del contexto. En esa investigación se propone un sistema de motores de juegos emergentes denominado EmerGENT, sustentado en autómatas celulares. En [7] muestran un marco para la selección de motores de juegos serios, usando tres criterios para el proceso de selección: 1. Fidelidad audiovisual y funcional, 2. Capacidad de composición y 3. Accesibilidad. Además, realizan dicha comparación en varios motores de juegos (Cry Engine, Source Engine, Unreal y Unity). Finalmente, en [8] se presentan cinco enfoques de narrativas emergentes: crear mundos creíbles, incorporar la experiencia del jugador en el juego, establecer espacios de múltiples opciones de decisión en los estados del juego, permitir la incertidumbre posibilitando crear situaciones inesperadas, posibilitar la co-autoría tal que el jugador es responsable de la historia y la dirección que toma el juego.

En específico, este trabajo propone un MJSE basado en ACO, el cual realiza el manejo de las tramas del juego guiados por el contexto educativo. De esta manera, el MJSE utiliza ACO para hacer emerger la dinámica del juego en función del contexto educativo. El artículo se organiza de la siguiente manera, la siguiente sección presenta los aspectos teóricos bases de este trabajo, seguidamente se presenta la arquitectura general del MJSE, para después detallar el componente que permite la emergencia del juego serio. La sección 3 presenta el diseño del MJSE basado en ACO. A continuación, se presenta un caso de estudio, y se compara el MJSE con otros trabajos similares, para finalmente terminar con las conclusiones.

2. Aspectos teóricos

2.1. Juegos serios emergentes

En [2, 7, 9] definen a los Juegos Serios (JS) como juegos diseñados y desarrollados desde un objetivo distinto a la pura diversión. Los JS proveen un ambiente motivador, un contexto de entretenimiento y auto-fortalecimiento, para que los jugadores "aprendan haciendo" a través de sus propios errores, gracias a desafíos adecuados a su nivel de competencia y a una realimentación constante.

Por otro lado, en [6] definen a un Juego Emergente (JE) como uno que se va desplegando de manera espontánea, autónoma, y sin leyes explícitas, adecuándose a los jugadores. En [3] proponen el JE "Metrópolis", cuyo funcionalismo parte de la premisa: Las ciudades son auto-gestionadas por decisiones tomadas en conjunto por sus habitantes (jugadores), sin que exista un habitante con un papel más importante. Concluyentemente, en Metrópolis emergen patrones urbanísticos en la ciudad por las decisiones que sus habitantes toman. [4] propone una extensión a Metrópolis con la incorporación de mecanismos emergentes a la dinámica del juego para adaptarla a sus jugadores. Proponen cinco niveles de emergencia en un JE:

1. *Comportamiento:* se generan nuevas tácticas y estrategias en el juego, siguiendo reglas con variantes.
2. *Secuencia:* se crean nuevos escenarios, tramas o temáticas en los juegos, cambiando el ambiente y el contexto del juego.
3. *Final:* patrones que reflejan resultados de los juegos, o continuar el juego de forma infinita (en el caso de los JS no es necesario que termine el juego ni que haya un ganador).
4. *Propiedad:* cambia las características en los objetos.
5. *Modelo de Negocio:* por el surgimiento de mercados y servicios alrededor de los juegos.
6. *Utilidad:* depende para que se va a utilizar el JE.

Finalmente, en un JSE la historia, la dinámica, el guion que va surgiendo, depende del contexto donde se va dando el juego. Así, el JSE posiciona al jugador en un entorno de realimentación de información y motivación al logro, guiado por un objetivo explícito distinto de la pura diversión, para superar desafíos adecuados a su capacidad, y aprender de sus propios errores. En específico, el comportamiento que va dándose en el JSE resulta espontáneo, autónomo, y sin leyes explícitas, adecuándose a los jugadores, a sus entornos, entre otras cosas.

En [5] definen a los motores de juegos como los ambientes computacionales que permiten realizar videojuegos. Pueden ser vistos como programas, librería o *framework*, para el desarrollo de videojuegos. Un motor de videojuegos es el núcleo general que une todas las partes de un juego. Así, los desarrolladores se centran en las mecánicas, las lógicas y las características específicas del juego que está concibiendo.

Por otro lado, en un JSE el MJSE maneja un conjunto de tramas, y las va seleccionando y fusionando en una única trama, según el contexto y el objetivo del juego. Para ello, el MJSE requiere realizar el siguiente conjunto de tareas:

- La búsqueda y selección del conjunto de tramas adecuadas al contexto donde funcionará el JSE,
- La fusión de algunas de las tramas seleccionadas en una única trama, según los objetivos del JS, que se desplegará inicialmente en el videojuego, y la supervisión de la dinámica del desarrollo del JSE, para adecuarlo a la dinámica del contexto donde funciona, a través de la adaptación de su trama.

2.2. Arquitectura de MJSE

Un MJSE debe mantener la relación-lógica entre la trama y el JSE, usando los submotores clásicos de los videojuegos para administrar gráficos e imágenes, controlar el movimiento físico de los objetos, gestionar el sonido, entre otras cosas. Pero ahora también debe integrar otro submotor, que hemos llamado submotor de tramas, para realizar las tareas de gestión de las tramas que componen el JSE. En [1] hemos propuesto una arquitectura general de un MJSE. En esta sección presentaremos brevemente dicha arquitectura (para más detalles ir a [1]).

2.2.1. Arquitectura general del MJSE

La arquitectura del MJSE está basada en capas jerárquicas, en las cuales están los diferentes submotores que la componen (ver Fig. 1).

1. *Núcleo del Motor de Videojuego:* es el elemento central del MJSE, en él se encuentran los seis submotores de base para cualquier videojuego, los cuales son:
   a. Submotor de Gráficos: realiza y maneja los gráficos, imágenes y dibujos primitivos, basados en sus características: texturización, mallas, terrenos, etc.
   b. Submotor Físico: se encarga de realizar los movimientos físicos de los objetos en un ambiente virtual.
   c. Submotor de Sonido: se encarga de gestionar todo lo referente a lo audible: música, audio, ruido, micrófonos, entre otras cosas.
   d. Submotor de Interacción: se encarga de configurar las interacciones dentro y fuera de los videojuegos.
   e. Submotor de Video: se encarga de la unión del sonido y las imágenes en secuencias fílmicas para realizar videoclips, caricaturas, cortes de películas, etc., usadas en el videojuego.
   f. Submotor de Renderización: se encarga de gestionar las imágenes en movimiento, considerando aspectos como: mejorar la iluminación, sombreado y oscuridad, definir sus efectos visuales, entre otros.
2. *Subsistema de Emergencia del Videojuego:* esta capa permite hacer emerger un juego, según los objetivos que se deben cumplir durante el juego o la dinámica que va ocurriendo en el mismo. En esta capa funciona el Submotor de Trama Emergente (STE), el cual interactúa con el jugador/contexto para hacer emerger el JSE, y el submotor de IA, que provee mecanismos requeridos en el proceso de emergencia del JSE.
3. *Subsistema de Adaptación del Videojuego:* esta capa permite adecuar un videojuego sin tener que hacer modificaciones profundas en él, actuando sobre sus características de base. Por ejemplo: puede establecer los valores de renderizados específicos del juego. Esta capa utiliza el SIA para adaptar esos valores de las características en los elementos, el ambiente y los eventos del videojuego.
   Como hemos visto, en estas dos últimas capas operan dos sub-motores:
   a. Submotor de Inteligencia Artificial (SIA): se encarga de introducir comportamientos inteligentes en los personajes y componentes del JSE, para adecuarlo a la dinámica y contexto en el que se está ejecutando. También, permite adaptar las narrativas, y en general los parámetros de los videojuegos, al contexto deseado.
   b. Submotor de Trama Emergente (STE): permite crear las narrativas de los videojuegos al contexto deseado, al objetivo del juego serio. Una vez recolectada la información precisa del contexto, realiza gestión de escenas y eventos, configuración de subtramas/guiones del juego, entre otras cosas.

2.2.2. Sub-motor de trama emergente

El STE establece la relación-lógica entre las tramas del JSE. El STE permite gestionar:

- El escenario, los personajes y eventos en la trama, de acuerdo a los requerimientos espacio-tiempo del tema.
- La coherencia y adecuación de la trama, con los requerimientos semánticos del contexto.
- La congruencia entre la actividad deseada a desarrollar y la trama del JSE.

Para ello, el STE posee las siguientes sub-capas:

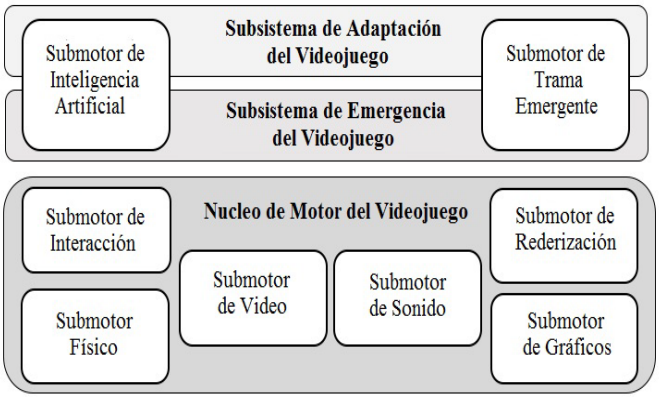


Figura 1: Arquitectura General del MJSE.
Fuente: Elaboración Propia.

1. *Gestor de Materia (GM):* determina la temática que se esta tratando en el contexto, para a partir de allí, establecer el tipo de trama que se debe aplicar en el JSE.
2. *Gestor de Videojuegos (GV):* busca los tipos de videojuegos (edugame, advergame, etc.) para esa temática, usando Repositorios de Objetos de Aprendizaje (ROA). Para esa busqueda, usa los metadatos de los OAs en un ROA y los compara con lo definido por el GM. Si no consigue al menos un videojuego parecido a lo buscado, llama al Módulo de Generación de JSE para generar un videojuego.
3. *Módulo de Generación de JSE (MGJSE):* es el responsable del ensamblaje, de un nuevo JSE, invocando para ello a los siguientes tres módulos de STE. Además, durante el juego, debido a la interacción entre el JSE y su contexto (ambiente, jugadores, etc.), pueden emerger nuevos comportamientos en el JSE por cambios que el MGJSE introduzca en el comportamiento, secuencia, final del juego, propiedad de sus componentes o utilidad del mismo.
4. *Storyboard (SB):* se encarga de generar guiones narrativos para el JSE, usando para ello la información del GM.
5. *Gestión de Escenas (GE):* se encarga de generar el ambiente, mundo o entorno, requeridos por las tramas del JSE.
6. *Sistemas de Eventos (SE):* este módulo se encarga de generar eventos especializados requeridos por el SB, para generar los comportamientos deseados en el JSE.

En específico, el STE se comporta de la siguiente manera (ver Fig. 2):

   a. El GM determina toda la información sobre la temática deseada, según el contexto donde se quiera usar el juego.
   b. El GV seleccionada de ROAs los JSs que sean más compatibles al uso deseado. Para ello, compara los metadatos de los JSs en el ROA, descritos bajo algunos de los estándares (LOM/SCORM) [10], con lo determinado por GM.
   c. El MGJSE determina "SI" se consiguen JSs que cubran la temática deseada; en ese caso los adecua y los envía al entorno donde serán usados (por ejemplo, un entorno virtual de aprendizaje, o VLE por sus siglas en inglés). De lo contrario, el MGJSE utiliza un algoritmo para hacer emerger un JSE compatible con el tema deseado. En este trabajo, se usa un algoritmo ACO para ello.

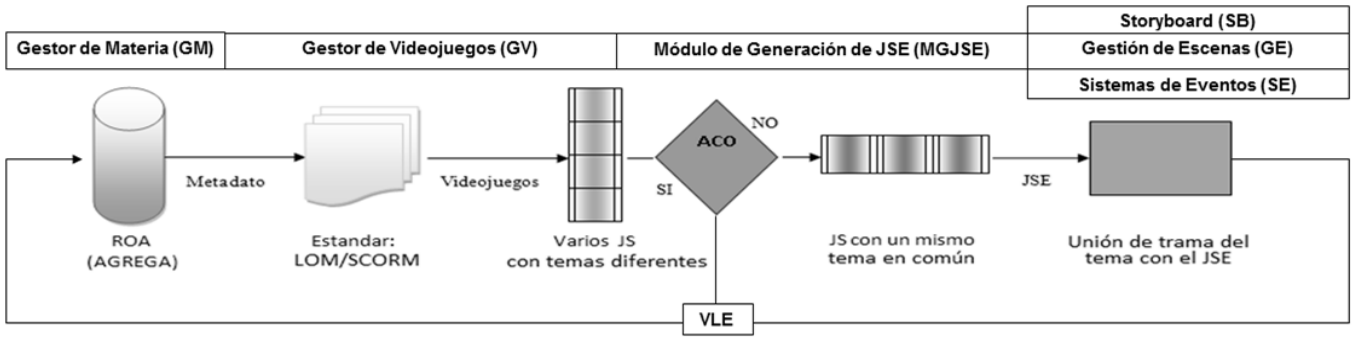


Figura 2. Componentes del STE.
Fuente: Elaboración Propia.

d. El GV seleccionada de ROAs los JSs que sean más compatibles al uso deseado. Para ello, compara los metadatos de los JSs en el ROA, descritos bajo algunos de los estándares (LOM/SCORM) [10], con lo determinado por GM.
e. El MGJSE determina "SI" se consiguen JSs que cubran la temática deseada; en ese caso los adecua y los envía al entorno donde serán usados (por ejemplo, un entorno virtual de aprendizaje, o VLE por sus siglas en inglés). De lo contrario, el MGJSE utiliza un algoritmo para hacer emerger un JSE compatible con el tema deseado. En este trabajo, se usa un algoritmo ACO para ello.
f. La solución final propuesta por el MGJSE, compuesta por uno o varios JSs, articula de manera natural sus bloques narrativos (SB), bajo los escenarios especificados en dichos JSs (GE), y los eventos definidos en ellos (SE).
g. El MJSE supervisa la dinámica del JSE bajo ejecución, para irlo adecuando al contexto de manera emergente, haciendo emerger nuevos comportamientos y secuencias (llama de nuevo a ACO), actualizando propiedades en los objetos, el final o su utilidad, en función de la misma.

3. STE basada en ACO

3.1. Especificación General de ACO

ACO es un tipo de meta heurística basada en población, el cual está inspirados en la conducta de las colonias de hormigas reales cuando buscan comida, para resolver problemas de optimización combinatoria [11,12]. En nuestro caso, ACO crea agentes hormigas, y cada una construirá un JSE para un mismo objetivo (temática), usando diferentes tramas. En particular, un videojuego seleccionado de un repositorio de juegos lo denominaremos subtrama (trama seleccionada), mientras que una trama de un JSE es la unión/fusión de una o más subtramas. ACO está compuesto por:

1. *Espacio de solución:* o espacio que recorrerán las hormigas para obtener soluciones. Es un grafo compuesto por nodos que describen las subtramas seleccionadas desde diferentes repositorios, y arcos que establecen las relaciones de dependencia entre ellas, cuando existen. También, el arco es usado por las hormigas para establecer la secuencia lógica entre las subtramas, para general la trama final del JSE, usando para ello feromonas.
2. *Hormigas:* caminan en el grafo de sub-tramas (tramas seleccionadas).
3. *Solución:* las sub-tramas (nodos) son marcadas por una feromona en el grafo, igual que los arcos que los interconectan. Cuando converge el algoritmo ACO, las sub-tramas son seleccionadas según si su feromona pasa un umbral, igual que los arcos que salen de ellas, los cuales establecen la secuencia lógica de ejecución de las subtramas.
4. *Feromonas:* hay dos tipos, una para las sub-tramas (nodos) y otro para los arcos entre las subtramas. La feromona define lo deseable de la subtrama y de los arcos que las interconectan, para pertenecer a la solución final.
5. *Función Feromona* actualiza cada tipo de feromona en función de la calidad del JSE propuesto.
6. *Función Heurística:* define la decisión heurística que toma una hormiga, al estar en una sub-trama (nodo), con respecto a que otra sub-trama (nodo) debe continuar a visitar después de ella.

ACO permite un proceso de aprendizaje colectivo entre las hormigas, para configurar el JSE [12, 13, 14]. Así, la solución no es más que una secuencia de sub-tramas tomadas del repositorio de tramas, ordenadas según una secuencia lógica entre ellas. Para seleccionar las tramas candidatas del repositorio de tramas que conformaran los nodos del grafo (sub-tramas), se considera la relación entre el contenido de la trama (definido en sus metadatos) y las características del JSE a desarrollar, basada en aspectos como: tema del juego serio, utilidad de la trama, etc.

3.2. Macroalgoritmo ACO para el STE

El macroalgoritmo a usar es el clásico de ACO [12, 13, 14]. En específico, en nuestro caso consiste de una fase de inicialización de parámetros, un proceso iterativo sobre dos componentes hasta que el sistema converja, y la construcción de la solución final. Dicho macroalgoritmo se muestra a continuación:

Inicializar parámetros, feromonas y grafo
Repita Mientras (no se cumpla condición de terminación)
ConstruirSolucionesporHormigas
ActualizarFeromona
ConstruirSolucionFinal

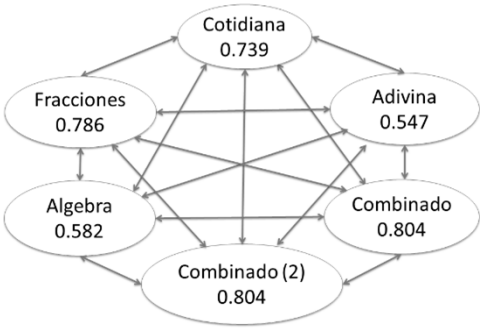


Figura 3: Grafo Teórico.
Fuente: Elaboración Propia



Figura 4: Nodo del grafo.
Fuente: Elaboración Propia.

a. Creación del grafo teórico de recorrido de las Hormigas (*Inicializar grafo*): El grafo teórico es definido como G = (N, E), donde N es un conjunto de nodos que representan las sub-tramas (JSs seleccionados por GV de ROAs), y E un conjunto de arcos que conectan todos los nodos de N (ver Fig. 3). Además, se establece una función de peso d_{ij} para determinar el peso de un arco (i, j) ∈ E, tal que es 1 si existe una relación de dependencia secuencial entre dos nodos (JS_i, JS_j, ∈ N), y 0 en caso contrario. Eso implica que $d_{ij}\neq 0$ cuando entre dos nodos hay una relación de dependencia entre ellos ver Fig. 3.

Los nodos del grafo guardan la información de la subtrama que representan (ID del nodo), pero adicionalmente almacenan el nivel de similitud entre el nodo y la temática tratada (basado en su metadato, y calculado por GV), y un nivel de feromona actualizado por las hormigas que transitan a través de ellos, que indica la deseabilidad de dicho nodo (ver Fig. 4).

b. Construcción de la solución por parte de las hormigas (*ConstruirSolucionesporHormigas*): En esta fase, algunas consideraciones se realizan:
   - Se define el número de individuos que integran la colonia.
   - El número de individuos de la colonia es invariable.
   - Cada hormiga inicialmente se coloca de modo aleatorio en el grafo para iniciar su recorrido.

Cada hormiga ejecuta una función heurística (o de transición) desde el nodo actual donde se encuentra, para determinar el próximo nodo que puede visitar que no haya previamente visitado. Esta función es definida como la probabilidad de visitar desde el nodo r a cada uno de sus nodos contiguos *s*, en función del nivel de feromona "γ(r,s)" del arco entre el nodo i y cada nodo s, y el índice de similitud "η(s)" de cada nodo *s* con respecto a la temática buscada, lo cual es calculado para todos los nodos aun no visitados por la hormiga k (J_r^k). Eso se expresa en la siguiente ecuación:

$$P_{(r,s)}^{k} = \frac{\gamma_{(r,s)} \cdot \eta_{(s)}}{\Sigma_{u \in J_r^k} \gamma_{(r,u)} \cdot \eta_{(s)}} \text{ Si } s \in J_r^k \qquad (1)$$

Particularmente, esta expresión se usa cuando no se quiere parar la construcción de una solución. Es decir, la hormiga puede culminar en cualquier momento la construcción de una solución, o continuar paseando por los nodos hasta recorrer a todos, basado en el siguiente algoritmo:

$$Recorrido\ Hormiga\ k = \begin{cases} parar, & num_{aleatorio} > umbral_parar \\ continuar\ constr.JSE\ basado\ ec.1, & caso\ contrario \end{cases}$$

3.3. Actualización de los feromonas

En nuestro caso hay dos feromonas, una para los arcos y otra para los nodos. Ambas son actualizadas al final de cada iteración. En ese sentido, cada hormiga actualizará la feromona de cada arista y cada nodo que visita. Para ello, se determina un índice de la calidad del JSE propuesto por cada hormiga, el cual será usado durante el proceso de actualización. Ese índice de calidad es calculado a partir del nivel de similitud del JSE propuesto por cada hormiga con respecto al tema deseado (definido por GV). El nivel de similitud del JSE propuesto por una hormiga k (η^k) no es más que la agregación de los índices de similitud "$\eta(s)^p$", para p=1… P, de las P subtramas que componen el JSE.

De esta manera, la feromona de cada nodo y arco se actualiza usándose las ecuaciones genéricas siguientes:

$$\gamma_{(r,s)} = \gamma_{(r,s)} + \Delta\gamma_{(r,s)}$$
$$\gamma_{(r)} = \gamma_{(r)} + \Delta\gamma_{(r)} \qquad (2)$$

Donde, $\Delta\gamma_{(r,s),}$ y $\Delta\gamma_{(r),}$ son el incremento de las feromonas, que vienen dadas por la sumatoria de las cantidades de feromona dejadas por las M hormigas en el arco (r, s) o nodo (r):

ID del nodo: JS
Índice de similitud "$\eta_{(s)}$"
Nivel de feromona "$\gamma_{(r)}$"

$$\gamma_{(r,s)} = \frac{\Sigma_{k=1}^{M} \Delta\gamma_{(r,s)}}{M}$$
$$\gamma_{(r)} = \frac{\Sigma_{k=1}^{M} \Delta\gamma_{(r)}}{M} \qquad (3)$$

y tanto $\Delta\gamma_{(r)}^{k}$ $\Delta\gamma_{(r)}^{k}$ como $\Delta\gamma_{(r,s)}^{k}$ son iguales a η^k

La actualización de las feromonas también tiene un proceso de evaporación de las mismas, la cual se ejecuta sobre todos los

nodos y arcos en el grafo al final de cada iteración, según la siguiente función:

$$\gamma_{(r,s)} = (1-\rho) + \Delta\,\gamma_{(r,s)} \qquad \gamma_{(r)} = (1-\rho) + \Delta\,\gamma_{(r)} \qquad (4)$$

Donde, $\rho \in (0,1]$ es el coeficiente de evaporación de feromona. En general, este proceso se realiza repetidamente hasta que la colonia converge en un grupo de soluciones (JSEs).

c. Construcción de la solución final *(ConstruirSolucionFinal):* Una vez que la colonia concluye su trabajo, se debe pasar a construir la solución final, es decir, el JSE que propondrá ACO. Para ello, se hace un recorrido sobre todos los nodos del grafo, seleccionándose los nodos con mayor valor de feromona, y los arcos que saldrán de cada uno de ellos serán seleccionados según un valor de feromona también (será el que tenga el valor mayor), tal que se garantice que todos los nodos (subtramas) conformen un camino (esa será la secuencia lógica del JSE propuesto).

3.4. Comparación entre las subtramas y el tema deseado

El nivel de similitud entre el nodo y la temática tratada, calculado por GV, consiste en comparar el metadato de la subtrama con respecto a la información del curso establecida por GM. Eso determina el interés/parecido de dicha subtrama con respecto al curso. Para realizar esa comparación se usará el estándar LOM [15], y en particular, los criterios siguientes:

1. *Title:* es el nombre del JS. En este caso, se compara si una o varias palabras del título es o son igual(es) a la temática que se está buscando. Por ejemplo: si se está buscando "Fracciones", se compara con el título del JS "Domino de Fracciones". Se da una puntuación en la siguiente escala: igual (1), parecida (0,9-0,8), sinónimos (0,7-0,6), algunas palabras (0,5-0,4), o pocas palabras (≤0,3).
2. *Language:* es el lenguaje para el que fue hecho el JS. En este caso, se compara el idioma deseado con el del JS, según la escala: mismo idioma (1), idiomas derivados (0,9-0,8), idiomas parecidos (0,7-0,6), escritura parecida (0,5-0,4), poco en común (≤0,3).
3. *Description:* contiene una descripción del contenido del JS. Por ejemplo: "juego de dominó interactivo que relaciona sus piezas según las diferentes representaciones fraccionarias gráficas o numéricas"). En este caso, se compara si una o varias palabras de la descripción es o son igual(es) a la que están buscando, usando la siguiente escala: igual (1), parecida (0,9-0,8), sinónimo (0,7-0,6), algunas palabras (0,5-0,4), o pocas palabras (≤0,3).
4. *Keyword:* palabras claves que representan el tema principal del JS, por ejemplo: fracciones, domino, cálculo y probabilidad. En este caso, se compara usando la misma escala de los ítems 1 y 3.
5. *Coverage:* describe la zona geográfica o región en la que es aplicable el JS. Se usa la siguiente escala: universal (1); además, cuando es nacional, regional, estadal y local, y coincide con lo que se busca, también es 1. De lo contrario es 0.
6. *Format:* identifica el software necesario para usar el JS. Si es compatible con lo que se busca su valor de comparación es 1, de lo contrario es 0.
7. *TypicalAgeRange:* edad intelectual del destinatario típico del JS, por ejemplo: "7-9", "0-5", "15", ">18", "adecuado para niños mayores de 7 años", "adults only". Si es compatible con lo que se busca su valor de comparación es 1, si es cercano 0.5, de lo contrario es 0.
8. *Dificulty:* este elemento describe lo difícil que resulta el JS para los destinatarios típicos, por ejemplo: escala muy alta, alta, media, baja o muy baja. En este caso, se compara usando la misma escala del ítem 7.
9. *Duration:* Tiempo aproximado o típico que necesitan para asimilar el JS los destinatarios objetivo. En este caso, se compara usando la misma escala del ítem 7.
10. *InteractivityLevel: e*l grado de interactividad que caracteriza a este JS. Se mide como muy alto, alto, medio, bajo, y muy bajo. Si es compatible con lo que se busca su valor de comparación es 1, si es cercana 0.5, de lo contrario es 0.
11. *SemanticDensity:* La densidad semántica de un JS puede ser estimada en función de su tamaño, ámbito o – en el caso de recursos auto-regulados tales como audio y vídeo duración. La densidad semántica de un JS es independiente de su dificultad. Se mide como: muy alto, alto, medio, bajo y muy bajo. En este caso, se compara usando la misma escala del ítem 10.
12. *IntendedEndUserRole:* El usuario(s) principal(es) para el que ha sido diseñado este JS, el cual puede ser un profesor, el autor, un aprendiz, entre otros. En este caso, se compara usando la misma escala del ítem 10.
13. *Context:* El entorno principal para el que fue diseñado el JS, utilizando para ello los siguientes valores: escuela, nivel educativo, entre otros. En este caso, se compara usando la misma escala del ítem 10.
14. *CognitiveProcess:* es el tipo específico del proceso cognitivo en el JS, y según el estándar OED:1989 pueden ser los siguientes valores: ejercicio, simulación, cuestionario, diapositiva, texto narrativo, examen, experimento, planteamiento de problema, autoevaluación, conferencia, entre otros. En este caso, se compara usando la misma escala del ítem 10.
15. *Cost:* Indicación de si el JS requiere pago para su uso, y puede ser si(0)/no(1). Si es compatible con lo que se busca su valor de comparación es 1, de lo contrario es 0.

Si no es especificado algunos de los ítems anteriores, su valor de comparación por defecto es 1. Una vez que se tienen los valores de esos criterios del estándar LOM, tanto del tema deseado (lo define GM) como de los JS recuperados de los ROAs, GV compara criterio por criterio para cada objeto recuperado y el tema deseado, para establecer el nivel de similitud entre ellos. Cada criterio donde coinciden aumenta el nivel de similitud entre ellos, es decir, se suman los criterios similares para calcular la similitud de una subtrama con respecto al tema deseado, y se divide entre el numero de criterios usados en la evaluación (en nuestro caso, 15).

4. Caso de estudio

A continuación, vamos a mostrar un ejemplo de cómo funcionaría el MJSE propuesto. Se parte de la hipótesis que se está en una clase de matemáticas, y se requiere definir un JSE

con el objetivo de explicar y resolver problemas con fracciones. Los datos del curso son definidos en la tabla 1. Además, los datos de los estudiantes y su contexto educativo son mostrados en la tabla 2.

Toda esa contextualización lo haría GM. Por otro lado, se usó el repositorio de aprendizaje https://goo.gl/otiH78, el cual usa los metadatos en formato SCORM [10] .

Con la información provista por GM, GV usa los metadatos SCORM de cada objeto de aprendizaje en AGREGA para hacer la comparación con el tema deseado. La Tabla 3 da un ejemplo de esa comparación entre un juego denominado "Domino de Fracciones" y el tema al que se le desea dar apoyo usando JSE (clase de matemáticas sobre problemas con fracciones), y el valor final de esa comparación.

Una vez que se realiza la comparación de todos los JS en los ROA con el tema deseado, el MJSE ejecuta el siguiente algoritmo:

Si ($\exists!_i$ Similitud (metadata RA_i, Tema_Deseado) >= 0.850) entonces

Envía RA_i con esa puntuación al VLE

Si (($\exists_i$ 0.4<=Similitud ($metadata_i$, Tema_Deseado)<=0.850) entonces

Invoca ACO

Tabla 1.
Datos del curso

Datos Básicos		Planificación	
a.	***Materia:*** *Matemática*	***a.***	***Tipo de Actividad:*** *Evaluación*
b.	***Modulo:*** *Número Racional*	*b.*	***Explicación:*** *5 minutos*
c.	***Tema:*** *Fracciones*	***c.***	***Uso del Juego:*** *30 minutos*
d.	***Clase:*** *45 Minutos*	***d.***	***Preguntas:*** *5 minutos*
e.	***OAs:*** *JSE*	***e.***	***Finalización:*** *5 minutos*

Fuente: Elaboración Propia

Tabla 2.
Datos de los estudiantes y del centro educativo

Datos Básicos	Datos Básicos SA
a. ***Idioma:*** *Español.*	**a. Nro. de Estudiantes:** 30 inscritos
b. ***Lugar:*** *Timotes - Venezuela*	**b. Promedio de Exámenes:** 1er parcial: 10 – 2do parcial: 15
c. ***Institución:*** *Canónigo Uzcátegui*	**c. Asistencia de Estudiantes:** 27 asisten
d. ***Carrera:*** *Ingeniería de Sistemas*	**d. Promedio total o SP** = 13 pts.
e. ***Pensum:*** *9° año*	**e. Nro. de Clases:** 20 clases de 30
f. ***Semestre****: 2do Lapso*	**f. Porcentaje de Asistencia:**86,5 %
g. ***Asignatura:*** *Matemática de 9° año*	

Fuente: Elaboración Propia

Es decir, el MJSE determina si hay algún JS que cumple con el tema deseado, de lo contrario, si consigue algunos más o menos similares, intenta hacer emerger un JS para el tema deseado usando ACO.

En nuestro caso, supongamos que ningún juego supera el umbral de similitud de 0.85, pero los 6 juegos de la Fig. 5 cumplen el valor de similitud de estar entre 0.85 y 0.4. Esos 6 juegos serán los usados por ACO. Con ellos se construye el grafo que él usará (serán sus nodos, ver Fig. 6).

Ahora se puede iniciar la construcción de soluciones por parte de las hormigas. Cada hormiga se coloca inicialmente aleatoriamente en cualquier nodo contenido en el grafo (ver Fig. 6), y se toma la decisión del nodo a ser visitado utilizando el modelo de Monte Carlo basado en la ecuación (1).

Supongamos que, en ese caso, la hormiga decide trasladarse al nodo "Combinado" usando la ec. (1), tal como se observa en la Fig. 7. Continuando con el proceso, de nuevo debe decidir donde moverse, y la hormiga decide ahora moverse al nodo "Combinado (2)" (ver Fig. 8). El puede continuar con la construcción de la solución o detenerse en cualquier nomento. En este caso, suponemos que culmina cuando revisa por última vez al nodo "Adivina" (ver Fig. 9).

Tabla 3.
Ejemplo de Comparación

LOM	Tema Deseado	Recurso de Aprendizaje	Puntuación
title	fracciones (VLE)	Dominó de **fracciones**	1
language	es (SA)	es	1
description	fracciones (VLE)	Varios juegos de dominó interactivos que relacionan sus piezas a partir de diferentes representaciones **fraccionarias** gráficas o numéricas.	0.9
keyword	fracciones (VLE)	**fracciones** equivalentes	1
coverage	universal (SA)	universal	1
format	javascript, html 5 o flash (ROA)	application/javascript	1
typicalAgeRange	15 (SA)	10	0,4
difficulty	very high (SA)	medium	0,5
duration	30 minutos (VLE)	PT0H10M0S	0,4
interactivityLevel	very high	very high	1
semanticDensity	very high (SA)	medium	0,5
intendedEndUserRole	learner (SA)	learner	1
context	schoolmate (SA)	schoolmate	1
cognitiveProcess	practise (SA)	practise	1
cost	no (ROA)	no	1
	Total		**11,8/15=0,786**

Fuente: Elaboración Propia

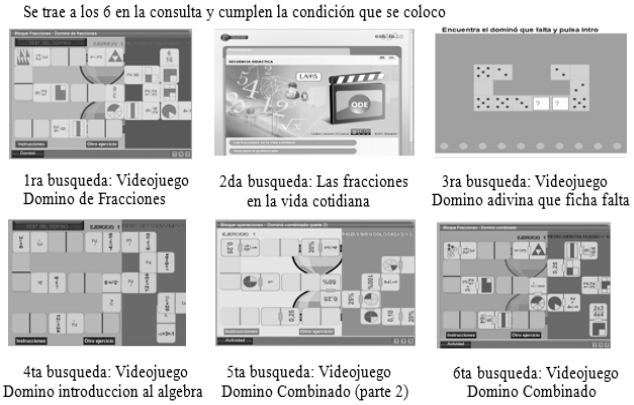


Figura 5. Videojuegos que usará ACO
Fuente: Elaboración Propia

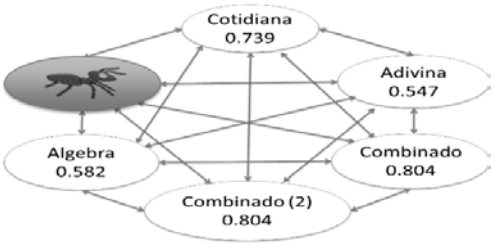


Figura 6. Elije aleatoriamente como nodo inicial "Fracciones".
Fuente: Elaboración Propia

En ese momento se inicia la actualización de los feromonas, lo cual es realizado usando la información de calidad de las propuestas de JSE de todas las hormigas de esa iteración (ver seccion 4.c, sobre el proceso de actualización). Al terminar la actualización, vuelve a comenzar cíclicamente el algoritmo con una nueva generación (iteración).

Una vez que el algoritmo converge, se pasa a construir la solución final. En ese caso, se escogen los nodos cuyo feromona pasa cierto umbral, y se conectan entre ellos según los valores más altos de los arcos que los unen. Si suponemos la Fig. 9 como la final, una vez que converge ACO, suponemos que los nodos que superan el umbral son solo 3, y los arcos que los unen (porque son los más altos) son los identificados con color rojo.

Basado en ello, el JSE creado esta compuesto por 3 sub-tramas, organizadas en la siguiente secuencia lógica:

- JS1: Fracciones – Combinado – Combinado (2)
- JS2: Algebra – Cotidiana
- JS3: Adivina – Fracciones

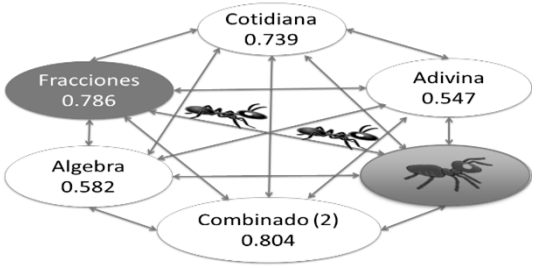


Figura 7. Elije moverse al nodo "Combinado"
Fuente: Elaboración Propia

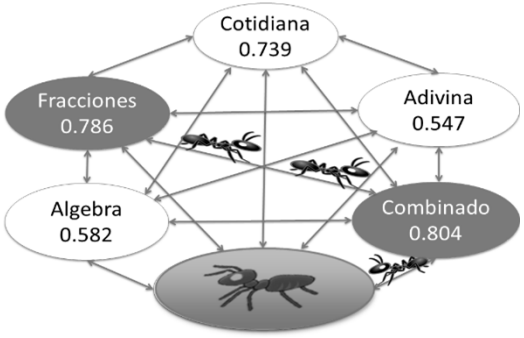


Figura 8. Elije aleatoriamente nodo "Combinado (2)"
Fuente: Elaboración Propia

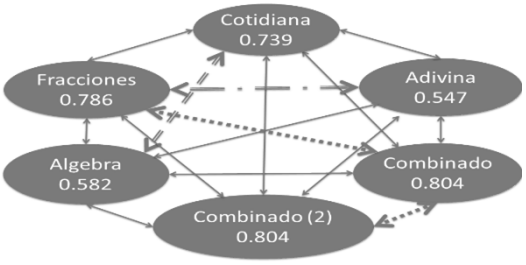


Figura 9. Solución final propuesta de JSE
Fuente: Elaboración Propia

Ese sería el JSE que emerge. Ese juego después sería observado durante su ejecución por el sistema adaptativo del MJSE, para determinar si debe ajustar parámetros, o recrear otro nuevo JSE.

5. Comparación con otras propuestas

Las bases teóricas de los JSE han sido introducidas en [6]. Es una investigación basada en mundos de juegos que manipulan la trama emergente, interactuando con el entorno, usando el motor de juegos emergentes (EmerGENT), cambiando el comportamiento del clima, y presentando en el entorno fenómenos como incendios, huracanes, inundaciones y terremotos. En [8] proponen un sistema para el desarrollo de narrativas para juegos emergentes con cinco enfoques: coherencia, agencia, espacio de posibilidad, incertidumbre y co-autoría. En [16] proponen entornos de aprendizaje inteligente basados en JS, se investiga sobre planificación narrativa en tiempo real, y sobre modelos para reconocer los estados emocionales en los estudiantes, proponiendo uno basado en una arquitectura que utiliza una red de decisión dinámica (RDD) y redes bayesianas dinámicas (RDB).

La principal diferencia de nuestra propuesta y los trabajos anteriores es que nuestra propuesta hace emerger un JSE utilizando diferentes subtramas, según las características del contexto donde será usado. Para ello, usa un algoritmo ACO que le permite generar posibles alternativas de JSE, para hacer emerger aquella que cumpla mejor los atributos que caracterizan al tema deseado.

En la Tabla 4 detallamos esa comparación, basado en varios criterios: Objetivo del juego, cual es la capacidad adaptativa que posee, cual MJS usa, la teoría de base que utiliza, y el tipo de emergencia que permite.

Tabla 4.
Comparación con otros trabajos recientes.

Criterios	[6]	[8]	[16]	Presente Trabajo
Objetivo del Videojuego	Construcción de mundos	Sistemas de narrativas para JE	Entornos de aprendizaje inteligente basados en JS	Orientado por la temática del contexto
Capacidad de Adaptación	Se adapta cambiando los elementos del ambiente	Incorpora narrativas emergentes en los juegos	Sistemas de tutoría inteligente	Se adapta al tema del del contexto
Motores para JSE	Motor de Juegos Emergentes (EmerGEnT)	No usa	Motor de juego multiplatafo rma Unity	MJSE
Teoría de base	Autómatas Celulares	Narrativas emergentes	RDD y (RDB)	ACO
Tipos de Emergencia	Comportamie nto, secuencia, final, propiedad, y utilidad	Coherencia, agencia, espacio de posibilidad, incertidum bre y co-autoría.	Comportami ento, secuencia y propiedades	Comportamie nto, secuencia, propiedad, modelo de negocio final y utilidad

Fuente: Elaboración Propia

Nuestro MJSE es el que permite más tipos de emergencias. En particular, pueden emerger comportamientos en la dinámica del juego, nuevas secuencias en los juegos, características, así como la forma de culminar según el fin del juego. Además, es el único que puede hacer emerger un nuevo JS guiado por el contexto.

6. Conclusiones

El uso de JSEs que se adecuen a un contexto dado (por ejemplo, a un aula inteligente), ayudan al proceso que esté ocurriendo en dicho contexto, haciéndolo más emocionante, entretenido y dinámico, motivando así a los actores en ese ambiente. Para ello, se requiere de un MJSE como el propuesto en este trabajo, con en particular un STE. La especificación de esto último es la innovación presentada en este trabajo, hecha a través de un algoritmo ACO.

Nuestra arquitectura permite emerger el JSE, pero, además, adecuarlo en tiempo de ejecución a la dinámica en el contexto. Esa es la principal diferencia de nuestro MJSE con respecto a trabajos anteriores.

ACO permite la emergencia de un JSE, a partir del manejo ordenado y sistemático de un conjunto de subtramas vinculadas a un contexto y dominio dado, para ser fusionadas en una única trama que lo represente. El algoritmo ACO de manera autónoma, selecciona las mejores subtramas que conformarán el JSE.

Como trabajo futuro, se probará el prototipo de ACO en diferentes contextos, se desarrollará el *sistema adaptativo de JSE*, que permite monitorear y adecuar el JSE a la dinámica de juego que en un momento se está dando en él. Para ello, se analizarán las diferencias emergencias posibles en un JSE (comportamiento, secuencia, final, propiedad o utilidad), y como gestionarlas desde el MJSE. También, se hará la especificación de un Agente de JSE para un Salón de Clases Inteligentes (SaCI) [17], que realizará la gestión del JSE en un aula inteligente usando nuestro MJSE; y la integración del MJSE en AmICL [18], para especificar el MJSE como un servicio en la nube.

Referencias

[1] Aguilar, J., Altamiranda, J., Díaz, F. and Mosquera, D., Motor de juego serios en ARMAGAeco-c. Revista UNET. 28, pp. 100-110, 2016.

[2] Bellotti, F., Berta, R. and De-Gloria, A., Designing effective serious games: opportunities and challenges for research, Special Issue: Creative learning with serious games. Intl. Journal of Emerging Technologies in Learning (IJET). 5, pp. 22-35, 2010. DOI: 10.3991/ijet.v5s3.1500

[3] Aguilar, J., Cardozo, J., González, C. and Rengifo, B., Una aproximación a los juegos emergentes, Metrópolis, simulador de ciudades autogestionada, Proceedings of the 47va Conferencia. Latinoamericana de Informática, 2013.

[4] Aguilar, J., Altamiranda, J. and Chávez, D., Extensiones a Metrópolis para una emergencia fuerte. Revista Venezolana de Computación, 3(2), pp. 38-46, 2016.

[5] Vallejo, D. and Martín, C., Desarrollo de videojuegos: Arquitectura del motor de videojuegos (2ª Ed.). Universidad Castilla la Mancha, España, 2013.

[6] Sweetser, P., An emergent approach to game design – Development and play, School of Information Technology and Electrical Engineering, The University of Queensland, Australia, 2006.

[7] Petridis, P., Duenwell, I., Panzoli, D., Arnab, S., Aristidis, P., Hendrix, M. and Freitas, S., Game engines selection framework for high-fedelity serious aplications. IBIMA Publishing, International Journal of Interactive Worlds. UK, 2012. DOI: 10.5171/2012.418638

[8] Chauvin, S., Levieux, G., Donnart, J. and Natkin, S., An out-of-character approach to emergent game narratives, Proceedings of the 9th International Conference on the Foundations of Digital Games, 2014.

[9] Chan, R., Zhang, H. and Tao, X., Serious game design for stroke rehabilitation. International Journal of Information Technology. 23, 2017.

[10] ADL, Advanced Distributed Learning Sharable Content Object Reference Model (ADL-SCORM), 2006.

[11] Aguilar, J., Introducción a los sistemas emergentes, Venezuela, Talleres Gráficos, Universidad de Los Andes, 2014.

[12] Dorigo, M. and Stutz, T., Ant colony optimization: overview and recent advances, In: Handbook of met heuristics, pp. 227-263, 2010. DOI:10.1007/978-1-4419-1665-5_8

[13] Aguilar, J., A general ant colony model to solve combinatorial optimization problems. Revista Colombiana de Computación. 2(1), pp. 7-18, 2001.

[14] Aguilar, J., Velasquez, L. and Pool, M., The combinatorial ant system, applied artificial intelligence. Taylor and Francis. 18(5), pp. 427-446, 2004. DOI: 10.1080/08839510490442067

[15] IEEE LTSCLOM. Draft Standard for Learning Object Metadata. IEEE 1484.12.1, [Consultado, el 2 de Noviembre de 2017], 2002.

[16] James, C., Eun, Y., Seung, Y., Bradford, W., Jonathan, P. and Jennifer, L., Serious games get smart: intelligent game-based learning environments. AI Magazine. pp. 31-49, 2013. DOI: 10.1609/aimag.v34i4.2488

[17] Valdiviezo, P., Cordero, J., Aguilar, J., Sánchez, M., A smart learning environment based on cloud learning. International Journal of Advanced Information Science and Technology. 39(39), pp. 39-52, 2015.

[18] Sanchez, M., Aguilar, J., Cordero, J. and Valdiviezo, P., Basic features of a Reflective Middleware for Intelligent Learning Environment in the Cloud (IECL), Proceedings of the Asia-Pacific Conference on Computer Aided System Engineering, 2015. DOI: 10.1109/APCASE.2015.8

[19] Heins, S. et al., Robotic-assisted serious game for motor and cognitive post-stroke rehabilitation, Proceedings of the 5th International Conference on Serious Games and Applications for Health, 2017. DOI: 10.1109/SeGAH.2017.7939262

[20] Ben-Sadoun, G., Manera, V., Alvarez, J., Sacco, G. and Robert, P., Recommendations for the design of serious games in

neurodegenerative diseases. Frontiers in Aging Neuroscience. 10, 2018. DOI: 10.3389/fnagi.2018.00013

[21] Jaramillo, A., Salvador, L. and Luján, S., A mobile serious games assessment tool for people with motor impairments, Proceedings of the 9th International Conference on Education Technology and Computers, pp. 172-177. DOI: 10.1145/3175536.3175569

J.L. Aguilar-Castro, es graduado en Ing. de Sistemas en 1987 en la ULA, MSc. en Ciencias de la Computación en 1991 de la Universite Paul Sabatier-Francia, Dr. en Ciencia de la Computación en 1995 de la Universite Rene Descartes-Francia. PhD en Ciencias de Computación en la Universidad de Houston, USA en 2000. Es profesor titular del Departamento de ULA, miembro de la Academia de Ciencias de Mérida y del Comité Técnico IEEE CIS sobre Redes Neuronales. Ha sido investigador postdoctoral en varias Universidades y publicado más de 500 trabajos en sistemas paralelo/distribuidos, inteligencia computacional, etc.
ORCID: 0000-0003-4194-6882

J.A. Altamiranda-Pérez, es graduado en Ing. de Sistemas en 2002, MSc. en Ciencias de la Computación en 2006 y Dr. en Ciencias Aplicadas de la ULA. Venezuela. Realizo pasantías de investigación en la Université de Rennes I en Francia. Realiza trabajos de investigación en el área de minería de datos, computación inteligente, sistemas multiagentes, bioinformática, en el CEMISID de la ULA.
ORCID:0000-0003-0339-3244

F.J. Díaz-Villarreal, es graduado de Ing. de Computación en el año 2004 en la UVM, MSc. en Informática Aplicada IUPTJE en el 2010, tutor de la comunidad de aprendizaje masterdrez PROEA de la UPTMKR desde 2014 y estudiante del Doctorado en Ciencias Aplicadas en la ULA desde 2017. Actualmente, es Ingeniero Informático del Servicio Autónomo de Registro Notarias (SAREN).
ORCID: 0000-0002-3859-476X

UNIVERSIDAD NACIONAL DE COLOMBIA
SEDE MEDELLÍN
FACULTAD DE MINAS

Área Curricular de Ingeniería
de Sistemas e Informática

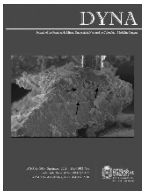
Oferta de Posgrados

Especialización en Sistemas
Especialización en Mercados de Energía
Maestría en Ingeniería - Ingeniería de Sistemas
Doctorado en Ingeniería- Sistemas e Informática

Mayor información:

E-mail: acsei_med@unal.edu.co
Teléfono: (57-4) 425 5365

UNIVERSIDAD NACIONAL DE COLOMBIA
SEDE MEDELLÍN
FACULTAD DE MINAS



DYNA
http://dyna.medellin.unal.edu.co/

A software tool to determine optical constants in thin film solar cell

Heiner Alexander Vargas-Perea [a], Robinson Rocha-González [a], Mónica Andrea Botero-Londoño [a], Alexander Sepúlveda-Sepúlveda [a] & Clara Lilia Calderón-Triana [b]

[a] *Escuela de Ingeniería Eléctrica, Electrónica y de Telecomunicaciones, Universidad Industrial de Santander, Bucaramanga, Santander, Colombia. heiner.vargas@correo.uis.edu.co, robinson.rocha@correo.uis.edu.co, mabotero@saber.uis.edu.co, fasepul@uis.edu.co*
[b] *Departamento de Física, Universidad Nacional de Colombia, Bogotá D.C., Colombia, clcalderont@unal.edu.co*

Received: January 25th, 2018. Received in revised form: July 25th, 2018. Accepted: August 2th, 2018

Abstract
In this work, it was developed a software tool that allows determining the optical properties of semiconductor materials, this tool is useful for researchers working on the characterization of semiconductor thin films. The software calculates the optical constants: index of refraction (*n*), coefficient of absorption (α) and prohibited energy gap (*Gap*), in addition to the approximate thickness of the film; with the developed program were calculated optical constants of thin films of ZnS, SnS:Bi, and SnS_2:Bi, which are used as buffer layers and absorbers in solar cells, this paper presents the results obtained with a SnS_2:Bi film. The software was created in the Python programming language within a simple English-Spanish interface and in order to develop it, the method proposed by Swanepoel, based on the experimental transmittance spectrum of the semiconductor material, was taken into account.

Keywords: manuscript software; optical constants; semiconductor thin films; solar cells.

Herramienta de software para determinar constantes ópticas en celdas solares tipo película delgada

Resumen
En este trabajo se desarrolló una herramienta de software que permite determinar las propiedades ópticas de materiales semiconductores, esta herramienta es de utilidad para investigadores que trabajan en la caracterización de películas delgadas semiconductoras. El software calcula las constantes ópticas: índice de refracción (*n*), coeficiente de absorción (α) y brecha de energía prohibida (*Gap*), además del espesor aproximado de la película; con el programa desarrollado se calcularon las constantes ópticas de películas delgadas de ZnS, SnS:Bi y SnS_2:Bi, que son usadas como capas buffer y absorbentes en celdas solares, en este trabajo se presentan los resultados obtenidos con una película de SnS_2:Bi. El software fue creado en el lenguaje de programación Python dentro de una interfaz sencilla inglés-español y para desarrollarlo se tuvo en cuenta el método propuesto por Swanepoel, el cual toma como base el espectro de transmitancia experimental del material semiconductor.

Palabras clave: software; constantes ópticas; películas delgadas semiconductoras; celdas solares.

1. Introducción

La creciente demanda mundial de energía ha guiado a los seres humanos a la búsqueda permanente de nuevos combustibles y fuentes alternativas de energía, principalmente las que provienen de fuentes naturales como la energía eólica, la mareomotriz y la solar, entre otras. La energía proveniente del Sol es una de las más utilizadas debido a sus grandes ventajas como disponibilidad en todos los lugares de la Tierra, no tiene costo, es silenciosa y es durable. La energía solar fotovoltaica encabeza la capacidad de generación de energía y se considera una nueva fuente de generación competitiva en muchos mercados emergentes en el mundo. La energía solar fotovoltaica fue la principal fuente de inclusión de capacidad de generación adicional en el año 2016 (48% más que en 2015) [1], debido en gran medida a la mejora en la competitividad, incremento en la demanda de energía eléctrica y a un mejor conocimiento del potencial de

How to cite: Vargas-Perea, H.A., Rocha-González, R., Botero-Londoño, M.A., Sepúlveda-Sepúlveda, A. and Calderón-Triana, C.L., Herramienta de software para determinar constantes ópticas en celdas solares tipo película delgada. DYNA, 85(206), pp. 321-328, September, 2018.

© The author; licensee Universidad Nacional de Colombia.

la energía solar fotovoltaica ya que los países tratan de reducir la contaminación y las emisiones de CO_2.

En la actualidad cerca del 90% del mercado de la tecnología de celdas solares está dominado por materiales basados en silicio, el cual ha demostrado ser una tecnología robusta en los módulos fotovoltaicos, pero teniendo en cuenta el alto costo de las láminas de silicio, su probabilidad de reducción del mismo tiende a disminuir, lo que lleva a la búsqueda de nuevas tecnologías y nuevos materiales que además puedan ofrecer ventajas como mayor disponibilidad, estabilidad y menor toxicidad. Entre los materiales más estudiados se encuentran películas delgadas de CdTe, kesteritas (CZTS), SnS, Cu(In,Ga)Se_2 y materiales compuestos como CuO/ZnO, CIS/TiO_2 [2].

Uno de los aspectos relevantes al realizar la caracterización de películas delgadas es, sin lugar a dudas, la determinación de constantes ópticas [3]; la cual constituye una de las fases iniciales en el proceso de diseño de celdas solares usando películas delgadas semiconductoras. Aunque existen varios métodos para la determinación de las constantes ópticas [4] se encuentra que el método de Swanepoel [5] es uno de los mejores y más usados para caracterización óptica de películas delgadas semiconductoras, aislantes o dieléctricos sobre sustratos transparentes [6-8].

En un principio las envolventes máxima y mínima del espectro se solían realizar a mano, lo que conducía a considerables errores, por lo cual se plantea el uso de algoritmos para ordenadores. Un primer algoritmo se propone en [9], el cual usa interpolación por curvas de Bezier. De manera casi contemporánea, en [10] se presenta un algoritmo basado en aproximaciones parabólicas entre puntos sucesivos del espectro, el cual fue desarrollado en MATLAB. Posteriormente, en [11] se presenta una formulación programación no-lineal sin restricciones sobre el método de Swanepoel, el cual se resuelve mediante el uso del método del gradiente espectral. *F*inalmente, en [12] se realiza un proceso de suavizado del espectro seguido de una interpolación mediante polinomios de Hermite; sin embargo, los cálculos los realiza sobre el espectro de reflectancia. En nuestro trabajo se propone usar el cálculo a partir del espectro de Transmitancia.

Este trabajo pretende aportar al estudio de las energías renovables, específicamente en la caracterización óptica de los materiales semiconductores usadas en la fabricación de celdas solares tipo película delgada. Las propiedades ópticas de un material semiconductor se determinan a través del conocimiento de sus constantes ópticas.

El enfoque principal de este trabajo fue diseñar una herramienta de software que permita la caracterización óptica de los materiales semiconductores con el fin de determinar su índice de refracción (*n*), coeficiente de absorción (α) y brecha de energía prohibida (*Gap*).

2. Software desarrollado

Las investigaciones, análisis de fórmulas y rutinas de código realizadas durante este trabajo dieron como resultado una herramienta de software creada en el lenguaje de programación Python, que lleva como nombre C.O.P.S® (Constantes Ópticas de Películas delgadas Semiconductoras); el software permite hallar las constantes ópticas de películas delgadas semiconductoras como índice de refracción, coeficiente de absorción y brecha de energía prohibida (*gap*) y una aproximación de su espesor, dentro de una interfaz sencilla inglés-español. Dentro de las librerías que se usaron para la construcción de la interfaz gráfica están entre otras: *Tkinter*, *Matplotlib*, *Scipy*, *Numpy*, todas con tareas específicas; en la Fig. 1 se presenta un diagrama donde se evidencia el proceso de construcción del software.

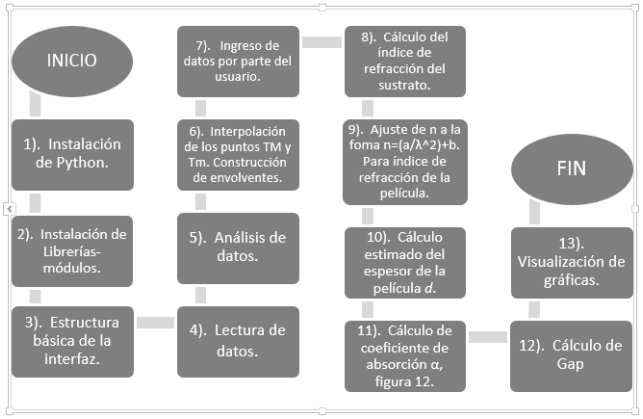


Figura 1. Diagrama de construcción del programa C.O.P.S.
Fuente: los autores.

El desarrollo del software se basó en el método propuesto por Swanepoel [5] y en [13], que parte de medidas de espectros de transmitancia experimentales. Un primer paso es la creación de la rutina de código encargada de abrir un archivo de texto (.txt) donde está registrado un espectro de transmitancia experimental (Transmitancia en función de longitud de onda - T vs λ), para realizar un análisis riguroso de dichos datos del espectro; se realiza la detección de los puntos máximos y mínimos del espectro de transmitancia, una vez extraídos estos puntos con sus respectivos valores de longitud de onda (λ en nm) se procede a hacer una interpolación para hallar las envolventes máxima y mínima continuas (*TM* y *Tm* respectivamente). Con las envolventes se pueden hallar los puntos *TM'* y *Tm'*, que son los valores de un máximo correspondiente a un mínimo dentro de la envolvente y viceversa. Los puntos *TM'* y *Tm'* se evidencian de una manera gráfica en la Fig. 2 y la rutina usada para el cálculo de los máximos y mínimos de transmitancia del espectro se presentan en la Fig. 3. En la rutina, T es el vector de transmitancia, *ma* es el vector de puntos máximos y mi es el vector de puntos mínimos.

En el programa el usuario debe ingresar un valor de espesor *(d)* si lo tiene, además del índice de refracción del sustrato *(s)*, si no es ingresado ninguno de estos valores el software hará los cálculos con el valor calculado automáticamente y el valor por defecto respectivamente. El cálculo de *s*, se calculará para muestras que el usuario decida no tomar este valor como constante a lo largo de todo el espectro de transmitancia como se presenta en la eq. (1).

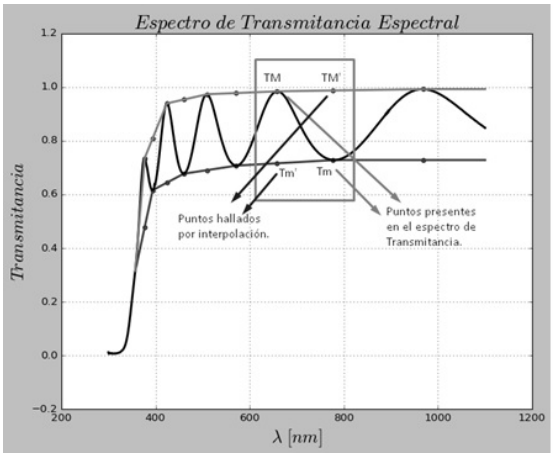


Figura 2. Espectro de transmitancia mostrando los puntos TM' y Tm'. Fuente: los autores.

$$s = 1/TM + (1/TM^2 - 1)^2 \quad (1)$$

Donde TM son los valores correspondiste a los puntos máximos en la matriz de máximos y mínimos calculados luego de realizar la interpolación.

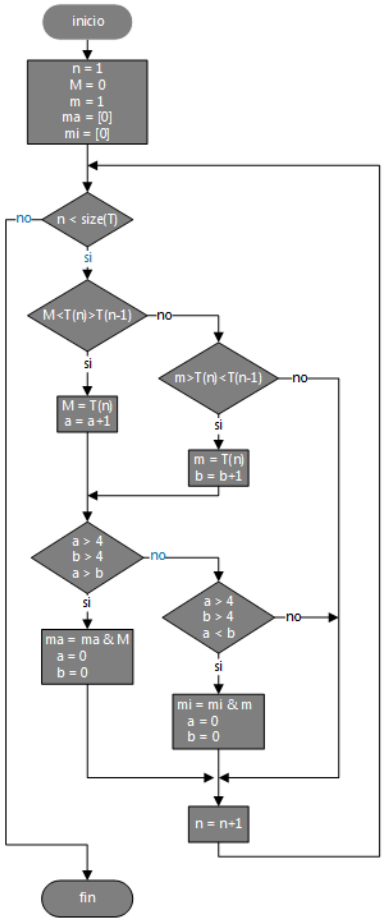


Figura 3. Rutina para el cálculo de los máximos y mínimos de transmitancia. Fuente: los autores.

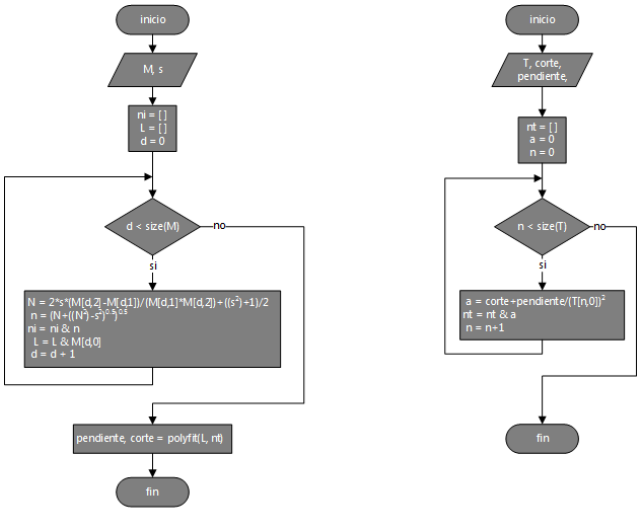


Figura 4. Método para el cálculo del índice de refracción del semiconductor. Fuente: los autores.

Para el cálculo del índice de refracción del material semiconductor (n), se tiene en cuenta la dispersión normal en el rango visible. Como las envolventes no existen en la zona de alta absorción no se puede hallar el índice de refracción de una forma analítica, por lo tanto, se aproxima por la ecuación Cauchy, eq. 2 [14].

$$n = \frac{a}{\lambda^2} + b \quad (2)$$

Este procedimiento se presenta en la imagen de flujo doble de la Fig. 4, donde *M* es una matriz con los máximos, mínimos y sus respectivas longitudes de onda y *s* es el índice de refracción del sustrato. Como resultado de este proceso se obtiene el índice de refracción de la película para todo el espectro en estudio denotado por *nt*.

Una vez calculado el índice de refracción para todo el rango del espectro experimental se procede con el cálculo del espesor de película si el usuario no ha ingresado el valor previamente.

Para el cálculo del coeficiente de absorción α, se presenta el método de bisección de la Fig. 5, donde s es el índice de refracción del sustrato, *d* es el espesor de la película, *n* es el vector de índice de refracción de la película en el rango de espectro estudiado y T es la matriz de transmitancia. *a* y *b* se definen al inicio de dicha rutina y son los límites del rango de *k*. La expresión *e=T[i,1]-Te* se refiere a la diferencia entre el valor de la transmitancia experimental y el valor de transmitancia teórica calculado con el valor de *k*.

Las iteraciones dentro de la rutina se realizan para cada valor de la longitud de onda hasta que el valor de e sea menor a 10^{-7}, si esto se cumple durante n iteraciones se da por terminado el ciclo, si no, se procede a preguntar por el valor de e de nuevo, si este es mayor a cero (0) se asigna el valor de k a b y vuelve a realizarse el proceso con un nuevo rango de k y si por el contrario es menor a cero (0) se le asigna el valor de k a a y se realiza el mismo proceso; el método reduce el rango de k en un 50% por cada iteración.

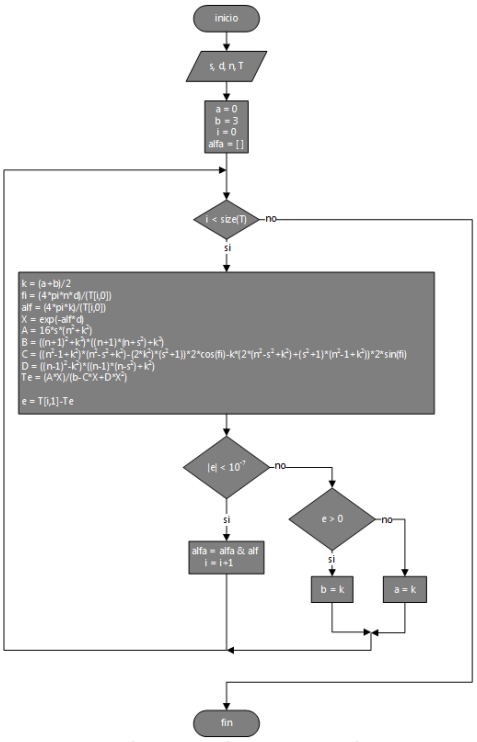


Figura 5. Rutina del método numérico para el cálculo del coeficiente de absorción.
Fuente: los autores.

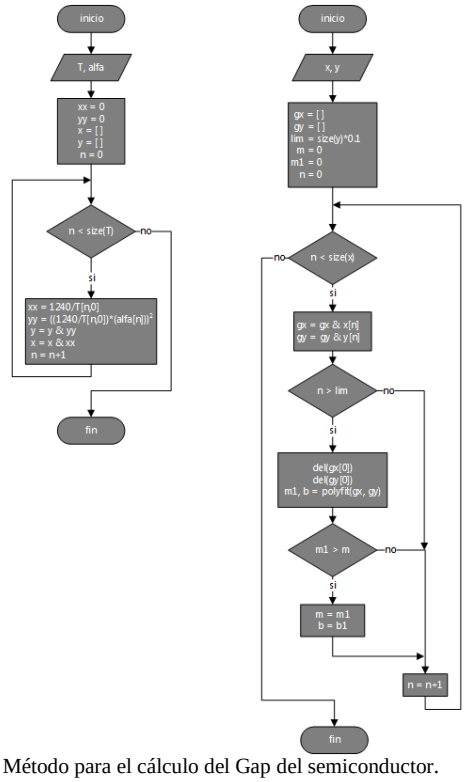


Figura 6. Método para el cálculo del Gap del semiconductor.
Fuente: los autores.

En la Fig. 6 se muestra la estructura para el cálculo del *Gap* de los materiales semiconductores, en esta rutina *T* es la matriz de transmitancia, *alfa* es el vector de coeficientes de absorción, *x* es el vector *hv*, *y* es el vector . En la rutina de la izquierda se crean los vectores *hv* y $(\alpha hv)^2$ y en la rutina de la derecha se halla la región de mayor pendiente sobre la cual se traza un recta paralela y su punto de corte con el eje *x* (*hv*) es el valor del *Gap*.

3. Comparación de resultados experimentales y simulados

Para verificar la confiabilidad del programa desarrollado se compararon los datos experimentales con los datos obtenidos de forma teórica para el espectro de transmitancia retomando la ecuación propuesta por Swanepoel [5], eq. 3.

$$T = \frac{Ax}{B - Cx + Dx^2} \tag{3}$$

Con la que se puede reconstruir el espectro de transmitancia espectral experimental, en la Fig. 7 podemos ver en forma gráfica esta reconstrucción.

La gráfica del espectro espectral experimental se presenta dentro de la Fig. 7 como una línea continua de color amarillo, el teórico está representado por una sucesión de puntos azules; se puede observar que el espectro teórico se

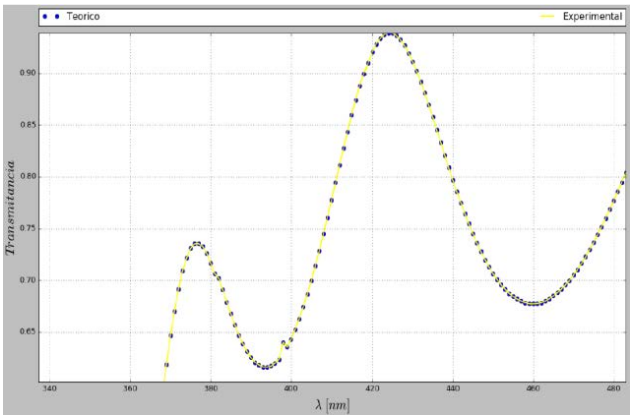


Figura 7. Espectros de transmitancia espectral experimental (línea amarilla) y teórico (puntos azules).
Fuente: los autores.

ajusta bastante bien al espectro experimental. De lo anterior se deduce que la aproximación que Swanepoel [5] propuso para reconstruir un espectro experimental de transmitancia, así como el software elaborado en este trabajo son adecuados para obtener valores confiables de las constantes ópticas de películas delgadas semiconductoras de espesor homogéneo.

Con el programa desarrollado se calcularon las constantes ópticas de películas delgadas de ZnS, SnS:Bi y SnS_2:Bi, que son usadas como capas buffer y absorbente en celdas solares [15]. Como ilustración, enseguida se presentan los resultados obtenidos con una película de SnS_2:Bi de espesor 638 nm.

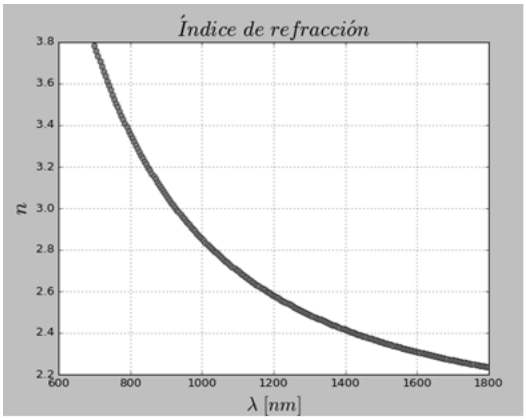


Figura 8. Índice de Refracción obtenido con el programa C.O.P.S. Fuente: los autores.

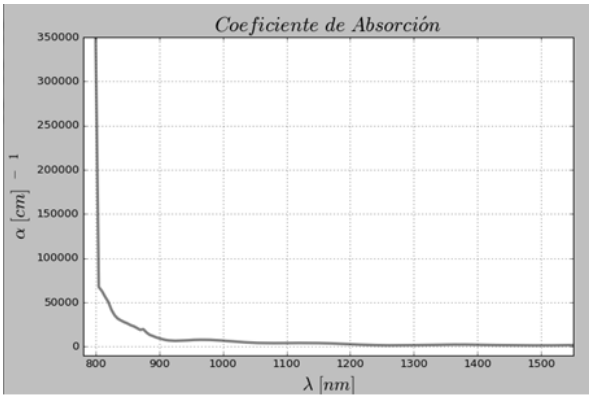


Figura 9. Coeficiente de absorción obtenido con el programa C.O.P.S. Fuente: los autores.

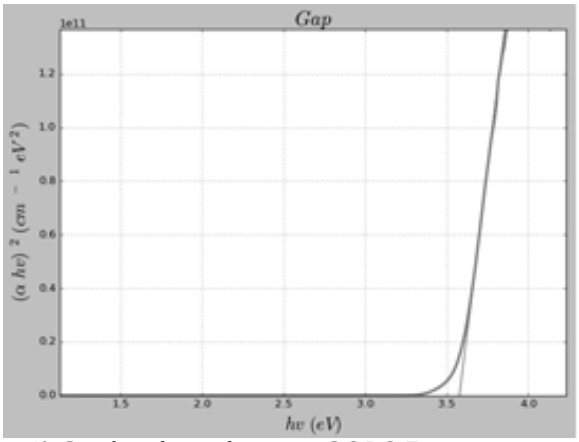


Figura 10. Gap obtenido con el programa C.O.P.S. Fuente: los autores.

Los espectros y valores de las constantes ópticas obtenidos con el programa C.O.P.S. se compararon con los obtenidos para las muestras en [16] y se obtuvieron resultados muy similares, por ejemplo para el caso del Gap de la ilustración (Fig. 10), con el programa C.O.P.S. se obtuvo un Gap de 3,58 eV y en el trabajo [16] un Gap de 3,57 eV, el índice de refracción n varió entre 3,80 y 2,35 para λ entre 700 y 1500 nm (Fig. 8) y el coeficiente de absorción α del orden de 10^5 cm^{-1} en ambos casos (Fig. 9).

4. Manejo del programa C.O.P.S.

La interfaz de usuario de C.O.P.S. se hizo pensando en que personas que no conozcan muy bien el tema pero estén incursionando en él tengan la facilidad de utilizarla. A continuación se muestran las ventanas y comandos básicos que debe manejar el usuario del programa.

Aparece la ventana de inicio del programa (Fig. 11):

Se genera la interfaz principal de C.O.P.S. (Fig. 13):

En esta ventana seleccionando "Acerca de C.O.P.S." se observa la siguiente ventana de Información del software (Fig. 14):

En la ventana de la interfaz principal de C.O.P.S. también se encuentran las funciones principales del software: al presionar el botón "Calcular Constantes" ubicado dentro de la ventana de transición en la parte superior derecha se abrirá la ventana presentada en la Fig. 15 (también se puede acceder desde la misma ventana de transición dirigiéndose a la barra de menú en la opción desplegable "Archivo" luego opción "Calcular").
Luego se debe seleccionar el idioma (Fig. 12):

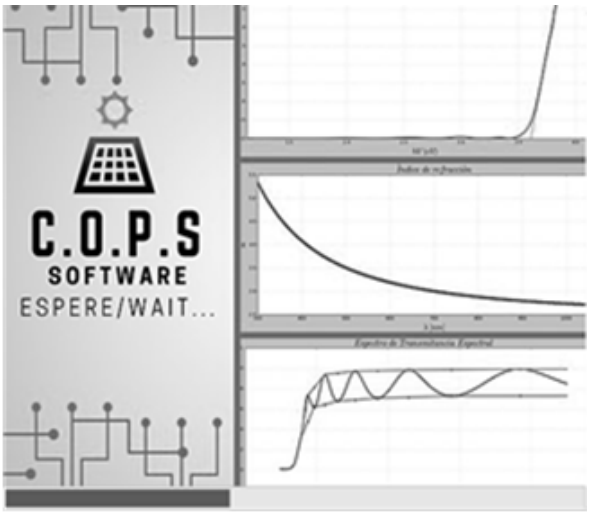


Figura 11. Entrando a C.O.P.S.
Fuente: los autores.



Figura 12. Selección de idioma.
Fuente: los autores.

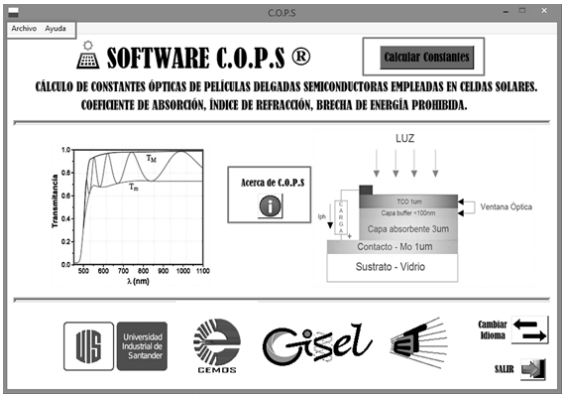


Figura 13. Ventana de interfaz principal de C.O.P.S.
Fuente: los autores.



Figura 14. Ventana de información ("Acerca de C.O.P.S").
Fuente: los autores.

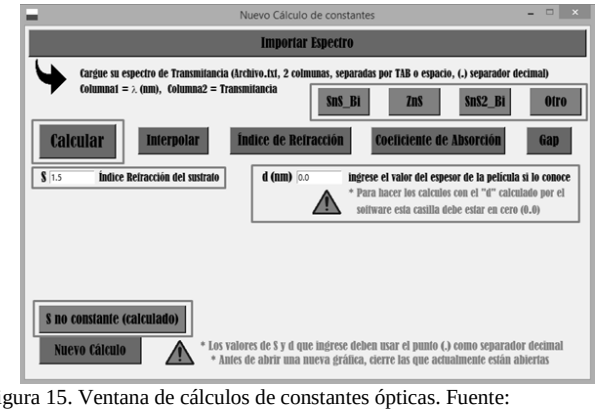


Figura 15. Ventana de cálculos de constantes ópticas. Fuente: los autores.

En esta ventana el usuario puede ingresar dos valores: el espesor de la película *d* (en nm) y el índice de refracción del sustrato *s* que por defecto viene con un valor igual a 1,5 (para vidrio soda-lime).Si el usuario desea analizar el espectro ingresado y hacer que C.O.P.S. calcule un índice de refracción del sustrato no constante, debe pulsar el botón "s no constante (calculado)" ubicado en la parte inferior izquierda de esta ventana. El espesor es calculado automáticamente por el software empleando el método propuesto por Swanepoel [5], si el usuario tiene el dato de una medida de espesor que se haya realizado con anterioridad puede ingresarla y el programa ajusta los cálculos a este espesor (cada vez que ingrese un nuevo dato debe pulsar sobre el botón calcular). Si el usuario no ingresa ningún valor de espesor el software toma el valor que se calcula automáticamente, para hacer los cálculos, si después de oprimir "Calcular" con este valor por defecto desea ingresar un nuevo valor de espesor se podrá hacer y oprimir nuevamente el botón "Calcular", de igual manera con el índice de refracción del sustrato.

El usuario también deberá seleccionar el tipo de compuesto del que se fabricó la película donde se presentan tres opciones: "ZnS, SnS:Bi y SnS_2:Bi", si otro compuesto se pulsa el botón "Otro".

Una vez definidos estos valores con los que se desea calcular, se procede a cargar el espectro de transmitancia espectral como un archivo .txt (archivo generado por la mayoría de los espectrofotómetros comerciales) que bebe tener dos columnas: la primera con los valores de λ (en nm) y la segunda con los valores de la Transmitancia, separadas por espacio o Tabulación y utilizando el punto (.) como separador decimal en las cantidades que las componen.

Esta carga del archivo se hace por el botón que se encuentra en la parte superior de la ventana de cálculo "Importar Espectro" (Fig. 15), una vez seleccionado el archivo .txt que contiene el espectro de transmitancia experimental se procede a oprimir el botón "Calcular", este proceso de cálculo toma alrededor de 0,5 a 2 segundos dependiendo la capacidad de cómputo del equipo donde se esté ejecutando C.O.P.S. Cuando el proceso de cálculo ha terminado la ventana de cálculo imprime el valor del espesor aproximado calculado de la película (*d*) y habilita los botones para poder ver las gráficas de la Interpolación (*TM, Tm, λ*), índice de refracción *n*, coeficiente de absorción α y *Gap*, como se muestra en la Fig. 16. Cada vez que un usuario abra una gráfica deberá cerrarla para abrir una nueva, esto evitará que las gráficas se sobrepongan dando lecturas erróneas; las gráficas se pueden mostrar aleatoriamente, una vez los botones estén habilitados no existe restricción en su orden.

Luego de presionar un botón ("Interpolar", "Índice de Refracción", "Coeficiente de Absorción", "Gap") para visualizar su respectiva gráfica aparecerá en la parte inferior de la ventana de cálculos un botón correspondiente a cada gráfica con el mismo nombre, que permitirá al usuario extraer los datos de dicha gráfica en un archivo .txt,; adicional a esto cuando la gráfica se esté mostrando se podrá guardar en diferentes formatos como png, jpg, pdf. Los archivos .txt son guardados en el directorio que el usuario le indique y poseen su respectiva demarcación, es decir nombre para cada columna según el tipo de gráfica seleccionada.

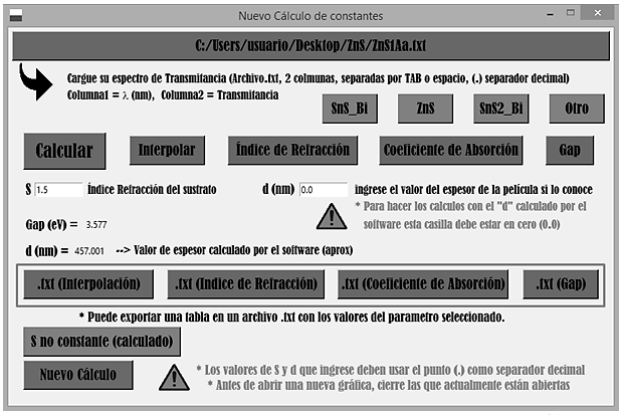


Figura 16. Botones para exportar archivos .txt y visualizar gráficas de las constantes ópticas.
Fuente: los autores.

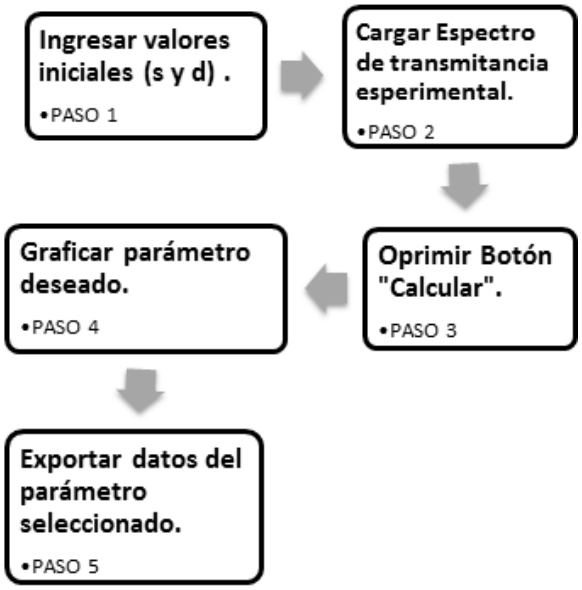


Figura 17. Pasos para el cálculo de constantes ópticas en C.O.P.S.
Fuente: los autores.

En la Fig. 17 se presenta el resumen del procedimiento que debe realizar el usuario para el cálculo de las constantes ópticas dentro del programa C.O.P.S.

5. Conclusiones

Se desarrolló una herramienta de software en el lenguaje de programación Python, la cual se nombró C.O.P.S. Se logró condensar todo dentro de un archivo .exe con el fin de ejecutarse sin la necesidad de tener instalado el lenguaje y sus múltiples librerías necesarias para el correcto funcionamiento de C.O.P.S. El software tomó como referencia el método propuesto por Swanepoel, que basa sus cálculos en medidas de transmitancia espectral experimentales. La herramienta permite hacer un ajuste automático para hallar los puntos máximos y mínimos de las envolventes del espectro de transmitancia experimental, para determinar las constantes ópticas de películas delgadas semiconductoras empleadas en la fabricación de celdas solares.

Se diseñó una interfaz gráfica de fácil manejo y multilenguaje (inglés-español), que permite al usuario entender de una manera sencilla los pasos que debe realizar para determinar las constantes ópticas a partir de un espectro de transmitancia tomado previamente y cargado en un archivo .txt, que es el formato que manejan los espectrofotómetros convencionales.

Se seleccionó el método de bisección para realizar las iteraciones en el cálculo de las constantes ópticas por facilidad y aplicabilidad, para este caso el método se ajustó correctamente y no consume una memoria computacional considerable, otros métodos numéricos pueden llegar a la respuesta en un tiempo más corto pero se debe tener cuidado en la selección de las condiciones para su evaluación ya que pueden alejar el valor esperado en vez de acercarlo en cada iteración.

El software desarrollado aporta a la caracterización y análisis para seleccionar las capas semiconductoras más adecuadas para la fabricación de celdas solares más eficientes. Se determinaron las constantes ópticas(n,α y Gap) de películas de diferentes compuestos: ZnS, SnS:Bi y SnS_2:Bi con el programa C.O.P.S. y los resultados obtenidos se compararon con los reportados para las mismas películas en otro trabajo, comprobándose que los datos arrojados por C.O.P.S son confiables.

Referencias

[1] Renewables 2017 Global Status Report 2017 [Online]. [date of reference: October 1st of 2017]. Available at: http.//www.ren21.net

[2] Ali, N., Hussain, A., Ahmed, R., Wang, M.K., Zhao, C., Ul-Haq, B. and Fu, Q.Y., Advances in nanostructured thin film materials for solar cell applications. Renewable and Sustainable Energy Reviews, 59, pp. 726-737, 2016. DOI: 10.1016/j.rser.2015.12.268

[3] Mesa, F., Ballesteros, V. and Dussan, A., Cálculo de constantes ópticas de películas delgadas de Cu3BiS3 a través del método de Wolfe. Universitas Scientiarum, 19(2), pp. 123-131, 2014. DOI: 10.11144/Javeriana.SC19-2.ccop

[4] Poelman, D. and Smet, P.F., Methods for the determination of the optical constants of thin films from single transmission measurements: a critical review. Journal of Physics D: Applied Physics, 36(15), pp. 1850-1857, 2003. DOI: 10.1088/0022-3727/36/15/316

[5] Swanepoel, R., Determination of the thickness and optical constants of amorphous silicon. J. Phys. E: Sci. Instrum., 16, pp. 1214-1222, 1983. DOI: 10.1088/0022-3735/16/12/023

[6] Shaaban, E.R., Yahia, I.S. and El-twally, E.G., Validity of Swanepoel's method for calculating the optical constants of thick films. Acta Physica Polonica A, 121, pp. 628-635, 2012. DOI: 10.12693/APhysPolA.121.628

[7] Ilican, S., Caglar, M. and Çağlar, Y., Determination of the thickness and optical constants of transparent indium-doped ZnO thin films by the envelope method. Materials Science-Poland, 25(3), pp. 709-718, 2007.

[8] Minkov, D.A., Gavrilov, G.M., Marquez, E., Fernandez-Ruano, S.M. and Stoynova, A.V., Development of algorithm for computer drawing envelopes of interference reflectance spectra for thin film specimens. Optik - International Journal for Light and Electron Optics, 132, pp. 320-328, 2017. DOI: 10.1016/j.ijleo.2016.12.063

[9] McClain, M., Feldman, A., Kahaner, D. and Ying, X., An algorithm and computer program for the calculation of envelope curves. Computers in Physics, 5(1), pp. 45-48, 1991. DOI: 10.1063/1.168405

[10] Minkov, D. and Swanepoel, R., Computer drawing of the envelopes of spectra with interference, Proceedings of the SPIE 1782: Thin Films for Optical Systems, 1993. DOI: 10.1117/12.141047.
[11] Birgin, E., Chambouleyron, I. and Martínez, J.M., Estimation of the optical constants and the thickness of thin films using unconstrained optimization. Journal of Computational Physics, 151(2), pp. 862-880, 1999. DOI: 10.1006/jcph.1999.6224
[12] Gavrilov, G.M., Minkov, D.A., Marquez, E. and Ruano, S.M.F., Advanced computer drawing envelopes of transmittance spectra of thin film specimens. International Advanced Research Journal in Science, Engineering and Technology, 3(9), 2016. DOI: 10.17148/IARJSET.2016.3931

H.A. Vargas-Perea, es Ing. Electrónico de la Universidad Industrial de Santander, Bucaramanga, Colombia en 2016. Actualmente Ingeniero de Servicio y Director Técnico en Inversiones M.D.ING S.A.S, Bogotá.
ORCID: 0000-0001-8282-0712

R. Rocha-González, es Ing. Electrónico de la Universidad Industrial de Santander, Bucaramanga, Colombia en 2017. Actualmente profesor, Innovación, Tecnología & Educación SAS, Bucaramanga.
ORCID: 0000-0001-7089-5864.

M.A. Botero-Londoño, es Ing. Electricista de la Escuela Colombiana de Ingeniería "Julio Garavito", Bogotá, Colombia en 1999; MSc. en Física, Universidad Nacional de Colombia, Manizales en 2004; Dra. en Ciencias Física, Universidad Nacional de Colombia, Bogotá en 2008. Actualmente profesora asociada de la Escuela de Ingenierías Eléctrica, Electrónica y de Telecomunicaciones, Universidad Industrial de Santander, Bucaramanga, Colombia.
ORCID: 0000-0003-1706-3182.

A. Sepúlveda-Sepúlveda, es Ing. Electrónico, MSc. en Automatización y Dr. en Ingeniería-Automática de la Universidad Nacional de Colombia, Manizales. Actualmente es profesor asociado de Escuela de Ingenierías Eléctrica, Electrónica y de Telecomunicaciones, Universidad Industrial de Santander, Bucaramanga.
ORCID: 0000-0002-9643-5193.

C.L. Calderón-Triana, es Lic. en Física, Universidad Distrital "Francisco José de Caldas", Bogotá, Colombia en 1994; Esp. en Ciencias Físicas, Universidad Nacional de Colombia, Bogotá, Colombia en 1996; MSc. en Ciencias Física, Universidad Nacional de Colombia, Bogotá en 1998; Dra. en Ciencias Física, Universidad Nacional de Colombia, Bogotá en 2003. Actualmente profesora titular del Departamento de Física, Universidad Nacional de Colombia, Bogotá.
ORCID: 0000-0002-3149-2939.

UNIVERSIDAD NACIONAL DE COLOMBIA
SEDE MEDELLÍN
FACULTAD DE MINAS

Área Curricular de Ingeniería
Eléctrica e Ingeniería de Control

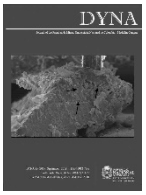
Oferta de Posgrados

Maestría en Ingeniería - Ingeniería Eléctrica

Mayor información:

E-mail: ingelcontro_med@unal.edu.co
Teléfono: (57-4) 425 52 64

UNIVERSIDAD NACIONAL DE COLOMBIA
SEDE MEDELLÍN
FACULTAD DE MINAS



DYNA
http://dyna.medellin.unal.edu.co/

Determination of glacier retreat at Nevado del Ruiz, Santa Isabel and Tolima volcanoes, Colombia through optical image and Din-SAR

Mario Fernando Monterroso-Tobar [a], Jhon Makario Londoño-Bonilla [a] & Sergey Samsonov [b]

[a] *Universidad Catolica de Manizales, Manizales, Colombia. mario.monterroso@ucm.edu.co, jmakario@ucm.edu.co*
[b] *Canada Centre for Mapping and Earth Observation Natural Resources Canada, Otawa, Canada. sergey.samsonov@nrcan-rncan.gc.ca*

Received: July 25th, 2017. Received in revised form: May 24th, 2018. Accepted: June 8th, 2018.

Abstract
We performed a quantification of glacier retreat of Nevado del Ruiz Volcano (VNR), Nevado de Santa Isabel Volcano (VNSI) and Nevado del Tolima Volcano (VNT), using satellite images Landsat 8 OLI TIRS and coherence images obtained by DinSAR technique of Radarsat II images. Spectral indexes and supervised image classification were calculated to differentiate the ice boundary. Between 2010 and 2015 the ice sheet of the volcanoes under study has reated 24%, 42% and 60% respectively. The coherence images show similar results as those obtained by optical images. The use of coherence images can be used for the delimitation of ice and rock in glacial areas. The ash on the ice sheet is a particular phenomenon on the VNR ice cap, which complicates the delimitation of the glacier surface for that volcano.

Keywords: optical images; glacier retreating; DinSAR; coherence images.

Estimación del retroceso glaciar en los volcanes Nevado del Ruiz, Tolima y Santa Isabel, Colombia a través de imágenes ópticas y Din-SAR

Resumen
Se realizó una cuantificación del retroceso glaciar del Volcán Nevado del Ruiz (VNR), Volcán Nevado de Santa Isabel (VNSI) y el Volcán Nevado del Tolima (VNT), utilizando imágenes satelitales Landsat 8 OLI TIRS. Se calcularon índices espectrales y clasificación supervisada de imágenes para diferenciar el límite entre hielo, se utilizó la técnica DinSAR usando imágenes de Radarsat II, específicamente las imágenes de coherencia. Entre 2010 y 2015 la capa de hielo de los volcanes en estudio ha retrocedido 24%, 42% y 60% respectivamente. Las imágenes de coherencia muestran resultados similares que los obtenidos mediante imágenes ópticas. El uso de las imágenes de coherencia puede utilizarse para la delimitación de hielo y roca en zonas glaciares. La ceniza sobre la capa de hielo es un fenómeno particular sobre el casquete glaciar del VNR, lo que complica la delimitación de la superficie glaciar para ese volcán.

Palabras clave: imágenes ópticas; DinSAR, retroceso glaciar; imágenes de coherencia.

1. Introducción

Como consecuencia del cambio climático, uno de los grandes impactos que se ha observado en todo el mundo es el derretimiento de glaciares. Existen tres nevados en Colombia que se encuentran en estructuras volcánicas clasificadas como activas: el Volcán Nevado del Ruiz (VNR), Volcán Nevado de Santa Isabel (VNSI) y Volcán nevado del Tolima (VNT), pertenecientes al Parque Nacional Natural los Nevados (PNNN), los cuales han sufrido disminución en su superficie de nieve debido al calentamiento global y otros factores. El Instituto de Hidrología, Meteorología y Estudios Ambientales IDEAM estima que para el año 1850 los glaciares colombianos

How to cite: Monterroso-Tobar, M.F., Londoño-Bonilla, J.M. and Samsonov, S., Estimación del retroceso glaciar en los volcanes Nevado del Ruiz, Tolima y Santa Isabel, Colombia a través de imágenes ópticas y Din-SAR. DYNA, 85(206), pp. 329-337, September, 2018.

© The author; licensee Universidad Nacional de Colombia.

ocupaban un área de 350 km^2, mientras que para la década 2000-2010 ocupaban un área de 45 km^2, representados en seis cuerpos de hielo con 300 km^2 menos en un período de 150 años. Ante estas circunstancias, determinar el retroceso glaciar se convierte en un aspecto importante para la gestión del impacto ambiental. La teledetección, mediante el uso de imágenes satelitales es una herramienta muy viable y útil para estudiar áreas o superficies de glaciares [1]. De igual forma, el uso de imágenes provenientes de sensores activos facilita aún más la obtención de información de superficies de desplazamiento, como lo es la Interferometria de Radar Diferencial -DinSAR- técnica que ha sido utilizada en distintas partes del mundo para el estudio de glaciares [2]. En el caso de Colombia, la técnica DinSAR no ha sido utilizada para el estudio de glaciares [3]. Este trabajo busca determinar los cambios en el área de la superficie glaciar que han sufrido el VNR, VNSI y VNT entre 2010 al año 2015, mediante el uso y procesamiento de imágenes satelitales ópticas y la técnica de DinSAR (el uso de imágenes de coherencia específicamente).

2. Métodos, datos y procesamiento

Existen diferentes técnicas para la extracción y mapeo de cobertura de nieve en una imagen de satélite [4-7]. Se han usado técnicas de Índices Espectrales (IE) [8,9] en imágenes satelitales del sensor Landsat 8 OLI TIRS el cual es un método que compara la información espectral de una banda con otra, para la distinción de la cobertura de nieve entre otras coberturas [4,11]. En la Tabla 1 se describen los IE aplicables para el estudio de glaciología.

Otra forma para la delimitación de área glaciar es la clasificación digital de imágenes [12,13]. Esta técnica implica en gran medida la interpretación visual del usuario para determinar diferentes categorías de cobertura de la tierra, a través de la utilización de distintos algoritmos que agrupan pixeles con la misma respuesta espectral.

Tabla 1
Índices Espectrales para el mapeo de coberturas de Nieve y Hielo mediante Imágenes Satelitales

Nombre del Índice	Formula	Descripción
Índice de Nieve Diferencial Normalizado -NDSI-	$\frac{\text{verde} - \text{SWIR}}{\text{verde} + \text{SWIR}}$	Para mapear la diferenciación de nieve-hielo en áreas cubiertas de nieve.
Índice de Nieve y Hielo Diferencial Normalizado -NDSII-	$\frac{\text{rojo} - \text{SWIR}}{\text{rojo} + \text{SWIR}}$	Para mapear la diferenciación de nieve y hielo en áreas cubiertas de nieve y hielo.
Índice Glaciar Diferencial Normalizado -NDGI-	$\frac{\text{verde} - \text{rojo}}{\text{verde} + \text{rojo}}$	Para mapear zonas de diferenciación entre nieve y hielo y una mezcla de hielo y flujos de nieve.
Índice de Nieve y Hielo Diferencial Normalizado -NDSII 2-	$\frac{\text{verde} - \text{NIR}}{\text{verde} + \text{NIR}}$	Para mapear diferentes zonas de hielo y nieve en distintas clases.

Fuente: Adaptada de [12].

Las tipologías más comunes de clasificación de imágenes son la clasificación supervisada en donde se requiere la participación del analista para valorar los diferentes pixeles de una imagen a partir de áreas de entrenamiento mediante un software, y la clasificación no supervisada, que está relacionada al valor y color relativo del tono o agrupamiento para la identificación de entidades. La clasificación supervisada se basa en aspectos tales como: las etiquetas de las clases espectrales en un ejercicio anticipado, determinación de parámetros clasificados a partir de la densidad de cada clase definida, es decir a partir del número de muestras tomadas en la imagen [14]. El autor plantea que las clases tomadas están en relación directa con la estructura espectral de la imagen, dependiendo del conocimiento que el usuario tenga al segmentar los pixeles comunes que a su vez es una representación numérica espectral de la imagen. Matemáticamente hablando, sean las clases espectrales predefinidas las siguientes:

$$\omega i, i = 1, 2, \ldots m \tag{1}$$

Para clasificar un pixel *r* en una de las clases es necesario conocer la siguiente probabilidad condicional:

$$p(\omega i \mid r), i = 1, 2, \ldots m \tag{2}$$

La cual es la probabilidad (verosimilitud) de que una clase ωi sea el correcto, dado un pixel en la posición *r*, que es el vector de posición del pixel en la imagen de muestra. Por esa razón, la clasificación se realizaría de acuerdo con el algoritmo de clasificación de Máxima probabilidad (o verosimilitud), el cual se puede definir como:

$$r \in \omega i, si\, p(\omega i \mid r) > p(\omega j \mid r), \forall\, i \neq j \tag{3}$$

Donde r pertenece a la clase ωi si la probabilidad $p(\omega j \mid r)$ es la mayor respecto a la probabilidad asociada a las clases a agrupar. La cantidad de muestras se traduce como la probabilidad condicional de tener la clase ωi dado el valor de pixel en *r*. Para cada pixel sería necesario conocer la probabilidad de que pertenezca a cada una de las clases definidas y se asignaría a la clase para la cual la probabilidad fuese la más alta; sin embargo, no es posible inferir esta probabilidad a partir de los datos prototipo [14]. Si se tiene una imagen multiespectral de dos bandas se pueden relacionar ambas en un histograma. Con los valores de los pixeles prototipo se puede llegar a tener una distribución espacial que muestra la frecuencia de ocurrencia en dos valores. Por otra parte, existen satélites que generan su propia fuente de radiación, como es el caso de la emisión artificial que generan los sensores activos. El sistema de Radar de Apertura Sintética -SAR- utilizado por distintos satélites europeos [16]. Este último, se fundamenta en el efecto Doppler, el cual está basado en el hecho de que cuando la fuente emisora de ondas observadas está en movimiento relativo, se acorta el ancho de banda hacia donde se mueve el emisor y se alarga hacia donde se aleja [14-16].

Una de las principales ventajas en las imágenes SAR es su uso para el estudio de deformaciones de la superficie terrestre a partir de dos imágenes SAR [15]. La

Interferometria de Radar de Apertura Sintética –InSAR- explora la diferencia de fase entre dos imágenes complejas SAR, las cuales observan la superficie terrestre desde diferentes posiciones. InSAR utiliza la fase, en donde la diferencia de ambas en un par interferómetrico (dos imágenes de SAR) genera una figura llamada Interferograma (representación geométrica del cambio de fase en dos imágenes), la cual representa los cambios de fase representados en 2π. InSAR se basa en la variación de la fase producida por una modificación de las

propiedades del terreno empleando dicho par, según la siguiente ecuación [17,18]:

$$\phi = -\frac{4\pi}{\lambda} * r + \phi_{(scatterring)} \quad (4)$$

En donde λ es la longitud de onda electromagnética r es el rango, y $\phi_{(scatterring)}$ es el cambio de fase debido a la dispersión producida por el blanco, siendo este segundo término, en general una variable que se considera aleatoria que se puede presentar en valores de 0 a 2π. El cambio de fase puede ser aprovechado para determinar cambios de elevación de la escena, generando con esto lo que se conoce como un Modelo Digital del Terreno -MDT-. El Interferograma registra un modelo de interferencia compuesto de franjas ("fringes") que contienen toda la información sobre la geometría relativa entre las dos imágenes [14]. Cada franja, que corresponde con un ciclo de fase, equivale a un cambio de distancia suelo-satélite, la cual se trata de una deformación escalar y no vectorial como la obtenida con sistemas GPS. Un parámetro a considerar al momento de analizar pares interferométricos es la coherencia *(γ)*, que es un número complejo cuya magnitud es una medida de la desviación estándar de la fase. Su valor va de 0 a 1; así, una coherencia de 1 significa una estimación perfecta de la fase (imagen sin decorrelación), mientras que un valor de cero quiere decir que la estimación de la fase es solo ruido (imagen totalmente decorrelacionada). Por lo general, valores por encima de 0.4 o 0.5 son considerados aceptables. La coherencia se expresa mediante la siguiente ecuación:

$$\gamma = \frac{\sum_k I_{1,k} I_{2,k}^*}{\sqrt{(\sum_k I_{1,k}^2)(\sum_k I_{2,k}^2)}} \quad (5)$$

Donde $I_{i,k}$ es la amplitud compleja del k-ésimo pixel en la imagen i, i = 1, 2. Para determinar y cuantificar el retroceso glaciar del VNR, VNSI y VNT, se utilizaron imágenes de Satélite Rapideye e imágenes Landsat 8 OLI TIRS. Para la generación de interferogramas e imágenes de coherencia se utilizaron imágenes en modo complejo del satélite canadiense RADARSAT II. En la Tabla 2 se presentan las características de las imágenes ópticas utilizadas en este estudio y en la Tabla 3 se presentan las características de las imágenes RADARSAT II.

Para cada una las imágenes satelitales Landsat 8 OLI TIRS se realizó una composición de bandas para generar una imagen multiespectral utilizando las bandas Aerosol Costero, Azul, Verde, Rojo, Infrarrojo Cercano y las dos imágenes del Infrarrojo de Onda Corta para cada fecha indicada. En el caso de la imagen Rapideye, la imagen tenía una composición previa de Azul, Verde, Rojo e Infrarrojo cercano. Cabe indicar que al realizar la composición de imágenes Landsat 8 OLI TIRS, la imagen multiespectral resultante quedó con una resolución espacial de 30 metros por cada pixel y una resolución radiométrica de 16 bits. Adicionalmente, para la composición de bandas de cada una de las imágenes Landsat 8 OLI TIRS se realizó una fusión de imágenes (Pan Sharpen), la cual es una técnica digital que pretende mejorar una imagen multiespectral potenciando su uso con una mayor resolución espacial. El resultado de este proceso fue una nueva imagen, en donde, en gran parte de ella se conserva la riqueza espectral original ganando una mejor resolución espacial.

Tabla 2
Características de las imágenes Rapideye y Landsat 8 OLI TIRS utilizadas en el estudio.

Sensor	Resolución Espacial	Bandas	Región Espectral	Resolución Temporal	Fecha de imágenes
Rapideye	7	1	Azul	1 Día	04 de enero 2010
		2	Verde		
		3	Rojo		
		4	Infrarrojo Cercano (NIR)		
Landsat 8 OLI TIRS	30	1	Aerosol Costero	16 Días	09/02/2014
		2	Azul		29/03/2014
		3	Verde		26/12/2014
		4	Rojo		24/09/2015
		5	Infrarrojo Cercano (NIR)		
		6	Infrarrojo de Onda Corta (SWIR 1)		
		7	Infrarrojo de Onda Corta (SWIR 2)		
	15	8	Pancromática		
	30	9	Cirrus		
	100	10	Infrarrojo Termal (TIRS 1)		
		11	Infrarrojo Termal (TIRS 2)		

Fuente: Adaptada de [20] y [21].

Tabla 3
Características de imágenes RADARSAT 2

Par	Fechas	Tamaño del Pixel (m^2)	Vistas	Modo	Línea de Base
Par 1	28 de septiembre 2014 22 de octubre 2014	Azimut: 61 Rango: 37	Azimut: 10 Rango: 8	Descendente	-51.59
Par 2	28 de septiembre 2014 09 de diciembre 2014	Azimut: 61 Rango: 37	Azimut: 10 Rango: 8	Descendente	13.34
Par 3	22 de octubre 2014 09 de diciembre 2014	Azimut: 61 Rango: 37	Azimut: 10 Rango: 8	Descendente	64.93
Par 4	02 de diciembre 2014 26 de diciembre 2014	Azimut: 61 Rango: 37	Azimut: 10 Rango: 8	Ascendente	-143.96

Fuente: Adaptada de [25]

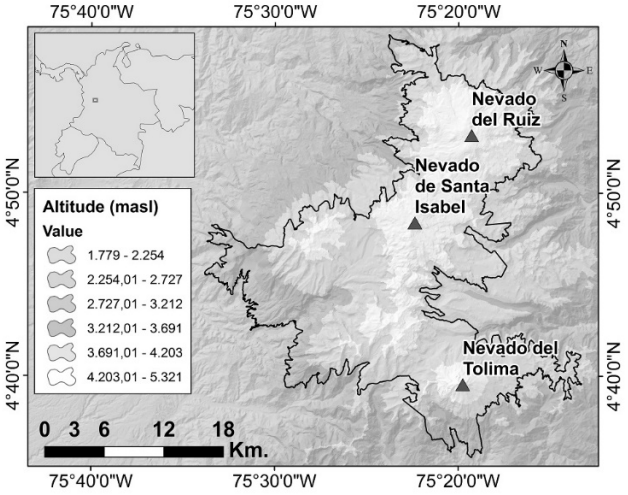


Figura 1. Parque Nacional Natural de Los Nevados (PNNN).
Fuente: Los autores

Todo este procedimiento se realizó utilizando la herramienta ATCOR (Atmospheric Correction) del software PCI Geomática 2014 [23]. Además, se utilizó un MDT de resolución 30 mts. Generado por el USGS (TOPO30) dentro del algoritmo de ATCOR, con el fin de minimizar las zonas con sombra dentro del área de estudio. En las imágenes Landsat 8 OLI TIRS se calcularon índices espectrales, los cuales se exportaron a formato vectorial para el cálculo en la determinación del retroceso glaciar. El procedimiento de clasificación de imágenes supervisada se aplicó a la imagen Rapideye con una resolución espacial de 7 metros (ver Tabla 2), en donde se tomaron en cuenta las coberturas nieve fresca, hielo glaciar, glaciar sucio (glaciar con ceniza), espacios sin vegetación y zonas con vegetación [23].

En cuanto a las imágenes RADARSAT II. Se generaron distintos interferogramas en los cuales se removió la fase topográfica con la intensión de simular un interferograma sintético, en este procedimiento se utilizó un MDT de la zona de trabajo con una resolución espacial de 90 mts. [24]. La generación de los interferogramas y mapas de desplazamiento se realizó usando el software GAMMA®. Posterior a lo anterior, se realizó el desenrollo de la fase ("phase unwrapping"), el cual consiste en la reconstrucción de la fase interferómetrica a partir de la representación enrollada, la cual está compuesta en rangos de 2π, es decir, se conoce menos un número entero de ciclos de 2π [14]. Para este procedimiento se usó el método de Mínimo Coste de Flujo para Desenrollo de la Fase (SNAPHU por sus siglas en inglés). Este algoritmo funciona con base a una red de pixeles irregulares, en donde la coherencia supere un umbral determinado [11].

3. Resultados y Discusión

3.1. Imágenes ópticas

La Fig. 2 muestra los resultados de la clasificación supervisada de la imagen para el año 2010 para los tres nevados utilizando imágenes Rapideye. Para el VNR se obtuvo un área de 9,47 km^2, para el VNSI de 2.35 km^2 y para el VNT de 1,25 km^2. En la Fig. 3 se presentan los Índices Espectrales utilizando imágenes Landsat 8 OLI TIRS para el VNR, también se muestra el cálculo de los diferentes IE para las imágenes ópticas Landsat utilizadas. Las escalas de colores de esta figura y las similares (5 y 7) van de -1 a 1. Los valores de los índices espectrales por encima de 0.4 se consideran área glaciar.

Al calcular los IE la presencia de ceniza en el VNR dificultó la identificación de valores por encima del 0,4 [11] para poder establecer la presencia de nieve o hielo en el casquete glaciar. Por esta razón, los vectores resultantes se ajustaron mediante métodos de digitalización manual en aquellas zonas en donde se confirmó que la ceniza recubría el área glaciar en la zona de estudio a partir de fotos y videos obtenidos en sobrevuelos disponibles (http://www2.sgc.gov.co/Manizales/Volcanes/Nevado-del-ruiz/Galeria-de-fotos.aspx). También se efectuaron modificaciones a valores de pixel catalogados con tipos de cobertura diferentes al verdadero; para ello, se eliminaron polígonos pequeños con un tipo de valor de pixel indefinido. La Fig. 4 muestra los resultados de la delimitación del área glaciar del VNR.

Para el 4 de enero de 2010, se obtuvo un área de superficie glaciar de 9,47 km^2; para el 29 de Marzo de 2014 de 7,78 km^2, para el 26 de Diciembre de 2014 de 7,57 km^2, y para el 24 de Septiembre de 2015 de 7,17 km^2, según las imágenes Landsat. Esto implica una disminución de la cobertura glaciar del 24,3% entre 2010 y 2015 para el VNR.

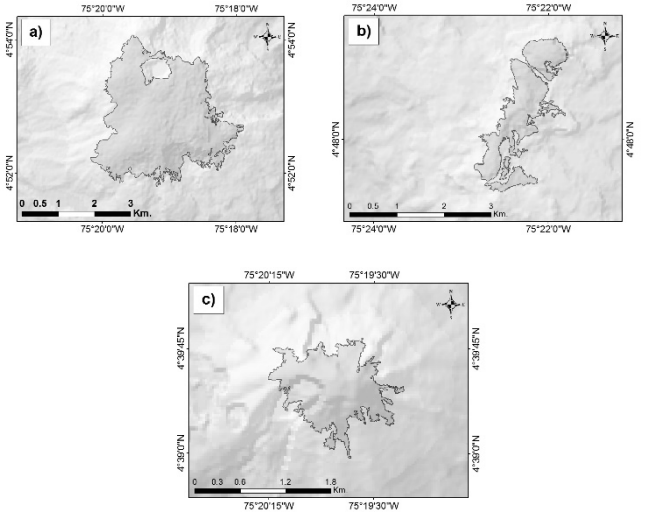


Figura 2. Delimitación de áreas glaciares para el VNR (a), VNSI (b) y VNT (c), mediante la clasificación supervisada de imágenes para la imagen Rapideye 2010.
Fuente: Elaboración propia.

3.1.1. Volcán Nevado de Santa Isabel

La Fig. 5 presenta los resultados del cálculo de los diferentes IE para el VNSI. Con el NDSI se obtuvieron mejores resultados en la delimitación del área glaciar que los con otros índices. La Fig. 6 muestra los resultados generados para cada imagen utilizada en la determinación de la superficie glaciar para el VNSI. Como se puede apreciar en dicha figura, la cobertura glaciar para el VNSI el 24 de marzo del año 2014 poseía un área de 1,32 km2, para el 26 de diciembre era de 1,30 km2, y para el 24 de septiembre de 2015 era de 0,92 km2, es decir una disminución del 69% en casi dos años.

3.12. Volcán Nevado del Tolima

La Fig. 7 presenta los resultados del cálculo de IE para el 29 de marzo y 26 de diciembre del año 2014 y 24 de septiembre del año 2015, para determinar el área glaciar del VNT. En esta figura se observa que el Índice NDSI delimita apropiadamente la cobertura glaciar. La Fig. 8 presenta la delimitación del área glaciar para cada año de estudio para el VNT. De esta figura se puede concluir que el área de superficie glaciar para el 29 de marzo de 2014 el área glaciar era de 0,83 km^2, para el 26 de diciembre del año 2014 fue de 0,82 km^2, y para septiembre el año 2015, fue de 0,72 km^2. Esto implica que el área glaciar del VNT ha disminuido en un 42% desde 2010 hasta 2015.

3.1.3. Imágenes Radar

La Fig. 9 presentan los mapas de desplazamiento en línea de vista -*LOS displacement*- de cada una de los interferogramas obtenidas en la investigación (Tabla 3), la cual presenta la deformación de la superficie, la Fig. 10 muestra los resultados de coherencia para los pares interferometricos para el PNNN. La Fig. 11 muestra la similitud del área de baja coherencia la cual hace referencia a la cobertura de nieve delimitada con la imagen Landsat 8 OLI TIRS.

De esta Figura es posible concluir que las deformaciones o desplazamientos obtenidos con la técnica InSAR no son útiles para delimitar el área glaciar o el límite hielo-roca en la zona del PNNN. Sin embargo, es posible usar la coherencia para tal fin.

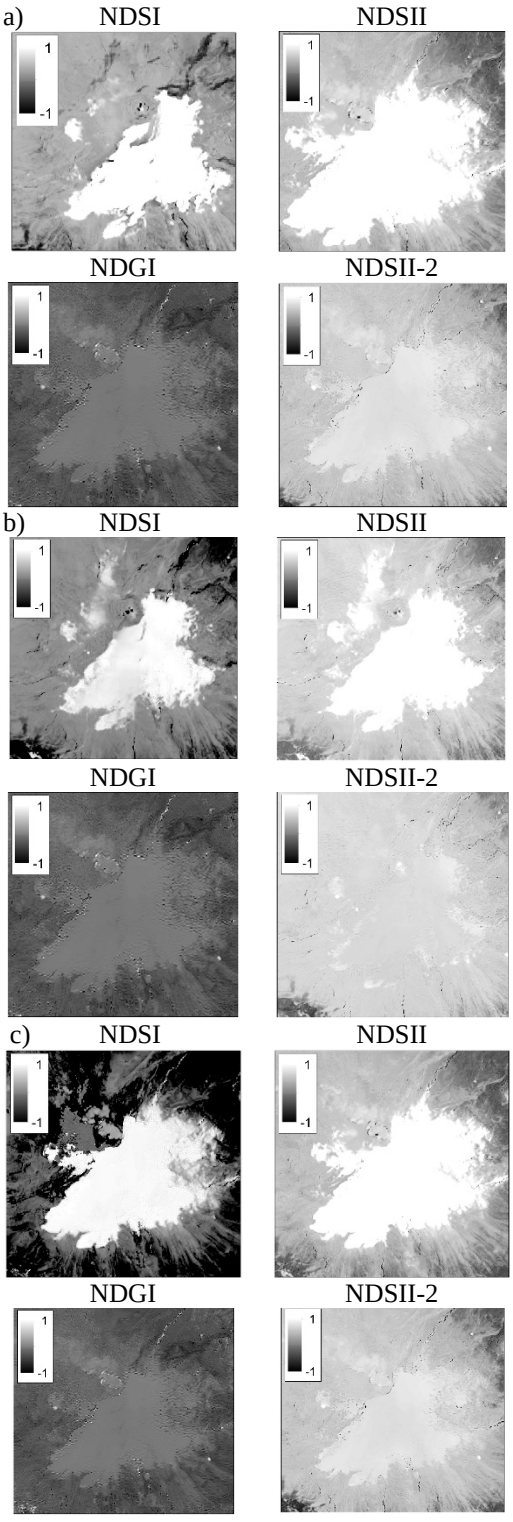


Figura 3. Cálculo de índices espectrales (Tabla 1) para el Volcán Nevado del Ruiz, a). 29 de marzo 2014. b). 26 de diciembre 2014. c). 24 de septiembre 2015.
Fuente: Elaboración propia.

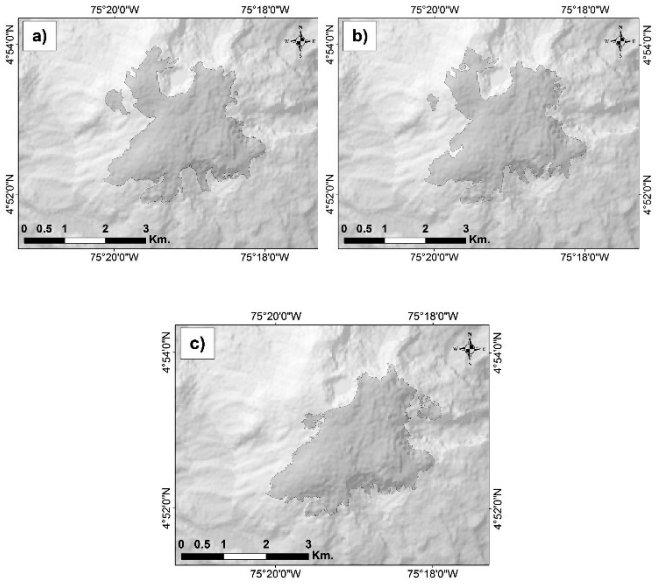


Figura 4. Delimitación área glaciar para el VNR para las siguientes fechas: a). 29 de marzo del 2014, b). 26 de diciembre 2014, c). 24 de septiembre del 2015. Usando índices espectrales. Los polígonos grises representan el área glaciar.
Fuente: Elaboración propia.

4. Análisis y conclusiones

La Tabla 4 presenta las variaciones de deshielo glaciar para los tres volcanes nevados en estudio entre 2010 y 2015 usando imágenes ópticas.

De acuerdo a los resultados, los tres nevados han presentado una disminución importante de la superficie glaciar en un período de cinco años. Entre el 2010 al año 2015, el VNR ha presentado un descenso de 24%, el VNSI un 60%, y el VNT un 42%. Con respecto a la técnica de InSAR, en la Fig. 10, se puede evidenciar que el área en estudio, para los cuatro interferogramas generados poseen una coherencia muy baja en tonos obscuros; principalmente en las zonas cubiertas de nieve y vegetación;

Aunque los mapas presentados anteriormente reflejan un descenso en la cobertura de nieve en las zonas de estudio, es importante indicar que las técnicas utilizadas para medir la cobertura glaciar presentan una serie de ventajas y desventajas las cuales son importantes tomarlas en cuenta para futuros trabajos de investigación. Entre las ventajas que estas técnicas poseen, se encuentra la disponibilidad de imágenes de satélite a utilizar para realizar cálculos de índices, interferogramas y mapas de desplazamiento, las cuales son amplias, por otro lado, las imágenes ópticas poseen tanto una resolución espacial como espectral adecuada para estudiar los cambios de cobertura de nieve,

Las desventajas en la interpretación de los datos SAR sobre glaciares es complicada en gran medida por la poca penetración en la nieve y el hielo glaciar. En cuanto a imágenes ópticas en estos métodos es importante recalcar que no todos los índices espectrales aplicados en glaciología son óptimos para diferenciar hielo y nieve sobre otras coberturas.

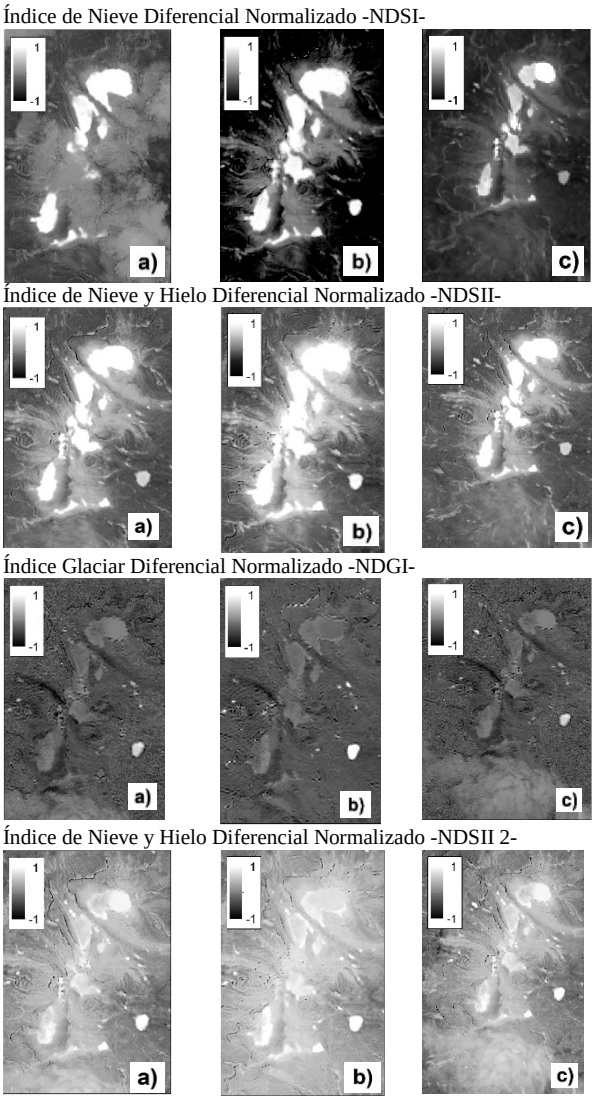


Figura 5. Índices Espectrales Nevado de Santa Isabel para las distintas fechas de estudio a) 29 de marzo 2014. b) 26 de diciembre 2014. c) 24 de septiembre 2015.
Fuente: Elaboración propia.

Para este caso, los índices óptimos a utilizar para la delimitación y cuantificación de área de nieve del VNR son NDSI y NDSII, ya que en estos índices se logra apreciar en mayor forma la cobertura glaciar. Es importante mencionar también que, debido a condiciones atmosféricas, se puede dificultar la selección adecuada de zonas de entrenamiento para una clasificación de imágenes óptima.

La utilización de Índices de Nieve Diferencial Normalizado -NDSI- es una herramienta adecuada que permite la delimitación de superficie glaciar. Sin embargo, en zonas de nieve cubiertas de ceniza, es importante acompañar esta técnica con procesos de digitalización manual para el re identificación de nieve o hielo en un objeto de estudio, basados en otros criterios como visitas a campo o fotos y videos de sobrevuelos.

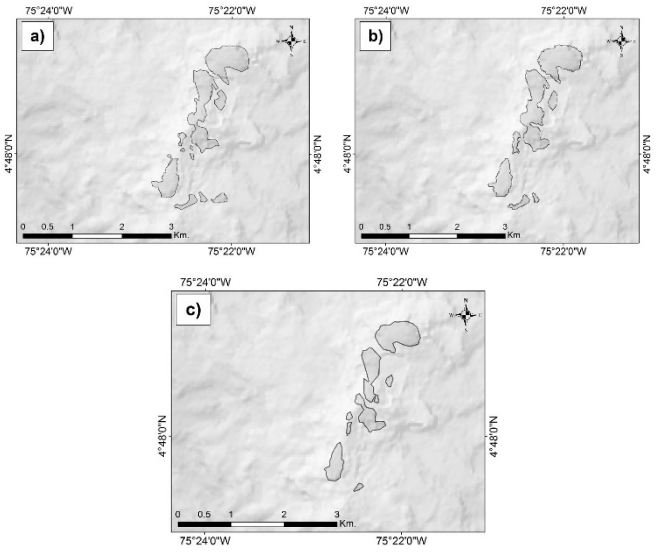
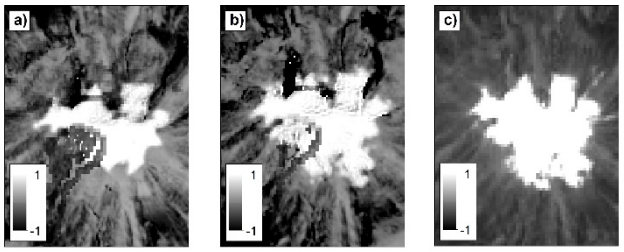
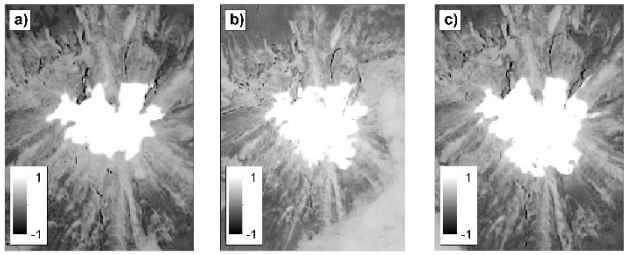


Figura 6. Delimitación área glaciar para el VNSI para las siguientes fechas: a). 29 de marzo del 2014, b). 26 de diciembre 2014, c). 24 de septiembre del 2015, usando índices espectrales. Los polígonos grises representan el área glaciar.
Fuente: Elaboración propia.

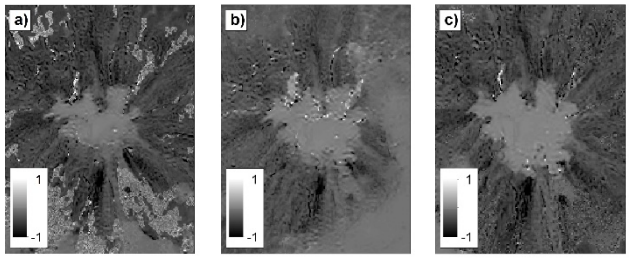
Índice de Nieve Diferencial Normalizado -NDSI-



Índice de Nieve y Hielo Diferencial Normalizado -NDSII-



Índice Glaciar Diferencial Normalizado -NDGI-



Índice de Nieve y Hielo Diferencial Normalizado -NDSII 2-

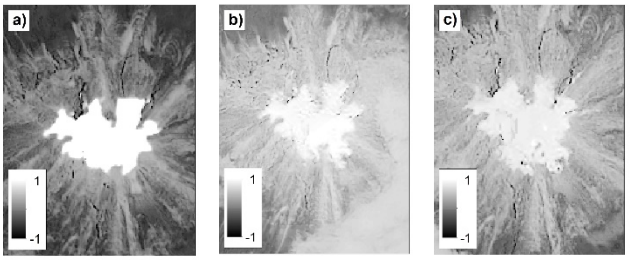


Figura 7. Índices Espectrales Nevado del Tolima, a) 29 de marzo 2014. b) 26 de diciembre 2014. c) 24 de septiembre 2015.
Fuente: Elaboración propia

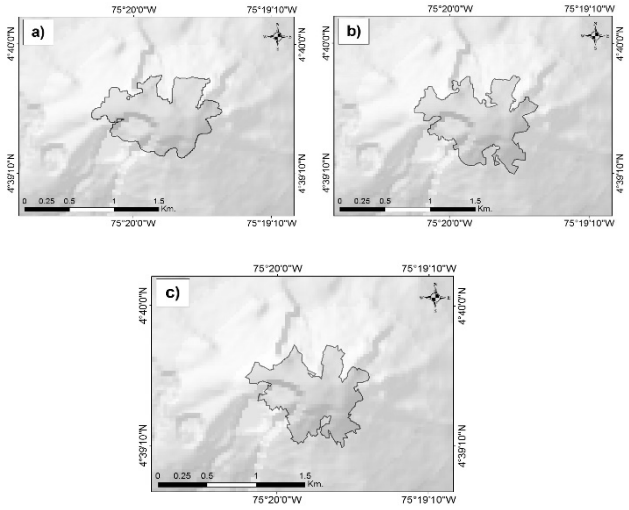


Figura 8. Delimitación área glaciar para el VNT para las diferentes fechas usando índices espectrales, a) 29 de marzo 2014. b) 26 de diciembre 2014. c) 24 de septiembre 2015. Los polígonos grises representan el área glaciar.
Fuente: Elaboración propia.

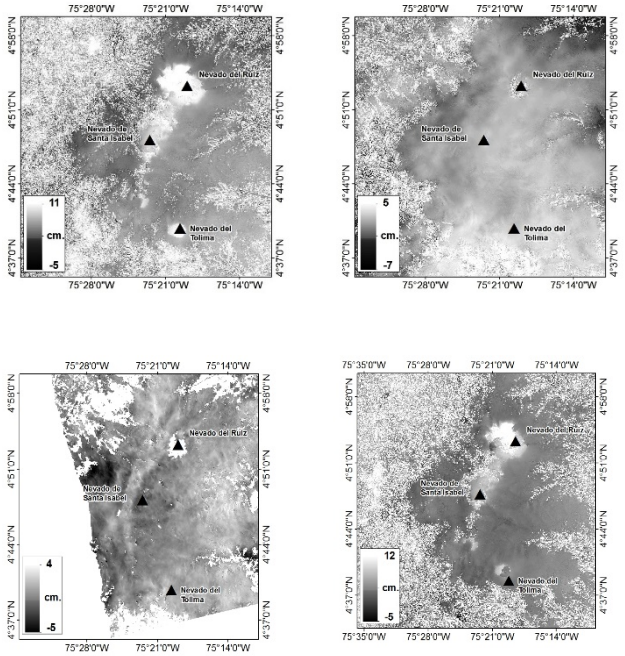


Figura 9. a) Línea de Vista de desplazamiento en cm., Parque Nacional Natural de los Nevados a partir de pares interferometricos de Radarsat II
Fuente: Elaboración propia

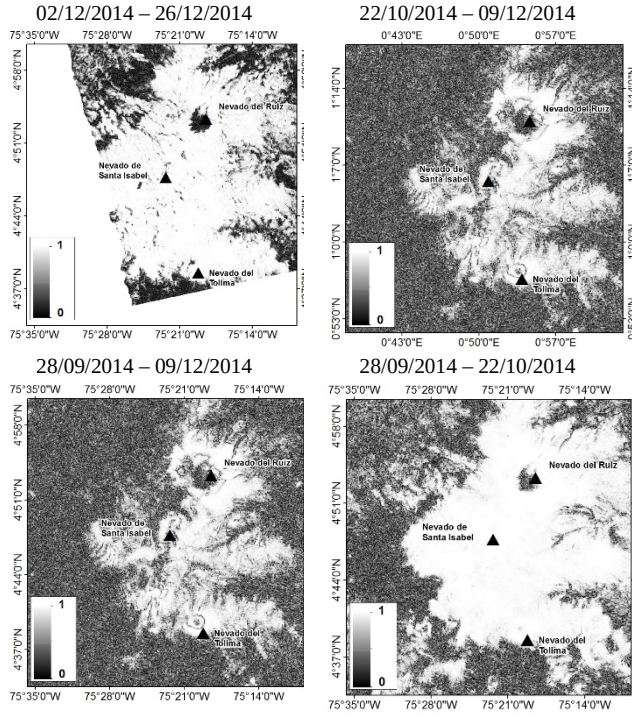


Figura 10: Resultados de Coherencia para cada par interferométrico.
Fuente: Elaboración propia.

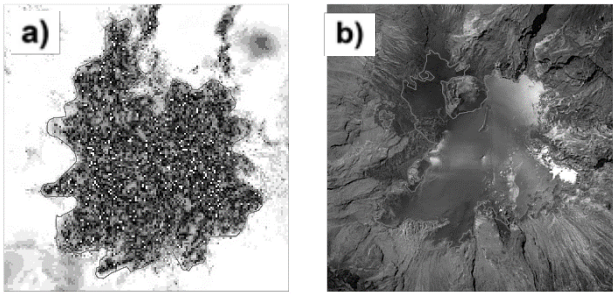
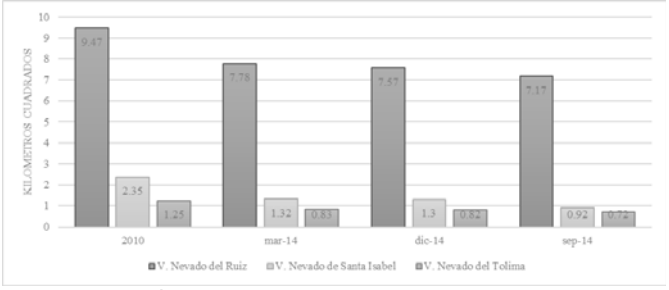


Figura 11: a). Delimitación del área glaciar VNR utilizando la imagen de decorrelación del par interferómetrico del 02/12/2014 – 26/12/2014. b). Imagen Landsat 8 OLI TIRS para el 26 de diciembre del año 2014.
Fuente: Elaboración propia.

Tabla 4.
Reducción de la superficie glaciar para los Nevados del Ruiz, Nevado de Santa Isabel y Nevado del Tolima 2010-2015.



Fuente: Elaboración Propia.

Por otra parte, una de las principales desventajas de la aplicación de DinSAR en superficies de los glaciares, es que la coherencia se ve afectada tanto por las condiciones meteorológicas, así como por la respuesta del hielo con el ruido que esta produce, ya que, al contener agua, la señal se pierde y no existe retorno alguno [19]. En otras palabras, La intensidad de la retrodispersión en la señal SAR reflejada en el hielo del glaciar y la nieve depende en gran medida de la longitud de onda, la polarización y el ángulo de incidencia, el cual se ve afectado en muchas ocasiones por las propiedades dieléctricas y geométricas del glaciar.

Dado que el área de estudio presenta actualmente una deformación debido a actividad volcánica o ascenso de magma [3], se hace muy difícil discriminar en los interferogramas qué parte del desplazamiento detectado es debida a retroceso glaciar y cuál a deformación volcánica.

Por su parte, las imágenes de coherencia parecen delimitar relativamente bien la zona de transición hielo-roca. En el caso del VNR se pudo obtener una superficie glaciar entre las fechas 02/12/2014 y 26/12/2014, de 9,65 km2 (Fig. 11), es decir, 0,2 km2 de diferencia con respecto a la imagen Landsat OLI TIRS de la misma fecha. Por tal motivo, se tomaron las zonas de baja coherencia como posibles indicadoras de presencia de hielo y nieve, donde la presencia de ceniza dificulta aún más la delimitación roca-hielo. Aprovechando que la nieve y el hielo poseen muy poca coherencia, esta se puede utilizar, como una buena aproximación al límite del hielo o nieve – roca, en un determinado sector que de antemano se sabe que posee dichos elementos. Es decir, las zonas de muy baja coherencia alrededor de los nevados, como la zona límite de la zona de hielo-nieve para diferenciarla de aquellas zonas con relativa alta coherencia (roca), que se consideraron ausentes de hielo o nieve, procedimiento que podría ser aplicado en otras zonas donde la delimitación de la masa glaciar con la técnica DinSAR es complicada.

Esto demuestra, que la coherencia puede ser un insumo en la delimitación de zonas con nieve-hielo, y parece ser apropiada y funcional siempre y cuando se tenga certeza de la presencia de la misma en la zona a estudiar. Se propone entonces que los valores bajos de coherencia alrededor de dichas zonas, en contraste con valores más altos en zonas aledañas, permite delimitar casquetes glaciares que estén cubiertos por ceniza y aquellos también que no lo estén. Para validar esta suposición se requiere de la aplicación en otras zonas volcánicas, aspecto que puede ser tema de estudio de trabajos posteriores.

De acuerdo con [26], las estimaciones en cuanto a superficie glaciar en los nevados de Colombia se habían reducido en un 60% en 60 años para el 2012 con un retiro anual del borde inferior del hielo que oscila entre 20 y 25 metros longitudinales. Si persisten las condiciones climáticas como las presentadas en el siglo pasado y en el año 2010, en el transcurso de tres o cuatro décadas, no existirán glaciares en Colombia [1]. Esto es un claro indicador de cambios en las condiciones climáticas y biológicas de estos cuerpos naturales, lo cual en gran medida es causado por factores climáticos, generando un grado de amenaza para los habitantes de la zona y sus medios de vida. Hay que tener en cuenta que El PNNN es una de las principales fuentes hídricas de municipios ubicados en las partes bajas de las cuencas que nacen en sus cimas tales como los municipios de

Chinchiná, Villa María, Manizales, Santa Rosa de Cabal principalmente, entre otros.

Agradecimientos

Los autores desean agradecer a la Universidad Católica de Manizales por el apoyo en el desarrollo del proyecto. Uno de los autores (MFM) desea agradecer al departamento de Geociencias de la Universidad de los Andes, Bogotá, Colombia, específicamente a la doctora Jill Pearse por su apoyo en el procesamiento de las imágenes de radar.

Referencias

[1] Arbelaez, J., Detección de cambios en el área del glaciar del Nevado del Ruiz entre los años 1985 y 2014 mediante el uso de imágenes Landsat [En línea]. Departamento de Geografía, Universidad del Valle, Cali, Colombia, 2014, 20 P. Disponible en: http://bibliotecadigital.univalle.edu.co/bitstream/10893/9942/1/CB-0551870.pdf

[2] Xiaobing, Z., Chang, N. and Shusun, L., Applications of SAR interferometry in earth and environmental science research. Sensors [Online]. 9(3), pp. 1876-1912, 2009. (date of reference: August 15th of 2015). Available at: http://www.mdpi.com/1424-8220/9/3/1876

[3] Lundgren, P., Samsonov, S., Lopez, V. and Ordoñez, M., Deep source model for Nevado del Ruiz Volcano, Colombia, constrained by interferometric synthetic aperture radar observations. Geophysical Research Letters [Online]. 42(12), pp. 4816-4823, 2015. (date of reference: October 5th of 2015). Available at: http://adsabs.harvard.edu/abs/2015GeoRL..42.4816L DOI :10.1002/2015GL063858

[4] Manoj, K., Aparna, S. and Ravi, P., Digital imagen information extraction techniques for snow cover mapping from remote sensing data. Encyclopedia of Snow, Ice and Glacers [Online]. 100, pp. 213-232, 2011. Available at: http://link.springer.com/referenceworkentry/10.1007%2F978-90-481-2642-2_498

[5] Recio, J., Ignacio, C. and Maestro, C., Análisis comparativo de distintos métodos de estimación de la superficie glaciar en el pirineo axial aragonés a partir de imágenes Landsat. Geofocus [En línea]. pp. 79-92, 2004. Disponible en: http://www.geofocus.org/index.php/geofocus/article/view/43/211

[6] Rignot, E.A., Contribution of the Patagonian icefields of South America to sea level rise. Science [Online]. 302, pp. 434-437, 2003. Available at: http://science.sciencemag.org/content/302/5644/434/tab-pdf

[7] Rakesh, B. and Tobias, B., Glacier mapping: a review with special reference to the Indian Himalayas. Progress in Physical Geography [Online]. pp. 672–704, 2009. Available at: http://journals.sagepub.com/doi/pdf/10.1177/0309133309348112

[8] Magsar, E., Pandi, K., Gombo, D. and Moondoi, O., Glacier change estimation using Landsat TM. International archives of the photogrammetry, remote sensing and spatial information science, 36(4), 2006.

[9] Hendriks, J. and Pelikka, P., Semi-automatic glacier delineation from Landsat imagery over Hintereisferner in the Austrian Alps. Zeitschriftur Gletscherkunde Undglazial geologie [Online]. 41, pp. 55-75, 2007. Available at: http://www.helsinki.fi/geography/geoinformatics/pdf/zgg_41_055-075_hendriks.pdf

[10] Chen, C., Statistical-cost network-flow approaches to two-dimensional phase unwrapping for radar interferometry [Online]. PhD Thesis, Stanford University, California, United States, 2001. 159 P. (date of reference: March 15th of 2016), Available at: http://web.stanford.edu/group/radar/people/Curtis_thesis_cpdf_print.pdf

[11] Dozier, J., Spectral signature of alpine snow cover from the Landsat thematic mapper. Remote Sensing of Environment [Online]. pp. 9-22, 1989. Available at: https://people.eri.ucsb.edu/~dozier/Pubs/DozierRSE1989.pdf

[12] Alva, M. and Meléndez, J., Aplicación de la Teledetección para el análisis multitemporal de la regresión glaciar en la Cordillera Blanca. Investigaciones Sociales [En línea] UNMSM/IIHS, 13, 2009. Disponible en: http://sisbib.unmsm.edu.pe/bibvirtualdata/publicaciones/inv_sociales/N22_2009/pdf/a04.pdf

[13] Vicens, Ll., Fuentes y Adquisición de Datos, Lección 9: Clasificación de Imágenes. Universidad de Girona, Valencia, España, 2007.

[14] Chavez, J.L., Tratamiento digital de imágenes multiespectrales. Instituto de Geofísica, Universidad Nacional Autónoma de México, México D.F., México, 2010. 618 P.

[15] Franceschetti, G. and Lanari, R., Synthetic Aperture Radar Processing. CRC Press: Boca Raton, Florida, USA, 1999.

[16] Jiménez, D., Movimientos de ladera en la vertiente meridional de Sierra Nevada (Granada, España): Identificación, análisis y cartografía de susceptibilidad y peligros mediante SIG. Departamento de Ingenieria Civil, Universidad de Granada, Granada, España, 2012.

[17] Hanssen, F., Radar interferometry: Data interpretation and error analysis. Delft University of Technology, The Netherlands, Kluwer Academic Publishers, 2001. DOI: 10.1007/0-306-47633-9

[18] Tomas, R., Estudio de la subsidencia de la ciudad de Murcia mediante Interferometria SAR diferencial avanzad, Tesis de doctorado, Universidad de Alicante, Alicante, España, 2008.

[19] Kjell, A., Rune, S. and Lauknes, T., SAR image of glaciers. In: Pellikka, P., Rees, G., Remote Sensing of Glaciers [Online], pp. 153-330, Taylor & Francis Group, Londres, Inglaterra, 2010. Available at: http://www.helsinki.fi/geography/geoinformatics/pdf/zgg_41_055-075_hendriks.pdf

[20] Ariza, A., Descripción y corrección de productos Landsat 8 LDCM, (Landsat Data Continuity Mission) [En línea], Versión 1.0, Bogotá, Colombia. Instituto Geográfico Agustín Codazzi, Centro de Investigación y Desarrollo CIAF, 2014. (fecha de referencia: 30 de Octubre de 2015). Disponible en: http://www.un-spider.org/sites/default/files/LDCM-L8.R1.pdf

[21] Garcia, M., Evora, J. and Arbelo, M., Satélites de teledetección para la gestión del territorio. Consejería de Agricultura, Ganadería, Pesca y Aguas del Gobierno de Canarias [En línea]. 2012. (fecha de referencia: 5 de Septiembre de 2015). Disponible en: http://www.gmrcanarias.com/wp-content/uploads/2016/01/20_catalogo_satelites_es.pdf

[22] PCI Geomatics, Manual de Usuario PCI Geomática, Procesamiento de Imágenes de Satélite, Corrección Atmosférica [En línea]. (fecha de referencia: 14 de Noviembre de 2015). Disponible en: http://www.pcigeomatics.com/pdf/training-guides/2016/Geomatica-1.pdf

[23] Pellikka, P. and Rees, G., Remote sensing of glaciers: techniques for topographic, spatial, and thematic mapping of glaciers. Taylor & Francis Group, Londres, Inglaterra, 2010.

[24] Gonzáles, P., Medida y caracterización de deformaciones usando técnicas geodésicas y de teledetección. Aplicación en vulcanología y sismotectónica. Tesis de Doctorado, Departamento de Física de la Tierra, Astronomía y Astrofísica, Facultad de Ciencias Matemáticas Universidad Complutense de Madrid, Madrid, España, 2010. 245 P.

[25] Sansonov, S., Interferogramas en cambio de fase (wrapping), Desenrollo de la Fase (Unwrapping) y Coherencias. Centro Canadiense de Estudios sobre Observación de la Tierra y Recursos Naturales. Comunicación Personal. 2015.

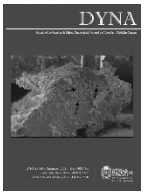
[26] Instituto de Hidrología, Meteorología y Estudios Ambientales., Glaciares de Colombia, más que montañas con hielo. Comité de comunicaciones y publicaciones IDEAM, Bogotá, Colombia, 2012.

M.F. Monterroso-Tobar, es estudiante de doctorado en Tecnológicas de Información y Comunicación e Ingeniería, Universidad Parthenope, y el Institute for Electromagnetic Sensing of the Environment, Nápoles, Italia. MSc. en Teledetección, Universidad Católica de Manizales; Colombia, Ing. en Administración de Tierras, Universidad de San Carlos de Guatemala. ORCID: 0000-0001-9442-7512

J.M. Londoño-Bonilla, es Geólogo de la Universidad de Caldas, MSc. en Ciencias, Geofísica de la Universidad de Kyoto, Japón, Dr. en Ciencias (Geofísica) de la Universidad de Kyoto, Japón. Docente de la Universidad Católica de Manizales, Colombia Profesional especializado del Servicio Geológico Colombiano.
ORCID: 0000-0003-1805-6048

S. Sansonov, es MSc., en Física de Lomonosov State University, Moscú. PhD. En Geofísica y Ciencias Ambientales de la Universidad de Western Ontario, Canada. Científico investigador del Canada Centre for Mapping and Earth Observation Natural Resources, Canada.
ORCID: 0000-0002-6798-4847.

UNIVERSIDAD NACIONAL DE COLOMBIA
SEDE MEDELLÍN
FACULTAD DE MINAS



DYNA
http://dyna.medellin.unal.edu.co/

Demolition and construction waste characterization for potential reuse identification

Lina María Chica-Osorio [a] & Juan Manuel Beltrán-Montoya [b]

[a] Grupo GICI. Facultad de Ingenierías, Universidad de Medellín, Medellín, Colombia. lmchica@udem.edu.co
[b] Facultad de Ingenierías, Universidad de Medellín, Medellín, Colombia. jmbeltranmontoya@outlook.com

Received: November 13th, 2017. Received in revised form: March 27th, 2018. Accepted: May 16th, 2018.

Abstract
Construction and demolition waste (CDW) have become a constant problem due to its volume of production and the lack of space for its final disposal. Several management strategies have been proposed to solve this problem as the reduction in the source of generation or the reuse as raw material. Nonetheless, for many cases this process is not consistent because CDW nature and its properties are not considered as an important variable in the identification of its possible reutilization. For this paper, an example of the potential reuse identification with regards to construction and demolition waste of Medellin city is presented. For this purpose, the physical, mineralogical and energetic properties were determined, as well as the specific amount of production. The results showed that the greatest potential reuse for CDW is associated to excavation waste and block masonry. Furthermore, based on the latter, a reuse model consisting in a soil-cement plate with 95% CDW was established.

Keywords: physical and chemical characterization, CDW reutilization.

Caracterización de residuos de demolición y construcción para la identificación de su potencial de reúso

Resumen
Los residuos de demolición y construcción (RCD), se han convertido en una problemática constante en el sector, debido a su volumen de producción y la falta de espacio para su disposición final. Para solucionar esta problemática se han propuesto diversas estrategias de gestión que consideran desde la disminución en la fuente hasta la reutilización como materia prima en la fabricación de diversos elementos. En este último aspecto, a nivel mundial, se han llevado a cabo esfuerzos por determinar el posible reúso de dichos residuos. Sin embargo, en muchos casos ese proceso parece ser inconsistente pues no se considera la naturaleza y propiedades del residuo como un condicional en la identificación de su posible reutilización. En este artículo, se presenta un ejemplo de aplicación de la identificación del potencial de reúso de residuos de demolición y construcción de la ciudad de Medellín, a partir de la determinación de las propiedades físicas, mineralógicas y energéticas, y del inventario específico de producción. Los resultados mostraron que, para el caso de estudio, los residuos con mayor potencial de uso para la reincorporación en la cadena productiva fueron los residuos de excavación y de mampostería de bloque, con los cuales, además, se probó un modelo de reutilización consistente en una placa suelo-cemento conformada por 95% de RCD.

Palabras clave: caracterización física y mineralógica, reutilización de RCD.

1. Introducción

Con el actual crecimiento demográfico, la demanda por entornos construidos seguirá en aumento. Las edificaciones, que son parte de ese entorno construido, tienen un enorme y continuo impacto sobre el medio ambiente. Indicadores de este impacto en los países industrializados es el hecho que en la construcción de infraestructura se utilizan alrededor del 40% de los recursos naturales extraídos, se emplea cerca del 70% de la electricidad, y se producen entre el 35% y el 65% de los residuos dispuestos en los botaderos. Esto implica, que la industria de la construcción es responsable del más alto porcentaje volumétrico de residuos totales en las naciones desarrolladas. En la Unión Europea, la cantidad total de

How to cite: Chica-Osorio, L.M. and Beltrán-Montoya, J.M., Caracterización de residuos de demolición y construcción para la identificación de su potencial de reúso. DYNA, 85(206), pp. 338-347, September, 2018.

© The author; licensee Universidad Nacional de Colombia.

residuos generados en el año 2013 fue de 2500 millones de toneladas, un 34% de los cuales resultan de la construcción y demolición [1]. En Asia, el porcentaje de residuos de demolición y construcción (RCD) que se generan por año, respecto del volumen total es 25% en Hong Kong y 48% en Corea del Sur [2]. Se estima entonces, que la cantidad de residuos, asociados a las actividades de construcción en las naciones desarrolladas, están a razón de 450 kg por año por habitante [3].

En países en vía de desarrollo, como los Latinoamericanos, no se encuentran disponibles cifras de producción de RCD. Las principales ciudades de Colombia presentan actualmente volúmenes de producción anuales altos de RCD, Bogotá produce alrededor de 12 millones de m^3, Medellín 860.000 m^3, para Cali 1 millón de m^3 anuales y Cartagena 190.000 m^3 [4]. En el Área Metropolitana del Valle de Aburrá el sector de la construcción produce 6.000 toneladas/día de residuos [5] de las cuales solo 1800 toneladas son almacenadas adecuadamente en centros de almacenamiento temporal de escombros CATES [6] lo que significa que más de 4000 toneladas son dispuestas de manera irregular. Estas cifras, muestran una problemática creciente, respecto del manejo y la disposición final de los RCD, y de los impactos que pueden generar.

A nivel mundial, se han planteado diversas estrategias para reducir la contaminación generada por los residuos de demolición y construcción. Se incluyen las asociadas a la reducción de los residuos en la fuente, pasando por la reutilización y el reciclaje [7,8]. Sin embargo, es claro que una gestión apropiada de los residuos debe incluir procesos que generen valor agregado a estos materiales y que permita su reincorporación a la cadena productiva, dando una solución sostenible a dicha problemática. Una búsqueda de alternativas de reutilización de los residuos estaría en concordancia con la promoción de desarrollo sostenible y fomento de nuevas oportunidades de negocio relacionadas con el manejo y aprovechamiento de los residuos sólidos provenientes de la construcción.

Aunque existen una gran cantidad de investigaciones que establecen la reutilización particular de residuos de demolición y construcción, pocos autores reportan la caracterización física y mineralógica de los mismos como un aspecto determinante en su potencial de reutilización. En este sentido, es pertinente plantear la pregunta sobre cómo generar estrategias para la identificación de posibles reúso si no existe una línea base de características tanto físicas como mineralógicas que condicionen una aplicación específica.

En este artículo, se presenta la caracterización completa de residuos de demolición y construcción producidos en la ciudad de Medellín, como el paso inicial en la determinación de su potencial de reúso. Además, se presentará un ejemplo de aplicación específico, obtenido a partir de un análisis de inventario y de las características físicas y mineralógicas de los RCD locales.

2. Identificación del potencial de reúso de RCD

En la actualidad, no existe una metodología precisa que permita la toma de decisiones sobre la oportunidad de reutilización de un residuo de demolición y/o construcción. Los criterios empleados usualmente están asociados con el volumen de producción y con las oportunidades de reincorporación disponibles. A pesar de ello, la naturaleza del residuo también se asocia con su reutilización. A continuación, se refieren estos criterios como punto de partida para la identificación del potencial de reúso.

2.1. Según inventario

El inventario o cantidad producida de residuos, es uno de los criterios con mayor peso, para identificar la oportunidad de reutilización de residuos de demolición y construcción. Dentro de los RCD que se producen en mayor cantidad a nivel mundial, los concretos se ubican el primer lugar en porcentaje de producción, seguidos de las roturas cerámicas y la mampostería, siendo estos residuos los que han concentrado la mayor cantidad de esfuerzos de reincorporación dentro de la cadena productiva de la construcción. La Tabla 1, muestra la producción porcentual de RCD discriminada, para algunos países de Europa.

En este sentido, un indicador importante de la factibilidad de reutilización de RCD como nueva fuente materias primas para el sector es el alto porcentaje de reciclaje, tal y como se observa en la Tabla 2. En Colombia, hasta el momento, no han sido encontrados reportes para los porcentajes de reúso para ninguna ciudad, pero para Medellín se estima que en 2023 para un área construida proyectada de 1.423.299m^2, se producirán 2.536.603 ton de RCD [9].

Tabla 1.
Producción porcentual discriminada de RCD en Europa.

Material	España 2004	Turquía 2005	Escocia 2015	España 2016
Concreto	12	40	45.64	69.8
Asfalto	5	-	19.33	-
Cerámicas	54	30	5.30	0.219
Mampostería	-	-	-	3.4
Agregados naturales	9	-	-	21.5
Madera	4	10	-	-
Metales	2.5	5	-	0.002
Plásticos	1.5	5	-	0.015
Yeso	0.2	-	-	0.103
Vidrio	0.5	-	0.07	-
Otros	4	10	1.59	0.001
Sin consolidar	7.3	-	28.06	-

Fuente: adaptado de [10-13]

Tabla 2.
Porcentaje de RCD reciclado en países europeos. *Millones de toneladas

País	RCD*	% Reciclado	País	RCD *	% Reciclado
Holanda	23.9	98	Polonia	38.19	28
Dinamarca	5.27	94	Finlandia	5.21	26
Estonia	1.51	92	Hungría	10.12	16
Alemania	72.40	86	España	31.34	14
Irlanda	2.54	80	Portugal	11.42	5
Inglaterra	99.10	75	Grecia	11.04	5
Lituania	3.45	60	Italia	46.31	0
Eslovenia	2.00	53	Rumania	21.71	0
Letonia	2.32	46	Suecia	10.23	0
Luxemburgo	0.67	46	Eslovaquia	5.38	0
Francia	85.65	45	Malta	0.8	0

Fuente: adaptado de [14].

Aunque habitualmente no son considerados dentro de las estadísticas de producción, los materiales producto de las excavaciones necesarias como etapa inicial para dar lugar a los desarrollos urbanísticos normalmente representan, en cantidad, el mayor residuo producido por la industria de la construcción. Este material en la mayoría de los casos es dispuesto en lugares autorizados o no, sin recibir ningún tipo de tratamiento o aprovechamiento [15].

2.2. Según oportunidades reportadas de reutilización

Respecto de la utilización de aquellos residuos que el inventario general a nivel mundial reportó con mayor oportunidad debido a su disponibilidad por su volumen de producción, a continuación, se describe los potenciales usos para cada uno de ellos.

2.2.1. Reutilización de residuos de concreto

Dentro de los residuos de construcción y demolición, los residuos de concreto sobresalen debido a que son el residuo con mayor volumen de producción [16]. Existen cuatro líneas principales de reutilización de residuos de concreto: Fabricación de concretos empleando RCD como sustituto total de áridos naturales o como de sustituto de las fracciones gruesas o finas; elaboración de prefabricados como bloques divisorios, bordillos y tuberías; uso en carreteras como base y sub-base; y aprovechamiento de los residuos de hormigón como materia prima para la producción de nuevos productos de alta calidad.

Las investigaciones referentes a la producción de concretos con áridos reciclados provenientes de hormigón se han enfocado principalmente en la determinación de las propiedades finales del concreto [17,18]. Los resultados obtenidos al emplear RCD para la fabricación de concretos son positivos, puesto que se han logrado producir concretos de hasta un 30% más de resistencia a la compresión en comparación con concretos fabricados con agregados convencionales [19]. Respecto de los prefabricados como bloques divisorios, bordillos y tubos, autores como [14] y [20] han estudiado estos productos encontrando resultados similares a los prefabricados convencionales con tasas de remplazo entre 40% y 60% e incluso se ha logrado mejorar propiedades como la resistencia al fuego y el aislamiento térmico y acústico [21] aunque la alta absorción de los productos finales debida a la porosidad de los agregados se plantea como un posible inconveniente al momento de climas extremos de hielo y deshielo.

La aplicación de los residuos de concreto dentro de las vías también ha sido motivo de estudio. En la aplicación como material de base y sub-base en carreteras se han obtenido resultados positivos al ser mezclados con cemento para lograr una estabilización adecuada [22]. También se ha evaluado la viabilidad de la utilización de los residuos de hormigón para la fabricación de mezclas asfálticas en frio sin alterar las propiedades mecánicas [23] y en algunos casos observando mejores comportamientos en condiciones de alta humedad y temperatura [24].

Por último, estudios se han enfocado en el aprovechamiento de los residuos de hormigón como materia prima para la producción de nuevos productos que van desde agregados gruesos y finos de alta calidad [25], placas suelo-cemento [26], coberturas para rellenos municipales [27], cenizas volantes para uso como aditivos en concretos de alta resistencia [28], e incluso con ayuda de tratamientos térmicos para la fabricación de cemento [29].

2.2.2. Reutilización de residuos de mampostería

Según estudios técnicos realizados por diversos autores [30-34] el uso de agregados reciclados provenientes de residuos de mampostería como sustituto de agregados naturales en la fabricación de concretos y morteros es el tipo de reutilización más común. Sin embargo, cualquier porcentaje de remplazo representa un decaimiento general de las propiedades físicas y mecánicas de los productos finales. Estos RCD pueden emplearse en la producción de ladrillos, bloques y adoquines, pues para estos elementos se requieren mezclas menos exigentes en cuanto a manejabilidad y resistencia (7MPa tránsito peatonal y bloques de mampostería tradicional). La tasa de absorción de agua que no debe superar el 6%, es la gran limitante en la aplicación de los residuos de mampostería para el uso en prefabricados [35]. De otro lado, residuos de mampostería con actividad puzolánica pueden emplearse como estabilizantes de terrenos o como materias primas para la fabricación de agregados expandidos [36, 37].

2.2.3. Reutilización de roturas cerámicas

A pesar que el volumen de producción de residuos derivados de la cerámica cocida es significativamente más bajo en comparación a otros residuos, desde la perspectiva de reutilización tienen un gran potencial de reúso gracias a su actividad puzolánica. Los residuos asociados a las roturas cerámicas pueden ser transformados siguiendo dos líneas de proceso: la reducción de tamaño o los procesos de alta temperatura. Como energéticamente la alta temperatura reduce las oportunidades de emplear un residuo cerámico como materia prima, las aplicaciones asociadas a este proceso son tecnológicamente de mayor impacto. Residuos de cerámica cocida son reactivados térmicamente para la fabricación de ecobloques [38] y de cerámica porosa [39] de especificaciones equivalentes a los productos fabricados a partir de materias primas nuevas. Por otro lado, los residuos de menor actividad puzolánica son empleados como agregados finos en la fabricación de adoquines, morteros de mampostería, y concretos tanto asfálticos como convencionales [40-43]. Se ha encontrado que en las sustituciones de agregado natural por residuos cerámicos usualmente se reduce la densidad y la trabajabilidad de las mezclas debido al incremento en el consumo de agua.

2.2.4. Reutilización de residuos de excavación

Se ha encontrado en diferentes lugares a nivel mundial que estos residuos pueden tener un gran potencial como agregados sustitutos a los habitualmente producidos en grandes canteras [15]. También se ha evidenciado que los residuos de excavación pueden ser utilizados como materia

prima para la fabricación de ladrillos o bloques estabilizados con diversos materiales como cemento [44], cemento y paja [45], cemento y escorias de alto horno [46] ente otros, encontrando que los bloques producto de estas mezclas cumplen a cabalidad las normas que los regulan y adicionalmente se puede generar una disminución de la energía de fabricación hasta en un 35% [44] y mejorar las propiedades de conductividad térmica [47-48]. Como materia prima también pueden ser utilizados como agregados para la fabricación de concretos en compañía de fibras [49], haciéndolos más económicos mientras cumplen con las resistencias y normas requeridas. Otros autores han encontrado que la utilización de residuos de excavación en compañía de cenizas volantes y otros aditivos como cal pueden generar mezclas sin aglutinantes cementicios destinadas para la fabricación de diversos elementos afines a la construcción o desarrollo urbano [50]. A pesar estos esfuerzos, se evidencia la falta profundidad en la información sobre el tema de reutilización de residuos de excavación [51] que apunten a la disminución de las tasas de disposición de estos residuos.

2.3. Según características fisicoquímicas

Como se indicó en la sección anterior, son pocos los investigadores que han reportado la caracterización de los residuos, como un criterio fundamental para decidir si un residuo tiene potencial aplicación. Debe considerarse que la reutilización de un residuo de demolición y construcción depende, por su puesto, de sus características y del efecto que estas pueden tener sobre las condiciones finales de un producto. Muchos autores presentan criterios asociados al tamaño que

Tabla 3.
Composición mineralógica de residuos mampostería según aplicación. Adaptado de varios autores.

Composición	Reutilización			
	Agregado mortero		Agregado concreto	Materia prima Cemento
	Xu et al (2014)	Martínez, et al (2013)	Silva et al (2014)	Galbenis & Tsimas (2006)
Al_20_3	5,25	13,29	15,50	9,7
CaO	11,71	26,09	8,73	26,77
Fe_20_3	8,36	4,93	9,84	4,58
K_20	3,48	0,83	1,29	1,49
MgO	-	3,82	3,50	2,31
$Si0_2$	71,35	47,43	54,09	44,59
MnO	-	0,08	0,18	-
$Ti0_2$	-	0,38	0,88	-
SO_3	-	-	0,14	-
P_2O_5	-	0,08	0,20	-
Na_20	-	2,21	1,92	-
Pérdidas ignición	-	0,86	3,40	9,14

Fuente: adaptado de varios autores [33,34,37,41]

Tabla 4.
Composición mineralógica de residuos de roturas cerámicas según aplicación. Adaptado de varios autores

Composición	Reutilización					
	Agregado mortero mampostería			Agregados Concreto		
	Saiz Martínez et al. (2016)	Martínez, Etxeberria et al. (2013)	Medina Banfill et al. (2013)	Medina et al. (2012)		Suzuki et al. (2009)
Al_20_3	10,1	13,29	9,83	24,46	9,1	5,25
CaO	15,7	26,09	17,98	0,63	11,8	63,88
Fe_20_3	2,44	4,93	2,49	0,94	0,91	2,97
K_20	2,31	0,83	3,17	2,8	1,63	0,34
MgO	1,81	3,82	1,85	0,19	0,67	1,38
$Si0_2$	45,5	47,43	48,75	68,41	58,2	20,84
MnO	-	0,08	0,04	-	-	-
$Ti0_2$	0,32	0,38	0,27	0,55	0,1	-
SO_3	3,12	-	2,64	-	-	2,12
P_2O_5	0,12	0,08	0,12	0,17	0,1	-
Na_20	0,95	2,21	0,86	1,65	2,38	0,23
$Zr0_2$	-	-	-	0,08	12,6	-
Pérdidas ignición	16,5	0,86	12,00	0,12	2,46	1,64

Fuente: adaptado de varios autores [40-43]

según el país y el tipo de aplicación debe cumplir una norma (en Colombia en el caso de los agregados para concretos y morteros la distribución de tamaño de partícula debe ajustarse a NTC 174 y en pavimentos a INV E- 213 y INV E- 214 y de absorción de agua. Respecto de la caracterización mineralógica, de la revisión bibliográfica, lograron extraerse algunos datos sobre la química de los minerales que los hacen susceptibles a ser usados. Para la reutilización como agregados se requieren altos contenidos de sílice y calcio (>20% y >10% respectivamente) y para reutilización como remplazo de cementantes o puzolanas elevados contenidos de CaO (>18%) y alúmina, como puede revisarse en las Tablas 3 y 4.

De otro lado, no se encontraron reportados índices asociados al consumo energético requerido para la reducción de tamaño de los residuos, previo a su reutilización.

3. Experimental: caracterización de RCD locales

3.1. Materiales y métodos

Los RCD's analizados consisten en residuos de mampostería de ladrillo y bloque-separadores de mortero, roturas cerámicas, y suelo de pobres características geotécnicas proveniente de residuos de excavación, fueron suministrados por la empresa Conconcreto S.A. Respecto de este último residuo, si bien es cierto la literatura no lo reporta de gran potencial y la reutilización más importante es el retrollenado, en el caso particular de estudio dado su inventario era el residuo con mayor problemática de vertido

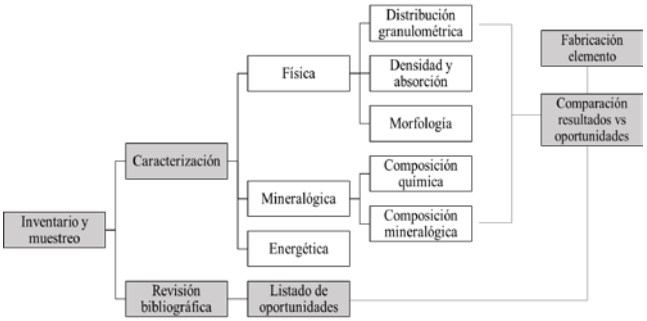


Figura 1. Metodología desarrollada.
Fuente: elaboración propia

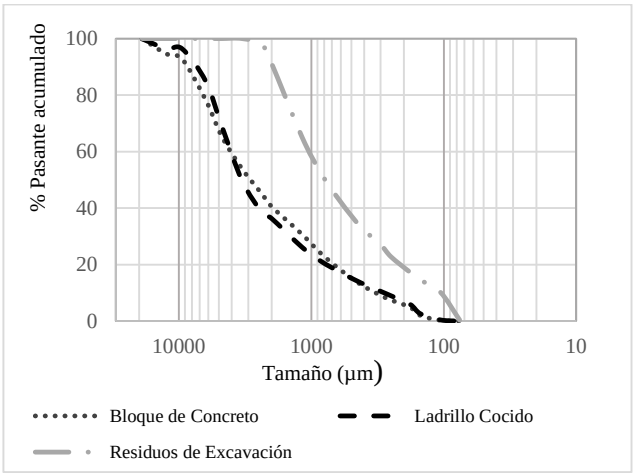


Figura 2. Curvas granulométricas de RCD estudiados.
Fuente: elaboración propia.

en obra. Las muestras fueron extraídas sin ningún tipo de proceso de separación, además sin trituración previa. La caracterización física realizada incluyó un análisis granulométrico convencional por tamizado, así como la determinación de la absorción y densidad según NTC 237 para los residuos de naturaleza cerámica. Este procedimiento se llevó a cabo en 4 intervalos granulométricos diferentes (en bruto, retenido en malla #6, entre la malla #6 y la malla #100, y pasante malla #100), con el fin de conocer los cambios en la absorción del material dependientes del tamaño de partícula. Las muestras también fueron analizadas para descripción morfológica por microscopía electrónica de barrido SEM con un equipo EVO LS 15 Zeiss a una distancia de trabajo WD: 8,5-9 mm y energía EHT: 20 kV. La caracterización química y mineralógica incluyó pruebas de difracción de rayos X en un equipo PANalytical con Goniómetro Omega/2 theta, y cuantificación por sonda EDS. Respecto de la caracterización energética, se obtuvieron medidas del índice de Bond, mediante una molienda escalonada de 700 cm^3 de material pasante malla #6 para estimar los gramos producidos por revolución (Gbp) y el índice de Bond correspondiente. El proceso garantiza la precisión de la medida al converger en las últimas 3 etapas.

Luego, con los resultados de la caracterización completa, se procede a comparar respecto del uso que la literatura reporta para los residuos que se identifican con el mayor potencial de utilización, ya sea por su calidad o por su inventario. Una vez realizada la toma de decisiones, se fabrica un modelo de aplicación. En la Fig. 1**,** se muestra un esquema de la metodología experimental empleada en este estudio.

3.2. Resultados y discusión

A continuación, se presentan los resultados obtenidos en la caracterización mineralógica física y energética de RCD's locales.

3.2.1. Caracterización física

La Fig. 2, presenta las curvas granulométricas para cada uno de los materiales en bruto, esto es, sin ningún proceso de separación o reducción de tamaño.

Las curvas granulométricas en ninguno de los casos pudieron ajustarse a una distribución estándar Rosin Ramler o Schuman, lo que indicaría que son bimodales. Como es de esperarse, los residuos de mampostería y las roturas cerámicas están enriquecidos en tamaños grandes (F80 en 7000 µm) y presentan fracciones importantes de tamaños finos (aproximadamente 10% pasante malla 100). Lo anterior, condiciona la aplicación sin procesar de estos residuos como agregado, debido a que la presencia de partículas tan finas, impide el empaquetamiento óptimo y aumenta la absorción de agua.

Respecto del suelo, según el tamaño máximo presente puede categorizarse como un suelo areno-arcilloso (SW-SC).

En la Tabla 5, se resumen los resultados obtenidos para absorción y densidad de residuos de mampostería y de roturas cerámicas. En el caso de los bloques-separadores que están compuestos de elevadas cantidades de cemento y cuyo tamaño de partícula es muy fino, no fue posible una determinación de la absorción por el método mencionado, pero se encontró que su densidad media es 3.01 g/cm^3.

Los resultados obtenidos muestran que, en el caso de las roturas, los tamaños superiores a la malla 6 controlan la absorción de agua, mientras que en bloque tanto el retenido como el pasante en la malla 6 tienen influencia sobre la absorción global. En el caso del bloque, en tamaños finos la absorción se encuentra al límite del valor máximo permitido para el uso de RCD como agregado (reutilización más usual) que es 9% [52-54].

Tabla 5.
Absorción de agua y densidad (g/cm^3) para RCD locales según NTC 237. Densidades: ρ1: muestra secada en el horno ρ2: muestra superficialmente seca, ρ3: relativa aparente.

Rotura cerámica	ρ1	ρ2	ρ3	Absorción
En bruto	2.00	2.25	2.67	**12.4%**
+6'	2.01	2.26	2.67	**12.5%**
-6 +100'	2.38	2.49	2.69	**4.9%**
-100'	2.54	2.57	2.62	**1.2%**

Mampostería bloque	ρ1	ρ2	ρ3	Absorción
En bruto	1.77	2.14	2.83	**21.3%**
+6'	2.18	2.40	2.80	**10.1%**
-6 +100'	2.53	2.63	2.81	**4.0%**
-100'	2.21	2.41	2.74	**8.7%**

Fuente: elaboración propia

Tabla 6.
Cuantificación de fases por XRD para RCD locales.

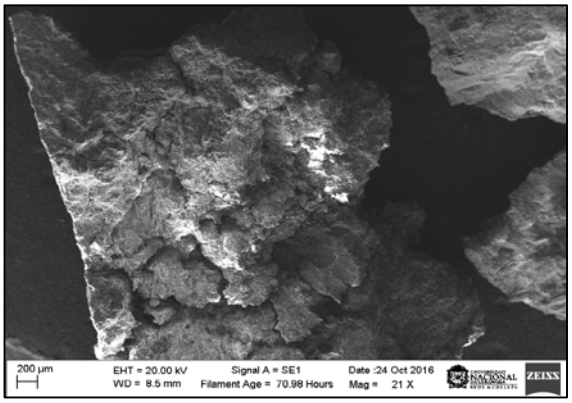
Muestra	Fases cristalinas	Fracción (%)
Mampostería de bloque y separadores	Cuarzo	21,8
	Calcita	19,8
	Albita	13,1
	Cinocloro	0,3
	Feldespato	21,8
	Biotita	2,2
	Cordierita	6,3
	Yeso	1,0
	Anortita	13,6
Mampostería de ladrillo	Cuarzo	51,1
	Calcita	7,8
	Albita	39,0
	Cordierita	1,7
	Caolinita	0,5
Roturas cerámicas	Cuarzo	29,2
	Calcita	9,2
	Albita	57,0
	Cordierita	2,1
	Biotita	2,2
	Caolinita	0,4
Residuos de excavación	Cuarzo	17,7
	Albita	15,7
	Caolinita	52,2
	Cordierita	3,3
	Moscovita	11,0

Fuente: elaboración propia

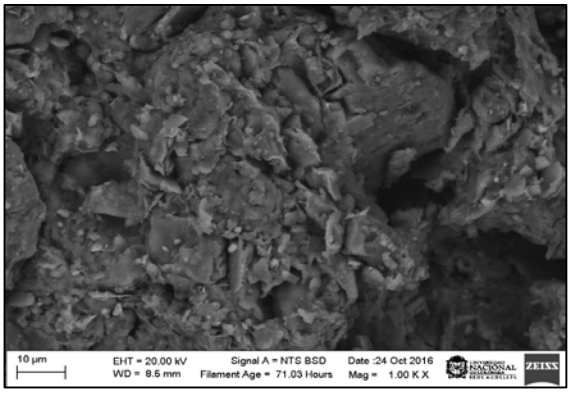
3.2.2. Caracterización mineralógica y morfológica

En la Tabla 6 se resume la caracterización mineralógica respectiva, obtenida por comparación de patrones de difracción. La fase cuarzo (SiO_2), los feldespatos: Albita, Anortita y Plagioclasa, y el carbonato de calcio son las fases dominantes en los residuos cerámicos analizados. Los residuos de excavación son los únicos que presentan fases arcillosas tales como moscovita y caolinita. Las cantidades disponibles de aluminio se reportan asociadas a minerales como la cordierita y algunos filosilicatos como la biotita.

Las Figs. 3 y 4 muestran la morfología tipo "blocky" de forma irregular con tamaños promedios de 200 a 600 µm, asociados tanto a los residuos de mampostería como a las roturas cerámicas. La cuantificación por EDS muestra la presencia de los elementos químicos: Fe, O, Si, C K, Al, S, Ca y Mg, elementos constituyentes de las fases reportadas por XRD. En la Fig. 5, se observa la imagen SEM respectiva del suelo proveniente de residuos de excavación, donde se observan las estructuras laminares de las arcillas y su diferencia de tamaño respecto de las partículas de arena. Así mismo, se presentan los espectros EDS para este residuo.



a) 21X



b) 100X

Figura 3 a) y b). Imágenes SEM de partículas de residuos de mampostería de bloque. Morfología tipo "blocky".
Fuente: presente estudio

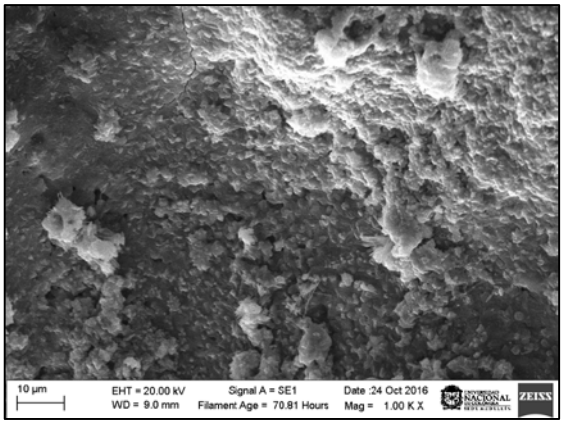
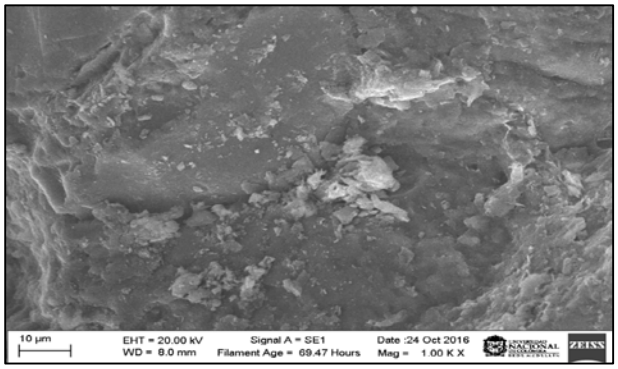


Figura 4. Imagen SEM de partículas de residuos cerámica. Morfología irregular. Imágenes obtenidas en el presente estudio.
Fuente: presente estudio

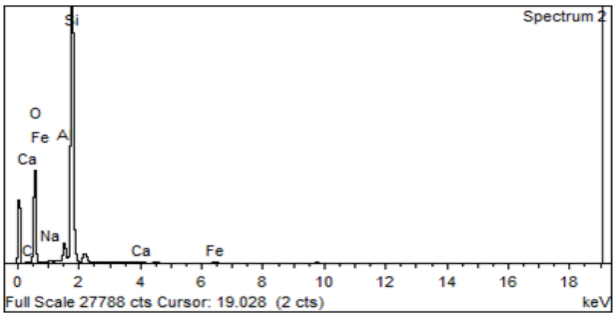
3.2.3. Caracterización energética

En la Tabla 7, se resumen los índices de trabajo para los residuos evaluados. Por sus condiciones naturales, los suelos no son materiales considerados para ser reducidos de tamaño.

Los resultados del Índice de Bond, indican que los RCD provenientes de roturas cerámicas, desde la perspectiva de consumo de energía, son los residuos con mayor potencial de aplicación pues tienen un índice de bond de 11 Kw-h/ton. Sin embargo, experimentalmente fue el procedimiento más complejo pues requirió de 10 ciclos para la convergencia lo que podría incidir en la precisión del ensayo. Así mismo, la pérdida de material fino en este RCD fue superior al 1%. Como en todos los casos, el índice de trabajo fue inferior a 20 kW-h/ton (estándar en plantas de producción de agregados naturales) todos los residuos son susceptibles de ser procesados con un consumo de energía del mismo orden (o en algunos casos menor) que el requerido en el beneficio de agregados naturales.



a)



b)

Figura 5 a) Imagen SEM de partículas de residuos de excavación. b) Caracterización química local por EDS para residuos de excavación. Imágenes obtenidas en el presente estudio.
Fuente: elaboración propia

Tabla 7.
Resumen del Índice de Bond como indicador del consumo energético.

Residuo	Gbp		WI (Kw-h/ton)	
	Muestra	Contramuestra	Muestra	Contramuestra
Ladrillo	2.234	2.121	12.142	11.435
Bloque	1.504	1.602	15.925	15.122
Roturas cerámicas	2.163	2.200	11.855	11.950

Fuente: elaboración propia

Idealmente la reutilización de un residuo debería hacerse en bruto, pero generalmente esto no es posible a nivel práctico. Técnicamente, un residuo puede cumplir con las condiciones de reúso, pero si energéticamente tiene un consumo mayor que obtener una materia prima nueva, esto imposibilitaría su reciclaje.

4. Análisis de resultados de caracterización y ejemplo de aplicación

Los resultados de caracterización física y mineralógica, así como un análisis de inventario específico, mostraron que los residuos con mayor potencial de uso para el caso local son los residuos de excavación. El elevado contenido de caolinita (mayor al 50%) y una distribución de tamaños muy cercanos a la arena con contenidos mínimos de partículas grandes, implica que puede ser empleado en la fabricación de elementos de tierra y cemento tal como fue reportado por [47, 48] sin requerir ninguna preparación adicional a un tamizado en una malla gruesa. Al comparar la composición mineralógica de los residuos de excavación y dicha literatura, se encuentra una correspondencia apropiada respecto de los minerales presentes. Sin embargo, el contenido de SiO_2 y CaO del suelo no son suficientes para generar elementos con alguna resistencia, según los reportes consultados. En este caso, la caracterización mineralógica del suelo, mostró un contenido de 17.7% de sílice cuando las referencias emplean fuentes de contenidos desde 47 a 85%; y para el CaO (fuente de Ca que tiene capacidad cementante) se emplea en contenidos que varían desde 1.5 a 2.5% y para el particular, no se reporta en ninguna proporción. Para potenciar el uso de los residuos de excavación, en la fabricación de elementos tierra-cemento, se requiere el aporte de material silíceo en tamaño arena como agregado, que será obtenido de los residuos de mampostería. Estos residuos, además de elevados contenidos de sílice, reportan calcita y yeso. Estos últimos minerales podrían actuar como cementantes o ayudantes del cemento, mejorando las propiedades de compactación y resistencia mecánica. En este sentido, tanto las fracciones gruesas como finas de residuos de mampostería presentan ventajas de uso respecto de los agregados naturales, pues además de aportar la fracción a áridos faltante, puede mejorar el desempeño. Evidentemente, para emplear RCD de mampostería se requiere de una reducción de tamaño para obtener un tamaño máximo nominal en la malla #6, que, reduzca la absorción de agua. El índice de Bond mostró ser el más elevado para todos los materiales analizados, aspecto que deberá considerarse como una restricción económica del proceso. Luego de identificar el potencial de uso de residuos de excavación y mampostería para la fabricación de elementos no estructurales tierra-cemento, se realizó un modelo tipo placa con los suelos residuos de excavación como base y los residuos de bloque de mampostería tanto como agregado (en tamaño +200) como remplazando una porción del cemento adicionado (en tamaño -200). Una revisión en la literatura referida a los métodos de fabricación referenciados en [47, 48], permitió definir un protocolo de mezclado y manufactura para estandarizar el proceso. Un resumen de dicho protocolo se muestra en la Fig. 6.

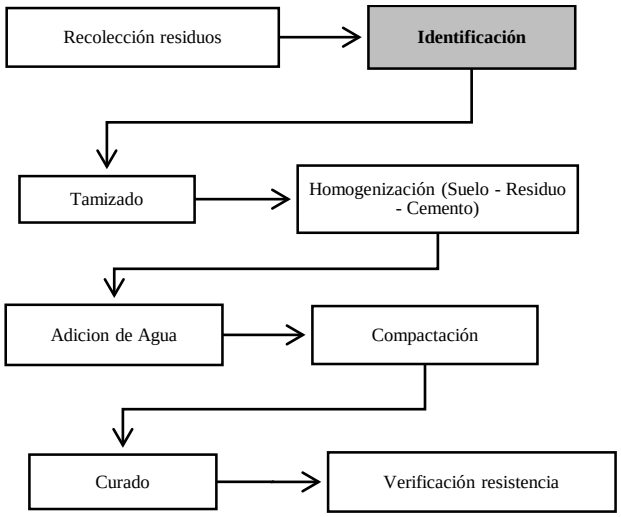


Figura 6. Protocolo de fabricación elementos tipo placa suelo – cemento – RCD.
Fuente: elaboración propia.

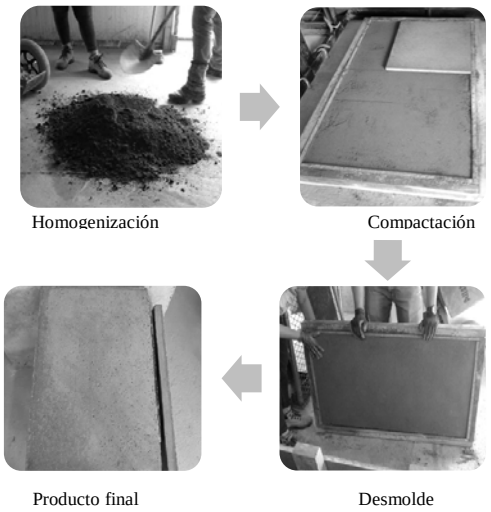


Figura 7. Proceso de fabricación modelo de reutilización de RCD, basado en la caracterización fisicoquímica
Fuente: elaboración propia.

Para el diseño de la dosificación se consideró el uso de 95% de residuos (entre suelo y bloque) y una relación A/C acorde con la humedad óptima de compactación. Se empleó compactación manual y una formaleta simple de madera para que el proceso pueda ser reproducido por cualquier usuario con materiales de composición mineralógica equivalente a la empleada. La resistencia a compresión final obtenida fue de 9MPa Una imagen general del proceso de fabricación y del resultado final se encuentra en a Fig. 7.

La composición química y física de los residuos de mampostería de ladrillo y de las roturas cerámicas, indican un mayor potencial de uso para aplicaciones en donde se requiera actividad puzolánica o sean permitidas grandes reducciones de tamaño. Sin embargo, para el caso de estudio, el volumen de producción fue muy bajo, lo que condicionó su aplicación.

5. Conclusiones

La determinación de las propiedades físicas y mineralógicas es una herramienta en la definición de la aplicación de cualquier material. En el caso de RCD's, esto es aún más relevante puesto que la viabilidad técnica de su reutilización depende, en gran medida de la cantidad producida, pero también está determinada por la composición mineralógica y propiedades como densidad, absorción de agua y distribución de tamaño de partícula. Así mismo, en el caso de RCD's que deban ser sometidos a procesos de reducción de tamaño, conocer su índice de trabajo es determinante para el diseño final del beneficio y para la evaluación del costo energético del reproceso. Aunque la caracterización fisicoquímica y la determinación del inventario pueden ser procesos demandantes en tiempo y dinero, los resultados obtenidos son un punto de partida no sólo para la identificación de los residuos con mayor potencial de reutilización, sino para la optimización del prototipo a fabricar, garantizando la incorporación de varios tipos de RCD en diferentes granulometrías, y con diferentes aportes a las características del producto final. En este sentido, la principal ventaja de conocer los residuos producidos, es desde la perspectiva técnica, eliminar la disposición en botadero de materiales que pueden ser transformados y ser tratados como materia prima.

En el caso local, a partir de los resultados de volumen de producción y de la caracterización física y mineralógica específica para cada residuo, se determina la aplicación que maximiza la reutilización. Se probó la metodología con un modelo consistente en placas suelo-cemento conformadas por 95% de RCD, con propiedades finales acordes con los requerimientos mínimos exigidos para elementos no estructurales. Además, se genera un protocolo de fabricación extensible a RCD de similares características.

Agradecimientos

Los autores agradecen el apoyo a Conconcreto S.A.y a la Universidad de Medellín, entidades financiadoras del proyecto de investigación "Caracterización y valoración de RCD para la identificación de su potencial uso como materiales de construcción", cuyos resultados se ven reflejados en el presente artículo.

Bibliografía

[1] Silva, R.V., de Brito, J. and Dhir, R.K., Performance of cementitious renderings and masonry mortars containing recycled aggregates from construction and demolition wastes. Construction and Building Materials, 105, pp. 400-415, 2016. DOI: 10.1016/j.conbuildmat.2015.12.171

[2] Won, J. and Cheng, J., Identifying potencial opportunities of building information modeling for construction and demolition waste management and minimization. Automatization in Construction, 79, pp. 3-18, 2017. DOI: 10.1016/j.autcon.2017.02.002

[3] Grettel, A. and Hernandez, L., Administración y manejo de los desechos en proyectos de construcción Etapa 2 Alternativas de manejo. Vicerrectoría de investigación, Instituto tecnológico de Costa Rica, 2007.

[4] Robayo-Salazar, R.A., Mattey-Centeno, P.E., Silva-Urrego, Y.F., Burgos-Galindo, D.M. and Delvasto-Arjona, S., Los residuos de la construcción y demolición en la ciudad de Cali: un análisis hacia su gestión, manejo y aprovechamiento. Tecnura, pp.157-170, 2015.

[5] Zapata-Ospina, G., Manejo de escombros, un reto para el Aburrá. El Colombiano, 18 de mayo de 2016.

[6] Loaiza-Bran, J.F., Normas en Medellin piden aprovechamiento progesivo de escombros. El Colombiano, 10 de Enero de 2016.

[7] Yuan, H. and Shen, L., Trend of the research on construction and demolition waste management. Waste Management, 31, pp. 670-679, 2011. DOI: 10.1016/j.wasman.2010.10.030

[8] Yuan, H.P., Shen, L., Jane, J.L. and Lu, W.S., A model for cost-benefit analysis of construction and demolition waste management throughout the waste chain. Resources. Conservation and Recycling, pp. 604-612, 2011. DOI: 10.1016/j.resconrec.2010.06.004

[9] Secretaría de Gestión y Control Territorial, Subsecretaría de Servicios Públicos y Secretaría de Medio Ambiente., Plan de Gestión Integral de Residuos Sólidos-PGIRS Municipio de Medellín 2016-2027. Medellín, Colombia, 2016.

[10] Eusko Jaurlaritza Gobierno Vasco., Monografía sobre residuos de construcción y demolición. IHOBE, 1, Sociedad Pública de Gestión Ambiental, 2004.

[11] Oikonomou, N.D., Recycled concrete aggregates. Cement and Concrete Composites, pp. 315-318, 2005.

[12] Medina, C., Zhu, W., Howind, T., Frías, M. and Sánchez-de Rojas, M.I., Effect of the constituents (asphalt, clay materials, floating particles and fines) of construction and demolition waste on the properties of recycled concretes. Construction and Building

Materials, 79, pp. 22-33, 2015 DOI: 10.1016/j.conbuildmat.2014.12.070

[13] Gómez-Meijide, B., Pérez, I. and Pasandín, A.R., Recycled construction and demolition waste in cold asphalt mixtures: evolutionary properties. Journal of Cleaner Production, 112, pp. 588-598, 2016. DOI: 10.1016/j.jclepro.2015.08.038

[14] Özalp, F., Dilsad-Yılmaz, H., Kara, M., Kaya, Ö. and Sahin, A., Effects of recycled aggregates from construction and demolition wastes on mechanical and permeability properties of paving stone, kerb and concrete pipes. Construction and Building Materials, 110, pp. 17-23, 2016. DOI: 10.1016/j.conbuildmat.2016.01.030

[15] Tokgöz, N., Use of TBM excavated materials as rock filling material in an abandoned quarry pit designed for water storage. Engineering Geology, 153, pp. 152-162, 2013. DOI: 10.1016/j.enggeo.2012.11.007

[16] Gomes, P.C., Ulsen, C., Pereira, F.A., Quattrone, M. and Angulo, S.C., Comminution and sizing processes of concrete block waste as recycled aggregates. Waste Management, 45, pp. 171-179, 2015. DOI: 10.1016/j.wasman.2015.07.008

[17] Bravo, M., de Brito, J., Pontes, J. and Evangelista, L., Durability performance of concrete with recycled aggregates from construction and demolition waste plants. Construction and Building Materials, 77, pp. 357-369, 2015. DOI: 10.1016/j.conbuildmat.2014.12.103

[18] Behera, M., Bhattacharyya, S.K., Minocha, A.K., Deoliya, R. and Maiti, S., Recycled aggregate from C&D waste & its use in concrete – A breakthrough towards sustainability in construction sector: A review. Construction and Building Materials, 68, pp. 501-516, 2014. DOI: 10.1016/j.conbuildmat.2014.07.003

[19] Wagih, A.M., El-Karmoty, H.Z., Ebid, M. and Okba, S.H., Recycled construction and demolition concrete waste as aggregate for structural concrete. HBRC Journal, 9, pp. 193-200, 2013. DOI: 10.1016/j.hbrcj.2013.08.007

[20] Soutsos, M.N., Tang, K. and Millard, S.G., Use of recycled demolition aggregate in precast products, phase II: Concrete paving blocks. Construction and Building Materials, 25, pp. 3131-3143, 2011. DOI: 10.1016/j.conbuildmat.2010.12.024

[21] Leiva, C., Solís-Guzmán, J., Marrero, M. and García-Arenas, C., Recycled blocks with improved sound and fire insulation containing construction and demolition waste. Waste Management, 33, pp. 663-671, 2013. DOI: 10.1016/j.wasman.2012.06.011

[22] Disfani, M.M., Arulrajah, A., Haghighi, H., Mohammadinia, A. and Horpibulsuk, S., Flexural beam fatigue strength evaluation of crushed brick as a supplementary material in cement stabilized recycled concrete aggregates. Construction and Building Materials, 68, pp. 667-676, 2014. DOI: 10.1016/j.conbuildmat.2014.07.007

[23] Gómez-Meijide, B., Pérez, I., Airey, G. and Thom, N., Stiffness of cold asphalt mixtures with recycled aggregates from construction and demolition waste. Construction and Building Materials, 77, pp. 168-178, 2015. DOI: 10.1016/j.conbuildmat.2014.12.045

[24] Gómez-Meijide, B. and Pérez, I., Effects of the use of construction and demolition waste aggregates in cold asphalt mixtures. Construction and Building Materials, 51, pp. 267-277, 2014. DOI: 10.1016/j.conbuildmat.2013.10.096

[25] de Brito, J., Ferreira, J., Pacheco, J., Soares, D. and Guerreiro, M., Structural, material, mechanical and durability properties and behaviour of recycled aggregates concrete. Journal of Building Engineering, 6, pp. 1-16, 2016. DOI: 10.1016/j.jobe.2016.02.003

[26] Jayasinghe, C., Fonseka, W.M.C.D.J. and Abeygunawardhene, Y.M., Load bearing properties of composite masonry constructed with recycled building demolition waste and cement stabilized rammed earth. Construction and Building Materials, 102, pp. 471-477, 2016. DOI: 10.1016/j.conbuildmat.2015.10.136

[27] Moussiopoulus, N.T., Papadopoulus, A.T., Iakovou, E.C., Achillas, H.C., Aidonis, D.T., Anastaselos, D.C. and Banias, G.C., Construction and demolition waste management: State of art trends, Proceedings of the 10th International Conference on Environmental Science and Tecnhnology, pp. A1009-A1016, 2007.

[28] Yu, R. and Shui, Z., Efficient reuse of the recycled construction waste cementitious materials. Journal of Cleaner Production, 78, pp. 202-207, 2014. DOI: 10.1016/j.jclepro.2014.05.003

[29] Galbenis, C.T. and Tsimas, S., Use of construction and demolition wastes as raw materials in cement clinker production. China Particuology, 4(2), pp. 83-85, 2006. DOI: 10.1016/S1672-2515(07)60241-3

[30] Corinaldesi, V., Mechanical and elastic behaviour of concretes made of recycled-concrete coarse aggregates. Construction and Building Materials, pp. 1616-120, 2010. DOI: 10.1016/j.conbuildmat.2010.02.031

[31] Li, X., Recycling and reuse of waste concrete in China: Part I. Material behaviour of recycled aggregate concrete. Resources, Conservation and Recycling, pp. 36-44, 2008. DOI: 10.1016/j.resconrec.2008.09.006

[32] Padmini, A.K., Ramamurthy, K. and Mathews, M.S., Influence of parent concrete on the properties of recycled aggregate concrete. Construction and Building Materials, pp. 829-836, 2009. DOI: 10.1016/j.conbuildmat.2008.03.006

[33] Xu, S., Wang, J., Ma, Q., Zhao, X. and Zhang, T., Study on the lightweight hydraulic mortars designed by the use of diatomite as partial replacement of natural hydraulic lime and masonry waste as aggregate. Construction and Building Materials, 73, pp. 33-40, 2014. DOI: 10.1016/j.conbuildmat.2014.09.062

[34] Silva, Y., Robayo, R., Matey, P. and Delvasto, S., Obtención de concretos autocompactantes empleando residuos de demolición. Revista latinoamericana de metalurgia y materiales, pp. 86-94, 2014.

[35] Poon, C.S. and Chan, D., Paving blocks made with recycled concrete aggregate and crushed clay brick. Construction and Building Materials, pp. 569-577, 2006. DOI: 10.1016/j.conbuildmat.2005.01.044

[36] Mueller, A., Schnell, A. and Ruebner, K., The manufacture of lightweight aggregates from recycled masonry rubble. Construction and Building Materials, 98, pp. 376-387, 2015. DOI: 10.1016/j.conbuildmat.2015.07.027

[37] Galbenis, C.T. and Tsimas, S., Use of construction and demolition wastes as raw materials in cement clinker production. China Particuology, 4(2), pp. 83-85, 2006. DOI: 10.1016/S1672-2515(07)60241-3

[38] Muñoz-Velasco, P., Morales-Ortíz, M.P., Mendívil-Giró, M.A. and Muñoz-Velasco, L., Fired clay bricks manufactured by adding wastes as sustainable construction material – A review. Construction and Building Materials, 63, pp. 97-107, 2014. DOI: 10.1016/j.conbuildmat.2014.03.045

[39] Hua, K., Shui, A., Xu, L., Zhao, K., Zhou, Q. and Xi, X., Fabrication and characterization of anorthite–mullite–corundum porous ceramics fromconstructionwaste. Ceramics International, 42, pp. 6080-6087, 2016. DOI: 10.1016/j.ceramint.2015.12.165

[40] Saiz-Martínez, P., González-Cortina, M., Fernández-Martínez, F. and Rodríguez-Sánchez, A., Comparative study of three types of fine recycled aggregates from construction and demolition waste (cdw), and their use in masonry mortar fabrication. Journal of Cleaner Production, 118, pp. 162-169, 2016. DOI: 10.1016/j.jclepro.2016.01.059

[41] Martínez, I., Etxeberria, M., Pavón, E. and Díaz, N., A comparative analysis of the properties of recycled and natural aggregate in masonry mortars. Construction and Building Materials, 49, pp. 384-392, 2013. DOI: 10.1016/j.conbuildmat.2013.08.049

[42] Suzuki, M., Sato, R. and Seddik-Meddah, M., Use of porous ceramicwaste aggregates for internal curing of high-performance concrete. Cement and Concrete Research, 39, pp. 373-381, 2009. DOI: 10.1016/j.cemconres.2009.01.007

[43] Medina, C., Sánchez-de Rojas, M. and Frías, M., Reuse of sanitary ceramic wastes as coarse aggregate in eco-efficient concretes. Cement & Concrete Composites, 34, pp. 48-54, 2012. DOI: 10.1016/j.cemconcomp.2011.08.015

[44] Venkatarama-Reddy, B.V. and Lokras, S.S., Steam-cured stabilised soil blocks for masonry construction. Energy and Buildings, 29, pp. 29-33, 1998. DOI: 10.1016/S0378-7788(98)00033-4

[45] Alam, I., Naseer, A. and Shah, A.A., Economical stabilization of clay for earth buildings construction in rainy and flood prone areas. Construction and Building Materials, 77, pp. 154-159, 2015. DOI: 10.1016/j.conbuildmat.2014.12.046

[46] Sekhar, D.C. and Nayak, S., Utilization of granulated blast furnace slag and cement in the manufacture of compressed stabilized earth blocks. Construction and Building Materials, 166, pp. 531-536, 2018.

[47] Lei, Z., Arild, G., Jelle, B.P., Liu, Y., Tao, G. and Yu, W., Thermal conductivity of cement stabilized earth blocks. Construction and Building Materials, 151, pp. 504-511, 2017. DOI: 10.1016/j.conbuildmat.2017.05.101
[48] Khedari, J., Watsanasathaporn, P. and Hirunlabh, J., Development of fibre-based soil–cement block with low thermal conductivity. Cement & Concrete Composites, 27, pp. 111-116, 2005.
[49] Voit, K. and Zimmermann, T., Characteristics of selected concrete with tunnel excavation material. Construction and Building Materials, 101, pp. 217-226, 2015. DOI: 10.1016/j.conbuildmat.2015.10.016
[50] Young-sang, K., Tan-Manh, D., Hyeong-ki, K. and Gyeongo, K., Utilization of excavated soil in coal ash-based controlled low strength material (CLSM). Construction and Building Materials, 124, pp. 598-605, 2016. DOI: 10.1016/j.conbuildmat.2016.07.053
[51] Magnusson, S., Lundberg, K., Svedberg, B. and Knutsson, S., Construction in urban areas implies use of construction materials from quarries and excavation of soil. Journal of Cleaner Production, 93, pp. 18-25, 2015. DOI: 10.1016/j.jclepro.2015.01.010
[52] Medina, C., Banfill, P.F.G., Sánchez-de Rojas, M.I. and Frías, M., Rheological and calorimetric behaviour of cements blended with containing ceramic sanitary ware and construction/demolition waste. Construction and Building Materials, 40, pp. 822-831, 2013. DOI: 10.1016/j.conbuildmat.2012.11.112
[53] Corinaldesi, V. and Moriconi, G., Behaviour of cementitious mortars containing different kinds of recycled aggregate. Construction and Building Materials, 23, pp. 289-294, 2009. DOI: 10.1016/j.conbuildmat.2007.12.006
[54] Soutsos, M.N., Tang, K. and Millard, S.G., Concrete building blocks made with recycled demolition aggregate. Construction and Building Materials, 25, pp. 726-735, 2011. DOI: 10.1016/j.conbuildmat.2010.07.014

L.M. Chica-Osorio, es profesora en Facultad de Ingeniería de la Universidad de Medellín, Colombia. PhD. en Ingeniería con énfasis en Ciencia y Tecnología de Materiales en 2014, de la Universidad Nacional de Colombia. Msc. En Ingeniería – Materiales y Procesos en 2009 e Ingeniera de Minas y Metalurgia, 2007. Integrante del grupo GICI.
ORCID: 0000-0001-8873-5017

J.M. Beltrán-Montoya, es Estudiante de Ingeniería Civil de la Universidad de Medellín, Colombia. Auxiliar de investigación con participación en proyectos relacionados con materiales de construcción.
ORCID: 0000-0001-9491-9867

UNIVERSIDAD NACIONAL DE COLOMBIA
SEDE MEDELLÍN
FACULTAD DE MINAS

Área Curricular de Ingeniería
Geológica e Ingeniería de Minas y Metalurgia

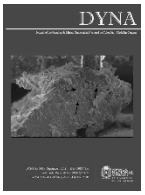
Oferta de Posgrados

Especialización en Materiales y Procesos
Maestría en Ingeniería - Materiales y Procesos
Maestría en Ingeniería - Recursos Minerales
Doctorado en Ingeniería - Ciencia y Tecnología de Materiales

Mayor información:

E-mail: acgeomin_med@unal.edu.co
Teléfono: (57-4) 425 53 68

UNIVERSIDAD NACIONAL DE COLOMBIA
SEDE MEDELLÍN
FACULTAD DE MINAS



DYNA
http://dyna.medellin.unal.edu.co/

Relationship between the particle size and the crystalline phases amount of an aluminum dross

Adriana Gómez-Gómez [a], Luz Elena Vinasco-Isaza [a], Nelson Batista de Lima [b] & Jorge Aberto Soares Tenório [c]

[a] *Departamento de Ingeniería Civil e Industrial, Pontificia Universidad Javeriana Cali, Cali, Colombia. adrianagomez@javerianacali.edu.co, levinasco@javerianacali.edu.co*
[b] *Departamento de Caracterización de Materiales, Instituto de Pesquisas Energéticas y Nucleares IPEN, Sao Paulo, Brasil. nblima@ipen.edu.co*
[c] *Departamento de Ingeniería Química, Universidad de Sao Paulo, Sao Paulo, Brasil. jtenorio@usp.br*

Received: August 15th, 2018. Received in revised form: September 06th, 2018. Accepted: September 18th, 2018.

Abstract
The Rietveld method was used in order to determine the amount of crystalline phases present in aluminum dross with particle size less than 3.35 mm. Initially, the dross was separated in four granulometric fractions by screening. Two samples of each granulometric size were obtained by means of quartering and homogenization. Each sample was grounded and subsequently analyzed by X-ray diffraction in order to identify and quantify the crystalline phases present in the dross. Metallic aluminum, aluminum oxide, spinel, defect spinel, diaoyudaoite and aluminum nitride were identified and then quantified by the Rietveld method. In order to observe the dependence of the particle size with the amount of each phase, statistical analyses was done by means of analyses of variance (ANOVA). The coefficient of determination R^2 was greater than 94% for all phases except for the $NaAl_{11}O_{17}$ phase. Thus, the amount of each crystalline phase is satisfactory explained by particle size.

Keywords: Rietveld method; characterization; aluminum dross; statistical analyses.

Relación entre el tamaño de partícula y el contenido de las fases cristalinas presentes en una escoria de aluminio

Resumen
En este trabajo se presenta la caracterización de una escoria de aluminio proveniente de la industria primaria, con tamaño de partícula inferior a 3.35 mm. Inicialmente el material fue separado en cuatro fracciones granulométricas las cuales fueron analizadas mediante difracción de rayos X con el fin de analizar la cantidad de cada una de las fases cristalinas presentes en la escoria. Se encontraron las siguientes fases: aluminio metálico, óxido de aluminio, espinelio, espinelio con defecto, diaoyudaoite y nitruro de aluminio. La dependencia del tamaño de partícula con la cantidad de cada una de las fases cristalinas fue analizada mediante un análisis de varianza (ANOVA) con un nivel de confianza del 99%. Del análisis estadístico se pudo concluir que la variación en el contenido encontrado de cada fase cristalina es explicada en un alto porcentaje por el tamaño de partícula.

Palabras clave: método de Rietveld; caracterización; escoria de aluminio; análisis estadístico.

1. Introducción

La escoria de aluminio es uno de los principales residuos que resultan del proceso de fusión de aluminio y se produce debido a la reacción química que ocurre entre el metal líquido y la atmósfera. En general este residuo representa más del 4% de la producción total de aluminio primario y 20% de la producción secundaria [1]. Aunque la composición exacta de la escoria de aluminio depende de la aleación que se está fundiendo y los parámetros del proceso, la escoria proveniente de la industria primaria está compuesta principalmente por aluminio en forma metálica, óxido de aluminio, nitruros y otros óxidos.

La escoria de aluminio se puede clasificar en tres tipos: escoria blanca, escoria negra y *saltcake* [2]. La escoria blanca proviene de la industria primaria, contiene grandes

How to cite: Gómez-Gómez, A., Vinasco, L.E., de Lima, N.B. and Tenório, J.A.S., Relación entre el tamaño de partícula y el contenido de las fases cristalinas presentes en una escoria de aluminio. DYNA, 85(206), pp. 348-354, September, 2018.

© The author; licensee Universidad Nacional de Colombia.

contenidos de aluminio y su color es claro, de ahí se deriva su nombre. La escoria negra se produce durante la producción secundaria de aluminio, es decir, por reciclaje en el que se utilizan flujos salinos los cuales oscurecen la escoria resultante. *Saltcake* resulta del reciclaje de escorias blancas y negras, y en este proceso también se utilizan sales que la hacen oscura, tiene menos cantidad de aluminio que los otros dos tipos de escorias.

A pesar de ser un residuo, la escoria de aluminio es considerada un material valioso principalmente por su alto contenido de aluminio metálico, el cual puede ser recuperado utilizando diferentes procesos [3-5]. Además, posee otros compuestos que la hacen apta para otras aplicaciones, como por ejemplo: fabricación de cemento de aluminato de calcio [6], obtención de materiales compuestos [7-8], fabricación de refractarios [9], refuerzo de materiales compuestos [10], y síntesis de diferentes compuestos [11-13].

Se ha considerado que debido a su estabilidad térmica hasta temperaturas de 1100 °C [14] tiene potencial para ser utilizada en almacenamiento de energía térmica. A pesar de todo esto, aún no se le ha encontrado un uso a la escoria a gran escala, lo cual es una preocupación ya que es descartada en rellenos sanitarios bajo condiciones especiales, esto acarrea costos para las empresas, y lo que es más preocupante un costo ambiental.

Los diversos usos de la escoria de aluminio muestran la importancia de su caracterización, ya que el primer paso para la reutilización de un material es saber su composición. Algunos trabajos muestran la caracterización química de este tipo de material [6,14], sin embargo, en estos casos se utiliza la técnica de fluorescencia de rayos X que en realidad solo detecta la presencia de los elementos presentes y no las fases cristalinas que se formaron durante el proceso de oxidación. La técnica de difracción de rayos X ha sido utilizada para identificar las fases cristalinas presentes en escorias de aluminio [4] y hasta para hacer análisis semicuantitativos [8].

El análisis cuantitativo de la escoria de aluminio es difícil debido a su heterogeneidad y a la gran cantidad de fases que la componen, sin embargo, la técnica de difracción de rayos X (DRX) es un método viable en este caso, pues permite no solo identificar las fases cristalinas presentes en un material, sino que también posibilita la cuantificación de las fases de una forma precisa [15].

La determinación de la relación entre el tamaño de partícula y la composición de la escoria es interesante con la finalidad de encontrar los posibles usos que se le podría dar, es decir, en términos de escoger el material con la composición más adecuada para una aplicación específica. Por ejemplo, la escoria con contenidos de Aluminio superiores al 20% se reprocesa para producción de aluminio secundario, sin embargo, si el contenido de aluminio es inferior se dificulta el reciclaje y es descartada. Por otro lado, la utilización de escoria con contenidos de aluminio de aproximadamente el 10%, que generalmente es el residuo del proceso de reciclaje, podría ser utilizada como una fuente de hidrógeno a partir del AlN [16] y para reducir las emisiones de CO_2 en la industria del acero [17]. Además, uno de los problemas de descartar la escoria de aluminio en rellenos es la generación amonia debido a la reacción del AlN con vapor de agua, por lo tanto, la cantidad de AlN debe ser lo suficientemente baja para poder descartarla en rellenos de manera segura [5].

Todo lo anterior muestra la importancia de conocer la composición de la escoria y su relación con el tamaño de partícula, sin embargo, poco trabajo ha sido realizado al respecto. Por ejemplo, Hiraki y Nagasaka (2015), encontraron el contenido de aluminio, nitruro de aluminio y cloro, para escorias con tamaño de partícula entre 20 y 800 µm.

El objetivo principal de este trabajo es determinar si hay una relación entre el tamaño de partícula y la cantidad de cada una de las fases cristalinas presentes en una escoria blanca de aluminio. Para el cálculo del porcentaje de cada una de las fases se utilizó la técnica de difracción de rayos X, específicamente el método de Rietveld [18]. Para determinar estadísticamente si la composición del material es influenciada por el tamaño de partícula, se realizó un análisis estadístico utilizando ANOVA.

2. Metodología

2.1. Caracterización del material

En este estudio se utilizó una escoria blanca proveniente de la producción primaria de aluminio, con tamaño de partícula inferior a 3.35 mm y una masa aproximada de 6 kg. Inicialmente, se realizó la separación granulométrica del material utilizando tamices con abertura de malla de 0.42, 0.85 y 1.68 mm. Se obtuvieron cuatro fracciones granulométricas: E1 (-0.42mm), E2 (+0.42mm, -0.85mm), E3 (+0.85mm, -1.68mm), E4 (+1.68mm, -3.35mm). De cada una estas fracciones se tomaron dos muestras representativas, de aproximadamente 10 g cada una. Los elementos químicos presentes en las muestras fueron determinados por microanálisis de rayos X (EDS) en un microscopio electrónico de barrido (SEM). Las fases cristalinas se identificaron utilizando los espectros de difracción de rayos X.

2.2. Método de Rietveld

Para el análisis cuantitativo con difracción de rayos X el tamaño de partícula fue reducido a un tamaño de 0.45 µm utilizando un molino de hierro de vibración excéntrica. Los ensayos de difracción se realizaron en un difractómetro Rigaku Multiflex operando a una potencia de 40 kV y 20 mA, geometría Bragg-Brentano θ/2θ, y radiación Cu kα. El barrido se hizo en el rango de 2θ desde 6 hasta 110°, a un paso de 0.02° y con un tiempo de barrido por paso de 8 s. Para determinar el porcentaje en peso de cada una de las fases se realizó un refinamiento de los espectros de difracción utilizando el método de Rietveld, utilizando el programa GSAS+EXPGUI [19-20]. La línea de base fue ajustada con la función analítica de Chebyschev, el perfil de los picos de difracción se ajustó utilizando una función Pseudo-Voigt modificada. Los factores refinados fueron: factor de escala individual, desplazamiento de la muestra, parámetros de red, factor de Gauss y factor de Lorentz del perfil de pico. El parámetro de asimetría se refinó únicamente para las fases que presentan picos a bajos ángulos. La orientación preferencial se corrigió utilizando la función de armónicos esféricos implementada en el programa. Finalmente se aplicó la función de Suortti para corregir rugosidad.

La calidad del refinamiento fue evaluada por el análisis de los factores R_E, R_{wp} y S (*goodness of fit*) que se definen a continuación [21]:

$$R_E = \left[\frac{N-P}{\sum w_i y_i^2}\right]^{1/2} \quad (1)$$

Donde N es el número de puntos medidos, P es el número de parámetros que se están refinando, y_i es la intensidad medida en el paso i, y $w_i = 1/y_i$.

R_E es el valor esperado de R_{wp} que se define como:

$$R_{wp} = \left\{\frac{\sum w_i(y_i - y_{ci})^2}{\sum w_i(y_{ci})^2}\right\} \quad (2)$$

Donde y_{ci} es la intensidad calculada en el paso i. Unos buenos resultados llevan a un valor de R_{wp} entre 2 y 10% [22]. Y finalmente,

$$S = \left[\frac{S_y}{N-P}\right]^{1/2} = \frac{R_{wp}}{R_E} \quad (3)$$

Donde:

$$S_y = \sum_i w_i(y_i - y_{ci})^2 \quad (4)$$

S_y se denomina residuo y es el valor mínimo de ajuste al realizar el refinamiento de los datos.

2.3. Análisis estadístico

Con el propósito de evaluar la precisión de los datos y determinar la variación en la composición del material con el tamaño de las partículas, se planteó un diseño experimental completamente al azar tomando como factor principal el tamaño de partícula con cuatro niveles, donde cada nivel es una fracción granulométrica (-0.42, +0.42 -0.85, +0.85 -1.68, +1.68 -0.35 mm). Como se explicó en la sección 2.1, de cada una de estas fracciones se analizaron dos muestras, teniendo como variables de respuesta cada una de las fases cristalinas encontradas en las muestras de escoria blanca de aluminio mediante al análisis de los espectros de difracción (Al, α-Al_2O_3, $MgAl_2O_4$, $Mg_{0.388}Al_{2.408}O_4$, $NaAl_{11}O_{17}$, AIN).

Los cálculos estadísticos se realizaron utilizando el paquete estadístico Minitab versión 15.0. Con el fin de observar la dependencia del tamaño de partícula sobre la cantidad encontrada en cada una de las fases cristalinas, se realizó un análisis de varianza (ANOVA) con un nivel de confianza del 99% y se validó el cumplimiento de los supuestos de normalidad, igualdad de varianzas y aleatoriedad e independencia de los errores, para cada una de las variables de respuesta evaluadas.

3. Resultados y discusión

3.1. Caracterización del material

En la distribución del tamaño de partículas de la escoria se obtuvieron los siguientes resultados: el 36.9% del material tiene un tamaño inferior a 0.42 mm (muestra E1), el 18.5% tiene un tamaño entre 0.42 mm y 0.85 mm (muestra E2), el 21.8% tiene un tamaño entre 0.85 mm y 1.68 mm (muestra E3), y el 22.8% tiene un tamaño entre 1.68 mm y 3.35 mm (muestra E4).

Los análisis de EDS mostraron que el material está compuesto principalmente de Al y en menor cantidad de O, Fe, Na, Mg, Si y K.

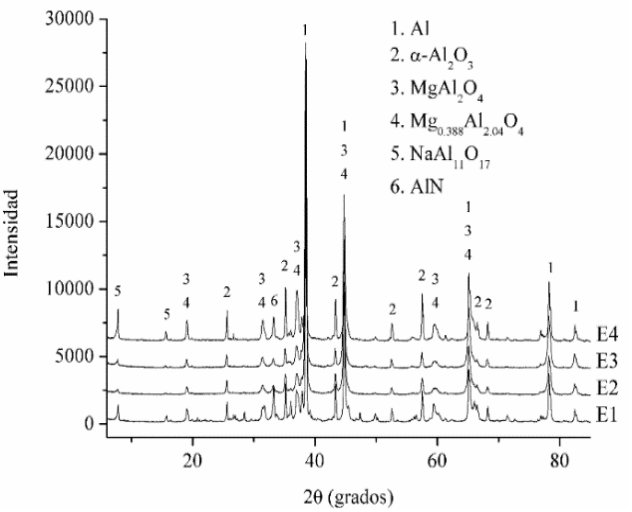


Figura 1. Identificación de las fases cristalinas de una escoria de aluminio. Fuente: Los autores

En la Fig. 1 se observa el difractograma de las muestras E1, E2, E3 y E4, donde se puede observar la presencia de las siguientes fases: aluminio metálico (Al), óxido de aluminio o corundo (α-Al_2O_3), espinelio ($MgAl_2O_4$), espinelio defectuoso ($Mg_{0.388}Al_{2.04}O_4$), diaoyudaoite ($NaAl_{11}O_{17}$) y nitruro de aluminio (AlN). Como se observa se identificaron la totalidad de los picos.

Las fases $MgAl_2O_4$ y $Mg_{0.388}Al_{2.04}O_4$ presentan picos en las mismas posiciones, sin embargo, al refinar las muestras solo con la fase $MgAl_2O_4$ no se obtenía un buen ajuste del patrón teórico al patrón experimental, este ajuste solo se obtuvo al refinar ambas fases al mismo tiempo. Las fases $NaAl_{11}O_{17}$, $Na_2O_{11}(Al_2O_3)$ y $K_{1.5}Al_{11}O_{17.25}$, denominadas alúminas-beta [23-25], también presentan picos en las mismas posiciones y con intensidades similares, por lo tanto, fue necesario hacer refinamientos con cada una de estas fases, al final los mejores ajustes se obtuvieron con la fase $NaAl_{11}O_{17}$.

3.2. Método de Rietveld

El método de Rietveld se aplicó en todas las muestras con el fin de determinar el porcentaje en masa de cada una de las fases cristalinas presentes. La calidad del refinamiento se verificó con los criterios numéricos y con la observación del ajuste, confirmando siempre que hubiera un buen ajuste de la curva teórica a los datos experimentales. En la Fig. 2 se puede observar el refinamiento de la muestra E1-1, en donde los puntos corresponden a los datos experimentales, la línea continua oscura es la curva ajustada con el método de Rietveld, y la curva clara corresponde a la diferencia entre los datos y el ajuste. Se puede observar en general un buen ajuste entre los datos y el modelo teórico, la calidad del ajuste fue muy similar en todas las muestras.

En la Tabla 1 se presentan los resultados de los refinamientos para cada par de muestras correspondientes a cada fracción granulométrica. Como se observa, en general cada par de muestras presenta porcentajes de composición muy similares, excepto para las muestras con porcentajes de composición inferiores al 5%.

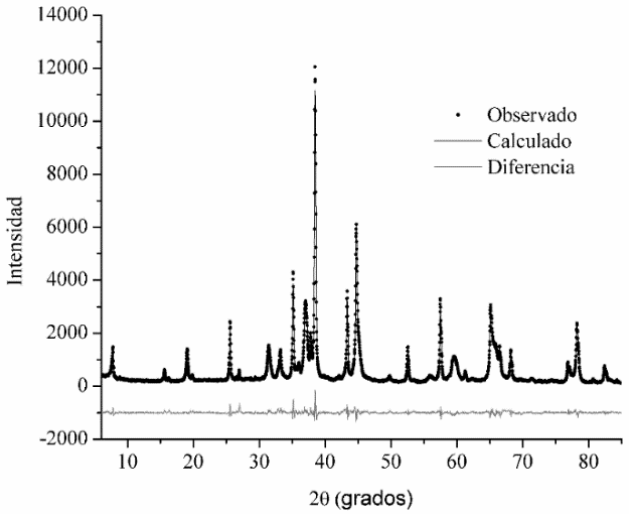


Figura 2. Resultado del refinamiento de la muestra E1-1.
Fuente: Los autores.

Tabla 1.
Resultados del refinamiento con el método de Rietveld de escorias de aluminio.

	E1-1	E1-2	E2-1
Al (wt%)	25.0 ± 0.2	24.2 ± 0.1	55.8 ± 0.1
α-Al_2O_3 (wt%)	28.7 ± 0.1	29.1 ± 0.1	17.0 ± 0.1
$MgAl_2O_4$ (wt%)	9.6 ± 0.2	10.6 ± 0.2	16.3 ± 0.2
$Mg_{0,388}Al_{2,408}O_4$ (wt%)	25.1 ± 0.21	24.6 ± 0.2	3.2 ± 0.2
$NaAl_{11}O_{17}$ (%)	4.93 ± 0.1	4.7 ± 0.1	3.0 ± 0.1
AlN (wt%)	6.6 ± 0.1	6.8 ± 0.1	4.7 ± 0.1
S	2.781	2.479	2.176
R_{wp} (%)	8.07	7.72	7.26
R_E (%)	4.84	4.9	4.92
	E2-2	**E3-1**	**E3-2**
Al (wt%)	55.5 ± 0.1	61.9 ± 0.1	63.5 ± 0.1
α-Al_2O_3 (wt%)	16.3 ± 0.1	12.4 ± 0.1	11.9 ± 0.1
$MgAl_2O_4$ (wt%)	14.9 ± 0.2	3.7 ± 0.2	3.6 ± 0.2
$Mg_{0,388}Al_{2,408}O_4$ (wt%)	6.4 ± 0.2	14.1 ± 0.2	13.8 ± 0.2
$NaAl_{11}O_{17}$ (%)	2.7 ± 0.1	2.5 ± 0.1	3.0 ± 0.1
AlN (wt%)	4.3 ± 0.1	5.5 ± 0.1	4.2 ± 0.1
S	2.203	2.325	2.475
R_{wp} (%)	7.39	7.37	7.59
R_E (%)	4.98	4.83	4.82

Fuente: Los autores

3.3. Análisis estadístico

A través del ANOVA se obtuvieron los siguientes coeficientes de determinación (R^2) para cada par de muestras: 99.93% para el Al, 99.9% para el α-Al_2O_3, 96.1% para $MgAl_2O_4$, 98.67% para $Mg_{0.388}Al_{2.04}O_4$, 72.19% para $NaAl_{11}O_{17}$ y AlN. Según estos resultados los R^2 estuvieron en su mayoría por encima del 94%, lo que indica que la variación en el contenido encontrado de cada fase cristalina es explicado en un alto porcentaje por el tamaño de partícula, la única excepción a este resultado se encontró en la fase $NaAl_{11}O_{17}$. Es interesante observar que esta fase es la única que presenta un contenido inferior al 5% en masa para todos los tamaños de partícula estudiados.

En la Fig. 3 se presentan los resultados de la variación de la composición, obtenido con el ANOVA, en función del tamaño de partícula para el Al y el α-Al_2O_3. Con las pruebas de comparación de medias para la fase cristalina de Aluminio, se comprobó con un nivel de confianza del 99% que existen diferencias significativas en la cantidad de Aluminio entre cada tamaño de partícula. También se observa que a medida que aumenta el tamaño de partícula, se incrementa significativamente el porcentaje de Aluminio, el mismo comportamiento fue observado por Hiraki & Nagasaka (2015), pero para escorias con tamaño de partícula mucho menor, 75 y 500 µm.

Para el material tamaño de partícula inferior a 0.42 mm se puede observar que el porcentaje de aluminio es muy bajo (24.635 ± 0.559) comparado con los tamaños de partícula mayores a 0.42 mm, los cuales presentaron cantidades de aluminio superiores al 55%.

Con base en las pruebas de comparación de medias para la fase cristalina de α-Al_2O_3, se comprobó con un nivel de confianza del 99% que existen diferencias significativas en el porcentaje de α-Al_2O_3 para cada uno de los tamaños de partícula. Además, a medida que aumenta el tamaño de partícula, disminuye el porcentaje de α-Al_2O_3.

Al contrario de lo ocurrido con el aluminio, se encontró que el material con un tamaño de partícula inferior a 0.42 mm presenta los valores más altos de α-Al_2O_3 (28.855% ± 0.276) en comparación con el material con tamaño de partícula superior a 0.42 mm donde el porcentaje de esta fase es inferior al 17%.

En la Fig. 4 se presentan los resultados de la variación de la composición, obtenido con el ANOVA, en función del tamaño de partícula para el $NaAl_{11}O_{17}$ y el AlN. En general se observa que la cantidad de ambas bases disminuye con el aumento del tamaño de partícula. Las pruebas de comparación de medias para la fase cristalina de $NaAl_{11}O_{17}$, con un nivel de confianza del 99%, mostraron diferencias significativas en el porcentaje de $NaAl_{11}O_{17}$ entre los diferentes tamaños de partícula, conformando dos grupos, como puede observarse en la Fig. 4.

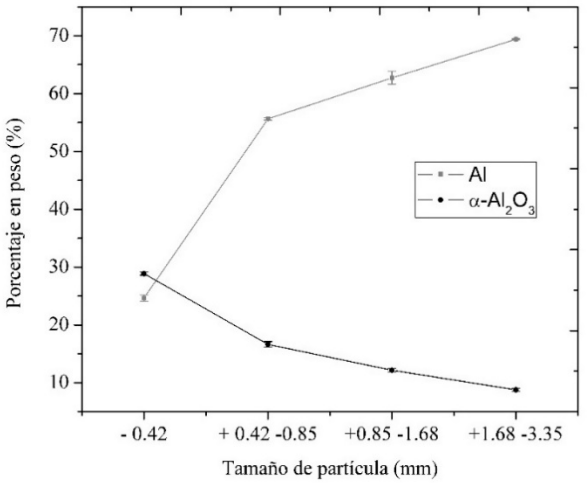


Figura 3. Cantidad de Al y α-Al_2O_3 en función del tamaño de partícula.
Fuente: Los autores

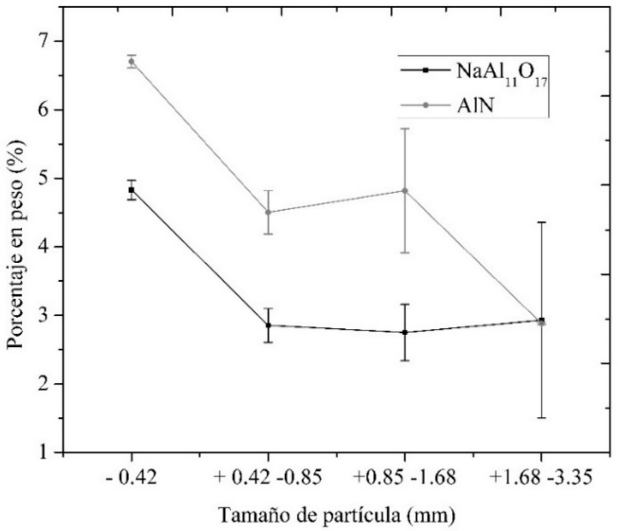


Figura 4. Cantidad de $NaAl_{11}O_{17}$ y AlN en función del tamaño de partícula.
Fuente: Los autores

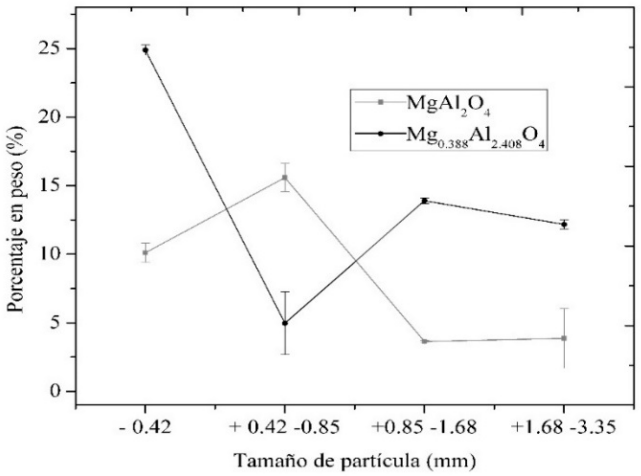


Figura 5. Cantidad de $MgAl_2O_4$, y $Mg_{0.388}Al_{2.408}O_4$ en función del tamaño de partícula.
Fuente: Los autores

El análisis realizado con el ANOVA muestra un alto error experimental sin embargo se evidencia diferencias significativas en el contenido de esta fase entre el tamaño de partícula 0.42 y los otros tamaños de partícula evaluados. Es importante anotar que para esta fase siempre se encontraron porcentajes inferiores al 5%.

Las pruebas de comparación de medias para la fase cristalina de AlN con un nivel de confianza del 99%, muestran que se forman tres grupos que son significativamente diferentes. El primer grupo consiste en el material con tamaño de partícula inferior a 0.42 mm, el segundo grupo conformado por los materiales con tamaño de partícula (+0.42 -0.85 y +0.85 -1.68) y el último grupo conformado por los materiales con tamaño de partícula (+1.68 -3.35), estos tres grupos presentan diferencias significativas en el porcentaje de AlN. El material con tamaño de partícula inferior a 0.42 mm presentó el mayor porcentaje de esta fase (6.705 % ± 0.092), en comparación con los tamaños de partícula superiores a 0.42 mm que presentaron un porcentaje por debajo del 6%. En general se observa que la cantidad de AlN disminuye al aumentar el tamaño de partícula, este mismo comportamiento también fue observado por Hiraky & Nagasaka (2015) para escorias de aluminio con tamaño de partícula entre 75 y 500 µm. Este material se forma debido a la reacción del aluminio fundido con el nitrógeno presente en la atmósfera.

En la Fig. 5 se pueden observar los resultados de la variación de la composición, obtenidos con el ANOVA, en función del tamaño de partícula para las fases $MgAl_2O_4$, y $Mg_{0.388}Al_{2.408}O_4$. Las pruebas de comparación de medias para la fase cristalina de $MgAl_2O_4$, con un nivel de confianza del 99%, muestran que se forman tres grupos que son significativamente diferentes en el porcentaje de $MgAl_2O_4$. Los dos primeros grupos lo conforman los tamaños de partícula -0.42 y +0.42 -0.85, el tercer grupo está conformado por los tamaños de partícula +0.85 -1.68 y +1.68 -3.35 pues estos dos últimos tamaños de partícula no presentan diferencias significativas en el porcentaje de $MgAl_2O_4$.

Para la fase cristalina $Mg_{0.388}Al_{2.408}O_4$, se observó con un nivel de confianza del 99% que se forman tres grupos que son significativamente diferentes en el porcentaje de esta fase. Los dos primeros grupos lo conforman los tamaños de partícula (-0.42 y +0.42 -0.85) y el tercer grupo está conformado por los tamaños de partícula (+0.85 -1.68 y +1.68 -3.35) pues estos dos últimos tamaños de partícula no presentan diferencias significativas en cuanto al porcentaje de $Mg_{0.388}Al_{2.408}O_4$.

Debido a que las fases $MgAl_2O_4$ y $Mg_{0.388}Al_{2.408}O_4$ son muy similares y presentan picos en posiciones muy próximas, el programa las puede confundir al momento de hacer el refinamiento, por lo tanto, se decidió analizar que ocurre al sumarlas. Se hizo nuevamente el análisis de varianza con la suma de estas fases con un nivel de confianza del 99% y se validó el cumplimiento de los supuestos de normalidad, igualdad de varianzas y aleatoriedad e independencia de los errores, y se obtuvo R^2 de 98.88%. La Fig. 6 muestra la cantidad de la suma de estas dos fases en función del tamaño de partícula.

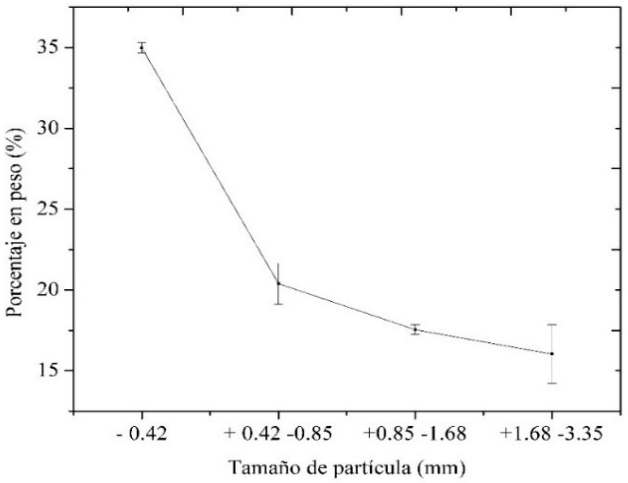


Figura 6. Cantidad de la suma $MgAl_2O_4$, y $Mg_{0.388}Al_{2.408}O_4$ en función del tamaño de partícula.
Fuente: Los autores

Al realizar las pruebas de comparación de medias para la suma de las fases cristalinas $MgAl_2O_4$ y $Mg_{0.388}Al_{2.408}O_4$, con un nivel de confianza del 99%, que se forman dos grupos que muestran diferencias significativas. El primer grupo conformado por el material con tamaño de partícula inferior a 0.42 mm y el segundo grupo conformado por el resto del material (+0.42 -0.85, +0.85 -1.68 y +1.68 -3.35), los materiales con estos tres tamaños de partícula no presentan diferencias significativas en el porcentaje de la suma de $MgAl_2O_4$ y $Mg_{0.388}Al_{2.408}O_4$.

Al sumar las dos fases, $MgAl_2O_4$ y $Mg_{0.388}Al_{2.408}O_4$ se observa en los resultados del ANOVA que el coeficiente de determinación aumentó a 98.88% lo que indica que al sumar estas dos fases se explica en mayor porcentaje la variabilidad de las fases en cada tamaño de partícula y tendrá mayor precisión reflejada en los intervalos de pronóstico más estrechos. Por otro lado, se observa en general una tendencia más clara, donde la cantidad de estas dos fases disminuye con el tamaño de partícula.

4. Conclusiones

En este trabajo se analizó una escoria de aluminio con tamaño de partícula inferior a 3.35 mm. Se encontró que este material está compuesto por Al metálico, α-Al_2O_3, $MgAl_2O_4$, AlN, $Mg_{0.388}Al_{2.04}O_4$ y $NaAl_{11}O_{17}$. El material fue separado por tamaño de partícula con el fin de determinar la influencia del tamaño de partícula en la composición del material.

Con respecto al análisis cuantitativo de las fases se pudo concluir que el contenido de aluminio presentó una tendencia a aumentar con el incremento del tamaño de partícula. Con tamaños de partícula superiores a 0.42 mm se observó que el porcentaje de aluminio es superior al 55%, llegando hasta 69.4%. Para las fases restantes se observó, en general, una tendencia contraria.

Del análisis estadístico se pudo concluir que los coeficientes de determinación estuvieron en su mayoría por encima del 94%, lo que indica que el contenido encontrado de cada fase cristalina es explicado en un alto porcentaje por el tamaño de partícula. La única excepción a este resultado se encontró para la fase $NaAl_{11}O_{17}$ donde se obtuvo un R^2 de 72.19%; es interesante observar que esta fase es la única que presenta un contenido inferior al 5% en masa para todos los tamaños de partícula estudiados.

Bibliografía

[1] Gutierrez, A., Miró, L., Gil, A., Rodríguez-Aseguinolaza, J., Barreneche, C., Calvet, N., et al., Advances in the valorization of waste and by-product materials as thermal energy storage (TES) materials. Renewable and Sustainable Energy Reviews, 59, pp. 763-783, 2016. DOI: 10.1016/j.rser.2015.12.071.

[2] Kulik, G.J. and Daley, J.C., Aluminum dross processing in the 90´s, Proceedings of the International symposium of recycling of metals and enginnering materials, pp. 427-437, 1990.

[3] David, E. and Kopac, J., Aluminum recovery as a product with high added value using aluminum hazardous waste. Journal of Hazardous Materials, 261, pp. 316-324, 2013. DOI: 10.1016/j.jhazmat.2013.07.042.

[4] Tsakiridis, P., Oustadakis, P. and Agatzini-Leonardou, S., Aluminum recovery during black dross hydrothermal treatment. Journal of Enviromental Chemical Engineering, 1(1-2), pp. 23-32, 2013. DOI: 10.1016/j.jece.2013.03.004.

[5] Hiraki, T. and Nagasaka, T., An easier upgrading process of aluminum dross residue by screening technique. Journal of Materials Cycles Waste Management, 17(3), pp. 566-573, 2015. DOI: 10.1007/s10163-014-0283-5.

[6] Ewais, E.M., Khalil, N.M., Amin, M.S., Ahmed, Y.M. and Barakat, M.A., Utilization of aluminum sludge and aluminum slag (dross) for the manufacture of calcium aluminate cement. Ceramics International, 35(8), pp. 3381-3388, 2009. DOI: 10.1016/j.ceramint.2009.06.008.

[7] Ibarra-Castro, M.N., Almanza-Robles, J.M., Cortés Hernández, D.A., Escobedo-Bocardo, J.C. and Torres-Torres, J., Development of mullite/zirconia composites from a mixture of aluminum dross and zircon. Ceramics International, 35(2), pp. 921-924, 2008. DOI: 10.*1016/j.ceramint*.2008.03.006.

[8] Huang, J., Fang, M., Huang, Z., Liu, Y., Yang, J., Huang, S., et al., Preparation, microstructure, and mechanical properties of Spinel-Corundum-Sialon composite materials from waste fly ash and aluminum dross. Advances in Materials Science and Engineering, 2014, pp. 1-10, 2014. DOI: 10.1155/2014/789867.

[9] Yoshimura, H., Abreu, A.P., Molisani, A., Portela, J. and Narita, N., Evaluation of aluminum dross waste as raw material for refractories. Ceramics international, 34(3), pp. 581-591, 2008. DOI: 10.1016/j.ceramint.2006.12.007.

[10] Kevorkijan, V.M., The quality of aluminum dross particles and cost-effective reinforcement for structural aluminum-based composites. Composites Science and Technology, 59(11), pp. 1745-1751, 1999. DOI: 10.1016/S0266-3538(99)00034-2.

[11] Hashishin, T., Kodera, Y., Yamamoto, T., Onhanagi, M. and Zuhair, A.M., Synthesis of $(Mg,Si)Al_2O_4$ Spinel from aluminum dross. Journal of the American Ceramic Society, 87(3), pp. 496-499, 2004. DOI: 10.1111/j.1551-2916.2004.00496.x.

[12] Kim, J., Biswas, K., John, K., Jeong, S. and Ahn, W., Synthesis of AlPO4-5 and CrAPO-5 using aluminum dross. Journal of Hazardous Materials, 169(1-3), pp. 919-925, 2009. DOI: 10.1016/j.jhazmat.2009.04.035.

[13] Murayama, N., Arimura, K., Okajima, N. and Shibata, J., Effect of structure-directing agent on AlPO4-n synthesis from aluminum dross. International Journal of Mineral Processing, 93(2), pp. 110-114, 2009. DOI: 10.1016/j.minpro.2009.07.002.

[14] Al-Naimi, K.M., Delclos, T. and Calvet, N., Industrial waste produced in the UAE, valuable high-temperature materials for thermal energy storage applications. Energy Procedia, 75, pp. 2087-2092, 2015. DOI: 10.1016/j.egypro.2015.07.320.

[15] Gómez-Gómez, A., Soares-Tenorio, J.A. and Batista-Lima, N., Quantitative analysis of aluminum dross by the Rietveld method. Materials Transactions, 49(4), pp. 728-732, 2008. DOI: 10.2320/matertrans.MRA2007129.

[16] Hiraki, T., Takeuchi, M., Hisa, M. and Akiyama, T., Hydrogen production from waste aluminum at different temperatures, with LCA. Materials Transactions, 46(5), pp. 1052-1057, 2005. DOI: 10.2320/matertrans.46.1052.

[17] Nakajima, K., Osuga, H., Yokoyama, K. and Nagasaka, T., Material flow analysis of Aluminum Dross and enviromental assessment for its recycling process. Materials Transactions, 48(8), pp. 2219-2224, 2007. DOI: 10.2320/matertrans.MRA2007070.

[18] Rietveld, H., A profile refinement method for nuclear and magnetics structures. Journal of Applied Crystallography, 2, pp. 65-71, 1969. DOI: 10.1107/S0021889869006558.

[19] Larson, A.C. and Von-Dreele, R.B., General structure analysis system (GSAS). Los Alamos National Laboratory Report LAUR, 1994.

[20] Toby, B.H., EXPGUI, a graphical user inteface for GSAS. Journal of Applied Crystallography, 34, pp. 210-213, 2001. DOI: 10.1107/S0021889801002242.

[21] Young, R., The Rietveld method. (R. Young, Ed.). New York: Oxford University Press, 1995.

[22] Bish, D. and Post, J., Reviews in mineralogy, v20: Modern Powder diffraction. Washington: The mineralogical society of America, 1989.

[23] Ferret, F.R., Roy, D. and Boulanger, C., Determination of alpha and beta alumina in ceramic alumina by X-Ray diffraction. Spectrochimica Acta Part B, 55(7), pp. 1051-1061, 2000. DOI: 10.1016/S0584-8547(00)00225-1.

[24] Massarotti, V., Camparivigano, G., Flor, G., Marini, A., Farrington, G.C. and Villa, M., X-ray powder diffraction of beta-aluminas. Jornal

of Applied Crystallography, 15, pp. 471-475, 1982. DOI: 10.1107/S0021889882012448.

[25] Kutty, T.R., Jayaraman, V. and Periaswami, G., Preparation of proton–β/β″-aluminas by the ion-exchange under hydrothermal conditions and their characterisation. Solid State Ionics, 128(1-4), pp. 161-175, 2000. DOI: 10.1016/S0167-2738(99)00341-0.

A. Gómez-Gómez, se graduó como Ing. Mecánica de la Universidad Nacional de Colombia en 2000 y Dra. en Ingeniería Metalúrgica de la Universidad de Sao Paulo, Brasil en 2006. PhD. en Ingeniería Mecánica de la Universidad de Sao Paulo, Brasil en 2010. Entre el 2006 y el 2010 trabajó como investigadora en el Laboratorio de Fenómenos de Superficies – LFS de la Universidad de Sao Paulo, Brasil. Actualmente es profesora asociada en la Pontificia Universidad Javeriana de Cali. Tiene experiencia en el área de Ingeniería de Materiales e Ingeniería Mecánica, trabajando en las siguientes áreas: caracterización de materiales, difracción de rayos x y esfuerzos residuales en películas delgadas.
ORCID: 0000-0002-3106-1397

L.E. Vinasco-Isaza, se graduó como Estadística de la Universidad del Valle en 1991, hizo MSc. en Ciencias en la Universidad Nacional de Colombia en 1998. Esp. en Creación de ambientes virtuales de aprendizaje–Argentina, en 2010. Esp. en Técnicas Avanzadas de Estadística Aplicada – España en 2011. Tiene experiencia docente en la Universidad del Valle, la Universidad ICESI y actualmente está vinculada como profesora asociada tiempo completo en el Departamento de Ingeniería Civil e Industrial de la Pontificia Universidad Javeriana, Cali, Colombia. Recibió la Certificación Internacional en Six Sigma Black Belt (IASSC) en 2015 y fue gestora de la Especialización en Ingeniería de la Calidad PUJ – Cali (2009), es consultora estadística a nivel empresarial en el área de calidad y productividad.
ORCID: 0000-0002-7631-2452

J.A.S. Tenório, es Ing. Metalúrgico de la Universidad de Sao Paulo, Brasil en 1984, tiene MSc. y Dr. en Ingeniería Metalúrgica de la Universidad de Sao Paulo, Brasil en 1988, 1992 respectivamente. Es profesor titular del Departamento de Ingeniería Química de la Universidad de Sao Paulo, Brasil. Se desempeña en las áreas de reciclaje, tratamiento de residuos sólidos y metalurgia extractiva. Fue presidente del Instituto de Ciencia y Tecnología en Residuos y Desarrollo Sostenible-ICTR entre el 2008 y el 2011. Fue editor de la Revista Brasileña de Ciencias Ambientales del ICTR entre el 2007 y el 2014 y de la Sección Metalurgia y Materiales de la Revista Escuela de Minas. Fue director del departamento de Ingeniería Metalúrgica y de Materiales de la Escuela Politécnica de la Universidad de Sao Paulo entre el 2010 y el 2014.
ORCID: 0000-0002-7849-7470

N.B. de Lima, se graduó como Físico en la Universidad de Sao Paulo, Brasil en 1979, hizo MSc. y Dr. en Tecnología Nuclear en la Universidad de Sao Paulo, Brasil en 1982 y 1991 respectivamente. Actualmente ocupa el cargo de Tecnólogo Senior III en la Comisión Nacional de Energía Nuclear de Brasil. Tiene experiencia en el área de ingeniería de materiales y metalúrgica con énfasis en estructura de los metales y aleaciones, trabajando principalmente en los siguientes temas: difracción de rayos X y textura.
ORCID: 0000-0002-6444-9224

UNIVERSIDAD NACIONAL DE COLOMBIA
SEDE MEDELLÍN
FACULTAD DE MINAS

Área Curricular de Ingeniería
Geológica e Ingeniería de Minas y Metalurgia

Oferta de Posgrados

Especialización en Materiales y Procesos
Maestría en Ingeniería - Materiales y Procesos
Maestría en Ingeniería - Recursos Minerales
Doctorado en Ingeniería - Ciencia y Tecnología de Materiales

Mayor información:

E-mail: acgeomin_med@unal.edu.co
Teléfono: (57-4) 425 53 68

Entregando
lo mejor de los
colombianos

Línea de atención al Cliente Nacional: **01 8000 111 210**
Línea de atención al Cliente Bogotá: **(57-1) 472 2000**
www.4-72.com.co

DYNA
85 (206), September, 2018
is an edition consisting of 100 printed issues
which was finished printing in the month of March of 2018
in Todograficas Ltda. Medellín - Colombia

The cover was printed on Propalcote C1S 250 g,
the interior pages on Propal Beige 90 g.
The fonts used are Times New Roman, Imprint MT Shadow

- Electrochemical analysis of the degradation of nitrided zirconia 3Y-TZP
- Dynamic adjustment of a MLFQ flow scheduler to improve cloud applications performance
- Use of BOF slag and blast furnace dust in asphalt concrete: an alternative for the construction of pavements"
- Impact on the direct costs of social interest and priority interest housing by including new construction standards: Cali case
- The use of GS1 standards to improve the drugs traceability system in a 3PL Logistic Service Provider
- Development of a parametric cable driven planar robot
- Effect of fly ash and silica fume on rheology, compressive strength and self-compacting in cement mixtures
- Using a non-reducing sugar in the green synthesis of gold and silver nanoparticles by the chemical reduction method
- Levelized avoided cost of electricity model based on power system operation
- Heavy metal contribution by runoff in a high-altitude megacity: a method based on the road-deposited sediment characterization
- Design, development, and implementation of an assistive technology device for shoulder telerehabilitation via the Internet
- Productive process improvement to elaborate cane train baskets, using Coloured Petri nets
- Active geodetic network: application in topography
- Application of OpenFoam solver SettlingFoam to bedload sediment transport analysis
- Encapsulation of β-carotene extracted from peach palm residues: A stability study using two spray-dried processes
- Synergistic effects in anaerobic codigestion of chicken manure with industrial wastes
- Palladium nanoparticles from a surfactant-modified hydroxysalt exchanged with tetrachloropalladate
- Morphological and nanomechanical characterization of Guadua Angustifolia kunth fiber by means of SEM and AFM
- Kinetic parameters of lactic acid bacterial isolated from fermented milk “Suero Costeño”
- Soft Pre-stressed PET Profiles as reinforcing fibers in structural elements made of concrete
- Entropy and negentropy of private electric vehicles in urban systems: homeostasis of mobility in Mexico
- Structural, thermal, rheological, morphological and mechanical properties of thermoplastic starch obtained by using hyperbranched polyester polyol as plasticizing agent
- An evaluation of the controlled release of ammoniacal nitrogen from residual cellulose/polyvinyl alcohol hydrogels as an alternative to traditional fertilization processes
- Design of metacognitive expectations of cognitive functions through ontological representations
- Simulation-optimization techniques for closed-loop supply chain design with multiple objectives
- Site characterization of a tropical soil by in situ tests
- Sugarcane molasses and vinasse as a substrate for polyhydroxyalkanoates (PHA) production
- Evaluation of water use in food SMEs: Case study of a poultry processing plant in Colombia
- Nutrient losses due to water erosion using simulated rainfall in southern Brazil
- Teratogenic effect on bone tissue development in Rattus norvegicus Wistar strain, induced by the presence of arsenic
- Design and Calculation of a Hybrid Solar-Hydraulic Power Station in Gran Canaria
- Electrocoagulation of indigo carmine dye solution with magnesium and AZ31 alloy anodes
- Integrating SOA and MAS in intelligent environments
- A planning algorithm in a class of discrete event systems
- Agronomic and environmental benefits of nitrogen fertilizers sources in Ocimum basilicum L
- Risk assessment in water treatment processes for the development of a Water Safety Plan – WSP
- Design of a serious emerging games engine based on the optimization algorithm of ant colony
- Palladium nanoparticles from a surfactant-modified hydroxysalt exchanged with tetrachloropalladate
- Estimación del retroceso glaciar en los volcanes Nevado del Ruiz, Tolima y Santa Isabel, Colombia a través de imágenes ópticas y Din-SAR
- Caracterización de residuos de demolición y construcción para la identificación de su potencial de reúso
- Relationship between the particle size and the crystalline phases amount of an aluminum dross

- Análisis electroquímico de la degradación de circonia 3Y-TZP nitrurada
- Ajuste dinámico de un programador de flujos MLFQ para mejorar el desempeño de aplicaciones en la nube
- Uso de escoria BOF y polvo de alto horno en concretos asfálticos: una alternativa para la construcción de pavimentos
- Impacto en costos directos de vivienda de interés social y de interés prioritario por inclusión de nuevas normas de construcción: caso Cali
- Uso de los estándares GS1 para la mejora del sistema de trazabilidad de medicamentos en un operador logístico 3PL
- Desarrollo de un robot cartesiano parametrizable comandado por cables
- Efecto de las cenizas volantes y el humo de sílice sobre la reología, resistencia a la compresión y autocompactación en mezclas de cemento
- Uso de una azúcar no reductora en la síntesis verde de nanopartículas de oro y plata por medio de reducción química
- Modelo de costo evitado nivelado de electricidad basado en la operación del sistema de potencia
- Contribución de metales pesados por escorrentía en una megaciudad de elevada altitud: un método basado en la caracterización del sedimento vial
- Diseño, desarrollo e implementación de una ayuda tecnológica para rehabilitación de hombro tele-operada vía Internet
- Mejora del proceso productivo para elaborar canastas para trenes cañeros, utilizando redes de Petri coloreadas
- Red geodésica activa: aplicación en topografía
- Aplicación del solucionador SettlingFoam de OpenFoam para el análisis del transporte de sedimento de carga de lecho
- Encapsulación de β-caroteno extraído a partir de residuos de chontaduro: Un estudio de estabilidad usando dos procesos de secado por atomización
- Efectos sinérgicos en la codigestión anaerobia de gallinaza y residuos industriales
- Nanopartículas de paladio a partir de una hidroxisal modificada con surfactante intercambiada con tetracloropaladato
- Caracterización morfológica y nanomecánica de la fibra de Guadua Angustifolia kunth mediante SEM y AFM
- Parámetros cinéticos de bacterias ácido-lácticas aisladas de la leche fermentada “Suero Costeño”
- Perfiles de PET ligeramente pretensados como fibras de refuerzo en elementos estructurales de concreto
- Entropía y negentropía del vehículo eléctrico particular en sistemas urbanos: homeostasis de la movilidad en México
- Propiedades térmicas, reológicas, morfológicas y mecánicas de almidón termoplástico obtenido usando un poliéster poliol altamente ramificado como agente plastificante
- Evaluación de la liberación controlada de nitrógeno amoniacal a partir de un hidrogel de celulosa residual/polivinil alcohol como una alternativa a los procesos de fertización tradicionales
- Diseño de expectativas metacognitivas de funciones cognitivas a través de representaciones ontológicas
- Técnicas de simulación-optimización para el diseño de cadenas de abastecimiento de ciclo cerrado con múltiples objetivos
- Caracterización de un suelo tropical por medio de ensayos in-situ
- Melazas y vinaza de la caña de azúcar como sustrato para la producción de polihidroxialcanoatos (PHA)
- Evaluación del uso del agua en PYMES de alimentos: Caso de estudio en una Planta de Beneficio Avícola en Colombia
- Pérdidas de nutrientes debido a la erosión hídrica con la lluvia simulada en el sur de Brasil
- Efecto teratogénico sobre el desarrollo del tejido óseo en la cepa Wistar de Rattus norvegicus, inducida por la presencia de arsénico
- Diseño y Cálculo de una Central Hibrida Solar-Hidráulica en Gran Canaria
- Electrocoagulación de soluciones de índigo carmín empleando ánodos de magnesio y de aleación AZ31
- Integración SOA-MAS en ambientes inteligentes
- Un algoritmo de planificación en una clase de sistemas de eventos discretos
- Beneficios agronómicos y ambientales de fuentes de fertilizantes nitrogenados en Ocimum basilicum L
- Evaluación del riesgo en procesos de tratamiento de agua para el desarrollo de un Plan de Seguridad del Agua – PSA
- Diseño de un motor de juegos serios emergentes basado en el algoritmo de optimización de colonia de hormigas
- Herramienta de software para determinar constantes ópticas en celdas solares tipo película delgada
- Determination of Glacier retreat at Nevado del Ruiz, Santa Isabel and Tolima Volcanoes, Colombia through optical image and Din-SAR
- Demolition and construction waste characterization for potential reuse identification
- Relación entre el tamaño de partícula y el contenido de las fases cristalinas presentes en una escoria de aluminio

DYNA
Publication admitted to the
Sistema Nacional de Indexación y Homologación de
Revistas Especializadas CT+I - PUBLINDEX, Category A1

Red Colombiana de Revistas de Ingeniería

UNIVERSIDAD NACIONAL DE COLOMBIA
SEDE MEDELLÍN
FACULTAD DE MINAS